Copyright 2019. De Gruyter. All rights reserved. May not be reproduced in any form without permission from the publisher, except fair uses permitted under U.S. or applicable copyright law.

DE GRUYTER

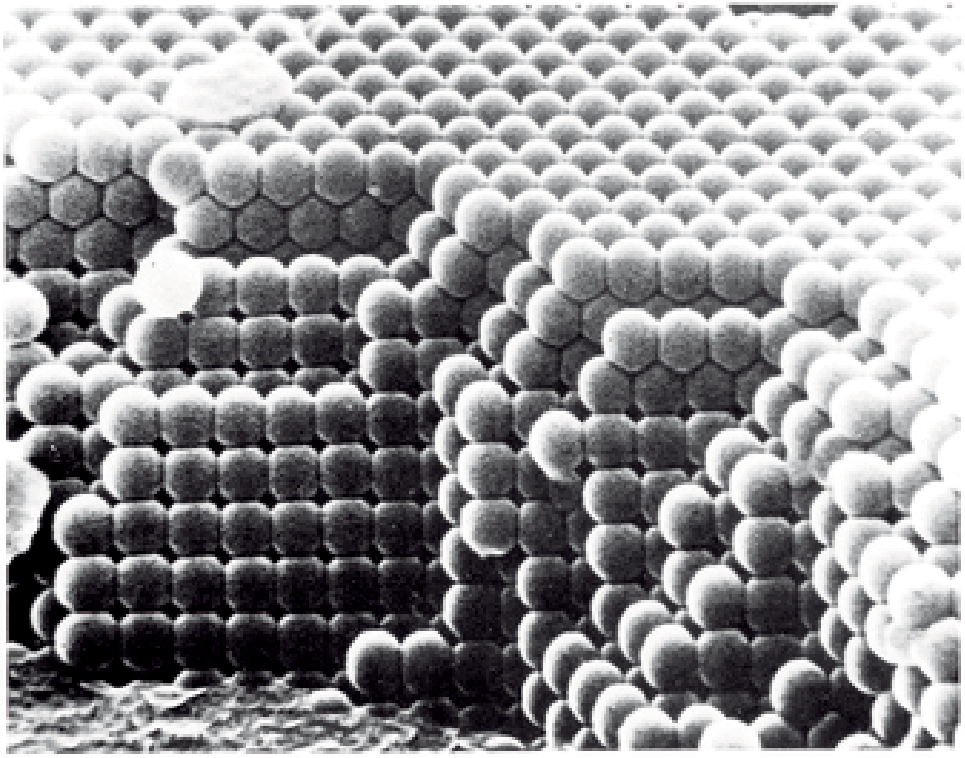


REVIEWS in
MINERALOGY
Volume 29

SILICA

PHYSICAL BEHAVIOR, GEOCHEMISTRY AND MATERIALS APPLICATIONS

P.J. Heaney, C.T. Prewitt
& G.V. Gibbs, *Editors*



Series Editor: Paul H. Ribbe
MINERALOGICAL SOCIETY OF AMERICA

EBSCO Publishing : eBook Collection (EBSCOhost) - printed on 2/13/2023 4:48 AM via
AN: 1[illegible]70 ; Peter J. Heaney, Charles T. Prewitt, Gerald V. Gibbs.; Silica : Physical Behavior, Geochemistry, and Materials Applications
Acco[illegible]ns335141

REVIEWS in MINERALOGY Volume 29

SILICA

PHYSICAL BEHAVIOR, GEOCHEMISTRY AND MATERIALS APPLICATIONS

Editors:

P.J. Heaney
Princeton University

C.T. Prewitt
Carnegie Institution of Washington, Geophysical Laborator

G.V. Gibbs
Virginia Polytechnic Institute & State University

Cover: Scanning electron micrograph of amorphous silica spheres closest packed in an Australian fire opal showing red interference colors. Sphere size is ~2500 Ångströms. Photo courtesy of Hans-Ude Nissen.

Series Editor: **Paul H. Ribbe**
Department of Geological Sciences
Virginia Polytechnic Institute & State University
Blacksburg, Virginia 24061 USA

MINERALOGICAL SOCIETY OF AMERICA
WASHINGTON, D.C.

EBSCOhost - printed on 2/13/2023 4:48 AM via . All use subject to https://www.ebsco.com/terms-of-use

COPYRIGHT 1994
MINERALOGICAL SOCIETY OF AMERICA
Printed by BookCrafters, Inc., Chelsea, Michigan.

REVIEWS IN MINERALOGY

(Formerly: SHORT COURSE NOTES)
ISSN 0275-0279

Volume 29: *SILICA: Physical Behavior, Geochemistry, and Materials Applications*

ISBN 0-939950-35-9

ADDITIONAL COPIES of this volume as well as those listed below may be obtained at moderate cost from the MINERALOGICAL SOCIETY OF AMERICA, 1130 Seventeenth Street, N.W., Suite 330, Washington, D.C. 20036 U.S.A.

Vol.	Year	Pages	Editor(s)	Title
1,3,4,5,6	*out*	*of*	*print*	
2	1983	362	P.H. Ribbe	FELDSPAR MINERALOGY (2nd edition)
7	1980	525	C.T. Prewitt	PYROXENES
8	1981	398	A.C. Lasaga R.J. Kirkpatrick	KINETICS OF GEOCHEMICAL PROCESSES
9A	1981	372	D.R. Veblen	AMPHIBOLES AND OTHER HYDROUS PYRIBOLES—MINERALOGY
9B	1982	390	D.R. Veblen, P.H. Ribbe	AMPHIBOLES: PETROLOGY AND EXPERIMENTAL PHASE RELATIONS
10	1982	397	J.M. Ferry	CHARACTERIZATION OF METAMORPHISM THROUGH MINERAL EQUILIBRIA
11	1983	394	R.J. Reeder	CARBONATES: MINERALOGY AND CHEMISTRY
12	1983	644	E. Roedder	FLUID INCLUSIONS (Monograph)
13	1984	584	S.W. Bailey	MICAS
14	1985	428	S.W. Kieffer A. Navrotsky	MICROSCOPIC TO MACROSCOPIC: ATOMIC ENVIRONMENTS TO MINERAL THERMODYNAMICS
15	1990	406	M.B. Boisen, Jr. G.V. Gibbs	MATHEMATICAL CRYSTALLOGRAPHY (Revised)
16	1986	570	J.W. Valley H.P. Taylor, Jr. J.R. O'Neil	STABLE ISOTOPES IN HIGH TEMPERATURE GEOLOGICAL PROCESSES
17	1987	500	H.P. Eugster I.S.E. Carmichael	THERMODYNAMIC MODELLING OF GEOLOGICAL MATERIALS: MINERALS, FLUIDS, MELTS
18	1988	698	F.C. Hawthorne	SPECTROSCOPIC METHODS IN MINERALOGY AND GEOLOGY
19	1988	698	S.W. Bailey	HYDROUS PHYLLOSILICATES (EXCLUSIVE OF MICAS)
20	1989	369	D.L. Bish, J.E. Post	MODERN POWDER DIFFRACTION
21	1989	348	B.R. Lipin, G.A. McKay	GEOCHEMISTRY AND MINERALOGY OF RARE EARTH ELEMENTS
22	1990	406	D.M. Kerrick	THE Al_2SiO_5 POLYMORPHS (Monograph)
23	1990	603	M.F. Hochella, Jr. A.F. White	MINERAL-WATER INTERFACE GEOCHEMISTRY
24	1990	314	J. Nicholls J.K. Russell	MODERN METHODS OF IGNEOUS PETROLOGY—UNDERSTANDING MAGMATIC PROCESSES
25	1991	509	D.H. Lindsley	OXIDE MINERALS: PETROLOGIC AND MAGNETIC SIGNIFICANCE
26	1991	847	D.M. Kerrick	CONTACT METAMORPHISM
27	1992	508	P.R. Buseck	MINERALS AND REACTIONS AT THE ATOMIC SCALE: TRANSMISSION ELECTRON MICROSCOPY
28	1993	584	G.D. Guthrie B.T. Mossman	HEALTH EFFECTS OF MINERAL DUSTS

EBSCOhost - printed on 2/13/2023 4:48 AM via . All use subject to https://www.ebsco.com/terms-of-use

FOREWORD

The Mineralogical Society of America has been sponsoring short courses in conjunction with their annual meetings with the Geological Society of America since 1974, and this volume represents the proceedings of the twenty-first in the sequence. Peter J. Heaney of Princeton University served as the primary scientific editor of this long-awaited volume on the silica polymorphs, with help from co-organizers Charlie Prewitt (Geophysical Laboratory) and Jerry Gibbs (Virginia Tech). As series editor of *Reviews in Mineralogy,* I thank Peter and the many authors for their heroic efforts to maintain the high quality of publication we have come to expect in the *Reviews* volumes. For the first time, a volume of *RiM* was handled almost exclusively between editors and authors by e-mail: it was free, fast, and efficient, saving uncounted numbers of hours of pain in the editorial office.

I am particularly grateful to Brett Macey for many hours of skilled work in assembling camera-ready copy for Volume 29. Margie Sentelle, who has contributed her secretarial skills to at least seventeen *RiM* volumes, continued her excellent work on this one.

Paul H. Ribbe
Series Editor
Blacksburg, VA
September 1, 1994

PREFACE AND ACKNOWLEDGMENTS

Oxygen and silicon are the two most common elements in the earth's crust, together constituting an estimated 74.32 weight % and 83.77 atom % of crustal rocks (Mason and Moore, 1982). Thus, it is not surprising that SiO_2, or silica, is the most abundant oxide on the earth's surface. In his widely cited survey, Clarke (1904) calculated that quartz alone comprises 12.0% of the crust by volume, ranking behind the mineral *groups* that include feldspar (59.5%) and amphibole/pyroxene (16.8%). Consequently, research into the silica system is motivated foremost by the prevalence of silica in man's immediate environment. The ubiquity of silica in igneous, metamorphic, and sedimentary rocks has led earth scientists to seek its uses as an indicator of large-scale geological processes, ranging from mountain-building to meteorite impacts. In industry, quartz has long played a prosaic but essential role as an inexpensive and relatively inert constituent of concrete aggregates, and modern electronics technology still relies on quartz oscillators. Silica phases also have played a prominent role in our understanding of the solid state. Physicists first discovered optical activity in crystals and the existence of soft modes during their investigations of quartz.

Many scientists have written substantial reviews documenting the importance of silica in the earth, materials, and physical sciences. Notable among these are Robert Sosman, who followed his *Properties of Silica* (1927) with *The Phases of Silica* (1965), and Clifford Frondel, who devoted the third volume of Dana's *System of Mineralogy* (1962) exclusively to the silica minerals. These treatises continue to serve as encyclopedic resources for those interested in silica, and their historical analyses and descriptions of

EBSCOhost - printed on 2/13/2023 4:48 AM via . All use subject to https://www.ebsco.com/terms-of-use

mineral varieties, morphologies, and localities will remain forever useful. Nevertheless, the past three decades have witnessed a first-order expansion of our knowledge of the silica system, and it is time to provide an updated silica review. The present volume focuses on the most recent developments, and it is intended to supplement rather than replace the earlier works of Sosman and Frondel.

The contributions to this volume cover silica chemistry in the following fashion:

• Chapters 1 through 3 describe the crystal structures and phase transitions of silica and its stuffed derivatives. Recent studies of the low-pressure polymorphs quartz, tridymite, and cristobalite have demonstrated unusual superperiodic phases and other anomalies associated with structural transformations (Chapter 1). Spectacular progress in multianvil and diamond cell technologies has made the high-pressure regime accessible, revealing new transitions in the coesite and stishovite systems as well as the phenomenon of pressure-induced amorphization (Chapter 2). Stoichiometric substitution of cations within the frameworks of both low- and high-pressure polymorphs produces a dizzying variety of derivative compounds that are of geological and industrial importance (Chapter 3).

• Chapters 4 through 9 bridge the relationship between the microstructural character of real silica minerals and the behavior of silica in the geological environment. Incorporation of small amounts of H dramatically weakens quartz exposed to stress (Chapter 4). Consequently, tectonic pressures may lead not to brittle fracture but to the production of high densities of dislocations and preferred orientation in polycrystalline quartz (Chapter 5). The low pressures and temperatures in sedimentary settings may promote the crystallization of highly defective silica phases that are frequently metastable (Chapter 6); through diagenetic processes, these minerals anneal to macrocrystalline quartz (Chapter 7). The nature of the surface structure of quartz strongly influences the mechanisms and kinetics of silica dissolution in aqueous fluids (Chapter 8).

• Chapters 9 through 13 treat the basic physical properties of the phases of silica. Recent calorimetric studies of some of the more unusual silica compounds have added insight into the stability of the silica framework (Chapter 9). Quantum mechanical considerations of the Si-O bond have yielded a fundamental understanding of the bond lengths and angles within the polymorphous silica system (Chapter 10). Calculations based upon first-principles theory have achieved significant success in explaining and predicting silica transitions at high temperatures and pressures (Chapter 11). Spectroscopic analyses of silica (Chapters 12 and 13) have revealed vibrational behaviors in response to variations in temperature, pressure, and composition that have deepened our understanding of the dynamic interactions within the silica structure.

• Chapters 14 through 16 detail the uses of silica for industrial purposes. For instance, doping silica with other cations produces ceramics with low expansion on heating (Chapter 14), and high-silica zeolites are being explored for their properties as catalysts and molecular sieves (Chapter 15). High concentrations of silica dust in the workplace long have been linked with the incidence of respiratory diseases, such as silicosis, and recent evidence suggests that crystalline silica may be carcinogenic (Chapter 16).

The assembly of this volume required the generous assistance of many, and the editors would like to thank them for their contributions. The Mobil Oil Corporation offered financial support. The following people provided external reviews of the chapters in this

EBSCOhost - printed on 2/13/2023 4:48 AM via . All use subject to https://www.ebsco.com/terms-of-use

volume: Fred Allen, Leland Allen, Phil Bennett, Guoqiu Gao, Robert MacChesney, Kurt Nassau, Shiv Sharma, Eugene Smelik, Jan Tullis (who heroically reviewed two manuscripts), and Hongwu Xu. In addition, many of our authors independently sought out reviewers, who are acknowledged at the end of their chapters. Of course, our deep gratitude goes to Paul Ribbe and his staff, who have worked unstintingly in their efforts to produce yet another professionally presented textbook in the RIM Series. Paul's patience and encouragement in our efforts to transfer edited and formatted manuscripts electronically (despite occasional mixups for which the editors take full credit) is especially appreciated.

Peter J. Heaney
Princeton, New Jersey
September 1, 1994

REFERENCES

Clarke FW (1904) Analyses of rocks from the laboratory of the United States Geological Survey, 1880 to 1903. Bull U S Geol Surv 228
Frondel C (1962) System of Mineralogy, 7th edn. Vol. 3. John Wiley, New York
Mason B, Moore CB (1982) Principles of Geochemistry, 4th edn. John Wiley, New York
Sosman RB (1927) The Properties of Silica. Chemical Catalog Co., New York
Sosman RB (1965) The Phases of Silica. Rutgers Univ Press, New Brunswick, NJ

EBSCOhost - printed on 2/13/2023 4:48 AM via . All use subject to https://www.ebsco.com/terms-of-use

EBSCOhost - printed on 2/13/2023 4:48 AM via . All use subject to https://www.ebsco.com/terms-of-use

SILICA: PHYSICAL BEHAVIOR, GEOCHEMISTRY, AND MATERIALS APPLICATIONS

TABLE OF CONTENTS, VOLUME 29

Page

Copyright; List of additional volumes of *Reviews in Mineralogy* ii
Foreword; Preface and Acknowledgments iii

Chapter 1 **P. J. Heaney**

STRUCTURE AND CHEMISTRY OF THE LOW-PRESSURE SILICA POLYMORPHS

Summary 1
Introduction 1
Phase Equilibria 2
Geological Occurrences 3
- Stable polymorphs 3
- Metastable polymorphs 3
  - Low-temperature tridymite and cristobalite 3
  - Other metastable polymorphs 4
- Amorphous silica 4
  - Biogenic silica 4
  - Abiogenic silica glass 5

Composition of Silica Polymorphs 5
- Quartz 5
  - Impurities 5
  - Geological applications 5
- Tridymite and cristobalite 6

Structure of Quartz 6
- Previous studies 6
- Crystal structures of α- and β-quartz 6
  - Framework topology 6
  - Cell settings 8
  - Structural vs. symmetrical chirality 10
  - Proper conventions 11
- Brazil twins 12
  - Occurrence and structure 12
  - Microcrystalline silica 12
  - Moganite 13
- Dauphiné twins 14
  - Imaging 14
  - Electrical properties and stress 15
  - Ferrobielasticity 15
- The α-β quartz transition 15
  - Dauphiné microtwins 15
  - Intermediate phase 17
  - Geological implications 18
- Real structure of β-quartz 18
  - Clusters of microtwins 18
  - Ordered single-potential model 19

Structure of Tridymite 19
- Stability of tridymite 19
- Crystal structure 19

EBSCOhost - printed on 2/13/2023 4:48 AM via . All use subject to https://www.ebsco.com/terms-of-use

HP-tridymite 20
OC-tridymite 22
OS-tridymite 23
OP-tridymite 23
MC-tridymite 23
MX-1 and PO-n tridymite 24
The Structure of Cristobalite 26
Crystal structure 26
Disorder in β-cristobalite 28
The α-β cristobalite transition 28
Cristobalite-tridymite relationships 29
Keatite 30
Acknowledgments 32
References 32

Chapter 2 **R. J. Hemley, C. T. Prewitt & K. J. Kingma**

HIGH-PRESSURE BEHAVIOR OF SILICA

Introduction 41
Overview of the SiO_2 system 43
Polymorphs 43
Low-pressure phases 43
High-pressure phases 43
Other polymorphs 44
Phase relations 44
Thermodynamic properties 46
Elastic and vibrational properties 47
Optical and electronic properties 48
High-Pressure Structures, Compression Mechanisms, and Transformations 49
Quartz 49
Cristobalite and tridymite 54
Coesite 56
Stishovite 57
Post-stishovite phases 60
Higher pressure behavior 62
Glass and lower density polymorphs 62
Comparison of High-Pressure Transformations 65
Transformation kinetics and metastability 65
Static versus dynamic compression 65
Comparisons of microstructures 66
Comparison with static deformation 69
Geophysical Implications 70
Impact phenomena and deformation 70
Lower crust and upper mantle 71
Deep mantle 71
References 73

Chapter 3 **D. C. Palmer**

STUFFED DERIVATIVES OF THE SILICA POLYMORPHS

Abstract 83
Introduction 83
Structures Derived From Quartz 84
β-eucryptite 87
Crystal structure 87

EBSCOhost - printed on 2/13/2023 4:48 AM via . All use subject to https://www.ebsco.com/terms-of-use

Structural behavior and phase transition 87
Crystal chemistry 88
Structures Derived From Keatite 90
β-spodumene 90
Ionic conductivity 91
Crystal chemistry 92
Structures Derived From Tridymite 92
Introduction to the nepheline–kalsilite series 96
Nepheline–kalsilite phase equilibria 97
Nepheline 98
Nepheline crystal chemistry 98
Structural behavior of nepheline 99
The incommensurate phase of nepheline 101
Other nepheline phases 102
Kalsilite 103
Kalsilite crystal chemistry 103
Structural behavior of kalsilite 104
Nepheline–kalsilite intermediates 105
Trikalsilite 105
Tetrakalsilite 105
Other $M\mathrm{AlSiO_4}$ phases 107
O1 structure 107
Icmm structure 110
Kaliophilite 110
Ca-rich derivatives of tridymite 111
Ba-rich derivatives of tridymite 112
Structures Derived From Cristobalite 112
Chemically-stabilized β-cristobalite 113
Carnegieite 113
Crystal structures 113
The high-low carnegieite phase transition 114
The nepheline–carnegieite reconstructive phase transition 115
Stuffed cristobalite phases: $\mathrm{Na_2}M\mathrm{SiO_4}$–$\mathrm{Na_2}M\mathrm{Si_2O_6}$ 115
Sodium zinc silicate 116
Sodium beryllium silicate 117
Sodium magnesium silicate 117
Sodium calcium silicate 117
Acknowledgments 118
References 118

Chapter 4 **A. K. Kronenberg**

HYDROGEN SPECIATION AND CHEMICAL WEAKENING OF QUARTZ

Introduction 123
Hydrogen Speciation 124
Infrared signatures of hydrogen 124
Surface species 127
Hydrogen point defects 132
Aggregated water and fluid inclusions 139
Hydrogen species at dislocations 145
Chemical Weakening 145
Stress corrosion cracking 146
Time-dependent frictional sliding 149
Solution transfer creep 152
Dislocation creep and water weakening 155
Single crystals 156

EBSCOhost - printed on 2/13/2023 4:48 AM via . All use subject to https://www.ebsco.com/terms-of-use

Polycrystalline quartz aggregates....161
Summary Remarks....165
Acknowledgments....166
References....166

Chapter 5 **H.-R. Wenk**

PREFERRED ORIENTATION PATTERNS IN DEFORMED QUARTZITES

Introduction....177
Creep Deformation and Deformation Mechanisms....177
Textures: Measurements and Representation....180
Experimental Deformation of Polycrystalline Quartz....184
Plasticity Theory....188
Some Natural Textures....193
Geological Applications: A Critical Assessment....195
Fabric zonation with metamorphic grade....195
Simple shear deformation and sense of shear....198
Differences in finite deformation at low and high metamorphic grade....200
Microstructural Information, Stress Estimates....202
Conclusions....204
Acknowledgments....204
References....204

Chapter 6 **H. Graetsch**

STRUCTURAL CHARACTERISTICS OF OPALINE AND MICROCRYSTALLINE SILICA MINERALS

Introduction....209
Chalcedony, Quartzine and Moganite....209
Microstructure....209
Crystal structure....212
Phase transitions....217
Water content....217
Microcrystalline Opals....219
Microstructure....220
Crystal structure....223
Phase transitions....226
Water content....226
Non-Crystalline Opals....226
Microstructure....226
Structure....228
Water content....229
Acknowledgments....229
References....229

Chapter 7 **L. P. Knauth**

PETROGENESIS OF CHERT

Abstract....233
Introduction....233
Common Silica Polymorphs in Sedimentary Rocks....234
Structural character of chert....234
Microcrystalline fibrous silica....234
Megaquartz....235

EBSCOhost - printed on 2/13/2023 4:48 AM via . All use subject to https://www.ebsco.com/terms-of-use

Opaline silica....237
Paragenesis of Authigenic Silica Phases....237
Diatoms and Their Conversion to Microcrystalline Quartz....238
Radiolarian Oozes, Spiculites, Ribbon Cherts and Novaculite....241
Radiolarians and sponges....241
Ribbon cherts....241
Novaculites....243
Nodular Cherts in Shallow Water Platform Carbonates and Epicontinental Sea Deposits....244
Mechanism of replacement....245
Rationale for early diagenesis....247
A generalized scenario for nodular chert formation....249
Magadi Cherts....249
Precambrian Cherts....251
Stromatolitic cherts....251
Iron formation chert....252
Archean cherts....252
Microquartz in Paleokarst Chert Breccias....253
Summary....255
References....256

Chapter 8 **P. M. Dove & J. D. Rimstidt**

SILICA-WATER INTERACTIONS

Introduction....259
Solubility....260
The dissolution reaction....260
Solubility of silica phases....261
Effect of temperature and pressure....262
Effect of pH....264
Effect of solution species....265
Solubility as a function of particle size....265
Equilibration temperature....267
Silica-Water Interface....268
Formation of the silica-water interface....268
Surface structures and properties....268
Electrical double layer of the silica-water interface....268
Ionization and surface charge....270
Kinetics....272
Basic principles....272
Aqueous diffusion....272
Dissolution and precipitation....273
Nucleation....277
Controls of temperature and solution composition on reactivity....278
Temperature dependence in deionized water....278
Catalysis by alkali cations....281
Solution pH....282
Combined temperature, electrolyte and pH relations....284
Organic acids....284
Ferrous-ferric iron complexing....285
Trivalent metals....287
Etch pit development....287
Surface and mechanistic controls on reactivity....288
Development of surface complexation models of dissolution....290
Solvent-surface controls on reactivity....293
Theoretical mechanistic models....297

EBSCOhost - printed on 2/13/2023 4:48 AM via . All use subject to https://www.ebsco.com/terms-of-use

Developments in applications of silica reactivity 298
Concluding Remarks 300
Acknowledgments 301
References 301

Chapter 9 **A. Navrotsky**

THERMOCHEMISTRY OF CRYSTALLINE AND AMORPHOUS SILICA

Introduction 309
Common Polymorphs 309
Quartz, cristobalite, glass, and melt 309
Tridymite 315
High pressure phases 316
Energy associated with dislocations in quartz 318
Metastable Silica Polymorphs 318
Microporous and mesoporous phases 318
Moganite 324
Amorphous silica 324
Conclusions 328
References 328

Chapter 10 **G. V. Gibbs, J. W. Downs & M. B. Boisen, Jr.**

THE ELUSIVE SiO BOND

Abstract 331
Introduction 332
Early Models for the SiO Bond 332
Geometries of Molecules and Crystals 334
The tetrahedral SiO_4 coordination polyhedron 334
The SiOSi disiloxy dimer 338
The Si_2O_7 dimer 339
The octahedral SiO_6 coordination polyhedron 341
Electron Density Distributions 344
Deformation electron density distributions 344
The efficacy of deformation electron density distributions 348
Gradient and Laplacian distributions 349
Laplacian distributions for minerals and molecules 352
The bonded radius of the oxide ion and SiO bond character 355
A Discussion 360
Acknowledgments 363
References 363

Chapter 11 **R. E. Cohen**

FIRST-PRINCIPLES THEORY OF CRYSTALLINE SiO_2

Abstract 369
Introduction 369
Role of theory in mineralogy and solid state physics 369
Electronic structure and bonding 370
Electronic structure methods 370
Self-consistent LDA computations 372
First-principles models 373
Gordon-Kim models 373

EBSCOhost - printed on 2/13/2023 4:48 AM via . All use subject to https://www.ebsco.com/terms-of-use

Potential models....374
Tight-binding models....374
Molecular Dynamics and Monte Carlo Simulations....374
Lattice dynamics....375
Electronic Structure and Bonding of Crystalline Silica....375
Structure and Equations of State....382
Gordon-Kim models....382
Potential models....383
Self consistent calculations....384
Lattice Dynamics and Elasticity....388
Models....388
Self-consistent calculations....392
Phase Transitions....392
The stishovite story....393
Displacive transitions in quartz, tridymite, and cristobalite....396
Conclusions....397
Acknowledgments....398
References....398

Chapter 12 **G. Dolino & M. Vallade**

LATTICE DYNAMICAL BEHAVIOR OF ANHYDROUS SILICA

Abstract....403
Introduction....403
Lattice Dynamics Measurements in Quartz....404
Introduction....404
Infrared studies....406
Raman studies....407
Room and low temperature studies....407
Uniaxial stress....409
High pressure....409
LO-TO splittings and polaritons....409
Non-linear optics....409
Brillouin measurements of acoustic modes....410
Dispersion curves measurements by inelastic neutron scattering....410
Soft mode in the α phase: Raman studies....410
Soft mode in the β phase....411
Neutron studies....411
Hyper-Raman study....413
Temperature-dependence of other vibrational modes....413
Raman measurements....413
Infrared measurements....413
Brillouin measurements....413
Elastic light scattering....414
Low frequency spectra in the incommensurate phase....415
Nature of the α-β transition....415
Lattice Dynamics of Other Silica Polymorphs....415
Introduction....415
Low pressure polymorphs....416
Cristobalite....416
Tridymite....418
High pressure polymorphs....418
Coesite....418
Stishovite....418
Amorphous silica....419
Theory of Lattice Dynamics of Silica Polymorphs....420

EBSCOhost - printed on 2/13/2023 4:48 AM via . All use subject to https://www.ebsco.com/terms-of-use

Empirical models....421
Ab initio calculations....423
Conclusion....424
References....425

Chapter 13 **G. R. Rossman**

COLORED VARIETIES OF THE SILICA MINERALS

Introduction....433
Reviews and techniques....433
Iron-Substitution in quartz....433
Association of color with iron....433
Iron sites in quartz....434
The $[FeO_4/Li]^0$ center = The S1 center....434
The $[FeO_4/H]^0$ center = The S2 center....435
The $[FeO_4/Na]^0$ center = The S3 center....435
The $[FeO_4]^0$ center = The S0 center = The I center....435
The Fe^{4+} site: $[FeO_4]^0$....435
The Fe^{2+} interstitial center: $[FeO_6]$ = The I6 site....436
The Fe^{2+} interstitial center: $[FeO_4]$ = The I4 site....436
Citrine....436
Classification....436
Natural orange-brown iron-containing citrine....436
Heated amethyst....437
Synthetic iron-containing quartz....439
Citrine color produced by irradiation....439
Greenish-yellow irradiation colors....439
New interpretations....441
Mössbauer spectra....442
Amethyst....442
Early ideas....442
Iron centers in amethyst....442
Color and optical spectrum....444
Synthesis of amethyst....445
Irradiation dose....445
Distribution of amethyst color....445
Analytical aspects....445
Color stability....446
Amethyst-citrine (ametrine)....446
Optical biaxial behavior....446
Green Quartz....447
Natural occurrences....448
Green color through irradiation....448
Synthesis of green quartz....448
Smoky Quartz....448
Aluminum centers....448
E centers....449
Optical spectra....449
E centers....451
Biaxiality....451
Electrolytic smoky quartz....452
Other irradiation colors related to smoky quartz....452
Thermal and optical stability....452
Rose Quartz....453
Massive vein rose quartz....453
Cause of color....453

EBSCOhost - printed on 2/13/2023 4:48 AM via . All use subject to https://www.ebsco.com/terms-of-use

Scattering and inclusions 454
Absorption intensity 454
Chemical analysis 455
Substitutional Ti 455
Radiation effects 455
Thermal stability 455
Photo stability 455
Single-crystal rose quartz 455
Synthetic rose quartz 456
Other Varieties of Silica Minerals Colored by Inclusions and Admixed Phase 456
Blue quartz 456
Natural blue quartz 456
Other blue colors 457
Chrysoprase 458
Jasper 460
Chert 460
Plasma 460
Prase 460
Heliotrope 460
Agate 460
Opal 460
Acknowledgments 462
References 462

Chapter 14 **G. H. Beall**

INDUSTRIAL APPLICATIONS OF SILICA

Introduction 469
The Crystalline Silica Polymorphs 469
α-quartz 469
Uses as a raw material 469
Natural quartz as a ceramic component 470
Single crystal quartz 470
Piezoelectric applications 471
Optical applications 473
Cristobalite 473
Cordierite-cristobalite glass-ceramics 473
Potassium fluorricherterite-cristobalite glass-ceramics 475
Stuffed Derivatives of Silica Polymorphs 479
Nomenclature of stuffed derivatives 479
β-quartz solid solutions 481
Composition and stability 481
Structure and properties 482
Glass-ceramics based on β-quartz solid solution 484
Stuffed derivatives of keatite (β-spodumene solid solution) 488
Composition and stability 488
Structure and properties 488
β-spodumene solid solution glass-ceramics 489
Vitreous Silica 492
Natural occurrences 492
Structure 493
Manufacture 493
Fused quartz 493
Vapor phase hydrolysis 494
Sol-Gel processes 495
Physical properties 495

EBSCOhost - printed on 2/13/2023 4:48 AM via . All use subject to https://www.ebsco.com/terms-of-use

Optical properties....495
Radiation effects....497
Thermal properties....497
Mechanical properties....498
Electrical properties....499
Other properties....499
Applications....499
Optical uses....499
Optical waveguides....499
Lighting....502
Thermal applications....502
Chemical applications....502
Electronic applications....503
Other applications....503
Summary....503
Acknowledgment....503
References....504

Chapter 15 **J. B. Higgins**

SILICA ZEOLITES AND CLATHRASILS

Introduction....507
Historical Development....508
Early history....509
Synthetic zeolite science....509
Early zeolite structures....509
The industrial era....510
Synthesis and commercialization....510
Catalytic applications....510
Synthesis with organic cations....511
High-silica zeolites....511
Pure silica zeolites (zeosils)?....511
Zeolites and Zeolitic Materials....511
What is a zeolite?....512
Zeolite nomenclature....513
Classification of tetrahedral framework materials....513
Tetrahedral frameworks & structure type codes....515
Aluminum content of porous silicates....515
Mineral silica polymorphs....515
Synthetic porous silicas....516
Preparation of Porosils....516
Solvothermal syntheses....516
Hydrothermal synthesis....516
The role of organic molecules....517
The role of alkali metals....518
Non-alkaline solvents: replacement of OH^- by F^-....518
Non-aqueous solvents....518
Framework modification....519
Porosil Materials....519
Zeosils....520
Si-theta-1 (TON)....520
Si-ZSM-23 (MTT)....520
Si-ferrierite (FER)....521
Si-ZSM-48....521
Si-ZSM-5 (MFI)....522
Si-ZSM-11 (MEL)....525

EBSCOhost - printed on 2/13/2023 4:48 AM via . All use subject to https://www.ebsco.com/terms-of-use

Si-ZSM-12 (MTW) 526
SSZ-24 (AFI) 527
Si-beta (*BEA) 527
Si-faujasite (FAU) 528
Clathrasils 529
melanophlogite (MEP) 529
dodecasil 1H (DOH) 532
dodecasil 3C (MTN) 532
deca-dodecasil 3R (DDR) 535
nonasil (NON) 535
sigma-2 (SGT) 536
Si-sodalite (SOD) 536
octadecasil (AST) 537
RUB-10 (RUT) 538
Acknowledgments 539
References 539

Chapter 16 **D. F. Goldsmith**

HEALTH EFFECTS OF SILICA DUST EXPOSURE

Abstract 545
Introduction and History 545
Biology and Physiology of Silica 546
Routes of exposure 546
Clearance of silica from the body 547
Clinical Description of Silica-Related Diseases 548
Acute silicosis 548
Accelerated silicosis 549
Chronic silicosis 549
Complications following silicosis 552
Epidemiology of Silica-Related Diseases 556
What is epidemiology? 556
Non-malignant pulmonary effects 557
Miscellaneous noncancer effects 560
Carcinogenicity of Crystalline Silica 561
Animal tumor research on silica 561
Cancer epidemiology research on silica-exposed workers 562
Studies of generalized silica exposure 563
Cancer risks and metal ore mining 563
Studies of iron ore miners 568
Studies of gold ore miners' cancer risk 570
Cancer risk for the granite industry, stone, and construction work 575
Cancer risks among ceramics, glass, and diatomaceous earth industries 578
Cancer risk among foundry workers and in metallurgical industries 581
Cancer risks among silicotics 586
Interaction between silica exposure or silicosis and cancer 592
Does silica exposure or silicosis cause lung cancer? 593
Strong relative risk 593
Consistent findings 594
Dose-response gradients 594
Controlled for confounding 594
Reliable exposure data 594
Biological specificity 595
Positive animal findings 595
Temporal cogency 595
Overall coherence 595

EBSCOhost - printed on 2/13/2023 4:48 AM via . All use subject to https://www.ebsco.com/terms-of-use

Summary of Human Health Related to Silica Exposure 596
Conclusion.....597
Acknowledgments 597
References 598

EBSCOhost - printed on 2/13/2023 4:48 AM via . All use subject to https://www.ebsco.com/terms-of-use

STRUCTURE AND CHEMISTRY OF THE LOW-PRESSURE SILICA POLYMORPHS

Peter J. Heaney

Department of Geological & Geophysical Sciences
Princeton University
Princeton, NJ 08544 U.S.A.

SUMMARY

This chapter reviews the geological occurrences, structures, and phase transitions of the low-pressure silica polymorphs—quartz, tridymite, and cristobalite. All these phases experience displacive transformations that involve structural contraction with decreased temperature, and research over the past three decades has sought out the mechanisms that control these transitions. The passage from β- to α-quartz is associated with an intermediate phase that is stable over a 1.3°C temperature interval. X-ray diffraction and transmission electron microscopy have revealed that this phase consists of Dauphiné microtwins that are incommensurately modulated. Meteoritic and synthetic tridymite experience a series of structural alterations with decreasing temperature during which the symmetry changes from hexagonal (HP) to orthorhombic (OC, OS, and OP) to monoclinic (MC). Phase transition behavior in terrestrial tridymite (PO-n and MX-1) is more complex, probably due to a greater degree of structural disorder. The transformation from cubic β-cristobalite to tetragonal α-cristobalite is marked by a high spontaneous strain and a large hysteresis in the transition temperature. The three high-temperature polymorphs—β-quartz, HP-tridymite, and β-cristobalite—exhibit evidence for dynamical disorder, but the nature of the atomic oscillations in these phases remains an active area of investigation.

INTRODUCTION

After von Laue's discovery of X-ray diffraction by crystalline solids in 1912, scientists mapped the structures of rock-forming minerals with breath-taking rapidity. In only two years, W.L. and W.H. Bragg charted the atomic frameworks of halite, pyrite, diamond, calcite, and fluorite, and they successfully delineated dozens of other minerals shortly thereafter (Bragg, 1937). However, crystallographers were frustrated in their earliest efforts to discern the structures of the silicon dioxide compounds, and it became clear that the compositional simplicity of these solids is accompanied by considerable structural complexity.

Researchers simplified the problem by exploiting the multiple phase transitions that characterize the silica system. The heating experiments of Le Chatelier (1889), Mallard (1890), and Fenner (1913) had hinted at the relative ease with which individual silica minerals permute to slightly different modifications. X-ray diffraction experiments indicated that the modifications for quartz, tridymite, and cristobalite are more highly symmetric at higher temperatures. Since structural modifications with higher symmetry involve fewer variable parameters, the atomic configurations of the silica polymorphs become more tractable at high temperatures. As a result, the structures of the high-temperature polymorphs of silica were determined before their low-temperature counterparts—β-quartz by Bragg and Gibbs (1925), β-cristobalite by Wyckoff (1925), and HP-tridymite by Gibbs (1927).

EBSCOhost - printed on 2/13/2023 4:48 AM via . All use subject to https://www.ebsco.com/terms-of-use

The following four decades witnessed surprisingly few investigations of a structural nature within the silica system, and our understanding of the silica polymorphs at the atomic scale remained little modified from these early studies. However, experimental interest in the silica minerals has flourished since the 1960's, and the rich chemistry that characterizes this most important geological system continues to surprise us. With the advent of more powerful microscopies, spectroscopies, and computer technologies, silica minerals now are appreciated as dynamical rather than as static entities, and the subtleties that attend the transformation of one polymorph to another have opened new roads in phase transition theory. As unexpected complexities in this end-member system are continually observed, researchers have been provoked to search for—and find—similar behaviors in other mineral groups.

PHASE EQUILIBRIA

The phase relationships among the low-pressure silica polymorphs first were sorted out by Fenner (1913), and the thermodynamic properties of these solids continue to be studied (see reviews by Richet et al., 1982; Swamy et al., 1994). In addition, metastable silica phases have assumed increasing importance in geological and materials research, and recent calorimetric investigations of high-silica zeolites and clathrates are described in the chapter by Navrotsky (this volume).

The transformation from α-quartz (or low quartz) to β-quartz (or high quartz) traditionally has been placed at 573°C at 1 bar (Fig. 1). Recent research (described below) has demonstrated the existence of an incommensurate phase that is stable between 573°C and 574.3°C. The transition from β-quartz to HP-tridymite at 1 bar occurs at 867°C, and HP-tridymite inverts to β-cristobalite at 1470°C. β-cristobalite melts to silica liquid at 1727°C. Increasing pressure strongly stabilizes the structure of α-quartz relative to β-quartz (Gibson, 1928; Yoder, 1950; Cohen and Klement, 1967; Koster van Groos and

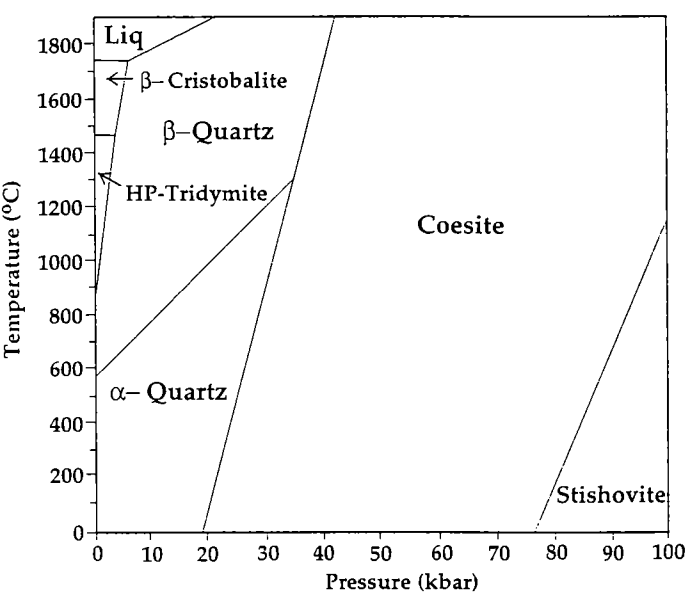


Figure 1. Phase diagram for the silica system. From Klein and Hurlbut (1993, Manual of Mineralogy, 21st edn., p. 527: © John Wiley & Sons). Reprinted with permission.

EBSCOhost - printed on 2/13/2023 4:48 AM via . All use subject to https://www.ebsco.com/terms-of-use

Ter Heege, 1973; Cohen et al., 1974), so that the slope (dT/dP) of the univariant curve separating the α- and β-quartz stability fields is strongly positive. Shen et al. (1993) have provided an expression for the change in the transition temperature T_c (in °C) as a function of hydrostatic pressure P (in kbar) using laser interferometry in a diamond anvil: $T_c = 574.3 + 25.59\ P - 6.406 \times 10^{-5}\ P^2$ (so that $dT/dP \approx 25.6$°C/kbar, in agreement with previous studies). Coe and Paterson (1969) demonstrated that the α-β quartz transition temperature increases more quickly when a nonhydrostatic stress is directed perpendicular rather than parallel to the **c** axis (10.6°C/kbar vs 5.0°C/kbar). The open structures of tridymite and cristobalite are especially unstable with increasing pressure, and phase equilibrium data (Kennedy et al., 1962; Ostrovsky, 1966; Jackson, 1976; Grattan-Bellew, 1978) place the slope of the univariant line between the tridymite and β-quartz stability fields at roughly 200°C/kbar; the slope of the cristobalite/β-quartz boundary is only slightly smaller.

GEOLOGICAL OCCURRENCES

Stable polymorphs

Even though most of the silica at the earth's surface has existed as β-quartz (and possibly β-cristobalite and HP-tridymite) at some point during its history, the predominant polymorph of silica within the crust is α-quartz, since the temperatures and pressures at which α-quartz is stable also characterize the bulk of the crust. The polymorphs β-quartz, HP-tridymite, and β-cristobalite usually are transient species that may crystallize during the cooling of igneous bodies, as can be indicated by the occurrence of quartz paramorphs after the high-temperature phases (Ray, 1947; Wager et al., 1953). Alternatively, tridymite and cristobalite may form stably in tectonically active zones or in regions associated with contact metamorphism, and they may convert to quartz with decreasing temperature (Moehlman, 1935; Van Valkenburg and Buie, 1945; Green and Fitz, 1993).

As a late-stage crystallization product in mature magmas, α-quartz is common in granites, granodiorites, rhyolites, and pegmatites, and α-quartz is an important constituent of metamorphic phyllites, mica schists, migmatites, and quartzites (Best, 1982; Shelley, 1993). Because α-quartz has a hardness of 7 on the Mohs scale of 10, it is fairly resistant to mechanical alteration. Similarly, its low solubility in water (see chapter by Dove and Rimstidt, this volume) preserves α-quartz during chemical weathering. As a result, α-quartz rivals feldspar as the most common mineral within sedimentary rocks, and α-quartz becomes relatively more abundant as beach sands age (Pettijohn, 1975). Moreover, α-quartz is the final product in the diagenetic crystallization sequence that begins with amorphous silica (opal-A) in ocean sediments (see chapter by Knauth), and it is the primary gangue mineral in hydrothermal veins of ore deposits (Fournier, 1985; Herrington and Wilkinson, 1993). Microcrystalline fibrous α-quartz, known as chalcedony, occurs as a secondary infilling of seams and cavities within rocks, sometimes creating concentrically banded agates or geodes (see chapter by Graetsch, this volume).

Metastable polymorphs

Low-temperature tridymite and cristobalite. Although the high-temperature phases of silica usually invert to α-quartz with time, metastable silica phases are not uncommon. For instance, both cristobalite and tridymite occur as metastable modifications at low temperature. In volcanic ejecta, the inversion from cristobalite or tridymite to quartz is inhibited by rapid quenching, as also occurs with many lunar rocks and meteorites (Dollase, 1967; Christie et al., 1971; Kawai et al., 1978). Likewise, cristobalite and tridymite form from the devitrification of volcanic glasses, such as obsidian.

EBSCOhost - printed on 2/13/2023 4:48 AM via . All use subject to https://www.ebsco.com/terms-of-use

Metastable cristobalite and tridymite also crystallize authigenically within sedimentary deposits as opal-CT (Jones and Segnit, 1971; 1972). The diagenetic reaction that transforms amorphous silica (opal-A) to macrocrystalline α-quartz involves intermediate phases that contain disordered mixtures of cristobalite and tridymite. The reactions that typify marine silica diagenesis may be expressed as follows: opal-A → opal-CT → chalcedony → α-quartz (see reviews by Williams et al., 1985 and Williams and Crerar, 1985). This same diagenetic sequence has been observed in the evolution of petrified wood (Stein, 1982). Opal-CT also is an important component of many soils (Drees et al., 1989), and it has been identified by X-ray diffraction within the culm (or stem) of bamboo (Deelman, 1986). Siliceous bamboo remains the only documented instance of crystalline silica that has been biogenically precipitated.

Other metastable polymorphs. Natural silica may adopt framework configurations that are topologically distinct from quartz, tridymite, and cristobalite. For instance, chert and chalcedony once were considered microcrystalline varieties of quartz, but it now is clear that these authigenic species represent nanoscale intergrowths of quartz and a metastable silica polymorph called moganite (Flörke et al., 1984). Although moganite is present in virtually every unaltered sample of microcrystalline "quartz" (Heaney and Post, 1992), it occurs in especially high concentrations in evaporitic environments (Heaney et al., 1992). Consequently, chert, chalcedony, flint, and the like should be regarded as rock rather than varietal names.

Less common is keatite, which is easily synthesized from silica glass at moderate temperatures and pressures (Keat, 1954) and may have been observed in stratospheric dust (Rietmeijer, 1988). In addition, several metastable compounds that are nearly pure silica can be found in nature. These would include clathrate structures, such as melanophlogite [$C_2H_{17}O_5 \cdot Si_{46}O_{92}$], which is often found in association with sulfur deposits (Skinner and Appleman, 1963; Zák, 1972). High-silica clathrates are described more fully in the chapter by Higgins. In addition, layered sodium silicate structures such as magadiite [$NaSi_7O_{13}(OH)_3 \cdot 3H_2O$] and kenyaite [$Na_2Si_{22}O_{41}(OH)_8 \cdot 6H_2O$] precipitate from highly alkaline carbonate-bicarbonate lakes (Eugster, 1967; Hay, 1968; Lagaly et al., 1975a,b). Leaching of sodium from magadiite deposits produces the layered mineral silhydrite [$3SiO_2 \cdot H_2O$] (Gude and Sheppard, 1972). These minerals diagenetically alter over timescales of thousands of years to form "Magadi-type" cherts (Sheppard and Gude, 1986).

Amorphous silica

Biogenic silica. Natural occurrences of amorphous silica also are widespread, particularly from biogenic sources, such as the skeletons of radiolaria, diatoms, and sponges (Simpson and Volcani, 1981). Siliceous tests that are not dissolved post mortem in highly undersaturated ocean waters will rain to the marine floor and lithify to form poorly crystalline opal, or porcellanite. In the absence of aggressive diagenesis, these opaline deposits can become quite extensive; in the Miocene Monterey Formation of California, diatomite sequences measure hundreds of meters thick (Garrison et al., 1981).

Amorphous silica also is cycled through the environment by organisms (Drees et al., 1989). Internal silicification of plant tissues promotes structural integrity and affords protection against plant pathogens and insects (Chen and Lewin, 1969). Some plants, such as members of the genus *Equisetum*, release exudates through the plant root that depolymerize silica in surrounding soil in order to facilitate silica uptake (Weiss and Herzog, 1977; Sangster and Hodson, 1986). Silica contents are especially high in grasses,

EBSCOhost - printed on 2/13/2023 4:48 AM via . All use subject to https://www.ebsco.com/terms-of-use

and silica accumulation can account for ~20% of the dry weight of rushes, rice, and sugarcane. The ash produced by burning the hulls of rice seeds may contain ~95 wt % silica (Kaufman et al., 1981). The ashing process may transform biogenic silica that is mostly amorphous to crystalline opal-CT (Deelman, 1986), thus posing potential health hazards for airborne ash (see chapter by Goldsmith, this volume). Likewise, trees can deposit nodules of amorphous silica as phytoliths within their leaves, and, after death and decomposition, this silica is returned to the soil. Geis (pers. comm. cited by Sangster and Hodson, 1986) estimates that the foliage and wood of sugar maples yield 90.1 kg/ha of particulate silica.

Abiogenic silica glass. Amorphous siliceous sinter, known as geyserite, precipitates from geyser fluids that contain high concentrations of dissolved silica. In addition, extrusive magmas may quench to form volcanic glasses upon sudden exposure to air or water. The structure of volcanic glass depends upon the composition of the starting liquid; basaltic glass (or tachylite) devitrifies fairly rapidly, but more silicic glasses (obsidian) may persist for millions of years in large deposits (O'Keefe, 1984). Silica glass also is found within tektites, which are spherical or teardrop-shaped silicate glass bodies associated with impact craters. Tektites usually are compositionally messy, but they may contain particles of pure silica glass known as lechatelierite (Glass, 1984). Lechatelierite also forms when lightening strikes unconsolidated sand or soil to create fulgurites, which adopt the shape of the lightening bolt (Rogers, 1946).

COMPOSITION OF SILICA POLYMORPHS

Quartz

Impurities. Quartz has a low tolerance for the incorporation of impurities because its void space is fairly cramped. Stoichiometric substitution of cation-anion pairs gives rise to *stuffed derivatives*, such as eucryptite [$LiAlSiO_4$]. These minerals are uncommon in nature, but they have important materials applications (see the chapters by Palmer and Beall). Small amounts of trivalent Al and Fe and monovalent Li, Na, and K are frequently incorporated in quartz. Depending on the oxidation states and the site distributions of these extraneous cations, the impurities may give rise to distinct coloration (see chapter by Rossman, this volume). The most generally abundant impurity is Al, which is present in the range of <13 ppm to 15,000 ppm in natural quartz (Smith and Steele, 1984) and up to 17,500 ppm in synthetic crystals (Ono, 1979); however, most quartz contains Al at the level of hundreds of ppm or less (Frondel, 1962). In their analytical survey of silica polymorphs, Smith and Steele (1989) observed a range for Na from 9 to 1420 ppm and for K from 3 to 290 ppm. Incorporation of impurities typically maintains electrical neutrality (Dennen, 1966), and plots of the contents of Li+Na+K vs. Al+Fe may reveal a 1:1 correspondence (Graetsch et al., 1987). Most commonly, however, the sum of the cations Li+Na+K is less than that of Al+Fe because of the important role played by interstitial H (see chapter by Kronenberg).

Geological applications. Attempts to exploit impurities in quartz for geological purposes have met with mixed success. Dennen et al. (1970) proposed that the solubility of Al in quartz increases linearly with temperature. Subsequent studies, however, have effectively discredited the Al geothermometer (Perry, 1971; Coveney and Kelly, 1971; and especially Scotford, 1975). Nevertheless, a review of the Russian literature by Hurst and Storch (1981) does indicate useful behavior patterns. Higher crystallization temperatures for quartz generally lead to: (1) lower total impurity contents; (2) lower ratios of interstitial to substitutional impurities; and (3) smaller unit cell volumes. Unfortunately, these trends

EBSCOhost - printed on 2/13/2023 4:48 AM via . All use subject to https://www.ebsco.com/terms-of-use

may be offset by such factors as pH of the solution, concentrations of impurities in the growth medium, growth rates, and orientation of the growth surface.

Geologists have examined impurities within quartz to shed light on rock paragenesis (Dennen, 1964). Suttner and Leininger (1972) found that cation contents are significantly more uniform in plutonic quartz than in metamorphic and volcanic quartz, and they found systematic variations in Ti, Mg, and Fe contents based on origin. Heynke et al. (1992) note that higher trace element concentrations may be found in hydrothermal vein quartz (700 to 4000 ppm) than in metamorphic quartz (200 ppm). Hurst and Storch (1981) demonstrated that impurity concentration and lattice parameters decrease with higher metamorphic grade. Goguel (1983) notes that Li/Al ratios in quartz of hydrothermal origin range from 0.35 to 0.57, which are much higher than the Li/Al ratios in magmatic quartz of 0.24 or less. Hervig and Peacock (1989) used Li distributions in deformed quartz as evidence for the absence of fluid flow in Santa Catalina mylonites.

Tridymite and cristobalite

Because of their more open frameworks, tridymite and cristobalite can more easily accommodate impurity elements than quartz, and stuffed derivatives based on tridymite and cristobalite occur with greater frequency and variety (see chapter by Palmer, this volume). Nevertheless, most natural tridymite and cristobalite crystals are relatively pure. Analyses of tridymite (Rubin and Keil, 1983; Smith and Steele, 1984; Schneider, 1986; Schneider and Flörke, 1982) and cristobalite (Peacor, 1973; Smith and Steele, 1984; Schneider, 1986; Graetsch et al., 1987) reveal concentrations of Al (~5000 ppm), Na (~3500 ppm), and K (~1500 ppm) at roughly ten times the levels observed in typical quartz samples. Larger grain sizes exhibit fewer impurities, with tridymite incorporating slightly higher amounts than cristobalite (Schneider, 1986).

STRUCTURE OF QUARTZ

Previous studies

The pioneering work of Bragg and Gibbs (1925) and Gibbs (1925) firmly established the topological conformation of the silica framework for α- and β-quartz. Refinement of this stucture was made possible by improved precision in single-crystal X-ray diffraction techniques (Young and Post, 1962; Smith and Alexander, 1963; Zachariasen and Plettinger, 1965; LePage and Donnay, 1976). Likewise, single-crystal high-temperature studies have allowed measurement of the structural changes that accompany the α-β quartz transition using X-rays (Young, 1962; Kihara, 1990) and neutrons (Wright and Lehmann, 1981). Low-temperature refinements of α-quartz have been reported by LePage et al. (1980) using single-crystal X-ray techniques and by Lager et al. (1982), who employed powder neutron diffraction. Quartz also has been approached through Rietveld refinement of standard X-ray (Thompson and Wood, 1983; Will et al., 1983) and synchrotron X-ray (Will et al., 1988) powder diffraction data. High-pressure refinements of quartz have been provided by Jorgensen (1978) to 25 kbar, D'Amour et al. (1979) to 68 kbar, Levien et al. (1980) to 61.4 kbar, and Ogata et al. (1987) to 22.6 kbar and 265°C. The high pressure behavior of quartz is complex, and it is reviewed in the chapter by Hemley et al.

Crystal structures of α- and β-quartz

Framework topology. The structure of α-quartz is most easily envisioned as a distortion of the high-temperature β modification. In β-quartz, paired helical chains of silica tetrahedra spiral in the same sense around 6_4 or 6_2 screw axes parallel to *c* (Fig. 2a).

EBSCOhost - printed on 2/13/2023 4:48 AM via . All use subject to https://www.ebsco.com/terms-of-use

The two helical chains are symmetrically related to each other by the twofold rotation within the sixfold screw, and the intertwined chains produce open channels parallel to c that appear hexagonal in projection. The framework of β-quartz contains 6- and 8-membered rings with irregular shapes, and the space group is either $P6_422$ or $P6_222$, depending on the handedness of the tetrahedral helices.

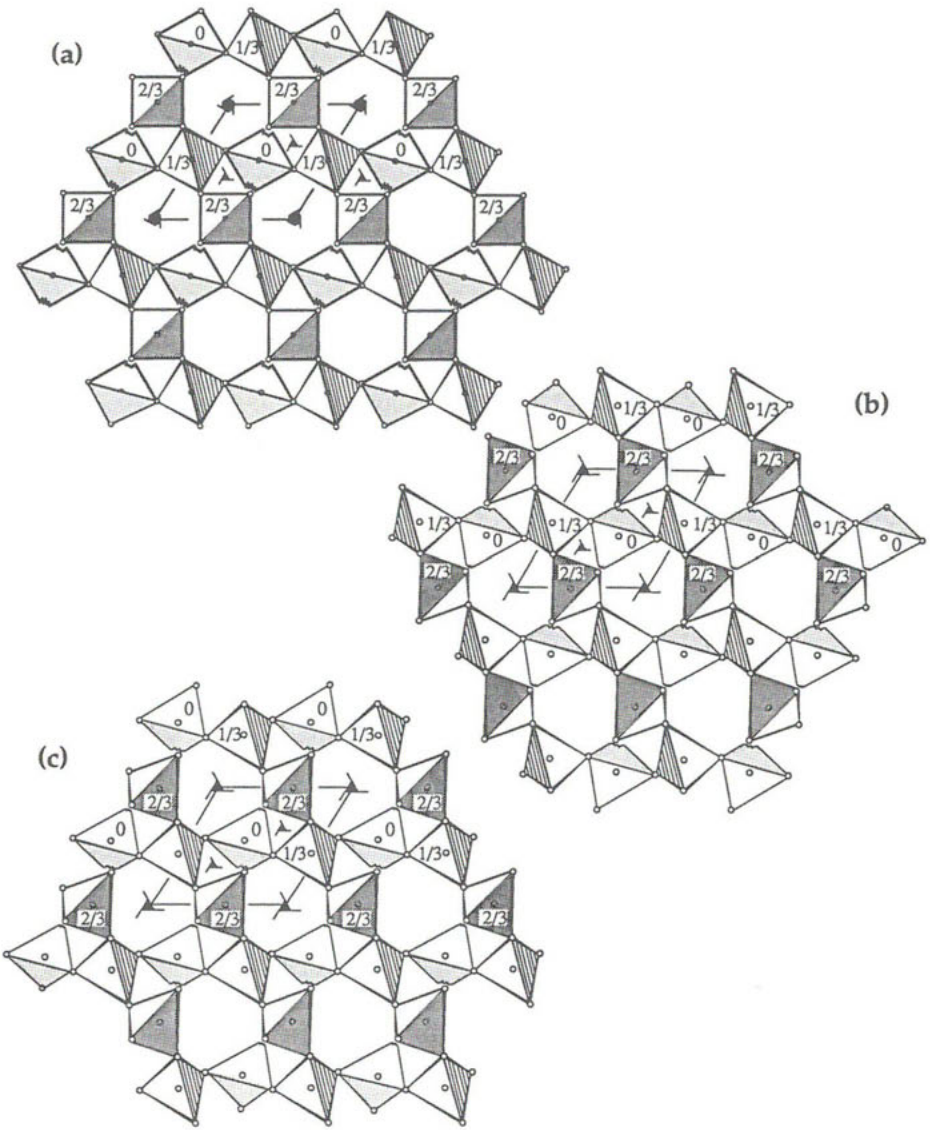


Figure 2. Projections of quartz along the c -axis. (a) β-quartz in space group $P6_422$ with the origin shifted by $1/3c$ with respect to the setting in the *International Tables* to facilitate com-parison with α-quartz. (b) α-quartz in space group $P3_121$ in the conventional obverse setting. (c) α-quartz in space group $P3_121$ in the reverse setting.

EBSCOhost - printed on 2/13/2023 4:48 AM via . All use subject to https://www.ebsco.com/terms-of-use

When β quartz is cooled below 573°C at 1 bar, the expanded β-quartz framework collapses to the denser α-quartz configuration (Fig. 2b,c). Mean Si-O bond distances hardly change (from 1.599 Å at 590°C to 1.609 Å at 25°C), but the Si-O-Si bond angle decreases dramatically from 150.9° at 590°C to 143.61° at room temperature (Wright and Lehmann, 1981). The contraction of the tetrahedral network may be described geometrically as the rotation of rigid tetrahedra about the ⟨100⟩ axes through an angle θ (Höchli and Scott, 1971; Megaw, 1973). In the β polymorph, θ is zero, but in α-quartz at room temperature, θ is 16.3°. As may be discerned from Figure 3, the sense of the tetrahedral rotation violates the twofold symmetry contained within the sixfold screw axes, and the space group symmetry decreases from $P6_422$ to its subgroup $P3_121$ (or from $P6_222$ to $P3_221$).

Although the handedness of the tetrahedral chains is preserved, the α-β quartz transformation yields two distinct α_1 and α_2 twin orientations, because the tetrahedral rotation may occur in one of two senses. If the tetrahedral tilt is as indicated in Fig. 3, then the structural variant portrayed in Fig. 2c appears, whereas rotation in the opposite direction yields the variant in Fig. 2b. These two twin orientations are known as the Dauphiné twins of α-quartz. As can be seen from the projections of the ditrigonal tunnels in Figures 2b and 2c, the two twin orientations are related to each other by the twofold symmetry lost during the transformation, as is expected for displacive transitions (Buerger, 1951). Structural continuity across Dauphiné twin boundaries is achieved by a gradual change in the tetrahedral tilt angle θ from +16.3° to -16.3° (McLaren and Phakey, 1969; Liebau and Böhm, 1982). Consequently, at the center of the domain wall θ is zero, and the structure assumes the ideal β-quartz configuration.

Cell settings. The atomic positions of the α and β polymorphs are listed in Table 1. As with all solids having threefold rotational symmetry, the hexagonal lattice of α-quartz exhibits a higher symmetry than does the trigonal structure. Consequently, α-quartz may be described in either an obverse or a reverse cell setting. Figure 2b represents left-handed α-quartz in the conventional obverse setting for space group $P3_121$, whereas the structure with the same space group is portrayed in the reverse setting in Figure 2c. (Obverse and reverse settings are related by a 180° rotation about *c*, which happens to be the Dauphiné twin law.) Right-handed α-quartz with space group $P3_221$ also may be described by obverse and reverse cell settings. Specification of the cell setting is critically important in discussions of those physical properties whose very existence arises from the absence of twofold rotational symmetry along *c*, such as the electric polarity of the twofold axes

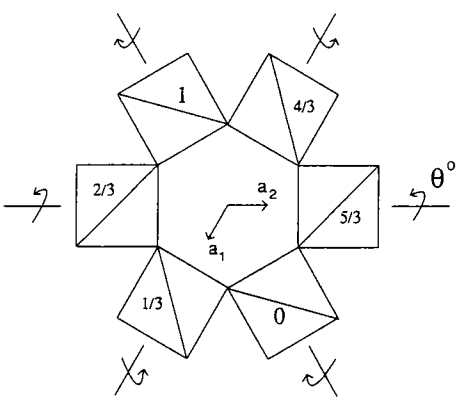


Figure 3. A projection of a single spiraling left-handed tetrahedral chain along *c* of the ideal hexagonal β structure. The Dauphiné twin orientation of Figure 2c can be produced by rotating individual tetrahedra in the senses indicated about the <100> directions. Rotation in the opposite sense results in the Dauphiné orientation of Figure 2b.

EBSCOhost - printed on 2/13/2023 4:48 AM via . All use subject to https://www.ebsco.com/terms-of-use

Table 1. Structural data for quartz

	β-Quartz		α-Quartz	
Unit Cell				
a (Å)	4.9977		4.91239(4)	
c (Å)	5.4601		5.40385(7)	
V (Å^3)	118.11		112.933	
ρ (g/cm^3)	2.5334		2.6495	
Space Group	$P6_422$	$P6_222$	$P3_121$	$P3_221$
Atom Positions				
x(Si)	1/2	1/2	0.4701	0.5299
y(Si)	0	0	0	0
z(Si)	0	0	1/3	2/3
x(O)	0.2072	0.2072	0.4139	0.5861
y(O)	0.4144	0.4144	0.2674	0.7326
z(O)	1/2	1/2	0.2144	0.7856

Note: Data for β-quartz at 590°C from Wright and Lehman (1981) and α-quartz at 25°C from Will et al. (1988)

perpendicular to *c*. Likewise, Miller indices are ambiguous unless the cell setting is known, since the *hkl* planes in one setting physically correspond to the $\bar{h}\,\bar{k}\,l$ planes of the other.

The degree of confusion that this fine detail has posed to some of our most eminent crystallographers should warm the heart of every struggling mineralogist. Over the years, different researchers have employed different conventions, creating an unholy quagmire (described by Lang, 1965b; Megaw, 1973, footnote, p. 267-268; Donnay and Le Page, 1978; Cady et al., 1993). The primary culprit appears to be Wyckoff (1922), who originated a left-handed coordinate system for trigonal and hexagonal space groups before such things were standardized. In his description of quartz, Wyckoff (1931) employed the conventional obverse setting in his left-handed system, but when the *International Tables for Crystallography* (Hermann, 1935) established the standard right-handed orientation, Wei (1935) and Wyckoff (1948; 1963) merely plotted the same coordinates using the new cell basis, thereby altering the handedness of the structure and changing the setting from obverse to reverse. Wyckoff's unconventional representations of the quartz structure have been reproduced by innumerable authors. Donnay and Le Page (1978) argue that the α-quartz setting may be standardized through the use of a single set of atomic coordinates that may be plotted in a right-handed coordinate system to obtain the obverse $P3_121$ structure or in a left-handed coordinate system to obtain the obverse $P3_221$ structure. However, their solution seems impractical in this age of computer programs for structure refinement and crystal drawing that assume right-handed coordinate systems.

Researchers also have differed in their choices for the origin of the unit cell. Admittedly, the origin selected in the International Tables is inconvenient, because the atom positions for the space groups $P6_422$ and $P6_222$ are displaced by 1/3*c* relative to their subgroups $P3_121$ and $P3_221$. But the publication of structures using unconventional origin positions (i.e., different from those presented in the International Tables) should be avoided. It is very easy to spend fruitless hours performing a Rietveld analysis of α-quartz that yields a bewilderingly poor goodness-of-fit when the user inputs atom positions referenced to a nonstandard origin.

EBSCOhost - printed on 2/13/2023 4:48 AM via . All use subject to https://www.ebsco.com/terms-of-use

Structural vs. symmetrical chirality. It is paradoxical but true that right-handed 3_1 screw axes are associated with *left*-handed tetrahedral helices in α-quartz (see also Burns and Glazer, 1990, p. 212-215). In Figure 2b, the tetrahedral chains are left-handed, because they spiral around *c* into the page in a counterclockwise fashion. However, the 3_1 screw axes in Figure 2b are right-handed screws, since the tetrahedra that are related by the threefold screw symmetry spiral downward in a *clockwise* fashion (i.e., every *other* tetrahedron surrounding a single ditrigonal tunnel spirals downward clockwise). Similarly, right-handed tetrahedral chains in α-quartz are associated with left-handed 3_2 screw axes.

It has been known since the work of Biot (1817) and Herschel (1822) that quartz crystals with different handedness will rotate the vibration plane of polarized light in opposite senses, but it was not until de Vries (1958) exploited intensity differences associated with anomalous X-ray scattering in quartz that a particular handedness of a tetrahedral spiral could be identified with a particular rotation of light. De Vries (1958) discovered that α-quartz with 3_1 screw symmetry is laevorotatory (the plane of polarization is rotated counterclockwise as light comes from the crystal towards the observer), whereas 3_2 screw symmetry causes dextral rotation of light.

De Vries (1958) wrongly claimed that the $P3_121$ "structure has right-handed spirals." Contrary to his interpretation, and the theoretical considerations of Ramachandran (1951) and Wooster (1953) before him, the sense of the rotation of light is *opposite* the sense of the tetrahedral helices: Right-handed tetrahedral chains induce dextrorotatory rotation of light. If the plane of polarization simply followed the sense of the right-handed tetrahedral chains, then to the observer the sense of rotation would be counterclockwise, or laevorotatory. (The reader may want to confirm this observation using a garden-variety wood screw with right-handed threads.)

To add to the perplexity, the handedness of the screw axis changes during the α-β transition, even though the handedness of the tetrahedral chain does not. In the $P6_422$ structure of β-quartz in Figure 2a, both the tetrahedral chains and the sixfold screw axes are left-handed. The tetrahedral chains of α-quartz in Figure 2b remain left-handed, but a right-handed 3_1 screw axis replaces the left-handed 6_4 screw axis that characterizes the structure in Figure 2a. Similarly, a left-handed 3_2 axis in α-quartz replaces a right-handed 6_2 screw axis in β-quartz.

Proper conventions. The handedness of α-quartz must refer to its structural handedness, *not* its symmetrical handedness. Otherwise, "right-handed" quartz transforms to "left-handed" quartz above 574.3°C! To relate this convention to macroscopic crystal form is difficult, because descriptions of morphological handedness have been inconsistently applied over the years. However, the crystal form with space group $P3_121$ as determined by de Vries (1958) is identical with the macroscopic crystal depicted by Frondel (1962, p. 14) as left-handed (Fig. 4). Therefore, in contrast to Frondel's statements (p. 12-13), α-quartz that is morphologically left-handed also contains left-handed tetrahedral helices. (The projected structure of "left-handed" quartz used by Frondel (1962, his Fig. 9, p. 18) was taken from Wyckoff and actually is right-handed, revealing the source of the confusion.)

Fortunately, the proper convention is easy to remember: Morphologically left-handed quartz is laevorotatory and has left-handed chains of silica tetrahedra. Left-handed quartz has space group symmetry $P3_121$, and right-handed quartz belongs to space group $P3_221$. Projections of the structures of left- and right-handed quartz in their obverse cell settings

EBSCOhost - printed on 2/13/2023 4:48 AM via . All use subject to https://www.ebsco.com/terms-of-use

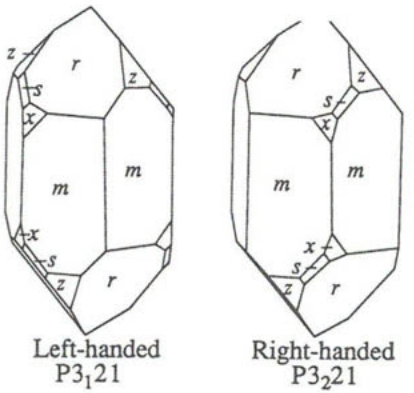


Figure 4. The crystal morphologies for left- and right-handed quartz. Minor faces *x*, *s*, and *z* follow a left-handed spiral in left-handed quartz and a right-handed spiral in right-handed quartz. (After Frondel, 1962)

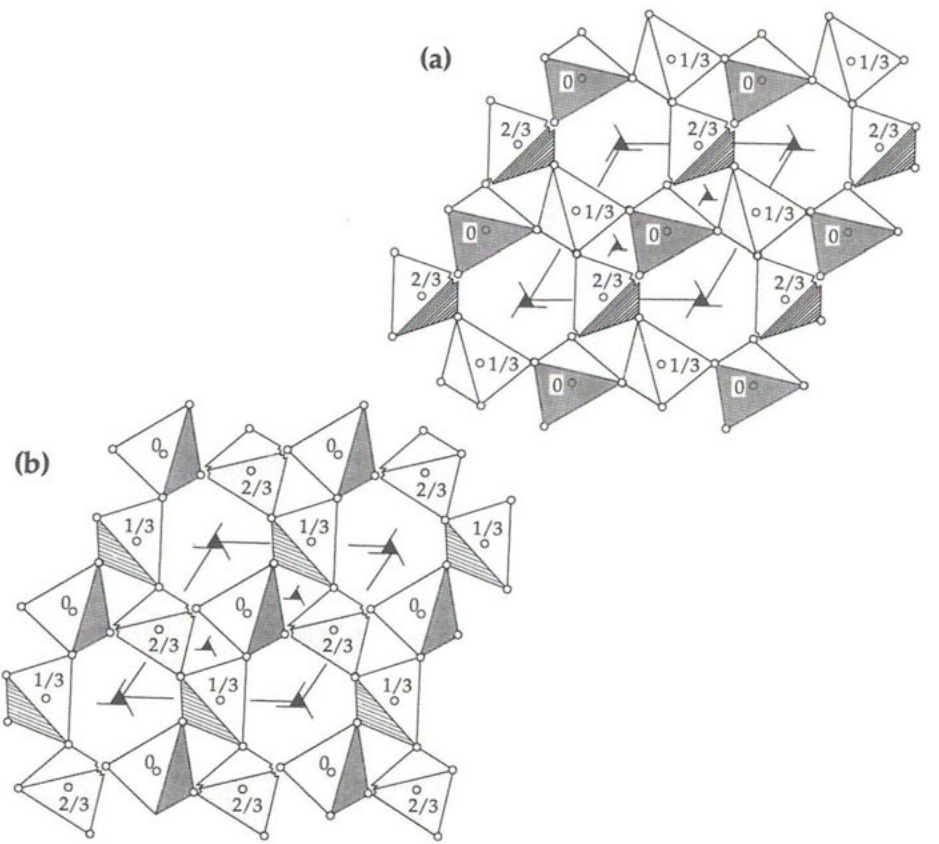


Figure 5. Projections of the structures of: (a) left-handed α-quartz with space group $P3_121$; and (b) right-handed α-quartz with space group $P3_221$. Both structures in obverse settings

EBSCOhost - printed on 2/13/2023 4:48 AM via . All use subject to https://www.ebsco.com/terms-of-use

are presented in Figure 5 (above). Atom coordinates in Table 1 are given with respect to the International Tables of Crystallography. Throughout this paper, Miller indices and axial orientations will be made with reference to quartz in the obverse setting of the cell.

Brazil twins

The multiple ways by which the structure of α-quartz may be (and has been) represented mimics the kinds of twins that naturally characterize α-quartz. Full descriptions of the twin laws that have been observed in quartz are provided by Frondel (1962, p. 75-99). Of these twins, the Brazil and the Dauphiné are by far the most common.

Occurrence and structure. The two enantiomorphs of α-quartz that are associated with the 3_1 and 3_2 screw symmetries are generally known as the Brazil twins. These twins are related by reflection across {110}, and they are depicted in Figures 4 and 5. In macroscopic crystals, high shear stress on (001) will induce Brazil twin domains bounded by (001) (McLaren et al., 1967). Among undeformed quartz crystals, Brazil twinning is especially prevalent in the violet variety known as amethyst. Light optical methods (Frondel, 1962, p. 87; Schmetzer, 1987) have indicated that {101} and more rarely {011} serve as the composition planes in Brazil twins formed during growth. Transmission electron microscopy (McLaren and Phakey, 1966; Balakirev et al., 1975; Van Goethem et al., 1977; McLaren and Pitkethly, 1982) has confirmed this orientation and further revealed the displacement vector R across the boundary as 1/2⟨110⟩. This twin boundary displacement yields minimal distortion of the oxygen framework across the composition plane, and 2/3 of the Si cations exactly coincide (McLaren and Pitkethly, 1982). On the basis of simulated X-ray topographs, González-Mañas et al. (1993) asserted that the boundaries are not simple planar defects but contain non-diffracting material.

In 1823, Brewster demonstrated that repetitive Brazil twin lamellae in amethyst are concentrated in the major {101} rhombohedral sectors. TEM (Balakirev et al., 1975; McLaren and Pitkethly, 1982) and optical (Schmetzer, 1987; Taijing and Sunagawa, 1990) studies indicate that within a given major rhombohedral sector, such as (101), composition planes corresponding to only the other two planes related by symmetry are observed, such as $(0\bar{1}1)$ and $(\bar{1}11)$. Therefore, the Brazil composition planes within a sector do not parallel the growing rhombohedral face.

Iron has long been known to play a part in the coloration of amethyst (see chapter by Rossman, this volume). By means of X-ray topography, Schlössin and Lang (1965) imaged Brazil twin lamellae in amethyst and demonstrated that iron is concentrated in the major rhombohedral sectors containing Brewster fringes. Although Baran et al. (1987) claim that X-ray topographs do not reveal an association of impurities with Brazil twin boundaries, synthesis of Brazil twinned quartz requires iron in the parent fluid, suggesting a formative role for iron in the initiation of Brazil twin defects in amethyst (McLaren and Pitkethly, 1982; Koivula and Fritsch, 1989).

Microcrystalline silica. Renewed interest in enantiomorphism in quartz has been raised by the observation that many microcrystalline varieties of quartz are polysynthetically twinned according to the Brazil law over very fine scales (see chapter by Graetsch, this volume). TEM investigations of fibrous chalcedony and equigranular chert (Miehe et al., 1984; Graetsch et al., 1987; Wenk et al., 1988; Heaney et al., 1994) reveal high concentrations of planar defects parallel to {101} that give rise to intense streaking along ⟨101⟩* in electron diffraction patterns. The orientations of these defect planes immediately led researchers to identify them as Brazil twin boundaries, and recent dark-field images by

EBSCOhost - printed on 2/13/2023 4:48 AM via . All use subject to https://www.ebsco.com/terms-of-use

Cady et al. (1993) have confirmed this interpretation. Heaney (1993) has proposed a spiral growth model for chalcedony that may explain the irregular changes in chirality.

By and large, the alternations in handedness within chert and chalcedony occur over length scales of ~100 Å. However, these silica species invariably contain regions in which the oscillation occurs with high regularity at the scale of the unit cell. This rigorous alternation of left- and right-handed twin lamellae parallel to {101} gives rise to a distinct silica polymorph called moganite (Fig. 6 and Table 2).

Moganite. Moganite was first described by Flörke et al. (1976; 1984) as a new silica phase found within cooling cracks of an ignimbrite in the Mogán Formation, Gran Canaria, Spain. The structure of moganite (Miehe et al., 1988; Miehe and Graetsch, 1992) may be described with reference to quartz, but it is not merely a subvariety of quartz. It has a lower symmetry than quartz ($I2/a$ rather than $P3_121$), and it produces a powder diffraction pattern with peaks that are not present in a quartz diffraction pattern (Miehe and

Table 2. Structural data for moganite

Space Group	$I\,1\,2/a\,1$		
Unit Cell			
a (Å)	8.758(2)		
b (Å)	4.876(1)		
c (Å)	10.715(2)		
β (°)	90.08(3)		
V (Å^3)	457.57		
ρ (g/cm^3)	2.616		
Atom	x	y	z
Si(1)	1/4	0.9908	0
Si(2)	0.0115	0.2533	0.1678
O(1)	0.9686	0.0680	0.2860
O(2)	0.1711	0.1770	0.1050
O(3)	0.8657	0.2148	0.0739

Note: Data from Miehe and Graetsch (1992)

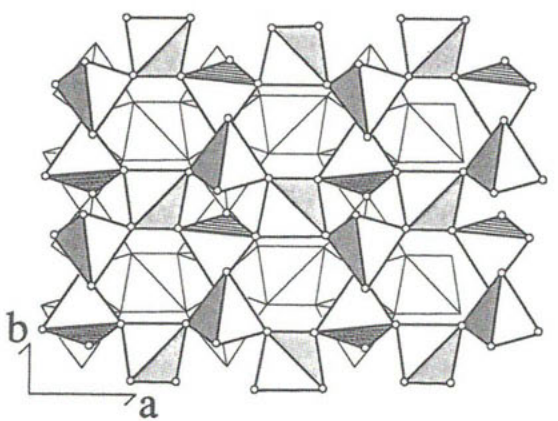


Figure 6. A projection of the structure of moganite along c in $I2_1/a$ setting. Pseudohexagonal tunnels that are open in α-quartz are blocked in moganite.

EBSCOhost - printed on 2/13/2023 4:48 AM via . All use subject to https://www.ebsco.com/terms-of-use

Graetsch, 1992). Calorimetric studies (Petrovic et al., 1993) have demonstrated that the enthalpy of moganite is comparable to the enthalpies of cristobalite and tridymite, and Raman spectroscopy reveals that moganite and quartz exhibit different vibrational modes (Kingma and Hemley, 1994). Heaney et al. (1992) have identified this phase as the discredited mineral known as lutecite (Michel-Lévy and Munier-Chalmas, 1892), and recent work by the author (Heaney and Vicenzi, 1994) strongly suggests that ferric iron promoted its transformation from quartz at Gran Canaria.

Dauphiné twins

Imaging. Because of the opposite rotatory activities associated with the Brazil twins of quartz, enantiomorphic domains may be observed in cross-polarized light with a standard petrographic microscope. However, Dauphiné twins will exhibit identical optical behavior and cannot be seen using conventional transmitted light microscopy. They can be viewed by reflected light in samples that have been etched with hydrofluoric acid, since the etching rate is dependent on the orientation of the *a* axes (Parrish and Gordon, 1945). Higher resolution information over bulk samples requires techniques that take advantage of the differences in scattering properties of the Dauphiné twins. Since an *hkl* diffracted intensity of one domain will superimpose upon $\bar{h}\bar{k}\bar{l}$ of the other, dark-field images formed from coincident diffractions with markedly different intensities will reveal the twin domains.

In this manner, Dauphiné twins were imaged first using X-ray topography (Lang, 1965a) and transmission electron microscopy (McLaren and Phakey, 1969). These studies have demonstrated that the Dauphiné twins are strikingly euhedral (Fig. 7). Constraints

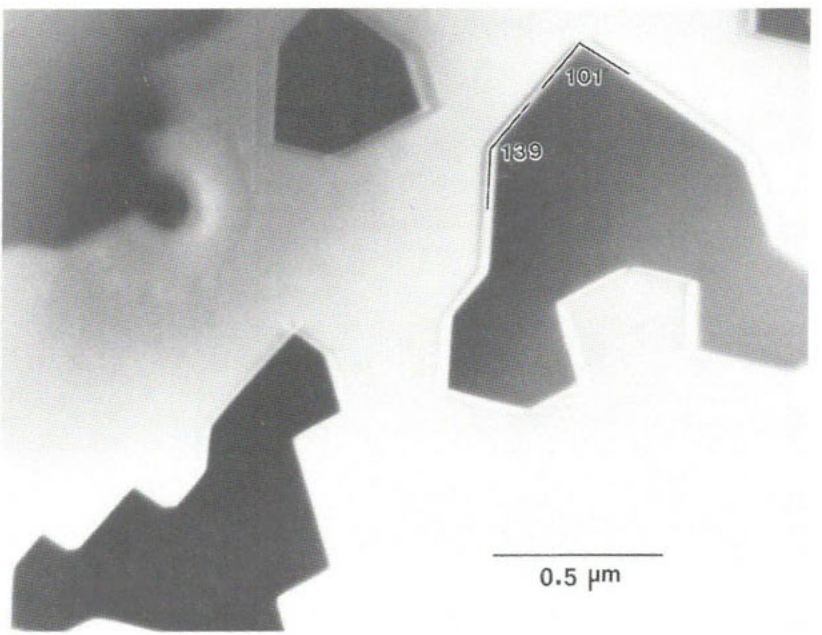


Figure 7. A dark-field (**g** = 301) image of α-quartz below the transition temperature. The two Dauphiné twin orientations appear as light and dark domains. These domains are polygonal, and boundary wall intersections are either 101° or 139°. (Courtesy of Hongwu Xu)

EBSCOhost - printed on 2/13/2023 4:48 AM via . All use subject to https://www.ebsco.com/terms-of-use

based on symmetry and strain require that the angle between boundary walls equal $120\pm2\varepsilon^{o}$, where ε is the angle between the boundary and the *a* axis (Walker, 1983; Walker and Gooding, 1985; Van Landuyt et al., 1985). As crystals are cooled from the α-β transition to room temperature, ε decreases from 9.5 to 3 (Yamamoto et al., 1988).

Electrical properties and stress. Dauphiné twins sometimes are called electric twins, because the electrically polarized diad axes normal to *c* in the two Dauphiné twin orientations are rotated 180° relative to each other. As a result, the piezoelectric charges induced in one set of twins by compression normal to *c* will cancel the electric charges created in the other. To be useful as oscillators, quartz crystals must be "detwinned"—that is, converted entirely to one of the two Dauphiné orientations (see chapter by Beall). [Brazil twins also will neutralize the piezoelectric charge.] Frondel (1945) describes his somewhat unsuccessful efforts to detwin quartz crystals by merely cycling specimens about the α-β transition temperature; these attempts were foiled by surprisingly strong memory effects exhibited by the twin boundaries (Heaney and Veblen, 1991a).

Schubnikov and Zinserling (1932) demonstrated that at room temperature α-quartz will form Dauphiné twins under an applied stress. This observation proved useful for materials scientists who found that the application of non-hydrostatic stress on defective crystals heated over 400°C proves to be an effective detwinning procedure (Wooster et al., 1947). Unfortunately for petrologists, the production of Dauphiné twins by stress prevents their use as geothermometers. However, Tullis and Tullis (1972) have found that mechanical twinning may give rise to preferred orientation textures in stressed quartzite (see chapter by Wenk), and mineral physicists have studied stress-induced twinning in α-quartz as an example of ferrobielastic behavior in geological materials.

Ferrobielasticity. α-quartz is a secondary ferroic (Aizu, 1973). The twins do not differ in terms of their spontaneous strain, as is the case with primary ferroics, but they do exhibit differences in elastic compliance. In α-quartz, the compliance coefficient s_{14} has opposite signs in the two Dauphiné configurations. As a result, an oriented stress on a crystal of α-quartz will generate different strains within the two twins. At a certain critical level, the stress will reverse the orientations within individual Dauphiné twin domains. This critical stress is known as the "coercive stress," and the orientational transformation is described as "switchover."

Acoustic and visual observations of ferrobielastic behavior in quartz by Laughner et al. (1979) indicate that the stress needed to twin quartz may be as low as 0.9×10^8 N/m^2 (= 0.9 kbar) at room temperature. As a uniaxial compressive stress approaches coercive levels, the Dauphiné twins adopt a striping pattern (Markgraaff, 1986). Switchover occurs at 2 to 5 kbar (Laughner et al., 1979; Bertagnolli et al., 1979), although the coercive stress decreases as the angle between the stress axis and [001] increases (Markgraaff, 1986). Likewise, the coercive stress is lower at higher temperatures, allowing specific domain patterns to be induced by laser heating (Anderson et al., 1976). Since the strength of quartz on compression is 20 to 30 kbar, Dauphiné twinning generally precedes brittle fracture. Ferrobielastic behavior is not readily detectable in fine-grained geological samples, such as agatoid chalcedony (Laughner et al., 1982). McLellan (1978) provides a thermodynamic treatment of Dauphiné twinning in stressed quartz.

The α-β quartz transition

Dauphiné microtwins. Detailed reviews of the α-β quartz transition may be found in Dolino (1990) and Heaney and Veblen (1991b). Although the structural changes

EBSCOhost - printed on 2/13/2023 4:48 AM via . All use subject to https://www.ebsco.com/terms-of-use

that attend the transformation appeared fairly straightforward after the work of Bragg and Gibbs (1925), anomalous behavior near the critical temperature had been detected by light scattering (Steinwehr, 1938; Yakovlev et al., 1956), Raman spectroscopy (Raman and Nedungadi, 1940; Kleinman and Spitzer, 1962; Shapiro and Cummins, 1968), and thermodynamic analysis (reviewed in Helgeson et al., 1978 and Ghiorso et al., 1979). The source of the peculiarities that attend the transition was first suggested by Young (1962), who inferred on the basis of high-temperature X-ray diffraction experiments that macroscopic Dauphiné twin domains are replaced by fine-scale microtwins as α-quartz transforms to β-quartz.

Proof of Young's (1962) conjecture was provided by Van Tendeloo et al. (1976) and Malov and Sonyushkin (1976), who observed the α-β quartz transition in situ with the transmission electron microscope. These groups found that as quartz is heated above the transition, large Dauphiné twins disperse into a mosaic of triangular microtwin prisms elongate parallel to *c* . Most surprisingly, Van Tendeloo et al. (1976) discovered that the prisms order into periodic honeycomb-like arrays, with the size of the microtwins decreasing with higher temperature (Fig. 8). Defect textures analogous to point defects and dislocations occur at the boundaries between arrays with unlike twin size to maintain continuity (Snoeck et al., 1986; Koh and Yamada, 1987). The Dauphiné twins do not transect Brazil twin walls, which serve as barriers between microtwinned regions (Van Goethem et al., 1977). Other defects in quartz, such as dislocations, create strain fields that pin the Dauphiné microdomains and stabilize them at temperatures below the critical point (Barber and Wenk, 1991).

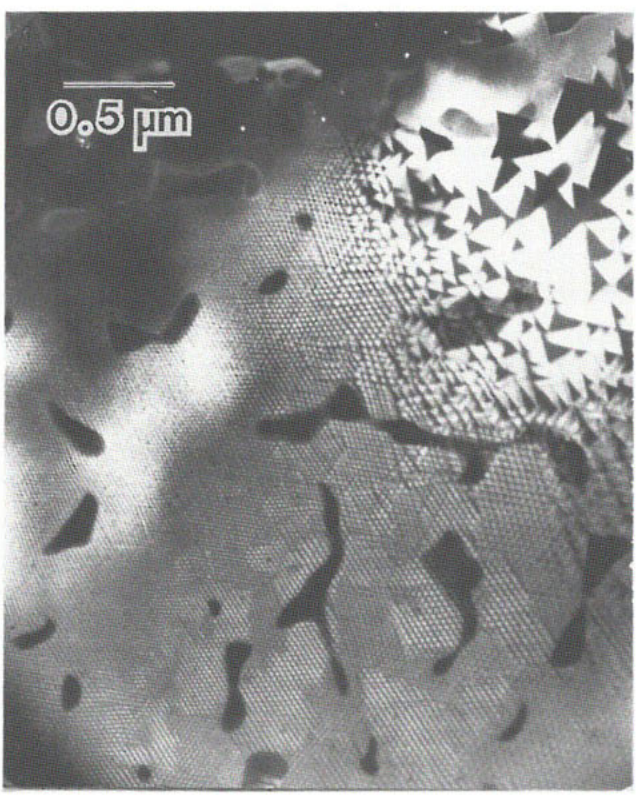


Figure 8. The intermediate phase of quartz. A temperature gradient exists across the specimen, with temperature increasing toward the lower left. Large Dauphiné twins can be seen to grade into triangular microtwins, which assemble into an ordered, honeycomb-like mosaic. Macrodomains appear as regions of differing contrast within the mosaic. Dark, irregularly shaped blobs are grains of Cu that were deposited on the specimen in an attempt to decrease thermal gradients. (From Heaney and Veblen, 1991b)

EBSCOhost - printed on 2/13/2023 4:48 AM via . All use subject to https://www.ebsco.com/terms-of-use

Intermediate phase. Höchli and Scott (1971) proposed that the transition from α to β quartz might be described by a Landau expansion in terms of an order parameter that corresponds to the tetrahedral tilt angle θ. More sophisticated Landau expansions (Grimm and Dorner, 1975; Banda et al., 1975; Bachheimer and Dolino, 1975) improved the agreement with experimentally measured physical parameters and supported the first-order nature of the transition. However, these models could not account for the microtwinned mosaic observed by TEM methods. Aslanian and Levanyuk (1979, 1984) and Aslanyan et al. (1983) solved this problem by recasting the Landau free energy with a term that couples the order parameter to spontaneous strain. This revised expression predicts the existence of two stable incommensurate phases between the stability fields of α- and β-quartz. One of the proposed intermediate structures exhibits periodicity in three directions (a so-called $3q$-phase), and the other is periodic in only one direction (a $1q$-phase).

Bachheimer (1980) provided experimental verification for the occurrence of at least one stable intermediate phase by monitoring thermal expansion, elastic compliance, and birefringence simultaneously about the transition. He found evidence for a first-order transition from α-quartz to an intermediate phase at 573°C (= T_c) and a second-order transition to β-quartz at 574.3°C (= T_i). Direct confirmation of the first-order nature of the phase transition between α-quartz and the intermediate phase has since been offered by differential scanning calorimetry (Zeyen et al., 1983; Drebushchak and Dement'ev, 1993), differential thermal analysis (Raz, 1983), and ac-calorimetry (Hatta et al., 1985). These results also are consistent with hysteresis effects reported in Raman experiments (Shapiro and Cummins, 1968) and γ-ray (Bastie and Dolino, 1985) and neutron (Dolino et al., 1984b) diffraction studies.

Researchers immediately identified the honeycomb mosaic observed by Van Tendeloo et al. (1976) with the $3q$ intermediate phase predicted by Aslanian and Levanyuk (1979). Zeyen et al. (1983) and Dolino et al. (1984a,b) demonstrated the incommensurate quality of this phase using neutron scattering techniques. These studies focused on the satellite diffraction intensities associated with the superperiodic microtwins, and they found that the reciprocal space vector from a primary spot to a satellite spot, denoted as q_o, decreases from 0.029 a^* at T_i to 0.015 a^* at T_c. This continuous variation corresponds to an increase in the microtwin periodicity from 150 Å at T_i to 288 Å at T_c. Subsequent γ-ray experiments (Bastie and Dolino, 1985) revealed maximum twin periodicities of 850 Å near T_c.

The satellite diffractions associated with the $3q$ incommensurate phase have been imaged using X-ray transmission topography (Gouhara and Kato, 1984; 1985a,b) and transmission electron microscopy (Snoeck et al., 1986; Yamamoto et al., 1988; Heaney and Veblen, 1991b). The X-ray topography experiments demonstrated that the satellite spots are actually split (Fig. 9); within the $hk0$ reciprocal lattice plane, q_o deviates from

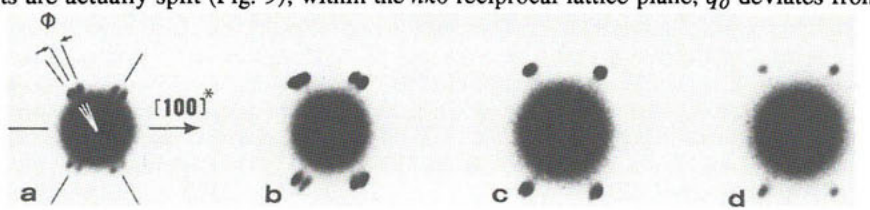


Figure 9. The 100 spot surrounded by split satellite diffractions. This splitting is produced by the relative rotation of the two sets of macrodomains in the incommensurate phase. As temperature increases from (a) to (d), the angle 2φ of splitting decreases and the satellite pairs merge. (Reprinted with permission from Yamamoto et al., 1988).

EBSCOhost - printed on 2/13/2023 4:48 AM via . All use subject to https://www.ebsco.com/terms-of-use

a^* by an angle $\pm\varphi$, which decreases on heating from $\varphi = 11^\circ$ near T_c to 1° near T_i. These results indicate that the $3q$ incommensurate phase contains two sets of macrodomains that are rotated by $2\varphi^\circ$ relative to each other, as was predicted by Walker (1983). Van Landuyt et al. (1985) delineate the macrodomains on TEM images of the incommensurate phase, and they also are visible in Figure 8. These macrodomains may be the large-scale striations (tens of μm in width) observed in X-ray topographs of the intermediate phase (Gouhara and Kato, 1985b), and they also may explain the cylindrical structures detected in the light scattering experiments of Dolino (1980).

The transition from a $3q$ to a $1q$ state may be induced by non-hydrostatic stress, and the appearance of the $1q$ incommensurate phase (which has stripes of Dauphiné microtwins) has been observed by elastic neutron scattering (Dolino et al., 1987), synchrotron X-ray diffraction (Zarka et al., 1988), and in situ transmission electron microscopy (Snoeck and Roucau, 1992). Bastie et al. (1988) offer evidence for a $3q$ to $1q$ transition at zero stress by high resolution neutron diffraction. This study finds no existence of macrodomains in the $1q$ incommensurate phase (so that $\varphi = 0$), which appears to be stable over a few hundredths of a degree. The observed coexistence of the $3q$ and the $1q$ phase supports the possibility that the transition is first order.

Geological implications. The discrete volume expansion caused by the first-order transition (Ghiorso et al., 1979) has been directly observed to anneal cracks in rhyolitic quartz (Massare et al., 1988), and it gives rise to strong low-frequency acoustic emissions (i.e., mineralogical screams) that are characteristic for different rock types (Schmidt-Mumm, 1991). The transition temperature decreases with increased impurity content (Keith and Tuttle, 1952; Smith and Steele, 1984) and with smaller grain size (Sosman, 1965; Dubrovinsky and Piloyan, 1986), although prolonged grinding lowered the inversion temperature by only 0.7°C (Moore, 1986). In addition, Molenaar and de Jong (1987) observe that the range of temperatures over which the α-β transition occurs depends upon paragenesis: Authigenic and vein quartz exhibit a broad range of transition temperatures in comparison with igneous and metamorphic quartz, perhaps because low-temperature quartz precipitates slowly in environments that are chemically diverse.

Real structure of β-quartz

What is the physical structure of β-quartz? Not long after Bragg and Gibbs (1925) reported their solution to this question, Buerger (1934) suggested that when framework structures are heated above a critical temperature, individual tetrahedra may experience dynamic group rotations. According to this model of displacive transitions (Buerger, 1951), the actual structure of quartz above 574.3°C may not conform to the idealized static image presented in Figure 2a. Instead, the hexagonal symmetry observed in early X-ray diffraction analyses may reflect temporal disorder, in which each atom oscillates between two positions that correspond to the Dauphiné twin configurations. If so, then β-quartz is not merely a spatial average but a time average of the Dauphiné twins, and each atom is associated with not one but two potential minima. The transition from β-quartz to α-quartz might then be perceived as an ordering event, in which the initially random motions of fluctuating tetrahedra begin to correlate over macroscopic distances as T_c is approached from higher temperatures, until the tetrahedra lock into one of the Dauphiné orientations at the critical temperature itself.

Clusters of microtwins. At present, the true nature of β-quartz remains unresolved, because different analytical techniques have generated results that are apparently contradictory. Dark-field TEM images of quartz near T_i are inherently ambiguous because the intermediate phase evolves from a domain-dominated structure to a boundary-

EBSCOhost - printed on 2/13/2023 4:48 AM via . All use subject to https://www.ebsco.com/terms-of-use

dominated one as the microtwins grow finer with higher temperature. Consequently, the imaging contrast becomes dramatically weaker as the twins decrease in size. Nevertheless, disorder within the β phase is indicated by the dynamical quality of the microtwins in the incommensurate phase and the aggregation of microdomains to form macrodomains as quartz is cooled below T_c (Van Tendeloo et al., 1976). Moreover, satellite spots associated with the microtwins have been observed to persist as diffuse intensities more than 200°C above T_i in electron diffraction patterns (Heaney and Veblen, 1991b). A refinement of β-quartz by single-crystal neutron diffraction yielded better results with a split-atom model that mimics disorder (Wright and Lehmann, 1981), and NMR spectroscopic data is consistent with oscillation of tetrahedra above the transition (Spearing et al., 1992). Recently, a number of lattice dynamical models have successfully simulated the α-β transition by assuming a dynamical disordering in β-quartz (Silvi et al., 1990; Tsuneyuki et al., 1990; Tautz et al., 1991).

Ordered single-potential model. By contrast, most spectroscopic analyses of the transition support an ordered structure for β-quartz. As detailed in the chapter by Dolino and Vallade, the α-β quartz transition is driven by a dynamical soft mode (Raman and Nedungadi, 1940; Axe and Shirane, 1970; Boysen et al., 1980; Tezuka et al., 1991) that couples briefly with a transverse acoustic mode to generate the incommensurate phase (Aslanian and Levanyuk, 1979). Observations of the soft mode about T_c are consistent with a simple displacive transition. In addition, Salje et al. (1992) report the disappearance of hard modes above T_i that are symmetrically forbidden in ordered β-quartz; these modes should be detected if β-quartz consists of clusters of α-quartz that persist over time scales longer than phonons. Likewise, unlike neutron scattering studies, high-temperature X-ray refinements of β-quartz produced better results for an ordered single-potential model (Young, 1962; Kihara, 1990). Kihara (1993) also reports a lattice dynamical calculation for β-quartz that agrees with his diffraction data.

The nature of this dynamical disorder remains an unanswered and exciting problem, and it applies not only to β-quartz but to the high-temperature modifications of tridymite and cristobalite.

STRUCTURE OF TRIDYMITE

Stability of tridymite

In his pioneering efforts to determine phase equilibria relationships within the silica system, Fenner (1913) observed that tridymite could be synthesized only with the aid of a "mineralizing agent" or flux, such as Na_2WO_4. When pure quartz is heated, it bypasses tridymite and transforms directly to cristobalite at ~1050°C (Mosesman and Pitzer, 1941). Early researchers also observed an extreme variability in powder X-ray diffraction and differential thermal analyses of natural and synthetic tridymite (see Sosman, 1965). The anomalous thermochemical properties of tridymite prompted some researchers to suggest that tridymite is not a pure silica polymorph with a true stability field within the silica system (Flörke, 1955; Eitel, 1957). In response to these ideas, Hill and Roy (1958) successfully synthesized tridymite from transistor-grade silicon and high-purity silica gel using only H_2O and D_2O as fluxes; confirmation of these results by subsequent researchers (e.g., Sato, 1963a) has convinced most scientists of the legitimacy of tridymite as a stable phase of silica.

Crystal structure

Determination of the structures of the low-temperature polymorphs of tridymite has proved one of the greater challenges in the crystal structure analysis of minerals. The difficulties are manifold: Tridymite almost invariably occurs as fine-grained crystals with

EBSCOhost - printed on 2/13/2023 4:48 AM via . All use subject to https://www.ebsco.com/terms-of-use

Table 3. Lattice parameters for synthetic/meteoritic tridymite

Type	Space Group	Temp Range (°C)	*a* (Å)	*b* (Å)	*c* (Å)	β (°)
HP	$P6_3/mmc$	>380	5.05 $=[100]_{HP}$	5.05 $=[010]_{HP}$	8.28 $=[001]_{HP}$	---
OC	$C222_1$	190-380	8.73 $=[210]_{HP}$	5.04 $=[010]_{HP}$	8.28 $=[001]_{HP}$	---
OS	Super-structure	150-190	95-65 $=n[210]_{HP}$	5.02 $=[010]_{HP}$	8.18 $=[001]_{HP}$	---
OP	$P2_12_12_1$	110-150	26.65 $=3[210]_{HP}$	5.02 $=[010]_{HP}$	8.15 $=[001]_{HP}$	---
MC	Cc	<110	18.49 $=[212]_{HP}$	4.991 $=[010]_{HP}$	25.83 $=-3[210]_{HP}$	117.75
MC_{DB}	Cc	<110	18.494 $=[212]_{HP}$	4.991 $=[0\bar{1}0]_{HP}$	23.758 $=2[21\bar{1}]_{HP}$	105.79

Note: All data from Nukui and Nakazawa (1980) except for MC_{DB} from Dollase and Baur (1976)

growth twins related by a sixfold rotation about the morphological pseudohexagonal axis (Dollase and Baur, 1976; Tagai et al., 1977). Tridymite also exhibits a high degree of stacking disorder, often due to intimate intergrowth with cristobalite. In addition, Smelik and Reeber (1990) demonstrated by a continuous X-ray diffraction study with increasing temperature that terrestrial tridymite experiences an almost uninterrupted series of structural modifications upon heating. Nevertheless, over the past three decades mineralogists have succeeded to a remarkable extent in characterizing this difficult mineral system (see review by Wennemer and Thompson, 1984a).

The different nomenclatures used to describe the modifications of tridymite are nearly as complicated as its crystal chemistry. This chapter will employ the two-letter terminology introduced by Nukui et al. (1978), in which the first letter signifies the crystal system of the polymorph and the second letter describes the unit cell type. The various polymorphs will be described in order of decreasing temperature and increasing complexity (Table 3).

HP-tridymite. The structure of ideal high-temperature tridymite is based upon a fundamental stacking module in which sheets of silica tetrahedra are arranged in hexagonal rings (Fig. 10). The tetrahedra within these rings point alternately above and below the plane defined by the basal oxygen atoms, and the sheets are stacked such that the hexagonal rings directly overlie one another, creating continuous tunnels normal to the sheets. Bonding of successive sheets in tridymite is achieved by mirror reflection of a given sheet relative to its neighboring sheets above and below, and the stacking sequence in tridymite is denoted by a doubled periodicity of the fundamental module...ABABAB...along the stacking direction, where A refers to a single sheet and B is its reflected equivalent (Fig. 11).

As originally determined by Gibbs (1927), HP-tridymite belongs to space group $P6_3/mmc$ with *c* normal to the layers, and it is isostructural with ice-*IH*, such that Si replaces O in ice and O replaces H (Fig. 11 and Table 4). Additional instances of structural

EBSCOhost - printed on 2/13/2023 4:48 AM via . All use subject to https://www.ebsco.com/terms-of-use

analogs in the SiO_2 and the H_2O systems are described in the chapter by Higgins (this volume). The stacking configuration in ideal HP-tridymite is destabilized by certain features. Planar basal oxygen atoms lie directly over each other in a cis orientation, thereby maximizing repulsive forces (Fig. 12); by contrast, the trans configuration minimizes repulsion (Flörke, 1967). In addition, the Si-O-Si bond angle is 180°, which Gibbs et al. (1981) have shown to be extremely unfavorable.

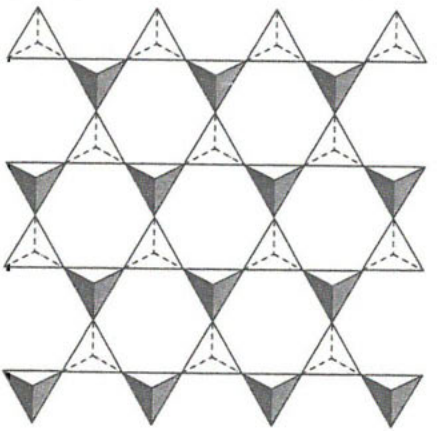
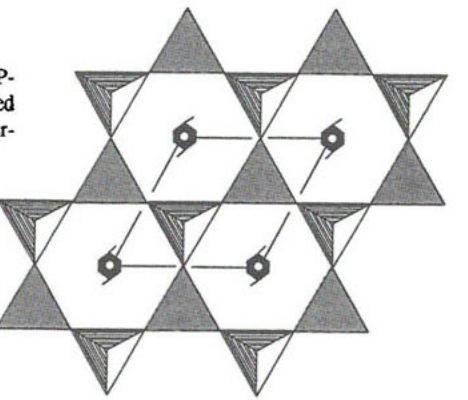


Figure 10. Diagram of the tetrahedral sheet that serves as the fundamental stacking module in tridymite and cristobalite. In tridymite, the layers are stacked in a doubled AB sequence parallel to *c*, and in cristobalite the sheets create a tripled ABC repeat along [111].

Figure 11. Projection of the structure of ideal HP-tridymite along *c*. Adjacent tetrahedral layers are related by mirror symmetry, and the six-membered rings superimpose exactly.



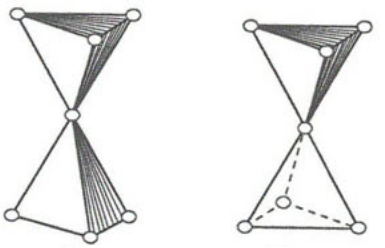


Figure 12. The cis and trans orientations of paired tetrahedra. HP-tridymite tetrahedra adopt the less stable cis orientation, which maximizes repulsion among basal oxygen ions. In β-cristobalite, the tetrahedra occur in the trans orientation.

Table 4. Structural data for HP-tridymite

Space Group		*P*63/*mmc*	
Unit Cell			
a (Å)		5.052(9)	
c (Å)		8.27(2)	
V (Å^3)		182.8(3)	
ρ (g/cm^3)		2.183	
Atom	x	y	z
Si(1)	1/3	2/3	0.0620(4)
O(1)	1/3	2/3	1/4
O(2)	1/2	0	0

Note: Data for 460°C from Kihara (1978)

EBSCOhost - printed on 2/13/2023 4:48 AM via . All use subject to https://www.ebsco.com/terms-of-use

Kihara et al. (1986a,b) examined the temperature coefficients of the oxygen atoms in HP-tridymite, and they have found that at 460°C the probability density function (PDF) for oxygen is circular about the nominal oxygen position. These circles have a radius of 0.4 Å, and they are oriented normal to the Si-Si bond vectors. The displacement of oxygen atoms from the central position effectively decreases the mean Si-O-Si bond angle from 180° to 149.2°, with a mean Si-O distance of 1.607 Å. In addition, the displacement of the oxygen atoms from their central positions introduces a transient ditrigonal character to the ring structure.

Kihara et al. (1986a,b) could not determine with certainty whether the annular PDFs contain minima or are perfectly uniform. If the oxygen atoms librate over circular arcs separated by low saddles, then HP-tridymite may consist of microdomains with 6 possible configurations that are statistically distributed with equal probability (Kihara, 1980); the local symmetry for the domain structure would conform to space group $Cc2m$ (Kihara, 1981). In their ^{29}Si MAS NMR study of the phase transitions in tridymite, Xiao et al. (1993) argue for correlated fluctuations of oxygen atoms in HP- and OC-tridymite with a frequency greater than 1 kHz. Alternatively, the absence of saddles within the PDF annuli would indicate that oxygen atoms in HP-tridymite rotate randomly about a central idealized position.

OC-tridymite. When HP-tridymite is cooled below ~380°C, the silica framework experiences a slight distortion, which lowers the space group symmetry from $P6_3/mmc$ to $C222_1$. As first revealed by Dollase (1967), during this transition pairs of tetrahedra in cis configuration are tilted from the c-axis in such a way that the tetrahedral sheets are offset in the b-axis direction (Fig. 13). Thus, this transition destroys the mirror symmetry parallel to (001) that relates the A and B stacking modules in HP-tridymite. The appearance of polysynthetic twin lamellae may be observed by light optical microscopy during the HP- to OC-tridymite transition (Nukui et al., 1978), and the transition is manifested by changes in intensities of certain X-ray diffractions (Kihara, 1978). However, differential scanning calorimetry does not reveal the HP-OC transformation (Wennemer and Thompson, 1984b; de Dombal and Carpenter, 1993), and single-crystal X-ray diffraction provides no evidence for hysteresis (Nukui et al., 1978).

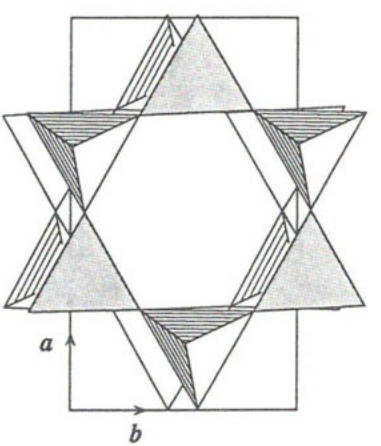


Figure 13. A projection of the structure of OC-tridymite along the c-axis. Tilting of tetrahedral pairs by 8° relative to c displaces adjacent tetrahedral sheets along b. (After Dollase, 1967)

EBSCOhost - printed on 2/13/2023 4:48 AM via . All use subject to https://www.ebsco.com/terms-of-use

Based on their analysis of lattice parameters using Guinier powder X-ray diffraction, de Dombal and Carpenter (1993) proposed that the transition from HP- to OC-tridymite occurs as *two* steps. This study documented a convergence in the lengths of the *a*-axes at 350°C, corresponding to the transition from an orthorhombic to a hexagonal cell. However, the rates of increase of the *c*-axis and volume with increasing temperature change at 465°C. Although the nature of this higher temperature transformation remains uncertain, it may be relevant that Kihara et al. (1986a) observed that the annular PDF distribution for the oxygen atoms in tridymite changed from a uniform symmetry at 460°C to a slightly bimodal asymmetry at 420°C. This bimodality became strongly evident in OC-tridymite at 220°C. Thus, it is possible that tridymite becomes metrically hexagonal at ~380°C, but that true hexagonal symmetry with respect to the structure is achieved at ~465°C.

OS-tridymite. Sato (1963b) observed that in the temperature range of 100° to 260°C, orthorhombic tridymite exhibits a superstructure along the *a*-axis direction of the orthorhombic cell (or the pseudohexagonal [210] direction). Subsequently, Dollase (1967) reported similar superperiodicities along a^* in orthorhombic tridymite from the Steinbach meteorite between 107° and 180°C with modulations that ranged from 105 to 65 Å with increasing temperature, and Nukui et al. (1978) observed a superstructure between 150° and 190°C in synthetic tridymite with a periodicity between 95 and 65 Å. Nukui et al. (1979) examined this incommensurate phase by X-ray precession between 150° and 190°C in 5°C steps and refined the structure in a 4-dimensional space group. Their results revealed amplitudes for atomic displacements relative to each atom in the unit cell that ranged from 0.04 Å to 0.56 Å. These displacements tend to transform the (time-averaged?) hexagonal rings within the tetrahedral sheets to ditrigonal six-membered rings. The transition from OC- to OS-tridymite may be visible as a broad peak from 165° to 197°C in DSC profiles (Thompson and Wennemer, 1979).

OP-tridymite. The ditrigonal distortions within the OS superstructure discerned by Nukui et al. (1979) presage the transformation to OP-tridymite, which belongs to space group $P2_12_12_1$. This polymorph is stable between ~110°C and ~150°C, and it represents a more advanced state of framework collapse. As determined by Kihara (1977), in OP-tridymite two-thirds of the tetrahedral rings are ditrigonal and one-third are oval in shape (Fig. 14). Within a single sheet, any two ditrigonal rings may adopt two orientations relative to each other: They may "point" in the same direction, or they may point in opposite directions. These orientations are related by a 180° rotation, and they are denoted as D and D' rings. Similarly, oval rings may be aligned parallel to one another, or their long axes may lie 90° to each other. When perpendicular, oval rings are differentiated as O and O' rings. Within OP tridymite, along the *a*-axis in Kihara's (1977) cell setting, the sequence of ring configurations is D' O' D D O D'. The fundamental stacking modules in OP tridymite are aligned such that identical types of distorted rings lie on top of one another.

MC-tridymite. At ~110°C, OP-tridymite transforms to a monoclinic structure with space group *Cc*. This transformation appears as a major lambda-type transition in differential scanning calorimetry (Mosesman and Pitzer, 1941; Thompson and Wennemer, 1979), and it is marked by a large hysteresis in single-crystal X-ray and optical studies (Nukui et al., 1978). The structure for this tridymite modification was solved simultaneously by Kato and Nukui (1976) and Dollase and Baur (1976), who obtained identical results within experimental error (Baur, 1977). Like OP-tridymite, the tetrahedral rings of the MC polymorph contain ditrigonal and oval rings in a 2:1 ratio. Moreover, the sequence of rings within a single sheet of OP-tridymite is the same as that within MC-tridymite. However, in contrast to OP-tridymite, the rings within a given layer do not

EBSCOhost - printed on 2/13/2023 4:48 AM via . All use subject to https://www.ebsco.com/terms-of-use

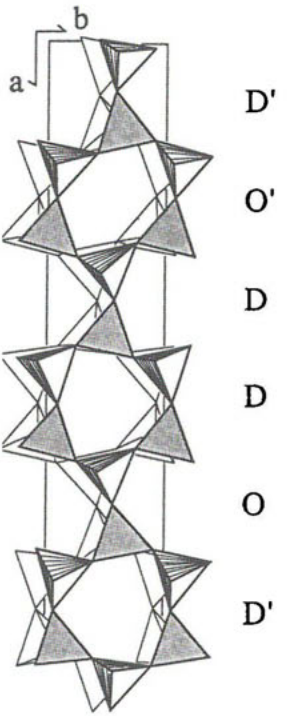


Figure 14. Projection of the structure of OP-tridymite along the *c*-axis. Framework collapse induces distortions of hexagonal rings to ditrigonal (D) and oval (O) configurations. Ditrigonal rings pointing in opposite directions are de-noted by D and D'. Oval rings oriented perpendicular to each other are denoted by O and O'. In OP-tridymite, identical rings are stacked upon one another along *c*. In MC-tridymite, different ring configurations are superimposed. (After Kihara, 1977)

overlie rings of the same type; along any single channel parallel to the stacking direction, the sequence is: O' O D' D D' D O O' D D' D D'. This stacking of unlike rings on top of one another forces a greater number of tetrahedral pairs that are aligned parallel to the stacking direction to adopt an orientation closer to the energetically favorable trans configuration (Wennemer and Thompson, 1984a).

MX-1 and PO-n tridymite. Most MC-tridymite occurs within meteoritic and synthetic samples, although Kawai et al. (1978) report MC-tridymite within the cavities of natural dacites. The thermochemical properties of different MC-tridymite specimens are fairly uniform. By contrast, low-temperature terrestrial tridymite exhibits an impressive diversity in structure and transition behavior (Graetsch and Flörke, 1991). Two distinct classes of room-temperature terrestrial tridymite have been described—MX-1 and PO-n tridymite. PO-n tridymite is pseudo-orthorhombic and characterized by different stacking periodicities among the fundamental modules. PO-1 tridymite is essentially identical with OP-tridymite, having a single AB stacking periodicity such that c = 8.20 Å. Superstructures based on pseudo-orthorhombic cells are known for n = 1, 2, 5, 6, and 10 (Table 5). Konnert and Appleman (1978) refined PO-10 tridymite from Plumas County, CA in the triclinic space group $F1$, and they found that all of the hexagonal rings are oval (Fig. 15). Due to the absence of large ditrigonal rings, the molar volume of PO-10 tridymite is 4.1% lower than that of meteoritic tridymite, and the isotropic temperature factors for Si and O in PO-10 tridymite tend to be lower than the corresponding values for meteoritic tridymite, indicating less positional disorder. Consequently, Konnert and Appleman (1978) suggest that PO-10 tridymite is thermodynamically more stable than MC-tridymite. The relationship between the superperiodicity (i.e., the value for n) and depositional environment remains unclear.

EBSCOhost - printed on 2/13/2023 4:48 AM via . All use subject to https://www.ebsco.com/terms-of-use

Table 5. Reported cells for room-temperature terrestrial tridymite

Type	*a* (Å)	*b* (Å)	*c* (Å)	β (°)	Source
PO-2	9.88 $=2[100]_{HP}$	17.10 $=2[120]_{HP}$	16.30 $=2[001]_{HP}$	90	Gibbs(1927)
PO-2	9.96 $=2[100]_{HP}$	17.18 $=2[120]_{HP}$	16.29 $=2[001]_{HP}$	90	Goetz(1962)
PO-2	17.072 $=2[210]_{HP}$	9.923 $=2[010]_{HP}$	16.291 $=2[001]_{HP}$	90	Smelik & Reeber(1990)
PO-5	9.91 $=2[100]_{HP}$	17.18 $=2[120]_{HP}$	40.78 $=5[001]_{HP}$	90	Lukesh & Buerger(1942)
PO-5	17.21 $=2[210]_{HP}$	9.94 $=2[010]_{HP}$	40.92 $=5[001]_{HP}$	90	Sato(1964)
PO-5	17.21 $=2[210]_{HP}$	9.93 $=2[010]_{HP}$	40.91 $=5[001]_{HP}$	90	Nukui et al. (1980)
PO-6	5.01 $=[100]_{HP}$	25.70 $=3[120]_{HP}$	48.60 $=6[001]_{HP}$	90	Shahid & Glasser(1970)
PO-10	9.91 $=2[100]_{HP}$	17.18 $=2[120]_{HP}$	81.57 $=10[001]_{HP}$	90	Lukesh & Buerger(1942)
PO-10	4.975 $=[100]_{HP}$	8.606 $=[120]_{HP}$	81.967 $=10[001]_{HP}$	90	Tagai & Sadanaga(1972)
PO-10	9.94 $=2[100]_{HP}$	17.17 $=2[120]_{HP}$	81.60 $=10[001]_{HP}$	90	Gardner & Appleman(1974)
PO-10	9.932 $=2[100]_{HP}$	17.216 $=2[120]_{HP}$	81.864 $=10[001]_{HP}$	90	Konnert & Appleman(1978)
MX-1	17.28 $=2[210]_{HP}$	10.04 $=2[010]_{HP}$	8.2 $=[001]_{HP}$	91.5	Nukui & Nakazawa(1980)
MX-1	5.0079 $=[100]_{HP}$	8.6004 $=[120]_{HP}$	8.2169 $=[001]_{HP}$	91.512	Hoffmann et al.(1983)

Note: After Nukui & Nakazawa (1980) and Smelik (1987)

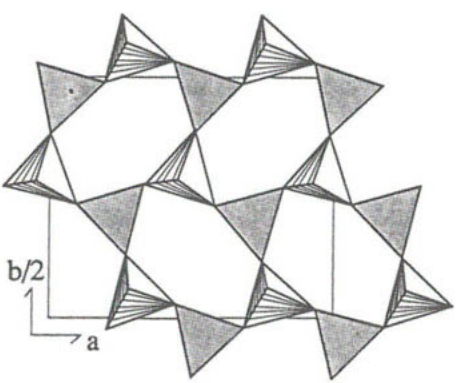


Figure 15. Projection along *c* of one of the ten tetrahedral sheets that comprise PO-10 tridymite. All rings adopt an oval configuration. Note the topological similarity with α-cristobalite in Figure 19. (After Konnert and Appleman, 1978)

EBSCOhost - printed on 2/13/2023 4:48 AM via . All use subject to https://www.ebsco.com/terms-of-use

Nukui and Nakazawa (1980) reported a terrestrial tridymite polymorph that is thermochemically distinct from both MC-tridymite and the PO series. This modification, called MX-1 tridymite, is monoclinic ($\beta = 91.50^\circ$) at room temperature (though a full refinement has not been reported), and it transforms to a pseudo-orthorhombic PO-1 tridymite at ~63°C; different specimens invert over a range from 35 to 80°C. Hoffmann et al. (1983) determined that MX-1 tridymite may be produced either by quenching MC-tridymite from temperatures between 110 and 160°C to -10°C or by exerting uniaxial pressure on MC-tridymite. In fact, the process of grinding MC-tridymite for powder X-ray diffraction is sufficient to effect the transition to the MX-1 modification. In addition, Hoffmann et al. (1983) revealed by single-crystal XRD that MX-1 tridymite exhibits an incommensurate superstructure. For the cell setting in Table 5, this modulated phase produces satellite reflections at $(h \pm nq_1, k, l \pm nq_2)$, with $q_1 = 0.663$, $q_2 = 0.498$ and n = 1,2.

Transmission electron microscope investigations of low-temperature tridymite have documented microstructural complexities that partially account for its variable transition behavior (Fig. 16). Carpenter and Wennemer (1985) observed that beam-heating always transforms MX-1 tridymite to PO-n tridymite, but that heating and cooling PO-n tridymite induces the formation of different superstructures. Similarly, Kim et al. (1992) reported that tridymite samples from different sources manifest varying degrees of stacking disorder, as indicated by streaking along c^* in electron diffraction patterns. In a study of twin relationships, Ashworth (1989) observed abundant pseudohexagonal twin boundaries related by 60° or 120° in PO-10 tridymite; for these twins, the composition planes are oriented parallel to the layer plane. By contrast, boundaries between PO-10 tridymite and MC-tridymite are curved, probably due to the misfit created by the mixture of oval and ditrigonal rings in MC-tridymite. The exclusive occurrence of oval rings in PO-10 tridymite may also explain the observation that α-cristobalite bonds only to PO-10 tridymite.

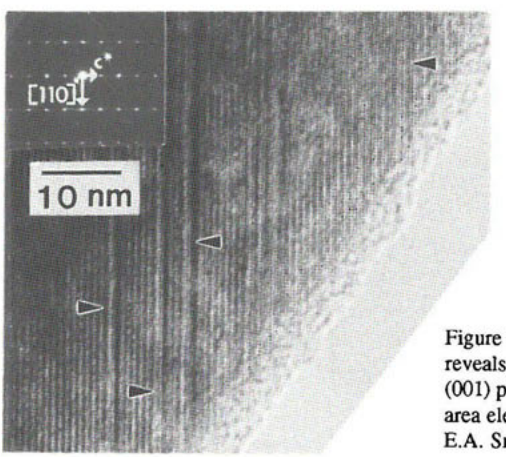


Figure 16. High-resolution TEM image of tridymite reveals numerous stacking faults (arrowed) along the (001) planes, giving rise to streaks along c^* in selected area electron diffraction patterns (inset). (Courtesy of E.A. Smelik)

THE STRUCTURE OF CRISTOBALITE

Crystal structure

Taking advantage of Mallard's (1890) observation that cristobalite transforms to an optically isotropic solid at high temperature, Wyckoff (1925) examined high or β-cristobalite by means of single-crystal X-ray diffraction by in situ heating methods. His

EBSCOhost - printed on 2/13/2023 4:48 AM via . All use subject to https://www.ebsco.com/terms-of-use

Table 6. Structural data for cristobalite

	β-Cristobalite	α-Cristobalite
Space Group	$Fd3m$	$P4_12_12$
Unit Cell		
a (Å)	7.12637	4.96937
c (Å)	—	6.92563
V (Å^3)	361.914	171.026
ρ (g/cm^3)	2.205	2.333
Atom Positions		
x(Si)	0	0.3006
y(Si)	0	0.3006
z(Si)	0	0
x(O)	1/8	0.2392
y(O)	1/8	0.1049
z(O)	1/8	0.1789

Note: Data for ideal β-cristobalite at 300°C and α-cristobalite at 30°C from Schmahl et al. (1992)

analysis revealed that β-cristobalite is a cubic analogue of diamond, such that Si occupies the same positions as C and O lies midway between any two Si atoms. The space group for this structure is $Fd3m$ (Table 6). Following the analysis of HP-tridymite by Gibbs (1927), it became clear that β-cristobalite and HP-tridymite are polytypic: Both minerals may be constructed from a fundamental stacking module that consists of sheets of silica tetrahedra in hexagonal rings (Fig. 10). Whereas in HP-tridymite the stacking sequence involves repetitions of two modules (AB), in β-cristobalite the stacking periodicity requires a three-layer repeat (ABC). As a result of this stacking arrangement, the hexagonal rings do not superimpose in β-cristobalite, and cristobalite lacks the continuous tunnels normal to the layers that are seen in tridymite (Fig. 17). With respect to the face-centered unit cell of β-cristobalite, these tetrahedral sheets are normal to [111]. Thus, tridymite and cristobalite bear a relationship similar to that between hexagonally and cubic closest packed solids.

Barth (1932a,b) recognized that the proposed Si-O bond distance of 1.54 Å in Wyckoff's model for β-cristobalite was too short in comparison with other silicates, but his investigations of β- and α-cristobalite resulted in erroneous space group assignments of $P2_13$ and $P2_12_12_1$, respectively. Nieuwenkamp (1935) determined that α-cristobalite actually has space group symmetry $P4_12_1$ (or $P4_32_1$), and in 1937 he confirmed $Fd3m$ as the symmetry for β-cristobalite. In addition, Nieuwenkamp (1937) argued that the O atoms in β-cristobalite rotate over a circular orbit with radius ~0.4 Å about the Si–Si bond vector.

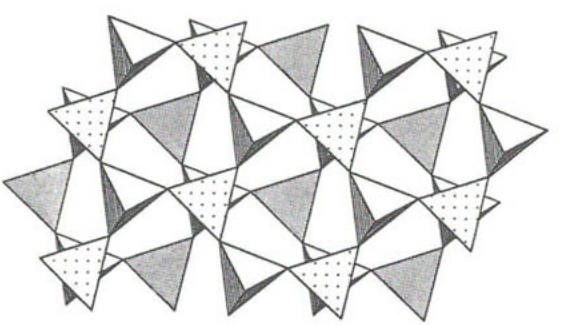


Figure 17. Projection of part of the structure of β-cristobalite normal to the stacking direction along [111]. Tetrahedra are arranged in trans orientation, and adjacent sheets block tunnels normal to sheets. Non-idealized ditrigonal ring configuration is shown. (Courtesy of E.A. Smelik)

EBSCOhost - printed on 2/13/2023 4:48 AM via . All use subject to https://www.ebsco.com/terms-of-use

The disordering of O along a circle about an idealized central position accounts not only for the apparent shortness of the Si-O bond length, it indicates an offset of the Si-O-Si bond angle from an energetically unfavorable 180°; displacement of O to the annular radius yields a Si-O distance of 1.61 Å and an Si-O-Si angle of ~148°.

Disorder in β-cristobalite. Recent studies of the high-temperature modification of cristobalite have revolved around the nature of the positional disorder involving the oxygen atoms. The questions are similar to those posed by β-quartz and HP-tridymite: Does β-cristobalite consist of transient clusters of α-cristobalite-like domains, or do the O annuli represent equipotential surfaces? In his single-crystal X-ray diffraction analysis of cristobalite over a range of temperatures, Peacor (1973) placed O atoms in the general position (192i) with 1/12th occupancy and found that they refined close to special positions 96h and 96g. Consequently, Peacor (1973) argued that the anions are distributed about the circles in non-random fashion, so that the tetrahedral rings in β-cristobalite have a ditrigonal configuration at any given point in time or space. Wright and Leadbetter (1975) achieved identical results, arguing for static disorder involving twin domains of a few unit cells with a local $I\bar{4}2d$ symmetry. Likewise, Hatch and Ghose (1991) employed Landau analysis to argue that the transition from α- to β-cristobalite has a fluctuation-induced first order character due to coupling between the order parameter (modeled as the departure of the Si-O-Si angle from 180°) and the spontaneous strain. Consequently, they suggest that β-cristobalite consists of microdomains that resonate among twelve distinct twin configurations.

By contrast, other studies weigh against the existence of α-like clusters within β-cristobalite. Hua et al. (1988) observed the appearance of intense streaking in electron diffraction patterns of cristobalite heated above T_c. Their Born-Karman force model for β-cristobalite indicates that these streaks represent planes of diffuse intensity in reciprocal space normal to the real space ⟨110⟩ direction. Thus, they assert that β-cristobalite is characterized by vibrational modes involving a concerted rotation of tetrahedra in columns parallel to ⟨110⟩. Hua et al. (1988) found no evidence for correlations among tetrahedra in different columns or for clusters of α-like domains. Likewise, lattice dynamical models based on Monte Carlo simulations of disorder in β-cristobalite (Welberry et al., 1989) and rigid unit modes (Swainson and Dove, 1993) produced uniform distributions of O atoms within annuli. Another Landau analysis of powder neutron diffraction data (Schmahl et al., 1992) employed only one scalar order parameter to describe the excess free energy of transition. Renormalization by strain did not produce a positive fourth-order term in the Landau expansion, suggesting that first-order behavior is not a result of strain coupling, contrary to the study of Hatch and Ghose (1991). This analysis indicates that correlated domains in β-cristobalite cannot be much larger than a unit cell in size.

As with β-quartz, spectroscopy results appear to counter the existence of fluctuating microdomains in β-cristobalite. Hard mode IR and Raman spectroscopy (Swainson and Dove, 1993) document the complete disappearance of symmetry-forbidden modes above T_c, and changes in the ^{27}Al quadrupole coupling constant over the transition in NMR spectroscopy (Phillips et al., 1993) suggest that if α-cristobalite-like domains occur in β-cristobalite, they exist for lifetimes shorter than 1 μs.

The α-β cristobalite transition. The phase transition between the low- and high-temperature modifications of cristobalite is thermochemically troublesome. The inversion temperatures displayed by different specimens range from 120 to 272°C (Sosman, 1965) with a hysteresis as large as 40°C (Phadke and Kshirsagar, 1986). For a single sample,

EBSCOhost - printed on 2/13/2023 4:48 AM via . All use subject to https://www.ebsco.com/terms-of-use

the transition temperature differs on heating and cooling. Peacor (1973) and Leadbetter and Wright (1976) followed changes in primary and satellite diffraction intensities with temperature and concluded that different transition temperatures characterize different subvolumes of a given crystal. These researchers also noted that the transition is accompanied by enormous changes in thermal expansion. The *a* and *c* axes of α-cristobalite increase rapidly at rates of 9.27×10^{-5} and 3.51×10^{-4} Å/°C, respectively, whereas in β-cristobalite *a* expands at only 2.08×10^{-5} Å/°C. This behavior translates to enormous spontaneous strains of -1.0% along *a* and -2.2% along *c* (Schmahl, 1993).

Examination of the α–β cristobalite transition using powder X-ray diffraction and DSC (Leadbetter and Wright, 1976; Schahl, 1993) reveals that the hysteresis does not result from limited reaction rates. The low- and high-temperature phases typically coexist over a ~20°C interval, and the degree of transformation does not alter even when samples are held at constant temperature for 17 h. However, the transformation is immediate upon temperature increase. This athermal transition behavior is reminiscent of martensitic transformations in metals, and Schmahl (1993) argues that the hysteresis arises from coherency strain at the interface between α- and β-cristobalite.

As delineated by Nord (1992), the transformation from space group $Fd3m$ to $P4_12_1$ (or $P4_32_1$) yields 12 distinct twin domains of three types: (1) three pseudomerohedral twins, related by the threefold axis lost during the transition from the cubic to tetragonal system; (2) two antiphase domains, related by the lost translation vector $1/2[110]_\beta$ $(= 1/2[111]_\alpha)$; and (3) two enantiomorphic merohedral twins, related by the lost inversion center. Pseudomerohedral twin and antiphase domains first were observed in TEM studies of lunar cristobalite (Fig. 18) by Christie et al. (1971). Withers et al. (1989) identified pseudomerohedral twins as lamellae bounded by $\{112\}_\alpha$ or $\{200\}_\alpha$ that are several microns thick. Unlike the Dauphiné twins of quartz, these pseudomerohedral twins exhibit no memory effects upon cycling about the transition temperature. Lally et al. (1978) obtained images in which antiphase domains appear as cylinders bounded by ragged edges. By dark-field TEM, Withers et al. (1989) observed striations measuring several hundred Å in thickness bounded by $\{10l\}_\alpha$. The nature of these domains is uncertain, but they may correspond to the enantiomorphs.

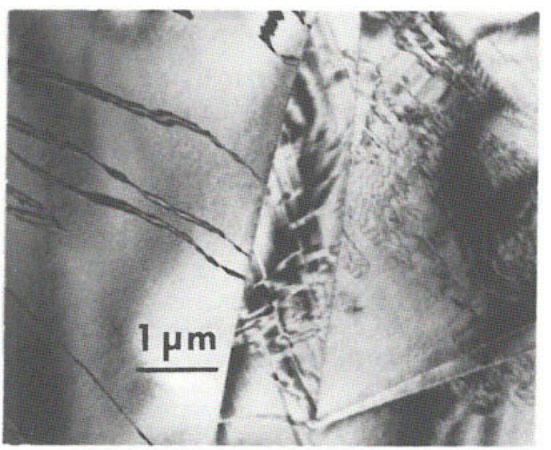


Figure 18. TEM image of pseudomerohedral twins with antiphase domains in late-crystallizing cristobalite from Apollo basalt 70017. (Courtesy of Gordon L. Nord)

Cristobalite-tridymite relationships. Like PO-10 tridymite, the tetrahedral rings within the stacking modules of α-cristobalite (Fig. 19) adopt only the oval configuration (Dollase, 1965; O'Keeffe and Hyde, 1976; Pluth et al., 1985). The similarity in ring

EBSCOhost - printed on 2/13/2023 4:48 AM via . All use subject to https://www.ebsco.com/terms-of-use

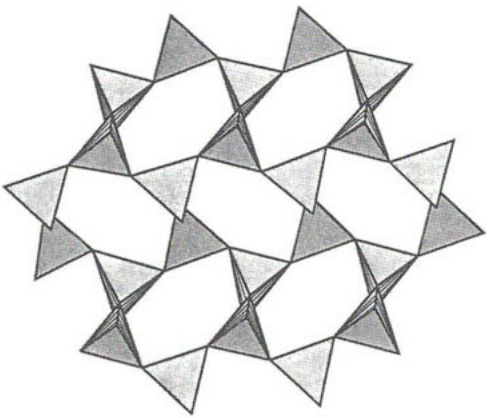


Figure 19. Projection of a single sheet of α-cristobalite close to the $[100]_{tet}$ direction (with *c* vertical and *b* horizontal). Ditrigonal rings of β-cristobalite have transformed to distorted oval rings.

configuration between terrestrial tridymite and low-temperature cristobalite suggests that these two structures can intergrow with little structural mismatch, accounting for the relative stability of opal-CT. The disordered intergrowth of cristobalite and tridymite strongly alters the transition behavior (Thompson and Wennemer, 1979; Wennemer and Thompson, 1984a). The transformation from OP-tridymite to OS- to OC-tridymite between 110°C and 190°C is associated with a change from a structure in which one-third of the rings are oval to a structure in which all of the rings are (at least transiently) ditrigonal. By contrast, the transformation from α- to β-cristobalite at ~235°C entails a single change from a structure with only oval rings to one with only ditrigonal rings. Consequently, when mixed-layer cristobalite-tridymite is heated, the oval rings of cristobalite will inhibit a low-temperature reconfiguration in tridymite to ditrigonal rings. On the other hand, interfacial strain will induce the oval rings in cristobalite to transform to ditrigonal rings. Thus, the transitions in tridymite increase in temperature while that in cristobalite decreases, and in DSC profiles the sharp lambda peak produced by the α-β cristobalite transformation merges with the lesser peaks produced by tridymite into a single broad peak.

Because the transformation of tridymite to cristobalite with high temperature involves a reconstructive layer change, stacking faults in tridymite serve as nucleation points that kinetically enhance the transition. Cristobalite lamellae that grow epitaxially within tridymite occur in two distinct orientations, which are related by a 180° rotation about $[111]_{\beta\text{-crist}}$ (Schneider and Flörke, 1986). Epitaxial replacement parallel to (001) is favored in highly defective tridymite, and the intergrown cristobalite lamellae are 100 nm to 2 μm in width. However, a TEM investigation of heated silica brick (Ashworth, 1988) has revealed that this transformation mechanism accounts for less than 1% of the replaced tridymite by volume. The more significant replacement mechanism involves nucleation of massive cristobalite at tridymite grain boundaries with no crystallographic relationship between the two polymorphs.

KEATITE

Keatite remains a somewhat enigmatic silica polymorph. Following the synthesis of this phase by Keat (1954), Shropshire et al. (1959) determined its tetragonal structure by single-crystal X-ray diffraction (Table 7). Keatite consists of corner-sharing silica tetrahedra that form fourfold spirals parallel to *c*. This arrangement produces 5-, 7- and

EBSCOhost - printed on 2/13/2023 4:48 AM via . All use subject to https://www.ebsco.com/terms-of-use

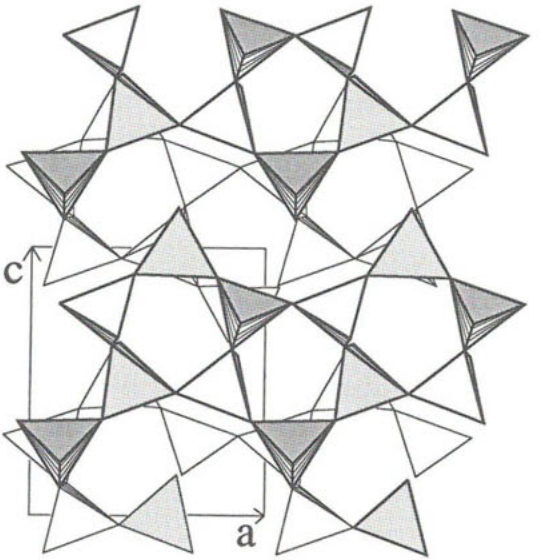


Figure 20. A projection along [100] of the tetragonal structure of keatite.

8- fold rings (Fig. 20). Keatite appears to have no field of thermodynamic stability, but it is easily synthesized in experiments that mimic the diagenesis of amorphous silica to quartz (Carr and Fyfe, 1958). Bettermann and Liebau (1975) determined semi-quantitative P-T-t diagrams for this transformation sequence, and their results suggest that crystallization of keatite is favored at moderate temperatures (200° to 400°C) and pressures (2 to 3 kbar). Weakly alkaline solutions also are required for its formation, since overly dilute solutions lead to the precipitation of cristobalite and high concentrations induce the crystallization of quartz (Keat, 1954). Martin and Röller (1990) report the synthesis of virtually pure keatite at pH = 12 with the addition of NaOH, KOH, and LiOH in 0.01 mol aqueous solutions.

Table 7. Structural data for keatite

Space Group	$P4_32_12$		
Unit Cell			
a (Å)	7.46		
c (Å)	8.61		
V (Å^3)	479		
ρ (g/cm^3)	2.50		
Atom	x	y	z
Si(1)	0.326	0.120	0.248
Si(2)	0.410	0.410	0
O(1)	0.445	0.132	0.400
O(2)	0.117	0.123	0.296
O(3)	0.344	0.297	0.143

Note: Data from Shropshire et al. (1959)

Despite the facility with which keatite is produced in the laboratory, its occurrence in nature remains uncertain. No studies of diagenetically altered opal have reported inclusions of keatite, suggesting that these transformations typically occur at temperatures and pressures lower than those that promote keatite crystallization. Keatite has been identified in Si-rich grains condensed in volcanic eruption clouds (Rietmeijer, 1988), but additional TEM and XRD studies are needed to confirm this observation. Although keatite appears rarely in nature, its stuffed derivatives comprise an industrially useful class of materials, and these compounds are described in chapters by Palmer and Beall (this volume).

EBSCOhost - printed on 2/13/2023 4:48 AM via . All use subject to https://www.ebsco.com/terms-of-use

ACKNOWLEDGMENTS

The author thanks David Veblen, Jeffrey Post, and George Guthrie for stimulating discussions on silica crystal chemistry, and Eugene Smelik, who kindly reviewed this manuscript and shared his extensive knowledge (and reprints) of tridymite mineralogy. Figures and photographs for this chapter were kindly supplied by Eugene Smelik, Gordon Nord, Hongwu Xu, and Naoki Yamamoto. Work presented in this review was supported by NSF grant EAR92-06031.

REFERENCES

Aizu K (1973) Second-order ferroic state shifts. J Phys Soc Japan 34:121-128

Anderson TL, Newnham RE, Cross LE, and Laughner JW (1976) Laser-induced twinning in quartz. Phys status solidi A37:235-245

Ashworth JR (1988) Transformation mechanisms of tridymite to cristobalite studied by transmission electron microscopy. Phys Chem Min 15:246-251

Ashworth JR (1989) Transmission electron microscopy of coexisting low-tridymite polymorphs. Min Mag 53:89-97

Aslanian TA, Levanyuk AP (1979) On the possibility of the incommensurate phase near α-β transition point in quartz. Sol Stat Comm 31:547-550

Aslanian TA, Levanyuk AP (1984) Fluctuation effects as a cause for the incommensurate phase formation. Ferroelectrics 53:231-234

Aslanyan TA, Levanyuk AP, Vallade M, Lajzerowicz J (1983) Various possibilities for formation of incommensurate superstructure near the α-β transition in quartz. J Phys C 16:6705-6712

Axe JC, Shirane G (1970) Study of the α-β quartz phase transformation by inelastic neutron scattering. Phys Rev B 1:342-348

Bachheimer JP, Dolino G (1975) Measurement of the order parameter of α-quartz by second harmonic generation of light. Phys Rev B 11:3195-3205

Bachheimer JP (1980) An anomaly in the β phase near the α-β transition of quartz. J Physique—Lett 41:L559-L561

Balakirev VG, Tsinober LI, Tsyganov EM (1975) Electron-microscope study of Brazil twins in synthetic amethyst. Sov Phys Crystallogr 19:517-520

Banda EJ, Craven RA, Parks RD, Horn PM, Blume M (1975) α-β transition in quartz: Classical versus critical behaviour. Sol Stat Comm 17:11-14

Baran Z, Godwod K, Warminski T (1987) X-ray study of Brazil twins in natural amethyst. Phys status solidi A101:9-24

Barber DJ, Wenk H-R (1991) Dauphiné twinning in deformed quartzites: Implications of an in situ TEM study of the α-β phase transformation. Phys Chem Min 17:492-502

Barth TFW (1932a) The cristobalite structures: I. High-cristobalite. Am J Sci 23:350-356

Barth TFW (1932b) The cristobalite structures: II. Low-cristobalite. Am J Sci 24:97-110

Bastie P, Dolino G (1985) γ-ray -diffraction of an incommensurate phase: Application to quartz. Phys Rev B 31:2857-2861

Bastie P, Mogeon F, Zeyen CME (1988) Direct neutron observation of a single-**q** incommensurate phase of quartz at zero stress. Phys Rev B 38:786-788

Baur WH (1977) Silicon-oxygen bond lengths, bridging angles Si-O-Si and synthetic low tridymite. Acta Cryst B33:2615-2619

Bertagnolli E, Kittinger E, Tichy J (1979) Ferrobielastic hysteresis in α-quartz. J Appl Phys 50:6267-6271

Best MG (1982) Igneous and metamorphic petrology. WH Freeman & Co., New York

Bettermann P, Liebau F (1975) The transformation of amorphous silica to crystalline silica under hydrothermal conditions. Contrib Min Petrol 53:25-36

Biot J-P (1817) Mémoire sur les rotations que certaines substances impriment aux axes de polarisation des rayons lumineux. Mémoires de l'Académie des Sciences de l'Institut 2:41-136

Boysen H, Dorner B, Frey F, Grimm H (1980) Dynamic structure determination for two interacting modes at the M-point in α- and β-quartz by inelastic neutron scattering. J Phys C 13:6127-6146

Bragg WL (1937) Atomic structure of minerals. Cornell Univ Press, Ithaca New York

Bragg WH, Gibbs RE (1925) The structure of α and β quartz. Proc Roy Soc Lond A109:405-427

Buerger MJ (1934) The temperature-structure-composition behavior of certain crystals. Proc Nat Acad Sci 20:444-453

EBSCOhost - printed on 2/13/2023 4:48 AM via . All use subject to https://www.ebsco.com/terms-of-use

Buerger MJ (1951) Crystallographic aspects of phase transformations. In: Smoluchowski R (ed) Phase transformations in solids. Wiley, New York, p 183-211

Burns G, Glazer AM (1990) Space groups for solid state scientists, 2nd edn. Academic Press, Boston

Cady SL, Wenk H-R, Kilaas R, Barber DJ (1993) Enantiomorphism and planar defects in length-fast chalcedony. In: Boland JN, FitzGerald JD (eds) Defects and processes in the solid state: Geoscience applications. Elsevier, Amsterdam, p 383-400

Carpenter M, Wennemer M (1985) Characterization of synthetic tridymites by transmission electron microscopy. Am Min 70:517-528

Carr RM, Fyfe WS (1958) Some observations on the crystallization of amorphous silica. Am Min 43:908-916

Chen CH, Lewin J (1969) Silicon as a nutrient element for *Equisetum arvense*. Can J Botany 47:125-131

Christie JM, Lally JS, Heuer AH, Fisher RM, Griggs DT, Radcliffe SV (1971) Comparative electron petrography of Apollo 11, Apollo 12, and terrestrial rocks. Proc Second Lun Sci Conf 1:69-89

Coe RS, Paterson MS (1969) The α-β inversion in quartz: A coherent phase transition under nonhydrostatic stress. J Geophys Res 74:4921-4948

Cohen LH, Klement W Jr (1967) High-low quartz inversion: Determination to 35 kilobars. J Geophys Res 72:4245-4251

Cohen LH, Klement W Jr, Adams HG (1974) Yet more observations on the high-low quartz inversion: Thermal analysis studies to 7 kbar with single crystals. Am Min 59:1099-1104

Coveney RM, Kelly WC (1971) Dawsonite as a daughter mineral in hydrothermal fluid inclusions. Contrib Min Petrol 32:334-342

D'Amour H, Denner W, Schulz H (1979) Structure determination of α-quartz up to 68 x 10^8 Pa. Acta Cryst B35:550-555

de Dombal, RF, Carpenter, MA (1993) High-temperature phase transitions in Steinbach tridymite. Eur J Min 5:607-622

Deelman JC (1986) Opal-CT in bamboo. Neues Jahrb Min Mon 9:407-415

de Jong BHWS, van Hoek J, Veeman WS, Manson DV (1987) X-ray diffraction and ^{29}Si magic-angle-spinning NMR of opals: Incoherent long- and short-range order in opal-CT. Am Min 72:1195-1203

Dennen WH (1964) Impurities in quartz. Geol Soc Am Bull 75:241-246

Dennen WH (1966) Stoichiometric substitution in natural quartz. Geochim Cosmochim Acta 30:1235-1241

Dennen WH, Blackburn WH, and Quesada A (1970) Aluminum in quartz as a geothermometer. Contrib Min Petrol 27:332-342

de Vries A (1958) Determination of the absolute configuration of α-quartz. Nature 181:1193

Dolino G (1980) Angular and polarization properties of light scattering at the α-β phase transition of quartz. Phys status solidi 60:391-401

Dolino G (1990) The α-inc-β transitions of quartz: A century of research on displacive phase transitions. Phase Transitions 21:59-72

Dolino G, Bachheimer JP, Berge B, Zeyen CME (1984a) Incommensurate phase of quartz: I. Elastic neutron scattering. J Physique 45:361-371

Dolino G, Bachheimer JP, Berge B, Zeyen CME, Van Tendeloo G, Van Landuyt J, Amelinckx S (1984b) Incommensurate phase of quartz: III. Study of the coexistence state between the incommensurate and the α-phases of neutron scattering and electron microscopy. J Physique 45:901-9128

Dolino G, Bastie P, Berge B, Vallade M, Bethke J, Regnault LP, Zeyen CME (1987) Stress-induced "3-q"-"1-q" incommensurate phase transition in quartz. Europhys Lett 3:601-609

Dollase WA (1965) Reinvestigation of the structure of low cristobalite. Z Kristallogr121:369-377

Dollase WA (1967) The crystal structure at 220°C of orthorhombic high tridymite from the Steinbach meteorite. Acta Cryst 23:617-623

Dollase WA and Baur WH (1976) The superstructure of meteoritic low tridymite solved by computer simulation. Am Min 61:971-978

Donnay JDH, Le Page Y (1978) The vicissitudes of the low-quartz crystal setting or the pitfalls of enantiomorphism. Acta Cryst A34:584-594

Drebushchak VA, Dement'ev SH (1993) Thermodynamic study of quartz in the vicinity of the α-β quartz transition. Geokhimia No. 9:1341-1353

Drees LR, Wilding LP, Smeck NE, Senkayi AL (1989) Silica in soils: Quartz and disordered silica polymorphs. In: Dixon JB, Weed SB (ed) Minerals in Soil Environments. Soil Science Society of America, Madison, WI, p 913-974

Dubrovinsky LS, Piloyan GD (1986) Effect of (micro) crystal size on the temperature of the polymorphic α-β transition in quartz. Doklad Akad Nauk SSSR 286:139-142

Eitel W (1957) Structural anomalies in tridymite and cristobalite. Am Ceram Soc Bull 57:142-148.

Eugster HP (1967) Hydrous sodium silicates from Lake Magadi, Kenya: Precursors of bedded chert. Science 157:1177-1180

EBSCOhost - printed on 2/13/2023 4:48 AM via . All use subject to https://www.ebsco.com/terms-of-use

Fenner CN (1913) The stability relations of the silica minerals. Am J Sci 36:331-384
Flörke OW (1955) Strukturanomalien bei Tridymit und Cristobalit. Berichte der Deutschen Keramischen Gesellschaft 32:369-381
Flörke OW (1967) Die Modifikationen von SiO_2. Fort Min 44:181-230
Flörke OW and Müller-Vonmoos M (1971) Displazive Tief-Hoch-Umwandlung von Tridymit. Z Kristallogr 133:193-202
Flörke OW, Jones JB, Schmincke H-U (1976) A new microcrystalline silica from Gran Canaria. Z Kristallogr 143:156-165
Flörke OW, Flörke OW, Giese U (1984) Moganite: A new microcrystalline silica-mineral. Neues Jahrb Min Abh 149:325-336
Flörke OW, Nukui A (1988) Strukturelle Pathologie von Tridymiten. Neues Jahrb Miner Abh 158:175-182
Fournier RO (1985) Silica minerals as indicators of conditions during gold deposition. U S Geol Surv Bull 1646:15-26
Frondel C (1945) Secondary Dauphiné twinning in quartz. Am Min 30:447-468
Frondel C (1962) The system of mineralogy, 7th edn, vol III. Wiley, New York
Gardner SP, Appleman DE (1974) X-ray crystallography and polytypism of naturally-occurring tridymite, SiO_2. Am Cryst Assn Prog & Abstr 2:271
Garrison RE, Douglass RB, Pisciotto KE, Isaacs CM, Ingle, JC (eds) (1981) The Monterey Formation and related siliceous rocks of California. Soc Econ Paleontol Min, Pacific Section, Los Angeles, California
Ghiorso MS, Carmichael ISE, Moret LK (1979) Inverted high-temperature quartz. Contrib Min Petrol 68:307-323
Gibbs GV, Meagher EP, Newton MD, Swanson DK (1981) A comparison of experimental and theoretical bond length and angle variations for minerals, inorganic solids, and molecules. In: O'Keeffe M, Navrotsky A (eds) Structure and Bonding in Crystals. Academic Press, New York, p 195-225
Gibbs RE (1925) The variation with temperature of the intensity of reflection of X-rays from quartz and its bearing on the crystal structure. Proc Roy Soc London A107:561-570
Gibbs RE (1927) The polymorphism of silicon dioxide and the structure of tridymite. Proc Roy Soc Lond 113A:351-367
Gibson RE (1928) The influence of pressure on the high-low inversion of quartz. J Phys Chem 32:1197-1205
Glass BP (1984) Tektites. J Non-Cryst Sol 67:333-344
Goetz W (1962) Untersuchungen am Tridymit des Siderophyrs von Grimma in Sachsen. Chem Erde 22:167-174
Goguel R (1983) The rare alkalies in hydrothermal alteration at Wairakei and Broadlands, geothermal fields, N.Z. Geochim Cosmochim Acta 47:429-437
González-Mañas M, Caballero MA, Capelle B, Epelboin Y (1993) Study of Brazil twin boundaries in synthetic quartz by means of simulations of X-ray topographs. J Appl Cryst 26:122-127
Gouhara K, Kato N (1984) Refined observations of the satellite reflections in the intermediate phase of quartz. J Phys Soc Jap 53:2177-2180
Gouhara K, Kato N (1985a) The intermediate phase of quartz. I. J Phys Soc Jap 54:1868-1881
Gouhara K, Kato N (1985b) The intermediate phase of quartz. II. Behaviour near the first-order transition temperature. J Phys Soc Jap 54:1882-1889
Graetsch H, Flörke OW, Miehe G (1987) Structural defects in microcrystalline silica. Phys Chem Min 14:249-257
Graetsch H, Flörke OW (1991) X-ray powder diffraction patterns and phase relationship of tridymite modifications. Z Kristallogr 195:31-48
Grattan-Bellew PE (1978) Quartz-tridymite transition under hydrothermal conditions. Explor Mineral 11:128-139
Green JC, Fitz TJ III (1993) Extensive felsic lavas and rheoignimbrites in the Keweenawan Midcontinent Rift plateau volcanics, Minnesota: Petrographic and field recognition. J Vol Geotherm Res 54:177-196
Grimm H, Dorner B (1975) On the mechanism of the α-β phase transformation of quartz. Phys Chem Sol 36:407-413
Gude AJ 3rd, Sheppard RA (1972) Silhydrite, $3SiO_2{\cdot}H_2O$, a new mineral from Trinity County, California. Am Min 57:1053-1065
Hatch DM, Ghose S (1991) The α-β phase transition in cristobalite, SiO_2. Phys Chem Min 17:554-562
Hatta I, Matsuura M, Yao H, Gouhara K, Kato N (1985) True behavior of heat capacity in α, incommensurate, and β phases of quartz. Thermo Act 88:143-148
Hay RL (1968) Chert and its sodium-silicate precursors in sodium-carbonate lakes of east Africa. Contrib Min Petrol 17:255-274

EBSCOhost - printed on 2/13/2023 4:48 AM via . All use subject to https://www.ebsco.com/terms-of-use

Heaney PJ (1993) A proposed mechanism for the growth of chalcedony. Contrib Min Petrol 115:66-74
Heaney PJ, Post JE (1992) The widespread distribution of a novel silica polymorph in microcrystalline quartz varieties. Science 255:441-443
Heaney PJ, Sheppard RA, Post JE (1992) Association of length-slow silica with evaporites. Geol Soc Am Abstr with Programs 24:A231
Heaney PJ, Veblen (1991a) Observation and kinetic analysis of a memory effect at the α-β quartz transition. Am Min 76:1459-1466
Heaney PJ, Veblen (1991b) Observations of the α-β phase transition in quartz: A review of imaging and diffraction studies and some new results. Am Min 76:1018-1032
Heaney PJ, Veblen DR, Post JE (1994) Structural disparities between chalcedony and macrocrystalline quartz. Am Min 79:452-460
Heaney PJ, Vicenzi EP (1994) A geochemical investigation of the silica polymorph moganite. (Abstr) Trans Am Gephys Union EOS 75:356
Helgeson HC, Delany JM, Nesbitt HW, Bird DK (1978) Summary and critique of the thermodynamic properties of rock-forming minerals. Am J Sci 278-A:1-229
Hermann C (1935) Internationale Tabellen zur Bestimmung von Kristallstrukturen. Bornträger, Berlin
Herrington RJ, Wilkinson JJ (1993) Colloidal gold and silica in mesothermal vein systems. Geol 21:539-542
Herschel JFW (1822) On the rotation impressed by plates of rock crystal on the planes of polarization of the rays of light, as connected with certain peculiarities in its crystallization. Trans Cambridge Phil Soc 1:43-51
Hervig RL, Peacock SM (1989) Implications of trace element zoning in deformed quartz from the Santa Catalina mylonite zone. J Geol 89:343-350
Heynke U, Leeder O, and Schulz H (1992) On distinguishing quartz of hydrothermal or metamorphogenic origin in different monomineralic veins in the eastern part of Germany. Min & Petrol 46:315-329
Hill VG, Roy R (1958) Silica structure studies. VI. On tridymite. Trans Brit Cer Soc 57:496-510
Höchli UT, Scott JF (1971) Displacement parameter, soft-mode frequency, and fluctuations in quartz below its α-β phase transition. Phys Rev Lett 26:1627-1629
Hoffmann W, Kockmeyer M, Löns J, Vach C (1983) The transformation of monoclinic low-tridymite MC to a phase with an incommensurate superstructure. Fort Miner 61:96-98
Hua GL, Welberry TR, Withers RL, Thompson JG (1988) An electron diffraction and lattice-dynamical study of the diffuse scattering in β-cristobalite, SiO_2. J Appl Cryst 21:458-465
Hurst VJ, Storch SP (1981) Regional variation in the cell dimensions of metamorphic quartz. Am Min 66:204-212
Jackson I (1976) Melting of the silica isotypes SiO_2, BeF_2 and GeO_2 at elevated pressures. Phys Earth Planet Inter 13:218-231
Jones JB, Segnit ER (1971) The nature of opal. I. Nomenclature and constituent phases. J Geol Soc Australia 18:57-68
Jones JB, Segnit ER (1972) Genesis of cristobalite and tridymite at low temperatures. J Geol Soc Australia 18:419-422
Jorgensen JD (1978) Compression mechanisms in α-quartz structures–SiO_2 and GeO_2. J Appl Phys 49:5473-5478
Kato K, Nukui A (1976) Die Kristallstruktur des monoklinen Tief-Tridymits. Acta Cryst B32:2486-2491
Kaufman PB, Dayanandan P, Takeoka Y, Bigelow WC, Jones JD, Iler R (1981) Silica in shoots of higher plants. In: Simpson TL, Volcani BE, (eds) Silicon and siliceous structures in biological systems. Springer-Verlag, New York, p 409-449
Kawai K, Matsumoto T, Kihara K, Sakurai K (1978) The first finding of monoclinic tridymite in terrestrial volcanic rocks. Min J (Japan) 9:231-235
Keat PP (1954) A new crystalline silica. Science 120:328-330
Keith ML, Tuttle OF (1952) Significance of variance in high-low inversion of quartz. Am J Sci 253a:203-280
Kennedy GC, Wasserburg GJ, Heard HC, Newton RC (1962) The upper three phase region in the system SiO_2-H_2O. Am J Sci 260:501-521
Kihara K (1977) An orthorhombic superstructure of tridymite existing between about 105 and 180°C. Z Kristallogr 146:185-203
Kihara K (1978) Thermal change in unit-cell dimensions, and a hexagonal structure of tridymite. Z Kristallogr 148:237-253
Kihara K (1980) On the split-atom model for hexagonal tridymite. Z Kristallogr 152:95-101
Kihara K (1981) Addenda and corrigendum for "On the split-atom model for hexagonal tridymite. Z Kristallogr 157:93
Kihara K (1990) An X-ray study of the temperature dependence of the quartz structure. Eur J Min 2:63-77

EBSCOhost - printed on 2/13/2023 4:48 AM via . All use subject to https://www.ebsco.com/terms-of-use

Kihara K (1993) Lattice dynamical calculations of anisotropic temperature factors of atoms in quartz, and the structure of β-quartz. Phys Chem Min 19:492-501
Kihara K, Matsumoto T, Imamura, M (1986a) High-order thermal-motion tensor analyses of tridymite. Z Kristallogr 177:39-52
Kihara K, Matsumoto T, Imamura M (1986b) Structural change of orthorhombic-I tridymite with temperature: A study based on second-order thermal-vibrational parameters. Z Kristallogr 177:27-38
Kim YJ, Xiao Y, Kirkpatrick RJ (1992) TEM investigation of tridymite polymorphs (Abstr.) Trans Am Gephys Union EOS 73:620
Kingma KJ, Hemley RJ (1994) Raman spectroscopic study of microcrystalline silica. Am Min 79:269-273
Klein C, Hurlbut CS Jr (1993) Manual of Mineralogy, 21st edn. John Wiley, New York
Kleinman DA, Spitzer WG (1962) Theory of the optical properties of quartz in the infrared. Phys Rev 125:16-30
Koh S-I, Yamada Y (1987) Kinetic process of formation of discommensuration pattern in SiO_2. Phase Transitions 8:261-272
Koivula JI, Fritsch E (1989) The growth of Brazil-twinned synthetic quartz and the potential for synthetic amethyst twinned on the Brazil law. Gems & Gemology 25:159-164
Konnert JH, Appleman DE (1978) The crystal structure of low tridymite. Acta Cryst B34:391-403
Koster van Groos AF, Ter Heege JP (1973) The high-low quartz transition up to 10 kilobars pressure. J Geol 81:717-724
Lagaly G, Beneke K, Weiss A (1975a) Magadiite and H-magadiite: I. Sodium magadiite and some of its derivatives. Am Min 60:642-649
Lagaly G, Beneke K, Weiss A (1975b) Magadiite and H-magadiite: II. H-magadiite and its intercalation compounds. Am Min 60:650-658
Lager GA, Jorgensen JD, Rotella FJ (1982) Crystal structure and thermal expansion of α-quartz SiO_2 at low temperatures. J Appl Phys 53:6751-6756
Lally JS, Nord GL Jr, Heuer AH, Christie JM (1978) Transformation-induced defects in α-cristobalite. Proc 9th Int'l Congress on Electron Microscopy, Electron Microscopy 1:476-477
Lang AR (1965a) Mapping Dauphiné and Brazil twins in quartz by X-ray topography. Appl Phys Lett 7:168-170
Lang AR (1965b) The orientation of the Miller-Bravais axes of α-quartz. Acta Cryst 19:290-291
Laughner JW, Cline TW, Newnham RE, Cross LE (1979) Acoustic emissions from stress-induced Dauphiné twinning in quartz. Phys Chem Min 4:129-137
Laughner JW, Newnham RE, Cross LE (1982) Mechanical twinning in small quartz crystals. Phys Chem Min 8:20-24
Leadbetter AJ, Wright AF (1976) The α-β transition in the cristobalite phases of SiO_2 and $AlPO_4$ I. X-ray studies. Phil Mag 33:105-112
Le Chatelier H (1889) Sur la dilatation du quartz. Com Rend de l'Acad Sciences 108:1046-1049
Le Page Y, Calvert LD, Gabe EJ (1980) Parameter variation in low-quartz between 94 and 298K. J Phys Chem Solids 41:721-725
Le Page Y, Donnay G (1976) Refinement of the crystal structure of low-quartz. Acta Cryst B32:2456-2459
Levien L, Prewitt CT, Weidner DJ (1980) Structure and elastic properties of quartz at pressure. Am Min 65:920-930
Liebau F, Böhm H (1982) On the co-existence of structurally different regions in the low-high quartz and other displacive phase transformations. Acta Cryst A38:252-256
Lukesh J, Buerger MJ (1942) The tridymite problem (Abstr.) Science 95:21
Mallard E (1890) Sur la tridymite et la christobalite. Bull Soc fran Min 13:161-180
Malov YV, Sonyushkin VE (1976) Direct electron-microscopic investigation of the α-β transition process in quartz. Sov Phys Crystal 20:644-645
Markgraaff J (1986) Elastic behavior of quartz during stress induced Dauphiné twinning. Phys Chem Min 13:102-112
Martin B, Röller K (1990) Keatite: Microstructure, growth fabric and crystal structure. I: Microstructure and texture. Neues Jahrb Min Mon 10:462-466
Massare D, Syffose G, Clocchiatti R (1988) Suivi optique et mesure de la température de transition α-β de quartz volcaniques sous pression de confinement entre 20 et 470 MPa. Com Ren Acad Sci Paris 307:375-378
McLaren AC, Phakey PP (1966) Electron microscope study of Brazil twin boundaries in amethyst quartz. Phys status solidi 13:413-422
McLaren AC, Phakey PP (1969) Diffraction contrast from Dauphiné twin boundaries in quartz. Phys status solidi 31:723-737
McLaren AC, Pitkethly DR (1982) The twinning microstructure and growth of amethyst quartz. Phys Chem Min 8:128-135

EBSCOhost - printed on 2/13/2023 4:48 AM via . All use subject to https://www.ebsco.com/terms-of-use

McLaren AC, Retchford JA, Griggs DT, Christie JM (1967) Transmission electron microscope study of Brazil twins and dislocations experimentally produced in natural quartz. Phys status solidi 19:631-644
McLellan AG (1978) The thermodynamic theory of the growth of Dauphiné twinning in quartz under stress. J Phys C 11:4665-4679
Megaw HD (1973) Crystal structures: A working approach. WB Saunders, Philadelphia
Michel-Lévy A, Munier-Chalmas CPE (1892) Mémoire sur diverses formes affectées par le réseau élémentaire du quartz. Bull Soc fran Minéral 15:159-190
Miehe G, Graetsch H (1992) Crystal structure of moganite: A new structure type for silica. Eur J Min 4:693-706
Miehe G, Graetsch H, Flörke OW (1984) Crystal structure and growth of fabric of length-fast chalcedony. Phys Chem Min 10:197-199
Miehe G, Graetsch H, Flörke OW, Fuess H (1988) Die monokline Kristallstruktur des SiO_2-Minerals Moganit. (Abstr) Z Kristallogr 182:183-184
Moehlman RS (1935) Quartz paramorphs after tridymite and cristobalite. Am Min 20:808-810
Molenaar N, de Jong AFM (1987) Authigenic quartz and albite in Devonian limestones: Origin and significance. Sediment 34:623-640
Moore GSM (1986) The α-β inversion in quartz and the effects of structural damage. Phase Transitions 7:25-40
Mosesman MA, Pitzer KS (1941) Thermodynamic properties of the crystalline forms of silica. J Am Chem Soc 63:2348-2356
Nieuwenkamp W von (1935) Die Kristallstruktur des tief-Cristobalits SiO_2. Z Kristallogr 92:82-88
Nieuwenkamp W von (1937) Über die Struktur von hoch-Cristobalit. Z Kristallogr 96:454-458
Nord GL Jr (1992) Imaging transformation-induced microstructuures. Rev Min 27:455-508
Nukui A, Nakazawa H (1980) Polymorphism in tridymite. (In Japanese) J Min Soc Japan 14(Spec Vol 2):364-386
Nukui A, Nakazawa H, Akao M (1978) Thermal changes in monoclinic tridymite. Am Min 63:1252-1259
Nukui A, Yamamoto A, Nakazawa H (1979) Non-integral phase in tridymite. In: Cowley JM, Cohen JB, Salamon MB, and Wuensch BJ (ed) Modulated Structures-1979. Am Inst Phys Conference Proc 53:327-329
Ogata K, Takéuchi Y, Kudoh Y (1987) Structure of α-quartz as a function of temperature and pressure. Z Kristallogr 179:403-413
O'Keefe JA (1984) Natural glass. J Non-Cryst Sol 67:1-17
O'Keeffe M, Hyde BG (1976) Cristobalites and topologically-related structures. Acta Cryst B32:2923-2936
Ono A (1979) Quartz solid solution in the system Li_2O-Al_2O_3-SiO_2-H_2O. (In Japanese with English abstr) J Japan Assn Min Petrol & Econ Geol 74:417-420
Ostrovsky IA (1966) PT-diagram of the system SiO_2-H_2O. Geol J 5:127-134
Parrish W, Gordon SG (1945) Orientation techniques for the manufacture of quartz oscillator-plates. Am Min 30:296-325
Peacor DR (1973) High temperature single-crystal study of the cristobalite inversion. Z Kristallogr 138:274-298
Perry EC Jr (1971) Implications for geothermometry of aluminum substitution in quartz from Kings Mountain, North Carolina. Contrib Min Petrol 30:125-128
Petrovic I, Heaney PJ, Navrotsky A (1993) Calorimetric study of the silica polymorph moganite. (Abstr) Trans Am Gephys Union EOS 74:160
Pettijohn FJ (1975) Sedimentary rocks, 3rd edn. Harper & Row, New York
Phadke AV, Kshirsagar LK (1986) Thermo-analysis of low cristobalite from Pune, Maharashtra, India: Paragenetic significance. Z Geol Wiss 14:559-567
Phillips BL, Thompson JG, Xiao Y, Kirkpatrick RJ (1993) Constraints on the structure and dynamics of the β-cristobalite polymorphs of SiO_2 and $AlPO_4$ from ^{31}P, ^{27}Al, and ^{29}Si NMR spectroscopy to 770K. Phys Chem Min 20:341-352
Pluth JJ, Smith JV, Faber, J Jr (1985) Crystal structure of low cristobalite at 10, 293, and 473 K: Variation of framework geometry with temperature. J Appl Phys 57:1045-1049
Ramachandran GN (1951) The theory of optical activity of crystals. III. Calculation of the rotatory power of β-quartz. Proc Indian Acad Sci 34:127-135
Raman CV, Nedungadi TMR (1940) The α-β transformation of quartz. Nature 145:147
Ray LL (1947) Quartz paramorphs after tridymite from Colorado. Am Min 32:643-646
Raz U (1983) Thermal and volumetric measurements on quartz and other substances at pressures up to 6 kbars and temperatures up to 700°C. Ph.D. dissertation, Swiss Federal Inst Tech, Zurich
Richet P, Bottinga Y, Denielou L, Petitet JP, Tequi C (1982) Thermodynamic properties of quartz, cristobalite and amorphous SiO_2: Drop calorimetry measurements between 1000 and 1800 K and a review from 0 to 2000 K. Geochim Cosmochim Act 46:2639-2658

EBSCOhost - printed on 2/13/2023 4:48 AM via . All use subject to https://www.ebsco.com/terms-of-use

Rietmeijer FJM (1988) Enhanced residence of submicron Si-rich volcanic particles in the lower stratosphere. J Vol Geotherm Res 34:173-184
Rogers AF (1946) Sand fulgurites with enclosed lechatelierite from Riverside County, California. J Geol 54:117-122
Rubin AE, Keil K (1983) Mineralogy and petrology of the Abee enstatite chondrite breccia and its dark inclusions. Earth Plan Sci Lett 62:118-131
Salje EKH, Ridgwell A, Güttler B, Wruck B, Dove MT, Dolino G (1992) On the displacive character of the phase transition in quartz: A hard-mode spectroscopic study. J Phys-Condensed Matter 4:571-577
Sangster AG, Hodson MJ (1986) Silica in higher plants. In: Evered D, O'Connor M (eds) Silicon Biochemistry. John Wiley, Chichester, UK, p 90-111
Sato M (1963a) X-ray study of tridymite (1): On tridymite M and tridymite S. Min J (Japan) 4:115-130.
Sato M (1963b) X-ray study of tridymite (2): Structure of low tridymite, Type M. Min J (Japan) 4:131-146
Sato M (1964) X-ray study of tridymite (3) Unit cell dimensions and phase transition of tridymite, Type S. Min J (Japan) 4:215-225
Schlössin HH, Lang AR (1965) A study of repeated twinning, lattice imperfections and impurity distribution in amethyst. Phil Mag 12:283-296
Schmahl WW (1993) Athermal transformation behaviour and thermal hysteresis at the SiO_2-α/β-cristobalite phase transition. Eur J Min 5:377-380
Schmahl WW, Swainson IP, Dove MT, Graeme-Barber, A (1992) Landau free energy and order parameter behaviour of the α/β phase transition in cristobalite. Z Kristallogr 201:125-145
Schmetzer K (1987) Microscopic observation of twinning microstructure in natural amethyst. Neues Jahrb Min Mon 1:8-15
Schmidt-Mumm A (1991) Low frequency acoustic emission from quartz upon heating from 90 to 610°C. Phys Chem Min 17:545-553
Schneider H (1986) Chemical composition of tridymite and cristobalite from volcanic and meteoritic rocks. Neues Jahrb Min Mon 10:433-444
Schneider H, Flörke OW (1982) Microstructure, chemical composition, and structural state of tridymite. Neues Jahrb Min Abh 145:280-290
Schneider H, Flörke OW (1986) High-temperature transformation of tridymite single crystals to cristobalite. Z Kristallogr 175:165-176
Schubnikow A, Zinserling K (1932) Über die Schlag- und Druck-Figuren und über die Mechanischen Quarzzwillinge. Z Kristallogr 83:243-264
Scotford DM (1975) A test of aluminum in quartz as a geothermometer. Am Min 60:139-142
Shahid KA, Glasser FP (1970) Thermal properties of tridymite: 25°C-300°C. J Therm Anal 2:181-190
Shapiro SM, Cummins HZ (1968) Critical opalescence in quartz. Phys Rev Lett 21:1578-1582
Shelley D (1993) Igneous and metamorphic rocks under the microscope. Chapman and Hall, London
Shen AH, Bassett WA, Chou I-M (1993) The α-β quartz transition at high temperatures and pressures in a diamond-anvil cell by laser interferometry. Am Min 78:694-698
Sheppard RA, Gude AJ 3rd (1986) Magadi-type chert-A distinctive diagenetic variety from lacustrine deposits. In: Mumpton FA (ed) Studies in Diagenesis. US Geol Surv Bull 1578:335-345
Shropshire J, Keat PP, Vaughan PA (1959) The crystal structure of keatite, a new form of silica. Z Kristallogr 112:409-413
Silvi B, D'Arco P, Causà M (1990) Periodic pseudopotential Hartree-Fock study of α-quartz structure SiO_2 and GeO_2. J Chem Phys 93:7225-7229
Simpson TL, Volcani BE (eds) (1981) Silicon and siliceous structures in biological systems. Springer, New York
Skinner BJ, Appleman DE (1963) Melanophlogite, a cubic polymorph of silica. Am Min 48:854-867
Smelik EA (1987) An X-ray diffraction study of displacive phase transitions in terrestrial tridymite. MS Thesis, Univ North Carolina, Chapel Hill, NC
Smelik EA, Reeber RR (1990) A study of the thermal behavior of terrestrial tridymite by continuous X-ray diffraction. Phys Chem Min 17:197-206
Smith GS, Alexander LE (1963) Refinement of the atomic parameters of α-quartz. Acta Cryst 16:462-471
Smith JV, Steele IM (1984) Chemical substitution in silica polymorphs. Neues Jahrb Min Mon 3:137-144
Snoeck E, Roucau C, Saint-Grégoire P (1986) Electron microscopy study of the modulated phases in berlinite $AlPO_4$ and quartz. J Physique 47:2041-2053
Snoeck E, Roucau C (1992) Electron microscope study of the triple-**q** to single-**q** phase transition in the incommensurate phase of quartz under stress. Phys Rev B 45:12,720-12,724
Sosman RB (1965) The phases of silica. Rutgers Univ Press, New Brunswick, NJ
Spearing DR, Farnan I, Stebbins JF (1992) Dynamics of the α-β phase transitions in quartz and cristobalite as observed by in-situ high temperature ^{29}Si and ^{17}O NMR. Phys Chem Min 19:307-321

EBSCOhost - printed on 2/13/2023 4:48 AM via . All use subject to https://www.ebsco.com/terms-of-use

Stein CL (1982) Silica recrystallization in petrified wood. J Sed Petrol 52:1277-1282
Steinwehr HE (1932) Umwandlung α-β Quartz. Z Kristallogr 99:292-313
Suttner LJ, Leininger RK (1972) Comparison of the trace element content of plutonic, volcanic, and metamorphic quartz from southwestern Montana. Geol Soc Am Bull 83:1855-1861
Swainson IP, Dove MT (1993) Low-frequency floppy modes in β-cristobalite. Phys Rev Lett 71:193-196
Swamy V, Saxena SK, Sundman B, Zhang J (1994) A thermodynamic assessment of silica phase diagram. J Geophys Res 99:11787-11794
Tagai T, Sadanaga R (1972) Tridymite, features of its high-low transitions and structure of its 20-layer polytype. Acta Cryst A28:S121
Tagai T, Sadanaga R, Takéuchi Y, Takeda, H (1977) Twinning of tridymite from the Steinbach meteorite. Min J (Japan) 8:382-398
Taijing L, Sunagawa I (1990) Structure of Brazil twin boundaries in amethyst showing Brewster fringes. Phys Chem Min 17:207-211
Tautz FS, Heine V, Dove MT, Chen X (1991) Rigid unit modes in the molecular dynamics simulation of quartz and the incommensurate phase transition. Phys Chem Min 18:326-336
Tezuka Y, Shin S, Ishigame M (1991) Observation of the silent soft phonon in β-quartz by means of hyper-raman scattering. Phys Rev Lett 66:2356-2359
Thompson AB, Wennemer M (1979) Heat capacities and inversions in tridymite, cristobalite, and tridymite-cristobalite mixed phases. Am Min 64:1018-1026
Thompson P, Wood IG (1983) X-ray Rietveld refinement using Debye-Scherrer geometry. J Appl Cryst 16:458-472
Tsuneyuki S, Aoki H, Tsukada M, Matsui Y (1990) Molecular-dynamics study of the α to β structural phase transition of quartz. Phys Rev Lett 64:776-779
Tullis J, Tullis T (1972) Preferred orientation of quartz produced by mechanical Dauphiné twinning: thermodynamics and axial experiments. Geophys Monogr 16:67-82
Van Goethem L, van Landuyt J, Amelinckx S (1977) The α-β transition in amethyst quartz as studied by electron microscopy and diffraction. Phys status solidi A41:129-137
Van Landuyt J, Van Tendeloo G, Amelinckx S, Walker MB (1985) Interpretation of Dauphiné-twin-domain configurations resulting from the α-β phase transition in quartz and aluminum phosphate. Phys Rev B31:2986-2992
Van Tendeloo G, Van Landuyt J, Amelinckx S (1976) The α-β phase transition in quartz and $AlPO_4$ as studied by electron microscopy and diffraction. Phys status solidi 33:723-735
Van Valkenburg A Jr, Buie BF (1945) Octahedral cristobalite with quartz paramorphs from Ellora Caves, Hyderabad State, India. Am Min 30:526-535
Wager LR, Weedon DS, Vincent EA (1953) A granophyre from Coire Uaigneich, Isle of Skye, containing quartz paramorphs after tridymite. Min Mag 30:263-275
Walker MB (1983) Theory of domain structures and associated defects in the incommensurate phase of quartz. Phys Rev B 28:6407-6410
Walker MB, Gooding RJ (1985) Properties of Dauphiné-twin domain walls in quartz and berlinite. Phys Rev B 32:7408-7411
Wei P-H (1935) The structure of α-quartz. Z Kristallogr 92:355-362
Weiss A, Herzog A (1977) Isolation and characterization of a silicon-organic complex from plants. In: Bendz G, Lindqvist I (eds) Biochemistry of silicon and related problems. Plenum Press, New York
Welberry TR, Hua GL, Withers RL (1989) An optical transform and Monte Carlo study of the disorder in β-cristobalite SiO_2. J Appl Cryst 22:87-95
Wenk H-R, Shaffer SJ, van Tendeloo G (1988) Planar defects in low temperature quartz. Phys status solidi A107:799-805
Wennemer M, Thompson AB (1984a) Tridymite polymorphs and polytypes. Schweiz min petrogr Mitt 64:335-353
Wennemer M, Thompson AB (1984b) Ambient temperature phase transitions in synthetic tridymites. Schweiz min petrogr Mitt 64:355-368
Will G, Bellotto M, Parrish W, Hart M (1988) Crystal structures of quartz and magnesium germanate by profile analysis of synchrotron-radiation high-resolution powder data. J Appl Cryst 21:182-191
Will G, Parrish W, Huang TC (1983) Crystal-structure refinement by profile fitting and least-squares analysis of powder diffractometer data. J Appl Cryst 16:611-622
Williams LA, Crerar DA (1985) Silica diagenesis. II. General mechanisms. J Sediment Petrol 55:312-321
Williams LA, Parks GA, Crerar DA (1985) Silica diagenesis. I. Solubility controls. J Sediment Petrol 55:301-311
Withers RL, Thompson JG, Welberry TR (1989) The structure and microstructure of α-cristobalite and its relationship to β-cristobalite. Phys Chem Min 16:517-523

EBSCOhost - printed on 2/13/2023 4:48 AM via . All use subject to https://www.ebsco.com/terms-of-use

Wooster WA (1953) Physical properties and atomic arrangements in crystals. Reports on Progress in Physics 16:62-82

Wooster WA, Wooster N, Ryecroft Il, Thomas LA (1947) The control and elimination of electrical (Dauphiné) twinning in quartz. J Inst Electr Eng 94:(Pt. 111), (16):926

Wright AF, Leadbetter AJ (1975) The structures of the β-cristobalite phases of SiO_2 and $AlPO_4$. Phil Mag 31:1391-1401

Wright AF, Lehmann MS (1981) The structure of quartz at 25 and 590°C determined by neutron diffraction. J Sol State Chem 36:371-380

Wyckoff RWG (1922) The analytical expression of the results of the theory of space-groups. Carnegie Inst Washington, Pub 318. Technical Press, Washington, DC

Wyckoff RWG (1925) The crystal structure of the high temperature form of cristobalite (SiO_2). Am J Sci 9:448-459

Wyckoff RWG (1931) The structure of crystals, 2nd edn. Chemical Catalog Co., New York

Wyckoff RWG (1948) Crystal structures, vol. I. Interscience, New York

Wyckoff RWG (1963) Crystal structures, vol. I, 2nd edn. Wiley, New York

Xiao Y, Kirkpatrick RJ, Kim YJ (1993) Structural phase transitions of tridymite: A ^{29}Si MAS NMR investigation. Am Min 78:241-244

Yakovlev IA, Mikheeva LF, Velichkina TS (1956) The molecular scattering of light and the α-β transformation in quartz. Sov Phys-Crystal 1:91-98

Yamamoto N, Tsuda K, Yagi K (1988) High voltage electron microscope study of incommensurate phase in quartz. J Phys Soc Jap 57:1352-1364

Yoder HS Jr (1950) High-low quartz inversion up to 10,000 bars. Trans Am Geophys Union 31:827-835

Young RA (1962) Mechanism of the phase transition in quartz. U S Air Force, Office of Scientific Research, Contract No. AF 49(638)-624

Young RA, Post B (1962) Electron density and thermal effects in alpha quartz. Acta Cryst 15:337-346

Zachariasen WH, Plettinger HA (1965) Extinction in quartz. Acta Cryst 18:710-714

Zák L (1972) A contribution to the crystal chemistry of melanophlogite. Am Min 57:779-796

Zarka A, Capelle B, Petit M (1988) Evidence of a single-q incommensurate phase in quartz by synchrotron X-ray diffraction. J Appl Cryst 21:72-73

Zeyen CME, Dolino G, Bachheimer JP (1983) Neutron and calorimetric observation of a modulated structure in quartz just above the α-β phase transition. Physica 120B:280-282

EBSCOhost - printed on 2/13/2023 4:48 AM via . All use subject to https://www.ebsco.com/terms-of-use

HIGH-PRESSURE BEHAVIOR OF SILICA

Russell J. Hemley, Charles T. Prewitt and Kathleen J. Kingma

Geophysical Laboratory and Center for High Pressure Research,
Carnegie Institution of Washington,
5251 Broad Branch Road, N.W.,
Washington, DC 20015 U.S.A.

INTRODUCTION

The response of silica to pressure touches many fields of human inquiry. Silica is ubiquitous in the Earth's crust, and silicon and oxygen are abundant elements in the solar system. As a result, the nature of silica within the Earth is a question as old as geology. Siliceous rocks suffering meteorite impact form a detailed record of high-pressure shocks on planetary surfaces. The manner in which SiO_2 responds to stress is central to technology, from primitive tool-making to the control of microstrains in modern nanolayer materials. The phases of silica serve as model systems for studies of high-pressure structures, phase transitions, vibrational dynamics, and chemical bonding. In view of the wide-ranging importance of the high-pressure behavior of SiO_2 the literature on this subject is vast, with the appearance of textbook completeness. However, recent high-pressure investigations have revealed a number of new phenomena in this ostensibly well-understood system. These include the discovery of new phases, amorphization transitions, and unusual behavior under dynamic compression. Thus, there has been resurgent interest in the high-pressure behavior of silica, with important implications for geology, planetary science, materials science, and fundamental physics.

The goal of this chapter is to review the behavior of crystalline and amorphous silica under high pressure and temperature conditions. This chapter considers the behavior of silica phases in both thermodynamically stable and metastable states, and it focuses principally on experimental static compression studies. Sosman (1965) published an extensive survey of early experimental work, and Heimann (1977) and Liu and Bassett (1986) provided briefer, more recent reviews. Numerous shock-wave studies of silica have been performed (especially since 1960), and it is instructive to compare the transformations observed with both static and dynamic compression techniques. A vast literature exists for silica glass at ambient pressure (Devine, 1988); here we describe the properties of amorphous SiO_2 at high pressure, with emphasis on recent *in situ* high-pressure investigations.

We begin with an overview of the silica system, including a general comparison of the high-pressure properties of the principal silica phases. This is followed by a more detailed discussion of the effects of pressure on structure, transformations, and physical properties of individual phases. In particular, we examine the relative contribution of pressure-induced coordination changes and alterations in the topology of the tetrahedral network for both crystalline and amorphous phases. We then compare the response of silica phases to static high pressure, dynamic compression, and static deformation. This is followed by a discussion of the geophysical implications.

EBSCOhost - printed on 2/13/2023 4:48 AM via . All use subject to https://www.ebsco.com/terms-of-use

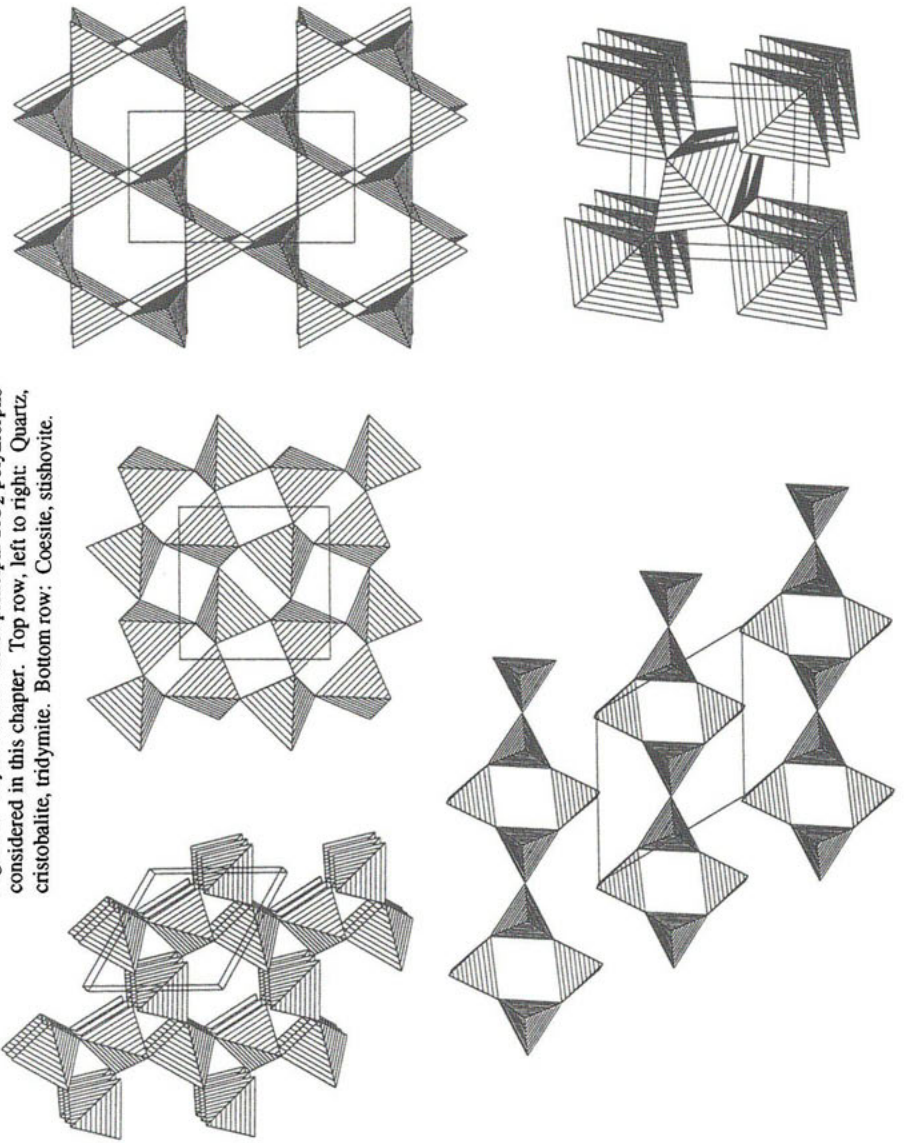


Figure 1. Crystal structures of principal SiO_2 polymorphs considered in this chapter. Top row, left to right: Quartz, cristobalite, tridymite. Bottom row: Coesite, stishovite.

EBSCOhost - printed on 2/13/2023 4:48 AM via . All use subject to https://www.ebsco.com/terms-of-use

OVERVIEW OF THE SiO_2 SYSTEM

Polymorphs

Low-pressure phases. The principal crystal structures considered here are shown in Figure 1. Low- or α-quartz is the stable phase of SiO_2 at ambient conditions and transforms to high- or β-quartz at 847 K and one atmosphere pressure. The α-quartz structure (space group $P3_121$) consists of two sets of chains of SiO_4 tetrahedra forming spirals parallel to the *c*-axis. When transformed to the β-quartz structure, the linkage among tetrahedra is maintained, but the symmetry of the spiral chains increases from threefold to sixfold.

The high-temperature, low-pressure forms of silica are tridymite and cristobalite. Because the reconstructive transformations of these polymorphs to quartz are hindered kinetically with decreasing temperature, tridymite and cristobalite can be preserved metastably at ambient conditions and thus are found commonly in nature. Their idealized structures are based upon stacking of sheets of SiO_4 tetrahedra in which the joined tetrahedra within each sheet alternate with their apical oxygens pointing up and down. In the tridymite structure, these sheets are joined such that a mirror plane lies between the sheets at the shared apical oxygens; the stacking sequence can be thought of as "ABAB," and the ideal structure has hexagonal symmetry and is isostructural with wurtzite. In the cristobalite structure, these sheets are joined such that an inversion point lies between the sheets at the shared apical oxygen; the cristobalite stacking sequence can be thought of as "ABCABC," and the ideal structure has cubic symmetry and is isostructural with sphalerite. These ideal structures are the high-temperature polymorphs. The lower-temperature structures, which can exist at ambient conditions, have reduced symmetries as compared to their high-temperature counterparts. A more detailed description of the crystal structures of quartz, tridymite, and cristobalite is given in the chapter by Heaney.

High-pressure phases. In 1953, a new, dense form of crystalline silica was synthesized at 3.55 GPa between 773-1073 K by Coes (1953). The new phase was named "coesite" or "silica C" by Sosman (1954). After its discovery in meteorite-impacted breccia at Meteorite Crater, Arizona, coesite gained status as a true mineral species (Chao et al., 1960), and it later was identified in kimberlites and low-temperature, high-pressure metamorphosed rocks (see below). The coesite unit cell parameters were first refined from Weissenberg and precession photographic data, which revealed monoclinic *C2/c* or *Cc* space group symmetry (second setting), originally determined to be hexagonal ($a \approx c$, $\beta = 120°$) (Ramsdell, 1955). The crystal structure was determined by Zoltai and Buerger (1959), and later refined by Araki and Zoltai (1969), Gibbs et al. (1977), Levien and Prewitt (1981), and Smyth et al. (1987). Corner-sharing tetrahedra join to form two symmetrically distinct four-membered rings. The first ring lies in the (001) plane and the rings are linked to form chains parallel to [010]. The chains at one level along the *c*-axis, while not linked to each other, are cross-linked to similar glide-related chains at the next level. This cross-linking serves to form the second type of four-membered SiO_4 rings, which lie approximately parallel to (010). Because of this close packing, coesite is the densest known silica polymorph that has a thermodynamic stability field and Si in tetrahedral coordination. The structure is similar to the silicate framework of the feldspar structure, which also consists of corner-sharing SiO_4 tetrahedra that are linked to form four-membered rings. These rings form chains parallel to the *c*-axis, and the chains, while not connected to each other in the *a-c* plane, are interconnected by offset chains above and below.

EBSCOhost - printed on 2/13/2023 4:48 AM via . All use subject to https://www.ebsco.com/terms-of-use

Stishovite, which has the rutile structure, was first synthesized in the laboratory (Stishov and Popova, 1961) and later was discovered in association with coesite at Meteor Crater, Arizona (Chao et al., 1962). The rutile structure consists of infinite chains of edge-shared SiO_6 octahedra parallel to the *c*-axis. Each chain is linked to four other chains related by the 4_2 screw axis of the $P4_2/mnm$ space group. Thus, each oxygen atom is coordinated by three silicon atoms, unlike the tetrahedral silica structures in which oxygen atoms are two-coordinated by silicon (Sinclair and Ringwood, 1978; Hill et al., 1983). This coordination results in a more efficient packing, even though the individual Si-O bond distances are longer than in quartz; the stishovite structure is approximately 46% denser than coesite. The high-pressure behavior of stishovite is of geophysical interest in view of its importance as a possible mantle constituent, and more generally, because of its role as an archetypal phase having octahedrally coordinated silicon. As discussed below, recent work shows that stishovite transforms to a closely related orthorhombic form at lower-mantle pressures (stishovite II).

Other polymorphs. In addition to the above polymorphs, a number of metastable silica phases exist at low pressure and exhibit high-pressure behavior of importance to geophysics and materials science. Of particular interest are the amorphous forms of silica, including synthetic silica glass (fused silica), the so-called diaplectic glass (pressure densified), and lechatelierite (natural melt-quenched glass). Indeed, one of the phenomena to be discovered and characterized in recent years is the pressure-induced "polymorphism" among the amorphous forms (e.g., Grimsditch, 1984). These transitions have parallels to structural transitions in crystalline polymorphs, despite the metastability and the sample history of the amorphous forms. The observations of these transformations have important implications for the behavior (e.g., density and rheology) of melts at very high pressures. Also, ultralow-density crystalline phases such as aerogels have interesting high-pressure properties, as described below. These are porous materials having cristobalite-like crystal structures.

Phase relations

Historically, the study of the silica phase diagram has been closely associated with the broad field of high-pressure research. Recent results are summarized in Figure 2. We first discuss relations among the equilibrium phases; metastable transitions are examined below. The pressure dependence of the α-β quartz transition was first studied by Gibson (1928), and later extended to 1.0 GPa by Yoder (1950). Cohen and Klement (1967) studied the transition to 3.5 GPa and estimated the coesite-α-β-quartz triple point at 1673 K and 3.7 GPa. Recently, Shen et al. (1993) determined the pressure dependence of the transition with a new diamond-cell interferometric technique, and the thermodynamics of the transition have been re-examined by Hosieni et al. (1985). An intermediate phase exists in a narrow temperature interval (1.3 K) between α- and β-quartz at ambient pressure (Dolino, 1988); the effect of stress on this incommensurate phase is described in the previous chapter. The cristobalite-tridymite-β-quartz triple point is located at 143 MPa and 1463 K (Jackson, 1976). Notably, the melting line of cristobalite is nearly pressure-independent.

The quartz-coesite and coesite-stishovite transitions have been particularly useful for calibration of pressure for high-pressure apparatus (e.g., Weaver et al. 1979; Mirwald and Massonne, 1980; Bohlen and Boettcher, 1982). The most recent determinations of the α-quartz-coesite and the β-quartz-coesite transitions are shown in Figure 2. A large number of determinations of the coesite-stishovite transition were carried out using

EBSCOhost - printed on 2/13/2023 4:48 AM via . All use subject to https://www.ebsco.com/terms-of-use

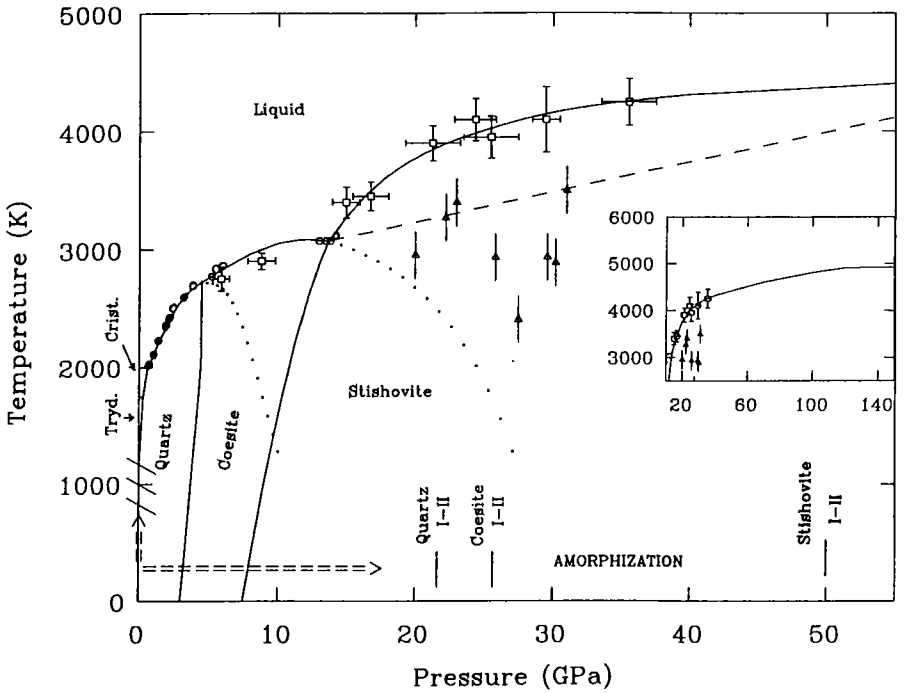


Figure 2. High *P-T* phase diagram of SiO_2 determined from static compression experiments. The solid lines are equilibrium phase boundaries consistent with the available data (see text). Data points for the high-pressure melting curves are shown: solid circles, Jackson (1976); open circles, Kanzaki (1990), Zhang et al. (1993); squares, Shen and Lazor (1994); triangles, shock-compression data from Kondo and Ahrens (1983) and Schmitt and Ahrens (1989). The dashed line is the stishovite melting line suggested by Zhang et al. (1993). The dotted lines are metastable extensions of quartz and coesite melting calculated from thermochemical data (Zhang et al., 1993). The stishovite I-II transition (Cohen, 1992; Kingma, 1994), and the (metastable) quartz I-II (Kingma et al., 1993b) and coesite I-II (Hemley, 1987) transitions, all observed at 300 K, are shown. The approximate pressures of extensive room-temperature static pressure amorphization are shown; progressive amorphization associated with microfracture begins at lower pressures (horizontal arrow) (Kingma et al., 1993a). The ambient-pressure amorphization of coesite and stishovite is indicated by the vertical arrow (e.g. Richet, 1988). *Inset*: Higher pressure range determined from shock-wave experiments, adapted from Schmitt and Ahrens (1989) and Lyzenga et al. (1983).

quenching techniques (see Akimoto and Syono, 1969). Yagi and Akimoto (1976) performed an *in situ* determination of this transition at 773 to 1373 K. Recent *in situ* measurements with reversals to 1700 K and 12 GPa are considered the most reliable, are consistent with thermochemical data (Swamy et al., 1994), and indicate that earlier work likely suffered from problems with metastability and kinetics (Zhang et al., 1994).

On the basis of shock-wave data, Davies (1972) inferred the location of the coesite-stishovite-liquid triple point at 12.5 GPa and 2500 K. Jackson (1976) studied the melting of cristobalite, quartz, and coesite to 4 GPa (along with the BeF_2 and GeO_2 isotypes). He found that the melting line of cristobalite is nearly independent of temperature and located the cristobalite-β-quartz-liquid triple point at 1973 K and 0.6 GPa. Jackson reported the β-quartz-coesite-liquid triple point at 4.0 to 4.5 GPa and 2373 to 2473 K, and found evidence that the coesite melting line increases with pressure. In order to reconcile

EBSCOhost - printed on 2/13/2023 4:48 AM via . All use subject to https://www.ebsco.com/terms-of-use

his data with the results of Davies (1972), he suggested that the melting curve must have a negative Clapyron slope at higher pressures (>4 GPa) or the coesite-stishovite-liquid triple point must be higher.

Kanzaki (1990) measured the melting relations of SiO_2 to 7 GPa and located the quartz-coesite-liquid triple point at 4.5 GPa and 2723 K. Zhang et al. (1993) extended the melting relations to 14 GPa and determined the coesite-stishovite-liquid triple point at 13.7 GPa and 3073 K. The results disagreed with the coesite-stishovite boundary calculated from thermochemical data, suggesting a significant uncertainty in the high *P-T* extrapolations of the heat capacity for the two minerals. The measured equilibrium melting curves for both quartz and coesite have a positive slope, although the curves are flat near the higher triple point for each. Thermochemical calculations indicate that the melting curves have pronounced negative slope in the extrapolated metastable range at higher pressure (Zhang et al., 1993), consistent with earlier proposals based on the observation of pressure-induced amorphization of the two minerals (Hemley et al., 1988).

Schmitt and Ahrens (1989) inferred melting temperatures of stishovite from shock-wave studies of SiO_2 glass. Their results provide a lower bound on the melting curve. New determinations by static compression include the multi-anvil study of Zhang et al. (1993) and the diamond-anvil laser-heating experiments of Shen and Lazor (1994). On the basis of shock temperature measurements from 60 to 140 GPa, Lyzenga et al. (1983) reported evidence for melting and proposed a melting line for stishovite over this range. The results are broadly consistent with lower pressure data and support the proposal that the shocked material relaxed to form stishovite, which in fact melted (see below). Sound speed data are also consistent with this interpretation (Chhabildas and Miller, 1985; McQueen, 1992).

Thermodynamic properties

The heat capacities of the high-pressure phases of silica have been measured by a number of researchers (Holm et al., 1967; Watanabe, 1982; Akaogi and Navrotsky, 1984; see also chapter by Navrotsky). Weaver et al. (1979) performed an experimental study of the α-β quartz and quartz-coesite transitions; they also assessed the thermochemical data on quartz, coesite, and stishovite, and found a number of inconsistencies with the higher *P-T* phase boundaries. More recent examinations have also encountered problems, particularly in the highest *P-T* range (Kuskov and Fabrichnaya, 1987). The most recent thermochemical data have been refined by Swamy et al. (1994). Their calculated phase diagram is in good agreement with phase equilibrium determinations, with the exception of the coesite-stishovite boundary at the highest temperatures (Zhang et al., 1994). Thermodynamic properties have also been calculated from model interatomic potentials (Belonoshko, 1994).

The pressure-volume relations (equations of state) for the different polymorphs are compared in Figure 3. The figure clearly shows the trend of increasing initial compressibility with increasing molar volume. In addition to the *P-V* relations, the thermal expansivity is a crucial thermochemical property and is important for geophysical modeling. The thermal expansion parameters of high-pressure silica phases have been measured, but only at zero pressure (Ito et al., 1974; Endo et al., 1986). The Grüneisen parameter (or ratio) γ is important for characterizing the thermal expansion at high pressure; it is defined as $\gamma = \alpha V K_T / C_V$ where α is the volume thermal expansion coefficient, V is the molar volume, K_T is the isothermal bulk modulus, and C_V is the constant volume specific heat. Values of γ have been determined from thermodynamic data for various polymorphs: 0.68 (±0.07) for α-quartz; 0.352 (±0.001) for coesite;

EBSCOhost - printed on 2/13/2023 4:48 AM via . All use subject to https://www.ebsco.com/terms-of-use

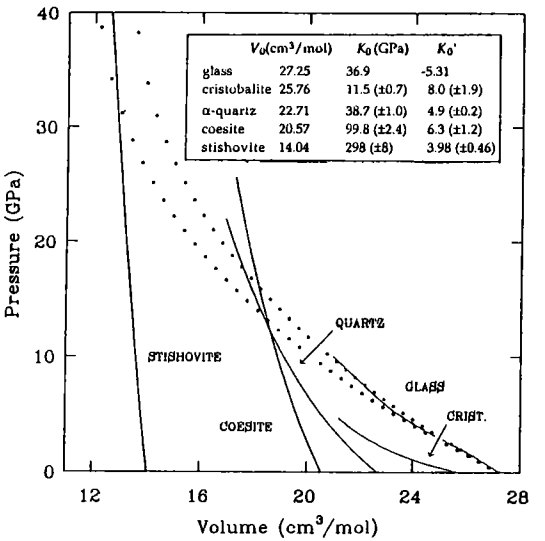


Figure 3. Comparison of *P-V* equations of state. The curves for the crystalline phases are least-squares fits to third-order Birch-Murnaghan equations of state (Liu and Bassett, 1986); parameters are shown in the inset. The fits are based on hydrostatic and quasi-hydrostatic measurements from the following sources: α-Quartz: quasihydrostatic data to 21 GPa (see text and Fig. 4). Coesite: Levien and Prewitt (1981), Hemley et al. (1988). Stishovite: Ross et al. (1990) and Shu et al. (1994, to be published). Cristobalite: Downs and Palmer (1994), Palmer and Finger (1994). Silica glass: the curve below 10 GPa represents a fit to ultrasonic measurements, Brillouin scattering, and static compression, with the equation-of-state parameters taken from Kondo et al. (1981); at higher pressure the envelope represents the dispersion in the data for shock compression (Wackerle, 1962; Marsh, 1980).

1.35(±0.03) for stishovite (Watanabe, 1982); 0.60(±0.01) for cristobalite (see Palmer et al., 1994). Boehler (1980) measured the pressure dependence of γ for quartz at 298 K, and found that it decreases slightly with increasing pressure; fitting his data one obtains $q = 0.76(\pm 0.18)$ where $q = -d \ln\gamma / d \ln V$. The Grüneisen parameter can also be estimated from high-pressure vibrational spectroscopy. High-pressure Raman and infrared data are close to the thermodynamic results for quartz, but some discrepancies are observed for other polymorphs (see Hemley, 1987; Williams et al., 1993).

Elastic and vibrational properties

Measurements of the elastic properties provide crucial geophysical information (e.g., for seismology) and give additional insight into compression mechanisms, phase transformations, and thermodynamic data (Fig. 3). In addition, many SiO_2 polymorphs have unusual elastic properties. Ultrasonic techniques have been used to determined the pressure and temperature dependence of the single-crystal elastic moduli of α-quartz (McSkimin et al. 1965; Wang et al., 1992, and references therein). Stishovite has the highest bulk modulus (Weidner et al., 1982), with coesite having an intermediate value (Weidner and Carleton, 1977; Levien and Prewitt, 1981). Because of their low density and open structures, tridymite and cristobalite have relatively low bulk moduli (high compressibility) (Yeganeh-Haeri et al., 1992). Also, cristobalite has a negative Poisson's ratio; i.e., it contracts laterally upon uniaxial compression (Yeganeh-Haeri et al., 1992). The lowest bulk modulus of this series is that of silica glass; it has been studied by ultrasonic measurements, Brillouin scattering, and static compression (see Zha et al., 1994).

EBSCOhost - printed on 2/13/2023 4:48 AM via . All use subject to https://www.ebsco.com/terms-of-use

In addition, the negative pressure derivative of the zero-pressure bulk modulus $K_0' = dK_0/dP$ (and positive dK_0/dT) of the glass is highly unusual.

Measurements of vibrational spectra provide detailed information on crystal chemistry, bonding, thermodynamic properties, phase equilibria, and phase transition mechanisms. Indeed, the first application of vibrational spectroscopy to study polymorphism was the pioneering light scattering study of the α-β transition in quartz by Raman and Nedungadi (1940). A general review of the vibrational spectroscopy and lattice dynamics of the SiO_2 polymorphs is given by Dolino and Vallade in this volume. Of the high-pressure phases measured at ambient conditions, infrared (Kieffer, 1979) and Raman (Sharma et al., 1981) spectra have been reported for coesite. For stishovite, Raman (Hemley et al., 1986b) and infrared (Hofmeister et al., 1990) spectra have been measured.

Vibrational spectroscopy is particularly useful for the study of compressional mechanisms and pressure-induced transformations. Asell and Nicol (1968) performed the first measurements of the Raman spectrum of α-quartz under pressure (to 4 GPa). More recent measurements have been carried out over a range of pressures by Dean et al. (1982), Jayaraman et al. (1987), Hemley (1987), and Kingma (1994); a general result of these studies is the observation of the strong pressure dependence of the 207 cm^{-1} mode, which is associated with the α-β quartz transition (Raman and Nedungadi, 1940). Hemley (1987) measured the spectrum of a series of polymorphs to ~50 GPa. Jayaraman et al. (1987) determined the Raman spectrum of α-quartz (and $AlPO_4$) to ~20 GPa. The infrared spectrum of quartz was measured under pressure to 5 GPa by Wong et al. (1986). More recently, Williams et al. (1993) carried out an infrared study of a series of silica polymorphs to maximum pressures of 45 GPa. Raman and IR spectra of silica glass were measured by Hemley et al. (1986a) and by Williams and Jeanloz (1988) to above 40 GPa. The results and implications of these studies are discussed below.

Optical and electronic properties

Studies of the optical properties (e.g., index of refraction, birefringence) of silica polymorphs date from the discovery of each of the phases (Sosman, 1965). There is a linear relationship between the density ρ and refractive index n for the tetrahedrally coordinated phases (Chao et al., 1962; Sclar et al., 1962; Skinner and Fahey, 1963; Maj 1984, 1988; Marler, 1988). Marler (1988) showed that the data can be represented by the following function: $n = 0.189\ \rho + 1.047$. The refractive index of silica glass has been measured to 57 GPa by Brillouin scattering (Zha et al., 1994).

Numerous experimental and theoretical studies indicate that the ionicity of the Si-O bond increases with Si coordination (see chapter by Cohen in this volume). Studies of the electron density distribution indicate that although stishovite is highly ionic, there is a pronounced polarization of the oxygens toward the Si atom (Hill et al., 1983; Cohen, 1991). ^{29}Si NMR is also sensitive to the coordination state of the cation and has been used to characterize the bonding in coesite, stishovite, and densified glass as well as to determine the relative abundance of phases in mixed phase samples (Smith and Blackwell, 1984; Yang et al., 1986; Assink et al., 1994; Cygan et al., 1994).

Few experimental studies of the electronic structure of the high-pressure phases at ambient pressure have been reported, nor have there been many studies of the general effect of pressure on these properties for any of the phases. Griscom (1977) reviewed spectroscopic and early theoretical data on the electronic structure of the SiO_2

EBSCOhost - printed on 2/13/2023 4:48 AM via . All use subject to https://www.ebsco.com/terms-of-use

polymorphs, principally quartz and glass. A large number of theoretical band-structure calculations have been performed in recent years (see Cohen's chapter). Exploiting the differences in the electronic structure of the phases, Jakubith and Lehmann (1981) measured X-ray photoelectron spectra of shock-loaded quartz to infer the existence of stishovite in the recovered samples.

HIGH-PRESSURE STRUCTURES, COMPRESSION MECHANISMS, AND TRANSFORMATIONS

Quartz

As pointed out by Jorgensen (1978), three mechanisms allow the structure of quartz and other tetrahedral silica phases to decrease in volume as pressure increases. These are: (1) a cooperative, rigid rotation of linked tetrahedra; (2) a distortion of tetrahedra due to changes in bond angles with constant bond length; and (3) a decrease in bond lengths. All of these mechanisms are active in compression of quartz, but the first is the most significant, thus accounting for a large fraction of volume change. A number of high-pressure compression and structural studies of quartz have been reported; the more recent include those by Jorgensen (1978), d'Amour et al. (1979), Levien et al. (1980), Ogata et al. (1987), Hazen et al. (1989), Glinnemann et al. (1992), and Kingma (1994). The compression data for quartz from different studies are compared in detail in Figure 4. The data of Kingma (1994) were obtained using powder and single-crystal synchrotron X-ray diffraction for quartz in a neon medium and are therefore considered to be the most reliable in the higher pressure range (e.g., > 10 GPa).

Rotation of tetrahedra with compression causes the Si-O-Si bond angles and the O-O distances to decrease. At room temperature and pressure, the Si-O-Si angle in quartz is 144°, and it decreases to 124.2° at 12.5 GPa (Hazen et al., 1989). Figure 5 shows the evolution of the structure with pressure with emphasis on the oxygen sublattice, including the extreme case when the angle approaches 120° and the oxygen atoms are in a quasi-

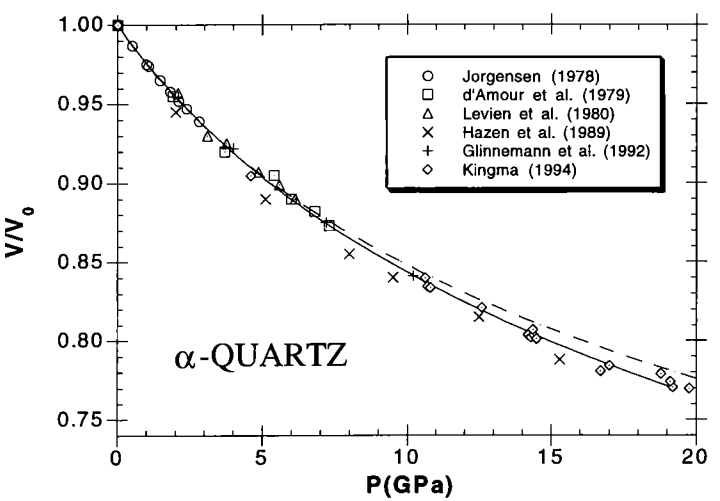


Figure 4. Comparison of *P-V* data for α-quartz. The solid line is the best-fit to all of the data (excluding Hazen et al., 1989)] with parameters K_0=38.7(±1.0) GPa and K_0'=4.9(±0.2). The dashed line is the equation of state with K_0=37.1 GPa and K_0'=6.0 (McSkimin et al., 1965; Hemley et al. 1988).

EBSCOhost - printed on 2/13/2023 4:48 AM via . All use subject to https://www.ebsco.com/terms-of-use

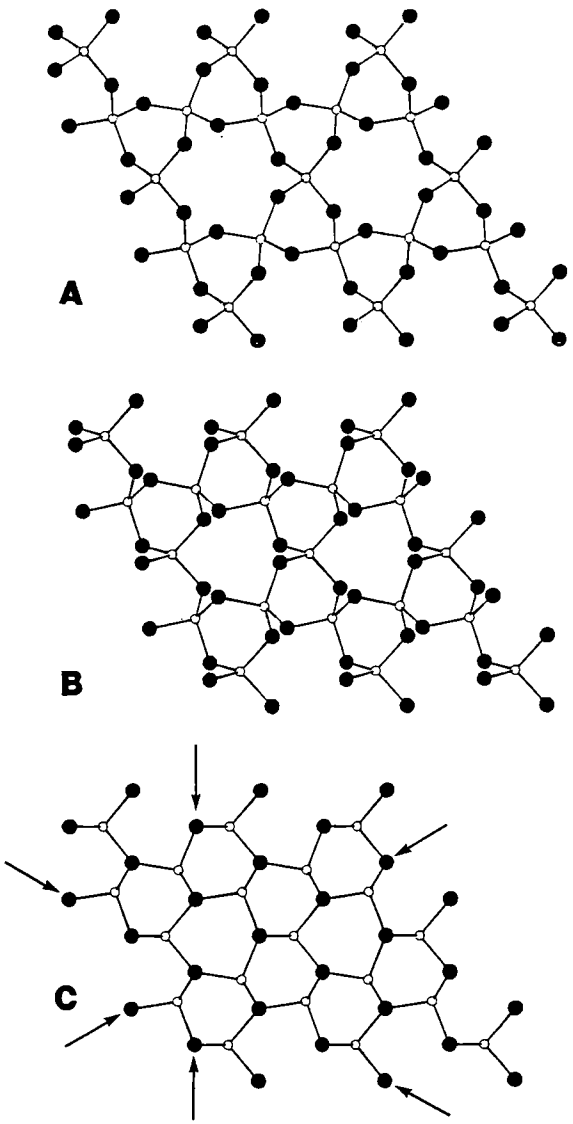


Figure 5. Effect of pressure on the structure of α-quartz as viewed down the *c*-axis (Hazen et al., 1989). (A) Zero-pressure; (B) 12.5 GPa; and (C) predicted high-pressure structure with Si-O-Si angle of 120°.

close-packed configuration. At room temperature, however, the structure transforms before the 120° angle is attained (see below). Si-O distances decrease slightly in the pressure range investigated thus far in structure refinements (Fig. 6a), but higher quality data should be obtained. The distances for Si-O(d2) are comparable, but for some undetermined reason, the d1 values from the two sources differ by a small but significant amount. Tetrahedral distortion increases with pressure, and the T-O distances decrease somewhat as pressure increases. Figure 6b shows the relationship between the distortion indices for intratetrahedral angles [DI(OTO)] and the O-O distances [DI(OO)] along the tetrahedral edges, revealing that distortion increases at a higher rate at the higher pressures.

EBSCOhost - printed on 2/13/2023 4:48 AM via . All use subject to https://www.ebsco.com/terms-of-use

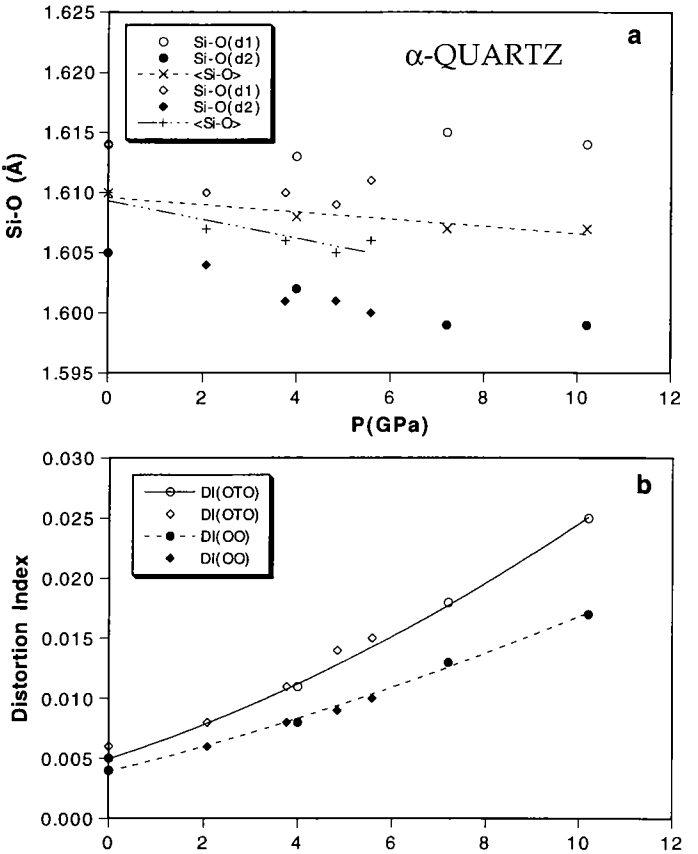


Figure 6. Effect of pressure on structural parameters of α-quartz. (a) Si-O distances from Glinnemann et al. (1992) shown with circles and Levien et al. (1980) with diamonds. (b) The distortion index (DI) plotted vs. pressure for the O-Si-O angles and O-O distances in quartz. Circles and diamonds are as above and the distortion index is defined in Glinnemann et al. (1992) as the sum of deviations from the mean divided by the mean value.

When α-quartz is pressurized well outside of its stability field at 300 K, it gradually transforms to an amorphous state, bypassing the equilibrium phase transformations to the high-pressure polymorphs coesite and stishovite. This was first observed by Raman scattering (Hemley, 1987) and subsequently by synchrotron X-ray diffraction (Hemley et al., 1988). These authors suggested that this pressure-induced amorphization parallels that previously found in the H_2O polymorph ice-I_h (Mishima et al., 1984). Since then a large number of experimental studies have been performed on this transition in quartz (Hazen et al., 1989; McNeil and Grimsditch, 1992; VerHelst-Voorhees and Wolf, 1992; Winters et al., 1992; Kingma et al., 1993a,b; Kingma, 1994). The thermodynamic driving force for the transformation is the higher density of the glassy (or disordered) state relative to that allowed for SiO_2 in the quartz structure (Fig. 3) (Hemley et al., 1988), an idea anticipated by DeCarli and Jamieson (1959) in their study of shocked quartz (see below).

EBSCOhost - printed on 2/13/2023 4:48 AM via . All use subject to https://www.ebsco.com/terms-of-use

At a microscopic level, the amorphization transition seems to be associated with a mechanical (or elastic) instability in the crystal. McSkimin et al. (1965) found that the pressure derivative of one of the shear moduli is negative (dC_{66}/dP = -2.69 at 298 K). This result suggested that quartz becomes elastically unstable at some critical pressure and that this may be related to the disordering (see Hemley, 1987). The resulting amorphous material achieves its high density relative to quartz by increasing Si coordination, as indicated by infrared spectroscopy (Williams et al, 1993). A large number of theoretical studies of this transformation have now been performed (e.g., Tse et al., 1992; Somayazulu et al., 1993; Binggeli et al. 1994). Calculations indeed predict an elastic instability in the structure at high pressure (Tse and Klug, 1991), although $B_3 = (C_{11} - C_{12})C_{44} - 2\,C_{14}^2$ becomes unstable instead of C_{66}. Thus, one of the three Born stability criteria for a hexagonal system is violated ($B_3 < 0$) (Binggeli and Chelikowsky, 1992). These calculations also show how the instability may be related to the coordination change.

Recently, transmission electron microscopy (TEM) studies have been performed on pressure-quenched samples to determine the scale of disorder and to further understand the mechanism of amorphization (VerHelst-Voorhees and Wolf, 1992; Winters et al.,

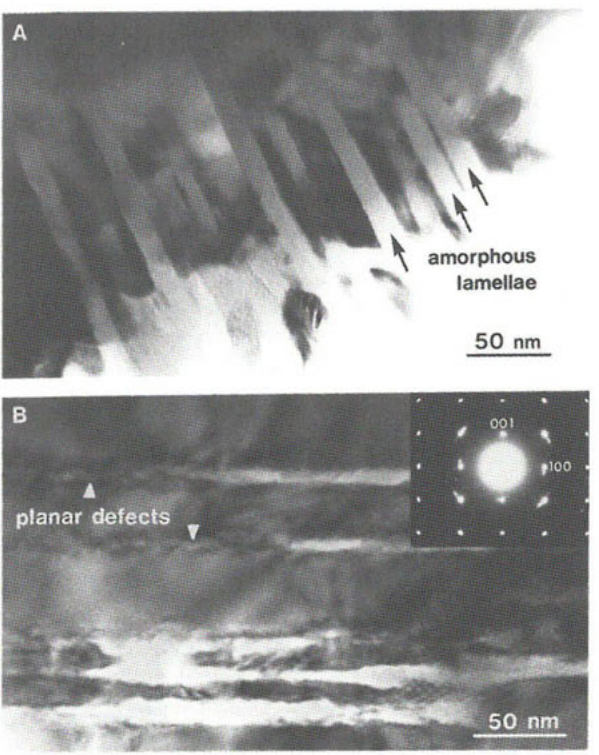


Figure 7. Representative TEM micrographs of quartz recovered from static compression (Kingma, 1994). (A) Central-beam image showing crystalline material (dark areas) and amorphous lamellae (light bands) formed by compression of quartz powder to 21-25 GPa without pressure medium. (B) Multiple-beam image from the same compression experiment showing growth of the amorphous lamella (light areas) on planar defects. Streaking and multiple spots in the selected area electron diffraction pattern (inset) indicate slight misorientation of crystalline blocks bounded by the amorphous lamellae that formed parallel to (001) in this grain.

EBSCOhost - printed on 2/13/2023 4:48 AM via . All use subject to https://www.ebsco.com/terms-of-use

1992; Cordier et al., 1993; Kingma et al., 1993a; Kingma, 1994). The transformation was shown to proceed via the formation of crystallographically-controlled planar defects followed by amorphous lamellae at pressures as low as 15 GPa (see Fig. 7, Kingma et al., 1993a; Cordier et al., 1993; Kingma, 1994). This result is also consistent with the shear-instability mechanism for the initiation of the transition; i.e., under pressure quartz becomes unstable with respect to shear along critical directions in the lattice (Goltrant et al., 1992). Moreover, these studies document that the samples are heterogeneous, with variable amounts of crystalline and amorphous material in coexistence (in the pressure-quenched samples) over a wide range of pressures. Indeed, the initial *in situ* Raman studies indicated that crystalline material persists to > 40 GPa (Hemley, 1987), and this likely depends on the stress state, orientation of crystals, and sample history.

Recent *in situ* spectroscopic and X-ray diffraction measurements also document that an intermediate crystalline-crystalline phase transition occurs at 21 GPa (Figs. 2 and 8) (Kingma et al., 1993b). Although amorphization occurs over a range of stress conditions, the extent of amorphization generally increases with pressure in the high-pressure phase (designated here as quartz II). Quartz II is not quenchable to ambient conditions (at room temperature), but characteristic optical-scale twin lamellae are observed in pressure-quenched single-crystal samples that have gone through the I-II phase transition during

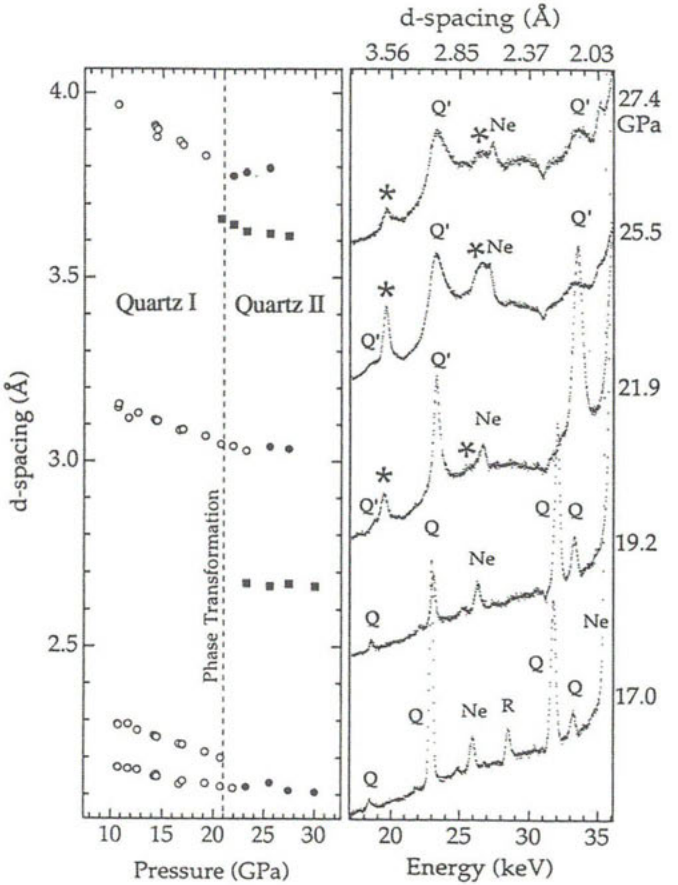


Figure 8. High-pressure synchrotron X-ray diffraction data for α-quartz showing the 21-GPa transition and gradual amorphization (Kingma et al., 1993b). Left: *d*-spacings. Right: Diffraction patterns. The labelling of the peaks is as follows: Q– α-quartz; Q'–peaks from high-pressure phase (Quartz II) that are similar to those of quartz; * – *new* peaks in the high-pressure phase; Ne – neon (pressure medium); R – ruby diffraction (pressure calibrant).

EBSCOhost - printed on 2/13/2023 4:48 AM via . All use subject to https://www.ebsco.com/terms-of-use

diamond-cell compression. These studies show that samples recovered from 20 to 30 GPa in a variety of pressure media are anisotropic because of residual crystalline SiO_2 rather than being a homogeneous anisotropic glass as proposed previously (McNeil and Grimsditch, 1992). Upon decompression, the high-pressure phase reverts to a quartz-like structure with an unusual twinned microstructure: the samples are strongly heterogeneous, with additional amorphization occurring on decompression; we believe that the transformation twinning and sample heterogeneity account for reported sign reversal in elasticity measurements (see Kingma et al., 1994; McNeil and Grimsditch, 1994). Somayazulu et al. (1994) have examined the 21-GPa transition theoretically.

There is evidence that a similar sequence of metastable transformations occurs under dynamic compression. Shock-induced polymorphism in quartz was first studied by DeCarli and Jamieson (1959), who found that shocked quartz becomes amorphous. They proposed that the transformation is driven thermodynamically by the higher density of the glass and that it could correspond to the crossing of the metastable extension of the quartz melting line (which would then have a negative slope.) Studies of quartz (and silica glass) under laser shock (Ng et al., 1991) found evidence for an anomalous increase in entropy (shock-induced disorder) at pressures prior to those expected for the formation of stishovite. The results are broadly consistent with the proposal that amorphization occurs along the principal Hugoniot for quartz (Hemley, 1987; Ahrens, 1988; Tan and Ahrens, 1990). Recent experiments suggest a previously undetected instability on the quartz Hugoniot at 23.5 GPa that may correspond to a shock-induced phase transformation (Grady and Zhugin, 1994). This is close to the 21-GPa transition observed in static compression experiments (at 298 K) (Kingma et al., 1993b). Thus, at sufficiently low temperatures in static pressure studies and in (transient) shock-wave experiments, the transformations from lower-pressure silica phases to the thermodynamically stable higher-pressure phases (i.e., stishovite and possibly post-stishovite) are not direct, despite the high temperatures involved in the latter experiments (see below).

Similar transformations occur in other compounds crystallizing in the quartz structure. Amorphization and the associated coordination change has been documented in GeO_2-quartz (Itie et al., 1989; Wolf et al., 1992; Yamanaka et al., 1992). Kruger and Jeanloz (1990) reported that α-berlinite ($AlPO_4$, isostructural with α-quartz) becomes amorphous at 18 GPa, but upon quenching it was found to revert back to the structure and orientation of the original crystal (see also Cordier et al., 1993, 1994; Polian et al., 1993). Notably, as for quartz, a negative dC_{66}/dP is also documented for $AlPO_4$ (Sidek et al., 1987).

Cristobalite and tridymite

As discussed above, the low density and open structures of tridymite and cristobalite result in relatively high compressibilities. Detailed information on the high-pressure behavior of cristobalite has been obtained from powder X-ray experiments (Tsuchida and Yagi, 1990; Miyoshi et al., 1993; Sugiura and Yamada, 1993; Parise et al., 1994) and single-crystal X-ray techniques (Downs and Palmer, 1994). Structural studies at the lower pressures show that under compression, the slightly distorted tetrahedra of the cristobalite structure remain rigid, and the structure compresses via rotation of the tetrahedra and bending of the Si-O-Si angle (Fig. 9a) (Downs and Palmer, 1994; Parise et al., 1994).

At ~1.5 GPa (well into the stability field of quartz), there is a phase transformation to a lower-symmetry phase, indicated by abrupt changes in the diffraction (Palmer and

EBSCOhost - printed on 2/13/2023 4:48 AM via . All use subject to https://www.ebsco.com/terms-of-use

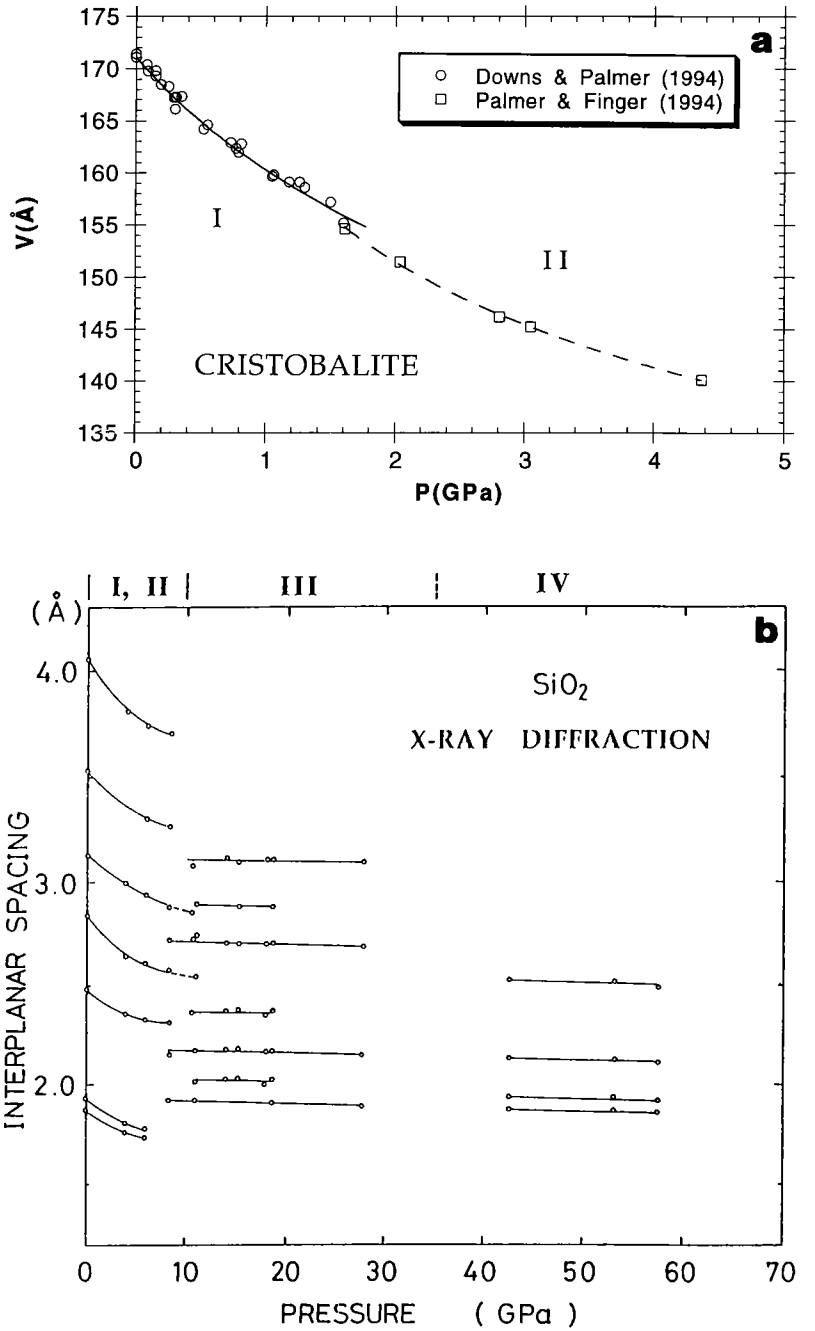


Figure 9. Room-temperature compression of cristobalite. (a) Comparison of low-pressure equation of state of Downs and Palmer (1994) and Palmer and Finger (1994). (b) Interplanar spacing versus pressure showing higher-pressure phase transitions to cristobalite III and IV (Tsuchida and Yagi, 1990). The structures of the higher-pressure phases have not been determined.

EBSCOhost - printed on 2/13/2023 4:48 AM via . All use subject to https://www.ebsco.com/terms-of-use

Finger, 1994; Parise et al., 1994), Raman (Palmer et al., 1994), and infrared (Yahagi et al., 1994) spectra. As noted above, low cristobalite is tetragonal (space group $P4_12_12$) and undergoes a phase transition at approximately 1.5 GPa to a monoclinic phase designated by Palmer et al. (1994) as cristobalite II. The Si-O distances and O-Si-O angles remain essentially unchanged up to the transition to cristobalite II. The only significant effect is in the Si-O-Si angle, which decreases from 146.49° at room pressure to 140.4° at 1.05 GPa. Because of twinning and the availability of only relatively poor diffraction patterns, Palmer and Finger (1994) were unable to refine the structure of cristobalite II. However, changes in cell parameters with increasing pressure indicate that the bulk modulus becomes somewhat larger after the transition takes place.

Recent work has resulted in new information about the higher pressure behavior of cristobalite. Two additional transitions were reported by Tsuchida and Yagi (1990) at 10 GPa and 35 GPa (Fig. 9b), but little is known about these transitions or the characteristics of the higher-pressure phases. For consistency, we designate these phases as cristobalite III and IV, although we recognize the structures may differ considerably from cristobalite. Raman and infrared spectroscopy (Palmer et al., 1994; Yahagi et al., 1994) indicate that the higher-pressure phases have dominantly tetrahedral Si; theoretical calculations predict new structures with mixed-coordination states (Tsuneyuki et al., 1989). Raman measurements of samples compressed above 10 GPa show evidence for amorphous material (Halverson and Wolf, 1990; Palmer et al., 1994; Hemley, unpublished). However, the extent of amorphization and heterogeneity of crystalline and amorphous material from static compression has not been examined in detail. Above 30 GPa, the Raman spectra show evidence for crystallization of stishovite, consistent with X-ray diffraction experiments (Tsuchida and Yagi, 1989). Shock-induced amorphization of cristobalite has been reported at 23-28 GPa on the basis of X-ray diffraction, TEM, and Raman spectroscopy of the quenched samples (Gratz et al., 1993). Pressure-induced amorphization of β-cristobalite has recently been studied theoretically (Zhang and Org, 1993); the existence of intermediate crystalline phases was not examined.

A similar sequence of transitions and high-pressure behavior is expected for tridymite, but few high-pressure experiments have been performed on this phase. Tridymite is a layer structure that often contains stacking faults; it is extremely difficult to obtain single crystals that give sharp, unambiguous diffraction patterns. In diamond-cell experiments at room temperature, Nukui et al. (1980) observed a reversible transition in a synthetic MC-type tridymite at 0.5 GPa. The symmetry changed from monoclinic to orthorhombic, and a twin boundary in the monoclinic phase (observed with an optical microscope) disappeared at the transition. In this study, no transition was observed up to 3 GPa in a natural pseudo-orthorhombic crystal. Cohen and Klement (1980) used differential thermal analysis (DTA) apparatus to examine the effect of pressure (up to 0.6 GPa) on the temperatures of transitions between "low," "middle," and "high" tridymite. However, this experiment identified no new phases. If one could obtain a good crystal or homogeneous powder sample, it would be useful to compare the bulk modulus of tridymite with that of cristobalite. It is interesting to note that $LiKSO_4$, which crystallizes in a stuffed tridymite structure, has been shown to undergo pressure-induced amorphization at 12 GPa (Sankaran et al., 1988).

Coesite

The coesite structure is composed of four-membered rings of silicate tetrahedra linked at corners to form chains parallel to *c*. There is one Si-O-Si angle constrained to

EBSCOhost - printed on 2/13/2023 4:48 AM via . All use subject to https://www.ebsco.com/terms-of-use

be 180° because this oxygen (O1 in Levien and Prewitt, 1981) is located on a center of symmetry. The structure and compression mechanism for coesite are shown in Figure 10. The four distinct Si-O-Si angles all decrease with pressure, the largest change being in Si2-O2-Si2, which decreases from 142.7° at room pressure to 136.4° at 5.19 GPa. This angle describes the kinking of chains parallel to c, whereas the other three describe distortions within the four-membered rings of tetrahedra. The mean Si-O bond lengths in each of the two symmetrically distinct silicate tetrahedra both exhibit significant contraction as a function of pressure; the Si1 tetrahedron becomes slightly more distorted, but the distortion of the Si2 tetrahedron does not change up to 5.19 GPa. The Si-Si distances decrease by as much as 0.07 Å over this pressure range, showing that the overall volume decrease is a result of the chains kinking and moving closer together.

Kirfel et al. (1979) reported the synthesis of a slightly denser form of coesite that crystallized with $P2_1/a$ symmetry. This apparent symmetry, however, was later found to result from twinning (Sasaki et al., 1983), and the $P2_1/a$ polymorph was retracted (Kirfel and Will, 1984). Twinning in coesite is found to be pervasive on (100). Despite the monoclinic distribution of components, the unit cell of coesite has strong pseudohexagonal symmetry, $a \cong 2b \cong c$, $\beta \cong 120°$. Thus, the reciprocal lattice net for one twin may coincide with that of another member (Sasaki et al., 1983). To reconcile thermochemical data, Hosieni et al. (1985) suggested that coesite may undergo a minor structural modification at high P-T conditions, but this has not been directly examined (i.e., by *in situ* experimental techniques).

Spectroscopic measurements provide additional information on the compressional behavior of coesite. The single-crystal elastic moduli under ambient conditions have been determined by Brillouin scattering (Weidner and Carleton, 1977). High-pressure Raman spectra show that, like quartz, the phase becomes amorphous on compression at room temperature, with amorphization beginning at 25 to 30 GPa (Hemley, 1987). These measurements also revealed that coesite undergoes a metastable crystalline-crystalline transition (coesite I-II) near 25 GPa (Hemley, 1987), subsequently documented by synchrotron X-ray diffraction (Hemley et al., 1988) and infrared spectroscopy (Williams et al., 1993). Spectroscopic data (Fig. 11) indicate that coesite II also has tetrahedral Si, and X-ray data suggest that the structure may be derived from a small distortion of the coesite structure. Crystal chemical arguments and theoretical calculations suggest that the transition involves a bending of characteristic linear Si-O-Si linkages in the coesite structure (Jackson and Gibbs, 1988).

Stishovite

Stishovite plays an important role as a prototype phase having octahedrally coordinated silicon. The significant variation among results of X-ray diffraction studies during static compression (e.g., Liu, 1974; Olinger, 1976; Sato, 1977; Sugiyama et al., 1987; Tsuchida and Yagi, 1989; Ross et al., 1990) indicates that the structural properties of stishovite at high pressure are highly sensitive to stress (Fig. 12a,b). The single-crystal elastic properties were determined at ambient conditions by Brillouin scattering (Weidner et al., 1982). The bulk modulus obtained from the average over the elastic moduli is close to that obtained by static compression for stishovite in a hydrostatic medium.

Stishovite is more compressible in the a than in the c direction (Fig. 12b), interpreted by Ross et al. (1990) as the result of significant Si-Si repulsion across the shared edges of octahedra that form chains in the c direction. However, the effect of Si-Si repulsion is reduced somewhat by shortening of the O-O distance along the octahedral shared edges,

EBSCOhost - printed on 2/13/2023 4:48 AM via . All use subject to https://www.ebsco.com/terms-of-use

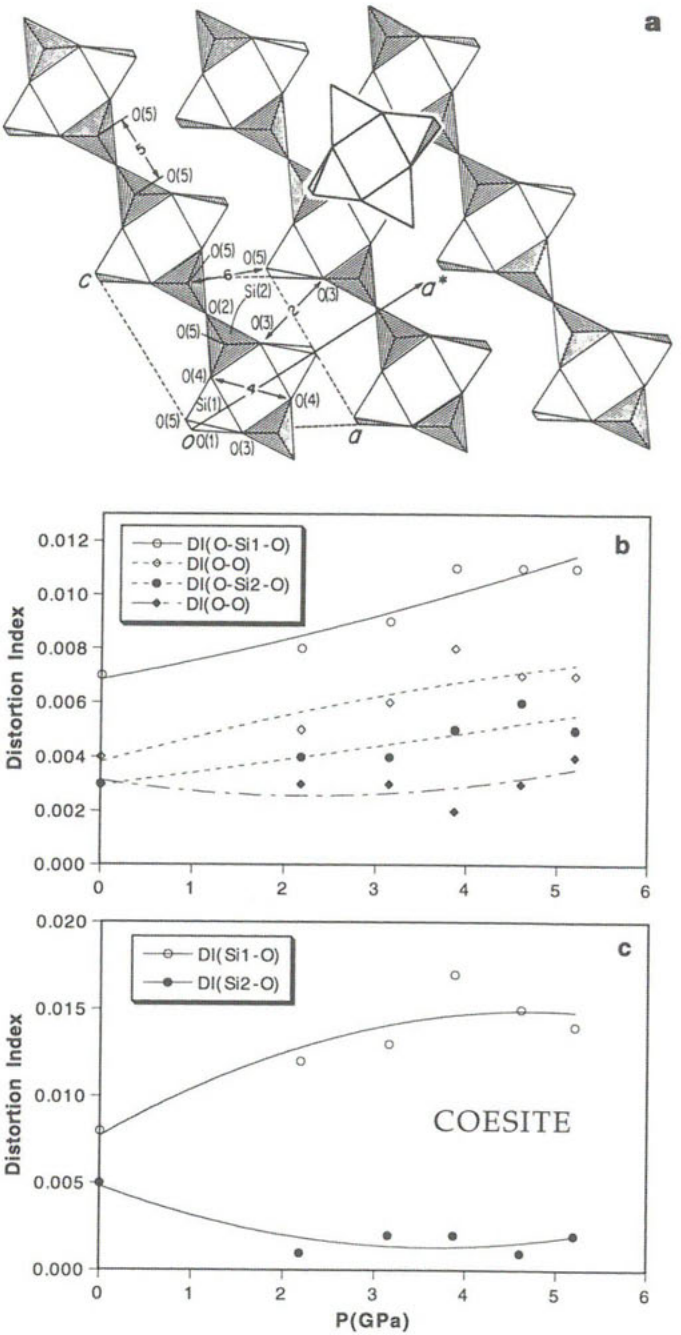


Figure 10. Effect of pressure on the structure of coesite (from Levien and Prewitt, 1981). (a) Crystal structure. (b) Distortion of O-Si-O angles and O-O distances along tetrahedral edges. (c) Distortion index for the Si-O bonds.

EBSCOhost - printed on 2/13/2023 4:48 AM via . All use subject to https://www.ebsco.com/terms-of-use

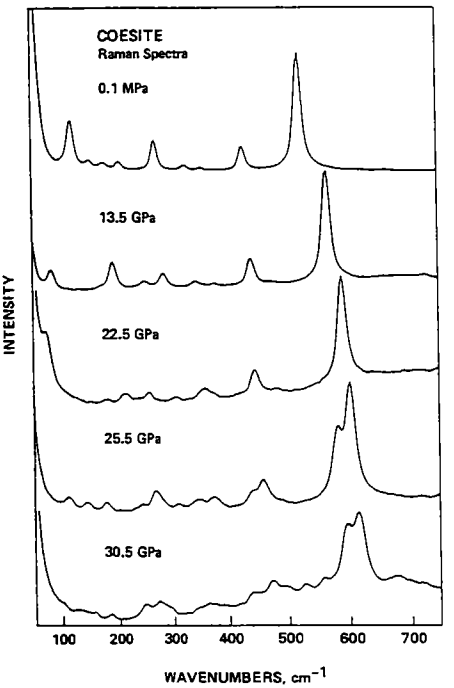


Figure 11. Evolution of the Raman spectrum of coesite (300 K) (Hemley, 1987). The doubling of the principal bands at 25 GPa is indicative of the high-pressure coesite I-II transition. At higher pressure, there is an increase in the diffuse scattering associated with the growth of the amorphous component in the sample.

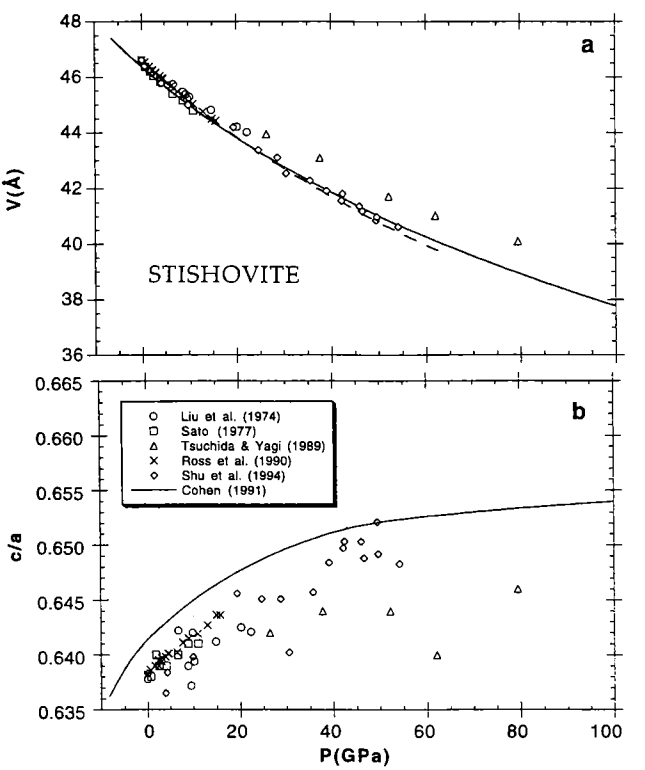


Figure 12. Comparison room-temperature experimental data and theoretical results (solid lines) for static compression of stishovite. (a) *P-V* equation of state. The dashed line is the equation of state fit to the data of Ross et al. (1990) and Shu et al. (1994, to be published) with K_0=298(±8) GPa and K_0'=3.98 (±0.46). (b) *c/a* ratio.

EBSCOhost - printed on 2/13/2023 4:48 AM via . All use subject to https://www.ebsco.com/terms-of-use

resulting in a shielding effect that reduces the repulsive forces between the Si ions. It has long been noticed that this (ambient condition) O-O distance of 2.29 Å is one of the shortest found in any oxide not containing hydrogen. In contrast to the tetrahedral forms of silica, the Si-O distances in stishovite change significantly as pressure is increased from ambient to 15 GPa. Not surprisingly, the equatorial Si-O bonds (involving the shared edges) are less compressible (Δ = 0.02 Å) than the apical Si-O bonds that are normal to the *c* direction (Δ = 0.04 Å). Compression is also accommodated by decreases in the O-O distances, but neither the O-Si-O nor the Si-O-Si angles show significant changes with pressure. Moreover, the large bulk modulus for stishovite (Fig. 3), is the largest known value both for oxides with the rutile structure or for any silicate; the compression mechanisms for the various silica phases are very different.

Post-stishovite phases

Since the discovery of stishovite, a major question has revolved around possible transformations to a denser structure at high pressures. Many post-stishovite structures have been proposed, including fluorite (CaF_2) (Syono and Akimoto, 1968), Fe_2N (modified niccolite, NiAs) (Liu et al., 1978; Sekine et al., 1987), α-PbO_2 (Liu, 1982; Ming and Manghnani, 1982), *I*2/a (modified α-PbO_2) (Tse and Klug, 1992), cotunnite (Liu, 1982), $CaCl_2$ (Nagel and O'Keeffe, 1971; Hemley et al., 1985; Tsuneyuki et al., 1989; Cohen, 1992; Lacks and Gordon, 1993) and $Pa\bar{3}$ (pyrite-like) (Park et al., 1988; Cohen, 1992). Experimental pursuit of this problem is impeded by the extreme pressure-temperature conditions and the possibility that the new phases are not quenchable. As a result, many of the proposed structures originate from theoretical calculations and studies of analog compounds (e.g., GeO_2, TiO_2, PbO_2). Evidence for the Fe_2N structure has been presented on the basis of static and shock-wave experiments on SiO_2 (Liu et al., 1978; Sekine et al., 1987), but it is likely that this phase can only exist metastably as it has a lower density than stishovite.

The transition of stishovite to the $CaCl_2$ structure involves a slight tilting of the SiO_6 octahedra, resulting in a closer packing (Fig. 13). Thus, it is not likely that the transition would be hindered by kinetic barriers that are present for reconstructive transformation mechanisms. Nagel and O'Keeffe (1971) pointed out that the distortions of the rutile-$CaCl_2$ transition have the same symmetry as the stishovite B_{1g} vibrational mode, which should therefore be a pressure-induced soft mode (i.e., the frequency decreases with pressure) and may drive the transformation. The softening of the B_{1g} mode during quasihydrostatic compression was documented in a Raman study of stishovite to a

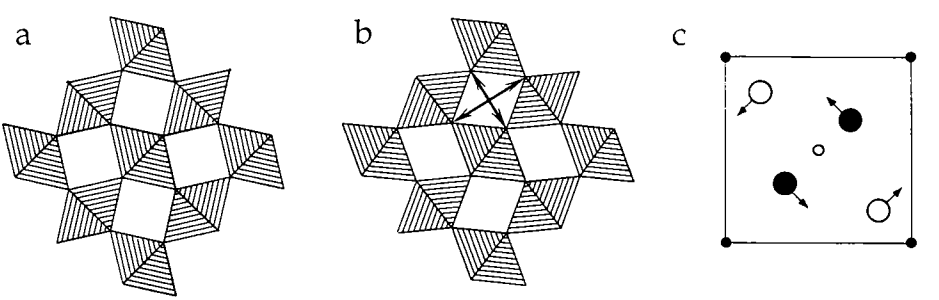


Figure 13. Relationship between (a) rutile and (b) $CaCl_2$ structures. Atomic displacements associated with the rutile B_{1g} Raman mode are shown in (c).

EBSCOhost - printed on 2/13/2023 4:48 AM via . All use subject to https://www.ebsco.com/terms-of-use

maximum pressure of 33 GPa, but no transition was observed (Hemley, 1987). It was also pointed out in this study that a shear instability will occur prior to the complete softening of the mode ($n \rightarrow 0$) (Miller and Axe, 1967). In the case of rutile, the B_{1g} mode contributes directly to the shear modulus $C_s=(C_{11}-C_{12})/2$ (Striefler, 1985). The synthesis of $CaCl_2$-structured silica has been reported on heating of both α-quartz and amorphous silica at pressures > 100 GPa (Tsuchida and Yagi, 1989) on the basis of the disappearance of two stishovite X-ray diffraction lines and the shift of a single line into a position consistent with the $CaCl_2$ structure. The nonhydrostatic nature of these experiments complicates an accurate characterization of the phase transition.

Lattice and molecular dynamics models have predicted the transition from stishovite to $CaCl_2$-silica in the megabar region (Hemley et al., 1985; Cohen, 1987; Matsui and Tsuneyuki, 1992; Tse and Klug, 1992; Lacks and Gordon, 1993). In contrast, a recent first-principles calculation predicted the transition to $CaCl_2$ at the much lower pressure of 45 GPa (Fig. 14; Cohen, 1992). Using the linearized-augmented plane-wave method, Cohen (1992) calculated that the B_{1g} mode vanishes around 75 GPa. The calculations predicted that stishovite becomes unstable at 45 GPa, when C_{11}-C_{12} goes to zero, while the semiempirical model of Striefler (1985) found the instability to occur at 30 GPa. Cohen's (1992) calculations predict that the stishovite-to-$CaCl_2$ transition is characterized by a reversal in the pressure shift of the lowest frequency Raman band from the soft B_{1g} mode (in the rutile structure) to the hard A_g mode (in $CaCl_2$); i.e., the B_{1g} correlates with the A_g mode across the transition. Further, the stishovite E_g mode splits into the $CaCl_2$ B_{2g} and B_{3g} at the transition. Thus, the formation of $CaCl_2$-structured silica from stishovite is expected to be readily detected by high-pressure Raman scattering.

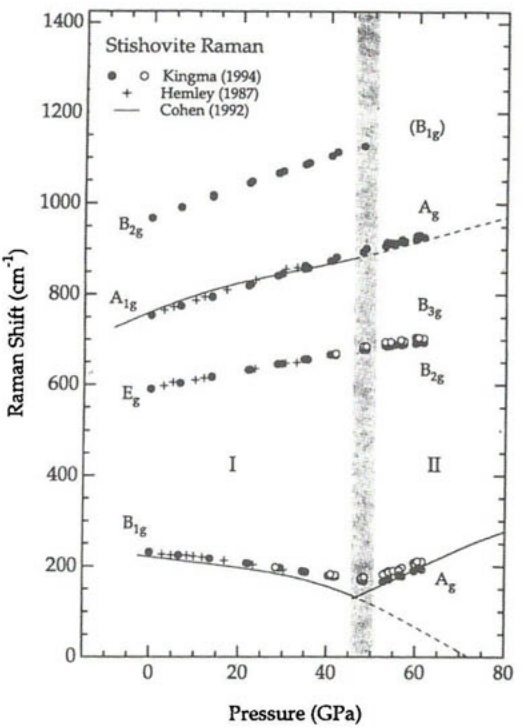


Figure 14. Pressure dependence of the Raman bands of stishovite showing the stishovite I-II transition (the rutile ⇔ $CaCl_2$-type structure) (300 K). From Kingma (1994).

EBSCOhost - printed on 2/13/2023 4:48 AM via . All use subject to https://www.ebsco.com/terms-of-use

Very recently, the high-pressure Raman spectum of stishovite was measured to pressures in excess of 60 GPa (Fig. 14; Kingma, 1994). The results are in excellent agreement with the earlier measurements of Hemley (1987) and the first-principles calculations of Cohen (1992). The new, higher pressure data demonstrate that stishovite transforms to the $CaCl_2$ structure (stishovite II) around ~50 GPa, considerably lower than that documented by powder X-ray diffraction (Tsuchida and Yagi, 1989), which is less sensitive to the orthorhombic distortion. If the transition is weakly first order, a small hysteresis loop is expected. The symmetries and assignments of the observed Raman lines of stishovite II were made using theory and analogy to $CaCl_2 \Leftrightarrow$ rutile transformations in other materials. In view of the similarity in the two structures, an alternative name for the high-pressure phase is β–stishovite.

Higher-pressure behavior

Several high-pressure studies carried out in the 1970s suggested that silica transforms to a conducting state in the 100-GPa range, but this work has been controversial (Liu and Bassett, 1986), and the available experimental and theoretical work indicate that the solid phases remain insulators at these pressures (see chapter by Cohen). Samples of silica (originally quartz) compressed to 200 GPa in a diamond cell remain transparent, although detailed measurements of optical properties have not been performed (Mao and Hemley, unpublished). Diffraction experiments on samples of quartz compressed at room temperature to 180 GPa show no evidence for the transition to fluorite-type silica, predicted theoretically to be dynamically unstable (Hemley et al., 1985; Susman et al., 1990; Miyoshi et al., 1993). Likewise, transformation to structures with space group $Pa\bar{3}$ (Park et al., 1988; Cohen, 1992) or *I2/a* (Tse and Klug, 1992) was not supported. It is possible that these transitions require heating. There have been reports of volume discontinuities above 100 GPa in magnetic compression shock experiments (Pavlovskii et al., 1978), but few details of these experiments are given and the results are not consistent with other studies (e.g., Trunin et al., 1971; Lyzenga et al., 1983). The transition from stishovite to the $Pa\bar{3}$ structure is predicted to occur with a 5% volume discontinuity above 150 GPa (at 0 K); the transition from the $CaCl_2$ structure should be shifted to higher pressures by a small amount due to the similarity of the $CaCl_2$ and rutile structures. Higher pressure shock-wave studies of quartz and quartzite rock, reportedly to 2 TPa (Trunin et al., 1971), probe the dense molten state.

Glass and lower-density polymorphs

Silica glass exhibits a number of unusual, if not anomalous, properties under pressure. First, the glass can be permanently densified by application of pressure (Bridgman and Simon, 1953; Roy and Cohen, 1961; Devine and Arndt, 1987), as well as by other means (Primak, 1975); that is, the material can be recovered in a densified state on quenching. Densification can exceed 20% and depends strongly on maximum *P-T* conditions, nonhydrostatic stress, and time. Numerous studies have been carried out to characterize the structural state of the densified materials. In general, evidence for a decrease in the mean Si-O-Si angle and a small increase in the Si-O bond has been obtained from radial distribution functions from X-ray (Couty and Sabatier, 1978) and neutron (Susman et al., 1990, 1991) diffraction, infrared and Raman spectroscopy (McMillan et al., 1984; Hemley et al., 1986a), electron spin resonance (Devine and Arndt, 1987), and X-ray spectroscopy (i.e., XANES) (Davoli et al., 1992).

Another anomalous property of silica glass is its initial decrease in bulk modulus with increase in pressure (negative K_0'). The bulk modulus reaches a minimum at

EBSCOhost - printed on 2/13/2023 4:48 AM via . All use subject to https://www.ebsco.com/terms-of-use

~2 GPa before increasing, as is the case for most materials (see Bridgman, 1939; Kondo et al., 1981; Schroeder et al., 1982; Meade and Jeanloz, 1987; Zha et al., 1994). Also, the Grüneisen parameter is negative. *In situ* spectroscopic studies (Fig. 15) reveal significant changes in structure and dynamical properties of the glass starting at a few GPa (Hemley et al., 1986a; Williams and Jeanloz, 1988; Suguira and Yamadaya, 1992; Williams et al., 1993; Zha et al., 1994). These studies indicate significant collapse in both the distribution and mean Si-O-Si angle in the glass over this pressure range. Irreversible compaction (>10 GPa) is accompanied by a shift in ring statistics toward smaller (more compact) ring structures of SiO_4 tetrahedra (Hemley et al., 1986a; Suguira and Yamadaya, 1992). The spectroscopic data indicate that above 20 GPa the SiO_4 tetrahedra become destabilized, and there is a gradual increase in Si coordination from 4 to 6. This was confirmed by X-ray diffraction using synchrotron radiation techniques (Fig. 16; Meade et al., 1992). A pressure-induced coordination change in GeO_2 glass has been documented by high-pressure EXAFS (Itie et al., 1989) and by Raman scattering (Durben and Wolf, 1991). Brillouin measurements for SiO_2 glass to 57 GPa show that Poisson's ratio increases from 0.19 at zero pressure to 0.30 to 0.35 above 23 GPa (Zha et al., 1994). The high-pressure value is close to that typically found for metals and is consistent with the decrease in shear strength at these pressures (Meade and Jeanloz, 1988).

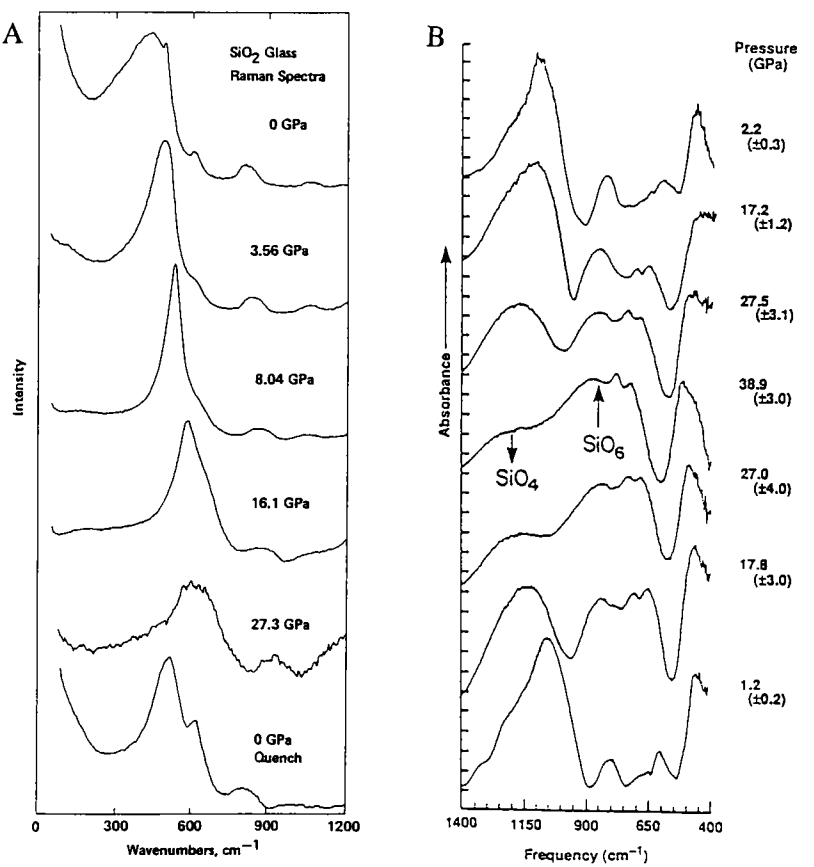


Figure 15. Pressure dependence of the vibrational spectrum of silica glass on increasing and decreasing pressure. (a) Raman spectrum (Hemley et al., 1986a). (b) Infrared spectrum (Williams and Jeanloz, 1988).

EBSCOhost - printed on 2/13/2023 4:48 AM via . All use subject to https://www.ebsco.com/terms-of-use

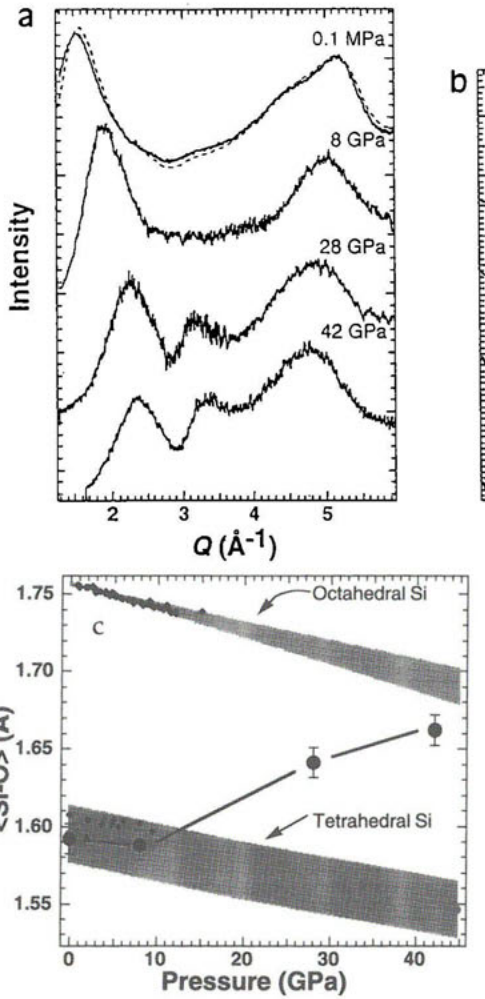


Figure 16. Pressure dependence of X-ray diffraction of silica glass (Meade et al., 1992). (a) Structure factor. (b) Pair correlation function. (c) Si-O bond length; the small symbols correspond to data from crystalline phases.

The first theoretical study of the change in structure of the glass under pressure was the pioneering molecular dynamics simulations of Woodcock et al. (1976). In particular, this study was able to accurately simulate the densification of silica under pressure; the glass transition temperature was also studied and predicted to decrease slightly with pressure (a prediction not yet tested directly by experiment). More recently, a variety of calculations have been performed with improved interatomic potentials. Recent simulations of the pressure-dependence of the structure factor and the large change in the first sharp diffraction feature (Jin et al., 1993) are in excellent agreement with the experimental results (Meade et al., 1992). Other high-pressure simulations include those of Kubicki and Lasaga (1988), Stixrude and Bukowinski (1991), and Tse and co-workers (Tse and Klug, 1992; Tse et al., 1992). Phenomenological models for high-pressure transformations in glasses include two-state models (Vucevich, 1972; Karpov and Grimsditch, 1993), and the continuous coordination change, bond-bending model of Stolper and Ahrens (1987).

EBSCOhost - printed on 2/13/2023 4:48 AM via . All use subject to https://www.ebsco.com/terms-of-use

The high-pressure behavior of ultralow-density silica phases (aerogels) has been studied by shock-wave techniques (Grover et al., 1992; Holmes and See, 1992; Rabie and Dick, 1992). Because of their exceedingly low density and enormous compressibility, very high temperatures are reached on the Hugoniot.

COMPARISON OF HIGH-PRESSURE TRANSFORMATION.

Transformation kinetics and metastability

From the foregoing discussion, it is clear that there are numerous examples of metastability in silica at high pressure. As a result, it is important to examine the kinetic factors that control transformations both experimentally and in nature. Pressure dramatically enhances the crystallization of quartz from glass; reaction rates are also strongly affected by the presence of impurities such as water (Fratello et al., 1980a,b). The kinetics of crystallization of coesite from glass and quartz have been studied in detail by Naka et al. (1976). We also point out here that differential stress can significantly alter the phase relations in the SiO_2 system. For example, Coe and Paterson (1969) studied the effect of differential stress on the α-β transition. Green (1972) demonstrated that coesite could be grown metastably from quartz in environments of high differential stress at confining pressures as low as 1.4 GPa. An even more striking example of metastability was reported by Alam et al. (1988), who found evidence for the formation of coesite, stishovite, and possibly Fe_2N-structure SiO_2 at ambient pressure by laser-heating 1-μm quartz particles. This intriguing result bears a close parallel to the metastable growth of diamond by chemical vapor deposition.

The kinetics and mechanism of the back transformations of the metastable high-pressure phases to the lower-pressure equilibrium phases is important for the use of these phases as geobarometers (or geospeedometers). The temperature dependence of the kinetics of the stishovite-to-glass back transformation has been studied by a number of workers (Skinner and Fahey, 1963; Dachille et al., 1963; Gigl and Dachille, 1968). These studies indicated that no stishovite formed in the Earth's interior would be preserved over geologic time in rocks at the surface. Skinner and Fahey (1963) found that stishovite rapidly reverts to glass at temperatures above 870 K and that the glass is essentially indistinguishable from normal SiO_2 glass (fused silica), although an intermediate short-lived structure may exist. The kinetics of the back transformation of both stishovite and coesite to glass have been studied more recently by Brazhkin et al. (1993). By use of ^{29}Si NMR, Xue et al. (1993) provide evidence that the stishovite transformation occurs via a heterogeneous nucleation and growth mechanism. Richet (1988) has shown that the amorphization process of stishovite (as well as that of coesite) can be understood in terms of (metastable) equilibrium thermodynamics.

Static versus dynamic compression

The state of silica samples compressed in shock-wave experiments is complex and has been controversial. An early observation was the very low yield of high-pressure crystalline phases (stishovite and coesite) in samples recovered in shock compression experiments above the transformation pressures. Typically, abundant glass is observed, although small amounts of stishovite were reported in later experiments (Stöffler, 1971; Ashworth and Schneider, 1985). It was proposed that glass recovered in shock experiments to pressures above the transformation to stishovite results from the back transformation of stishovite at high temperatures of the shock (McQueen et al., 1963), although melting is not required (Skinner and Fahey, 1963). Reasonable yields of

EBSCOhost - printed on 2/13/2023 4:48 AM via . All use subject to https://www.ebsco.com/terms-of-use

stishovite were generated in laboratory shocks by designing experiments to allow removal of heat (see Kleeman and Ahrens, 1973). Kieffer et al. (1976) suggested that fluids played a role in the formation and preservation of the high-pressure phases at Meteor Crater.

In early shock studies, the formation of glass was associated with melting. The observation in recent static-compression experiments of pressure-induced transformation of crystalline silica to an amorphous phase suggests that amorphization in shock compression could also occur via a solid-state process. DeCarli and Jamieson (1959), whose experiments were performed prior to the discovery of stishovite, had proposed that the recovered glass formed directly from quartz. The recent observations of solid-state amorphization in static compression experiments support this original proposal. Recent shock studies are also consistent with the prominent role of solid-state amorphization (e.g., Gratz et al., 1992), although it is clear that glass forms upon decompression from melts at higher shock conditions (i.e., > 50 GPa on the quartz Hugoniot).

Sound velocity measurements in shocks have provided additional insight into the behavior of silica on dynamic compression (Grady et al., 1975; Pavlovskii, 1976; Chhabildas and Miller, 1985; McQueen, 1992) (Fig. 17). At about 70 GPa for silica glass and about 110 GPa for quartz, the sound velocities decrease and abrupt changes in emitted thermal radiation are observed; both of these phenomena are consistent with shock-induced melting. Above these pressures, the measured Hugoniot velocity corresponds to the bulk sound speed. These measurements indicate a loss of material strength behind the shock front in the transformation ("mixed phase") region (20 to 40 GPa); in the high-pressure phase regime (40 to 110 GPa) the shear modulus is non-zero, and the sound speed drops to the bulk value above 108 GPa. Swegle's (1990) analysis of unloading paths allows for a 2-GPa strength at 30 GPa, reduced relative to the value of about 6 GPa at the elastic limit. Moreover, Figure 17 shows that the Hugoniot sound velocities in silica glass above the melting point are broadly consistent with the trend defined by the bulk sound velocities measured under static compression (Zha et al., 1994). Thus, within the pressure regime of the shock-induced high-pressure silica glass, compressional and bulk sound velocities are similar under both static and dynamic loading, despite temperature differences of 4500 K or more.

In their study of shocked silica glass, Schmitt and Ahrens (1989) found evidence for heterogeneous deformation below 26 GPa, which significantly complicates the characterization of the thermodynamic state (including melting) of the material. Tan and Ahrens (1990) assume that most of the material transforms to high-pressure phases via a molten state associated with optical features identified as high-temperature shear bands. There may be parallels to optical properties of deformed silica in diamond-cell experiments: laser-induced luminescence of heavily deformed quartz samples has been observed at confining pressures above 20 GPa (Hemley, unpublished). The nature of this luminescence is not understood, but appears to be associated with the formation of defects in metastable samples undergoing pressure-induced transformation. Similar results have been observed in samples of alkaline earth oxides undergoing the B1-B2 transition (Hemley, unpublished). These observations indicate that low-lying electronic excitations (i.e., in the visible) in such highly metastable states could complicate temperature measurements if similar types of deformation occur in shock experiments.

EBSCOhost - printed on 2/13/2023 4:48 AM via . All use subject to https://www.ebsco.com/terms-of-use

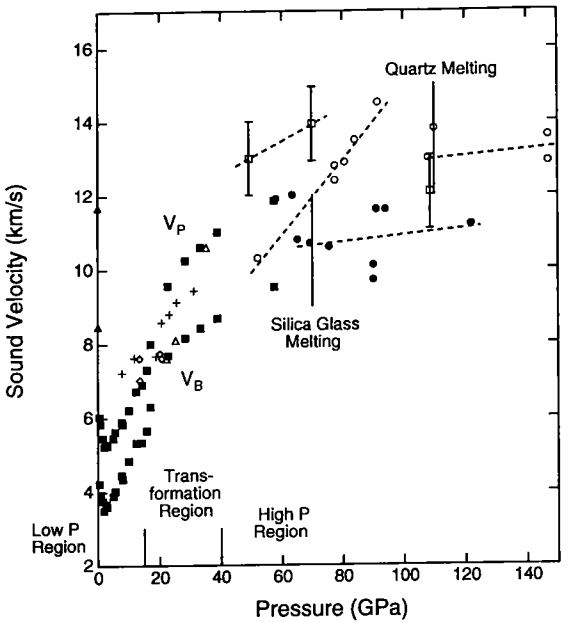
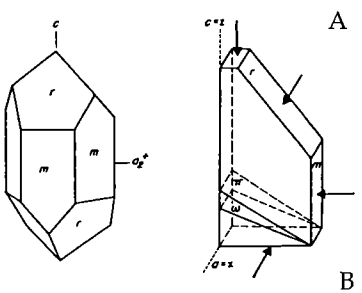
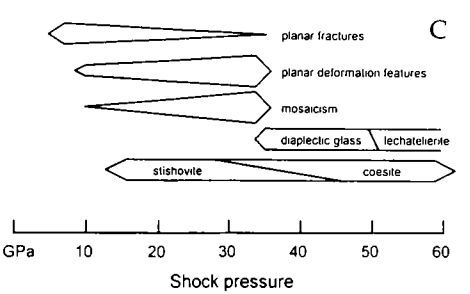


Figure 17. Sound velocities in silica glass and quartz under shock compression compared with compressional and bulk velocities under static compression (filled squares) (Zha et al., 1994). Vertical lines at 70 and 110 GPa show approximate locations of melt boundaries under shock compression for silica glass and quartz, respectively. Hugoniot data for silica glass are shown by the solid circles (McQueen, 1992), diamonds (Chhabildas and Miller, 1985); for quartz starting material + (Pavloskii 1975). Dashed lines connect different data sets at high pressure. The filled triangles show the 1-bar compressional and bulk sound velocities in stishovite (Weidner et al., 1982).



Quartz Crystal Forms	$C \wedge \perp$ Form
c - {0001} - basal pinacoid	0°
ω - {10$\bar{1}$3} ω' - {01$\bar{1}$3} - rhombohedra	22°57'
π - {10$\bar{1}$2} π' - {01$\bar{1}$2} - rhombohedra	32°25'
r - {10$\bar{1}$1} z - {01$\bar{1}$1} - unit rhombohedra	51°47'
s {11$\bar{2}$1} s' {2$\bar{1}$1$\bar{1}$} - trigonal bipyramids ξ {11$\bar{2}$2} ξ' {2$\bar{1}$1$\bar{2}$}	65°33' 47°44'
m - {10$\bar{1}$0} - first order prism	90°
a - {11$\bar{2}$0} - second order prism	90°

Figure 18. Summary of shock compression effects in α-quartz (after Huffman et al., 1993; Stoffler and Langenhorst, 1994). (A) Crystal forms and orientation of shock propagation directions studied experimentally (Huffman et al., 1993). (B) List of common forms along with their Miller indices and angle between *c* and the pole to the form. (C) Classification of observed microstructure and transformations in recovered samples.



EBSCOhost - printed on 2/13/2023 4:48 AM via . All use subject to https://www.ebsco.com/terms-of-use

Comparisons of microstructures

Numerous detailed petrologic and mineralogical studies of material from natural meteorite-shocked areas around the world have been performed (see below). In addition, material from laboratory shock experiments has been studied extensively (e.g., Avé Lallement and Carter, 1971; Christie and Ardell, 1974; Mashimo, 1980; Ashworth and Schneider, 1985; Gratz et al., 1988, 1992; McMillan et al., 1992; Tattevin et al., 1990; Langenhorst et al., 1992). The studies of natural and laboratory shocked samples document a unique set of features, including the presence of high-pressure phases, shock lamellae in quartz (as well as feldspar) grains, shock-induced transformation of crystals into glass without melting, as well as melt-related features (Fig. 18).

Recently, changes produced in quartz by static diamond-cell compression have been studied by optical and TEM methods (Winters et al., 1992; VerHelst-Voorhees and Wolf, 1992; Kingma et al., 1993a,b; Kingma, 1994). The microscopic observations of Cordier et al. (1993) provide a useful comparison with both the high-pressure shock experiments (with high transient stress) and the nominally hydrostatic diamond-cell experiments. There are striking similarities between the microstructures produced in quartz by static and dynamic compression. Every microstructure observed in quartz samples experiencing diamond-cell compression has been previously documented in the shock literature.

The characteristic microstructures produced in quartz by diamond-cell compression are crystallographically controlled planar features (planar defects and amorphous lamellae) that are recognized at both the optical and TEM scales (Kingma et al., 1993a,b; Cordier et al., 1993; Kingma, 1994). In comparison, the most widely used petrographic evidence for an impact event is the identification of planar deformation features (PDFs), a name chosen to describe all optical-scale planar microstructures produced in quartz by shock compression (Grieve, 1990). The orientations, density, and distribution of PDFs have been correlated to peak shock pressures (Hörz, 1968; Müller and Defourneaux, 1968; Avé Lallement and Carter, 1971), and more recent studies have investigated the effects of starting sample temperature on shock-related microstructures (Gratz et al., 1992; Langenhorst et al., 1992; Huffman et al., 1993). The generally accepted progression of PDF orientations with increasing peak shock pressure is as follows: basal {001} features appear first when shock pressure is above ~9 GPa; {103} PDFs appear between 15 and 17 GPa; {102} PDFs occur when peak pressure is about 20 GPa; and finally, for peak shock pressures greater than ~36 GPa, quartz is completely transformed to a high-density amorphous phase. Above peak pressures of ~20 GPa, {102} PDFs are most common, but other orientations are observed, such as {111}, {110}, {100}, {112}, {211}, and {511} (Huffman et al., 1993). Planar features are observed in identical orientations in statically compressed samples, with {102} and {103} being most common (Kingma et al., 1993a,b; Kingma, 1994). A correlation between peak pressure and lamellar orientation has not been established for statically compressed quartz samples.

TEM of quartz samples recovered from diamond-cell compression indicates that amorphous lamellae nucleate and grow on planar defects, and that the amorphous phase forms entirely in the solid state (pressure-induced amorphization) (Fig. 7; Kingma et al., 1993a). In a study of shocked quartz, Gratz et al. (1988) also found amorphous lamellae that terminated in dislocations, but they used this microstructure to hypothesize that hot, fluid silica was injected along a plane of weakness (tensional crack) in the quartz during the release phase of the shock, thus forming an amorphous lamella. The lack of high-temperature effects (such as recrystallization, flow texture, or diffuse boundaries) in close association with the amorphous lamellae produced by both shock (e.g., Kieffer et al., 1976; Ashworth and Schneider, 1985; Gratz et al., 1988; Goltrant et al., 1991; Huffman et

EBSCOhost - printed on 2/13/2023 4:48 AM via . All use subject to https://www.ebsco.com/terms-of-use

al., 1993) and diamond-cell compression of quartz strongly suggests that the amorphous phase forms in shock samples via a solid-state process (e.g., Huffman et al., 1993). In their recent review, Stöffler and Langenhorst (1994) agree that PDFs form by solid-state amorphization, but only for shock pressures < 25 GPa; they propose that PDFs originate as high-pressure melt bands for shock pressure between 25 and 35 GPa.

Surface ripples and subtle variations of orientation within the micron-scale optical lamellae of single-crystal quartz fragments experiencing compression in a diamond cell may be related to crystallographic misorientations reported for recovered shocked quartz (Kingma, 1994); streaking and asterism in electron and X-ray diffraction patterns consistent with rotational misorientations (4-10°) of the crystalline blocks separated by the amorphous lamellae have been observed in both shock and static samples (Ashworth and Schneider, 1985; Kingma et al., 1993a). It has been reported that quartz having the characteristic planar features breaks with pronounced undulatory surfaces that have a pearly, iridescent luster (Chao, 1967); these surfaces may reflect lattice misorientations. Slight changes in crystallographic orientation have also been detected in association with deformation lamellae produced by uniaxial compression of quartz with a load of 0.1-0.3 GPa (673-1023 K) (McLaren et al., 1970; Christie and Ardell, 1974).

Refinement of d values measured by X-ray diffraction of quartz samples experiencing peak shock pressures around 30 GPa have shown that the average unit cell of the quartz (or quartz-like) material recovered from shock is approximately 3% larger than that of unshocked quartz (Ashworth and Schneider, 1985, McMillan et al., 1992). Further, powder diffraction of shocked quartz has shown asymmetric broadening of lines, especially those with low l indices (Schneider et al., 1984). Naturally shocked quartz shows a high abundance of tangled curved dislocations, straight dislocations decorated by bubbles and inclusions, extensive fracturing, and evidence for annealed fractures (Engelhardt and Bertsch, 1969; Goltrant et al., 1991; Huffman et al., 1993). These microstructures can be associated with the high strain rates and brittle behavior from the shock event; similar features are not observed in the recovered diamond-cell samples.

Comparison with static deformation

Parallels may be drawn between microstructures and transformations documented by static and dynamic high-pressure experiments and those found in deformation and rock mechanics studies. Low-pressure deformation experiments with high strain rates show networks of tangled dislocations and evidence for plastic deformation (McLaren et al., 1970; Christie and Ardell, 1974; Twiss, 1974). The formation of silica glass upon grinding of quartz was inferred in comminution experiments dating back to the last century (see Lin et al., 1975). Griggs (1936) observed amorphous silica on fracture and sliding surfaces of quartz, as well as the appearance of cristobalite adjacent to the shear surfaces. Subsequently, numerous studies have provided evidence for amorphization in rock deformation experiments (for a review, see Yund et al., 1990). Yund et al. (1990) studied high-strain experimental fault gouge and found abundant amorphous material along with submicron crystalline fragments in deformed quartzite samples. These studies suggest a connection between deformation, micro-fracture, and amorphization, with similarities to observations of higher pressure (and higher stress) diamond-cell experiments (Kingma et al., 1993a). This is supported by the close similarity in features measured in the Raman spectra of quartz samples recovered from shock compression, static compression, and ball-milling (Fig. 19). Also, there are some notable similarities between these spectra and those of quartz and glass exposed to high radiation doses and electron impact (Primak, 1975). In particular, growth of bands near 500 and 620 cm^{-1} suggest similar defects, e.g., ring structures (McMillan et al., 1984; Hemley et al., 1986a).

EBSCOhost - printed on 2/13/2023 4:48 AM via . All use subject to https://www.ebsco.com/terms-of-use

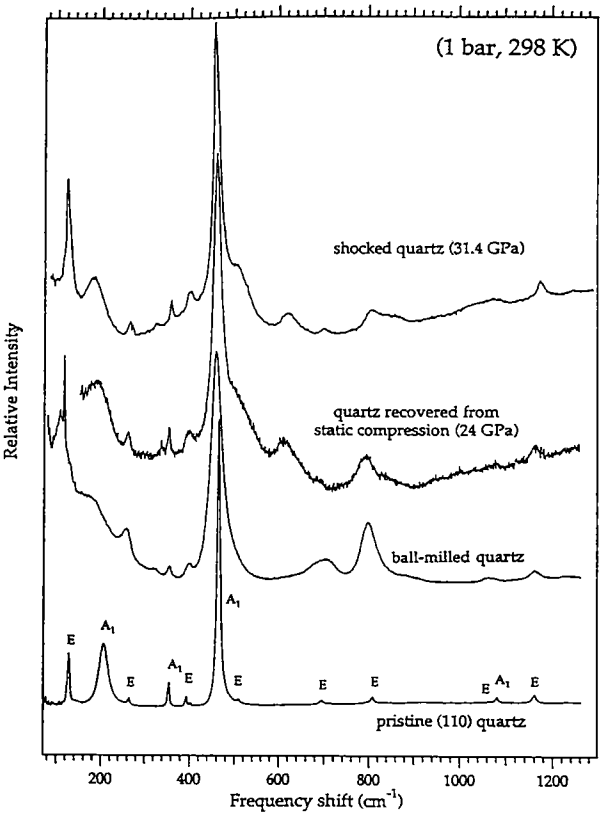


Figure 19. Comparison of Raman spectra of pristine quartz and quartz recovered from ball-milling and static compression (Kingma, 1992), and from shock compression (McMillan et al., 1992).

GEOPHYSICAL IMPLICATIONS

Impact phenomena and deformation

There is a high probability that a meteorite striking the Earth will impact some amount of quartz because of the mineral's widespread distribution. If so, then quartz with shock lamellae, and the presence of coesite and stishovite form key indicators of an impact site. As stated above, detailed petrologic and mineralogical studies have identified a set of features unique to material from natural meteorite-impact sites (e.g., Chao, 1967; French and Short, 1968, and the references therein; Engelhardt and Bertsch, 1969; Stöffler and Hornemann, 1972; Kieffer et al., 1976; Bohor et al., 1984, 1987; Alexopoulox, et al., 1988; Goltrant, et al., 1991; Huffman, et al., 1993). The earliest investigations were motivated by the debate between a volcanic (Bucher, 1963) versus impact (Dietz, 1963) origin of cryptoexplosion structures, while the later studies have been inspired by the bolide hypothesis for the Cretaceous-Tertiary boundary extinctions (Alvarez et al., 1980). Although coesite and stishovite were identified by X-ray diffraction in Vredefort Dome, South Africa (Martini, 1978, 1991), an impact origin for this structure is still in dispute due do lack of convincing microstructures in quartz (Reimold, 1992). There is also evidence for coesite in tektites (Walter, 1965).

EBSCOhost - printed on 2/13/2023 4:48 AM via . All use subject to https://www.ebsco.com/terms-of-use

Amorphous silica has been observed in natural and experimental high-strain fault gouge (see Wenk, 1978, Yund et al., 1990; Dell'Angelo, 1991). Although such observations were often taken as evidence for shear heating and melting, the formation of amorphous material in the solid state is a more likely alternative mechanism, especially in view of the absence of petrographic features indicative of a melt. Indeed, the similarities in the microstructures and other physical properties associated with amorphous material by grinding, nonhydrostatic stress, and quasihydrostatic compression in the diamond cell suggests that natural material is formed by a solid-state transformation (i.e., without melting) (Kingma et al., 1993a). On the other hand, the population of planar defects and extent of amorphization is significantly lower in the comminution experiments. Hence although there are similarities in the initial stages of the transformation, material recovered from higher pressure (e.g., >30 GPa) can be distinguished from that experiencing simple comminution.

Lower crust and upper mantle

Although most commonly associated with impact metamorphism, coesite has also been found in association with environments of static compression. The first such discovery was of coesite crystals in xenoliths from a kimberlite (Sobolev et al., 1976; Smyth and Hatton, 1977). The presence of coesite indicates equilibration of the kimberlite source at ~3 GPa (100 km); rapid quenching during ascent preserves the high-pressure phase. There have now been numerous reports of coesite as inclusions in diamond (Sobolev et al., 1976; Meyer, 1987). In high-grade metamorphic rocks (e.g., eclogites), cracks found in host grains (garnet, pyroxene) which radiate from quartz inclusions are believed to form during the slow release of pressure and temperature (uplift) by the volume increase of the coesite-quartz transformation. More recently, there have been numerous observations of relict coesite in these rocks. For instance, coesite has recently been reported from eclogites in central China (Okay et al., 1989; Wang et al. 1989), and it has been used as an indicator of high-pressure, low-temperature metamorphism in crustal rocks. While coesite may be regarded as a mineral produced during plate collision, only rarely does it survive transport to the Earth's surface (Smith, 1984). The question of how coesite can be naturally preserved in any scenario but extremely rapid ascent remains under debate. It is argued that some relict coesite is found because its host grain offers either protection from fluids (preventing retrograde metamorphism) or overpressure to prevent back transformation on slow uplift. Chopin (1984) has reported coesite inclusions in pyrope from metasedimentary rock, which suggests that coesite is a metamorphic product (along with pyrope) resulting from burial of upper crustal material.

Pawley et al. (1993) have shown that stishovite can store significant amounts of hydrogen and that it could therefore be a storage site for water in deep subducting slabs. As discussed above, the relatively rapid kinetics for inversion of stishovite to glass at moderate temperatures is consistent with the fact that no stishovite formed within the Earth has yet been observed in crustal rocks. On the other hand, it may be possible to observe stishovite as inclusions in diamond (stabilized by high compressive stresses of the diamond host). The effect of differential stress on the stability field and transformation kinetics of the high-pressure phases needs to be examined further.

Deep mantle

Stishovite is of geophysical interest in view of its wide field of stability through much of the mantle. Indeed, prior to the discovery of silicate perovskites, stishovite plus (Mg,Fe)O and other oxides were considered to be major components of the lower mantle

EBSCOhost - printed on 2/13/2023 4:48 AM via . All use subject to https://www.ebsco.com/terms-of-use

(post-spinel phases). Subsequently, stishovite has been ruled out as a major constituent, in part on the basis of its high sound velocity (measured at zero pressure) (Weidner et al., 1982). However, the evidence for the softening shear modulus under pressure inferred from the soft Raman mode (Hemley, 1987), from theoretical calculations (Cohen, 1987, 1992), and from the observation of the stishovite I-II transition, which is driven by a shear-instability (Kingma, 1994), indicates that the shear and bulk sound velocities may be lower than expected from the ambient pressure measurements; the effect of shear mode softening is expected over a range of pressures prior to the phase transition.

The stishovite I-II transition is expected to have significant geophysical implications. Theoretical calculations (see Cohen's chapter) and studies of analog materials indicate that temperature weakly stabilizes the rutile structure, giving rise to a slightly positive Clapyron slope for the stishovite-$CaCl_2$ transition (Cohen, 1992). Although suitable high-temperature experiments have not been performed on stishovite, the stable high-temperature phase in analog compounds such as $CaBr_2$ (Raptis et al., 1989) and PtO_2 (Weber et al., 1990) is rutile. Depending upon the magnitude of the *dP/dT* slope of the stishovite I-II transition, free silica in the $CaCl_2$ structure may exist in the lower mantle below depths of 1200 km. Models predicting a perovskite composition for the lower mantle require enrichment of silica and/or iron relative to the upper mantle (e.g., Knittle et al., 1986; Stixrude et al., 1992). The existence of a stable silica phase with free energy lower than that of stishovite drives the following reaction to the right:

$$\underset{\text{(perovskite)}}{(Mg,Fe)SiO_3} \leftrightarrow \underset{\text{(magnesiowüstite)}}{(Mg,Fe)O} + SiO_2$$

Additionally, if iron enrichment is significant, the production of magnesiowüstite and a silica phase is further promoted by the inability of perovskite to accommodate large amounts of iron (e.g., Stixrude et al., 1992)..

Even without a significant abundance of free SiO_2 in the lower mantle, the new transition may be important. Diamond-cell experiments indicate that silicates react with molten iron to form free SiO_2 in addition to magnesiowüstite and iron sulfides at pressures of the deep lower mantle (Knittle and Jeanloz, 1991). The observations suggest that anomalous seismic signatures of *D"*, the 100- to 300-km layer between the lower mantle and core, may arise from chemical or mineralogical heterogeneity associated with such reactions. The recent studies of the stability of the $CaCl_2$-structured SiO_2 indicate that this is the likely phase under these conditions. The effect of trace impurities and possible pressure-induced solid-solution behavior (cf., Pawley et al., 1993) on the stability of stishovite II and its physical properties needs to be investigated.

Finally, there are important geophysical consequences of the high-pressure studies of melts and glasses for the behavior of deep-seated melts. The flat fusion curves for stishovite indicate that the density of the coexisting liquid and solid phases are very close. This conjecture is further supported upon comparing the recent static pressure work of Shen and Lazor (1994), and the shock data of Lyzenga et al. (1983). The result would support the notion that the siliceous melts could remain neutrally buoyant in the lower mantle (see Rigden et al., 1984). The effect of the stishovite I-II transition on the fusion curve is expected to be small in view of the small change in structure. Although comparison between the high-temperature melts and glasses is not direct, it is notable that the experimentally documented coordination change is found to be complete by ~40 GPa (Meade et al., 1992), above which the compression mechanism is expected to change. The evident flattening the stishovite fusion curve thus plausibly arises from the structural similarity of the octahedrally coordinated liquid and solid above 40 GPa.

EBSCOhost - printed on 2/13/2023 4:48 AM via . All use subject to https://www.ebsco.com/terms-of-use

We are grateful to Q. Williams, R.E. Cohen, T.S. Duffy, and H.K. Mao for very useful discussions and correspondence during the preparation of this review. This work was supported by N.S.F.

REFERENCES

Ahrens TJ (1988) A new theory for the shock production of glasses and high pressure phases in planetary silicates. Proc 19th Lunar Planet Sci Conf 1:3-4, Lunar and Planet Inst, Houston, TX

Akaogi M, Navrotsky A (1984) The quartz-coesite-stishovite transformations: new calorimetric measurements and calculation of phase diagrams, Phys Earth Planet Int 36:124-134.

Akimoto S, Syono Y (1969) Coesite-stishovite transition, J Geophys Res 74:1653-1659.

Alam M, DebRoy T, Roy R, Breval E (1988) High-pressure phases of SiO_2 made in air by Fedoseev-Derjaguin laser process, Appl Phys Lett 53:1687-1689.

Alexopoulox JS, Grieve RAF, Robertson PB (1988) Microscopic lamellar deformation features in quartz: Discriminative characteristics of shock-generated varieties, Geology 16:796-799.

Alvarez LW, Alvarez W, Asaro F, Michel HV (1980) Extraterrestrial cause for the Cretaceous-Tertiary extinction, Science 208:1095-1108.

Araki T, Zoltai T (1969) Refinement of the coesite structure, Z Kristallogr 129:381-387.

Asell JF, Nicol M (1968) Raman spectrum of α quartz at high pressures, J Chem Phys 49:5395-5399.

Ashworth JR, Schneider H (1985) Deformation and transformation in experimentally shock-loaded quartz, Phys Chem Min 11:241-249.

Assink RA, Boslough MB, Cygan RT (1994) Characterization of amorphous material in shocked quartz by NMR spectroscopy. In: High-Pressure Science and Technology - 1993, Schmidt SC et al. (eds) p 383-386, Am Inst of Physics, New York.

Avé Lallement HG, Carter NL (1971) Pressure dependence of quartz deformation lamellae orientations, Am J Sci 270:218-235.

Belonoshko AB (1994) Molecular dynamics of silica at high pressures—equation of state, structure, and phase transitions, Geochim Cosmochim Acta 58:1557-1566.

Binggeli N, Chelikowsky JR (1992) Elastic instability in α-quartz under pressures, Phys Rev Lett 69:2220-2223.

Binggeli N, Chelikowsky JR, Wentzcovitch R (1994) Simulating the amorphization of a-quartz under pressure, Phys Rev B 49:9336-9340.

Boehler R (1980) Adiabats of quartz, coesite, olivine, and magnesium oxide to 50 kbar and 1000 K, and the adiabatic gradient in the Earth's mantle, J Geophys Res 87:5501-5506.

Bohlen SR, Boettcher AL (1982) The quartz↔coesite transformation: a precise determination and the effects of other components, J Geophys Res 87:7073-7078.

Bohor BF, Foord EE, Modreski PJ, Triplehorn DM (1984) Mineralogical evidence for an impact event at the Cretaceous-Tertiary boundary, Science 224:867-869.

Bohor BF, Modreski PJ, Foord EE (1987) Shocked quartz in the Cretaceous-Tertiary boundary clays: evidence for a global distribution, Science 236:705-709.

Brazhkin VV, Voloshin RN, Popova SV (1961) The kinetics of the transition of the metastable phases of SiO_2, stishovite and coesite to the amorphous state, J Non-Cryst. Solids 136:241-248.

Bridgman PW (1939) The high pressure behavior of miscellaneous minerals, Am J Sci 237:7-18.

Bridgman PW, Simon I (1953) Effects of very high pressures on glass, J Appl Phys 24:405-413.

Bucher WH (1963) Cryptoexplosion structures caused from without or from within the Earth? ("astroblemes" or "geoblemes"?), Am J Sci 261:547.

Chao ECT (1967) Shock effects in certain rock-forming minerals, Science 156:192-202.

Chao ECT, Fahey JJ, Littler J, Milton DJ (1962) Stishovite, a new mineral from Meteor Crater, Arizona, J Geophys Res 67:419-421.

Chao ECT, Shoemaker EM, Madsen BM (1960) First natural occurrence of coesite, Science 132:220-222.

Chhabildas LC, Miller JM (1985) Release-adiabat measurements in crystalline quartz, Sandia National Laboratory Report SAND 85-1092.

Chopin C (1984) Coesite and pure pyrope in high-grade blueschists of the Western Alps: A first record and some consequences, Contrib Min Petrol 86:107-118.

Christie JM, Ardell AJ (1974) Substructures of deformation lamellae in quartz, Geology 2:405-408.

Coe RS, Paterson MS (1969) The alpha-beta inversion in quartz; a coherent phase transition under nonhydrostatic stress, J Geophys Res 74:4921-4948.

Coes L (1953) A new dense crystalline silica, Science 118:131-132.

Cohen LH, Klement Jr WK (1980) Tridymite: Effect of hydrostatic pressure to 6 kbar on temperatures of two rapidly reversible transitions, Contrib Min Petrol 71:401-405.

EBSCOhost - printed on 2/13/2023 4:48 AM via . All use subject to https://www.ebsco.com/terms-of-use

Cohen LH, Klement Jr. WK (1967) High-low quartz inversion: determination to 35 kilobars, J Geophys Res 73:4245-4251.

Cohen RE (1987) Calculation of elasticity and high pressure instabilities in corundum and stishovite with the potential induced breathing model, Geophys Res Lett 14:37-40.

Cohen RE (1991) Bonding and elasticity of stishovite SiO_2 at high pressure: linearized augmented plane wave calculations, Am Min 76:733-742.

Cohen RE (1992) First-principles predictions of elasticity and phase transitions in high pressure SiO_2 and geophysical implications. In: High-Pressure Research: Application to Earth and Planetary Sciences. Syono Y, Manghnani MH, (eds), p 425-431, Terra Scientific, Tokyo-Am Geophys Union, Washington, DC

Cordier P, Doukhan JC, Peyronneau J (1993) Structural transformations of quartz and berlinite $AlPO_4$ at high pressure and room temperature: A transmission electron microscopy study, Phys Chem Min 20:176-189.

Cordier P, Gratz AJ, Doukhan JC, Nellis WJ (1994) Microstructures of $AlPO_4$ subjected to high shock pressures, Phys Chem Min 21:133-139.

Couty R, Sabatier G (1978) Contribution a l'etude de l'enthalpie du verre de silice densifie, J Chim Phys 75:843-848.

Cygan RT, Boslough MB, Kirkpatrick RJ (1994) NMR spectroscopic examination of shocked sandstone from Meteor Crater. In: High-Pressure Science and Technology—1993, Schmidt SC et al. (eds) p 807-810, Am Inst of Physics, New York.

d'Amour H, Denner W, Schulz H (1979) Structure determination of α-quartz up to 68 x 10^8 Pa, Acta Crystallogr B35:550-555.

Dachille F, Zeto RJ, Roy R (1963) Coesite and stishovite--stepwise reversal transformations, Science 140:991-993.

Davies GF (1972) Equations of state and phase equilibria of stishovite and a coesitelike phase from shock-wave and other data, J Geophys Res 77:4920-4933.

Davoli I, Paris E, Stizza S, Benfatto M, Fanfoni M, Gargano A, Bianconi A, Seifert F (1992) Structure of densified vitreous silica: Silicon and oxygen XANES spectra and multiple scattering calculations, Phys Chem Min 19:171-175.

Dean KJ, Sherman WF, Wilkinson GR (1982) Temperature and pressure dependence of the Raman active modes of vibrations of α-quartz, Spectrochim Acta 38A:1105-1108.

DeCarli PS, Jamieson JC (1959) Formation of an amorphous form of quartz under shock conditions, J Chem Phys 31:1675-1676.

Dell'Angelo LN (1991) Formation of an amorphous phase in experimentally produced high-pressure faults: Evidence for shear heating? (abstr), EOS Trans Am Geophys Union 71:458.

Devine RA (ed) (1988) The Physics and Technology of Amorphous SiO_2. Plenum, New York.

Devine RAB, Arndt J (1987) Si-O bond-length modification in pressure-densified amorphous SiO_2, Phys Rev B35:9376-9379.

Dietz RS (1963) Cryptoexplosion structures: A discussion, Am J Sci 261:650.

Dolino G (1988) Incommensurate phase transitions in quartz and berlinite. In: Structural and Magnetic Phase Transitions in Minerals. Adv Physical Geochem 7:17-38, Springer-Verlag, New York.

Downs RT, Palmer DC (1994) The pressure behavior of α cristobalite, Am Min 79:9-14.

Durben DJ, Wolf GH (1991) Raman spectroscopic study of the pressure-induced coordination change in GeO_2 glass, Phys Rev B 43:2355-2363.

Endo S, Akai T, Akahama Y, Wakatsuki M, Nakamura T, Tomai Y, Koto K, Ito Y, Tokonami M (1986) High temperature X-ray study of single crystal stishovite synthesized with Li_2WO_4 as flux, Phys Chem Min 13:146-151.

Engelhardt Wv, Bertsch W (1969) Shock induced planar deformation structures in quartz from the Ries Crater, Germany, Contrib Min Petrol 20:203-234.

Fratello VJ, Hays JF, Spaepen F, Turnbull D (1980a) The mechanism of growth of quartz crystals into fused silica, J Appl Phys 51:6160-6164.

Fratello VJ, Hays JF, Turnbull D (1980b) Pressure dependence of crystallization of quartz from fused silica, J Appl Phys 51:4718.

French BM, Short NM (1968) Shock Metamorphism of Natural Materials, Mono Book, Baltimore, 664 p

Gibbs GV, Prewitt CT, Baldwin KJ (1977) A study of the structural chemistry of coesite, Z Kristallogr 145:108-123.

Gibson (1928) The influence of pressure on the high-low inversion of quartz, J Phys Chem 32:1197-1205.

Gigl PD, Dachille F (1968) Effect of pressure and temperature on the reversal transitions of stishovite, Meteoritics 4:123-136.

Glinnemann J Jr., HEK, Schulz H, Hahn T, Placa SJL, Dacol F (1992) Crystal structures of the low-temperature quartz-type phases of SiO_2 and GeO_2 at elevated pressure, Z Kristallogr 198:177-212.

EBSCOhost - printed on 2/13/2023 4:48 AM via . All use subject to https://www.ebsco.com/terms-of-use

Goltrant O, Cordier P, Doukhan J-C (1991) Planar deformation features in shocked quartz: A transmission electron microscopy investigation, Earth Planet Sci Lett 106:103-115.

Goltrant O, Leroux H, Doukhan J-C, Cordier P (1992) Formation mechanisms of planar deformation features in naturally shocked quartz, Phys Earth Planet Inter 74:219-240.

Grady DE, Murri WJ, DeCarli PS (1975) Hugoniot sound velocities and phase transformations in two silicates, J Geophys Res 80:4857-4861.

Grady DE, Zhugin YN (1994) Critical transition stress in the shock compression of SiO_2, Bull. Am Phys Soc 39:410-411.

Gratz AJ, DeLoach LD, Clough TM, Nellis WJ (1993) Shock amorphization of cristobalite, Science 259:663-666.

Gratz AJ, Nellis WJ, Christie JM, Brocious W, Swegle J, Cordier P (1992) Shock Metamorphism of quartz with initial temperatures -170 to +1000 C, Phys Chem Min 19:267-288.

Gratz AJ, Tyburczy J, Christie J, Ahrens T, Pongratz P (1988) Shock metamorphism of deformed quartz, Phys Chem Min 16:221-223.

Green HW (1972) Metastable growth of coesite in highly strained quartz, J Geophys Res 77:2478-2482.

Grieve RAF (1990) Shocked minerals and the K/T controversy, Eos Trans Am Geophys Union 71:1792.

Griggs DT (1936) Deformation of rocks under high confining pressure, J Geol. 44:541-577.

Grimsditch M (1984) Polymorphism in amorphous SiO_2, Phys Rev Lett 52:2379-2381.

Griscom DL (1977) The electronic structure of SiO_2: A review of recent spectroscopic and theoretical advances, J Non-Cryst Solids 24:155-234.

Grover R, Ree F, Holmes N (1992) Equation-of-state from SiO_2 aerogel Hugoniot data In: Shock Compression of Condensed Matter - 1991, Schmidt SC et al. (eds), p 95-98, Elsevier, New York.

Halverson K, Wolf GH (1990) Pressure-induced amorphization of cristobalite: Structural relationships of crystal-amorphous transitions and polymorphic glass transitions in silica polymorphs (abstr), EOS Trans Am Geophys Union 71:1671.

Hazen RM, Finger LW, Hemley RJ, Mao HK (1989) High-pressure crystal chemistry and amorphization of α-quartz, Solid State Comm 72:507-511.

Heimann RB (1977) High-temperature and high-pressure polymorphs of silica: A review, Minerals Sci Eng. 9:57-67.

Hemley RJ (1987) Pressure dependence of Raman spectra of SiO_2 polymorphs: α-Quartz, coesite, and stishovite. In: High-Pressure Research in Mineral Physics, Manghnani MH, Syono Y (eds) p 347-359, Terra Scientific-Tokyo–Am Geophys Union, Washington, DC

Hemley RJ, Jackson MD, Gordon RG (1985) Lattice dynamics and equations of state of high pressure mineral phases studied with electron gas theory (abstr), EOS Trans Am Geophys Union 66:357.

Hemley RJ, Jephcoat AP, Mao HK, Ming LC, Manghnani MH (1988) Pressure-induced amorphization of crystalline silica, Nature 334:52-54.

Hemley RJ, Mao HK, Bell PM, Mysen BO (1986a) Raman spectroscopy of SiO_2 glass at high pressure, Phys Rev Lett 57:747-750.

Hemley RJ, Mao HK, Chao ECT (1986b) Raman spectrum of natural and synthetic stishovite, Phys Chem Min 13:285-290.

Hill RJ, Newton MD, Gibbs GV (1983) A crystal chemical study of stishovite, J Solid State Chem 47:185-200.

Hofmeister A, J Xu, Akimoto S (1990) Infrared spectroscopy of synthetic and natural stishovite, Am Min 75:951-955.

Holm JL, Kleppa OJ, Westrum Jr. EF (1967) Thermodynamics of polymorphic transformations in silica. Thermal properties from 5 to 1070°K and pressure-temperature stability fields for coesite and stishovite, Geochim Cosmochim Acta 31:2289-2307.

Holmes NC, See EF (1992) Shock compression of low-density microcellular materials. In: Shock Compression of Condensed Matter - 1991. Schmidt SC et al. (eds) p 91-94, Elsevier, New York.

Hörz R (1968) Statistical measurements of deformation structures and refractive indices in experimentally shock-loaded quartz. In: Shock Metamorphism of Natural Materials, p 243-254 Mono Book, Baltimore, MD.

Hosieni KR, Howald RA, Scanlon MW (1985) Thermodynamics of the lambda transition and the equation of state of quartz, Am Min 70:782-793.

Huffman AR, Brown JM, Carter NL, Reimold WU (1993) The microstructural response of quartz and feldspar under shock loading at variable temperatures, J Geophys Res 98:22171-22197.

Itie JP, Polian A, Calas G, Petiau J, Fontaine A, Tolentino H (1989) Pressure-induced coordination changes in crystalline and vitreous GeO_2, Phys Rev Lett 63:398-401.

Ito H, Kawada K, Akimoto S (1974) Thermal expansion of stishovite, Phys Earth Planet Int 8:277-281.

Jackson I (1976) Melting of silica isotypes SiO_2, BeF_2 and GeO_2 at elevated pressures, Phys Earth Planet Int 13:218-231.

EBSCOhost - printed on 2/13/2023 4:48 AM via . All use subject to https://www.ebsco.com/terms-of-use

Jackson MD, Gibbs GV (1988) A modeling of the coesite and feldspar framework structure types of silica as a function of pressure using modified electron gas methods, J Phys Chem 92:540-545.

Jakubith M, Lehmann G (1981) An X-ray photoelectron spectroscopic study of shock-loaded quartz, Phys Chem Min 7:165-168.

Jayaraman A, Wood DL, Maines RG (1987) High-pressure Raman study of the vibrational modes in $AlPO_4$ and SiO_2 (α-quartz), Phys Rev B35:8316-8321.

Jin W, Kalia RK, Vashishta P, Rino JP (1993) Structural transformation, intermediate-range order and dynamical behavior of SiO_2 glass at high pressures, Phys Rev Lett 71:3146-3149.

Jorgensen JD (1978) Compression mechanisms in α-quartz structures—SiO_2 and GeO_2, J Appl Phys 49:5473-5478.

Kanzaki M (1990) Melting of silica up to 7 GPa, J Am Ceram Soc 73:3706-3707.

Karpov VG, Grimsditch M (1993) Pressure-induced transformations in glasses, Phys Rev B48:6941-6948.

Kieffer SW (1979) Thermodynamics and lattice vibrations of minerals: 2. vibrational characteristics of silicates, Rev. Geophys. Space Phys 17:20-34.

Kieffer SW, Phakey PP, Christie JM (1976) Shock processes in porous quartzites: Transmission electron microscopy observations and theory, Contrib Min Petrol 59:41-93.

Kingma KJ (1994) Pressure-induced transformations in SiO_2, PhD Dissertation, Johns Hopkins University, Baltimore, MD.

Kingma KJ, Meade C, Hemley RJ, Mao HK, Veblen DR (1993a) Microstructural observations of α-quartz amorphization, Science 259:666-669.

Kingma KJ, Hemley RJ, Mao H-K, Veblen DR (1993b) New high-pressure transformation in α-quartz, Phys Rev Lett 70:3927-3930.

Kingma KJ, Hemley RJ, Mao HK, Veblen DR (1994) Response to Comment by McNeil and Grimsditch, Phys Rev Lett 72:1302.

Kirfel A, Will G (1984) Ending the "$P2_1/a$ coesite" discussion, Z Kristallogr 167:287-291.

Kirfel A, Will G, Arndt J (1979) A new phase of coesite SiO_2, Z Kristallogr 149:315-326.

Kleeman J, Ahrens TJ (1973) Shock-induced transition of quartz to stishovite, J Geophys Res 78:5954-5960.

Knittle E, Jeanloz R (1991) Earth's core-mantle boundary: Results of experiments at high pressures and temperatures, Science 251:1438-1443.

Knittle E, Jeanloz R, Smith GL (1986) Thermal expansion of silicate perovskite and stratification of the Earth's mantle, Nature 319:214-216.

Kondo K-I, Ahrens TJ (1983) Shock-induced spectra of fused quartz, J Appl Phys 54:4383-4385.

Kondo K-I, Ito S, Sawaoka A (1981) Nonlinear pressure dependence of the elastic moduli of fused quartz up to 3 GPa, J Appl Phys 52:2826-2831.

Kruger M, Jeanloz R (1990) Memory glass: an amorphous material formed from $AlPO_4$, Science 249:647-649.

Kubicki JD, Lasaga AC (1988) Molecular dynamics simulations of SiO_2, melt and glass: Ionic and covalent models, Am Min 73:941-955.

Kuskov OL, Fabrichnaya OB (1987) The SiO_2 polymorphs: the equations of state and thermodynamic properties of phase transformations, Phys Chem Min 14:58-66.

Lacks DJ, Gordon RG (1993) Calculations of pressure-induced phase transitions in silica, J Geophys Res 98:22147-22155.

Langenhorst F, Deutsch A, Stöffler D, Hornemann U (1992) Effect of temperature on shock metamorphism of single-crystal quartz, Nature 356:507-509.

Levien L, Prewitt CT (1981) High-pressure crystal structure and compressibility of coesite, Am Min 66:324-333.

Levien L, Prewitt CT, Weidner DJ (1980) Structure and elastic properties of quartz at pressure, Am Min 65:920-930.

Lin IJ, Nadiv S, Grodzian DJM (1975) Changes in the state of solids and mechano-chemical reactions in prolonged comminution processes, Minerals Sci Eng 7:313-336.

Liu L-G (1974) Silicate perovskite from phase transformations of pyrope-garnet at high pressure and temperature, Geophys. Res Lett 1:277-280.

Liu L-G (1982) High-pressure phase transformations of the dioxides: implications for structure of SiO_2 at high pressures. In: High-Pressure Research in Geophysics, Akimoto S, Manghnani MH, (eds), p 349-360, Center for Academic Publications, Tokyo.

Liu L-G, Bassett WA (1986) Elements, Oxides, Silicates - High-Pressure Phases with Implications for the Earth's Interior. Oxford, New York.

Liu L-G, Bassett WA, Sharry J (1978) New high-pressure modifications of GeO_2 and SiO_2, J Geophys Res 83:2301-2305.

Lyzenga GA, Ahrens TJ, Mitchell AC (1983) Shock temperatures of SiO_2 and their geophysical implications, J Geophys Res 88:2431-2444.

EBSCOhost - printed on 2/13/2023 4:48 AM via . All use subject to https://www.ebsco.com/terms-of-use

Maj S (1984) On the relationship between refractive index and density of SiO_2 polymorphs, Phys Chem Min 10:133-136.
Maj S (1988) Energy gap and density in SiO_2 polymorphs, Phys Chem Min 15, 271-273.
Marler B (1988) On the relationship between refractive index and density for SiO_2 polymorphs, Phys Chem Min 16:286-290.
Marsh SP (1980) LASL Shock Hugoniot Data, Univ. of Calif. Press, Berkeley, CA, p 321-323.
Martini JEJ (1978) Coesite and stishovite in the Vredefort Dome, South Africa, Nature 272:715-717.
Martini JEJ (1991) The nature, distribution and genesis of the coesite and stishovite associated with the pseudotachylite of the Vredefort Dome, South Africa, Earth Planet. Sci Lett 103:285-300.
Mashimo T, Nishii K, Soma T, Sawaoka A (1980) Some physical properties of amorphous SiO_2 synthesized by shock compression of α quartz, Phys Chem Min 5:367-377.
Matsui Y, Tsuneyuki S (1992) Molecular dynamics study of rutile-$CaCl_2$-type phase transition of SiO_2. In: High-Pressure Research: Application to Earth and Planetary Sciences. Syono Y, Manghnani MH, (eds) p 433-439, Terra Scientific, Tokyo-Am Geophys Union,Washington, DC.
McLaren AC, Turner RG, Boland JN (1970) Dislocation structure of the deformation lamellae in synthetic quartz: A study by electron and optical microscopy, Contrib Min Petrol 29:104-115.
McMillan P, Piriou B, Couty R (1984) A Raman study of pressure-densified vitreous silica, J Chem Phys 81:4234-4236.
McMillan PF, Wolf GH, Lambert P (1992) A Raman spectroscopic study of shocked single crystalline quartz, Phys Chem Min 19:71-107.
McNeil L, Grimsditch M (1994) Comment on "New high-pressure transformation in α-quartz", Phys Rev Lett 72:1301.
McNeil LE, Grimsditch M (1992) Pressure-amorphized SiO_2 α-quartz: An anisotropic amorphous solid, Phys Rev Lett 68:83-85.
McQueen RG (1992) The velocity of sound behind strong shocks in SiO_2. In: Shock Compression of Condensed Matter - 1991. Schmidt SC et al. (eds) p 75-78, Elsevier, New York.
McQueen RG, Fritz JN, Marsh SP (1963) On the equation of state of stishovite, J Geophys Res 68:2319-2322.
McSkimin HJ, Andreatch P, Thurston RN (1965) Elastic moduli of quartz versus hydrostatic pressure at 25°C and -195.8°C, J App. Phys 36:1624-1632.
Meade C, Hemley RJ, Mao HK (1992) High-pressure X-ray diffraction of SiO_2 glass, Phys Rev Lett 69:1387-1390.
Meade C, Jeanloz R (1987) Frequency-dependent equation of state of fused silica to 10 GPa, Phys Rev B35:236-244.
Meade C, Jeanloz R (1988) Effect of a coordination change on the strength of amorphous SiO_2, Science 241:1072-1074.
Meyer HOA (1987) Inclusions in diamond. In: Mantle Xenoliths. Nixon PH (ed) p 501-522, John Wiley & Sons, New York.
Miller PB, Axe JD (1967) Internal strain and Raman-active vibrations in solids, Phys Rev 163:924-926.
Ming LC, Manghnani MH (1982) High-pressure phase transformations in rutile-structured dioxides. In: High-Pressure Research in Geophysics. Akimoto S, Manghnani MH, (eds) p 329-347, Center for Academic Publications, Tokyo.
Mirwald PW, Massonne H-J (1980) The low-high quartz and quartz-coesite transition to 40 kbar between 600° and 1600°C and some reconnaissance data on the effect of $NaAlO_2$ component on the low quartz-coesite transition, J Geophys Res 85:6983-6990.
Mishima O, Calvert LD, Whalley E (1984) 'Melting Ice' I at 77 K and 10 kbar: A new method of making amorphous solids, Nature 310:393-395.
Miyoshi M, Endo M, Suito K, Onadera A, Shimomura O, Takemura K, Kikegawa T (1993) Phase transition of cristobalite. In: Progr Abstracts 30th High Pressure Symposium, p 90-91.
Müller WF, Defourneaux W (1968) Deformations-strukturen in Quartz als Indikator für Stosswellen: eine experimentelle Untersuchung an Quartz-Einkristallen, Z. Geophys. 34:483-504.
Nagel L, O'Keeffe M (1971) Pressure and stress induced polymorphism of compounds with rutile structure, Mat Res Bull 6:1317-1320.
Naka S, Ito S, Kameyama T, Inagaki M (1976) Crystallization of coesite, Memoirs, Faculty of Engineering, Nagoya University 28:265-316.
Ng A, Godwal BK, Waterman J, DaSilva L, Ashcroft NW, Jeanloz R (1991) Nonequilibrium shock behavior of quartz, Phys Rev B 44:4872-4876.
Nukui A, Yamaoka S, Nakazawa H (1980) Pressure-induced phase transitions in tridymite, Am Min 65:1283-1286.
Ogata K, Takéuchi Y, Kudoh Y (1987) Structure of α-quartz as a function of temperature and pressure, Z Kristallogr 179:403-413.

EBSCOhost - printed on 2/13/2023 4:48 AM via . All use subject to https://www.ebsco.com/terms-of-use

Okay AI, Shutong X, Sengor AMC (1989) Coesite from Dabie Shan eclogites, central China, Eur J Min 1:595-598.

Olinger B (1976) The compression of stishovite, J Geophys Res 81:5341-5343.

Palmer DC, Finger LW (1994) Pressure-induced phase transition in cristobalite: An X-ray powder diffraction study to 4.4 GPa, Am Min 79:1-8.

Palmer DC, Hemley RJ, Prewitt CT (1994) Raman spectroscopic study of high-pressure phase transitions in cristobalite, Phys Chem Min (in press).

Parise JB, Yeganeh-Haeri A, Weidner DJ, Jorgensen JD, Saltzberg MA (1994) Pressure-induced phase transition and pressure dependence of crystal structure in low (α) and Ca/Al-doped cristobalite, J Appl Phys 75:1361-1367.

Park KT, Terakura K, Matsui Y (1988) Theoretical evidence for a new ultra-high pressure phase of SiO_2, Nature 336:670-672.

Pavlovskii MN (1976) Measurements of the velocity of sound in shock-compressed quartzite, dolomite, anhydrite, sodium chloride, paraffin, plexiglas, polyethylene, and fluoroplast-4, Z. Prik. Mek. Tek. Fiz. 17:136-139.

Pavlovskii AI, Kolokol'chikov NP, Dolotenko MI, Bykov AI (1978) Isoentropic compression of quartz by the pressure of a superstrong magnetic field, JETP Lett 27:264-266.

Pawley AR, McMillan PF, Hollaway JR (1993) Hydrogen in stishovite, with implications for mantle water content, Science 261, 10124-1026.

Polian A, Grimsditch M, Philippot E (1993) Memory effects in pressure induced amorphous $AlPO_4$, Phys Rev Lett 71:3143-3145.

Primak W (1975) Compacted States of Vitreous Silica - Studies of Radiation Effects in Solids, Gordon and Breach, New York

Rabie R, Dick JJ (1992) Equation of state and crushing dynamics of low-density silica aerogels. In: Shock Compression of Condensed Matter - 1991, Schmidt SC et al. (eds) p 87-91, Elsevier, New York.

Raman CV, Nedungadi TMK (1940) The α-β transformation of quartz, Nature 145:147.

Ramsdell LS (1955) The crystallography of "coesite", Am Min 40, 975-982.

Raptis C, McGreevy RL, Seguier DG (1989) Temperature-induced structural phase transition in $CaBr_2$ studied by Raman spectroscopy, Phys Rev B39:7996-7999.

Reimold WU, Colliston WP, Wallmach T (1992) Comment on "The nature, distribution and genesis of the coesite and stishovite associated with the pseudotachylite of the Vredefort Dome, South Africa", by JEJ Martini, Earth PLanet. Sci Lett 112:213-217.

Richet P (1988) Superheating, melting and vitrification through decompression of high-pressure minerals, Nature 331:56-58.

Rigden SM, Ahrens TJ, Stolper EM (1984) Densities of liquid silicates at high pressures, Science 226:1071-1074.

Ross NL, Shu J-F, Hazen RM (1990) High-pressure crystal chemsitry of stishovite, Am Min 75:739-747.

Roy R, Cohen HM (1961) Effects of high pressure on glass: a possible piezometer for the 100-kilobar region, Nature 190:798-799.

Sankaran H, Sikka SK, Sharma SM, Chidambaram R (1988) Pressure-induced noncrystalline phase of $LiKSO_4$. Phys Rev B38:170-173.

Sasaki S, Chen H-K, Prewitt CT, Nakajima Y (1983) Re-examination of "$P2_1/a$ coesite", Z Kristallogr 164:67-77.

Sato Y (1977) Pressure-volume relationship of stishovite under hydrostatic compression, Earth Planet Sci Lett 34:307-312.

Schmitt DR, Ahrens TJ (1989) Shock temperatures in silica glass: implications for modes of shock-induced deformation, phase transformation, and melting with pressure, J Geophys Res 94:5851-5871.

Schneider H, Vasudevan R, Hornemann U (1984) Deformation of experimentally shock-loaded quartz powders: X-ray line broadening studies, Phys Chem Min 10:142-147.

Schroeder J, Dunn KJ, Bundy F (1982) Brillouin scattering from amorphous SiO_2 under hydrostatic pressure. In: High Pressure in Research and Industry, Proc 8th AIRAPT Conf Blackman, CK, Johannison T, Tegner L (eds) p 259-267, Arkitektkopia, Uppsala, Sweden.

Sclar CB, Carrison LC, Schwartz CM (1962) Optical crystallography of coesite, Am Min 47:1292-1303.

Sekine T, Akaishi M, Setaka N (1987) FeN_2-type SiO_2 from shocked quartz, Geochim Cosmochim Acta 51:379-381.

Sharma SK, Mammone JF, Nicol MF (1981) Raman investigation of ring configurations in vitreous silica, Nature 292:140-141.

Shen G, Lazor P (1994) Melting of minerals under lower mantle conditions: I. Experimental results, J Geophys Res submitted for publication.

Shen AH, Bassett WA, Chou I-M (1993) The α-β quartz transition at high temperatures and pressures in a diamond-anvil cell by laser interferometry, Am Min 78:694-698.

EBSCOhost - printed on 2/13/2023 4:48 AM via . All use subject to https://www.ebsco.com/terms-of-use

Sidek HAA, Saunders GA, Hong W, Bin X, Jianru H (1987) Elastic behavior under hydrostatic pressure and acoustic-mode vibrational anharmonicity of single-crystal berlinite, Phys Rev B36:7612-7619.
Sinclair W, Ringwood AE (1978) Single crystal analysis of the structure of stishovite, Nature 275:714-715.
Skinner BJ, Fahey JJ (1963) Observations on the inversion of stishovite to silica glass, J Geophys Res 68:5595-5604.
Smith DC (1984) Coesite in clinopyroxene in the Caledonides and its implications for geodynamics, Nature 310:641-644.
Smith JV, Blackwell CS (1984) Nuclear magnetic resonance of silica polymorphs, Nature 303:223-225.
Smyth JR, Hatton CJ (1977) A coesite-sanidine grospydite from the Roberts Victor kimberlite, Earth Planet Sci Lett 34:284-290.
Smyth JR, Smith JV, Artioli G, Kvick Å (1987) Crystal structure of coesite, a high-pressure form of SiO_2, at 15 and 298 K from single crystal neutron and X-ray diffraction data: Test of bonding models, J Phys Chem 91:988-992.
Sobelev NV, Yefimova ES, Koptil VI, Lavrent'yev YG, Sobelev VS (1976) Inclusions of coesite, garnet, and omphacite in Yakutian diamond: First discovery of coesite paragenesis, Dokl. Akad. Nauk. SSSR 230:1441-1444.
Somayazulu MS, Sharma SM, Garg N, Chaplot SL, Sikka SK (1993) The beahvior of α-quartz and pressure-induced SiO2 glass under pressure: a molecular dynamics study, J Phys C: Cond Mat 65:6345-6456.
Somayazulu MS, Sharma SM, Sikka SK (1994) On the structure of the new high pressure phase in α-quartz by molecular dynamics studies, Phys Rev Lett 73:98-101.
Sosman RB (1954) New high-pressure phases of silica, Science 119:738-739.
Sosman RB (1965) The Phases of Silica. Rutgers University Press, New Brunswick, N.J.
Stishov SM, Popova SV (1961) A new dense modification of silica, Geochemistry (USSR) 10:923-926.
Stixrude L, Bukowinski MST (1991) Atomic structure of SiO_2 glass and its response to pressure, Phys Rev B 44:2523-2534.
Stixrude L, Hemley RJ, Fei Y, Mao HK (1992) Thermoelasticity of silicate perovskite and magnesiowüstite and stratification of the Earth's mantle, Science 257:1099-1101.
Stöffler D (1971) Coesite and stishovite in shocked crystalline rocks, J Geophys Res 76:5474-5488.
Stöffler D, Hornemann U (1972) Quartz and feldspar glasses produced by natural and experimental shock, Meteoritics 7:371-395.
Stöffler D, Langenhorst F (1994) Shock metamorphism of quartz in nature and experiment: I. Basic observation and theory, Meteoritics 29:155-181.
Stolper EM, Ahrens TJ (1987) On the nature of pressure-induced coordination changes in silicate melts and glasses, Geophys Res Lett 14:1231-1233.
Striefler ME (1985) On the nature of the structural instability in stishovite (abstr), EOS Trans Am Geophys Union 66:358.
Suguira H, Yamadaya T (1992) Raman scattering in silica glass in the permanent densification region, J Non-Cryst Solids 144:151-158.
Sugiura H, Yamadaya T (1993) Pressure induced phase transition of low-cristobalite. In: Progr Abstracts 30th High Pressure Symp, p 134-135
Sugiyama M, Endo S, Koto K (1987) The crystal structure of stishovite under pressure up to 6 GPa, Min J 13:455-466.
Susman S, Volin KJ, Liebermann RC, Gwanmesia GD, Wang Y (1990) Structural changes in irreversibly densified fused silica: Implications for the chemical resistance of high level nuclear waste glasses, Phys Chem Glasses 31:144-150.
Susman S, Volin KJ, Price DL, Grimsditch M, Rino JP, Kalia RK, Vashishta P, Gwanmesia G, Wang Y, Liebermann RC (1991) Intermediate-range order in permanently densified SiO_2: A neutron-diffraction and molecular-dynamics study, Phys Rev B 43:1194-1197.
Swamy V, Saxena SK, Sundman B, Zhang J (1994) A thermodynamic assessment of silica phase diagram, J Geophys Res 99:11787-11794.
Swegle JW (1990) Irreversible phase transitions and wave propagation in silicate geological materials, J Appl Phys 68:1563-1579.
Syono Y, Akimoto S (1968) High pressure synthesis of fluorite-type PbO_2, Mat. Res Bull. 3:153-157.
Tan H, Ahrens TJ (1990) Shock induced polymorphic transitions in quartz, carbon, and boron nitride, J Appl Phys 67:217-224.
Tattevin H, Syono Y, Kikuchi M, Kusabe K, Velde B (1990) Shock deformation of alpha quartz: Laboratory experiments and TEM investigation, Eur J Min 2:227-234.
Trunin RF, Simakov GV, Poduets MA, Moiseyev BN, Popov LV (1971) Dynamic compressibility of quartz and quartzite at high pressure, Izvest. Phys Solid Earth 1:8-12.
Tse JS, Klug DD (1991) Mechanical instability of α-quartz: A molecular-dynamics study, Phys Rev Lett 67:3559.

EBSCOhost - printed on 2/13/2023 4:48 AM via . All use subject to https://www.ebsco.com/terms-of-use

Tse JS, Klug DD (1992) Novel high pressure phase of silica, Phys Rev Lett 69:3647-3649.
Tse JS, Klug DD, Le Page Y (1992) High-pressure densification of amorphous silica, Phys Rev B46:5933-5938.
Tsuchida Y, Yagi T (1989) A new, post-stishovite high-pressure polymorph of silica, Nature 340:217-220.
Tsuchida Y, Yagi T (1990) New pressure-induced transformations of silica at room temperature, Nature 347:267-269.
Tsuneyuki S, Matsui Y, Aoki H, Tsukada M (1989) New pressure-induced structural transformations in silica obtained by computer simulation, Nature 339:209-211.
Twiss RJ (1974) Structure and significance of planar deformation features in synthetic quartz, Geology 2:329-332.
VerHelst-Voorhees M, Wolf GH (1992) HREM and Raman spectroscopic investigations of the pressure-induced amorphization in α-quartz (abstr), EOS Trans Am Geophys Union 73:581.
Vucevich MR (1972) A new interpretation of the anomlous properties of vitreous silica, J Non-cryst Solids 11:25-63.
Wackerle J (1962) Shock-wave compression of quartz, J Appl Phys 33:922-937.
Walter LS (1965) Coesite discovered in tektites, Science 147:1029.
Wang Q, Saunders GA, Lambson EF, Tschaufeser P, Parker SC, James BJ (1992) Temperature dependence of the acoustic-mode vibrational anharmonicity of quartz from 243 to 393 K, Phys Rev B 45:10242-10254.
Wang X, Liou JG, Mao HK (1989) Coesite-bearing ecolgite from the Dabie Mountains in central China, Geology 12:1085-1088.
Watanabe H (1982) Thermochemical properties of synthetic high-pressure compounds relevant to the Earth's mantle. In: High-Pressure Research in Geophysics, Akimoto S, Manghnani MH (eds) p 441-464, Center for Academic Publications, Tokyo.
Weaver JS, Chipman DW, Takahashi T (1979) Comparison between thermochemical and phase stability data for the quartz-coesite-stishovite transformations, Am Min 64:604-614.
Weber WH, Graham GW, McBride JR (1990) Raman spectrum of β-PtO_2: Evidence for the D_{2h}-to-D_{4h} phase transition, Phys Rev B 42:10969-10975.
Weidner DJ, Bass JD, Ringwood AE, Sinclair W (1982) The single-crystal elastic moduli of stishovite, J Geophys Res 87:4740-4746.
Weidner DJ, Carleton HR (1977) Elasticity of coesite, J Geophys Res 82:1334-1346.
Wenk HR (1978) Are pseudotachylites products of fracture or fusion? Geology 6:507-511.
Williams Q, Hemley RJ, Kruger MB, Jeanloz R (1993) High pressure infrared spectra of α-quartz, coesite, stishovite, and silica glass, J Geophys Res 98:22157-22170.
Williams Q, Jeanloz R (1988) Spectroscopic evidence for pressure-induced coordination changes in silicate glasses and melts, Science 239:902-905.
Winters RR, Garg A, Hammack WS (1992) High-resolution transmission electron microscopy of pressure-amorphized α-quartz, Phys Rev Lett 69:3751-3753.
Wolf GH, Wang S, Herbst CA, Durben DJ, Oliver WF, Kang ZC, Halvorson K (1992) Pressure-induced collapse of the tetrahedral framework in crystalline and amorphous GeO_2. In: High-Pressure Research: Application to Earth and Planetary Sciences. Syono Y, Manghnani MH (eds) p 503-517, Terra Scientific, Tokyo–Am Geophys Union, Washington, DC.
Wong PTT, Beaudais FL, Moffatt DJ (1986) Hydrostatic pressure effects on the TO-LO splitting and softening of infrared active phonons on α-quartz, J Chem Phys 84:671-674.
Woodcock LV, Angell CA, Cheeseman PA (1976) Molecular dynamics studies of the vitreous state: Simple ionic systems and silica, J Chem Phys 65:1565-1577.
Xue X, Stebbins JF, Kanzaki M (1993) A ^{29}Si MAS NMR study of sub-T_g amorphization of stishovite at ambient pressure, Phys Chem Min 19:480-485.
Yagi T, Akimoto S (1976) Direct determination of coesite-stishovite transition by in situ X-ray measurements, Tectonophysics 35:259-270.
Yahagi Y, Yagi T, Yamawaki H, Aoki K (1994) Infrared absorption spectra of the high-pressure phases of cristobalite and their coordination numbers of silicon atoms, Solid State Comm 89:945-948.
Yamanaka T, Shibata T, Kawasaki S, Kume S (1992) Pressure induced amorphization of hexagonal GeO_2. In: High-Pressure Research: Application to Earth and Planetary Sciences. Syono Y, Manghnani MH (eds) p 493-501, Terra Scientific, Tokyo–Am Geophys Union, Washington, DC.
Yang WH, Kirkpatrick RJ, Vergo N, McHone J, Emilsson TI, Oldfield E (1986) Detection of high-pressure silica polymorphs in whole-rock samples from Meteor Crater, Arizona, impact sample using solid-state silicon-29 nuclear magnetic resonance spectroscopy. Meteoritics 21:117-124.
Yeganeh-Haeri A, Weidner DJ, Parise JB (1992) Elasticity of α-cristobalite: A silicon dioxide with a negative Poisson's ratio, Science 257:650-652.
Yoder HS (1950) High-low quartz inversion up to 10,000 bars, Trans Am Geophys Union 31:827-835.

EBSCOhost - printed on 2/13/2023 4:48 AM via . All use subject to https://www.ebsco.com/terms-of-use

Yund RA, Blanpied ML, Tullis TE, Weeks JD (1990) Amorphous material in high strain experimental fault gouges, J Geophys Res 95:15589-15602.

Zha CS, Hemley RJ, Mao HK, Duffy TS, Meade C (1994) Acoustic velocities and refractive index of SiO_2 glass to 57.5 GPa by Brillouin scattering, Phys Rev B (in press).

Zhang J, Li B, Utsumi W, Liebermann RC (1994) Reversal of the coesite-stishovite transformation (abstr), EOS Trans Am Geophys Union 75:346.

Zhang J, Liebermann RC, Gasparik T, Herzberg CT, Fei Y (1993) Melting and subsolidus relations of SiO_2 at 9-14 GPa, J Geophys Res 98:19785-19793.

Zhang X, Org CK (1993) Pressure-induced amorphization of β-cristobalite, Phys Rev B 48:6865-6870.

Zoltai T, Buerger MJ (1959) The crystal structure of coesite, the dense, high-pressure form of silica, Z Kristallogr 111:129-141.

EBSCOhost - printed on 2/13/2023 4:48 AM via . All use subject to https://www.ebsco.com/terms-of-use

EBSCOhost - printed on 2/13/2023 4:48 AM via . All use subject to https://www.ebsco.com/terms-of-use

STUFFED DERIVATIVES OF THE SILICA POLYMORPHS

David C. Palmer

Department of Earth Sciences, University of Cambridge
Downing Street, Cambridge CB2 3EQ U.K.

ABSTRACT

The framework structures of silica polymorphs provide the common structural basis for a wide variety of technological and geological materials. Phases can be classified as "stuffed silica derivatives" if they comprise a silica framework topology with (alkali or alkaline earth) cations "stuffed" into the framework cavities, with appropriate subsitition of framework cations to ensure charge balance. This review examines each of the tetrahedral silica polymorphs: quartz, keatite, tridymite and cristobalite, investigating the structural controls for cationic stuffing and substitutions. The structures of the major derivative phases are outlined, in relation to their crystal chemistry and stability range. The resulting structural behavior and properties are discussed.

INTRODUCTION

Buerger (1954) first used the term *stuffed derivatives* of silica to refer to those phases in which non-tetrahedral cations reside in the voids of a three-dimensional silica framework structure. The exact nature of the stuffing species is determined by the size (and shape) of the framework cavities, and the need to maintain charge balance. Framework topology, and the framework density—the number of tetrahedral sites per unit volume are clearly important factors. Corner-sharing tetrahedral frameworks can generally accommodate different sized cavity cations, by polyhedral tilting about the cavity sites (expanding or contracting). To maintain charge balance, framework silicon is replaced by ions of lower valence, most notably Al^{3+}.

Different framework distortions around the "stuffing cations" can lead to a variety of derivative structures with different ring/channel configurations. Changing temperature may lead to *reconstructive* transitions between different stuffed silica polymorphs (e.g., α-eucryptite–β-spodumene; nepheline–carnegieite, etc.). The strain associated with extensive stuffing of *larger* cations into framework cavities may be alleviated by changes in the framework *topology*. Reconstructive transitions from stuffed silica polymorphs to non-silica-derivative phases may then occur (e.g., kalsilite–beryllonite-*Icmm* phase).

Quartz and keatite have structures derived from 3-, 4- or 6-fold *spirals* of SiO_4 tetrahedra. The cavities in quartz and keatite are too small to incorporate ions much larger than Li. Nevertheless, a wide variety of phases in the Li_2O - Al_2O_3 - SiO_2 ("LAS") ternary system have been synthesized. Many of these phases have useful properties such as low thermal expansion, or superionic Li conduction. Lithium aluminosilicates are the major crystalline phases of low-expansion, Li-bearing "glass-ceramics": microcrystalline solids which are stronger than conventional glasses, expand less, and can withstand thermal shocks much better. (Applications of such low-thermal-expansion glass ceramics are legion, ranging from ceramics hobs to laser casings).

There is some disagreement in the literature about the naming of Li-stuffed silica polymorphs. There are three polymorphs of $LiAlSi_2O_6$. The stable phase at ambient conditions is the mineral *spodumene* (also referred to as α-spodumene, or $LiAlSi_2O_6$–I),

EBSCOhost - printed on 2/13/2023 4:48 AM via . All use subject to https://www.ebsco.com/terms-of-use

which is a clinopyroxene. The first phase to form on annealing glasses of composition $LiAlSi_2O_6$ is a stuffed β-quartz phase, variously referred to as "$LiAlSi_2O_6$-III", "γ-spodumene", or "β-quartz solid solution". Li (1968) preferred to use the formula $LiAlSi_2O_6$ -with a suffix denoting the structure type (I = clinopyroxene; II = keatite; III = β-quartz). This system avoids the confusion between similar phases related by displacive phase transitions (e.g., α-/β-quartz). However, Li's nomenclature does not seem to have gathered much support in the literature, perhaps because of the cumbersome formula names; it is also inappropriate for a range of compositions with the same structure. Thus, for this chapter, the following terminology is used for Li-bearing phases in the LAS system:

Structure Type	*Composition Range*	*Generic name*
Phenacite	$LiAlSiO_4$	α-eucryptite
β-quartz	$LiAlSiO_4$ - SiO_2 solid solution	β-eucryptite
Keatite	$LiAlSi_2O_6$ - SiO_2 solid solution	β-spodumene

α-eucryptite has a structure derived from that of phenacite, Be_2SiO_4 (Hesse, 1984), and so cannot be considered a "stuffed silica derivative". Another polymorph, γ-eucryptite, may be crystallized from Li-exchanged silica zeolites (Dondur et al., 1988), but its structure has yet to be determined.

Tridymite and cristobalite have structures derived from sheets of six-fold *rings* of SiO_4 tetrahedra. The "cavities" formed between the tetrahedral sheets can accommodate a wide range of cations, from Na, to Ca. This gives rise to tremendous structural flexibility, emphasized by the diverse mineralogy of the nepheline–kalsilite series. These represent the most *thoroughly* studied group of stuffed silica-derivatives, and so comprise the bulk of this review. Larger cations (e.g., Rb and Cs) are too large for either kalsilite, or nepheline frameworks, and synthetic phases $RbAlSiO_4$ and $CsAlSiO_4$ have the beryllonite (*Icmm*) structure (Klaska et al., 1979).

The high-pressure phases of silica, coesite and stishovite, are too dense to permit extensive inclusion of other atoms or ions (Table 1)

A final group of structures that could be regarded as stuffed silica derivatives are the silica clathrates, which include melanophlogite and dodecasil. These phases are discussed in detail in Chapter Higgins. Clathrates are synthetic phases with a silica-based framework structure containing very large cages. These low-density phases are synthesized around template molecules. The guest molecules, such as xenon, CO_2 and CH_3NH_2, are neutral, unlike the stuffing cations in the other silica polymorphs.

In the following review the tetrahedral silica polymorphs (quartz, keatite, tridymite, cristobalite) are considered in turn, focussing on the structural control of ionic substitutions, the resulting phases, and their structural behavior.

STRUCTURES DERIVED FROM QUARTZ

The idealized, β-quartz structure (spacegroup $P6_422$) comprises parallel 3- and 6-fold helices of SiO_4 tetrahedra, forming an interlinked framework with distorted 6- and 8-fold tetrahedral rings. A channel structure is defined by double helices (6_2 or 6_4 symmetry) along [001]. Distorted tetrahedral cavities are created between the two helices, sharing edges with one SiO_4 tetrahedra from each helix (Fig. 1). The distance from the centre of the interstice to the centres of the surrounding oxygen atoms is ~1.94 Å, so if we take the

EBSCOhost - printed on 2/13/2023 4:48 AM via . All use subject to https://www.ebsco.com/terms-of-use

Table 1. Framework densities for silica polymorphs in comparison with other tectosilicates (italics).

Mineral Name	Framework density (Al,Si /1000 Å^3)	Reference
Faujasite	*12.7*	*Baur (1964)*
Sodalite	*17.15(1)*	*Hazen and Sharp (1988)*
Leucite	*20.466(3)*	*Palmer (1990)*
Tridymite	22.6	Dollase and Baur (1976)
Cristobalite	23.378(1)	Downs and Palmer (1994)
Albite	*24.082(4)*	*Angel et al. (1988)*
Keatite	25.0	Shropshire et al. (1959)
Quartz	26.411(9)	Glinnemann et al. (1992)
Coesite	29.279(3)	Levien and Prewitt (1981)
Stishovite	42.927(1)	Ross et al. (1990)

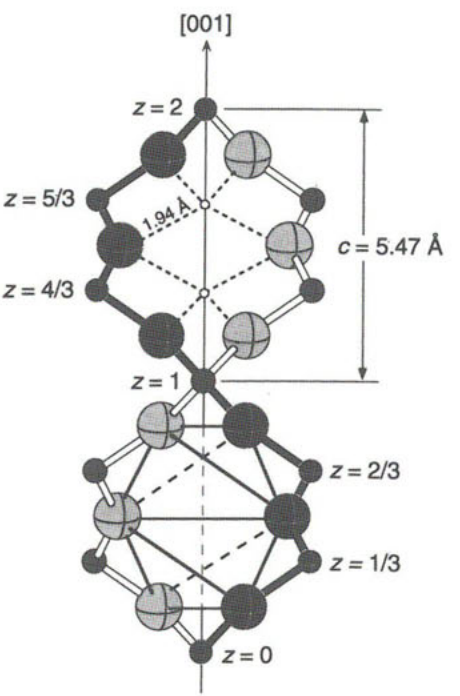


Figure 1. The double helix structure of β-quartz, viewed down [100]. Oxygen atoms shown as large spheres, with Si atoms as smaller, darker spheres. The two helices run parallel to [001] and are distinguished by different shading. The fractional z-coordinates of Si atoms in one helix are given. Tetrahedral interstices exist between the helices, at the same heights as the Si atoms, and spaced at *c*/3 along [001]. Bonds from the centers of the interstices to the coordinating oxygen atoms are shown in the upper part of the diagram; tetrahedra are illustrated in the lower half of the diagram.

EBSCOhost - printed on 2/13/2023 4:48 AM via . All use subject to https://www.ebsco.com/terms-of-use

"crystal radius" of O to be 1.35 Å (Shannon, 1976), and assume an undistorted framework, this site is only just big enough for Li (crystal radius = 0.59Å). The distances between adjacent tetrahedral cavities are small ($c/3 \approx 1.82$ Å), so adjacent tetrahedral cavities cannot be occupied simultaneously. The *midpoint* between two tetrahedral cavities is at the centre of a highly-distorted octahedron, with two very small oxygen distances (~1.74 Å).

The restricted nature of framework cavities means that only significant Li substitution has been observed. Charge balance may be achieved by replacing a proportion of the silicon atoms by Al^{3+}.

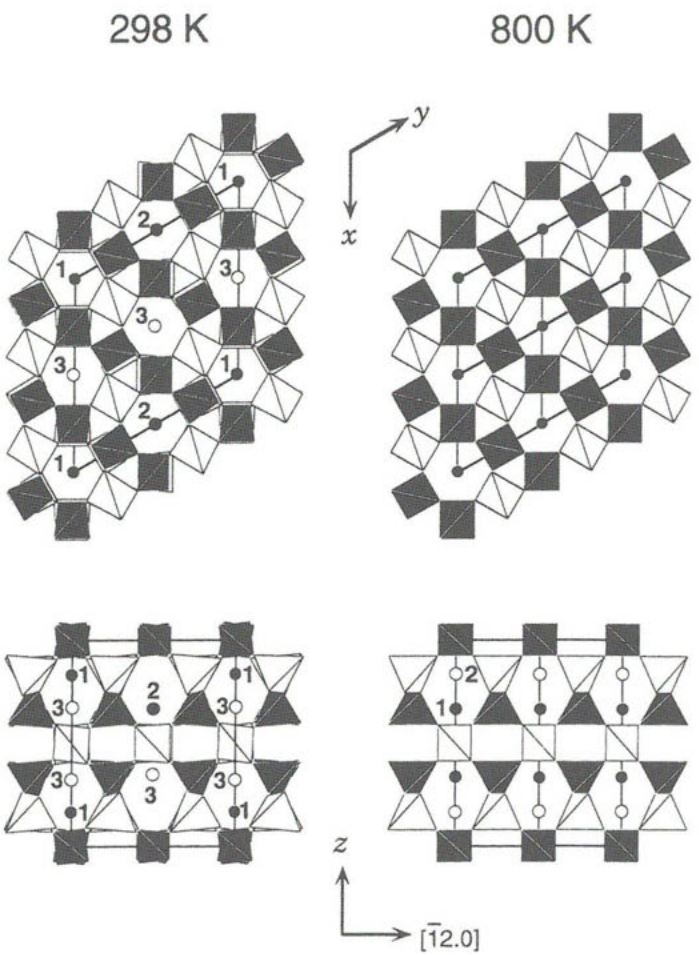


Figure 2. Projections of the structures of β-eucryptite. Si-containing tetrahedra are plotted in black; Al tetrahedra are white. The view directions are: [001] (upper diagrams) and [100] (lower). At low temperatures the Li ions reside on three distinct sites, Li1–3 (numbered). Above T_c ~ 755 K, the Li ions become disordered over the two sites Li1 and Li2. Structural data from Guth and Heger (1979).

EBSCOhost - printed on 2/13/2023 4:48 AM via . All use subject to https://www.ebsco.com/terms-of-use

β-eucryptite

Beta-eucryptite, $LiAlSiO_4$, is the lithium-stuffed derivative of β-quartz. It is of considerable technological importance because of its very low thermal expansion (hence its use in very-low thermal expansion ceramics), and superionic conductivity of lithium (possible use as a solid electrolyte in lithium-based electric batteries).

Crystal sructure. The structure of β-eucryptite was shown to be based on that of β-quartz by Winkler (1948). Ordering of Al and Si over the tetrahedral sites causes a doubling of the *c* axis, with the appearance of weak, "superlattice" reflections of the type *hkl*, *l* = odd. The "Al-avoidance rule" is satisfied because each Si is surrounded by four Al tetrahedra, and vice versa. Winkler (1948) also reported that the Li atoms reside in the same planes as the Al atoms, and that they are tetrahedrally-coordinated by oxygen. The LiO_4 tetrahedra share edges with adjacent AlO_4 tetrahedra (Fig. 1). Buerger (1948) discovered additional superlattice reflections indicating that the unit cell is doubled along *a* and *b* axes The superlattice reflections have been classified as "a" and "c" reflections by Schulz (1974):

Main (β-quartz) reflections: h, k, l = even

Superlattice reflections: l = odd; h, k = even (*c* reflections)

h, k = odd, *or* $h + k$ = odd (*a* reflections)

Structure refinements on the room-temperature phase of β-eucryptite (Tscherry et al., 1972a; Tscherry et al., 1972b; Pillars and Peacor, 1973; Guth and Heger, 1979) confirm that the unit cell is doubled along *x, y* and *z* relative to the β-quartz structure, and that the Al and Si tetrahedra are ordered on alternate layers parallel to *z*. The Li atoms are also ordered, as Winkler had suggested, but the actual ordering scheme is not the one he had suggested. There are four six-fold channels in the unit cell, each containing Li ions. In only one channel do the Li atoms reside within layers of Al atoms (this is the Li1 site); the remaining three channels (which are symmetrically-equivalent) contain Li2 and Li3 sites, which reside within layers of SiO_4 tetrahedra (Fig. 2). Along each channel axis, there is an alternation of occupied and vacant Li tetrahedral sites, and the sequence of occupied and vacant sites is reversed in adjacent channels parallel to **a** or **b**. This gives rise to the possibility of antiphase domains, related by an **a**/2 translation vector, which may be imaged with an electron microscopy (Müller and Schulz, 1976).

At ambient conditions, Guth and Heger (1979) observed additional, weak reflections of the type $00l$, $l \neq 3n$, which are forbidden by the previously-assumed spacegroup, $P6_222$. They suggested that the *true* symmetry of the room-temperature phase is only pseudo-hexagonal, and proposed orthorhombic (e.g., *C*222) or monoclinic (e.g., *P*2) spacegroups. They speculated that the extra reflections relate to small distortions of the Li distribution parallel to [001]. The fact that no splitting of x-ray reflections could be observed must indicate that merohedric twinning operates: the superposition of at least three twin domains thus gives apparently hexagonal symmetry.

Structural Behavior and Phase Transition

Thermal expansion. The temperature dependence of lattice constants has been well studied (Hummel, 1951; Gillery and Bush, 1959; Pillars and Peacor, 1973; Schulz, 1974). On increasing temperature there is an expansion in the (001) plane, but a contraction along *c* so that the overall unit cell volume decreases. This somewhat anomalous

EBSCOhost - printed on 2/13/2023 4:48 AM via . All use subject to https://www.ebsco.com/terms-of-use

behavior can be explained by the edge-sharing of Li- and (Al,Si)-containing tetrahedra. At ambient conditions, the Li–(Al,Si) distance is very small (~2.63 to 2.65 Å). Now, the four atoms associated with the edge sharing (i.e., Li, Al/Si and two oxygen atoms) are all coplanar. The repulsive force between the Li and the Al/Si can be reduced by thermal *expansion* in the *xy* plane, but to maintain the Li–O and (Al,Si)–O bond distances, the shared edge length (O–O) must *decrease*. This causes a net decrease in the *c* cell edge, illustrated in Figure 3.

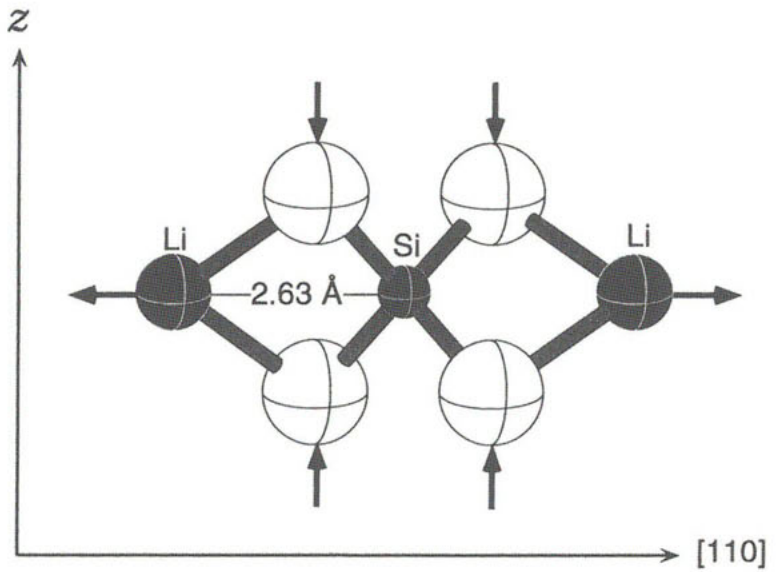


Figure 3. Structural rationalization of the thermal expansion behavior for β-eucryptite. The Li and Al/Si atoms are coplanar normal in (001), and the LiO_4- and $(Al/Si)O_4$-tetrahedra share edges. Thermal *expansion* in the (001) plane reduces the repulsive force between Li and Al/Si. However, to maintain the metal-oxygen bond distances requires a *contraction* along [001]. Thus, *a* and *b* increase with increasing temperature, whilst *c* decreases.

Phase transition. On increasing temperature the "a" superlattice reflections become weaker and very diffuse. In contrast, the "c" reflections remain sharp at all temperatures. This suggests a progressive disordering of the Li distribution, with a phase transition to a smaller (**a**/2) unit cell. However, verifying the positions of the 2-electron Li^+ ions using x-ray diffraction is not easy. Neutron diffraction has a clear advantage because of the scattering length of Li. Guth and Heger (1979) carried out single-crystal neutron diffraction experiments on the high temperature phase at 800 K. The unit cell was found to be equivalent to that of β-quartz, but with a doubled *c*-axis. There was no evidence of Al/Si disorder at this temperature, and the spacegroup was taken as being $P6_222$. Difference Fourier analysis revealed a *smeared distribution* of Li along the structural channels, with two symmetrically-distinct "nodes" designated Li1 (68% occupancy) and Li2 (22% occupancy). The total Li site occupancy is then only 90%, compared with a refined 99% occupancy at room-temperature. Clearly there are anharmonic effects associated with Li diffusion (disordered Li distribution within and/or between the neighboring channels) which cannot be approximated by classical probability ellipsoids.

EBSCOhost - printed on 2/13/2023 4:48 AM via . All use subject to https://www.ebsco.com/terms-of-use

Ionic conductivity. Significant diffuse intensity is observed in single-crystal diffraction patterns above T_c (Alpen et al., 1977). The *a* reflections become diffuse layers perpendicular to [001] and the intensity distribution suggests strong one-dimensional correlation between Li ions in the structural channels (although the original three-dimensional ordering pattern has been destroyed). The same study showed that at temperatures above T_c there is very high Li-ion conductivity parallel to [001], but virtually none in the (001) plane. β-eucryptite can thus be considered a one-dimensional "superionic" conductor of Li. The Li diffusion is thermally-activated, and occurs as a cooperative, "single file" process between occupied and vacant sites (Li1 and Li2) parallel to [001]. The activation energy for the "site hopping" has been determined as ~0.74–0.83 eV from the temperature-dependence of the ionic conductivity (Alpen et al., 1977), the dielectric loss (Böhm, 1975) and NMR spectroscopy (Follstaedt and Richards, 1976).

Incommensurate phase. Close to T_c, Guth and Heger observed satellite reflections in the vicinity of the superlattice reflections. An incommensurate (IC) phase thus appears to bridge the boundary between a low-temperature phase with ordered Li distribution, and the high-temperature state of Li disorder. Guth and Heger speculated that there was a modulation of Li occupation probability in neighboring structural channels. Comparison with other IC phases (see McConnell, 1983) suggests that the IC phase may be stabilized by favorable coupling between Li ordering, and some other process—possibly a framework distortion at low temperatures.

Crystal Chemistry

SiO_2–($Li_2O.Al_2O_3$) solid solution. At high temperatures the β-eucryptite structure is stable over a wide solid solution range along the join SiO_2–($Li_2O.Al_2O_3$) (Skinner and Evans, 1960). Munoz (1969) synthesized phases along the join SiO_2 ("Qz") – $LiAlSi_2O_6$ ("Sp"). At pressures above 1.0 GPa there appears to be complete solid solution of Li in a stuffed β-quartz structure. The only naturally-occurring phase reported in this range is the mineral virgilite (French et al., 1978) occurring as microscopic crystals in clear, high-alumina volcanic glass, from Peru. The samples reported have a composition corresponding to $Qz_{39}Sp_{61}$.

More extensive solid solution can be achieved metastably since stuffed β-quartz phases are the first to grow from annealed lithium-aluminosilicate glass. (The stable phase for SiO_2-rich compositions is β-spodumene, a stuffed derivative of keatite). The crystal structure of a metastable $LiAlSi_2O_6$ phase was determined by Li (1968), who referred to it as "$LiAlSi_2O_6$-II". The structure is virtually identical to that of β-eucryptite, except that Al and Si are disordered over the tetrahedral sites, and Li can occupy one of three symmetrically-equivalent positions. Like β-eucryptite, there is very low net thermal expansion: *a* and *b* expand on increasing temperature, but the *c* axis contracts. Prolonged annealing leads to a reconstructive phase transition to β-spodumene.

Solid solution with $AlPO_4$. Extensive solid solution of $AlPO_4$ (up to 48 mol%) in β-eucryptite has been observed by Perrotta and Savage (1967). P^{5+} substitutes for Si^{4+}, the number of *vacant* Li sites increases, and the lattice parameters decrease. $AlPO_4$-rich compositions show some split diffraction peaks, suggesting a symmetry-reducing phase transition (presumbably a displacive framework collapse). The ionic conductivity increases with the phosphate content: diffusion is clearly facilitated by the increased number of vacant sites. In addition, Tindwa et al. (1982) suggest that the phosphate

EBSCOhost - printed on 2/13/2023 4:48 AM via . All use subject to https://www.ebsco.com/terms-of-use

addition reduces the strength of the bonding between the Li and the surrounding channel oxygens.

Boron substitution. There is extensive solid solution of boron in β-eucryptite, the B substituting for Al in the compositional range: $LiAl_{1-x}B_xSiO_4$ ($0 \leq x \leq 1$). Mazza and Lucco-Borlera (1994) were able to synthesize phases with up to 40% B replacing Al. Unlike pure $LiAlSiO_4$, the substituted phases did not show weak *a* reflexions, indicating that the Al/Si/B distribution is disordered. The cell dimensions *a* and *c* decrease with increasing B replacement of Al, reflecting the smaller ionic radius of B.

STRUCTURES DERIVED FROM KEATITE

Keatite (or *silica K*) is a high-pressure form of SiO_2 which has not been recognized in nature. The phase may be synthesized at 0.1 GPa and 800 K, from silica gel, water, and small quantities of alkali ions. Keatite is tetragonal, with spacegroup $P4_1$ (Shropshire et al., 1959). The structure comprises four-fold spirals of corner-connected SiO_4 tetrahedra (Si1 sites). The spirals are linked together by additional tetrahedra (Si2 sites), each of which shares its corners with tetrahedra in four different spirals (Fig. 4). The tetrahedral framework contains 5-, 7- and 8-fold rings. The 5-fold rings form channels parallel to [100] and [010].

β-spodumene

The mineral spodumene, a clinopyroxene, undergoes a reconstructive transformation at high temperatures to a Li-stuffed derivative of keatite, generally referred to as "β-spodumene" (or "$LiAlSi_2O_6$-II"). This phase may also be synthesized from a glass by annealing at high temperature to transform the primary stuffed-quartz phase.

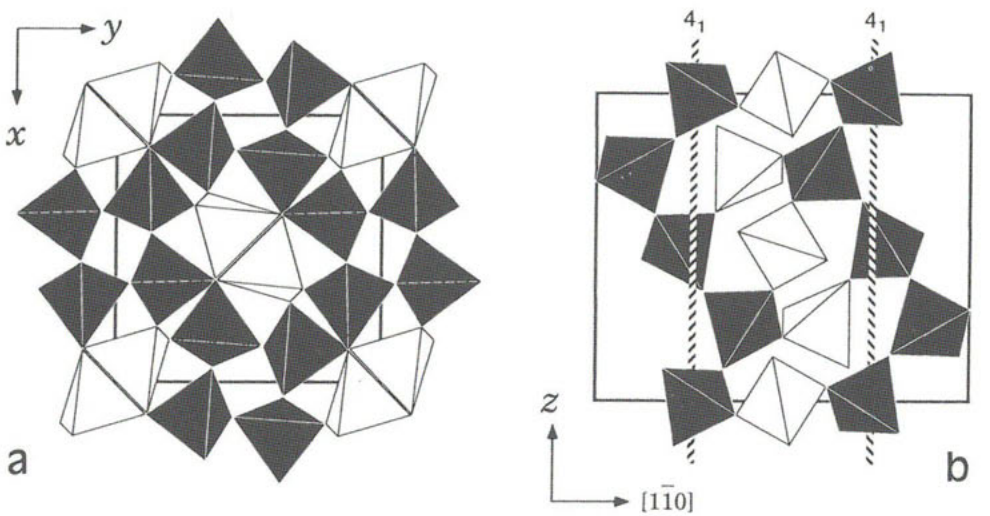


Figure 4. The crystal structure of keatite, SiO_2. The structure contains 4-fold spirals of SiO_4 tetrahedra (Si1 sites, in black) which are cross-linked by additional tetrahedra (Si2 sites, in white), each of which shares its corners with tetrahedra in four different spirals. (a) Projection of the structure on (001). (b) Projection of two silicate spirals on (110). The 4_1 screw axes are indicated by the hatched lines. Atomic coordinates are from Shropshire et al. (1959).

EBSCOhost - printed on 2/13/2023 4:48 AM via . All use subject to https://www.ebsco.com/terms-of-use

Skinner and Evans (1960) investigated the stability of β-spodumene. They reported that this phase has tetragonal symmetry, and proposed a stuffed-keatite structure. A full crystal structure refinement was carried out in spacegroup $P4_32_12$ by Li and Peacor (1968) and later by Clarke and Spink (1969). The aluminosilicate framework is virtually identical to that of keatite, but the tetrahedral bond lengths suggest that Al and Si atoms are disordered over the two independent tetrahedral sites. Li ions are disordered over four sets of paired sites. Each pair comprises two distorted tetrahedral sites, and the midpoint between the two sites is octahedrally-coordinated by oxygen. The distance between the sites in a pair is too small for them both to be occupied by Li, and 50% occupancy is assumed. The Li ions "cling" to the edges of the five-fold tetrahedral rings (Fig. 5). The thermal expansion is highly anisotropic (Ostertag et al., 1968), echoing that of the "parent" phase, keatite.

Ionic Conductivity

β-spodumene has a well-defined channel structure, and one might expect the ionic conductivity to reflect the framework anisotropy. However, Roth and Bohm (1987) obtained the same values for conductivity along ***a*** and **c**. Clearly the conduction mechanism is more complex than a simple geometric model might suggest. Experiments on $LiAlSi_2O_6$ glasses suggest that ion-ion interactions and short-range order determine the conduction, rather than well-defined, long-range diffusion pathways. The conduction is thermally-activated, with an activation energy, E_a = 0.81 eV—similar to that for β-eucryptite.

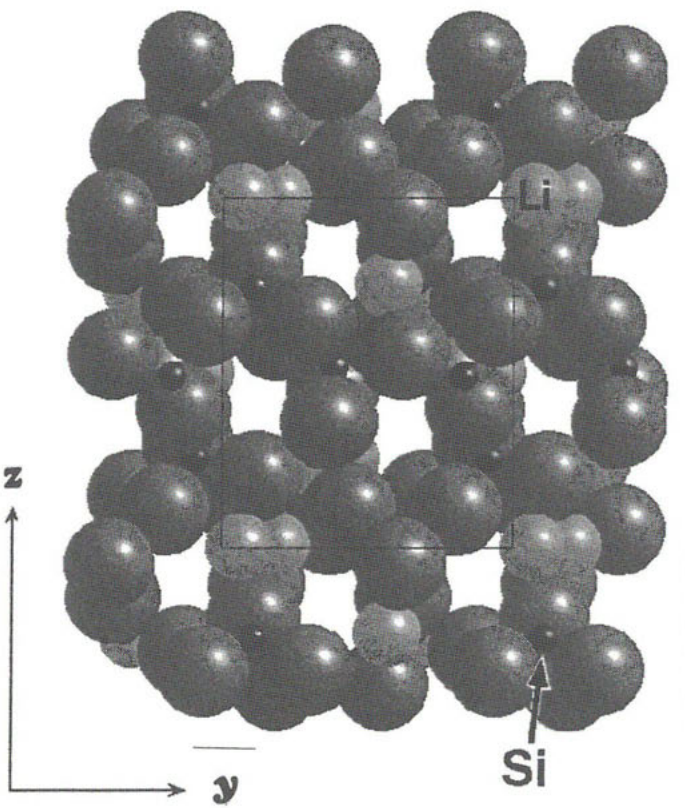


Figure 5. Space-filling model of the β-spodumene structure, viewed along [100]. Large dark spheres are oxygens; medium-sized gray spheres are Li, and small dark spheres are Al/Si atoms. Li sites occur in pairs (50% occupancy in each), at the edges of 5-fold rings.The Li-O coordination polyhedron is a distorted tetrahedron. The structural data are from Li and Peacor (1968); atomic radii are from Shannon (1976).

EBSCOhost - printed on 2/13/2023 4:48 AM via . All use subject to https://www.ebsco.com/terms-of-use

Crystal Chemistry

β-spodumene has, like β-eucryptite, been extensively studied by materials scientists interested in exploiting its ionic conductivity and thermal expansion properties. Varous combinations of "doping" and substitutions have been tried in order to enhance these properties.

β-spodumene–silica solid solution. There is extensive solid solution along the join (Li_2O, Al_2O_3)–SiO_2 at high temperatures. Roy et al. (1950) gave a tentative phase diagram for this join, proposing "β-spodumene" solid solution from about 60–78 wt % SiO_2 at temperatures above 800 K, with two phase fields (petalite + spodumene; α-eucryptite + spodumene) at low temperatures.

Boron substitution. Mazza and Lucco-Borlera (1994) reported that $LiAlSiO_4$ phases with more than 60% of the Al replaced by B crystallized as β-spodumene. With increased B content, the cell parameters decreased (*c* decreases more rapidly than *a*).

Ca/Si substitution. Wang and Hon (1993) were able to substitute 5–13 wt % CaO for SiO_2. This proved counter-productive, because the resulting thermal expansion coefficients are higher than the original, calcium-free β-spodumene.

STRUCTURES DERIVED FROM TRIDYMITE

The idealized tridymite structure comprises hexagonal sheets of SiO_4 tetrahedra arrayed in six-fold rings, with adjacent tetrahedra directed in opposite directions (the sequence around the ring is summarized as "UDUDUD" where "U" and "D" refer to tetrahedra pointing upwards and downwards respectively). Successive sheets are stacked in an "ABAB..." sequence parallel to [001], analogous to "hexagonal close packing" in metals. The resulting structure, illustrated in Figure 6, has wide channels parallel to [001]. This idealized phase has topological symmetry $P6_3/mmc$. A 6_3 axis runs parallel to [001] through the centre of each six-fold ring, and a triad axis passes through the centre of each tetrahedron. The Si–O–Si linkage between sheets is therefore constrained to be 180°, which is energetically unfavorable (Liebau, 1985). This angle can be reduced to a more favorable value by off-centering the apical oxygens, which then occupy three symmetrically-equivalent positions about the triad axis.

Natural tridymite has a range of structural phase transitions, but different samples exhibit different behavior. The actual behavior appears to be crucially dependent on both the starting material—terrestrial, meteoritic, or synthetic—and its thermal history. Not only do samples vary chemically, but the layer structure is amenable to a high degree of stacking disorder and defects, and to the possibility of long-range superstructures. Carpenter and Wennemer (1985) emphasized the diversity of superstructures observed in different synthetic samples, which appeared to underscore the varying transformation behavior amongst different samples. Because of the lamentable paucity of well-characterized synthetic samples, the emphasis here is on natural, rather than synthetic derivatives.

The high-temperature hexagonal phase undergoes a series of displacive phase transitions involving rotations of essentially rigid SiO_4 tetrahedra, leading to a progressive crumpling of the framework and collapse of the six-fold rings (the behavior of meteoritic tridymite is detailed in de Dombal and Carpenter, 1993). Figure 7 illustrates two distortion mechanisms, which reduce the size of the [001] channels. Both oval and

EBSCOhost - printed on 2/13/2023 4:48 AM via . All use subject to https://www.ebsco.com/terms-of-use

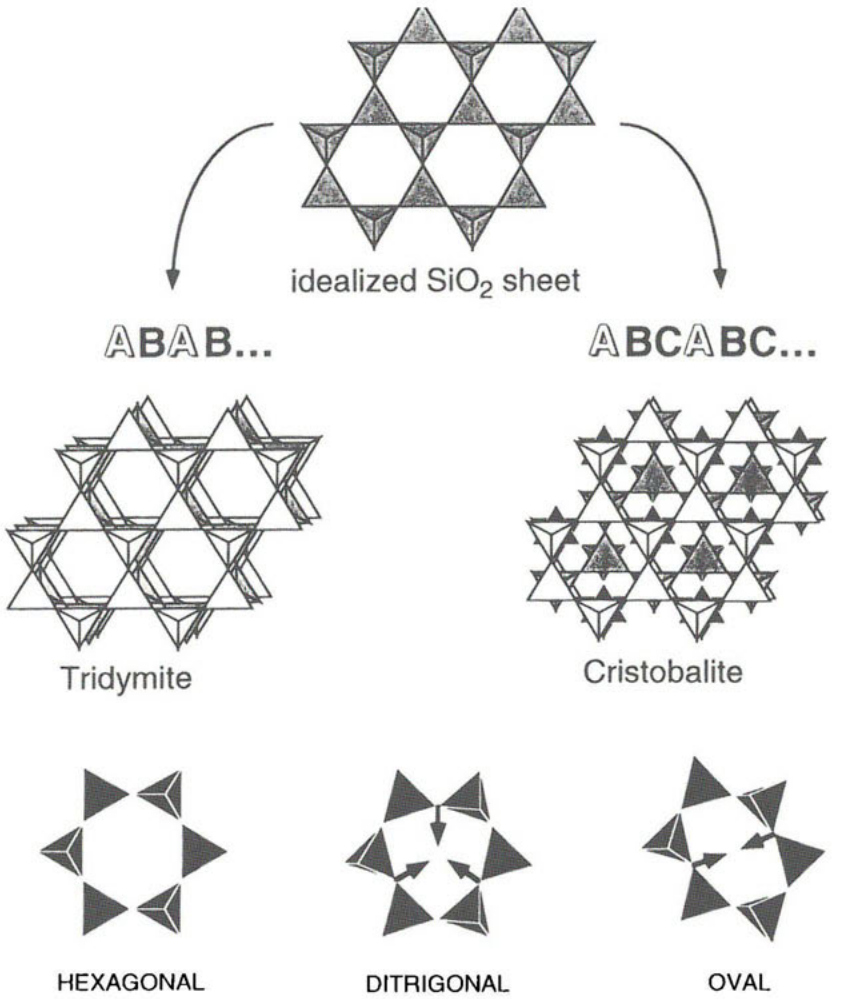


Figure 6 (top). Two methods of stacking identical tetrahedral sheets. A simple two-layer "AB" repeat sequence (analogous to hexagonal close packing in metals) gives the idealized tridymite structure. A three-layer "ABC" repeat (analogous to cubic closest packing in metals) gives the idealized cubic cristobalite structure. Successive tetrahedral layers are slightly offset, for clarity.

Figure 7 (bottom). Ring distortions in tridymite phases.

ditrigonal ring distortions are observed in the low-temperature, monoclinic phase (Fig. 8), and all three ring types are to be found in stuffed tridymite derivatives (Fig. 9).

Ionic substitutions in tridymite. The tridymite structure is very tolerant to ionic substitutions. Natural tridymites contain small amounts of large alkali and alkaline earth elements, which appear to stabilize the structure down to low temperatures. Large cations, most notably Na, K and Ca, can be accommodated within the [001] structural channels, residing between successive sheets of silicate tetrahedra, with nine nearest-

EBSCOhost - printed on 2/13/2023 4:48 AM via . All use subject to https://www.ebsco.com/terms-of-use

EBSCOhost - printed on 2/13/2023 4:48 AM via . All use subject to https://www.ebsco.com/terms-of-use

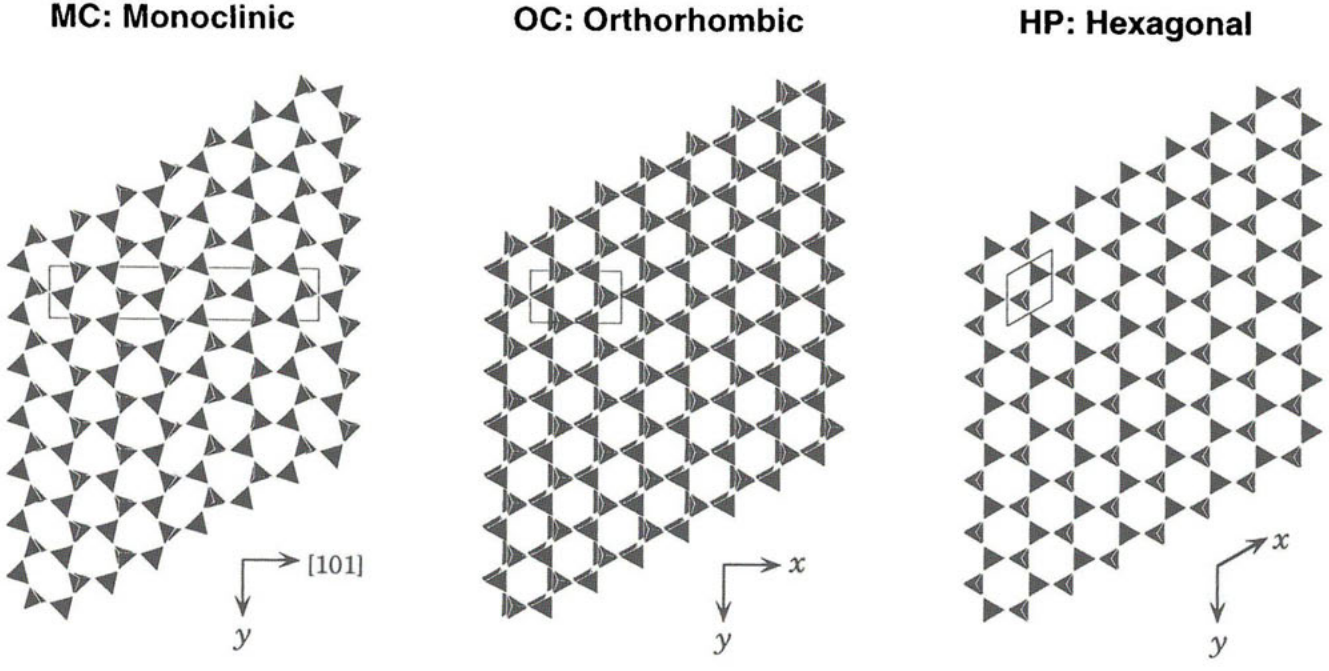


Figure 8. Structural modifications of tridymite from the Steinbach Meteorite. The structures are plotted at the same scale with their *y*-axes parallel. On decreasing temperature, the high-temperature hexagonal phase (after Kihara, 1978) undergoes a displacive phase transition to an orthorhombic phase (Dollase 1967) and then to a monoclinic phase (Dollase and Baur, 1976), which is metastable at room temperature.

Figure 9. Stuffed derivatives of tridymite. The structures are plotted at the same scale, viewed down [001] with the unit cells outlined. K = dark circles; Na = light circles; SiO_4 = dark tetrahedra; AlO_4 = light tetrahedra. Crystal structure data from: Hahn and Buerger (1955); Bonaccorsi et al. (1988) ; Merlino et al. (1985); Perrotta and Smith (1965).

EBSCOhost - printed on 2/13/2023 4:48 AM via . All use subject to https://www.ebsco.com/terms-of-use

neighbor oxygen atoms. Charge balance is attained by the partial replacement of silicon by a lower-valence cation (e.g., Al or Mg).

Substituted tridymite phases show a remarkably diverse chemistry, attributable, in no small part, to the intrinsic flexibility of Al–O–Si linkages which allows geometrically non-rigid frameworks, and crumpling to accommodate crystal-chemical influences. Superstructures are relatively easy to form, and there is much scope for order-disorder of framework cations, and cavity cations and vacancies. With the addition of temperature- and pressure-driven displacive phase transitions, the overall behavior can become highly complex and intriguing.

Introduction to the Nepheline–Kalsilite Series

The most important stuffed derivatives of tridymite have compositions in the range $NaAlSiO_4$ to $KAlSiO_4$. In nature the main representatives are the potassium end-member, kalsilite, and nepheline (ideal formula: $Na_3KAl_4Si_4O_{16}$), which is a stable intermediate phase. At high temperatures there is extensive solid solution between sodium and potassium end members, and natural nephelines also show extensive solid solution towards SiO_2 (Fig. 10).

Nepheline-Kalsilite phases are characterized by distortions of the tridymite parent structure, about the cavity cations. In kalsilite one observes a ditrigonal distortion of the six-membered rings about K. In nepheline on the other hand, the K ions reside in open, six-fold rings. The K sites remain expanded because of the large contraction around the adjoining Na sites, which causes an oval distortion. For natural nephelines with an Na:K

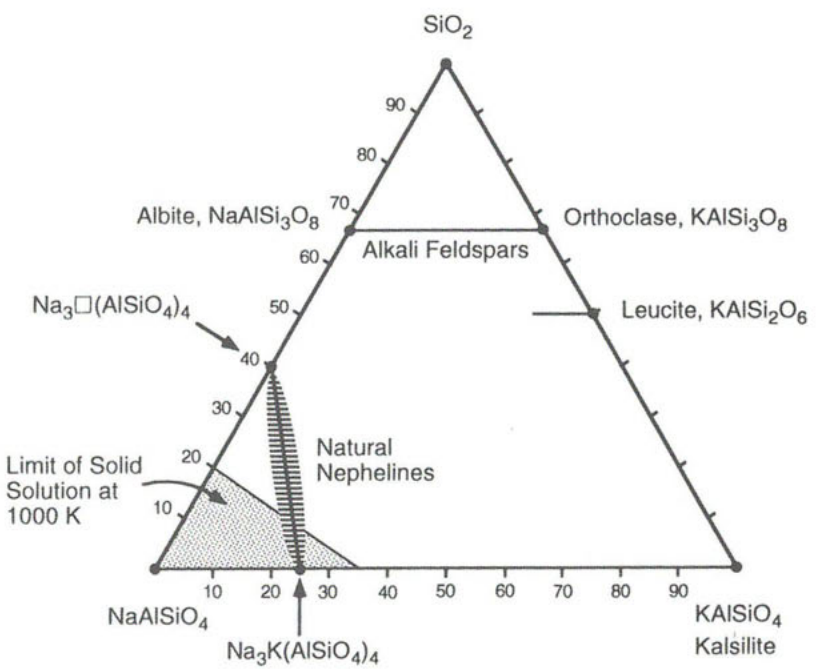


Figure 10. Ternary diagram showing compositions of phases in the nepheline–kalsilite–SiO_2 system.

EBSCOhost - printed on 2/13/2023 4:48 AM via . All use subject to https://www.ebsco.com/terms-of-use

ratio close to 3:1, there appears to be complete ordering of Na and K into the two ring types. Trikalsilite and tetrakalsilite are intermediate structures, consisting of hexagonal, ditrigonal and oval rings in varying proportions (Fig. 9).

Nepheline–Kalsilite Phase Equilibria

Tuttle and Smith (1958) presented a phase diagram for the $NaAlSiO_4$–$KAlSiO_4$ system, which had been determined from annealing experiments on synthetic samples. They suggested extensive solid solution of K in nepheline above 1200 K, with a solvus extending to the nepheline and kalsilite compositions at room temperature. The remaining high temperature part of the phase diagram was less certain, however—particularly towards the K end, where a series of phase fields involving orthorhombic kalsilite ("O1" phase) and tetrakalsilite ("H4" phase) were proposed.

Many details of the nepheline–kalsilite phase diagram remain unresolved. Part of the problem lies with the very rapid exsolution of nepheline and kalsilite from solid solution, even at low temperatures (Yund et al., 1972). *In-situ* studies are essential to the elucidation of phase relations. In intrusive rocks complete unmixing of nepheline and kalsilite is usually observed, but in volcanic rocks the scale of exsolution tends to be less, leading to perthitic intergrowths of nepheline and kalsilite (Fig. 11). Conversely, it is relatively easy to "homogenize" Ne-Ks perthites by annealing at high temperature; but a rapid quench is required to preserve the solid solution. Ferry and Blencoe (1978) noted that phases synthesized at high temperatures might react and re-equilibrate at lower temperatures if quench rates are too low; with this in mind, a redetermination of the nepheline-kalsilite solvus (Fig. 12) yielded rather different results from the original Tuttle and Smith (1958) work.

The rapid exsolution rates in nepheline-kalsilite can be related to the high mobility of Na and K ions in tridymite-type frameworks. Diffusion is facilitated by well-defined channels parallel to [001] with "side-channels" connecting alkali sites in the (001) plane. Gregorkiewitz (1986) demonstrated the high ionic conductivity, with maximum conduction of Na and K parallel to [001]. Structure refinements of nepheline show the framework about the large, hexagonal channel, appears rigid and unable to adjust to ions of smaller size (e.g., Na substituting for K). The rigidity of this wide pathway also minimizes momentum interchange with the diffusing ions.



Figure 11. Back-scattered electron image of a phenocryst from a nephelinite lava (Belgian Congo). Perthitic texture with exsolution lamellae of nepheline (dark) and kalsilite (light). The white bar represents 200 μm. The groundmass contains crystals of nepheline, melilite, clinopyroxene, and ilmenite. Photo reproduced by kind permission of Dr. Daniella Cellai, University of Cambridge.

EBSCOhost - printed on 2/13/2023 4:48 AM via . All use subject to https://www.ebsco.com/terms-of-use

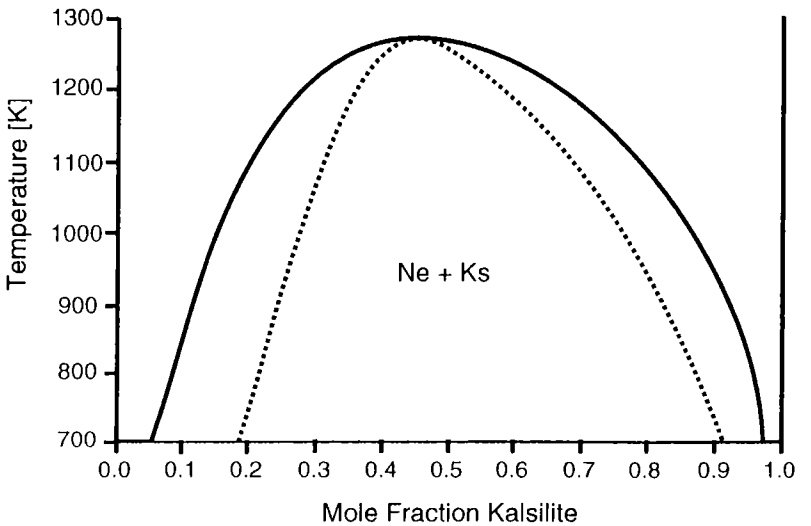


Figure 12. Solvus (solid curve) and spinodal (dashed curve) for the nepheline-kalsilite solid solution at 0.2 GPa. After Ferry and Blencoe (1978).

Nepheline

Nepheline is a characteristic mineral of alkaline igneous rocks and is the most common feldspathoid mineral. It occurs as a primary phase in plutonic, hypabyssal and volcanic rocks of widely-differing mineralogy and composition.

Nepheline Crystal Chemistry

The crystal structure of nepheline was first solved by Buerger et al. (1954), with later refinements by Hahn and Buerger (1955). The refinements confirmed earlier suggestions that the mineral is a stuffed derivative of tridymite. The alkali cations, sodium and potassium, are ordered in two different sites: the K ions reside in open hexagonal rings (K is 9-fold coordinated by O), whilst the Na sites are distorted, oval rings, leading to a coordination number of 8 oxygens around each Na. The ratio of oval to hexagonal rings is thus 3:1 (Fig. 13a).

Two sets of tetrahedral sites can immediately be recognized. One set resides on special equivalent positions, along the [001] triads, with three Na nearest neighbors. A second set lies on general equivalent positions (forming the hexagonal rings), with one K and two Na nearest neighbors. For Al/Si ordering, each set must be further divided, giving a total of four tetrahedral sites.

The apical oxygen atom which connects adjacent layers of AlO_4 and SiO_4 tetrahedra in special equivalent positions (i.e., T1, T2 sites) is off-centered by ~0.3 Å from the triad axis, and disordered over three sites. The off-centering reduces the Al—O—Si bond angle from an energetically-unfavorable 180°, to 133.5° (Fig. 13b).

Excess SiO_2. Compared with the "ideal" nepheline formula $Na_3K(AlSiO_4)_4$, most natural nephelines contain an excess of Si at the expense of Al. Charge-balance is

EBSCOhost - printed on 2/13/2023 4:48 AM via . All use subject to https://www.ebsco.com/terms-of-use

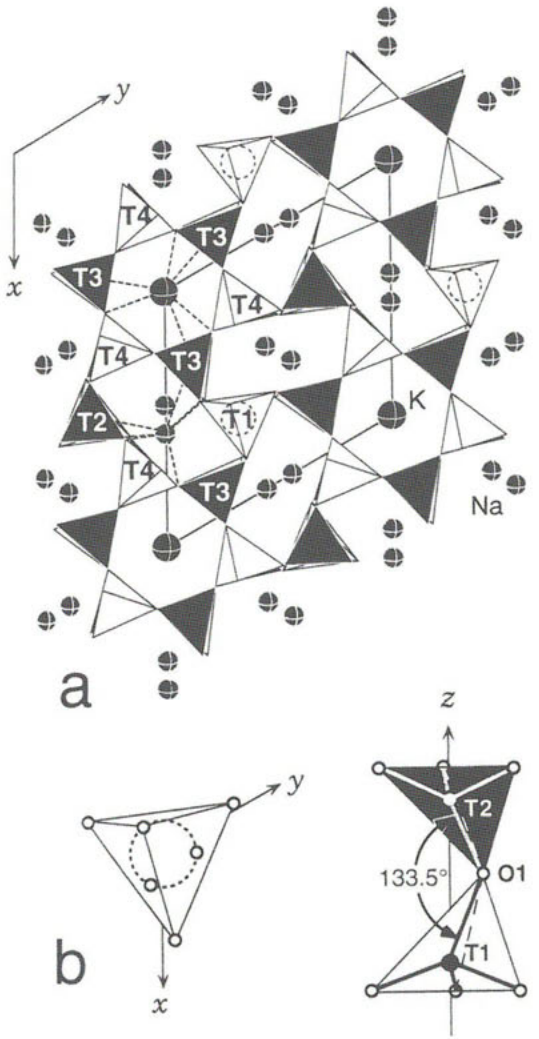


Figure 13. The crystal structure of nepheline plotted using the coordinates of Hahn and Buerger (1955). (a) Projection along [001]. Black spheres represent K; grey spheres represent Na. The bonds to nearest-neighbor oxygen atoms are indicated by the dashed lines. SiO_4 tetrahedra are shown in black, pointing downwards; AlO_4 tetrahedra are white, and point upwards. A triad axis passes vertically through the T1 and T2 sites; oxygen is off-centered from this axis (represented by the dashed circles), and disordered over three sites. (b) Detail showing the effects of apical oxygen (O1) off-centering. The T1 (Al)–O–T2 (Si) bond angle is reduced from 180° to 133.5°.

accomplished by a deficiency of potassium, leaving vacancies ([ ]) on the hexagonal sites, according to the exchange: $K^{+}Al^{3+} \Leftrightarrow [\,]Si^{4+}$ (Fig. 9).

Structural Behavior of Nepheline

Single-crystal x-ray structure refinements suggest that natural "Na_3K" nephelines do not undergo significant changes on heating (Foreman and Peacor, 1970). The framework topology remains unchanged, but the T1 and T2 tetrahedra rotate about [001], thereby expanding the oval sites. Birefringence measurements (Sahama, 1962) and electron microscopy (McConnell, 1962) suggest another story: there is evidence for a major structural change at temperatures as low as 473 K.

EBSCOhost - printed on 2/13/2023 4:48 AM via . All use subject to https://www.ebsco.com/terms-of-use

Sahama (1962) measured the birefringence of 34 nepheline samples representing different geological environments, at temperatures up to 1300 K. He was able to define two types of behavior: so-called "Type I" nephelines are generally from plutonic environments and have a high birefringence at room temperature, which eventually *decreases* on prolonged heating. When cooled to room temperature, type I samples showed a permanent decrease in birefringence, which Sahama attributed to the *disordering* of the nepheline. Type II nephelines have lower birefringence at room-temperature, but this increases on heating. These nephelines were interpreted as being the "least-well ordered". Nephelines from *volcanic* environments showed a continuous gradation in behavior between types I and II. Various explanations have been suggested, all involing order/disoder of different sets of cations and/or vacancies.

Al/Si order-disorder. By analogy with feldspars and other tectosilicates, one might expect the degree of Al/Si order in natural nephelines to correlate with the geological history and cooling rate. In ideal nepheline with a 1:1 Al-Si ratio, it is possible to have full ordering. The structure allows for a simple ordering scheme with alternating Al-Si tetrahedra.

Originally, X-ray structure refinements were used to estimate the degree of ordering. Because the atomic scattering factors for Al and Si are very similar, researchers have resorted to measuring the tetrahedral cation-to-oxygen *bond distances* (Al^{3+} being larger than Si^{4+}). Nevertheless, there are still difficulties associated with possible averaged domain effects, pseudo symmetry, and the existence of fine-scale twinning. Perhaps not surprisingly then, there has been considerable confusion regarding ordering schemes deduced from x-ray diffraction experiments. Hahn and Buerger (1955) studied a nepheline of volcanic origin which they concluded was only partially ordered. They deduced full Al/Si ordering on the four tetrahedra in special positions (T1, T2), but Al/Si disorder over the remaining twelve tetrahedra located on general-equivalent-positions (T3, T4). This ordering scheme was contradicted by a later x-ray structure refinement on the same sample. Simmons and Peacor (1972) claimed that the T3 and T4 sites were fully ordered, and that there was a "high degree of Al/Si disorder" on the T1, T2 sites. However, structure refinements on other nephelines indicated full ordering of Al and Si over all tetrahedral sites (Foreman and Peacor, 1970). Dollase and Peacor (1971) suggested a decrease in the degree of Al/Si ordering with increasing cooling rate, so that volcanic nephelines are the least-well ordered. Their ordering scheme involved polar crystals, with Al-rich tetrahedra all pointing along the positive *c*-axis, and Si-rich tetrahedra all pointing the other way. The T1 and T2 sites were found to be less-well ordered than T3 and T4. This could be rationalized by considering the differences in site environments: T1 and T2 are bonded to the positionally-disordered O1 atom and surrounded by Na cations; by contrast, the T3 and T4 sites are surrounded by Na and K cations (and/or vacancies) and in some samples by Ca. They concluded that "non-uniform ordering probably involves correlations between O1 disorder, tetrahedral-site occupancy and K-site occupancy" and invoked a "domain" model for the ordering pattern.

The difficulties in determining Al/Si site occupancies using traditional x-ray techniques are largely overcome by using magic-angle spinning nuclear magnetic resonance spectroscopy (NMR), which provides information on a much smaller length scale than x-ray diffraction. Two separate studies (Stebbins et al., 1986; Hovis et al., 1992) found complete Al/Si order in all samples. Any *excess* Si was found to substitute randomly on the Al sites. The authors concluded that the disorder effects in volcanic nephelines, reported in earlier x-ray studies, are the result of averaging domains with complete short-range order.

EBSCOhost - printed on 2/13/2023 4:48 AM via . All use subject to https://www.ebsco.com/terms-of-use

Na/K ordering. Samsonova (1969) measured the changes in intensity ratios of certain reflections following heat treatment at 1000°C for a suite of nephelines. Theoretical calculations appeared to support the notion of a Na/K order-to-disorder transition. However, there is no evidence for Na/K disordering from high-temperature x-ray structure refinements (Foreman and Peacor, 1970). Even if such a Na/K disordered phase existed, the very high exsolution rate of Na and K ions would prevent this phase from being quenched to room temperature. There are very strong reasons why Na/K disordering should not occur: the two ions have different sizes, and occupy very different site environments. K could not be accommodated within the highly-distorted oval Na site without substantial framework strain. Although Na has been reported in the large K site for Na-rich nephelines, it is positionally-disordered in a one-sided bonding arrangement with the cavity wall: an energetically unfavorable environment.

K-[ ] ordering. Most natural nephelines have an excess of Si over Al, which is accommodated by a deficiency in K, creating vacancies ([ ]) on the large alkali sites. There is now compelling evidence that at low temperatures these nephelines may have ordered K-[ ] distributions along [001]. A combination of K-[ ] ordering and a displacive distortion has been invoked to explain an incommensurate structure for nepheline.

The Incommensurate Phase of Nepheline.

Sahama (1958) noted the presence of layer lines of weak reflections corresponding to $l \pm 1/9$ on x-ray single-crystal rotation photographs. He argued that the "conventional" unit cell of nepheline is a pseudo cell, and that the true cell is much larger: $a = \sqrt{3}\, a_0$; $c \approx 9c_0$. The *a*-axis of the true cell is at 30° to that of the pseudo cell. McConnell (1962) used transmission electron microscopy (TEM) to study the additional maxima in a large number of different natural nephelines. Some samples (e.g., nepheline from a phonolite) showed very sharp maxima, whilst others (e.g., pegmatite and potassic lava samples) showed diffuse streaks. The maxima occur in *pairs* in reciprocal space, with coordinates $(\pm 1/3, \pm 1/3, \pm\delta)$ where δ is irrational and was found to vary with composition from 0.207(1)–0.213(1). Schematic diffraction patterns from this *incommensurate* phase are illustrated in Figure 14. After heating for several hours at 400–500°C, the satellites became weak and diffuse (significantly broadened in the x^*y^* plane), but could not be completely eliminated. In addition, diffuse streaks appeared, connecting diffuse satellites to their corresponding Bragg maxima.

From his heating experiments, McConnell (1962) noted two main processes: (i) an instantaneous, and reversible, decrease in intensity on heating—this, he suggested, must relate to a *displacive* mechanism, such as the off-centering of the O1 apical oxygen atoms; and (ii) a kinetically-controlled process, manifested in the slow, irreversible decrease in the intensity of satellite reflections at constant temperature. The fact that such "disorder" could be induced at temperatures as low as 200°C ruled out the possibility of Al/Si disordering. From the time- and temperature-dependence of the satellite intensity, McConnell (1981) calculated decay constants, and hence an *activation energy* of disordering of ~80 kJ mol^{-1} was determined. McConnell (1981) argued that this value is in good agreement with values of K-ion diffusion from other experiments on different minerals, and it suggested an irreversible disordering of K ions and vacancies on the large alkali sites. The incommensurate phase was rationalized as arising from the interaction, or "resonance," of (K-[ ]) ordering and (O1) displacement modes in nepheline.

Further support for the McConnell model comes from actual measurements of ionic conductivity in nepheline: Gregorkiewitz (1986) measured an activation energy for

EBSCOhost - printed on 2/13/2023 4:48 AM via . All use subject to https://www.ebsco.com/terms-of-use

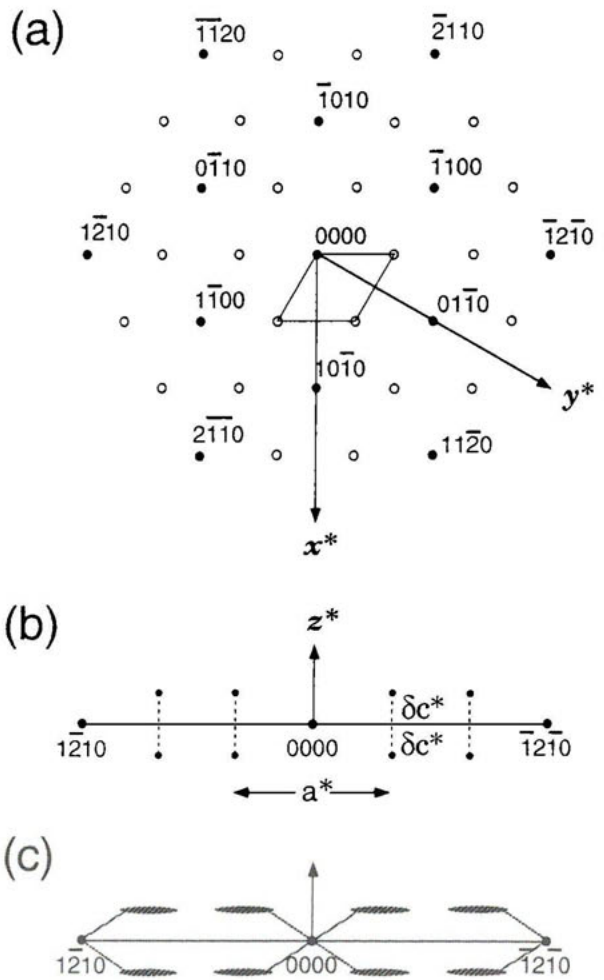


Figure 14. Schematic diffraction patterns from the incommensurate phase of nepheline. (a) The x^*y^* section of the reciprocal lattice. Open circles are the *projections* of the satellite reflections onto this plane. (b) The $y\,z^*$ section. The satellite reflections are at a height δc^* above and below the zero-layer. (c) The effect of heating. As the incommensurate phase disorders, the satellite maxima become diffuse and are connected to the Bragg maxima by diffuse streaks. After McConnell (1962).

diffusion of K along [001] in nepheline of 76 kJ mol^{-1}, in good agreement with the results of McConnell's kinetic analysis. de Dombal (1992) showed that the IC phase can be interpreted within the scope of Landau Theory, using two interacting order parameters: Q_{OD} (K-[] order-disorder) and Q (O1 displacement).

Other Nepheline Phases

Potassic nepheline. Sahama (1957) managed to homogenize nepheline-kalsilite exsolution lamellae, yielding a highly-potassian (72 mol % K) nepheline. Single crystals of nepheline-kalsilite perthite were heated to 1100°C and quenched in water. When examined by x-ray powder diffraction, the crystals displayed patterns similar to that of pure nepheline. More recently, Hovis et al. (1992) used ion-exchange to synthesize a composition series ranging from nepheline, to kalsilite. The most K-rich nepheline phase corresponded to 63 mol % K, beyond which tetrakalsilite or kalsilite were observed. The

EBSCOhost - printed on 2/13/2023 4:48 AM via . All use subject to https://www.ebsco.com/terms-of-use

unit cell parameters increase as K fills vacant sites along the nepheline hexagonal channels. With increasing K content these sites become fully-occupied, and K has to substitute for Na on the smaller, oval sites. The point at which this occurs is marked by a sudden increase in slope of cell parameters plotted versus K-content.

Sodic nepheline. For nephelines containing more than 6 sodium atoms per unit cell, the excess Na must be accommodated on the large alkali site. Ions smaller than K cannot achieve full contact with the surrounding channel oxygens, so Na substitution must involve either collapse of the hexagonal channels, or an off-centering of Na towards the channel wall. It is significant that in nature, nepheline avoids the problem of Na substitution for K, preferring an omissional solid solution ($K \Leftrightarrow [\,]$) coupled with the substitution of Si for Al.

Dollase and Thomas (1978) prepared a Na-rich nepheline by ion exchanging crystals of natural nepheline in molten NaCl. The resulting composition was reported as: $K_{0.03}Ca_{0.05}Na_{7.30}Al_{7.48}Fe_{0.03}Si_{8.50}O_{32}$. Structure refinements showed that although the smaller sodium cation replaces potassium in the hexagonal channels, the overall volume decrease is rather small, with no framework collapse. Instead, the Na ions were found to be off-centered by ~ 0.3 Å, residing on three off-axis positions with one-third occupancy in each. This results in a tendency for "one-sided" bonding to oxygen atoms in the channel wall, similar to that observed for adsorbed cations in zeolites. The off-centered Na positions have been confirmed for a variety of Na-rich nephelines (Gregorkiewitz, 1984; Hippler and Bohm, 1989). The degree of Al/Si ordering correlates with the stoichiometry: partial disorder is required when the Si/Al ratio is greater than unity.

Henderson and Roux (1977) studied the effects of substituting Na for K using synthetic samples of composition $Na_{8-x}K_xAl_8Si_8O_{32}$. As the fraction of K decreased to $x < 0.2$, the symmetry was observed to decrease from hexagonal to orthorhombic, accompanied by the onset of lamellar twinning. The new unit cell was a superstructure, with dimensions: $a_o \approx a_H$, $b_o \approx \sqrt{3}a_h$, $c_o \approx 3c_h$ (the subscript 'h' refers to the hexagonal nepheline cell), suggesting framework collapse about the small Na ion in the large alkali sites. The distorted, orthorhombic phase could be transformed to the "conventional" hexagonal cell by heating. The temperature of the *displacive* phase transition ($T_c \approx 430$ K for pure Na-nepheline) decreased with increasing K content (Henderson and Thompson, 1980).

Klaska et al. (1979) have reported the synthesis of a pure Na-nepheline with the beryllonite-*Icmm* structure. Work with germanate analogues (Barbier and Fleet, 1988) suggests that this may be the stable $NaAlSiO_4$ phase.

Kalsilite

Kalsilite, $KAlSiO_4$, is typically found in volcanic rocks, such as K-rich lavas (Uganda and Zaire). It is commonly associated with nepheline, the two minerals occurring in phenocrysts, with a perthitic relationship.

Kalsilite Crystal Chemistry

Perrotta and Smith (1965) confirmed earlier suggestions by Claringbull and Bannister (1948) that kalsilite has a tridymite-type tetrahedral framework structure. The main features of the kalsilite structure include: (1) Al/Si ordering in adjacent sites, causing a reduction in symmetry from the idealized tridymite "topological symmetry" $P6_3/mmc$ to

EBSCOhost - printed on 2/13/2023 4:48 AM via . All use subject to https://www.ebsco.com/terms-of-use

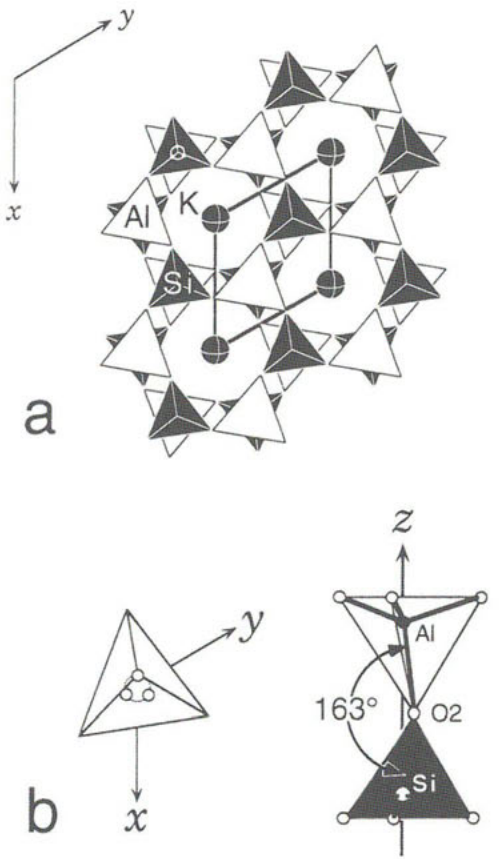


Figure 15. The crystal structure of kalsilite. (a) Projection of the *average*, $P6_3$ structure along [001], plotted using the coordinates of Perrotta and Smith (1965). (b) The effect of apical oxygen (O2) displacement from the triad axis. The off-centered O2 atom can occupy one of three possible sites, indicated by open circles, at a distance of 0.25 Å from the [001] triad. The off-centering reduces the Al–O2–Si bond angle from 180° to a more energetically-favorable 163°.

$P6_3mc$; (2) collapse of the six-fold tetrahedral rings in a ditrigonal pattern about a centrally-located K atom. Potassium is surrounded by nine nearest oxygens: three apical (O2) oxygens linking the upper and lower tetrahedral sheets, plus two sets of three basal oxygens from the upper and lower ditrigonal rings (Fig. 15a). The mean K–O bond distance is 2.90 Å. The apical oxygen atoms (O2) linking the tetrahedral sheets along [001] show very high temperature factors, and appear to be disordered over three sites—related by a triad—in the same manner as the O1-sites in nepheline. The off-centering of the apical oxygens reduces the T–O–T bond angle from 180° to 163° (Fig. 15b), a somewhat higher angle than observed for nepheline, although the mean T–O–T angle is 146°, which is very close to the ideal value of 142° suggested by Liebau (1985) for an "unstrained" Si–O–Al bond. The presence of weak "superstructure" reflections may be due to the ordering of the apical oxygen displacements, perhaps coupled with an ordering of the channel species (K, plus minor Na and H_2O).

Structural Behavior of Kalsilite

The kalsilite structure can be viewed as a stuffed tridymite derivative with adjacent layers rotated through 180°. On increasing temperature there are various possibilities for structural modification: (1) an expansion of the framework in the (001) plane, involving

EBSCOhost - printed on 2/13/2023 4:48 AM via . All use subject to https://www.ebsco.com/terms-of-use

the opening of the six-fold rings from ditrigonal to hexagonal cross section; (2) a change in the off-centering of the apical O2 oxygens; (3) disorder of Al and Si over the tetrahedral sites.

Henderson and Taylor (1988) measured the thermal expansion of synthetic kalsilite to 1163 K, noting that c decreases on heating, in contrast to the behavior of nepheline. This might be explained by an increased disorder of the apical oxygens which would further decrease the T–O–T angle parallel to [001].

Andou and Kawahara (1982) proposed a displacive transition from the low-temperature $P6_3$ phase to $P6_3mc$ at 1138 K, with the possibility of Al/Si disordering at higher temperatures. The existence of a high temperature $P6_3mc$ phase was later confirmed by a structure refinement carried out at 1223 K by Kawahara et al. (1987).

The accepted $P6_3$ symmetry of low-temperature kalsilite was challenged by Capobianco and Carpenter (1989). They examined natural kalsilite in the electron microscope, observing a high density of *lamellar* twins with their composition planes parallel to (001) (Fig. 16). The diffraction patterns can be interpreted as arising from the superposition of three sets of *orthorhombic* twin domains stacked parallel to [001] and rotated through 120° about this axis. Such an orthorhombic cell would have to be pseudo-hexagonal, C-face centered, and include a c-glide. A possible spacegroup is $Cmc2_1$.

On heating kalsilite, a rather more complex picture emerges. Capobianco and Carpenter (1989) report that the pseudo-hexagonal $?Cmc2_1$ phase undergoes a reversible, displacive phase transition at $T_c \approx 1133$ K to another pseudo-hexagonal phase. The transition is highly first-order, and thus there is a degree of coexistence between the two orthorhombic phases; this is *not* a kinetic effect, because the actual phase transition is very rapid. The high temperature orthorhombic phase is characterized by the appearance of new superstructure reflections, 410 and 120, and $a \approx 3\sqrt{3}\ b$. This phase is therefore referred to as "$3\sqrt{3}$ kalsilite". At 1183–1223 K, reflections of the type hhl (l = odd) vanished, and the sample appeared to transform to the $P6_3mc$ phase of Kawahara et al. (1987).

Nepheline–Kalsilite Intermediates

Minerals with compositions between nepheline and kalsilite are rare, but there are intermediate structures which have varying proportions of the three tridymite ring types (hexagonal, oval and ditrigonal) in order to achieve the most favorable cation environments.

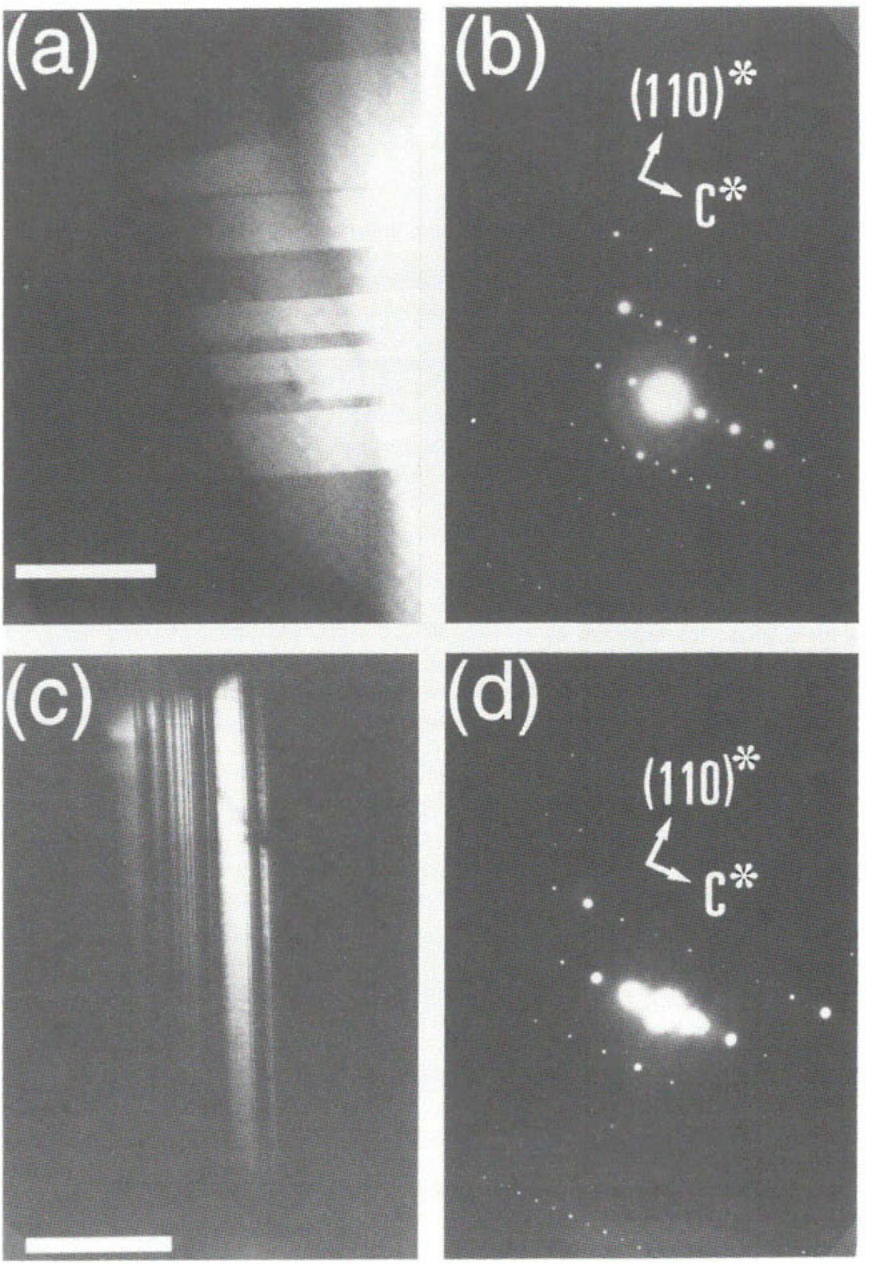
Trikalsilite

Trikalsilite is hexagonal, $P6_3$, with its a-axis repeat three times that for kalsilite. The crystal structure was solved by Bonaccorsi et al. (1988) who showed that the structure comprises elements of both nepheline and kalsilite structures: hexagonal, ditrigonal and

---

Figure 16 (next page). Twinning in a natural kalsilite observed by transmission electron microscopy. (a) Bright-field image showing multiple twin lamellae (scale bar = 200 nm) (b) Diffraction pattern for a twinned crystal, showing weak {00l, $l = 2n+1$} twin reflections along the **c*** direction. (c) Dark-field image obtained using an $l = 2n + 1$ reflection. (d) Diffraction pattern in the same orientation as (b), but from an untwinned region of the crystal. From Capobianco and Carpenter (1989).

EBSCOhost - printed on 2/13/2023 4:48 AM via . All use subject to https://www.ebsco.com/terms-of-use



EBSCOhost - printed on 2/13/2023 4:48 AM via . All use subject to https://www.ebsco.com/terms-of-use

oval rings, in the ratio 1:2:6 (Fig. 17). Adjacent tetrahedral layers are in the same orientation, unlike kalsilite where they are rotated through 180°. Full Al/Si ordering was assumed, with adjacent tetrahedral occupied by Al and Si. The alkali cations are disordered over the oval (M2, M3) sites.

Crystals of natural trikalsilite were described by Sahama and Smith (1957), occurring in association with nepheline, inside a porphyritic lava. The formation of trikalsilite from a heat-treated nepheline-kalsilite perthite was reported by Sahama (1957), but Bonaccorsi et al. (1988) were unable to reproduce this result.

Tetrakalsilite

Synthetic tetrakalsilite was described by Smith and Tuttle (1957) in their study of the nepheline-kalsilite system. The "H4" phase (in their terminology) could be produced by heating a glass of composition 30% nepheline 70% kalsilite for six hours at 1793 K. Sahama (1957) was also able to synthesize this phase, by heating a natural nepheline/kalsilite perthite at 1273 K, followed by a rapid quench. Hovis et al. (1992) produced tetraksilite during ion-exchanging experiments on natural and synthetic nephelines; their phase had a composition corresponding to 72% kalsilite, 28% nepheline. The name "tetrakalsilite" was suggested by Sahama (1960) on account of the *a* dimension (~ 20.5 Å) being almost exactly four times that of kalsilite.

In nature tetrakalsilite occurs as the mineral "panunzite"—named after Dr. Achille Panunzi (University of Naples) who discovered the pyroxene-rich volcanic blocks in which the mineral occurs. Crystals were first described by Benedetti et al. (1977) in metamorphic ejecta at Mt. Somma–Vesuvio, Italy. The occurrence is typically a "micro-perthitic" association with nepheline, or kalsilite. The composition was given as $Na_{0.30}K_{0.70}AlSiO_4$. Crystals from the same locality were also described by Franco and Gennaro (1988).

The crystal structure of panunzite was refined by Merlino et al. (1985). The space group was reported as $P6_3$, with cell dimensions: a = 20.513(8), c = 8.553(3) Å. The structure is very similar to that of nepheline, containing hexagonal rings surrounded by oval rings. There are also kalsilite-type ditrigonal rings in the structure, grouped in threes about the [001] triad, but unlike kalsilite, adjacent (001) tetrahedral layers are in eclipsed configuration. Of the six alkali sites, only three are fully ordered: "Na1" (oval rings) contains 100% Na; K3 (ditrigonal rings) and K5 (hexagonal rings) contain 100% K. The remaining sites contain different amounts of sodium. K1 (ditrigonal), K2 (oval) and K4 (oval) contain 12%, 22% and 17% Na, respectively. Merlino et al. (1985) also reported Al/Si ordering, with no Al-O-Al linkages. The Al and Si tetrahedra point in opposite directions along [001] (Fig. 18).

Other MAlSiO$_4$ Phases

The O1 Structure

A high-temperature polymorph of $KAlSiO_4$ was described by Smith and Tuttle (1957), who noted that it had orthorhombic symmetry, and named it "O1"; it was suggested kalsilite undergoes a *reconstructive* transformation to the O1-$KAlSiO_4$ phase at high temperatures. Cook et al. (1977) carried out high-temperature x-ray diffraction measurements on this phase, confirming the orthorhombic symmetry, and measuring unit cell parameters for quenched samples of a = 9.057(2), b = 15.642(2), c = 8.582(2) Å.

EBSCOhost - printed on 2/13/2023 4:48 AM via . All use subject to https://www.ebsco.com/terms-of-use

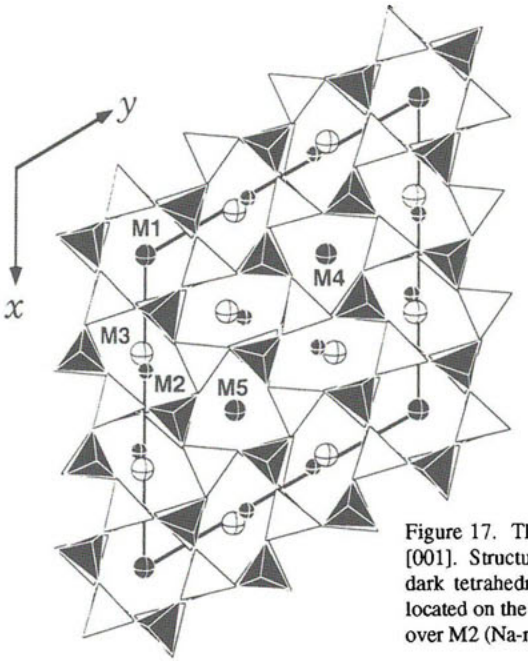


Figure 17. The crystal structure of trikalsilite viewed along [001]. Structure determined by Bonaccorsi et al. (1988). The dark tetrahedra contain Si, and the light contain Al. K is located on the M1, M4 and M5 sites; K and Na are disordered over M2 (Na-rich) and M3 (K-rich).

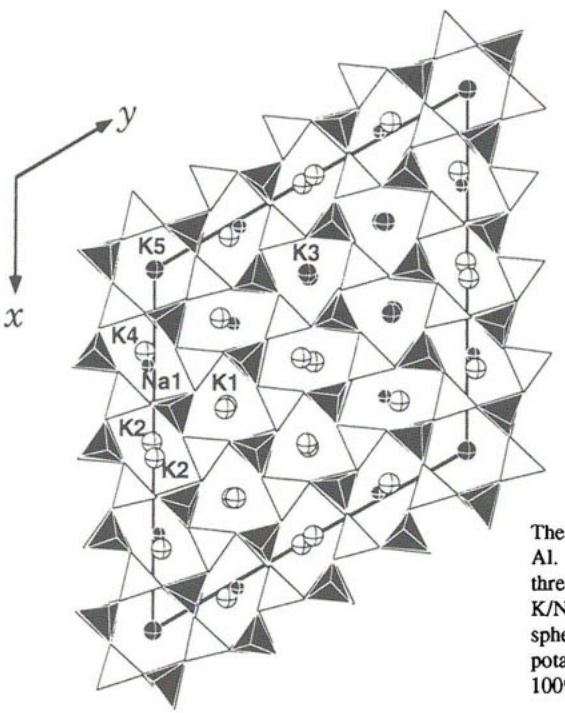


Figure 18. The crystal structure of tetrakalsilite, viewed along [001], using the coordinates of Merlino et al. (1985). The dark tetrahedra contain Si, the light contain Al. There are six alkali sites, spread amongst three different ring types. The sites on which K/Na disorder occurs are shown as white spheres. The dark spheres (K3 & K5) contain potassium; the grey spheres (Na1 site) contain 100% sodium.

EBSCOhost - printed on 2/13/2023 4:48 AM via . All use subject to https://www.ebsco.com/terms-of-use

The crystal structure was determined by Gregorkiewitz (1980) as part of a doctoral dissertation and details are published in an abstract (Gregorkiewitz and Schäfer, 1980). The structure refinement was complicated by pseudo-symmetry and twinning. Macroscopically, the structure appears to be orthorhombic, with spacegroup $Pn2_1m$. However, diffuse streaks parallel to **b*** in the diffraction pattern indicate possible stacking disorder, and there is evidence of a domain structure. The true, *local* symmetry, may be monoclinic.

O1-$KAlSiO_4$ is related to other stuffed tridymite derivatives in that it consists of sheets of six-fold rings of $(Al,Si)O_4$ tetrahedra, but the actual ring topologies differ from the simple **UDUDUD** tridymite sequence. Within the (001) plane there are two ring types: **UUDDUD** and **UUUDDD**, in the proportional 2:1. These rings are oval in section, and connection of successive rings creates eight- and ten-fold tetrahedral rings parallel to [001], which contain K (Fig. 19).

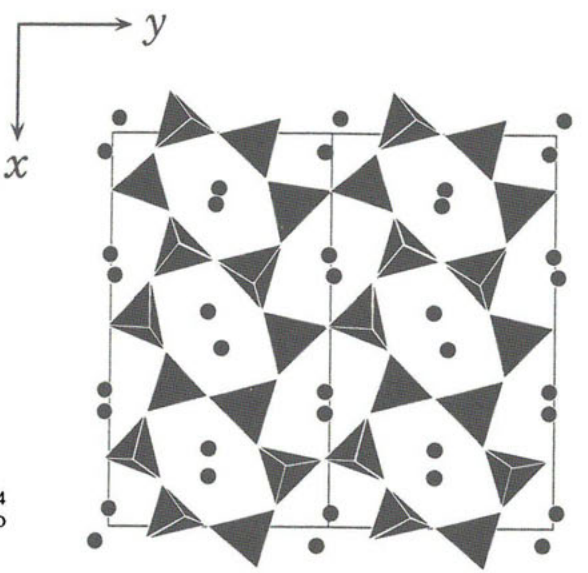


Figure 19. The structure of O1-$KAlSiO_4$ viewed down [001]. After Merlino (1984).

Structural behavior of O1-$KAlSiO_4$. Cook et al. (1977) studied a synthetic O1-$KAlSiO_4$ using x-ray diffraction, reporting a phase transition to another orthorhombic phase with a larger unit cell at temperatures above 1723–1758 K. Lower-temperature work, also with a synthetic sample, and using differential-scanning calorimetry (Lange et al., 1986) showed pronounced "lambda" anomalies at 695 K and 817 K, indicative of first-order, displacive phase transitions. (Measurements on the iron analog, $KFeSiO_4$ revealed only one phase transition, at 730 K). Somewhat different results were obtained by Capobianco and Carpenter (1989) who studied a specimen derived from a metamorphic kalsilite, using x-ray powder diffraction. A break–in–slope of the *c/a* ratio at 813 K, with a progressive curvature below this temperature, suggested a single, *continuous* displacive phase transition at $T_c = 813$ K. The *b/a* ratio remained close to $\sqrt{3}$ at all temperatures and the unit cell appears to be close to hexagonal in its dimensions on both sides of the phase transition.

EBSCOhost - printed on 2/13/2023 4:48 AM via . All use subject to https://www.ebsco.com/terms-of-use

Icmm Structure

Cations larger than K cannot easily be accommodated within the tridymite framework. Synthesis of $RbAlSiO_4$ (Klaska and Jarchow, 1975) yields a new framework topology in which the orientation of half the tetrahedra is reversed, (a **UUUDDD** sequence), creating eight-fold rings parallel to [010]. There is a reduction in topological symmetry from hexagonal to orthorhombic, *Icmm*. Further, distortions around the Rb ions lead to the space group $Pc2_1n$. Rb is surrounded by 11 nearest-neighbor oxygens, at a mean distance of 3.3 Å. The structure is illustrated in Figure 20. The T–O–T bond angle between adjacent tetrahedral sheets is 179.3°, which is energetically unfavorable. Liebau (1985) reported synthetic $CsAlSiO_4$ in which Cs is 13-fold coordinated by oxygen. Ion-exchange of $RbAlSiO_4$ can be used to produce a potassium analog, referred to as $KAlSiO_4$-*Icmm* (Minor et al., 1978).

Kaliophilite

Kaliophilite, isochemical with kalsilite, remains something of a mystery phase. Although the mineral was discovered before kalsilite, its structure has never been satisfactorily solved. In nature, kaliophilite is restricted to volcanic rocks, specifically ejected blocks that have become incorporated into pyroclastic deposits. The main localities are Mt. Vesuvius (biotite-pyroxenite ejecta), described by Bannister and Hey (1931), and the Alban Hills, Rome, described by Barbieri et al. (1970). Tuttle and Smith (1958) synthesized a kaliophilite-like phase, which they considered to be metastable. However, their sample had different cell dimensions from the *natural* kaliophilite described by other groups.

Crystallography. Kaliophilite appears to have hexagonal symmetry, and is characterized by an a repeat of ~ 27 Å ($= 3\sqrt{3}a_0$, where a_0 is the cell dimension of the idealized tridymite unit cell), and $c = 8.56$ Å (i.e., the same as for tridymite and kalsilite).

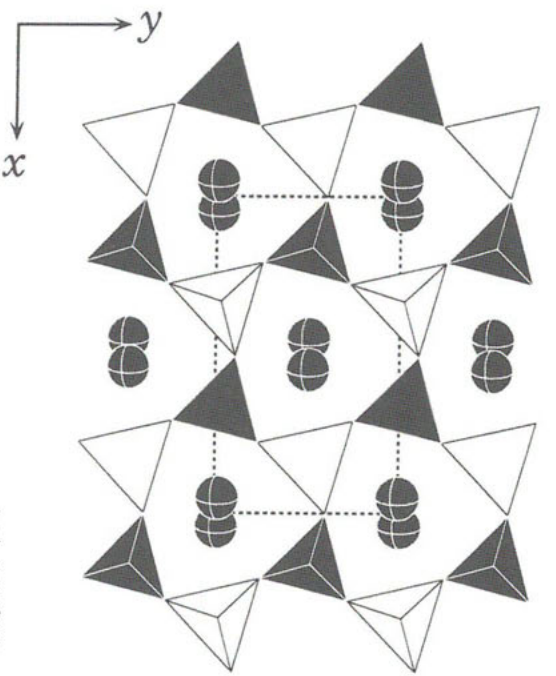


Figure 20. The structure of $RbAlSiO_4$-*Icmm*, viewed along [001]. The unit cell outline is shown by the dashed line. Tetrahedra are occupied by Si (black) and Al (white). The grey circles represent Rb atoms. Structure determined by Klaska and Jarchow (1975).

EBSCOhost - printed on 2/13/2023 4:48 AM via . All use subject to https://www.ebsco.com/terms-of-use

Lukesh and Buerger (1942) reported a space group of $P6_322$, but the presence of merohedric twinning (Cellai et al., 1992) would suggest that the true space group is of lower symmetry, presumably a subgroup, e.g., $P6_3$. Dark field TEM images using kaliophilite superstructure reflections reveal stacking disorder of the 27 Å *a* repeat (Cellai et al., 1992).

Structural behavior. Cellai et al. (1992) report heating experiments on natural kaliophilite. On increasing temperature the cell parameters show a pronounced curvature, with a break in slope at Tc ≈ 998 K, indicative of a displacive phase transition. There is no change in crystal system, so the high-temperature space group is most probably $P6_322$. The displacive phase transition to the subgroup is therefore consistent with merohedric twinning observed by electron microscopy.

Is kaliophilite a stuffed derivative of tridymite? Kaliophilite has traditionally been regarded as a stuffed derivative of tridymite, which would imply a relationship to kalsilite. This now seems highly unlikely. Firstly, the *c* dimension of kaliophilite (8.56 Å) is rather less than that of kalsilite (8.69 Å), and very similar to that for the O1-$KAlSiO_4$ phase (Sandomirskiy and Urusov, 1988). Secondly, there is a marked difference in thermal expansion: the *c*-dimension of kaliophilite increases with temperature (Cellai et al., 1992), as does that for the O1-$KAlSiO_4$ phase (Sandomirskiy and Urusov, 1988); by contrast, kalsilite shows a *decrease* in *c* with increasing temperature (Henderson and Taylor, 1988). Thirdly, ion-exchange experiments on kaliophilite, replacing K by Na, result in a small change in unit cell size, but not a switch to the nepheline structure observed for similar experiments on kalsilite. This evidence points to kaliophilite *not* being a stuffed derivative of tridymite, but having a different framework topology, possibly related to that of the O1 polymorph (**UUUDDD** and **UDUDUD** rings).

Ca-rich derivatives of tridymite

Synthetic nepheline, containing small amounts of calcium, has been reported by Rossi et al. (1989). There is evidence for some ordering of K, Na, and Ca cations along the hexagonal channels parallel to [001]: The K-site of nepheline is statistically occupied by Ca, Na, K; a second site, 1.25 Å above the K site along [001], is occupied by Ca + Na.

$CaAl_2SiO_6$ (yoshiokaite). Ca-rich tridymite derivatives, which include the lunar mineral *yoshiokaite,* have been reported in the solid-solution range

$$Ca_{8-0.5x}[\,]_{0.5x}Al_{16-x}Si_xO_{32}\,,\quad x \approx 2.8 \text{ to } 6.0$$

(Yoshioka, 1970; Vaniman and Bish, 1990). The crystal structure of an intermediate phase was determined by Steele and Pluth (1990) and shown to be very similar to that of nepheline—comprising hexagonal and oval rings of tetrahedra arrayed in sheets parallel to (001). Unlike nepheline, the rings in adjacent sheets are distorted in opposite senses, which causes the *c* axis to be doubled. The Ca ions reside in the oval rings (the Na sites in nepheline), and the hexagonal rings remain empty (Fig. 21). In order their refinement, Steele and Pluth assigned half-occupancy to the Si and O sites on the triad axis. This would seem to require tetrahedral *face-sharing* along the triad axis; but the authors argued that this is an artifact caused by a [110] twin axis which superposes the reciprocal lattices of two twin components. (The components differ only in the orientation of their tetrahedra along the triad axis). The *true* crystal symmetry is the $P\bar{3}$, and not the *average* $P\,\bar{3}c$ space group observed in diffraction experiments.

$CaAl_2O_4$. Increased Ca substitution (with a corresponding replacement of Si by Al to maintain charge balance) forces Ca into the hexagonal site of the nepheline structure. For the end-member, $CaAl_2O_4$, there is no longer any distinction between the "oval"

EBSCOhost - printed on 2/13/2023 4:48 AM via . All use subject to https://www.ebsco.com/terms-of-use

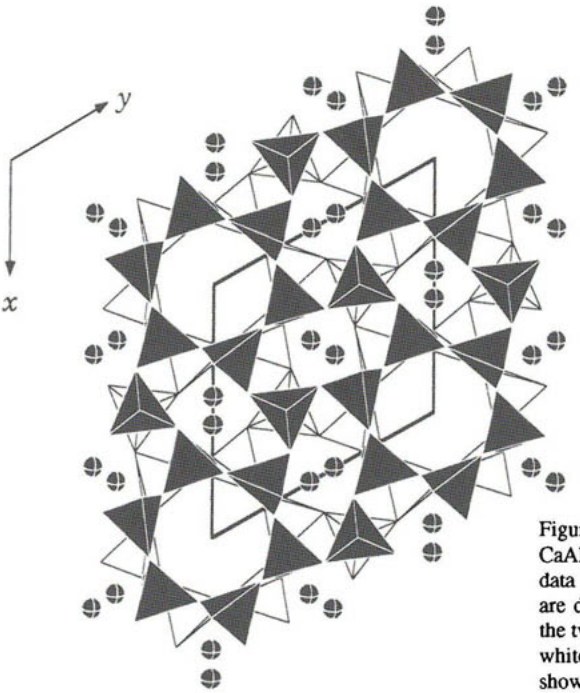


Figure 21. Crystal structure of yoshiokaite, $CaAl_2SiO_6$. viewed along [001]. Structural data from Steele and Pluth (1990). Al and Si are disordered over the tetrahedral sites, in the two layers of the unit cell (lower layer in white; upper layer in black). Ca atoms are shown as grey spheres.

and "hexagonal" rings of the nepheline structure, and the outcome is a stuffed-kalsilite phase. A crystal structure refinement (Hörkner and Müller-Buschbaum, 1976) revealed monoclinic symmetry, space group $P2_1/c$, with the tetrahedral sheets parallel to (010).

Ba-Rich Derivatives of Tridymite

Liu and Barbier (1993) claim to have synthesized a range of Ba-stuffed kalsilite phases, $BaMSiO_4$ (M = Co, Mg, Zn). Unfortunately they did not report the *final composition* of their crystals, apparently assuming that exact stoichiometry was maintained throughout the synthesis. Their crystals were hexagonal, with a $\sqrt{3}$A superstructure, and ordered tetrahedral sites.

STRUCTURES DERIVED FROM CRISTOBALITE

Cristobalite is the highest-temperature polymorph of silica. The crystal structure is related to that of tridymite: the ideal structures differ only in the stacking sequence of otherwise identical layers of SiO_4 tetrahedra (Fig. 6). The "ABCABC" stacking sequence of tetrahedral sheets gives a maximum topological symmetry of $Fd\bar{3}m$. Although cristobalite shows *macroscopic* cubic symmetry at high temperatures, the true microscopic symmetry is probably much lower, indicated by the observation of diffuse intensity in diffraction patterns (Hua et al., 1988), and the non-disappearance of "symmetry-forbidden" vibrational modes (Swainson et al., 1994). The idealized $Fd\bar{3}m$ structure contains structural "cages", each comprising an hexagonal ring of

EBSCOhost - printed on 2/13/2023 4:48 AM via . All use subject to https://www.ebsco.com/terms-of-use

tetrahedra "plugged" by one upwards-pointing- and one downwards-pointing tetrahedron. The resulting cavity is large enough for alkali and alkaline earth cations, in 12-fold coordination by oxygen (Fig. 22).

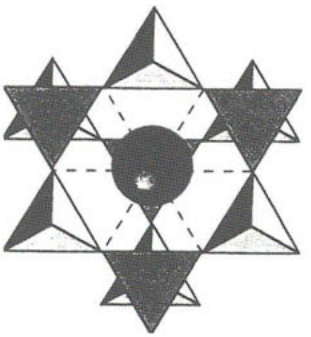


Figure 22. Cation residing in a cristobalite structural cage. The cavity is ringed by a six-fold ring of tetrahedra, and "plugged" by (111) tetrahedral sheets above and below. (The upper tetrahedral sheet has been omitted for the sake of clarity.) Bonds to oxygen atoms at the same height are shown as dashed lines.

Chemically Stabilized β-Cristobalite

The cubic-to-tetragonal phase transition in cristobalite involves a large (5%) volume change, which can cause single-crystals and ceramics to shatter. Not surprisingly, there has been much technological interest in inhibiting the phase transition. The high-temperature β-cristobalite phase cannot be preserved by quenching because the α-β transition is displacive in nature. Attention has therefore been focused on chemically stuffing cristobalite in an attempt to expand the framework into a cubic topology.

Perrotta et al. (1989) synthesized cristobalite-like phases containing Na_2O or CaO and with some Si^{4+} replaced by Al^{3+} for charge balance. Although these phases showed diffraction patterns characteristic of the β-phase rather than α-cristobalite, the samples also contained some crystalline and amorphous impurities. More recently Saltzberg et al. (1992) were able to synthesize single-phase cristobalite-like materials by a "wet chemical" method, starting with colloidal silica and then adding a range of dopants, including Ca, K, Na, Li, etc. The phase with composition $Ca_{0.02}Al_{0.09}Si_{0.91}O_2$ was characterized by Gai-Boyes et al. (1993). This material has sharp β-cristobalite X-ray diffraction peaks, and it has a relatively defect-free microstructure. Electron diffraction patterns contain considerable diffuse intensity, and the sample displays a broad ^{29}Si NMR resonance. The Ca is believed to be located inside cages between tetrahedral layers. The presence of Ca ions in cavities and Al in the tetrahedral framework induces local, static distortions, which might account for the broadened NMR resonance.

Carnegieite

Carnegieite is the high-temperature polymorph of $NaAlSiO_4$, and is stable up to its melting point of 1800 K There is a reconstructive phase transformation from the low-temperature polymorph, nepheline, to carnegieite, at temperatures above 1523 K. A steep rise in transition temperature for increasingly-potassic nepheline suggests that carnegieite is relatively intolerant to K substitution.

Crystal Sructures

The first refinements of carnegieite, using synthetic specimens, were somewhat speculative in nature. Barth and Posnjak (1932a) measured the intensities of 16 powder X-ray diffraction lines, and concluded that the high-temperature structure was cubic, with possible space group $P2_13$ or $F\bar{4}3m$—but expressing a preference for the

EBSCOhost - printed on 2/13/2023 4:48 AM via . All use subject to https://www.ebsco.com/terms-of-use

former. Substituting excess Na_2O into high Carnegieite results in an expanded structure with space group $F\bar{4}3m$ (Borchert and Keidel, 1947), which is also the space group of high cristobalite. This space group was used in later work on $NaAlSiO_4$ carnegieite by Thompson et al. (1993) and Withers and Thompson (1993). The tetrahedral framework contains a series of large cavities, in half of which reside sodium atoms (Fig. 23a).

The High-Low Carnegieite Phase Transition

Carnegieite undergoes a displacive "high-low" phase transition on cooling, reminiscent of the α-β cristobalite transition. Low-carnegieite is *metastable*, but the high activation energy for transformation to the stable phase, nepheline, opposes conversion.

Determination of the low-temperature crystal structure has proved difficult. Synthesis of carnegieite is complicated by the possibility of Na_2O-loss from oxide mixtures, leading to non-stoichiometric run products, and this problem is further exacerbated by the very long annealing times needed to achieve a homogeneous phase. The problem was highlighted when Klingenberg et al. (1981) claimed to index a powder X-ray diffraction pattern on the basis of a large, *triclinic* unit cell. This result was discredited by Thompson et al. (1993) in a detailed study incorporating a variety of synthesis techniques, and extensive sample characterization.

Given that the high-low carnegieite transition is displacive, one would expect a simple relationship between the two structures. Thompson et al. (1993) and Withers and Thompson (1993) proposed that low-carnegieite is orthorhombic, with space group $Pb2_1a$. The *b* axis of the orthorhombic phase is parallel to the cubic (high-carnegieite) cell edge and double the length; the *a* and *c* axes are oriented 45° to their cubic counterparts, illustrated in Figure 23. ^{29}Si and ^{27}Al NMR spectroscopy confirms that Al and Si are fully ordered (Stebbins et al., 1986; Thompson et al., 1993).

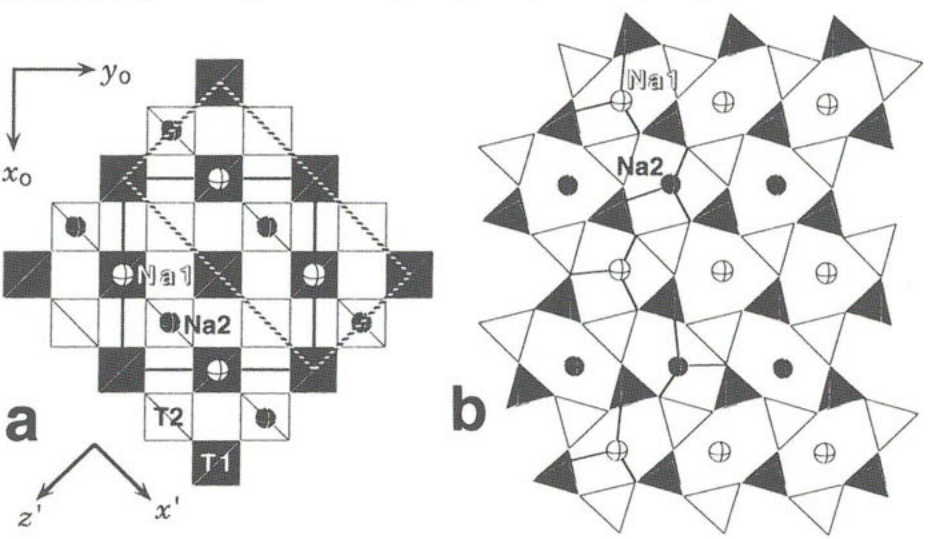


Figure 23. Crystal structures of carnegieite, $NaAlSiO_4$. (a) Projection of the high-carnegieite structure on (001) after Thompson et al. (1993). The axes of the cubic unit cell are indicated by x_o, y_o; the low-temperature unit cell is indicated by the hatched lines. (b) One tetrahedral sheet of the low-carnegieite (orthorhombic) structure. The plane corresponds to (111) of the cubic phase. Na has four closest oxygen neighbors, giving it approximately tetrahedral coordination. Bonds to the three coplanar neighbours are shown; the fourth is in the next tetrahedral layer.

EBSCOhost - printed on 2/13/2023 4:48 AM via . All use subject to https://www.ebsco.com/terms-of-use

The Nepheline–Carnegieite Reconstructive Phase Transition

The high-temperature form of carnegieite is a stuffed derivative of cubic ("beta-") cristobalite and so the nepheline/carnegieite transition would appear to be analogous to the tridymite/cristobalite phase transition: both involving a change in stacking sequence of otherwise identical tetrahedral sheets (ABAB layers to ABCABC layers). The tridymite/cristobalite transition requires breaking the T–O–T connections between adjacent sheets, rotation of tetrahedra, and shifting of layers (Schneider and Flörke, 1986). The nepheline/carnegieite transformation is also coherency-controlled (the planes of carnegieite tetrahedral sheets are parallel to those of the nepheline structure) but occurs at a lower temperature, and has much faster kinetics (Schneider et al., 1994). Rapid movement of "interstitial" Na ions at high temperature may catalyze the phase transition, which is further facilitated by the presence of weaker Al–O–Si bonds between the tetrahedral layers.

Stuffed Cristobalite Phases: Na_2MSiO_4–$Na_2MSi_2O_6$

A wide variety of phases exhibit a framework structure based on that of cristobalite, but containing various *divalent* framework cations (M = Ca, Be, Zn, Mg) in place of Si^{4+} or Al^{3+}. Compared to the carnegieite structure, these phases have twice as many sodium atoms, filling all the possible "cage" sites. Many of these phases show extensive solid solution in the ternary system $Na_2O - MO - SiO_2$. Synthetic phases with compositions of the form $Na_x[\,]_{2-x}[M_{x/2}Si_{2-x/2}O_4]$ ($2.0 \geq x \geq 1.33$), along the join Na_2MSiO_4 to $Na_2MSi_2O_6$ have been well studied (Table 2) because of their potential as superionic conductors of sodium.

Table 2. Stuffed derivatives of tridymite, $ABSiO_4$: A = channel cation; B = framework cation.

A	*B*	Formula	Structure	Reference
K	Al	$KAlSiO_4$	Kalsilite	Kawahara et al. (1987)
K	Fe	β-$KFeSiO_4$	Kalsilite	Bentzen (1983)
K	Fe	γ-$KFeSiO_4$	"Kaliophilite"	Bentzen (1983)
K,Na	Al	$Na_{0.28}K_{0.72}AlSiO_4$	K-rich nepheline	Sahama (1957)
K,Na	Al	$Na_{0.3}K_{0.7}AlSiO_4$	Tetrakalsilite	Benedetti et al. (1977)
K,Na	Al	$Na_{0.33}K_{0.67}AlSiO_4$	Trikalsilite	Bonaccorsi et al. (1988)
Na	Al	$NaAlSiO_4$	Na-rich nepheline	Gregorkiewitz (1984)
Na,K	Al	$Na_{0.75}K_{0.25}AlSiO_4$	Nepheline	Dollase (1970)
Na,K	Ga	$Na_{0.70}K_{0.30}GaSiO_4$	√3 A Kalsilite	Barbier et al. (1993)
Na,Ca,K	Al	$K_{0.03}Na_{0.83}Ca_{0.07}Al_{0.99}Si_{1.01}O_4$	Nepheline	Rossi et al. (1989)
Ca	Al	$Ca_{0.66}Al_{1.34}Si_{0.66}O_4$	Yoshiokaite	Steele and Pluth (1990)
Ca	Al	$CaAl_2O_4$	Kalsilite	Hörkner and Müller-Buschbaum (1976)
Ba	Co	$BaCoSiO_4$	Kalsilite	Liu and Barbier (1993)
Ba	Mg	$BaMgSiO_4$	Kalsilite	Liu and Barbier (1993)
Ba	Zn	$BaZnSiO_4$	Kalsilite	Liu and Barbier (1993)

EBSCOhost - printed on 2/13/2023 4:48 AM via . All use subject to https://www.ebsco.com/terms-of-use

Grins (1982) defined four main structure types for stuffed sodium silicates, three of which are stuffed cristobalite derivatives. The cristobalite derivative structures are cubic (type "K") and orthorhombic (types "A" and "C"). The cell parameters of the "C" phase may be related to those of the cubic, "K" phase by the relation: $a_c = \sqrt{2}\, a_k$; $b_c \approx 2a_k$; $c_c \approx a_k/\sqrt{2}$. A monoclinic phase which could not be related to a cristobalite unit cell was designated type "M". Examples of the phases, "A", "C", "M" and "K" are given in Table 3.

Sodium Zinc Silicate

The best Na-ion conductors with the cristobalite structure lie in the range $Na_xZn_{x/2}Si_{2-x/2}O_4$ (Grins, 1982), but details of structures and phase relations for this system are still somewhat sketchy. The Na_2ZnSiO_4 end member ($x = 2$) appears to have two, orthorhombic, modifications. The high-temperature structure (denoted type 'C' by Grins) can be preserved on quenching from 1375 K, and presumably there is a *reconstructive* phase transition to the low-temperature phase, type 'A' on slow cooling.

Table 3. Structure refinements of Na_2MSiO_4 – $Na_2MSi_2O_6$ stuffed cristobalite phases

M	Composition	Structural details	Reference
Zn	Na_2ZnSiO_4	Low-T, type A: $a = 7.037$; $b = 5.440$; $c = 5.250$ Å High-T, type C: $a = 10.482$; $b = 14.435$; $c = 5.242$ Å	Grins (1982)
	$Na_4Zn_2Si_3O_{10}$	Type K (carnegieite): $a = 7.316$ Å	Grins (1982)
	$Na_2ZnSi_2O_6$	Monoclinic; non-cristobalite	Grins (1982)
Be	Na_2BeSiO_4	Orthorhombic, C-type, $Pca2_1$ $a = 9.861$; $b = 13.875$; $c = 4.911$ Å	Frostäng et al.. (1988a)
	$Na_{1.8}Be_{0.9}Si_{1.1}O_4$	Orthorhombic, *Pcba;* disordered C-type. $a = 4.920$; $b = 9.876$; $c = 13.922$ Å	Frostäng et al.. (1990)
	$Na_2BeSi_2O_6$	Orthorhombic, Chkalovite structure $a = 21.096$; $b = 6.870$; $c = 21.142$ Å	Simonov et al. (1976) Frostäng et al.. (1988)
Mg	Na_2MgSiO_4	Orthorhombic, $Pmn2_1$ $a = 7.015$; $b = 10.968$; $c = 5.260$ Å	Shannon (1979)
	$Na_4Mg_2Si_3O_{10}$	Low-T, type C: $a = 10.584$; $c = 14.328$; $c = 5.233$ Å High-T, type K: $a = 7.440$ Å	Shannon (1979)
Ca	Na_2CaSiO_4	Carnegieite	Barth and Posnjak (1932b)

EBSCOhost - printed on 2/13/2023 4:48 AM via . All use subject to https://www.ebsco.com/terms-of-use

At high temperatures, sodium-poor phases ($x < 1.75$) are cubic, with structure type 'K'. At lower temperatures there is evidence for a solvus between the type 'A' structure, and a non-cristobalite, monoclinic phase, type 'B' ($x < 1.31$). The Na-ion conductivity initially increases with increasing Na content, reaching a maximum at $x = 1.85$, and then decreases. This may be explained as the outcome between changing size of "bottle necks" in an expanding framework, and the decreasing number of vacant Na sites.

Sodium Beryllium Silicate

The crystal structure of the synthetic phase Na_2BeSiO_4 was refined by Frostäng et al. (1988a). The structure is orthorhombic, with space group $Pca2_1$, and the cell dimensions suggest that it is a "type C" phase. The cristobalite-type framework comprises alternating BeO_4 and SiO_4 tetrahedra. There are two Na sites, two of which are five-fold coordinated by oxygen, and the remaining two four-fold coordinated.

The solid solution $Na_xBe_{x/2}Si_{2-x/2}O_4$ ($2 \geq x \geq 1.80$) was investigated by Frostäng et al. (1988b). Decreasing sodium content leads to Be/Si disorder over the tetrahedral sites. The solid solution was reported to extend to the composition $Na_{1.8}Be_{0.9}Si_{1.1}O_4$ ($x = 1.8$). The crystal structure of this end-member was determined by Frostäng et al. (1990). The disordered distribution of Be and Si leads to a space group *Pbca*, but the structure is otherwise isostructural with Na_2BeSiO_4 (type "C"). The conductivity of sodium ions increases across the solid solution, with decreasing Na content. Because the framework structures of the "end members" appear very similar, with no significant change in the sizes of the sodium cages, the increase in conductivity must be due to the increased number of vacant sodium sites.

Chkalovite. $Na_2BeSi_2O_6$ occurs naturally as the mineral *chkalovite*. The crystal structure was refined by Simonov et al. (1976) in space group *Fdd*2, with $Z = 24$. This is another stuffed cristobalite derivative with an ordered distribution of Be and Si on almost regular tetrahedral sites. There are four distinct sodium sites, with each sodium approximately *octahedrally*-coordinated by the nearest neighbor oxygens. The thermal expansion behavior was investigated by Henderson and Taylor (1989).

Sodium Magnesium Silicate

Shannon (1979) studied the ionic conductivity of sodium magnesium silicates, synthesizing phases with composition near Na_2MgSiO_4 and $Na_4Mg_2Si_3O_{10}$. The former has cell dimensions corresponding to a type "A" structure with a doubled b dimension. As with other sodium cristobalites, the ionic conductivity increases with the number of vacant Na sites (i.e., as the amount of "stuffed" sodium decreases).

The $Na_4Mg_2Si_3O_{10}$ phase corresponds to type "C" orthorhombic structure. There is a reversible phase tradition at 870–920 K to a cubic, type "K" structure, which Shannon related to cation disordering.

Sodium Calcium Silicate

Although Ca^{2+} ions may reside in structural cavities in "chemically-stabilized" beta-cristobalite, they may also be incorporated into the tetrahedral framework. This is somewhat unexpected: the large ionic radius of calcium normally leads to coordination by six to nine nearest neighbor oxygen atoms. The synthetic phase Na_2CaSiO_4 was studied by Barth and Posnjak (1932b) who observed it to be a stuffed cristobalite

EBSCOhost - printed on 2/13/2023 4:48 AM via . All use subject to https://www.ebsco.com/terms-of-use

derivative, with a similar structure to that of carnegieite: Al^{3+} being replaced by Ca^{2+} ions, and with extra Na^{+} ions to maintain charge balance.

ACKNOWLEDGMENTS

I thank Drs Daniela Cellai and Michael Carpenter (University of Cambridge) for their invaluable advice during the preparation of this manuscript. Crystal structure drawings were produced on the Apple Macintosh computer, using *CrystalMaker* (an interactive crystallography program available from the author).

REFERENCES

Alpen U, Schulz H, Talat GH, Böhm H (1977) One-dimensional cooperative Li-diffusion in β-eucryptite. Sol State Commun 23:911–914.

Andou Y, Kawahara A (1982) The existence of high-low inversion point of kalsilite. Mineral J 11:72–77.

Angel RJ, Hazen RM, McCormick TC, Prewitt CT, Smyth JR (1988) Comparative compressibility of end-member feldspars. Phys Chem Min 15:313–318.

Bannister FA, Hey MH (1931) A chemical, optical and X-ray study of nepheline and kaliophilite. Min Mag 22:569–608.

Barbier J, Fleet ME (1988) Investigation of phase relations in the $(Na,K)AlGeO_4$ system. Phys Chem Min 16:276–285.

Barbier J, Liu B, Weber J (1993) Crystal chemistry of the $(Na,K)GaSiO_4$ system. Eur J Min 5:297–305.

Barbieri M, Federico M, Tolomeo L (1970) Contributi alla conoscenza della caliofilite in relazione a recenti ritrovamenti nella regione vulcanica dei Colli Albani. Period Mineral 39:323–341.

Barth TFW, Posnjak E (1932a) Silicate structures of the cristobalite type I. The crystal structure of α-carnegieite ($NaAlSiO_4$). Zeits Krist 81:135–141.

Barth TFW, Posnjak E (1932b) Silicate structures of the cristobalite type II. The crystal structure of Na_2CaSiO_4. Zeits Krist 81:370–375.

Baur WH (1964) On the cation and water positions in faujasite. Am Min 49:697–704.

Benedetti E, Gennaro MD, France E (1977) Primo rinvenimento in natura de tetrakalsilite. Rendiconti Accademia Nazionale Lincei Series 8, vol. 62:835–838.

Bentzen JJ (1983) Three crystalline polymorphs of $KFeSiO_4$, potassium ferrisilicate. J Am Ceram Soc 66:475–479.

Böhm H (1975) Dielectric properties of β-eucryptite. Phys Stat Sol A30:531–536.

Bonaccorsi E, Merlino S, Pasero M (1988) Trikalsilite: its structural relationships with nepheline and tetrakalsilite. Neues Jahrbuch für Mineralogie Mittheilungen 12:559–567.

Borchert W, Keidel J (1947) Die Strukturen Na_2O-reicher Carnegieite. Heidelberger Beiträge Mineralogie Petrographica 1:17–30.

Buerger MJ (1948) Crystals based on the silica structures. Am Min 33:751–752.

Buerger MJ (1954) The stuffed derivatives of the silica structures. Am Min 39:600–614.

Buerger MJ, Klein GE, Donnay G (1954) Determination of the crystal structure of nepheline. Am Min 39:805–818.

Capobianco C, Carpenter M (1989) Thermally induced changes in kalsilite ($KAlSiO_4$). Am Min 74:797–811.

Carpenter MA, Wennemer M (1985) Characterization of synthetic tridymites by transmission electron microscopy. Am Min 70:517–528.

Cellai D, Carpenter MA, Heaney PJ (1992) Phase transitions and microstructures in natural kaliophilite. Eur J Min 4:1209–1220.

Claringbull GF, Bannister FA (1948) The crystal structure of kalsilite. Acta Cryst 1:42–.

Clarke PT, Spink JM (1969) The crystal structure of β-spodumene, $LiAlSi_2O_6$-II. Zeits Krist 130:420–426.

Cook LP, Roth RS, Parker HS, Negas T (1977) The system K_2O-Al_2O_3-SiO_2. Part I. Phases on the $KAlSiO_4$-$KAlO_2$ join. Am Min 62:1180–1190.

de Dombal RF (1992) Phase transitions in nepheline and tridymite. Ph.D. thesis, University of Cambridge

de Dombal RF, Carpenter MA (1993) High-temperature phase transitions in Steinbach tridymite. Eur J Min 5:607–622.

EBSCOhost - printed on 2/13/2023 4:48 AM via . All use subject to https://www.ebsco.com/terms-of-use

Dollase WA (1967) The crystal structure at 220°C of orthorhombic high tridymite from the Steinbach Meteorite. Acta Cryst 23:617–623.

Dollase WA (1970) Least-squares refinement of the structure of a plutonic nepheline. Zeits Krist 132:27–44.

Dollase WA, Baur WH (1976) The superstructure of meteorite low tridymite solved by computer simulation. Am Min 61:971–978.

Dollase WA, Peacor DR (1971) Si-Al ordering in nepheline. Contrib Mineral Petrol 30:129–134.

Dollase WA, Thomas WM (1978) The crystal chemistry of silica-rich, alkali-deficient nepheline. Contrib Mineral Petrol 66:311–318.

Dondur V, Dimitrijevi R, Petranovic N (1988) Li^+ ion mobility in eucryptite phases. J Mater Sci 23:4081–4084.

Downs RT, Palmer DC (1994) The pressure behavior of α-cristobalite. Am Min 79:9–14.

Ferry JM, Blencoe JG (1978) Subsolidus phase relations in the nepheline-kalsilite system at 0.5, 2.0 and 5.0 kbar. Am Min 63:1225–1240.

Follstaedt DM, Richards PM (1976) NMR relaxation in the superionic conductor β-$LiAlSiO_4$. Phys Rev Lett 37:1571–1574.

Foreman N, Peacor DR (1970) Refinement of the nepheline structure at several temperatures. Zeits Krist 132:45–70.

Franco E, Gennaro Md (1988) Panunzite, a new mineral from Mt. Somma—Vesuvio, Italy. Am Min 73:420–421.

French BM, Jezek PA, Appleman DE (1978) Virgilite: a new lithium aluminum silicate mineral from the Macusani glass, Peru. Am Min 63:461–465.

Frostäng S, Grins J, Louër D, Werner P-E (1988a) The structure of Na_2BeSiO_4 obtained by the Rietveld profile refinement technique. Solid State Ionics 31:131–138.

Frostäng S, Grins J, Nygren M (1990) Rietveld refinement of $Na_{1.8}Be_{0.9}Si_{1.1}O_4$ - an ionic conductor with a cristobalite-related structure. Solid State Ionics 44:51-54.

Frostäng S, Grîns J, Nygren M (1988b) Ionic conductivity studies and phase analysis of the Na_2BeSiO_4 – $Na_2BeSi_2O_6$ system. J Solid State Chem 72:92–99.

Gai-Boyes PL, Saltzberg MA, Vega A (1993) Structures and stabilization mechanisms in chemically stabilized ceramics. J Solid State Chem 106:35-47.

Gillery FH, Bush EA (1959) Thermal contraction of β–eucryptite ($Li_2O{\cdot}Al_2O_3{\cdot}2SiO_2$) by x-ray and dilatometer methods. J Am Ceram Soc 42:175–177.

Glinnemann J, King HE, Schultz H, Hahn T, La Placa SJ, Dacol F (1992) Crystal structures of the low-temperature quartz-type phases of SiO_2 and GeO_2 at elevated pressure. Zeits Krist 198:177–212.

Gregorkiewitz M (1980) Synthese und Charakterisierung poröser Silicate. Ph.D. thesis, Technische Hochschule Darmstadt

Gregorkiewitz M (1984) Crystal structure and Al/Si ordering of a synthetic nepheline. Bull Minéral 107:499–507.

Gregorkiewitz M (1986) Alkali ion diffusion in M'($AlSiO_4$) compounds with frameworks of the tridymite topology and its variants. Solid State Ionics 18:534–538.

Gregorkiewitz M, Schäfer H (1980) The structure of $KAlSiO_4$—kaliophilite O1: application of the subgroup-supergroup relations to the quantitative space group determination of pseudosymmetric crystals. Sixth European Crystallogr Meeting, Barcelona. Abstracts with Program, 155.

Grins J (1982) Ionic conductivity of sodium zinc silicates in the compositional region Na_2ZnSiO_4–$Na_2ZnSi_2O_6$. Solid State Ionics 7:157–164.

Guth H, Heger G (1979) Temperature dependence of the crystal structure of the one-dimensional Li^+-conductor β-eucryptite ($LiAlSiO_4$). In: Vashista, Mundy and Shenoy (ed.), Fast ion transport in solids. pp. 499–502. Elsevier North Holland, New York.

Hahn T, Buerger MJ (1955) The detailed structure of nepheline, $KNa_3Al_4Si_4O_{16}$. Zeits Krist 106:308–388.

Hazen RM, Sharp ZD (1988) Compressibility of sodalite and scapolite. Am Min 73:1120–1122.

Henderson CMB, Roux J (1977) Inversions in sub-potassic nephelines. Contrib Min Petrol 61:279–298.

Henderson CMB, Taylor D (1988) The structural behaviour of the nepheline family: (3) Thermal expansion of kalsilite. Min Mag 52:708–711.

Henderson CMB, Taylor D (1989) Structural behavior of chkalovite, $Na_2BeSi_2O_6$—a member of the cristobalite family. Min Mag 53:117-119.

Henderson CMB, Thompson AB (1980) The low-temperature inversion in sub-potassic nephelines. Am Min 65:970–980.

EBSCOhost - printed on 2/13/2023 4:48 AM via . All use subject to https://www.ebsco.com/terms-of-use

Hesse (1984) The crystal structure of α-eucryptite, $LiAlSiO_4$. Acta Cryst A40, supplement:
Hippler B, Bohm H (1989) Structure investigation of sodium nephelines. Zeits Krist 187:39–53.
Hörkner W, Müller-Buschbaum H (1976) Zur Kristallstruktur von $CaAl_2O_4$. J Inorganic Nuclear Chem 38:983–984.
Hovis GL, Spearing DR, Stebbins JF, Roux J, Clare A (1992) X-ray powder diffraction and ^{23}Na, ^{27}Al, and ^{29}Si MAS-NMR investigation of nepheline–kalsilite crystalline solutions. Am Min 77:19–29.
Hua GL, Welberry TR, Withers RL, Thompson JG (1988) An electron diffraction and lattice-dynamical study of the diffuse scattering in β-cristobalite, SiO_2. J Appl Cryst 21:458–465.
Hummel FA (1951) Thermal expansion properties of some synthetic lithio minerals. J Am Ceram Soc 34:235–239.
Kawahara A, Andou Y, Marumo F, Okuno M (1987) The crystal structure of high temperature form of kalsilite ($KAlSiO_4$) at 950°C. Mineral J 13:260–270.
Kihara K (1978) Thermal change in unit-cell dimensions, and a hexagonal structure of tridymite. Zeits Krist 148:237–253.
Klaska R, Jarchow O (1975) Die Kristallstruktur und die Verzwillingung von $RbAlSiO_4$. Zeits Krist 142:225–238.
Klaska R, Klaska KH, Jarchow O (1979) Struktur und verwachsung zweier topologisch unterschiedlicher tetraedergerüste der pseudosymmetrie *Icmm*. Zeits Krist 149:135–136.
Klingenberg R, Felsche J, Miehe G (1981) Crystal data for the low-temperature form of carnegieite $NaAlSiO_4$. J Appl Cryst 14:66–68.
Lange RA, Carmichael ISE, Stebbins JF (1986) Phase transitions in leucite $KAlSi_2O_6$, orthorhombic $KAlSiO_4$, and their iron analogues ($KFeSi_2O_6$, $KFeSiO_4$). Am Min 71:937–945.
Levien L, Prewitt CT (1981) High-pressure crystal structure and compressibility of coesite. Am Min 66:324–333.
Li (1968) The crystal structure of $LiAlSi_2O_6$ III (high-quartz solid solution). Zeits Krist 127:327–348.
Li CT, Peacor DR (1968) The crystal structure of $LiAlSi_2O_6$-II ("β-spodumene"). Zeits Krist 126:46–65.
Liebau F (1985) Structural chemistry of silicates. Springer-Verlag, Berlin. 347 p.
Liu B, Barbier J (1993) Structures of the stuffed tridymite derivatives, $BaMSiO_4$ (M = Co, Zn, Mg). J Solid State Chem 102:115-125.
Lukesh JS, Buerger MJ (1942) The unit cell and space group of kaliophilite. Am Min 27:226–227.
Mazza D, Lucco-Borlera M (1994) Effect of the substitution of boron for aluminium in the beta-eucryptite $LiAlSiO_4$ structure. J Eur Ceram Soc 13:61–65.
McConnell JD (1981) Time-temperature study of the intensity of satellite reflections in nepheline. Am Min 66:990–996.
McConnell JDC (1962) Electron diffraction study of subsidiary maxima of scattered intensity in nepheline. Min Mag 33:114–124.
McConnell JDC (1983) A review of structural resonance and the nature of long-range interactions in modulated mineral structures. Am Min 68:1–10.
Merlino S (1984) Feldspathoids: their average and real structures. In: WL Brown (ed.), Feldspars and Feldspathoids. pp. 435–470. D Reidel, Dordrecht, The Netherlands
Merlino S, Franco E, Mattia CA, Pasero M, Gennaro MD (1985) The crystal structure of panunzite (natural tetrakalilite). N Jahrb Mineral Mitt 7:322–328.
Minor DB, Roth RS, Brower WS, Daniel MC (1978) Alkali ion exchange reactions with $RbAlSiO_4$: a new metastable polymorph of $KAlSiO_4$. Materials Res Bull 13:575–581.
Müller WF, Schulz H (1976) Antiphase domains in β–eucryptite ($LiAlSiO_4$). Naturwiss 63:294.
Munoz JL (1969) Stability relations of $LiAlSi_2O_6$ at high pressures. Mineralogical Soc of America Spec Paper 2:203–209.
Ostertag W, Fischer GR, Williams JP (1968) Thermal expansion of synthetic b-spodumene and b-spodumene-silica solid solutions. J Am Ceram Soc 51:651–654.
Palmer D (1990) Volume anomaly and the impure ferroelastic phase transition in leucite. In: EKH Salje (ed.), Phase Transitions in Ferroelastic and Coelastic Crystals. pp. 350–366. Cambridge University Press, Cambridge, UK
Perrotta AJ, Savage RO (1967) Beta eucryptite crystalline solutions involving P^{5+}. J Am Ceram Soc 50:112.
Perrotta AJ, Smith JV (1965) The crystal structure of kalsilite $KAlSiO_4$. Min Mag 35:588–595.
Perrotta NJ, Grubbs DK, Martin ES, Dando NR, McKinstry HA, Huang CY (1989) Chemical stabilization of β-cristobalite. J Am Ceram Soc 61:441–447.

EBSCOhost - printed on 2/13/2023 4:48 AM via . All use subject to https://www.ebsco.com/terms-of-use

Pillars WW, Peacor DR (1973) The crystal structure of beta eucryptite as a function of temperature. Am Min 58:681–690.

Ross NL, Shu J-F, Hazen RM, Gasparik T (1990) High-pressure crystal chemistry of stishovite. Am Min 75:739–747.

Rossi G, Oberti R, Smith DC (1989) The crystal structure of a K-poor Ca-rich silicate with the nepheline framework, and crystal-chemical relationships in the compositional space (K, Na, Ca, [])8-(Al,Si)16O32. Eur J Min 1:59–70.

Roth G, Bohm H (1987) Ionic-conductivity of beta-spodumene ($LiAlSi_2O_6$) single-crystals. Solid State Ionics 22:253-256.

Roy RD, Roy D, Osborn EF (1950) Compositional and stability relationships among the lithium aluminosilicates, eucryptite, spodumene, and petalite. J Am Ceram Soc 33:152–159.

Sahama TG (1957) Complex nepheline-kalsilite pheocrysts in Kabfumu lava, Nyirangongo area, North Kivu in Belgian Congo. J Geol 65:515–526.

Sahama TG (1958) A complex form of natural nepheline from Iivaara, Finland. Am Min 43:165–166.

Sahama TG (1960) Kalsilite in the lavas of Mt. Nyiragongo. J Petrology 1:146.

Sahama TG (1962) Order-disorder in natural nepheline solid solutions. J Petrology 3:65–81.

Sahama TG, Smith JV (1957) Trikalsilite, a new mineral. Am Min 42:42–.

Saltzberg MA, Bors SL, Bergna H, Winchester SC (1992) Synthesis of chemically stabilized cristobalite. J Am Ceram Soc 75:89–95.

Samsonova NS (1969) Order and disorder in the arrangement of sodium and potassium atoms in the nepheline structure. Translated in: Doklady Earth Sciences Section 187:134–137.

Sandomirskiy PA, Urusov VS (1988) Phase relationships and thermal expansion for $KAlSiO_4$ polymorphs. Geochim Intl 25:62–73.

Schneider H, Flörke OW (1986) High-temperature transformation of tridymite single crystals to cristobalite. Zeits Krist 175:165–176.

Schneider H, Flörke OW, Stoeck R (1994) The $NaAlSiO_4$ nepheline–carnegieite solid-state transformation. Zeits Krist 209:113–117.

Schulz H (1974) Thermal expansion of beta eucryptite. J Am Ceram Soc 57:313–317.

Shannon RD (1976) Revised effective ionic radii and systematic studies of interatomic distances in halides and chalcogenides. Acta Cryst A23:751–761.

Shannon RD (1979) Ionic conductivity in sodium magnesium silicates. Phys Chem Min 4:139–148.

Shropshire J, Keat PP, Vaughan PA (1959) The crystal structure of keatite, a new form of silica. Zeits Krist 112:409–413.

Simmons WB, Peacor DR (1972) Refinement of the crystal structure of a volcanic nepheline. Am Min 57:1711–1719.

Simonov MA, Egorow-Tismenko YK, Belov NV (1976) Refined crystal structure of chkalovite $Na_2Be[Si_2O_6]$. Soviet Phys Doklady 20:805–807.

Skinner BJ, Evans HT (1960) β-spodumene solid solutions on the join $Li_2O.Al_2O_3$–SiO_2. Am J Sci 258–A:312–324.

Smith JV, Tuttle OF (1957) The nepheline-kalsilite system: I. X-ray data for the crystalline phases. Am J Sci 255:282–305.

Stebbins JF, Murdoch JB, Carmichael ISE, Pines A (1986) Defects and short-range order in nepheline group minerals: a silicon-29 nuclear magnetic resonance study. Phys Chem Min 13:371–381.

Steele IM, Pluth JJ (1990) Crystal-structure of synthetic yoshiokaite, a stuffed derivative of the tridymite structure. Am Min 75:1186-1191.

Swainson IP, Dove MT, Palmer DC, Poon WC-K (1994) Infrared and Raman spectroscopic studies of the α–β phase transition in cristobalite. Phys Chem Min (to be submitted):

Thompson JG, Withers RL, Whittaker AK, Traill RM, Gerald JDF (1993) A reinvestigation of low-carnegieite by XRD, NMR, and TEM. J Solid State Chem 104:59-73.

Tindwa RM, Perrotta AJ, Jerus P, Clearfield A (1982) Ionic conductivities of phosphorous-substituted β-eucryptite ceramics. Materials Res Bull 17:873–881.

Tscherry V, Schulz H, Laves F (1972a) Average and super structure of β-eucryptite ($LiAlSiO_4$). Zeits Krist 135:161–174.

Tscherry V, Schulz H, Laves F (1972b) Average and super structure of β-eucryptite ($LiAlSiO_4$). Part II. Superstructure. Zeits Krist 135:175–198.

Tuttle OF, Smith JV (1958) The nepheline–kalsilite system. II. Phase relations. Am J Sci 256:571–589.

EBSCOhost - printed on 2/13/2023 4:48 AM via . All use subject to https://www.ebsco.com/terms-of-use

Vaniman DT, Bish DL (1990) Yoshiokaite, a new Ca,Al-silicate mineral from the Moon. Am Min 75:676–686.

Wang MC, Hon MH (1993) Properties and crystallization of Li_2O-CaO-Al_2O_3-SiO_2-TiO_2 glasses. J Mater Res 8:890-898.

Winkler HGF (1948) Synthese und Kristallstruktur des Eukryptits, $LiAlSiO_4$. Acta Cryst 1:27–34.

Withers RL, Thompson JG (1993) Modulation wave approach to the structural parameterization and Rietveld refinement of low carnegieite. Acta Cryst B49:614-626.

Yoshioka T (1970) Metastable solid solution with nepheline-type structure in the CaO–Al_2O_3–SiO_2 system. J Chem Soc Japan 43:1981–1987.

Yund RA, McCallister RH, Savin SM (1972) An experimental study of nepheline-kalsilite exsolution. J Petrol 13:255–272.

EBSCOhost - printed on 2/13/2023 4:48 AM via . All use subject to https://www.ebsco.com/terms-of-use

HYDROGEN SPECIATION AND CHEMICAL WEAKENING OF QUARTZ

Andreas K. Kronenberg

Department of Geology and Geophysics
Center for Tectonophysics
Texas A and M University
College Station, TX 77843 U.S.A.
e-mail: a.kronenberg@tamu.edu

INTRODUCTION

Hydrogen resides on the surfaces, at structural defects, and within the crystalline interiors of quartz crystals, and its diversity in speciation and site occupancy belies the apparent simplicity of stoichiometric quartz. Hydrogen complexes may saturate surface sites of crystal faces and fractures. Similarly, hydrogen complexes may occupy sites on dislocations and other crystalline flaws in order to satisfy "dangling" bonds. Hydrogen point defects occur in a large number of distinguishable sites to compensate charges associated with impurity cations. Fine-scale clusters of molecular water and fluid inclusions are common and may be incorporated during crystal growth, deformation, and crack healing. Hydrogen contents of quartz range from 10^1 to 10^2 ppm (H/10^6 Si) for clear, vug-grown crystals devoid of inclusions, whose hydrogen speciation is dominated by point defects, to 10^3-10^5 ppm for milky quartz, amethyst, citrine, and rapidly grown synthetic quartz crystals. Much larger hydrogen contents are characteristic of microcrystalline quartz and chalcedony due to the incorporation of molecular water (up to 1-2 wt %) during low-temperature growth.

Although hydrogen contents of quartz are generally small, effects of hydrogen defects on the physical and chemical properties of quartz can be substantial. Hydrogen species adsorbed on the surfaces of quartz influence a wide range of properties that depend on surface and interfacial energies (Parks, 1984). They control rates of dissolution, precipitation, and grain growth (e.g., Blum and Lasaga, 1988). Surficial hydrogen species influence inelastic mechanical properties through their involvement in processes of crack growth, crack healing, and adhesion during frictional sliding (Atkinson, 1984; Dieterich and Conrad, 1984; Smith and Evans, 1984). Within the quartz interior, hydrogen point defects increase the diffusional mobility of oxygen (Farver and Yund, 1991a), and they may influence silicon mobilities and electrical transport properties (Kronenberg and Kirby, 1987). Mobile hydrogen defects promote exchange between fluid inclusions and grain exteriors and may thereby affect inclusion compositions (Hall and Bodnar, 1990). The mechanical resonator properties of rapidly grown synthetic quartz crystals may be influenced by clusters of molecular water that introduce anelastic loss (e.g., King, 1959; Dodd and Fraser, 1965). Hydrogen defects, molecular water clusters, and fluid inclusions appear to have multiple roles in promoting ductile deformation of quartz (Paterson, 1989). Dislocations may be generated at molecular water clusters and fluid inclusions. Moreover, molecular water appears to facilitate dislocation glide and climb, processes of dislocation reorganization and recovery, and dynamic recrystallization that may accompany deformation.

Much of our information regarding hydrogen defects in quartz comes from infrared (IR) and near-IR spectroscopy (McMillan and Hofmeister, 1988), and excellent reviews of hydrogen speciation in quartz and other minerals have previously been given by Aines

EBSCOhost - printed on 2/13/2023 4:48 AM via . All use subject to https://www.ebsco.com/terms-of-use

and Rossman (1984a) and Rossman (1988). Hydrogen in quartz is bonded to oxygen and, owing to the strongly polar nature of hydroxyl (OH) groups, can be detected in trace quantities by examining the absorption of radiation due to O-H vibration in the IR. Hydrogen defects on a variety of sites can be distinguished by examining OH absorption band frequencies, band widths, and polarizations that are sensitive to the local crystalline environment. Hydroxyl groups can be distinguished from water molecules by examining stretching vibrations at low temperatures and by comparing fundamental and combination vibrational modes. Hydrogen defects have also been characterized in detail by electron paramagnetic resonance (EPR) studies (e.g., Weil, 1984), and fine-scale molecular water clusters and fluid inclusions have, respectively, been studied by transmission electron microscopy (TEM) and Raman micro-spectroscopy (e.g., Gerretsen et al., 1989; Wopenka et al., 1990). Although many defects have yet to be characterized fully, a wealth of information is available regarding the majority hydrogen defects.

Of physical properties that are affected by water and derivative hydrogen defects, the mechanical properties of quartz have received the most attention. Many of the mechanisms involved in brittle failure and ductile deformation of quartz are influenced by chemical interactions with water (e.g., Atkinson, 1984; Paterson, 1989), and failure and flow strengths depend critically upon access of hydrogen species to surfaces and structural flaws. Significant advances have been made in characterizing those conditions in the laboratory that promote chemical weakening of quartz and correlating mechanical properties with majority hydrogen species present. In addition, studies of such processes as diffusion, dissolution and precipitation that influence or accompany deformation have revealed roles of internal and surficial hydrogen species that contribute to our understanding. However, many questions regarding chemical weakening by hydrogen species remain to be answered, and applications of experimental results to deformation of quartz in nature must await their clarification.

In the first half of this chapter, hydrogen species commonly found in quartz are reviewed, drawing upon results primarily of IR and near-IR absorption studies. In the second half of the chapter, the roles of hydrogen defects in deformation processes are reviewed, and remaining questions are examined with emphasis placed on chemically-assisted crack growth, frictional sliding, solution transfer, and dislocation creep.

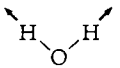
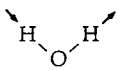
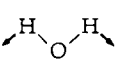
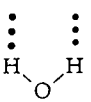
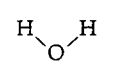
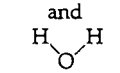
HYDROGEN SPECIATION

Infrared signatures of hydrogen

The vibrational motions of hydroxyl (OH) ions and water molecules (H_2O) give rise to strong, characteristic absorption bands (Alpert et al., 1970; Nakamoto, 1978) associated with fundamental O-H stretching and H-O-H bending modes (Table 1) in the IR (at wavenumbers ν less than 4000 cm^{-1} or wavelengths λ greater than 2.5 μm) and weaker combination modes and overtones in the near-IR (at ν greater than 4000 cm^{-1}). As isolated molecules, OH ions exhibit a single stretching vibration at $\nu \cong 3735$ cm^{-1}. However, O-H stretching vibrations are sensitive to local hydrogen bonding, and absorption bands of OH groups that interact with nearby oxygens are shifted systematically to lower wavenumbers as O-H···O bond lengths are decreased (Nakamoto et al., 1955; Novak, 1974) and hydrogen bond strengths are increased. At quartz surfaces, isolated hydroxyl groups may absorb at wavenumbers near 3735 cm^{-1}. Within quartz, hydrogen point defects give rise to multiple, sharply defined OH absorption bands at wavenumbers between 3650 and 3200 cm^{-1} that reflect variations in local hydrogen bonding amongst multiple defect sites.

EBSCOhost - printed on 2/13/2023 4:48 AM via . All use subject to https://www.ebsco.com/terms-of-use

TABLE 1. Characteristic vibrations of OH and H_2O

Species	Vibrational Mode	Wavenumber υ (cm^{-1})
Infrared		
O – H	OH Stretch (isolated)	3735
O – H • • • O	OH Stretch (hydrogen - bonded to nearby oxygen)	between 3700 - 1800
	Symmetric OH Stretch (isolated)	3657
	Antisymmetric OH Stretch (isolated)	3756
	HOH Bend (isolated)	1595
	OH Stretch (symmetric ~3219 cm^{-1} antisymmetric ~3445 cm^{-1})	~3400 (extending over 3700-3100 cm^{-1})
	HOH Bend (liquid water)	1630
Near - Infrared		
Si – O – H and Al – O – H	Combination Modes OH Stretch (~3500cm^{-1}) + XOH Bend (e.g. SiOH at ~870 cm-1)	~4400 - 4500
	Combination OH Stretch (~3500 cm^{-1}) +HOH Bend (1630 cm-1)	~5200
O – H • • • O and 	First Overtone of OH Stretch (~3500cm^{-1})	~7000

Isolated H_2O molecules exhibit symmetric and antisymmetric stretching vibrations (Table 1) at 3657 and 3756 cm^{-1}, respectively, and a bending mode at 1595 cm^{-1}. The vibrational modes of H_2O are influenced by hydrogen bonding as well, and both symmetric and antisymmetric stretching modes shift to lower wavenumbers as hydrogen bond strengths are increased. In its common form as water, H_2O exhibits a broad absorption at ~3400 cm^{-1} that extends over 3700 to 3100 cm^{-1} due to widely distributed O-H···O bond lengths among molecules of the liquid. H_2O is commonly incorporated in

EBSCOhost - printed on 2/13/2023 4:48 AM via . All use subject to https://www.ebsco.com/terms-of-use

quartz as fluid inclusions and fine nm-scale clusters; corresponding IR spectra exhibit broad absorption bands at ~3400 cm^{-1} that resemble the OH absorption band of liquid water (e.g., Aines and Rossman, 1984a), although marked differences in band character may be noted for crystals with fine-scale water clusters. H-O-H bending vibrations of molecular water in quartz are masked by strong interferences with intrinsic Si-O vibrations (Spitzer and Kleinman, 1961; Moenke, 1974). However, OH and H_2O may be distinguished if combination modes (Table 1) at near-IR frequencies are large enough to be detected. Combination O-H stretch/H-O-H bend vibrations, diagnostic of H_2O, appear at ~5200 cm^{-1} ($\cong \nu_{OHstretch} + \nu_{HOHbend}$), clearly offset from combination modes involving O-H stretch and Si-O-H bend motions at ~4400 to 4500 cm^{-1} ($\cong \nu_{OHstretch} + \nu_{SiOHbend}$).

Additional constraints on the hydrogen speciation of quartz may be obtained by examining polarizations of OH absorption bands and any changes in character or frequency with changes in temperature. Using polarized incident radiation, absorption band intensities due to crystallographically aligned O-H stretching vibrations may vary with changes in vibration direction **E** according to the orientation of **E** relative to a particular O-H bond and its symmetrical equivalents. O-H vibrations of fluid inclusions have no crystallographic alignment and broad absorptions of quartz are commonly isotropic. At low temperatures, OH absorptions due to hydrogen point defects increase in band height and decrease in band width. They may also shift in frequency, but only by a few wavenumbers (cm^{-1}). In contrast, molecular water within fluid inclusions may freeze, and its presence can often be recognized by a significant spectral shift of the broad band at ~3400 cm^{-1} (characteristic of liquid water measured at room temperature) upon cooling to ~3200 cm^{-1} (characteristic of ice measured at low temperatures, e.g., 77 K). Molecular water within nm-scale clusters gives rise to a broad absorption at ~3400 cm^{-1}; however, changes in band character and wavenumber at low temperatures are negligible, and freezing appears to be inhibited for water clusters below some threshold size.

Many hydrogen defects in quartz have been characterized by their association with other point defects, particularly impurity cations (Brunner et al., 1961; Kats, 1962; Kats et al., 1962; Krefft, 1975). Evidence for these associations comes from electrolytic exchange, diffusion experiments, and the observed growth and decline of OH absorptions with the introduction and loss of specific cations.

Despite the introduction of several alternative methods of measuring trace concentrations of hydrogen in minerals (McLaren and Payling, 1980; Moze et al., 1980; Yurimoto et al., 1989), IR spectroscopy remains one of the most sensitive tools for hydrogen analysis. Absorption bands due to O-H stretching scale in size with the concentrations (c) of hydrogen defects and IR path length (l) through the specimen, as described by the Beer-Lambert relation

$$A = k\,c\,l \qquad (1)$$

where A is the peak absorbance relative to background and k is a molar absorption coefficient that must be determined by calibration (Alpert et al., 1970). Since measures of peak absorbance may vary with temperature and, for narrow bands, spectrometer resolution, integral absorbances A* (based on numerical integration of the absorption band above background levels) are generally preferred for concentration determinations, using a relation of the same form as (1) and a calibrated value of the integral molar absorption coefficient k*. In principle, absorption coefficients can differ, depending on local hydrogen bonding, for each type of hydrogen defect. The sharp absorption bands associated with hydrogen interstitials in clear, natural quartz appear to have similar

EBSCOhost - printed on 2/13/2023 4:48 AM via . All use subject to https://www.ebsco.com/terms-of-use

absorption coefficients; using charge transport measurements during electrolysis to determine concentrations of cation-paired hydrogen defects, Kats (1962) found

$$c\ (H/10^6\ Si) = 0.812\ \Delta\ (cm^{-2})$$

where $\Delta = A^*/l$ and A^* is summed over all O-H bands. However, broad absorption bands of synthetic quartz have integral absorption coefficients closer to that of liquid molecular water; based on hydrogen extraction measurements, calibration yields

$$c\ (H/10^6\ Si) = 1.05\ \Delta\ (cm^{-2})$$

where Δ is determined over 3750 to 2400 cm^{-1}, correcting for background Si-O absorptions (Aines et al., 1984). Absorption coefficients of OH stretching modes are generally observed to increase with decreasing wavenumber, and Paterson (1982) proposed that concentrations of various forms of hydrogen species can be estimated by numerical integration of

$$c = \frac{1}{l} \int \frac{A(\upsilon)}{k(\upsilon)}\, d\upsilon \qquad (2)$$

using a linear dependence of $k(\nu)$ upon ν, as determined from reported absorption coefficients for hydrogen species in a number of crystalline and amorphous compounds.

Surface species

Hydrogen complexes are readily formed at the surfaces of quartz and other phases of silica by reaction with H_2O. Silanol SiOH groups (Fig. 1) replace siloxanes ≡ Si-O-Si ≡ that are highly strained at surfaces (e.g., Hair, 1967; Snoeyink and Weber, 1972). SiOH groups then provide sites for the adsorption of water, first as isolated molecules, and later as hydrogen-bonded clusters and continuous layers. Spectroscopic assignments of surficial hydrogen species (Table 2) come largely from studies of amorphous silica phases (e.g., silica gel, fused or precipitated silica) with high surface areas and variable states of hydration (McDonald, 1957, 1968; Benesi and Jones, 1959; Folman and Yates, 1959; Anderson and Wickersheim, 1964; Anderson, 1965; Klier et al., 1973; Morrow and Cody, 1973; Klier and Zettlemoyer, 1977; Shen and Klier, 1980; Stone and Walrafen, 1982). However, comparisons with spectroscopic results for finely ground α-quartz, fibrous chalcedony, and crystalline opals (Soda, 1961, 1962; Takamura et al., 1964; Segnit et al., 1965; Gallei and Parks, 1972; Langer and Flörke, 1974; Flörke et al., 1982;

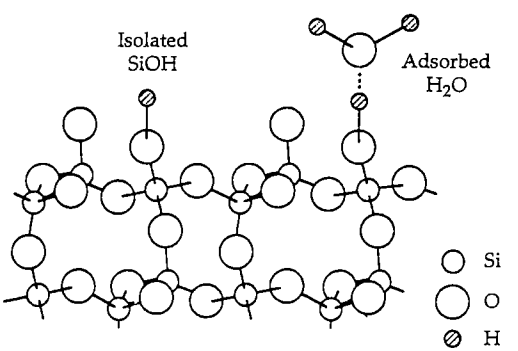


Figure 1. Hydrogen species adsorbed at quartz surfaces. Silanol SiOH groups are stable over a wide range of conditions, replacing the highly strained siloxanes, ≡ Si-O-Si ≡ . SiOH groups may be isolated, but they may also form hydrogen bonds with neighboring silanols or water molecules. H_2O adsorbs to surfaces forming hydrogen bonds between the molecule's oxygen and a surface silanol in early stages of hydration. In advanced stages of hydration, H_2O forms hydrogen-bonded clusters and continuous layers.

EBSCOhost - printed on 2/13/2023 4:48 AM via . All use subject to https://www.ebsco.com/terms-of-use

TABLE 2. Absorption bands assigned to surficial hydrogen species

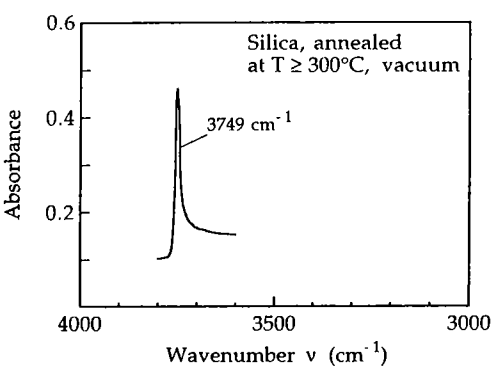
Wavenumber (cm^{-1})	Species and Mode	Silica Surface	Reference
7326	Isolated SiOH, OH stretch overtone	amorphous (dehydrated gel)	1
7305-7300	Isolated SiOH, OH Stretch overtones	amorphous (precipitated, degassed)	2, 3, 4
7260-7100	Hydrogen-bonded SiOH, OH stretch overtones	amorphous (fused)	5
7180-7130	Individual H_2O and hydrogen-bonded SiOH, OH stretch overtones	amorphous (precipitated)	2, 3
7090 6850	H_2O, OH stretch overtones	chalcedony, opal, amorphous (gel, low levels of hydration)	1, 6, 7, 8
5290 5260 5180	H_2O, Combination OH Stretch/HOH bend vibrations	chalcedony, opal, amorphous (gel, precipitated, low levels of hydration)	1, 2, 3, 6, 7, 8
4550 4450 4420	SiOH, Combination OH Stretch/SiOH bend vibrations	chalcedony, opal, amorphous (gel, fused)	1, 5, 6, 7, 8
3750-3748	Isolated SiOH, OH Stretch	amorphous (precipitated, fumed, and degassed)	9, 10, 11, 12, 13
3740	SiOH (very weak hydrogen-bonding), OH stretch	chalcedony, amorphous (dehydrated gel, precipitated and fumed)	1, 8, 11, 14
3740-3700	Hydrogen-bonded SiOH, OH stretch	amorphous (dehydrated gel, fumed)	11, 15
3680-3660	Hydrogen-bonded SiOH and H_2O, OH stretch	amorphous (precipitated and fused)	5, 11
3665-3660	Hydrogen-bonded SiOH and H_2O, OH stretch	chalcedony, opal, amorphous (gel, fused, low levels of hydration)	1, 5, 8, 16
3649	Isolated SiOH, OH stretch	α - quartz	17
3627	Isolated SiOH, OH stretch	α - quartz	17

EBSCOhost - printed on 2/13/2023 4:48 AM via . All use subject to https://www.ebsco.com/terms-of-use

TABLE 2. (continued)

Wavenumber (cm^{-1})	Species and Mode	Silica Surface	Reference
3540-3500	Hydrogen-bonded SiOH and H_2O, OH stretch	amorphous (gel, precipitated and low levels of hydration)	1, 5, 11
~3400 (broad, shoulder at ~3320)	Hydrogen-bonded H_2O, OH stretch	α- quartz, cristobalite, chalcedony, opal, amorphous (hydrated gel, fused, and precipitated)	1, 6, 8, 11, 14, 16, 18, 19, 20, 21
3500-2800 (very broad)	Hydrogen-bonded H_2O, OH stretch	amorphous (hydrated, precipitated and fumed)	11
1650-1635	H_2O, HOH bend	α- quartz, cristobalite, amorphous (hydrated gel)	15, 20

1. Anderson and Wickersheim 1964
2. Klier et al. 1973
3. Klier and Zettlemoyer 1977
4. Shen and Klier 1980
5. Stone and Walrafen 1982
6. Langer and Florke 1974
7. Florke et al. 1982
8. Graetsch et al. 1985
9. McDonald 1957
10. Folman and Yates 1959
11. McDonald 1968
12. Morrow and Cody 1973
13. Anderson 1965
14. Frondel 1982
15. Benesi and Jones 1959
16. Bartoli et al. 1990
17. Gallei and Parks 1972
18. Soda 1961
19. Soda 1962
20. Takamura et al. 1964
21. Segnit et al. 1965



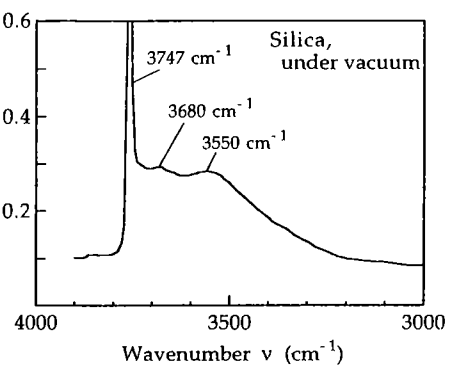


Figure 2 (left). IR absorption spectrum of amorphous silica powder (Aerosil 2491) with a surface area of 2 × 10^5 m^2/kg after annealing at T ≥ 300°C under vacuum for several days. In the absence of adsorbed H_2O, surfaces of silica are populated by isolated silanols (SiOH) with OH stretching vibrations giving rise to absorption at ν = 3749 cm^{-1} (after McDonald, 1957).

Figure 3 (right). IR absorption spectrum of fumed, high-surface-area amorphous silica (Cabosil) placed under vacuum at 27°C for 3 hours. A sharp absorption band at ν = 3747 cm^{-1} may be assigned to isolated surface SiOH; however, the spectrum is dominated by a broad absorption extending over 3600 to 3200 cm^{-1} due to adsorbed H_2O. Absorption bands at ~3680 and ~3550 cm^{-1} may be due to both hydrogen-bonded SiOH and H_2O (after McDonald, 1968).

EBSCOhost - printed on 2/13/2023 4:48 AM via . All use subject to https://www.ebsco.com/terms-of-use

Frondel, 1982; Graetsch et al., 1985; Bartoli et al., 1990) suggest that the same species populate crystalline SiO_2 surfaces even though specific surface sites may differ.

Silanol groups may be expected to saturate the surfaces of quartz at all conditions of geologic interest. They appear on silica surfaces for all but the most rigorously anhydrous conditions and seem to be stable at temperatures up to 940°C (under vacuum, McDonald, 1968). OH stretching vibrations of isolated silanols at amorphous silica surfaces give rise to a sharp, well-defined absorption band (Fig. 2) at 3749 cm^{-1} (McDonald, 1957, 1968; Folman and Yates, 1959; Morrow and Cody, 1973; Anderson, 1965). However, this band may shift as hydrogen bonds are formed with neighboring silanols or with adsorbed water molecules (Benesi and Jones, 1959; Anderson and Wickersheim, 1964; Anderson, 1965; McDonald, 1968; Stone and Walrafen, 1982), and silanol absorption bands at low levels of hydration are observed at wavenumbers ranging from 3740 to 3660 cm^{-1} (Table 2). The assignment of these sharp bands to surficial SiOH was originally confirmed by Benesi and Jones (1959) by exchanging dehydrated silica gels with deuterated water (D_2O) and examining the growth of absorption bands corresponding to O-D stretching vibrations. Within relatively short periods of time (30 minutes) at room temperature, a sharp band was observed at 2760 cm^{-1} with similar character to that at 3730 cm^{-1} and with the expected isotopic shift for SiOD groups.

Near-IR O-H stretching overtones of isolated SiOH groups have been detected at 7326 to 7300 cm^{-1} ($\cong 2\nu_{OHstretch}$) both in transmission (Anderson and Wickersheim, 1964) and reflectance (Klier et al., 1973; Klier and Zettlemoyer, 1977; Shen and Klier, 1980; Stone and Walrafen, 1982), and combination O-H stretch/SiOH bend modes have been detected at ~4550 cm-1 (Anderson and Wickersheim, 1964; Stone and Walrafen, 1982). Corresponding modes for hydrogen-bonded silanols are shifted to lower wavenumbers and appear, respectively, at 7260 to 7100 cm^{-1} and 4420 to 4450 cm^{-1} (Anderson and Wickersheim, 1964; Klier et al., 1973; Klier and Zettlemoyer, 1977; Stone and Walrafen, 1982).

With increasing degrees of hydration, absorption bands at 3749 to 3740 cm^{-1} and 7326 to 7300 cm^{-1} are observed to decrease, while absorptions at wavenumbers of 3680 to 2800 cm^{-1} (Fig. 3, above), ~7090 to 6850 cm^{-1} and ~5200 cm^{-1} (Fig. 4) are observed

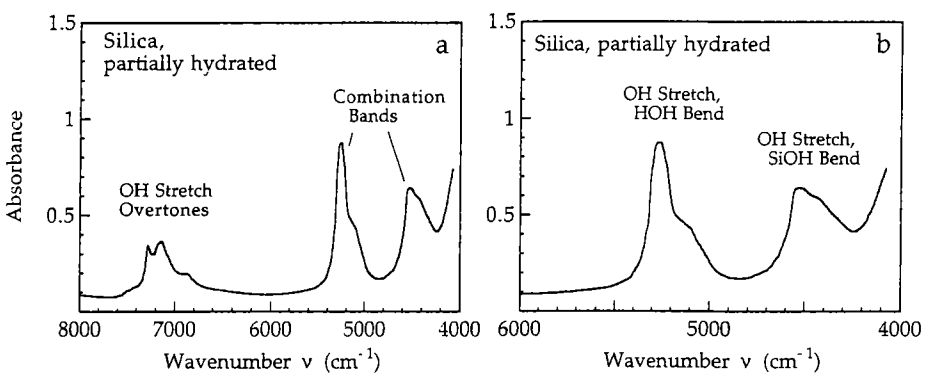


Figure 4. Near-IR absorption spectra of partially hydrated silica gel (measured at 100°C in air). (a) OH stretching overtones are apparent at ν = 7326 cm^{-1} due to isolated silanols and at ~7100 and 6850 cm^{-1} due to hydrogen-bonded SiOH and H_2O. (a,b) Combination OH stretch/HOH bend modes of molecular water appear at wavenumbers of ~5290-5180 cm^{-1}, and OH stretch/SiOH bend modes of silanol groups appear at ~4550-4420 cm^{-1} (after Anderson and Wickersheim, 1964).

EBSCOhost - printed on 2/13/2023 4:48 AM via . All use subject to https://www.ebsco.com/terms-of-use

to grow (Anderson and Wickersheim, 1964; McDonald, 1968; Klier et al., 1973; Klier and Zettlemoyer, 1977; Shen and Klier, 1980). Isolated silanols become rare and absorption spectra are dominated by bands due to both hydrogen-bonded silanols and water molecules. H_2O forms hydrogen bonds with surficial silanols (Fig. 1); as individual adsorbed molecules, it gives rise to O-H stretching modes at 3660 and 3540 cm^{-1}, O-H overtones at 7090 and 6850 cm^{-1}, and combination O-H stretch/HOH bend modes at 5290 and 5180 cm^{-1} (e.g., Anderson and Wickersheim, 1964). With further hydration, clusters of H_2O form, and increased hydrogen bonding further reduces O-H stretching frequencies until continuous hydrogen-bonded networks of water molecules give rise to a very broad absorption at ~3400 cm^{-1}, extending over 3500 to 2800 cm^{-1}.

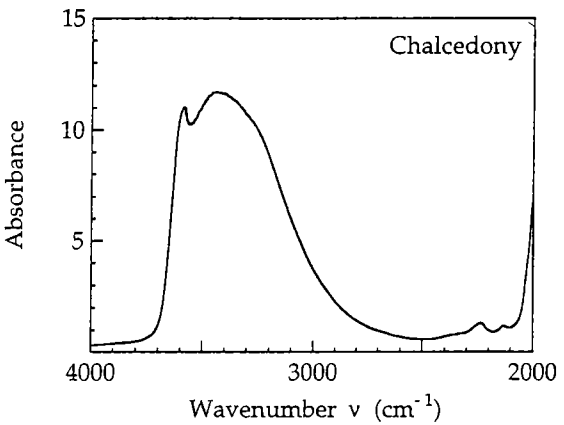


Figure 5. IR absorption spectrum of chalcedony (from the Kofa Mtns, Arizona, GRR #1143, normalized to specimen thickness l of 1 mm) with broad absorption band at ~3400 cm^{-1} associated with H-bonded molecular water (courtesy of G.R. Rossman).

IR spectra of fibrous chalcedony, crystalline opals, and fine particulate α-quartz with high surface areas exhibit similar absorption bands (Fig. 5) to those investigated for amorphous silica phases. Isolated silanols at the surfaces of chalcedony fibers give rise to an absorption band at 3740 cm^{-1} (Frondel, 1982; Graetsch et al., 1985) while hydrogen-bonded silanols of chalcedony and opals lead to IR absorptions at 3650 and 3440 cm^{-1} and near-IR bands at 4560 and 4380 cm^{-1} (Langer and Flörke, 1974; Flörke et al., 1982; Graetsch et al., 1985; Bartoli et al., 1990). Silanols at quartz surfaces, as detected in reflectance spectra (Gallei and Parks, 1972), give rise to two sharp absorption bands, one at 3649 cm^{-1} and the other at 3627 cm^{-1}, corresponding to at least two distinguishable sites of the crystalline surface (Table 2). Gallei and Parks (1972) assigned these bands to OH stretching modes of isolated silanols, although some hydrogen bonding may be suggested by the relatively low frequencies. Hydrogen-bonded molecular water appears at the surfaces of quartz, cristobalite, chalcedony, and crystalline opals with spectroscopic signatures similar to those of amorphous silica surfaces, with a broad IR absorption band centered at ~3400 cm^{-1} (Fig. 5) and a near-IR band at ~5200 cm^{-1} (Soda, 1961, 1962; Takamura et al., 1964; Segnit et al., 1965; Langer and Flörke, 1974; Flörke et al., 1982; Frondel, 1982; Graetsch et al., 1985; Bartoli et al., 1990).

The first several layers of adsorbed water molecules may have structures that differ from that of normal liquid water, and thin films of H_2O (< 10 molecules in dimension) between silica and mineral surfaces exhibit unusual physical and chemical properties (Pashley and Israelachvili, 1984; Magda et al., 1985; Horn et al., 1989; Gee et al., 1990; Israelachvili, 1992). Densities of H_2O at silica surfaces are lower than that of bulk liquid water (Etzler and Fagundus, 1987), and specific heat capacities are higher than that measured for water (Etzler, 1988). Dissolved ions may be attracted to charged surface

EBSCOhost - printed on 2/13/2023 4:48 AM via . All use subject to https://www.ebsco.com/terms-of-use

sites and may establish a diffuse layer charge (e.g., Li and Bruyn, 1966). In addition,thin H_2O films may possess ordered structures (Israelachvili, 1992) that influence diffusional and electrical transport properties (Anderson and Parks, 1968; Schoen et al., 1988) and near-surface viscosities (Peschel and Adlfinger, 1970; Israelachvili, 1986). Thin ordered films of H_2O may even exhibit thresholds to flow that cannot be described by linear Newtonian viscosity (Pashley and Israelachvili, 1984; Israelachvili and Kott, 1989; Gee et al., 1990).

Hydrogen species adsorbed at quartz surfaces may influence hydrogen defects within the interior of quartz by exchange and diffusional transport. Studies of hydrogen and oxygen diffusion rates in quartz exposed to hydrous conditions indicate that exchange reactions between hydrogen species at the surface and within the quartz interior are rapid in comparison with intracrystalline mobilities (Kats, 1962; Kats et al., 1962; Freer and Dennis, 1982, 1984; Giletti and Yund, 1984; Elphick et al., 1986; Kronenberg et al., 1986; Farver and Yund, 1991a); however, little is known regarding the mechanisms by which exchange between surface and internal hydrogen species occurs.

Hydrogen point defects

Hydrogen-occupied sites drop off dramatically below quartz surfaces, and clear natural crystals have hydrogen defect concentrations that do not often exceed 150 ppm ($H/10^6$ Si). Milky quartz, amethyst, citrine, and rapidly grown synthetic quartz may have hydrogen contents of ~300 to 4000 ppm, significantly larger than those of clear natural crystals; however, much of this hydrogen occurs as fine-scale aggregated clusters of water and fluid inclusions, not as isolated point defects on structural sites. Despite their trace concentrations, more is known about hydrogen point defects in natural clear quartz crystals than is known about hydrogen species in wet varieties of quartz. Early IR absorption studies of natural quartz (Wood, 1960; Brunner et al., 1961; Bambauer et al., 1962, 1963; Dodd and Fraser, 1965), particularly those of Kats (1962) and Kats et al. (1962), were successful in assigning absorption bands between ~3600 and 3200 cm^{-1} to specific hydrogen defects and constraining their nearby structural and chemical environments. More recent studies have built upon these earlier investigations, making use of both IR (Krefft, 1975; Chakraborty and Lehmann, 1976a,b, 1978; Markes and Halliburton, 1979; Pankrath, 1991; Shinoda and Aikawa, 1993) and EPR spectroscopies (Halliburton et al., 1981; Nuttall and Weil, 1981a,b; Goshen et al., 1983; Isoya et al., 1983). Hydrogen point defects of natural milky and synthetic quartz, amethyst, and citrine have not been characterized in the same detail as those in clear colorless natural crystals. Some of the absorption bands exhibited by these varieties of quartz are common to clear natural quartz, and the same structural, electrical, and thermodynamic variables are likely to control the concentrations of hydrogen defects in these species as in natural colorless quartz. However, many of the hydrogen defects that give rise to sharp absorption bands for synthetic quartz, amethyst, and citrine, but not natural clear quartz, remain unidentified.

IR spectra of large, clear, vug-grown quartz crystals are marked by numerous, closely spaced absorption bands between 3610 and 3205 cm^{-1} (Table 3) that are strongly polarized, appear relatively narrow at room temperature (Fig. 6), and become very sharp and resolvable (Fig. 7) at low temperatures (e.g., 77 K). In a single, extraordinary study of hydrogen defects in quartz, Kats (1962) examined the characteristics of nearly all of the absorption bands assembled in Table 3 and demonstrated that they correspond, with only a few exceptions (i.e., Si-O overtones at ~3300 and 3200 cm^{-1}), to O-H stretching vibrations involving intrinsic, structural oxygens and extrinsic hydrogen interstitials.

EBSCOhost - printed on 2/13/2023 4:48 AM via . All use subject to https://www.ebsco.com/terms-of-use

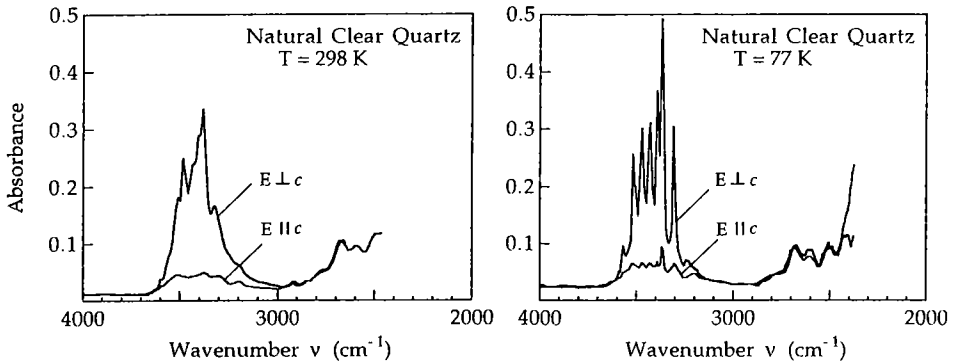


Figure 6 (left). IR absorption spectra of clear colorless natural quartz (from Pasto Bueno, Peru) measured at room temperature (T = 298 K) with **E** ∥ *c* and **E** ⊥ *c* (normalized to specimen thickness l of 1 mm). Multiple sharp, strongly polarized absorption bands appear between 3600 and 3200 cm^{-1} that may be assigned to OH vibrations where oxygens occupy normal structural sites and hydrogens occupy interstitial sites (courtesy of G.R. Rossman).

Figure 7 (right). IR absorption spectra of clear colorless natural quartz (Pasto Bueno, Peru, same as in Fig. 6) measured at low temperature (T = 77 K, cooled using liquid N_2) with **E** ∥ *c* and **E** ⊥ *c* (normalized to l = 1 mm; courtesy of G.R. Rossman).

Quartz specimens were systematically annealed at elevated temperatures in the presence of H_2O and D_2O, and changes in absorption bands recorded. The growth of some absorption bands at the expense of others for specimens annealed in H_2O was taken as evidence for multiple defect sites and for changes in distribution of hydrogen amongst sites. New, sharply defined absorption bands between 2678 and 2390 cm^{-1} emerged for quartz crystals annealed in D_2O, superposed on intrinsic Si-O bands of quartz, and Kats (1962) was able to assign them to O-D stretching modes corresponding to O-H stretching vibrations at higher wavenumbers. Given the small concentrations of hydrogen defects in natural quartz crystals, combination and overtone absorption bands are very weak; nevertheless, Kats (1962) observed several small absorption bands at 4625, 4575, and 4515 cm^{-1} due to OH stretch/SiOH bend vibrations.

Of the multiple O-H absorption bands exhibited by clear natural quartz, many have intensities that correlate with the presence of other trace impurities, particularly Al, Li, Na, and K. Kats (1962) was able to manipulate the infrared spectra of quartz by means of electrolytic exchange experiments and identify defect associations between hydrogen and a variety of cation impurities (Table 3). Charge neutrality in natural quartz appears to be maintained by

$$[Al_{Si}] + [Fe_{Si}] = [H_i] + [Li_i] + [Na_i] + [K_i], \quad (3)$$

a balance between Al and Fe^{3+} substitutions for Si that are relatively immobile and interstitial hydrogen and monovalent cation impurities with concentrations that may be altered by electrolysis or diffusional exchange at high temperatures (e.g., Bambauer, 1961; Bambauer et al., 1962, 1963; Kats, 1962; Snow and Gibbs, 1964; Park and Nowick, 1974; Markes and Halliburton, 1979; Halliburton et al., 1981). By examining the growth and decline of O-H absorptions and correlating these with the introduction and

EBSCOhost - printed on 2/13/2023 4:48 AM via . All use subject to https://www.ebsco.com/terms-of-use

TABLE 3. IR absorption bands assigned to OH stretching modes of internal hydrogen species

Wavenumber (cm^{-1}) at ~77K	Wavenumber (cm^{-1}) at ~298K	Point Defect Association	Type of Quartz	References
3654	—	—	synthetic	1
3634	—	—	synthetic	1
3615	3615	—	synthetic, amethyst	2, 3, 4
3610	3610	K^+	natural clear, synthetic	2, 5, 6
3600	3595	—	natural clear, synthetic, amethyst	2, 4, 6, 7
3594	—	B^{3+}	synthetic	8
3590	—	H^+	natural clear	2, 9, 10
3585	—	K^+	natural clear	1, 2, 6
3585	3585	—	synthetic, amethyst, citrine	1,2,3,4,8
3578	—	K^+	natural clear	2
3567	—	K^+	natural clear, synthetic, amethyst	2, 4
3556	—	Na^+	natural clear, synthetic	2, 8
3550	—	K^+	natural clear	2, 4, 10
3540	—	Cu^+	natural clear	2
3538	—	K^+	natural clear	2
3535	—	Ag^+	natural clear	2
3534	—	Na^+	natural clear	2
3530	—	H^+	natural clear	2
3524	—	Ag^+	natural clear	2
3520	3517	Li^+	natural clear, synthetic, amethyst, citrine	2, 4, 7, 11
3514	—	Cu^+	natural clear	2
3513	3517	Na^+	natural clear, synthetic	1, 2, 8
3510	3510	Li^+	natural clear	2, 7, 9, 10, 11, 12
3507	—	—	natural clear, synthetic, citrine	2, 4, 8
3500	—	Ag^+	natural clear	2
3500	—	—	amethyst	4
3485	—	H^+	natural clear	2, 3
3478	3485	Li^+	natural clear, synthetic, amethyst, citrine	2, 4, 5, 7, 8, 10, 11, 12, 13
3470	3474	—	natural clear	1, 2, 4, 9, 11
3462	—	Cu^+	natural clear	2
3462	3468	H^+	natural clear	2, 3, 9
3460	—	K^+	natural clear	2
3454	—	Ag^+	natural clear	2
3453	—	Na^+	natural clear	2
3440	3436	—	synthetic, amethyst	2, 3, 4
3440	3443	Li^+	natural clear, synthetic, citrine	2, 8, 9, 10, 11, 12
3430	—	—	natural clear, citrine	4, 11
3428/3435*	3432	Al^{3+}	natural clear, synthetic, citrine	1, 2, 4, 5, 6, 7, 9, 10
3422	—	H^+	natural clear	2, 9
3415	—	Cu^+	natural clear	2
3414	—	K^+	natural clear	2
3400	—	H^+	natural clear	2
3400	—	Ag^+	natural clear	2
3400	—	Na^+	natural clear	2
~3400 (very broad	~3650-2500 cm^{-1})	—	synthetic, amethyst, citrine	2, 3, 4, 8, 14, 15, 16, 17, 18, 19

EBSCOhost - printed on 2/13/2023 4:48 AM via . All use subject to https://www.ebsco.com/terms-of-use

TABLE 3. (continued)

Wavenumber (cm^{-1}) at ~77K	Wavenumber (cm^{-1}) at ~298K	Point Defect Association	Type of Quartz	References
3396	3405	Li^+	natural clear, synthetic, citrine	1, 2, 4, 5, 7, 8, 9, 11, 12
3382	—	Na^+	natural clear	2
3380	—	—	natural clear	2
3375	—	—	amethyst	2, 4
3364/3371*	3380/3383*	Al^{3+}	natural clear, synthetic, citrine	1, 2, 3, 4, 5, 6, 7, 9, 10, 11, 12, 13
3355	—	—	synthetic, amethyst	2, 4, 8
3305	—	H^+	natural clear, synthetic	1, 2, 4, 9
3305/3310*	3310/3318*	Al^{3+}	natural clear, synthetic, amethyst, citrine	2, 3, 4, 5, 6, 7, 10, 11
3250	—	—	amethyst, citrine	4
3210 (shoulders at 3365 and 3130 cm^{-1})	~3400 (broad)	H_2O	natural milky	2, 20
3205	—	—	natural clear, synthetic, amethyst	1, 2, 4, 10

*Absorption band wavenumbers reported in some early studies (e.g. Wood 1960; Brunner et al. 1961; Kats 1962; Kats et al. 1962; Bambauer et al. 1963) appear to be high (see Aines and Rossman 1984a)

1. Wood 1960
2. Kats 1962, Kats et al. 1962
3. Rovetta et al. 1989
4. Chakraborty and Lehmann 1976a,b, 1978
5. Krefft 1975
6. Pankrath 1991
7. Brunner et al. 1961
8. Kopp and Staats 1970
   Staats and Kopp 1974
9. Kronenberg et al. 1986
10. Yurimoto et al. 1989
11. Bambauer et al. 1963
12. Shinoda and Aikawa 1993
13. Bukanov and Markova 1969
14. Dodd and Fraser 1965 1967
15. Griggs and Blacic 1965, Griggs 1967
16. Kekulawala et al. 1978, 1981
17. Kirby and McCormick 1979
    Linker and Kirby 1981
18. Aines et al. 1984
19. Cordier and Doukhan 1989
20. Aines and Rossman 1984a

loss of alkali ions, Kats (1962) identified hydrogen defects that are associated with Al substitutions for Si, as well as with nearby alkali interstitials and other, neighboring hydrogen defects. Hydrogen interstitials near aluminum substitutions provide local charge balance and give rise to prominent absorptions at 3435, 3364, and 3305 cm^{-1} (measured at 77 K) that appear to be stable over a wide range of conditions (e.g., Kats, 1962; Kronenberg et al., 1986; Rovetta et al., 1986, 1989). Hydrogen interstitials paired with alkali interstitials and neighboring hydrogen defects are common as well (Table 3); however, the nature of these defect associations and the means by which charge is locally balanced remain to be determined. Stabilities of hydrogen-monovalent cation pairs appear to be limited to low temperatures, and many absorption bands assigned to them disappear from quartz crystals annealed in the presence of H_2O or D_2O (e.g., Kats et al., 1962; Aines and Rossman, 1985; Kronenberg et al., 1986; Rovetta et al., 1986).

EBSCOhost - printed on 2/13/2023 4:48 AM via . All use subject to https://www.ebsco.com/terms-of-use

The vibrational frequencies, band widths, and polarizations displayed by O-H absorptions of clear natural quartz all provide clues to the sites upon which hydrogen resides. The range of vibrational frequencies provides a measure of the range of hydrogen bond lengths among the various defect sites. The narrow band widths of OH absorptions at low temperatures indicate that hydrogen bonding at each site is closely controlled by nearby structural oxygens. Moreover, the pronounced polarizations of sharp bands indicate that O-H stretching vibrations are strongly aligned. Kats (1962) proposed two model sites for hydrogen interstitials near Al substitutions, based partly on the polarizations of OH bands and partly on their vibrational frequencies. Both models place hydrogen near apical oxygens of tetrahedra filled by substitutional aluminum; however, O-H bonds associated with absorptions at 3428 and 3364 cm^{-1} extend into *c*-axis channels, while hydrogen bonds of OH groups associated with absorption at 3305 cm^{-1} must be relatively short. Kats (1962) suggested that this hydrogen is situated between two non-equivalent oxygens of an Al tetrahedron. O-H stretching vibrations at 3428 and 3364 cm^{-1} are intense for **E** perpendicular to *c* (Fig. 7), and comparisons with much weaker band intensities for **E** parallel to *c* suggest an orientation of O-H bonds of ~75° relative to *c* (Kats, 1962). The absorption band at 3305 cm^{-1} is also polarized, though not to the same extent as the other bands associated with Al, and OH groups associated with this band are probably inclined at lower angles to *c*. More recently, Pankrath (1991) reported O-H stretching vibrations of synthetic quartz crystals that exhibit anisotropy within the (001) plane due to symmetrically degenerate Al substitutions introduced during growth; making use of these observations, Pankrath (1991) showed that O-H bonds responsible for absorption at 3365 cm^{-1} are inclined at 36° to *a*-axes, as projected onto the (001) plane (Fig. 8), while O-H vibrations at 3305 cm^{-1} are inclined at 34° and involve different oxygen sites than those of OH absorptions at higher wavenumbers.

While hydrogen may occupy many more sites than those proposed by Kats (1962) and Pankrath (1991), there are probably fewer interstitial positions than implied by the number of absorption bands in Table 3. Absorption bands at 3396, 3382, 3354 cm^{-1}, for example, may be due to hydrogen at equivalent structural positions (Kats, 1962; Aines and Rossman, 1984a) that differ only in their associations with nearby Li, Na, Ag interstitials, respectively. EPR studies confirm many of the associations between Al, H, Li, and Na point defects (Weil, 1975; Markes and Halliburton, 1979; Halliburton et al., 1981; Nuttall and Weil, 1981a,b; Goshen et al., 1983; Isoya et al., 1983) and have provided detailed information regarding their local energy levels and crystalline environments.

The IR spectra of rapidly grown synthetic quartz, amethyst, citrine, and milky quartz (Figs. 9, 10, and 11) are dominated by broad absorption bands at ~3400 cm^{-1} of variable shape (as discussed in the next section) superposed by smaller, sharp absorption bands

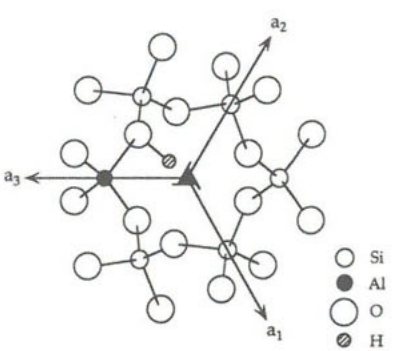
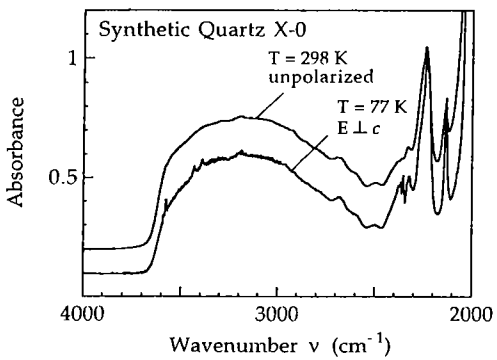


Figure 8. Proposed interstitial hydrogen site (model site 1, Kats, 1962) near substitutional aluminum responsible for OH vibrations at 3428 and 3364 cm^{-1} as shown projected on (001) of left-handed α-quartz (after Pankrath, 1991).

EBSCOhost - printed on 2/13/2023 4:48 AM via . All use subject to https://www.ebsco.com/terms-of-use



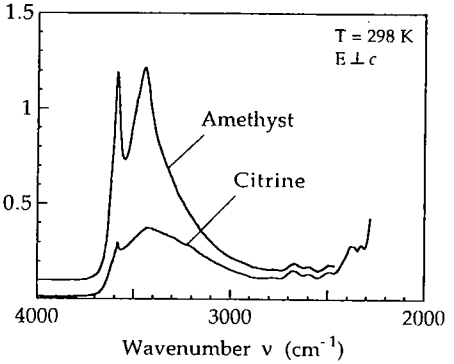
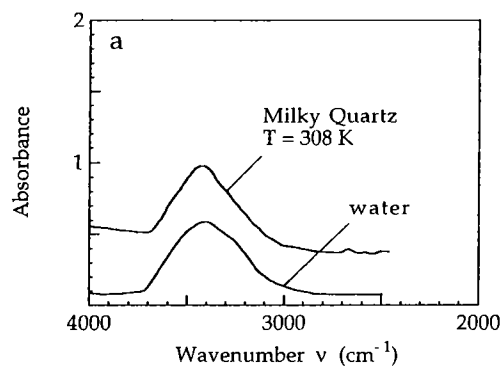


Figure 9 (left). IR absorption spectra of rapidly grown synthetic quartz (crystal X-0 obtained from Bell Labs, Griggs and Blacic, 1965) with broad, isotropic band due to OH stretching modes of molecular water clusters, extending from 3650 to ~2500 cm^{-1} (normalized to l = 1 mm, polarized and unpolarized spectra obtained using beam perpendicular to a and c of (010) specimen). Small sharp absorption bands are apparent in spectra measured at low temperature (77 K, with $\mathbf{E} \perp c$); however, the broad absorption band does not change in shape or shift significantly at low temperatures (courtesy of G.R. Rossman).

Figure 10 (right). IR absorption spectra of amethyst (Rio Grande do Sul, Brazil) and citrine (Anahi Mine, Bolivia) measured at room temperature with $\mathbf{E} \perp c$ (normalized to l = 1 mm) exhibit a broad OH absorption band at ~3400 cm^{-1} and a sharp band at 3585 cm^{-1} (courtesy of G.R. Rossman).



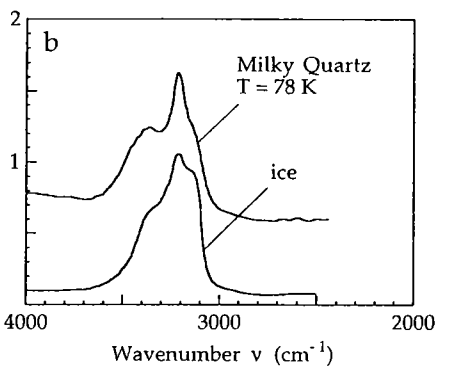


Figure 11. IR absorption spectra of polycrystalline milky quartz (Dillsburg, PA, CIT # 3027, normalizing to l = 1 mm) measured at (a) room temperature and at (b) low temperature (78 K). The broad band at ~3400 cm^{-1} measured at room temperature closely resembles that of liquid H_2O and exhibits a shift to 3200 cm^{-1} at low temperatures due to freezing of H_2O inclusions to ice (after Aines and Rossman, 1984a).

that are due to O-H vibrations of hydrogen point defects (Kats, 1962; Dodd and Fraser, 1965, 1967; Kopp and Staats, 1970; Staats and Kopp, 1974; Chakraborty and Lehmann, 1976a,b, 1978; Hosaka and Taki, 1981a,b; Hosaka et al., 1981; Aines and Rossman, 1984a). Many of the sharp bands of very dry synthetic quartz crystals with small or negligible broad band absorptions (Hosaka and Taki, 1981a; Pankrath, 1991) are the same as those observed in spectra of clear natural crystals. Amethyst and citrine also exhibit many of the bands (Table 3) identified in clear natural quartz (Chakraborty and Lehmann, 1976a,b, 1978; Aines and Rossman, 1984a). However, a number of absorption bands that are prominent in the spectra of rapidly grown, wet synthetic quartz (e.g., at ν = 3585 cm^{-1}, Table 3) are generally absent from the spectra of natural clear crystals.

EBSCOhost - printed on 2/13/2023 4:48 AM via . All use subject to https://www.ebsco.com/terms-of-use

Whereas many associations between hydrogen and cation defects in clear natural quartz crystals have been established, absorption bands of synthetic quartz crystals do not always show good correlations with alkali impurity concentrations (Kats, 1962; Dodd and Fraser, 1965; Kopp and Staats, 1970; Staats and Kopp, 1974; Hosaka and Taki, 1981a,b; Hosaka et al., 1981). Associations between aluminum substitutions and alkali interstitials in synthetic quartz may prevail over defect pairs involving hydrogen. Alternatively, impurity cations of rapidly grown, wet synthetic quartz crystals may enter aggregated clusters of molecular water. Given this situation, assignments of sharp bands of synthetic quartz have often relied on comparisons with absorption bands of clear natural quartz. Many of those bands that appear to be unique to wet synthetic quartz have not been assigned.

In addition to hydrogen interstitials that occur in association with aluminum substitutions, EPR studies of synthetic quartz (Nuttall and Weil, 1980; Weil, 1984; Cordier et al., 1994) have suggested the occurrence of hydrogen clusters near silicon vacancies ($4H_i + V_{Si}$) with structures similar to substitutional hydrogen defects (i.e., H_4O_4 groups for SiO_4 tetrahedra) of hydrogrossular (Foreman, 1968). While such defects have not been identified in IR absorption studies of synthetic quartz, IR spectra of hydrogarnets (Aines and Rossman, 1984b; Rossman and Aines, 1991; Cho and Rossman, 1993) reveal a number of sharp absorption bands near 3600 cm^{-1} that resemble unidentified sharp bands at high wavenumbers of synthetic quartz, amethyst, and citrine (Table 3). Given that H_4O_4 substitutions are electrically neutral, no strong associations with alkali point defects are expected. However, of the many OH absorption bands observed for hydrogen-bearing garnets, only two (one at 3662 cm^{-1} and one at 3598 cm^{-1}) are due to H_4O_4 defects, and many other modes of hydrogen incorporation may be responsible for sharp bands of the wet varieties of quartz. Several approaches have been taken to evaluate the structure and stability of H_4O_4 in quartz (Doukhan and Paterson, 1986; Paterson, 1986; Purton et al., 1992). These studies suggest solubilities of H_4O_4 substitutions that are very low at ambient conditions but that may reach ~20 to 40 ppm at elevated temperatures (T) and water pressures (P_{H2O}) (e.g., T = 1000°C, P_{H2O} = 1000 MPa).

Hydrogen interstitials make up the majority of hydrogen defects in quartz over a wide range of conditions. However, other minority defects that are difficult to study by spectroscopy may be important as well. Point defects consisting of isolated water interstitials have not been identified by IR spectroscopy, and their solubilities, even at high water pressures, must be very small (<10 ppm, Kronenberg et al., 1986; Rovetta et al., 1986; Cordier and Doukhan, 1989, 1991; Gerretsen et al., 1989); yet studies of oxygen volume diffusion under hydrothermal conditions suggest their presence. Oxygen diffusion rates in quartz are enhanced at high water pressures (Freer and Dennis, 1982; Dennis, 1984; Giletti and Yund, 1984; Elphick et al., 1986; Farver and Yund, 1991), with diffusion coefficients that scale linearly with the fugacity of water (f_{H2O}) (Farver and Yund, 1991a). Thus, oxygen diffusion appears to depend upon the motion of interstitial water molecules with very small concentrations. Rates of diffusional transport depend on both the concentrations and mobilities of point defects that effect transport. Given that mobilities of different hydrogen species may vary by many orders of magnitude (e.g., Kats, 1962; Elphick and Graham, 1988; Farver and Yund, 1991a), low-concentration, minority defects may control rates of diffusion if their mobilities are sufficiently large (Zhang et al., 1991).

Concentrations of hydrogen interstitials can be altered in relatively short experimental times; yet true equilibrium populations of hydrogen species within quartz

EBSCOhost - printed on 2/13/2023 4:48 AM via . All use subject to https://www.ebsco.com/terms-of-use

may require long time scales. Hydrogen interstitials have high mobilities (Kats, 1962; Sosin, 1975; Kronenberg et al., 1986), as do monovalent interstitial cations that can migrate along *c*-axis channels (Harris and Waring, 1937; Gibson and Vogel, 1950; Verhoogen, 1952; Snow and Gibbs, 1964; Rybach and Laves, 1967; Frischat, 1970; Krefft, 1975; Markes and Halliburton, 1979; Jain and Nowick, 1982a,b). However, changes in defect populations that require oxygen transport (e.g., Freer and Dennis, 1982; Dennis, 1984; Farver and Yund, 1991a), such as the introduction or loss of molecular water interstitials, may take long times, even at high water fugacities. Rates of silicon and aluminum diffusion in silicates are very slow (Jaoul et al., 1981; Yund, 1986; Houlier et al., 1988, 1990; Yund and Snow, 1989) and the introduction and loss of hydrogen defects associated with silicon vacancies ($4H_i + V_{Si}$) may occur only over very small length scales. Changes in defect pairs involving Al and interstitial hydrogen and alkali impurities have been achieved only by the exchange and migration of the relatively mobile interstitial defects. Al defects appear to be immobile in experimental times (Krefft, 1975; Markes and Halliburton, 1979; Halliburton et al., 1981; Jain and Nowick, 1982a,b), and equilibrium concentrations may be very difficult to achieve.

Aggregated water and fluid inclusions

Most of the hydrogen in rapidly grown synthetic and milky quartz occurs as fine-scale clusters of aggregated molecular water and fluid inclusions. IR spectra of synthetic quartz crystals exhibit a broad prominent band at ~3400 cm^{-1} (Fig. 9) that may extend from 3650 to 2500 cm^{-1} with integrated absorbances that yield hydrogen contents of up to 4000 ppm (Kats, 1962; Dodd and Fraser, 1965, 1967; Kekulawala et al., 1978, 1981; Kirby and McCormick, 1979; Hosaka and Taki, 1981a,b; Hosaka et al., 1981; Aines et al., 1984; Cordier and Doukhan, 1989). The broad character of this absorption is comparable to those of absorption bands assigned to H_2O at surfaces and within the interiors of chalcedony and opal (Segnit et al., 1965; Langer and Flörke, 1974; Frondel, 1982; Graetsch et al., 1985; Bartoli et al., 1990), suggesting the occurrence of similarly wide distributions of O-H···O bond lengths. Unlike the sharp, polarized OH absorption bands associated with structurally incorporated hydrogen defects, the broad absorption of synthetic quartz does not appear to be crystallographically controlled, and absorbance (for **E** varying relative to *c*) is nearly isotropic (Fig. 9).

IR spectra of synthetic quartz crystals measured at low temperatures ($T < 0°C$) exhibit reversible changes with decreasing temperature; sharp absorption bands increase in peak intensity and decrease in band width (Chakraborty and Lehmann, 1976b, 1978; Hosaka et al., 1981) while the broad band may show only subtle changes in shape. However, at high temperatures, spectra of synthetic crystals change irreversibly, with the permanent reduction of some sharp absorption bands and the growth of others (e.g., Kats, 1962; Kekulawala et al., 1978, 1981); in addition, significant changes in the character of the broad band correlates with loss of clarity (Brunner et al., 1961; Dodd and Fraser, 1965, 1967; Bambauer et al., 1969; Jones, 1978; Kekulawala et al., 1978, 1981; Kirby and McCormick, 1979; Paterson and Kekulawala, 1979; McLaren et al., 1983, 1989; Gerretsen, 1988). Broad absorption bands of synthetic quartz crystals annealed at $T > 500°C$ (Fig. 12) begin to resemble absorption bands measured for natural milky quartz crystals (Fig. 11) as they take on a "milky" appearance due to internal scattering of light. The broad absorptions at 3400 cm^{-1} of both heat-treated synthetic and milky quartz resemble the OH absorption band of liquid water (Fig. 11), and they shift to ~3200 cm^{-1} at low temperatures (e.g., $T = 77$ K), with shoulders that consist of composite bands characteristic of O-H stretching modes of ice. While optical-scale fluid inclusions are

EBSCOhost - printed on 2/13/2023 4:48 AM via . All use subject to https://www.ebsco.com/terms-of-use

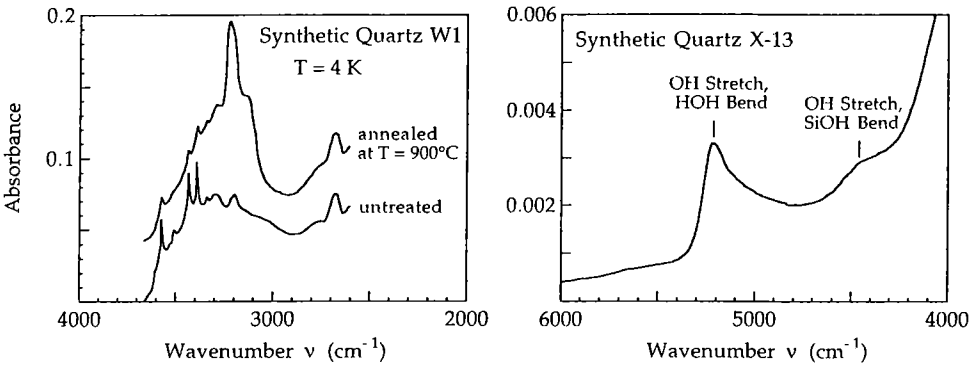


Figure 12. IR absorption spectra of synthetic quartz (crystal W1 obtained from Western Electric, Hobbs et al., 1972) measured at low temperature (T = 4 K, cooled using liquid He, unpolarized beam parallel to *c*, normalized to l = 1 mm) before and after annealing at T = 900°C (in air for 7 hours). The character of the broad OH absorption band of synthetic quartz changes as a result of heat-treatment; the broad band of untreated crystals does not shift significantly upon cooling to 4 K, while the broad band of heat-treated crystals shifts to 3200 cm^{-1} (after Kekulawala et al., 1982).

Figure 13. Near-IR absorption spectrum of rapidly grown synthetic quartz (X-13 obtained from Bell Labs) with E ∥ *c* (normalized to specimen thickness l = 1 mm). Combination bands associated with OH stretch/HOH bend modes of molecular water and OH stretch/SiOH bend modes of OH groups appear at ~5200 cm^{-1} and ~4500 cm^{-1}, respectively (after Aines et al., 1984).

generally abundant in milky quartz, inclusions that give rise to scattering in heat-treated synthetic quartz are below optical resolution.

Near-IR spectra of synthetic quartz are marked by relatively weak absorption bands at ~5200 and ~4500 cm^{-1} (Fig. 13) associated, respectively, with combination OH stretch/HOH bend modes of molecular water and OH stretch/SiOH bend (or OH stretch/AlOH bend) modes of structural hydroxyl groups. By comparing these band intensities relative to absorbance at ~3400 cm^{-1} for synthetic crystals of varying hydrogen content, Aines et al. (1984) demonstrated unambiguously that the broad absorption band of synthetic quartz corresponds to molecular water, before and after heat-treatment. The size and shape of the broad band produced by synthetic quartz crystals vary both with growth rate and growth direction (Wood, 1960; Dodd and Fraser, 1967; Chakraborty and Lehmann, 1976a; Lias and Grudenski, 1973), and molecular water contents appear to be well above equilibrium values; high growth rates for any particular growth sector favor high water contents, while low growth rates result in broad absorptions that are vanishingly small (Hosaka and Taki, 1981a; Pankrath, 1991). IR spectra of synthetic quartz crystals grown at low rates are dominated by sharp absorptions similar to those of clear natural crystals, and near-IR spectra exhibit combination OH stretch/SiOH bend bands at ~4500 cm^{-1} that are large relative to the ~5200 cm^{-1} band (Aines et al., 1984; Cordier and Doukhan, 1989, 1991). Absorption intensities at ~5200 and ~4500 cm^{-1} vary systematically with increasing hydrogen content, and wet synthetic quartz crystals grown rapidly are dominated in the near-IR by absorption at ~5200 cm^{-1}.

While H_2O inclusions in heat-treated synthetic quartz crystals may freeze, no spectral shift (from 3400 to 3200 cm^{-1}) is observed at low temperatures (at either 77 K or 4 K) for synthetic crystals that have not been altered by annealing (Fig. 12). Despite this observation, IR and TEM studies of wet synthetic quartz crystals indicate that molecular

EBSCOhost - printed on 2/13/2023 4:48 AM via . All use subject to https://www.ebsco.com/terms-of-use

water taken up during growth occurs as discrete clusters, not as isolated point defects. The broad nature of the 3400 cm^{-1} band is strong evidence for an extended network of hydrogen bonds with distributions of O-H···O bond lengths that may exceed, at ambient conditions, that of liquid water. Moreover, the lack of absorption anisotropy suggests an absence of crystallographic control of H_2O molecule orientations, inconsistent with H_2O point defects, yet readily explained if H_2O occurs as aggregated clusters. TEM studies of synthetic quartz in regions of high hydrogen content have shown that fine-scale inclusions are abundant (Fig. 14a) with characteristic oblate ellipsoidal (lens) shapes; aspect ratios of these inclusions average 1:4, and long axes within {100} planes may range from 10 to 60 nm (McLaren et al., 1983, 1989; Gerretsen, 1988; Gerretsen et al., 1989; Cordier et al., 1988). TEM observations of synthetic quartz in regions of low hydrogen content exhibit inclusions as well; however, their occurrence tends to be

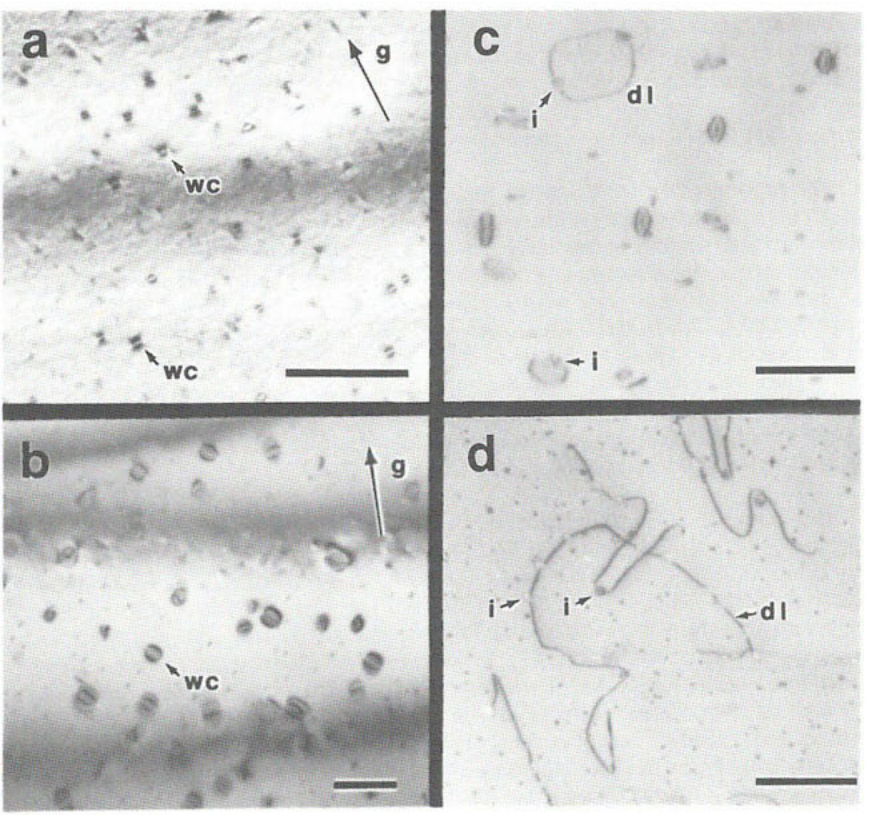


Figure 14. Transmission electron micrographs (bright field) of fine-scale molecular water clusters, fluid inclusions, and dislocations in synthetic quartz (scale bars represent 0.5 μm). (a) Ellipsoidal clusters of molecular water (wc) within untreated, rapidly grown quartz (g = 101). Diffraction contrast surrounding H_2O clusters indicate that local deviatoric stresses are large. (b) Clusters of molecular water in early stages of coarsening (corresponding to the nucleation of dislocation loops) within sample annealed at T = 407°C for 65 hours (g = 100). (c) Fluid inclusions (i) and dislocation loops (dl) in synthetic quartz annealed at T = 550°C for 24 hours. (d) Spheroidal fluid inclusions (i) decorating dislocations (dl) in synthetic quartz annealed at T = 806°C for 1 hour (courtesy of P. Cordier).

EBSCOhost - printed on 2/13/2023 4:48 AM via . All use subject to https://www.ebsco.com/terms-of-use

heterogeneous, and their dimensions are even smaller (2 to 3 nm) than the ellipsoidal inclusions of rapidly grown wet regions (McLaren et al., 1983; Cordier and Doukhan, 1991).

Lack of diffraction contrast within ellipsoidal inclusions indicates that they are amorphous, while strain contours surrounding the inclusions indicate large local deviatoric stresses associated with their incorporation (McLaren et al., 1983; Gerretsen, 1988). By measuring inclusion dimensions and densities, and summing over large populations of ellipsoidal inclusions, Gerretsen (1988) was able to account for all of the broad-band water of synthetic quartz without appealing to contributions from structural H_2O. The minimum dimensions of ellipsoidal H_2O inclusions in synthetic quartz (measured along their short axes) are comparable to those of thin, vicinal fluid films between silica surfaces, which exhibit enhanced hydrogen bonding and structural order relative to those of bulk liquid water (Bassett et al., 1970; Peschel and Adlfinger, 1970; Etzler and Fagundus, 1987; Etzler, 1988; Horn et al., 1989; Israelachvili and Kott, 1989; Israelachvili, 1992). Thus, H_2O within fine-scale clusters may exhibit similar departures from the properties of water. As is apparent from IR spectra measured at low temperatures, ellipsoidal H_2O clusters do not exhibit freezing, and they can be distinquished from larger fluid inclusions on this basis.

The pronounced changes in the broad band absorption of synthetic quartz crystals annealed at elevated temperatures coincide with significant changes in inclusion geometries and defect substructures (Fig. 14). TEM observations of heat-treated synthetic quartz reveal nearly equant, spheroidal inclusions with mean sizes (30-120 nm) that appear to coarsen with time at elevated temperature (Griggs, 1967; Baeta and Ashbee, 1973; Kirby and McCormick, 1979; Paterson and Kekulawala, 1979; Kekulawala et al., 1981; McLaren et al., 1983, 1989; Cordier et al., 1988; Gerretsen, 1988; Gerretsen et al., 1989). Minimum inclusion dimensions in heat-treated crystals are much larger than those of the original ellipsoidal H_2O clusters, increasing the propensity of H_2O in these inclusions to freeze. Diffraction contrast in the surrounding quartz is lost, and deviatoric stresses appear to be relaxed.

Spheroidal inclusions in heat-treated synthetic quartz are found to intersect with dislocations (Fig. 14c,d), and their development and growth appears to be linked during early stages of coarsening to the growth of prismatic {110} dislocation loops (Kirby and McCormick, 1979; McLaren et al., 1983, 1989; Cordier et al., 1988; Gerretsen, 1988). The process of fluid inclusion coarsening requires the net transport of H_2O to larger inclusions and the transport of SiO_2 away from growing inclusions. Rates of hydrogen diffusion in quartz (Kats, 1962; Kronenberg et al., 1986) are sufficiently rapid to explain the observed rates of coarsening (Paterson and Kekulawala, 1979; McLaren et al., 1983; Cordier et al., 1988); however, the effective rate-limiting diffusivities inferred from inclusion coarsening results are somewhat larger than diffusivities of oxygen (e.g., Dennis, 1984; Giletti and Yund, 1984; Farver and Yund, 1991a) and are much larger than diffusivities expected for silicon (Jaoul et al., 1981; Yund, 1986; Houlier et al., 1988, 1990; Yund and Snow, 1989).

Exchange of H_2O and SiO_2 may be facilitated by pipe diffusion along dislocations (McLaren et al., 1983; Cordier et al., 1988; Gerretsen, 1988). The prismatic dislocation loops that intersect fluid inclusions during early stages of coarsening exhibit Burgers vectors $1/3\langle 110\rangle$ that are everywhere normal to the plane of the loop (McLaren et al., 1983, 1989; Cordier et al., 1988; Gerretsen, 1988). Thus, dislocations that develop during the early stages of annealing have an edge character along all segments of any particular loop

EBSCOhost - printed on 2/13/2023 4:48 AM via . All use subject to https://www.ebsco.com/terms-of-use

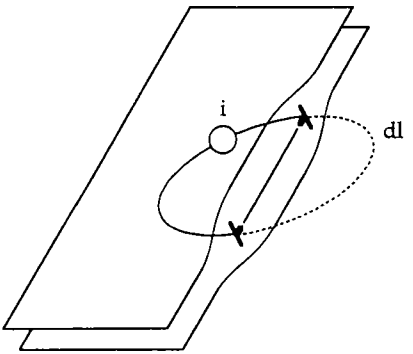


Figure 15. Interstitial-type dislocation loops (dl) with edge character (⊥) grow by the addition of SiO_2 to the edge of the dislocation half-plane (presumably transported by pipe diffusion of Si and O defects) as fluid inclusions (i) coarsen by the counter-flux of H_2O.

(Fig. 15), and growth of interstitial-type loops appears to involve dislocation climb and the addition of SiO_2 to the dislocation half-plane. Given that the effective diffusivities determined by Paterson and Kekulawala (1979), McLaren et al. (1983), and Cordier et al. (1988) are large compared with rates of volume diffusion, they may reflect rates of pipe diffusion as H_2O migrates to coarse, growing inclusions (presumably as mobile protons and slower molecular water defects) and SiO_2 is transported (as separate Si and O defects) from the walls of coarse, growing inclusions to fine, collapsing inclusions and to dislocation jogs (unit-cell steps within the half plane of dislocations).

Fluid inclusions are abundant in natural milky quartz, both at the optical and TEM scales, and they commonly give rise to a broad absorption band at 3400 cm^{-1} that closely resembles that of bulk liquid H_2O (Fig. 11a). Measured at low temperatures, the broad band shifts to 3200 cm^{-1}, and a large fraction of H_2O within milky quartz appears to be freezable (Fig. 11b). Optical-scale fluid inclusions in milky quartz crystals from a wide variety of geologic settings have been studied extensively with the goal of constraining past thermodynamic conditions and chemistries of fluids using thermometric methods (Roedder, 1984) and high-sensitivity Fourier transform IR and micro-Raman spectroscopic methods (Rosasco and Roedder, 1979; Cheilletz et al., 1984; Touray et al., 1985; Vry et al., 1987; Wopenka et al., 1990). Inclusions may be incorporated during growth, and measurements of homogenization and freezing temperatures of scattered primary inclusions may provide information relative to the time of crystal growth (e.g., Roedder and Skinner, 1968; Roedder and Kopp, 1975). However, optical-scale fluid inclusions may also be formed by imperfect crack healing (e.g., Shelton and Orville, 1980; Smith and Evans, 1984), and planar arrays of fluid inclusions may provide information about the fluids introduced after crystallization during later events of brittle deformation and recovery (e.g., Kerrich, 1976; Wilkins and Barkas, 1978; Pecher et al., 1985; Jang et al., 1989).

A third group of fluid inclusions in milky quartz has dimensions of 30 to 200 nm and is microstructurally similar to fluid inclusions in heat-treated synthetic quartz (McLaren and Hobbs, 1972; White, 1973; Christie and Ord, 1980; Ord and Christie, 1984; Stenina et al., 1984; Kronenberg et al., 1990). Further investigations are needed to understand the mechanisms by which these inclusions are formed, but their occurrence in natural quartz tectonites and their association with dislocations suggest mechanisms of nucleation and growth similar to those inferred for nm-scale inclusions in synthetic quartz during annealing and high-temperature deformation (Baeta and Ashby, 1973; Kirby and McCormick, 1979; Kekulawala et al., 1981; McLaren et al., 1983, 1989; Cordier et al., 1988; Cordier and Doukhan, 1989).

EBSCOhost - printed on 2/13/2023 4:48 AM via . All use subject to https://www.ebsco.com/terms-of-use

Natural amethyst and citrine crystals exhibit broad band absorptions (Fig. 10) at ~3400 cm^{-1} (Chakraborty and Lehmann, 1976a,b, 1978; Kekulawala et al., 1978; Aines and Rossman, 1984a) that resemble those of synthetic quartz crystals; these bands appear to be related to fine (20 to 100 nm) inclusions that lie preferentially along Brazil twin boundaries (McLaren and Phakey, 1965, 1966; McLaren et al., 1983). As with synthetic quartz crystals, the broad absorptions of amethyst and citrine measured at low temperatures show only subtle changes in shape (Kekulawala et al., 1978; Aines and Rossman, 1984a). Amethyst and citrine lose clarity at elevated temperatures ($T \geq 600°C$), and significant changes in the broad band parallel the irreversible changes in spectra of heat-treated synthetic quartz. The broad band of heat-treated amethyst, measured at room temperature, resembles that of water, and, at low temperatures ($T = 4$ K), it resembles that of ice (Kekulawala et al., 1978). Fine-scale clusters of molecular water in amethyst and citrine are replaced at high temperatures by spheroidal fluid inclusions that decorate both twin boundaries and dislocations (McLaren and Phakey, 1965, 1966). Although hydrogen species of amethyst and citrine have not been studied in the same detail as have hydrogen species in synthetic quartz, ratios of molecular water to hydroxyl appear to differ for amethyst and citrine. Near-IR absorption bands at 5200 and 4500 cm^{-1} indicate that molecular water is the predominent hydrogen species in citrine, while hydroxyl defects are more common in amethyst (Aines and Rossman, 1984a).

The replacement of fine-scale clusters of molecular water by freezable fluid inclusions and subsequent inclusion growth may depend upon the pressure imposed during annealing (Kekulawala et al., 1981; Gerretsen, 1988; Cordier and Doukhan, 1989; McLaren et al., 1989). McLaren et al. (1983, 1989) and Cordier and Doukhan (1989) have suggested that H_4O_4 substitutions for SiO_4, or, equivalently, defect clusters of the form

$$4H_i + V_{Si} + 4O_O = V_{SiO2} + 2(H_2O)_i \quad (4)$$

may serve as nuclei for clusters of molecular water. If so, development and growth of molecular water clusters and fluid inclusions may depend upon pressure through changes in H_4O_4 solubility and the concentrations of H_4O_4 clusters in excess of their solubility (Doukhan and Paterson, 1986; Paterson, 1986; Cordier et al., 1994).

Interactions and chemical exchange may also occur between coarse, optical-scale fluid inclusions and fine, TEM-scale H_2O clusters and inclusions. Hydrogen volume diffusion in quartz is rapid, and recent investigations of optical-scale fluid inclusions containing CO_2, CH_4, and chalcopyrite daughter crystals have shown that fluid inclusions may not be closed systems relative to hydrogen (Hall and Bodnar, 1990; Morgan et al., 1993; Mavrogenes and Bodnar, 1994). Thus, inclusions within quartz grains of rocks subjected to elevated temperatures after the time of trapping may re-equilibrate with respect to new values of f_{H2} and may no longer record original fluid compositions or the original conditions of f_{H2} or f_{O2}. By comparison, rates of oxygen volume diffusion are slow, and fluid inclusions are not expected to gain or lose H_2O unless fracture causes decrepitation or crystalline flaws such as dislocations provide high-diffusivity paths. Dislocations may interact with optical-scale inclusions as well as nearby nm-scale inclusions, and recent studies have documented changes in H_2O-CO_2 inclusion compositions that may result from H_2O loss by pipe diffusion (Bakker and Jansen, 1990, 1991, 1994; Hollister, 1990). Pipe diffusion in experimental studies may serve to redistribute H_2O amongst inclusions of differing sizes, but exchange may occur between inclusions and grain boundaries over longer, geologic times.

EBSCOhost - printed on 2/13/2023 4:48 AM via . All use subject to https://www.ebsco.com/terms-of-use

Hydrogen species at dislocations

Hydrogen species have often been inferred to occupy sites on dislocations in quartz, beginning with the first explanations of hydrolytic weakening (Griggs and Blacic, 1965; Griggs, 1967) and continuing with the most recent theories of water-assisted creep (see Paterson, 1989). Nevertheless, the hypothesis that silanol groups replace distorted siloxanes at dislocation cores as they do at free quartz surfaces remains as plausible and untested today as when it was first proposed. *Ab initio* models of molecular structures of the silica-water system suggest that hydrolysis of siloxanes

$$\equiv \text{Si-O-Si} \equiv + \text{H}_2\text{O} \rightarrow \equiv \text{Si-O-H} \cdots \text{H-O-Si} \equiv \quad (5)$$

may proceed once Si-O bonds of siloxanes are stretched by > 4% (Heggie and Jones, 1987). Thus, hydrogen-bonded silanols (as described by Eqn. 5) are not expected in the otherwise undisturbed structure of quartz, whereas they may be common at crystalline flaws where strains are large. Formation energies of model dislocation structures (Heggie and Nylen, 1984, 1985; Heggie et al., 1985) are significantly reduced by the introduction of hydrolysed bonds (Heggie and Jones, 1986; Heggie, 1992). Energies of dislocation kinks (or unit cell offsets within the glide plane) may be reduced by the introduction of hydrogen-bonded silanols (Eqn. 5) as well as by ($4H_i + V_{Si}$) complexes (Heggie and Jones, 1986).

H_2O pipe diffusion in silicates may be rapid relative to rates of volume diffusion (e.g., Yund et al., 1981), and several lines of microstructural evidence suggest that pipe diffusion is rapid in quartz. The simultaneous growth of dislocation loops by climb and of fine-scale fluid inclusions along these dislocation loops in synthetic quartz suggest that rates of H_2O and SiO_2 exchange may be governed by pipe diffusion (Paterson and Kekulawala, 1979; McLaren et al., 1983; 1989; Cordier et al., 1988; Gerretsen, 1988). In studies of H_2O-CO_2 inclusions, the observed loss of H_2O relative to CO_2 from optical-scale inclusions suggests that H_2O may be transported by pipe diffusion while CO_2 remains trapped (Bakker and Jansen, 1990, 1991, 1994). Rates of H_2O pipe diffusion depend upon both the concentrations and the mobilities of H_2O defects along dislocations, so that rapid pipe diffusion implies finite concentrations of hydrogen-oxygen complexes within dislocation cores.

Despite the many clues that hydrogen defects populate dislocations, OH absorptions assigned to hydrogen species on dislocations have not been identified by spectroscopy. Even if the dangling bonds of dislocation cores are saturated with respect to hydrogen species, detection and identification of their IR bands may prove challenging; given dislocation densities as large as 10^9 cm^{-2} (cm/cm^3), silanols within dislocation cores may not account for more than a small fraction (1 to 2 ppm H/10^6 Si) of the hydrogen found in quartz (Griggs, 1967; Paterson, 1989), regardless of whether the crystals are dominated by small concentrations of point defects (~30 to 150 ppm) or large quantities of aggregated H_2O (~300 to 4000 ppm).

CHEMICAL WEAKENING

The inelastic mechanical properties of rocks are strongly influenced by the presence of aqueous fluids (Kirby, 1984; Carter et al., 1990), both through physical changes in the state of stress associated with the introduction of internal pore pressures and through chemical interactions that change the energetics of breaking bonds. The influence of pore fluids on the effective stress of porous and fractured materials and the conditions required

EBSCOhost - printed on 2/13/2023 4:48 AM via . All use subject to https://www.ebsco.com/terms-of-use

for fracture and frictional sliding were recognized with the early studies of Terzaghi (1936, 1945), and elevated fluid pressures may be important over a wide range of geologic conditions (Hubbert and Rubey, 1959; Handin et al., 1963; Brace and Martin, 1968; Raleigh et al., 1976; Etheridge et al., 1984; Kerrich, 1986; Byerlee, 1990; Sibson, 1990; Rice, 1992). Pore fluid pressures (P_f) act in opposition to externally applied pressures and reduce the shear stresses (τ) required for fracture and frictional sliding, given respectively by the Mohr-Coulomb expressions

$$\tau = \tau_o + \mu_f (\sigma_n - P_f) \quad (6a)$$

and

$$\tau = \mu (\sigma_n - P_f) \quad (6b)$$

where σ_n is the normal stress, τ_o is a cohesive strength, μ_f is referred to as the coefficient of internal friction, and μ is the friction coefficient for a particular surface. The fracture and frictional strengths of rocks may thus vary widely with local values of P_f, which in turn depend upon the sources and subsurface transport of fluids.

Enhanced rates of crack growth and frictional sliding may also be observed in the absence of significant fluid pore pressures; instead, they may depend on chemical interactions with H_2O, relative humidity, solution pH, and ionic strength. Experimental investigations of quartz deformation suggest a variety of chemical roles for water and the hydrogen species adsorbed at quartz surfaces. Reactions that lead to hydrogen-bonded silanols may reduce fracture energies, while enhanced diffusion rates of hydrated surfaces and thin H_2O films may promote grain growth, recrystallization, and solution transfer creep.

Intracrystalline mechanisms of ductile deformation are not generally sensitive to variations in mean stress (or the hydrostatic pressure) and thus are not affected directly by changes in fluid pressure as described by effective pressure laws (Eqns. 6). However, dislocations in quartz may be nucleated at internal clusters of molecular water, and their motion by glide and climb may be accelerated by internal hydrogen species that influence the populations and mobilities of dislocation kinks and jogs or increase rates of solid state diffusion. These processes of deformation may ultimately depend upon pore fluid pressures and compositions through equilibrium relationships between internal hydrogen defect concentrations and the imposed thermodynamic conditions. However, equilibrium point defects have been difficult to achieve experimentally, and the deformation of quartz by dislocation creep mechanisms cannot be understood without addressing the distributions of hydrogen defects and the rates at which they may be transported.

Stress corrosion cracking

Hydrogen species adsorbed at quartz surfaces lead to significant reductions in surface energies (γ) that alter the energetics of crack growth (Parks, 1984), and the kinetics of reactions between atmospheric H_2O and OH and Si-O bonds at crack tips appears to govern the rates of crack growth over a wide range of time scales (Michalske and Freiman, 1982; Freiman, 1984). Surface energies of quartz may decrease by an order of magnitude as hydrogen species are adsorbed; based on theoretical estimates of γ for pristine quartz surfaces and calorimetric measurements of heats of adsorption and immersion (Axelson and Piret, 1950; Hackerman and Hall, 1958; Young and Bursh, 1960; Wade et al., 1961; Whalen, 1961a,b; Anderson, 1965; Parks, 1984), surface energies may drop from values in excess of 2 J/m^2 for quartz surfaces exposed to high vacuum to γ = 0.5 to 0.7 J/m^2 for surfaces dominated by silanol groups, γ = 0.4 to

EBSCOhost - printed on 2/13/2023 4:48 AM via . All use subject to https://www.ebsco.com/terms-of-use

0.45 J/m^2 for surfaces saturated with H_2O, and $\gamma = 0.3$ to 0.4 J/m^2 for surfaces in contact with water. If energy losses during crack growth associated with acoustic emissions, microplasticity, and generation of heat are neglected, similar trends may be expected for fracture surface energies (γ_f) (see Parks, 1984), and stored strain energies released during tensile crack growth may vary with the availability of environmental H_2O. In the absence of H_2O or OH at crack tips, crack growth may be catastrophic once a critical threshold stress is achieved, and rates may reach acoustic velocities. In humid environments, crack growth may proceed at much lower quasi-static rates with velocities that depend either upon processes of stress corrosion at the crack tip or upon diffusive transport of the reactive hydrogen species to the crack tip.

Tensile crack growth in quartz, as in glass and other crystalline silicates, occurs when the local stress at the crack tip exceeds its local strength. While local stresses may vary with crack dimensions and orientation relative to those of tractions applied at the far field, the conditions for crack growth can be examined by comparing the mechanical strain energy (G) available for crack propagation, normalized by unit area of crack, with $2\gamma_f$. For tensile plane strain loading configurations

$$G = K_I^2 (1 - p^2)/E \tag{7}$$

where K_I is a local stress intensity factor for tensile (mode I) cracking, p is Poisson's ratio, and E is Young's modulus. Crack extension may proceed under anhydrous conditions once G reaches a critical value G_c related to the surface energy of pristine quartz surfaces. However, crack growth experiments performed on quartz and silica glass specimens loaded in air, in atmospheres with controlled humidities, or in water indicate that crack extension may occur at values of G much less than G_c with growth rates that depend on the concentrations of atmospheric hydrogen species (Brace and Walsh, 1962; Wiederhorn, 1967, 1969; Wiederhorn and Bolz, 1970; Martin, 1972; Scholz, 1972; Hartley and Wilshaw, 1973; Martin and Durham, 1975; Ball and Payne, 1976; Atkinson, 1979; Dunning et al., 1980, 1984; Atkinson and Meredith, 1981, 1987a,b; Meredith and Atkinson, 1982; Michalske and Freiman, 1982; Dunning and Huf, 1983; Freiman, 1984; Parks, 1984).

Crack growth rates of specimens loaded in any particular environment may show complex behavior (Fig. 16a) at stress intensity factors K_I (e.g., Wiederhorn, 1967; Atkinson, 1984; Frieman, 1984) less than K_{Ic} (associated with G_c). Widely varying crack velocities v may be measured at low values of K_I (regime 1) that are governed by stress corrosion processes and thermally activated rates of reaction at the crack tip, with

$$v = v_0 K_I^n \exp(-H/RT) \tag{8}$$

where v_0 and n may depend upon the hydrogen species present, H is an activation enthalpy, R is the gas constant, and T is absolute temperature. As crack velocities increase, diffusive transport of hydrogen species to the crack tip may become important, and a plateau in velocity may be reached (regime 2) in association with diffusion-controlled propagation; crack velocities in this regime are insensitive to K_I and are limited by depletion of hydrogen species at the crack tip and by the mobilities of atmospheric H_2O and OH. Diffusion-controlled crack growth is replaced as values of K_I approach K_{Ic} (regime 3), crack growth becomes unstable, and the v - K_I relationship shows little sensitivity to environmental hydrogen species.

Tensile crack growth experiments performed on single crystal specimens of quartz have shown that reaction-controlled (regime 1) crack growth operates over a wide range

EBSCOhost - printed on 2/13/2023 4:48 AM via . All use subject to https://www.ebsco.com/terms-of-use

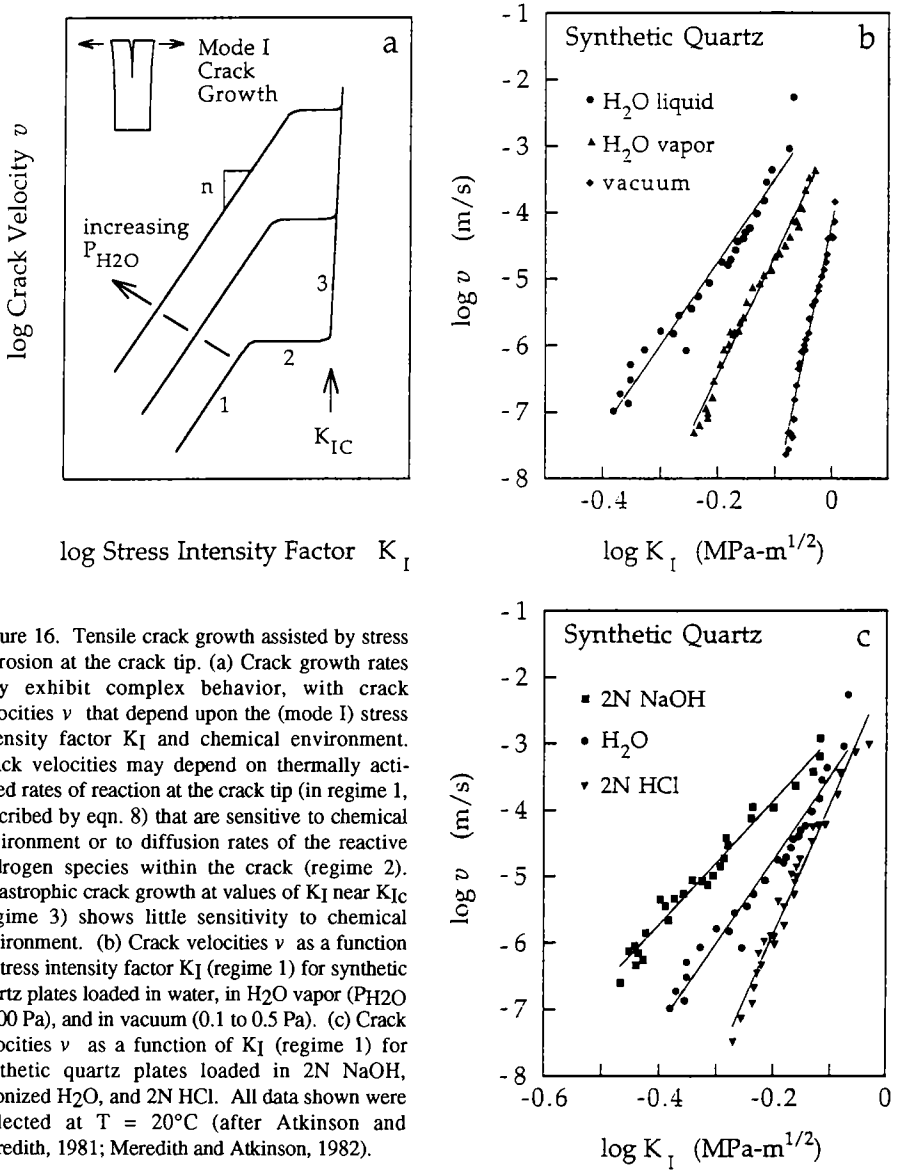


Figure 16. Tensile crack growth assisted by stress corrosion at the crack tip. (a) Crack growth rates may exhibit complex behavior, with crack velocities v that depend upon the (mode I) stress intensity factor K_I and chemical environment. Crack velocities may depend on thermally activated rates of reaction at the crack tip (in regime 1, described by eqn. 8) that are sensitive to chemical environment or to diffusion rates of the reactive hydrogen species within the crack (regime 2). Catastrophic crack growth at values of K_I near K_{Ic} (regime 3) shows little sensitivity to chemical environment. (b) Crack velocities v as a function of stress intensity factor K_I (regime 1) for synthetic quartz plates loaded in water, in H_2O vapor (P_{H2O} = 300 Pa), and in vacuum (0.1 to 0.5 Pa). (c) Crack velocities v as a function of K_I (regime 1) for synthetic quartz plates loaded in 2N NaOH, deionized H_2O, and 2N HCl. All data shown were collected at T = 20°C (after Atkinson and Meredith, 1981; Meredith and Atkinson, 1982).

of laboratory time scales and chemical environments (Scholz, 1972; Hartley and Wilshaw, 1973; Ball and Payne, 1976; Atkinson, 1979, 1984; Dunning et al., 1980, 1984; Atkinson and Meredith, 1981; Meredith and Atkinson, 1982; Dunning and Huf, 1983). Thus, stress corrosion mechanisms are likely to control crack growth during slow natural deformations of silicates in the Earth's crust. As shown in Figure 16b, crack velocities exhibit kinetics consistent with Equation (8) for specimens immersed in water during loading, for samples exposed to controlled vapor pressures (P_{H2O} = 300 Pa), and even for samples loaded in a vacuum of 0.1 to 0.5 Pa (Atkinson and Meredith, 1981; Meredith and

EBSCOhost - printed on 2/13/2023 4:48 AM via . All use subject to https://www.ebsco.com/terms-of-use

Atkinson, 1982). However, pronounced increases in velocity for any given K_I are apparent as atmospheric H_2O is made available, and systematic changes in the relationship between v and K_I are observed that may be described by decreasing values of n with increasing exposure to H_2O. Crack velocities depend on environmental OH concentrations as well (Atkinson and Meredith, 1981), with similar trends expressed by v - K_I relationships as pH is increased (Fig. 16c).

Activation enthalpies describing the temperature dependence of crack growth fall within the range of 46 to 99 kJ/mol (Scholz, 1972; Martin and Durham, 1975; Atkinson, 1979; Meredith and Atkinson, 1982); these values may provide clues to reactions that occur between hydrogen species and quartz at crack tips. Michalske and Freiman (1982) proposed an elegant model for stress corrosion in silicates in which rates of reaction between H_2O and Si-O bonds are controlled by the simultaneous process of electron transfer and proton transfer. H_2O molecules that migrate to the crack tip may readily form a hydrogen bond with oxygen in quartz without undergoing dissociation (Fig. 17). The rate-limiting steps then consist of: (1) Bond formation between oxygen of the water molecule and silicon in the region of the crack tip, replacing a Si-O bond in quartz; and (2) Replacement of the hydrogen bond between hydrogen in the water molecule and surficial oxygen with an O-H bond, which results in two silanol groups that are hydrogen bonded. Crack growth then proceeds by breaking the weak hydrogen bond and extending crack surfaces that are populated by silanol groups. The model of Michalske and Freiman (1982) suggests that stress corrosion may proceed given the presence of any environmental molecules that have electron donor sites on one end and proton donor sites on the other, and experiments performed on quartz plates exposed to solutions of varying pH (e.g., Atkinson and Meredith, 1981; Dunning et al., 1984) suggest that OH molecules may contribute to crack extension reactions.

Crack healing may occur for values of $G < 2\gamma$ where γ refers to the surface energy of surfaces saturated with respect to reactive molecules present in the environment. Activation enthalpies for crack healing (Smith and Evans, 1984; Brantley et al., 1990) are comparable (35 to 80 kJ/mol) to those of crack growth, and rates of healing similarly depend upon fluid chemistry (Brantley, 1992; Brantley et al., 1990). However, crack growth and healing do not generally proceed by identical, reversible processes. Crack healing is often imperfect, leading to the development of fluid inclusions, and the mechanisms of SiO_2 dissolution, precipitation, and redistribution that govern crack healing differ from the stress corrosion mechanisms that do not require silica transport.

Time-dependent frictional sliding

Surficial hydrogen species appear to influence frictional sliding, leading to significant reductions in the friction coefficient μ and the introduction of time and sliding velocity effects that may give rise to unstable, stick-slip frictional response. Frictional sliding between silicate surfaces occurs once shear stresses become sufficiently large relative to the normal stress imposed, as given by Equation (6b). Sliding displacements between quartzite surfaces under anhydrous conditions require significantly larger shear stresses for a given normal stress (Fig. 18a) than those required for sliding in humid environments. Friction coefficients determined for quartzite surfaces in dry argon following heat treatment at 300°C range from 0.85 to 1.0 (Dieterich and Conrad, 1984), while surfaces exposed to air or other humid environments exhibit friction coefficients of 0.55 to 0.70 (e.g., Byerlee, 1978; Dieterich and Conrad, 1984; Dunning and Miller, 1984).

EBSCOhost - printed on 2/13/2023 4:48 AM via . All use subject to https://www.ebsco.com/terms-of-use

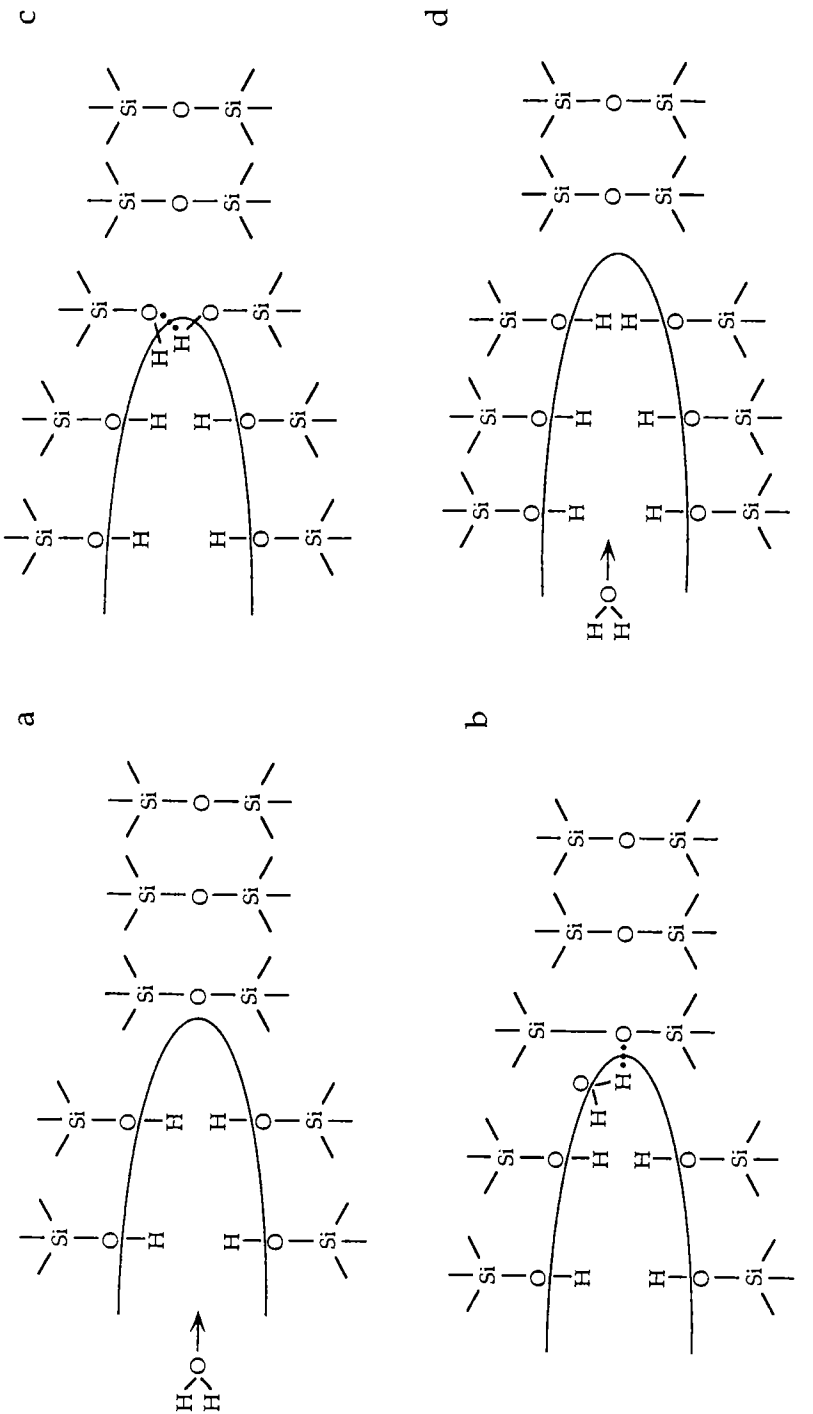


Figure 17. Stress corrosion reaction at crack tip proposed by Michalske and Freiman (1982) involving (a) transport of H_2O to the crack tip, (b) formation of a hydrogen bond between H_2O and structural oxygen, (c) simultaneous replacement of the hydrogen bond just formed by an O-H bond, replacement of an O-H bond of the water molecule by a hydrogen bond, and exchange of oxygens bonded to nearby Si, and (d) loss of hydrogen bonding between paired silanols. The hydrogen bond between silanols offers negligible resistance to crack extension compared with breaking a Si-O bond, and the energies of proton and electron transfer reactions are expected to be low relative to that of extending a Si-O bond.

EBSCOhost - printed on 2/13/2023 4:48 AM via . All use subject to https://www.ebsco.com/terms-of-use

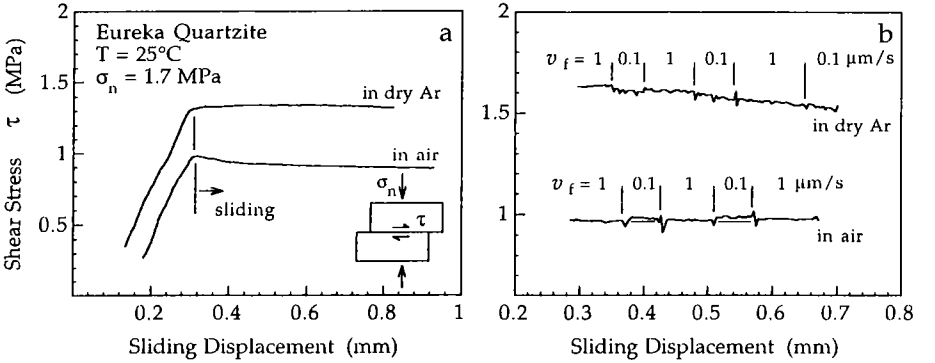


Figure 18. Frictional sliding resistance of quartzite sliding blocks loaded at room temperature in air and in dry argon atmosphere. (a) Larger shear stresses τ are required at a given normal stress σ_n (=1.7 MPa) to initiate sliding along surfaces of Eureka quartzite dried at 300°C and loaded in dry argon than along quartzite surfaces exposed to air (sliding velocity v_f = 1.0 μm/s). (b) Variations in shear resistance τ during velocity-stepping experiments at v_f = 0.1 and 1.0 μm/s. Velocity weakening of quartzite surfaces, associated with changes in the frictional surface state (or Ψ, see text), may be observed in humid environments (as reductions in τ with increases in v_f from 0.1 to 1.0 μm/s or as increases in τ with reductions in v_f) but not in dry argon (σ_n = 1.7 MPa, after Dieterich and Conrad, 1984).

Friction coefficients μ for silicate surfaces exposed to humid environments also vary as a function of time and sliding velocity v_f, as given by constitutive relationships (Dieterich, 1979, 1981; Ruina, 1983) of the form

$$\mu = \mu^* + a\, ln\left(\frac{v_f}{v_{f^*}}\right) + b\,\Psi \qquad (9)$$

where

$$\frac{d\Psi}{dt} = -\left(\frac{v_f}{L_c}\right)\left[\Psi + ln\left(\frac{v_f}{v_{f^*}}\right)\right] \qquad (10)$$

The first term of Equation (9), μ^*, is the friction coefficient determined at a reference steady state defined at sliding velocity v_f^*, while the second and third terms describe departures from μ^* that depend upon sliding velocity v_f and transient changes in surface state. Frictional resistance to sliding may increase as sliding velocities are increased, and the second term of (9) describes the instantaneous increase in μ observed in experiments in which the velocity is step-wise increased with a magnitude given by material parameter a and the change in velocity imposed. Following the initial rise in μ, frictional resistance to sliding may decay at the increased sliding velocity, and the third term of (9) describes the long-term transient response of sliding surfaces associated with changes in state where b is a material parameter and the state variable Ψ depends on sliding displacements following the step in velocity, as given by Equation (10). L_c is a characteristic displacement for strength decay and is independent of sliding velocity. Silicates that exhibit increases in steady state friction coefficients with increasing velocity (i.e., $a - b > 0$) are referred to as velocity strengthening while those that display decreases in steady state values in μ with increases in velocity ($a - b < 0$) are referred to as velocity weakening. Velocity weakening may lead to accelerations in sliding velocities when shear stresses are increased, resulting in unstable, stick-slip response.

Friction experiments performed with quartzite sliding blocks in argon and in air incorporated sliding velocities that were step-wise changed between 0.1 and 1.0 μm/s

EBSCOhost - printed on 2/13/2023 4:48 AM via . All use subject to https://www.ebsco.com/terms-of-use

(Dieterich and Conrad, 1984), and a comparison of the results reveals differences in frictional response associated with the third term of Equation (9) due to changes in surface state during sliding (Fig. 18b). Shear stresses measured at a given normal stress for surfaces exposed to air were observed to rise initially as velocity was increased, followed by a reduction in stress to values below those measured at the original, slower sliding velocity, indicating that $a - b < 0$. Similarly, shear stresses showed an initial decrease for reductions in sliding velocity, after which stresses gradually increased, reaching values that exceeded shear stresses originally measured at slower velocities (Fig. 18b). Shear stresses for quartzite surfaces measured in a dry argon environment exhibited small, instantaneous changes as sliding velocities were changed, consistent with the second term of Equation (9). However, transient response leading to velocity-weakening was not observed; thus, the third term of Equation (9) and changes in surface state given by (10) appear to be negligible.

The mechanisms by which hydrogen species at quartz surfaces influence time-dependent frictional properties have not been identified. Hydrogen species may affect cracking at asperity contacts by stress corrosion processes, and they may thereby influence the development of gouge. Alternatively, hydrogen species may alter adhesion between surfaces at points of contact; changes in surface state may occur through changes in bonding and local redistribution of silica and hydrogen species. The constitutive parameters of Equations (9) and (10) are essentially phenomenological, and further studies are needed before the effects of surficial hydrogen species on frictional surface states can be identified.

Significant reductions in apparent friction coefficients for silicate surfaces with thin layers of gouge between them may result if fluids promote dissolution and precipitation and act to seal regions of the sliding surfaces from fluid transport. Once sealed, compaction of gouge may lead to locally elevated pore pressures P_f (Eqn. 6b), resulting in apparent friction coefficients as low as 0.22 (Blanpied et al., 1992). Sealing by dissolution and precipitation may often be incomplete; yet thin, nm-scale films of vicinal water between quartz surfaces can be difficult to remove (Peschel and Adlfinger, 1970; Israelachvili, 1986; Horn et al., 1989; Israelachvili and Kott, 1989; Gee et al., 1990). These films may continue to serve as an internal pore fluid that reduces apparent friction coefficients (Byerlee, 1990).

Solution transfer creep

Compaction and viscous creep of quartz sands and porous polycrystalline aggregates may occur through a variety of solution transfer (or pressure solution) processes if intergranular and thin vicinal fluids are present between quartz grains to promote silica transport. Solution transfer creep involves the simultaneous dissolution of quartz at grain contacts and precipitation within pores or at free surfaces, leading to densification and shape changes by porosity reduction and rearrangement of quartz grains. A number of driving forces may be responsible for dissolution and precipitation, and rates of deformation may be controlled either by reaction kinetics at quartz-fluid interfaces or by rates of diffusional transport within intergranular fluid films. Silica solubilities may be increased locally and lead to dissolution at elastically loaded grain contacts where normal stresses resolved on quartz-fluid interfaces are greater than the mean fluid pressure within pores (Weyl, 1959; Kamb, 1961; Elliott, 1973; Paterson, 1973; deBoer, 1977a; Rusanov, 1978; Raj, 1982; Pharr and Ashby, 1983; Lehner and Bataille, 1984). Alternatively, dissolution may result from inelastic deformation if stresses at grain contacts are sufficient to introduce microcracks or dislocations, which increase local strain energies

EBSCOhost - printed on 2/13/2023 4:48 AM via . All use subject to https://www.ebsco.com/terms-of-use

(deBoer, 1977a; Wintsch and Dunning, 1985; Tada and Siever, 1986; Tada et al., 1987) or local dissolution rates (Brantley et al., 1986; Blum et al., 1990).

As dissolution proceeds at grain contacts, quartz may be precipitated at quartz-fluid interfaces subjected to low normal stresses. However, continued dissolution and precipitation require silica transport from sources to sinks by diffusion within connected intergranular fluid films. Solution transport may occur at the grain scale (Rutter, 1976, 1983; Robin, 1978), giving rise to grain impingement and overgrowth textures (e.g., Ernst and Blatt, 1963; Pittman, 1972; Elliott, 1973). At much larger scales. solution transport generates spaced cleavages, stylolites and veins (e.g., Lerbekmo and Platt, 1962; Fletcher and Pollard, 1981; Etheridge et al., 1984; Dewers and Ortoleva, 1989).

The rates of solution transfer creep may depend upon the kinetics of dissolution at grain contacts, precipitation at free surfaces, or diffusion of silica within intergranular fluid films. Assuming that creep rates are controlled by reaction rates at quartz-fluid interfaces (Raj, 1982; Pharr and Ashby, 1983), uniaxial strain rates $\dot{\varepsilon}$ may be expressed by

$$\dot{\varepsilon} = \beta \frac{(\sigma_1 - \sigma_3)}{d} \frac{k_i c \Omega}{RT} \tag{11}$$

where σ_1 and σ_3 are the maximum and minimum principal stresses applied (and $\sigma_1 - \sigma_3$ is commonly referred to as differential stress), d is the grain size, the product $k_i c$ represents the linear growth velocity of a crystal interface where k_i is a rate parameter for reaction at the quartz-fluid interface and c is the solubility of silica in the fluid, Ω is the molar volume of quartz, R is the gas constant, T is measured in K, and β is a numerical factor whose value depends on textural geometries and internal stress distributions. Reaction rates depend on temperature and k_i is given by

$$k_i = k_o \exp(-H/RT) \tag{12}$$

where k_o is a constant and H is an activation enthalpy. Similarly, rates of densification $\dot{\rho}$ by porosity reduction may be controlled by reaction kinetics, and expressions derived for compaction (e.g., Raj, 1982) exhibit a linear dependence of $\dot{\rho}$ upon the effective pressure P_e (or more generally upon an effective mean stress), much as uniaxial strain rates depend linearly upon differential stress (Eqn. 11). Densification rates $\dot{\rho}$ depend similarly upon silica solubility (c) and thermally activated reaction rates (k_i), and they show a reciprocal relationship with grain size (d).

Solution transfer creep may, alternatively, be controlled by diffusion of silica within intergranular fluid films (Elliott, 1973; Rutter, 1976, 1983; Raj, 1982; Pharr and Ashby, 1983), and uniaxial strain rates may be given by

$$\dot{\varepsilon} = \alpha \frac{(\sigma_1 - \sigma_3)}{d^3} \frac{c D_b \delta}{RT} \tag{13}$$

where D_b is the diffusion coefficient within intergranular fluid films of thickness δ, and α is constant for a given texture. Diffusion is thermally activated, and D_b varies with temperature as

$$D_b = D_o \exp(-H/RT) \tag{14}$$

where D_o is a constant and H is an activation enthalpy for diffusion. Rates of densification $\dot{\rho}$ may be controlled by diffusion, and expressions for $\dot{\rho}$ (Raj, 1982) are similar in form to (13) with linear dependences upon the effective pressure P_e (or mean stress),

EBSCOhost - printed on 2/13/2023 4:48 AM via . All use subject to https://www.ebsco.com/terms-of-use

diffusion coefficient D_b and silica solubility c, and a strong non-linear dependence on grain size ($1/d^3$).

Many of the processes leading to solution transfer creep have been documented in laboratory studies of fluid-saturated quartz aggregates, including dissolution (Renton et al., 1969; Sprunt and Nur, 1976, 1977; deBoer et al., 1977; Gratier and Guiguet, 1986; Elias and Hajash, 1992; Schutjens, 1991) and microcracking (Renton et al., 1969; deBoer et al., 1977; Schutjens, 1991) at grain contacts, precipitation within pores and development of quartz overgrowths (Ernst and Blatt, 1963; Sprunt and Nur, 1976, 1977; deBoer et al., 1977; Gratier and Guiguet, 1986; denBrok and Spiers, 1991), and net reductions in porosity (Ernst and Blatt, 1963; Sprunt and Nur, 1976, 1977; deBoer et al., 1977; Gratier and Guiguet, 1986; Elias and Hajash, 1992). Rates at which these processes occur depend strongly upon fluid chemistries (Ernst and Blatt, 1963; Renton et al., 1969; Gratier and Guiguet, 1986), and measurements of compaction rates demonstrate the effects of effective pressure and grain size (Renton et al., 1969; deBoer, 1977b; Schutjens, 1991; Elias and Hajash, 1992). Such effects generally are consistent with theoretical creep relationships (Raj, 1982), with a temperature dependence given by an activation enthalpy H of 61 to 76 kJ/mol (Schutjens, 1991). However, several discrepancies are apparent amongst the results of these experimental studies; in particular, reported functional dependencies of $\dot{\rho}$ upon fluid compositions, stress, inelastic strain, and grain size appear to differ, and there is little agreement on the rate-limiting processes. The kinetics of dissolution may control deformation rates over some conditions (Schutjens, 1991; Elias and Hajash, 1992), while rates of precipitation (Mullis, 1991, 1993), crack extension (Schutjens, 1991) or diffusion (Gratier and Guiguet, 1986; Gratz, 1991) may govern deformation rates at others. Rate-controlling mechanisms may depend on textures as well, particularly grain size (d) and irregularities in intergranular fluid films (e.g., Gratz, 1991). While aqueous fluids promote processes of dissolution, precipitation, and silica transport, they also accelerate rates of grain growth resulting in increased values of d (Tullis and Yund, 1982), which will tend to decrease creep rates (Eqns. 11 and 13) and possibly alter the rate-controlling mechanisms.

Thin fluid films between grains play several essential roles in all models of solution transfer creep. They provide channels of high diffusivity between the solute sources and sinks; yet at grain contacts, they must also transmit normal stresses that are locally higher than mean fluid pressures (e.g., Kamb, 1961; Elliott, 1973; Rutter, 1976, 1983; Robin, 1978; Raj, 1982). Rates of diffusion along quartz grain boundaries are rapid compared with diffusivities within the interiors of quartz grains (Farver and Yund, 1991b). However, diffusion coefficients within aqueous fluid films (several molecules in dimension) are still greater than those of grain boundaries by many orders of magnitude (Olejnik and White, 1972; Magda et al., 1985; Schoen et al., 1988). Significant rates of grain convergence have been observed only when thin fluid films are present between grains under load (Hickman and Evans, 1991, 1992; Hickman et al., 1993), and conditions that lead to the replacement of fluid films by grain boundaries cannot give rise to steady creep rates. Since interfacial energies in pure quartz aggregates favor grain boundaries at textural equilibrium to thin fluid films (Watson and Brenan, 1987; Lee et al., 1991; Holness, 1993), secondary solid phases such as layer silicates may be required for significant deformation by solution transfer creep (Hickman and Evans, 1991).

Intergranular fluid films must also sustain shear stresses that are associated with gradients in normal stresses at fluid-quartz interfaces if gradients in chemical potential are to be maintained (e.g., Robin, 1978; Rutter, 1983). Shear stresses may be supported by thin vicinal fluid films (< 10 molecules in dimension) if they possess ordered structures

EBSCOhost - printed on 2/13/2023 4:48 AM via . All use subject to https://www.ebsco.com/terms-of-use

(e.g., Peschel and Adlfinger, 1970; Horn et al., 1989; Israelachvili and Kott, 1989; Gee et al., 1990); thus, gradients in normal stress and chemical potential are likely to depend upon the dimensions and non-linear mechanical properties of thin fluid films.

Fluid compositions and interfacial hydrogen species may influence rates of solution transfer creep in several ways. If deformation is rate-limited by reaction kinetics, creep rates may be influenced by fluid compositions that alter silica solubilities (c) or reaction rates (k_i) (Eqn. 11). Rates of quartz dissolution are strongly affected by fluctuations in pH (Fig. 19) caused by variations in dissolved and interfacial hydrogen species (Lasaga, 1984; Blum and Lasaga, 1988; Brady and Walther, 1989, 1990, 1992; Casey and Sposito, 1992); greater numbers of $\equiv Si\text{-}OH_2^+$ groups populate quartz interfaces at low pH while greater numbers of $\equiv Si\text{-}O^-$ surface groups appear at high pH. Dissolution rates are substantially larger at higher values of pH, and they appear to exhibit a minimum (Brady and Walther, 1990, 1992; Casey and Sposito, 1992) for surfaces dominated by silanol $\equiv Si\text{-}OH$ groups at the pH of zero surface charge (pH ~ 2, Parks, 1984). Activation enthalpies of dissolution change systematically with pH, from H = 44 kJ/mol at pH = 4 to H = 97 kJ/mol at pH = 11 (Brady and Walther, 1990; Casey and Sposito, 1992), suggesting that the mechanisms by which silica dissolves change with the dominant surface species. Rates of quartz dissolution are also affected by ionic strengths of electrolyte solutions as a result of exchange reactions between surface protons and monovalent cations (Dove and Crerar, 1990; Gratz et al., 1990).

If solution transfer creep is rate-limited by diffusion, creep rates may depend on fluid composition through changes in silica solubility (c) and potential changes in diffusion coefficient (D_b) (Eqn. 13). Moreover, diffusional transport rates depend on the presence of intergranular fluid films, which at textural equilibrium are favored by low interfacial (quartz-fluid) energies relative to the energies of grain boundaries (Hickman and Evans, 1991, 1992; Hickman et al., 1993). Wide variations in wetting characteristics of fluids in contact with quartz have been observed for fluid compositions of varying $H_2O\text{-}CO_2$ compositions and electrolyte concentrations (Watson and Brenan, 1987; Lee et al., 1991; Holness, 1993). Bulk diffusivities of quartz aggregates, which depend on mobilities both along grain boundaries and quartz-fluid interfaces, increase markedly as grain textures become wetted (Farver and Yund, 1992).

Dislocation creep and water weakening

Molecular water clusters, fluid inclusions, and hydrogen defects within the interior of quartz may promote mechanisms of crystal plasticity through a variety of chemical and

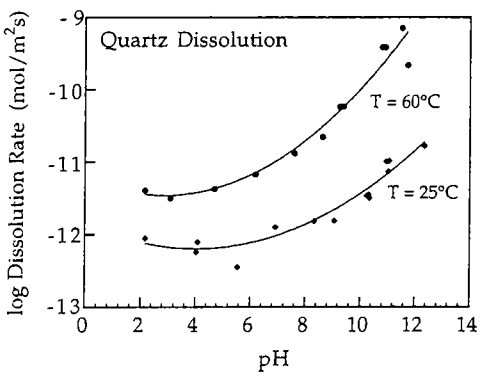


Figure 19. Dissolution rates for a clear natural quartz (from Hot Springs, Arkansas) as a function of solution pH (normalized to a common ionic strength of solution of 10^{-3} M) with a minimum, at a given temperature, near the pH of zero surface charge (pH ~ 2). Hydrogen species at the quartz-fluid interface that control dissolution rates may give rise to parallel trends for solution transfer creep with solution pH if creep rates are rate-limited by reaction kinetics (after Brady and Walther, 1990).

EBSCOhost - printed on 2/13/2023 4:48 AM via . All use subject to https://www.ebsco.com/terms-of-use

mechanical interactions with dislocations (e.g., Paterson, 1989). These may lead to pronounced reductions in ductile yield strengths. Fine-scale H_2O clusters and inclusions contribute to the nucleation of dislocations, and they may serve as internal reservoirs of water, which may exchange with hydrogen species that facilitate dislocation motion. Given that hydrogen species enter the cores of dislocations, rates of dislocation glide and climb may be accelerated through increases in the concentrations and mobilities of dislocation kinks and jogs. Recovery of dislocation substructures within grain interiors by dislocation climb and annihilation may be assisted by hydrogen point defects, which accelerate rates of oxygen and silicon diffusion. Reductions in dislocation density at grain margins due to dynamic recrystallization may be assisted by water at grain boundaries. Grain boundary constraints may be further relaxed if fluids within pores and at grain boundaries give rise to creep by solution transfer.

Within a few years of the identification of hydrogen defects in quartz (Brunner et al., 1961; Bambauer et al., 1962, 1963; Kats, 1962; Kats et al., 1962), Griggs and Blacic (1964, 1965) discovered that the ductile strengths of quartz single crystals may differ by over an order of magnitude depending upon their hydrogen contents. These researchers (Griggs and Blacic, 1965; Griggs, 1967; Blacic, 1975) assumed that dangling bonds within the cores of dislocations are satisfied by hydrogen defects and that hydrolysis of Si-O bonds near advancing dislocations could reduce the energy barrier to dislocation glide. This proposed mechanism of hydrolytic weakening stimulated numerous investigations of quartz and other silicates deformed under hydrothermal conditions; yet, this model continues to be debated, and several alternative hypotheses have since been offered. Experimental evidence of water weakening in quartz comes from comparisons of compressive strengths of dry and wet single crystals with majority hydrogen defects characterized by IR spectroscopy, and also from comparisons of the strengths of polycrystalline quartz aggregates deformed in the presence and in the absence of water. While clear advances have been made in the correlation of mechanical properties of quartz with majority hydrogen species present, no single mechanism of chemical weakening is supported by all of the experimental results. Thus, internal hydrogen species may play multiple roles in the deformation of quartz.

Single crystals. Clear vug-grown quartz crystals with sharp IR absorption bands due to trace concentrations of hydrogen interstitials are mechanically strong. Dry natural single crystals fail by fracture at confining pressures appropriate to the crust (Fig. 20), and they yield only at high confining pressures ($P_c > 1000$ MPa) with the onset of limited basal (001) ⟨110⟩ slip at differential stresses (> 2000 MPa at $T < 900°C$ and $\dot{\varepsilon} = 10^{-5}s^{-1}$) that approach theoretical limits for uniform shear failure (Christie et al., 1964a,b; Griggs, 1967; McLaren et al., 1967; Heard and Carter, 1968; Blacic, 1975; Christie and Ardell, 1976; Blacic and Christie, 1984; Doukhan and Trepied, 1985; Kronenberg et al., 1986).

In contrast, quartz crystals that display broad IR absorption bands associated with non-freezable molecular water clusters are weak. Rapidly grown synthetic quartz crystals with large absorption bands at ~3400 cm^{-1} yield at differential stresses (< 200 MPa) well below those exhibited by natural clear crystals under the same conditions (Fig. 20). Dislocation glide is readily activated on the prismatic slip systems {110} ⟨001⟩ and {100} ⟨010⟩ and several other secondary systems (Griggs and Blacic, 1965; Baeta and Ashbee, 1967, 1969a,b, 1970a,b; Griggs, 1967; McLaren and Retchford, 1969; McLaren et al., 1970; Hobbs et al., 1972; Balderman, 1974; Twiss, 1974, 1976; Blacic, 1975; Morrison-Smith et al., 1976; Ayensu and Ashbee, 1977; Kirby, 1977; Kekulawala et al., 1978, 1981; Ball and Glover, 1979; Kirby and McCormick, 1979; Linker and Kirby,

EBSCOhost - printed on 2/13/2023 4:48 AM via . All use subject to https://www.ebsco.com/terms-of-use

1981; Blacic and Christie, 1984; Linker et al., 1984; Doukhan and Trepied, 1985; Boulogne et al., 1988a,b; Cordier et al., 1988; Cordier and Doukhan, 1989). Amethyst single crystals with nm-scale clusters of molecular water have strengths comparable to those of wet synthetic quartz (Kekulawala et al., 1978), while milky quartz crystals with freezable, optical-scale fluid inclusions exhibit somewhat higher yield strengths (Kekulawala et al., 1978). As shown in Figure 20, wet synthetic quartz and amethyst crystals exhibit increased yield strengths if they are annealed prior to deformation at conditions that favor the replacement of non-freezable water clusters by freezable fluid inclusions (Kekulawala et al., 1978, 1981; Paterson and Kekulawala, 1979). By contrast,

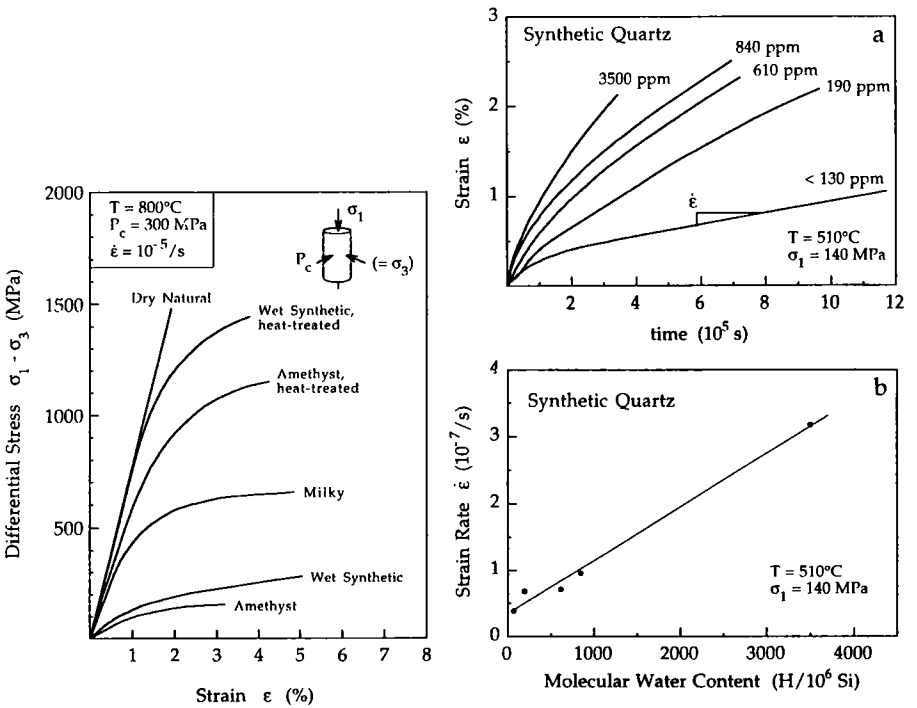


Figure 20 (left). Differential stress (σ_1 - σ_3)-strain (ε) response of quartz single crystals with varying water contents (and internal H_2O distributions) shortened perpendicular to *m* (100) at T = 800°C in triaxial compression experiments ($\sigma_1 > \sigma_3$, $P_C = \sigma_3 = 300$ MPa) at a constant strain rate $\dot{\varepsilon} = 10^{-5}$/s. Dry natural single crystals exhibit linear elastic behavior until failure at large differential stresses, while rapidly grown synthetic quartz and amethyst exhibit ductile yielding at low stresses. Milky quartz crystals exhibit yielding at intermediate differential stresses, while single crystals of synthetic quartz and amethyst that have been heat-treated prior to deformation (at T = 900°C for 49 and 17 hours, respectively) exhibit yielding at intermediate to high differential stresses (after Kekulawala et al., 1978).

Figure 21 (right). Mechanical response of synthetic quartz single crystals with varying water contents (from < 130 to 3500 ppm H/10^6Si) shortened perpendicular to *m* (100) at T = 510°C and constant stress (σ_1 = 140 MPa) in uniaxial compression experiments ($P_C = \sigma_3 = 0$; experiments LC-75, LC-73, LC-74, LC-45, and LC-69 performed on specimens prepared from crystals X-0, X-41, X-507veil, X-507, and X-125 with water contents of 3500, 840, 610, 190, and < 130 ppm, respectively). (a) Creep strain-time data exhibit systematic increases in transient strain rates (at constant stress) with molecular water content (as determined from absorption intensities at 3400 cm^{-1} and 5200 cm^{-1}). (b) Maximum strain rates prior to strain hardening scale with water content (courtesy of M.F. Linker and S.H. Kirby).

EBSCOhost - printed on 2/13/2023 4:48 AM via . All use subject to https://www.ebsco.com/terms-of-use

dry natural quartz crystals can be weakened by the introduction of fluid inclusions (Griggs and Blacic, 1965; Mackwell and Paterson, 1985; Ord and Hobbs, 1986), through processes involving crack extension and healing prior to deformation (Kronenberg et al., 1986; Fitzgerald et al., 1991).

The low strengths of rapidly grown synthetic quartz crystals correlate directly with their broad OH absorption bands (Kekulawala et al., 1978, 1981) that are assigned to molecular water clusters (Aines et al., 1984; Gerretsen, 1988). Strain rates measured for synthetic quartz crystals for a given differential stress (Linker and Kirby, 1981; and unpublished results) vary systematically with molecular water content (Fig. 21, above), as determined from absorption intensities at 3400 and 5200 cm^{-1}. Moreover, the transient mechanical response of synthetic quartz depends on inclusion coarsening and changes in inclusion distribution. Decreases in stress beyond the yield point for crystals loaded at constant strain rates are more subdued at elevated confining pressures (e.g., Baeta and Ashbee, 1970a; Hobbs et al., 1972; Balderman, 1974; Kekulawala et al., 1981; Linker and Kirby, 1981) due to a lowered rate of fluid inclusion coarsening with pressure (Baeta and Ashbee, 1973; Kekulawala et al., 1978, 1981; Kirby and McCormick, 1979; McLaren et al., 1983, 1989; Cordier and Doukhan, 1989, 1991; Paterson, 1989).

Strain rates ($\dot{\varepsilon}$) resulting from the glide of dislocations depend upon the densities (ρ) of mobile dislocations, their glide velocities (v_g), and the magnitude of their Burgers vector (b), as given by the Taylor-Orowan relation

$$\dot{\varepsilon} = \rho\, v_g\, b \ . \tag{15}$$

Changes in the mechanical response of synthetic quartz crystals at low strains can be explained by increases in dislocation densities (ρ) with time; strain rates measured during constant stress experiments (and stresses measured during constant $\dot{\varepsilon}$ experiments) have been matched successfully by models of dislocation multiplication and observed increases in ρ (Hobbs et al., 1972; Griggs, 1974; Kirby and McCormick, 1979; Linker et al., 1984). Stress concentrations in quartz surrounding H_2O clusters and inclusions may serve to nucleate dislocations, and McLaren et al. (1989) and Gerretsen et al. (1989) have suggested that stress-induced processes of nucleation and growth of prismatic dislocation loops at inclusions increase dislocation densities, particularly during inclusion coarsening, and that increased dislocation densities may explain the low yield strengths of synthetic quartz. However, chemical interactions that lead to increased rates of dislocation glide and climb appear to be important as well. While nucleation of dislocations may be required for deformation of quartz crystals with low initial densities of structural flaws, dislocation densities present in quartzites are commonly large at the onset of deformation; yet, quartzites are resistant to creep, and they exhibit high compressive strengths at low water pressures (e.g., Heard and Carter, 1968; Mainprice and Paterson, 1984). Once dislocations are nucleated, dislocation substructures that develop in relatively dry quartz single crystals and quartzites deformed without added H_2Oreveal processes of work-hardening, whereas substructures of wet quartz crystals and quartzites deformed with added H_2O exhibit recovery textures with evidence of dislocation climb and recrystallization (e.g., Carter et al., 1964; Hobbs, 1968; McLaren and Retchford, 1969; Green et al., 1970; Baeta and Ashbee, 1973; Trepied and Doukhan, 1982; Koch et al., 1989; Tullis and Yund, 1989; Hirth and Tullis, 1992; Gleason et al., 1993).

Dislocation glide velocities (v_g) may be increased if hydrogen species increase either the concentrations or mobilities of dislocation kinks (Griggs, 1967, 1974; Hirsch, 1979, 1981; Hobbs, 1981, 1984, 1985; Heggie and Jones, 1986). The original hypothesis of Griggs, Blacic, and Frank (Griggs and Blacic, 1965; Griggs, 1967, 1974) involved hydrolysis reactions between H_2O and the dangling bonds of edge dislocations (Fig. 22),

EBSCOhost - printed on 2/13/2023 4:48 AM via . All use subject to https://www.ebsco.com/terms-of-use

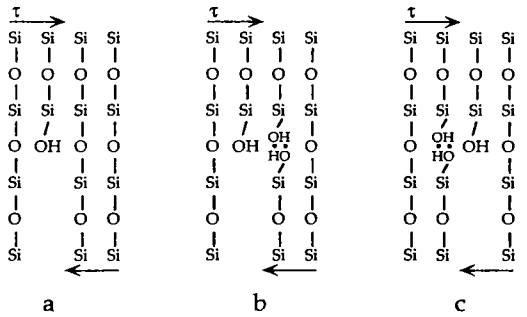


Figure 22. Hydrolytic weakening mechanism proposed by Griggs, Blacic, and Frank (Griggs, 1967; Blacic, 1975) involving (a) silanols (or other hydrogen species) within dislocation cores that replace distorted siloxanes; (b) hydrolysis reactions in the neighborhood of an advancing edge dislocation that replace strong ≡ Si-O-Si ≡ bridges by hydrogen-bonded silanols ≡ Si-O-H ··· H-O-Si ≡ ; and (c) promotion of dislocation glide (after Griggs, 1967).

similar to those that occur at crack tips, to form weak hydrogen-bonded silanols. Water was originally thought to enter dislocation cores by diffusive transport of hydrogen point defects from the surrounding quartz structure (Griggs, 1967; Blacic, 1975, 1981) and to reach dislocation kinks by a combination of volume diffusion and pipe diffusion (Griggs, 1974). Hydrolysis reactions of the type proposed by Griggs and Blacic (1965) appear to be supported by recent modeling efforts (Heggie and Jones, 1987). However, formation energies of dislocation kinks may be influenced by ($4H_i + V_{Si}$) defects as well as by H_2O defects (Heggie and Jones, 1986), and revisions to the original models of H_2O transport are required if solubilities of all hydrogen point defects other than hydrogen interstitials are very small (Doukhan and Paterson, 1986; Kronenberg et al., 1986; Paterson, 1986; Cordier and Doukhan, 1989, 1991; Gerretsen et al., 1989). Most of the molecular water of synthetic quartz crystals occurs as aggregated clusters and inclusions (Aines et al., 1984; Gerretsen, 1988, Gerretsen et al., 1989). Much of the H_2O at dislocation kinks is supplied by fluid inclusions that intersect the dislocations, and it may be transported by pipe diffusion (Fig. 23) (McLaren et al., 1983; Cordier et al., 1988; Gerretsen, 1988). Thus, milky quartz single crystals with water contents similar to those of synthetic quartz crystals are stronger, perhaps because fluid inclusions within them are coarse and widely spaced, and transport by pipe diffusion must proceed over greater distances.

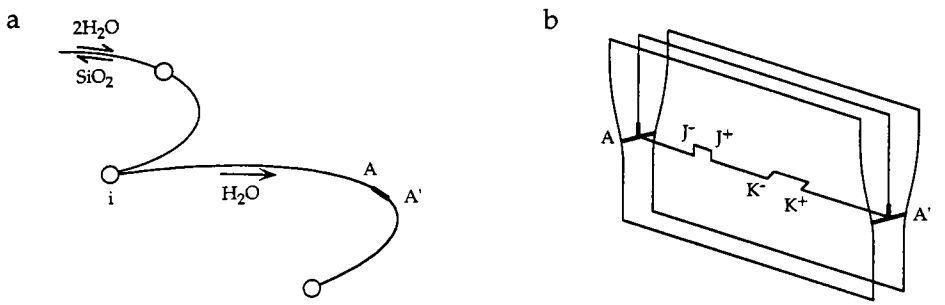


Figure 23. Transport of H_2O (or other reactive hydrogen species) and Si and O defects by pipe diffusion. Rates of dislocation glide may depend upon (a) delivery of H_2O by pipe diffusion from fluid inclusions (i) to advancing segments (A—A') of dislocations where hydrolysis (or other reactions) increase the concentrations of (b) dislocation kinks, K^+ and K^- (unit cell offsets within the glide plane, of positive and negative sign) and/or increase their mobilities. Dislocation climb may depend similarly upon exchange of H_2O and SiO_2 by pipe diffusion between fluid inclusions and dislocation jogs, J^+ and J^- (unit cell steps in the edge of the dislocation half plane) where the loss or gain of SiO_2 may be promoted by the counter-flux of H_2O, resulting in the increase of jog concentrations and mobilities.

EBSCOhost - printed on 2/13/2023 4:48 AM via . All use subject to https://www.ebsco.com/terms-of-use

If hydrolysis reactions (Eqn. 5) replace strong Si-O bonds near advancing dislocations with hydrogen-bonded silanols SiOH, energy barriers that inhibit breaking and rearranging bonds during glide can be reduced. However, variations in the strength of quartz are observed at hydrogen contents much greater than are needed to saturate dislocation cores (1 to 2 ppm H/10^6 Si for $\rho = 10^7$ mm^{-2}; Griggs, 1967, 1974). Thus, hydrogen defects at dislocations represent only a small fraction of hydrogen species within the quartz interior that may be resupplied as dislocations move. The rate-controlling step offered by the Griggs-Blacic-Frank model for quartz deformation involves the transport of H_2O to dislocation kinks. Creep rates ($\dot{\varepsilon}$) of synthetic quartz crystals are thermally activated, given by

$$\dot{\varepsilon} = A\ (\sigma_1 - \sigma_3)^n \exp(-H/RT) \qquad (16)$$

where A and n are material parameters and the activation enthalpy H takes on values ranging from 69 to 213 kJ/mol for α-quartz and 88 to 192 kJ/mol for β-quartz, depending on the slip systems activated (Baeta and Ashbee, 1970b; Balderman, 1974; Ayensu and Ashbee, 1977; Kirby and McCormick, 1979; Linker and Kirby, 1981; Linker et al., 1984). Variations in the activation barrier associated with different slip systems and structures between α- and β-quartz suggest that thermal barriers to glide may involve dislocation kink motions once hydrolysis reactions have occurred. Alternatively, if transport is rate-controlling, variations in activation enthalpies may reflect differences in the energetics of H_2O pipe diffusion due to dislocations having different orientations and Burgers vectors (Linker and Kirby, 1981; Linker et al., 1984).

Once significant strains (>1-2%) are achieved and dislocation densities are increased, dislocation glide velocities may be limited by obstacles within the glide plane, and mean values of v_g may depend upon rates of dislocation climb and recovery (Hobbs, 1968, 1981, 1984, 1985; McLaren and Retchford, 1969; Baeta and Ashbee, 1973; Doukhan and Trepied, 1985). Just as mobilities of dislocation kinks may be increased by the introduction of hydrogen defects along dislocations, dislocation jogs may have higher concentrations and mobilities as well. However, in addition to the delivery of H_2O (or other reactive hydrogen species) to jogs, dislocation climb requires the removal (or addition) of SiO_2 at jogs and pipe diffusion of silicon and oxygen defects (Fig. 23).

Recent measurements of diffusion rates in quartz (e.g., Dennis, 1984; Giletti and Yund, 1984; Cordier et al., 1988; Farver and Yund, 1991a) indicate that H_2O transport is slow relative to proton transport (e.g., Kats et al., 1962), in support of the original premise of the Griggs-Blacic-Frank model that rates of diffusive transport control creep rates. However, competing models of hydrolytic weakening (Hirsch, 1979, 1981; Hobbs, 1981, 1984, 1985) have been proposed in which changes in the concentrations of dislocation kinks [K] and jogs [J] do not require local hydrolysis reactions, but depend instead on relationships between [K] and [J] and populations of distributed point defects, which may be altered by the introduction of hydrogen species. If so, chemical weakening of quartz must depend upon trace, minority hydrogen species such as interstitial water $(H_2O)_i$ or H_4O_4 clusters, since concentrations of majority species, hydrogen interstitials H_i, have no measurable effect on strength (Kekulawala et al., 1981; Kronenberg et al., 1986). Moreover, equilibrium populations of dislocation kinks and jogs and distributed point defects cannot be achieved throughout quartz crystals of macroscopic dimensions in laboratory times (Paterson, 1989), since they depend on diffusive transport. Thus, while the definitive experiments to distinguish between these models of water weakening have yet to be performed, rates at which hydrogen species are transported are critical and are likely to control rates of dislocation glide and climb.

EBSCOhost - printed on 2/13/2023 4:48 AM via . All use subject to https://www.ebsco.com/terms-of-use

Polycrystalline quartz aggregates. In quartzites, intragranular hydrogen species may influence dislocation creep by the same mechanisms that weaken quartz single crystals, while fluids at grain boundaries promote recrystallization and solution transfer processes. Compressive strengths of quartzites vary systematically over an order of magnitude with the amount of water available during deformation; quartzites deformed in the presence of water (~0.1 to 0.4% by weight) are weak (Parrish et al., 1976; Jaoul et al., 1984; Kronenberg and Tullis, 1984; Koch et al., 1989; den Brok and Spiers, 1991; den Brok, 1992; Hirth and Tullis, 1992; Post and Tullis, 1993), while quartzites deformed without added water, but with their original intragranular water contents (ranging from 600 to 4000 ppm H/10^6Si) have intermediate strengths (Heard and Carter, 1968; Parrish et al., 1976; Tullis et al., 1979; Ross et al., 1983; Jaoul et al., 1984; Kronenberg and Tullis, 1984; Mainprice and Paterson, 1984; Koch et al., 1989; Hirth and Tullis, 1992; Kronenberg and Wolf, 1990), and quartzites that were vacuum-dried at elevated temperatures prior to deformation are strong (Jaoul et al., 1984; Kronenberg and Tullis, 1984). Much as in dry single crystals of quartz, dislocations in quartzites that are deformed without added water (at a given $T \leq 800°C$ and $\dot{\varepsilon} = 10^{-5}$ to 10^{-6}/s) are distributed heterogeneously, and slip on planes other than (001) appears to be limited. In addition, dislocation substructures reflect low rates of recovery (e.g., Heard and Carter, 1968; Jaoul et al., 1984; Kronenberg and Tullis, 1984; Mainprice and Paterson, 1984; Koch et al., 1989; Tullis and Yund, 1989; Hirth and Tullis, 1992). In contrast, quartzites deformed in the presence of water exhibit homogenous densities of prismatic and basal dislocations and organized dislocation configurations that result from climb and recovery. Activation enthalpies associated with deformation of vacuum-dried quartzites are large (H = 300 kJ/mol, Kronenberg and Tullis, 1984), whereas values of H determined for quartzites deformed in the presence of water (H = 120 to 148 kJ/mol, e.g., Jaoul et al., 1984; Kronenberg and Tullis, 1984; Koch et al., 1989) are comparable to those determined for dislocation creep in wet synthetic quartz crystals.

Intragranular water contents of quartzites are comparable to those of rapidly grown synthetic quartz; however, several observations suggest that direct comparisons of their mechanical properties may not be appropriate. IR spectra of individual grains of quartzites resemble those of milky quartz crystals, with broad absorption bands at ~3400 cm^{-1} that shift to ~3200 cm^{-1} at low temperatures, unlike the broad absorptions of synthetic quartz (Mainprice and Paterson, 1984; Koch et al., 1989; Kronenberg and Wolf, 1990; den Brok, 1992; den Brok et al., 1994). Moreover, optical and TEM observations of quartzites reveal fluid inclusions of widely varying sizes (e.g., Mainprice and Paterson, 1984; Koch et al., 1989), much as in milky quartz, without any clear evidence of non-freezable H_2O clusters. As indicated by the spectral differences between quartzites and synthetic quartz crystals, quartzites are strong at low confining pressures P_c and exhibit water weakening only at high P_c (Heard and Carter, 1968; Tullis et al., 1979; Mainprice and Paterson, 1984; Kronenberg and Tullis, 1984), whereas synthetic quartz crystals with non-freezable H_2O clusters exhibit low strengths at atmospheric pressure. Elevated water pressures (P_{H2O}) may increase the solubilities of hydrogen species in quartz, and the low strengths of quartzites deformed at high P_{H2O} have been thought to result from diffusional uptake of the same hydrogen species as are initially present in wet synthetic quartz. However, recent IR studies of quartzites deformed at high pressures in the presence and absence of water (Kronenberg and Wolf, 1990; den Brok, 1992; den Brok et al., 1994) have failed to detect changes in either water content or in the predominent hydrogen species within grain interiors.

While the microstructures of quartzites deformed in the presence of water provide evidence for intragranular deformation by dislocation creep (Carter et al., 1964; Koch et

EBSCOhost - printed on 2/13/2023 4:48 AM via . All use subject to https://www.ebsco.com/terms-of-use

al., 1989; Tullis and Yund, 1989; Hirth and Tullis, 1992; Gleason and Tullis, 1994), den Brok and Spiers (1991) and den Brok et al. (1994) have suggested that solution transfer processes assisted by intergranular fluids may contribute to water weakening. Rheologies associated with dislocation creep are generally nonlinear with stress exponents $n \geq 3$ (Eqn. 16), whereas rheologies associated with solution transfer processes exhibit more nearly linear viscous behavior with values of $n = 1$ (Eqns. 11 or 13). Quartzites deformed at elevated pressures without added water exhibit values of n ranging from 3.0 to 6.5 (e.g., Heard and Carter, 1968; Parrish et al., 1976; Kronenberg and Tullis, 1984; Gleason and Tullis, 1994), consistent with models of dislocation creep. However, quartzites deformed in the presence of intergranular fluids exhibit values of n between 1 and 3 (e.g., $1.3 \leq n \leq 2.7$, Parrish et al., 1976; Jaoul et al., 1984; Kronenberg and Tullis, 1984; Koch et al., 1989; den Brok and Spiers, 1991), which may reflect varying amounts of intragranular fluid present during deformation and varying contributions from dislocation and solution transfer processes to deformation.

Molecular water contents within the grain interiors of coarse-grained (~100 to 200 μm) quartzites may not readily be altered, given the rates of oxygen volume diffusion (e.g., Dennis, 1984; Giletti and Yund, 1984; Farver and Yund, 1991a) or pipe diffusion (McLaren et al., 1983; Cordier et al., 1988), and equilibrium with intergranular fluids may not be achieved over experimental time scales. However, water contents may be increased at grain margins where water-assisted dislocation creep may satisfy inhomogeneous strains imposed by neighboring quartz grains and allow for homogeneous deformation by dislocation glide within grain interiors without altering water contents. Homogeneous hydrogen defect populations in equilibrium with intergranular fluids may be achieved only in fine-grained quartz aggregates with grain dimensions that are less than characteristic diffusion distances (several μm for oxygen transport). Thus, water-weakening of polycrystalline quartz aggregates with equilibrium concentrations of hydrogen species may be examined only by experiments performed on fine-grained synthetic quartz aggregates, flints, and novaculites (Mainprice, 1981; Kronenberg and Tullis, 1984; Paterson and Luan, 1990; Luan and Paterson, 1992).

Dislocation glide and climb in fine-grained synthetic quartz aggregates (prepared from silica gel or silicic acid), in natural flints with large initial water contents (Mainprice, 1981; Paterson and Luan, 1990; Luan and Paterson, 1992), and in novaculites deformed in the presence of water (Kronenberg and Tullis, 1984; Gleason et al., 1993) may be influenced by internal hydrogen species, as observed in synthetic quartz single crystals. Strengths exhibited by these fine-grained quartz aggregates are uniformly low, and creep activation enthalpies ($H = 110$ to 150 kJ/mol) compare favorably with those of wet synthetic quartz. Rates of dislocation glide and climb may be controlled by the transport of H_2O, silicon, and oxygen defects along dislocations by pipe diffusion. However, fluid films at grain boundaries of fine-grained quartz aggregates may serve as sources of H_2O, so that grain size in association with transport distances between dislocation kinks and grain boundaries may affect strength. Fluid films may also assist solution transfer processes; contributions to deformation by these mechanisms may lead to additional grain size effects on creep strength (as described by either Eqns. 11 or 13), and they may produce low values for the stress exponent n (e.g., $n = 2.3$ for gel-origin synthetic quartz aggregates, Luan and Paterson, 1992; $n = 2.5$ for novaculite deformed in the presence of water, Kronenberg and Tullis, 1984).

Given that the solubilities of molecular water and other hydrogen species (such as H_4O_4) may increase with the fugacity of H_2O (Doukhan and Paterson, 1986; Paterson, 1986; Cordier and Doukhan, 1989; Farver and Yund, 1991a), reductions in strength as a

EBSCOhost - printed on 2/13/2023 4:48 AM via . All use subject to https://www.ebsco.com/terms-of-use

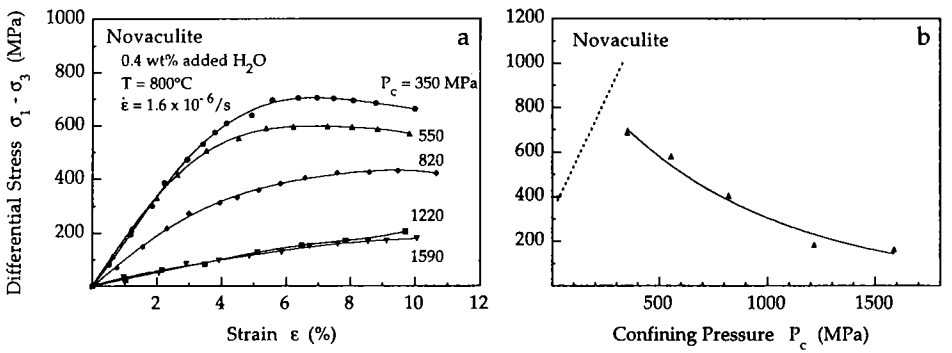


Figure 24. Water weakening of fine-grained quartz aggregates (Arkansas novaculites with grain sizes of 3.6 to 4.9 μm) deformed in the presence of H_2O at confining pressures P_C from 350 to 1590 MPa. The ductile strengths of polycrystalline quartz aggregates appear to depend on P_{H_2O} (or f_{H_2O}) with pronounced reductions in strength at high P_{H_2O}, as revealed by (a) differential stress-strain curves of novaculites deformed at T = 800°C and a constant strain rate $\dot{\varepsilon}$ = 1.6 x 10^{-6}/s. (b) Ductile strengths of novaculites, recast as σ_1 - σ_3 (measured at a strain ε of 10%, or choosing maximum values of σ_1 - σ_3 for samples that soften with strain) versus P_C (dashed line represents Mohr-Coulomb criterion for brittle failure, after Kronenberg and Tullis, 1984).

function of confining pressure for fine-grained quartz aggregates (Fig. 24) that were deformed in the presence of water (Kronenberg and Tullis, 1984) may reflect changes in hydrogen species that assist dislocation creep with increasing f_{H2O}. As in synthetic quartz, the hydrogen species responsible for chemical weakening may be restricted to dislocation cores, hydrolysing bonds locally. Alternatively, hydrogen species may occur as distributed point defects, altering local concentrations and mobilities of dislocation kinks and jogs. Depending upon the mechanism of water weakening and the types of point defects that influence dislocation creep (Hirsch, 1979, 1981; Hobbs, 1981, 1984, 1985), creep rates may also depend on the fugacity of oxygen f_{O2}, and the pre-exponential parameter A of Equation (16) may be given by some function $A = B\ (f_{H2O})^p\ (f_{O2})^q$ where B, p, and q are constants that depend on the point defect populations of quartz. However, significant changes in the rates of solution transfer creep may also be expected with changes in silica solubility of the intergranular fluid at elevated water pressures. Thus, the relative contributions of dislocation creep and solution transfer creep will need to be examined before the effects of f_{H2O} and f_{O2} on dislocation creep can be quantified.

While very high water pressures (or high f_{H2O} > ~1000 MPa) appear to be required for water weakening of polycrystalline quartz aggregates at experimental strain rates, greenschist facies conditions appear to be sufficient for water weakening of quartz tectonites deformed at geologic strain rates. Aqueous fluids may preferentially infiltrate the crust along shear zones (e.g., Fricke et al., 1992) and lead to strain localization (e.g., Kronenberg et al., 1990). Populations of fluid inclusions within crustal shear zones are observed to change with the introduction of deformation microstructures associated with microcrack extension and healing, dislocation creep, and recrystallization (Kerrich, 1976; Wilkins and Barkas, 1978; Passchier, 1984). While fluid inclusions observed at the optical scale commonly define the traces of healed microcracks, TEM observations of naturally deformed quartz reveal nm-scale fluid inclusions (McLaren and Hobbs, 1972; White, 1973; Christie and Ord, 1980; Ord and Christie, 1984; Stenina et al., 1984;

EBSCOhost - printed on 2/13/2023 4:48 AM via . All use subject to https://www.ebsco.com/terms-of-use

Kronenberg et al., 1990) that decorate dislocations (Fig. 25) and closely resemble inclusions in experimentally deformed synthetic quartz and quartzites deformed at high P_{H2O}.

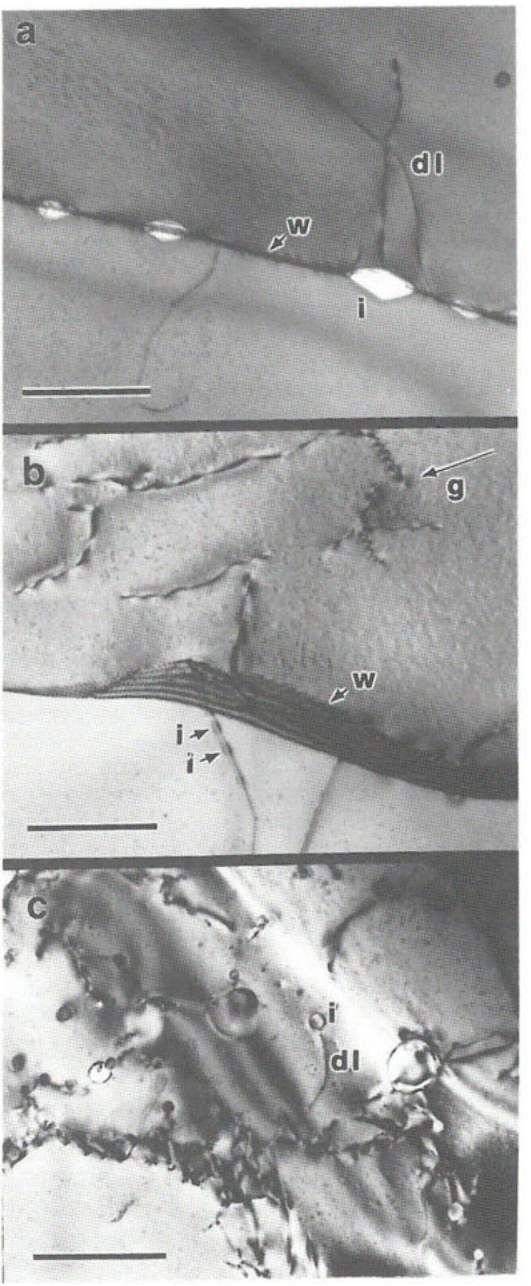


Figure 25. Transmission electron micrographs of fine-scale fluid inclusions (i) and dislocations (dl) of quartz grains (within a natural granodiorite shear zone of the Sierra Nevada, California) deformed at greenschist facies conditions (scale bars represent 0.5 μm).

(a) Fluid inclusions and subgrain walls (w) decorate the trace of a healed microcrack.

(b) Fluid inclusions (i) along dislocation that terminates within subgrain wall (w) (g = 011).

(c) Densely distributed fluid inclusions within quartz grains near center of shear zone are commonly found to intersect with dislocations (after Kronenberg et al., 1990).

EBSCOhost - printed on 2/13/2023 4:48 AM via . All use subject to https://www.ebsco.com/terms-of-use

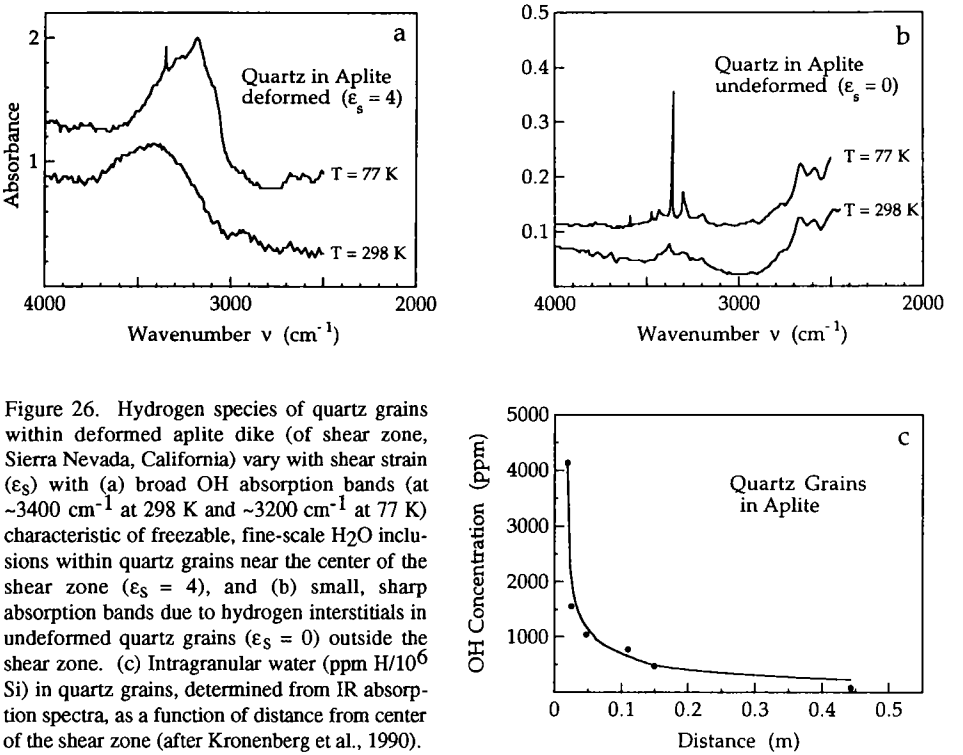


Figure 26. Hydrogen species of quartz grains within deformed aplite dike (of shear zone, Sierra Nevada, California) vary with shear strain (ε_S) with (a) broad OH absorption bands (at ~3400 cm^{-1} at 298 K and ~3200 cm^{-1} at 77 K) characteristic of freezable, fine-scale H_2O inclusions within quartz grains near the center of the shear zone (ε_S = 4), and (b) small, sharp absorption bands due to hydrogen interstitials in undeformed quartz grains (ε_S = 0) outside the shear zone. (c) Intragranular water (ppm H/10^6 Si) in quartz grains, determined from IR absorption spectra, as a function of distance from center of the shear zone (after Kronenberg et al., 1990).

Broad OH absorption bands of quartz grains within naturally deformed shear zones (Fig. 26) resemble those of milky quartz with intragranular water contents that may reach ~2000 to 10,000 ppm (H/10^6 Si) (Kronenberg and Wolf, 1990; Kronenberg et al., 1990; Nakashima et al., 1994). Given that hydrogen point defects such as interstitial molecular water or H_4O_4 substitutions for silica tetrahedra may have solubilities no greater than ~20 ppm under greenschist conditions (Doukhan and Paterson, 1986; Kronenberg et al., 1986; Paterson, 1986; Cordier and Doukhan, 1989, 1991; Gerretsen et al., 1989), most of the H_2O presently within fluid inclusions must have been incorporated as aggregated H_2O at the time of deformation, and only small fractions could have been dissolved within the quartz structure. Water contents associated with fluid inclusions of quartz grains deformed by dislocation creep may vary systematically across shear zones (Kronenberg et al., 1990; Nakashima et al., 1994) and correlate with localized shear strains. Thus, dislocation glide and climb in naturally deformed quartz appear to be assisted by aggregated forms of H_2O, much as in experimentally deformed quartz, and mechanisms of water weakening may involve delivery of H_2O by pipe diffusion and chemical interactions between H_2O and the dangling and distorted bonds of dislocation kinks and jogs.

SUMMARY REMARKS

Quartz is populated by a wide variety of hydrogen species that influence its physical and chemical properties. As a framework silicate with strong Si-O bonds arranged in a fully linked three-dimensional network, quartz may be expected to be strong and refractory, an expectation that is satisfied by the properties of dry quartz deformed under

EBSCOhost - printed on 2/13/2023 4:48 AM via . All use subject to https://www.ebsco.com/terms-of-use

anhydrous conditions. However, hydrogen species at the surfaces and interior of quartz serve to interrupt its strong Si-O-Si network and assist processes of inelastic deformation that depend on breaking bonds, ranging from crack growth and frictional sliding to solution transfer and dislocation creep. As a result, deformation of quartz is possible at the relatively low temperatures encountered in the Earth's crust.

The hydrogen species of quartz and their effects on mechanical properties have been studied extensively with the view that mechanisms of water weakening in quartz may also serve to weaken other silicates. In spite of these efforts, we still have much to discover regarding the critical hydrogen species that influence deformation and the mechanisms by which quartz is weakened.

ACKNOWLEDGMENTS

Many thanks go to G. Rossman for generously providing high quality IR spectra for a wide range of quartz crystals, to P. Cordier for providing fine electron micrographs of synthetic quartz illustrating processes of inclusion coarsening, and to M. Linker and S. Kirby for permission to use some of their exceptional, unpublished creep results for synthetic quartz. I am grateful to O. Kwon for efficiently crafting figures, serving as my software expert, and for dependably being my right-hand man. I am indebted to A. Raymond for her love and for putting up with me over the last few months. This review has benefitted from constructive comments of J. Tullis, G. Rossman, A. Post, and N. Carter as well as discussions over the years with many of my colleagues; in particular, I thank R. Aines, J. Blacic, N. Carter, J. Christie, P. Cordier, W. Durham, J. Farver, J. Fitzgerald, H. Green, B. Herbert, S. Hickman, B. Hobbs, O. Jaoul, S. Kirby, D. Kohlstedt, W. Lamb, M. Linker, S. Mackwell, D. Mainprice, S. Nakashima, A. Ord, M. Paterson, G. Rossman, M. Rovetta, P. Segall, J. Tullis, T. Tullis, G. Wolf, and R. Yund.

REFERENCES

Aines RD, Rossman GR (1984a) Water in minerals? a peak in the infrared. J Geophys Res 89:4059-4071

Aines RD, Rossman GR (1984b) The hydrous component in garnets: pyralspites. Am Min 69:1116-1126

Aines RD, Rossman GR (1985) The high temperature behavior of trace hydrous components in silicate minerals. Am Min 70:1169-1179

Aines RD, Kirby SH, Rossman GR (1984) Hydrogen speciation in synthetic quartz. Phys Chem Min 11:204-212

Alpert NL, Keiser WE, Szymanski HA (1970) IR Theory and Practice of Infrared Spectroscopy. Plenum, New York

Anderson JH (1965) Calorimetric vs infrared measures of adsorption bond strengths on silica. Surface Sci 3:290-291

Anderson JH, Parks GA (1968) The electrical conductivity of silica gel in the presence of adsorbed water. J Phys Chem 72:3662-3668

Anderson JH, Wickersheim KA (1964) Near infrared characterization of water and hydroxyl groups on silica surfaces. Surface Sci 2:252-260

Atkinson BK (1979) A fracture mechanics study of subcritical tensile cracking of quartz in wet environments. Pure Appl Geophys 117:1011-1024

Atkinson BK (1984) Subcritical crack growth in geological materials. J Geophys Res 89:4077-4114

Atkinson BK, Meredith PG (1981) Stress corrosion cracking of quartz: a note on the influence of chemical environment. Tectonophysics 77:T1-T11

Atkinson BK, Meredith PG (1987a) The theory of subcritical crack growth with applications to minerals and rocks. In Atkinson BK (ed) Fracture Mechanics of Rock, Academic Press, London, p 111-166

Atkinson BK, Meredith PG (1987b) Experimental fracture mechanics data for rocks and minerals. In: Atkinson BK (ed) Fracture Mechanics of Rock, Academic Press, London, p 477-525

Axelson JW, Piret EL (1950) Crushing of single particles of crystalline quartz. Ind Eng Chem 42:665-670

Ayensu A, Ashbee KHG (1977) The creep of quartz single crystals, with special reference to the mechanism by which water accommodates dislocation glide. Phil Mag 36:713-723

EBSCOhost - printed on 2/13/2023 4:48 AM via . All use subject to https://www.ebsco.com/terms-of-use

Baeta RD, Ashbee KHG (1967) Plastic deformation and fracture of quartz at atmospheric pressure. Phil Mag 15:931-938
Baeta RD, Ashbee KHG (1969a) Slip systems in quartz I—experiments. Am Min 54:1551-1573
Baeta RD, Ashbee KHG (1969b) Slip systems in quartz II—interpretation. Am Min 54:1574-1582
Baeta RD, Ashbee KHG (1970a) Mechanical deformation of quartz I. constant strain-rate compression experiments. Phil Mag 22:601-623
Baeta RD, Ashbee KHG (1970b) Mechanical deformation of quartz II. stress relaxation and thermal activation parameters. Phil Mag 22:625-635
Baeta RD, Ashbee KHG (1973) Transmission electron microscopy studies of plastically deformed quartz. Phys stat sol (a) 18:155-170
Bakker RJ, Jansen JBH (1990) Preferential water leakage from fluid inclusions by means of mobile dislocations. Nature 345:58-60
Bakker RJ, Jansen JBH (1991) Experimental post-entrapment water loss from synthetic CO_2-H_2O inclusions in natural quartz. Geochim Cosmochim Acta 55:2215-2230
Bakker RJ, Jansen JBH (1994) A mechanism for preferential H_2O leakage from fluid inclusions in quartz, based on TEM observations. Contrib Min Pet 116:7-20
Balderman M (1974) The effect of strain rate and temperature on the yield point of hydrolytically weakened synthetic quartz. J Geophys Res 79:1647-1652
Ball A, Glover G (1979) Dislocation climb deformation in quartz. Bull Min102:188-194
Ball A, Payne BW (1976) The tensile fracture of quartz crystals. J Mat Sci 11:731-740
Bambauer HU (1961) Spurenelementgehalte und γ-Farbzentrum in Quarzen aus Zerrklüften der Schweizer Alpen. Schweiz mineral petrogr Mitt 41:335-369
Bambauer HU, Brunner GO, Laves F (1962) Wasserstoff-Gehalte in Quarzen aus Zerrklüften der Schweizer Alpen und die Deutung ihrer regionalen Abhängigkeit. Schweiz mineral petrogr Mitt 42:221-236
Bambauer HU, Brunner GO, Laves F (1963) Merkmale des OH-Spektrums alpiner Quarze (3μ-Gebiet). Schweiz mineral petrogr Mitt 43:259-268
Bambauer HU, Brunner GO, Laves F (1969) Light scattering of heat-treated quartz in relation to hydrogen containing defects. Am Min 54:718-724
Bartoli F, Bittencourt Rosa D, Doirisse M, Meyer R, Philippy R, Samama J-C (1990) Role of aluminium in the structure of Brazilian opals. Eur J Mineral 2:611-619
Bassett DR, EA Boucher, Zettlemoyer AC (1970) Adsorption studies on ice-nucleating substrates. Hydrophobed silicas and silver iodide. J Colloid Interface Sci 34:436-446
Benesi HA, Jones AC (1959) An infrared study of the water-silica gel system. J Phys Chem 63:179-182
Blacic JD (1975) Plastic deformation mechanisms in quartz: the effect of water. Tectonophysics 27:271-294
Blacic JD (1981) Water diffusion in quartz at high pressure: tectonic implications. Geophys Res Letters 8:721-723
Blacic JD, Christie JM (1984) Plasticity and hydrolytic weakening of quartz single crystals. J Geophys Res 89:4223-4239
Blanpied ML, Lockner DA, Byerlee JD (1992) An earthquake mechanism based on rapid sealing of faults. Nature 358:574-576
Blum A, Lasaga A (1988) Role of surface speciation in the low-temperature dissolution of minerals. Nature 331:431-433
Blum AE, Yund RA, Lasaga AC (1990) The effect of dislocation density on the dissolution rate of quartz. Geochim Cosmochim Acta 54:283-297
Boulogne B, Cordier P, Doukhan J-C (1988a) Defects and hydrolytic weakening in α-berlinite $AlPO_4$ a structural analog of quartz. Phys Chem Min 16:250-261
Boulogne B, Francois P, Cordier P, Doukhan J-C (1988b) Plastic deformation of synthetic wet α-berlinite $AlPO_4$. Phil Mag A 57:411-430
Brace WF, Martin RJ III (1968) A test of the law of effective stress for crystalline rocks of low porosity. Int'l J Rock Mech Min Sci 5:415-426
Brace WF, Walsh JB (1962) Some direct measurements of the surface energy of quartz and orthoclase. Am Min 47:1111-1122
Brady PV, Walther JV (1989) Controls on silicate dissolution rates in neutral and basic pH solutions at 25°C. Geochim Cosmochim Acta 53:2823-2830
Brady PV, Walther JV (1990) Kinetics of quartz dissolution at low temperatures. Chemical Geol 82:253-264
Brady PV, Walther JV (1992) Surface chemistry and silicate dissolution at elevated temperatures. Am J Sci 292:639-658
Brantley SL (1992) The effect of fluid chemistry on quartz microcrack lifetimes. Earth and Planet Sci Letters 113:145-156

EBSCOhost - printed on 2/13/2023 4:48 AM via . All use subject to https://www.ebsco.com/terms-of-use

Brantley SL, Crane SR, Crerar DA, Hellmann R, Stallard R (1986) Dissolution at dislocation etch pits in quartz. Geochim Cosmochim Acta 50:2349-2361

Brantley SL, Evans B, Hickman SH, Crerar DA (1990) Healing of microcracks in quartz: implications for fluid flow. Geology 18:136-139

Brunner GO, Wondratschek H, Laves F (1961) Ultrarotuntersuchungen über den Einbau von H in natürlichem Quarz. Z Elektrochemie 65:735-750

Bukanov VV, Markova GA (1969) The smoky and citrine color of natural quartz. Acad Sci USSR Earth Science Proc 187:115-117 [translated from Doklady Akademi Nauk SSSR 187:645-647]

Byerlee J (1978) Friction of rocks. Pure Appl Geophys 116:615-626

Byerlee J (1990) Friction, overpressure and fault normal compression. Geophys Res Letters 17:2109-2112

Carter NL, Christie JM, Griggs DT (1964) Experimental deformation and recrystallization of quartz. J Geol 72:687-733

Carter NL, Kronenberg AK, Ross JV, Wiltschko DV (1990) Control of fluids on deformation of rocks. In Knipe RJ, Rutter EH (eds) Deformation Mechanisms, Rheology and Tectonics, Geol Soc Spec Publication 54:1-13

Casey WH, Sposito G (1992) On the temperature dependence of mineral dissolution rates. Geochim Cosmochim Acta 56:3825-3830

Chakraborty D, Lehmann G (1976a) Distribution of OH in synthetic and natural quartz crystals. J Solid State Chem 17:305-311

Chakraborty D, Lehmann G (1976b) On the structures and orientations of hydrogen defects in natural and synthetic quartz crystals. Phys stat sol (a) 34:467-474

Chakraborty D, Lehmann G (1978) On the fine structure in the infrared spectra of clear natural quartz, amethyst, citrine and synthetic quartz crystals in the 3400 cm^{-1} region. Z Naturforsch 33a:290-293

Cheilletz A, Dubessy J, Kosztolanyi C, Masson-Perez N, Ramboz C, Zimmermann J-L (1984) Les fluides moléculaires d'un filon de quartz hydrothermal: comparaison de techniques analytiques ponctuelles et globales, contamination des fluides occlus par des composés carbonés. Bull Min 107:169-180

Cho H, Rossman GR (1993) Single-crystal NMR studies of low-concentration hydrous species in minerals: grossular garnet. Am Min 78:1149-1164

Christie JM, Ardell AJ (1976) Deformation structures in minerals. In Wenk HR (ed) Electron Microscopy in Mineralogy, Springer Verlag, Berlin, p 374-403

Christie JM, Ord A (1980) Flow stress from microstructures of mylonites: example and current assessment. J Geophys Res 85:6253-6262

Christie JM, Griggs DT, Carter NL (1964a) Experimental evidence of basal slip in quartz. J Geol 72:734-756

Christie JM, Heard HC, LaMori PN (1964b) Experimental deformation of quartz single crystals at 27 to 30 kilobars confining pressure and 24°C. Am J Sci 262:26-55

Cordier P, Doukhan J-C (1989) Water solubility in quartz and its influence on ductility. Eur J Mineral 1:221-237

Cordier P, Doukhan J-C (1991) Water speciation in quartz: a near infrared study. Am Min 76:361-369

Cordier P, Boulogne B, Doukhan J-C (1988) Water precipitation and diffusion in wet quartz and wet berlinite $AlPO_4$. Bull Minéral 111:113-137

Cordier P, Weil JA, Howarth DF, Doukhan J-C (1994) Influence of the $(4H)_{Si}$ defect on dislocation motion in crystalline quartz. Eur J Mineral 6:17-22

deBoer RB (1977a) On the thermodynamics of pressure solution-interaction between chemical and mechanical forces. Geochim Cosmochim Acta 41:249-256

deBoer RB (1977b) Pressure solution: theory and experiment. Tectonophysics 39:287-301

deBoer RB, Nagtegaal PJC, Duyvis EM (1977) Pressure solution experiments on quartz sand. Geochim Cosmochim Acta 41:257-264

denBrok SWJ (1992) An Experimental Investigation into the Effect of Water on the Flow of Quartzite. PhD Dissertation, Rijksuniversiteit Utrecht, 178 p

denBrok SWJ, Spiers CJ (1991) Experimental evidence for water weakening of quartzite by microcracking plus solution-precipitation creep. J Geological Soc London 148:541-548

denBrok SWJ, Meinecke J, Roller K (1994) FTIR-determination of intragranular water content in quartzites experimentally deformed with and without added water in the ductile deformation field. J Geophys Res: in press

Dennis PF (1984) Oxygen self-diffusion in quartz under hydrothermal conditions. J Geophys Res 89:4047-4057

Dewers T, Ortoleva PJ (1989) Mechano-chemical coupling in stressed rocks. Geochim Cosmochim Acta 53:1243-1258

Dieterich JH (1979) Modelling of rock friction: 1. experimental results and constitutive equations. J Geophys Res 84:2161-2168

EBSCOhost - printed on 2/13/2023 4:48 AM via . All use subject to https://www.ebsco.com/terms-of-use

Dieterich JH (1981) Constitutive properties of faults with simulated gouge. In Carter NL, Friedman M, Logan JM, Stearns DW (eds) Mechanical Behavior of Crustal Rocks (The Handin Volume) Geophys Monogr 24:103-120 Am Geophys Union, Washington, DC

Dieterich JH, Conrad G (1984) Effect of humidity on time- and velocity-dependent friction in rocks. J Geophys Res 89:4196-4202

Dodd DM, Fraser DB (1965) The 3000-3900 cm^{-1} absorption bands and anelasticity in crystalline α-quartz. J Phys Chem Solids 26:673-686

Dodd DM, Fraser DB (1967) Infrared studies of the variation of H-bonded OH in synthetic α-quartz. Am Min 52:149-160

Doukhan J-C, Paterson MS (1986) Solubility of water in quartz-a revision. Bull Minéral 109:193-198

Doukhan J-C, Trepied L (1985) Plastic deformation of quartz single crystals. Bull Minéral 108:97-123

Dove PM, Crerar DA (1990) Kinetics of quartz dissolution in electrolyte solutions using a hydrothermal mixed flow reactor. Geochim Cosmochim Acta 54:955-969

Dunning JD, Huf WL (1983) The effects of aqueous chemical environments on crack and hydraulic fracture propagation and morphologies. J Geophys Res 88:6491-6499

Dunning JD, Miller ME (1984) Effects of pore fluid chemistry on stable sliding of Berea sandstone. Pure Appl Geophys 122:447-462

Dunning JD, Lewis WL, Dunn DE (1980) Chemomechanical weakening in the presence of surfactants. J Geophys Res 85:5344-5354

Dunning JD, Petrovski D, Schuyler J, Owens A (1984) The effects of aqueous chemical environments on crack propagation in quartz. J Geophys Res 89:4115-4123

Elias BP, Hajash A Jr (1992) Changes in quartz solubility and porosity due to effective stress: an experimental investigation of pressure solution. Geology 20:451-454

Elliott D (1973) Diffusion flow laws in metamorphic rocks. Geol Soc Am Bull 84:2645-2664

Elphick SC, Dennis PF, Graham CM (1986) An experimental study of the diffusion of oxygen in quartz and albite using an overgrowth technique. Contrib Min Pet 92:322-330

Elphick SC, Graham CM (1988) The effect of hydrogen on oxygen diffusion in quartz: evidence for fast proton transients? Nature 335:243-245

Ernst WG, Blatt H (1963) Experimental study of quartz overgrowths and synthetic quartzites. J Geol 72:461-470

Etheridge MA, Wall VJ, Cox SF, Vernon RH (1984) High fluid pressures during regional metamorphism and deformation: implications for mass transport and deformation mechanisms. J Geophys Res 89:4344-4358

Etzler FM (1988) Enhancement of hydrogen bonding in vicinal water: heat capacity of water and deuterium oxide in silica pores. Langmuir 4:878-883

Etzler FM, Fagundus DM (1987) The extent of vicinal water: implications from the density of water in silica pores. J Colloid Interface Sci 115:513-519

Farver JR, Yund RA (1991a) Oxygen diffusion in quartz: dependence on temperature and water fugacity. Chem Geology 90:55-70

Farver JR, Yund RA (1991b) Measurement of oxygen grain boundary diffusion in natural, fine-grained, quartz aggregates. Geochim Cosmochim Acta 55:1597-1607

Farver JR, Yund RA (1992) Oxygen diffusion in a fine-grained quartz aggregate with wetted and nonwetted microstructures. J Geophys Res 97:14017-14029

FitzGerald JD, Boland JN, McLaren AC, Ord A, Hobbs BE (1991) Microstructures in water-weakened single crystals of quartz. J Geophys Res 96:2139-2155

Fletcher RC, Pollard DD (1981) Anticrack model for pressure solution surfaces. Geology 9:419-424

Flörke OW, Köhler-Herbertz B, Langer K, Tönges I (1982) Water in microcrystalline quartz of volcanic origin: agates. Contrib Min Pet 80:324-333

Folman M, Yates DJC (1959) Infrared studies of physically adsorbed polar molecules and of the surface of a silica adsorbent containing hydroxyl groups. J Phys Chem 63:183-187

Foreman DW Jr (1968) Neutron and X-ray diffraction study of $Ca_3Al_2(O_4D_4)_3$, a garnetoid. J Chem Phys 48:3037-3041

Freer R, Dennis PF (1982) Oxygen diffusion studies. I. a preliminary ion microprobe investigation of oxygen diffusion in some rock-forming minerals. Min Mag 45:179-192

Freiman SW (1984) Effects of chemical environments on slow crack growth in glasses and ceramics. J Geophys Res 89:4072-4076

Fricke HC, Wickham SM, O'Neil JR (1992) Oxygen and hydrogen isotope evidence for meteoric water infiltration during mylonitization and uplift in the Ruby Mountains-East Humboldt Range core complex, Nevada. Contrib Min Pet 111:203-221

Frischat GH (1970) Sodium diffusion in natural quartz crystals. J Am Ceramic Soc 53:357

Frondel C (1982) Structural hydroxyl in chalcedony (type B quartz). Am Min 67:1248-1257

EBSCOhost - printed on 2/13/2023 4:48 AM via . All use subject to https://www.ebsco.com/terms-of-use

Gallei E, Parks GA (1972) Evidence for surface hydroxyl groups in attenuated total reflectance spectra of crystalline quartz. J Colloid Interface Sci 38:650-651

Gee ML, McGuiggan PM, Israelachvili JN, Homola AM (1990) Liquid to solidlike transitions of molecularly thin films under shear. J Chem Phys 93:1895-1906

Gerretsen J (1988) The Occurrence of Water in Quartz. Implications for the Process of Water Weakening. PhD dissertation. Australian National Univ, Canberra, 224 p

Gerretsen J, Paterson MS, McLaren AC (1989) The uptake and solubility of water in quartz at elevated pressure and temperature. Phys Chem Min 16:334-342

Gibson G, Vogel RC (1950) Migration of lithium and several multicharged ions through quartz plates in an electric field II. J Chem Phys 18:1094-1097

Giletti BJ, Yund RA (1984) Oxygen diffusion in quartz. J Geophys Res 89:4039-4046

Gleason GC, Tullis J (1994) A flow law for dislocation creep in quartzite and its implications for the strength of the crust. EOS Trans Am Geophys Union 75:329

Gleason GC, Tullis J, Heidelbach F (1993) The role of dynamic recrystallization in the development of lattice preferred orientations in experimentally deformed quartz aggregates. J Struct Geol 15:1145-1168

Goshen S, Friedman M, Thieberger R, Weil JA (1983) Models for the hydrogen atom confined within crystalline quartz. J Chem Phys 79:4363-4366

Graetsch H, Flörke OW, Miehe G (1985) The nature of water in chalcedony and opal-C from Brazilian agate geodes. Phys Chem Min 12:300-306

Gratier JP, Guiguet (1986) Experimental pressure solution-deposition on quartz grains: the crucial effect of the nature of the fluid. J Struct Geol 8:845-856

Gratz AJ (1991) Solution-transfer compaction of quartzites: progress toward a rate law. Geology 19:901-904

Gratz AJ, Bird P, Quiro GB (1990) Dissolution of quartz in aqueous basic solution, 106-236°C: surface kinetics of "perfect" crystallographic faces. Geochim Cosmochim Acta 54:2911-2922

Green HW, Griggs DT, Christie JM (1970) Syntectonic and annealing recrystallization of fine-grained quartz aggregates. In Paulitsch P (ed) Experimental and Natural Rock Deformation, Springer-Verlag, Berlin, p 227-235

Griggs DT (1967) Hydrolytic weakening of quartz and other silicates. Geophys J Roy Astr Soc 14:19-31

Griggs DT (1974) A model of hydrolytic weakening in quartz. J Geophys Res 79:1653-1661

Griggs DT, Blacic JD (1964) The strength of quartz in the ductile regime. EOS Trans Am Geophys Union 45:102

Griggs DT, Blacic JD (1965) Quartz: anomalous weakness of synthetic crystals. Science 147:292-295

Hackerman N, Hall AC (1958) The adsorption of water vapor on quartz and calcite. J Phys Chem 62:1212-1214

Hair ML (1967) Silica surfaces. In Infrared Spectroscopy in Surface Chemistry, Marcel Dekker, NY, p 79-139

Hall DL, Bodnar RJ (1990) Methane in fluid inclusions from granulites: a product of hydrogen diffusion? Geochim Cosmochim Acta 54:641-651

Halliburton LE, Koumvakalis N, Markes ME, Martin JJ (1981) Radiation effects in crystalline SiO_2: the role of aluminum. J Appl Phys 52:3565-3574

Handin J, Hager RVJr, Friedman M, Feather JN (1963) Experimental deformation of sedimentary rocks under confining pressure: pore pressure tests. Am Assoc Petrol Geol Bull 47:717-755

Harris PM, Waring CE (1937) Diffusion of lithium ions through quartz in an electric field. J Phys Chem 41:1077-1085

Hartley NEW, Wilshaw TR (1973) Deformation and fracture of synthetic α-quartz. J Mat Sci 8:265-278

Heard HC, Carter NL (1968) Experimentally induced "natural" intragranular flow in quartz and quartzite. Am J Sci 266:1-42

Heggie M (1992) A molecular water pump in quartz dislocations. Nature 355:337-339

Heggie M, Jones R (1986) Models of hydrolytic weakening in quartz. Phil Mag A 53:L65-L70

Heggie M, Jones R (1987) Density functional analysis of the hydrolysis of Si-O bonds in disiloxane. application to hydrolytic weakening in quartz. Phil Mag Letters 55:47-51

Heggie M, Nylen M (1984) Dislocation core structures in α quartz derived from a valence force potential. Phil Mag B 50: 543-555

Heggie M, Nylen M (1985) Dislocations without deep states in α-quartz. Phil Mag Letters B 51: L69-L72

Heggie M, Jones R, Nylen M (1985) Electronic structure of α-quartz, the [1010] surface and perfect stoichiometric dislocations. Phil Mag B 51: 573-580

Hickman SH, Evans B (1991) Experimental pressure solution in halite: the effect of grain/interphase boundary structure. J Geol Soc London 148:549-560

EBSCOhost - printed on 2/13/2023 4:48 AM via . All use subject to https://www.ebsco.com/terms-of-use

Hickman SH, Evans B (1992) Growth of grain contacts in halite by solution-transfer: implications for diagenesis, lithification, and strength recovery. In Evans B, Wong T-F (eds) Fault Mechanics and Transport Properties of Rocks, Academic Press, London, p 253-280

Hickman S, Evans B, Katz G (1993) Growth of grain-to-grain contacts through solution-transport processes. Abstracts Spring MRS Meeting, Materials Research Society, 414

Hirsch PB (1979) A mechanism for the effect of doping on dislocation mobility. J Phys Colloque C6 40:C6-117-C6-121

Hirsch PB (1981) Plastic deformation and electronic mechanisms in semiconductors and insulators. J de Physique Colloque C3 42:C3-149–C3-160

Hirth G, Tullis J (1992) Dislocation creep regimes in quartz aggregates. J Struct Geol 14:145-159

Hobbs BE (1968) Recrystallization of single crystals of quartz. Tectonophysics 6:353-401

Hobbs BE (1981) The influence of metamorphic environment upon the deformation of minerals. Tectonophysics 78:335-383

Hobbs BE (1984) Point defect chemistry of minerals under a hydrothermal environment. J Geophys Res 89:4026-4038

Hobbs BE (1985) The hydrolytic weakening effect in quartz. In Schock RN (ed) Point Defects in Minerals, Geophys Monogr 31:151-170, Am Geophys Union, Washington, DC

Hobbs BE, McLaren AC, Paterson MS (1972) Plasticity of single crystals of synthetic quartz. In Heard HC, Borg IY, Carter NL, Raleigh CB (eds) Flow and Fracture of Rocks (The Griggs Volume), Geophys Monograph 16:29-53, Am Geophys Union, Washington, DC

Hollister LS (1990) Enrichment of CO_2 in fluid inclusions in quartz by removal of H_2O during crystal-plastic deformation. J Struct Geol 12:895-901

Holness MB (1993) Temperature and pressure dependence of quartz-aqueous fluid dihedral angles: the control of adsorbed H_2O on the permeabilities of quartzites. Earth Planet Sci Letters 117:363-377

Horn RG, Smith DT, Haller W (1989) Surface forces and viscosity of water measured between silica sheets. Chem Phys Letters 162:404-408

Hosaka M, Taki S (1981a) Hydrothermal growth of quartz crystals in pure water. J Crystal Growth 51:640-642

Hosaka M, Taki S (1981b) Hydrothermal growth of quartz crystals in KCl solutions. J Crystal Growth 53:542-546

Hosaka M, Taki S, Nagai K, Asahara J (1981) Synthetic quartz crystals grown in NaCl, KCl solutions and pure water, and their low temperature infrared absorption. Proc Annual Symp on Frequency Control 35:1-9

Houlier B, Jaoul O, Abel F, Liebermann RC (1988) Oxygen and silicon self-diffusion in natural olivine at T = 1300°C. Phys Earth Planet Interiors 50:240-250

Houlier B, Cheraghmakani M, Jaoul O (1990) Silicon diffusion in San Carlos olivine. Phys Earth Planet Interiors 62:329-340

Hubbert MK, Rubey WW (1959) Role of fluid pressure in the mechanics of overthrust faulting. Geol Soc Am Bull 70:115-205

Isoya J, Weil JA, Davis PH (1983) EPR of atomic hydrogen ^1H and ^2H in α-quartz. J Phys Chem Solids 44:335-343

Israelachvili JN (1986) Measurements of the viscosity of liquids in very thin films. J Colloid Interface Sci 110:263-271

Israelachvili JN (1992) Adhesion forces between surfaces in liquids and condensable vapours. Surface Sci Reports 14:109-159

Israelachvili JN, Kott SJ (1989) Shear properties and structure of simple liquids in molecularly thin films: the transition from bulk (continuum) to molecular behavior with decreasing film thickness. J Colloid Interface Sci 129:461-467

Jain H, Nowick AS (1982a) Electrical conductivity of synthetic and natural quartz crystals. J Appl Phys 53:477-484

Jain H, Nowick AS (1982b) Radiation-induced conductivity in quartz crystals. J Appl Phys 53:485-489

Jang B-A, Wang HF, Ren X, Kowallis BJ (1989) Precambrian paleostress from microcracks and fluid inclusions in the Wolf River batholith of central Wisconsin. Geol Soc Am Bull 101:1457-1464

Jaoul O, Poumellec M, Froidevaux C, Havette A (1981) Silicon diffusion in forsterite: a new constraint for understanding mantle deformation. In Stacy FD et al. (eds) Anelasticity in the Earth 4:95-100, Am Geophys Union, Washington, DC

Jaoul O, Tullis J, Kronenberg AK (1984) The effect of varying water contents on the creep behavior of Heavitree quartzite. J Geophys Res 89:4298-4312

Jones ME (1978) The influence of hydrostatic pressure on the precipitation of structure-bound water in micro-inclusions in quartz. Phil Mag A 37:703-706

Kamb WB (1961) The thermodynamic theory of nonhydrostatically stressed solids. J Geophys Res 66:259-271

EBSCOhost - printed on 2/13/2023 4:48 AM via . All use subject to https://www.ebsco.com/terms-of-use

Kats A (1962) Hydrogen in alpha quartz. Philips Research Reports 17:1-31, 133-195, 201-279
Kats A, Haren Y, Stevels JM (1962) Hydroxyl groups in β-quartz. Phys Chem Glasses 3:69-75
Kekulawala KRSS, Paterson MS, Boland JN (1978) Hydrolytic weakening in quartz. Tectonophysics 46:T1-T6
Kekulawala KRSS, Paterson MS, Boland JN (1981) An experimental study of the role of water in quartz deformation. In Carter NL, Friedman M, Logan JM, Stearns DW (eds) Mechanical behavior of crustal rocks (The Handin Volume) Geophysical Monogr 24:49-60, Am Geophys Union, Washington, DC
Kerrich R (1976) Some effects of tectonic recrystallization on fluid inclusions in vein quartz. Contrib Min Pet 59:195-202
Kerrich R (1986) Fluid infiltration into fault zones: chemical, isotopic and mechanical effects. Pure Appl Geophys 124:225-268
King JC (1959) The anelasticity of natural and synthetic quartz at low temperatures. Bell Syst Tech J 38:573-602
Kirby SH (1977) The effects of the α-β phase transformation on the creep properties of hydrolytically-weakened synthetic quartz. Geophys Res Letters 4:97-100
Kirby SH (1984) Introduction and digest to the special issue on chemical effects of water on the deformation and strengths of rocks. J Geophys Res 89:3991-3995
Kirby SH, McCormick JW (1979) Creep of hydrolytically weakened synthetic quartz crystals oriented to promote {2110}<0001> slip: a brief summary of work to date. Bull Min 102:124-137
Klier K, Zettlemoyer AC (1977) Water at interfaces: molecular structure and dynamics. J Colloid Interface Sci 58:216-229
Klier K, Shen JH, Zettlemoyer AC (1973) Water on silica and silicate surfaces I. partially hydrophobic silicas. J Phys Chem 77:1458-1465
Koch PS, Christie JM, Ord A, George RP Jr (1989) Effect of water on the rheology of experimentally deformed quartzite. J Geophys Res 94:13975-13996
Kopp OC, Staats PA (1970) Characterization of RbOH-grown quartz by infrared and mass spectroscopy. J Phys Chem Solids 31:2469-2476
Krefft GB (1975) Effects of high-temperature electrolysis on the coloration characteristics and OH-absorption bands in alpha quartz. Radiation Effects 26:249-259
Kronenberg AK, Kirby SH (1987) Ionic conductivity of quartz: DC time dependence and transition in charge carriers. Am Min 72:739-747
Kronenberg AK, Tullis (1984) Flow strengths of quartz aggregates: grain size and pressure effects due to hydrolytic weakening. J Geophys Res 89:4281-4297
Kronenberg AK, Wolf GH (1990) Fourier transform infrared spectroscopy determinations of intragranular water content in quartz-bearing rocks: implications for hydrolytic weakening in the laboratory and within the earth. Tectonophysics 172:255-271
Kronenberg AK, Kirby SH, Aines RD, Rossman GR (1986) Solubility and diffusional uptake of hydrogen in quartz at high water pressures: implications for hydrolytic weakening. J Geophys Res 91:12723-12744
Kronenberg AK, Segall P, Wolf GH (1990) Hydrolytic weakening and penetrative deformation within a natural shear zone. In Duba AG, Durham WB, Handin JW, Wang HF (eds) The Brittle-Ductile Transition in Rocks (The Heard Volume) Geophysical Monogr 56:21-36, Am Geophys Union, Washington, DC
Langer K, Flörke OW (1974) Near infrared absorption spectra (4000-9000 cm^{-1}) of opals and the role of "water" in these $SiO_2 \cdot nH_2O$ minerals. Fortschr Min 52:17-51
Lasaga AC (1984) Chemical kinetics of water-rock interactions. J Geophys Res 89:4009-4025
Lee VW, Mackwell SJ, Brantley SL (1991) The effect of fluid chemistry on wetting textures of novaculite. J Geophys Res 96:10023-10037
Lehner FK, Bataille J (1984) Nonequilibrium thermodynamics of pressure solution. Pure Appl Geophys 122:53-85
Lerbekmo JF, Platt RL (1962) Promotion of pressure-solution of silica in sandstones. J Sed Petrol 32:514-519
Li HC, de Bruyn PL (1966) Electrokinetic and adsorption studies on quartz. Surface Sci 5:203-220
Lias NC, Grudenski EE (1973) The growth of high acoustic Q quartz at high growth rates. J Crystal Growth 18:1-6
Linker MF, Kirby SH (1981) Anisotropy in the rheology of hydrolytically weakened synthetic quartz crystals. In Carter NL, Friedman M, Logan JM, Stearns DW (eds) Mechanical behavior of crustal rocks (The Handin Volume) Geophysical Monogr 24:29-48, Am Geophys Union, Washington, DC
Linker MF, Kirby SH, Ord A, Christie JM (1984) Effects of compression direction on the plasticity and rheology of hydrolytically weakened synthetic quartz crystals at atmospheric pressure. J Geophys Res 89:4241-4255

EBSCOhost - printed on 2/13/2023 4:48 AM via . All use subject to https://www.ebsco.com/terms-of-use

Luan FC, Paterson MS (1992) Preparation and deformation of synthetic aggregates of quartz. J Geophys Res 97:301-320
Mackwell SH, Paterson MS (1985) Water-related diffusion and deformation effects in quartz at pressure of 1500 and 300 MPa. In Schock RN (ed) Point defects in minerals. Geophysical Monograph 31:141-150, Am Geophys Union, Washington, DC
Magda JJ, Tirrell M, Davis HT (1985) Molecular dynamics of narrow, liquid-filled pores. J Chem Phys 83:1888-1901
Mainprice DH (1981) The Experimental Deformation of Quartz Polycrystals. PhD dissertation, Australian National University, Canberra, 171 p
Mainprice DH, Paterson MS (1984) Experimental studies of the role of water in the plasticity of quartzites. J Geophys Res 89:4257-4269
Markes ME, Halliburton LE (1979) Defects in synthetic quartz: radiation-induced mobility of interstitial ions. J Appl Phys 50:8172-8180
Martin RJIII (1972) Time-dependent crack growth in quartz and its application to the creep of rocks. J Geophys Res 77:1406-1419
Martin RJIII, Durham WB (1975) Mechanisms of crack growth in quartz. J Geophys Res 80:4837-4844
Mavrogenes JA, Bodnar RJ (1994) Hydrogen movement into and out of fluid inclusions in quartz: experimental evidence and geologic implications. Geochim Cosmochim Acta 58:141-148
McDonald RS (1957) Study of the interaction between hydroxyl groups and aerosil silica and adsorbed non-polar molecules by infrared spectrometry. J Am Chem Soc 79:850-854
McDonald RS (1968) Surface functionality of amorphous silica by infrared spectroscopy. J Phys Chem 62:1168-1178
McLaren AC, Hobbs BE (1972) Transmission electron microscope investigation of some naturally deformed quartzites. In Heard HC, Borg IY, Carter NL, Raleigh CB (eds) Flow and Fracture of Rocks, Geophys Monograph 16:55-66, Am Geophys Union, Washington, DC
McLaren AC, Payling R (1980) The determination of hydrogen concentration in silicates using ion-beam spectrochemical analysis (IBSCA). Phys Chem Min 5:315-326
McLaren AC, Phakey (1965) A transmission electron microscope study of amethyst and citrine. Australian J Phys 18:135-141
McLaren AC, Phakey (1966) Transmission electron microscope study of bubbles and dislocations in amethyst and citrine quartz. Australian J Phys 19:19-24
McLaren AC, Retchford JA (1969) Transmission electron microscope study of the dislocations in plastically deformed synthetic quartz. Phys stat sol 33:657-668
McLaren AC, Retchford JA, Griggs DT, Christie JM (1967) Transmission electron microscope study of Brazil twins and dislocations experimentally produced in natural quartz. Phys stat sol 19:631-644
McLaren AC,Turner RG, Boland JW, Hobbs BE (1970) Dislocation structure of the deformation lamellae in synthetic quartz: a study by electron and optical microscopy. Contrib Min Pet 29:104-115
McLaren AC, Cook RF, Hyde ST, Tobin RC (1983) The mechanisms of the formation and growth of water bubbles and associated dislocation loops in synthetic quartz. Phys Chem Min 9:79-94
McLaren AC, Fitzgerald JD, Gerretsen J (1989) Dislocation nucleation and multiplication in synthetic quartz: relevance to water weakening. Phys Chem Min 16:465-482
McMillan PF, Hofmeister AM (1988) Infrared and Raman spectroscopy. In Hawthorne FC (ed) Spectroscopic Methods in Mineralogy and Geology, Rev Min 18:99-159
Meredith PG, Atkinson BK (1982) High-temperature tensile crack propagation in quartz: experimental results and application to time-dependent earthquake rupture. Earthquake Prediction Res 1:377-391
Michalske TA, Freiman SW (1982) A molecular interpretation of stress corrosion in silica. Nature 295:511-512
Moenke HHW (1974) Silica, the three-dimensional silicates, borosilicates, and beryllium silicates. In Farmer VC (ed) The Infrared Spectra of Minerals, Min Soc (London) Monogr 4:365-382
Morgan GB VI, Chou I-M, Pasteris JD, Olsen SN (1993) Re-equilibration of CO_2 fluid inclusions at controlled hydrogen fugacities. J Metamorphic Geol 11:155-164
Morrison-Smith DJ, Paterson MS, Hobbs BE (1976) An electron microscope study of plastic deformation in single crystals of synthetic quartz. Tectonophysics 33:43-79
Morrow BA, Cody IA (1973) Infrared spectra of the isolated hydroxyl groups on silica. J Phys Chem 77:1465-1474
Moze O, Hicks TJ, McLaren AC (1980) Determination of the hydrogen content of synthetic quartz by neutron polarization analysis. Phys Chem Min 5:309-314
Mullis AM (1991) The role of silica precipitation kinetics in determining the rate of quartz pressure solution. J Geophys Res 96:10007-10013
Mullis AM (1993) Determination of the rate-limiting mechanism for quartz pressure dissolution. Geochim Cosmochim Acta 57:1499-1503

EBSCOhost - printed on 2/13/2023 4:48 AM via . All use subject to https://www.ebsco.com/terms-of-use

Nakamoto K (1978) Infrared and Raman Spectra of Inorganic and Coordination Compounds. J Wiley & Sons, New York

Nakamoto K, Margoshes M, Rundle RE (1955) Stretching frequencies as a function of distances in hydrogen bonds. J Am Chem Soc 77:6480-6488

Nakashima S, Matayoshi H, Yuko T, Michibayashi K, Masuda T, Kuroki N, Yamagishi H, Ito Y, Nakamura A (1994) Infrared microspectroscopy analysis of water distribution in deformed and metamorphosed rocks. Tectonophysics (in press)

Novak A (1974) Hydrogen bonding in solids. Correlation of spectroscopic and crystallographic data. Structure and Bonding 18:177-216

Nuttall RHD, Weil JA (1980) Two hydrogenic trapped-hole species in α-quartz. Solid State Comm 33:99-102

Nuttall RHD, Weil JA (1981a) The magnetic properties of the oxygen-hole aluminum centers in crystalline SiO_2. II. $[AlO_4/H^+]^+$ and $[AlO_4/Li^+]^+$. Can J Phys 59:1709-1718

Nuttall RHD, Weil JA (1981b) The magnetic properties of the oxygen-hole aluminum centers in crystalline SiO_2. III. $[AlO_4]^+$. Can J Phys 59:1886-1892

Olejnik S, White JW (1972) Thin layers of water in vermiculites and montmorillonites-modification of water diffusion. Nature Phys Sci 236:15-16

Ord A, Christie JM (1984) Flow stresses from microstructures in mylonitic quartzites of the Moine thrust zone, Assynt area, Scotland. J Struct Geol 6:639-654

Ord A, Hobbs BE (1986) Experimental control of the water-weakening effect in quartz. In Hobbs BE, Heard HC (eds) Mineral and Rock Deformation: Laboratory Studies (The Paterson Volume), Geophys Monogr 36:1-72 Am Geophys Union, Washington, DC

Pankrath R (1991) Polarized IR spectra of synthetic smoky quartz. Phys Chem Min 17:681-689

Park DS, Nowick AS (1974) Dielectric relaxation of point defects in α-quartz. Phys stat sol (a) 26:617-626

Parks GA (1984) Surface and interfacial free energies of quartz. J Geophys Res 89:3996-4008

Parrish DK, Krivz AL, Carter NL (1976) Finite-element folds of similar geometry. Tectonophysics 32:183-207

Pashley RM, Israelachvili JN (1984) Molecular layering of water in thin films between mica surfaces and its relation to hydration forces. J Colloid Interface Sci 101:511-523

Passchier CW (1984) Fluid inclusions associated with the generation of pseudotachylyte and ultramylonite in the French Pyrenees. Bull Minéral 107:307-315

Paterson MS (1973) Nonhydrostatic thermodynamics and its geologic applications. Rev Geophys Space Phys 11:355-389

Paterson MS (1982) The determination of hydroxyl by infrared absorption in quartz, silicate glasses and similar materials. Bull Minéral 105:20-29

Paterson MS (1986) The thermodynamics of water in quartz. Phys Chem Min 13:245-255

Paterson MS (1989) The interaction of water with quartz and its influence in dislocation flow-an overview. In Karato S-I, Toriumi M (eds) Rheology of Solids and of the Earth. Oxford University Press, Oxford, p 107-142

Paterson MS, Kekulawala KRSS (1979) The role of water in quartz deformation. Bull Min 102:92-98

Paterson MS, Luan FC (1990) Quartzite rheology under geological conditions. In Knipe RJ, Rutter EH (eds) Deformation Mechanisms, Rheology and Tectonics, Geol Soc Special Publ 54:299-307

Pecher A, Lespinasse M, Leroy J (1985) Relations between fluid inclusion trails and regional stress field: a tool for fluid chronology-an example of an intragranitic uranium ore deposit (northwest Massif Central, France). Lithos 18:229-237

Peschel G, Adlfinger KH (1970) Viscosity anomalies in liquid surface zones IV. the apparent viscosity of water in thin layers adjacent to hydroxylated fused silica surfaces. J Colloid Interface Sci 34:505-510

Pharr GM, Ashby MF (1983) On creep enhanced by a liquid phase. Acta Metall 31:129-138

Pittman ED (1972) Diagenesis of quartz in sandstones as revealed by scanning electron microscopy. J Sed Petrol 42:507-519

Post AD, Tullis J (1993) Reversibility of hydrolytic weakening of experimentally deformed quartz aggregates. EOS Trans Am Geophys Union 74:600

Purton J, Jones R, Heggie M, Oberg S, Catlow CRA (1992) LDF pseudopotential calculations of the α-quartz structure and hydrogarnet defect. Phys Chem Min 18:389-392

Raj R (1982) Creep in polycrystalline aggregates by matter transport through a liquid phase. J Geophys Res 87:4731-4739

Raleigh CB, Healy JH, Bredehoeft JD (1976) An experiment in earthquake control at Rangely, Colorado. Science 191:1230-1237

Renton JJ, Heald MT, Cecil CB (1969) Experimental investigation of pressure solution of quartz. J Sed Petrol 39:1107-1117

EBSCOhost - printed on 2/13/2023 4:48 AM via . All use subject to https://www.ebsco.com/terms-of-use

Rice JR (1992) Fault stress states, pore pressure distributions, and the weakness of the San Andreas fault. In Evans B, Wong T-F (eds) Fault Mechanics and Transport Properties of Rocks, Academic Press, London, p 475-503

Robin P-YF (1978) Pressure solution at grain-to-grain contacts. Geochim Cosmochim Acta 42:1383-1389

Roedder E (1984) Fluid Inclusions, Reviews in Mineralogy, Vol 12, Min Soc Am, Washington, DC, 644 p

Roedder E, Skinner BJ (1968) Experimental evidence that fluid inclusions do not leak. Economic Geology 63:715-730

Roedder E, Kopp OC (1975) A check on the validity of the pressure correction in inclusion geothermometry, using hydrothermally grown quartz. Fortschr Min 52:431-446

Rosasco GJ, Roedder E (1979) Application of a new Raman microprobe spectrometer to nondestructive analysis of sulfate and other ions in individual phases in fluid inclusions in minerals. Geochim Cosmochim Acta 43:1907-1915

Ross JV, Bauer SJ, Carter NL (1983) Effect of the α-β quartz transition on the creep properties of quartzite and granite. Geophys Res Letters 10:1129-1132

Rossman GR (1988) Vibrational spectroscopy of hydrous components. In Hawthorne FC (ed) Spectroscopic Methods in Mineralogy and Geology, Rev Min 18:193-206

Rossman GR, Aines RD (1991) The hydrous components in garnets: grossular-hydrogrossular. Am Min 76:1153-1164

Rovetta MR, Holloway JR, Blacic JD (1986) Solubility of hydroxyl in natural quartz annealed in water at 900°C and 1.5 GPa. Geophys Res Lett 13:145-148

Rovetta MR, Blacic JD, Hervig RL, Holloway JR (1989) An experimental study of hydroxyl in quartz using infrared spectroscopy and ion microprobe techniques. J Geophys Res 94:5840-5850

Ruina AL (1983) Slip instability and state variable friction laws. J Geophys Res 88:10359-10370

Rusanov AI (1978) On the thermodynamics of deformable solid surfaces. J Colloid and Interface Sci 63:330-345

Rutter EH (1976) The kinetics of rock deformation by pressure solution. Phil Trans R Soc London A 283:203-219

Rutter EH (1983) Pressure solution in nature, theory and experiment. J Geological Soc London 140:725-740

Rybach L, Laves F (1967) Sodium diffusion experiments in quartz crystals. Geochim et Cosmochim Acta 31:539-546

Schoen M, Cushman JH, Diestler DJ, Rhykerd CL (1988) Fluids in micropores. II. self-diffusion in a simple classical fluid in a slit pore. J Chem Phys 88:1394-1407

Scholz CH (1972) Static fatigue of quartz. J Geophys Res 73:3295-3302

Schutjens PMTM (1991) Experimental compaction of quartz sand at low effective stress and temperature conditions. J Geological Soc London 148:527-539

Segnit ER, Stevens TJ, Jones JB (1965) The role of water in opal. J Geol Soc Australia 12:211-226

Shelton KL, Orville PM (1980) Formation of synthetic fluid inclusions in natural quartz. Am Min 65:1233-1236

Shen JH, Klier K (1980) Water on silica and silicate surfaces V. amorphous, porous, hydrophilic, phosphorous-doped silicas. J Colloid Interface Sci 75:56-67

Shinoda K, Aikawa N (1983) Polarized infrared absorbance spectra of an optically anisotropic crystal: application to the orientation of the OH^- dipole in quartz. Phys Chem Min 20:308-314

Sibson RH (1990) Conditions for fault-valve behaviour. In Knipe RJ, Rutter EH (eds) Deformation Mechanisms, Rheology and Tectonics, Geol Soc Special Publication No 54, p 15-28

Smith DL, Evans B (1984) Diffusional crack healing in quartz. J Geophys Res 89:4125-4135

Snoeyink VL, Weber WJ (1972) Surface functional groups on carbon and silica. In Progress in Surface Membrane Sciences vol 5, p 63-119

Snow EH, Gibbs P (1964) Dielectric loss due to impurity cation migration in alpha-quartz. J Appl Phys 35:2368-2374

Soda R (1961) Infrared absorption spectra of quartz and some other silica modification. Bull Chem Soc Jap 34:1491-1495

Soda R (1962) Deformation vibration of SiOH. Bull Chem Soc Jap 35:1897-1898

Sosin A (1975) The kinetics of an atom diffusing in one dimension: hydrogen in quartz. Radiation Effects 26:267-271

Spitzer WG, Kleinman DA (1961) Infrared lattice bands of quartz. Phys Rev 121:1324-1335

Sprunt ES, Nur A (1976) Reduction of porosity by pressure solution: experimental verification. Geology 4:463-466

Sprunt ES, Nur A (1977) Destruction of porosity through pressure solution. Geophys 42:726-741

Staats PA, Kopp OC (1974) Studies on the origin of the 3400 cm^{-1} region infrared bands of synthetic and natural α-quartz. J Phys Chem Solids 35:1029-1033

EBSCOhost - printed on 2/13/2023 4:48 AM via . All use subject to https://www.ebsco.com/terms-of-use

Stenina NG, Bazarov LSh, Shcherbakova MYa, Mashkovtsev RI (1984) Structural state and diffusion of impurities in natural quartz of different genesis. Phys Chem Min 10:180-186
Stone J, Walrafen GE (1982) Overtone vibrations of OH groups in fused silica optical fibers. J Chem Phys 76:1712-1722
Tada R, Siever R (1986) Experimental knife-edge pressure solution of halite. Geochim Cosmochim Acta 50:29-36
Tada R, Maliva R, Siever R (1987) A new mechanism for pressure solution in porous quartzose sandstone. Geochim Cosmochim Acta 51:2295-2301
Takamura T, Yoshida H, Inazuka K (1964) Infrared characteristic bands of highly dispersed silica. Kolloid Zeitschrift 195:12-16
Terzaghi K (1936) Simple tests determine hydrostatic uplift. Engineering New-Record 116:872-875
Terzaghi K (1945) Stress conditions for the failure of saturated concrete and rock. Am Soc Testing Materials Proc 45:777-792
Touray JC, Beny-Bassez C, Dubessy J, Guilhaumou N (1985) Microcharacterization of fluid inclusions in minerals by Raman microprobe. Scanning Electron Microscopy I:103-118
Tullis J, Yund RA (1982) Grain growth kinetics of quartz and calcite aggregates. J Geol 90:301-318
Tullis J, Yund RA (1989) Hydrolytic weakening of quartz aggregates: the effects of water and pressure on recovery. Geophys Res Letters 16:1343-1346
Tullis J, Shelton GL, Yund RA (1979) Pressure dependence of rock strength: implications for hydrolytic weakening. Bull Minéral 102:110-114
Twiss RJ (1974) Structure and significance of planar deformation features in synthetic quartz. Geology 2:329-332
Twiss RJ (1976) Some planar deformation features, slip systems, and submicroscopic structures in synthetic quartz. J Geol 84:701-724
Verhoogen J (1952) Ionic diffusion and electrical conductivity in quartz. Am Min 37:637-655
Vry J, Brown PE, Beauchaine J (1987) Application of micro-FTIR spectroscopy to the study of fluid inclusions. EOS Trans Am Geophys Union 68:1538
Wade WH, Cole HD, Meyer DE, Hackerman N (1961) Adsorptive behavior of fused quartz powders. Adv Chem Ser 33:35-41
Watson EB, Brenan JM (1987) Fluids in the lithosphere, 1. experimentally-determined wetting characteristics of CO_2-H_2O fluids and their implications for fluid transport, host-rock physical properties, and fluid inclusion formation. Earth Planet Sci Letters 85:497-515
Weil JA (1975) The aluminum centers in α-quartz. Radiation Effects 26:261-265
Weil JA (1984) A review of electron spin spectroscopy and its application to the study of paramagnetic defects in crystalline quartz. Phys Chem Min 10:149-165
Weyl PK (1959) Pressure solution and the force of crystallization-a phenomenological theory. J Geophys Res 64:2001-2025
Whalen JW (1961a) Thermodynamic properties of water adsorbed on quartz. J Phys Chem 65:1676-1681
Whalen JW (1961b) Heats of immersion in silica-water systems. Adv Chem Ser 33:281-290
White S (1973) Dislocations and bubbles in vein quartz. Nature Phys Sci 243:11-14
Wiederhorn SM (1967) Influence of water vapor on crack propagation in soda-lime glass. J Am Ceram Soc 50:407-414
Wiederhorn SM (1969) Fracture surface energy of glass. J Am Ceram Soc 52:99-105
Wiederhorn SM, Bolz LH (1970) Stress corrosion and static fatigue of glass. J Am Ceram Soc 53:543-548
Wilkins RWT, Barkas JP (1978) Fluid inclusions, deformation and recrystallization in granite tectonites. Contrib Min Pet 65:293-299
Wintsch RP, Dunning J (1985) The effect of dislocation density on the aqueous solubility of quartz and some geologic implications: a theoretical approach. J Geophys Res 90:3649-3657
Wood DL (1960) Infrared absorption of defects in quartz. J Phys Chem Solids 13:326-336
Wopenka B, Pasteris JD, Freeman JJ (1990) Analysis of individual fluid inclusions by Fourier transform infrared and Raman microspectroscopy. Geochim Cosmochim Acta 54:519-533
Young GJ, Bursh TP (1960) Immersion calorimetry studies of the interaction of water with silica surfaces. J Colloid Sci 15:361-369
Yund RA (1986) Interdiffusion of NaSi-CaAl in peristerite. Phys Chem Min 13:11-16
Yund RA, Snow E (1989) Effects of hydrogen fucacity and confining pressure on the interdiffusion rate of NaSi-CaAl in plagioclase. J Geophys Res 94:10662-10668
Yund RA, Smith BM, Tullis J (1981) Dislocation-assisted diffusion of oxygen in albite. Phys Chem Min 7:185-189
Yurimoto H, Kurosawa M, Sueno S (1989) Hydrogen analysis in quartz crystals and quartz glasses by secondary ion mass spectrometry. Geochim Cosmochim Acta 53:751-755
Zhang Y, Stolper EM, Wasserburg GJ (1991) Diffusion of a multi-species component and its role in oxygen and water transport in silicates. Earth Planet Sci Letters 103:228-240

EBSCOhost - printed on 2/13/2023 4:48 AM via . All use subject to https://www.ebsco.com/terms-of-use

PREFERRED ORIENTATION PATTERNS IN DEFORMED QUARTZITES

H.-R. Wenk

Department of Geology and Geophysics
University of California
Berkeley, CA 94720 U.S.A.

INTRODUCTION

Traditionally there has been little interaction between mineralogists and structural geologists. Within the *Reviews in Mineralogy* series, deformation of minerals (particularly of polycrystalline aggregates) has only been addressed in depth in the treatment of feldspar minerals (Tullis, 1983). The lack of attention is unfortunate, and this chapter tries to correct it for quartz. The intent is to make mineralogists aware of the tectonic significance of this mineral and to illustrate the way in which mineralogical methodology can be applied to interpret deformation features. The inclusion of such a chapter in a mineralogy book should also highlight to structural geologists the fact that mineral deformation obeys crystallographic laws based on physical principles. This brief overview emphasizes the requirement for close interaction between research in mineralogy and structural geology. Quartz is of considerable tectonic interest because under many conditions it is one of the most ductile phases in crustal rocks, and its rheology dominates the deformation behavior. The literature on quartz deformation is extensive and beyond the scope of this chapter. We will merely touch the surface to give the reader access to this large field of investigation and to stimulate future work.

CREEP DEFORMATION AND DEFORMATION MECHANISMS

Minerals like quartz may plastically deform under conditions of constant stress and temperature. This "creep deformation" occurs through a combination of slip motion, which may be described as a sliding of successive planes of atoms across one another, and a recovery mechanism, such as dislocation climb normal to the slip plane or grain boundary diffusion and recrystallization. Because creep is thermally activated, its role in deformation usually becomes more significant with higher temperature. Creep obeys an Arrhenius relationship of the form $d\varepsilon/dt = A\ \sigma^n\ e^{-Q/RT}$, where $d\varepsilon/dt$ is the strain rate, σ is the differential flow stress ($\sigma_1 - \sigma_3$), Q is activation energy, R is the gas constant, and T is the absolute temperature. In this flow law, A and n are experimentally determined constants that are characteristic for a given material.

The way in which a mineral deforms is strongly dependent on its structure. α–quartz has trigonal symmetry, with point group 32 (Fig 1). In many quartzites, the "trigonality," or the difference in orientation patterns for positive and negative rhombs, is very pronounced. At high temperature, α-quartz transforms to hexagonal β–quartz, with point group 622 (see chapter by Heaney). In high grade metamorphic rocks, deformation occurs in the β-quartz stability field (Fig. 2). The displacive phase transition from α– to β–quartz measurably changes the susceptibility to deformation. Linker and Kirby (1981), Kirby (1977) and Kirby and McCormick (1979) performed creep experiments on hydrolytically weakened quartz single crystals that were oriented identically and deformed on the same slip systems. These researchers observed different flow behaviors for α– and β–quartz, such that the high-temperature β phase exhibited an activation energy three time higher than

EBSCOhost - printed on 2/13/2023 4:48 AM via . All use subject to https://www.ebsco.com/terms-of-use

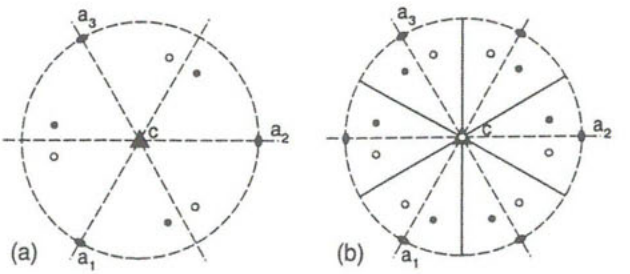


Figure 1. Point group symmetries of α quartz (32) (a), and calcite ($\bar{3}2/m$) (b). The centrosymmetric group is generally used in texture studies.

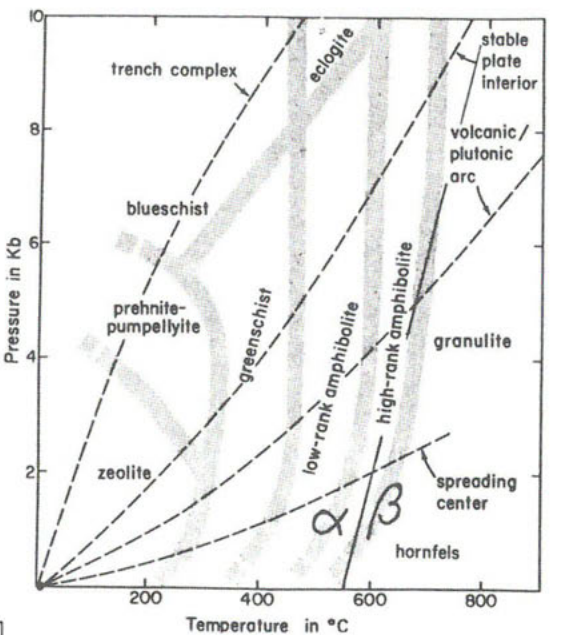


Figure 2. Pressure-temperature diagram illustrating metamorphic facies and the stability fields for α– and β–quartz (as modified from Ernst, 1976).

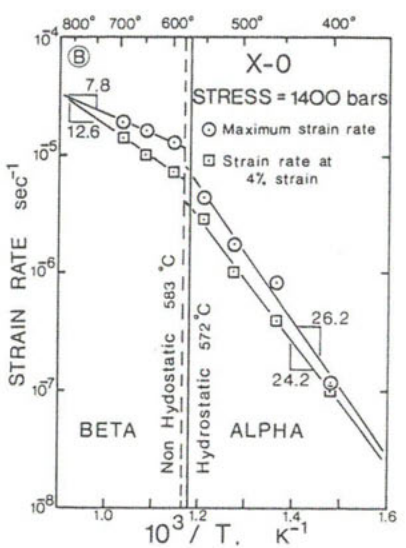


Figure 3. Experimental creep deformation of synthetic single crystals of quartz oriented for prism *c*-slip illustrating in a strain rate vs. inverse temperature diagram that α– and β–quartz have different activation energies for slip (Kirby and McCormick, 1979).

EBSCOhost - printed on 2/13/2023 4:48 AM via . All use subject to https://www.ebsco.com/terms-of-use

that of α–quartz (Fig. 3). They also determined the strain rate sensitivity of the flow stress and obtained a stress exponent (n) of 3.7.

Both α– and β–quartz lack a center of symmetry and may exist as right- or left-handed structures. The absence of a center of symmetry gives rise to such properties as piezoelectricity, and several investigations confirm the presence of a piezoelectric effect in polycrystalline quartz even though the dominance of one hand in a polycrystalline aggregate remains unconfirmed (e.g., Bishop, 1981; Parkhomenko, 1971; Ghomshei and Templeton 1989). In many deformation studies and particularly investigations of preferred orientation, enantiomorphism cannot be identified, and a higher crystal symmetry is used by adding a center of symmetry to 32. This produces pointgroup $\bar{3}2/m$, which is the same as that of calcite and will be used in representations in this chapter (Fig. 1b).

Slip systems that are active during ductile deformation of quartz can be established by experimental deformation of oriented single crystals or by identifying dislocations and their Burgers vector through contrast experiments with the TEM (e.g., McLaren and Phakey, 1965). The best established slip system is (001)⟨110⟩ (Christie et al., 1964; Beata and Ashbee, 1967; Griggs and Blacic, 1965; Blacic, 1975); this system appears to dominate at low temperature. At higher temperature prismatic slip {100} ⟨001⟩ becomes active (Beata and Ashbee, 1969, 1970; Blacic, 1975), and in such samples Burgers vectors of ⟨110⟩ and [001] have been identified (e.g., Ardell et al., 1974; McLaren et al., 1967; Morrison-Smith et al., 1976; Doukhan and Trepied, 1985). Evidence for other slip systems, such as prismatic {100}⟨010⟩, rhombohedral {101} or {011}⟨010⟩ or ⟨$\bar{1}\bar{1}$1⟩, and pyramidal {2$\bar{1}$1} ⟨$\bar{1}\bar{1}$1⟩ is more circumstantial and largely based on the fact that quartz crystals do deform if they are compressed parallel to the *c*-axis (Baeta and Ashbee, 1969; Hobbs et al., 1972). These slip systems are restricted to high temperature deformation. So far, Burgers vectors ⟨111⟩ have not been identified by electron microscopy. There is no reliable information with respect to critical shear stresses and their dependence on strain rate and temperature. It also is not certian whether slip on positive and negative rhombs is equivalent or whether there is a preference for the sense of shear, as in rhombohedral carbonates. The well established slip systems have a higher hexagonal symmetry, and if only those systems were active, one would expect orientation distributions in polycrystals to display hexagonal symmetry.

There are several reasons for the relative paucity of mechanical data for this well-studied solid in comparison with other minerals, such as carbonates and olivine. Induction of dislocation creep in natural quartz requires a high-pressure solid medium apparatus, and the procurement of high-quality data is experimentally difficult. Moreover, as described in Chapter Kronenberg, traces of water drastically alter the strength of quartz (Griggs and Blacic, 1965). The incorporation of only 1000 to10,000 ppm H_2O decreases the strength by an order of magnitude (Griggs, 1967; Hobbs, 1984; Koch et al., 1989). Models of hydrolytic weakening have been reviewed in depth by Paterson (1989), but there is little agreement over several issues: What is the speciation of hydrogen in quartz (Cordier and Doukhan, 1991)? Which species is responsible for the weakening effect, and how does hydrogen control dislocation movement?: Some authors (Griggs, 1967; Kekulawala et al., 1981) argue that intrinsic structural defects occur as Si-O-Si bonds that have been replaced with weaker hydrolized silicon-oxygen bridges (i.e., Si-OH:HO-Si). Others, on the other hand, believe that molecular water associated with concentrated dislocations produces a mechanical instability at a much larger scale (McLaren et al., 1983; Den Brok and Spiers, 1991).

Another difficulty with determining slip systems in quartz is that the mineral is extremely susceptible to radiation damage, making it very difficult to perform contrast

EBSCOhost - printed on 2/13/2023 4:48 AM via . All use subject to https://www.ebsco.com/terms-of-use

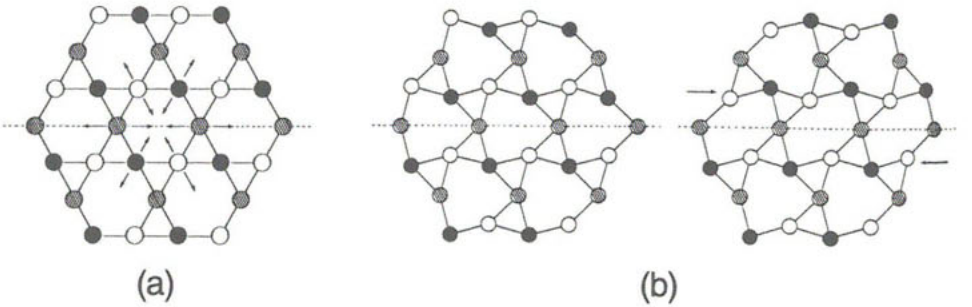


Figure 4. Dauphiné twinning in quartz can be induced (a) thermally during the α–β phase transformation, or (b) mechanically by shear on (100) [010].

experiments with the TEM to identify the Burgers vectors associated with dislocations. There is experimental evidence for slip in the ⟨110⟩ and [001] directions, but slip planes are more difficult to establish because dislocations are often curved, and they are generally not concentrated in discrete planes, which makes trace analysis impossible.

It has long been known that high stresses induce mechanical Dauphiné twinning (Zinserling and Shubnikov, 1933). Dauphiné twins are geometrically related by a 2-fold rotation about the *c*-axis. They can be produced by a slight distortion of the structure, either by cooling through the β–α phase transformation (Fig. 4a) or by shear (Fig. 4b). Mechanical twinning has also been documented in polycrystalline quartz experimentally deformed or loaded in the α field (Tullis, 1970; Tullis and Tullis, 1972). Barber and Wenk (1991) described the influence of dislocation microstructures on the appearance of twins during the β–α phase transformation (Fig. 5). Twins created during the transition typically are mobile at temperatures just below the critical point, but in deformed quartzites dislocations appeared to pin the domain boundaries.

High shear stresses also may induce Brazil twinning in α-quartz (McLaren et al., 1967). The structural changes required to induce Brazil twins with right- and left-handed lamellae are much more profound than those associated with Dauphiné twinning, since the Brazil twin boundary requires both distortion of the oxygen framework and displacement of some Si cations (McLaren and Phakey, 1966). Therefore, higher differential stresses are required to produce Brazil twin domains. In some deformation lamellae in experimentally deformed quartz, thin layers of glass and arrays of dislocations have been identified (Christie and Ardell, 1974). Amorphous lamellae also are typical of quartz subjected to shock (e.g., Müller and Défourneaux, 1968; Gratz et al., 1992). These results suggest that deformation lamellae in similar orientations with high dislocation concentrations in some naturally deformed quartzites may originally have been amorphous.

TEXTURES: MEASUREMENTS AND REPRESENTATION

Crystal deformation can be studied at different scales. Within a single crystal, it may be manifested through linear and planar defects, especially as systematic dislocation microstructures. On the larger scale of the polycrystal, the petrographic microscope may reveal that grains in a recrystallized quartzite are equant (Fig. 6a), whereas in some granulitic gneisses the quartz crystals are extremely flattened (Fig. 6b). Such shape preferred orientation is clearly related to deformation history. The grain shape has been used to estimate the finite strain, although it should be noted that complete recrystallization

EBSCOhost - printed on 2/13/2023 4:48 AM via . All use subject to https://www.ebsco.com/terms-of-use

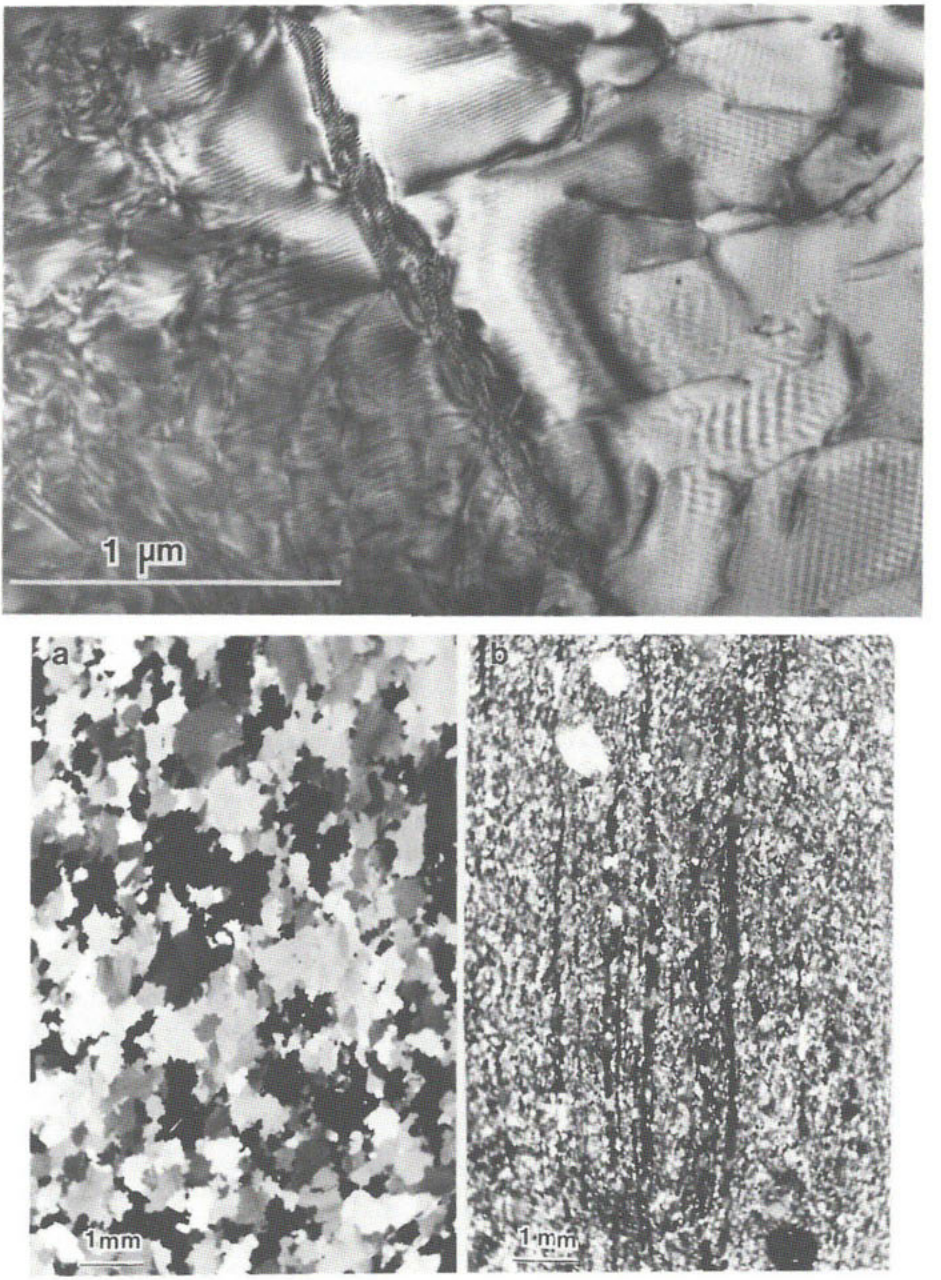


Figure 5 (above). Naturally deformed quartz heated to the critical temperature in the HVEM. Dauphiné twins (regular linear or grid pattern) are pinned by dislocations (dark lines) (Barber and Wenk, 1991).

Figure 6 (below). Photomicrographs of naturally deformed quartz. (a) Recrystallized quartzite from the Bergell Alps, greenschist facies (Brg 420) and (b) Highly flattened quartz grains (dark stringers) in granulite grade leucogranitic gneisses from Palm Canyon, California (PC 253). Traces of foliation plane and lineation are N-S.

EBSCOhost - printed on 2/13/2023 4:48 AM via . All use subject to https://www.ebsco.com/terms-of-use

of a quartz aggregate limits the usefulness of grain shape in determining the total rock strain, since the shape is continually reset. Other bulk deformation features become visible when a gypsum plate is inserted and the sample is viewed in cross-polarized light. Under these conditions, color patterns that change uniformly as the stage is rotated may be observed. These patterns are indicative of an alignment of crystal axes, known as crystallographic (or lattice) preferred orientation or "texture," which is not to be confused with "petrographic texture." Particular orientation patterns may develop as crystals are rotated during deformation, and thus they reflect the deformation mechanisms and the strain history. The crystallographic preferred orientation may or may not be related to the shape preferred orientation.

Texture is a characteristic property of many deformed materials. The two most important mechanisms of texture development, slip and recrystallization, are closely related to dislocation structures. Recrystallization refers specifically to an isocompositional creation of high-angle grain boundaries, and during recrystallization the dislocation density controls the stability of grains and the orientations of the grain boundaries. Dislocations are a temporary record of the deformation history, and they are modified by each successive event. Furthermore, they are local features and are representative of only small volumes of the material. Consequently, they typically are characterized at a microscopic level. By contrast, macroscopic texture patterns are the accumulated product of the whole deformation history, and they represent an average over large volumes of material. In this sense they are similar to mechanical properties, such as stress-strain curves, which are often used to assess a plasticity model. But in contrast to a one-dimensional stress-strain curve, textures are complex three-dimensional distributions that are often a unique indicator of underlying processes. This is especially true for low-symmetry compounds that are characterized by complicated crystal structures, few and symmetrically unrelated slip systems, high plastic anisotropies, and high strain-rate sensitivities of stress.

Texture can be measured quantitatively grain by grain with a universal stage microscope. However, in the case of quartz with no cleavage or visible twins, only the *c*-axis orientation can be determined. Recently, different diffraction techniques (X-ray, neutron or electron) have been used to record orientation densities. Texture results are represented in pole figure (or fabric) diagrams, which are projections of a sphere on which poles to a lattice plane *hkl* for many crystallites are collected. Usually, pole figure diagrams are contoured, expressed as pole densities, and normalized to represent pole densities in multiples of a reference sample with a random orientation pattern (m.r.d.= multiples of a random distribution). Figure 7 illustrates the distribution of axes *c*-axes [001] and *a*-axes ⟨110⟩ for a recrystallized quartzite.

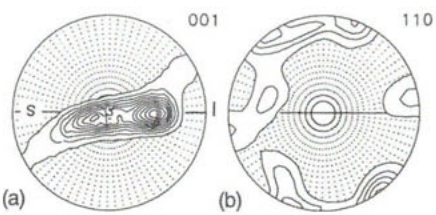


Figure 7. Description of the texture in quartzite Brg 420 with (a) *c*-axis; and (b) *a*-axis pole figures. The foliation plane s and the lineation direction l are indicated. Equal area projection on upper hemisphere. Pole densities are contoured. Contour interval is 1 m.r.d. (multiples of a random distribution). Dots are a 5° × 5° grid below 1 m.r.d.

Pole figures are quantitative but still incomplete representations of preferred orientations. The *c*-axis pole figure does not contain information about the orientation distribution of *a*-axes, for example, except that in each crystal the *a*-axis has to be at a 90° angle from

EBSCOhost - printed on 2/13/2023 4:48 AM via . All use subject to https://www.ebsco.com/terms-of-use

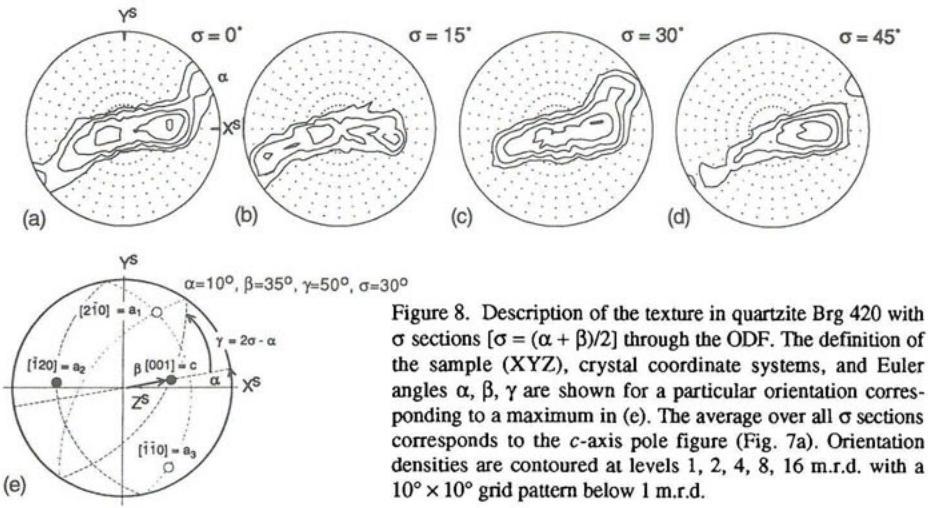


Figure 8. Description of the texture in quartzite Brg 420 with σ sections [σ = (α + β)/2] through the ODF. The definition of the sample (XYZ), crystal coordinate systems, and Euler angles α, β, γ are shown for a particular orientation corresponding to a maximum in (e). The average over all σ sections corresponds to the *c*-axis pole figure (Fig. 7a). Orientation densities are contoured at levels 1, 2, 4, 8, 16 m.r.d. with a 10° × 10° grid pattern below 1 m.r.d.

the *c*-axis. A more complete representation is the orientation distribution function (ODF), which relates the crystal coordinate system in all crystallites to a sample coordinate system. This can be done with three angles, such as Euler angles α, β and γ (Fig. 8e). Figures 8a-d shows a three-dimensional orientation density (or probability) distribution for the same quartzite, represented as four diagonal or oblique σ-sections that are least distorted (Helming et al., 1988). The angle σ is defined as $\sigma = (\alpha + \gamma)/2$. Each section displays the *c*-axes of those crystallites for which the *a*-axes are oriented in a particular direction. This is a more complete representation of texture and is generally preferred. The ODF can be calculated from measured pole figures using various methods.

The ODF in Figures 8a-d can be viewed as an elongated tube of high orientation density which extends at α = 0° and β at low angles along $\sigma = (\alpha + \gamma)/2$. How does one read such a diagram? It is necessary first to define the coordinate system. The sample coordinate X is chosen parallel to the lineation and Z parallel to the pole of the schistosity. Crystal coordinates of this trigonal mineral are chosen such that z is parallel to the pole of (001) = *c* and x is parallel to the pole of (2-10) = a_1 (Figs. 1b and 8e). It then is possible to reconstruct the orientation of any position in the ODF and find the corresponding crystal orientation.

As an example, consider the maximum density in the section with σ = 30° (Fig. 8c). The orientation of a quartz crystal may be viewed as a boat on the Earth's surface. Two angles (α: longitude, β: colatitude) define its location (i.e., the *c*-axis orientation), and a third angle [γ or $\sigma = (\alpha + \gamma)/2$] defines the direction in which it is heading (Wenk and Kocks, 1987). With this picture of the boat, it is possible to determine that the masts (*c*-axes) are at α = 10° and β = 35°. The heading (i.e., the *a*-axis direction relative to the reference boat in the North pole) is σ = 30°. The full crystal orientation is indicated in the stereogram in Figure 8e.

Pole figure diagrams for fibrous textures are special because the pole figures are axially symmetric. Figure 9a displays some pole figures for chalcedony. Here only the symmetry (fiber) axis is of interest, and it is customary to represent orientation information on inverse pole figures that show the density of fiber axes relative to crystal coordinates. The inverse pole figures are also calculated from measured pole figures through the ODF.

EBSCOhost - printed on 2/13/2023 4:48 AM via . All use subject to https://www.ebsco.com/terms-of-use

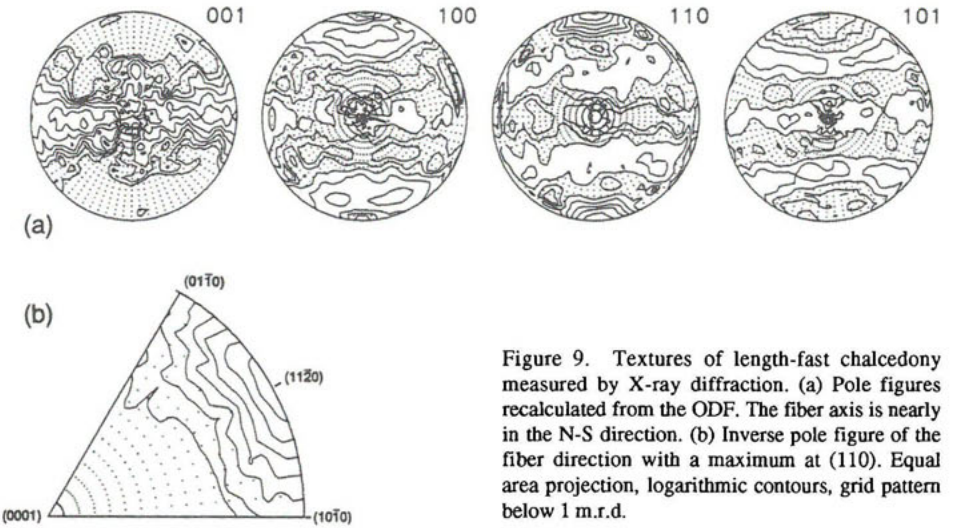


Figure 9. Textures of length-fast chalcedony measured by X-ray diffraction. (a) Pole figures recalculated from the ODF. The fiber axis is nearly in the N-S direction. (b) Inverse pole figure of the fiber direction with a maximum at (110). Equal area projection, logarithmic contours, grid pattern below 1 m.r.d.

Figure 9b shows an inverse pole figure for this length-fast chalcedony with a concentration at [110], indicating that *a*-axes rather than poles to *m* prisms are parallel to the fiber direction.

Texture analysis is a large field of investigation in materials science and structural geology, and it has been reviewed in several books (e.g., Bunge, 1982; Bunge and Esling, 1982). Wenk (1985) provides summaries that earth scientists may find useful as an introduction to various aspects of texture research—such as measurement, representation, ODF analysis, and interpretation—with an emphasis on geological systems.

EXPERIMENTAL DEFORMATION OF POLCRYSTALLINE QUARTZ

Preferred orientation is easily induced experimentally in quartz aggregates during ductile deformation. Figure 10 shows, by inverse pole figures and *c*-axis profiles, typical texture types that developed during plastic deformation of fine-grained flint (Green et al., 1970). At low temperatures, *c*-axes orient near the compression axis for samples deformed in the α- as well as in the β-field (Figs. 10a,b,e,f). At higher temperature a distinct maximum develops near $r = \{101\}$ (Fig. 10c), and correspondingly a "small circle girdle" of *c*-axes develops (Fig. 10g). It is generally agreed that at low temperature basal $c = (001)$ slip is the dominant mechanism, whereas at higher temperature prismatic and rhombohedral slip become active (see section 2). The distinct difference between positive (*h0l*) and negative (0*hl*) rhombs (e.g., Fig. 10c) can be partially attributed to mechanical Dauphiné twinning. In fact, Tullis and Tullis (1972) documented strong preferred orientation in flint and quartzite samples subjected to stress but with almost no permanent strain, and they attributed it to Dauphiné twinning. Dauphiné twins do not change the *c*-axis orientation, which is random in the case of Figure 10d, but they do reverse positive and negative rhombs (Fig. 10d). Tullis et al. (1973) observed similar texture patterns in axially compressed quartzite, documenting a transition from a "*c*"- (Figs. 11a,d) to an "*r*"-fabric (Figs. 11c,f). The angle of the *c*-axis small circle girdle increased as temperature became higher and the strain rate decreased, probably as a result of increasing proportions of prismatic slip (Fig. 12).

EBSCOhost - printed on 2/13/2023 4:48 AM via . All use subject to https://www.ebsco.com/terms-of-use

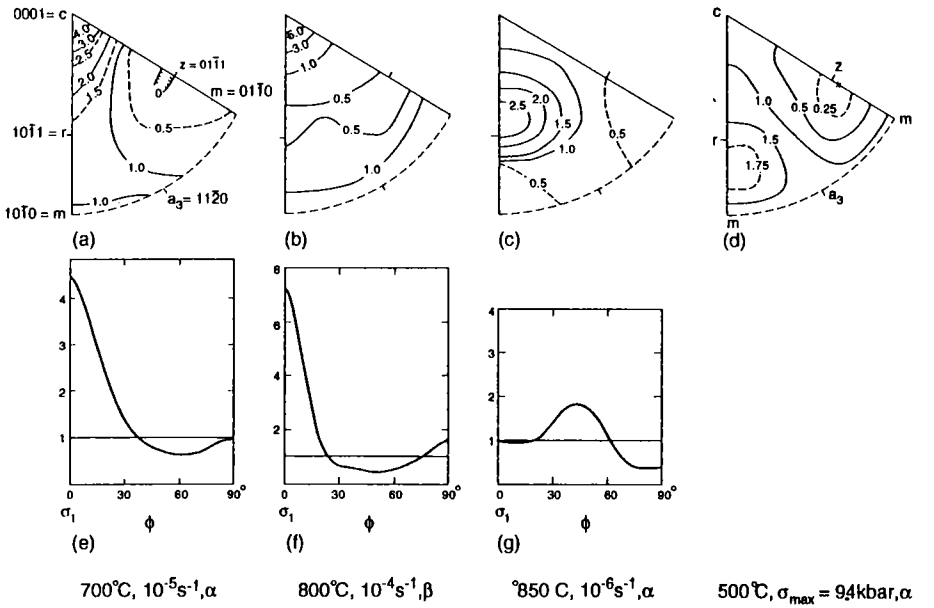


Figure 10. Typical textures developing during axial compression of flint. (a-d) inverse pole figures of the compression direction. (e-g) corresponding *c*-axis profiles from parallel to perpendicular to the compression direction. Deformation conditions and contour levels (in m.r.d.) are indicated. (a-c) from Green et al. (1970) (d) from Tullis and Tullis (1972). Sample (d) was stressed but without permanent deformation.

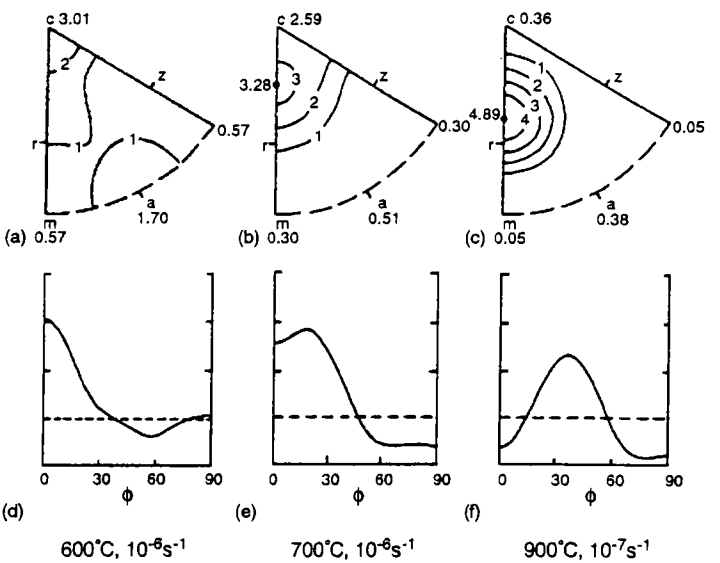


Figure 11 Typical texture patterns in experimentally axially compressed quartzites represented as inverse pole figures (a-c) and *c*-axis profiles from parallel to perpendicular to the compression direction (d-f). Temperature and strain rate are indicated. The sample in (c) is about 80% recrystallized. (Tullis et al., 1973).

EBSCOhost - printed on 2/13/2023 4:48 AM via . All use subject to https://www.ebsco.com/terms-of-use

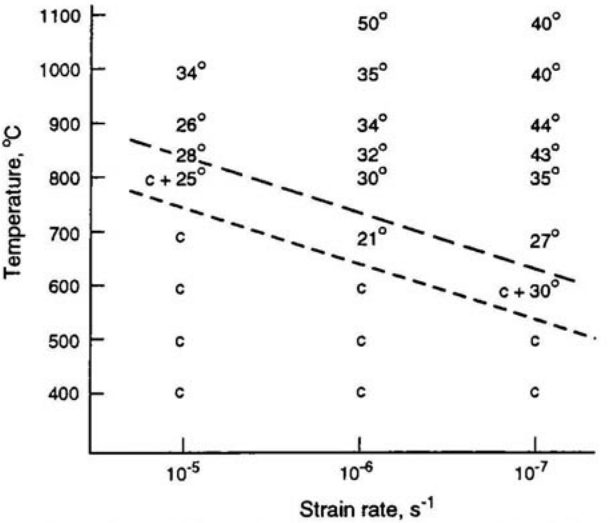


Figure 12. Texture patterns in experimentally deformed quartzite in a temperature vs. strain rate diagram. At low temperature a *c*-maximum type fabric forms, and at higher temperature and lower strain rates a *c* small circle girdle develops. The opening angle is indicated. Recognizable recrystallization occurs above the upper dashed line. (Tullis et al., 1973).

Experimental investigations also addressed the behavior of quartz during dynamic recrystallization. Hirth and Tullis (1992) used microstructures to identify three different recrystallization mechanisms with increasing temperature, decreasing strain rate, and thus decreasing flow stress: (1) Strain-induced grain boundary migration; (2) Progressive subgrain rotation; and (3) Progressive subgrain rotation with rapid boundary migration. Gleason et al. (1993) document the fact that textures in experimentally recrystallized quartzites are characteristic of these mechanisms. When grain boundary migration dominates, *c*-axes in recrystallized grains are oriented parallel to the compression direction (Fig. 13a). When subgrain rotation is important, a small circle girdle of *c*-axes develops

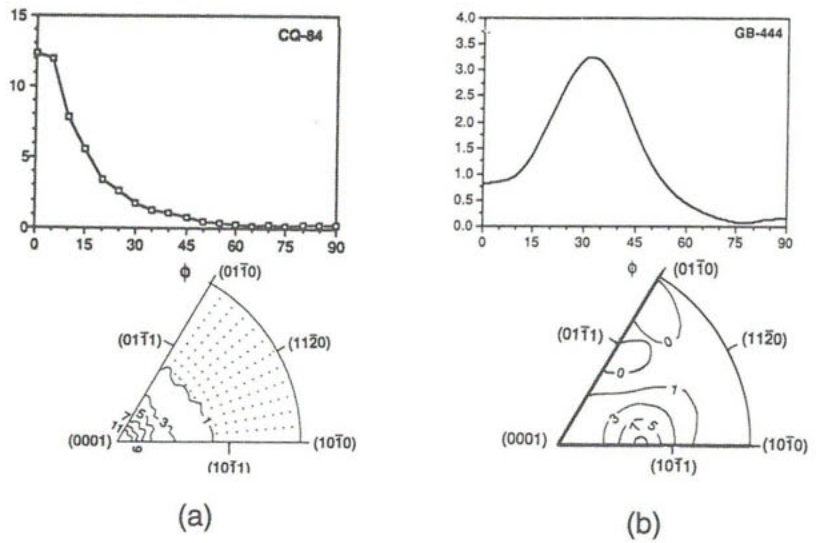


Figure 13. Textures in dynamically recrystallized quartzites represented as *c*-axis profiles from parallel to perpendicular to the compression direction (top) and inverse pole figures (bottom). (a) Texture typical of grain boundary migration. Novaculite shortened 57% at 900°C. (b) Texture of recrystallized grains attributed to subgrain rotation. Quartzite shortened 75% at 900°C, 60% recrystallized (Gleason et al., 1993).

EBSCOhost - printed on 2/13/2023 4:48 AM via . All use subject to https://www.ebsco.com/terms-of-use

(Fig. 13b). These patterns are similar to those observed in non-recrystallized quartzites deformed under similar conditions.

Only a few experiments address the effect of second phases on texture development. Tullis and Wenk (1994) have revealed that the addition of minor amounts of mica attenuates preferred orientation of quartz by causing heterogeneous deformation with strain concentrating in zones of mica, which facilitates grain boundary sliding (Fig. 14).

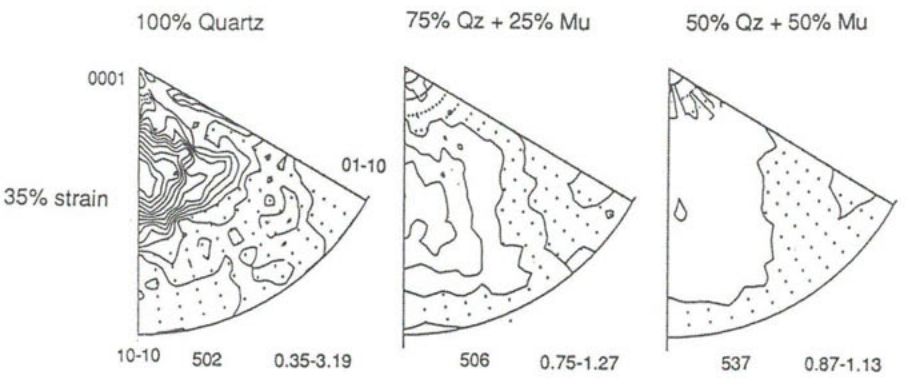


Figure 14. Textures in experimentally deformed quartz-muscovite mixtures represented as inverse pole figures. Addition of 25% mica strongly reduces the texture of quartz. Dot pattern below 1 m.r.d. Pole density maximum and minimum are indicated (Tullis and Wenk, 1994).

All experiments described above were performed using axial compression. Experimental fabric studies that examine plane strain are more relevant to geological conditions, but these include only a few pure shear experiments by Tullis (1977) and simple shear experiments by Dell'Angelo and Tullis (1989). These latter authors observed that samples with small deformation and no appreciable recrystallization exhibit a *c*-axis maximum that is displaced from the shear plane normal and is oriented against the sense of shear. When a highly recrystallized matrix is present, the *c*-axis maximum for unrecrystallized porphyroclasts is displaced *with* the sense of shear (Figs. 15a,b). In other quartzites, *c*-axes are more or less aligned perpendicular to the shear plane .

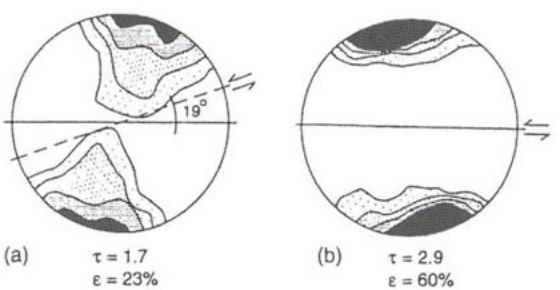


Figure 15. Two *c*-axis pole figures of experimentally sheared quartzite. At low strain the *c*-axis maximum at high angles to the shear plane is rotated against the sense of shear (a). At higher strain where recrystallization occurs, *c*-axes of old non-recrystallized grains are rotated with the sense of shear (b). The implied shear plane and sense of shear are indicated. After Dell'Angelo and Tullis (1989).

EBSCOhost - printed on 2/13/2023 4:48 AM via . All use subject to https://www.ebsco.com/terms-of-use

PLASTICITY THEORY

A real polycrystal that deforms and remains coherent has to fulfill both stress equilibrium and strain compatibility, and from the mechanical point of view there is a unique solution to its mode of deformation. However, solving this problem analytically is very difficult. Two extreme model approaches are most tractable: One assumes that each crystal deforms as an isolated grain with no knowledge of its neighbors in a uniform stress field. This approach, which provides stress equilibrium, is a lower bound limit for stress. In the second approach it is assumed that a grain is totally controlled by its neighbors and suffers the identical strain as the aggregate; this model guarantees compatibility at grain boundaries, and it provides an upper bound limit for stress. As long as many equivalent slip systems are available (in other words, there is low plastic anisotropy, as in fcc metals), the differences between predictions from the two approaches are small. However, for minerals with low crystal symmetry and few slip systems, a compatibility and an equilibrium model can give very different answers, and such systems need to be approached with more sophisticated theories that have recently been developed. This chapter will now illustrate a few aspects of equilibrium and compatibility theories, and then some extensions will be discussed. For a detailed review, see Wenk and Christie (1991).

In 1928 Schmid compressed single crystals of Zn, and he observed that the active component of an applied force is that which may be resolved on the slip plane and in the slip direction. More formally, $\tau = F/A \cos \phi \cos \lambda$, where τ is the shear stress, F is the applied compressional or tensional force, A is the cross-sectional area of the slip plane, ϕ is the angle between the slip plane normal and the applied force, and λ is the angle between the slip direction and the applied force. The critical resolved shear stress τ_c is associated with the critical force F_c required to initiate slip, and in crystals with few slip systems τ_c is a material constant that is independent of crystal orientation. This slip behavior can be explained by movements of dislocations whose geometry is crystallographically controlled. According to this concept, if a stress is applied, no plastic deformation occurs until the shear stress resolved on the slip system reaches its critical limit τ_c. The shear stress is maximized if the applied compressive force is halfway between the slip plane normal and the slip direction. During slip, an unconstrained crystal changes its shape but does not rotate (Figs. 16 a,b). However, in a compression experiment the ends of the crystal must remain in contact with the piston. Accordingly, the slip plane normal rotates toward the compression direction (Fig. 16c). In polycrystals, neighboring grains impose similar constraints that induce rotation, leading to the development of preferred orientation.

In the case of stress equilibrium, each grain in a polycrystal deforms according to the external stress. As the applied stress is increased, the grains strain only elastically. However, at some point those grains in an optimal orientation start to deform. As they rotate they become less favorably oriented. For deformation to proceed, the stress must be

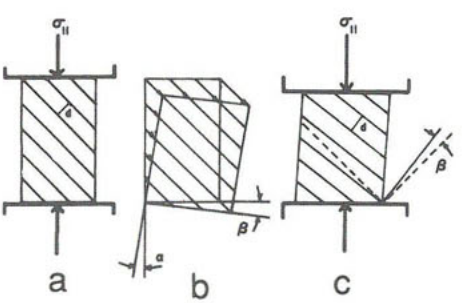


Figure 16. Schematic diagram to illustrate rotation of a crystal between pistons resulting from slip solid lines show a slip plane. If pistons are applied (a), shear deformation occurs which produces a new shape (b), leading to a lattice rotation β, if pistons stay in contact with the sample.

EBSCOhost - printed on 2/13/2023 4:48 AM via . All use subject to https://www.ebsco.com/terms-of-use

increased. As the stress is increased, the resolved shear stress increases on other slip systems, and grains with different orientations also become active, all rotating along trajectories towards the corresponding slip plane normal. In a compression experiment the compression axis can never reach the slip plane normal, because at that point the resolved shear stress is zero and an infinitely high stress would be required to activate slip. This model, which Schmid (1928) applied to Zn, is a rather crude approach. It accurately describes very small deformations for materials with a single slip system, but it does not apply very well to trigonal minerals like quartz. It assumes that each grain is isolated from its environment, but in reality a grain deforms independently of its neighbors only at very small deformations. For instance, when a dislocation reaches a grain boundary, that dislocation will project stresses into the neighboring grain, and the neighbor, depending on its orientation, will impose backstresses. If neighbors have a similar orientation, backstresses may be assumed to be small. On the other hand, if orientations are different, these stresses may be very high.

In 1938 Taylor proposed an ingenious and simple solution to avoid gaps and overlaps at grain boundaries. His solution was to impose homogeneous strain; in other words, he assumed that all grains undergo the same shape change regardless of their orientations. Homogeneous strain requires that each grain is able to undergo the macroscopically imposed shape change. Because the 3×3 strain tensor is symmetrical and if the volume is preserved the product of the diagonal elements remains constant, there are five variables, which require five degrees of freedom. Each independent slip system contributes one degree of freedom, and up to five independent slip systems are necessary to produce an arbitrary shape change. For special strain conditions and crystal orientations, fewer systems may suffice (e.g., in pure shear 2, in axial compression at least 3 are necessary), but never more than five need to be activated. In many crystals, including quartz, there are more than five potential slip systems. Taylor proposed selecting that combination of five which requires the least amount of plastic work; this combination depends on critical resolved shear stresses and orientation. Once the five active slip systems have been selected, shears on each system can be determined, as can the rotation of each grain. The application of the Taylor theory to trigonal quartz (Lister et al., 1978) provided the first physical basis for the interpretation of deformation textures in rocks. However, the original model had several deficiencies.

One of them is the assumption of rigid-plastic behavior, which is inconsistent with the viscoplastic behavior established experimentally for quartz (e.g., Linker and Kirby, 1981 in the equation, $d\varepsilon/dt = A\ \sigma^n\ e^{-Q/RT}$). Quartz has a stress exponent n of 3, and it is therefore very sensitive to strain rate, in contrast to metals where the stress exponent approaches infinity. Deformation occurs on a given slip system before its critical shear stress is reached, but it proceeds at a lower rate. Sensitivity to strain rate profoundly influences the texture pattern (Figs. 17a-c). The viscoplastic texture is smoother than the rigid-plastic texture (Wenk et al., 1989), corresponding better to natural textures (Schmidt, 1925) (Fig. 17d).

Another deficiency of the Taylor model is the assumption of homogeneous strain, which is not realistic in the case of quartz. Strain is least likely to be homogeneous at lower temperatures where few slip systems operate and recrystallization occurs by grain boundary migration. Strain tends to be much more homogeneous at higher temperatures where climb is easy and recrystallization occurs by subgrain rotation. Natural quartzite frequently exhibits highly deformed and relatively undeformed grains within the same sample, as has been evaluated quantitatively by measurements of aspect ratios (Bouchez, 1977). Bouchez (1977) noted that strongly deformed grains have different orientations (Fig. 18b) from weakly deformed grains (Fig. 18a).

EBSCOhost - printed on 2/13/2023 4:48 AM via . All use subject to https://www.ebsco.com/terms-of-use

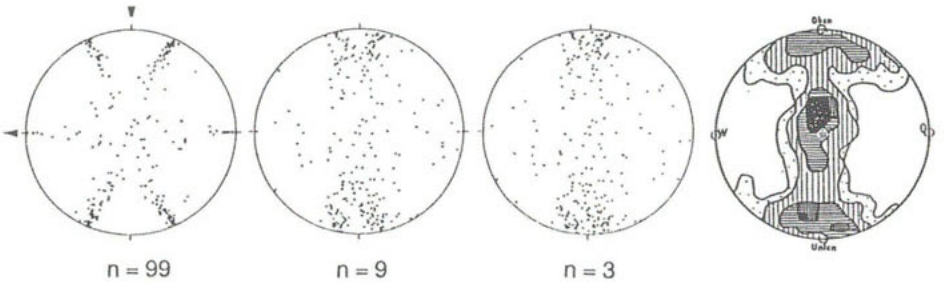


Figure 17. Taylor simulations for quartz in pure shear illustrating the effect of strain rate sensitivity (Wenk et al., 1989). Compression is N-S, extension E-W. The stress exponent, n, gives the most realistic texture and compares well with the measured quartz texture on the right side (Schmidt, 1925).

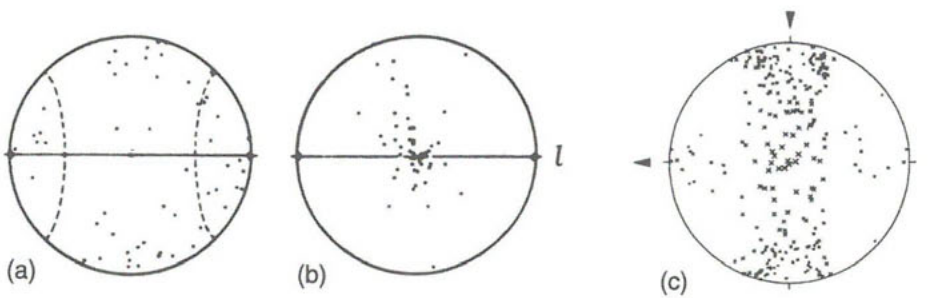


Figure 18. *c*-axis pole figures of quartz. (a) Naturally deformed quartzite, foliation horizontal and lineation l E-W. Collection of grains with an aspect ratio <4 (weakly deformed grains). (b) Same sample as in (a) but a collection of strongly deformed grains with an aspect ration >8 (Bouchez, 1977). (c) Viscoplastic self-consistent simulations of pure shear deformation. Symbol sizes are proportional to strain (Wenk et al., 1989). Compression is N-S, and extension is E-W. Note that in the simulations, highly deformed grains have a pattern as in (b); less deformed grains have a pattern resmbling (a).

Heterogeneous strain can be approached with a viscoplastic self-consistent theory (Molinari et al., 1987) that compromises between stress equilibrium and strain compatibility, requiring fewer slip systems and allowing most of the deformation to be activated by weak ones with a high resolved shear stress. While the Taylor theory does not permit heterogeneous deformation, in the viscoplastic self-consistent model, unfavorably oriented grains are allowed to deform more slowly, and each grain has the freedom to follow an optimum strain path that may be different from the one macroscopically imposed. The symbol sizes in Figure 18c are a measure of the grain deformation and agree very well with naturally observed microstructures (Figs. 18a,b).

Texture simulations using the self-consistent theory for simple shear deformation of a quartz aggregate have been performed with the following slip systems:

(1) Basal (001) ⟨010⟩ (normalized critical shear stress $\tau_c = 1$);

(2) Prismatic {100} [001] ($\tau_c = 2.0$ (a) and 0.4 (b));

(3) Prismatic {100} ⟨010⟩ ($\tau_c = 0.4$ (a) and 2.0 (b)); and

(4) Pyramidal {101} ⟨010⟩ ($\tau_c = 6$) and {101} ⟨101⟩ ($\tau_c = 6$).

EBSCOhost - printed on 2/13/2023 4:48 AM via . All use subject to https://www.ebsco.com/terms-of-use

These slip systems correspond to deformation at moderate and high temperature (Wenk et al., 1989). Several features are observed in (001) and (110) pole figures after a shear of $\gamma = 1.732$, and in rotation trajectory diagrams of several representative grains (Fig. 19). The rotation trajectories reveal that crystals rotate relative to the shear plane in the sense of the shear. There are no stable orientations in simple shear, and rotations are particularly fast for rate sensitive materials with a small stress exponent, such as quartz. This result runs counter to intuition, which suggests that the slip plane orients itself parallel to the shear plane ("easy slip").

Texture develops in simple shear because rotations occur at different rates for different orientations, with maxima in the pole figures corresponding to orientation regions in which rotations are slowest. The texture maxima of the *a* and *c*-axes are inclined to the shear plane, and the *c*-axes of the most highly deformed grains (large symbols) are contained in the shear plane perpendicular to the shear direction. The simulation that favors prism *a* slip (Fig. 19a) produces a *c*-maximum at high angles to the shear plane, as is typical of natural quartzites deformed at low and medium metamorphic grade. Grains in the center of (001) pole figures have large symbols, indicative of high strain, even though trajectories indicate that *c*-axes do not rotate much. The model in which prism *c* slip dominates (Fig. 19b) has a

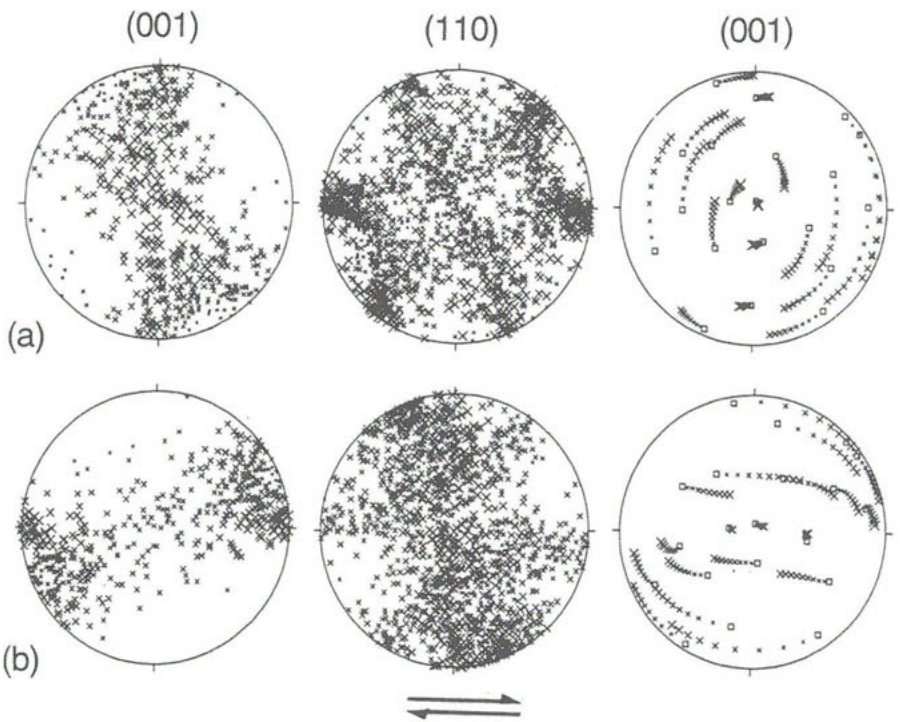


Figure 19. Viscoplastic self-consistent simulations for quartz (n = 3) illustrating the development of texture during simple shear. (001) and (110) pole figures for 500 grains after a shear of $\gamma = 0.87$. Large symbols represent plastically "hard" grains (a,b). (001) rotation trajectories for selected grains. The box indicates the starting orientation. Shear plane is horizontal and the sense of shear is indicated. (a) Conditions favoring prism *a*-slip; (b) conditions favoring prism *c*-slip (see text).

EBSCOhost - printed on 2/13/2023 4:48 AM via . All use subject to https://www.ebsco.com/terms-of-use

maximum of *c* axes at low angles to the shear plane; this case is less frequently observed, and prism *c* slip (which has been documented experimentally) is probably subordinate at tectonic conditions (see next section for a more detailed discussion).

Quantitative plasticity models such as that of Taylor are mainly applicable to single phase materials for which all components have similar mechanical properties. For polyphase materials composed of strong and weak particles, as are most quartz-bearing rocks, mechanical interactions between grains are much more complicated and deformation is locally heterogeneous. A few attempts have been made to model such systems, including quartz-bearing aggregates (Canova et al., 1992), but the field of polyphase polycrystal plasticity is still in its infancy. Finite element models may ultimately prevail over analytical solutions (Wenk, 1994).

The process of recrystallization is closely linked to deformation by slip, and a short discussion is appropriate because recrystallization, whether static or dynamic, frequently is responsible for preferred orientation in rocks. The driving force for recrystallization is internal strain, such as dislocations. There is a general tendency for a grain boundary to move towards and consume the grains containing the higher dislocation densities, thereby reducing the free energy of the system. The result is a preferential selection of grains with no, or few, dislocations. This process appears to characterize low-temperature regimes, and it has been impressively documented by in situ observations of recrystallization during deformation in two-dimensional model systems such as octa-chloropropane (e.g., Jessell 1986). In these experiments there is a general tendency for less deformed grains to replace more highly deformed grains, which are more favorably oriented for slip.

Recrystallization is much less understood than deformation by slip (e.g., Gottstein and Mecking 1985; Doherty et al., 1988). It is not clear whether preferred nucleation or preferred grain growth governs recrystallization, even for fcc metals. No general model is available to predict texture development. However, in all materials investigated so far (including quartz), there appears to be a close orientation relationship between host and newly nucleated grains. Therefore, a recrystallization texture generally emphasizes some components.of the deformation texture. Jessell (1988) has devised a model for texture development during recrystallization that assumes that grain boundary migration is the dominant mechanism, and Jessell and Lister (1990) have applied it to quartz. In this case the less deformed grains consume the more highly deformed grains. The degree of deformation of individual grains is assessed with the Taylor factor, i.e., the plastic work that a crystal has to undergo to satisfy homogeneous deformation. This may not be a valid assumption, since in real rocks plastically "hard" grains with a high Taylor factor may not deform at all.

Wenk et al. (1989) have noted that in self-consistent simulations of quartz deformed in pure and simple shear the most highly deformed grains (Figs. 18c and 19) have the same orientation as recrystallized grains in quartzite mylonites, specifically, a concentration of *c*-axes in the intermediate fabric direction Y (Fig. 7a). They concluded that in such a case nucleation of new grains may occur in the same orientation as those grains that are most highly deformed. These grains would grow and dominate the ultimate texture pattern. But quartz remains enigmatic, and the typical recrystallized mylonite texture with a *c*-axis maximum in the foliation plane and perpendicular to the lineation (Y) so far has not been reproduced in axial compression experiments (Gleason et al., 1993), probably because there are different regimes of dynamic recrystallization, as implied by Hirth and Tullis (1992).

EBSCOhost - printed on 2/13/2023 4:48 AM via . All use subject to https://www.ebsco.com/terms-of-use

SOME NATURAL TEXTURES

Textures have been measured from many naturally deformed quartzite specimens. Most of these texture investigations were based upon (001) pole figures obtained with a petrographic microscope equipped with a universal rotation stage. Sander (1950) has classified these textures into *c*-axis maximum fabrics, small circle girdles, great circle girdles, and crossed girdles (Fig. 20).

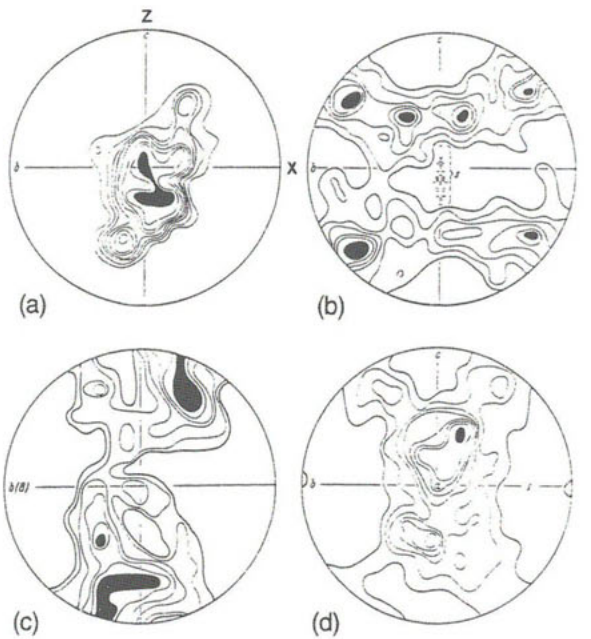


Figure 20. Typical quartz textures of naturally deformed quartzites represented as *c*-axis pole figures, where *c* is the pole to the foliation (Z), *b* the lineation (X) and *a* the intermediate fabric direction (Y).

(a) Typical Y maximum texture, common in mylonites (Saualpe, Austria).

(b) Small circle girdle observed in granulites (Burgstädt, Saxony).

Crossed girdles in metamorphic rocks: (c) from a quartz lens in marble (Hintertux, Tirol), (d) from deformed pegmatite (Melibokus, Odenwald, Germany).

(Sander, 1950)

These *c*-axis pole figures are incomplete texture representations. There is no information on the orientation of *a*-axes, on differences between positive and negative rhombs, and on possible enantiomorphism. Since Sander's work, several ODF descriptions of quartzites based on X-ray and neutron diffraction data have been obtained (e.g., Baker and Wenk 1972; Bunge and Wenk 1977; Schmid and Casey 1986; Mancktelow, 1987a,b; Mainprice et al., 1993; Helming et al., 1994). Quartz textures display a wide variability, which may be complicated partially due to the diversity of recovery mechanisms, such as dislocation glide and climb and recrystallization, but it also results from deformation histories. Figures 21a,b,c illustrate pole figures measured by neutron diffraction for some typical quartz textures, including a Y-maximum (a), small circle girdle (b) and crossed girdle (c). The *c*- and *a*-axes of Figures 21a,b have a very similar distribution to that predicted by the simple shear simulations, which favor prism *a* slip and subordinate basal slip (Fig. 19a). Figures 22a,b,c illustrate the corresponding ODF's in σ-sections. A σ-rotation of 30° corresponds to a crystal rotation of 60° (or 180°) about the *c*-axis and thus to a Dauphiné twin or a hexagonal character. Sample Sci 490 (Fig. 22b) is more closely "hexagonal" than the other two since sections σ and σ + 30° are similar. This sample was probably deformed in the β-quartz stability field near a granite contact.

An elegant method of texture representation that uses "tripods" was suggested by Schmid et al. (1981) and Schmid and Casey (1986). It has been applied in a modified

EBSCOhost - printed on 2/13/2023 4:48 AM via . All use subject to https://www.ebsco.com/terms-of-use

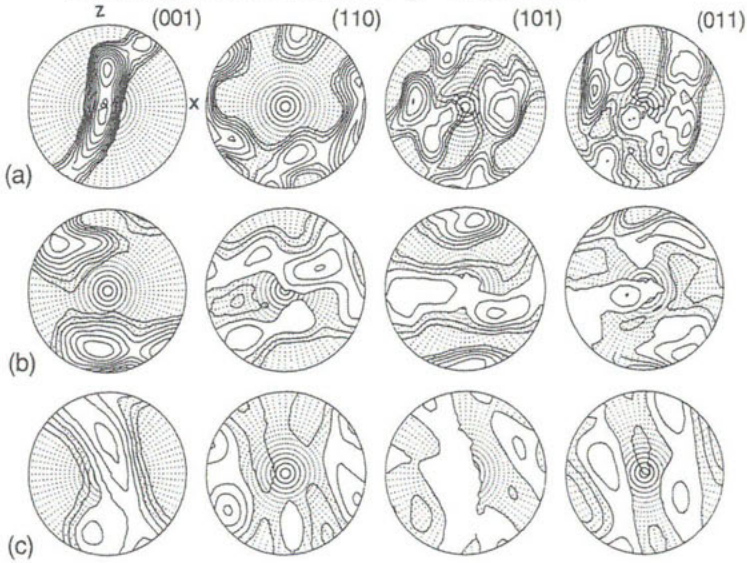


Figure 21. Typical quartz textures represented as pole figures for 4 different crystal directions, which were recalculated from the ODF. Notice the asymmetry in all patterns (X = lineation and Z = pole to the foliation are indicated). (a) Y maximum in recrystallized quartzite Brg 420 from the Bergell Alps. (b) Asymmetric small circle girdle in Sci 490 from a granite contact in the Bergell Alps. (c) Crossed girdle in W106 from Wildrose Canyon, Death Valley, California. Equal area projection. Logarithmic contour intervals (0.5, 0.71, 1.0, 1.41, 2.0 r.m.d., etc.). Dot pattern below 1 m.r.d.

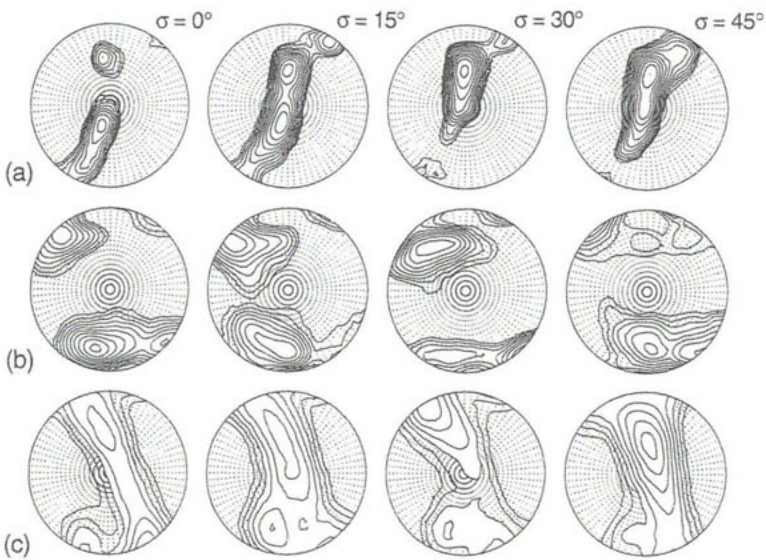


Figure 22. Typical quartz textures represented as ODF σ-sections. Same samples as in Figure 21. (a) Y maximum in recrystallized quartzite Brg 420 from the Bergell Alps. (b) Asymmetric small circle girdle in Sci 490 from a granite contact in the Bergell Alps. (c) Crossed girdle in W106 from metamorphic conglomerates in Wildrose Canyon, Death Valley, California. An average over all σ-sections is a (001) pole figure. Equal area projection. Logarithmic contour intervals. Dot pattern below 1 m.r.d.

EBSCOhost - printed on 2/13/2023 4:48 AM via . All use subject to https://www.ebsco.com/terms-of-use

version to the quartz textures illustrated above (Fig. 23). A complex quartz texture is divided into components that represent concentrations of orientation density (Helming et al., 1994). Each component is then expressed with a tripod, in which the legs point towards *a*-axes and the intersection illustrates the *c*-axis orientation. The size of the tripod is proportional to the volume in orientation space. The diagram for the single maximum fabric displays components with similar *c*-axis orientations but opposite *a*-axis orientations. Such components are related by Dauphiné twinning. [Caution: A representation by components is compact and may be easy to visualize, but it is purely descriptive. It should not be extended to imply deformation mechanisms, such as that *a*-axes are slip directions and are aligned in the macroscopic shear direction!]

The presence of Dauphiné twins cannot be verified with orientation distribution data because X-ray as well as neutron data collection averages over the whole sample, and local correlation information is lost. Recently, electron diffraction methods have been developed to study orientation relationships between neighboring grains. Electron backscatter diffraction pattern (EBSP) analysis is performed using a scanning electron microscope (for review see Wright, 1993), and it can reveal the existence of twin boundaries in naturally deformed quartzites (Fig. 24). If one calculates a misorientation map in a density space that depicts the rotation axis and the rotation angle required to bring neighboring grains to coincidence, there is a strong concentration for a 60° rotation around the *c*-axis; this rotation corresponds to the Dauphiné twin law (Fig. 25, Kunze et al., 1994).

GEOLOGICAL APPLICATIONS: A CRITICAL ASSESSMENT

Why are structural geologists interested in texture analysis? Textures contain information about the deformation history. An anisotropic orientation distribution in a portion of the crust constrains models of rheology for that region. In addition, rocks with texture have anisotropic physical properties. It is possible to determine finite strain from the orientation of phyllosilicates in slates and schists (e.g., Oertel, 1983). In carbonate rocks one can use texture patterns to distinguish between pure shear and simple shear deformation and, in the latter case, to infer the sense of shear (e.g., Ratschbacher et al., 1991). Interpretations rely either on empirical correlations of patterns with a known (or implied) geological history or they are based on comparisons with predictions from polycrystal plasticity theory. The latter has been quite successful for explaining preferred orientation in calcite, olivine, and phyllosilicate. However, plasticity theory is less satisfactory for quartz. First, quartz textures are often quite irregular so that it is difficult to assess which features are really significant. Second, interpretations of natural quartzite textures are much less convincing, even though individual publications present plausible explanations. Some inconsistencies need to be addressed in future research.

As with other minerals, quartz textures have been used to interpret changes in metamorphic grade, the deformation history, and particularly to infer the sense of shear in shear zones. Quartz is important because of its wide occurrence and its high ductility under most metamorphic conditions. Because of its high plastic anisotropy in comparison with calcite, preferred orientation may also affect the rheology of quartz-bearing rocks.

Fabric zonation with metamorphic grade

The relative ease with which certain slip systems operate depends on the physical conditions of the deformation. Temperature is the most important factor affecting critical resolved shear stresses. Since the texture patterns are linked to slip system activity, one should observe changes in active slip system with increases in temperature. Such changes

EBSCOhost - printed on 2/13/2023 4:48 AM via . All use subject to https://www.ebsco.com/terms-of-use

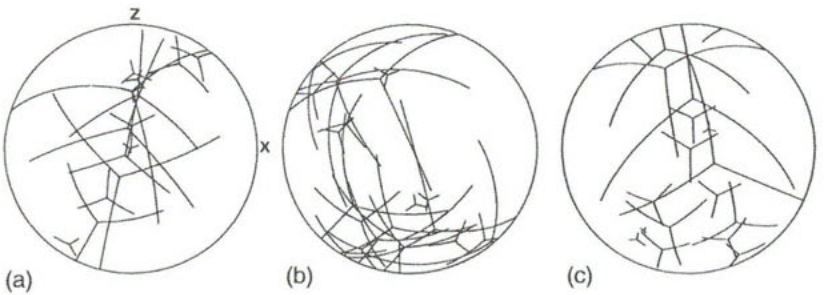


Figure 23. Tripod representation of texture components in the three quartzites of Figures 21 and 22. Center indicates the *c*-axes and "legs" point to the a-axes. The length of the legs is proportional to orientation volume of the component. Note that several components are related by the Dauphiné twin law (180° rotation about *c*) (Helming et al., 1994).

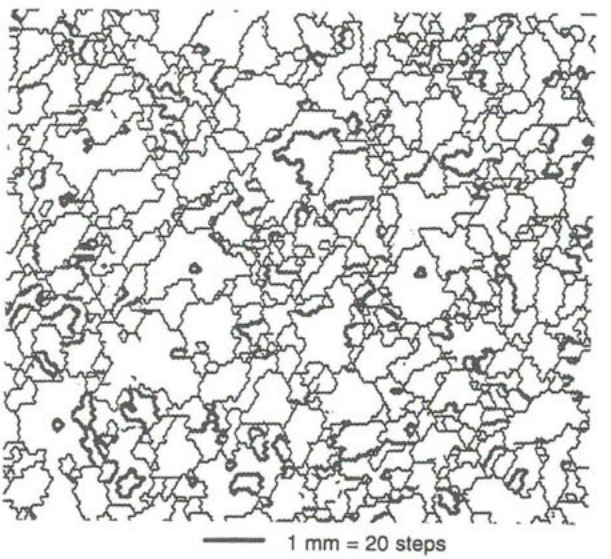


Figure 24. Grain boundary map for recrystallized quartzite Brg 420 based on local orientation determinations by EBSP with the SEM. The sample was scanned on a hexagonal pattern with 50 μm step size. Light lines are any grain boundaries with a misorientation of more than 10°, and heavy lines are grain boundaries between crystals with a Dauphiné twin relationship (Kunze et al., 1994).

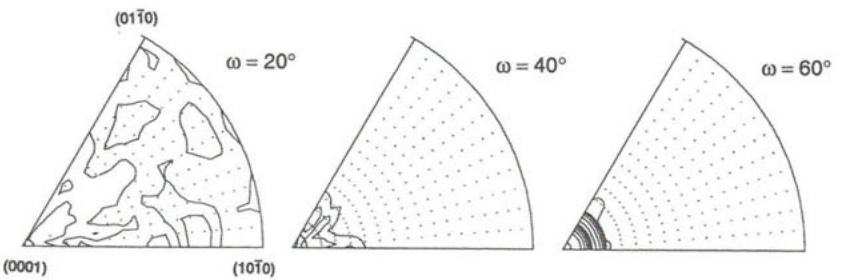


Figure 25. Misorientation distribution function (MDF) in axis-angle space relating misorientations between neighbor pairs for recrystallized quartzite Brg. 420. The maximum at c = (001) and ω = 60° corresponds to a Dauphiné twin (Kunze et al., 1994).

EBSCOhost - printed on 2/13/2023 4:48 AM via . All use subject to https://www.ebsco.com/terms-of-use

have been well established through experiments (e.g., Tullis et al., 1973) and simulations (Lister et al., 1978; Wenk et al., 1989; e.g., Fig. 19). As a result, one would expect to observe changes in deformation mechanisms in naturally deformed rocks wherever there are temperature gradients.

Behr (1964) documented with increasing metamorphic grade a transition from a crossed girdle (Fig. 26 top) to a small circle girdle type texture (Fig. 26 bottom) in the Erzgebirge and the Saxony granulites (Behr, 1961; 1968). The *c*-axis pole figures have almost orthorhombic symmetry (Fig. 26 left), except in the vicinity of a gabbro intrusion, where they become distinctly triclinic (Fig. 26 right). These papers were summarized in English and interpreted by Lister and Dornsiepen (1982). The difference in fabrics was thought to be due to a change from predominantly basal to prismatic and pyramidal slip. Wilson (1973) describes variations in microstructures associated with fabric changes from prograde quartzites of Mount Isa, Australia and there are several other documented natural texture transitions.

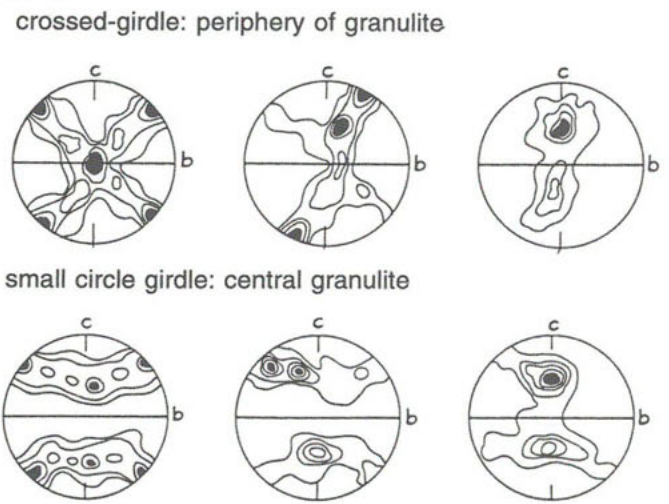


Figure 26. Quartz *c*-axis pole figures from the Saxony granulites. Top: crossed girdle from the peripheral northern part of the granulite of assumed lower metamorphic grade. Bottom: small circle girdles in the central part of the granulite of higher metamorphic grade. From left to right increasing triclinic distortion towards an emplaced gabbro (Behr, 1964).

Other factors that affect fabrics include changes in strain history (Hofmann, 1974), such as a transition from compressional deformation with small circle girdles (s tectonite, Fig. 27, bottom) to an extensional or plane strain deformation with crossed girdles (b tectonite, Fig. 27, top). Recently Fueten (1992) interpreted fabric changes in the Thompson belt, Manitoba, by dividing the *c*-axis fabric diagram into eight components (Fig. 28) in an elaboration of diagrams of Behr (1961), and he attributed to each component a mechanism or a geologic episode. These simplifications are common in the literature on natural quartz fabrics, but they lack any physical justification. The orientation distribution is more or less continuous, and it represents the integrated product of history and active deformation mechanisms. A texture cannot be divided into sets of grains that deform by particular mechanisms and remain in particular orientations (Wenk and Christie, 1991). The reader is again referred to the trajectories of Figure 19, which illustrate the dynamic nature of preferred orientation. Unfortunately, there are very few studies in which

EBSCOhost - printed on 2/13/2023 4:48 AM via . All use subject to https://www.ebsco.com/terms-of-use

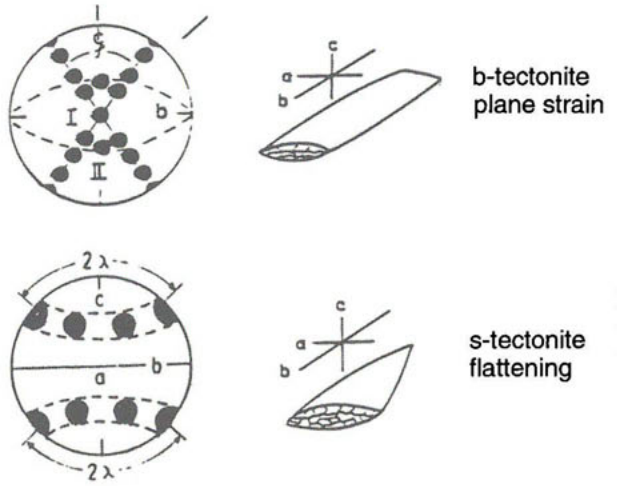


Figure 27. Interpretation of *c*-axis crossed girdle (top) and small circle girdle (bottom) textures from the Erzgebirge (Saxony), due to the strain history, i.e., plane strain and flattening (Hofmann, 1974).

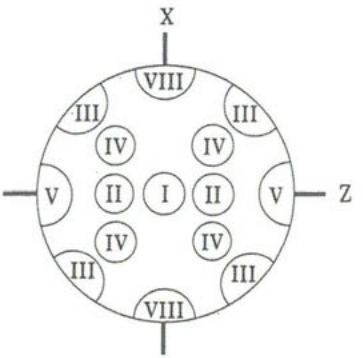


Figure 28. Decomposition of a quartz *c*-axis pole figure into eight components, each of which is attributed to a different mechanism or a different tectonic event (Fueten, 1992).

texture patterns have been correlated with quantitative TEM investigations of actual dislocation mechanisms. Admittedly, such studies are not easy. A notable exception is the work by Blumenfeld et al. (1986), who documented a change from prism *a* to basal *c* slip at very high temperature.

The asymmetric *c*-axis small circle fabric with an opening angle of 110-120° observed in granulites (Figs. 26 bottom, 27 bottom) has generally been associated with high temperature deformation. We have been surprised to find recently two almost identical small circle fabrics, one in the vicinity of a granite contact, the second one at a distance of 30 km from the contact in low-grade greenschist facies (Helming et al., 1994).

Simple shear deformation and sense of shear

One of the universal principles of texture interpretation is symmetry: The texture symmetry cannot be lower than the symmetry of the strain path (Paterson and Weiss, 1962). Quartz textures often deviate from orthorhombic symmetry, suggesting non-coaxial deformation or superposition of different deformation events. Non-coaxial experiments (e.g., Fig. 15) and simulations (e.g., Fig. 19) produce monoclinic textures.

EBSCOhost - printed on 2/13/2023 4:48 AM via . All use subject to https://www.ebsco.com/terms-of-use

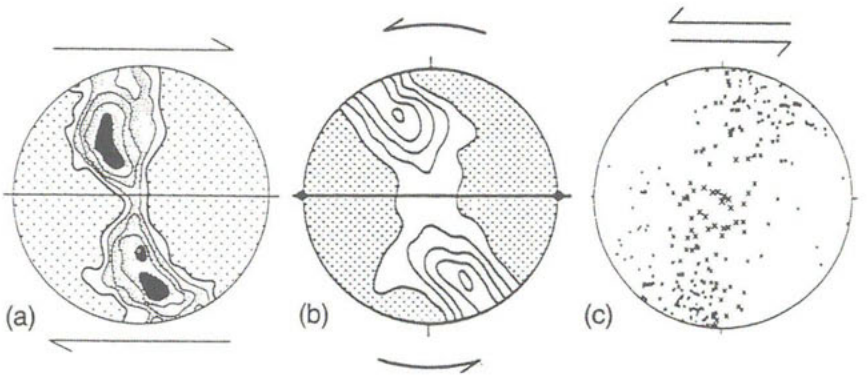


Figure 29. Asymmetric (monoclinic) quartz *c*-axis pole figures on which the sense of shear is indicated. In the natural samples the sense is inferred from geological evidence. (a) Carreras et al. (1977) from the Pyrenees; (b) Law (1990) from Moine thrust, Scotland; and (c) Viscoplastic self-consistent polycrystal plasticity simulations (Wenk et al., 1989).

Lister and Williams (1979) used the results of Taylor simulations to cautiously interpret asymmetric *c*-axis diagrams of Carreras et al. (1977; Fig. 29a), and in this case the plasticity theory predictions agreed with geologic evidence. The *c*-axis girdle is inclined against the sense of shear relative to the shear plane. In other cases such interpretations of quartz *c*-axis pole figures did not agree with independent geological shear indicators. For example, Law (1990) and Law et al. (1990) suggest a sense of shear opposite to that predicted by the Taylor theory for mylonites along the Moine thrust, Scotland (Fig. 29 b). To remedy the discrepancy, observed in several locations, researchers have resorted to various solutions. One possibility is to assume that the quartz texture is a superposition of different deformation events (Christie, 1963). Also, a kinematic model which minimizes misfits between grains was developed by Etchecopar (1977) and predicts a different sense of shear. It has been applied by Behrmann and Platt (1982), Schmid and Casey (1986) and Simpson (1980) as a basis to interpret quartz textures, even though Schmid and Casey recognized deficiencies (p. 283: "A serious shortcoming of the model of Etchecopar (1977) is that it is physically unrealistic..."). This conflict is further highlighted in the study of Law et al. (1990) which invokes the Scmid factor for a single slip. The fact remains that, contrary to the contention of Law (1990, p. 339), the Taylor and Etchecopar models do *not* "only differ in detail" and do *not* predict the same textures for simple shear.

There has also been an obsession with Schmidt's (1927) concept that in simple shear the slip direction orients itself in the shear direction. As documented by *a*-axis pole figures there is no *a*-axis maximum near the lineation direction in most quartzites (e.g., Fig. 21). Also, there is no single slip direction in quartz for most slip systems but rather a set of directions related by symmetry. Moreover, Schnidt's (1927) concept is not predicted by any theory (Fig. 19).

In the interpretation of quartz textures, it appears that models are often selected arbitrarily on the basis of predicting the "correct" results rather than for their physical relevance. Clearly there are problems with the interpretation of quartz textures: In many cases the shear sense cannot be predicted correctly with conventional polycrystal plasticity theory. In addition, the most common natural fabric type with a strong *c*-axis maximum in the intermediate fabric direction Y has not been produced with plasticity theory nor with axial compression experiments.

EBSCOhost - printed on 2/13/2023 4:48 AM via . All use subject to https://www.ebsco.com/terms-of-use

The natural samples described above are recrystallized, so there is some question as to whether plasticity theory and kinematic slip models should be applied in the first place. The simple shear experiments of Dell'Angelo and Tullis (1989) with low strain and no recrystallization produced texture patterns that agree with plasticity theory (Fig. 15a), whereas at high strain with significant recrystallization the asymmetry is reversed (Fig. 15b). In the recrystallized samples only the non-recrystallized quartz grains were measured, and those may float like passive markers in a recrystallizing matrix. In such a case one would expect rigid body rotations in the sense of shear for the isolated porphyroclasts, while the fine-grained recrystallized matrix or large grains that are in contiguous contact may behave differently.

In some recrystallized quartzites there is not much difference in orientation between recrystallized and old grains (Bell and Etheridge, 1976; Law, 1986). Also angles between *c*-axes of recrystallized and adjacent old grains display a pattern which can be explained with the bulk texture and is not specific for misorientations between neighbors. In a crossed girdle texture, Kirschner and Teyssier (1991, 1992) observed that grains in a Y orientation are all recrystallized, and they interpret the texture as a result of two events, deformation and recrystallization. Hippert and Borba (1992) suggest that the textures may be explained by a single event, with recrystallization affecting old grains in a Y orientation; this model is similar to that proposed above (Wenk et al., 1989; strongly deformed grains with large symbols in Fig. 19a). In detailed studies of local features with the SEM, Lloyd and Freeman (1991) also document that newly recrystallized grains within a large grain do not form very clear misorientation relationships. Jessel (1986) inferred grain boundary movements from microstructures in a quartzite with weak texture and suggests that grains in Y orientation are growing at the expense of others, even though fabric coordinates are not easily assigned in this sample. Such observations are very important and should be extended to other samples with stronger textures. Experimental studies also are ambiguous in determining whether the orientations of dynamically recrystallized grains are controlled by the orientation of the host or the stress/strain field (Hobbs, 1968). It should be pointed out that in quartzites dynamic recrystallization is usually associated with a grain size reduction. Therefore, subgrain rotations and nucleation appear to be more important than boundary migration, as implied in the model of Jessell and Lister (1990). This is also suggested by the fact that quartz textures in pure quartzites are similar to those in polymineralic rocks where grain boundary migration cannot occur.

Differences in finite deformation at low and high metamorphic grade

Texture development can have a profound influence on the mechanical properties of a rock, as is illustrated by quartzites. Understanding the process again requires polycrystal plasticity theory. Quartz deforms at low temperature primarily by basal slip (001) and at higher temperature by prismatic slip (100). Figure 30 shows Taylor simulations for axial compression and extension for low and high temperature. Textures are represented as inverse pole figures of the symmetry axis (Takeshita and Wenk, 1988). In these inverse pole figures, the Taylor factor, which indicates the plastic strength of a particular orientation, is contoured. Regions of lowest Taylor factor, where deformation is easiest, are dashed. They are oriented at about 45° to (001) and (100), corresponding to the highest Schmid factor for basal and prismatic slip. Also shown are rotation trajectories for selected grains. For example, for crystals in compression at low temperature, rotations take place towards "soft" areas, indicating that the polycrystal weakens during deformation. By contrast, in extension grains rotate towards "hard" areas. The opposite is true for high-temperature prismatic slip. This trend is highlighted in Figure 31, which shows the relationship between the average Taylor factor (corresponding to the yield stress) and

EBSCOhost - printed on 2/13/2023 4:48 AM via . All use subject to https://www.ebsco.com/terms-of-use

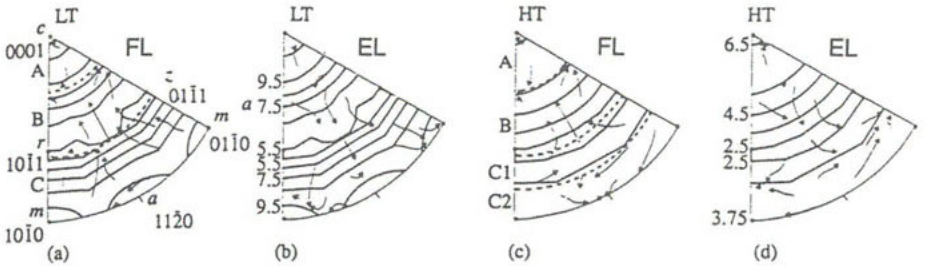


Figure 30. Taylor factor (high Taylor factor is shaded) and Taylor rotation trajectories for deformation in compression (a,c) and in extension (b,d) at low (LT) and high (HT) temperature conditions (Takeshita and Wenk, 1988).

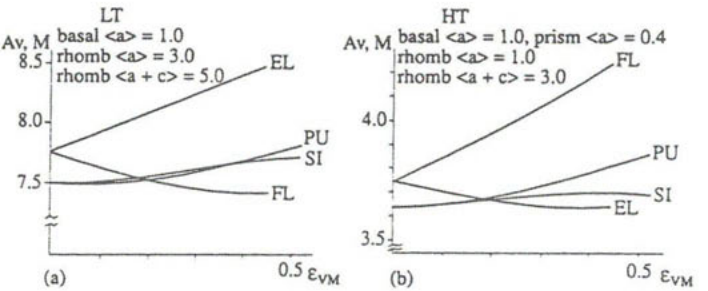


Figure 31. Changes of the average Taylor factor (equivalent to yield strength) with increasing strain for different deformation modes. EL = elongation, FL = flattening, PU = pure shear and SI = simple shear at low temperature conditions (a) and high temperature conditions (b) with different slip system activities (Takeshita and Wenk, 1988).

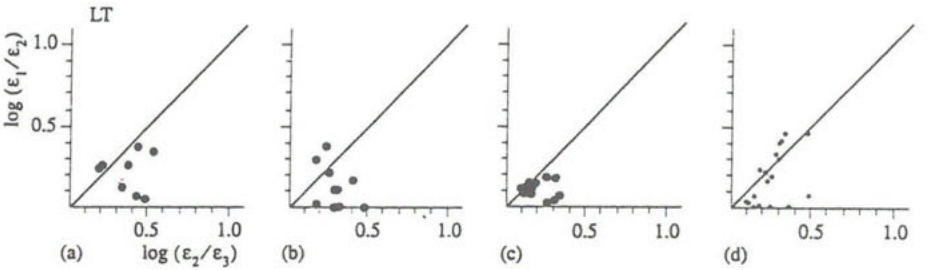


Figure 32. Grain aspect ratios plotted in a Flinn diagram for various low grade metamorphic rocks: (a) Moine thrust, Scotland, (b) Ormiston nappe, Australia, (c) Brittany, France and (d) Shimanto belt, Japan (Takeshita and Wenk, 1988). At these low grade conditions deformation occurs in plane strain and by flattening.

different strains. At low temperature, flattening is energetically favored, whereas at high temperature the most favorable path is elongation. In a literature survey, Takeshita and Wenk (1988) found that in many low grade metamorphic areas (such as Moine Thrust, Scotland; Ormiston Nappe, Australia; Brittany, France; Shimanto Belt, Japan), quartzites deform in a field between flattening and plane strain (Fig. 32), whereas in high grade metamorphic areas (such as Angers, France; Ryoke Belt, Japan) quartzites deform in

EBSCOhost - printed on 2/13/2023 4:48 AM via . All use subject to https://www.ebsco.com/terms-of-use

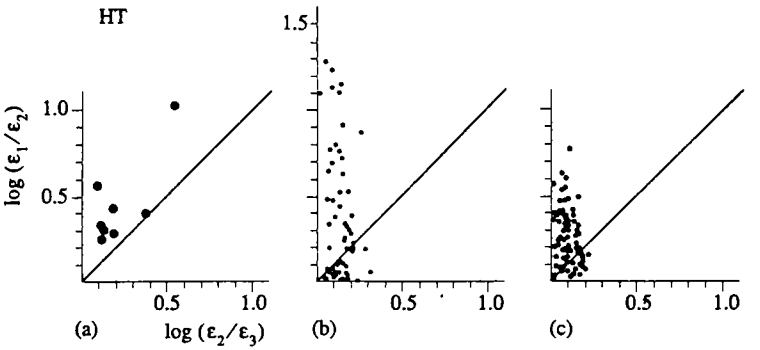


Figure 33. Grain aspect ratios plotted in a Flinn diagram for various high grade metamorphic rocks: (a) Angers, France, (b) Sambagawa belt, Japan, and (c) Ryoke belt, Japan (Takeshita and Wenk, 1988). In these high grade conditions, quartzite deformation was largely by elongation.

elongation (Fig. 33). Takeshita and Wenk concluded that the strain distribution in a large geological body may depend on internal anisotropic plastic properties of the material, such as preferred slip systems, as well as imposed external boundary conditions. However, the trends in these examples are different from those in quartzites and granulites in Saxony, for which Hofmann (1974) describes compression textures at high temperatures and plane strain/extension textures at lower metamorphic grade. The relationship between strain geometry and metamorphic grade needs to be investigated further.

MICROSTRUCTURAL INFORMATION, STRESS ESTIMATES

Qualitative information about deformation conditions can often be inferred from general investigations of microstructures. Some of these can be observed with the optical microscope, and J. Tullis and coworkers have reproduced in the laboratory petrographic textures that are common in metamorphic rocks (e.g., Dell'Angelo and Tullis, 1989; Hirth and Tullis, 1992; Gleason et al., 1993). There are numerous TEM studies of dislocation microstructures in naturally deformed rocks (e.g., Liddell et al., 1976; White et al., 1971). Although it is difficult to identify the Burgers vector of dislocations or slips systems, it is relatively straightforward to distinguish cold-worked quartzites with high dislocation densities and irregular tangles (Fig. 34a) from hot-worked recovered quartzites with residual dislocations organized in cell walls (Fig. 34b).

If recovery and recrystallization accompany dislocation movements as polycrystals deform under steady state conditions during creep, then dislocation density, recrystallized grain size, and subgrain size are a function of the magnitude of the applied stress. This relationship is well documented in metals (e.g., Takeuchi and Argon, 1976) and is applicable to minerals (Twiss, 1986). It has been established experimentally for quartz (Fig. 35 from Twiss, 1986; using data from UCLA Ph.D. theses of P.S. Koch and J.W. McCormick). In principle, such information could be used to infer paleostresses during tectonic deformation of quartzites in natural environments, and this has been attempted for some mylonites (Christie and Ord, 1980; Etheridge and Wilkie, 1981; Hacker et al., 1992; Ord and Christie, 1984). Unfortunately, the application is limited by changes in microstructure during post-tectonic annealing and also by the fact that grain size and dislocation density are also a function of water content, which may be variable in space and time, even in a single sample (Ord and Hobbs, 1986; den Brock and Spiers, 1991).

EBSCOhost - printed on 2/13/2023 4:48 AM via . All use subject to https://www.ebsco.com/terms-of-use

EBSCOhost - printed on 2/13/2023 4:48 AM via . All use subject to https://www.ebsco.com/terms-of-use

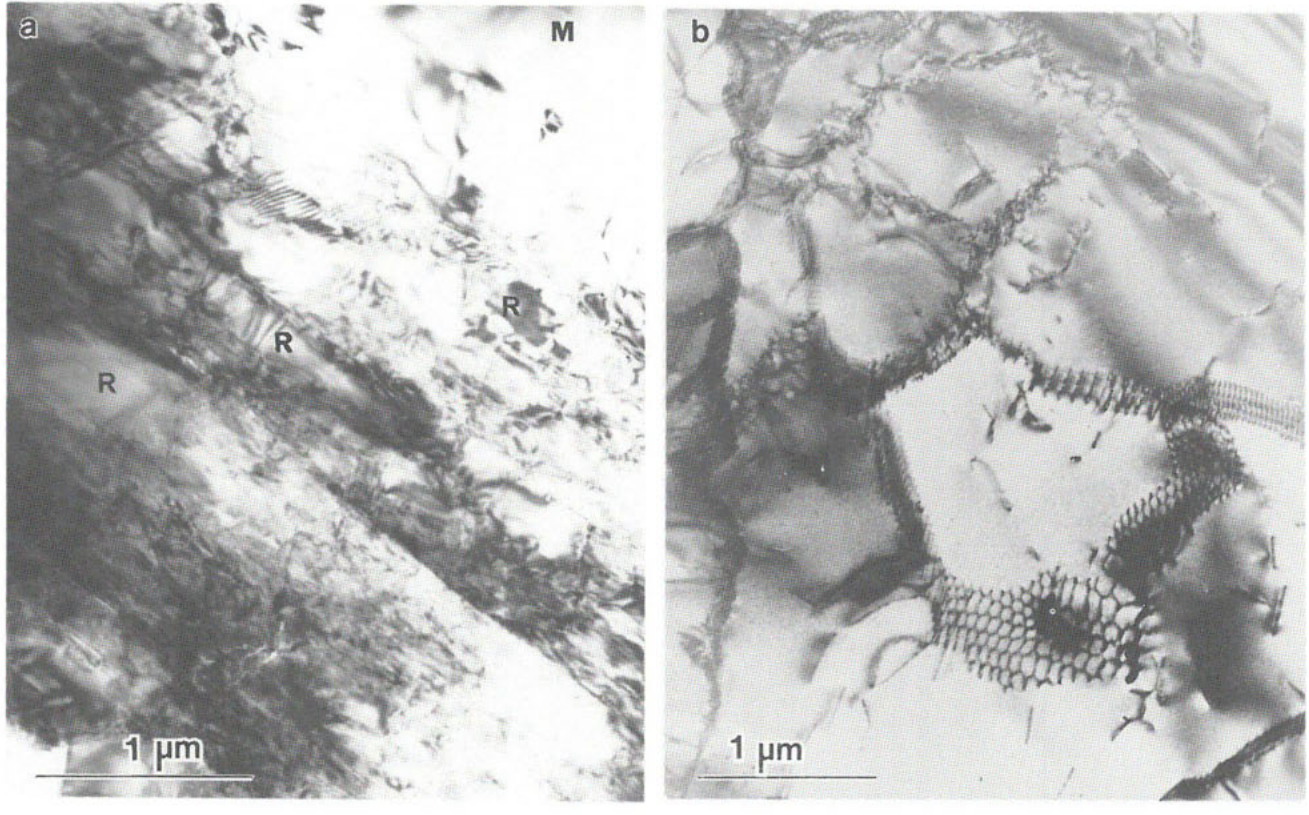


Figure 34. Dislocation microstructures in metamorphic quartzites from the Bergell Alps. (a) Greenschist grade conditions with high dislocation densities and irregular tangles. Some dislocation-free recrystallized regions (R). (b) High-grade amphibolite facies conditions with recovery and arrangment of dislocations in subgrain boundaries (Liddell et al., 1976).

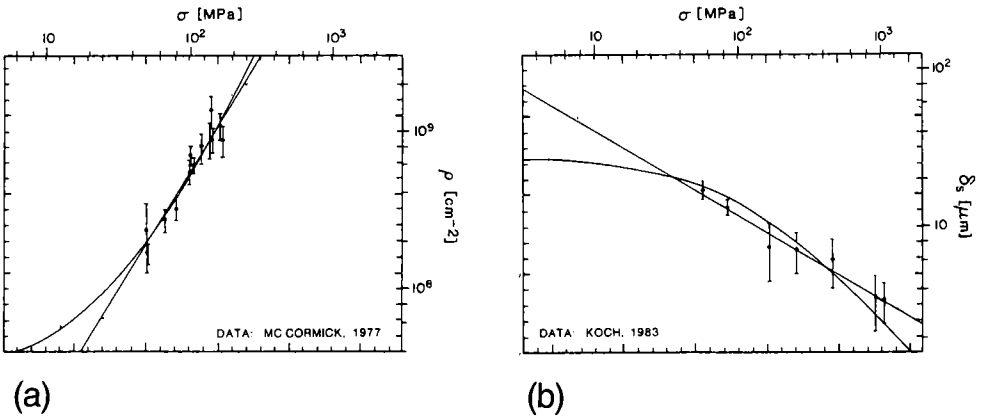


Figure 35. Relationship between magnitude of applied stress σ and dislocation density ρ (a) and subgrain diameter δ (b) for experimentally deformed quartzites in steady state creep (Twiss, 1986). (a) is from synthetic quartz single crystals and (b) from quartzite. The lines indicate different models to fit the data.

CONCLUSIONS

The understanding of deformation features requires detailed knowledge of many of the topics addressed in other chapters, including water content of quartz, trace elements, crystal structure, phase transformations, plasticity theory and materials science. Quartz deformation and quartz textures are still challenging subjects. Indeed, it may seem somewhat surprising to find so many open questions that can be addressed at all levels of sophistication. For example, with the U-stage one can determine the distribution of right- and of left-handed quartz; with the TEM one can identify slip systems in samples with typical textures to determine if there is an interrelationship; with IR spectroscopy one can analyze the speciation of water in quartz-bearing tectonites. The unusually strong textural variations and the discrepancies among textures that are observed in experiments, in simulations, and in nature make this mineral very interesting. Quartz may potentially be the key to help us understand dynamic recrystallization, just as fcc metals were used to derive principles of dislocation slip, calcite to develop theories of mechanical twinning, and phyllosilicates to understand rigid body rotations.

ACKNOWLEDGMENTS

I am indebted to Peter Heaney, Florian Heidelbach, Toru Takeshita and Jan Tullis for constructive reviews of the manuscript, to S. Cady, F. Heidelbach and K. Helming for providing unpublished data and to NSF EAR90-17237 and IGPP-LANL for financial support.

REFERENCES

Ardell AJ, Christie JM, McCormick, JW (1974) Dislocation images in quartz and the determination of Burgers vectors. Phil Mag 29:1399-1411

Baeta RD, Ashbee KGH (1967) Plastic deformation and fracture of quartz at atmospheric pressure. Phil Mag 15:931-938

Baeta RD, Ashbee KHG (1969a) Slip systems in quartz. I. Experiments. Am Min 54:1551-1573

Baeta RD, Ashbee KHG (1969b) Slip systems in quartz. II. Interpretation. Am Min 54:1574-1582

EBSCOhost - printed on 2/13/2023 4:48 AM via . All use subject to https://www.ebsco.com/terms-of-use

Baeta RD, Ashbee KGH (1970) Mechanical deformation of quartz: I Constant strain-rate compression experiments. Phil Mag 22:601-623
Baker DW, Wenk H-R (1972) Preferred orientation in a low symmetry quartz mylonite. J Geol 80:81-105
Barber DJ, Wenk H-R (1991) Dauphiné twinning in deformed quartzites: implications of an in situ TEM study of the α–β phase transformation. Phys Chem Min 17:492-502
Behr H-J (1961) Beiträge zur petrographischen und tektonischen Analyse des sächsischen Granulitgebirges. Freiberger Forsch C119:7-134
Behr H-J (1964) Die Korngefügefazies der Zweigürteltektonite im kristallinen Grundgebirge Sachsens. Abh Deutsch Akad Wiss Berlin, Kl Bergbau 1:1-46
Behr H-J (1968) Zur tektonischen Analyse magmatischer Körper unter besonderer Berücksichtigung des Quarz Korngefüges II. Freiberger Forsch C219:33-98
Behrmann JH, Platt JP (1982) Sense of nappe emplacement from quartz *c*-axis fabrics; an example from the Betic Cordilleras (Spain). Earth Planet Sci Lett 59:208-215
Bell TH, Etheridge MA (1976) The deformation and recrystallization of quartz in a mylonite zone, central Australia. Tectonophysics 32:235-267
Bishop JR (1981) Piezoelectric effects in quartz-rich rocks. Tectonophysics 77:297-321
Blacic JD (1975) Plastic deformation mechanisms in quartz: The effect of water. Tectonophysics 27:271-294
Blumenfeld P, Mainprice D, Bouchez, JL (1986) C-slip in quartz from subsolidus deformed granite. Tectonophysics 127:97-115
Bouchez, JL (1977) Plastic deformation of quartzites at low temperature in an area of natural strain gradient. Tectonophysics 39:25-50
Bunge HJ (1982) Texture Analysis in Materials Science. Butterworths, London
Bunge HJ, Esling C (1982) Quantitative Texture Analysis. Deutsch Gesell Metallkunde, Oberursel, Germany
Bunge HJ, Wenk H-R (1977) Three dimensional texture analysis of three quartzites (trigonal crystal and triclinic specimen symmetry). Tectonophysics 40:257-285
Canova GR, Wenk H-R, Molinari A (1992) Simulation of texture development in polyphase materials. Acta Metall Mater 40:1519-1530
Carreras J, Estrada A, White, S (1977) The effects of folding on the *c*-axis fabrics of a quartz mylonite. Tectonophysics 47:15-42
Christie JM (1963) The Moine thrust zone in the Assynt region, northwest Scotland. Univ Calif Publ Geol Sci 40:345-440
Christie JM, Ardell AJ (1974) Substructures of deformation lamellae in quartz. Geology 2:405-408
Christie JM, Ord A (1980) Flow stress from microstructures of mylonites: Example and current assessment. J Geophys Res 85:6253-6262
Christie JM, Griggs DT, Carter NL (1964) Experimental evidence of basal slip in quartz. J Geol 72:734-756
Cordier P, Doukhan JC (1991) Water speciation in quartz: A near-infrared study. Am Min 76:361-369
Dell'Angelo LN, Tullis J (1989) Fabric development in experimentally sheared quartzites. Tectonophysics 169:1-21
Den Brok SWJ, Spiers CJ (1991) Experimental evidence for water weakening of quartzite by microcracking plus solution-precipitation creep. J Geol Soc London 14:541-548
Doherty R D, Gottstein G, Hirsch J, Hutchinson W B, Lücke K, Nes E, Wilbrandt P (1988) Report on panel recrystallization textures: mechanisms and experiments. In: Proc 8th Int'l Conf on Textures of Materials (Kallend JS, Gottstein G, eds), Metall Soc, Warrendale, Pennsylvania, 563-572
Doukhan JC, Trepied L (1985) Plastic deformation of quartz single crystals. Bull Min 108:97-123
Ernst WG (1976) Petrologic Phase Equilibria. WH Freeman, San Francisco, 333 p
Etchecopar A (1977) A plane kinematic model of progressive deformation in a polycrystalline aggregate. Tectonophysics 39:121-139
Etheridge MA, Wilkie JC (1981) An Assessment of dynamically recrystallized grain size as a paleopiezometer in quartz-bearing mylonite zones. Tectonophysics 78:475-508
Fueten F (1992) Tectonic interpretations of systematic variations in quartz *c*-axis fabrics across the Thompson belt. J Struct Geol 14:775-789
Ghomshei MM, Templeton T L (1989) Piezoelectric and *a*-axis fabric along a quartz vein. Phys Earth Planet Int 55:374-386
Gleason GC, Tullis J, Heidelbach, F (1993) The role of dynamic recrystallization in the development of lattice preferred orientations in experimentally deformed quartz aggregates. J Struct Geol 15:1145-1168
Gottstein G, Mecking H (1985) Recrystallization. In: Preferred Orientation in Deformed Metals and Rocks, an Introduction to Modern Texture Analysis (Wenk H-R, ed) Academic Press, Orlando, 183-218
Gratz AJ, Nellis WJ, Christie JM, Brocious W, Swegle J, Cordier, P (1992) Shock metamorphism of quartz with initial temperatures -170 to +1000°C. Phys Chem Min 19:267-288

EBSCOhost - printed on 2/13/2023 4:48 AM via . All use subject to https://www.ebsco.com/terms-of-use

Green HW, Griggs DT, Christie, JM (1970) Syntectonic and annealing recrystallization of fine-grained quartz aggregates. In: Experimental and Natural Rock Deformation (Paulitsch P, ed). Springer-Verlag, Berlin, 272-335

Griggs DT (1967) Hydrolytic weakening of quartz and other silicates. Geophys J Roy Astron Soc 14:19-31

Griggs DT, Blacic JD (1965) Quartz: anomalous weakness of synthetic crystals. Science 147:292-295

Hacker BR, An Yin, Christie JM, Davis GA (1992) Stress magnitude, strain rate, and rheology of extended middle continental crust inferred from quartz grain sizes in the Whipple Mountains, California. Tectonics 11:36-46

Helming K, Matthies S, Vinel GW (1988) ODF representation by means of σ-sections. In: Proc 8th Int'l Conf Textures of Materials. (Kallend J, Gottstein G, eds) TMS-AIME, Warrendale, Pensylvania, 55-60

Helming K, Wenk H-R, Choi CS, Schäfer W (1994) Description of quartz textures by components. Examples from metamorphic rocks. In: Textures in Geological Materials (Bunge HJ et al., eds) Deutsch Gesell Metallkunde, Oberursel, Germany (in press)

Hippert JFM, Borba RP (1992) Quartz *c*-axis fabric differences between porphyroclasts and recrystallized grains: Discussion. J Struct Geol 14:627-630

Hirth G, Tullis J (1992) Dislocation creep regimes in quartz aggregates. J Struct Geol 14:145-159

Hobbs BE (1968) Recrystallization of single crystals of quartz. Tectonophysics 6:353-401

Hobbs BE (1984) Point defect chemistry of minerals under a hydrothermal environment, J Geophys Res 89:4026-4038

Hobbs BE, McLaren AC, Paterson MS (1972) Plasticity of single crystals of synthetic quartz. Am Geophys Union, Geophys Monogr 16:29-53

Hofmann J (1974) Die Quartzteilgefüge von Metamorphiten und Anatexiten, dargestellt am Beispiel des Osterzgebirges (DDR). Freiberger Forsch C297:107 p

Jessel MW (1986) Grain boundary migration and fabric development in experimentally deformed octachloropropane. J Struct Geol 8: 527-542

Jessel MW (1988) Simulation of fabric development in recrystallizing aggregates-I. Description of the model. J Struct Geol 10:771-778

Jessel MW, Lister GS (1990) A simulation of the temperature dependence of quartz fabrics. In: Deformation Mechanisms, Rheology and Tectonics (Knipe RJ, Rutter EH, eds). Geol Soc (London) Spec Publ 54:353-362

Kekulawala KRSS, Paterson MS, Boland JN (1981) An experimental study of the role of water in quartz deformation. Am Geophys Union Monogr 24:49-60

Kirby SH (1977) The effects of the α–β phase transformation on the creep properties of hydrolytically-weakened synthetic quartz. Geophys Res Lett 4:97-100

Kirby SH, McCormick JW (1979) Creep of hydrolytically weakened synthetic quartz crystals oriented to promote {2110} [0001] slip: a brief summary of work to date. Bull Min 102:124-137

Kirschner D, Teyssier C (1991) Quartz *c*-axis differences between porphyroclasts and recrystallized grains. J Struct Geol 13:105-109

Kirschner D, Teyssier C (1992) Quartz *c*-axis differences between porphyroclasts and recrystallized grains: Reply. J Struct Geol 14:631-634

Koch PS, Christie JM, Ord A, George RP (1989) Effect of water on the rheology of experimentally deformed quartzite. J Geophys Res 94:13975-13996

Kunze K, Adams BL, Heidelbach F, Wenk H-R (1994) Local microstructural investigations in recrystallized quartzite using orientation imaging microscopy. Proc 10th Int'l Conf Textures of Materials. Solid State Phenomena (in press)

Law RD (1986) Relationships between strain and quartz crystallographic fabrics in the Roche Maurice quartzites of Plougastel, western Brittany. J Struct Geol 8:493-515

Law RD (1990) Crystallographic fabrics: a selective review of their applications to research in structural geology. In: Deformation Mechanisms, Rheology and Tectonics (Knipe RJ, Rutter EH, eds). Geol Soc (London) Spec Publ 54:335-352

Law RD, Schmid SM, Wheeler J (1990) Simple shear deformation and quartz crystallographic fabrics: a possible natural example from the Torridon area of NW Scotland. J Struct Geol 12:29-45

Liddell NA, Phakey PP, Wenk H-R (1976) The microstructures of some naturally deformed quartzites. In Electron Microscopy in Mineralogy (Wenk H-R, ed) Springer-Verlag, Berlin, p 419-427.

Linker MF, Kirby SH (1981) Anisotropy in the rheology of hydrolytically weakened synthetic quartz crystals. Am Geophys Union Monographs 24:29-48

Lister GS, Dornsiepen VF (1982) Fabric transitions in the Saxony granulite terrain. J Struct Geol 4:81-92

Lister GS, Paterson MS, Hobbs BE (1978) The simulation of fabric development during plastic deformation and its application to quartzite: The model. Tectonophysics 45:107-158

Lister GS, Williams PF (1979) Fabric development in shear zones: Theoretical controls and observed phenomena. J Struct Geol 1:283-297

EBSCOhost - printed on 2/13/2023 4:48 AM via . All use subject to https://www.ebsco.com/terms-of-use

Lloyd GE, Freeman B (1991) SEM electron channeling analysis of dynamic recrystallization in a quartz grain. J Struct Geol 13:945-953

Mainprice D, Lloyd GE, Casey M (1993) Individual orientation measurements in quartz polycrystals: advantages and limitations for texture and petrophysical property determinations. J Struct Geol 15:1169-1187

Mancktelow NS (1987a) Quartz textures from the Simplon fault zone, southwest Switzerland and North Italy. Tectonophysics 135:133-153

Mancktelow NS (1987b) Atypical textures in quartz veins from the Simplon fault zone. J Struct Geol 8:995-1005

McLaren AC, Phakey PP (1965) Dislocations in quartz observed by transmission electron microscopy. J Appl Phys 36:3244-3246

McLaren AC, Phakey PP (1966) Electron microscope study of Brazil twin boundaries in amethyst quartz. Phys status solidi 13:413-422

McLaren AC, Retchford JA, Griggs DT, Christie JM (1967) Transmission electron microscopy study of Brazil twins and dislocations experimentally produced in natural quartz. Phys status solidi 19:631-644

McLaren AC, Cook RF, Hyde ST, Tobin RC (1983) The mechanisms of the formation and growth of water bubbles and associated dislocation loops in synthetic quartz. Phys Chem Min 9:79-94

Molinari A, Canova GR, Ahzi S (1987) A self-consistent approach of the large deformation polycrystal viscoplasticity. Acta Metall 35:2983-2994

Morrison-Smith DJ, Paterson MS, Hobbs BE (1976) An electron microscope study of plastic deformation in single crystals of synthetic quartz. Tectonophysics 33:43-79

Müller WF, Défourneaux M (1968) Deformationsstrukturen in Quarz als Indikator für Stosswellen: Eine experimentelle Untersuchung an Quarz-Einkristallen. Zeits Geophys 34:483-504

Oertel G (1983) The relationship of strain and preferred orientation of phyllosilicate grains in rocks - review. Tectonophysics 100:413-447

Ord A, Christie JM (1984) Flow stresses from microstructures in mylonitic quartzites of the Moine Thrust zone, Assynt area, Scotland. J Struct Geol 6:639-654

Ord A, Hobbs BE (1986) Experimental control of the water-weakening effect in quartz. Am Geophys Union Geophys Monogr 36:51-72

Parkhomenko EI (1971) Electrification Phenomena in Rocks. (Translation by Keller GV) Plenum Press, New York, 285 p

Paterson MS (1989) The interaction of water with quartz and its influence in dislocation flow - an overview. In: Rheology of Solids and of the Earth (Karato SI, Toriumi M, eds), p 107-142. Oxford Univ Press, Oxford, UK

Paterson MS, Weiss LE (1961) Symmetry concepts in the structural analysis of deformed rocks. Geol Soc Am Bull 72:841-872

Ratschbacher L, Wenk H-R, Sintubin M (1991) Calcite textures: examples from nappes with strain-path partitioning. J Struct Geol 13: 369-384

Sander B (1950) Einführung in die Gefügekunde der Geologischen Körper, Vol 2, Springer, Vienna, 409 p

Schmid E (1928) Zn-normal stress law. In: Proc Int'l Congress Applied Mechanics, Delft, p 342

Schmid SM, Casey M, Starkey J (1981) An illustration of the advantages of a complete texture analysis described by the orientation distribution function (ODF) using quartz pole figure data. Tectonophysics 78:101-117

Schmid SM, Casey M (1986) Complete fabric analysis of some commonly observed quartz *c*-axis patterns. Am Geophys Union Geophys Monogr 36:263-286

Schmidt W (1925) Gefügestatistik. Tschermaks min petrog Mitt 38:392-423

Schmidt W (1927) Zur Quarzgefügeregel. Fortschr Min Krist Petrog 11:334-343

Simpson C (1980) Oblique girdle orientation patterns of quartz *c*-axes from a shear zone in the basement core of the Maggia nappe, Ticino, Switzerland. J Struct Geol 2:243-247

Takeshita T, Wenk H-R (1988) Plastic anisotropy and geometric hardening in quartzites. Tectonophysics 149:345-361

Takéuchi S, Argon AS (1976) Review: Steady state creep of single phase crystalline matter at high temperatures. J Mater Sci 11:1542-1566

Taylor GI (1938) Plastic strain in metals. J Inst Metals 632:307-324

Tullis J (1970) Quartz: Preferred orientation in rocks produced by Dauphiné twinning. Science 168:1342-1344

Tullis J (1977) Preferred orientation of quartz produced by slip during plane strain. Tectonophysics 39:87-102

Tullis J (1983) Deformation of feldspars. Rev Min 2:297-323

Tullis J, Christie JM, Griggs DT (1973) Microstructure and preferred orientations of experimentally deformed quartzites. Geol Soc Am Bull 84:297-314

Tullis J, Tullis T (1972) Preferred orientation of quartz produced by mechanical Dauphiné twinning: thermodynamics and axial experiments. Am Geophys Union Geophys Monogr 16:67-82

EBSCOhost - printed on 2/13/2023 4:48 AM via . All use subject to https://www.ebsco.com/terms-of-use

Tullis J, Wenk H-R (1994) The effect of muscovite on the strength and lattice preferred orientations of experimentally deformed quartz aggregates. Mat Sci Eng A175:209-220
Twiss RJ (1986) Variable sensitivity piezometric equations for dislocation density and subgrain diameter and their relevance to olivine and quartz. Am Geophys Union Geophys Monogr 36:247-261
Wenk H-R, ed (1985) Preferred Orientation in Deformed Metals and Rocks: An Introduction to Modern Texture Analysis. Academic Press, Orlando, Florida, 610 p
Wenk H-R, ed (1994) Polyphase Polycrystal Plasticity. Special Issue: Mat Sci Eng A175:1/2
Wenk H-R, Christie JM (1991) Review paper: Comments on the interpretation of deformation textures in rocks. J Struct Geol 13:1091-1110
Wenk H-R, Canova G, Molinari A, Kocks UF (1989) Viscoplastic modeling of texture development in quartzite. J Geophys Res 94B:17895-17906
Wenk H-R, Kocks UF (1987) The representation of orientation distributions. Metall Trans 18A:1083-1092
White SH, Crosby A, Evans PE (1971) Dislocations in naturally deformed quartzite. Nature Phys Sci 231:85-86
Wilson CJL (1973) Preferred orientation in quartz ribbon mylonites. Geol Soc Am Bull 86:968-974
Wright SI (1993) A review of automated orientation imaging microscopy (OIM). J Computer-Assisted Micros 5:207-221
Zinserling K, Shubnikov A (1933) Über die Plastizität des Quarzes. Z Kristallogr 85:454-461

EBSCOhost - printed on 2/13/2023 4:48 AM via . All use subject to https://www.ebsco.com/terms-of-use

STRUCTURAL CHARACTERISTICS OF OPALINE AND MICROCRYSTALLINE SILICA MINERALS

Heribert Graetsch

Ruhr-Universität Bochum
Institut für Mineralogie
D-44780 Bochum, Germany

INTRODUCTION

From the structural point of view, micro- and non-crystalline silica minerals can be divided into three major groups: microcrystalline quartz and moganite, microcrystalline opals with a disordered cristobalite/tridymite structure, and non-crystalline opals and glasses. The structural state of the microcrystalline minerals is mainly characterized by a small crystallite size and planar structural defects (twin and stacking faults). In addition, both micro- and non-crystalline modifications are further characterized by a variable amount of non-essential water. The $SiO_2 \cdot nH_2O$ minerals are usually rather pure and non-volatile impurities are below 1 mol % in most samples and often even below 0.5 mol %. By contrast, silica glass may contain high concentrations of impurities, and the demarcation between natural silica glass and silicate glass is not well-defined. Only fulgurites and Libyan Desert glass are comparably pure (cf. Frondel, 1962). Due to their different growth fabric and microstructure, several varieties and subvarieties of microcrystalline silica have been distinguished, and additional synonymous names can be found in the literature. In this paper the current nomenclature compiled by Flörke et al. (1991) is used (Table 1). Keatite, an additional length-slow fibrous silica modification, is not included since it has not been identified in nature with certainty (Keat, 1954; Shropshire et al., 1959; Martin and Röller, 1990). A recent review on the structures and properties of crystalline and non-crystalline silica phases has been published by Flörke and Martin (1993).

CHALCEDONY, QUARTZINE AND MOGANITE

Microstructure

Investigating fibrous microcrystalline quartz with a polarizing microscope, Michel-Lévy and Munier-Chalmas (1892) distinguished between length-fast chalcedony, length-slow quartzine, and length-slow "lutecite." Quartzine and "lutecite" are often referred to as length-slow chalcedony (Folk and Pittman, 1971; Kastner, 1980; Keene, 1983). X-ray pole figure diagrams reveal that the fibers of length-fast chalcedony are elongated perpendicular to the *c*-axis of quartz, parallel to [110] and in some samples parallel to $[1\bar{1}0]$ (Correns and Nagelschmidt, 1933; Braitsch, 1957). The fiber axis of quartzine is parallel to the *c*-axis (Braitsch, 1957). "Lutecite" has been less well characterized by X-ray diffraction methods, but some researchers (Heaney et al., 1992) identify this phase with the newly discovered polymorph moganite (discussed below).

In agate geodes chalcedony forms either wall-lining or horizontally layered bands. The growth fabric differs in these varieties. The horizontal chalcedony layers consist of closely packed radiating spherulites (Figs. 1a and 2b). In wall-lining bands, the chalcedony fibers radiate towards the center of the geode from many nucleation points on the wall surface, forming parabolic fiber bundles. Interference of neighboring bundles results in a parallel-texture of the fibers (Figs. 1b and 2a; Frondel, 1978). A plate cut parallel to the fibers

EBSCOhost - printed on 2/13/2023 4:48 AM via . All use subject to https://www.ebsco.com/terms-of-use

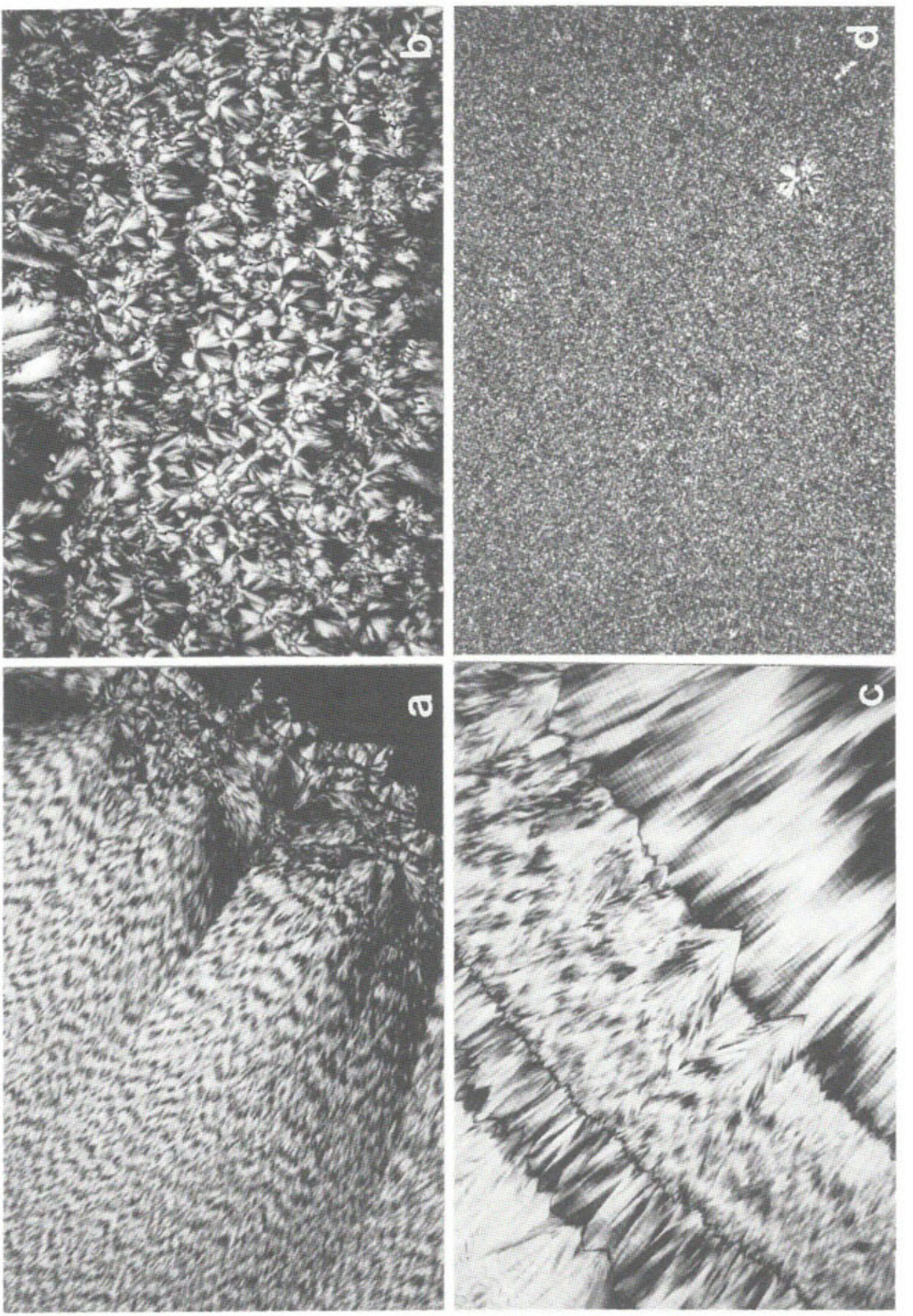
EBSCOhost - printed on 2/13/2023 4:48 AM via . All use subject to https://www.ebsco.com/terms-of-use

Table 1. Micro- and non-crystalline silica minerals*

crystal structure or phase	variety	subvariety/ synonymous name	microstructure	optical character	water content in weight %
quartz	microquartz		granular	⊕	<0.4
disordered quartz**	chalcedony		fibrous [11$\bar{2}$0]	length-fast	0.5 - 2
	quartzine		fibrous [0001]	length slow	0.5 - 1
moganite			platy (110), lepidospheric	length slow	1.5 - 3
disordered cristobalite	opal-C	lussatine	platy (111)***	length-fast	1 - 3
cristobalite/tridymite	opal-CT	lussatite	fibrous [110]***	length-slow	3 - 8
		common massy opal	platy , lepidospheric	nearly isotropic	3 -10
non-crystalline	opal-AG	precious opal	close packing of homometric spheres	play of color, anomalous birefringence	4 - 8
		potch opal	heterometric spheres	isotropic	4 - 8
	opal-AN	hyalite	botryoidal crusts and masses	strain birefringence	3 - 7
	lechâtelierites	fulgurites	vitrified impact tubes	isotropic	<0.3
		meteoritic silica glass	vitreous masses	isotropic	<0.3

C: cristobalite, T: tridymite, A: amorphous, G: gel-like, N: network (glass)-like
* after Flörke et al. (1991)
** very often contains minor amounts of moganite
*** the indices refer to cubic setting of cristobalite

Figure 1 (opposite page). Microstructure of some microcrystalline quartz varieties. (a) length-fast parabolic chalcedony with rhythmic extinction banding forming a wall-lining band in an agate geode. (b) length-fast spherulitic chalcedony in a horizontal agate layer. (c) length-slow quartzine (QN) between length-fast chalcedony (CH) with oscillatory compositional zonation. (d) chalcedony in a flint nodule. The long edge of the micrographs is 1.11 mm long in nature; crossed polars.



EBSCOhost - printed on 2/13/2023 4:48 AM via . All use subject to https://www.ebsco.com/terms-of-use

polarizes transmitted light (Raman and Jayaraman, 1955). Between crossed polars, wall-lining chalcedony exhibits a rhythmic extinction banding (Runzelbänderung or wrinkle banding) normal to the direction of fiber elongation. The extinction banding is due to simultaneous twisting of the *c*-axis around the fiber axes (Bernauer, 1927; Frondel, 1978). Frondel (1978) and Heaney (1993) suggest that the twisting might be caused by screw dislocations.

The chalcedony bands occasionally show additional smooth striations (Jones, 1952) which might be produced by a zonation of the OH content (Frondel, 1985). Whereas the extinction banding is unique for wall-lining chalcedony, the compositional zonation also occurs in other microcrystalline silica minerals and in non-crystalline hyalite as well (Fig. 1; see Fig. 15, below). In flint and chert the chalcedony fibers generally do not show a preferred orientation. The term flint is used for compact silica nodules from Cretaceous chalk beds, whereas chert refers to massive bedded silica deposits formed by diagenesis of biogenic sea floor sediments and abiogenic saline lake beds (Frondel, 1962; Eugster, 1967; Calvert, 1983). For classification and genesis of siliceous rocks also see Füchtbauer (1988).

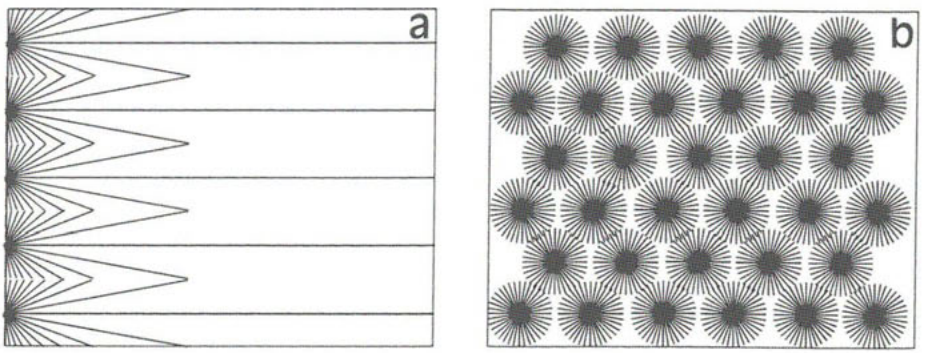


Figure 2. Schematic sketch of fibrous growth of chalcedony, quartzine and lussatite resulting in a parallel-texture after nucleation on the surface wall (a) and in a close packing of radiating spherulites after nucleation in the whole agate band (b).

Crystal structure

Initially, Correns and Nagelschmidt (1933) assumed that chalcedony contains some interstitial non-crystalline opal in order to explain the water content and the lower refractive indices in comparison to coarse quartz crystals (Fig. 3). Further investigations have provided no evidence for the presence of opal. Therefore, chalcedony was considered to consist of microcrystalline quartz with water in submicroscopic pores of the particles (Weymouth and Williamson, 1951; Midgley, 1951; Folk and Weaver, 1952). Pelto (1956) and Micheelsen (1966) assumed that additional lattice imperfections occur in chalcedony.

X-ray powder diffraction patterns of chalcedony and quartzine exhibit broad quartz reflections and very weak additional intensity maxima. Extra reflections with the indices $h\pm1/2$, k, $l\pm1/2$ (Fig. 4) are also visible in electron diffraction patterns together with 3 systems of diffuse streaks due to planar defects (Fig. 5; Miehe et al., 1984; Heaney et al., 1994). These patterns indicate coherent intergrowth of quartz with minor amounts of a phase with a larger unit cell and lower symmetry than quartz. Transmission electron

EBSCOhost - printed on 2/13/2023 4:48 AM via . All use subject to https://www.ebsco.com/terms-of-use

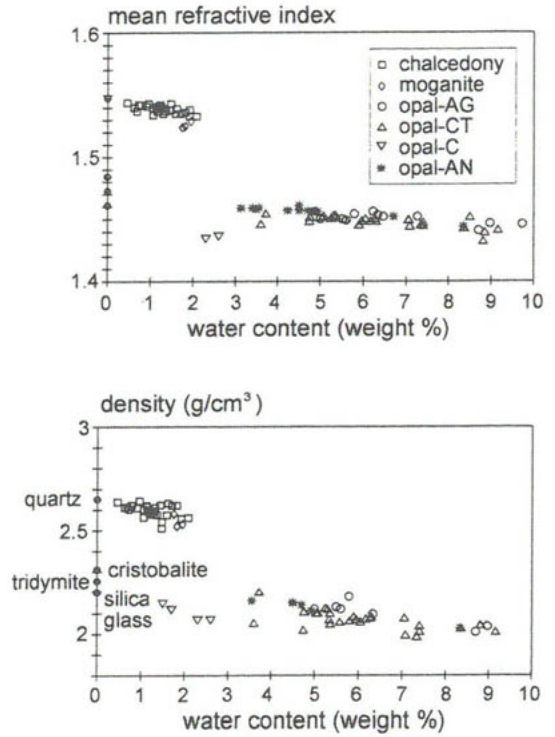


Figure 3. Mean refractive indices and densities of microcrystalline quartz, moganite and opals vs the total water content. Data from Flörke et al. (1982), (1985); Frondel (1982); Graetsch et al. (1985); Langer and Flörke (1974); Micheelsen (1966); Midgley (1951); Pelto (1956); Plyusnina (1979); Taliaferro (1935); Weymouth and Williamson (1951)

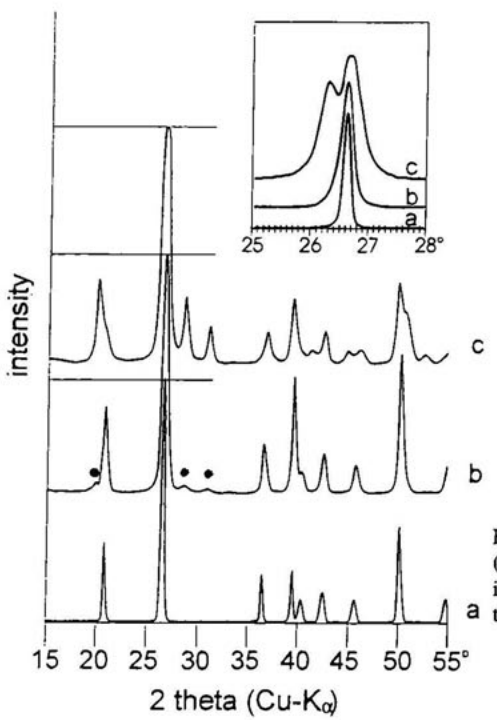


Figure 4. X-ray powder diffraction patterns of (a) quartz, (b) chalcedony, (c)moganite. Stars indicate additional weak "moganite" reflections in the diffraction pattern of chalcedony.

EBSCOhost - printed on 2/13/2023 4:48 AM via . All use subject to https://www.ebsco.com/terms-of-use

microscopy has revealed that chalcedony fibers are not single-crystalline but polysynthetically twinned according to the Brazil law; right- and left-handed slabs are bounded by the composition plane (101) (Fig. 6; Miehe et al., 1984; Cady et al., 1993). The intergrown phase frequently occurs as thin slabs (up to 100 Å) at the twin boundaries. This structural element has close similarities to the structure of moganite (Graetsch et al., 1987).

Moganite is a microcrystalline silica mineral found in the ignimbrite flows at Gran Canaria (Flörke et al., 1976a, 1984). The crystal structure of moganite has been refined with the Rietveld method using X-ray powder diffraction data (Miehe and Graetsch, 1992). The structure can be described as an alternating stacking of (101) lattice-slices of right- and left-handed quartz. This can be considered as periodically repeated twinning according to the Brazil law on the unit cell scale (Fig. 7). The relation of the lattice parameters of quartz and pseudo-orthorhombic moganite are listed in Table 2.

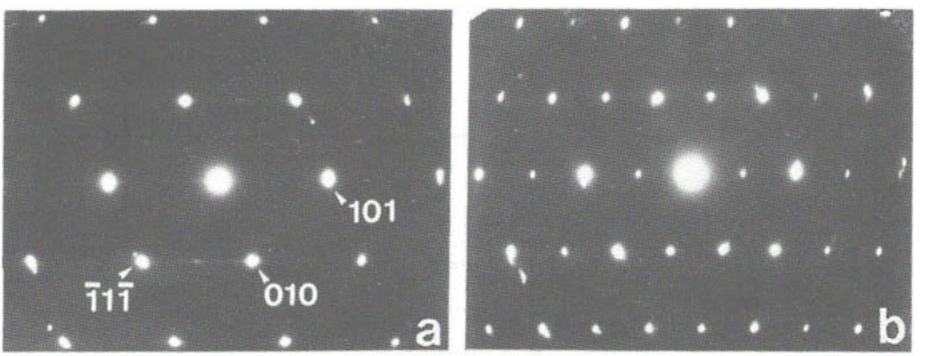


Figure 5. Selected area electron diffraction patterns of length-fast chalcedony (a) and moganite (b). Diffuse streaks and additional weak intensity maxima in chalcedony indicate planar faults and coherent intergrowth with moganite-like structural elements. From Graetsch et al. (1987).

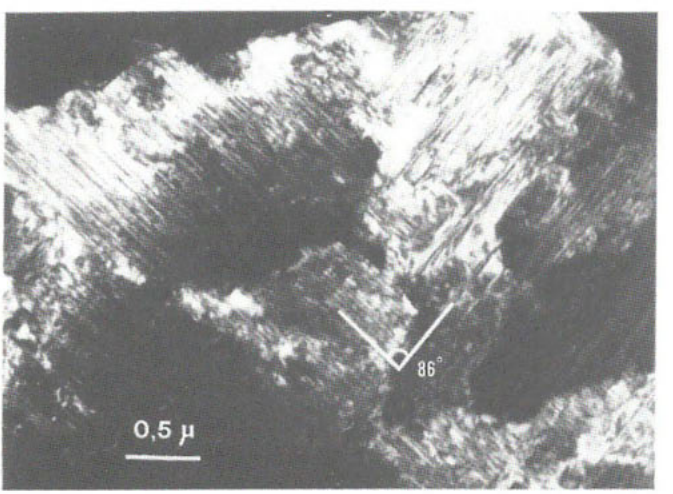


Figure 6. Transmission electron micrograph of a length-fast chalcedony showing polysynthetic twinning according to the Brazil law. Dark field image with **g** = 112 as working reflection. From Miehe et al. (1984).

EBSCOhost - printed on 2/13/2023 4:48 AM via . All use subject to https://www.ebsco.com/terms-of-use

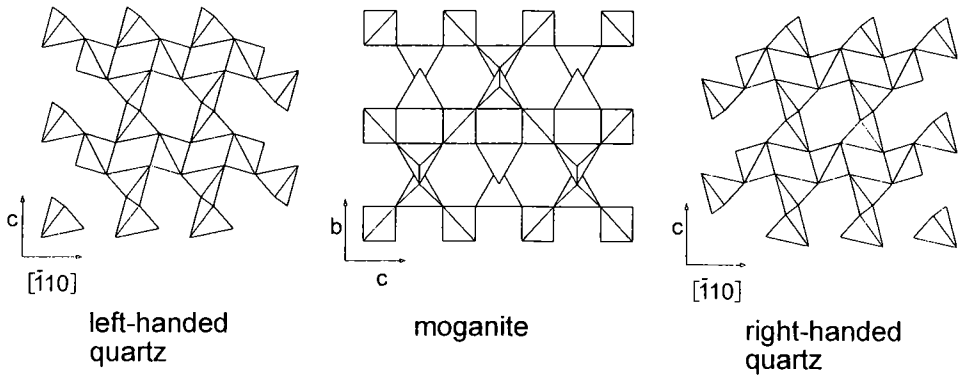


Figure 7. Crystal structures of right- and left-handed quartz and moganite.

Table 2. Lattice parameters of moganite and quartz*

	moganite	quartz**
a =	8.758(2)Å	8.510Å = $\sqrt{3}$ a (trigonal)
b =	4.876(1)Å	4.913Å
c =	10.715(2)Å	10.810Å = 2 c (trigonal)
α =	90°	90°
β =	90.08(3)°	90°
γ =	90°	90°
space group:	I 1 2/a 1	P $3_1$21, P$3_2$21

* after Miehe and Graetsch (1992)
** orthohexagonal setting for quartz

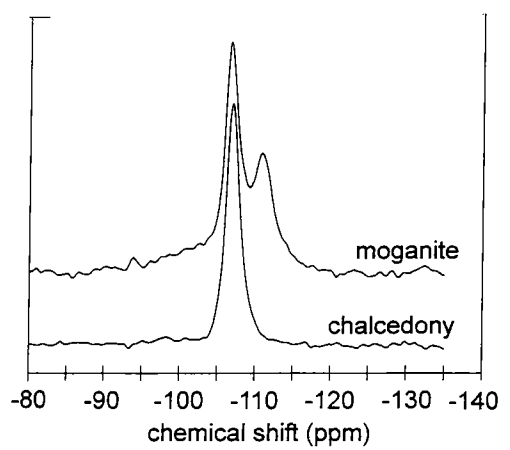


Figure 8. ^{29}Si MAS NMR spectra of moganite and chalcedony. Chemical shift relative to tetramethylsilane. Spectra are displaced vertically.

EBSCOhost - printed on 2/13/2023 4:48 AM via . All use subject to https://www.ebsco.com/terms-of-use

The slices are displaced by the vector $\pm 1/2[110]_{quartz}$, as in the structural model proposed by McLaren and Phakey (1966) and McLaren and Pitkethly (1982) for the Brazil twin boundaries in amethyst. This structural model implies that at the Brazil twin boundaries, the interstitial I_4 position with pseudotetrahedral oxygen coordination is occupied by silicon. The formation of the new tetrahedral site requires adjustment of the tetrahedral framework (Miehe and Graetsch, 1992). ^{29}Si MAS NMR spectra (Fig. 8) confirm the existence of two sites for silicon atoms in moganite with different local environments by showing two signals instead of a single signal for quartz (Graetsch et al., 1994a). Due to the lower symmetry, the infrared absorption spectrum of the lattice vibrations of moganite also differs from that of quartz (Fig. 9). With Raman spectroscopy, Kingma and Hemley (1994) found striking differences in the vibrational spectra of moganite and quartz, and they also identified additional vibrational bands of moganite in the spectrum of chalcedony.

Moganite consists of thin plates with the indices (110) corresponding to (100) of quartz. In length-fast chalcedony, however, the intergrown slabs correspond to the (101) face of quartz (Miehe and Graetsch, 1992). The broadness of the X-ray reflections and the ^{29}Si MAS NMR signals indicate that moganite usually contains a large number of structural defects (Graetsch et al., 1994a). In intermediate samples from Gran Canaria the intergrowth of quartz and moganite is much coarser than in common chalcedony. The examination of more than 150 specimens of microcrystalline quartz varieties by Heaney and Post (1992) revealed that at least traces of moganite occur in every sample.

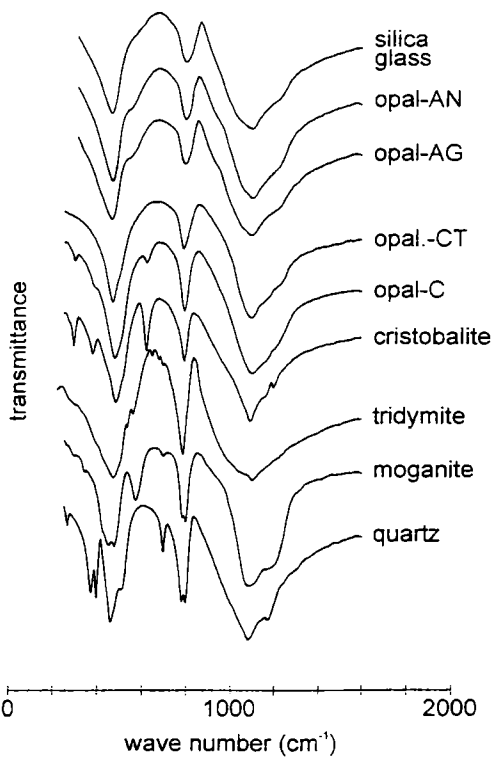


Figure 9. Infrared absorption spectra of fundamental Si-O stretching and bending vibrations in micro- and non-crystalline silica minerals and the ordered silica modifications: low-cristobalite, low-tridymite (L3-T_O(MX-1) and quartz. KBr technique. Spectra are displaced vertically.

EBSCOhost - printed on 2/13/2023 4:48 AM via . All use subject to https://www.ebsco.com/terms-of-use

Microquartz, for example in agates, occurs in horizontally layered bands as fine-grained granular crystals with a size below 0.02 mm. The water content ranges from about 0.1 to 0.3 wt % and the properties are very close to macroscopic quartz (Flörke et al., 1982, 1991).

Phase transitions

When heated above 900°C, moganite and chalcedony reconstructively transform to cristobalite with moderate stacking disorder. Below 900°C moganite does not show any phase transition (Flörke et al., 1984; Miehe and Graetsch, 1992). In chalcedony the displacive inversion from low to high quartz is still detectable with X-ray diffraction at about the same temperature as coarse quartz crystals, but no or only a very small heat effect is found by differential thermal analysis (Flörke, 1962). This behavior can probably be explained by the small crystallite size (Moore and Rose, 1973, Moore, 1986) and the high density of twin defects.

Water content

The water in microcrystalline quartz is responsible for the low refractive indices and density as compared with coarse quartz crystals (Fig. 1). With thermogravimetry and infrared spectroscopy Pelto (1956) and Frondel (1982) distinguished 3 kinds of water in chalcedony: (1) Molecular water loosely held in pores; (2) Hydrogen-bonded (OH) located on internal surfaces and imperfectly crystalline regions; and (3) Hydrogen-bonded (OH) located on structural sites. The infrared spectra of chalcedony are characterized by broad band absorption centered at about 3,500 cm^{-1}, a band at 3430 cm^{-1} superimposing the broad band and a relatively sharp band near 3,600 cm^{-1} (Fig. 10). The latter consists of two components at about 3,615 and 3,585 cm^{-1}.

The sharp bands are assigned to fundamental stretching vibrations of structural silanol groups and the broad continuous absorption to stretching vibrations of molecular water and

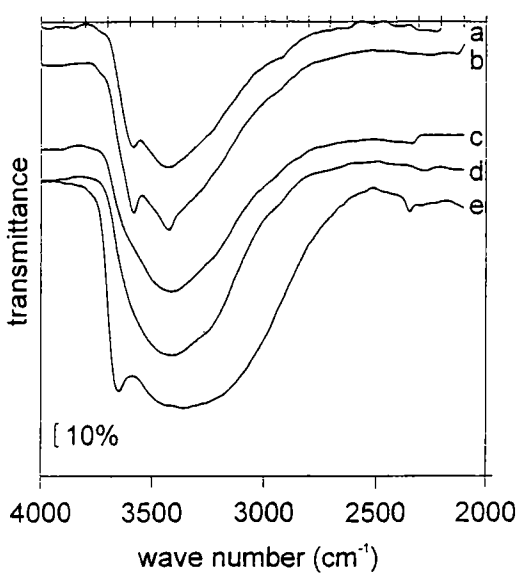


Figure 10. Infrared absorption spectra of fundamental O-H stretching vibrations in (a) Chalcedony, (b) Moganite, (c) Opal-C, (d) Opal-CT, and (e) Opal-AN. Recorded using plane polished plates with a thickness of 0.03 mm. Spectra are displaced vertically.

EBSCOhost - printed on 2/13/2023 4:48 AM via . All use subject to https://www.ebsco.com/terms-of-use

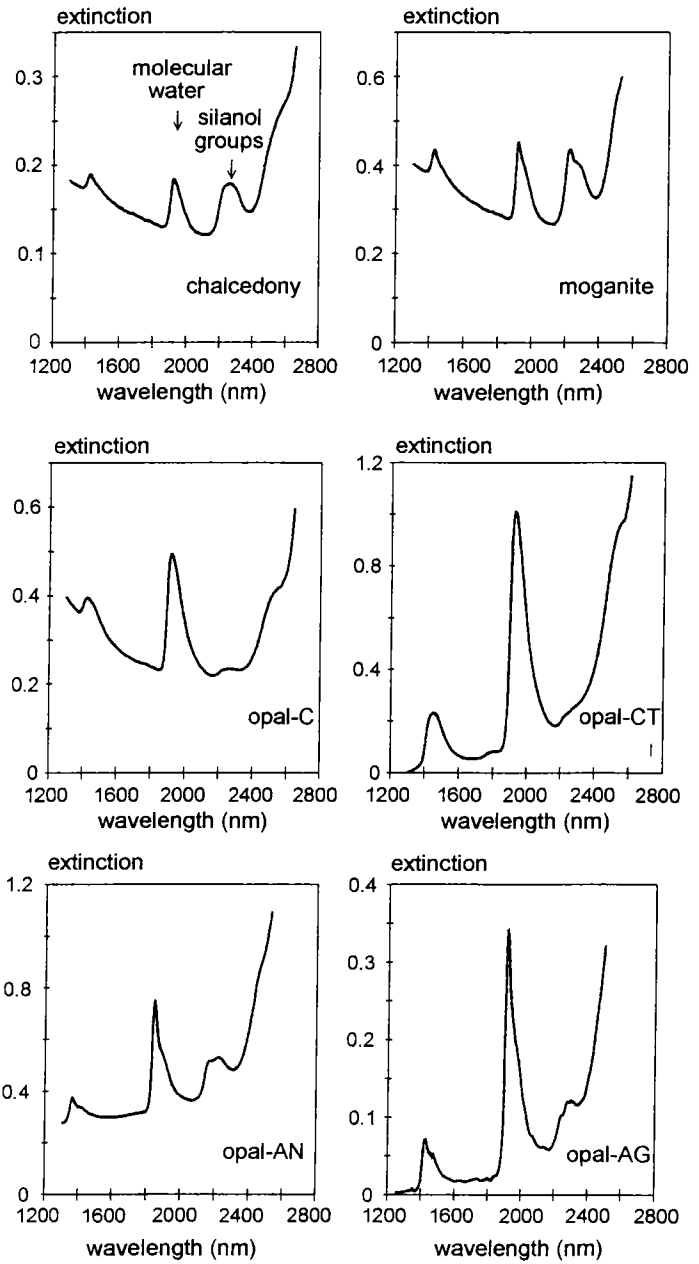


Figure 11. Near infrared absorption spectra of chalcedony, moganite and opals. The bands near 4,500 cm^{-1} are due to the combination of bending and stretching vibrations of silanol groups. The bands near 5,200 cm^{-1} stem from molecular water. The band near 7,000 cm^{-1} is the first overtone of O-H stretching vibrations of both molecular and silanol group water. Thickness of the plates: chalcedony 0.45 mm, moganite 0.62 mm, opal-C 0.96 mm, opal-CT 0.93 mm, opal-AG 0.50 mm and opal-AN 0.37 mm.

EBSCOhost - printed on 2/13/2023 4:48 AM via . All use subject to https://www.ebsco.com/terms-of-use

surface silanol (Si-OH) groups. According to Frondel (1982), the broad band absorption is characteristic for quartz formed at low temperatures, like amethyst and chalcedony. Infrared spectra of natural and synthetic quartz formed at higher temperatures exhibit a large number of sharp bands, most of which are assigned to hydroxyl groups associated with alkali ions that are incorporated in the quartz structure (Kats, 1962; Chakraborty and Lehmann, 1976 and 1978; Aines and Rossman, 1984; Pankrath, 1991). In chalcedony, most of the silanol groups are not coupled to non-volatile impurities (Flörke et al., 1982).

In near-infrared spectra the bands of molecular water and silanol group water do not overlap since the combination of bending and stretching vibrations cause absorption at 5,200 cm^{-1} and 4,500 cm^{-1}, respectively (Fig. 11; Scholze, 1960), so that both kinds of water can be identified unambiguously and determined quantitatively. The content of silanol group water ranges from 0.2 to 0.9 and of molecular water from 0.5 to 1.4 wt % in chalcedony (Flörke et al., 1982; Graetsch et al., 1987).

With near-infrared absorption spectroscopy Aines et al. (1984) showed that most of the molecular water in chalcedony freezes at low temperature like liquid water and only a small amount of water is entrapped in the crystallites as isolated water molecules. Near-infrared absorption spectra of partly dehydrated samples reveals that the combination band of silanol group water consists of at least two components at 4,500 and 4,400 cm^{-1}. The latter is due to surface silanol groups strongly interacting with adsorbed water molecules and the former to the silanol groups located at structural defects (Fig. 12).

On heating, molecular water from surfaces and open porosity is lost at about 150°C. Molecular water in closed pores and nearly all of the silanol groups are lost in a second dehydration step near 600°C (Micheelsen, 1966; Frondel, 1982; Flörke et al., 1982; Graetsch et al., 1985). The second step in the dynamic dehydration experiments may by chance nearly coincide with the inversion temperature of quartz. But it could also indicate additional mobilization of the protons by the structural changes during the phase transition.

The infrared spectrum of water in moganite (Fig. 10) is similar to that of chalcedony. The absorption bands of structural silanol at 3,600 cm^{-1} and of surface silanol groups at 3,430 cm^{-1} are better resolved, and the overall water content is slightly higher than in chalcedony. In the near-infrared absorption spectrum (Fig. 11), the high wave number component near 4,500 cm^{-1} is enhanced with respect to the component at 4,400 cm^{-1}, indicating that the content of silanols at structural defects is higher in moganite than in chalcedony (Miehe and Graetsch, 1992).

Two different models for the incorporation of hydrogen in the quartz structure are described in Chapter Kronenberg. Brunner et al. (1961) proposed location of hydrogen at ruptures of silicon-oxygen bridges (Fig. 12b). Chains or clusters of such hydroxyl-bearing defects could contribute to the isotropic broad band absorption (Aines and Rossman, 1984). McLaren et al. (1983) suggested the occupation of silicon vacancies by four protons (the so-called hydrogarnet substitution). Clustering of these $4H_{Si}$ defects results in the formation of tiny water bubbles. The bubbles are associated with dislocation loops in synthetic quartz. Although there is no experimental evidence for the occurrence of these defects in chalcedony or moganite, some of the surface silanol and the molecular water that does not freeze at low temperature might be located in such bubbles or clusters.

MICROCRYSTALLINE OPALS

The group of opal minerals can be divided into two categories: (a) non-crystalline opals and (b) microcrystalline opals. The latter yield X-ray diffraction patterns with few

EBSCOhost - printed on 2/13/2023 4:48 AM via . All use subject to https://www.ebsco.com/terms-of-use

broad intensity maxima. Due to the lack of reflections that are characteristic for low-cristobalite, microcrystalline opals were initially thought to consist of submicroscopic high-cristobalite (Levin and Ott, 1933). With better X-ray techniques, Flörke (1955a,b) has shown that the X-ray patterns of these opals are caused by low-cristobalite with extensive stacking disorder due to intercalated structural elements of tridymite. Jones and Segnit (1971) sub-divided microcrystalline opals into opal-CT, which consists of cristobalite/tridymite with strong stacking disorder, and opal-C, which contains disordered low-cristobalite with minor evidence for tridymitic stacking (Fig. 13).

Microstructure

Opal-CT commonly occurs as tiny spherical aggregates (so-called lepispheres) formed by thin crystal blades (Fig. 14, Segnit et al., 1970; Flörke et al., 1975). The blades correspond to the {111} faces of cristobalite and {001} faces of tridymite (cubic setting for cristobalite and hexagonal setting for tridymite is used throughout for simplicity). The opal-CT blades are often intergrown according to the (304) and (106) twin law of tridymite (Flörke et al., 1976b).

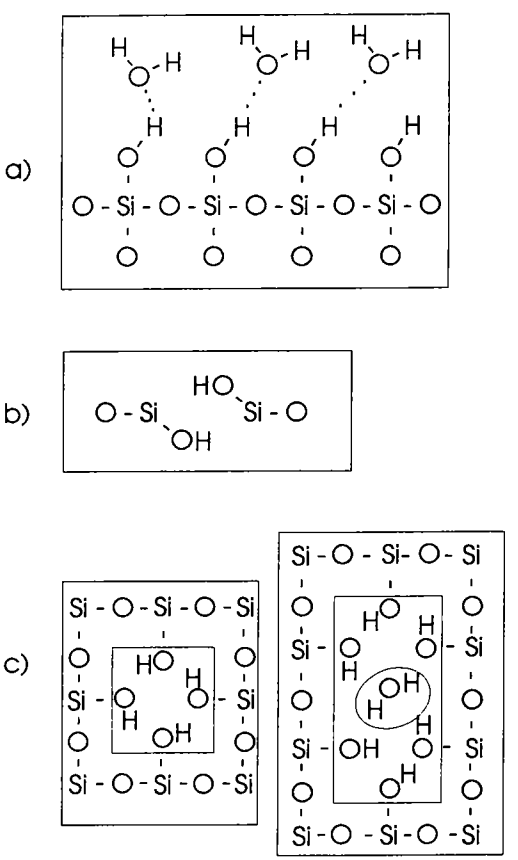


Figure 12. Models for incorporation of water in quartz. (a) Surface silanol groups interacting with adsorbed water molecules.
(b) Protons located at ruptures of Si-O-Si bridging bonds, after Brunner et al. (1961).
(c) occupation of a silicon vacancy by four protons (left side) and cluster of two $4H_{Si}$ defects containing additionally a water molecule (right side).
After McLaren et al. (1983).

EBSCOhost - printed on 2/13/2023 4:48 AM via . All use subject to https://www.ebsco.com/terms-of-use

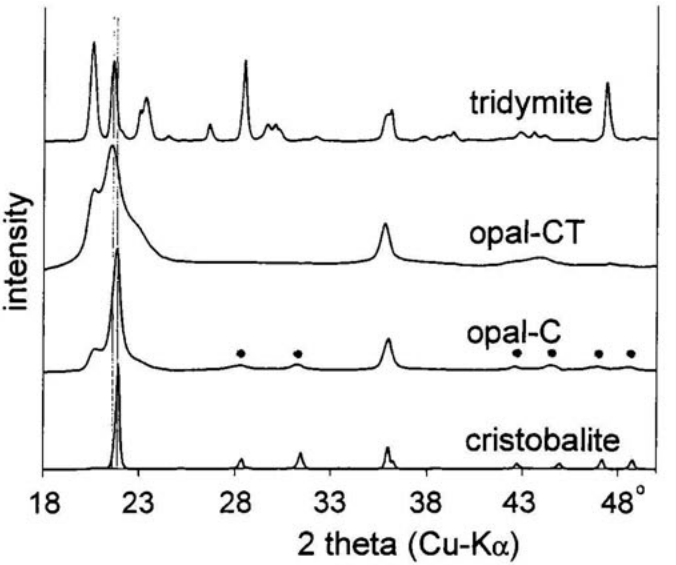


Figure 13. X-ray powder diffractograms of cristobalite, tridymite L3-T_O(MX-1), opal-C and opal-CT. The stars indicate weak superstructure reflections of low-cristobalite in the diffractogram of opal-C. The vertical lines indicate the difference of the *d*-spacings in cristobalite (4.04 Å) and tridymite (4.10 Å).

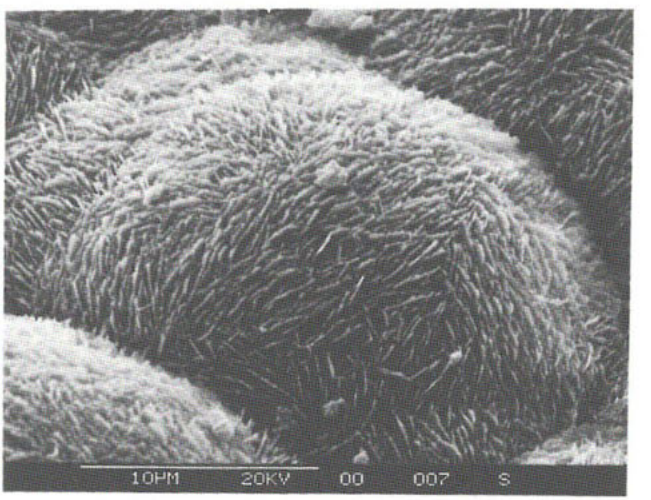


Figure 14. Scanning electron micrograph of an opal-CT lepisphere consisting of small crystal blades.

Whereas massy common opal-CT appears almost isotropic, fibrous lussatite shows length-slow birefringence (Mallard 1890). Like chalcedony, lussatite occurs as radiating spherulites or fiber bundles with a parallel texture (Fig. 15). The fiber axis is <110> for cubic setting of cristobalite (Braitsch, 1957). The fiber axis does not coincide with the direction of stacking disorder (<111>) (Braitsch, 1957; Graetsch et al., 1994b).

EBSCOhost - printed on 2/13/2023 4:48 AM via . All use subject to https://www.ebsco.com/terms-of-use

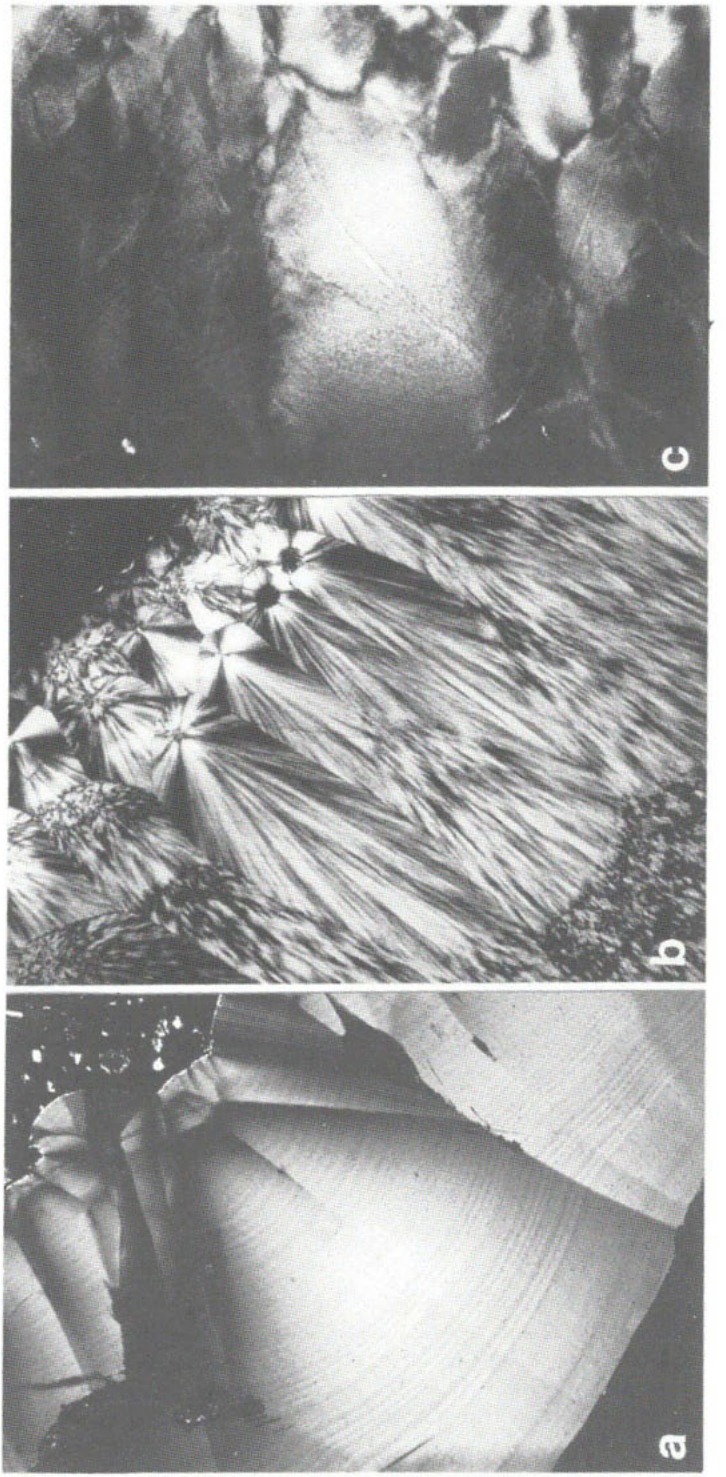


Figure 15. Microstructure of (a) lussatine (opal-C), (b) lussatite (fibrous opal-CT) and (c) hyalite (opal-AN). The long edge of the micrographs is 1.11 mm in nature, crossed polars.

EBSCOhost - printed on 2/13/2023 4:48 AM via . All use subject to https://www.ebsco.com/terms-of-use

Originally, the term lussatine had been coined by Laves (1939) for length-fast cristobalite prepared by devitrifying silica glass. With pole figure diagrams, Braitsch (1957) has shown that lussatine from horizontally layered agate bands consists of lamellar platelets parallel to {111} (cubic setting of cristobalite). The birefringence is wavy due to small changes in the orientation of blocks of parallel platelets (Fig. 15). The direction of preferred orientation is <111>, which coincides with the direction of the stacking disorder (Braitsch, 1957). Both lussatine and lussatite exhibit diffuse, anisotropic small-angle X-ray scattering caused by defects containing water (Graetsch et al., 1994b).

Crystal structure

The framework structures of high-cristobalite and high-tridymite are both constructed from layers formed by six-membered rings of tetrahedra. Cristobalite has a 3-layer sequence and tridymite a 2-layer sequence with the same stacking vectors as in cubic and hexagonal closest packing, respectively. In tridymite, however, every second layer is rotated by 180° around the hexagonal *c*-axis. In cristobalite all neighboring tetrahedra are in trans-configuration, whereas in the stacking direction of tridymite the tetrahedra are in cis-configuration (Fig. 16; Gibbs, 1927; Flörke, 1967; Flörke and Nukui, 1988). In high-cristobalite and high-tridymite the spacings between the layers are approximately equal (4.12 Å). At room temperature, however, the *d*-spacings are 4.04 and 4.10 Å in low-cristobalite and low-tridymite, respectively. This variation has been ascribed to different

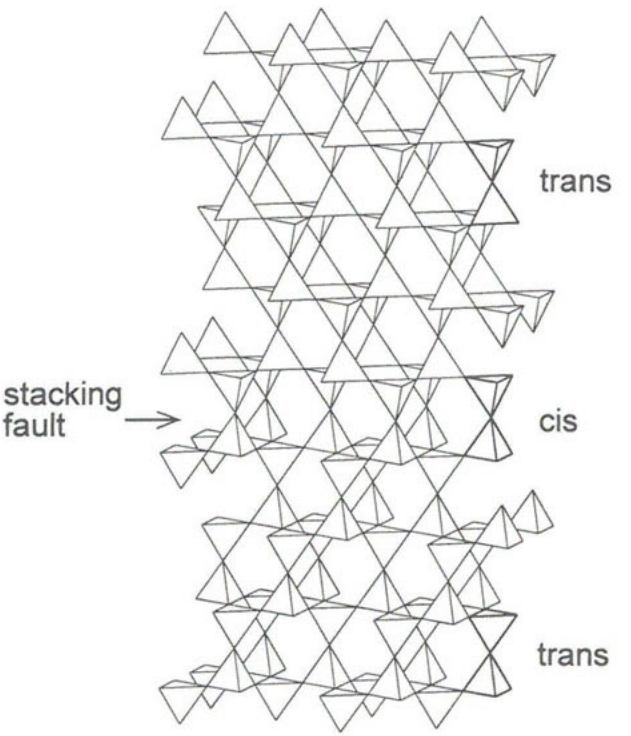


Figure 16. Structural model for a tridymitic stacking fault in cristobalite. Idealized by drawing straight Si-O-Si bridges. (1120) slice (hexagonal setting). Stacking direction ([0001] tridymite / [111] cristobalite) vertical.

EBSCOhost - printed on 2/13/2023 4:48 AM via . All use subject to https://www.ebsco.com/terms-of-use

non-Coulombic repulsive forces associated with the oxygen atoms in trans- and cis-configurations (Flörke, 1967; Graetsch and Flörke, 1991) leading to larger interlayer Si-O-Si angles and smaller intralayer Si-O-Si angles in tridymite (Nukui and Nakazawa, 1980).

In microcrystalline opals from sea floor sediments non-crystalline silica is diagenetically transformed first to opal-CT and then to opal-C. The gradual change of the *d*-spacings from about 4.12 to 4.04 Å has been exploited as an indicator for structural "ripening" with depth and age (Murata and Nakata, 1974; Mitsui and Tagushi, 1977; Mizutani, 1977; Rad, 1979; Iijima and Tada, 1981; Kano, 1983). The assumption is that diagenesis leads to a reduction of tridymitic stacking, creating a more ordered low-cristobalite. The apparent *d*-spacing of the largest peak in the X-ray diffraction patterns of microcrystalline opals together with the intensity distribution can be taken as a rough measure of the structural state. From calculated X-ray diagrams simulating stacking disordered cristobalite/tridymite, it can be estimated that in most strongly disordered opal-CT, the stacking is about 50% tridymitic and 50% cristobalitic. Evidence for extended domains with predominating tridymitic or cristobalitic stacking is lacking in most cases. Opal-C from agate geodes contains about 20 to 30% tridymitic stacking (Graetsch et al., 1994b). The predominant cristobalitic stacking is revealed by weak superstructure reflections that are characteristic of low-cristobalite (Flörke et al., 1990; Fig. 13).

^{29}Si MAS NMR spectra of opals exhibit a single resonance near -111 ppm (Fig. 17;

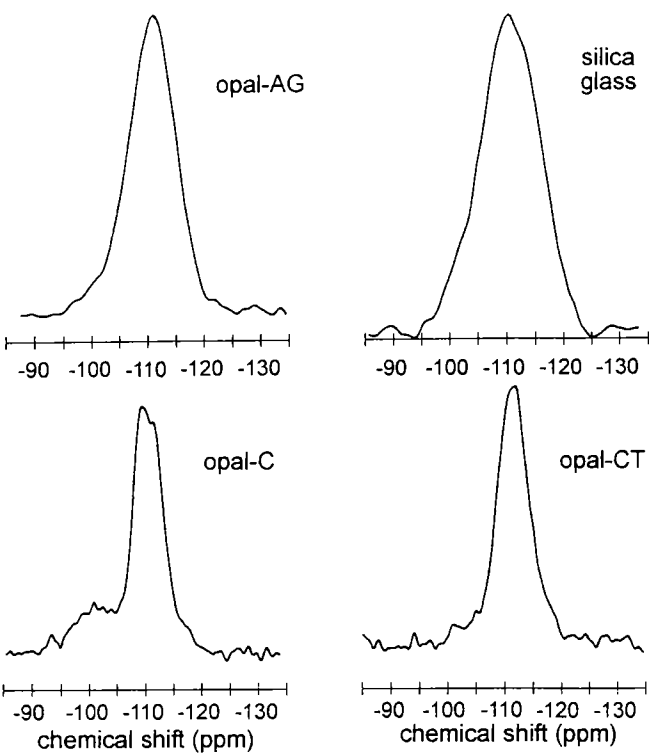


Figure 17. ^{29}Si MAS NMR spectra of opals and natural silica glass (Libyan desert glass). The small signal near -100 ppm in the spectrum of opal-C is due to defect silanol groups (silicon in Q3(1OH) configuration). Chemical shift relative to tetramethylsilane.

EBSCOhost - printed on 2/13/2023 4:48 AM via . All use subject to https://www.ebsco.com/terms-of-use

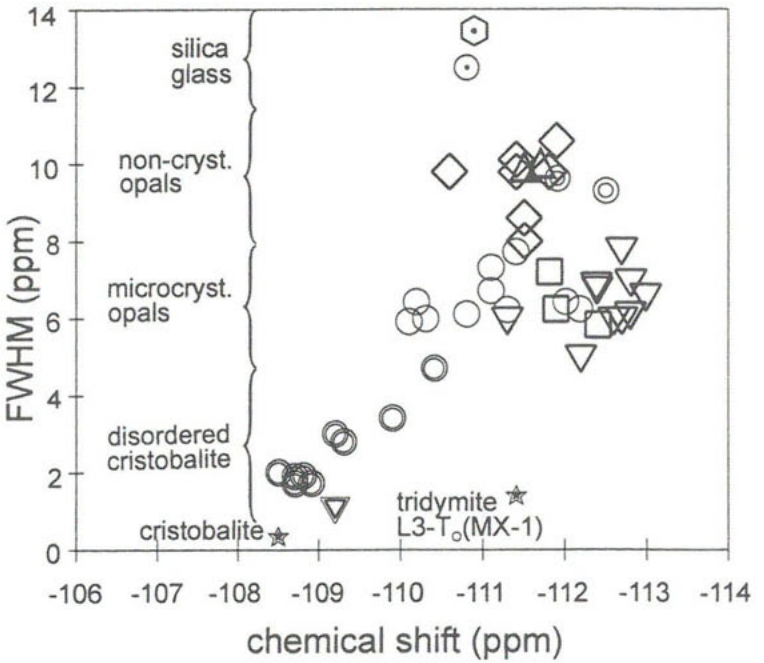


Figure 18. Full width at half maximum (FWHM) versus the chemical shift of the ^{29}Si MAS NMR signal of opals. The disordered cristobalite samples were produced by annealing various opals at 1,350°C for 1 h. Squares: data from deJong et al. (1987), triangles: data from Adams et al. (1991), hexagon: data from Murdoch et al. (1985), circles: data from Graetsch et al. (1994b).

deJong et al., 1987; Adams et al., 1991; Graetsch et al., 1994b). Chemical shifts and half-widths of the signal exhibit considerable scatter but vary with the degree of stacking disorder (Fig. 18). NMR spectroscopy is sensitive to the local environments of the atoms, and the spectra indicate an increase of the mean intertetrahedral Si-O-Si angle with increasing tridymitic stacking from opal-C to opal-CT in accordance with the results from X-ray powder diffraction. (For the correlation between chemical shift and Si-O-Si angles see Smith and Blackwell, 1983 and Engelhardt and Michel, 1987.) Moreover, the increase of the half-width of the ^{29}Si MAS NMR signal indicates an increase in local disorder with decreasing long-range order (Fig. 18). The most strongly disordered opal-CT has a very large d-spacing of 4.12 Å, which exceeds the value of 4.10 Å in low tridymite, which has an ordered two-layer stacking sequence. The additional local disorder detected by NMR may explain the increased stacking distance. The six-membered rings of tetrahedra in low-cristobalite have an oval shape (Dollase, 1965; Peacor, 1973). By contrast, the different room-temperature modifications of tridymite contain rings that are either exclusively oval (Konnert and Appleman, 1978), 2/3 ditrigonal and 1/3 oval (Kato and Nukui, 1977; Baur, 1977), or exclusively ditrigonal (Löns and Hoffmann, 1987). In opal-C, the rings probably are oval as in low-cristobalite, but in opal-CT they are presumably so heavily distorted that a comparison with the ordered crystal structures of the low temperature forms of cristobalite and tridymite becomes meaningless.

EBSCOhost - printed on 2/13/2023 4:48 AM via . All use subject to https://www.ebsco.com/terms-of-use

Infrared absorption spectra of stacking disordered cristobalite in the range corresponding to lattice vibrations show reduced absorption for the bands at 620, 380 and 300 cm^{-1}, which are characteristic for low-cristobalite (Rey, 1966). These bands can still be detected in infrared spectra of opal-C but are lacking for opal-CT (Fig. 9; Graetsch et al., 1994b). Clearly, the atomic displacements are no longer correlated due to the loss of translational periodicity caused by stacking faults and small particle size, and only localized Si-O vibrations remain when the crystallite size approaches the wavelength of infrared light (Shuker and Gammon, 1970; Brawer, 1975). The absorption bands at 1,100, 790 and 480 cm^{-1} are common to all silicates with tetrahedrally coordinated silicon. These bands grow increasingly broad as silica ranges from opal-C to opal-CT to non-crystalline opal, indicating variations of the dipole moments due to slightly varying surroundings of the $SiO_{4/2}$ tetrahedra. These findings are in accordance with the results obtained from NMR spectroscopy and X-ray diffraction

Phase transitions

Unlike microcrystalline quartz, the inversion temperature of cristobalite is sensitive to disorder (Flörke, 1955b, 1956; Walker et al., 1958; Flörke, 1967). Cristobalite with strong stacking disorder displacively transforms below 200°C and well ordered cristobalite at 270°C upon heating.Similarly, the hysteresis and the thermal effects associated with the low-high cristobalite inversion are reduced or absent in opal. In opal-C the structural disorder is so high that no thermal effect is observed with differential thermal analysis (Jones and Segnit, 1971), but the displacive transformation remains detectable with X-ray diffraction by the disappearance of the weak superstructure reflections. Below 900°C no reconstructive transformation occurs in opal-CT (Wahl et al., 1961). Heating to temperatures above 1,000°C reduces the number of stacking faults, and microcrystalline opals are gradually transformed to more highly ordered forms of cristobalite (Jones and Segnit, 1971).

Water content

The amount of water in microcrystalline opals ranges from about 1.5 in opal-C to more than 10 wt % in some opal-CT samples reducing the density and the mean refractive index (Fig. 3). The very low refractive index and density of the opal-C samples in Figure 3 might be explained by air in the cavities of the microstructure. Dehydration experiments and infrared spectroscopy reveal that most H_2O in opal is molecular water (Fig. 10). Near-infrared absorption spectroscopy at room temperature (Langer and Flörke, 1974) and at low temperatures (Aines et al., 1984) has shown that isolated water molecules form a small part of the molecular water. The rest is liquid water. The content of silanol group water is lower than in microcrystalline quartz and in non-crystalline opals. Most silanol groups are found at the surface and interact with molecular water. Shoulders at 3,650 cm^{-1} in the range of the fundamental O-H stretching vibrations and at 4,550 cm^{-1} in near-infrared spectra indicate the presence of some silanols located at structural defects.

NON-CRYSTALLINE OPALS

Microstructure

Langer and Flörke (1974) distinguished between non-crystalline opal-AG and non-crystalline opal-AN (or hyalite). The former is an amorphous gel-like aggregate of spherical silica particles with water filling the interstices (Jones et al., 1964). The latter is a water-containing amorphous (network-forming) silica glass (Flörke et al., 1973).

EBSCOhost - printed on 2/13/2023 4:48 AM via . All use subject to https://www.ebsco.com/terms-of-use

Opal-AN occurs as millimeter-thick botryoidal crusts on volcanic rocks. It forms by transport of silica via steam to the surfaces of cold rocks, which quench the vapor (Flörke et al., 1973). Under the polarizing microscope, opal-AN shows strain-induced birefringence, some water inclusions, gas bubbles, and striations that are presumably caused by variations in the water content (Fig. 15, Flörke et al., 1985).

Precious opal consists of close-packed homometric silica spheres (Fig. 19). The diameter of the spheres is approximately half of the wavelength of light (Jones et al., 1964). As noted in Chapter Rossman, the ordered arrangement of non-crystalline silica spheres and interstices with different refraction index causes the diffraction of light which is the origin of the colors of precious opal (Sanders, 1964 and 1968). The size of the spheres and the orientation of the crystal-like packing determine which color is visible.

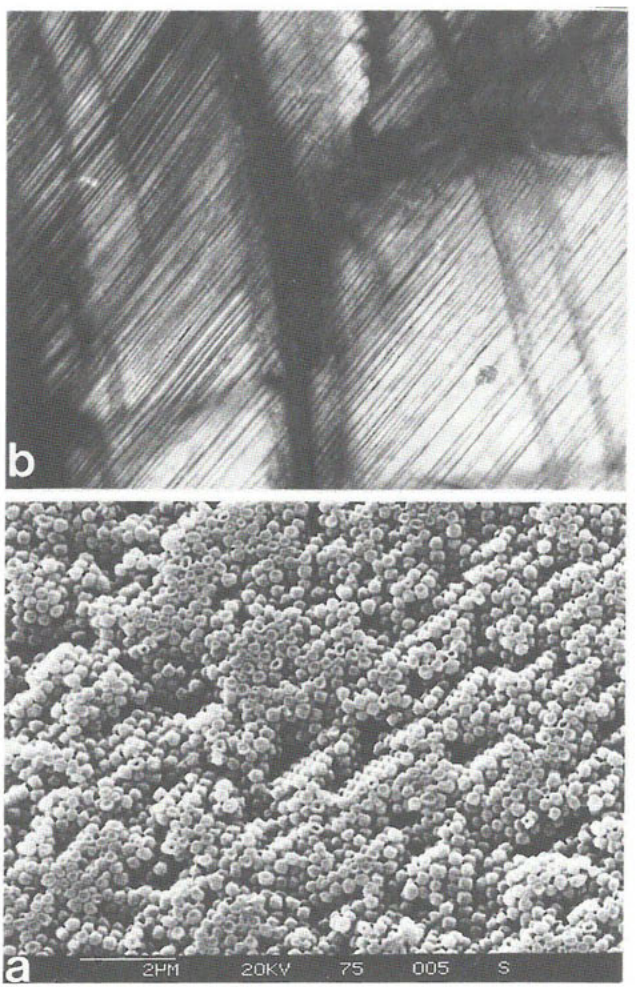


Figure 19. Scanning electron micrograph (a) and petrographic thin section micrograph (b) of precious opal. The long edge of micrograph (b) is 1.11 mm long in nature; crossed polars.

EBSCOhost - printed on 2/13/2023 4:48 AM via . All use subject to https://www.ebsco.com/terms-of-use

"Grains" with coherent stacking but different mutual orientation cause the typical play of color when the stone is turned. The water content and specific surface area as determined by the BET method are usually smaller than values calculated for closest-packed spheres. This discrepancy is due to the presence of additional silica cement partly filling the interstices (Jones and Segnit, 1969). The spheres often consist of a core and one or two shells (Fig. 19), indicating that they were probably formed by aggregation of smaller spheres (Darragh et al., 1965; Jones and Segnit, 1969). The stacking of the spheres is usually faulty. Twinning and stacking faults are abundant (Sanders, 1968; Monroe et al., 1969) and cause stripes or striations in the color patches when viewed in reflected light. Due to anomalous birefringence which also originates from the diffraction of light, the stripes are also visible between crossed polars (Fig. 19).

Unlike silica glass, micro- and non-crystalline silica minerals yield diffuse small-angle X-ray and neutron scattering caused by the inhomogeneous microstructure (Flörke et al., 1991). In precious opals, interparticular interferences superimpose upon the diffuse scattering to yield a few broad intensity maxima (Fig. 20; Graetsch and Ibel, 1991). Diffraction effects are lacking in potch opal due to irregular packing of heterometric spheres, non-spherical shapes, or complete filling of the interstices with silica cement (Fig. 20).

Structure

Radial distribution curves obtained by large-angle X-ray scattering show that the atomic arrangement in non-crystalline opals and silica glass differ from strongly stacking disordered opal-CT by the smaller range of order, not exceeding about 9 Å in the non-crystalline silica phases. ^{29}Si MAS NMR spectroscopy reveals some differences in the local tetrahedral configurations of silica glass and non-crystalline opals (Graetsch et al., 1990). The most striking difference is the larger half-width of the NMR signal of silica glass than those of opals (Fig. 17 and 18), indicating a broader spread of Si-O-Si angles in the random network of glass. The signals of silica glass, opal-AG, and opal-AN exhibit chemical shifts of -110.9 (Murdoch et al., 1985), -111.9 and -112.5 ppm, respectively; these shifts reveal a smaller mean Si-O-Si angle in silica glass than in opals. The greater disorder in silica glass could imply that not all tetrahedral rings contain six members (Mozzi and Warren, 1969; Hosemann et al., 1986). Such structural elements seem to be less frequent or absent in non-crystalline opals.

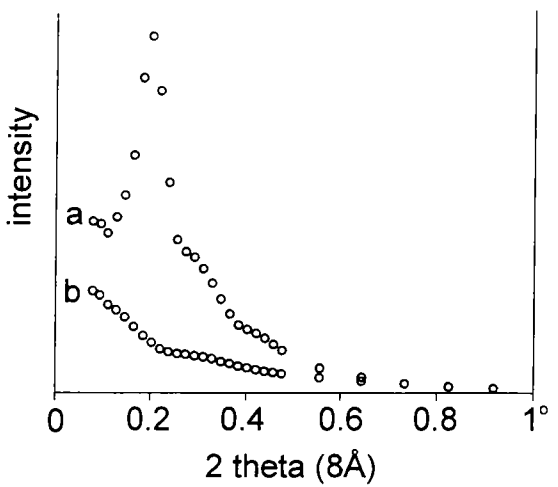


Figure 20. Small angle neutron scattering of a precious opal (a) and a potch opal (b). Wavelength = 8.0 Å; sample to detector distance: 31.25 m. After Graetsch and Ibel (1991).

EBSCOhost - printed on 2/13/2023 4:48 AM via . All use subject to https://www.ebsco.com/terms-of-use

Water content

Most of the water in non-crystalline opals is molecular water. Two different species have been distinguished with near-infrared absorption spectroscopy: a) Isolated water molecules trapped in the network and b) Liquid water in voids or interstices of the microstructure (Langer and Flörke, 1974; Aines et al., 1984). The content of isolated water molecules is highest in opal-AN, causing a sharp combination band at 5,270 cm^{-1}. The shoulder near 5,150 cm^{-1} arises from liquid water (Fig. 11). Similar to microcrystalline quartz and microcrystalline opals, two types of silanol group water can be distinguished: a) Internal silanols located at defects and b) Surface silanols interacting with water molecules. The number of defect silanols is highest in opal-AN (Langer and Flörke, 1974). $^{29}Si/\{^{1}H\}$ MAS NMR cross polarization experiments have shown that geminal silanols (two hydroxyls attached to one silicon atom) do not occur in detectable amounts in micro- and non-crystalline silica minerals (Graetsch et al., 1994 a,b). In opals, most of the water is lost below 400°C with a broad maximum of dehydration at about 200°C (Jones and Segnit, 1971; Langer and Flörke, 1974).

ACKNOWLEDGMENTS

I thank Profs. O.W. Flörke and Peter Heaney for critically reading the manuscript.

REFERENCES

Adams SJ, Hawkes GE, Curzon EH (1991) A solid state ^{29}Si nuclear magnetic resonance study of opal and other hydrous silicas. Am Min 76:1863-1871

Aines RD, Kirby SH, Rossman GR (1984) Hydrogen speciation in synthetic quartz. Phys Chem Min 11:204-212

Aines RD, Rossman GR (1984) Water in minerals ? A peak in the infrared. J Geophys Res 89:4059-4071

Baur WH (1977) Silicon-oxygen bond lengths, bridging angles Si-O-Si and synthetic low tridymite. Acta Cryst B33:2615-2619

Bernauer F (1927) Über Zickzackbänderung und verwandte Polarisationserscheinungen an Kristallen und Kristallaggregaten. N Jahrb Mineral Beil 55:92-143

Braitsch O (1957) Über die natürlichen Faser- und Aggregationstypen beim SiO_2, ihre Verwachsungsformen, Richtungsstatistik und Doppelbrechung. Heidelbg Beitr Mineral Petrogr 5:331-372

Brawer S (1975) Theory of the vibrational spectra of some network and molecular glasses. Phys Rev B 11:3173-3194

Brunner GO, Wondratschek H, Laves F (1961) Ultrarotuntersuchungen über den Einbau von H in natürlichen Quarzen. Z Elektrochem 65:735-750

Cady SL, Wenk H-R, Kilaas R, Barber DJ (1993) Enantiomorphism and planar defects in length-fast chalcedony. In: Boland JN, FitzGerald JD (eds) Defects and processes in the solid state: Geoscience applications. Elsevier, Amsterdam, pp 383-400

Calvert SE (1983) Sedimentary geochemistry of silicon. In Aston SR (ed.) Silicon geochemistry and biogeochemistry. Academic Press, London

Chakraborty D, Lehmann G (1976) On the structure and orientation of hydrogen defects in natural and synthetic quartz crystals. Phys status solidi 34:467-474

Chakraborty D, Lehmann G (1978) On the fine structure in the infrared spectra of clear natural quartz, amethyst, citrine and synthetic quartz in the 3,400 cm^{-1} region. Z Naturforsch 330:290-293

Correns CW, Nagelschmidt G (1933) Über Faserbau und optische Eigenschaften von Chalzedon. Z Kristallogr 85:199-213

Darragh PJ, Gaskin AJ, Terrell BC, Sanders JV (1965) Origin of precious opal. Nature 209:13-16

deJong BHWS, van Hoeck J, Veeman WS, Manson DV (1987) X-ray diffraction and ^{29}Si magic angle spinning NMR of opals: Incoherent long- and short-range order in opal-CT. Am Min 72:1195-1203

Dollase WA (1965) Reinvestigation of the structure of low cristobalite. Z Kristallogr 121:369-377

Engelhardt G, Michel D (1987) High-resolution solid-state NMR of silicates and zeolites. Wiley, Chichester, UK

Eugster HP (1967) Hydrous sodium silicates from Lake Magadi, Kenya: Precursors of bedded chert. Science 157:1177-1180

EBSCOhost - printed on 2/13/2023 4:48 AM via . All use subject to https://www.ebsco.com/terms-of-use

Flörke OW (1955a) Zur Frage des "Hoch-Cristobalit" in Opalen, Bentoniten und Gläsern. N Jahrb Mineral Mh:217-224
Flörke OW (1955b) Strukturanomalien bei Tridymit und Cristobalit. Ber Deut Keram Ges 32:369-381
Flörke OW (1956) Über die Hoch-Tief Umwandlung und die thermische Ausdehnung von Cristobalit. Ber Deut Keram Ges 33:319-321
Flörke OW (1962) Untersuchungen an feinstkristallinem Quarz. Schweiz min petrogr Mitt 41:311-324
Flörke OW (1967) Die Modifikationen des SiO_2. Fortschr Min 44:181-230
Flörke OW, Jones JB, Segnit ER (1973) The genesis of hyalite. N Jahrb Min Mh:82-89
Flörke OW, Jones JB, Segnit ER (1975) Opal-CT crystals. N Jahrb Min Mh:369-377
Flörke OW, Jones JB, Schmincke H-U (1976a) A new microcrystalline silica from Gran Canaria. Z Kristallogr 143:156-165
Flörke OW, Hollmann R, Rad Uv, Rösch H (1976b) Intergrowth and twinning in opal-CT lepispheres. Contrib Mineral Petrol 58:235-242
Flörke OW, Köhler-Herbertz B, Langer K, Tönges I (1982) Water in microcrystalline quartz of volcanic origin: agates. Contrib Mineral Petrol 80:324-333
Flörke OW, Flörke U, Giese U (1984) Moganite:a new microcrystalline silica-mineral. N Jahrb Min Abh 149:325-336
Flörke OW, Flux S, Schröder B (1985) Hyalith vom Steinwitzhügel bei Kulmain (W'Teil des Egergrabens. N Jahrb Min Abh 151:87-97
Flörke OW, Nukui A (1988) Strukturelle Pathologie von Tridymiten. N Jahrb Min Abh 158:175-182
Flörke OW, Graetsch H, Jones JB (1990) Hydrothermal deposition of cristobalite. N Jahrb Min Mh:81-95
Flörke OW, Graetsch H, Martin B, Röller K, Wirth R (1991) Nomenclature of micro- and non-crystalline silica minerals, based on structure and microstructure. N Jahrb Min Abh 163:19-42
Flörke OW, Martin B (1993) Silica modifications and products. Ullmann's Encyclopedia of Industrial Chemistry Vol A23:583-598, 654-655
Folk RL, Weaver CE (1952) A study of the texture and composition of chert. Am J Sci 250:498-510
Folk RL, Pittmann, JS (1971) Length-slow chalcedony: a new testament for vanished evaporites. J Sediment Petrol 41:1045-1058
Frondel C (1962) The System of Mineralogy, 7th edn, vol 3, Wiley, New York
Frondel C (1978) Characters of quartz fibers. Am Min 63:17-27
Frondel C (1982) Structural hydroxyl in chalcedony (Type B quartz). Am Min 67:1248-1257
Frondel C (1985) Systematic compositional zoning in the quartz fibers of agates. Am Min 70:975-979
Füchtbauer H (1988) Sedimente und Sedimentgesteine. Sediment-Petrologie Teil II. Schweizerbart, Stuttgart
Gibbs RE (1927) The polymorphism of silicon dioxide and the structure of tridymite. Proc Roy Soc A113:351-368
Graetsch H, Flörke OW, Miehe G (1985) The nature of water in chalcedony and opal-C from Brazilian agate geodes. Phys Chem Min 12:300-306
Graetsch H, Flörke OW, Miehe G (1987) Structural defects in microcrystalline silica. Phys Chem Min 14:249-257
Graetsch H, Mosset A, Gies H (1990) XRD and ^{29}Si MAS-NMR study on some non-crystalline silica minerals. J Non-Cryst Solids 119:173-180
Graetsch H, Flörke OW (1991) X-ray powder diffraction pattern and phase relationship of tridymite modifications. Z Kristallogr 195:31-48
Graetsch H., Ibel, K. (1991) Neutronenkleinwinkelstreuung von Opalen und Chalzedon (abstract). Z Kristallogr Suppl 3:86
Graetsch H, Topalovic I, Gies H (1994a) NMR spectra of chalcedony and moganite. Eur J Min 6:459-464
Graetsch H, Gies H, Topalovic I (1994b) NMR, XRD and IR study on microcrystalline opals. Phys Chem Min 21:166-175
Heaney PJ, Post JE (1992) The widespread distribution of a novel silica polymorph in microcrystalline quartz varieties. Science 255:441-443
Heaney PJ, Sheppard RA, Post JE (1992) Association of length-slow silica with evaporites. GSA Abstr with Programs 24:A231
Heaney PJ (1993) A proposed mechanism for the growth of chalcedony. Contrib Mineral Petrol 115:66-74
Heaney PJ, Veblen DR, Post JE (1994) Structural disparities between chalcedony and macrocrystalline quartz. Amer Mineral 79:452-460
Hosemann R, Hentschel MP, Schmeisser U, Brückner R (1986) Structural model of vitreous silica based on microcrystalline principles. J Non-Cryst Solids 83:223-234
Iijima A, Tada R (1981) Silica diagenesis of neogene diatomaceous and volcanoclastic sediments in northern Japan. Sedimentology 28:185-200
Jones FT (1952) Iris agate. Am Min 37:578-587
Jones JB, Sanders JV, Segnit ER (1964) Structure of opal. Nature 204:990-991

EBSCOhost - printed on 2/13/2023 4:48 AM via . All use subject to https://www.ebsco.com/terms-of-use

Jones JB, Segnit ER (1969) Water in sphere-type opal. Min Mag 37:357-361
Jones JB, Segnit ER (1971) The nature of opal. I. Nomenclature and constituent phases. J Geol Soc Australia 18:57-68
Kano K (1983) Ordering of opal-CT in diagenesis. Geochem J 17:87-93
Kastner M (1980) Length-slow chalcedony: the end of the new testament (abstract). Trans Am Geophys Union 61:399
Kato K, Nukui A (1977) Die Kristallstruktur des monoklinen Tief-Tridymits. Acta Cryst B32:2486-2491
Kats A (1962) Hydrogen in alpha-quartz. Philips Res Rep 17:133-279
Keat PP (1954) A new crystalline silica. Science 120:328-330
Keene JB (1983) Chalcedonic quartz and occurrence of quartzine (length-slow chalcedony) in pelagic sediments. Sedimentology 30:449-454
Kingma KJ, Hemley RJ (1994) Raman spectroscopic study of microcrystalline silica. Am Min 79: 269-273
Konnert JH, Appleman DE (1978) The crystal structure of low tridymite. Acta Cryst B34:391-403
Langer K, Flörke OW (1974) Near infrared absorption spectra (4,000 - 9,000 cm^{-1}) of opals and the role of "water" in these $SiO_2 \cdot nH_2O$ minerals. Fortschr Min 52:17-51
Laves F (1939) Über den Einfluß von Spannungen auf die Regelung von Quarz- und Cristobalit Kriställchen in Chalzedon, Quarzin und Lussatit. Naturwiss 42:705-717
Levin I, Ott E (1933) X-ray study of opals, silica glass and silica gel. Z Kristallogr 85:305-318
Löns J, Hoffmann W (1987) Zur Kristallstruktur der inkommensurablen Raumtemperaturphase des Tridymits (abstract). Z Kristallogr 178:141-143
Mallard E (1890) Sur la Lussatite, nouvelle variété minérale cristallisée de silice. Bull Soc Franç Min 13:63-66
Martin B, Röller K (1990) Keatite: microstructure, growth fabric and crystal structure. I. Microstructure and texture. N Jahrb Min Mh:462-466
McLaren AC, Phakey PP (1966) Electron microscope study of Brazil twin boundaries in amethyst. Phys status solidi 13:413-422
McLaren AC, Pitkethly DR (1982) The twinning microstructure and growth of amethyst quartz. Phys Chem Min 8:128-135
McLaren AC, Cook RF, Hyde ST, Tobin RC (1983) The mechanisms of the formation and growth of water bubbles and associated dislocation loops in synthetic quartz. Phys Chem Min 9:79-94
Micheelsen H (1966) The structure of dark flint from Stevns, Denmark. Dansk Geol Medd Kobenhavn 16:285-368
Michel-Lévy A, Munier-Chalmas CPE (1892) Mémoire sur diverses formes affectées par le réseau élémentaire du quartz. Bull Soc Franç Min 15:159-190
Midgley HG (1951) Chalcedony and flint. Geol Mag 88:179-184
Miehe G, Graetsch H, Flörke OW (1984) Crystal structure and growth fabric of length-fast chalcedony. Phys Chem Min 10:197-199
Miehe G, Graetsch H (1992) Crystal structure of moganite: a new structure type for silica. Eur J Min 4:693-706
Mitsui K, Taguchi K (1977) Silica mineral diagenesis in neogene tertiary shales in the Tempoku district, Hokkaido, Japan. J Sediment Petrol 47:158-167
Mizutani S (1977) Progressive ordering in cristobalitic silica in the early stage of diagenesis. Contrib Mineral Petrol 61:129-140
Monroe EA, Sass DB, Cole SH (1969) Stacking faults and polytypism in opal, $SiO_2 \cdot nH_2O$. Acta Cryst A25:578-580
Moore GSM, Rose HE (1973) The structure of powdered quartz. Nature 242:187
Moore GSM (1986) The alpha-beta inversion in quartz and effects of structural damage. Phase Transitions 7:25-40
Mozzi RL, Warren BE (1969) The structure of vitreous silica. J Appl Cryst 2:164-172
Murata KL, Nakata K (1974) Cristobalitic stage in the diagenesis of diatomaceous shale. Science 184:567-568
Murdoch JB, Stebbins JF, Carmichael ISE (1985) High-resolution ^{29}Si NMR study of silicate and aluminosilicate glasses: the effect of network-modifying cations. Am Min 70:332-343
Nukui A, Nakazawa H (1980) Polytypism in tridymite. J Min Soc Japan 14, Spec Vol 2:364-386 (in Japanese)
Pankrath R (1991) Polarized IR spectra of synthetic smoky quartz. Phys Chem Min 17:681-689
Peacor DR (1973) High-temperature single crystal study of the cristobalite inversion. Z Kristallogr 138:274-298
Pelto CR (1956) A study of chalcedony. Am J Sci 254:32-50
Plyusnina II (1979) Infrared study of cryptocrystalline formations of silica. I. Chalcedonies. Archiwum Mineralogiczne 35:19-31
Rad Uv (1979) SiO_2-Diagenese in Tiefseesedimenten. Geol. Rundschau 68:1025-1036

EBSCOhost - printed on 2/13/2023 4:48 AM via . All use subject to https://www.ebsco.com/terms-of-use

Raman CV, Jayaraman A (1955) On the optical behaviour of cryptocrystalline quartz. Proc Indian Acad Sci 41A:1-6

Rey Th (1966) Ultrarotabsorption von $AlPO_4$ und SiO_2 in Abhängigkeit von Fehlordnung und Temperatur. Z Kristallogr 123:263-314

Sanders JV (1964) Colour of precious opal. Nature 204:1151-1153

Sanders JV (1968) Diffraction of light by opals. Acta Cryst A24:427-434

Scholze H (1960) Zur Frage der Unterscheidung zwischen H_2O-Molekülen und OH-Gruppen in Gläsern und Mineralien. Naturwiss 47:226-227

Segnit ER, Anderson CA, Jones JB (1970) A scanning microscope study of the morphology of opal. Search 1:349-351

Shorpshire J, Keat PP, Vaughan PA (1959) The crystal structure of keatite, a new form of silica. Z Kristallogr 112:400-413

Shuker R, Gammon RW (1970) Raman-scattering selection-rule breaking and the density of states in amorphous materials. Phys Rev Lett 25:222-225

Smith JV, Blackwell, CS (1983) Nuclear magnetic resonance of silica polymorphs. Nature 303:223-225

Taliaferro, N.L. (1935) Some properties of opal. Am J Sci 30:450-474

Wahl FM, Grim RE, Graf RB (1961) Phase transformations in silica as examined by continuous X-ray diffraction. Am Min 44:196-208

Walker RF, Zerfoss S, Holley SF, Gross LJ (1958) Temperature of the inversion in cristobalite. J Res Nat Bur Standards 61:251-261

Weymouth JH, Williamson WO (1951) Some physical properties of raw and calcined flint. Min Mag 29:573-593

EBSCOhost - printed on 2/13/2023 4:48 AM via . All use subject to https://www.ebsco.com/terms-of-use

PETROGENESIS OF CHERT

L. Paul Knauth

Department of Geology
Arizona State University
Tempe, AZ 85287-1404 U.S.A.

ABSTRACT

Authigenic quartz is found abundantly in sedimentary rocks in the form of chert nodules, chert beds, finely disseminated grains, and cavity infillings. Common cherts consist of interlocking grains of complexly twinned, hydrous, granular microcrystalline quartz that has replaced pre-existing sediments such as carbonate, opal, or evaporite minerals. Fibrous quartz and megaquartz (normal α–quartz) occur in lesser amounts as cavity and fracture fillings.

Silica sedimentation has been dominated by diatoms for the past 50 million years. Bedded chert can form when diatom oozes composed of opal-A are buried and transformed into opal-CT and then into microquartz via a series of solution-reprecipitation steps. Ribbon cherts and novaculites appear to have formed from radiolarian oozes that followed a similar diagenetic sequence.

Prior to the explosive evolution of diatoms, opal-A sponge spicules were a common constituent of shallow-water carbonate environments. During early diagenesis, opal-A spicules dissolved and nodular zones of carbonate became replaced with the mobilized silica. Replacement probably occurred in coastal environments during the conversion of metastable biogenic carbonate into calcite and dolomite. Microquartz was probably precipitated as nodular chert in zones of highest permeability where carbonate dissolved in response to solubility changes at groundwater interfaces (fresh water/marine water, oxic/anoxic) and/or in response to force of crystallization of growing quartz crystals.

Silica precipitated on a large scale in Archean and early Proterozoic sedimentary environments, and was often associated with massive precipitation of iron oxides and siderite. The nature of the original silica precipitate is unknown, but any transformation from precursor opaline phases into microquartz probably occurred at shallow burial depths. Archean sediments are silicified with microquartz to a degree unknown in younger rocks, suggesting warmer climatic temperatures or pervasive later alteration.

Microquartz has formed in a wide array of sedimentary environments that have evolved over geologic time. The transformation sequence of opal-A→opal-CT→ microquartz for siliceous oozes is the most widely known mechanism for chert formation, but most ancient cherts are not the maturation products of siliceous oozes. It is likely that many of the more common cherts in the ancient record formed by direct diagenetic precipitation of microquartz without any precursor opaline phases.

INTRODUCTION

Silica is, and always has been, a common precipitate in the world's seas, lakes, rivers, and soils. Its mineralogy and geochemistry is today overwhelmingly dominated by the biologic activity of diatoms. However, these opal-secreting algae have been abundant only

EBSCOhost - printed on 2/13/2023 4:48 AM via . All use subject to https://www.ebsco.com/terms-of-use

for about the last 50 Ma. Prior to the explosive evolution of diatoms, the environments and manner in which silica formed were quite different. Silica is precipitated today primarily as opal, but ancient deposits are composed of quartz cherts. Some of these deposits represent opal that converted to quartz during burial diagenesis, but many appear to have a more subtle and complicated origin with no modern analogs. Investigations into the origin of cherts have been summarized in excellent reviews by Hesse (1990) and Carozzi (1993). Isotopic studies have been summarized by Knauth (1992). The review presented here focuses on the manner in which authigenic microcrystalline quartz has formed in sedimentary rocks of various types throughout geologic time.

COMMON SILICA POLYMORPHS IN SEDIMENTARY ROCKS

The crystallinity of naturally occurring authigenic silica covers the complete spectrum from X-ray-amorphous to well ordered α–quartz. Opaline forms are common in rocks younger than Miocene, but become progressively rarer with increasing age. With the exception of a few deep sea deposits, opal in rocks older than 60 Ma is essentially unknown. A popular explanation for this time trend is that authigenic silica is generally precipitated as opal, which then inverts to quartz over tens of millions of years. However, as will be discussed below, it is also possible that biogenic production of opal is currently at an all- time high in earth history. Climatic temperatures also play a key role in silica deposition, and these temperatures may have been cooler than average during this recent interval of widespread opal deposition.

Structural character of chert

The crystalline varieties of sedimentary silica have been classified into three types: granular microcrystalline quartz, fibrous silica, and megaquartz. These authigenic varieties contain many structural complexities and peculiarities (see chapter by Graetsch). Most appear to have measurable amounts of hydroxyl and molecular water at dislocations, along planar defects, and at other sites yet to be determined. Fibrous silica is ubiquitous in cherts and has received much attention because of its interesting crystallographic properties. However, it is almost always a minor component. The dominant phase in cherts is granular microcrystalline quartz, or "microquartz". This material has a crystallographic complexity probably equal to that of the fibrous varieties. It is a remarkable intergrowth of birefringent, α–quartz grains that range in size from less than1 to 50 μm (Fig. 1). The average grain size in ancient cherts has never been statistically determined, but is probably on the order of 8 to 10 μm.

The water content in chert ranges from about 0.2 to 2.0 wt % (Knauth and Epstein 1976; Graetsch et al., 1985) and is about 50‰ depleted in deuterium relative to the water from which silica precipitates. This depletion is similar to that observed for hydroxyl in clay minerals, and it suggests that the water is primarily hydroxyl. However, it is possible that 2 Si-OH groups originally present at dislocations could combine upon aging to form a Si-O bond with release of H_2O. With this annealing mechanism, the microquartz could retain molecular water in submicroscopic fluid inclusions that was originally isotopically fractionated as OH.

Microcrystalline fibrous silica

Microcrystalline fibrous silica, or chalcedony, usually forms botryoidal arrays in cavities, fractures, and vugs in host rocks. Due to numerous tiny fluid inclusions and other impurities, fibrous silica often is a pale yellow-brown color in thin section in plane

EBSCOhost - printed on 2/13/2023 4:48 AM via . All use subject to https://www.ebsco.com/terms-of-use

polarized light. It can be length fast or length-slow. Folk and Pittman (1971) suggested that length-slow fibrous quartz usually forms when sulfate is present in the parent fluid, and Kastner (1979) noted that length-slow chalcedony precipitates from Mg-rich solutions with high ionic strength (>3). Fibers typically twist about the fiber axes, creating oscillatory extinction textures in cross-polarized light known as "zebraic chalcedony." Other peculiarities of fibrous growth abound, as discussed in Chapter Graetsch. Water is present in fibrous silica as structural OH and several types of non-structural water (Pelto, 1956, Frondel, 1982). The water content typically comprises about 1 to 2 wt % (Knauth, 1973; Graetsch et al., 1985).

Moganite is a variety of length-slow fibrous silica that has been defined on the basis of detailed X-ray diffraction studies (Flörke et al., 1976) and micro-Raman spectroscopy (Kingma and Hemley, 1994). Heaney and Post (1992) have shown that moganite is widespread in natural chert samples. The significance of moganite for petrologic studies is still being explored; it may prove useful as an indicator of vanished evaporites.

Megaquartz

For lack of a more accurate term, well-defined crystals of authigenic, α–quartz of any size are called megaquartz (Folk, 1950). These crystals (Fig. 2) are ordered over the long range and do not contain the crystallographic complexities of microquartz and fibrous silica. They can occur as megascopic, subhedral, drusy quartz crystals in cavities or as

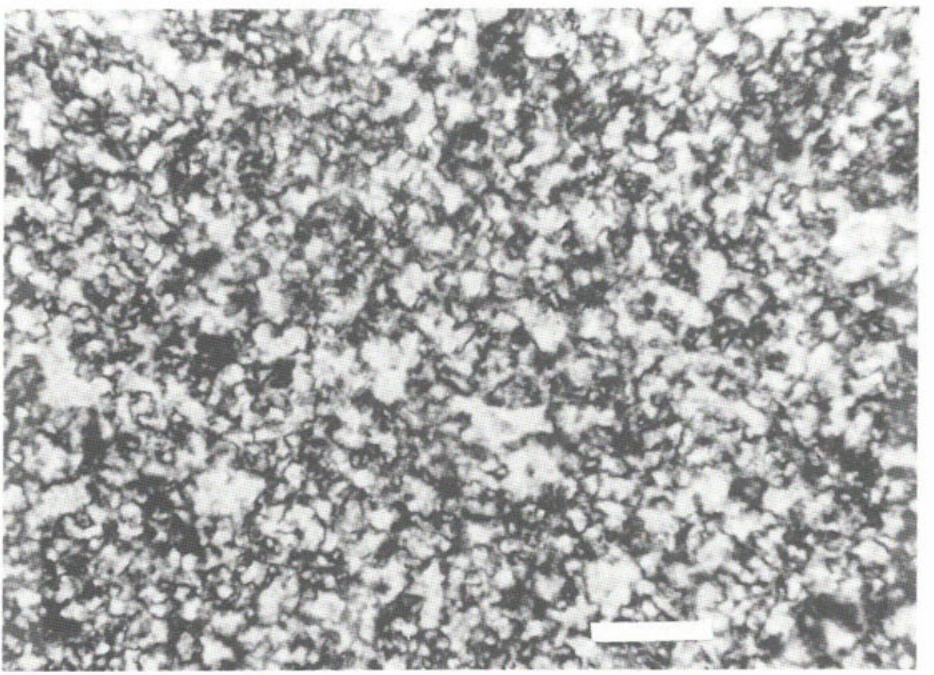


Figure 1. Crossed nicols. Granular microcrystalline quartz, or "microquartz," from the Miocene Humboldt Formation, Nevada. This texture is typical for well-preserved ancient cherts. The grain size ranges from about 5 to 60 μm, and is somewhat coarser in this example than the normal 8 to 10 μm found in most cherts. Bar = 100μm.

EBSCOhost - printed on 2/13/2023 4:48 AM via . All use subject to https://www.ebsco.com/terms-of-use

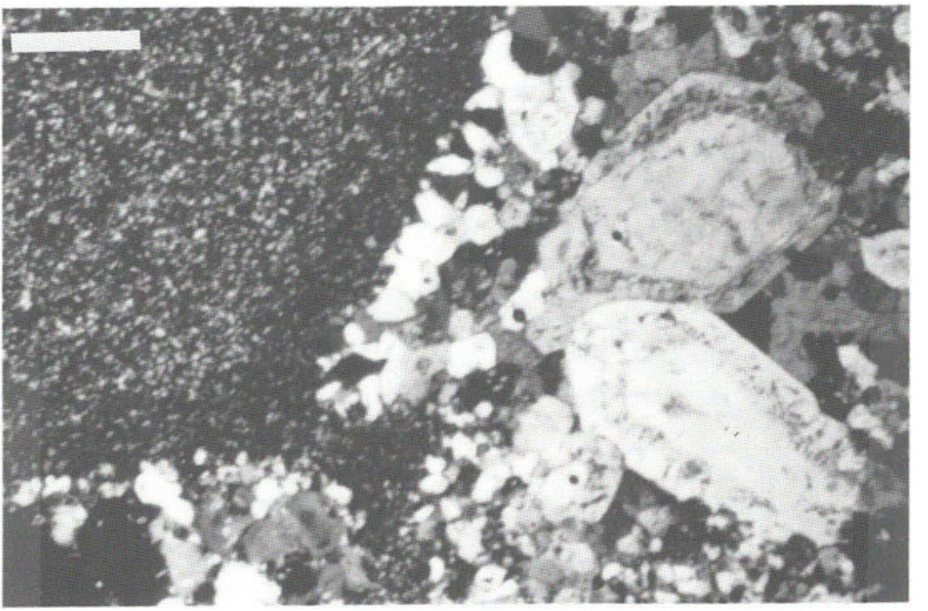
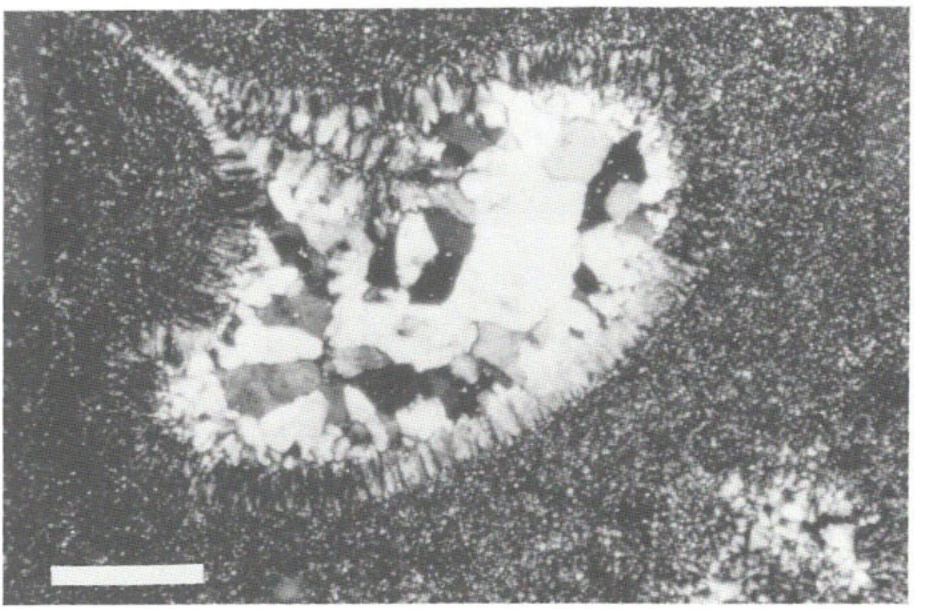


Figure 2. Crossed nicols. Megaquartz from the Cretaceous Edwards Limestone, Texas. Fine-grained, dark material is microquartz. Megaquartz crystals range in size from ~50 μm to 1 mm. Megaquartz in unmetamorphosed cherts such as this typically represents growth into free space, such as micro-cavities and fracture openings. It can also form during metamorphic recrystallization of microquartz. Bar = 500 μm.

Figure 3. Crossed nicols. Fossil mold lined with fibrous silica that grades inward into megaquartz. Matrix is microquartz. This common petrographic texture probably indicates declining silica concentrations and/or a decrease in the rate of crystal growth during cavity infilling. Edwards Limestone, Texas. Bar = 250μm.



EBSCOhost - printed on 2/13/2023 4:48 AM via . All use subject to https://www.ebsco.com/terms-of-use

intergrown, microscopic grains. In many infilled cavities, the walls are lined with fibrous silica that grades inward into megaquartz (Fig. 3). A common interpretation (Folk and Weaver, 1952; Heaney, 1993) is that the textural transformation from microquartz to megaquartz represents declining silica concentrations and/or slower crystal growth during cavity infilling (possibly a response to decreasing permeability and diminished flow of diagenetic fluids as the cavity fills up). Megaquartz and drusy quartz are extremely common in ancient sabkha limestone and dolostone where abundant sulfate blebs and nodules have been dissolved away during early diagenesis and then infilled by direct growth of quartz. The equilibrium solubility of megaquartz is probably about 4 ppm (Mackenzie and Gees, 1971).

Megaquartz also forms when chert composed of microquartz is metamorphosed or hydrothermally altered. A mosaic texture of grains generally much larger than 10 microns develops in which each grain goes to pinpoint extinction. This texture is easily distinguishable from the microquartz and fibrous quartz textures of unaltered cherts and is a reliable guide to "preserved" versus "recrystallized" cherts. A "triple-point" texture can even develop in severely metamorphosed cherts (Keller et al., 1977). Individual grains of megaquartz that form during metamorphic recrystallization of microquartz are not readily distinguishable optically from individual grains of diagenetic megaquartz. However, the overall texture (pure mosaic of megaquartz versus cavity-fill, presence or absence of fibrous quartz and microquartz) usually allows some assessment of the likelihood of a metamorphic origin for the megaquartz. This issue is critical to many geochemical and paleontological studies, and petrographic screening of samples in these cases is invaluable.

Opaline silica

Opaline forms of authigenic silica include opal-A, opal-CT, and opal-C (Jones and Segnit, 1971). Of these, only opal-A and opal-CT figure prominently in the origin of cherts in sedimentary rocks. Opal-A is the most common amorphous form and is abundantly precipitated by modern organisms. It contains up to 12 wt % water, including both hydroxyl and molecular water (Knauth and Epstein, 1982). The equilibrium solubility at 25°C of opal-A is on the order of 70 to 150 ppm (Iler, 1979).

Opal-CT is a near amorphous, weakly birefringent phase with weak diffraction peaks of cristobalite and tridymite. Knauth and Epstein (1975) measured a water content of 1.2 wt %, but Keene (1976) found values as high as 13 wt %. Questions remain regarding the speciation of water in this material, but it appears to contain a major OH component (Knauth and Epstein,1975). Opal-CT is found as a common diagenetic alteration product of biogenic oozes initially composed of opal-A, but it is rare in the other varieties of chert. The solubility is difficult to measure, but it is inferred to be intermediate between that of opal-A and that of quartz (Kastner, 1981).

PARAGENESIS OF AUTHIGENIC SILICA PHASES

The careful documentation of silica diagenesis in siliceous oozes (e.g., Murata and Larsen, 1975) has strongly influenced the popular view of how the silica phases discussed above originate. However, the origin of authigenic quartz is so variable and complicated that extreme caution should be used in porting diagenetic schemes from one geologic setting to another. Authigenic silica found in diagenetically altered diatomite has an utterly different origin from that found in the alkaline-lake deposits of East Africa. Similarly, nodular cherts in limestone are early diagenetic replacement features; they are not maturation products of biogenic oozes. If ancient cherts now composed of microquartz had

EBSCOhost - printed on 2/13/2023 4:48 AM via . All use subject to https://www.ebsco.com/terms-of-use

precursor phases such as opal-CT, these must be inferred from indirect methods. Because of this, there is much uncertainty regarding the origin of most authigenic quartz.

A common misconception is that quartz cannot precipitate directly from an aqueous solution at room temperature and that all authigenic quartz must have an opaline precursor. In fact, quartz does precipitate directly from solution in the laboratory. Mackenzie and Gees (1971) grew 10 μm-sized subhedral quartz crystals in sea water at 20°C in 2 years. This is the size of the most common microquartz grains in cherts. There is therefore no reason to believe that quartz cherts cannot form directly from solutions carrying >4 ppm dissolved silica.

The common forms of authigenic silica and the waters in which they dissolve and precipitate are shown schematically in Figure 4. Several diagenetic pathways for silica diagenesis are shown, and these are dependent on the particular geologic setting. In all cases studied, the silica transformations involve changes in oxygen isotope composition (e.g., Murata et al., 1977), so the transformations are dissolution/precipitation reactions rather than solid-solid inversions. Pathways shown in Figure 4 are discussed below for the major types of cherts.

DIATOMS AND THEIR CONVERSION TO MICROCRYSTALLINE QUARTZ

The modern oceans contain an immense number of silica-secreting organisms, about 70% of which are diatoms (Lisitzin, 1972). Second in importance are the radiolaria, followed by the silica sponges. Silicoflagellates and higher organisms also precipitate silica, but on a much smaller scale. Biogenic silica is opal-A in all cases that have been investigated.

Diatoms live in the surface waters and can settle out on the ocean floor as extensive oozes when productivity is particularly high. The most extensively investigated example is the Monterey Formation, California. About 300 to 500 m of diatomaceous ooze accumulated in several basins off the California coast during the Miocene-Pliocene. The deposits were subsequently buried to various depths and then uplifted along this tectonically active coastline. Bramlette (1946) noted that burial had apparently converted the Monterey diatomite into a hard rock with a porcelain-like texture. Murata and Nakata (1974) made detailed studies of a continuously exposed stratigraphic section and showed that the "porcellanite" was composed largely of opal-CT. Porcellanite that had been buried to even greater depths was composed of α-quartz.

About the same time as the work of Murata and Nakata, cores from deep ocean basins were revealing a similar diagenetic sequence for radiolarian oozes. Oxygen isotope studies (Knauth and Epstein, 1975; Kolodny and Epstein, 1976; Murata et al., 1977; Pisciotto 1981) and consideration of the geothermal gradient in cored deep sea sections (Kastner, 1981) suggested that biogenic opal-A converts wholesale to opal-CT when burial temperatures reach about 45°C. Quartz forms extensively when temperatures reach about 80°C.

During the course of this diagenetic transformation, void spaces in microfossil molds and microcavities are often filled with bladed spherules of silica about 5 to 12 μm in diameter. Based on bulk X-ray analysis, these "lepispheres" appear to be composed of opal-CT (Weaver and Wise, 1972). While lepispheres may be made of opal-CT, it does not follow that all opal-CT occurs as lepispheres. The lepispheres appear to represent opal-CT

EBSCOhost - printed on 2/13/2023 4:48 AM via . All use subject to https://www.ebsco.com/terms-of-use

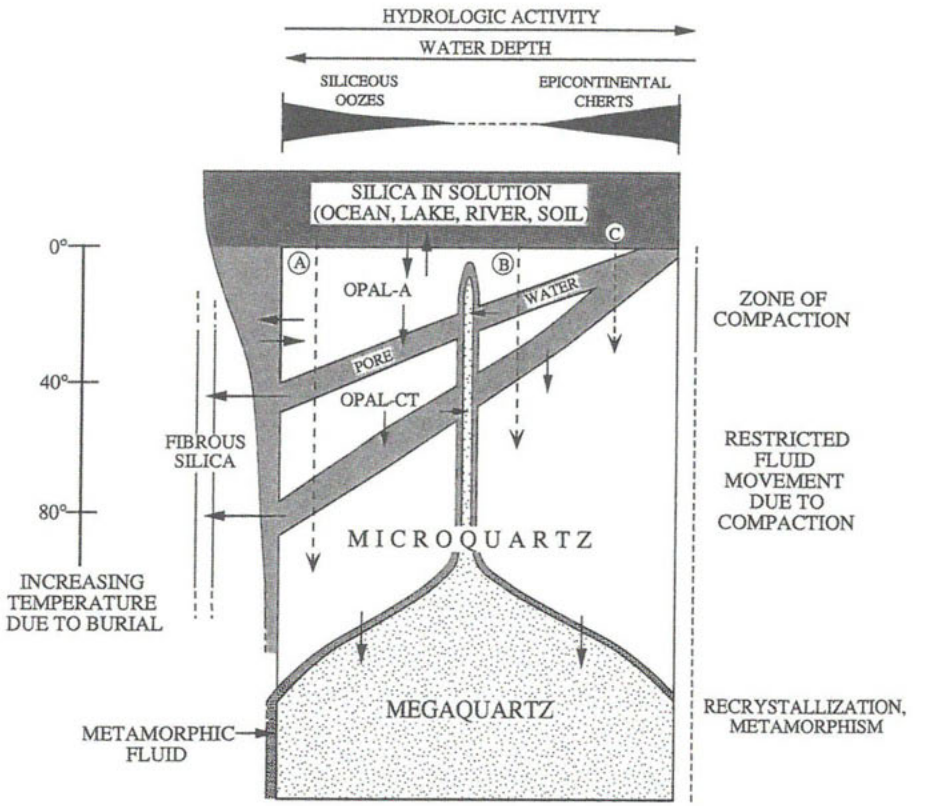


Figure 4. Schematic diagram of major authigenic silica phases and their possible diagenetic transformations. Vertical dimension represents qualitative burial depth with associated increase in temperature and loss of permeability. Horizontal scale represents qualitative depth of initial depositional environment. In general, deep sea oozes lie to the left of the diagram, while epicontinental deposits lie toward the right. Diagenetic path "A" represents silica initially deposited as opal-A (diatoms, radiolarians) which then transforms to opal-CT and then microquartz via solution-reprecipitation steps. Path "C" represents early diagenetic cherts in which microquartz forms during shallow burial. Megaquartz forms by metamorphic recrystallization of microquartz or by direct growth into voids at any stage of burial. Fibrous silica can grow in vugs and fractures at all burial depths.

that has grown into free space. The massive matrix of typical opal-CT porcellanite may or may not contain lepispheres.

The importance of temperature in the opal-A→opal-CT→quartz transition was stressed in most of the initial studies of siliceous ooze diagenesis. For example, Hein et al. (1978) correlated the opal-A→opal-CT transition with a regional acoustic reflector and suggested that the reflector thereby defined a subterranean isothermal surface that could be mapped over a wide area. However, the importance of temperature in the transformations has probably been overestimated. Based on empirical trends, Isaacs (1982) suggested that the silica transformation rates are influenced by the impurity content of the silica. Williams et al. (1985) argued that dissolution-precipitation during the transformations is accompanied

EBSCOhost - printed on 2/13/2023 4:48 AM via . All use subject to https://www.ebsco.com/terms-of-use

by significant changes in surface area and is therefore subject to Ostwald ripening (in which larger particles with low solubilities grow at the expense of smaller particles with higher solubilities). While the process may proceed faster at higher temperatures, there is an inherent tendency for more soluble opal-A with higher surface area to be replaced by opal-CT and then quartz at any temperature.

Matheney and Knauth (1993) have shown that the oxygen isotope temperatures of the earlier work on siliceous ooze diagenesis were often based on measurements that were not corrected for the internal water component. In addition, most studies made an implicit assumption that water/rock ratio was infinite throughout burial diagenesis. Using a stepwise fluorination method to remove water prior to isotopic analysis and using a model for the evolution of water/rock ratios during burial diagenesis, Matheney and Knauth (1993) argued that much Monterey opal-CT forms at least as low as 17 to 21°C (rather than the 35 to 50°C range normally inferred). Based on new isotopic data, Behl (1992) also concluded that much Monterey opal-CT forms at ~2 to 33°C.

To those familiar with nodular or bedded cherts in ancient strata exposed on the continents, the quartz cherts of the Monterey Formation are a surprising sight. Rather than the usual hard, translucent silica with conchoidal fracture, the quartz cherts often have the texture of indurated shale. Upon moderate weathering, some varieties even spray grains when hit with a hammer, and might be mistaken for a sandstone. Black, shiny, "glassy" cherts with conchoidal fracture do occur, but they have usually been considered anomalous (Isaacs 1982). Behl (1992) has argued that much of the "glassy" chert is quartz that filled voids directly and did not go through the opal-A→opal-CT→quartz transformation. $\delta^{18}O$ for quartz cherts in the Monterey Formation ranges from 25‰ to 31‰ (Behl, 1992), a much greater range than reported in earlier papers. Many quartz cherts appear to have formed at temperatures as low as 30-40°C rather than the 80°C value often quoted.

Most Monterey diatomite appears to have followed a trajectory represented as path "A" in Figure 4, the sequence originally proposed by Murata and Nakata (1974). The more recent work suggests that in some areas the transformations occurred during shallower burial, and these could be represented by numerous alternative pathways that lie more toward the right side of the diagram. Path "C", for example, would represent a black, "glassy" chert that formed below 45°C.

It is important to note that diatoms precipitate and survive in surface sea water that is strongly undersaturated with respect to dissolved silica. The particle surfaces are apparently armored with metals to impede dissolution (Lewin, 1961). In spite of this, more than 99% of all diatoms dissolve during settling and the first meter of burial (e.g., Hein et al., 1978); only those diatoms most resistant to dissolution are left to participate in silica diagenesis. Deeper burial leads to increased compaction, which decreases porosity and permeability. As a result, fluid flow is inhibited, further impeding diagenetic transformations that depend on the solution-reprecipitation mechanism. The formation of porcellanite involves a further reduction in permeability, and the transformation to quartz via solution-precipitation reactions becomes very difficult, possibly proceeding preferentially in zones that become fractured and thereby subject to fluid invasion. Opal-A in diatom oozes is therefore strongly resistant to diagenetic alteration. Nevertheless, the diatom-to-microquartz transformation scheme has become well known and widely applied, even to cherts that do not form as maturation products of siliceous oozes (e.g., Maliva and Siever, 1988a; Gao and Land, 1991). However, with the possible exception of radiolarian oozes (which are even more resistant to dissolution), the diagenetic scheme deduced for

EBSCOhost - printed on 2/13/2023 4:48 AM via . All use subject to https://www.ebsco.com/terms-of-use

diatomaceous oozes should probably be viewed as an extreme situation rather than a model to be applied to the petrogenesis of all cherts.

RADIOLARIAN OOZES, SPICULITES, RIBBON CHERTS AND NOVACULITE

Radiolarians and sponges

Radiolarians and silica-secreting sponges have been abundant since the beginning of Phanerozoic time and have given rise to various types of "bedded cherts." Radiolarians are an open-ocean fauna that live throughout the water column and accumulate as deep water oozes. The oozes are purest in environments that lie below the Carbonate Compensation Depth and are located far from clastic source areas.

Silica sponges were common in shallow platform sediments until the Cenozoic. Today, they are most abundant in the deep oceans and usually make up only a minor part of shallow water communities. It is possible that the Cenozoic explosion of diatoms so lowered the silica concentration of surface sea water that the sponges were displaced into the more silica-rich waters of the deep ocean. Sediment composed predominantly of opaline sponge spicules (spiculite) occurs today, but it is not nearly as abundant as radiolarian ooze.

The diagenetic transformation of radiolarian oozes and spiculites into quartz chert may commonly proceed similar to the sequence of diatomaceous oozes as shown by trajectory "A" in Figure 4. Drill cores from deep sea sediments rich in biogenic silica frequently contain layers of porcellanite and radiolarian molds partially filled with opal-CT lepispheres (e.g., Lancelot, 1973; Rad, 1978). Quartz cherts lie at deeper burial depths. The simplest explanation for most of the cherts and porcellanites encountered by deep sea drilling is that biogenic opal-A has been converted to opal-CT and then to quartz as a result of increasing burial temperature (see Kastner, 1981, for an excellent review that argues this viewpoint). Of course, deeper portions of the sediment pile generally represent progressively older times, when sea-floor conditions may have been quite different. (By contrast, in the Monterey Formation, the same stratigraphic horizon was buried to various depths and then uplifted to allow examination of fabulous surface exposures.) Deep bottom water in the Cretaceous and earlier times may have been over 15°C warmer than in today's ocean (Savin, 1977). Diagenesis of radiolarian oozes may have proceeded much faster and at much shallower depths of burial under those conditions.

Ribbon cherts

Because of plate tectonics, deep ocean sediments are eventually subducted and/or deformed and attached to the sides of continents as long fold belts. Bedded cherts with a distinctive "pinch and swell" texture (Fig. 5) are commonly found in these fold belts. These "ribbon" cherts are particularly abundant in Mesozoic strata. They are often found associated with ophiolites, where they are deposited directly on pillow basalts. The association of these cherts with volcanic rocks suggested to early workers that hydrothermal fluids served as the major source of dissolved silica for these rocks—"exhalite" cherts on a grand scale (Grunau, 1965). However, gentle etching techniques and petrographic examination have subsequently revealed abundant radiolarians, many layers of which appear to have been deposited via turbidity currents. The exhalative origin is now less popular, and most recent workers have concluded that ribbon cherts were once radiolarian oozes that were diagenetically altered into quartz chert.

EBSCOhost - printed on 2/13/2023 4:48 AM via . All use subject to https://www.ebsco.com/terms-of-use

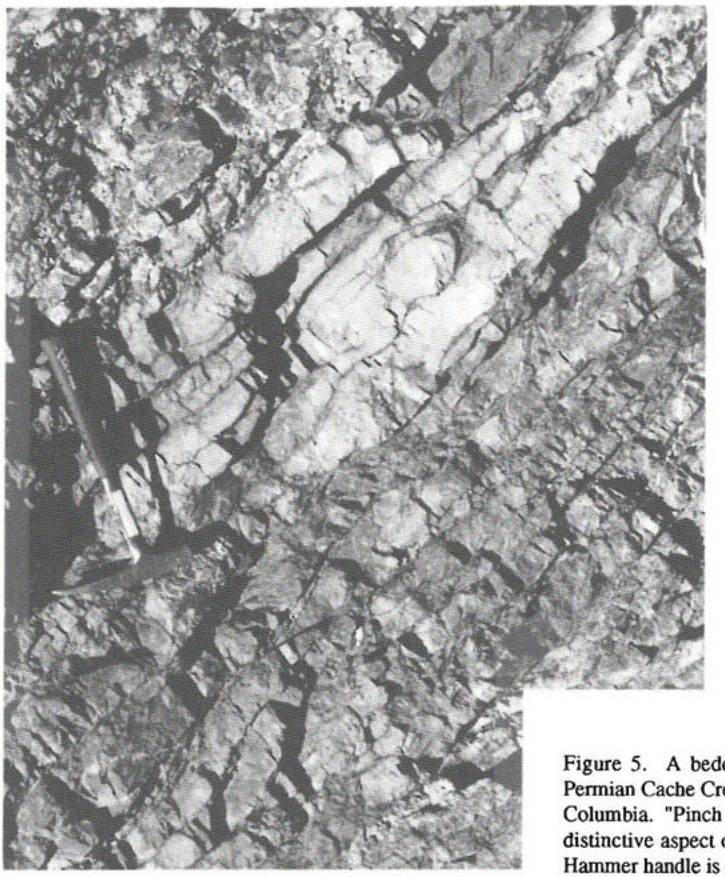


Figure 5. A bedded radiolarian chert, Permian Cache Creek Formation, British Columbia. "Pinch and swell" texture is a distinctive aspect of these ribbon cherts. Hammer handle is 0.4 m.

Where unmetamorphosed, the ribbon cherts are composed predominantly of microquartz. One common explanation for the pinch and swell structure is that the thicker portions of the bed represent zones that became lithified prior to compaction, and that the "pinched" parts of the beds compacted around these zones. However, etched-out radiolarians often show no signs of deformation due to compaction. It is possible that portions of these oozes converted to either opal-CT or quartz prior to significant burial (thus following a transformation path like "B" in Fig. 4). Folk and McBride (1978) have even presented intriguing evidence that some radiolarian oozes were intermittently uplifted before significant burial and exposed to subaerial diagenesis (suggesting a possible path in Fig. 4 to the right of "B").

Jenkyns and Winterer (1982) noted that deep sea drilling in modern ocean basins has never encountered anything resembling the ribbon cherts so commonly exposed in fold belts. There are no thick sequences of ribbon cherts or chert-shale couplets. Rather, there are radiolarian oozes interbedded with clays and carbonates. Jenkyns and Winterer (1982) suggested that the ribbon cherts had accumulated during previous times when there were numerous small basins rich in radiolaria. However, Murray et al. (1992) argued that the post-Mesozoic radiolarian populations became diluted by the explosive radiation of diatoms and calcareous plankton to produce the kinds of Cenozoic depositional sequences cored in the modern ocean basins. Prior to this time, radiolarians could accumulate slowly into

EBSCOhost - printed on 2/13/2023 4:48 AM via . All use subject to https://www.ebsco.com/terms-of-use

oozes of considerable purity and thickness. The geochemical data of Murray et al. (1992) suggest that the chert-shale couplets were produced via diagenetic segregation of silica during burial diagenesis; silica migrated out of the shale and into the horizons now holding chert. It is not clear what this scenario implies regarding a pathway on Figure 4. Ribbon cherts are now all quartz, so evidence for diagenetic pathways will have to be inferred from petrographic "ghost" features observed in thin-section or from forms etched out of slabs.

Novaculites

Novaculites are bedded quartz cherts similar to radiolarian ribbon cherts except that they are commonly pure white and more evenly bedded than the typical "ribbon" chert. The Devonian Arkansas-Caballos Novaculite of Arkansas-Texas is the best-known example (Fig. 6). The northern part of this unit stretches west from Little Rock, Arkansas for 350 km. As observed by Jones and Knauth (1979), fossil radiolarians and sponge spicules are typically visible in thin-section and indicate a probable siliceous ooze precursor. "Ghost" lepispheres are observed in some samples, suggesting that opal-CT was an intermediate phase between the original opal-A and the microquartz final product. $\delta^{18}O$ of chert at the western end ranges from +30‰ to +34‰ , while the eastern part of the belt ranges from +25‰ to +30‰. Jones and Knauth (1979) inferred from all this that the novaculite was mainly a radiolarian ooze that converted to quartz over a burial temperature range of about 15 to 30°C in the western area and at 30 to 55°C in the eastern area.

The overall isotopic range of the novaculite is the same as that observed for the Monterey cherts, suggesting that pathways similar to "A" and "B" in Figure 4 were common during crystallization of the novaculite. The transformations proceeded at significantly shallower burial depths to the west, and the presence of length-slow fibrous quartz may indicate localized precipitation in evaporitic environments. Folk and McBride (1976) and Hovorka (1981) have also presented evidence for evaporitic environments and



Figure 6. Caballos Novaculite, Ft. Pena picnic grounds, near Marathon, Texas. The novaculite is the left-dipping white bed extending from lower right to upper left. The extreme resistance of this radiolarian chert to erosion is the cause of the topographic relief in the area shown. Trees in foreground provide scale.

EBSCOhost - printed on 2/13/2023 4:48 AM via . All use subject to https://www.ebsco.com/terms-of-use

subaerial exposure prior to significant burial of the Caballos Novaculite in West Texas. The "maturation" of siliceous oozes from biogenic opal to quartz likely occurred at variable depths and in widely different depositional environments. Opal-CT may or may not have been an intervening phase in the maturation sequence, and factors other than burial temperature were probably important in determining when diagenetic quartz crystallized. A diagenetic pathway along the right side of Figure 4 is possible for some areas. As in the case of the ribbon cherts, localized metamorphic recrystallization of the original microquartz into megaquartz further complicates the study of these ancient bedded cherts.

NODULAR CHERTS IN SHALLOW WATER PLATFORM CARBONATES AND EPICONTINENTAL SEA DEPOSITS

Sedimentary rocks deposited on cratons have a high preservation potential relative to ocean basin deposits because they tend to escape subduction and the intense deformation associated with collisional plate boundaries. Because of this, many cratonic sequences are well-preserved and beautifully exposed on the continents. Nodular cherts in limestones are a common occurrence in these sequences and are probably the most familiar form of chert to most geologists.

Chert nodules in these limestones are composed of microquartz and typically occur in the form of oblate spheroids, with the long axis lying in the bedding plane of the host carbonate (Fig. 7). They range in size from cm-sized blebs to meter-sized lenses. Most are smaller than a half-meter, and the majority of the authigenic microquartz in carbonates may actually be finely disseminated throughout the host rock matrix. Thin "stringers" of microquartz are common along bedding planes. Conchoidal fracture is a distinctive feature of unmetamorphosed nodular cherts. A peculiar physical property is that fractured pieces flex enough to keep them from fitting perfectly back together.



Figure 7. Nodular chert in limestone. Naco Formation, Tonto Creek, Arizona. This typical replacement chert is an oblate spheroid with its major axis lying in the bedding plane of the host limestone. The chert nodule stands in relief because it is more resistant to weathering than the host limestone. Horizontal dimension of nodule is about 25 cm.

EBSCOhost - printed on 2/13/2023 4:48 AM via . All use subject to https://www.ebsco.com/terms-of-use

An early view of nodular chert formation was that colloidal silica precipitated as gels, which rolled around on the sea floor as nodular masses. These then converted to quartz with burial and aging (Tarr, 1917). Starting with Van Tuyl (1918), evidence has steadily mounted that most nodular cherts form as replacement of limestone rather than crystallization from a gel. Every gradation from weakly silicified zones to near-100% replacement is observed. The purer cherts are translucent, and the luster becomes duller with increasing impurities (such as unreplaced carbonate, clay, or organic matter). Crystallization from a gel is still invoked for some Precambrian examples (Oehler and Schopf, 1971), but most nodular cherts in carbonate rocks appear to result from a diagenetic episode in which carbonate was replaced incrementally on a volume-for-volume basis by silica (analogous to petrified wood, where silica has replaced organic matter with near-perfect preservation of organic structures).

Mechanism of replacement

The mechanism of replacement has never been fully explained. Biggs (1957) invoked Ramberg's (1952) ideas in which a growing quartz crystal has a higher thermodynamic "force of crystallization" than limestone or dolomite, leading to quartz replacement of carbonate. Correns (1969) pointed out that calcite solubility increases with decreasing pH while silica solubility first decreases and then remains relatively constant (below pH $\cong$ 9). Thus, diagenetic waters undergoing a steady decrease in pH can be expected to dissolve calcite while silica precipitates, and silicification of carbonate can occur.

Knauth (1979) proposed that dissolved silica concentrations in seaward-moving, coastal ground waters progressively rise by dissolution of opal-A sponge spicules until the meteoric waters begin mixing with sea water pore fluids. It is thermodynamically possible for the fluid mixture to become undersaturated with respect to calcite, even if the waters that mixed were initially saturated with respect to calcite (but have different CO_2 partial pressures or different temperatures). Silica can replace limestone under these conditions, and the mechanism accounts for observed isotopic ratios, typical field relationships, and many other features associated with the cherts (Knauth, 1979).

Clayton (1986) suggested that oxidation of microbial H_2S lowers pH during mixing of oxic and anoxic pore fluids. The decrease in alkalinity allows pore fluids saturated in silica from the dissolution of co-existing biogenic opal-A to replace carbonate. The mechanism was invoked to explain rows of chert nodules in the Cretaceous Chalk of western Europe. While this is a deep sea deposit, the mechanism could work as well during diagenesis of epicontinental carbonates.

Maliva and Siever (1988b) could not find dissolution textures in thin sections of silicified carbonates and argued that a mechanism for replacement that does not involve changes in pore water chemistry is therefore required to explain silicification. They re-invoked the idea of force of crystallization and explained it in terms of enhanced carbonate solubility due to pressure exerted by growing quartz crystals.

Numerous authors from Biggs (1957) onward have noted that chert nodules in epicontinental carbonate units are often found as clasts in the strata immediately overlying them, indicating syn-sedimentary chert formation rather than a late-diagenetic origin, as in the case of the deep-sea cherts. In addition, chert nodules are typically found scattered in disarray in paleokarst horizons that develop during exposure to meteoric water (e.g., Robertson, 1967; Meyers, 1977). Calcite allochems and early depositional textures, including oolitic texture and crossbedding, are commonly preserved in cherts, while primary textures in the host carbonate have been completely obliterated by subsequent neomorphism and/or dolomitization. Compaction laminae are typically draped around chert

EBSCOhost - printed on 2/13/2023 4:48 AM via . All use subject to https://www.ebsco.com/terms-of-use

nodules (Fig. 8), indicating silicification prior to compaction. Isolated dolomite rhombs within cherts are common, and these are normally interpreted to indicate that preferential silicification of calcite and aragonite occurred after inception of dolomitization but before it could proceed beyond formation of isolated crystals. In short, virtually every study of nodular chert formation has included evidence that the nodules were formed during early diagenesis and before compaction.

It is possible that chert nodules form early but are originally composed of some precursor phase such as opal-A or opal-CT. Because opal-CT lepispheres are so distinctive and common in Tertiary deep sea cherts, various authors have tried to find evidence that opal-CT precedes microquartz in nodular cherts. Maliva and Siever (1988a) observed quartz microspheroids that they interpreted as former opal-CT lepispheres that had inverted to quartz. They suggested that the opal-A→opal-CT→quartz maturation sequence observed in diatomaceous oozes appears to have been operative in the formation of many Mesozoic and Paleozoic nodular cherts. In another study, Gao and Land (1991) boiled Ordovician nodular cherts in concentrated HF and observed textures with the SEM that they interpreted to be former opal-CT lepispheres that had inverted to quartz. By analogy with diagenesis in deep sea oozes, these authors suggested that microquartz formation in these nodular cherts did not form until 25 to 50 my after formation of the putative lepispheres.

Some replacement cherts occur in the shape of anhydrite nodules ("cauliflower cherts") and other evaporite mineral fabrics. Cauliflower chert appears to have formed when evaporite minerals in carbonate sabkha deposits were flushed out by meteoric groundwaters prior to compaction (Chowns and Elkins, 1974). Microquartz precipitated as the evaporite was dissolved on a "volume for volume" basis, and megaquartz grew into the voids.

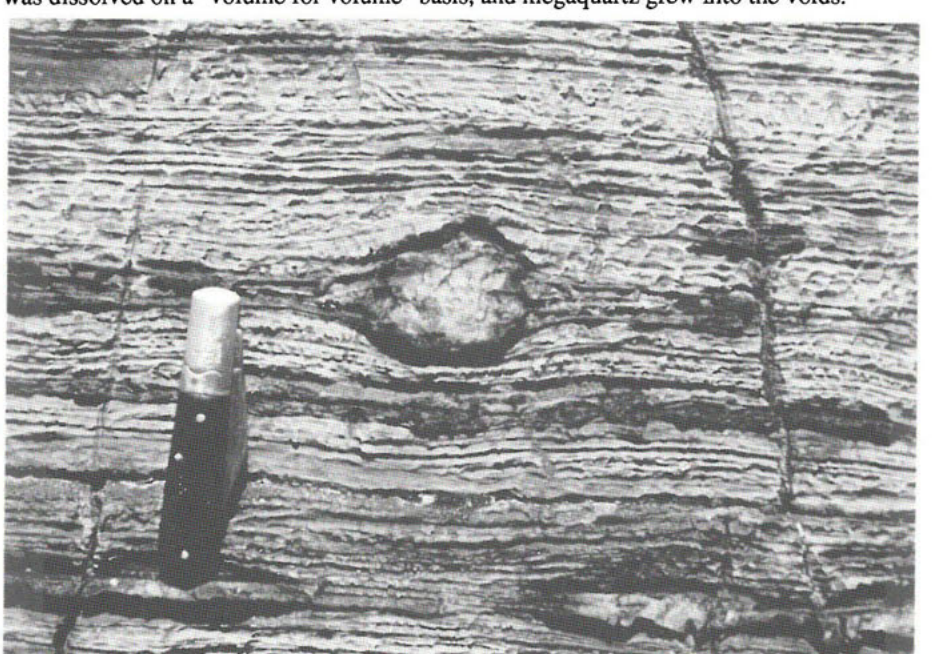


Figure 8. Nodular chert in Precambrian Bass Limestone, Mineral Canyon, Grand Canyon, Arizona. Laminated beds are compacted around the chert nodule, indicating early diagenetic silicification prior to compaction. Laminae are probably stromatolitic. Pocket knife length is 8 cm.

EBSCOhost - printed on 2/13/2023 4:48 AM via . All use subject to https://www.ebsco.com/terms-of-use

Taking the literature at its face value, any number of diagenetic pathways can be drawn in Figure 4 for silicification of epicontinental carbonates. For example, path A would be consistent with the arguments of Gao and Land (1991), path "C" with the mixing zone model of Knauth (1979) and the evaporitic interpretation of Chowns and Elkins (1974), and anything in between for the force of crystallization ideas of Maliva and Siever (1988b). However, a critical assessment of these pathways is warranted in order to direct future mineralogical investigations. Moreover, paleoenvironmental reconstruction requires a geochemical and paleontological understanding of ancient cherts to determine their temporal relationship with the host carbonate. For example, stable isotope variations in selected microquartz have been interpreted as products of early diagenesis, and they have been used to infer past climatic temperatures (e.g., Knauth and Epstein, 1976). Likewise, microfossils in Precambrian silicified stromatolites provide important information about the early history of life. The time at which isotopes and microfossils became "locked" in microquartz is critical to these studies.

Rationale for early diagenesis

The following observations and arguments support the interpretation that most microquartz in epicontinental carbonates is early diagenetic and follows pathways along the right side of Figure 4 rather than the maturation sequence so frequently invoked for diatomaceous oozes and deep sea sediments:

1. Pre-compaction of chert within meters (or, at most, tens of meters) of burial appears to have been common. The incorporation of already-formed chert nodules and chert fragments into overlying units and paleokarst breccias precludes any 25 to 50 my time lag as proposed for deep sea cherts.

2. The host carbonate is originally precipitated biologically as aragonite, high-magnesium calcite, and calcite. During early diagenesis, the metastable phases dissolve and reprecipitate as low-magnesium calcite and/or dolomite during the carbonate "stabilization" process. Shallow water carbonate environments are riddled with islands made up of storm and tide-deposited metastable carbonate that originally precipitated offshore. Stabilization is particularly rapid in the fresh water lenses under these islands and in any offshore areas receiving groundwaters from them. The islands grow and shrink depending upon the vagaries of storm tracks and carbonate productivity patterns. Over long times, huge volumes of metastable sediments are eventually subjected to meteoric groundwaters as coastlines prograde and islands form and reform over broad geographic areas.

Throughout the Paleozoic and Mesozoic, silica sponges were common in shallow-water carbonates. Opal-A spicules should therefore have been abundant in unstabilized carbonate debris, and they were subject to diagenetic mobilization during carbonate stabilization. Stabilization is a dissolution/reprecipitation event, so that this stabilization process would have provided a favorable environment for silica to replace carbonate. Moreover, this idea is consistent with isotope data and the numerous arguments for "early" chert formation.

3. There is no compelling evidence that opal-CT was a necessary, or even common, precursor to microquartz in epicontinental replacement cherts. Quartz can clearly precipitate directly from aqueous solution at low temperatures, as proven in lab experiments by Mackenzie and Gees (1971) and as inferred from the common occurrence of drusy quartz in sedimentary rocks. The quartz spheroids figured by Maliva and Siever (1988a) and taken to indicate opal-CT precursors for cherts appear to occur in former voids.

EBSCOhost - printed on 2/13/2023 4:48 AM via . All use subject to https://www.ebsco.com/terms-of-use

Megaquartz and fibrous quartz are also found in voids, but this does not imply that these species are a precursor for microquartz that replaces carbonate.

Gao and Land (1991) do not give the petrographic context or frequency of occurrence for the textures that they claim are opal-CT. It remains to be confirmed that microquartz will reveal an array of former opal-CT lepispheres if powerfully etched. Acid etching is not necessary to see former lepispheres in microquartz that formed in former siliceous oozes (e.g., Jones and Knauth, 1979); they are readily visible in thin-section as ghost structures in former cavities. It should also be noted that cavity infilling of fossil molds by fibrous silica botryoids is ubiquitous in nodular cherts. The botryoids come in all sizes, and the smaller varieties might be mistaken for "lepispheres" in casual SEM views. Additionally, as will be discussed below, features relating to paleokarst and subaerial exposure surfaces are surprisingly common in ancient platform carbonates, and these features have generally been overlooked. Cavity-fill fibrous silica is common in this material, and could easily be mistaken for "precursor" lepispheres and mistakenly attributed to the type of maturation sequence observed in deep sea sediments.

In addition, Schubel and Simonson (1990) have figured spherical aggregates of quartz platelets that strongly resemble the putative ghost-lepispheres described above. Schubel and Simonson show clearly that these represent replacement of the mineral magadiite [$NaSi_7O_{13}(OH)_3 \cdot 3H_2O$]. Spherical aggregates of quartz apparently originate in a variety of ways; their presence does not immediately indicate the former presence of opal-CT lepispheres.

4. Maliva and Siever (1988b) have proposed that the force of crystallization mechanism is the dominant mechanism of silicification and that pore water chemistry and pH are not controlling factors. The argument is based mainly upon their claim that solution features in carbonate are not visible in thin-section. However, solution/precipitation occurs pervasively when carbonate grains are stabilized during early diagenesis, and this surely occurred in the carbonates hosting their samples as well. Stabilization, compaction, and neomorphism in the host carbonate around chert nodules have probably obliterated the kinds of vugs, etch pits, and any other solution features for which they searched. Replacement has always been considered to be a process that works incrementally and at the microscopic scale. Force of crystallization may well be an operative process, but the geochemical effects of diagenetic fluids may also play an important role.

5. Stable isotope data show clearly that the microquartz sampled today from epicontinental carbonates has precipitated from waters that were either purely meteoric or had a meteoric water component (e.g., Knauth and Epstein, 1976; Kolodny et al., 1980). Gao and Land (1991) have argued that meteoric water interacts with cherts during deep burial and modifies their isotopic composition. However, the idea of late reequilibration of cherts in stabilized, compacted, limestones and dolostones is not supported by hydrogen isotope data (Knauth and Epstein, 1976), the overall trends of $\delta^{18}O$ variations for cherts over geologic time (Knauth, 1992), or evidence that groundwater moves preferentially along bedding planes and fractures in indurated rocks instead of diffusing through the hard matrix.

Matrix flow of groundwater is most active prior to compaction and during stabilization of metastable carbonate phases. Movement diminishes with progressive burial, and the water/rock ratio decreases. Thus, the indurated zones tend to become progressively rock-buffered with respect to oxygen isotopes. It is reasonable that megaquartz may fill vugs at any time in the rock's burial history, but the complete reequilibration of microquartz long after deposition seems unlikely. The simplest explanation of large isotopic variation in

EBSCOhost - printed on 2/13/2023 4:48 AM via . All use subject to https://www.ebsco.com/terms-of-use

unmetamorphosed nodular cherts is that variable amounts of meteoric waters were involved in the original silicification event and that nodular chert formation is particularly vigorous in or near coastal carbonate environments.

A generalized scenario for nodular chert formation

Based on the arguments above, a possible scenario for the formation of microquartz in many nodular cherts in limestone is shown in Figure 9. In this model, metastable carbonate grains and opaline sponge spicules are washed up on islands by tides and storms. Meteoric waters infiltrating the land surface percolate toward the sea preferentially along zones of greatest permeability. The carbonate becomes stabilized via numerous solution/reprecipitation episodes, and opal-A is dissolved and transported seaward. The dissolved silica concentration rises progressively and quartz precipitation can occur when the concentration rises above 4 ppm. Cementation can occur in voids; replacement can occur wherever carbonate dissolves simultaneously. Carbonate dissolution may result during stabilization, mixing zone undersaturation, pH decreases at oxic/anoxic groundwater interfaces, force of crystallization at quartz/carbonate interfaces, or from processes yet to be identified. Nodules can be expected to form along zones of greatest groundwater flux where transport of silica is most active. In areas where the dissolved silica concentration rises to levels above opal-CT or opal-A saturation (probably uncommon in this setting), these phases may precipitate as well as quartz.

MAGADI CHERTS

Not all cherts can be related to diagenetic pathways on Figure 4. Eugster (1969) has described Pleistocene cherts associated with alkaline lakes in the rift valley of east Africa in which the initial precipitates are hydrous Na-silicates (such as magadiiite) that were deposited in varve-like layers. Following removal of Na by meteoric waters, the residual silica crystallizes as quartz chert.

O'Neil and Hay (1973) found that $\delta^{18}O$ of cherts from Lake Magadi ranged from $+31‰$ to $+44.1‰$. This is possibly the most ^{18}O-rich terrestrial material ever measured, and the isotopic data are hard to reconcile with Eugster's proposed mechanism, since low ^{18}O meteoric waters would have to have leached out Na without affecting the ^{18}O-rich Si-O bonds. Schubel and Simonson (1990) appear to have solved the problem by showing that the conversion to quartz chert takes place in stages with volume-for-volume replacement of magadiite by quartz and considerable addition of void-filling fibrous quartz. The high $\delta^{18}O$ indicates that the diagenetic fluids were ^{18}O-rich evaporite fluids, consistent with the evaporite environment of Lake Magadi. Rectilinear arrays of submicroscopic quartz crystals described by Schubel and Simonson (1990) produce a distinctive petrographic texture which may be an indicator of replaced magadiite in ancient cherts.

Sheppard and Gude (1986) provide a useful review of possible ancient examples of magadi-type cherts. Many of their examples include abundant evidence of quartz crystal growth into vugs and crystal molds of former evaporite minerals. Eugster (1969) suggested that magadi-type cherts are possible analogs of chert in Precambrian iron formations. This idea has faded, but identification of these unusual chert types in the ancient record provides an important indication of alkaline, lacustrine environments.

EBSCOhost - printed on 2/13/2023 4:48 AM via . All use subject to https://www.ebsco.com/terms-of-use

EBSCOhost - printed on 2/13/2023 4:48 AM via . All use subject to https://www.ebsco.com/terms-of-use

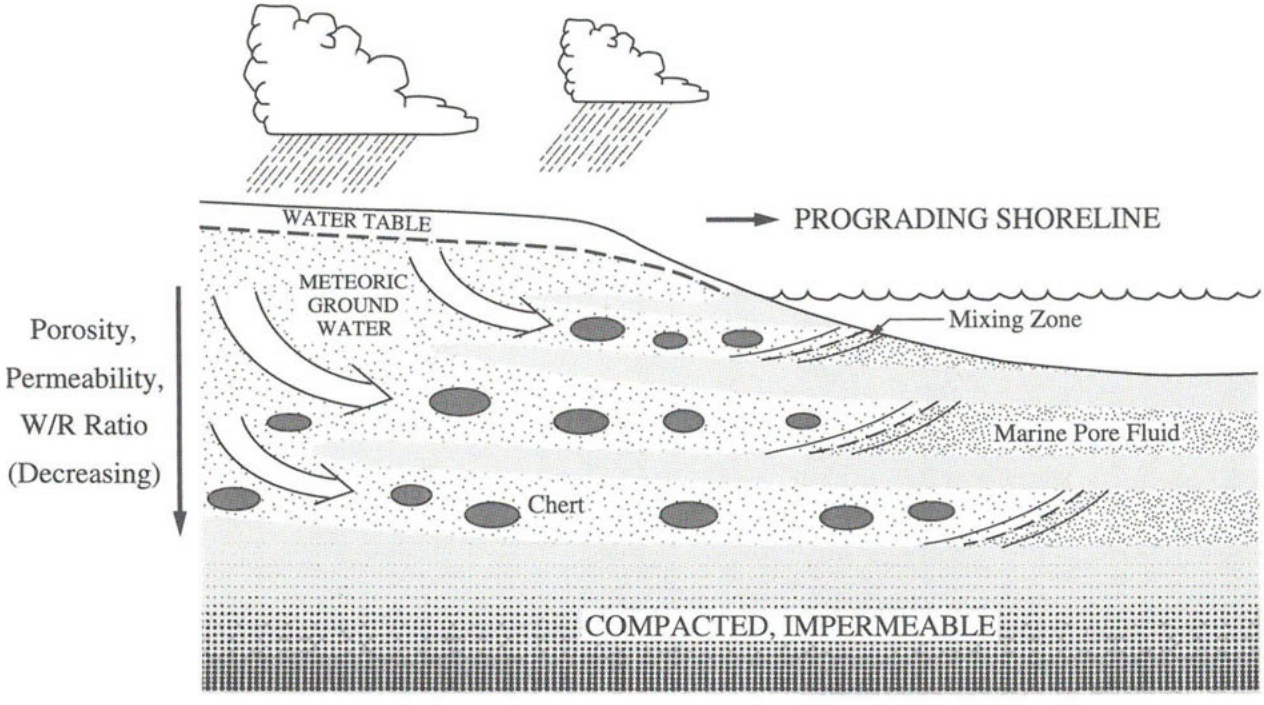


Figure 9. Possible diagenetic setting of nodular chert formation. Meteoric water moves through coastal carbonate sediments and becomes progressively richer in dissolved silica by dissolution of sponge spicule opal-A. Chert replaces biogenic calcite and aragonite shell debris that dissolve during stabilization or in response to mixing zone undersaturation, pH decreases at oxic/anoxic ground water interfaces, and/or force of crystallization at quartz/carbonate interfaces. Replacement occurs preferentially in zones of greatest permeability and highest ground water flux.

PRECAMBRIAN CHERTS

With the exception of the Magadi-type cherts, the silica source for all the cherts described above was probably originally diatom, radiolarian, or sponge opal-A. These organisms were not present in the Precambrian, so Precambrian cherts need to be considered separately. Chert is abundant in Precambrian sedimentary rocks and is found in stromatolitic carbonates, iron formations, Archean greenstone belts, beds in argillites, stratiform jasper beds in silicic volcanic sequences, and a variety of other occurrences. The cherts are now all microquartz, fibrous silica, or megaquartz. Many have been metamorphosed to mosaics of megaquartz. Little is known about the silica sources or the nature of possible precursor phases for most of these examples.

Although modern examples are unknown, it is possible that species of opal-producing bacteria were present in the Precambrian. Bacteria currently occupy nearly all sedimentary environments. In the absence of Precambrian megascopic grazers, there is little to limit their explosive occupation of all ecological niches. Bacteria are so small that they are rarely preserved or observed in ancient rocks. Furthermore, extremely strict criteria have been established for demonstrating biogenicity of putative Precambrian fossils (e.g., Schopf and Walter, 1983). While such criteria prevent paleontological blunders, they should not have the unintended effect of downplaying the potentially enormous role that microbes may have played in Precambrian sedimentation and diagenesis. Bacterial precipitation of silica gel (opal-A) may have been widespread in the Precambrian.

Stromatolitic cherts

Most Precambrian carbonates are laminated deposits probably precipitated by cyanobacteria or, in some cases, as inorganic "whitings." Oolitic horizons are common in many Proterozoic units. Chert is found as replacement nodules (Fig. 8) similar to Phanerozoic examples, but it is more common as small, irregular blebs and stringers along laminations.

The nodular cherts are similar to their Phanerozoic counterparts and are probably early diagenetic replacements. Erikkson (1983) has described one example compatible with the scenario shown in Figure 9. Bacterial silica, volcanic ash, fine-grained terrigeneous debris, and sea water are possible silica sources. If bacterial precipitation of silica was not widespread, the silica content of sea water may have risen to the level of quartz saturation. Based on the absence of definitive evidence of silica-secreting organisms, Maliva et al. (1990) suggested that silica was introduced into peritidal carbonates principally via abiologic precipitation. An interesting question is whether quartz precipitation could have kept dissolved silica at its equilibrium value of 4 ppm. If not, higher values may have been achieved and opal-CT or opal-A may have precipitated.

Microfossils are sometimes preserved in the pure silica stromatolites. It is possible that organic microbial mats were directly permineralized with colloidal silica that later devitrified to quartz (Oehler, 1976). Petrographic textures for cherts hosting microfossils have not been extensively described. Numerous, (even close-packed) spherulitic arrays of fibrous silica are sometimes observed and could represent a devitrification texture (by analogy with devitrification of industrial glasses and obsidian). It is not known whether this texture occurs more commonly in microfossil-bearing cherts.

EBSCOhost - printed on 2/13/2023 4:48 AM via . All use subject to https://www.ebsco.com/terms-of-use

Iron formation chert

Cherts are found interbedded with siderite and/or iron oxides throughout much of Precambrian time. The iron-oxide/chert banded iron formations are a famous example and seem to have reached peak abundance prior to 2 Ga. Fe^{+2} was apparently as common in the early Precambrian seas as Ca^{+2} is today, either because atmospheric oxygen was less abundant, or the oceans were stratified with respect to dissolved oxygen (with anoxic deep water). The flux of dissolved silica through the oceans must have been high to account for the large amount of authigenic quartz. Depending upon how "iron formations" are defined, they ceased to form in any abundance in the upper Proterozoic.

Where unmetamorphosed, iron formation cherts are composed of microquartz with varying amounts of fibrous quartz and megaquartz. Synsedimentary chert breccias and chert arenites are common, indicating lithification near the sediment/water interface (pre-compaction, within reach of synsedimentary erosion). Diagenetic pathways probably lay toward the right side of Figure 4. Dimroth and Chauvel (1973) described what amounts to path C (where opal-A = "silica gel") for the Sokoman Iron Formation. Simonson's (1987) detailed petrographic studies of iron formation arenites show that megaquartz and fibrous quartz were commonly direct, early, and voluminous precipitates (7 vol %) between and within clastic grains. In order to explain the direct precipitation of so much quartz, Simonson (1987) suggested that hydrothermal fluids had invaded these shelf deposits during early diagenesis. However, in view of the demonstration by Mackenzie and Gees (1971) that quartz can precipitate directly from sea water at room temperature, there is probably no need to invoke an influx of hydrothermal fluids from unknown regions.

Archean cherts

The world's oldest sedimentary rocks are cherts. They contain the paleontological record of the earliest life and a possible geochemical record of early climatic conditions. There is, however, considerable controversy over how these ancient cherts formed and whether or not hydrothermal alteration and metamorphism have obliterated the mineralogical and geochemical record of early diagenesis.

The least metamorphosed Archean cherts occur in the 3.5 Ga Onverwacht Group in South Africa and formed largely by replacement of pre-existing volcaniclastic sediments. The degree of silicification in this deposit is extraordinary: A 10-km thick section of sedimentary and volcanic rocks has been replaced by chert! Much of the silicification is clearly hydrothermal and is associated with syn-depositional volcanic activity. There is clear evidence that carbonates and evaporites were also deposited and replaced by chert, and certain thin, white beds may even have been deposited directly from sea water (Lowe and Knauth, 1977).

The cherts are now all composed of microquartz, megaquartz, and minor amounts of fibrous silica. Metamorphic recrystallization has generally coarsened the crystal size of the microquartz, although samples can be found that are virtually indistinguishable in thin section from Phanerozoic examples. Fibrous quartz has generally been converted to radiating arrays of megaquartz. Synsedimentary breccias and petrographic characteristics indicate that lithification was early for most types of Onverwacht cherts, occurring in many cases before the overlying layers were deposited (e.g., Lowe and Knauth, 1977). Aggressive silicification clearly accompanied early diagenesis. Biologic sources of silica may have been locally important, but volcanic glasses (including shards, lappilli, and other pyroclastic debris) are an alternative source.

EBSCOhost - printed on 2/13/2023 4:48 AM via . All use subject to https://www.ebsco.com/terms-of-use

Lowe and Knauth (1977) and Knauth and Lowe (1978) argued that a spectrum of chert types and diagenetic styles exist for the Onverwacht. Megaquartz associated with volcanic rocks and cross-cutting veins is most easily interpreted in terms of hydrothermal silicification. Microquartz cherts, particularly in the upper, sediment-rich part of the section, are more readily interpreted as early diagenetic silicification of carbonates and evaporites. The correlation of $\delta^{18}O$ with these chert types is excellent, with the most ^{18}O-rich material occurring in beds interpreted as early diagenetic based on field and petrographic arguments. The lowest $\delta^{18}O$ values occur for the megaquartz associated with volcanic rocks.

Paris et al. (1985) argued that the synsedimentary breccias were not syn-depositional, but rather were hydrothermal breccias and sheared zones. They argued that all Onverwacht cherts originated during late hydrothermal alteration of the entire sediment pile. Hot waters supposedly rose through the pile and silicified the entire mass, a process they also proposed for the diagenesis of Tertiary deep sea siliceous oozes. Hanor and Duchac (1990) studied the hydrothermal silicification of komatiite lavas and questioned whether all Onverwacht cherts might be hydrothermal in origin. Hydrothermal silicification clearly occurred in many horizons of Onverwacht strata, and this has been noted by all who have investigated these horizons. However, claims or inferences that the complete spectrum of cherts in the 10-km thick Onverwacht section originated in this way are unduly simplified.

What accounts for the extraordinary amount of silicification of the Onverwacht and other Archean examples? One possibility is that the early earth was substantially warmer in the Archean, so that ocean environments were conducive to silicification. Archean cherts are depleted in ^{18}O by over $10‰$ relative to their Phanerozoic counterparts (see review by Knauth, 1992). It now seems likely that $\delta^{18}O$ of the oceans is held within several parts-per-thousand of the present value by the interaction of sea water with hot basalts at spreading centers, so the popular idea that an ^{18}O-depleted ocean was responsible for the Archean chert δ-values is now less viable. Some dismiss the chert isotope data because of concerns over possible metamorphic alteration and late diagenetic overprinting. However, if this is the case, prodigious amounts of low-^{18}O waters would have been required to penetrate some of the most impermeable rocks in nature. [Solely heating a chert does not change $\delta^{18}O$!]

A 10-km thick section of impermeable chert is probably rock-dominated with respect to the oxygen reservoir, except along fractures and bedding planes. $\delta^{18}O$ was probably fixed during early diagenesis at temperatures in excess of 50°C. While surprisingly warm, there is nothing to preclude earth surface temperatures of this magnitude in the Archean. Archean microfossils are similar to cyanobacteria that live at this temperature today, and greenhouse heating in response to higher CO_2 levels can easily account for the warm conditions. The entire earth's surface in the Archean may have been an open hydrothermal system characterized by intense silicification and quartz precipitation. Under such conditions, all diagenetic pathways in Figure 4 would correspond to burial depths of only a few meters.

MICROQUARTZ IN PALEOKARST CHERT BRECCIAS

When chert-bearing carbonates are exposed to meteoric water (either through uplift or lowering of sea-level), chert/terra rosa breccias can develop as insoluble weathering residues (Fig. 10). In extreme cases, the finer, terra rosa particles can be washed out completely. Individual chert clasts are flushed free of carbonate impurities. The voids between and within clasts can fill with fibrous silica and drusy quartz. Isotopic data for

EBSCOhost - printed on 2/13/2023 4:48 AM via . All use subject to https://www.ebsco.com/terms-of-use

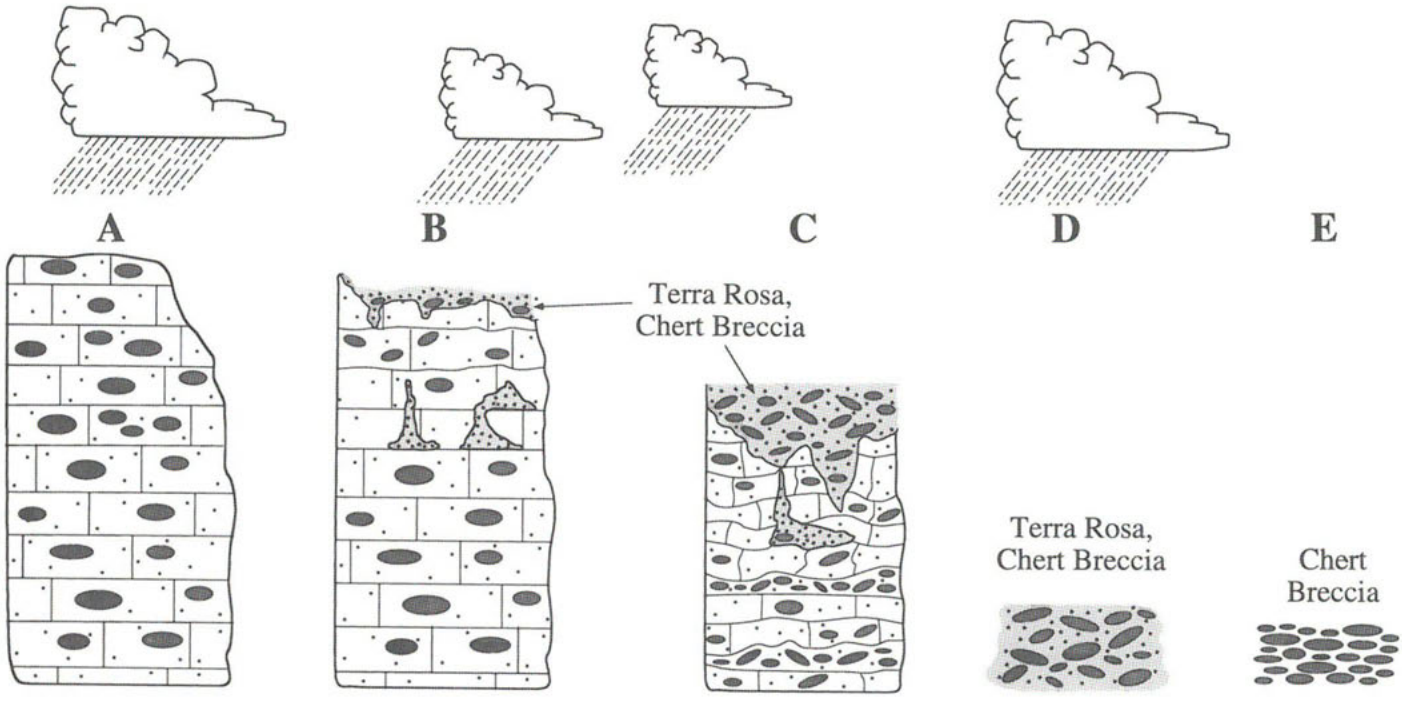


Figure 10. Stages in the development of karst chert breccias. Examples of all stages are represented in the geologic record and have been commonly overlooked. Some "bedded cherts" have been created in this fashion. (A) Flat-lying cherty limestone subjected to subaerial exposure by eustatic sea-level drop or tectonic uplift. (B) Down-flowing meteoric waters dissolve limestone along joints and bedding planes. Terra rosa (red soil) and chert breccias develop as insoluble residues at the exposed surface, in caverns, and along bedding planes. (C) Chert breccia in terra rosa matrix develops extensively in karst pits. Dissolution along subsurface bedding planes with greatest permeability removes limestone and concentrates insoluble cherts. (D) Extreme dissolution leaves rubble of chert and terra rosa. (E) Complete dissolution of carbonate turns terra rosa into pure chert rubble, which can be recemented with quartz to produce a bedded chert. Renewed deposition from eolian, fluvial, or marine sources can arrest the karst process and preserve the unit at any stage shown.

EBSCOhost - printed on 2/13/2023 4:48 AM via . All use subject to https://www.ebsco.com/terms-of-use

these secondary phases can be used to document their subaerial origin and to deduce continental paleotemperatures (Kenny and Knauth, 1992). In cases where cementation is particularly thorough, a massive, smooth chert bed that superficially resembles a primary bedded chert can be produced. A spectacular example of this is the Grand Falls chert described by Robertson (1967).

Chert "beds" and breccias of this sort have generally gone unrecognized. Wright (1994) has pointed out how common and generally unappreciated subaerial exposure is within carbonate sequences of all kinds. Even stratigraphic horizons many meters below the exposure surface can undergo dissolution. Chert nodules and finely-disseminated chert can concentrate along these subsurface horizons without production of a paleosol (Fig. 10C). Former supratidal carbonate horizons rich in sulfate and other evaporite phases are particularly susceptible to such dissolution. Zones that have undergone dissolution are readily recognized by the slumping and disorientation of the chert nodules that originally had long axes parallel to bedding.

In thin section, cherts from these horizons contain numerous vugs that become filled with fibrous silica and megaquartz during the karst event. Apparently, finely disseminated chert is dissolved and reprecipited by the through-going groundwaters via Ostwald ripening. Botryoidal cavity-fill of vugs vacated by carbonate is ubiquitous and many of these botryoidal forms can easily be mistaken for relict opal-CT lepispheres that matured into quartz. These karst-related structures are so common that any investigation of silica phases in shallow water carbonates should involve an evaluation of whether or not a paleokarst lies above the horizon of interest. Multiple silica phases in a single thin-section of karst breccia cherts can represent drastically different geologic settings and events separated in time by millions of years or even hundreds of millions of years!

SUMMARY

Biogenic precipitation of opal-A by diatoms has dominated silica input into sediments for the past 50 million years. Diatom frustules resist dissolution at the low ground temperatures of the modern world and transform slowly into opal-CT and then into microquartz. Radiolarian oozes in deep sea sediments also resist dissolution and follow a similar sequence of silica transformations to produce the bedded cherts typically found in deformed mountain belts along continental margins.

Prior to the explosive evolution of diatoms, silica sponges were common in shallow water carbonate environments. During stabilization and early diagenesis of the carbonate sediments, silica was mobilized and precipitated as microquartz in the form of concretionary-like nodules, seams, stringers, and disseminated blebs. Microquartz appears to have replaced the carbonate at extremely shallow burial depths, prior to compaction and often within reach of syn-sedimentary erosion. Similar replacement of stromatolitic carbonate occurred throughout the Precambrian, but the silica source for these cherts remains problematic.

Silica precipitated on a large scale in Archean and early Proterozoic sedimentary environments, and was often associated with massive precipitation of iron oxides and siderite. The nature of the original silica precipitate is unknown, but any transformation from precursor phases into quartz probably occurred at extremely shallow burial depths.

Diagenetic pathways for silica precipitation and transformation of opaline phases to quartz are summarized in Figure 4. No single trajectory through this diagram can be

EBSCOhost - printed on 2/13/2023 4:48 AM via . All use subject to https://www.ebsco.com/terms-of-use

considered typical for all authigenic silica; the diagenetic pathway is specific to the depositional system in question. Temperature is an important, but not exclusive, factor that governs the character and speed of silica diagenesis. Dissolution kinetics and the degree to which ground waters and pore fluids can physically transport dissolved silica are probably equally important factors. Microquartz precipitation is probably earliest in systems that have active hydrologic flow prior to compaction.

Chert types and the manner in which they formed have evolved over geologic time in response to the amount and type of silica deposited into sediments and possibly in response to major climatic temperature changes. Most of our understanding of silica transformations has been based on a limited number of phases defined and identified largely on the basis of petrography. Detailed mineralogical studies are likely to define new silica types which will have to be interpreted and considered in terms of the many depositional settings and different diagenetic pathways that produce authigenic microcrystalline quartz.

REFERENCES

Behl RJ (1992) Chertification in the Monterey Formation of California and deep-sea sediments of the west Pacific. PhD dissertation: Univ of California, Santa Cruz, 287 p

Biggs DL (1957) Petrography and origin of Illinois nodular cherts. Illinois State Geol Surv Cir 245, 25 p

Bramlette MN (1946) The Monterey Formation of California and the origin of its siliceous rocks. US Geol Surv Prof Paper 212, 57 p

Carozzi AV (1993) Sedimentary Petrography. Prentice Hall, New Jersey

Chowns TM, Elkins JE (1974) The origin of quartz geodes and cauliflower cherts through silicification of anhydrite nodules. J. Sediment Petrol 44:885-903

Clayton CJ (1986) The chemical environment of flint formation in Upper Cretaceous chalks. In: Sieveking GdG, Hart, MB (eds) The Scientific Study of Flint and Chert. Cambridge Univ Press, NY 45-54

Correns CW (1969) Introduction to mineralogy. Springer-Verlag, New York

Dimroth E, Chauvel JJ (1973) Petrography of the Sokoman Iron Formation in part of the central Labrador trough, Quebec, Canada. Geol Soc Am Bull 84:111-134

Eriksson KA (1983) A paleohydrologic model for early Proterozoic dolomitization and silicification. Precambrian Res 21:299-321

Eugster HP (1969) Inorganic bedded cherts from the Magadi area, Kenya. Contrib Min Petrol 22:1-31

Flörke, OW, Jones JB, Schmincke H-U (1976) A new microcrystalline silica from Gran Canaria. Zeits Krist 143:156-165

Folk RL (1950) Petrology of authigenic silica in the Beekmantown group of central Pennsylvania. M.S. thesis, Penn State College, State College, PA, 114 p

Folk RL, McBride EF (1976) The Caballos Novaculite revisited Part I: Origin of novaculite members. J Sediment Petrol 46:659-669

Folk RL, McBride EF (1978) Radiolarites and their relation to subjacent "oceanic crust" in Liguria, Italy. J Sediment Petrol 48:1069-1102

Folk RL, Pittman JS (1971) Length-slow chalcedony: a new testament for vanished evaporites. J Sediment Petrol 41:1045-1058.

Folk RL, Weaver E (1952) A study of the texture and composition of chert. Am J Sci 250:498-510

Frondel C (1982) Structural hydroxyl in chalcedony (Type B quartz). Am Min 67:1248-1257

Gao G, Land LS (1991) Nodular chert from the Arbuckle Group, Slick Hills, SW Oklahoma: a combined field, petrographic and isotopic study. Sedimentology 38:857-870

Graetsch H, Flörke OW, Miehe G (1985) The nature of water in chalcedony and opal-C from Brazilian agate geodes. Phys Chem Min 12:300-306

Grunau HR (1965) Radiolarian cherts and associated rocks in space and time. Eclogae Geol Helv 58:157-208

Hanor JS, Duchac KC (1990) Isovolumetric silicification of early Archean komatities: geochemical mass balances and constraints on origin. J Geol 98:863-877

Heaney PJ, Post JE (1992) The widespread distribution of a novel silica polymorph in microcrystalline quartz varieties. Science 255:441-443

EBSCOhost - printed on 2/13/2023 4:48 AM via . All use subject to https://www.ebsco.com/terms-of-use

Heaney PJ (1993) A proposed mechanism for the growth of chalcedony. Contrib Min Petrol 115:66-74
Hein JR, Scholl DW, Barron JA, Jones MG, Miller, J (1978) Diagenesis of Late Cenozoic diatomaceous deposits and formation of the bottom simulating reflector in the southern Bering Sea. Sedimentology 25:155-181
Hesse R (1990) Origin of chert and silica diagenesis. In: McIlreath IA, Morrow DW (ed) Diagenesis. Geol Assoc Canada, Geoscience Canada, Reprint Ser 4:227-275
Hovorka SD (1981) Stratigraphy and petrography of the upper chert and shale member, Caballos Formation, Brewster County, West Texas. MS thesis, Univ of Texas, Austin, TX, 273 p
Iler R (1979) The Chemistry of Silica. Wiley, New York
Isaacs CM (1982) Influence of rock compositions on kinetics of silica phase changes in the Monterey Formation, Santa Barbara area, California. Geology 10:304-308
Jenkyns HC, Winterer EL (1982) Paleoceanography of Mesozoic ribbon radiolarites. Earth Planet Sci Lett 60:351-375
Jones DL, Knauth LP (1979) Oxygen isotopic and petrographic evidence relevant to the origin of the Arkansas Novaculite. J Sediment Petrol 49:581-597
Jones JB, Segnit ER (1971) The nature of opal: I. Nomenclature and constituent phases. J Geol Soc Australia 18:57-68
Kastner M (1979) Length-slow chalcedony: The end of the new testament. (abstr) Trans Am Geophys Union EOS 61:399
Kastner M (1981) Authigenic silicates in deep-sea sediments: formation and diagenesis. In: Emiliani C (ed) The Sea 7:915-980, Wiley, New York
Keene JB (1976) The distribution, mineralogy, and petrography of biogenic and authigenic silica from the Pacific Basin. PhD dissertation, Scripps Inst of Oceanography, 264 p
Keller WD, Viele GW, Johnson CH (1977) Texture of Arkansas Novaculite indicates thermally induced metamorphism. J Sediment Petrol 47:834-843.
Kenny R, Knauth LP (1992) Continental paleoclimates from δD and $\delta 18O$ of secondary silica in paleokarst chert lags. Geology 20:219-222
Kingma KJ, Hemley RJ (1994) Raman spectroscopic study of microcrystalline silica. Am Min 79:269-273
Knauth LP (1973) Oxygen and hydrogen isotope ratios in cherts and related rocks. PhD dissertation, California Inst Tech, Pasadena, CA, 369 p
Knauth LP (1979) Origin of chert in limestone. Geology 7:274-277
Knauth LP (1992) Origin and diagenesis of cherts: An isotopic perspective. In: Clauer N, Chaudhuri S (eds) Isotopic Signatures and Sedimentary Records. Springer-Verlag, Berlin, p 123-152
Knauth LP, Epstein S (1975) Hydrogen and oxygen isotope ratios in silica from the JOIDES deep sea drilling project. Earth Planet Sci Lett 25:1-10
Knauth LP, Epstein S (1976) Hydrogen and oxygen isotope ratios in nodular and bedded cherts. Geochim Cosmochim Acta 40:1095-1108.
Knauth LP, Epstein S (1982) The nature of water in hydrous silica. Am Min 67:510-520
Knauth LP, Lowe DR (1978) Oxygen isotope geochemistry of cherts from the Onverwacht Group (3.4 billion years), Transvaal, South Africa, with implications for secular variations in the isotopic composition of cherts. J Geol 41:209-222
Kolodny Y, Epstein S (1976) Stable isotope geochemistry of deep sea cherts. Geochim Cosmochim Acta 40:1195-1209
Kolodny Y, Taraboulos A, Frieslander U (1980) Participation of fresh water in chert diagenesis: evidence from oxygen isotopes and boron α-track mapping. Sedimentology 27:305-316
Lancelot Y (1973) Chert and silica diagenesis in sediments from the Central Pacific. In: Initial Repts Deep Sea Drill Proj 17:377-506, US Govt Printing Office, Washington, DC
Lewin JC (1961) The dissolution of silica from diatom walls. Geochim Cosmochim Acta 21:182-198
Lisitzin AP (1972) Sedimentation in the World Oceans. Soc Econ Paleontol Min Spec Pub 17:218 p
Lowe D, Knauth LP (1977) Sedimentology of the Onverwacht Group (3.4 billion years), Transvaal, South Africa, and its bearing on the characteristics and evolution of the early earth. J Geol 85:699-723
Mackenzie FT, Gees R (1971) Quartz: synthesis at earth-surface conditions. Science 173:533-535
Maliva RG, Siever R (1988a) Pre-Cenozoic nodular cherts: evidence for opal-CT precursors and direct quartz replacement. Am J Sci 288:798-809
Maliva RG, Siever R (1988b) Diagenetic replacement controlled by force of crystallization. Geology 16:688-691

EBSCOhost - printed on 2/13/2023 4:48 AM via . All use subject to https://www.ebsco.com/terms-of-use

Maliva RG, Knoll AH, Siever R (1990) Secular change in chert distribution: A reflection of evolving biological participation in the silica cycle. Palaios 4:519-532

Matheney RK, Knauth LP (1993) New isotopic temperature estimates for early silica diagenesis in bedded cherts. Geology 21:519-522

Meyers WJ (1977) Chertification in the Mississippian Lake Valley Formation, Sacramento Mountains, New Mexico. Sedimentology 24:75-105

Micheelsen H (1966) The structure of dark flint from Stevns, Denmark. Medd Dansk Geol Foren 16:285-368

Murata KJ, Larsen (1975) Diagenesis of of Miocene siliceous shales, Temblor Range, California. US Geol Surv J Res 3:553-566

Murata KJ, Nakata JK (1974) Cristobalitic stage in the diagenesis of diatomaceous shale. Science 184:567-568

Murata KJ, Friedman I, Gleason JD (1977) Oxygen isotope relations between diagenetic silica minerals in Monterey Shale, Temblor Range, California. Am J Sci 277:259-272

Murray RW, Jones DL, Bucholtz ten Brink MR (1992) Diagenetic formation of bedded chert: evidence from chemistry of the chert-shale couplet. Geology 20:271-274

Oehler JH (1976) Experimental studies in Precambrian paleontology: Structural and chemical changes in blue-green algae during simulated fossilization in synthetic chert. Geol Soc Am Bull 87:117-129

Oehler JH, Schopf JW (1971) Artificial microfossils: Experimental studies of permineralization of blue-green algae in silica. Science 174:1229-1231

O'Neil JR, Hay RL (1973) $^{18}O/^{16}O$ ratios in cherts associated with the saline lake deposits of East Africa. Earth Planet Sci Lett 19:257-266

Paris I, Stanistreet G, Hughes MJ (1985) Cherts of the Barberton Greenstone Belt interpreted as products of submarine exhalative activity. J Geol 93:111-129

Pelto CR (1956) A study of chalcedony. Am J Sci 254:32-50

Pisciotto KA (1981) Diagenetic trends in the siliceous facies of the Monterey Shale in the Santa Maria region, California. Sedimentology 28:547-571

Rad U von, Riech, V, Rösch H (1978) Silica diagenesis in continental margin sediments off Northwest Africa. In: Initial Repts Deep Sea Drill Proj 41:879-897, US Govt Printing Office, Washington, DC

Ramberg H (1952) The Origin of Metamorphic and Metasomatic Rocks. Univ Chicago Press, Chicago, IL

Robertson CE (1967) The Elsey Formation and its relationship to the Grand Falls Chert. Missouri Geol. Surv Rept Invest No. 38, 62p

Savin SM (1977) The history of the earth's surface temperature during the past 100 million years. In: Ann Rev Earth Planet Sci 5:319-355

Schubel KA, Simonson BM (1990) Petrography and diagenesis of cherts from Lake Magadi, Kenya. J Sediment Petrol 60:761-776

Schopf JW, Walter MR (1983) Archean microfossils: New evidence of ancient microbes. In: Schopf JW (ed) Earth's Earliest Biosphere. Princeton Univ Press, Princeton, NJ, p 214-239

Sheppard RA, Gude AJ (1986) Magadi-type chert--A distinctive diagenetic variety from lacustrine deposits. In: Mumpton FA (ed) Studies in Diagenesis. US Geol Surv Bull 1578:335-345

Simonson B (1987) Early silica cementation and subsequent diagenesis in arenites from four Early Proterozoic iron formations of North America. J Sediment Petrol 57:494-511

Tarr WA (1917) Origin of the chert in the Burlington Limestone. Am J Sci 44:409-452

Van Tuyl FM (1918) The origin of chert. Am J Sci 45:449-456

Weaver FM, Wise SW (1972) Ultramorphology of deep sea cristobalitic chert. Nature 237:56-57

Williams LA, Parks GA, Crerar DA (1985) Silica diagenesis, I. solubility controls. J Sediment Petrol 55:301-311

Wright PV (1994) Paleosols in shallow marine carbonate sequences. Earth Sci Rev 35:367-395

EBSCOhost - printed on 2/13/2023 4:48 AM via . All use subject to https://www.ebsco.com/terms-of-use

SILICA-WATER INTERACTIONS

P. M. DOVE

School of Earth and Amospheric Sciences
Georgia Institute of Technology
Atlanta, GA 30332 U.S.A.

J. D. RIMSTIDT

Department of Geological Sciences
Virginia Polytechnic Institute & State University
Blacksburg, VA 24061 U.S.A.

INTRODUCTION

In this chapter, we explore the mineral-water geochemistry of the silica polymorphs. At least nine different SiO_2 phases are found in natural and engineered earth systems in the forms of quartz, cristobalite, tridymite, moganite, coesite, stishovite, lechatelierite (silica glass), opal and inorganic amorphous silica (Drees et al., 1989). The interactions of aqueous fluids with the SiO_2 polymorphs are important for several reasons. The first is the abundance of silica, as these phases are found extensively in diverse aqueous environments and also have important economic roles in the materials industry. Table 1 lists several low temperature and hydrothermal silica-rich systems for which an understanding of silica solubilities and rates of dissolution and precipitation may be important. In the lower temperature environments, it is generally agreed that mineral-solution reaction rates are critically dependent upon reaction kinetics, since virtually all mineral-solution reactions are controlled by disequilibrium processes and therefore can only be described through irreversible thermodynamics and kinetics.

A second motivation for understanding silica-water interactions is the unique role of these polymorphs as the end-member oxides to the myriad classes of silicate minerals and glasses. As such, the fundamental control of crystal structure and crystallinity on the reactivity of these relatively simple Si-O bonded phases offer an important baseline to understanding the behavior of more complex aqueous, polymeric, amorphous and crystalline silicate minerals and materials. For example, the behavior of polymeric and amorphous silica compounds may have properties that can be useful in understanding some of the complex aluminosilicate gels, polymers and sols that are now being detected in soil environments (e.g., Casey et al., 1993). Likewise, quartz, which makes up 12% of the minerals in the earth's crust, is the pure oxide representative of the silicates, which comprise 90% of the minerals in the earth's crust and dominate virtually every water-rock system.

We begin by examining the structure, properties and behavior of aqueous silica in the bulk solution. This is followed by a discussion of the solubility of silica in both the silica-water and silica-water-vapor saturated systems. Recent advances in studies of the kinetics of SiO_2 dissolution show the integral role of mineral surface geochemistry in unraveling mineral reactivity. This leads us to describe briefly the current view of the SiO_2 surface in aqueous solutions and to describe some properties and behavior of both the surface and solvent at the silica-water interface. With this information, we examine the state of our knowledge in the kinetics of silica-water reactions with particular emphasis on the effects of ions and compounds that catalyze and inhibit silica reaction rates. We conclude with a brief review of the way in which silica-water interactions influence the behavior of two geological and geophysical systems. Although past work investigated many different silica

EBSCOhost - printed on 2/13/2023 4:48 AM via . All use subject to https://www.ebsco.com/terms-of-use

Table 1. SiO_2-rich natural processes and engineered systems.

An understanding of rate-enhancing and -inhibiting influence of dissolved ions on silica reactivity improves our ability to quantify the past and future evolution of these systems.

Natural Processes
Dissolution of silica in marine sediments
(Hurd, 1972, 1973; Wollast, 1974; DeMaster, 1981; Van Bennekom, 1981; Wollast, 1983; Gehlen et al., 1993)
Polymorphs: biogenic silica, opaline phases, inorganic amorphous silica, detrital quartz
Soil development
(Evans, 1965; Drees et al., 1989; White and Peterson, 1990; White et al., 1992; Swoboda-Colberg and Drever, 1993)
Polymorphs: virtually all, particulary quartz, disordered cristobalite, opal
Pressure solution, ductile creep and compaction
(Mullis, 1993; Sleep, 1994; Sleep and Blanpied, 1992)
Polymorphs: quartz
Engineered Earth Systems
Repository behavior
(Verma and Pruess, 1987)
Polymorphs: virtually all, particularly quartz, volcanic and synthetic glasses
Geothermal HDR (Hot Dry Rock) reservoirs
(Tester et al., 1994)
Polymorphs: virtually all, particularly quartz, and amorphous silica
Oil-field reservoirs
Polymorphs: virtually all, particularly quartz, and amorphous silica

polymorphs, the majority of effort in the earth science literature has centered on quartz. Thus, it receives disproportionate attention in our discussions.

Several recent review articles have examined specific aspects of silica-water interactions in detail and are not repeated here. For example, Parks (1990) presents surface free energy thermodynamic principles and applies them to oxide surfaces. Likewise, theoretical studies of silica water interactions are only briefly discussed as this subject received extensive treatment in Lasaga (1990).

In reading this chapter, you may agree that while progress has been made, much remains to be understood, particularly in the area of geochemical kinetics. Recent studies have built on previous work to significantly advance our understanding of silica reactivity in simple solutions. Yet quantified relationships for all but the most simple mineral-fluid systems are still unknown. We hope this review will bring the readers up to date on the current knowledge in this area and point to continuing gaps where future efforts are needed.

SOLUBILITY

The dissolution reaction

Silica dissolves in water by the reaction

$$SiO_2(s) + 2\ H_2O = H_4SiO_4(aq) \qquad (1)$$

EBSCOhost - printed on 2/13/2023 4:48 AM via . All use subject to https://www.ebsco.com/terms-of-use

$$K = \frac{a_{H_4SiO_4}}{a_{SiO_2} a^2_{H_2O}} \quad (2)$$

It is important to realize that although Equation (1) seems to explain most of the solubility behavior of silica, there are reasons to believe that the ratio of SiO_2:H_2O in the aqueous species may not be exactly 1:2 (Walther and Helgeson, 1977) so that some prefer to generalize Equation (1) to

$$SiO_2(s) + n\ H_2O = SiO_2 \cdot nH_2O(aq) \quad (3)$$

The SiO_2:H_2O ratio is less than 1:2 if hydrogen bonded waters of hydration are counted into the stoichiometry of the aqueous species. On the other hand, the formation of polynuclear species eliminates water molecules and thus increases the SiO_2:H_2O ratio. NMR (Cary et al,, 1982), Raman (Alvarez and Sparks, 1985) and diffusion rate (Applin, 1987) studies of dilute silica solutions all provided evidence for the presence of silica dimers formed by the reaction

$$2\ H_4SiO_4(aq) = H_6Si_2O_7(aq) + H_2O \quad (4)$$

Figure 1, based on K = 330 for Reaction (4) (Applin, 1987), suggests that this dimer contributes little to the solubility of quartz but accounts for about 40% of dissolved silica in equilibrium with amorphous silica. Thus, representing dissolved silica as H_4SiO_4 is a bit of fiction similar to representing dissolved CO_2 as H_2CO_3 even though there is clear evidence that CO_2 solutions contain both $CO_2(aq)$ and $H_2CO_3(aq)$ species. This representation of dissolved silica creates no problems in thermodynamic calculations but is undoubtedly inadequate for understanding the kinetics of silica-water reactions.

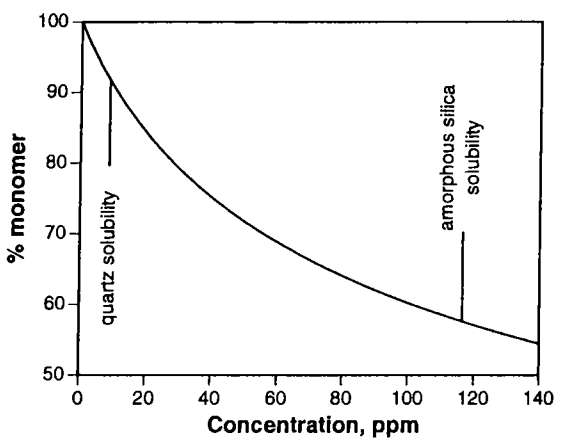


Figure 1. Percent of dissolved silica in the monomer form (H_4SiO_4) as a function of total dissolved silica concentration. The balance of the dissolved silica occurs as dimers ($H_6Si_2O_7$). This diagram is based on the association constant of 330 at 25°C reported by Applin (1987).

Solubility of silica phases

By convention, the activity of a pure crystalline solid is defined as one and the activity of the pure solvent is defined as one. Thus, $a_{SiO_2} = 1$ and $a_{H_2O} = 1$ so that Equation (2) simplifies to

$$K = a_{H_4SiO_4}. \quad (5)$$

The effect on solubility of varying the ΔG_f° of the silica phase is illustrated in Figure 2, which shows quartz, cristobalite, and amorphous silica solubility along the three phase

EBSCOhost - printed on 2/13/2023 4:48 AM via . All use subject to https://www.ebsco.com/terms-of-use

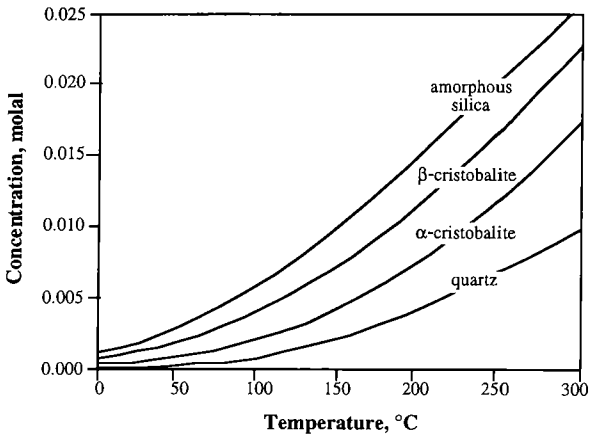


Figure 2. Solubilities of quartz, cristobalite, and amorphous silica along the three-phase curve, $SiO_2(s)$–$H_2O(l)$–$H_2O(v)$ based on equations from Rimstidt and Barnes (1980).

curve $SiO_2(s)$–$H_2O(l)$–$H_2O(v)$. The solubility of silica phases increases from quartz to α-cristobalite to β-cristobalite to amorphous silica because $\Delta G_f°$(quartz) < $\Delta G_f°$(α-cristobalite) < $\Delta G_f°$(β-cristobalite) < $\Delta G_f°$(amorphous silica). This variation in the $\Delta G_f°$ of these silica phases is conventionally reflected by assigning successively higher values of K for their dissolution equilibria. It is instructive, however, to change the convention so that K is always constant and the variation of solubility is expressed by changing a_{SiO_2} (Table 2). This table shows that at 25°C , the activity of cristobalite is twice that of quartz and amorphous silica is ten times that of quartz. Inserting these values into Equation (2) and using the value of K for quartz, the solubility of these other phases can be calculated from

$$a_{H_4SiO_4} = a_{SiO_2} K_{qz} \tag{6}$$

The activities of silica phases relative to quartz at temperatures up to 1200°C are shown in Figure 3. The solubility of these phases can be found by multiplying quartz solubility by a_{SiO_2} for these polymorphs. On this diagram, the phase with the lowest activity is the most stable, and therefore, the least soluble. Note that although this convention is a convenient way to show the relative solubilities of silica phases, it creates certain computational difficulties, and therefore it is not used for most thermodynamic calculations.

Effect of temperature and pressure. The solubility of quartz increases both with increasing temperature and with increasing pressure (Fig. 4), except for a small region near the critical point of water not shown on the figure (Fournier et al., 1982a; Manning, pers. com.). The increase in quartz solubility with increasing pressure is related to the interaction of the OH groups of H_4SiO_4 with dipolar water molecules. This hydrogen-bonding reaction was investigated by Chakoumakos and Gibbs (1986) who found that two water molecules arranged around the OH groups of H_4SiO_4 as shown in Figure 5 is the lowest energy configuration. Increasing pressure results in increasing density of water so there are more water molecules in the neighborhood of the OH groups increasing the frequency of encounters between the H_4SiO_4 and H_2O molecules. Thus, increasing pressure increases the number of molecules oriented in the most stable configuration (Fig. 5) and lowers the $\Delta G_f°(H_4SiO_4, aq)$ resulting in greater silica solubility. The solubility minimum near the critical point of water is a result of a density minimum in this region. However, only a few shallow hydrothermal systems attain pressures and temperatures near the critical point of water so this minimum plays only a minor role in geological systems. Increasing pressure makes ΔG_r for Reaction (1) more negative because

EBSCOhost - printed on 2/13/2023 4:48 AM via . All use subject to https://www.ebsco.com/terms-of-use

Table 2. Comparison of the solubility of silica phases at 25°C based on data from Robie et al. (1978). The conventional values of the equilibrium constant in column K assume that $a_{SiO2} = 1$. The values in column a_{SiO2} assume that $K = 1.11 \times 10^{-4}$, the solubility constant for quartz, for all dissolution reactions.

Phase	$\Delta G_f°$, kJ mol^{-1}	K	a_{SiO2}
quartz	-856.288	1.11×10^{-4}	1.00
cristobalite	-854.512	2.28×10^{-4}	2.05
tridimite	-853.812	3.02×10^{-4}	2.71
coesite	-850.85	9.98×10^{-4}	8.97
glass	-850.559	1.12×10^{-3}	10.08

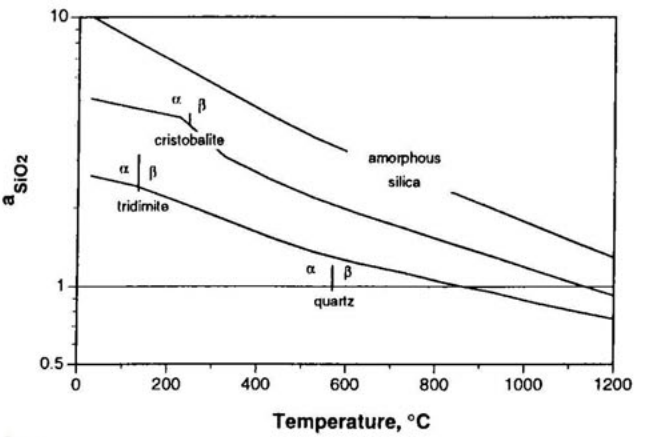


Figure 3. Activity of silica phases relative to quartz as a function of temperature. Free energy data from Robie et al. (1978) were adjusted slightly (within the reported 1σ reported uncertainty) to make the quartz-tridymite and quartz-cristobalite phase transitions fall at the correct temperatures.

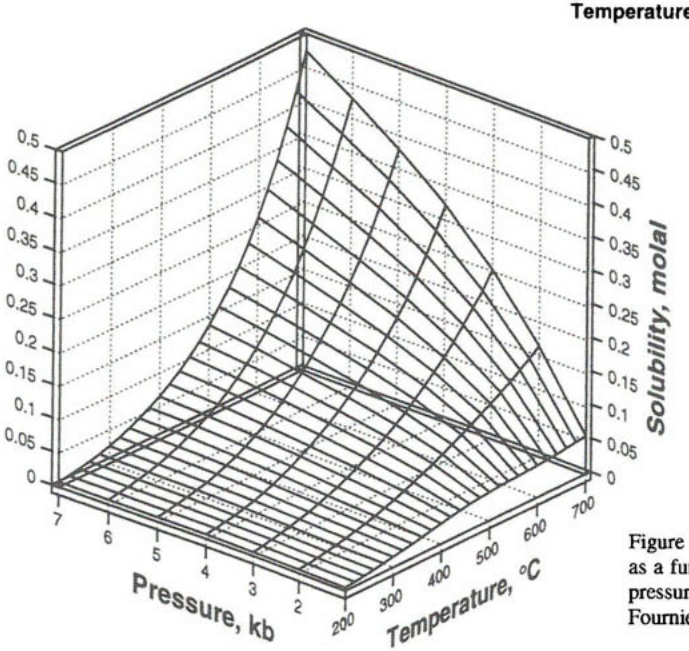


Figure 4. The solubility of quartz as a function of temperature and pressure based on the equation of Fournier and Potter (1982b).

EBSCOhost - printed on 2/13/2023 4:48 AM via . All use subject to https://www.ebsco.com/terms-of-use

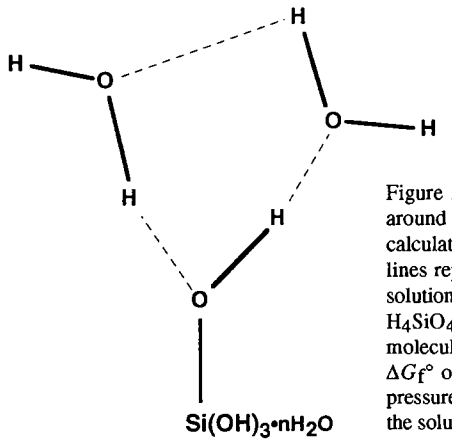


Figure 5. The most stable arrangement of water molecules around a single OH group of a H_4SiO_4 molecule based on calculations by Chakoumakos and Gibbs (1986). The dashed lines represent hydrogen bonds. Increasing the pressure on a solution increases the concentration of water molecules around H_4SiO_4 and thus increases the amount of time that water molecules exist in this most stable configuration. Because the ΔG_f° of H_4SiO_4 is lowest in this configuration, increasing pressure makes dissolved silica more stable and thus increases the solubility of silica minerals.

it makes the ΔH_r term of the $\Delta G_r = \Delta H_r - T\Delta S_r$ equation more negative. On the other hand, increasing temperature causes the $T\Delta S_r$ to become larger which makes ΔG_r more negative so that quartz solubility increases. Thus, the increase in quartz solubility with temperature and pressure is attributable to two different effects. Note that the solubility of other silica phases as a function of pressure and temperature can be estimated by multiplying quartz solubility shown in Figure 3 by the a_{SiO_2} values shown in Figure 2.

Effect of pH. H_4SiO_4 is a weak acid that dissociates appreciably about two pH units above neutrality. The first dissociation reaction

$$H_4SiO_4 = H_3SiO_4^- + H^+ \quad (7)$$

is an important buffer for some natural systems where free silica is present. If a reaction consumes enough hydrogen ions to drive the pH above the pK for Reaction (7), silica dissolves by the reaction

$$SiO_2(s) + 2\ H_2O = H_3SiO_4^- + H^+ \quad (8)$$

and supplies one mole of hydrogen ions per mole of silica that dissolves. As a result only highly unusual, low-silica environments like carbonatites and serpentinites can attain a pH above the first pK of silica. This buffering effect ensures that the second and higher dissociation reactions,

$$H_3SiO_4^- = H_2SiO_4^{2-} + H^+ , \quad (9)$$

$$H_2SiO_4^{2-} = HSiO_4^{3-} + H^+ , \quad (10)$$

$$HSiO_4^{3-} = SiO_4^{4-} + H^+ , \quad (11)$$

are of little geological importance. However, the second and third dissociation Reactions (9) and (10), which occur about two pH units above the first (Fig. 6), are important in alkali silicate solutions used in a variety of technological processes such as zeolite synthesis. Note that when a solution is in equilibrium with amorphous silica, ionized polymers such as $H_6Si_4O_7^{2-}$ also occur at significant concentrations as shown on Figure 6. The solubility of quartz follows the same pattern as is depicted in Figure 6, but the total solubility is about one-tenth that of amorphous silica; only very small concentrations of polymers form at these lower silica concentrations. The solid solubility and the first dissociation constant of silica changes with increasing temperatures to produce a fairly

EBSCOhost - printed on 2/13/2023 4:48 AM via . All use subject to https://www.ebsco.com/terms-of-use

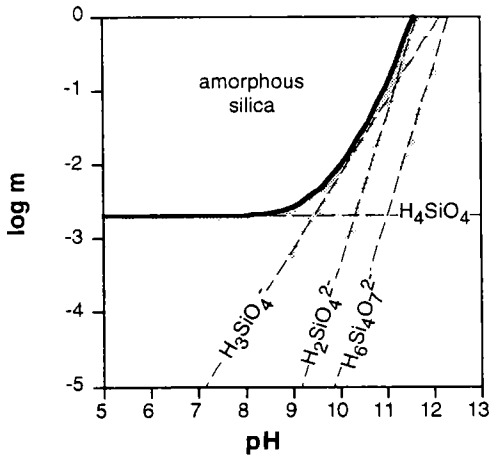


Figure 6. Solubility of amorphous silica as a function of pH (solid line). The dashed lines show the concentration of aqueous species. The shaded area indicates the approximate conditions where polynuclear species make up a significant fraction of the aqueous species. Diagram is based on equilibrium constants from Stumm and Morgan (1981) for solutions with $I = 0.5$.

complex behavior for quartz solubility as a function of pH and temperature (Fig. 7) for conditions along the three phase curve $SiO_2(s)$–solution–$H_2O(v)$. The decrease in solubility above 250°C is a result of the rapidly decreasing density of the solution making it a progressively poorer solvent for ionized species.

Effect of solution species. The presence of dissolved constituents can affect silica solubility in two ways. Some solutes react with H_4SiO_4 to form complexes and others interact with water molecules to change the hydration energy of H_4SiO_4. The activity (≈concentration) of H_4SiO_4 is fixed by Reaction (1) so that if some of the H_4SiO_4 reacts with a solute species to form a complex, more solid dissolves to replenish the reacted H_4SiO_4. Because the total amount of dissolved silica is the sum of all of the silica-containing aqueous species, these complex-forming reactions increase the solubility of silica. There is evidence that aqueous silica interacts with a variety of organic and inorganic species to form complexes. Reported values of equilibrium constants show the following decreasing affinity for reaction with $H_3SiO_4^-$: $H^+ > Fe^{3+} > UO_2^+ >> Mg^{2+} > Ca^{2+} >> Na^+$ (Porter and Webber, 1971; Olsen and O'Melia, 1973). In addition, F^- interacts strongly with silica displacing OH groups to form SiF_6^{2-} (Roberson and Barnes, 1978). Finally, there are several silica-organic complexes (Bennett, 1991), some of which may be quite important in weathering reactions. Other solutes can increase silica solubility by changing the solvent properties of the solution. Quartz solubility is greater in NaCl solutions (Fournier, 1982a; Xie and Walther, 1993) than in pure water presumably because Na^+ and/or Cl^- ions change the structure of water in such a way to increase its hydrogen bonding with H_4SiO_4. This effect is called salting-in and is illustrated in Figure 8.

Solubility as a function of particle size

When a silica particle is fractured, work must be done to create the new surface. The amount of work required to create a unit area of new surface is called the surface free energy (σ, erg/cm^2). The growth of silica particles produces new surface area so that the free energy, ΔG_f(particle), required to form a particle with a surface area of A cm^2 containing n moles of substance is

$$\Delta G_f(\text{particle}) = n\,\Delta G_f(\text{bulk solid}) + A\,\sigma. \qquad (12)$$

This relationship can be recast in terms of the radius of the particle (r, cm) (assuming that it is spherical):

EBSCOhost - printed on 2/13/2023 4:48 AM via . All use subject to https://www.ebsco.com/terms-of-use

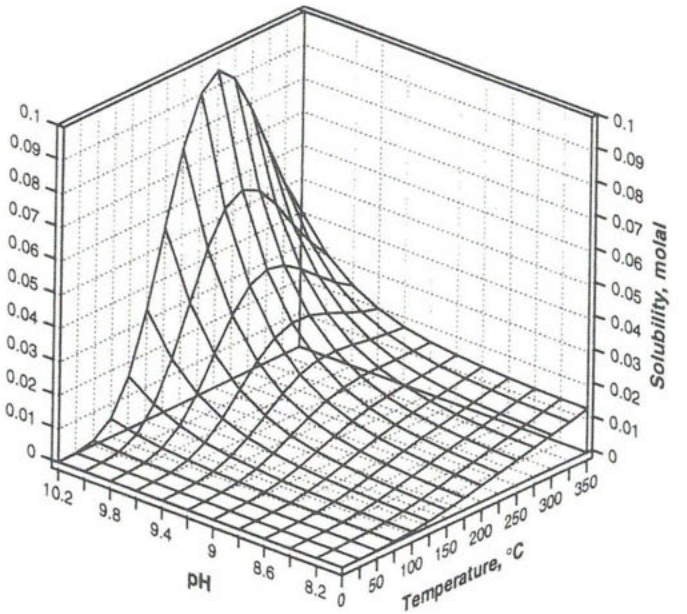
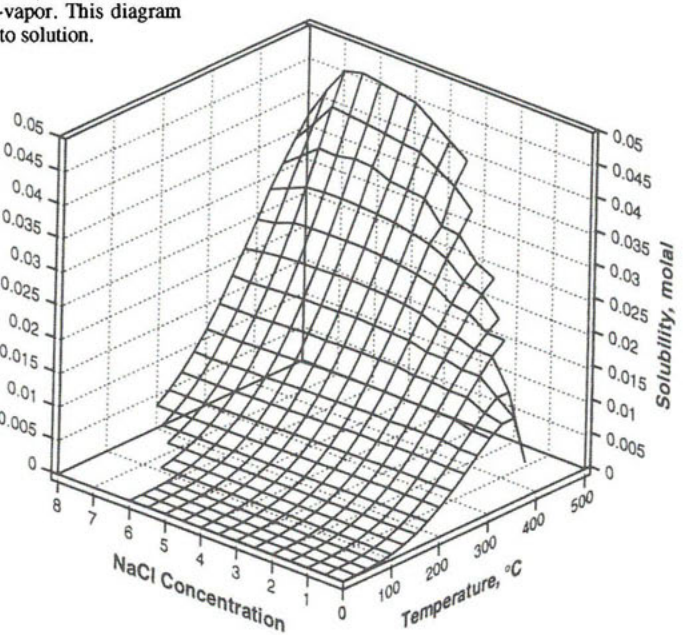


Figure 7 (above). Solubility of quartz as a function of pH and temperature for conditions along the three-phase curve (quartz-solution-vapor) based on data from Fleming and Crerar (1982).

Figure 8 (below). Solubility of quartz in sodium chloride solutions along the three-phase curve quartz-solution-vapor based on the model of Fournier (1983). The solubility surface is terminated along the upper right edge by the critical point of the solution and on the lower left corner by the four-phase field quartz-halite-solution-vapor. This diagram shows that silica is salted into solution.



EBSCOhost - printed on 2/13/2023 4:48 AM via . All use subject to https://www.ebsco.com/terms-of-use

$$\Delta G_f(\text{particle}) = \frac{-4\pi r^3 \Delta G_f^\circ}{3\,V_m} + 4\text{x}10^{10}\pi r^2\sigma \qquad (13)$$

where V_m is the molar volume of the solid ($cm^3\ mol^{-1}$). This relationship can be further modified to give the solubility of the particle (c, arbitrary units) relative to the bulk solubility of the substance (c°, arbitrary units)

$$\ln\left(\frac{c}{c^\circ}\right) = \frac{\frac{2}{3}\,10^{-7}\,\sigma\,V\,B}{r\,R\,T} \qquad (14)$$

where B is a geometric factor (16.8 for spheres), and R is the gas constant (8.314 $J\ mol^{-1}K^{-1}$). The surface free energy of amorphous silica in contact with solution is around 45 erg cm^{-2} (Alexander, 1957), and the surface free energy of quartz in contact with solution is around 120 erg cm^{-2} based on an estimate by Rimstidt and Cole (1983). Figure 9 shows the solubility of quartz and amorphous silica as a function of the radius of curvature of the silica surface. The solubility of convex surfaces (positive radius of curvature) increases with decreasing particle size so that for radii less than ~0.1 μm the particles have a measurably increased solubility. This causes small silica particles to dissolve away while large particles increase in size. This phenomenon is widely known as Ostwald ripening. On the other hand, Equation (14) predicts that the solubility of silica at concave surfaces (negative radius of curvature) decreases with decreasing radius of curvature. This causes silica to precipitate at or near the tips of cracks to cause the cracks to grow closed. Details about the rate of the crack healing process are available in Brantley (1992). Together Ostwald ripening and crack healing promote the growth of large particles with smooth faces or spherical shape.

Equilibration temperature

Experience shows that quartz equilibrates with geothermal solutions so rapidly at temperatures above 200°C that it is reasonable to assume that most solutions are in equilibrium with quartz above this temperature (Fournier, 1985; Cline et al., 1992). Although modest concentrations of alkali and alkaline earth cations increase the reaction rate between quartz and solution by as much as 100 times, the activation energies for the dissolution and precipitation reactions are so high that this catalytic effect reduces the equilibration temperature only about 10°C. Thus, it is reasonable to assume that most brines are in equilibrium with quartz at temperatures above about 190°C. Furthermore,

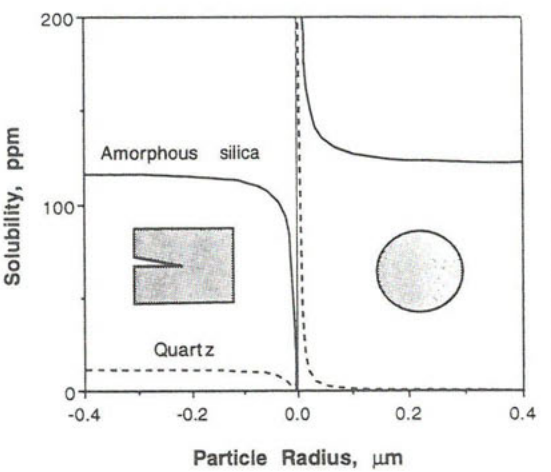


Figure 9. The solubilities of quartz and amorphous silica at 25°C as a function of the radius of curvature of the surface of the solid. Note that the solubility of particles with convex surfaces increases with decreasing radius of curvature and the solubility of concave regions decreases with decreasing radius of curvature. This causes small particles to dissolve and small fractures to be filled.

EBSCOhost - printed on 2/13/2023 4:48 AM via . All use subject to https://www.ebsco.com/terms-of-use

because the reaction rates are so fast above these temperatures, metastable silica phases (i.e., glass, opal, silica gel, etc.) convert to quartz by means of dissolution and precipitation quite rapidly in terms of geologic time so that it is quite unlikely that any metastable silica phase can persist above 200°C. Below this temperature the departure of solutions from equilbirium with quartz depends upon a wide variety of factors including *A/M* ratio, flow rates, and temperature (Rimstidt and Barnes, 1980). Thus, it is reasonable to assume that essentially all hydrothermal solutions hotter than 200°C are in equilibrium with quartz. Moreover, if these solutions are tapped by wells and brought to the surface quickly, their silica content can be used to estimate the temperature of the aquifer. This is the basis for the quartz geothermometer (Fournier, 1972) widely used in geothermal exploration.

SILICA-WATER INTERFACE

Formation of the silica-water interface

Processes governing the kinetics of silica-water interactions originate at the mineral-solution interface. Recent advances in understanding the reactivity of silica and perhaps all mineral phases have emphasized the role of surface structure and chemistry. Because of this, our kinetics discussion begins by considering the nature of this interface. Silica surface geochemistry has been extensively discussed elsewhere (e.g., Iler, 1979; Parks, 1990) and the reader is referred to these works. Our purpose is to focus on information most pertinent to communicating the recent advances in quantifying the kinetics of silica-water interactions and the mechanistic surface controls on these reaction rates.

One way to understand the silica-water interface is to begin with a freshly broken quartz surface and then hydrate it in a stepwise fashion to a fully wetted surface. Figure 10, from Parks (1984), shows that when quartz is fractured in vacuum to expose a fresh surface, the initial surface (Fig. 10.I) is composed of 'dangling' silicon and oxygen bonds. These 'sites' and the corresponding surface structures are quite unstable and hydroxylate easily with available water within seconds, even at ultra high vacuum conditions. This hydroxylated surface (Fig. 10.II) is dominated by >SiOH or silanol groups. The initial adsorbed water adjacent to the surface is oriented and has properties (e.g., entropy, mobility, and dielectric constant) different from those of bulk water (e.g., Sermon, 1980). As this adsorbed water film increases beyond approximately three monolayers (Fig. 10.III), its properties become more like bulk water (Parks, 1984). In the presence of molecular water, the silanol groups ionize, producing mobile protons that associate/dissociate with the surface to impart an electrical conductivity to the surface. As these groups dissociate, hydronium ions are produced that diffuse from the surface to develop a pH-dependent surface charge and potential. This surface charge, in turn, attracts a diffuse cloud of counterions to preserve electroneutrality. The resulting surface-solution interface that exists at virtually all wetted mineral surfaces (Fig. 10.IV) is called the electrical double layer (e.g., Yates et al., 1974; Davis et al., 1978). Detailed discussions of the mechanisms that develop these interfacial fields at quartz-water and other oxide material interfaces are considered elsewhere (e.g., references in Iler, 1979).

Surface structures and properties

Electrical double layer of the silica-water interface. A closer look at the chemical structure of the electrical double layer shows three electrostatically charged regions. Figure 11a shows that these regions are defined as the o, β, and d planes, and each is associated with an electric potential and surface charge. Comparing Figures 11a and 11b, these idealized planar surfaces correspond to the decreasing charge distribution

EBSCOhost - printed on 2/13/2023 4:48 AM via . All use subject to https://www.ebsco.com/terms-of-use

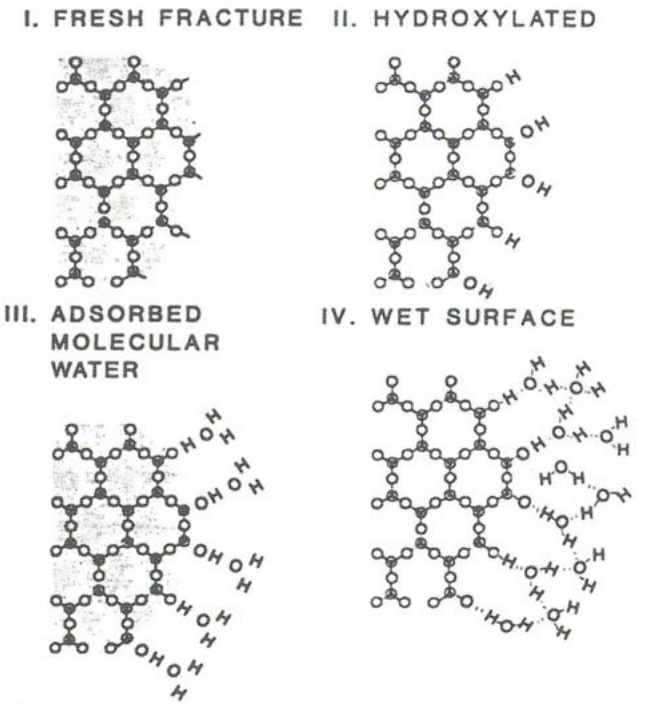


Figure 10. A schematic diagram illustrating stepwise water-surface interactions with freshly cleaved or fractured quartz (from Parks, 1984).

and electrical potential that occurs with increasing distance from the surface. Hydrogen ions coordinate with the unsaturated sites of the interface at the innermost o layer (as an 'inner-sphere complex'). Sodium and other weakly bound cations are positioned at the β layer (as an 'outer-sphere complex') or the d layer (near the bulk solution). Low-temperature surface complexation models do not permit sodium to interact specifically with the surface because surface titration data suggest it is not specifically bound to the surface due to shielding by its own solvation sphere. However, sodium may exist in the β layer in an 'ion pair' coordination with the surface that promotes its partial dehydration and water dissociation within the charged interface (Conway, 1981; Fokkink et al., 1990). Although hydration spheres are implicitly ignored in this representation, the same relative surface-metal distances are predicted for the surface coordination of H^+ and Na^+ at o and β, planes, respectively. At hydrothermal temperatures, recent experiments show that a significant proportion of sodium may specifically bind to the surface at the o layer (see later discussion of Berger et al., 1994).

Investigations of SiO_2 surface chemistry have produced a generally accepted model for the distributions of quartz surface sites in aqueous solutions (see references in Iler, 1979). Briefly, quartz in contact with a simple solution composition containing only an alkali salt (i.e., quartz-water-sodium chloride system) has surface structures that can be described by three 'complexes' that are denoted by a '>' symbol and have a population balance of

$$\theta_{>SiOH} + \theta_{>SiO^-} + \theta_{>SiO\text{-}Na^+} = 1.0 \qquad (15)$$

where $\theta_{>SiOH}$ = fraction of total sites as >SiOH species

$\theta_{>SiO^-}$ = fraction of total sites as $>SiO^-$ species

$\theta_{>SiO\text{-}Na^+}$ = fraction of total sites as $>SiO\text{-}Na^+$ species.

EBSCOhost - printed on 2/13/2023 4:48 AM via . All use subject to https://www.ebsco.com/terms-of-use

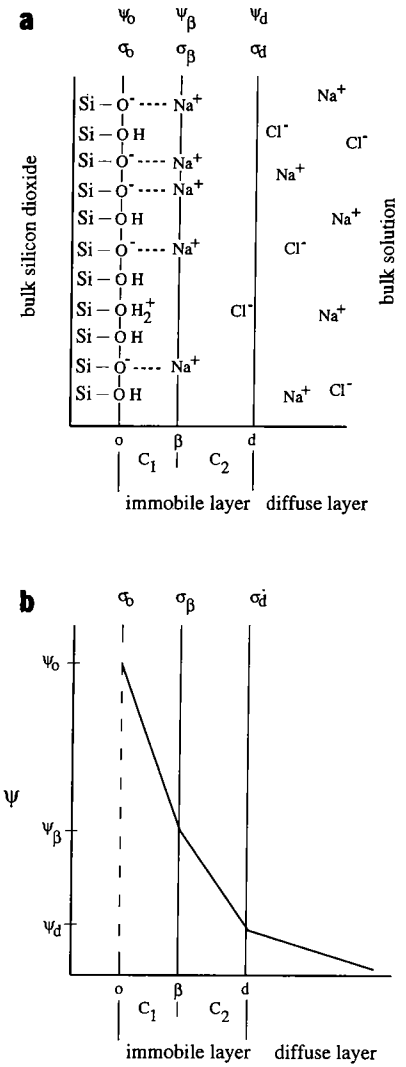


Figure 11. Schematic illustration of the triple layer model (modified from Hayes and Leckie, 1987) of an idealized planar quartz-water-sodium chloride interface.

Note that these 'species' are constructs describing surface titration data and the surface charge relationships of oxides. Of the three complexes listed, only >SiOH has been directly observed using spectroscopic methods (Anderson and Wickersheim, 1964; Gallei and Parks, 1972; Morrow and Cody, 1976a,b). The other two complexes may or may not have physical meaning as they describe the time-averaged degree of surface ionization. For the purpose of later relating surface complex distributions to dissolution kinetic data, the $>SiO^-$ and $>SiO\text{-}Na^+$ are co-dependent upon changes in solution pH and sodium concentration and cannot be evaluated independently. These terms are added and referred to as $>SiO^-_{tot}$.

Ionization and surface charge. Most of what is known about the surfaces of silica polymorphs has come from studies of amorphous silica and quartz. The surface complexes describing silica-solution interfaces are not static, but are rather calculated distributions reflecting an average electronic state resulting from proton, cation, and hydroxyl ion interactions with the undersaturated oxygens at the mineral surface (Prigogine and Fripiat, 1974). The population balance is largely controlled by the surface reactions listed in Table 3 and the relative magnitudes of their association constants to form negative surface charge as $>SiO^-_{tot}$ complexes. The pK_a for ionization by Reaction 16 in Table 3 is about 6.8, indicating that the surface is only weakly acidic. These interactions lead to the pH and sodium dependence of average $>SiO^-_{tot}$ distributions as shown in Figure 12. In general, net negative charge increases with increasing solution pH and/or alkali cation concentration until about pH 10 or 11. Above this pH, further pH increases or addition of alkali have smaller effects on net negative charge.

(a) Each layer has an associated interfacial potential, ψ_i (volts), and charge density, σ_i (coulomb m^{-2}), that determine the inner (C_1) and outer (C_2) layer capacitance (Faraday m^{-2}), by the relationship $C_j = \Delta\sigma_i(\Delta\psi_i)^{-1}$. The magnitude of these parameters decreases with increasing distance from the mineral surface into the solution side of the interface and finally to the bulk solution. In this model, the bulk uncharged solution is beyond the diffuse d layer. Strongly sorbed ions such as hydrogen interact closely with unsaturated oxygens in the innermost o layer, whereas weakly sorbed ions such as sodium are thought to interact only from distances associated with the β layer at low temperatures. (b) Schematic representation of the corresponding charge distribution and the potential decay away from the surface.

EBSCOhost - printed on 2/13/2023 4:48 AM via . All use subject to https://www.ebsco.com/terms-of-use

Table 3. Acid-base quartz surface complex reactions and corresponding association constants at 25°C.

Reaction	K_a	Reference	Eqn.
$>SiOH = >SiO^- + H^+$	$10^{-6.8}$	a	(16)
$>SiOH + Na^+ = >SiO\text{-}Na^+ + H^+$	$10^{-7.1}$	b	(17)
$>SiOH_2^+ = >SiOH + H^+$	$10^{-2.3}$	c	(18)
$>SiOH + H^+ + Cl^- = >SiOH_2Cl$	$10^{-6.4}$	d	(19)

a) Schindler and Kamber,1968; b) Kent et al., 1988; Dugger et al., 1964; c) Schindler and Stumm, 1987; d) Kent et al., 1988.

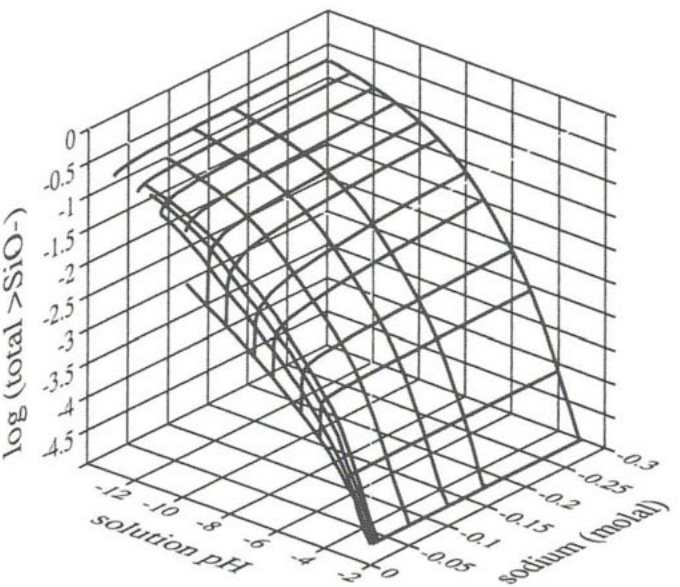


Figure 12. The three-dimensional dependence of fractional surface charge upon bulk solution pH and sodium concentration for the quartz-water-sodium chloride system at 25°C. The fractional sum of calculated $>SiO^-$ and $>SiO\text{-}Na^+$ populations is plotted as a function of solution pH and sodium concentration (see Dove, 1994). Three general environments are recognized. At low pH, negative surface charge is low and independent of sodium concentration. At near-neutral pH, surface charge is sensitive to the addition of small concentrations of sodium. At high pH, sodium has only a small effect on net surface charge as the basic solution inherently contains sodium as sodium hydroxide and surface ionization nears saturation.

Other metals besides the alkali cations also interact with silica surfaces, some quite strongly. Interaction mechanisms appear to range from simple ion exchange into the β plane to cation-surface specific binding at the innermost o layer. For example, surface association constants, K_a, vary from $10^{-7.8}$ for lithium (Dugger et al., 1964) to $10^{-1.8}$ for ferric iron (Schindler et al., 1976) at 25°C . Later discussion will show that certain metal-surface interactions can dramatically enhance or inhibit silica reactivity. The direction and degree of these effects are partially related to interaction strengths although the specifics are considerably more complex.

EBSCOhost - printed on 2/13/2023 4:48 AM via . All use subject to https://www.ebsco.com/terms-of-use

KINETICS

Basic principles

Aqueous diffusion. The rates of reactions between minerals and solutions are either limited by diffusion of aqueous species to or from the surface or by rates of bond breaking and formation at the mineral's surface. At temperatures below 300°C, bond breaking and formation is clearly the rate limiting step for silica dissolution or precipitation. This interpretation is supported by the relatively high activation energies for these reactions. As a rule-of-thumb, the activation energy for a bond-breaking reaction is about 20% of the enthalpy of formation of that bond. The ΔH_f° of quartz is -910.700 kJ mol^{-1} (Robie et al., 1978) and each mole of quartz contains four moles of Si–O bonds so the ΔH_f° (Si–O) is -227.675 kJ mol^{-1}. Twenty percent of this value is 45.5 kJ mol^{-1}, which is low, but consistent with experimental measurements of the activation energy for quartz dissolution and precipitation (see Table 4). The activation energy for diffusion of aqueous species is

Table 4. Summary of some activation energies reported for the precipitation and dissolution kinetics of the silica polymorphs.

Reference	Solution Composition	Temperature °C	E_a kJ mol^{-1}
Precipitation- Quartz			
Bird et al. (1986)	deionized water	121-255	51-55
Precipitation- Cristobalite			
Renders et al. (1994)	deionized water	150-300	53.7
Precipitation- all silica polymorphs			
Rimstidt and Barnes (1980)	deionized water	25-300	49.8
Dissolution-Quartz			
Rimstidt and Barnes (1980)	deionized water	25-300	67-4-76.6
Gratz et al. (1990)	pH 10 to 13	148-236	86.4[1]-90.2[2]
Casey et al. (1990)	pH 3, 11	20-70	36[3], 53[4]
Brady and Walther (1990)	pH 2-11.7	25, 60	54[5], 96[6]
Dove and Crerar (1990)	pH 5.7, Na^+ 0 to 0.2	150-300	
Gratz and Bird (1993)	pH 10 to 13	148-236	78.6
Tester et al. (1994)	deionized water	25-625	89±5
Dove (1994)	pH 2 to 12, Na^+ 0 to 0.3	25-300	66.0[7]-82.7[8]
House & Hickenbotham (1992)	pH 10	5-35	83.2
Dissolution-Cristobalite			
Rimstidt and Barnes (1980)	deionized water	25-300	68.7[9], 65.7[10]
Dissolution-Amorphous silica			
Rimstidt and Barnes (1980)	deionized water	25-300	60.9-64.9
Fleming (1986)	deionized water	25-100	54.8±3.8
Liang and Readey (1987)	hydrofluoric acid	24-70	33, 30, 26[11]

[1]prism average; [2]rhomb average; [3]pH 3; [4]pH 11; [5]pH 3; [6]pH 11; [7]low pH range with transition to [8]high pH range; [9]α-cristobalite; [10]β-cristobalite; [11]10%HF, 25%HF, 49% HF, respectively.

EBSCOhost - printed on 2/13/2023 4:48 AM via . All use subject to https://www.ebsco.com/terms-of-use

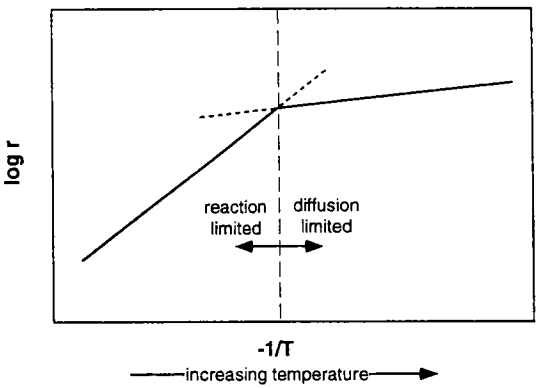


Figure 13. Schematic diagram illustrating the relationship between the surface reaction limited rate and the rate of diffusion of H_4SiO_4 away from the mineral surface as a function of temperature. At low temperatures the rate limiting step for silica dissolution is bond breaking at the surface, but this reaction has a high activation energy so that its rate increases rapidly with increasing temperature. At some temperature, depending on the geometry of the system and the relative fluid velocity, the reaction limited rate releases silica to the solution faster than it can diffuse away from the surface. The rate of dissolution is limited by diffusion at this and higher temperatures.

on the order of 20 kJ mol^{-1}. However, because the activation energy for the bond-breaking reaction is higher than the activation energy for the diffusion reaction, some temperature exists where these two rates are equal, as illustrated in Figure 13. This temperature varies from system to system depending on the rate of the geometry- and flow-controlled diffusion process. An analysis of this problem by Casey (1987) shows that the cross-over point for quartz reactions occurs at temperatures above 300°C for most geologically reasonable situations.

Dissolution and precipitation. A fundamental reference point in describing the kinetics of silica dissolution and precipitation is the equilibrium solubility relationship between the mineral phase and the solution. Considering the simplest scenario for opposing forward and reverse reactions, we can write the expression

$$SiO_2 + 2\ H_2O(l) = H_4SiO_4 \tag{16}$$

where dissolution and precipitation, respectively, proceed by

$$SiO_2 + 2\ H_2O = (*)^{\ddagger} \tag{17}$$

$$(SiO_2{\bullet}2H_2O)^{\ddagger} = H_4SiO_4 \tag{18}$$

and

$$H_4SiO_4 = (*)^{\ddagger} \tag{19}$$

$$(*)^{\ddagger} = SiO_2 + 2\ H_2O \tag{20}$$

The $(*)^{\ddagger}$ indicates an activated intermediate species whose stoichiometry is unknown. At equilibrium, Reactions (18) and (20) proceed at equal rates. From this basis, Rimstidt and Barnes (1980) derived an integrated rate equation which accounted for both reaction directions such that

$$r_+ = (dn_{H_4SiO_4}/dt)_+ = Ak_+a_{SiO_2}\,a^2\,{}_{H_2O} \tag{21}$$

EBSCOhost - printed on 2/13/2023 4:48 AM via . All use subject to https://www.ebsco.com/terms-of-use

and

$$r_- = (dn_{H_4SiO_4}/dt)_- = Ak_-a_{H_4SiO_4} \quad (22)$$

where $n_{H_4SiO_4}$ is the number of moles of H_4SiO_4, A is the interfacial area (m^2) and k_+ and k_- are the dissolution and precipitation rate constants, respectively. The net rate is the sum of (21) and (22):

$$r = (dn_{H_4SiO_4}/dt) = A\ (k_+a_{SiO_2}\ a^2_{H_2O} - k_-a_{H_4SiO_4}). \quad (23)$$

Since $n_{H_4SiO_4}$ can be recast as $a_{H_4SiO_4}$ for

$$n_{H_4SiO_4} = m_{H_4SiO_4}\ (M) \quad (24)$$

where M is the mass of water in the systems is constant, the reaction rate can be expressed relative to the rate in a system containing 1 kg of water such that (23) is written

$$r = (dm_{H_4SiO_4}/dt) = (A/M)\ \ (k_+a_{SiO_2}\ a^2_{H_2O} - k_-a_{H_4SiO_4}). \quad (25)$$

Rimstidt and Barnes (1980) designed the A/M term to quantify the extent of the system, that is, the ratio of the relative surface area to the relative mass of water present. Normalizing the reaction rate to 1 kg water and 1 m^2 of interfacial surface area, they defined apparent rate constants, k'_+ and k'_-, that included A/M such that

$$k'_+ = (A/M)\gamma_{H_4SiO_4}\ a_{SiO_2}\ a^2_{H_2O}\ k_+ \quad (26)$$

$$k'_- = (A/M)\gamma_{H_4SiO_4}\ a_{SiO_2}\ a^2_{H_2O}\ k_- \quad (27)$$

Fundamental rate constants that can be compared must separate this A/M contribution from the measured apparent constants. Substituting Equation (26) and (27) into (23) converts the rate equation to the simple form

$$r = k'_+ - k'_-\ a_{H_4SiO_4}. \quad (28)$$

Since $$K = k_+ /k_- \quad (29)$$

then (28) is rearranged to $$r = k'_+ (1 - Q/K) \quad (30)$$

where Q is the activity quotient of the system,

$$Q = (a_{H_4SiO_4}) /(a_{SiO_2})\ (a_{H_2O})^2. \quad (31)$$

Equation (30) gives the dissolution rate of quartz as a first order expression written in terms of silicic acid release. Numerous studies have assumed first order behavior of quartz dissolution since Rimstidt and Barnes (1980) presented Equation (30). However, this was confirmed experimentally only recently. Berger et al. (1994) measured quartz dissolution rates in *deionized water* containing 0 to 10 mmoles of silica at 300°C and found that the reaction rate follows a first order rate law in silicic acid concentration over the tested range of reaction affinity as shown in Figure 14a. In contrast, Figures 14b and 14c show that the rate law deviates significantly from first order behavior in the presence of low sodium or lead concentrations. This difference in behavior is explained in terms of competitive adsorption between dissolved cations and H_4SiO_4 at the silica surface.

While the rate equations developed by Rimstidt and Barnes (1980) are consistent with thermodynamics, mineral-water reaction rates are perhaps better understood in terms of processes occurring at the mineral-solution interface. This means removing emphasis on

EBSCOhost - printed on 2/13/2023 4:48 AM via . All use subject to https://www.ebsco.com/terms-of-use

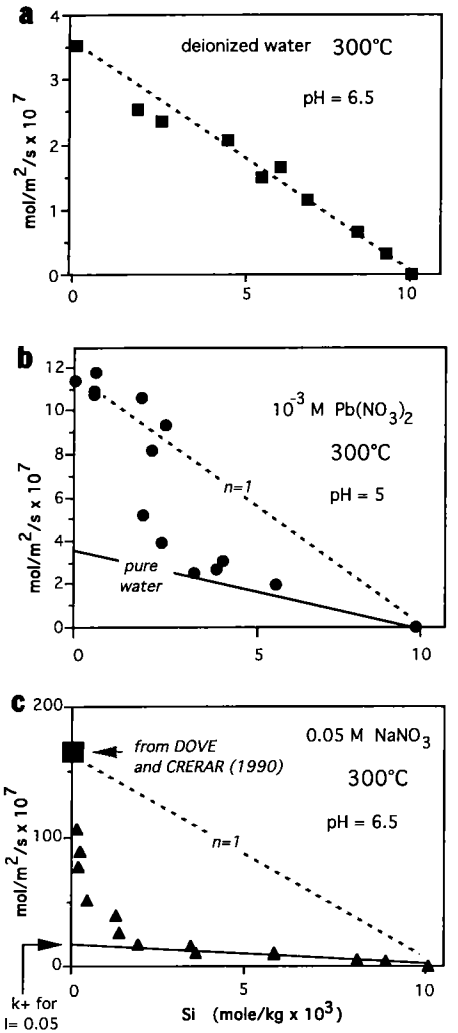


Figure 14. Experimental quartz dissolution rates at 300°C in solutions of various silica concentrations. The dotted lines represent calculated rates.
(a) Deionized water;
(b) 10^{-3} molal $Pb(NO_3)_2$;
(c) 0.05 molal $NaNO_3$
(from Berger et al., 1994).

the behavior of the bulk solution and refocusing it on the reactants, that is, the surface site densities and interfacial solvent population and behavior.

Transition state theory (TST) has been developed to describe the energetics of elementary reactions on a molecular level, and recent reviews of this subject have shown its direct application to describing mineral-water reaction rates (Lasaga, 1981; Lasaga, 1990). We briefly use TST here to show how silica-dissolution and precipitation reaction rates can be reformulated from Equation (25) to a kinetic expression based on the surface and solvent reactant concentrations. For simple rate-limiting dissolution reactions of the forms,

$$A + B = AB^{\ddagger} \rightarrow C + D \tag{32a}$$

$$A = A^{\ddagger} \rightarrow P, \tag{32b}$$

EBSCOhost - printed on 2/13/2023 4:48 AM via . All use subject to https://www.ebsco.com/terms-of-use

the absolute identity of A, B and the activated intermediates, $AB^{\ddagger}$ or $A^{\ddagger}$, are not usually known, but can be assumed to have one of these stoichiometries with reasonable certainty. Dove and Crerar (1990) proposed that the rate-determining step for quartz dissolution involves the attack of silica surfaces by H_2O to break Si-O bridging bonds by the simple reaction

$$>\text{Si-O-Si}< + H_2O = (>\text{Si-O-Si}< \bullet H_2O)^{\ddagger} \rightarrow 2(>\text{Si-O-H}), \quad (33)$$

which is analogous to Equation (32a). The TST formulation of the rate constant, k_+, describing the frequency that an adsorbed water molecule binds a silica surface to form an activated complex is conventionally written as

$$k'_+ = \left(\frac{kT}{h}\right)\left(\frac{\gamma_{ads}}{\gamma^{\ddagger}}\right)\left(\exp\frac{\Delta S^{\ddagger}}{R}\right)\left(\exp\frac{-\Delta H^{\ddagger}}{RT}\right) \quad (34)$$

where k'_+ = apparent rate constant (sec^{-1})

$\frac{kT}{h}$ = frequency factor (9.85×10^{12} sec^{-1} at 200°C)

$\frac{\gamma_{ads}}{\gamma^{\ddagger}}$ = activity coefficients for adsorbed H_2O and intermediate species

$\Delta S^{\ddagger}$ = standard activation entropy (J mol^{-1} K^{-1})

$\Delta H^{\ddagger}$ = standard activation enthalpy (kJ mol^{-1}).

The k'_+ in Equation (24) has units of (sec^{-1}) because it represents the rate that an individual adsorbed water molecule attacks the quartz structure. However, when BET or geometric mineral surface areas are known, experimental dissolution rate data give the reaction rate, $r_{H_4SiO_4}$, for a population of water molecules that reacts per unit area of mineral surface. The parameters k'_+ and $r_{H_4SiO_4}$ are linked by recasting the net reaction rate in terms of the number of moles of water molecules per reactive area (mol m^{-2}) such that the reaction rate, $r_{H_4SiO_4}$, is equal to the number of adsorbed H_2O molecules multiplied by the apparent rate, k'_+, or

$$\text{number moles of adsorbed } H_2O \text{ per square meter} = X_{H_2O}\, N_{t,ads} \quad (35)$$

where X_{H_2O} = mole fraction of sites accessible to water molecules

$N_{t,ads}$ = moles of reactive sites on the mineral surface (mol m^{-2})

so that the forward rate is expressed

$$r = X_{H_2O}\, N_{t,ads}\, k_+. \quad (36)$$

The forward reaction rate in Equation (17) is given by

$$r = k_+ (a_{SiO_2})(a_{H_2O})^2 . \quad (37)$$

Solving for k_+ from Equations (36) and (37) gives

$$k_+ = \frac{X_{H_2O}\, N_{t,ads}}{(a_{SiO_2})(a_{H_2O})^2} k'_+ \quad (38)$$

Substituting (34) for k'_+, we obtain the rate constant for the reaction of water molecules with the quartz surface

$$k_+ = \frac{X_{H_2O}\, N_{t,ads}}{(a_{SiO_2})(a_{H_2O})^2}\left(\frac{kT}{h}\right)\left(\frac{\gamma_{ads}}{\gamma^{\ddagger}}\right)\left(\exp\frac{\Delta S^{\ddagger}}{R}\right)\left(\exp\frac{-\Delta H^{\ddagger}}{RT}\right) \quad (39)$$

EBSCOhost - printed on 2/13/2023 4:48 AM via . All use subject to https://www.ebsco.com/terms-of-use

where k_+, the fundament rate constant has units of (mol m^{-2} sec^{-1}). Dove and Crerar (1990) showed that this description of the rate constant has a number of advantages over the *A/M* convention used in Equation (25). First, the standard state for the activated reaction becomes one mole of sites per square meter. The units of this standard state are physically consistent with the activated complex concentration that exists within the two-dimensional space of the interface. Second, it produces a system which describes the thermodynamic variables, and thus, r and k_+ with internally consistent units (e.g., Lasaga, 1981, p. 143).

Another advantage of using this convention is that general rate equations can be written with multiple rate *constants* to describe the kinetics of silica-water dissolution over a range of conditions, such as solution pH, where multiple rate-limiting reactions are operative. Thus, a net rate equation can be described by a sum of processes as shown later in Equations (53 to 55).

Although the previous discussion focuses on dissolution, Renders et al. (in review) suggests that the reverse reaction rate of silica precipitation can also be described with this convention for the rate constant as shown in Figure 15. Briefly, we can rewrite Equations (25) and (26) as

$$r_+ = (dn_{H_4SiO_4}/dt)_+ = k_+ a_{SiO_2} a^2_{H_2O} \quad (40)$$

and $$r_+ = (dn_{H_4SiO_4}/dt)_- = k_- a_{H_4SiO_4} \quad (41)$$

where k_+ and k_- are described by Equation (25) for a single forward and reverse rate-limiting reaction, respectively.

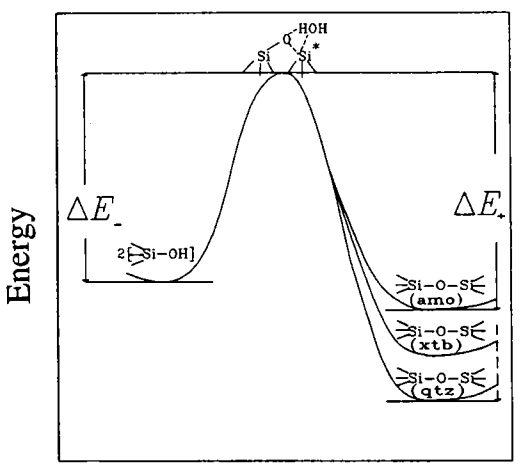


Figure 15. A schematic illustration showing the similarity between forward and reverse reaction path for microscopically reversible silica dissolution and precipitation. Activation energy, E_a,- is thought to be a constant for the precipitation of all silica polymorphs, but E_a,+ varies with the silica polymorph. (from Renders et al., in review).

Nucleation. The precipitation of the first silica particles from a homogeneous supersaturated solution is inhibited by the high solubility of very small silica particles. This high solubility, which is the result of the work required to form silica surfaces as described in the section on silica solubility and particle size, can be visualized as an energy barrier that must be crossed via an activated complex, which is called the critical nucleus as illustrated in Figure 16. The rate of formation of critical nuclei has been modeled by Nielsen (1959), who showed that the flux of aqueous species to the growing nuclei, J, is given by:

EBSCOhost - printed on 2/13/2023 4:48 AM via . All use subject to https://www.ebsco.com/terms-of-use

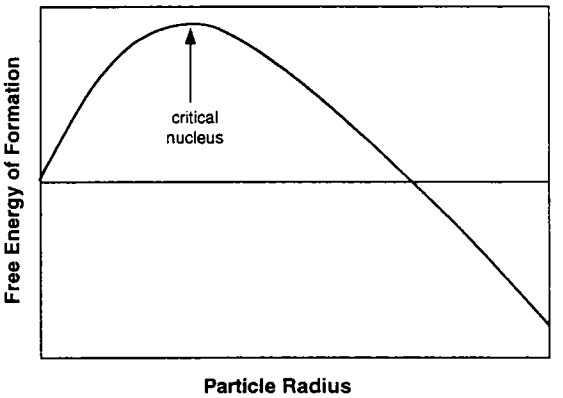


Figure 16. Schematic illustration of the change in free energy of formation of a growing particle as a function of size. Particles smaller than the size of the critical nucleus will tend to dissolve while those larger than the critical nucleus will tend to grow to macroscopic size.

$$J = A\ exp\left(\frac{-\Delta G^*}{k\,T}\right) \tag{42}$$

where A is a factor relating to the collision rate of the aqueous species involved in the formation of the nuclei (it is on the order of 10^{30} for most systems), k is the Boltzman constant, T is temperature in degrees Kelvin, and ΔG^* is the free energy of formation of a critical nucleus as given by the following expression:

$$\Delta G^* = \frac{16\,\pi\,\sigma^3\,V^2}{3\left[k\,T\,ln\left(\frac{c}{c_o}\right)\right]^2} \tag{43}$$

where s is the surface free energy of the solid, V is its molar volume, c is the concentration of aqueous species, and c_0 is the equilibrium concentration of the aqueous species. This equation shows that high values of σ produce slow rates of nucleation. Because quartz has a high surface free energy, it is much more difficult to nucleate than is amorphous silica. As a result, amorphous silica often precipitates from solutions instead of quartz. This effect is illustrated in Figure 17, which shows the flux of silica onto growing nuclei as a hydrothermal solution is cooled. This explains the formation of opal and siliceous sinter in hydrothermal systems that are substantially supersaturated with respect to quartz. In general, more soluble phases have a lower surface free energy than less soluble phases so that the most soluble polymorph of a material forms first from a supersaturated solution and this polymorph transforms stepwise to less soluble polymorphs until the most stable, least soluble polymorph finally forms. This phenomenon is called Ostwald's step rule (Stumm, 1992). In the case of silica, opal A often precipitates first from solution; it transforms to opal CT, which has a lower solubility than opal A; and finally, opal CT transforms to quartz.

Controls of temperature and solution composition on reactivity.

Numerous investigations have qualitatively and quantitatively investigated aspects of silica-water reaction rates such as saturation state, temperature, solution pH, salinity, dissolved metals and organics. Although these categories are interrelated, we group these investigations somewhat arbitrarily to review some of the most important findings.

Temperature dependence in deionized water. The dissolution and precipitation kinetics of the silica polymorphs in deionized water have been investigated in several studies over the temperature range of 25° to 300°C. One motivation for these studies,

EBSCOhost - printed on 2/13/2023 4:48 AM via . All use subject to https://www.ebsco.com/terms-of-use

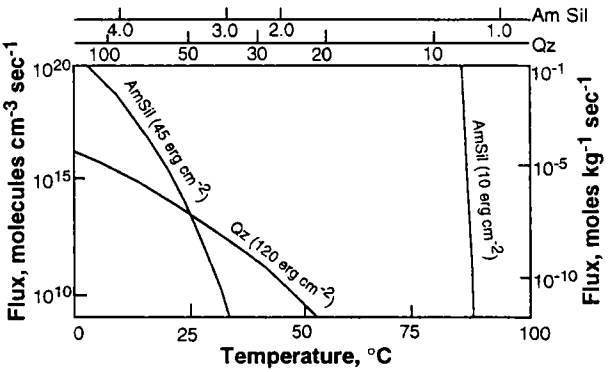


Figure 17. If a hot solution of silica (345 ppm, saturated with respect to quartz at 230°C) is cooled, this diagram shows that the flux of dissolved silica (J) to form nuclei of quartz (Qz) or amorphous silica (Am Sil) by homogeneous nucleation is essentially zero (rates below $1x10^{-7}$ mol kg^{-1} sec^{-1} precipitate less than 10% of the dissolved silica per day) until the solution reaches 25°C. Observations of siliceous sinter formation shows that amorphous silica forms near 100°C, suggesting that heterogeneous nucleation (probably on iron and manganese oxyhydroxides), illustrated by the line on the right, occurs. The axes at the top of the diagram indicate the degree of saturation of quartz and amorphous silica. This figure was adapted from Rimstidt and Cole (1983).

particularly at hydrothermal conditions, is to understand the corrosion and precipitation of silica in both natural and engineered geothermal systems listed in Table 1.

In perhaps the first most comprehensive investigation of silica reactivity in hydrothermal systems, Rimstidt and Barnes (1980) determined the dissolution rate of four silica polymorphs as empirical functions of temperature. As seen in Table 4, within the error of their experiments, they found that the activation energies for dissolution of these polymorphs were similar with values ranging from 60 to 76 kJ mol^{-1}. Bird et al. (1986) also investigated the dissolution of natural quartz in oil-sands with the goal of understanding silica transport during steam injection into these silica-rich systems. There is some question concerning whether these early experiments are representative of silica reactivity in a pure SiO_2-H_2O system since we know that dissolved components derived from the reactors or the bulk rock sample could affect dissolution rates. More recently, Tester et al. (1994) combined new data with existing rates published in ten different studies to determine an updated temperature function (spanning 25° to 625°C) for the dissolution kinetics of quartz in deionized water. Their experiments were careful to consider the potential rate-enhancing or inhibiting effects of dissolved components from fluids or bomb walls on the reaction rate. One finding of this study was that both geometric and BET-derived surface areas were successfully used to normalize dissolution rates and determine a simple Arrhenius expression for quartz dissolution rate in deionized water. Figure 18 illustrates the fit of both temperature functions to the dissolution rate data.

The precipitation kinetics of the silica polymorphs in deionized water has also been studied. Rimstidt and Barnes (1980) found that a single rate constant expression with an activation energy of 40 kJ mol^{-1} described the precipitation of quartz, α-cristobalite, β-cristobalite and amorphous silica. Renders et al. (in review) recently studied the precipitation kinetics of synthetic cristobalite to investigate the reactivity of this polymorph, which often forms preferentially over other thermodynamically-favored forms of silica (see *Nucleation* section). They found that cristobalite precipitates hydrothermally only when

EBSCOhost - printed on 2/13/2023 4:48 AM via . All use subject to https://www.ebsco.com/terms-of-use

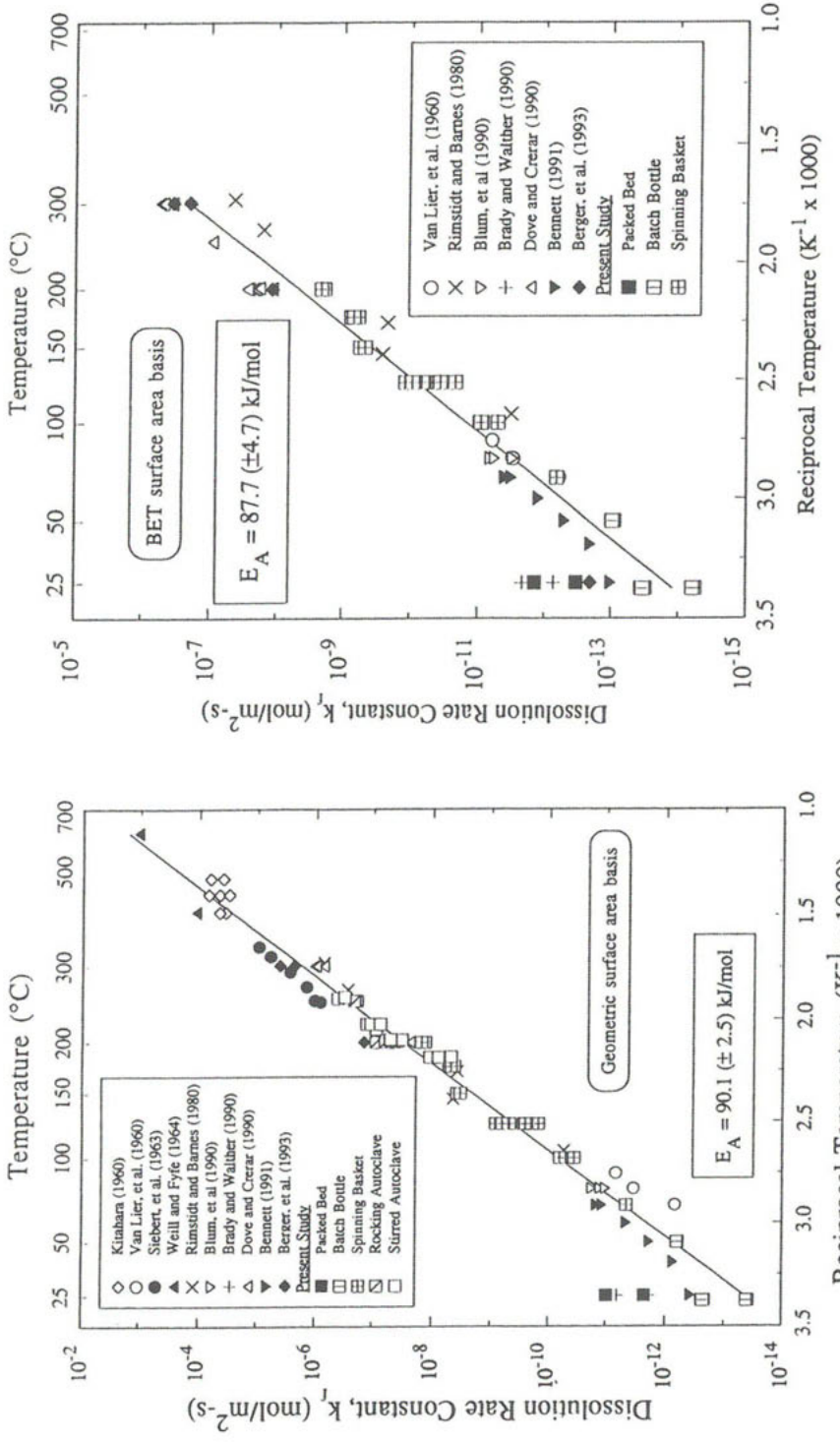


Figure 18. Quartz dissolution kinetics in pure water from 25° to 300°C using (a) a geometric surface area basis and Arrhenius coordinates; (b) BET-determined surface area basis and Arrhenius coordinates (from Tester et al., 1994).

EBSCOhost - printed on 2/13/2023 4:48 AM via . All use subject to https://www.ebsco.com/terms-of-use

precursor cristobalite nuclei are present and when silica concentrations are above cristobalite thermodynamic saturation. Like Rimstidt and Barnes (1980), they found that the activation energy for precipitation is similar to values determined for quartz and amorphous silica (see Table 4). This led them to conclude that all silica polymorphs precipitate by the same rate-limiting elementary reaction. Renders et al. (in review) also showed that the presence of cristobalite catalyzes the metastable precipitation of hydrothermal cristobalite. This has important implications for the quartz geothermometer (e.g., Arnórsson et al., 1983a,b) as cristobalite precipitation could lower *in situ* silica concentrations to result in significantly cooler predicted temperatures.

Catalysis by alkali cations. Numerous studies have qualitatively shown that the presence of alkali cations markedly increases the dissolution rate of quartz and amorphous silica (Diénert and Wandenbulcke, 1923; Sasaki, 1952; Van Lier et al., 1960; Weigel, 1964; Kamiya and Shimokata, 1976; Fleming, 1986). Recent work by Dove and Crerar (1990) quantified the magnitude of this effect on quartz dissolution in hydrothermal solutions. They showed that quartz dissolution rates at near-neutral pH are increased by a factor of 33 with the addition of as little as 0.05 molal sodium or potassium chloride solutions to deionized water at 100° to 300°C (Fig. 19a,b). Further, they found that the magnitude of this rate increase is cation-dependent where the effect of Na ≈ K > Li > Mg.

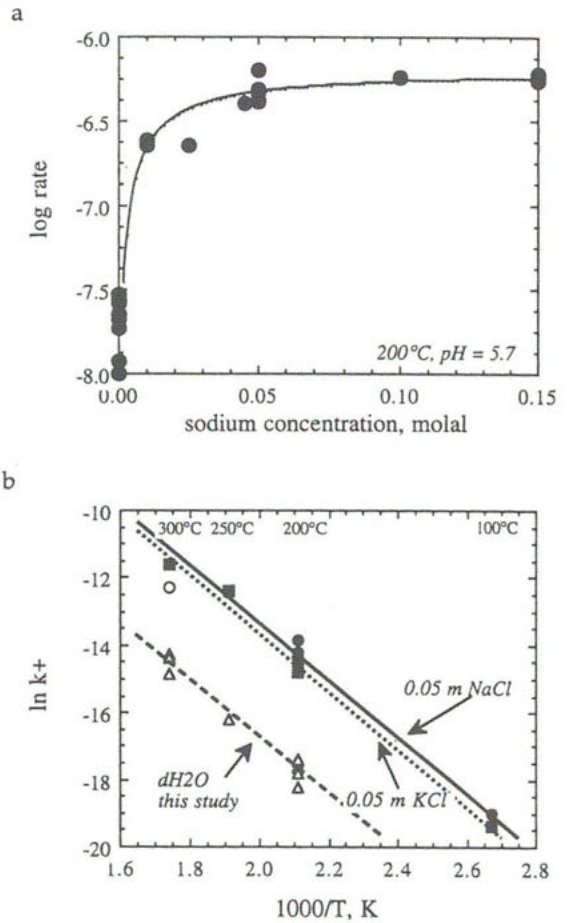


Figure 19. Electrolytes significantly increase the dissolution kinetics of quartz. (a) Effect of small NaCl concentrations on dissolution rate at 200°C. (b) Arrhenius plot of temperature-dependence of dissolution rate in deionized water, 0.05 molal NaCl and 0.05 molal KCl (from Dove and Crerar, 1990).

EBSCOhost - printed on 2/13/2023 4:48 AM via . All use subject to https://www.ebsco.com/terms-of-use

It has since been shown that alkali cations also enhance quartz and amorphous silica dissolution rates in near-neutral pH solutions at lower temperatures, albeit the effect declines with decreasing temperature. Bennett (1991) found that sodium and potassium chloride increase rates at 25° to 70°C by a factor of only 5 to 8. Likewise, Dove and Elston (1992) and Berger et al. (1994) determined that electrolytes cause a similar rate increase (factor of 6) for quartz dissolution at pH 6.5 to 7 and 25°C .

While little work has investigated the effect of electrolyte solutions on the precipitation kinetics of silica polymorphs, previous workers have shown that quartz precipitation rates increase as salinity increases (Corwin and Swinnerton, 1951; Laudise, 1959). Hosaka and Taki (1981a,b) found that quartz growth rates are faster in solutions of NaCl and KCl than in deionized water at 350° to 500°C. Like Dove and Crerar (1990), they also found that NaCl increased rates slightly more than KCl. At much more extreme electrolyte concentrations, Bohlmann et al. (1980) examined rates of silica deposition in reactors packed with several forms of silica (α–quartz, polycrystalline α-quartz, porous Vycor) in NaCl brine solutions at pH 5 to 8 and temperatures of 60° to 120°C. They found little difference between precipitation rates of silica in 0.09 and 1.0 molal NaCl , but increasing salt content to 4.0 molal increased dissolution rates by one order of magnitude. Kinetic interpretation of the data was complicated since much of the silica removal appeared to be dominated by nucleation onto the silica surfaces, but these experiments yielded a silica deposition rate that predicts rapid plugging of underground geothermal systems. This prediction is consistent with field observations when waste geothermal brines are reinjected into their host formations.

These reaction rate dependences of both dissolution and precipitation on simple dissolved components have profound implications for the accuracy of geochemical models as these numerical codes have often incorporated kinetic constants from dissolution experiments conducted in deionized water. Recent work quantifying the effect of simple salts suggests that predicted rates of silica dissolution from these models are likely much slower than what actually occurs in the natural surface waters or geothermal fluids that contain significant concentrations of Ca, Mg, Na and K. The rate-enhancing effect of alkali is also important for interpreting experimental studies. Cation-bearing solutions are often used in rate experiments to examine ligand effects (e.g., Bennett et al., 1988), control ionic strength or to buffer solution pH (e.g., Thornton and Radke, 1988; Knauss and Wolery, 1988; Schwartzentruber et al., 1987). Bennett (1991) offers a good example of the careful experimental design and analysis needed to separate clearly alkali effects from the reaction of interest.

Solution pH. Numerous studies have investigated both the general pH-dependent behavior of silica dissolution rates and specifics of behavior at particular ranges of solution pH. In general, the silica polymorphs appear to have a dissolution rate minimum near the zero point of net proton charge, ZPNPC, of pH 2 for silica. At both low temperatures (Liang and Readey, 1987; Knauss and Wolery, 1988; Wollast and Chou, 1988; Bennett, 1991) and hydrothermal temperatures (Dove and Crear, 1991; Berger et al., 1994) dissolution rates increase in solutions that are more acidic or basic on either sides of this pH minimum. In this discussion, we focus on rates measured in the pH range of about 2 to 12, which covers the most common solution pH's observed in natural systems. The reader is encouraged to consult Iler (1979) for discussions of silica reactivity in extremely acidic and basic solutions.

Baumann (1955) made perhaps the first observations of the pH-dependence of silica dissolution with a qualitative study of a commercial silica gel (Aerosil) at 30°C. Figure 20

EBSCOhost - printed on 2/13/2023 4:48 AM via . All use subject to https://www.ebsco.com/terms-of-use

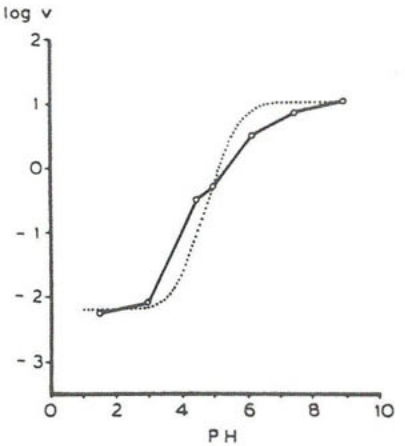
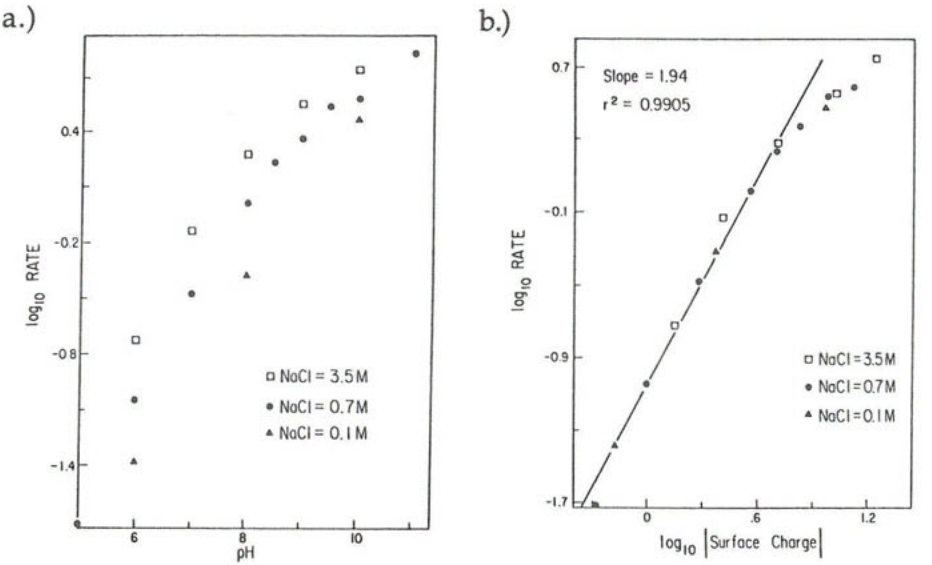


Figure 20 (left). Early work showing the pH dependence of Aerosil dissolution rates at 23°C (from Baumann, 1955).

Figure 21 (below). Dissolution rate (mol cm^{-2} s^{-1}) of amorphous silica in three concentrations of sodium chloride plotted as (a) a function of bulk solution pH, and (b) a logarithm of absolute surface charge (from Wirth and Gieskes, 1979).



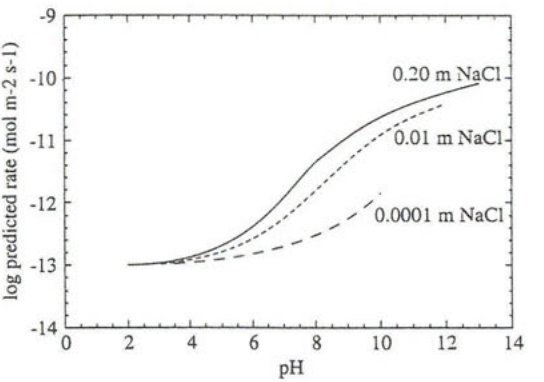


Figure 22. The predicted dissolution rates of quartz at 25°C as a function of pH and contoured by sodium concentration. The reaction rate is independent of cation concentration below approximately pH four (from Dove and Elston, 1992).

EBSCOhost - printed on 2/13/2023 4:48 AM via . All use subject to https://www.ebsco.com/terms-of-use

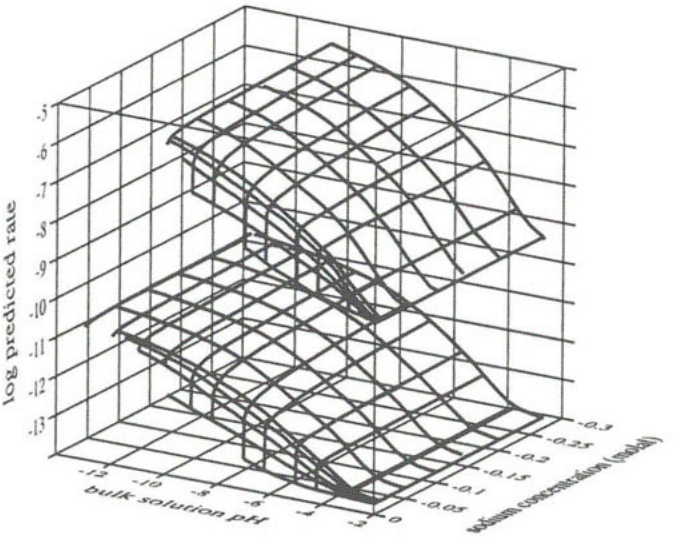
shows the general pH-dependence of dissolution where rates have a minimum near the ZPNPC of pH 2 for silica and increases exponentially until leveling off near pH 10. Studies of quartz dissolution rates versus pH have since shown similar trends in reactivity (Henderson et al., 1970; Knauss and Wolery, 1988; Wollast and Chou, 1988; Brady and Walther, 1990; House and Orr, 1992).

Silica dissolution behavior exhibits a complex rate dependence upon both pH and electrolyte concentration. Wirth and Gieskes (1979) noted the dependence of both parameters in measurements of vitreous silica dissolution rates. Figure 21a shows that rates of amorphous silica dissolution plotted versus solution pH show considerable scatter with variable sodium concentration. In contrast, these same data form the single trend shown in Figure 21b when rates are replotted in terms of calculated negative surface charge at the interface. A later analysis of the pH-dependence of quartz dissolution rate by Dove and Elston (1992) showed that a direct comparison of experimental values reported by seven laboratories showed a disconcerting amount of scatter among investigators. Recasting the reported rate data in terms of the influence of both solution pH and electrolyte concentration on the predominant negative surface complex distributions (see Fig. 12 and section on *Mechanisms*), most of the discrepancies between investigators could be explained by the pH-dependent influence of alkali cations contained in the pH and ionic strength buffers. This led to remarkable congruency among the data reported by seven laboratories using different sources of quartz and experimental methods. Figure 22 shows the complex pH- and alkali cation- rate dependence of quartz dissolution that resulted from this data analysis. More recently, Berger et al. (1994) conducted a parallel study of the effects of sodium and lead on quartz dissolution rate in conjunction with sorption studies of these same metals on silica surfaces. They observed a similar pH and cation dependence of quartz dissolution that held from 25° to 300°C. This is supported in Dove (1994).

Combined temperature, electrolyte and pH relations. The numerous kinetic studies of pH, temperature and electrolyte dependence that are listed in the previous discussions have been put together to develop a more comprehensive model of quartz reactivity. Dove (1994) combines new hydrothermal data with reported rate measurements to determine a general rate equation that quantifies reaction kinetics from 25° to 300°C in solutions having a pH_T (in situ pH at temperature of experiment) of 2 to 12, and 0 to 0.3 molal sodium. The rate equation gives a good fit to experimental data that span reaction rates over a range of 10^{11}. The expression has several properties suggesting robustness: It describes the pH dependence of dissolution rates, cation-specific effects observed at near-neutral pH, the diminishing effects of cations at higher solution pH, and the increasing rate-enhancing effects of alkali with increasing temperature. The expression also has a reaction order near one, implying first order behavior. The rate equation is based upon a surface reaction model that relates changes in modeled surface complexes to their reactivity in aqueous solutions (see later discussion of *Mechanisms*). The behavior of this predictive expression is illustrated for two temperatures in Figure 23.

Organic acids. Field evidence has suggested that high concentrations of dissolved silica are often found in association with organic rich environments. These environments include soil pore waters, oil field formation waters and lake and marine sediment pore waters. In a study of a glacio-fluvial sand aquifer that had been contaminated by crude petroleum, Bennett and Siegel (1987) found evidence for organo-enhanced complexing and reactivity of silica. They observed that quartz sand grains from uncontaminated and contaminated regions of the aquifer showed considerably different etching patterns. While uncontaminated quartz grains showed a complete lack of chemical etch pits, contaminated grains revealed the extensive development of triangular pits and a general roughening of the

EBSCOhost - printed on 2/13/2023 4:48 AM via . All use subject to https://www.ebsco.com/terms-of-use



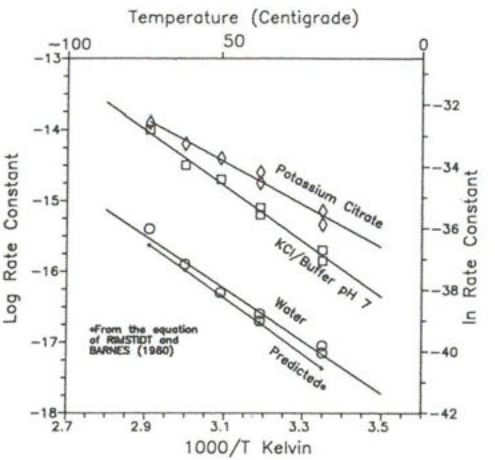


Figure 23 (above). The dissolution rate of quartz in solutions of variable pH_T and sodium concentration at two temperatures. The predicted rates at 25°C (lower surface) and 200°C (upper surface) show the dissolution behavior predicted by Equation (57). The observed pH-dependence of dissolution rate is low in pure water at 25°C but increases with either increasing sodium concentration or temperature (from Dove, 1994).

Figure 24 (left). The effect of potassium citrate, KCl buffer, and deionized water on the dissolution rate of quartz between 25° and 70°C (from Bennett, 1991).

surface. These observations led to experimental studies (Bennett et al., 1988) that quantified the rates of quartz dissolution in dilute solutions of salicylic, oxalic and humic acids. Citrate was found to increase dissolution rates by a factor of 8 to 10. Bennett (1991) later resolved individual contributions of these competing mixed organic-inorganic electrolyte solutions to silica reactivity as seen in Figure 24. Organic acids appear to increase dissolution rates by a factor of four by decreasing the activation energy 20% and increasing apparent quartz solubility.

Ferrous-ferric iron complexing. Field and laboratory observations of iron-stained quartz supports titration studies showing that iron binds strongly with silica surfaces. Iron may also affect silica reactivity. If true, this could be important to understanding the genesis of Banded Iron Formations as some studies have concluded that formation of these deposits was not controlled by the solubility of iron. Rather, BIF

EBSCOhost - printed on 2/13/2023 4:48 AM via . All use subject to https://www.ebsco.com/terms-of-use

development may have been controlled by the rate of quartz removal. Morris and Fletcher (1987) conducted experiments to test this hypothesis by measuring quartz solubility at 60°C in a series of iron and sodium-bearing solutions over a pH range of 4 to 8.6. Figure 25a shows that fine grained quartz ($A_{sp} = 0.22\ m^2\ g^{-1}$) exposed to starting solutions containing ferrous iron for 1 to 9 days became significantly more soluble following an 'oxidizing period'. In this period samples were aerated continuously with bubbling oxygen and without significant abrasion of the quartz grains. The observed increases in solubility were further enhanced by delaying the oxidizing period to later times. Although the results are somewhat difficult to interpret, the data clearly suggest a significant effect on apparent solubility or dissolution rates.

Morris and Fletcher (1987) suggested that these effects on quartz reactivity are caused by surface reactions of iron with silica. Figure 25b shows their proposed multistep reaction of ferrous iron with the quartz surface, exposure to oxidizing conditions, then re-exposure to reducing conditions. If the effects are real, they could also be important to understanding silica mobility in a range of modern environmental settings where soil and groundwaters undergo alternating reducing and oxidizing conditions.

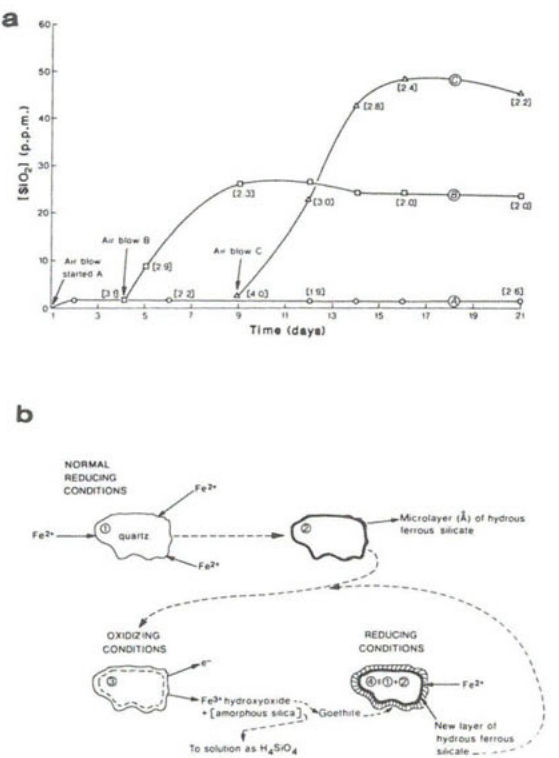


Figure 25. (a) Experimental data for silica accumulation during quartz dissolution at 60°C in solutions containing ferrous iron and an initial pH of 6.6. A indicates aeration at the start of the experiment, B, aeration after 4 days of reaction, and C, aeration after 9 days of reaction. pH values are shown in square brackets. (b) Proposed reaction of iron with quartz surfaces: (1) quartz reacts with ferrous iron in groundwater to form a hydrous ferrous iron/silica surface layer; (2) layer breaks down under oxidizing conditions to a goethite precursor, (3) silica is released to solution (both from Morris and Fletcher, 1987).

EBSCOhost - printed on 2/13/2023 4:48 AM via . All use subject to https://www.ebsco.com/terms-of-use

Trivalent metals. It is qualitatively well-documented that minute concentrations of aqueous aluminum as well as other bi- and trivalent metals can dramatically affect the surface properties, apparent solubility and dissolution of quartz, biogenic silica, and amorphous inorganic silica (Lewin, 1961; Iler, 1973). The scientific significance of these interactions for diverse natural and engineered systems led to extensive studies of silicic acid chemistry in natural waters, biological systems, soil systems and industrial processes (Lewin, 1961; Matijevic et al., 1971; Allen and Matijevic, 1971; Hem et al., 1973; Hurd, 1973; Brown and Hem, 1975; Jardine, 1985a, 1985b; many others). Table 5 lists several ions found to decrease rates of dissolution for many of the SiO_2 polymorphs. Of these, aluminum and ferric iron (previously discussed) occur the most extensively in natural environments, albeit in low concentrations for the pH range of most natural waters. Estimates of the reduction in dissolution rates by aluminum range from three to eight orders of magnitude (Hurd, 1973). New work is integrating quantitative kinetic and surface geochemical studies at low and hydrothermal temperatures to understand the rates and mechanistic controls of aluminum on silica reactivity (e.g., Dove et al., 1994).

Etch pit development

Dissolution under sufficiently undersaturated conditions results in the formation of etch pits on the mineral surface. If the silica mineral is unstrained the free energy of

Table 5. Experimental investigations reporting ions qualitatively observed to inhibit the dissolution kinetics of the SiO_2 polymorphs.

Reference	*Polymorph, silica-rich phase*
Al^{3+}	
Lewin (1961)	diatoms
Jones and Handreck (1963)	monosilicic acid, natural soil
Wiegel (1961)	silica glass
Iler (1973)	amorphous silica
Hudson and Bacon (1958)	sodic glass (71% silica)
Ballou et al. (1973)	silica glass (96% silica)
Fe^{3+}	
Lewin (1961)	diatoms
Jones and Handreck (1963)	monosilicic acid, natural soil
Wiegel (1961)	silica glass
Hudson and Bacon (1958)	sodic glass (71% silica)
Ballou et al. (1973)	silica glass (96% silica)
Zn^{2+}	
Wiegel (1961)	silica glass
Hudson and Bacon (1958)	sodic glass (71% silica)
Cu^{2+}	
Wiegel (1961)	silica glass
Hudson and Bacon (1958)	sodic glass (71% silica)
Be^{2+}	
Lewin (1961)	diatoms
Hudson and Bacon (1958)	sodic glass (71% silica)
Ga^{3+}, Gd, Sc, Ti^{4+}, Y, Yb	
Lewin (1961)	diatoms

EBSCOhost - printed on 2/13/2023 4:48 AM via . All use subject to https://www.ebsco.com/terms-of-use

formation of an etch pit in the mineral's surface, ΔG_p, is the sum of the free energy driving the dissolution, ΔG_v, and the work needed to create the new surface area of the etch pit, ΔG_s (Lasaga and Blum, 1986; Brantley et al., 1986):

$$\Delta G_p = \Delta G_v + \Delta G_s = \frac{\pi r^2 a RT ln\left(\frac{c}{c_o}\right)}{V} + 2\pi r a \sigma \quad (44)$$

where r is the radius of the pit, a is the depth of the pit, c is the concentration of silica in solution, c_o is the equilibrium solubility of the silica mineral, V is the molar volume of the silica mineral, R is the gas constant, T is temperature in Kelvins, and s is the surface free energy of the mineral. According to this equation, there is always a free energy barrier to the growth of etch pits in undeformed silica minerals, but the magnitude of this barrier decreases as the solution becomes more and more undersaturated (see Fig. 1a in Brantley et al., 1986). There is an additional source of free energy, ΔG_d, in deformed crystals that is present where dislocations intersect the surface so that Equation (44) aquires an additional term:

$$\Delta G_p = \Delta G_v + \Delta G_s + \Delta G_d = \frac{\pi r^2 a RT ln\left(\frac{c}{c_o}\right)}{V} + 2\pi r a \sigma - \frac{a K b^2 ln\left(\frac{r}{r_o}\right)}{4} \quad (45)$$

where K is an energy factor, b is the Burgers vector of the dislocation, and r_o is the radius of the dislocation core. See Lasaga and Blum (1986) for an extensive discussion of ways to model the ΔG_d term. The ΔG_d term has the effect of removing the barrier to nucleation of etch pits for low values of c/c_o so that etch pits easily nucleate and spontaneously grow. Brantley et al. (1986) determined that for quartz in water at 300°C etch pits would nucleate and spontaneously grow when $c/c_o < 0.75 \pm 0.15$. Thus, silica phases in contact with highly undersaturated aqueous solutions will develop etch pits at places where dislocations outcrop on the crystal surface. Above some critical degree of undersaturation, $c/c_o > 0.75$, there is little or no etch pit formation.

Recent work on the kinetics of etch pit development on quartz surfaces led to the *negative crystal method* for isolating the rates of dissolution of specific crytallographic faces (Gratz et al., 1990). Figure 26 shows four types of etch pit features that are produced when quartz is reacted in alkaline solutions. Gratz et al. (1990) estimated dissolution rates of individual negative crystals by measuring the sizes of individual crystals during a sequence of dissolution steps. This method has powerful advantages over other studies that measure rates by changes in bulk solution composition in that it acknowledges the large variations in dissolution rate with crystal orientation and cracks. With recent developments in scanning probe microscopy, this direct observational method for estimating reaction rates has become more practical for a wider range of materials. Using scanning force microscopy (SFM), Gratz et al. (1991) showed that monolayer steps (Fig. 27) can be observed in the floors and walls of etch pits such as those in Figure 26. These types of SFM studies will certainly lead to a better understanding of surface controls on silica and other mineral reactivities in the future. Gratz and Bird (1993a,b) further advanced these ideas with a rate law describing the dissolution kinetics of all single crystals and powders in terms of surface roughening and the mathematics of monolayer step motion.

Surface and mechanistic controls on reactivity

Numerous experimental and theoretical studies of silica polymorph reactivity in aqueous solutions have led to some consensus on the mechanism of silica nucleation, growth and dissolution. This discussion of mechanisms draws from the earlier description

EBSCOhost - printed on 2/13/2023 4:48 AM via . All use subject to https://www.ebsco.com/terms-of-use

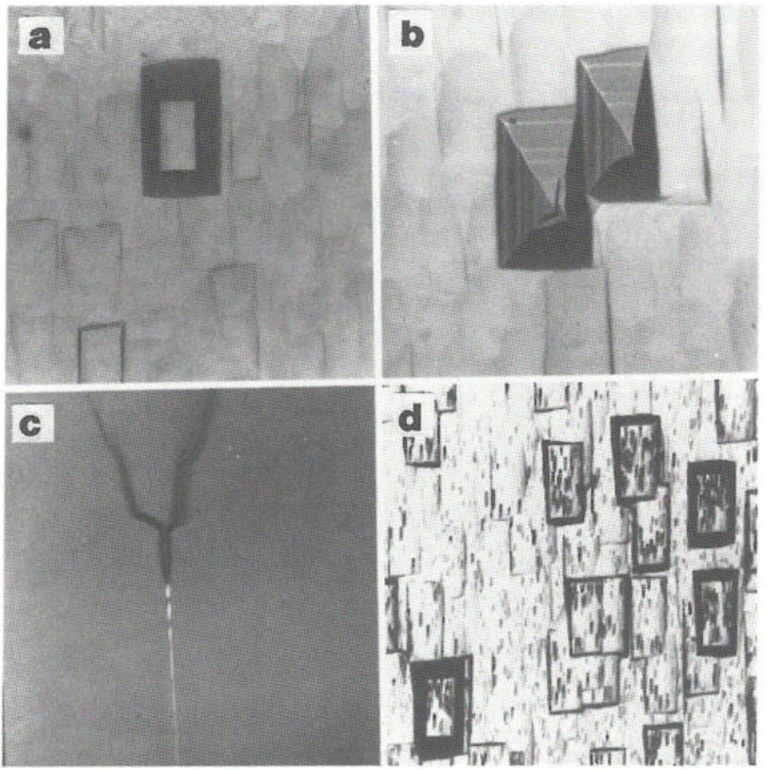


Figure 26 (above). Features produced by etching prismatic faces of quartz in alkaline solution: (a) large negative crystal—a flat bottomed pit with crystallographic walls; (b) two jumbo pits—large depressions with pointed centers and curved walls; (c) etch tunnel undercutting the surface; and (d) abundant small pits superimposed on negative crystals. All figures are scaled to the 100 micron bar shown in (c) (from Gratz et al., 1990).

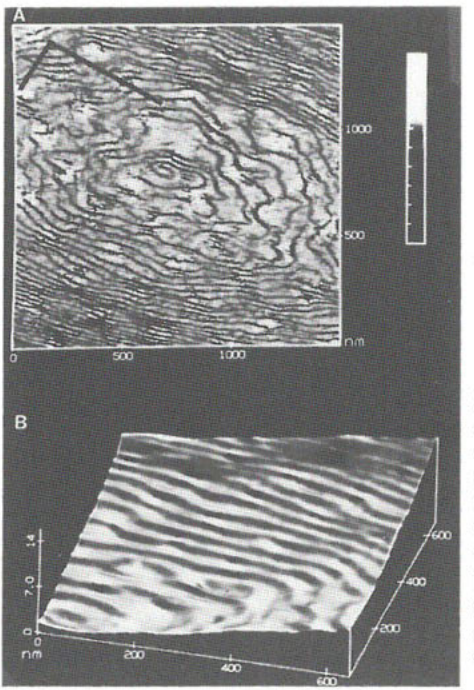


Figure 27 (left). SFM images of a microscopic quartz etch pit formed at 148°C, then scanned in ethanol with $<10^{-8}$ Newton of applied force (from Gratz et al., 1991). (A) Map view of an etch pit that is image-enhanced to show the edges between topographic levels. Image area is 1490 × 1490 nm with a height difference of 20 nm between the bottom of the pit and the highest edge of the surface. (B) Surface plot of one quadrant of the etch pit. Image size is 650 × 650 × 14 nm (used with permission of authors).

EBSCOhost - printed on 2/13/2023 4:48 AM via . All use subject to https://www.ebsco.com/terms-of-use

of the silica-water interface to emphasize the roles of mineral surface charge and coordination chemistry in reactivity, surface-solvent interactions and reaction processes.

Development of surface complexation models of dissolution. The work of Wieland et al. (1988) established surface coordination chemistry as a basis for correlating the surface-controlled dissolution kinetics of many oxides and silicate minerals and materials with observed pH-dependence of dissolution. They proposed that general surface-controlled dissolution can be represented by the simplified multistep reactions

$$>M + L(aq) = >ML \quad (46)$$

$$>ML = >ML^{\ddagger} \quad (47)$$

$$>ML^{\ddagger} = ML(aq) \quad (48)$$

and the dissolution rate, r, is generally proportional to the surface concentration of the precursor site, [>ML], such that

$$r = k\,[>ML]. \quad (49)$$

This approach produces a more satisfactory description of the pH dependence of mineral dissolution than rate laws based on proton activities in solution such that

$$r = k\,[H^+]^n \quad (50)$$

where r and k are the experimental dissolution rate (mol m^{-2} s^{-1}) and rate constant, respectively. The rate constant typically exhibits a fractional dependence upon reaction order, n. Wieland et al. (1988) predicted that surface complexation models (see Silica-Water Interface) would "prove to be essential tools for the quantitative description of reactive surface species in dissolution". While equilibrium surface complexation models are finding success in describing the solution-composition dependence of silica (and other mineral) dissolution kinetics, it is important to keep in mind that these rate equations still employ only simple correlations between equilibrium surface complexes and do not represent actual stoichiometries.

The first applications of surface complexation concepts to describing silica reactivity predates Wieland et al. (1988). A study by Wirth and Gieskes (1979) found that the logarithm of the dissolution rate of vitreous silica in solutions having a pH range of 5 to 11 correlated linearly with the logarithm of the net negative surface excess charge (as $[>OH^-]$) with a slope of 1.94, suggesting a second order dependence of reaction. They also showed that different dissolution rates measured for solutions containing different sodium concentrations, but similar pH, could be condensed into the single trend shown in Figure 21b. Similar findings were reported by Fleming (1986) who measured the pH and salt dependence of amorphous silica (Ludox) polymerization kinetics. Rates of aqueous silica condensation were described in terms of the surface concentration of negatively charged >SiO- complexes:

$$r \propto k_O A\ [SiO^-]C \quad (51)$$

where the rate is described by the rate constant, k_O , in mol sec^{-1}, surface area of the reactant, A,, surface concentration of the ionized surface sites, $[SiO^-]$ and the reaction affinity, A.

Brady and Walther (1990) showed that quartz dissolution rates also correlate with negative surface charge. They related surface speciation at the quartz-solution interface to the kinetics of dissolution as a function of solution pH and salt concentration to write a rate

EBSCOhost - printed on 2/13/2023 4:48 AM via . All use subject to https://www.ebsco.com/terms-of-use

equation as a sum of near-neutral pH (assumed proportional to the detachment rate of >SiOH) and basic pH mechanisms:

$$r = k_n [\text{SiOH}] + k_b [\text{SiO}^-] \quad (52)$$

where k_i is the dissolution rate constant and surface concentrations are given as the number of species per unit area. Like Wirth and Gieskes (1979) and Bohlmann et al. (1980), the data suggest that the reaction order approaches two at higher solution pH.

A similar rate expression is based on a multiple activated complex (MAC) model to include a variety of activated complexes (Hiemstra and van Riemsdijk, 1989a,b; Hiemstra and van Riemsdijk, 1990). These complexes were hypothesized as silica species that were singly, doubly and triply bound to the surface. Using their approach, only two protonation reactions (16) and (18) were required to describe reactions occurring over the pH 0 to 14 range. This gave the rate equation

$$r = k_{r1} \{[\text{SiO}^-]^n + [\text{SiOH}_2^+]^n\} + k_{r2} [\text{SiOH}^0]^n. \quad (53)$$

By setting the reaction order, n, to assume first or second order behavior, they fitted the reaction rate constant. They found that different reaction orders for [SiO^-] were required to fit rate data from different investigators. For example, the Knauss and Wolery (1988) and Wollast and Chou (1987) quartz dissolution rate data fit Equation (53) if they assumed second or first order behavior, respectively.

An analysis of quartz dissolution rate data at 25°C by Dove and Elston (1992) also found that a single reaction order could not describe the reported rates of multiple investigators. They used a surface reaction model similar to Hiemstra and van Riemsdijk (1990) to suggest that dissolution rates have both a first and second order dependence upon $\theta_{>\text{SiOtot}}$, the fractional sum of >SiO^- and >SiO^-Na^+ complexes by the rate expression

$$r = k_1 [>\text{SiOH}]^* + k_2 [>\text{SiO}_{\text{tot}}]^1 + k_3 [>\text{SiO}_{\text{tot}}]^2 \quad (54)$$

where $\theta_{>\text{SiOH}}$ is the fraction of >SiOH surface complexes and * indicates that the reaction order dependence on this species is ill-determined (but likely first order).

These studies investigated dissolution rate behavior and surface charge dependence over numerous small ranges of solution composition and/or temperature. A single comprehensive model describing all of these effects (Dove, 1994) combined the rate data from these individual studies with new rate data and supporting evidence from the surface chemistry literature to extend these surface reaction models (See section on *Combined temperature, pH, sodium relations*) to obtain:

$$r = k_{>\text{SiOH}} \left(\theta_{>\text{SiOH}}\right)^{n_{>\text{SiOH}}} + k_{>\text{SiO}^-_{\text{tot}}} \left(\theta_{>\text{SiO}^-_{\text{tot}}}\right)^{n_{>\text{SiO}^-_{\text{tot}}}} \quad (55)$$

where

k_i = rate constant for the reaction of surface species i,

n_i = reaction order of surface species, i

$\theta_{>\text{SiOH}}$ = fraction of total surface sites occupied by hydrogen ion as >SiOH,

$\theta_{>\text{SiO}^-_{\text{tot}}}$ = sum of the fractions of total sites existing as deprotonated >SiO^- site and as a complex with sodium ion interaction as >$SiO\text{-}Na^+$.

The temperature dependence of Equation (55) is introduced by expanding the rate constants, k_i, into their components per Equation (39) for mineral-solution reactions. It is not straightforward to determine the temperature dependence of the hydrothermal kinetic data because the mineral surface complex distributions (i.e., $\theta_{>\text{SiOH}}$) cannot be directly

EBSCOhost - printed on 2/13/2023 4:48 AM via . All use subject to https://www.ebsco.com/terms-of-use

measured. Existing surface complexation models have been developed from titration experiments conducted at 25°C and so the behavior of these complexes is still largely unknown at hydrothermal temperatures. Dove (1994) estimated surface site complex distributions at higher temperatures by making the following assumptions:

- total surface site number remains constant with changing temperature,
- distributions of surface complexes are primarily controlled by the relative magnitudes of the surface association constants,
- these distributions are, in turn, primarily controlled by changes in the dissociation constant of water with temperature (Lyklema, 1987; Fokkink et al., 1989; Blesa et al., 1990; Brady, 1992),
- therefore, site *distributions* at the *in situ* pH at temperature (pH_T) remain approximately constant.

Thus, equilibrium surface complex distributions can be estimated for the temperature of each experiment by using pH_T and the association constants of Equations (16) and (17).

The regression fit of rate data and the corresponding site distributions for each experiment listed in Dove (1994) obtained estimates of five parameters for the expression

$$r = \exp^{-10.7\pm1.1}T \ \exp\left(\frac{-66.0\pm2.3}{10^{-3}RT}\right)\left(\theta_{>SiOH}\right)^{1} + \exp^{4.7\pm0.8}T \ \exp\left(\frac{-82.7\pm2.1}{10^{-3}RT}\right)\left(\theta_{>SiO^-_{tot}}\right)^{1.1\pm0.06} \quad (56)$$

where the dissolution rate in mol m^{-2} s^{-1}. The '±' values give two standard errors of each estimate. The reaction order associated with $\theta_{>SiOH}$, was indeterminate from the fitting procedure but is inferred to equal one from investigations of quartz dissolution rates and probable reaction mechanisms (Rimstidt and Barnes, 1980; Lasaga and Gibbs, 1990; Berger et al., 1994). Equation (56) describes quartz dissolution rates from 25° to 300°C for pH 2 to 12, variable ionic strength, and sodium concentrations from 0 to as high as 0.5 molal. The first and second terms in Equation (56) contributes to total reaction rate at the solution composition where the corresponding surface complexes are predominant. That is, the first term largely describes rates at acidic solution pH near the ZPNPC. The second term describes dissolution rates in higher pH solutions and the contribution of alkali cations to reactivity.

Although Equation (56) is an empirical description of quartz dissolution kinetics, it has properties suggesting robustness. First, a comparison of measured and predicted rates for seven temperatures illustrates the generally good quality of this expression over reaction rates spanning a factor of 10^{11} (Dove, 1994). The model predicts dissolution rates in variable solution compositions and temperatures including the numerous data at 25°C and extends to give dissolution rates comparable to estimates at 385° to 430°C by Murphy and Helgeson (1989). Second, the reaction order associated with the $>SiO^-_{tot}$ term is near one, implying first order behavior. This near-integer value suggests physical meaning. Third, estimates of apparent enthalpy and entropy associated with the higher pH conditions (where the $>SiO^-_{tot}$ term dominates rates) give good agreement with other investigations (see later discussion). Finally, the good quality of fit is also manifested by the model's ability to predict large increases in dissolution rate with the introduction of sodium ion to solutions having near-neutral pH and by the smaller effect at higher pH. Figure 23 illustrates the relationship between sodium chloride concentration and the dissolution rate of quartz at near-neutral pH. Plotting the rate predicted by Equation (56) for two temperatures as surfaces, shows that the ability of sodium to increase dissolution rates at near-neutral pH is temperature dependent. This is consistent with observations that sodium has only a small

EBSCOhost - printed on 2/13/2023 4:48 AM via . All use subject to https://www.ebsco.com/terms-of-use

effect on quartz dissolution rate at 25°C compared to hydrothermal temperatures (see *Catalysis by Alkali Cations*).

The terms in Equation (56) describe the *combined* reactions leading to and including the formation of an activated complex and so is necessarily empirical. It gives no indication of reaction stoichiometry, water properties, attachment geometry or specific site chemistry for individual rate-limiting reactions. These processes must be evaluated with evidence external to the dissolution rate data. While this method is still an indirect approach to describing the detailed reactivity of surface bonds, it is an improvement over rate models which correlate reaction rates with solution composition parameters (i.e., pH) or bulk surface charge. Ideally, we would like to relate changes in quartz reactivity to detailed changes in electronic structure of mineral surfaces. However, this is not yet possible. As a beginning, this representation provides a means of relating reaction rates to average surface compositions to relate the site fractions of the modeled surface complexes to quartz reactivity. The end result quantifies silica dissolution rates in solutions of variable pH and sodium concentration and provides insight into mechanisms of solvent-surface controls on reactivity.

Solvent-surface controls on reactivity. From the most simple view of dissolution and precipitation, silica polymorph reactivity in aqueous solutions is determined by interactions with the solvent near the mineral-solution interface in hydration-dehydration reactions. Dove (1994) describes the dynamic changes in surface and solvent behavior that occur with changing solution composition. The net result of this behavior is its close correlation with the reported pH and solute dependencies of quartz dissolution rates. Three aspects are summarized here:

• *Dissolution rates mimic net surface charge and solvent behavior at interface.* At the slow reaction rates associated with a low solution pH and and thus, a relatively uncharged surface (see Fig. 12), surface charge and potential are small and will have little influence on the structure of water near the surface compared to bulk water (Conway, 1981). Under these conditions, hydrogen bonding among the water molecules themselves and between the water molecules and >SiOH groups at the surface control structure (Eisenberg and Kauzmann, 1969; Tait and Franks, 1971; Klier and Zettlemoyer, 1977). This view of the interface is supported by dielectric constant measurements of water at low field strengths that are approximately equal to the bulk value of 78 (Davies and Rideal, 1963). Extensive intermolecular hydrogen bonding results in a relatively large proportion of molecular water adjacent to the surface (Bérubé and deBruyn, 1968; Zhu and Robinson, 1991) and is the primary species available for reaction. The weak nucleophilic properties of molecular water are manifested by the relatively slow dissolution rate of quartz in low pH solutions (Casey et al., 1990). The low entropy change associated with this environment is suggested by the low value of the preexponential in the first term of Equation (56) and its correspondingly low $\Delta S_{xp,>SiOH}$ (-244 J mol^{-1} K^{-1}). This low value of ΔS_{xp} is supported by House and Hickenbotham (1992) and Gratz and Bird (1993). It has been proposed that in this environment, the electronegative oxygen of water is the primary reactant in a mechanism where the interaction of oxygen with a surface silicon atom forms a silicon-oxygen complex having five-fold coordination with oxygen (Lasaga and Gibbs, 1990). (See later Fig. 30 for a possible rate-limiting mechanism for the hydrolysis by molecular water.) At very acidic (positive surface charge) and ZPNPC (net neutral surface charge) solution pH, this mechanism may dominate by reaction of the electronegative oxygen of the water dipole with the quartz surface. If true, this may also explain the lower observed $\Delta H_{xp,>SiOH}$ of 66 kJ mol^{-1} (Dove, 1994) since little additional energy of water dissociation is involved.

EBSCOhost - printed on 2/13/2023 4:48 AM via . All use subject to https://www.ebsco.com/terms-of-use

At higher solution pH, the accumulated negative charge (see Fig. 12) results in increased polarization of the solvent (Fig. 12). Increased negative charge affects near-surface water structure to induce a locally different pH at the mineral-solution interface (e.g., Dove, 1994). This increased ionization of water is confirmed by dielectric measurements of water at high field strengths showing a decreased dielectric constant to values near eight (Davies and Rideal, 1963). This environment is also suggested by the larger pre-exponential term, A, shown in Equation (56). The increase in preexponential from the first and second terms is indicative of a change in the reaction mechanism and/or the properties of the surface-solution interface. Equation (39) shows that increases in the pre-exponential must be derived from increases in the product of the activity coefficients, C_S, X_{H_2O}, or ΔS. Although individual contributions of these terms cannot be evaluated from dissolution rate data, it appears that ΔS is the only term that can make significant contributions to the larger $A_{>SiO^-_{tot}}$. Dove (1994) suggests that high interfacial charge gradients promote reorientation of water in the interfacial environment by affecting local solvent dissociation or rates of near-surface solvent exchange. This is supported by IR studies showing that water molecules at quartz-water interfaces have a strong orientational and bond ordering dependence upon solution pH and sodium concentration (Du et al., 1994).

Another indication that interfacial water properties are important to dissolution are the diminishing cation-specific effects observed at higher solution pH. At near-neutral pH, cation-specific effects on dissolution rate were observed by Dove and Crerar (1990) where rates increased by a factor of 6 to 25 from solutions containing lithium or magnesium to sodium or potassium. In contrast, rates measured by Gratz et al. (1990) conducted at pH 12 found that dissolution rates in solutions containing lithium, sodium, or potassium are similar within a factor of two. This difference is predicted by Dove (1994) which suggests that at conditions of higher surface charge, or where solution pH is greater than near-neutral, transition to faster dissolution mechanism is nearly complete, and the second term of Equation (56) controls dissolution rates at these conditions. Thus, cation specific effects are expected to diminish at higher solution pH because of smaller differences between the hydration properties of cations impose little additional effect on water striction and polarization to promote further the hydroxyl dominated reaction (e.g., examine Fig. 12).

One proposed mechanism for a hydroxide-surface interaction is the oriented sorp-tion of the proton of a hydroxyl group onto the bridging oxygen of a >Si-O-Si< surface group. Experimental evidence for the reactivity of a bridging oxygen at silica surfaces has been reported (Morrow and Cody, 1975; Morrow and Cody, 1976a,b; Foley, 1986; Gallei and Parks, 1972). Molecular orbital and ab initio calculations of silicon-oxygen-bonded analogs estimate that a bridging oxygen bears a net negative charge ranging from -0.7 to -0.9 esu (deJong and Brown, 1980; Geerlings et al., 1984; Foley, 1986) and is sensitive to adsorbing molecules (Mortier et al., 1984). Susceptibility of negative charge at the bridging oxygen to a hydrogen ion in proximity to the surface at a charged interface suggests that hydrolysis could involve proton or oriented hydroxyl sorption at the bridging oxygen. *Ab initio* calculations indicate that the process is accompanied by a net flow of charge from the bridging oxygen to the proton (Ugliengo et al., 1990). Following this step, redistribution of electronic charge may permit a reaction of oxygen (as hydroxide?) with the adjacent silicon atom to form a five-coordinated transition state complex (Fig. 30). Casey et al. (1990) called for early transfer of hydrogen to a bridging oxygen, followed by nucleophilic attack of silicon by hydroxyl ion. These mechanisms may involve higher net energies as water dissociation is folded into the apparent enthalpy (and entropy). This is consistent with the larger observed $D\!H_{>SiO^-_{tot}}$ discussed earlier.

EBSCOhost - printed on 2/13/2023 4:48 AM via . All use subject to https://www.ebsco.com/terms-of-use

• *Dissolution rates in alkali cation solutions correlate with $\Delta G_{hy,cation}$.* Dove (1994) suggested an indirect role for alkali cations in enhancing quartz dissolution rates by affecting solvent properties to promote a faster reaction mechanism involving hydroxyl ion. Fokkink et al. (1990) suggested that cadmium ions (having similar behavior to alkali cations) are 'stuck' in the interfacial region in a passive way by their waters of hydration and weak attraction for the surface. This 'ion-pair' surface-interaction results in partial release and polarization of low-entropy waters of hydration (Conway, 1981) to affect water dissociation to a degree proportional to the free energy of hydration, ΔG_{hy}, of each alkali cation. Alkali cations added to a solution at near-neutral pH may behave similarly as hydrated cations in the negatively charged interface by their weak association with the surface. At pH conditions where interfacial charge is sensitive to the addition of alkali (see Fig. 12), it would be expected that dissolution rates would be sensitive to the hydration properties of individual alkali ions. This was observed by Wijnen et al. (1990), who found a relationship between the hydration properties of cations and the dissolution rates of silica gel. This relationship is again observed for cation-specific quartz dissolution rates. Figure 28 shows that rates of quartz dissolution in solutions containing a variety of alkali cations correlate with ΔG_{hy} of the corresponding alkali cation. Extrapolating this trend to a zero ΔG_{hy} (standard state for proton) yields $10^{-13.2}$ mol m^{-2} s^{-1}. This value is very close to the predicted rate of $10^{-12.9\pm0.7}$ mol m^{-2} s^{-1} at 40°C for pure water (Dove, 1994) and also near to 40°C rates measured by Bennett (1991), Tester et al. (1994) and predicted by Rimstidt and Barnes (1980) and Dove and Elston (1992).

• *Temperature dependence of alkali catalysis correlates with surface interaction strengths.* The increasing catalysis of silica dissolution rates by alkali cations with increasing temperature was described earlier. Processes responsible for this behavior were investigated by Berger et al. (1994). They conducted experiments comparing the effect of sodium and lead ion on quartz dissolution rates (25°, 200°, 300°C) in parallel with adsorption experiments (25°, 150°C) of the same cations on amorphous silica surfaces. These data compared results of quartz and amorphous silica studies with the assumption that degree of crystallinity of the polymorph does not change the nature of the chemical reactions at the solid-solution interface.

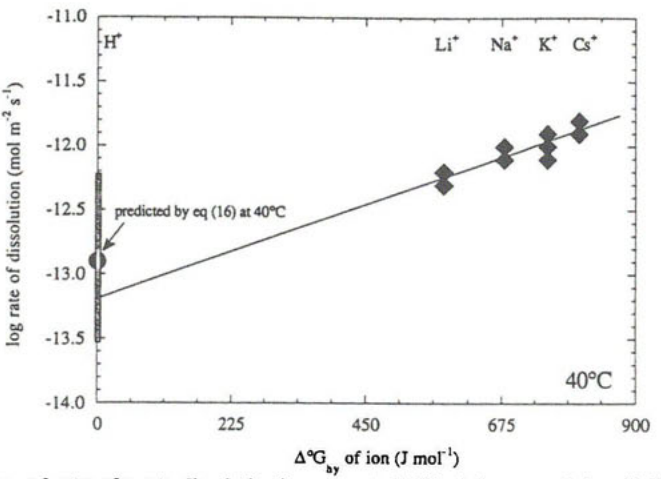


Figure 28. Measured rates of quartz dissolution in near-neutral pH solutions containing alkali metal cations correlate with the standard free energy of hydration of the ion. This trend extrapolates to the dissolution rate of quartz in the absence of cations by predicting a rate of $10^{-13.2}$ mol m^{-2} s^{-1} for pure water in good agreement with $10^{-12.9}$ predicted by Equation (57) for rates at 40°C. The shaded area indicates the 95 percent confidence interval for the predicted rate in DIW (from Dove, 1994).

EBSCOhost - printed on 2/13/2023 4:48 AM via . All use subject to https://www.ebsco.com/terms-of-use

The Berger et al. (1994) sorption experiments revealed a surprising change in the behavior of sodium sorption on silica surface with increasing temperature. Figure 29a shows that at 25°C , sodium sorption edges shift with increasing concentration, suggesting that sodium interacts only weakly with the surface and is easily displaced by either an ionic strength effect or by other electrolytes or protons (see Fig. 11a,b). This behavior is indicative of 'outer sphere' sorption of the metal, meaning that the cation interacts only weakly with the surface through its primary (and perhaps secondary?) solvation layer(s). In contrast, Figure 29b shows that sodium exhibits a much different sorption behavior at 150°C . The sodium sorption edge is now independent of ionic strength (if metal ions are absent, which still out-compete sodium for surface interaction). This implies an important change in the sodium-silica surface speciation with increasing temperature and suggests that the hydration energy is lower and the solvation sphere is lost upon sorption. Thus, at higher temperatures, sodium displaces protons for specific surface adsorption. These

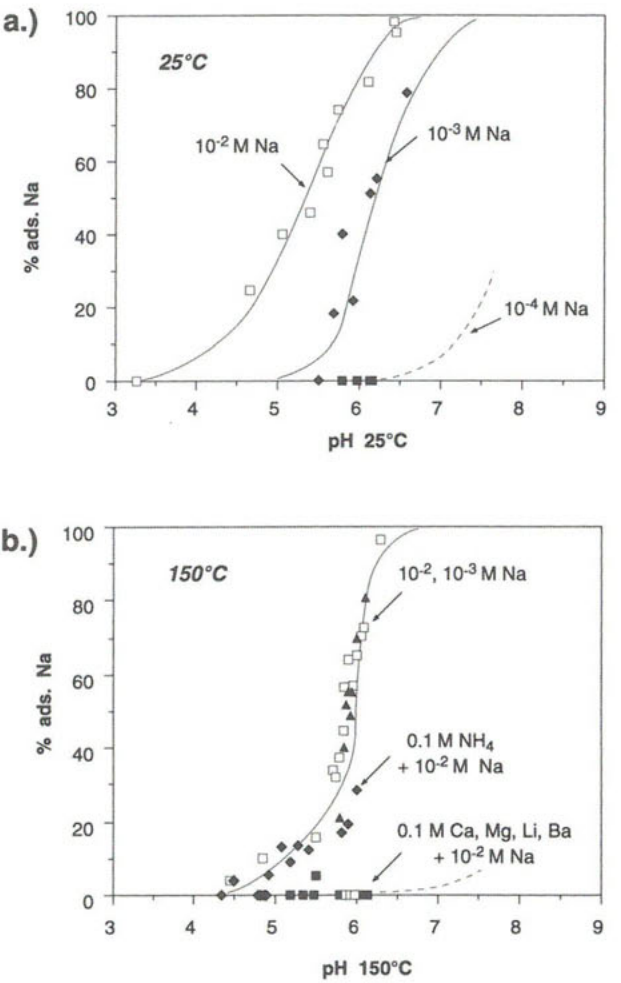


Figure 29. Adsorption isotherms of sodium and lead on amorphous silica powder at (a) 25°C, and (b) 150°C from nitrate-bearing solutions of variable ionic strength (from Berger et al., 1994).

EBSCOhost - printed on 2/13/2023 4:48 AM via . All use subject to https://www.ebsco.com/terms-of-use

findings directly support the mechanistic model proposed in Dove and Crerar (1990) for quartz dissolution rates at hydrothermal temperatures. Berger et al. (1994) suggest that this transition in sorption behavior is directly responsible for the increasing catalysis by sodium with increasing temperature. They predict similar alkali-dependent dissolution rates for amorphous silica.

A somewhat different, but related interpretation of the temperature dependence of sodium catalysis is suggested by Dove (1994). This study found consistency in the data by assuming that changes in surface association constants were directly related to the temperature dependent changes in the association constant of water. Measured and predicted rates show that the $>SiO^-_{tot}$ term in Equation (56) increasingly dominates bulk reaction rates with increasing temperature. Equation (56) suggests that this behavior is caused by the increasing contribution of $T\Delta S_{>SiO^-_{tot}}$ to the overall reaction rate. This is consistent with the behavior of an endothermic reaction and could indicate a transition in either the reaction mechanism or solvent and/or cation behavior near the surface. This shift to a rate dependence upon contributions by the $>SiO^-_{tot}$ term could explain the very small increases in ΔH reported by Dove and Crerar (1990) between quartz dissolution rates in water versus solutions containing sodium or potassium. At the temperature and pH regime of their experiments, the dissolution rate in water or sodium-bearing solutions is mostly $>SiO^-_{tot}$ -reaction controlled, and at these conditions only the large increases in the preexponential term were measurable.

Theoretical mechanistic models. Several theoretical investigations have used molecular orbital and ab initio studies to simulate solvent-silica interactions. In early work, deJong and Brown (1980) investigated the qualitative effects of water, hydronium and protons on the energy of the Si-O bond in a $H_6Si_2O_7$ cluster. One of their goals was to understand physical properties and reactivity of silicates in terms of the details of water attachment to the Si-O bond in a melt or aqueous environment. They were perhaps the first to model the relative effects of different ions and molecules on the strength of the bridging oxygen, O(br) and found that the degree of weakening followed the sequence: $H^+ > OH^- > H_3O^+ > H_2O$ where the H^+ adion perturbs this bond the most. Foley (1986) found a similar trend for hydronium ion and water interactions with $H_6Si_2O_7$ and quantified large minimum energy differences between these two interaction mechanisms.

Ab initio methods have also been used to investigate the dynamic process of water sorption and interaction with a disiloxane group. Using fully optimized models, Lasaga and Gibbs (1990) showed that water-silica interactions involve at least the three steps of adsorption, activated complex formation and hydrolysis. Figure 30 suggests that for

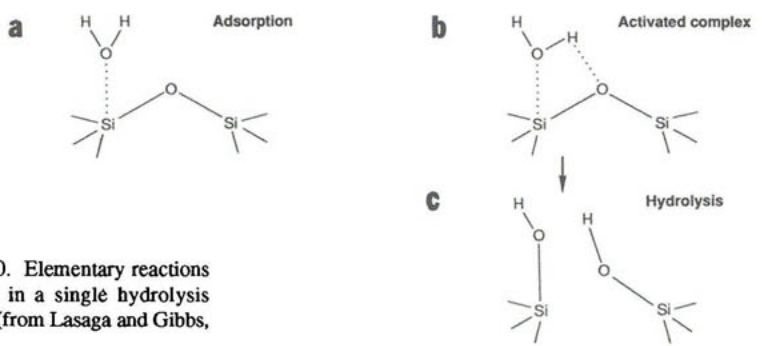


Figure 30. Elementary reactions involved in a single hydrolysis reaction (from Lasaga and Gibbs, 1990).

EBSCOhost - printed on 2/13/2023 4:48 AM via . All use subject to https://www.ebsco.com/terms-of-use

reactions with H_2O, the reaction involves rapid transfer of H^+ to the bridging oxygen followed by the formation of the transition state complex. The complex is a five-coordinated silicon species that forms by binding with the transient hydroxyl ion. These findings prompted Lasaga and Gibbs (1990) to suggest that dissolution rates of silica should exhibit a distinct isotope kinetic effect. Such an effect was reported by Scholze (1977) in silicate glasses that measured rates of SiO_2 release in HCl and DCl solutions. In a similar study, Casey et al. (1990) predicted that rates of quartz dissolution in D_2O and H_2O solutions should differ by more than a factor of four.

More recently, Xiao and Lasaga (1994) conducted high level *ab initio* calculations investigating the interaction of H_2O and H^+ (H_3O^+) with Si-O-Si and Si-O-Al structures to investigate mechanisms for surface reactions with similar stoichiometries. They found that proton transfer to the bridging oxygen has no energy barrier and occurs near the outset of the calculation. This attack by H_3O^+ significantly weakens the bridging bonds of both of these species. Calculated activation energies of hydrolysis for the Si-O-Si and Si-O-Al linkages by H_2O are 134 and 113 kJ mol^{-1}, respectively. For H_3O^+ catalysis, they find 92 and 67 kJ mol^{-1} respectively. These values, particularly for the H_3O^+ catalysis, are much larger than reported experimental values (compare Table 4), but these estimates likely cannot include all of the chemical processes that contribute to the actual hydrolysis process measured in the laboratory (see below).

While these molecular orbital models are generally consistent with the reported rate data, they cannot prove particular reaction mechanism(s). Part of the reason for this limitation is that these theoretical calculations become tractable only after assuming conditions of zero Kelvin and zero pressure to predict minimum energy configurations of isolated molecules. These conditions are far removed from hydrogen-bonded environments at charged interfaces. When comparing theoretical calculations with actual experimental rate data, we must remember that present techniques for measuring dissolution and precipitation rates offer only an indirect view of possibly many different surface reaction processes. Individual reaction processes are folded together and simply reveal a time-dependent change in bulk solution composition. As a result, we are still a distance from determining which (if any) of these theoretically-determined mechanisms offer the 'most correct' representation of mineral-solvent interactions. In the absence of more sophisticated spectroscopic methods for directly probing the transition state, theoretical evidence offers a powerful guide to designing clever tests that probe silica reactivity.

Developments in applications of silica reactivity

One outgrowth of recent studies of silica-water kinetics is an increased recognition that bulk solution composition has a dramatic impact on the reactivity of silica surfaces. This has led to a focus on understanding the effects of solution pH and salinity on solvent structure and behavior at charged mineral surfaces in aqueous solutions. There are several areas of research where these relations are finding application. First, the controls of solution composition on surface reactivity may also contribute to our understanding of pressure solution (Gratier and Guiguet, 1986) and the creep, rupture and subsequent mineralization of silica-rich fault zones (e.g., Sibson, 1987; Sleep and Blanpied, 1992). Recent work shows the dynamic equilibrium that may exist between grain size reduction by fracture and grinding of quartz as balanced against grain growth by nucleation and Ostwald ripening (Sleep, 1994). This work uses a one-dimensional model to relate the porosity and resultant mineral-water interaction that results from shear processes. Results indicate that ductile creep is a plausible mechanism for increasing fluid pressure within sealed fault zones so that failure can occur at relatively low shear tractions. This leads to repeatable and

EBSCOhost - printed on 2/13/2023 4:48 AM via . All use subject to https://www.ebsco.com/terms-of-use

predictable earthquake cycles. Continued advances in understanding the reactivity of silica-water reactivity could refine models of this nature.

There is considerable evidence that the electrical fields induced at silica surfaces with different solution compositions affect interfacial water properties such as the dissociation constant, viscosity, rates of water exchange, and proton transfer (Fripiat et al., 1965; Anderson and Parks, 1968; Peschel and Aldfinger, 1970; Tait and Franks, 1971; Churaev et al., 1972; Drost-Hansen, 1977; Davies and Rideal, 1963; Roberts and Zundel, 1979; Sermon, 1980; Parks, 1984; Sposito, 1989; Zhu and Robinson, 1991; Israelachvili, 1992). These effects likely impact geophysical rock properties such as electrical conductivity, streaming potential and acoustic signatures (e.g., Sermon, 1980; Knight and Nur, 1987; Morgan et al., 1989; Knight and Dvorkin, 1992). Solution composition may also affect silica surface reactivity in fracture initiation and propagation (e.g., Weiderhorn and Johnson, 1973; Atkinson and Meredith, 1981; Parks, 1984; White et al., 1987). Findings from these studies suggest that these 'physical' phenomena may be better understood by incorporating models of 'chemical' phenomena occurring at silica surfaces. Despite the scientific and economic potential of these ideas, they have received insufficient attention in the earth sciences.

There are remaining questions about the relationships between solution composition and silica reactivity in natural systems. While the catalyzing effects of alkali salts have been investigated, there is evidence that the dissolution rates and/or apparent solubilities of natural silica surfaces may be inhibited. For example, the 'silica problem' revolves around the continuing controversy of whether dissolved silica concentrations in the marine water column is anomalously low because of reduced solubility or reduced rates of reaction. In either case, aluminum is believed to cause the reduced concentration of natural silica (Lewin, 1961; Hurd, 1973; Van Bennekom and van der Gaast, 1976; Van Bennekom, 1981, 1988; Van Bennekom et al., 1989, 1991), although evidence for this relationship is circumstantial. Surface and solution compositional controls on silica reactivity in determining rates of soil development are also controversial. In some cases, field-measured rates are much slower than rates measured in the laboratory using simple solution compositions (White and Peterson, 1990; White et al., 1992; Swoboda-Colberg and Drever, 1993). Presently, this disparity is largely attributed to hydrologic control (Swoboda-Colberg and Drever, 1993). However, if common soil-water constituents such as aluminum or iron species drastically inhibit reaction rates of silica phases, the differences between lab and field reaction rates of the silica polymorphs may be attributed to presently unrecognized geochemical controls. While the effect of certain inhibitory metals has been documented qualitatively (see earlier discussions), these controls on silica reactivity are now receiving renewed attention in integrated surface spectroscopic and kinetic studies.

Finally, an accurate representation of solution and surface compositional controls for silica surface reactivity is central to developing representative models of silica-water interactions in geochemical systems. In lower temperature environments, it is generally agreed that mineral-solution reaction processes are critically dependent upon reaction kinetics, as virtually all mineral-solution reactions are controlled by disequilibrium processes and therefore can only be described through irreversible thermodynamics and kinetics. In most hydrothermal environments, silica-water reactions make a transition from kinetic to thermodynamic control. Numerical models have found that local equilibrium assumptions begin to apply near the 150° to 250°C range when

- rates of dissolution for the SiO_2-deionized water system are used
- fluid movement is modeled using long time and length scales

EBSCOhost - printed on 2/13/2023 4:48 AM via . All use subject to https://www.ebsco.com/terms-of-use

(e.g., Helgeson, 1968, 1979; Parkhurst et al., 1980; Lasaga, 1984; Lichtner, 1988, 1993; Evans and Huang, 1983; Evans and Nicholson, 1987; Steefel and Lasaga, 1994). Many of these models have quantified silica reactivity using experimental reaction rates measured in deionized water. These rates are unlikely to be representative of processes occurring in earth systems as natural fluids have variable solution pH and contain numerous dissolved solutes. Discussion in this review has shown that constituent solutes are known to have *both* significant rate-inhibiting and enhancing effects on behavior, *even when present at very low concentrations*. If we begin to quantify and consider both rate inhibiting and catalyzing effects, then equilibrium versus kinetic controls on the evolution of natural and engineered systems may become less clear. For example, processes now considered borderline between equilibrium versus kinetic control, such as the development of pressure solution or silica precipitation in certain geothermal systems, may come into the rate-limited regime when the effect of inhibitory ions are considered. This understanding becomes still more urgent when we consider societal needs for predictive models which describe the evolution of diverse current and future earth systems. From the behavior of radioactive waste repositories to the chemical controls on geothermal and oil-field scales and the biogeochemical cycling of silicon, silica-water interactions will play a key role in interpreting these environments.

CONCLUDING REMARKS

The intent of this chapter was to review the literature leading to the current state of our knowledge of solubility behavior and the kinetics of silica dissolution and precipitation reactions in aqueous solutions. These topics have received considerable study in recent years owing to the extensive occurrence of these phases in diverse natural and engineered systems and the enormous scientific and applied need for understanding their behavior. The mutual interaction of water with these silica phases is central to quantifying the mobility and cycling of the second-most abundant element in the earth's crust. Further, quantifying silica mobility in diverse chemical and physical environments is fundamental to determining the mechanistic controls on silica-water interactions as analogs for understanding compositionally more complex silicate minerals and glasses.

The equilibrium solubilities of quartz and amorphous silica have been investigated numerous times and over a wide range of temperatures, pressures, and solution compositions. As a result, our knowledge of the solubility of these phases is generally satisfactory for most geochemical or technological applications. This is not true for some other less common, but perhaps quite important phases, like opal-CT or moganite where there are almost no solubility data. In addition, there is sufficient evidence of the presence of aqueous polynuclear silica species to warrent the quantification of the equilibrium between them and H_4SiO_4. While polynuclear silica species are likely not significant in solutions in equilibrium with quartz they may make up a large proportion of the species in solutions in equilibrium with the more soluble silica polymorphs. This may have a profound impact on how we model both the equilibrium solubilities and the precipitation kinetics of these phases. Thus, although there is a tendency to think of silica solubility research as a mature field, several interesting problems remain.

Our understanding of the kinetics of silica-water interactions continues to be much less developed than the equilibrium system. Recent advances have quantified the kinetics of quartz dissolution at variable pH, salinities, and temperature, yet experimental difficulties associated with studying the precipitation kinetics continues the existing gaps in our quantitative understanding of quartz nucleation and growth. Reactivities of the other silica

EBSCOhost - printed on 2/13/2023 4:48 AM via . All use subject to https://www.ebsco.com/terms-of-use

polymorphs are also largely unknown despite the widespread occurrence of amorphous silica in diverse environments

Recent developments in the kinetics of silica-water interactions have recognized the importance of detailed processes occurring at the silica-water interface. This key to mechanistic control on reactivity cannot be overstated and has led us from an emphasis on casting rates in terms of bulk solution composition to conceptually viewing kinetics closer to the reaction site, that is, the silica-water interface. This advance produces a more satisfactory representation of silica surface reactivity. Yet, existing rate laws are still lacking as these relations are correlations of bulk reaction rate with bulk surface charge. Current rate laws do not reveal the details of solvent structure, properties, transition state complex or the detailed reaction mechanism. Theoretical calculations of reaction path complexes provide important insights, but computational limitations continue to place uncomfortable assumptions on the conditions and structure of the modeled systems. Continued advances in understanding mechanistic controls will necessarily entail integrated studies of *in situ* surface reactivity using near-surface spectroscopic and microscopic techniques in conjunction with solution studies and theoretical modeling.

It is well to remember that although many of the silica-water interactions described in this review have been conducted in experimental and theoretical settings, most natural environments have more complicated fluid chemistries than those used in laboratory studies. Yet many of the resulting principles are already directly applicable to the study of natural processes as we begin to quantify the interaction of individual aqueous components in solutions with silica surfaces and the effects of these interactions on reactivity. It is now imperative to understand how these components interact to control bulk reactivity of minerals in solutions. With this basis in understanding we will acquire a full quantitative and mechanistic description of silica-water interactions and gain a powerful basis for understanding other mineral-water systems.

ACKNOWLEDGMENTS

We thank P.C. Bennett and P.J. Heaney for their reviews of this chapter.

REFERENCES

Alexander GB (1957) The effect of particle size on the solubility of amorphous silica in water. J Phys Chem 61:1563-1564

Allen LH, Matijevic E (1971) Stability of colloidal silica. III. Effect of hydrolyzable cations. J Coll Interface Sci 35:66-76

Alvarez R, Sparks D L (1985) Polymerization of silicate anions in solutions at low concentrations. Nature 318:649-651

Anderson JH, Parks GA (1968) The electrical conductivity of silica gel in the presence of adsorbed water. J Phys Chem 72:3662-3668

Anderson JH, Wickersheim KA (1964) Near infrared characterization of water and hydroxyl groups on silica surfaces. Surf Sci 2:252-260

Applin KR (1987) The diffusion of dissolved silica in dilute aqueous solutions. Geochim Cosmochim Acta 51:2147-2151

Arnórsson S, Gunnlaugsson E (1983a) The chemistry of geothermal waters in Iceland. III. Chemical geothermometry in geothermal investigations. Geochim Cosmochim Acta 47:567-577

Arnórsson S, Gunnlaugsson W (1983b) The chemistry of geothermal waters in Iceland. II. Mineral equilibria and independent variables controlling water compositions. Geochim Cosmochim Acta 47:547-566

Atkinson BK, Meredith PG (1981) Stress corrosion cracking of quartz: a note on the influence of chemical environment. Tectonophysics 77:T1-T11

EBSCOhost - printed on 2/13/2023 4:48 AM via . All use subject to https://www.ebsco.com/terms-of-use

polymorphs are also largely unknown despite the widespread occurrence of amorphous silica in diverse environments

Recent developments in the kinetics of silica-water interactions have recognized the importance of detailed processes occurring at the silica-water interface. This key to mechanistic control on reactivity cannot be overstated and has led us from an emphasis on casting rates in terms of bulk solution composition to conceptually viewing kinetics closer to the reaction site, that is, the silica-water interface. This advance produces a more satisfactory representation of silica surface reactivity. Yet, existing rate laws are still lacking as these relations are correlations of bulk reaction rate with bulk surface charge. Current rate laws do not reveal the details of solvent structure, properties, transition state complex or the detailed reaction mechanism. Theoretical calculations of reaction path complexes provide important insights, but computational limitations continue to place uncomfortable assumptions on the conditions and structure of the modeled systems. Continued advances in understanding mechanistic controls will necessarily entail integrated studies of *in situ* surface reactivity using near-surface spectroscopic and microscopic techniques in conjunction with solution studies and theoretical modeling.

It is well to remember that although many of the silica-water interactions described in this review have been conducted in experimental and theoretical settings, most natural environments have more complicated fluid chemistries than those used in laboratory studies. Yet many of the resulting principles are already directly applicable to the study of natural processes as we begin to quantify the interaction of individual aqueous components in solutions with silica surfaces and the effects of these interactions on reactivity. It is now imperative to understand how these components interact to control bulk reactivity of minerals in solutions. With this knowledge we will acquire a full quantitative and mechanistic description of silica-water interactions and gain a powerful basis for understanding other mineral-water systems.

ACKNOWLEDGMENTS

We thank P.C. Bennett and P.J. Heaney for their reviews of this chapter.

REFERENCES

Alexander GB (1957) The effect of particle size on the solubility of amorphous silica in water. J Phys Chem 61:1563-1564

Allen LH, Matijevic E (1971) Stability of colloidal silica. III. Effect of hydrolyzable cations. J Coll Interface Sci 35:66-76

Alvarez R, Sparks D L (1985) Polymerization of silicate anions in solutions at low concentrations. Nature 318:649-651

Anderson JH, Parks GA (1968) The electrical conductivity of silica gel in the presence of adsorbed water. J Phys Chem 72:3662-3668

Anderson JH, Wickersheim KA (1964) Near infrared characterization of water and hydroxyl groups on silica surfaces. Surf Sci 2:252-260

Applin KR (1987) The diffusion of dissolved silica in dilute aqueous solutions. Geochim Cosmochim Acta 51:2147-2151

Arnórsson S, Gunnlaugsson E (1983a) The chemistry of geothermal waters in Iceland. III. Chemical geothermometry in geothermal investigations. Geochim Cosmochim Acta 47:567-577

Arnórsson S, Gunnlaugsson W (1983b) The chemistry of geothermal waters in Iceland. II. Mineral equilibria and independent variables controlling water compositions. Geochim Cosmochim Acta 47:547-566

Atkinson BK, Meredith PG (1981) Stress corrosion cracking of quartz: a note on the influence of chemical environment. Tectonophysics 77:T1-T11

EBSCOhost - printed on 2/13/2023 4:48 AM via . All use subject to https://www.ebsco.com/terms-of-use

Ballou EV, Leban MI, Wydeven T (1973) Solute rejection by porous glass membranes III. Reduced silica dissolution and prolonged hyperfiltration service with feed additives. J Appl Chem Biotech 23:119-130

Baumann H (1955) Über die auflösung von SiO_2 in wasser. Beiträge zur silikose Forschung 37:47-71

Bennett P, Siegel DI (1987) Increased solubility of quartz in water due to complexing by organic compounds. Nature 326:684-686

Bennett PC (1991) Quartz dissolution in organic-rich aqueous systems. Geochim Cosmochim Acta 55:1781-1797

Bennett PC, Melcer ME, Siegel, DI, Hassett, JP (1988) The dissolution of quartz in dilute aqueous solutions of organic acids at 25°C. Geochim Cosmochim Acta 52:1521-1530

Berger G, Cadore E, Schott J, Dove PM (1994) Dissolution rate of quartz in lead and sodium electrolyte solutions between 25 and 300°C: Effect of the nature of surface complexes and reaction affinity. Geochim Cosmochim Acta 58:541-551

Bérubé YG, de Bruyn PL (1968) Adsorption at the rutile-solution interface. J Coll Interface Sci, 28:92-105

Bird G, Boon J, Stone T (1986) Silica transport during steam injection into oil sands 1. Dissolution and precipitation kinetics of quartz: New results and review of existing data. Chem Geol 54:69-80

Blesa MA, Maroto AJG, Regazzoni AE (1990) Surface acidity of metal oxides immersed in water: A critical analysis of thermodynamic data. J Coll Interface Sci 140:287-290

Bohlmann EG, Mesmer RE, Berlinski P (1980) Kinetics of silica deposition from simulated geothermal brines. Soc Petrol Engin J 239-248

Brady PV (1992) Silica surface chemistry at elevated temperatures. Geochim Cosmochim Acta 56:2941-2946

Brady PV, Walther JV (1990) Kinetics of quartz dissolution at low temperatures. Chem Geol 82:253-264

Brantley SL (1992) The effect of fluid chemistry on quartz microcrack lifetimes. Earth Planet Sci Lett 113:145-156

Brantley SL, Crane SR, Crerar DA, Hellman R, Stallard R (1986) Dissolution at dislocation etch pits in quartz. Geochim Cosmochim Acta 50:2349-2361

Brown DW, Hem JD (1975) Reactions of aqueous aluminum species at mineral surfaces. U S Geol Surv Water Supply Paper, Washington DC:1827-F

Cary LW, deJong BHWS, Dibble Jr WE (1982) A 29Si NMR study of silica species in dilute aqueous solutions. Geochim Cosmochim Acta 46:1317-1320

Casey WH (1987) Heterogeneous Kinetics and Diffusion Boundary Layers: The Example of Reaction in a Fracture. J Geophys Res 92:8007-8013

Casey WH, Lasaga AC, Gibbs GV (1990) Mechanisms of silica dissolution as inferred from the kinetic isotope effect. Geochim Cosmochim Acta 54:3369-3378

Casey WH, Westrich HR, Banfield J, Ferruzi G, Arnold GW (1993) Leaching and reconstruction at the surfaces of dissolving chain-silicate minerals. Nature 366:253-256

Chakoumakos BC, Gibbs GV(1986) Theoretical molecular orbital study of silanol-water interactions. J Phys Chem 90:996-998

Churaev NV, Sobolev VD, Zheleznyi BV (1972) Thermal expansion of water in thin quartz capillaries. Russian J Phys Chem 46:1320-1322

Cline JS, Bodnar RJ, Rimstidt JD (1992) Numerical simulation of fluid flow and silica transport and deposition in boiling hydrothermal solutions: Application to epithermal gold deposits. J Geophys Res 97:9085-9103

Conway BE (1981) Ionic Hydration in Chemistry and Biophysics, Elsevier Scientific, Amsterdam, 773 p.

Corwin JF, Swinnerton AC (1951) The growth of quartz in alkali halide solutions. J Am Chem Soc 73:3598-3601

Davies JT, Rideal EK (1963) Interfacial Phenomena, 2nd Edn. Academic Press, New York, 480 p

Davis JA, James RO, Leckie JO (1978) Surface ionization and complexation at the oxide/water interface. J Coll Interface Sci 63:480-499

deJong BHWS, Brown Jr GE (1980) Polymerization of silicate and aluminate tetrahedra in glasses, melts and aqueous solutons- II. The network modifying effects of Mg^{2+}, K^+, Na^+, Li^+, H^+, OH^-, F^-, Cl^-, H_2O, CO_2 and H_3O^+ on silicate polymers. Geochim Cosmochim Acta 44:1627-1642

DeMaster DJ (1981) The supply and accumulation of silica in the marine environment. Geochim Cosmochim Acta 45:1715-1732

Diénert F, Wandenbulcke F (1923) Sur le dosage de la silice dans les eaux. Comptes rendus des seances de l'academié des sciences, 176:1478-1480

Dove PM (1994) The dissolution kinetics of quartz in sodium chloride solutions at 25° to 300°C. Am J Sci 294:665-712

Dove PM, Crerar DA (1990) Kinetics of quartz dissolution in electrolyte solutions using a hydrothermal mixed flow reactor. Geochim Cosmochim Acta 54:955-969

EBSCOhost - printed on 2/13/2023 4:48 AM via . All use subject to https://www.ebsco.com/terms-of-use

Dove PM, Elston SF (1992) Dissolution kinetics of quartz in sodium chloride solutions: Analysis of existing data and a rate model for 25°C. Geochim Cosmochim Acta 56:4147-4156

Dove PM, Krishnan V, Murovitz JR (1994) Controls on the surface reactivity of silica: The effect of aluminum on the kinetics of quartz dissolution. Geol Soc Am Abstracts, Seattle, WA (in press)

Drees LR, Wilding LP, Smeck NE, Senkayi AL (1989) Silica in soils: Quartz and disordered silica polymorphs. In: Dixon JB, Weed SB (eds) Minerals in Soil Environments, p 913-974, Soil Sci Soc Am, Madison, WI

Drost-Hansen W (1977) Effects of vicinal water on colloidal stability and sedimentation processes. J Coll Interface Sci 58:251-262

Du Q, Freysz E, Shen YR (1994) Vibrational spectra of water molecules at quartz/water interfaces. Phys Rev Letters 72:238-241

Dugger DL, Stanton JH, Irby BN, McConnell BL, Cummings WW, Maatman RW (1964) The exchange of twenty metal ions with the weakly acidic silanol group of silica gel. J Phys Chem 68:757-760

Eisenberg D, Kauzmann W (1969) The Structure and Properties of Water. Oxford Univ Press, New York, 296 p

Evans DD, Huang C (1983) Role of desaturation on transport through fractured rock. In: Mercer JW, Rao PS, Marine IW (eds) Role of the unsaturated zone in radioactive and hazardous waste disposal. p 165-178 Ann Arbor Sci Publ, Ann Arbor, MI

Evans DD, Nicholson TJ (1987) Flow and Transport Through Unsaturated Fractured Rock. Am Geophys Union Geophys Monogr 42, Washington, DC

Fleming BA (1986) Kinetics of reaction between silicic acid and amorphous silica surfaces in NaCl solutions. J Coll Interface Sci 110:40-64

Fleming BA, Crerar DA (1982) Silicic acid ionization and calculation of silica solubility at elevated temperature and pH. Geothermics, 11:15-29

Fokkink LGJ, De Keizer A, Lyklema J (1989) Temperature dependence of the electrical double layer on oxides: rulite and hematite. J Coll Interface Sci 127:116-131

Fokkink LGJ, De Keizer A, Lyklema J (1990) Temperature dependence of cadmium adsorption on oxides. J Coll Interface Sci 135:118-131

Foley JA (1986) Hydronium ion and water interactions with SiOSi, SiOAl, and AlOAl tetrahedral linkages. MS thesis, Virginia Polytechnic Inst & State University, Blacksburg, VA

Fournier RA, Potter III RW (1982b) An equation correlating the solubility of quartz in water from 25°C to 900°C at pressures up to 10,000 bars. Geochim Cosmochim Acta 46:1969-1973

Fournier RO (1972) Silica in thermal waters: Laboratory and field investigations. Symp Hydrogeochemistry and Biochemistry 1:122-139

Fournier RO (1983) A method of calculating quartz solubilities in aqueous sodium chloride solutions. Geochim Cosmochim Acta 47:579-586

Fournier RO (1985) Silica minerals as indicators of conditions during gold deposition. In: Tooker EW (ed) Geologic Characteristics of Sediment- and Volcanic-Hosted Disseminated Gold Deposits—Search for an Occurrence Model. U S Geological Survey

Fournier RO, Rosenbauer, RJ, Bischoff, JL (1982a) The solubility of quartz in aqueous sodium chloride solution at 350°C and 180 to 500 bars. Geochim Cosmochim Acta 46:1975-1978

Fripiat JJ, Jelli A, Poncelet G, Andre J (1965) Thermodynamic properties of adsorbed water molecules and electrical conduction in montmorillonites and silicas. J Phys Chem 69:2185-2197

Gallei E, Parks GA (1972) Evidence for surface hydroxyl groups in attenuated total reflectance spectra of crystalline quartz. J Coll Interface Sci 38:650-651

Geerlings P, Tariel N, Botrel A, Lissilour R, Mortier WJ (1984) Interaction of surface hyroxyls with adsorbed molecules. A quantum-chemical study. J Phys Chem 88:5752-5759

Gehlen M, van Raaphorst W, Wollast R (1993) Kinetics of silica sorption on North Sea sediments. In: Kump LR (ed) Geochemistry of the Earth's Surface; abstracts for 3rd Int'l Symp on Geochemistry of the Earth's Surface, p 359-361, Chem Geol

Gratier JP, Guiguet R (1986) Experimental pressure solution-deposition on quartz grains: The crucial effect of the nature of the fluid. J Struct Geol 8:845-856

Gratz AJ, Bird P (1993a) Quartz dissolution: Negative crystal experiments and a rate law. Geochim Cosmochim Acta 57:965-976

Gratz AJ, Bird P (1993b) Quartz dissolution: Theory of rough and smooth surfaces. Geochim Cosmochim Acta 57:977-989

Gratz AJ Bird P, Quiro GB (1990) Dissolution of quartz in aqueous basic solution, 106-236°C: Surface kinetics of "perfect" crystallographic faces. Geochim Cosmochim Acta 54:2911-2922

Gratz AJ, Manne S, Hansma PK (1991) Atomic force microscopy of atomic-scale ledges and etch pits formed during dissolution of quartz. Science 251:1343-1346

Hayes KF, Leckie JO (1987) Modeling ionic strength effects on cation adsorption at hydrous oxide/solution interfaces. J Coll Interface Sci 115:564-572

EBSCOhost - printed on 2/13/2023 4:48 AM via . All use subject to https://www.ebsco.com/terms-of-use

Helgeson HC (1968) Evaluation of irreversible reactions in geochemical processes involving minerals and aqueous solutions-I. Thermodynamic relations. Geochim Cosmochim Acta 32:853-877
Helgeson HC (1979) Mass transfer among minerals and hydrothermal solutions. In: Barnes HL (ed) Geochemistry of Hydrothermal Ore Deposits, p 568-610, John Wiley, New York
Hem JD, Roberson CE, Lind CJ, Polzer WL (1973) Chemical interactions of aluminum with aqueous silica at 25°C. U S Geol Surv Water Supply Paper, Washington, DC, 1827-E
Henderson JH, Syers JK, Jackson, ML (1970) Quartz dissolution as influenced by pH and the presence of a disturbed surface layer. Israel J Chem 8:357-372
Hiemstra T, Van Riemsdijk WH (1990) Multiple activated complex dissolution of metal(hydr)oxides: A thermodynamic approach to quartz. J Coll Interface Sci 136:132-150
Hiemstra T, Van Riemsdijk WH, Bolt GH (1989a) Multisite proton adsorption modeling at the solid/solution interface of (hydr)oxides: A new approach I. Model description and evaluation of intrinsic reaction constants. J Coll Interface Sci 133:91-104
Hiemstra T, Van Riemsdijk WH, Bolt GH (1989b) Multisite Proton adsorption modeling at the solid/solution interface of (hydr)oxides: A new approach II. Application to various important (hydr)oxides. J Coll Interface Sci 133:105-117
Hosaka M, Taki S (1981a) Hydrothermal growth of quartz crystals in NaCl solutions. J Crystal Growth 52:837-842
Hosaka M, Taki S (1981b) Hydrothermal growth of quartz crystals in KCl solutions. J Crystal Growth 53:542-546
House WA, Hickinbotham LA (1992) Dissolution kinetics of silica between 5 and 35°C. J Chem Soc Faraday Trans 88:2021-2026
House WA, Orr DR (1992) Investigation of the pH dependence of the kinetics of quartz dissolution at 25°C. J Chem Soc Faraday Trans 88:233-241
Hudson GA, Bacon FR (1958) Inhibition of alkaline attack on soda-lime glass. Ceramic Bull 37:185-188
Hurd DC (1973) Interactions of biogenic opal sediment and seawater in the Central Equatorial Pacific. Geochim Cosmochim Acta 37:2257-2282
Hurd DC (1972) Factors affecting the solution rate of biogenic opal in seawater. Earth Planet Sci Lett 15:411-417
Iler R (1979) The Chemistry of Silica. John Wiley and Sons, New York, 865 p.
Iler RK (1973) Effect of adsorbed alumina on the solubility of amorphous silica in water. J Coll Interface Sci 43:399-408
Israelachvili J (1992) Interfacial and Surface Forces, 2nd Edn. Academic Press, New York, 450 p
Jardine PM, Zelazny LW, Parker JC (1985a) Mechanisms of aluminum adsorption on clay minerals and peat. Soil Sci Soc Am J 49:862-867
Jardine PM, Zelazny LW, Parker JC (1985b) Kinetics and mechanisms of aluminum adsorption on kaolinite using a two-site nonequilibrium transport model. Soil Sci Soc Am J 49:862-867
Jednacak J, Pravdic V (1974) The electrokinetic potential of glasses in aqueous electrolyte solutions. J Coll Interface Sci 49:16-23
Jones LHP, Handreck KA (1973) Effects of iron and aluminum oxides on silica in solution in soils. Nature 198:852-853
Kamiya H, Shimokata K (1976) The role of salts in the dissolution of powdered quartz. In: Cadek J, Paces T (eds) Proc Int'l Symp Water-rock Interaction. Czechoslovakian Geological Survey, Prague
Kent DB, Tripathi VS, Ball NB, Leckie JO, Siegel MD 1988 Surface-complexation modeling of radionuclide adsorption in subsurface environments: Sandia National Labs, Albuquerque, U S Nuclear Regulatory Commission Rpt NUREG/CR-4807, 113 p
Klier K, Zettlemoyer AC (1977) Water at interfaces: Molecular structure and dynamics. In Kerker M, Zettlemoyer AC, Rowell RL (eds) Colloid and Interface Science 1:231-244
Knauss KG, Wolery TJ (1988) The dissolution kinetics of quartz as a function of pH and time at 70°C. Geochim Cosmochim Acta 52:43-53
Knight R, Dvorkin J (1992) Seismic and electrical properties of sandstones at low satrurations. J Geophys Res 97:17425-17432
Knight RJ, Nur A (1987) Geometrical effects in the dielectric response of partially saturated sandstones. The Log Analyst 513-519
Lasaga AC (1981) Transition state theory. In: Lasaga AC, Kirkpatrick RJ (eds) Kinetics of Geochemical Processes. Rev Mineral 8:135-169
Lasaga AC (1984) Chemical kinetics of water-rock interactions. J Geophys Res 89:4009-4025
Lasaga AC (1990) Atomic treatment of mineral-water surface reactions. In: Hochella Jr MF, White AF (eds) Mineral-Water Interface Geochemistry Rev Mineral 23:17-85
Lasaga AC, Blum AE (1986) Surface chemistry etch pits and mineral-water reactions. Geochim Cosmochim Acta 50:2363-2379

EBSCOhost - printed on 2/13/2023 4:48 AM via . All use subject to https://www.ebsco.com/terms-of-use

Lasaga AC, Gibbs GV (1990) Ab-initio quantum mechanical calculations of water-rock interactions: Adsorption and hydrolysis reactions. Am J Sci 290:263-295
Laudise RA (1959) Kinetics of hydrothermal quartz crystallization. J Am Chem Soc 81:562-566
Lewin JC (1961) The dissolution of silica from diatom walls. Geochim Cosmochim Acta 21:82-198
Liang D, Readey DW (1987) Dissolution kinetics of crystalline and amorphous silica in hydrofluoric-hydrochloric acid mixtures. J Am Ceram Soc 70:570-577
Lichtner PC (1988) The quasi-stationary state approximation to coupled mass transport and fluid-rock interaction in a porous media. Geochim Cosmochim Acta 52:143-165
Lichtner PC (1993) Scaling properties of time-space kinetic mass transport equations and the local equilibrium limit. Am J Sci 293:257-296
Lyklema J (1987) Electric double layers on oxides: Disparate observations and unifying principles. Chem and Industry 2:741-747
Manning CE (in press) The solubility of quartz in H_2O in the lower crust and upper mantle. Geochim Cosmochim Acta
Matijevic E, Mangravite Jr FJ, Cassell EA (1971) Stability of colloidal silica. IV. The silica-alumina system. J Coll Interface Sci 35:560-568
Morariu VV, Mills R (1973) A study of water adsorbed on silica. The effect of surface nature temperature and coverage on the spin-spin relaxation time. II. Z Physikal Chemie Neue Folge 83:41-53
Morgan FD, Williams ER, Madden TR (1989) Streaming potential properties of westerly granite with applications. J Geophys Res 94:12449-12461
Morris RC, Fletcher AB (1987) Increased solubility of quartz following ferrous-ferric iron reactions. Nature 330:558-561
Morrow BA, Cody IA (1975) An infrared study of some reactions with reactive sites on dehydroxylated silica. J Phys Chem 79:761-762
Morrow BA, Cody IA (1976a) Infrared studies of reactions on oxide surfaces. 5. Lewis acid sites on dehydroxylated silica. J Phys Chem 80:1995-1998
Morrow BA, Cody IA (1976b) Infrared studies of reactions on oxide surfaces. 6. Active sites on dehydroxylated silica for the chemisorption of ammonia and water. J Phys Chem 80:1998-2004
Mortier WJ, Sauer J, Lercher JA, Noller H (1984) Bridging and terminal hydroxyls. A structural and chemical quantum chemical discussion. J Phys Chem 88:905-912
Mullis AM (1993) Determination of the rate-limiting mechanism for quartz pressure solution. Geochim Cosmochim Acta 57:1499-1503
Murphy WM, Helgeson HC (1989) Thermodynamic and kinetic constraints on reaction rates among minerals and aqueous solutions. IV. Retrieval of rate constants and activation parameters for the hydrolysis constants of pyroxene wollastonite olivine andalusite quartz and nepheline. Am J Sci 289:17-101
Nielsen AE (1959) The kinetics of crystal growth in barium sulfate precipitation. II. Temperature Dependence and Mechanism. Acta Chem Scand 13:784-802
Olsen LL, O'Melia CR (1973) Interactions of Fe(III) with Si(OH)4. J Inorg Nucl Chem 35:1977-1985
Parkhurst LC, Thorstenson DC, Plummer LN (1980) PHREEQE-A computer program for geochemical calculations. U S Geol Surv Water Res Invest 80-96
Parks GA (1967) Aqueous surface chemistry of oxides and complex oxide minerals. Adv Chem Ser 67:121-160
Parks GA (1984) Surface and interfacial free energies of quartz. J Geophys Res 89:3997-4008
Parks GA (1990) Surface energy and adsorption at mineral-water interfaces: An introduction. In: Hochella Jr MF, White AF (eds) Mineral-Water Interface Geochemistry Rev Mineral 23:133-175
Peschel G, Aldfinger KH (1970) Viscosity anomalies in liquid surface zones. IV. Apparent viscosity of water in thin layers adjacent to hydroxylated fused silica surfaces. J Coll Interface Sci 34:505-510
Porter RA, Weber Jr WJ (1971) The interaction of silicic acid with iron (III) and uranyl ions in dilute aqueous solution. J Inorg Nucl Chem 33:2443-2449
Prigogine M, Fripiat JJ (1974) A possible mechanism of the interaction of adsorbed water molecules with a silica surface. Bull Soc Royale Sciences de Liego 43:449-458
Renders PJN, Gammons C, Barnes HL Precipitation and dissolution rate constants for cristobalite at 150 to 300°C. Geochim Cosmochim Acta (in press)
Rimstidt JD, Barnes HL (1980) The kinetics of silica-water reactions. Geochim Cosmochim Acta 44:1683-1699
Rimstidt JD, Cole DR (1983) Geothermal mineralization I: The mechanism of formation of the Beowawe Nevada siliceous sinter deposit. Am J Sci 283:861-875
Roberson CE, Barnes RB (1978) Stability of fluoride complex with silica and its distribution in natural water systems. Chem Geol 21:239-256
Roberts NK, Zundel G (1979) IR studies of long-range surface effects-excess proton mobility in water in quartz pores. Nature 278:726-728

EBSCOhost - printed on 2/13/2023 4:48 AM via . All use subject to https://www.ebsco.com/terms-of-use

Robie RA, Hemingway BS, Fisher JS (1978) Thermodynamic Properties of Minerals and Related Substances at 298.15 K and 1 Bar (105 Pascals) Pressure and at Higher Temperatures. U S Geol Surv, Washington, DC, 456 p

Sasaki B (1952) The corrosive action of aqueous solutions of several electrolytes on the silicic acid solid surface. Part 1: Tohoku Daigaku Hisui Yoeki Kagaku Kenkyujo Hokoku 113-121

Schindler P, Kamber HR (1968) Die aciditat von silanolgruppen. Helv Chim Acta 51:1781-1786

Schindler P, Stumm W (1987) The surface chemistry of oxides hydroxides and oxide mineral. In: Stumm W (ed) Aquatic Surface Chemistry, p 83-110. John Wiley and Sons, New York

Schindler PW, Furst B, Dick R, Wolf PU (1976) Ligand properties of surface silanol groups I. Surface complex formation with Fe^{3+} Cu^{2+} Cd^{2+} and Pb^{2+}. J Coll Interface Sci 55:469-475

Scholze H (1977) Evidence of control of dissolution rates of glasses by H+ mobility. J Am Ceram Soc-Discussions and Notes 60:186

Schwartzentruber J, Furst W, Renon H (1987) Dissolution of quartz into dilute alkaline solutions at 90°C: A kinetic study. Geochim Cosmochim Acta 51:1867-1874

Sermon PA (1980) Interaction of water with some silicas. J Chem Soc Faraday I 76:885-888

Sibson RH (1987) Earthquake rupturing as a mineralizing agent in hydrothermal systems. Geology 15:701-704

Sleep N (1994) Grain size and chemical controls on the ductile properties of mostly frictional faults at low-temperature hydrothermal conditions. Pure Appl Geophys (in press)

Sleep NH, Blanpied ML (1992) Creep compaction and the weak rheology of major fault. Nature 359:687-692

Sposito G (1989) The Chemistry of Soils. Oxford Univ Press, New York 277 p

Stanton J, Maatman RW (1963) The reaction between aqueous uranyl ion and the surface of silica gel. J Coll Sci 18:132-146

Steefel CI, Lasaga AC (1994) A coupled model for transport of multiple chemical species and kinetic precipitation/dissolution reactions with application to reactive flow in single phase hydrothermal systems. Am J Sci 294:529-592

Stumm W (1992) Chemistry of the Solid-Water Interface. John Wiley & Sons, New York, 428 p

Stumm W, Morgan JJ (1981) Aquatic Chemistry. John Wiley & Sons, New York, 780 p

Swoboda-Colberg NG, Drever JI (1993) Mineral dissolution rates in plot-scale field and laboratory experiments. Chem Geol 105:51-70

Tait MJ, Franks F (1971) Water in biological systems. Nature 230:91-94

Tester JW, Worley WG, Robinson BA, Grigsby CO, Feerer JL (1994) Correlating quartz dissolution kinetics in pure water from 25 to 625°C. Geochim Cosmochim Acta 58:xxx

Thornton SD, Radke CJ (1988) Dissolution and condensation kinetics of silica in alkaline solution. Soc Petrol Eng 743-752

Ugliengo P, Saunders V, Garrone E (1990) Silanol as a model for the free hydroxyl of amorphous silica: Ab initio calculations of the interaction of water. J Phys Chem 94:2260-2267

Van Bennekom A (1981) On the role of aluminum in the dissolution kinetics of diatom frustrules. In: Ross R (ed) 6th Diatom Symp, p 445-456. Otto Koeltz, Koenigstein, Germany

Van Bennekom AJ (1988) Deep-water transit times in the Eastern Indonesian basins calculated from dissolved silica in deep and interstitial waters. Netherlands J Sea Res 22:341-354

Van Bennekom AJ, van der Gaast SJ (1976) Possible clay structures in frustrules of living diatoms. Geochim Cosmochim Acta 40:1149-1152

Van Bennekom AJ, Jansen HJF, van der Gaast SJ, van Iperen JM, Pieters J (1989) Aluminum-rich opal: an intermediate in the preservation of biogenic silica in the Zaire (Congo) deep-sea fan. Deep-Sea Res 36:173-190

Van Bennekom AJ, Buma AGJ, Nolting RF (1991) Dissolved aluminum in the Weddell-Scotia confluence and effect of Al on the dissolution kinetics of biogenic silica. Mar Chem 35:423-434

Van Lier JA, de Bruyn PL, Overbeek JTG (1960) The solubility of quartz. J Phys Chem 64:1675-1682

Verma A, Pruess K (1987) Effects of silica redistribution on performance of high-level nuclear waste repositories in saturated geologic formations. In: Coupled Processes Associated with Nuclear Waste Repositories, p 541-563. Academic Press, New York

Walther JV, Helgeson HC (1977) Calculation of the thermodynamic properties of aqueous silica and the solubility of quartz and its polymorphs at high pressures and temperatures. Am J Sci 277:1315-1351

Weiderhorn SM, Johnson H (1973) Effect of electrolyte pH on crack propagation in glass. J Am Ceram Soc 56:192-197

Weigel VE (1964) Über die Heißauslaugung von Silikätglasern durch Neutralsalzlösungen. Glastechnische Ber 37:141-147

Weigel VE (1964) Über die Beeinflussung der Heibauslaugung von silikatgläsern durch neutralzalzösungen. Glastechnische Ber 37:141-147

EBSCOhost - printed on 2/13/2023 4:48 AM via . All use subject to https://www.ebsco.com/terms-of-use

White AF, Peterson ML (1990) Role of reactive-surface area characterization in geochemical kinetic models. In: Melchoir DC, Bassett RL (eds) Chemical Modeling of Aqueous Systems II:461-475. Am Chem Soc Symp Ser 416, Washington, DC

White AF, Blum AE, Bullen TD, Peterson ML, Schulz MS, Harden JW (1992) A three million year weathering record for a soil chronosequence developed in granitic alluvium Merced California, U S A. In Kharaka YK, Maest AS (ed) Water Rock Interactions, p 607-610 AA Balkema, Rotterdam

White GS, Freiman SW, Wiederhorn SM, Coyle TD (1987) Effects of counterions on crack growth in vitreous silica. J Am Ceram Soc 70:891-895

Wieland E, Wehrli B, Stumm W (1988) The coordination chemistry of weathering: III. A generalization on the dissolution rates of minerals. Geochim Cosmochim Acta 52:1969-1981

Wijnen PWJG, Beelen TPM, De Haan JW, Van De Ven LJM, Van Santen RA, (1990) The structure directing effect of cations in aqueous silicate solutions. A 29Si-nmr study. Coll Surf 45:255-268

Wirth GS, Gieskes JM (1979) The inital kinetics of dissolution of vitreous silica in aqueous media. J Coll Interface Sci 68:492-500

Wollast R (1974) The silica problem. In: Goldberg ED (ed) The Sea, p 359-392. John Wiley, New York

Wollast R (1983) The global cycle of silica. In Aston S (ed) Silicon Geochemistry and Biogeochemistry, p 39-76. Academic Press, London

Wollast R, Chou L (1988) Rate control of weathering of silicate minerals at room temperature and pressure. In: Lerman A, Meybeck M (ed) Physical and Chemical Weathering in Geochemical Cycles. NATO ASI Series No. 251:11-31. D Reidel, Dordrecht, Netherlands

Xiao Y, Lasaga AC (1994) Ab initio quantum mechanical studies of the kinetics and mechanisms of silicate dissolution: $H^+(H3O^+)$ catalysis. Geochim Cosmochim Acta (in review)

Xie Z, Walther JV (1993) Quartz solubilities in NaCl solutions with and without wollastonite at elevated temperatures and pressures. Geochim Cosmochim Acta 57:1947-1955

Yates DE, Levine S, Healy TW (1974) Site-binding model of the electrical double layer at the oxide/water interface. J Chem Soc Farad Trans 70:1807-1818

Zhu SB, Robinson GW (1991) Structure and dynamics of liquid water between plates. J Phys Chem 94:1403-1410

EBSCOhost - printed on 2/13/2023 4:48 AM via . All use subject to https://www.ebsco.com/terms-of-use

THERMOCHEMISTRY OF CRYSTALLINE AND AMORPHOUS SILICA

Alexandra Navrotsky

Department of Geological & Geophysical Sciences
Princeton Materials Institute
Princeton University
Princeton, New Jersey 08544 U.S.A.

INTRODUCTION

SiO_2 is rich in polymorphism. Polymorphs having P-T fields of thermodynamic stability include stishovite, coesite, quartz, tridymite (possibly), cristobalite, and liquid. Metastable phases include moganite, many zeolitic forms, glass, amorphous gels, and a range of micro and mesoporous materials having different degrees of crystallinity. This diversity of structures largely reflects the variety of ring, cage, and framework topologies that can be constructed by linking SiO_4 tetrahedra. The numerous structures, both stable and metastable, must all be energetically accessible to be formed easily, especially under low-temperature aqueous or hydrothermal conditions. This review explores the energetics of silica, with emphasis on relating the trends seen in enthalpies, entropies, and heat capacities to features of structure and bonding for phases that are either pure SiO_2 or close to pure SiO_2 in composition. Hydrated forms (e.g., opal) are excluded.

Thermochemical properties of silica polymorphs are crucial for calculating high-pressure phase equilibria (since stishovite may occur in the lower mantle), for studying meteorite impacts (which can form coesite, stishovite, and glass), for characterizing igneous and metamorphic rocks (where quartz, cristobalite, and tridymite occur), and for understanding both silica solubility and the kinetics of silica dissolution and precipitation in the low-temperature aqueous environment. In the latter, metastable, hydrated, and amorphous silicas frequently are encountered.

The thermochemistry of sol-gel silicas, fumed silica, and siliceous zeolites is important to the industrial use of these materials as catalysts, molecular sieves, drying agents, and ceramics. The behavior of silica as a phase in cements and other building materials is controlled by both kinetic and thermodynamic factors.

Finally, an understanding of the thermochemistry of silica polymorphs provides insights into bonding and framework topology and links theoretical considerations arising from quantum mechanical descriptions of the Si-O bond to macroscopic physical properties.

COMMON POLYMORPHS

Quartz, cristobalite, glass, and melt

Much work has been done on the thermodynamics of these important phases. Rather than refer to earlier studies, I rely on the excellent critical review of Richet et al. (1982). Thermodynamic properties are summarized in Tables 1, 2, and 3 for quartz, cristobalite, and the amorphous state (glass and melt) respectively.

EBSCOhost - printed on 2/13/2023 4:48 AM via . All use subject to https://www.ebsco.com/terms-of-use

Table 1. Thermodynamic properties of quartz

	J/mol K			kJ/mol	Formation from the elements		
T(K)	C_p	$S°_T$	$-(G°_T - H°_{298})/T$	$H°_T - H°_{298}$	$\Delta H°_f$	$\Delta G°_f$	Log K_f
0	0.000	0.000	0.000	-6.910			
50	5.808	2.630	2.766	-6.815			
100	15.696	9.685	9.748	-6.278			
150	24.868	17.827	17.862	-5.258			
200	32.622	26.076	26.095	-3.815			
250	39.152	34.074	34.082	-2.017			
273	41.819	37.658	37.662	-1.079			
298	44.509	41.439	41.439	0.000	-910.700	-856.281	150.017
300	44.700	41.715	41.400	0.083	-910.709	-855.944	149.033
400	53.429	55.842	43.307	5.014	-910.864	-837.649	109.386
500	59.649	68.469	47.100	10.684	-910.543	-819.375	85.599
600	64.382	79.778	51.621	16.894	-909.894	-801.198	69.750
700	68.696	90.023	56.386	23.546	-908.973	-783.150	58.439
800	75.255	99.561	61.191	30.695	-907.696	-765.257	49.966
847		104.164	63.445	34.489	-906.704	-756.914	46.679
847	67.386	104.937	63.445	35.144	-906.049	-756.914	46.679
900	67.974	109.045	66.010	38.731	-905.649	-747.594	43.389
1000	68.959	116.259	70.680	45.579	-904.891	-730.073	38.135
1100	69.833	122.873	75.128	52.519	-904.126	-712.628	33.840
1200	70.629	128.984	79.365	59.543	-903.353	-695.253	30.264
1300	71.372	134.667	83.403	66.643	-902.571	-677.943	27.240
1400	72.075	139.982	87.257	73.816	-901.775	-660.694	24.651
1500	72.750	144.978	90.940	81.057	-900.964	-643.502	22.409
1600	73.402	149.694	94.466	88.365	-900.134	-626.365	20.449
1700	74.037	154.163	97.847	95.737	-949.793	-608.830	18.707
1800	74.659	158.413	101.095	103.172	-948.632	-588.807	17.087
1900	75.270	162.466	104.219	110.669	-947.428	-568.849	15.639
2000	75.873	166.342	107.229	118.226	-946.180	-548.956	14.337

Temperature of transition = 847 K
Enthalpy of transition = 0.655 kJ/mol^{-1}
Temperature of fusion = 1700 K
Enthalpy of fusion = 9.395 kJ/mol^{-1}

Reproduced from Richet et al. (1982) with permission

EBSCOhost - printed on 2/13/2023 4:48 AM via . All use subject to https://www.ebsco.com/terms-of-use

Table 2. Thermodynamic properties of cristobalite

	J/mol K			kJ/mol	Formation from the elements		
T(K)	C_p	$S°_T$	$-(G°_T - H°_{298})/T$	$H°_T - H°_{298}$	$\Delta H°_f$	$\Delta G°_f$	Log K_f
0.	0.000	0.000	0.000	-7.039			
50.	6.548	3.841	3.979	-6.911			
100.	15.986	11.208	11.272	-6.353			
150.	25.276	19.479	19.514	-5.324			
200.	33.010	27.844	27.863	-3.854			
250.	39.535	35.935	35.943	-2.043			
273.	42.246	39.548	39.552	-1.090			
298.	44.885	43.363	43.363	0.000	-907.864	-854.019	149.620
300.	45.069	43.641	43.364	0.083	-907.872	-853.685	148.640
400.	53.601	57.829	45.241	5.035	-908.006	-835.587	109.116
500.	60.723	70.570	49.053	10.758	-907.633	-817.516	85.405
525.	62.400	73.574	50.150	12.298	-907.466	-813.014	80.890
525.	60.250	76.080	50.150	13.614	-906.150	-813.013	80.890
600.	62.775	84.300	53.913	18.232	-905.720	-799.737	69.623
700.	65.132	94.165	58.972	24.635	-905.048	-782.125	58.363
800.	66.833	102.979	63.932	31.237	-904.318	-764.614	49.924
900.	68.150	110.929	68.720	37.989	-903.555	-747.196	43.366
1000.	69.231	118.167	73.308	44.859	-902.774	-729.865	38.124
1100.	70.156	124.810	77.692	51.830	-901.979	-712.612	33.839
1200.	70.976	130.950	81.878	58.887	-901.173	-695.432	30.271
1300.	71.722	136.661	85.875	66.023	-900.355	-678.320	27.255
1400.	72.413	142.002	89.695	73.230	-899.525	-661.272	24.672
1500.	73.065	147.021	93.351	80.504	-898.681	-644.283	22.436
1600.	73.686	151.756	96.855	87.842	-897.822	-627.351	20.481
1700.	74.283	156.241	100.217	95.240	-947.454	-610.024	18.744
1800.	74.863	160.504	103.449	102.698	-946.270	-590.209	17.127
1900.	75.427	164.566	106.560	110.212	-945.048	-570.461	15.683
2000.	75.980	168.449	109.558	117.783	-943.787	-550.778	14.385

Temperature of transition = 525 K
Enthalpy of transition = 1.316 kJ/mol^{-1}
Temperature of fusion = 1999 K
Enthalpy of fusion = 8.92 kJ/mol^{-1}

Reproduced from Richet et al. (1982) with permission

EBSCOhost - printed on 2/13/2023 4:48 AM via . All use subject to https://www.ebsco.com/terms-of-use

Table 3. Thermodynamic properties of amorphous SiO_2

	J/mol K			kJ/mol			
					Formation from the elements		
T (K)	C_p	$S°_T$	$-(G°_T - H°_{298})/T$	$H°_T - H°_{298}$	$\Delta H°_f$	$\Delta G°_f$	Log K_f
0.	0.000	5.108	0.000	-6.967			
50.	6.572	8.950	9.087	-6.840			
100.	16.047	16.383	16.446	-6.276			
150.	25.034	24.632	24.667	-5.244			
200.	32.715	32.915	32.934	-3.795			
250.	38.866	40.901	40.909	-2.000			
273.	41.465	44.456	44.460	-1.070			
298.	44.061	48.475	48.475	0.000	-901.554	-849.233	148.782
300.	44.243	48.748	48.476	0.082	-901.564	-848.909	147.808
400.	52.392	62.666	50.318	4.939	-901.793	-831.308	108.558
500.	58.071	75.003	54.046	10.478	-901.603	-813.702	85.007
600.	62.170	85.972	58.471	16.501	-901.141	-796.161	69.312
700.	65.208	95.795	63.113	22.877	-900.496	-778.714	58.108
800.	67.497	104.659	67.762	29.518	-899.727	-761.367	49.712
900.	69.238	112.714	72.316	36.359	-898.875	-744.123	43.188
1000.	70.563	120.081	76.729	43.352	-897.972	-726.976	37.973
1100.	71.565	126.856	80.983	50.460	-897.039	-709.922	33.711
1200.	72.309	133.116	85.069	57.656	-896.094	-692.953	30.163
1300.	72.845	138.927	88.992	64.915	-895.152	-676.062	27.164
1400.	73.209	144.339	92.754	72.219	-894.225	-659.244	24.597
1480.	73.396	148.413	95.653	78.084	-893.501	-645.837	22.794
1480.	81.373	148.413	95.653	78.084	-893.501	-645.837	22.794
1500.	81.373	149.505	96.364	79.712	-893.163	-642.493	22.374
1600.	81.373	154.757	99.851	87.849	-891.504	-625.836	20.431
1700.	81.373	159.690	103.228	95.986	-940.398	-608.831	18.707
1800.	81.373	164.341	106.495	104.124	-938.534	-589.381	17.103
1900.	81.373	168.741	109.656	112.261	-936.689	-570.034	15.671
2000.	81.373	172.915	112.716	120.398	-934.862	-550.784	14.385

Glass transition near 1480 K

Reproduced from Richet et al. (1982) with permission.

EBSCOhost - printed on 2/13/2023 4:48 AM via . All use subject to https://www.ebsco.com/terms-of-use

Both quartz and cristobalite undergo displacive α-β transitions (see Fig. 1).. Richet et al. (1982) treat these as first-order, more as a matter of convenience in tabulation than for any other reason. This approximation does not introduce major errors when considering the properties of quartz at pressures and temperatures far from the transition. However, in the transition region, strong peaks and/or divergences in heat capacity, compressibility, thermal expansion, and other properties (see Fig. 1) are seen. The α-β

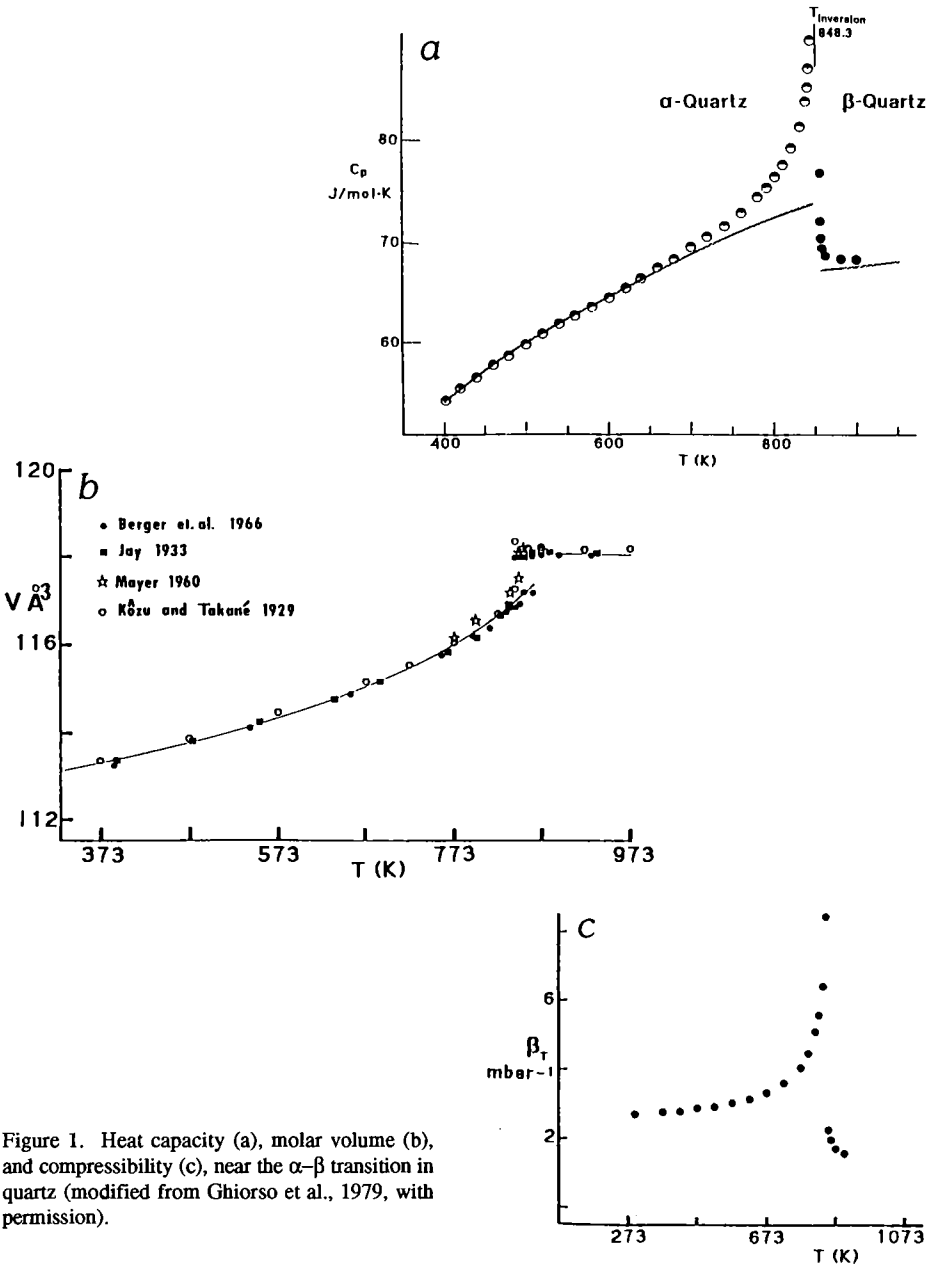


Figure 1. Heat capacity (a), molar volume (b), and compressibility (c), near the α–β transition in quartz (modified from Ghiorso et al., 1979, with permission).

EBSCOhost - printed on 2/13/2023 4:48 AM via . All use subject to https://www.ebsco.com/terms-of-use

transition, which certainly is not simply first order, is further complicated by the probable occurrence over a small temperature range of incommensurate structures (see review in Heaney and Veblen, 1991). The exact shape of the transition peak is still a matter of controversy; Ghiorso et al. (1979) compare various analyses and Gronvold et al. (1989) offer more recent, and somewhat different, data. The details of the α-β transition vary with sample characteristics (purity, thermal history, grain size). The α-β transition rises sharply with pressure (Cohen and Klement, 1975; Klement and Cohen, 1968).

Despite the complexity in the region of the α-β transition, the rather small overall integrated enthalpy associated with this transition (0.5 to 0.7 kJ/mol) makes the details of the transition unimportant in influencing thermodynamic properties in P-T regions away from the transition itself. Thus the final data sets chosen by Richet et al. (1982) and by Gronvold et al. (1989) are in very good agreement far from the transition region.

It is well established that cristobalite is the stable, high temperature polymorph, but whether β-quartz transforms directly to cristobalite, or whether there is a stable phase field for tridymite (see below) has been disputed. The "best" data selected by Richet et al. (1982) place the β-quartz - β-cristobalite transition at 1108 K, stable melting of β-cristobalite at 1999 K, and metastable melting of β-quartz at 1700 K. A semi-schematic phase diagram consistent with these thermodynamic parameters is shown in Figure 2.

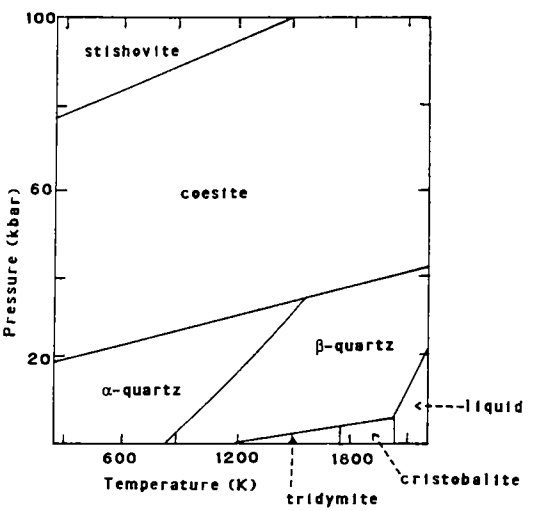


Figure 2. Semi-schematic diagram of the P-T stability relations among silica polymorphs near atmospheric pressure. The α–β quartz transformation is shown as a dashed line to stress it is not a simple first order transition.

Molten silica supercools easily to form a glass. Silica is a very "strong" liquid, in the sense of Angell (1985). Changes in heat capacity, thermal expansivity, and other physical properties at the glass transition temperature, T_g, are not pronounced; indeed T_g is not easily detected. Richet et al. (1982) suggest a glass transition at about 1480 K for slowly cooled SiO_2 glass and about 1600 K for fast-quenched samples. For the supercooled liquid they suggest a heat capacity, independent of temperature, of 81.4 J/mol·K, with a jump of about 10% at T_g, although their drop calorimetric data do not show T_g very clearly. Recent high temperature differential scanning calorimetry (Navrotsky, unpublished) confirms the data and interpretation of Richet et al. (1982) and shows the glass transition quite clearly (Fig. 3).

EBSCOhost - printed on 2/13/2023 4:48 AM via . All use subject to https://www.ebsco.com/terms-of-use

Table 4. Thermodynamics of phase transitions among stable silica polymorphs

	T (K)	ΔH (kJ/mol)	ΔS (J/mol·K)
α-quartz = β-quartz	847[a,b]	0.65 ± 0.20[d]	0.77 ± 0.24[d]
α-cristobalite = β-cristobalite	525[a,b]	1.32 ± 0.30[d]	2.51 ± 0.57[d]
β-quartz = liquid	1700[a,b,c]	9.39 ± 1.00[d]	5.52 ± 0.59[d]
β-cristobalite = liquid	1999[a]	8.92 ± 1.00[d]	4.46 ± 0.50[d]
β-quartz = β-cristobalite	1108[a]	2.15 ± 1.00[d]	1.94 ± 0.90[d]
α-quartz = coesite		2.93 ± 0.29[e]	-2.93 ± 0.80[e]
coesite = stishovite		48.95 ± 1.72[e]	-4.19 ± 1.67[e]

a. Data from Richet et al. (1982), equilibrium at 1 atm
b. Treated as first order transition
c. Metastable melting equilibrium at 1 atm
d. ΔH, ΔS at equilibrium temperature shown
e. Data from Akaogi et al. (1984), ΔH°_{298} and ΔS°_{298}

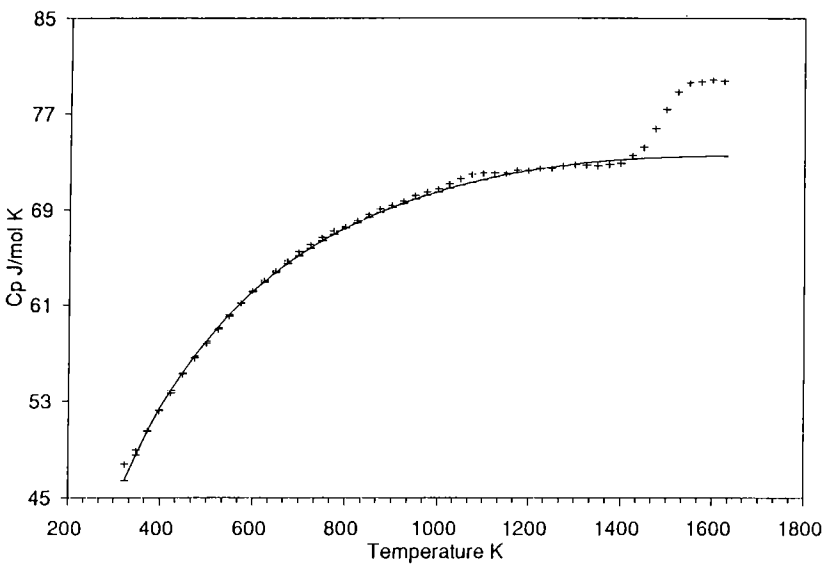


Figure 3. Heat capacity (Navrotsky, unpublished) of SiO_2 glass obtained by differential scanning calorimetry in a Netzsch 404 calorimeter, scan rate of 20 K/min. The glass transition is seen clearly. Crosses represent measured heat capacity, curve is that of Richet et al., (1982).

Tridymite

Tridymite is a somewhat enigmatic phase. Though it occurs in nature and can be synthesized, for example by growth using a Na_2WO_4 flux, it is not clear whether tridymite has a stability field in the pure SiO_2 system, though such a field is shown in Figure 2. Furthermore, several types of tridymite modifications exist. These include pseudo-orthorhombic forms (PO-*n*) and two monoclinic forms MC and MX-1 (Graetsch and Flörke, 1991; DeDombal and Carpenter, 1993). MX-1 tridymite can be produced

EBSCOhost - printed on 2/13/2023 4:48 AM via . All use subject to https://www.ebsco.com/terms-of-use

from the MC polymorph by quenching MC from 383-433 K to below 273 K, or by grinding MC at room temperature. The MX-1 form contains two incommensurate structural modulations. All three polymorphs undergo a complex series of structural phase transitions on heating, with lambda-type, sharp, and/or gradual heat capacity anomalies, depending on the sample. Furthermore, stacking faults are prevalent in tridymites, and their energetics, though assumed small, are unknown. (Thompson and Wennemer, 1979; Graetsch and Flörke, 1991; DeDombal and Carpenter, 1993; Xiao et al., 1993, 1994). Mixed phases representing tridymite-cristobalite interlayering have also been reported (Thompson and Wennemer, 1979).

A recent calorimetric study of the MC polymorph shows its enthalpy of formation from quartz to be 5.1 ± 1.0 kJ/mol, in reasonable agreement with an earlier value for a less well characterized tridymite, 3.3 ± 3.6 kJ/mol (see Table 5). The MX-1 material produced by ball-milling MC is somewhat higher in enthalpy, 7.7 ± 2.0 kJ/mol above quartz. The results suggest that tridymite is a variable material in terms of energetics as well as structure. More work on these materials is needed.

Table 5. Thermochemistry of various tridymites

Sample	**Enthalpy at 298 K relative to quartz** (kJ/mol)	**Reference**
Synthetic flux grown Monoclinic MC	5.1 ± 1.0	1
Synthetic MX-1, Ball milled 8 min from MC	7.7 ± 2.0	1
Uncertain	3.3 ± 3.6	2

1. Calorimetry of Petrovic and Navrotsky (unpublished), using samples of Xiao et al. (1993, 1994).
2. Robie et al. (1978).

High pressure phases

Coesite, with Si in tetrahedral coordination and stishovite, with Si in octahedral coordination are quenchable high pressure polymorphs, the former formed near 25 kbar, the latter near 90 kbar (see Fig. 4). Solution calorimetry in molten lead borate by Akaogi et al. (1984) (see Tables 4 and 6) provide thermochemical data which, when used to calculate the quartz-coesite and coesite-stishovite equilibrium, gave good agreement with experiments in the 700-1400 K range (see Fig. 4). Recent experiments at much higher temperature (2000-3000 K) (Zhang et al., 1993) explored melting as well as phase transitions (see Fig. 5). The data for the coesite-stishovite transition appear to show a much steeper dP/dT at high temperature than at low temperature. To fit this apparent curvature by thermochemical calculation would require somewhat unlikely pressure and temperature derivatives for bulk modulus, thermal expansivity, and/or heat capacity. Uncertainties in P-T calibration, sluggishness of reactions at low temperature, or other sources of error may be responsible. We are currently redetermining the enthalpy of stishovite to refine our earlier study.

An internally consistent thermodynamic data set for the silica system, based on existing thermochemical and phase diagram information, has been evaluated by Swamy et al. (1994). The uncertainties associated with stishovite (mentioned above) and

EBSCOhost - printed on 2/13/2023 4:48 AM via . All use subject to https://www.ebsco.com/terms-of-use

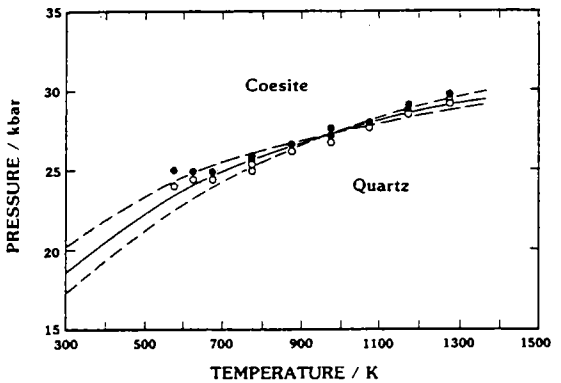


Figure 4 (top). The quartz-coesite transition boundary (solid curve) calculated from thermochemical data (Akaogi et al., 1984). Dashed curves show the uncertainty of the slope of the calculated boundary. Experimental data (circles) are by Bohlen and Boettcher (1982). Reproduced with permission.

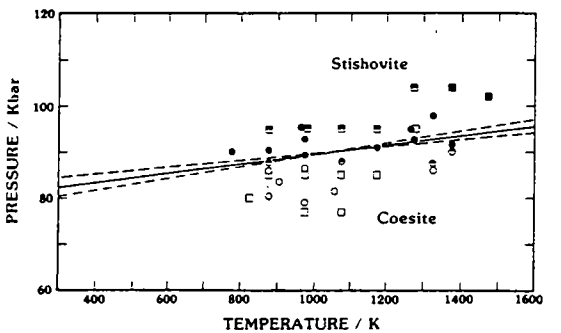


Figure 4 (bottom). The coesite-stishovite transiton boundary (solid line) calculated from thermochemical data (Akaogi et al., 1984). Dashed lines represent the uncertainty of the slope of the calculated boundary. Circles and squares are experimental data by Yagi and Akimoto (1976) and Suito (1977), respectively. Reproduced with permission.

Table 6. Thermophysical parameters for silica phases participating in high pressure phase equilibria

Parameters[a]	Quartz	Coesite	Stishovite	Liquid
V_{298}, cm^3/mol[b]	22.69	20.64	14.01	26.71[c]
K_{298}, GPa	68.42	96.00	314.0	14.43
$(dK_T/dP)_T$	6.40	8.40	6.40	4.30
$(dK_T/dT)_P$, GPa/K	—	-0.02	-0.047	—
α_0, 10^{-4}	-0.065	0.0543	0.1023	0.100
α_1, 10^{-8}	—	0.8320	1.3500	—
α_3	—	-0.0610	—	—
a	78.812	78.746	58.129	81.37
b, 10^{-3}	1.205	0.6974	7.002	—
c, 10^7	0.1731	-0.2963	-1.2689	—
e, 10^9	0.1202	0.5858	1.7928	—
g, 10^4	-1.2130	-0.6689	1.7040	—

a. Data as tabulated by Zhang et al. (1993)

b. $V°_{298}$ is molar volume at 298 K and 1 atm; K_{298} is bulk modulus, with $(\partial K_T/\partial P)_T$ and $(\partial K_T/\partial T)_P$ its pressure and temperature derivatives; α_0, α_1, and α_2 are coefficients in thermal expansion equation, $\alpha = \alpha_0 + \alpha_1 T + \alpha_2 T^{-2}$; a, b, c, e, g are coefficients in heat capacity equation C_P (J/mol·K) = $a + bT + cT^{-2} + eT^{-3} + gT^{-1}$

c. Extrapolated ignoring glass transition, volume of supercooled liquid reference state.

EBSCOhost - printed on 2/13/2023 4:48 AM via . All use subject to https://www.ebsco.com/terms-of-use

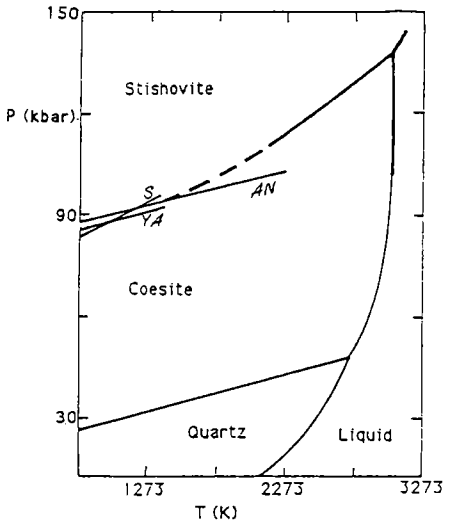


Figure 5. Phase diagram of silica at high pressure and temperature, including melting relations. Thick curves are new data of Zhang et al. (1993), light curves represent earlier data (modified from Zhang et al. 1993). Used with permission.

uncertainties in physical properties (high P-T equations of state) suggest that additional work is indeed desirable.

Energy associated with dislocations in quartz

The energy associated with dislocations has been considered to be important in many mineralogical processes. High temperature drop-solution calorimetry in lead borate ($2PbO{\cdot}B_2O_3$) solvent was recently employed to study the energy associated with dislocations in quartz by measuring the enthalpy difference between undeformed and deformed single crystals of synthetic quartz (Liu et al., 1994).

Two sets of calorimetric experiments have been conducted: (1) using a Pt capsule as a container for powdered sample; and (2) using pellets made from sample powder without any container. For the first set of experiments, the undeformed sample with a dislocation density of $<10^5$ cm^{-2} yielded a measured enthalpy (the sum of heat content and enthalpy of solution) of 39.2 ± 1.0 kJ/mol, while the sample with a dislocation density from 5.9×10^{10} to 1.2×10^{11} cm^{-2} gave an enthalpy of 38.6 ± 0.8 kJ/mol. For the second set of experiments, the measured enthalpy of the undeformed sample is 38.9 ± 0.3 kJ/mol and that of a deformed sample with a dislocation density from 3.0×10^{10} to 1.2×10^{11} cm^{-2} is 38.2 ± 0.6 kJ/mol.

The enthalpy difference from both sets of experiments is about 0.6 kJ/mol with an uncertainty of about ± 0.6 kJ/mol. This result is consistent with theoretical calculations and clearly indicates that the energy associated with dislocations is small. For geologically realistic dislocation densities ($<10^9$ cm^{-2}), the maximum excess energy would be less than 0.1 kJ/mol.

METASTABLE SILICA POLYMORPHS

Microporous and mesoporous phases

Since the synthesis of the first high-silica zeolites, β and ZSM-5, high-silica zeolites and molecular sieves have attracted attention and triggered major research efforts both in industry and academia (see chapter by Higgins). Numerous new, high- and pure-silica

EBSCOhost - printed on 2/13/2023 4:48 AM via . All use subject to https://www.ebsco.com/terms-of-use

structures have been reported and their number is growing rapidly. Three classes of materials are presently known: (1) clathrasils, in which isolated cavities of 0.4 to 1.0 nm diameter are interconnected, separated by small "windows" of < 0.3 nm; (2) zeolites proper, which contain pores with diameters of 0.5 to 1.0 nm; and (3) mesoporous materials, with periodically arranged pores in the 1 to 10 nm range, but with seemingly amorphous frameworks. All these materials are generally made by co-assembly, crystallization from aqueous or hydrothermal solution containing organic and/or inorganic structure-directing agents that participate in the crystallization and initially occupy the cages. Often, but not always, such agents can be burned out at 500 to 1000 K, leaving an anhydrous, organic-free framework that, upon further heating, converts to amorphous silica or cristobalite for phases of SiO_2 composition.

From an energetic point of view, several questions arise. How are energies, entropies, and heat capacities of these materials related to each other? Why are there so many phases? Is there an energetic limit to the pore size that can form? Why do the mesoporous materials have noncrystalline silicate frameworks? Does the structure-directing agent play a thermodynamic or kinetic role?

Recent calorimetric studies (Petrovic et al., 1993, 1994) address these questions. Table 7 lists the enthalpies relative to quartz of various low density silicas. The energetics of the pure silica zeolites may be viewed in comparison with those of dense silica polymorphs, which include stishovite and the tetrahedral frameworks of coesite,

Table 7. Energetics of low density metastable silica polymorphs

Material	**Molar Volume** (cm^3/mol)	**Enthalpy relative to quartz** (kJ/mol)
Zeolites		
ZSM-12	31.05	8.7 ± 0.8[a]
ZSM-5	33.65	8.2 ± 0.8[a]
ZSM-11	34.02	8.2 ± 1.0[a]
SSZ-24	34.42	7.2 ± 0.9[a]
ZSM-18	42.12	13.9 ± 0.4[e,f]
EMT (hexagonal faujasite)	46.51	10.5 ± 0.9[a]
FAU (faujasite)	47.43	13.6 ± 0.7[a]
Mesoporous silicas		
MCM-41 (28)[b]		14.8 ± 1.0[e]
MCM-41 (32)[b]		14.4 ± 0.4[d]
MCM-41 (35)[b]		14.6 ± 0.6[d]
MCM-41 (50)[b]		14.8 ± 0.5[d]
MCM-41(collapsed)[c]		11.2 ± 1.0[d]
Other		
Glass	26.32	9.2 ± 0.5[d]
Moganite	23.02	3.3 ± 0.6[e]

a. at 298 K (Petrovic et al., 1993)
b. number in ( ) refers to XRD d-spacing of the first diffraction line in Å
c. collapsed to an amorphous phase after several months standing in air
d. at 298 K (Richet et al., 1982)
e. at 298 K (Petrovic et al., in prep.)
f. contains 3-membered rings

EBSCOhost - printed on 2/13/2023 4:48 AM via . All use subject to https://www.ebsco.com/terms-of-use

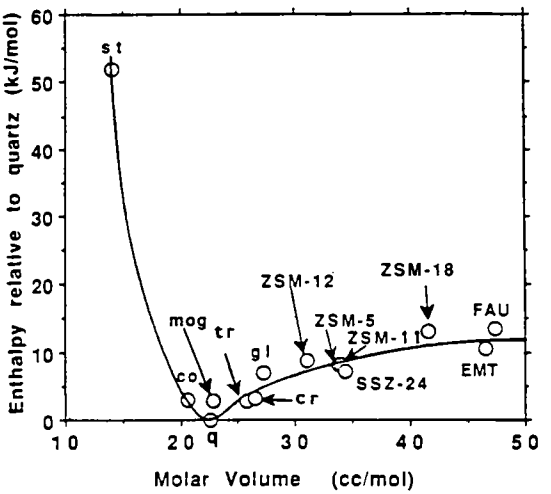


Figure 6. Enthalpies of crystalline silica polymorphs relative to quartz versus molar volume (modified from Petrovic et al., 1993 to include new data). Curve is suggestive, not fit to any equation.

quartz, tridymite, cristobalite, and silica glass. Quartz is the thermodynamically stable form at 298 K and must lie at a minimum of any curve relating energy (enthalpy) and molar volume (see Fig. 6). This curve rises steeply to stishovite, with octahedral Si and a molar value of 14.01 cm^3/mol. Any hypothetical tetrahedrally coordinated structure with equally high density would be metastable with respect to stishovite and even higher in energy. Thus it is clear that energy and enthalpy rise sharply with decreasing molar volume. A similar trend is seen for amorphous silicas densified by pressure or radiation damage (see below).

For molar volumes greater than (and densities less than) that of quartz, the trend is quite different (Petrovic et al., 1993) (see Table 7 and Fig. 6). The enthalpy increases only slowly with increasing molar volume. Indeed, comparing silica faujasite (FAU) with a molar volume of 47.43 cm^3/mol to quartz, with a molar volume of 22.69 cm^3/mol, the difference is only 13.6 kJ/mol; thus, a more than 2-fold expansion of the structure raises the energy by an amount only 1.5 times the enthalpy of vitrification. It is clear that framework silica structures are energetically very tolerant of changes in the topological linkages of tetrahedra to form rings and cages of different sizes. It appears that in zeolitic silicas the large cavities are beginning to act as "external" pores, with increase in their volume fraction (decrease in framework density) affecting the energy in only a minor way. Thus, 5-8 Å diameter pores may mark the transition, at least in terms of energetics, from a uniform structure to a heterogeneous one in which the interior of the pores is not strongly interacting with the framework, and is beginning to act like a second phase. Whether this is true in microporous materials in general remains to be determined.

To a first approximation, all zeolitic silicas studied so far are strikingly similar to each other in enthalpy, generally 10-15 kJ/mol less stable than quartz and only 0-5 kJ/mol higher in energy than silica gels (Petrovic et al., 1993). Thus, formation of these zeolitic materials from a silica gel under hydrothermal conditions is not an energetically costly process, but one for which thermal energy (RT = 3 kJ/mol at 373 K) suffices. The structure-directing agent (template or guest molecule) does not have to stabilize an otherwise energetically prohibitive structure, but to select among numerous structures of similar energy. This suggests a kinetic or entropic role for the structure-directing agent in

EBSCOhost - printed on 2/13/2023 4:48 AM via . All use subject to https://www.ebsco.com/terms-of-use

zeolite synthesis. Whether structure-directing agents are present under natural hydrothermal conditions when zeolite minerals crystallize is unknown.

The small differences in energy among the silica zeolites might be related to the distribution of Si-O-Si angles which connect relatively undistorted SiO_4 tetrahedra. *Ab initio* molecular orbital calculations find that the potential energy curve for the Si-O-Si angle shows a small barrier to linearity and does not rise sharply with decreasing intertetrahedral angle until that angle is less than about 135° (see chapter by Gibbs et al., this volume). The distribution of Si-O-Si angles observed in silicates in general, and in "dense" SiO_2 polymorphs in particular, follows a similar trend, with angles between 140° and 180° very common, but angles below 135° infrequent, or absent in the case of dense silica polymorphs. In quartz there is a single Si-O-Si angle of 143.6°, near the optimum angle from the potential energy curve, and cristobalite also has a single angle, 146.7°. All others, including tridymite, show a distribution of angles. The average angle ranges from 141° to 154° and does not appear to correlate with energetics. Coesite, a high-pressure polymorph and the densest tetrahedral SiO_2 structure, has been reported to have a 180° angle, but there is still some debate about its structure. The silica zeolites all have some Si-O-Si angles between 145° and 170°; however, ZSM-12, EMT, and FAU have a population of Si-O-Si angles ≤ 140°. Though these are very likely in small four-membered rings, such rings in a structure do not automatically imply the presence of small angles, as is illustrated by ZSM-5 and ZSM-11. Faujasite is an extreme case, with two distinct populations of rings, one four- and six-membered, and the other twelve-membered. The presence of small rings in a structure does not imply a higher density, because the region between three- or four-membered rings contains larger rings and cages and is less dense. Indeed, ZSM-18 contains 3-membered rings, and is somewhat higher in enthalpy than the other zeolites studied (see Table 7).

The shape of the potential energy curve from quantum calculations suggests that small Si-O-Si angles are more destabilizing than large ones. Figure 7 shows the enthalpy of silica zeolites relative to quartz plotted against the fraction of Si-O-Si angles ≤ 140°. A reasonable correlation is seen, which is more pronounced than that for energy versus average Si-O-Si angle, framework density, or molar volume (Petrovic et al., 1993).

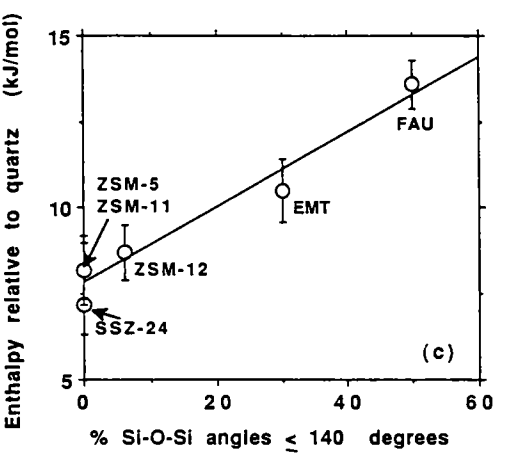


Figure 7. Enthalpy of zeolitic silicas relative to quartz (kJ/mol) plotted against fraction of Si-O-Si angles ≤ 140° (from Petrovic et al., 1993, with permission). Line is suggestive only.

EBSCOhost - printed on 2/13/2023 4:48 AM via . All use subject to https://www.ebsco.com/terms-of-use

Thus, Si-O-Si angles between 130° and 140° indeed appear to destabilize silica zeolites slightly. This observation provides the basis for a hypothesis as to why very large pore frameworks seem harder to make in silicate and aluminosilicate zeolites than in aluminophosphates or zeolites containing boron, beryllium, or zinc. The hypothesis is that the pure-silica materials having large pores are destabilized not by their large cages, but by the small rings with angles between 120° and 135°. This is consistent with the observed large pore materials being those with P, Be, B, or Zn in the framework (i.e., in 4-fold coordination), since the optimum T-O-T, T-O-Si, or T-O-Al angles for these cations are indeed shifted to lower values, as seen both from observed angles in other materials and from molecular orbital calculations.

Recently, a new family of mesoporous materials, with pore diameters in the 2 to 10 nm range, has been synthesized using surfactants as structure-directing agents (Beck et al., 1992). These phases have a periodic arrangement of regularly sized pores but an amorphous framework, as inferred from X-ray diffraction, Raman spectroscopy, and nuclear magnetic resonance. We have recently measured the enthalpy of formation of several of these so-called MCM-41 materials (Petrovic et al., 1994) and found them to be only 14-15 kJ/mol less stable than quartz at room temperature (see Fig. 8). Thus, even such large pore silicas are similar in energy to zeolites with small cages and to amorphous sol-gel silica.

Recent evidence on the synthesis of mesoporous aluminosilicates using surfactant structure-directing techniques (Monnier et al, 1993; McGehee et al., 1994) suggests that the process of assembly is complex. Formation of the surfactant mesophase does not necessarily precede silica precipitation; the silica does not just petrify a preexisting organic framework. The forces involved in micellar interactions are known to be small and delicately balanced. We have shown that the energy differences between various silicate arrangements are also small and on the order of thermal energy. Thus, although the bonding within an organic molecule and within a silicate is strong, as is the electrostatic interaction between charged species in solution and in the evolving framework, the energy differences between alternative mesoscopic configurations are likely to be small, and the change in energy during synthesis is probably only a very weak driving force. This scenario of small differences in energy between competing strongly bonded species sets the stage for self-assembly, with the framework and the structure-directing agent influencing each other's geometrical arrangement, and with the structuring driven by small energetic differences occurring in a ternary or multicomponent system in the thermodynamic sense. These small differences are the key to why so many different structures can form, just as is the case for more conventional self-assembly, e.g., protein folding or phospholipid bilayer mesophase formation. Indeed, were the differences in energy between alternative mesostructures large, only one structure (of distinctly lowest free energy) would form, rather than the complexity of zeolites and mesophases seen.

The hypotheses above, though based on data for silica, are expected to apply to a wide range of porous materials. Thus, for the aluminum phosphate (ALPO) family, for example, the low framework density structures are also likely to be very similar in energy to each other, though one cannot predict the value of this energy relative to berlinite (the most stable polymorph), or the framework density at which this energy plateau is attained. Work to characterize energetics in such systems is in progress.

Interestingly, the heat content, H_{977}-H_{298}, appears to scale with framework density, with the denser silica materials having the higher average heat capacity in this temperature range (see Fig. 9). Since the less dense phases generally have the higher

EBSCOhost - printed on 2/13/2023 4:48 AM via . All use subject to https://www.ebsco.com/terms-of-use

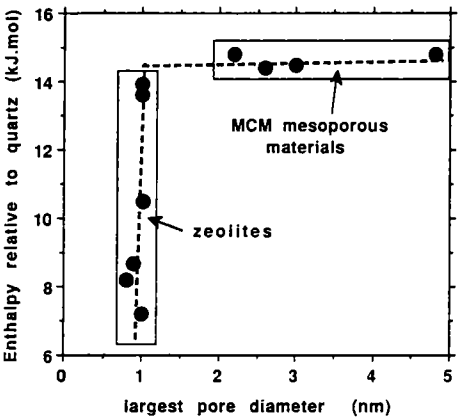


Figure 8. Enthalpy of zeolitic and mesoporous silicas vs largest pore diameter. Data from Petrovic et al. (1994) and additional unpublished data (Petrovic et al., in preparation). Two dashed lines show regions where enthalpy depends significantly on pore diameter (<1 nm) and varies only weakly, if at all, with pore diameter (>1 nm).

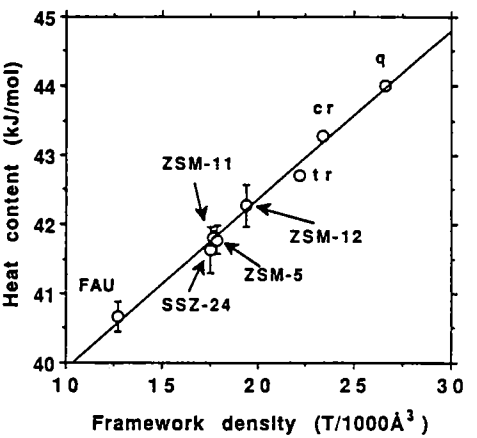


Figure 9. Heat content (H_{977} - H_{298}) of dense and zeolitic silicas vs framework density (modified from Petrovic et al., 1993, with permission). Only essentially pure SiO_2 materials are shown. The line is a least-squares fit.

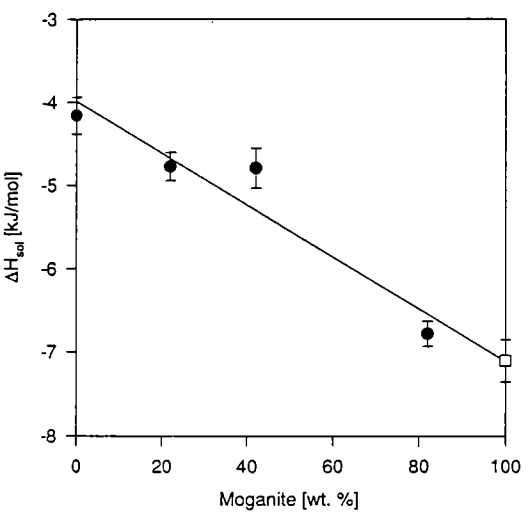


Figure 10. Enthalpies of solution in molten $2PbO{\cdot}B_2O_3$ at 975 K of samples (which are intergrowths of quartz and moganite) vs moganite content derived by Rietveld refinement. Data from Petrovic, Heaney, and Navrotsky, in preparation. Solid circles represent data, open square is extrapolated value (with uncertainties) for moganite.

EBSCOhost - printed on 2/13/2023 4:48 AM via . All use subject to https://www.ebsco.com/terms-of-use

entropy at room temperature, $S°_{298}$, some crossovers in heat capacity curves appear likely. Detailed C_p measurements and lattice dynamical modelling would be instructive.

Moganite

High temperature solution calorimetry using lead borate ($2PbO{\cdot}B_2O_3$) solvent was recently employed to study the thermochemical stability of moganite, a novel silica polymorph present in microcrystalline quartz varieties (Heaney and Post, 1992). A series of chert specimens with different moganite contents has been studied. Moganite concentrations were determined by Rietveld refinement of powder X-ray diffraction patterns, and for each specimen the complementary phase was pure quartz.

The enthalpies of solution at 977 K are shown in Figure 10 (above). When these values are taken together with the value for quartz they define a linear trend that extrapolates to -7.1 kJ/mol for pure moganite. The observed thermochemical instability of moganite relative to quartz of 2.9 ± 1.5 kJ/mol at 977 K is similar to that of cristobalite. These results strongly support powder X-ray diffraction studies showing that moganite is indeed a distinct silica phase. Though moganite has virtually the same density as quartz, its enthalpy is 3.3 kJ/mol higher at 298 K. Thus volume (density) is not the only factor in determining the energetics of metastable silicas polymorphs. Structurally, this instability may be related to the presence of 4- and 8-membered rings of SiO_4 tetrahedra containing Si-O-Si angles of 137, 146 and 147°, in contrast to quartz, which contains only 6-membered rings with a single Si-O-Si angle of 144°. The metastability of moganite relative to quartz also may explain the apparent scarcity of moganite in rocks older than 130 million years.

Amorphous silica

Apart from a variable water content too small (< 0.1%) to be significant for bulk energetics, normal silica glass (fused silica slowly cooled from the molten state) is a fairly well defined material. Its energy is only 9.1 kJ/mol higher than that of quartz at room temperature, while the enthalpy of fusion of cristobalite at its melting point is only 8.9 kJ/mol. These values represent the smallest heats and entropies of fusion of any oxides, and are comparable to values for phase transitions among the stable crystalline polymorphs. They suggest that the structural reorganization upon destruction of long-range order to form glass or melt is not profound; nor is the change from glass to melt (glass transition) a pronounced phenomenon in silica.

Amorphous forms of SiO_2 that are much more metastable can be made (see Table 8). Huffman et al. (1986) measured the energetics of low-pressure chemically vapor deposited (LPCVD) silica films and powder ("snow") produced from $SiH_4 + O_2$ (see Table 8 and Fig. 11). The excess enthalpy relative to fused silica increased with decreasing temperature of deposition, reaching as much as 67 kJ/mol (8 times the enthalpy of fusion) for the powder made at the lowest temperature. Though part of this may be an effect of surface area, the majority of the energetics is a bulk effect. Radial distribution functions (RDF) defined by X-ray methods showed definite differences between the CVD silica and bulk glass (Konnert et al., 1987). Large differences in the RDF in the 0.4 to 0.6 nm region indicate that the ring statistics are very different for the two phases. Six-membered rings are favored in the bulk silica. Very possibly the differences in the RDF indicate the presence of more rings of different sizes in the CVD material. The absence of significant oscillations in the snow RDF beyond 1.0 nm indicates much less mesoscopic order than in bulk silica.

EBSCOhost - printed on 2/13/2023 4:48 AM via . All use subject to https://www.ebsco.com/terms-of-use

Table 8. Energetics of metastable amorphous silicas

Sample	Enthalpy relative to bulk glass (kJ/mol)
LPCVD films made from $SiH_4 + O_2$ deposited at	
523 K	43.8 ± 2.2
643 K	33.3 ± 0.4
703 K	22.1 ± 0.5
LPCVD "snows" made from $SiH_4 + O_2$ deposited at	
327-455 K	59.9 ± 1.6
344-673 K	47.0 ± 7.0
Flame hydrolyzed at 1073 K from $SiCl_4 + O_2$	0 ± 0.5
Colloidal silica gel, from fumed silica	
no additives	10.6 ± 4.2
polyvinyl acetate binder	13.9 ± 9.7
Alkoxide derived silica gel	
acid catalyzed	
no additives	7.3 ± 1.0
no additives	11.8 ± 7.2
base catalyzed	
strong base, no additives	66.8 ± 1.8
strong base, no additives	53.5 ± 7.1
weak base, no additives	17.2 ± 4.3
two step catalyzed, strong acid followed by partial neutralization	
no additives	6.6 ± 8.5
glycerol added	0.7 ± 8.8
formamide added	16.2 ± 5.3
oxalic acid added	5.9 ± 4.2
supercritically dried gels, two step acid catalyzed	
normal preparation	1.4 ± 2.2
excess ethanol	2.7 ± 4.0
Pressure densified silica	
~ 17% densified	23.7 ± 1.5
~ 17% densified	16.5 ± 1.4
13.8% densified	15.9 ± 2.0
18.4% densified	19.2 ± 2.0
Neutron irradiated silica	
Corning 7960 glass	12.1 ± 1.1
originally quartz	10.2 ± 2.0

Table modified from Navrotsky (1991).

The widths of the Si-O, O-O, and Si-Si distance distributions were used to estimate the potential energy that is associated with observed distortions of bond distances and angles from equilibrium values for bulk glass (Konnert et al., 1987). Each observed distance distribution was assumed to be the convolution of a thermal motion distribution with a positional disorder distribution. Force constants for Si-O stretching and tetrahedral and intertetrahedral bending were then used to calculate the excess energy. The largest energy contribution comes from the O-O distortions, which result in a significantly different mean O-Si-O angle for snow (107.8 ± 0.5°) than for bulk glass (109.9 ± 0.4°). The smaller energy terms arise from differences in Si-O and Si-Si distributions, which do

EBSCOhost - printed on 2/13/2023 4:48 AM via . All use subject to https://www.ebsco.com/terms-of-use

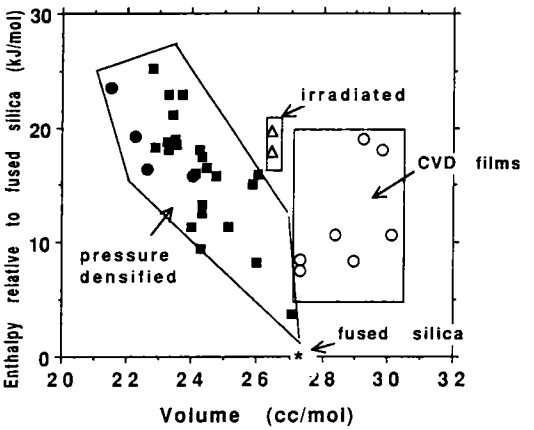


Figure 11. Enthalpy relative to bulk SiO_2 glass of various amorphous silica materials as a function of their molar volume. Solid circles - pressure densified silica (Navrotsky et al., in prep); solid squares, pressure densified silica (Couty, 1977); open triangles - radiation damaged silica (Navrotsky et al., in prep); open circles, CVD silica (Huffman et al., 1986).

not significantly change the mean values but substantially increase the variance in the Si-O distance and the Si-Si distance in snow. The total energetic contributions reflect a balance between the energy needed for a given distortion and the extent to which that distribution differs from snow to glass. Although the force constants and energy calculations used cannot represent a unique set of parameters, one can conclude that the major distortions and the major source of excess energy come from bond bending rather than changes in Si-O distances.

Infrared and Raman spectra of LPCVD SiO_2 films and of those annealed at 1173 K have been published (Huffman and McMillan, 1985). Raman spectra show the initial presence of bands at 500 cm^{-1} (D1 defect) and 600 cm^{-1} (D2 defect) in all films. The intensity of the D2 band on annealing at 1173 K decreases to that of fused silica glass. Infrared and Raman spectra of all films detect a peak near 880 cm^{-1}, which is most prominent for the 643 and 523 K samples, barely discernible for the 703 K film, and absent in the annealed films. The band near 500 cm^{-1} is associated with 4-fold siloxane rings, that near 600 cm^{-1} is associated with 3-fold siloxane rings, and the band near 880 cm^{-1} is associated with 2-fold rings.

The interpretation of the excess energy in LPCVD films as being mainly due to the presence of small rings is consistent with infrared and Raman spectra of the original and annealed films and diffraction studies on related "snows." Annealing studies show that this excess energy can be eliminated near 1073 K, consistent with the zero stored energy in the flame hydrolysis material prepared at 1073 K.

Two sol-gel silicas were studied by Maniar et al. (1990). Thermochemical cycles were developed to correct for the evolution of volatile impurities (water and organics) and determine the energy associated with the silica framework. More recent work on a series of colloidal and alkoxide silica gels was performed by Ying et al. (1993a,b) (see Table 8).

The small metastability of the colloidal silicas (Ying et al., 1993a) puts an upper limit of about 10 kJ/mol (a more likely value is 5 kJ/mol) on effects due to reduction of surface area and porosity. These materials are derived from fumed silica, analogous to the flame hydrolysis material, and they cannot undergo significant polymerization-depolymerization reactions during the early stages of processing once they are

EBSCOhost - printed on 2/13/2023 4:48 AM via . All use subject to https://www.ebsco.com/terms-of-use

precipitated. Thus the large (> 20 kJ/mol) excess energies in the LPCVD films and snows and in the base-catalyzed gels reflect conditions (anhydrous low-temperature deposition and rapid precipitation during drying, respectively) where the ring structure initially deposited is not able to rearrange to a more stable configuration.

Amorphous SiO_2 denser than bulk silica glass can be produced by pressure densification or by radiation damage. The former produces permanent densification of up to 22% for samples treated at 15 to 20 GPa at room temperature, while the latter produces 3% densification. Based on neutron diffraction and vibrational spectroscopy, Susman et al. (1990) propose that both types of glasses have similar changes in mid-range order relative to bulk silica, although in the irradiated samples the damage may be concentrated along highly densified ionization tracks and displacement cascades within a less altered matrix, while the distortions in the pressure densified material are presumably more uniformly distributed. The neutron diffraction studies of glass pressurized at 298 K and 16 GPa show the following: From 6 $Å^{-1}$ to the maximum momentum transfer in the experiment (i.e. for distances in real space corresponding to the first coordination shell), the structure factors of the densified and undensified silica are essentially the same. This implies that the SiO_4 tetrahedron changes very little, and there is no evidence for octahedrally coordinated silicon. Nor is octahedral Si seen by NMR (J. Stebbins, pers. comm.).

There are striking differences in the second shell arising from O-O correlations. There is a broadening of the bond angle distribution about oxygen, a 10% increase in the coordination of oxygen by oxygen, and a doubling of the r.m.s. displacement. These data are consistent with an increase in the population of smaller (3-fold and 4-fold) rings. The enhanced D1 and D2 bands seen in Raman spectroscopy of the pressure densified glass support this contention. In addition, the 434 cm^{-1} band in bulk glass, which involves symmetric Si-O-Si stretching, is much less intense in the pressure densified glass, suggesting less freedom about the bridging oxygen, consistent with smaller rings. Similar changes are seen in the Raman spectra of neutron compacted fused silica, consistent with analogous densification mechanisms.

Using the diamond anvil cell with synchrotron radiation, Meade et al. (1992) studied the effect of pressure (at room temperature) in situ to 42 GPa. Below 8 GPa, they found little change in the Si-O distances but a decrease in the Si-Si distance, consistent with distortion of the Si-O-Si angles between relatively rigid SiO_4 tetrahedra. At 28 GPa, the Si-O distance has lengthened, and by 42 GPa it approaches that in stishovite. A gradual change to octahedral coordination is thus inferred and is consistent with earlier in situ Raman spectra above 30 GPa (Hemley et al., 1986). Thus, silica loses its tetrahedral framework at very high pressure, but much of this coordination change appears reversible and nonquenchable. The energetics of this change in coordination have not been studied, but this process is probably energetically more costly than the quenchable lower pressure densification described below. The behavior of silica at very high pressure is discussed in Chapter Kingma.

The enthalpies associated with quenched pressure densified glass (up to 16 GPa) and neutron irradiated glass are shown in Table 8 and Figure 11. Both types of sample show substantially higher energy than normal atmospheric pressure bulk melted glass.

Somewhat surprisingly, the irradiated samples (with only 3% densification) show over half the excess energy shown by the sample pressurized at 16 GPa with 17-22% densification. This suggests that, although radiation damage may be localized in the sample rather than uniformly distributed (leading to less overall compaction), the extent

EBSCOhost - printed on 2/13/2023 4:48 AM via . All use subject to https://www.ebsco.com/terms-of-use

of local damage may be greater than in the pressure densified silica when normalized to the same number of tetrahedra involved. This supports the proposal by Susman et al., (1990) that the radiation damaged silica may indeed be significantly more chemically reactive than bulk glass. This may have important implications for high-level nuclear waste disposal.

In contrast to the CVD "snow," the quenched pressure-densified silica on which calorimetry was done shows essentially no distortion of the SiO_4 tetrahedron. Since in the "snow," about half the total excess energy comes from distortions in the O-Si-O angle, it is reasonable to suppose that the pressure-densified glass would have half the excess energy of the "snow" if both had an approximately energetically equal broadening of the Si-O-Si angle distribution, but the densified glass had no O-Si-O distortions. This energetic relation is indeed seen (roughly 20 vs. 40 kJ/mol), but an energy calculation from the neutron diffraction data for pressure densified silica analogous to that for CVD "snow" was not done because the neutron study could not sufficiently resolve the Si-Si peak.

CONCLUSIONS

The wealth of polymorphism, both stable and metastable, in SiO_2 reflects the low energetic cost of changing the angles linking SiO_4 tetrahedra to produce a variety of crystalline and amorphous framework structures. Most forms of crystalline and amorphous silica lie within 15 kJ/mol of quartz in enthalpy. Exceptions contain distortions within their SiO_4 tetrahedra or Si in higher coordination. The closely balanced energetics of the many forms of silica give this material rich, diverse, and complicated mineralogical and geochemical behavior.

REFERENCES

Akaogi M, Navrotsky A (1984) The quartz-coesite-stishovite transformations: new calorimetric measurements and calculation of phase diagrams. Phys Earth Planet Int 36:124-134

Akimoto S, Syono Y (1969) Coesite-stishovite transition. J Geophys Res 74: 1653-1659

Beck JS, Vartuli JC, Roth WJ, Leonowicz ME, Kresge CT, Schmitt KD, Chu CFW, Olson DH, Sheppard EW, McCullen, SB, Higgins JB, Schlenker JL, (1992) A new family of mesoporous molecular sieves prepared with liquid crystal templates. J Am Chem Soc 114:10834-10843

Bohlen SR, Boettcher AL (1982) The quartz ⇔ coesite transformation: a precise determination and the effects of other components. J Geophys Res 87:7073-7078

Cohen LH, Klement W Jr (1975) Differential thermal analysis investigation of the high-low cristobalite inversion under hydrostatic pressure to 7 kbars. J Am Ceram Soc 58:206-208

Couty R, (1977) Etude par la calorimetrie et la diffusion des rayons X des effets des hautes pressions sur un corps amorphe: le verre de silice. PhD dissertation, Univ. Pierre et Marie Curie (Paris VI), Paris, France.

DeDombal RF, Carpenter MA (1993) High-temperature phase transitions in Steinbach tridymite. Eur J Min 5:607-622

Ghiorso MS, Carmichael ISE, Moret LK (1979) Inverted high-temperature quartz. Unit cell parameters and properties of the α–β inversion. Contrib Min Petrol 68:307-323

Graetsch H, Flörke OW (1991) X-ray powder diffraction patterns and phase relationship of tridymite modifications. Zeits Krist 195:31-48

Gronvold F, Stolen S, Svendsen SR (1989) Heat capacity of α quartz from 298.15 to 847.3 K, and of β quartz from 847.3 to 1000 K—Transition behaviour and revaluation of the thermodynamic properties. Thermochim. Acta 139: 225-243

Heaney PJ, Veblen DR (1991) Observations of the α–β phase transitions in quartz: a review of imaging and diffraction studies and some new results. Am Min 76:1010-1032

Heaney PJ, Post JE (1992) The widespread distribution of a novel silica polymorph in microcrystalline quartz varieties. Science 255:441-443

Hemley RJ, Mao HK, Bell PM, Mysen BO (1986) Raman spectroscopy of SiO_2 glass at high pressure. Phys Rev Lett 57:747-750

EBSCOhost - printed on 2/13/2023 4:48 AM via . All use subject to https://www.ebsco.com/terms-of-use

Huffman M, McMillan P (1985) Infrared and raman studies of chemically vapor deposited amorphous silica. J Noncryst Solids 76:369-379

Huffman M, Navrotsky A, Pintchovski F (1986) Thermochemical and spectroscopic studies of chemically vapor deposited amorphous silica. J Electrochem Soc 133:164-171

Klement W Jr., Cohen LH, (1968) High-low quartz inversion: Thermodynamics of the lambda transition. J Geophys Res 73:2249-2259

Konnert S, D'Antonio P, Huffman M, Navrotsky A (1987) Diffraction studies of a highly metastable form of amorphous silica. J Am Ceram Soc 70:192-196

Liu M, Yund RA, Tullis J, Topor L, Navrotsky, A (1994) Energy associated with dislocations: a calorimetric study using synthetic quartz. Phys Chem Min (submitted)

Maniar PD, Navrotsky A, Rabinovich EM, Ying JY, Benziger JB (1990) Energetics and structure of sol-gel silicas. J Noncryst Solids 124:101-111

McGehee MD, Gruner SM, Yao N, Chun CH, Navrotsky A, Aksay IA (1994) Synthesis of mesoscopic structures by co-assembly. Microscopy Soc Am Annual Meeting, abstract (submitted)

Meade C, Hemley RJ, Mao HK, (1992) High pressure X-ray diffraction of SiO_2 glass. Phys. Rev. Lett. 69:1387-1390

Monnier A, Schüth F, Huo Q, Kumar D, Margolese D, Maxwell RS, Stucky GD, Krishnamurty M, Petroff P, Firouzi A, Janicke M, Chimelka BF (1993) Cooperative formation of inorganic-organic interfaces in the synthesis of silicate mesostructures. Science 261:1299-1303

Navrotsky A (1991) Structure and energetics of vitreous and crystalline tectosilicates. Trans Am Cryst Assoc 27:1-12

Petrovic I, Navrotsky A, Davis ME, Zones SI (1993) Thermochemical study of the stability of frameworks in high silica zeolites. Chem Mater 5:1805-1813

Petrovic I, Navrotsky A, Chen CY, Davis ME (1994) High temperature calorimetry of MCM-41. Proc Int'l Zeolite Conference (submitted)

Richet P, Bottinga Y, Denielou L, Petitet JP, Tequi C (1982) Thermodynamic properties of quartz, cristobalite and amorphous SiO_2: Drop calorimetry measurements between 1000 and 1800 K and a review from 0 to 2000 K. Geochim Cosmochim Acta 46:2639-2658

Susman S, Volin KJ, Liebermann RC, Gwanmesia GD, Wang Y (1990) Structural chantes in irreversibly densified fused silica: implications for the chemical resistance of high level nuclear waste glasses. Phys Chem Glasses 31:144-149

Swamy V, Saxena SK, Sundman B, Zhang J (1994) A thermodynamic assessment of silica phase diagram. Jour. Geophys. Res. 99: 11,787-11,794

Thompson AB, Wennemer M (1979) Heat capacities and inversions in tridymite, cristobalite, and tridymite-cristobalite mixed phases. Amer. Mineral. 64: 1018-1026

Xiao Y, Kirkpatrick RJ, Kim YJ (1994) Investigations of MX-1 tridymite by ^{29}Si MAS NMR - modulated structures and structural phase transitions. Phys Chem Min (submitted)

Xiao Y, Kirkpatrick RJ, Kim YJ (1993) Structural phase transitions of tridymite: a ^{29}Si MAS NMR investigation. Am Min 78:241-244

Yagi T, Akimoto S (1976) Direct determination of coesite-stishovite transition by in situ X-ray measurements. Tectonophysics 35:259-270

Ying JY, Benziger JB, Navrotsky A (1993a) The structural evolution of colloidal silica gels to ceramics. J Am Ceram Soc 76:2561-2570

Ying JY, Benziger JB, Navrotsky A (1993b) The structural evolution of alkoxide silica gels to ceramics: Effects of catalyst pH. J Am Ceram Soc 76:2571-2582

Zhang J, Liebermann RC, Gasparik T, Herzberg CT (1993) Melting and subsolidus relations of SiO_2 at 9-14 GPa. J Geophys Res 98:19,785-19,793

EBSCOhost - printed on 2/13/2023 4:48 AM via . All use subject to https://www.ebsco.com/terms-of-use

EBSCOhost - printed on 2/13/2023 4:48 AM via . All use subject to https://www.ebsco.com/terms-of-use

THE ELUSIVE SiO BOND

10 **G.V. Gibbs[1], J.W. Downs[2] and M.B. Boisen, Jr.[1]** 10

[1] *Departments of Geological Sciences, Materials Science and Engineering and Mathematics Virginia Tech, Blacksburg, VA 24061, U.S.A.*

e-mail: popeye@vtvm1.edu

[2] *Department of Geological Sciences Ohio State University, Columbus, OH 43210, U.S.A*

Contemporary quantum chemistry presents a quandary. Solution of the Schrödinger equation proceeds to higher and higher accuracy, and molecular properties are computed ever more precisely. But the understanding of molecular properties seems thereby not enhanced. The beauty that is chemistry eludes us. – Robert G. Parr

ABSTRACT

The character of the SiO bond is examined in terms of observed and calculated structures and electron density distributions recorded for siloxane and silicic acid molecules and silicate crystals. The similarity of SiO bond length and SiOSi angle data together with similar electron density distributions indicate that the forces that bind Si and O together behave as if localized and largely independent of the long–range forces of the ions that comprise the periodic field of a silicate crystal. Despite the generation of accurate structures with improved robust basis sets and quantum mechanical models, little insight has been provided into the character of the bond. Observed and calculated deformation electron density distributions which often show significant accumulations of electron density between bonded Si and O ions have also provided little insight into the character of the bond. On the other hand, the eigenvalues and eigenvectors of the Hessian of observed and calculated electron density distributions, evaluated at the bond critical points of the SiO bonds in the disilicic molecule, coesite and danburite, indicate a closed–shell interaction between Si and O and an SiO bond that is intermediate in character between covalent and ionic. They also indicate that the ionic character of the bond increases as its length increases. The bonded radius of the oxide ion provided by experimental electron density maps indicates that the bonds in octahedral SiO_6 coordination polyhedra are $\sim$25% more ionic than those in tetrahedral SiO_4 polyhedra. The electron density distribution in the disilicic acid molecule is indicated to be locally depleted away from the valence shell of the oxide ion where the shell crosses the bond with the electron density distribution of the ion being highly concentrated along the bond toward Si. As the SiOSi angle widens, electron density is revealed to be progressively more concentrated in the bond. The ellipticity of the cross–section of the bond decreases as the angle widens, suggesting the presence of a π–system. The d–type orbitals used on Si in theoretical calculations are indicated to play a small but important role in governing the geometry, electron density distribution and spectral properties of small hydroxy acid and siloxane molecules and silicate crystals.

EBSCOhost - printed on 2/13/2023 4:48 AM via . All use subject to https://www.ebsco.com/terms-of-use

INTRODUCTION

Our knowledge and understanding of the SiO bond comes from both observational data and mathematical models. Of the observables that depend in some way on the nature of the binding forces that link Si and O together, only a handful can be uniquely identified with an individual SiO bond. Of these, bond length is special in the sense that it provides a reliable measure of the strength of a bond: the shorter a particular bond, the greater its strength and its force constant. Over the years, bond length and angle variations observed for silica and silicate crystals, organosiloxane molecular crystals and gas phase molecules have played a key role in improving our knowledge of the bond. Electron density distributions have also provided important insight into the properties of the bond by defining where the electron density distributions of Si and O are locally concentrated upon bond formation. Valuable information has also been provided by model calculations on representative molecules and on infinite periodic structural representations of the silica polymorphs. Despite the small number of atoms in a molecule compared with that of a chemically similar crystal, molecular orbital calculations have provided valuable insight into the force fields that govern the local geometries, bond length and angle variations and electron density distributions of the silica polymorphs. Model calculations based upon such fields have not only served to generate the structures and the elastic properties of the known structure types of silica, but they have also been used to generate new ones. Calculations on such silica crystals as quartz, cristobalite, coesite, and stishovite using the modified electron gas method, the Hartree–Fock–Roothaan periodic crystal method with Gaussian basis sets and the linearized augmented and the local density functional pseudopotential methods with plane wave basis functions have provided important information on the energetics, band structures, elastic and bulk properties, vibrational spectra and the electron density distributions of the silica polymorphs. Finally, X–ray emission and photoelectron spectra have provided important information on the electronic structure of the silica polymorphs. As the results of these latter studies have been carefully examined elsewhere by Tossell and Vaughan (1992), they will not be discussed in detail other than how they may bear on the nature of the SiO bond.

This review paper is divided into four major parts. In the first part, several early models for the SiO bond are examined. Observed and calculated SiO bond lengths and SiOSi angles for assorted hydroxy silicic acid and siloxane molecules and silicate crystals are compared in the second. This is followed by a comparison of the properties of experimental and theoretical electron density distributions in the third. The final part concludes with a discussion of the character of the bond and the extent to which the $3d$ atomic orbitals on Si may be used in π–bonding and bond formation in light of the evidence presented in parts two and three.

EARLY MODELS FOR THE SiO BOND

A number of models have been proposed for the structure of the SiO bond ranging from a model that is ionic to one that is covalent. One of the earliest was proposed by G. N. Lewis (1923), who considered the SiO_4 silicate coordination polyhedron as consisting of an Si atom sharing electron pairs and forming a covalent bond with four coordinating O atoms each disposed at a corner of a tetrahedron. As each electron pair was considered to be equally shared between the two atoms, the model requires that the formal charges on Si and O be zero. Lewis went on to predict that the structure of silica, both in its vitreous and crystalline states, can be viewed as

EBSCOhost - printed on 2/13/2023 4:48 AM via . All use subject to https://www.ebsco.com/terms-of-use

a molecule of corner sharing silicate polyhedra of indeterminate extent, a prediction that was later verified when the structures of quartz, cristobalite and vitreous silica were determined.

At the time Lewis (1916) was developing his model, the Born–Landé (1918) ionic bonding model was enjoying success in representing the bonding and the thermochemical properties of a wide variety of highly symmetrical inorganic compounds (Sherman, 1932). Rather than considering the atoms in a material like quartz as neutral, the Born–Landé model considers them as charged Si^{+4} cations and O^{-2} anions linked together by ionic bonds (see Burnham, 1990 for a comprehensive review of the ionic model as it applies to oxides and silicates). During the same period, early quantum mechanical calculations were enjoying success in generating a binding energy (912 kJ/mol) that matches that observed (914 kJ/mol) for the cubic crystal LiH without introducing any empirical data (Hylleras, 1930). However, because of their difficult and protracted nature, such calculations were impossible at that time with the existing facilities for even small molecules like SiO_2 much less for a crystal like quartz. On the other hand, assuming an atomic model and using nodeless radial wave functions for the valence electrons on Si and O, Slater (1930) was successful in the generation of an SiO bond length, R(SiO) = 1.62Å, in close agreement with the values observed for SiO_4 coordination polyhedra in molecules and crystals. The successful calculation of the binding energy of LiH provided some early hints of what was to be accomplished in the not too distant future with the advancement of the theory of quantum mechanics, computers and computational algorithms.

It was in this context that Linus Pauling (1927; 1929) derived his ionic radii and formulated his famous set of rules for determining the structures of stable ionic compounds. Using arguments based in part on the Born–Landé model, he proposed that the SiO_4^{-4} silicate tetrahedral oxyanion consists of a small Si^{+4} cation bonded to four much larger O^{-2} oxide anions. Later, with the development of his widely used electronegativity scale, Pauling (1939) modified his ionic model and asserted, on the basis of the electronegativity difference between Si and O, that each SiO bond, rather than being purely ionic, has ~50% covalent character. With his hybrid orbital model for the atom, he combined the valence $3s-$ and $3p-$ atomic orbitals (AOs) on Si into four orthogonal sp^3–hybrid AOs that overlap with the valence AOs on the oxide ions. The result is the formation of four equivalent single bonds that not only account for the tetrahedral geometry of the silicate coordination polyhedron but also for the relatively large strength of the SiO bond. As this single bond hybrid model endows a formal charge of ~+2 on Si (in violation of his electroneutrality principle) and as the mean SiO bond distance observed for a monosilicate crystal (1.63Å) is shorter than that (1.76Å) calculated for a single bond with the Schomaker–Stevenson additivity rule (1941), he added a $(p-d)\pi$ system to the model that involves the $2p$–AOs on O and two of the relatively low-lying $3d-$AOs on Si in resonance with the sp^3–framework (Pauling, 1952). Not only did this $(p-d)\pi$ model reduce the charge on Si to ~+1, it also generated a bond length that matches that observed (see also Jaffe, 1954; Cruickshank, 1961).

Since Pauling advanced his $(p-d)\pi$ model, there has been a running debate in the literature as to the extent to which the $d-$type AOs on Si are actually used in forming the wave function of the SiO bond (cf. Jaffe, 1954; Fyfe, 1954; Stone and Seyferth, 1955; Verhoogen, 1958; Cruickshank, 1961; Noll, 1968; Mitchell, 1969; Brown et al., 1969; Brown and Gibbs, 1970; Baur, 1971; Dyatkina and Klimenko, 1973; Voronkov et al., 1975; Kwart and King, 1977; Griscom, 1977; Oberhammer and Boggs, 1980; Stewart et al., 1980; Pauling, 1980; Kutzelnigg, 1984; Apeloig, 1989; Sheldrick, 1989; Sauer, 1989; Boisen et al., 1990 and references therein). For

EBSCOhost - printed on 2/13/2023 4:48 AM via . All use subject to https://www.ebsco.com/terms-of-use

example, Brown et al. (1969) have argued that the tetrahedral bond lengths and angles in framework silicates can be interpreted in terms of a $(p-d)\pi$ model with shorter SiO bonds being involved with wider SiOSi angles in accordance with the prediction that, as the angle widens, the overlap between the $d-$AOs on Si and the $p-$AOs on O should increase and the SiO bond should shorten (Cruickshank, 1961). On the other hand, Baur (1971) has argued that it is not necessary to invoke such a model as the bond lengths and angles in a silicate can be simply explained in terms of an extention of Pauling's (1929) electrostatic valence rule since the SiO bond length variations are not a function of the SiOSi angle but are determined by a more fundamental relationship between bond length and the bond strength sums that reach each oxide anion. He concluded by recommending that the $(p-d)\pi$ model be discarded as a general bonding model for silicates. However, as correlations between bond length and angle and bond strength sums can tell us little about the role played by the $d-$AOs in bonding, further clarification of the properties of the SiO bond had to await improvements in atomic basis sets, computer hardware and software for modeling and computing wave functions, electronic structures, minimum energy theoretical structures, theoretical electron density distributions and other properties of molecules and crystals. It also had to await the development of methods and software for analyzing experimental and theoretical electron density distributions and their topological properties.

Next, we will examine minimum energy structures obtained in molecular orbital calculations for the tetrahedral SiO_4 and octahedral SiO_6 coordination polyhedra of several hydroxy silicic acid molecules, for the SiOSi disiloxy dimer of the disiloxane molecule and for the Si_2O_7 dimer of the disilic acid molecule. The results will be compared with data observed and calculated for several silicate crystals. A comparison will show that the SiO bond lengths and SiOSi angles observed and calculated for the molecules match those observed for chemically similar crystals despite the huge size difference that obtains between a molecule and a crystal.

GEOMETRIES OF MOLECULES AND CRYSTALS

The tetrahedral SiO_4 coordination polyhedron

The monosilicic acid molecule, H_4SiO_4, is the smallest molecule to contain the basic building block of a silicate crystal, the tetrahedral SiO_4 coordination polyhedron (Fig. 1a). The first theoretical self-consistent field (SCF) non empirical molecular orbital (MO) calculations to be completed on the molecule were undertaken by Collins et al. (1972) using a minimum basis set of Slater type AOs, each expanded with three Gaussian type functions with the basis augmented with $d-$type functions on Si. They concluded from single point calculations, assuming an SiO bond length of 1.62Å and D_{2d} point symmetry, that each of the five $3d-$type AOs makes a meaningful contribution to the wave functions of the molecule with a total Mulliken population of ~1.45 electrons in these AOs. With these functions, they found that they could reproduce the observed $L_{2,3}$ X-ray emission spectra for silica rather well; this could not be done when the $d-$type basis functions were omitted from the calculations. In addition, an SCF Xα scattered wave cluster MO calculation of the electronic structure of the silicate SiO_4^{+4} anion undertaken by Tossell (1975) indicates that $Si_{3d}O_{2p}$ bonding occurs, but that it plays a minor role compared with $Si_{3s,3p}O_{2p}$ bonded interactions. He concluded that the wavefunctions of the SiO bond include both σ and π type $d-$functions in about equal amounts. In a subsequent SCF MO calculation, Newton and Gibbs (1980) obtained a Mulliken population of ~0.65 electrons in the $d-$AOs when a relatively robust 6-31G* basis set was used (For a discussion of basis set

EBSCOhost - printed on 2/13/2023 4:48 AM via . All use subject to https://www.ebsco.com/terms-of-use

nomenclature, see Hehre et al., 1986). A calculation of Mulliken overlap populations reveals that the SiO σ–bond overlap population, $n[Si_{3d(t_2)}O_{2s,2p}]_\sigma = 0.11$ electrons, is modest and somewhat smaller than the SiO π–bond overlap population, $n[Si_{3d(e)}O_{2p}]_\pi = 0.16$ electrons. These results also indicate that the d–AOs on Si form σ as well as π–bonded interactions with the coordinating oxide ions. Since the overall population is in close agreement with that calculated for the SiO_2 molecule with a relatively robust basis set (Pacansky and Hermann, 1978), Newton and Gibbs (1980) concluded that

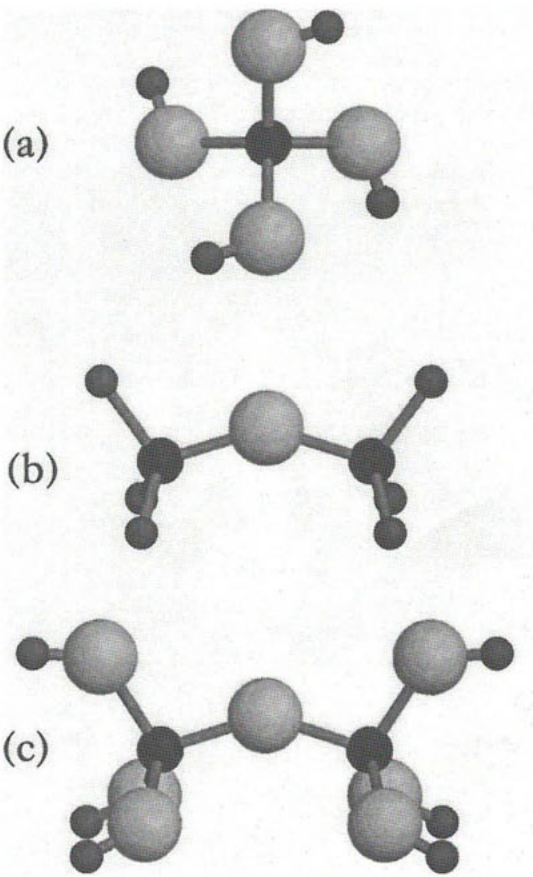


Figure 1. Drawings of the molecules (a) monosilicic acid, H_4SiO_4, (b) disiloxane, H_6Si_2O and (c) disilicic acid, $H_6Si_2O_7$. The large light–gray spheres represent the oxygen atoms, the intermediate–sized black spheres represent silicon atoms and the small dark–gray spheres represent hydrogen atoms. No significance is attached to the sizes of the spheres. The drawings were constructed with *XTALDRAW*, an interactive program written for the PC by Dr. Robert T. Downs of the Geophysical Laboratory, Washington DC 20015 and Dr. Kurt L. Bartelmehs of the Department of Geological Sciences, University of Texas at Austin, Austin, Texas 78712.

EBSCOhost - printed on 2/13/2023 4:48 AM via . All use subject to https://www.ebsco.com/terms-of-use

the electronic population of the $d-$AOs on Si is meaningful and not an artifact of a deficient s and p basis set.

Sauer (1983) has since completed MO calculations on the molecule using 6–31G and 6–31G* bases sets in an evaluation of the role played by the $d-$AOs on Si. A step–by–step energy minimization of the geometry of the molecule with three point parabola fits revealed that the SiO bond increases in length from 1.630Å to 1.635Å, rather than decreasing, when $d-$type AOs were added to the basis set. These bond lengths are in close agreement with that observed (1.637Å), on average, for the monosilicates. However, as the change in bond length, upon adding the $d-$AOs, was in a direction opposite to that proposed by Pauling (1952), Sauer (1983) expressed doubt about the nature of the contribution made by the $d-$AOs in determining the length of the SiO bond. On the other hand, a Mulliken population analysis of the resulting wave functions for the molecule indicates a moderate charge transfer of electrons from the oxide ions of ~0.65 electrons into the empty $d-$AOs on Si. Later, a full minimization of the energy of the monosilicic acid molecule using 6–31G and 6–31G* basis sets (Hess et al., 1986; O'Keeffe et al., 1985), assuming S_4 point symmetry as determined by Gibbs et al. (1981), shows that the SiO bond contracts from 1.662Å to 1.629Å, a fraction of that proposed by Pauling (1952) when $d-$functions are added to the basis set.

In a study of the role played by the $d-$functions on bond strengths (bond energies), the minimum energy geometries for a number of singly bonded saturated silyl H_3SiX molecules with four coordinated Si were calculated by Luke et al. (1986). They observed that the SiX ($X = OH^{-1}$, H^{-1}, SH^{-1}, CH_3^{-1}, etc.) bond energies calculated for these molecules increase regularly with the electronegativity of the substituent X anion, with the energies increasing with the polarity and the ionic character of the bond. As SiX bonds for X anions with similar electronegativities were observed to have similar energies, they conclude that the transfer of electrons into the vacant $d-$AOs on Si contributes little to the resulting bond energies. For example, the energies of the SiS and SiC bonds for the gas phase molecules H_3SiSH and H_3SiCH_3 are very similar (348 kJ/mole and 358 kJ/mole, respectively), yet $(SH)^{-1}$ anion has lone–pairs to participate in $(p-d)\pi$ bonding while the CH_3^{-1} methyl anion has none. However, lone–pairs are not required for bond formation if the $d-$type AOs participate in σ bonds with both C and S. Considering the complex nature of the bonds, Luke et al. (1986) were careful to stress that it is difficult to separate the $(p-d)\pi$ bonding effects from contributions from ionic bonding effects such as those embodied in the structure of $H_3Si^+X^-$. In concluding their study, they observed that a more elaborate study is needed to assess the relative importance of the ionicity and $(p-d)\pi$ bonding in determining the energies of the bonds to Si. Comprehensive reviews of these results together with those generated in a variety of theoretical calculations on organosiloxane molecules persuaded Apeloig (1989) and Sheldrick (1989) to concur with earlier workers that the $d-$type AOs contribute little to the SiO bonding picture. This was considered to be true inasmuch as the strengthening and the resulting shortening of the bond with the inclusion of the $d-$AOs is much smaller than that predicted by Pauling's model (1960).

For this review, electron correlated wave functions were calculated for the H_4SiO_4 molecule at the full MP2 level to assess the role played by the $d-$type AOs in the wave functions of the molecule when the correlated motions of the electrons are modeled. The minimum energy geometry was calculated assuming S_4 point symmetry. Unfortunately, because $d-$type basis functions can be viewed as larger–sized versions of $s-$ and $p-$type basis functions, it is difficult if not impossible to determine from such calculations whether electron populated $d-$AOs are related to a meaningful

EBSCOhost - printed on 2/13/2023 4:48 AM via . All use subject to https://www.ebsco.com/terms-of-use

$d-$orbital participation or to a deficiency in the $s-$ and $p-$basis sets of the Si atom. Also, as the SiO bond is believed to have a significant component (~50%) of ionic character (Pauling, 1960), the electron density should be displaced upon bond formation from Si toward the more electronegative oxide ion, imparting a natural polarity to the bond. In such a case, the $d-$type AOs on Si can serve as polarization functions in an MO modeling of the wave functions of the ionic component of the bond. With these factors in mind, it becomes apparent that it can be difficult to determine from the occupancies of the $d-$AOs whether the orbitals play a meaningful role in defining the wavefunction of the bond, whether the $s,p-$basis set is incomplete or whether the bond is polar.

Calculations at the MP2/6-31G** level with $d-$type functions on the heavy atoms and $p-$type functions on the remaining H atoms yield minimum energy bond lengths that typically agree to within ~0.02Å and minimum energy bond angles that agree to within ~5° with observed geometries for a wide variety of molecules (Hehre et al., 1986). The minimum energy geometry of the H_4SiO_4 molecule calculated at the MP2/6-31G** level has an SiO bond length of 1.643Å compared with 1.637Å observed, on average, for the monosilicates. A Mulliken population analysis of the resulting wave function indicates that ~0.45 electrons are distributed among the $d-$type AOs with a charge of ~+1.5 on Si. If the magnitude of the charge is meaningful, then the bond can be concluded to possess a relatively large component of ionic character. A study of the theoretical electron density distribution and the dimerization of silanol by Kudo and Nagase (1985) also indicates that the SiO bond has a relatively large ionic component. Deformation maps calculated for the molecule display peaks of electron density along the SiO bonds displaced toward the more electronegative oxide ions. This displacement of peaks was viewed as enhancing both the net charge on the oxide ion and the polar character and the ionicity of the bond.

The energy of the H_4SiO_4 molecule was also minimized at the MP2/6-31G level without polarization functions, yielding a single bond length of 1.701Å and a charge on Si of ~+2.0. The charge matches that assigned to Si in the single bond sp^3 hybrid model for the silicate polyhedron (see Part 1). However, the resulting single bond length is shorter than that (1.76Å) calculated with the Schomaker-Stevenson additivity rule (1941). Kutzelnigg (1984) has presented evidence based on the spatial distributions of the valence electrons that implies that second-row atoms like Si should form strong single bonds and relatively weak multiple bonds compared with first-row atoms like C which should form weak single bonds and relatively strong multiple bonds. If this is the case, then the SiO single bond should be shorter than that calculated with the Schomaker-Stevenson rule (1941). As observed above, the value calculated for the bond is indeed shorter by ~0.06Å. It is noteworthy that the minimum energy CO single bond length (1.433Å) calculated here for the monocarbonate molecule, H_4CO_4, at the MP2/6-31G level agrees exactly with the single bond length calculated with the Schomaker-Stevenson equation (1.43Å). Also, any shortening of the SiO bond accompanying the formation of a $(p-d)\pi$ bond should be less than that (0.12Å) predicted by Pauling's model. A minimization of the energy of the H_4SiO_4 molecule at the MP2 level using a robust 6-311+G(2d, 2p) basis set with two $d-$type AOs on both Si and O and two $p-$type AOs on H, completed for this review, resulted in an SiO bond length of 1.637Å, in exact agreement with the average bond length observed for the monosilicates. These calculations suggest that the maximum shortening that one can expect for the SiO bond with the addition of polarization functions is ~0.06Å. This shortening is about half that predicted by Pauling's semi-empirical model, a result that can be ascribed to the combined effect of a strong single bond and a relatively weak double bond. The charge on Si is also reduced but again

EBSCOhost - printed on 2/13/2023 4:48 AM via . All use subject to https://www.ebsco.com/terms-of-use

to a lesser extent than that proposed. Thus, given the qualitative nature of Pauling's model and the observations given above, the reduction in charge and the shortening in the SiO bond length generated in the calculations can be considered to conform with the trends predicted by his model.

It is generally accepted that polarization functions are an essential ingredient for a correct description of molecular geometries. These functions have also been found to be essential in periodic Hartree–Fock crystal calculations for the correct reproduction of the experimental geometries of quartz and stishovite (Noda et al., 1990). In addition, the Si $L_{2,3}$ X–ray spectral results for quartz cannot be easily interpreted without a small contribution of $d-$orbital participation to the wave functions of the silicate coordination polyhedron (Tossell and Vaughan, 1992). As such a participation is believed to be necessary to explain the spectra, some of the strengthening and the shortening of the SiO bond can be ascribed to the $d-$orbitals on Si forming both σ and π bonded interactions within an SiO_4 coordination polyhedron. The extent of the involvement is probably small with a little participation having a large effect on the geometry of the coordination polyhedron, the strength of the SiO bond and the charges on Si and O (see Tossell and Vaughan, 1992 and references therein).

The monosilicic acid molecule is a relatively simple representative model for a locally charge–balanced SiO_4 coordination polyhedron in a silicate crystal. Despite its small size, its bond lengths calculated at the MP2 level with basis functions that include $d-$type polarization functions nonetheless match those observed on average for monosilicate crystals and organosiloxane gas phase molecules (1.637Å). As the H_4SiO_4 molecule has not been isolated for a structural analysis, the observed and calculated geometries of the molecule have yet to be compared. On the other hand, the structure of the gas phase molecule disiloxane has not only been determined several times with experimental methods but minimum energy structures calculated for the SiOSi disiloxy dimer of the molecule have been generated numerous times with a variety of basis sets.

The SiOSi disiloxy dimer

Disiloxane, $H_3SiOSiH_3$, is the simplest molecule to contain the SiOSi disiloxy dimer, the fundamental link that binds corner sharing silicate coordination polyhedra into a structure of condensed silicate tetrahedra (Fig. 1b). A structure analysis of the molecule by Almennigen et al. (1963), using electron diffraction methods, reveals that its SiO bond length (1.634Å) and SiOSi angle (144.1°) closely resembles that observed, on average, for a number of silicate crystals (Liebau, 1961; Gibbs et al., 1981; Gibbs, 1982). Not only did Almennigen et al. (1963) conclude from this result that the bonding picture of the molecule and the crystal can be viewed as similar, but they also observed that the bonding in the two systems can be pictured in terms of a π-bonding model that involves two lone–pairs on O and the $3d-$AOs on Si.

Oberhammer and Boggs (1980) completed one of the first energy minimizations for the molecule using a split 4–31G* basis set and a relatively large Gaussian orbital exponent on the $d-$type AOs of 0.8. Their calculations generated a minimum energy SiO bond length of 1.629Å and an SiOSi angle of 143.3° when $d-$type functions were included in the basis set for Si and polarization functions were included for O, but an angle of 180° was generated when these functions were omitted in the calculations. As the $\pi-$overlap population for the SiO bond was found to be small, they concluded that the $(p-d)\pi$ bonding model is of minor importance and that the ionic character of the bond is much greater than that indicated by a consideration of the electronegativities of Si and O. They ascribed the short bond length observed for the molecule to the highly ionic character of the bond and the wide SiOSi angle to

EBSCOhost - printed on 2/13/2023 4:48 AM via . All use subject to https://www.ebsco.com/terms-of-use

electrostatic repulsions between the Si cations. It is noteworthy that the geometry of the molecule has also been optimized by other workers with varying degrees of success depending on the basis sets used in the calculations (Sauer and Zurawski, 1979; Meier and Hu, 1980; Newton, 1981; Ernst et al., 1981; Gibbs et al., 1987a; Grigoras and Lane, 1987; Koput, 1990; Nicholas et al., 1992a). For example, Nicholas et al. (1992a) have completed calculations on the molecule with a series of basis sets of increasing quality, including extended basis sets and one including electron correlation with a frozen core. The geometries generated with double/triple zeta split valence sets with the basis sets augmented with two or three $d-$type polarizations were found to be in good agreement with the experimental data. Using the equation $i(\mathrm{SiO}) = 50[\mathrm{Q(Si)} - \mathrm{Q(O)}]$ where Q(Si) and Q(O) are the Mulliken charges for Si and O, they concluded that the ionicity of SiO bond, i(SiO), increases by ~25% as the SiOSi angle widens from 130 to 180° and the SiO bond shortens. This result conforms with an earlier suggestion made by Oberhammer and Boggs (1980) that the ionic character of the bond increases as the length of the bond decreases. The SiO bond lengths calculated for disiloxane as a function of the SiOSi angle were found to decease nonlinearly with the resulting bond lengths, agreeing with those observed for the silica polymorphs to within ~0.01Å (Hill and Gibbs, 1979). Nicholas et al. (1992b) also completed additional MO calculations on several structural analogues of the disiloxane H_3TOTH_3 (T = Si, Al, B and P) molecule that were used to model the geometries, the force constants and the relative acidities of the hydroxly groups at the surfaces and defect sites of various substituted zeolites. The good agreement that obtains between the calculated and the observed bond lengths and angles, the force constants and the trends in acidity led them to state that the molecules themselves are but very small fragments of the crystal structure of a chemically similar zeolite crystal. Not only does this good agreement provide support for the Almenningen et al. (1961) observation that the bonding picture of the gas phase molecule disiloxane is similar to that of a silicate crystal, but it may also indicate that the observation is more general and that it holds for a variety of substituted zeolite crystals as well. Collectively, these results indicate that the force field that governs the TO bond lengths and TOT angles and the stretching and bending force constants behave as if short ranged and largely independent of the long–range forces of the ions comprising the periodic field of a crystal.

As shown above, the structural analogues of the disiloxane molecule have been successfully used as models for studying the defects and the surface structure of a zeolite. On the other hand, the disiloxane molecule is unsatisfactory for modeling structures with condensed corner sharing silicate coordination polyhedra because it lacks tetrahedral OSiO angles. The disilicic acid molecule (Fig. 1c) is more suitable for modeling such structures not only because it contains tetrahedral angles, but because it contains an SiOSi dimer that links two corner sharing coordination polyhedra into an Si_2O_7 dimer.

The Si_2O_7 dimer

For corner sharing T_2O_7 dimers (T = Si, P, S, Cl), the tendency for the TOT angle to widen as T changes from Cl to Si can be ascribed to a systematic increase in the ionic character of the TO bond with the SiO bond having the largest ionic component, the longest average bond length and the smallest stretching force constant in the series. With the opening of the TOT angle, the $(p - d)\pi$ bond order of the bridging bonds of a T_2O_7 dimer is expected to increase and the TO bond lengths are expected to decrease (Cruickshank, 1961; Brown et al., 1969). In an examination of the bonding properties of the Si_2O_7 dimer, Newton and Gibbs (1980) completed

EBSCOhost - printed on 2/13/2023 4:48 AM via . All use subject to https://www.ebsco.com/terms-of-use

STO–3G and STO–3G* calculations on the $(HO)_3SiOSi(OH)_3$ molecule and found that the calculated SiO bridging bond length for the molecule decreases non–linearly with an increase in the SiOSi angle, regardless of whether d–type basis functions are included in the basis set or not (see also Pietsch and Hubner, 1986). They also observed that bond lengths calculated for the SiO bonds comprising the SiOSi angle are negatively correlated with the fraction of s–character of the bridging oxide ion, $f_s(O) = \cos\Theta/(\cos\Theta - 1)$ where $\Theta = <$SiOSi. Scatter diagrams of R(SiO) observed for the siloxanes and the silica polymorphs vs. $f_s(O)$ conform with these results (Hill and Gibbs, 1979; Chakoumakos et al., 1981; Karle et al., 1986; Boisen et al., 1990) with the SiO bridging bond lengths decreasing as the SiOSi angle widens.

The minimum energy SiOSi angle calculated for the disilicic acid molecule was found to be straight rather than bent when polarization functions were not included in split valence basis set 3–21G and 6–31G calculations. However, when polarization functions are added, calculations have resulted in bent angles that match the average value observed for a variety of silicate crystals and glasses and siloxane crystals reasonably well (cf. Uchino et al., 1992). Because of the agreement obtained among the observed bond lengths and angles and those calculated with a 6–31G* basis set, it was concluded that polarization functions are a necessary ingredient for a correct description of the geometry of such molecules (O'Keeffe et al., 1985). We note in passing that the SiO bond length vs. <SiOSi trend can also be interpreted in terms of a simple qualitative MO argument. This model is based on the HOMO–LUMO energy gap (Tossell, 1984; Sheldrick, 1989) of the dimer and concentrates on the energy difference between the π–nonbonding HOMO and the σ–antibonding LUMO of a linear dimer. As the argument goes, the larger the energy difference, the wider the angle as in the case of the SiOSi angle. As the energy difference increases from Cl to Si, the model predicts, as observed, that the TOT angle should increase, on average, in the series with the SiOSi angle being the widest.

The energy of the disilicic acid molecule has also been minimized with a full MP2/6-31G model with two d–type polarization functions added to the Si atoms and one added to the bridging O atom (Downs, 1992). Because of the extensive computer time required to minimize the energy of such a large molecule, its geometry was assumed to exhibit C_{2v} point symmetry (Fig. 1c). By fixing the geometry of the molecule so that its terminating H atoms are directed away from the nonbridging O atoms of the second silicate coordination polyhedron at a distance greater than 3Å, the formation of one or more O···H bridging bonds involving the H atoms of one silicate coordination polyhedron and the O atoms of the other is avoided. If such a geometry is not adopted, the formation of the O···H bonds can affect the resulting SiOSi angles as observed in a careful study by Burkhard et al. (1991). For example, as reported by Kubicki and Sykes (1993), when two such bridges are formed, an SiOSi angle of 128.3° is adopted by the molecule; when one bridge results, an SiOSi angle of 141.5° is adopted, but when no bridges are formed, a straight SiOSi angle is adopted when 3–21G* basis set calculations are made.

The MP2 level energy minimization of the molecule undertaken by Downs (1992) within the constraints of C_{2v} point symmetry resulted in a structure with all O···H bridging distances in excess of 3.05Å. As the distances are ~1.0Å longer than those obtained by Kubicki and Sykes (1993), it was concluded that the SiOSi angle adopted by the molecule is largely independent of the formation of bridging O···H bonds. The minimum energy bridging SiO bond length (1.616Å) and the bridging SiOSi angle (143.7°) calculated for the molecule matches the SiO bond length (1.610Å) and the SiOSi angle (143.7°) observed for quartz as well as can be expected (Downs, 1992). In addition, the SiO bridging bond length was optimized for a set of SiOSi

EBSCOhost - printed on 2/13/2023 4:48 AM via . All use subject to https://www.ebsco.com/terms-of-use

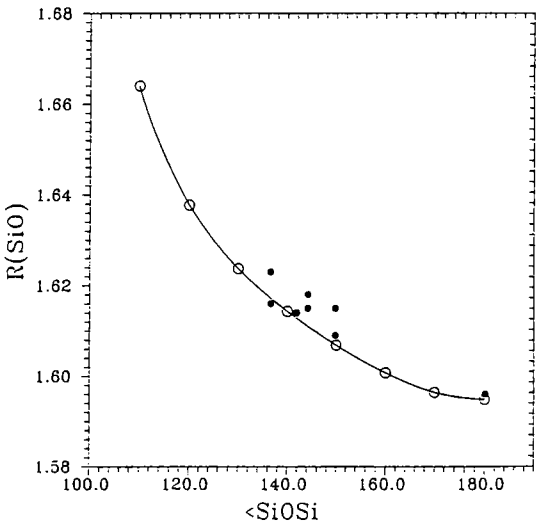


Figure 2. The SiO bridging bond lengths, R(SiO), for an $H_6Si_2O_7$ molecule plotted as a function of its SiOSi angle as open bullets (Data taken from Downs, 1992). The SiO bond lengths of the molecule were calculated at the MP2/6–31G level with two sets of d–type AOs on the Si atoms and the bridging O. In the calculations, the SiOSi angles were fixed successively at 10° intervals between 110° and 180°, the OSiO angles were clamped at $\cos^{-1}(-1/3)$ and the SiO bond lengths were varied until the energy of the molecule was minimized. The R(SiO) and SiOSi angle data recorded for coesite are plotted in the figure as solid bullets.

angles ranging between 110 and 180°. The resulting SiO bond lengths and SiOSi angles are compared with those observed for coesite in Figure 2. The bond lengths and angles, when subjected to a linear regression analysis of R(SiO) vs. $f_s(O)$, generates the equation $R(SiO) = 1.731 - 0.271f_s(O)$. This equation yields bond lengths that match those observed for the silica polymorphs to within ~0.01Å, on average (Hill and Gibbs, 1979; Boisen et al., 1990). These results show that the bond lengths and angles calculated for the molecule at the MP2/6-31G level augmented with polarization functions match those observed for silica crystals with four coordinated Si reasonably well. They also indicate that that the bonding picture of the locally charge–balanced Si_2O_7 dimer of the disilicic acid molecule is similar to that of the dimers in the silica polymorphs quartz, cristobalite and coesite.

The octahedral SiO_6 coordination polyhedron

While the vast majority of silicates that contain SiO_4 coordination polyhedra crystallize at the temperatures and pressures typically encountered in the crust of the earth, those like $K_2Si_4O_9$, which contain both SiO_4 and SiO_6 polyhedra (Swanson and Prewitt, 1983), and others like stishovite and an $MgSiO_3$ perovskite structure type, which contain SiO_6 polyhedra, crystallize at the higher temperatures and pressures that are typically encountered in the mantle (Finger and Hazen, 1991; Bukowinski, 1994). But silicates like thaumasite, $Ca_3Si(OH)_6$, which possess six coordinate $Si(OH)_6$ polyhedra, crystallize at the temperatures and pressures that are typically encountered near the surface of the earth. In addition, a number of organosiloxane molecular and silicon phosphate crystals synthesized in the laboratory and Si–organic compounds in aqueous solutions have been described with SiO_6 coordination polyhedra (Liebau, 1985). As reported by Liebau (1985), the individual SiO bond lengths in these materials range between 1.70 and 1.84Å with an average value of 1.77Å, a value that agrees with the average SiO bond length observed for stishovite (Hill et al., 1983). SiO_4 and SiO_6 are the only Si containing coordination polyhedra that have been reported for silicates, although an SiO_5 coordination polyhedron has been re-

EBSCOhost - printed on 2/13/2023 4:48 AM via . All use subject to https://www.ebsco.com/terms-of-use

ported for a molecule. Liebau (1985) has suggested that the $3d-$type AOs on Si mix with its $3s-$ and $3p-$AOs to form a set of six equivalent sp^3d^2 hybrid orbitals directed toward the corners of an octahedron, forming six covalent bonds with the $2p-$AOs on O. In an examination of the mean SiO bond lengths, <R(SiO)>, recorded for SiO_6 polyhedra in crystal and molecules, Baur (1977) found that the bond length varies between 1.73Å to 1.80Å, with <R(SiO)> increasing in a regular way with the mean coordination number, <CN(O)>, of the oxide ion. A similar correlation has been shown to obtain between <R(SiO)> and <CN(O)> for silicates with four coordinate Si (Smith and Bailey, 1963).

A minimization of the energy of the SiO_6 coordination polyhedron in a H_8SiO_6 molecule using a 6–31G* basis set yielded an SiO bond length of 1.76Å in agreement with the average value reported for crystals and molecules with six coordinate Si. In a study of the stishovite structure as a function of pressure using the LAPD method, Cohen (1991) observed a hybridization that involves the $s-$, $p-$ and $d-$AOs on Si with a valence electron density of 0.2 in the $3s-$, 0.3 in the $3p-$ and 0.1 in the $3d-$AOs on each Si atom. The small dispersion of the individual bands and a large band gap of the calculated band structure were taken as evidence that the structure of the SiO bond consists of a mixture of ionic and covalent bonding conferring a charge ~-1.4 on O and $\sim+2.8$ on Si. If, as asserted by Catlow and Stoneham (1983), the partitioning of charges in band energy calculations is more naive than it is for small molecules, then the magnitudes of such charges for crystals, and for molecules as well (cf. Tossell and Vaughan, 1992), may not be very meaningful.

The close agreement that obtains between the SiO bond length calculated for the hypothetical molecule H_8SiO_6 and that observed on average for crystals and molecules with six coordinate Si indicates that the force field that governs the average bond length for a locally charge-balanced SiO_6 coordination polyhedron in a crystal like stishovite is short ranged in its behavior as observed for the silica polymorphs and several substituted zeolites. Any model that is proposed for the tetrahedral bonds in silicates and zeolites and the SiO bonds in crystals and molecules with six coordinate Si should include an explanation of why the bond lengths and angles in chemically related molecules and crystals are nearly identical on average (Almennigen et al., 1963; Gibbs et al., 1981; Gibbs, 1982; Burdett and Caneva, 1985).

In periodic Hartree–Fock calculations completed for quartz and stishovite, Noda et al. (1991) observed that the addition of $d-$type AOs to a 6–21G basis set resulted in improved structures for both quartz and stishovite. For both of these structure types, the population of the $d-$AOs is relatively high ($\sim$0.50 electrons in quartz and $\sim$0.45 in stishovite). When the $d-$AOs were omitted from the basis sets, stishovite was calculated to be more stable than quartz by $\sim$24 kJ/mol, but when the orbitals were added to the basis, quartz was calculated to be the more stable polymorph by $\sim$30 kJ/mol. This result plus the relatively large number of electrons in the $d-$AOs were taken as crucial evidence (Noda et al., 1991) that the $d-$AOs on Si play a meaningful role and are extensively used in bond formation in both quartz and stishovite.

As observed by Noda et al. (1990), the first principle crystal calculations completed for the silica polymorphs quartz and stishovite and those completed by others (Allan and Teter, 1990; Cohen, 1991; Keskar and Chelikowsky, 1991; Liu et al., 1994, Bukowinski, 1994, for example) are much more powerful than calculations completed on a molecule like $(HO)_3SiOSi(OH)_3$. In such calculations, unlike a calculation on a molecule, the field of a crystal is explicitly taken into account. Also, the problems of attaching H atoms to the nonbridging O atoms of the molecule to approximate the crystal field is avoided. Without a doubt, when it comes to modeling both the bulk and dynamic properties of a crystal, first principle crystal calculations are un-

EBSCOhost - printed on 2/13/2023 4:48 AM via . All use subject to https://www.ebsco.com/terms-of-use

surpassed in their potential for modeling the structures and properties of crystals for a variety of conditions (for an excellent review of such calculations see Bukowinski, 1994). Not only have they reproduced the structures of a number of relatively high symmetry materials, but they have also reproduced zero pressure elastic properties, deformation electron densities and the pressure dependences of molar volumes and selected Raman frequencies. But, on the other hand, when it comes to understanding the local properties and structures of a crystal or a glass, calculations and arguments based on molecules have provided support and understanding for a number of experimental trends and principles in crystal chemistry that have yet to be achieved by first principle crystal calculations. For example, calculations on molecules have not only reproduced bond length and angle variations observed for the silica polymorphs, but they have also reproduced the bond length and bond strength trends (Gibbs, 1982; Gibbs et al. 1987b) discovered by Smith (1953) for a silicate and extended by Baur (1970) and Brown and Shannon (1973) for oxide crystals. Such trends have been established by calculations on molecules for sulfide, nitride and fluoride crystals as well (Bartelmehs et al., 1989; Buterokos et al., 1992; Nicoll et al., 1994) . Molecular calculations have also provided insight into the effects of the non–tetrahedral cations on the variability of the bridging TOT angles and the thermochemical properties for silicates and silicate glasses (Gibbs, 1982; Geisinger et al., 1985; Navrotsky et al., 1985) as well as how quadratic stretching force constants vary with bond length and angle (O'Keeffe and McMillian, 1986; Hess et al., 1988; Hill et al., 1995) and how Raman active breathing mode frequencies for rings vary with Al content (Kubicki and Sykes, 1993). In addition to reproducing the local structures of alkali–metal silicate glasses, calculations on $(H_2M)O_3SiOSiO_3(MH_2)$ ($M = Li^+$, Na^+, K^+) molecules have satisfactorly reproduced observed trends in photoelectron, X–ray emission and UV excitation energies recorded for such glasses (Uchino et al., 1992). They have also been used to generate the structure and bulk modulus of quartz (Lasaga and Gibbs, 1987) as well as to generate a large number of new structure types for silica using a potential energy function based on the force field of the disilicic acid molecule (Boisen et al., 1994). Thus, when it comes to providing an understanding and a quantum mechanical underpinning of systematic trends involving bond length and angle variations, force constants and spectral properties and to generating new structure types (see the review by Sauer (1989) on molecular models and Tossell and Vaughan (1992), Chapters 4–7), MO calculations on small molecules will continue to find use despite their obvious limitations. Nonetheless, it should be observed in passing that semi–empirical extended Hückel type calculations completed for crystals employing the tight–binding approach have been used with some success in interpreting Pauling's rules (Burdett and MaLarnan, 1984) and the bond length–bond strength correlations discussed above (Burdett and Hawthorne, 1991).

In summary, the theoretical calculations examined in the second part of this review paper show that with more robust basis sets, the geometries of molecules and crystals are computed with more accuracy. But, what have these calculations taught us about the SiO bond? Actually, they have provided us with little insight into the nature of the bond other than that $d-$type AOs are required in the calculations to reproduce the observed SiO bond lengths and SiOSi angles. They have also provided evidence for the assertion that the forces that govern the geometry of a locally charge balanced silicate polyhedron behave as if short ranged and largely independent of the long–range forces exerted on the polyhedron by the ions of the periodic field of a silicate crystal. But, because deficient $sp-$type AOs and polar bonds can masquerade as $d-$type AOs, the calculations have nonetheless provided little or no meaningful insight into either the role or the extent played by the $d-$AOs in the formation of $\pi-$bonds. But, as will become evident below, electron density distributions, observed and

EBSCOhost - printed on 2/13/2023 4:48 AM via . All use subject to https://www.ebsco.com/terms-of-use

calculated for molecules and crystals, have provided evidence that seems to improve our understanding of the character of the bond and its π–system.

ELECTRON DENSITY DISTRIBUTIONS

In his pioneering work on the crystalline state, Bragg (1921) proposed that the electron density distribution, $\rho(\mathbf{r})$, in a crystal like diamond can be modeled by a superposition of free atoms with spherically averaged electron density distributions. Since then crystallographers have collected diffraction data for thousands of crystals and have found that they can account for their diffraction records reasonably well with a procrystal model: a model that assumes that the electron density distribution of a crystal consists of a superposition of spherically and thermally averaged atomic $\rho(\mathbf{r})$ distributions, each atom placed at its observed position in the crystal (Craven and Stewart, 1993). The close agreement that often obtains in such studies between observed and calculated structure factor moduli has been taken as evidence that the electron density distributions in these crystals are largely atomic in nature despite any reorganization of the electron density that may occur upon bond formation (Slater, 1965; Spackman and Maslen, 1986; Trefry et al., 1987; Gibbs et al., 1992; Tossell and Vaughan, 1992). For example, electron density maps recently calculated for bromellite, BeO, phenakite, Be_2SiO_4, danburite, $CaB_2Si_2O_8$, and coesite, SiO_2, assuming a procrystal model are similar to those retrieved from observed single crystal intensity data (Downs and Gibbs, 1987; Downs, 1990; Downs and Swope, 1992; Downs, 1994).

As indicated above, the differences that exist between the observed electron density distribution of a crystal like coesite and that of a procrystal model are relatively small (Figs. 3a and 3b). During the last two decades, maps of such differences, referred to as deformation electron density maps, have been published for a variety of silicate crystals (Tsirelson et al., 1990). Not only have these maps been used to assess the rearrangement of the electron density distribution that can occur upon bond formation relative to that of a procrystal model, but they have also been compared with theoretical deformation density maps calculated for hydroxy silicic acid molecules and silicate crystals. They have also been used to make inferences about the covalent and double bond character of the SiO bond. It is noteworthy that total electron density maps generated with experimental data with a generalized X–ray scattering factor (gsf) model also show a close correspondence with those generated in MO calculations for the disilicic acid molecule (Figs. 3a and 3c). The close correspondence in the electron density distributions of the two suggests that the long–range forces of the crystal field in coesite exerts a small effect on its electron density distributions. As observed by Tsirelson et al. (1990), the role played by 3*d* AOs of Si in the double character of the SiO bond has been extensively discussed, but that there has been no general consensus on the solution to the problem as documented in Part 2 of this review paper. They continued by observing that experimental deformation electron density distributions may not only serve as a basis for studying the double bond character of the SiO bond in silicate crystals, particularly in the silica polymorphs, but also for studying the effect of the crystal field on the electron density distribution of the SiO bonds in such crystals.

Deformation electron density distributions

A deformation electron density map for a crystal can be obtained by evaluating the function

$$\Delta\rho(\mathbf{r}) = \frac{1}{V}\sum_{hk\ell}(F_o/\kappa - F_{IAM})\exp\{-2\pi(\mathbf{h}\cdot\mathbf{r})\} \qquad (1)$$

EBSCOhost - printed on 2/13/2023 4:48 AM via . All use subject to https://www.ebsco.com/terms-of-use

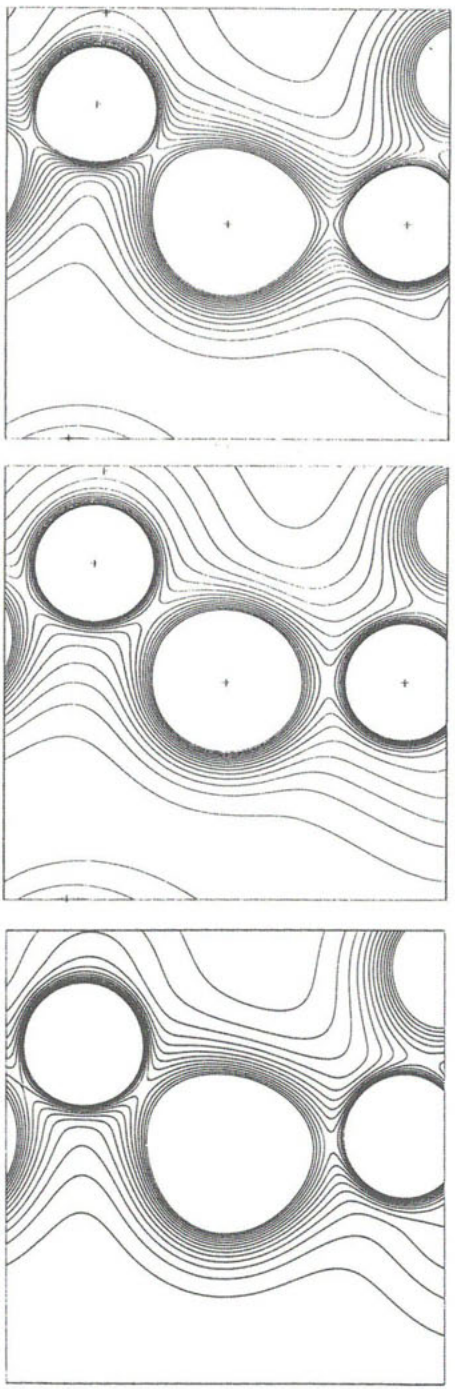


Figure 3. Total electron density distributions for an Si_2O_7 dimer (a) generated from experimental X–ray diffraction data with a gsf model for the Si(1)O(5)Si(2) dimer in coesite (Downs, 1994), (b) generated with an IAM model for the dimer (Downs, 1994) and (c) generated in an Hartree–Fock MO calculation using a 6–31G** basis set for a $H_6Si_2O_7$ molecule whose geometry was fixed at the geometry of the Si_2O_7 group in coesite (Hill, 1995). Each map is contoured with level lines of electron density evenly spaced at intervals of 0.1 e/Å^3.

EBSCOhost - printed on 2/13/2023 4:48 AM via . All use subject to https://www.ebsco.com/terms-of-use

at each point **r** in 3-space where F_O/κ is a scaled and model-phased observed structure factor modulus, F_{IAM} is a structure factor calculated for an independent atom (procrystal) model (IAM) of a crystal consisting of spherical atoms with their positional and thermal parameters fixed at observed values and **h** is the Bragg diffraction vector.

With the goal of improving our understanding of the properties of the electron density distribution of the SiO bonds in the silica polymorphs with four coordinate Si, diffraction data was recorded and $\Delta\rho(\mathbf{r})$ maps constructed for coesite (Geisinger et al., 1987). Coesite is ideally suited for studying SiO bond length, SiOSi angle and electron density variations because it contains two nonequivalent silicate tetrahedra with eight nonequivalent SiO bonds linked together by five nonequivalent SiOSi angles into a framework of corner-sharing silicate tetrahedral oxyanions. As observed earlier, the bond lengths in the structure decrease in a regular way from 1.621Å to 1.595Å as the SiOSi angle widens from 137° to 180°. Maps of the deformation electron density distributions for the five SiOSi angles reveal peaks on or near all of the SiO bonds in coesite, with an average peak height of $\sim$0.45 eÅ^{-3}. The peaks in each SiO bond, situated closer to the more electronegative oxide ions than to the Si cation, are connected by ridges of deformation electron density that extend across the interior of each bent angle to a saddle point in $\Delta\rho(\mathbf{r})$. The location of the peaks next to the oxide ions can be ascribed to a polarity of the bond; the closer the peak to the oxide ion, the greater the polar character of the bond. As discussed in part 2, whether these features represent the effects of double bonding or the ionicity of the bond is unclear. Deformation electron density, localized on the exterior sides of the obtuse SiOSi angles next to only two of the oxide ions (O2 and O5) has been interpreted as lone-pair electron density (Geisinger et al., 1987). However, no meaningful trends obtain between the heights of the peaks in the bonds and SiO bond length.

The gross features of these maps roughly match those calculated for the SiOSi dimers of the molecules $H_3SiOSiH_3$, $(HO)_3SiOSi(OH)_3$ and $H_8Si_4O_4$ with either a 6-31G* or a 6-31G** basis set (Geisinger et al., 1987; Gibbs et al., 1987a). As observed for coesite, these maps show peaks displaced off the SiO bonds toward the interior of the SiOSi angle and toward the oxide ions. They also show ridges of deformation electron density localized in the bent angles between the peaks of the bonds (Fig. 4). But, unlike the experimental maps, sharp peaks ascribed to localized lone-pair electron density exist on all of the oxide ions at the exterior side of each bent SiOSi angle. The absence of such peaks for the O3 and O4 ions in coesite has been ascribed to the limited resolution of the diffraction data which were only recorded to a $\sin\Theta/\lambda$ value of 0.91Å^{-1}. The displacement of the peaks off the SiO bonds toward the interior of the SiOSi angle can be ascribed to lone-pair bond-pair nonbonded repulsions (Gillespie, 1963). Also, the peaks in the theoretical maps are not as high ($\sim$0.35 eÅ^{-3}) as those observed for coesite. The progressive accumulation of lone-pair charge density in the antibinding region of the molecule with a narrowing of the SiOSi angle has been used to explain some of the lengthening of the SiO bond that accompanies the narrowing of the angle. The features of a deformation density map calculated in a periodic Hartree-Fock study of quartz with a 6-21G** (Noda et al., 1990) are strikingly similar to those calculated for $H_3SiOSiH_3$ (Gibbs et al., 1987a) with the peaks along the bonds being higher (0.47 eÅ^{-3}) than those calculated for the molecule but in close agreement with those observed for coesite (when one compares Figure 4 with a deformation map calculated for quartz, Figure 7 in Noda et al. (1990), this close agreement is apparent). Model deformation density maps have also been calculated for the quartz structure within the local-density approximation of density functional theory, using the plane wave pseudopotential method (Binggeli et al., 1991). The resulting plane wave density maps also show a strong similarity with

EBSCOhost - printed on 2/13/2023 4:48 AM via . All use subject to https://www.ebsco.com/terms-of-use

the experimental maps recorded for coesite with peak heights in the SiO bonds of the theoretical map of $\sim$0.45 eÅ^{-3} in close agreement with those observed. On the other hand, these maps are in relatively poor agreement with a static deformation density map observed for quartz which shows bond peaks $\sim$0.9 eÅ^{-3} in height (Spackman et al., 1981). This discrepancy may be ascribed to the fact that the data set used to construct the map for quartz suffers from extinction and therefore is believed to be of poorer quality than those recorded for coesite (Spackman, personnel communication). Binggeli et al. (1991) conclude, from the bridge of deformation electron density on the internal side of the SiOSi angle and the accumulation of electron density along the SiO bond at a distance of $\sim$0.50Å from the oxide ion, that a significant fraction of the valence electrons on Si has been transferred to the oxide ion. They continue by observing that the electrons come in large part from valence density distribution of the Si atom in the region of the SiO bond and from the region of the distribution located furthest away from the oxide ion. Based on these results, they conclude that the bond can be described as a blend of strong ionic and covalent interactions with coexisting nonbonded features.

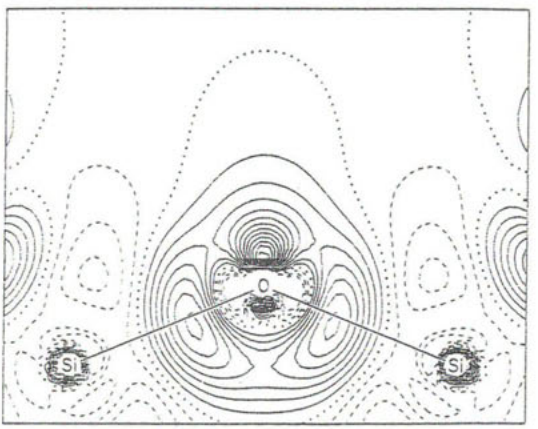


Figure 4. Deformation electron density map calculated for the gas phase molecule disiloxane, H_6Si_2O, using a 6–31G** basis set with two *d*–AOs on Si and one on O. The map passes through atoms of the SiOSi dimer of the molecule, it is contoured with level lines of electron density evenly spaced at intervals of 0.05e/Å^3 with the positive level lines drawn as solid lines, the zero level lines drawn with dotted lines and the negative lines drawn as dashed lines. The maximum contour plotted is 1.3 e/Å^3. The position of the oxide ion is indicated by the symbol O and that of the two Si ions by the symbol Si. The line connecting Si and O denote the interatomic vector that connect Si and O. The $\Delta\rho(\mathbf{r})$ electron density is concentrated about the more electronegative oxide ion with bonding peaks directed toward the Si ions and a lone–pair peak situated next to the oxide ion just above the apex of the SiOSi angle. The bonding peaks are displaced off the SiO bond vector toward the interior side of the SiOSi angle and they are connected by ridge of electron density with an intervening saddle point. A ridge of electron density also exists on the exterior side of the angle where the bonding and lone pair–peaks coalesce.

Stishovite contains six coordinate Si and three coordinate O unlike quartz, cristobalite and coesite which have four coordinate Si and two coordinate O. An exploration of the deformation electron density for stishovite was undertaken to clarify the properties of the electron density distributions of the SiO bonds in a six coordinate polyhedron (Hill et al., 1983; Spackman et al., 1987). Deformation electron density maps calculated for the two nonequivalent bonds in the six coordinate polyhedron

EBSCOhost - printed on 2/13/2023 4:48 AM via . All use subject to https://www.ebsco.com/terms-of-use

display peaks that have statistically identical heights, $\sim$0.3 eÅ^{-3}, a value that is less than the peak heights typically observed for a four coordinate SiO bond. It is possible that the smaller peaks recorded for stishovite are an indication that the six coordinate SiO bond has a larger component of ionic character than a four coordinate bond. Deformation electron density maps calculated in a modeling of the stishovite structure using a linearized augmented plane wave model are similar to those observed with the heights of the peaks in the bonds being close ($\sim$0.35e/Å^3) to those observed (Cohen, 1991). With calculations based on a self–consistent local–density approximation, Xu and Ching (1991) obtained a band structure that is in excellent agreement with the structure obtained by Cohen (1991), yet, on the basis of the calculated electron density maps, they concluded that the SiO bond in stishovite is more covalent than it is in the other silica polymorphs. As the calculated electron density maps show extraneous peaks where there are no atoms in the crystals, the significance of their conclusion is unclear. Also, their conclusion that the SiO bond in the denser, close–packed stishovite structure is more covalent than it is in the more open framework structures of the other silica polymorphs runs counter to observations by Catlow and Stoneham (1983) who expect that ionic crystals will favor close–packed structures whereas the directed bonds of a covalent crystal will favor more open framework structures.

As with silicates, the peaks of deformation electron density in the SiO bonds of stishovite are located closer (0.68Å) to more electronegative oxide ions. Their heights and positions are similar to those calculated by Hill et al. (1983) for a hypothetical $(2/3H)_{12}SiO_6$ molecule using a 6–31G* basis set. Each oxide ion in stishovite is bonded to three Si atoms at the corners of a triangle. Deformation electron density maps calculated in planes perpendicular to the triangle and along the two nonequivalent bonds each show peaks adjacent to the oxide ion localized above and below the plane of the triangle with peak height of $\sim$0.45 eÅ^{-3}. These lone–pair peaks are well developed in the maps calculated with the LAPW method (Cohen, 1991). A similar feature is displayed as a natural progression of the lone–pair deformation density near the bridging oxide ion of the disilicic acid molecule as the SiOSi angle closes from 180° to 137°. The fact that the oxide ion in stishovite is three rather than two coordinate should not affect this feature, although it might result in a reduction of the electron density concentrated along the SiO bonds and the strengths of the bonds (Spackman et al., 1987)

Tsirelson et al. (1990) have undertaken an extensive review of experimentally determined deformation electron density distributions recorded for more than 25 silicate crystals ranging from monosilicates like forsterite to framework silicates like coesite. With few exceptions, the dominant features in the resulting maps are peaks situated near the SiO bonds typically displaced in the direction of the oxide ion, as observed for coesite, with a height of $\sim$0.5 eÅ^{-3}, on average. They concluded from these features that the SiO bond is predominantly covalent in character. In addition, bridges of deformation electron density that typically occur on the interior side of an SiOSi angle and that connect peaks in the bonds were taken as evidence for SiO double bond character.

The efficacy of deformation electron density distributions

In the explorations of the electron density distributions reviewed by Tsirelson et al. (1990), attention was focused on $\Delta\rho(\mathbf{r})$ rather than on the total electron density distribution, $\rho(\mathbf{r})$. Although it has been asserted that $\Delta\rho(\mathbf{r})$–maps delineate regions where electron density is either accumulated or depleted, such maps are generated in such a way that the resulting distributions are dependent on a reference electron density distribution model. Moreover, with the discovery of slightly negative or very small

EBSCOhost - printed on 2/13/2023 4:48 AM via . All use subject to https://www.ebsco.com/terms-of-use

deformation density peaks along some of the SiO bonds in orthopyroxene, (Sasaki et al., 1982), tourmaline (Belokoneva and Tsirelson, 1993) and topaz (Belokoneva et al., 1993), the question arises whether a mapping of a $\Delta\rho(\mathbf{r})$ distribution always provides a meaningful measure of the redistribution of the electron density accompanying bond formation. Also, maps obtained for the H_2O_2 molecule show negative peaks of deformation electron density in the OO bond (Savariault and Lehmann, 1980), and negative or very small peaks of deformation densities have been observed in the NN, CN and CO bonds for a number of other molecules (Dunitz and Seiler, 1983). These predominantly covalent bonds have been described as bonds "without bonding electron density". In contrast with the results obtained in the $\Delta\rho(\mathbf{r})$–maps for the OO bond, Cremer and Krakar (1984) have calculated the Laplacian distribution of $\rho(\mathbf{r})$, $\nabla^2\rho(\mathbf{r})$, for the H_2O_2 molecule and found that electron density is indeed locally concentrated in the bond. Hence, a $\nabla^2\rho(\mathbf{r})$ distribution seems to be a more meaningful probe of charge concentration than a $\Delta\rho(\mathbf{r})$ distribution (see below). One problem with $\Delta\rho(\mathbf{r})$ densities is the choice that is made in defining reference promolecule and procrystal density distributions. Usually, these densities are constructed with spherically and thermally averaged, noninteracting, neutral free atoms located at the positions they adopt in the molecule and the crystal. But one could elect to use oriented atomic electron density distributions or the electron density distributions of those states to which the system will dissociate as the reference density. Plainly, the resulting $\Delta\rho(\mathbf{r})$–maps would be different and open to alternative interpretations. Thus, such a distribution is not without its problems. In the next part, the gradient and Laplacian of the total electron distribution will used to probe the character of the SiO bond, its polarity and its π–system. As observed below, the gradient and the Laplacian of an electron density distribution, unlike a deformation electron density distribution, are both independent of reference models and basis sets.

Gradient and Laplacian distributions

The topological features of the electron density distribution of a molecular or a crystalline system, as revealed by its Laplacian distribution, have provided important insights into the nature of bonding in general and the SiO bond in particular by highlighting those regions in the system where the electron density is either concentrated or depleted (Bader, 1990; Downs, 1990; Downs and Swope, 1992; Hill, 1995). As asserted by Morse and Feshbach (1953) and used by Bader (1990), a scalar function of $\rho(\mathbf{r})$ has a tendency to be locally concentrated such that the Laplacian of $\rho(\mathbf{r})$

$$\nabla^2\rho(\mathbf{r}) = \partial^2\rho(\mathbf{r})/\partial x^2 + \partial^2\rho(\mathbf{r})/\partial y^2 + \partial^2\rho(\mathbf{r})/\partial z^2 \qquad (2)$$

has a negative sign; the greater the magnitude of $-\nabla^2\rho(\mathbf{r})$, the greater the local concentration of the electron density. On the other hand, the electron density is asserted to have a tendency to be locally depleted where the Laplacian has a positive sign, so that the greater the value of $\nabla^2\rho(\mathbf{r})$, the greater the depletion. These same statements also hold for each of the three curvatures, $\partial^2\rho(\mathbf{r})/\partial x^2$, $\partial^2\rho(\mathbf{r})/\partial y^2$ and $\partial^2\rho(\mathbf{r})/\partial z^2$ in their respective directions.

In exploring the structure of an atom like Si, Bader and Essén (1984) and Bader et al. (1984) found that the Laplacian of the electron density distribution delineates the shell structure of the atom where each shell is displayed as a spherical node consisting of two regions with the electron density being locally concentrated in one and locally depleted in the other (Shi and Boyd, 1988). The spike at the center of the $-\nabla^2\rho(\mathbf{r})$ map for the Si atom (IAM model) displayed in Figure 5a corresponds to the K–shell, the next outermost node to the L–shell and the outermost very low lying shell to the very diffuse M–shell. The shells corresponding to the core K–shell and the

EBSCOhost - printed on 2/13/2023 4:48 AM via . All use subject to https://www.ebsco.com/terms-of-use

valence L–shell of an IAM modeled O atom are displayed in Figure 5b. Clearly, the valence shell concentration of the O atom is much more prominent than the low lying valence shell concentration on Si. As we shall see, the electron density distribution of the valence shell of the oxide ion seems to play a more dominant role in the formation of the SiO bond relative to that played by the diffuse electron density distribution of the shell that corresponds to the M–shell on Si.

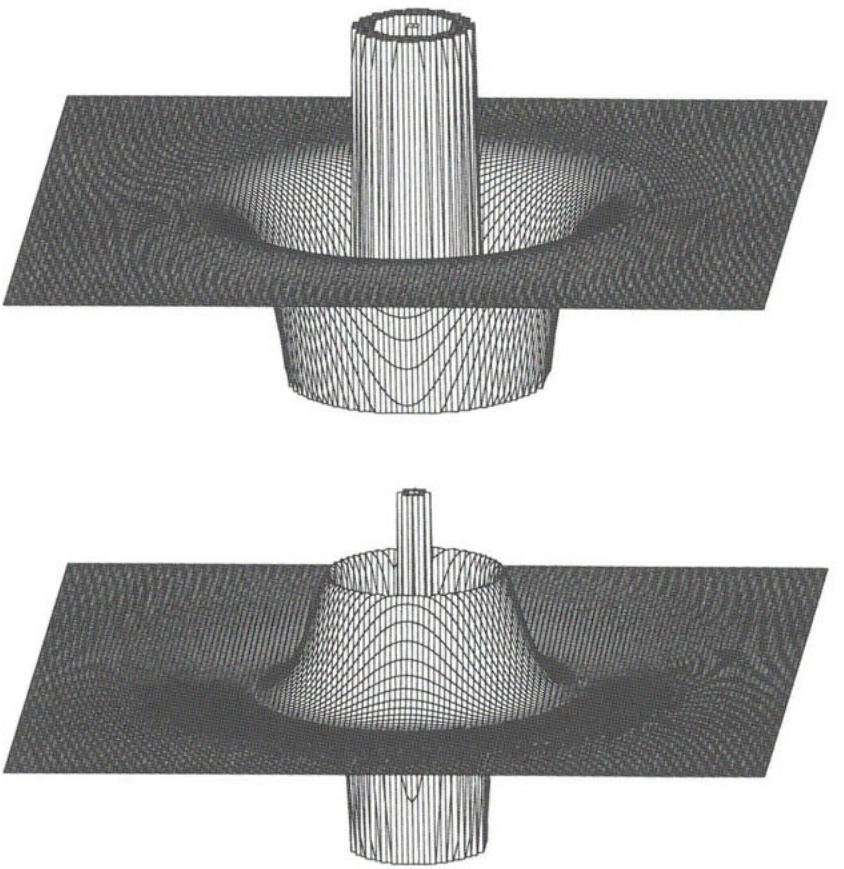


Figure 5. Relief maps of the negative Laplacian of the electron density distributions, $\nabla^2\rho(\mathbf{r})$, for planes 3Å on a side passing through the nucleus of a spherically averaged ground state (a) Si atom and (b) O atom calculated with Clementi–Roetti wave functions. Both maps are truncated at ± 150 eÅ^{-5}.

Bader and Essén (1984) have also found that the components of $\nabla^2\rho(\mathbf{r_c})$ can be used to classify the interaction between a pair of bonded atoms and their bond type when evaluated at a saddle point (a bond critical point $\mathbf{r_c}$). Bader (1990) has asserted that such a saddle point resides between each pair of bonded atoms. With the construction of a gradient vector field map of $\rho(\mathbf{r})$, a special pair of gradient lines can be defined (Bader, 1990), both originating at a saddle point with one terminating at one of the bonded atoms and the second terminating at the other. Such a pair of lines that connects the nuclei of the bonded atoms and the saddle point in a bound system is called a bond path. The path defines a line along which $\rho(\mathbf{r})$ is a maximum

EBSCOhost - printed on 2/13/2023 4:48 AM via . All use subject to https://www.ebsco.com/terms-of-use

with respect to any neighboring gradient lines, and therefore, it runs along the top of the ridge of electron density that links the saddle point to the peaks centered on a pair of bonded atoms. This line is close to, but it may not necessarily lie along the straight line that connects a pair of bonded atoms. The saddle point is a special point along the bond path at which the electron density attains a minimum value. By evaluating the Laplacian at this point, the energetics and atomic interactions between a pair of bonded atoms can be characterized in a consistent way, as discussed by Bader and Essén (1984) and by Bader (1990). In molecules with strained bonds, the difference between the length of the bond path and the bond length provides a measure of the strain and the degree to which electron density is relaxed away from the constraints imposed on the molecule by the nuclear framework (Bader, 1990).

The energetics that govern the electron density distribution of a molecule or a crystal are closely tied to the Laplacian of the distribution. As observed by Bader (1990),

$$(\hbar^2/4\pi^2 m)\nabla^2\rho(\mathbf{r}) = 2G(\mathbf{r}) + \mathcal{V}(\mathbf{r}) \tag{3}$$

where $\mathcal{V}(\mathbf{r})$ is the potential energy density, which is negative, and $G(\mathbf{r})$ is the local kinetic energy density, which is positive. As the sign of $\mathcal{V}(\mathbf{r})$ is negative everywhere in a bonded system and as $2G(\mathbf{r})$ is necessarily positive, the sign of $\nabla^2\rho(\mathbf{r})$ determines which of these two energy density terms is larger in magnitude. In a region where $\nabla^2(\mathbf{r}) < 0$, not only is the electron density locally concentrated, but also $\mathcal{V}(\mathbf{r})$ locally exceeds the average value of $2G(\mathbf{r})$. Thus, by making a map of those regions where $\nabla^2\rho(\mathbf{r}) < 0$, those regions where the potential energy density makes a dominant contribution to the energy of the system are delineated (Bader et al., 1984). Likewise, by determining where the Laplacian of the electron density is positive, a map can be obtained that delineates those regions where the kinetic energy density makes a dominant contribution to the energy of the system.

In determining the nature of a bond, the value of the electron density $\rho(\mathbf{r_c})$ and its Laplacian, $\nabla^2\rho(\mathbf{r_c})$, are determined at the saddle point in the internuclear region between the two atoms comprising the bond (Bader, 1990). For purposes of simplicity, the three principal curvatures of $\rho(\mathbf{r_c})$ that define $\nabla^2\rho(\mathbf{r_c})$ are denoted λ_i, $i = 1, 2, 3$. Because $\rho(\mathbf{r})$ attains a minimum value along the bond path, the curvature in this direction measured at $\mathbf{r_c}$, denoted λ_3, is always positive. The remaining two curvatures, denoted λ_1 and λ_2 have mutually perpendicular eigenvectors that are also perpendicular to the eigenvector associated with the third curvature denoted λ_3. Both λ_1 and λ_2 have negative signs, corresponding to a local concentration of $\rho(\mathbf{r})$ in the binding region along the bond path between the bonded atoms. The value of $\rho(\mathbf{r_c})$ evaluated at the internuclear critical point $\mathbf{r_c}$ has been found to correlate with bond length for a given bond type; the greater the value of $\rho(\mathbf{r_c})$, the greater the amount of electron density and the shorter the bond (Bader et al., 1984). In addition, the ellipticity of a bond, $\epsilon = |(\lambda_1 - \lambda_2)/\lambda_2|$ where $|\lambda_1| > |\lambda_2|$, has been used as a probe of the π–character of a bond by measuring the extent to which the electron density is preferentially concentrated in a π–system; that is, in a plane or planes on opposite sides of the bond. The polar nature of a bond has been taken as proportional to the ratio $G(\mathbf{r_c})/\rho(\mathbf{r_c})$ (Cremer, 1987).

In a study of a number of diatomic molecules with a range of atomic interactions and bond types, Bader and Essén (1984) observed that the interactions can be classified into two limiting classes: (1) shared interactions typical of a covalent type bond and (2) closed shell interactions typical of an ionic type bond. In shared interactions, the electron density is locally concentrated in the binding region between a pair of bonded atoms. In this case, the curvatures of $\rho(\mathbf{r_c})$ perpendicular to the path are both large in magnitude and negative in sign (–25 to –45 $e\text{Å}^{-5}$). On the other

EBSCOhost - printed on 2/13/2023 4:48 AM via . All use subject to https://www.ebsco.com/terms-of-use

hand, λ_3, the positive curvature of $\rho(\mathbf{r})$ at the critical point along the bond path can take on a range of values between 0.0 and 45 eÅ^{-5}. Hence, in this case, $\nabla^2\rho(\mathbf{r_c})$ is negative, indicating that the electron density is concentrated in the binding internuclear region and that the potential energy density makes a dominant contribution in the region, over the kinetic energy density, to the energy of the system. The end result is a local concentration of electron density between the nuclei of the bonded atoms. For such a bonded interaction, the value of the electron density evaluated at the critical point is typically large, roughly between 2 and 4 eÅ^{-3}. On the other hand, for ionic interactions between closed-shell atoms, the curvatures perpendicular to the bond path, albeit both negative in sign, are sufficiently small in magnitude (−1 to −2 eÅ^{-5}) such that $\nabla^2\rho(\mathbf{r_c})$ is positive, indicating a local depletion of the electron density in the vicinity of the bond and a concomitant concentration of the electron density in the vicinity of the bonded atoms. In this case, the kinetic energy density makes a dominant contribution, over the potential energy density, to the energy of the system in the region of the interatomic surface. In all of the cases studied with closed shell ionic interactions, $|\lambda_1|/\lambda_3 < 1$, indicating a concentration of $\rho(\mathbf{r})$ toward the nuclei of the bonded atoms. Such a ratio is expected when closed shell wave functions are dominant in defining the wave functions of a bond. Also, for ionic bonds, the electron density at the critical point is typically small, roughly between 0.2 to 0.4 eÅ^{-3}. Between the two limiting classes of shared and closed-shell interactions, there exists an intermediate class of interactions where the critical point is located close to a nodal surface of $-\nabla^2\rho(\mathbf{r})$. As in the case of closed-shell interactions, $\nabla^2\rho(\mathbf{r})$ is typically large. On the other hand, the value of the electron density at the critical point is of intermediate value between those exhibited by ionic and covalent bonds. Furthermore, the ratio $|\lambda_1|/\lambda_3$ lies roughly between 0.2 and 1.4 with the more ionic bonds exhibiting values at the lower end of the scale.

Laplacian distributions for minerals and molecules

Downs and Swope (1992) have mapped the Laplacian of the generalized X-ray scattering factor pseudoatom electron density distribution recorded for danburite and displayed the shell structures of the valence and core electrons of its constituent atoms. The resulting $\nabla^2\rho(\mathbf{r})$ relief maps indicate that the CaO, BO and SiO interactions in the structure are mainly closed shell in nature with a concentration of the electron density in the valence shell about each O atom, each residing in the vicinity of a bond path. In addition to these bonded interactions, concentrations of nonbonded electron density occur on the O atom on the exterior sides of the bridging SiOSi, SiOB and BOB angles. Also, an evaluation of $\rho(\mathbf{r_c})$ and $\nabla^2\rho(\mathbf{r_c})$ at the saddle points between the SiO and BO bonds indicates that these bonds are of intermediate bond type between ionic and covalent while the CaO bond is indicated to be predominantly ionic in character. A similar analysis for bromellite, BeO, indicates that the BeO bond is more ionic in character than the SiO and the BO bonds but more covalent than the CaO bonds, as expected from electronegativity considerations (Downs, 1990). Interestingly, Downs (1990) found that electron density distributions calculated for (1) a superposition of Be cations and oxide ions, (2) a procrystal distribution calculated for a superposition of spherically averaged neutral atoms and (3) the experimental pseudoatom model of the electron density distribution are surprisingly similar. In addition, $\nabla^2(\mathbf{r_c}) > 0$ for all three models, indicating that interaction between Be and O is a closed shell interaction regardless of whether they are considered to be noninteracting atoms or ions or interacting bonded atoms. The values of $\rho(\mathbf{r_c})$ for these bonds ($\sim$0.55 eÅ^{-3}) are similar to that (0.6 eÅ^{-3}) obtained for the bond in an MgO molecule and significantly smaller than the values obtained for the SiO ($\sim$0.95

EBSCOhost - printed on 2/13/2023 4:48 AM via . All use subject to https://www.ebsco.com/terms-of-use

eÅ^{-3}) and BO (~1.05 eÅ^{-3}) bonds in danburite (Downs, 1990; Downs and Swope, 1992). However, the values of $\rho(\mathbf{r_c})$ for the CaO bonds in danburite (~0.15 eÅ^{-3}) are much smaller than the intermediate SiO and BO bond types and slightly smaller than that (0.25 eÅ^{-5}) calculated for the bond in the NaCl molecule (Bader, 1990). For closed shell interactions, the ratio $|\lambda_1|/\lambda_3$ is expected to be less than 1. The average ratio for the CaO bonds in danburite is 0.15. It is 0.25 for the BeO bonds in BeO and it is 0.30 for the SiO bond and 0.35 for the BO bonds in danburite. In other words, of these bonds, the electron density distribution is indicated to be concentrated toward the ions comprising the CaO bond, as expected from electronegativity considerations, with the CaO bond being the most ionic bond in the series. Also, the BO bond is indicated to be more covalent in character than the SiO bond, as expected from electronegativity considerations.

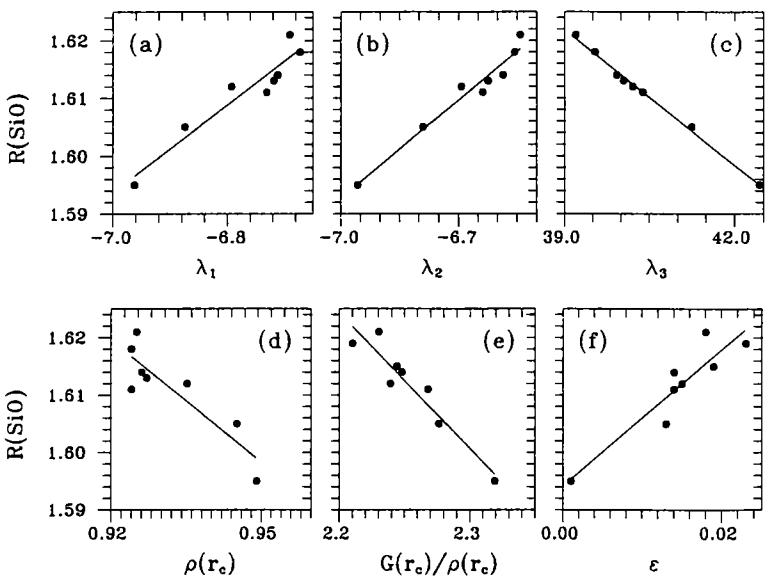


Figure 6. A summary of the properties of the electron density distribution of the SiOSi dimers in a set of $H_6Si_2O_7$ molecules with geometries fixed at those observed for the Si_2O_7 units in coesite. In (a), (b) and (c), the individual SiO bond lengths, R(SiO), observed for coesite are plotted against λ_1, λ_2 and λ_3, the curvatures of the electron density distribution calculated for the molecules at their saddle points, $\mathbf{r_c}$. In (d), R(SiO) is plotted against the value of the electron density, $\rho(\mathbf{r_c})$. In (e) R(SiO) is plotted against $G(\mathbf{r_c})/\rho(\mathbf{r_c})$ where $G(\mathbf{r_c})/\rho(\mathbf{r_c})$ is the kinetic energy density and in (f) R(SiO) is plotted vs. the ellipticity, ϵ, of the bonds.

Using the X–ray diffraction data recorded by Geisinger et al. (1987), Downs (1994) evaluated the Laplacian of the gsf pseudoatom electron density distribution at the saddle points along the SiO bonds in coesite. The average value of the λ_3–curvature (~30 eÅ^{-5}) observed at the eight nonequivalent saddle points is smaller than that calculated (~40 eÅ^{-5}) for an ionic model and marginally larger than that calculated (~28 eÅ^{-5}) for an independent atom model of the electron density distribution of the structure. In addition, the average values of the λ_1– and λ_2–curvatures observed at the saddle points (–9 eÅ^{-5}) are larger in magnitude than those calculated for the IAM (–4 eÅ^{-5}) and the ionic models (–6 eÅ^{-5}). This result indicates that the electron density in coesite is concentrated to a greater extent perpendicular to its SiO bonds than that exhibited by either an ionic or an IAM electron density distri-

EBSCOhost - printed on 2/13/2023 4:48 AM via . All use subject to https://www.ebsco.com/terms-of-use

bution. On the other hand, the observed concentration of the electron density along the bonds in coesite is 0.25 $e\text{Å}^{-3}$ larger than that exhibited by the independent atom model ~0.85 $e\text{Å}^{-3}$ and ~0.4 $e\text{Å}^{-3}$ larger than that exhibited by the ionic model (0.68 $e\text{Å}^{-3}$) of the electron density. The value of the electron density observed at the bond critical points for coesite, ~ 1.1 $e\text{Å}^{-3}$, is larger than that expected for both types of bonds. Collectively, these results are expected for a bond of intermediate type with the concentration of the electron density distribution along the bond being largely atomic in nature.

The Laplacian distribution for coesite has been modeled by Hill (1995) in a calculation completed on five $(HO)_3SiOSi(OH)_3$ molecules, using a 6–311++G** basis set. The geometry of each of the Si_2O_7 dimers in the molecules was adjusted to match that observed for each of the five nonequivalent dimers in coesite. The hydrogen atoms used to neutralize each dimer were placed at 0.97Å in the directions of the Si atoms bonded to the 'nonbridging' oxides of the dimer in coesite. The Laplacian of the distributions and the λ_i values obtained in the calculations are plotted in Figures 6a, 6b and 6c as functions of the SiO bond lengths observed for coesite. As the magnitudes of λ_1 and λ_2 both increase as the SiO bond length shortens, the electron density is seen to be progressively concentrated in a direction perpendicular to the bond as the SiO bond shortens and the SiOSi angle widens. This results in a progressive increase in the local concentration of the electron density between Si and O as the angle widens, typifying an increased covalent interaction between the two atoms. The systematic increase in these λ–values also indicates that the potential energy density makes a progressively greater contribution to the energy of the system in the region of the SiO bond as the bond lengths shorten and the angle widens. Because the magnitude of λ_3 increases as the SiO bond length shortens, the electron density is also indicated to be concentrating along the bonds toward both Si and O. These results suggest that the covalent character of the SiO bond increases as the SiOSi angle widens. This observation is borne out by Figure 6d, in which it is seen that the electron density evaluated at the critical points increases from ~0.92 $e\text{Å}^{-3}$ to ~0.95 $e\text{Å}^{-3}$ as the bond length shortens and the angle widens; this also typifies an increase in the covalent character of the bond as the angle widens. As the electron density increases, the $G(\mathbf{r_c})/\rho(\mathbf{r_c})$ vs. R(SiO) plot in Figure 6e indicates that the polarity of the bond increases as well. This result can be ascribed to either an increase in the ionicity of the bond or to an increase in the participation of the $d-$AOs on Si in $(p-d)\pi$ bond formation as the SiO bond shortens. If the latter is important, then the ellipticity of the SiO bond should be zero when the SiOSi angle is straight and both π–systems are involved in bonding (Cruickshank, 1961). Moreover, it should increase in a regular way as the SiOSi angle narrows and as one of the π–systems becomes dominant (Cruickshank, 1961). A plot of ϵ vs. R(SiO) shows that $\epsilon = 0$ when the SiOSi = 180° and that it increases in a regular way as the angle narrows (Fig. 6f). These results indicate that the increased polarization and shortening of the SiO bond accompanying the widening of the SiOSi angle can be interpreted in terms of π–bond formation.

Deformation electron density distributions calculated for $(HO)_3SiOSi(OH)_3$ and $H_3SiOSiH_3$ molecules and observed for coesite show peaks along the SiO bonds that are displaced toward the interior of each bent SiOSi angle (Fig. 4). This result suggests that the bond paths that connect the nuclei of Si and O and the bond critical point are curved away from the line connecting Si and O, indicating strained SiO bonds. As observed above, in molecules with strained bonds, the bond paths are usually curved and depart from the straight lines between the bonded atoms, the greater the departure, the greater the strain energy embodied in a bond. In an examination of the strained character of the bonds, Hill (1995) calculated the

EBSCOhost - printed on 2/13/2023 4:48 AM via . All use subject to https://www.ebsco.com/terms-of-use

bond path lengths for the SiO bridging bonds in each of the five $(HO)_3SiOSi(OH)_3$ molecules and found in each case that that they match the SiO bond lengths of the molecules to within 0.0005Å. With this result, she concluded that the bond paths in the SiOSi dimers follow the line between each pair of Si and O atoms in the molecule very closely and that the SiO bonds that comprise the molecules are largely strain free.

Relief and contour maps of $-\nabla^2\rho(\mathbf{r})$ for each of the $(HO)_3SiOSi(OH)_3$ molecules were calculated by Hill (1995) to learn where the electron density in the vicinity of each bond is either locally concentrated or depleted. Each map displays nodes that correspond to the K– and L–shells for both Si and O with the nodes of the valence L–shells on the oxide ions being prominent features in the maps. Because of the very diffuse nature of the valence electrons of Si, the nodes corresponding to the M–shell of Si are not prominent features in the maps (Fig. 7a). In fact, a mapping of the valence electron density distribution for coesite, using the data recorded by Geisinger et al. (1987), shows peaks of electron density centered at the position of each oxide ion with little or no density in the vicinity of the Si atoms (see Fig. 1, Jackson and Gibbs, 1988), with a polarization of $\rho(\mathbf{r})$ along the SiO bonds toward each Si cation. The $-\nabla^2\rho(\mathbf{r})$ maps for the five molecules show a depletion of the L–shell electron density concentration for each oxide ion where the shell crosses the SiO bond, with electron density being locally concentrated away from the shell along the bond in the direction of the Si cation. Figure 7b is a map of the positive contours of $-\nabla^2\rho(\mathbf{r})$ for the molecular model of the Si(1)O(5)Si(2) dimer in coesite. It shows that the electron density distribution of the O(5) oxide ion is highly polarized in its concentration in the directions of Si(1) and Si(2). Its also shows that electron density is locally concentrated in the shell on the external side of the SiOSi angle. All of the features seen in Figure 7 are displayed by all of the molecular models for the nonequivalent SiOSi dimers in coesite. The features exhibited by the SiO bonds in the disilicic acid molecule are observed for coesite, but the trends are much more poorly developed. It has been proposed by Bader (1990) that the nonbonded maxima in a $-\nabla^2(\mathbf{r})$ distribution can be used to identify sites of potential electrophilic attack, whereas regions of maximum depletion highlight sites of potential nucleophilic attack. According to his arguments, the peaks of lone–pair pair density observed to occur next to each oxide ion in danburite and coesite represent sites of potential electrophilic attack (Downs, 1994). The mechanism proposed by Michalske and Bunker (1982) for the cleavage of the SiOSi dimer by attack by the water molecule conforms with an attraction of the protons of the molecule by the lone–pair electron density (also see Lasaga and Gibbs, 1990).

The bonded radius of the oxide ion and SiO bond character

The bonded radii of the atoms comprising a bond can be determined by measuring the distances between the nuclei of a pair of bonded atoms like Si and O and the critical point of minimum electron density along the bond path (Bader, 1990). As these radii are measured in the direction of the bond, they have little or no meaning in other directions (O'Keeffe, 1981; Gibbs and Boisen, 1986; Gibbs et al., 1992). In fact, a single ion like the oxide ion can exhibit several radii with a different radius along each of the nonequivalent bonds that it forms in a molecule or a crystal with nearest neighbor cations (Johnson, 1973). For example, the oxide ions in danburite exhibit bonded radii that range between ~0.94 and ~1.23Å (Downs and Swope, 1992). Three of the ions are bonded to three different cations, four coordinate ^{IV}B and ^{IV}Si and seven coordinate ^{VII}Ca at distances of ~1.47, ~1.62 and ~2.44Å, respectively. In the direction of the BO bonds, the oxide ions exhibit a radius of ~1.00Å, in the direction

EBSCOhost - printed on 2/13/2023 4:48 AM via . All use subject to https://www.ebsco.com/terms-of-use

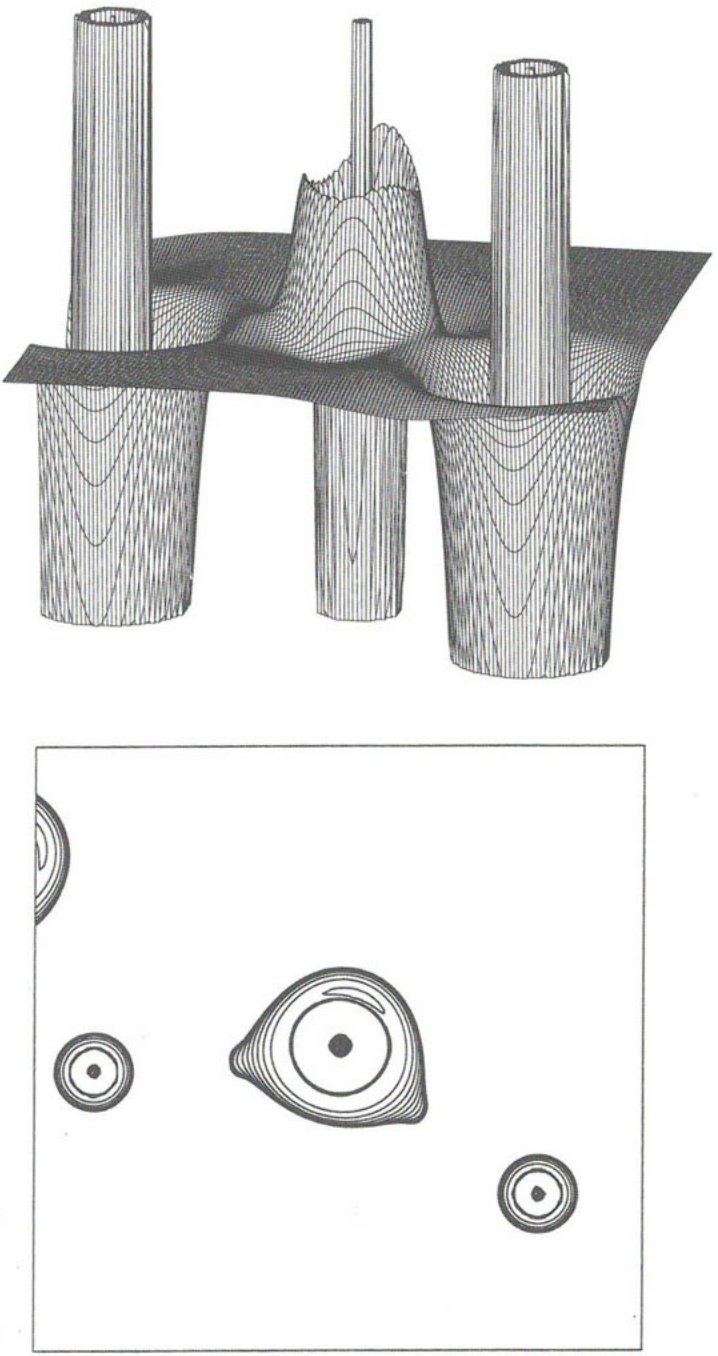


Figure 7. (a) A relief map of $-\nabla^2\rho(\mathbf{r})$ and (b) a map of the positive level line contours of $-\nabla^2\rho(\mathbf{r})$ passing through the SiOSi plane of a $H_6Si_2O_7$ molecule (Hill, 1995). The molecules for which the calculations were completed are described in the legend of Figure 2.

EBSCOhost - printed on 2/13/2023 4:48 AM via . All use subject to https://www.ebsco.com/terms-of-use

of the SiO bonds, a radius of ~0.94Å while in the direction of the CaO bonds, a radius of ~1.23Å. Of the two remaining nonequivalent oxide ions, one is bonded to two equivalent ^{IV}B cations and a ^{VII}Ca cation and has a radius of ~1.18Å in the direction of the CaO bond and a radius of ~0.97Å in the direction of the two BO bonds. The remaining oxide ion is bonded to two equivalent ^{IV}Si atoms and exhibits a single radius of ~0.94Å. As will be shown below, such radii can be related to the fractional ionic character of a bond, such that the larger the radius of the oxide ion, the more ionic the bond. The cations in danburite also show variable radii but the variability is much smaller than that of the oxide ion.

Bonded radii measured for the atoms in coesite, stishovite, bromellite and danburite agree to within 0.02Å, on average, with the procrystal and promolecule radii calculated for these minerals (Gibbs et al., 1992; Feth et al., 1993; Nicoll et al., 1994). The procrystal radii were obtained from electron density distributions calculated with a procrystal model for each crystal whereas the promolecule radii were calculated for a promolecule model of the nonequivalent coordinated polyhedra in each of the crystals with the bond lengths and angles fixed at observed values. The observation that the procrystal and the promolecule radii obtained in these calculations agree with the bonded radii to within ~0.002Å indicates that the position of the bond critical point along the bond path is determined almost entirely by the electron density distributions of the atoms that define the bond (Nicoll et al., 1994). Also, the observation that the bonded radii for the oxide ions are only ~0.02Å larger than both procrystal and promolecule radii indicates that the reorganization of the electron density that occurs upon bond formation has a small effect on the position of the critical point that defines the minimum in the electron density. In fact, promolecule radii calculated for XO bonds for X cations of the first four rows of the periodic table correlate with Shannon's (1976) crystal radii for the oxides (Feth et al., 1993). As observed for bonded radii, the promolecule radii calculated for the oxide ion vary regularly from ~0.60Å, when bonded to a highly electronegative cation like ^{III}N^{+5}, to ~1.35Å, when bonded to a highly electropositive cation like ^{XII}K^{+}. This result suggests that the promolecule radius of the oxide ion changes regularly with the electronegativity of the X cation, as observed by Feth et al. (1993). A similar correlation has been described between the bonded radius of the H atom, r_b(H), and the electronegativity of the atoms bonded to H in the series of XH$_n$ molecules where X = Li, Be, $\cdots$, F (Cremer, 1987). Also, as shown by Gibbs et al. (1992), r_b(H) increases in a regular way with increasing XH bond length.

Using the bonded radii for the oxide ions obtained from experimental electron density maps recorded for coesite, stishovite, danburite and bromellite, a derivation was undertaken for this review of the expression

$$f_i(XO) = 1 - \exp\{-1/4(-0.85 + 2.64r_b(O))^2\} \quad (4)$$

which relates the fractional amount of ionic character, $f_i(XO)$, of an XO bond to the bonded radius of the oxide ion, r_b(O), comprising the bond. This expression indicates that the fractional ionic character of the SiO bonds, f_i(SiO), recorded for coesite decreases from 0.48 to 0.46 as the SiO bond length decreases from 1.62 to 1.60Å compared with 0.51 given by the electronegativity difference between Si and O (Pauling, 1960). These values are ~25% less than the average fractional ionic character, 0.63, calculated for the bonds in stishovite. The larger f_i(SiO) value calculated for stishovite conforms with the assertion by Noda et al. (1991) that the SiO bond in the mineral is ~20% more ionic than it is in quartz. It also agrees with the observation made by Hill et al. (1983) that Mulliken charges on Si increase with coordination number from a value of ~+0.5 for one coordinate Si in SiO to ~+1.5 for six coordinate Si in $(2/3H)_{12}SiO_6$, if such charges can be considered as meaningful. The

EBSCOhost - printed on 2/13/2023 4:48 AM via . All use subject to https://www.ebsco.com/terms-of-use

SiO bond length in this sequence also increases with coordination number, suggesting that the ionic character of the bond increases in a regular way with increasing bond length. However, these results are at odds with Mulliken population analyses calculated for the disiloxane molecule that were used by Oberhammer and Boggs (1980) and later by Nicholas et al. (1992a) as evidence that the covalent character of the SiO bond increases dramatically as the bond lengthens (Nicholas et al., 1992a). According to these results, the longer SiO bond in stishovite should be considered to be more covalent than the shorter bond in quartz. It is also at odds with a band energy calculation completed for stishovite (Xu and Ching, 1991) which was also interpreted as indicating that the longer SiO bond in stishovite is more covalent than it is in silicates with four coordinate Si.

Total electron density maps recorded for coesite, danburite and stishovite indicate that the bonded radii for both Si and O in these materials decrease in a regular way with a shortening of the SiO bond (Fig. 8; see also Gibbs et al., 1992 and Nicoll et al., 1994). Unlike the crystal radius of the oxide anion which decreases by only ~0.02Å with a decrease in coordination number from 6 to 4 (Shannon and Prewitt, 1969), the bonded radius of the anion decreases by ~0.2Å from 1.1 to 0.9Å. On the other hand, the bonded radius of the Si cation decreases by only ~0.02Å while the crystal radius of the cation is indicated to decrease by 0.14Å. In other words, the crystal radius of the oxide anion is indicated to change a small amount with the bond length change that accompanies a change in the coordination number of the Si cation unlike the bonded radius of the anion which changes much more with bond length and coordination number change.

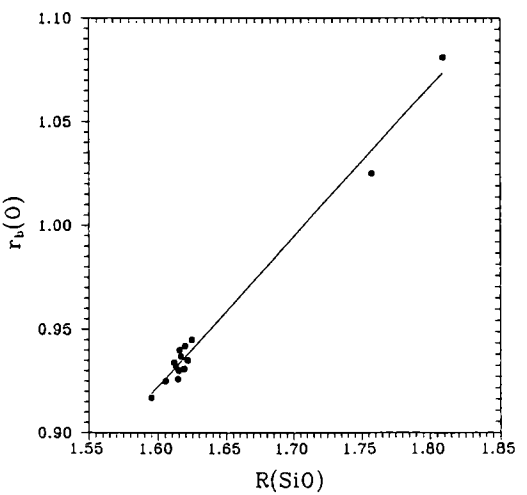


Figure 8. The SiO bond lengths, R(SiO), observed for danburite, coesite and stishovite plotted against the bonded radius of the oxide ion, $r_b(O)$, obtained from experimental electron density maps.

The relatively large decrease in the bonded radius of the oxide anion with decreasing bond length suggests that the size of the oxide anion in the direction of a bond decreases at a faster rate with increasing pressure and is more compressible along the bond than the Si cation. An APW calculation of the equation of state of the fluorite structure type of silica by Bukowinski and Wolfe (1986) indicates that the radius of the oxide ion, measured at the critical point along the SiO bond, decreases nearly three times faster with increasing pressure than does the radius of the Si cation. Also, the bonded radius of the Si cation at room pressure was also measured to be 0.74Å, ~0.30Å larger than that expected (0.46Å) for the crystal radius of the

EBSCOhost - printed on 2/13/2023 4:48 AM via . All use subject to https://www.ebsco.com/terms-of-use

cation from radius vs. coordination number considerations (Shannon and Prewitt, 1969). A smaller bonded radius of ~0.70Å was measured for the six–coordinate Si cation in stisovite (Spackman et al., 1987). An extrapolation of the regression line drawn in Figure 8 to the minimum energy SiO bond length (1.963Å) calculated for the fluorite structure type yields bonded radii for the oxide anion and the Si cation of 1.18Å and 0.78Å, respectively. The extrapolated value for the bonded radius for oxide ion is only 0.04Å smaller than the bonded radius of the ion (1.22Å) given by the minimum in the electron density distribution measured along the SiO bond. The greater compressibility of the oxide ion observed by Bukowinski and Wolfe (1969) conforms with a high pressure study of forsterite (Mg_2SiO_4) that shows that its O···O separations decrease about four times faster than its Si···Mg and Mg···Mg separations with increasing pressure (O'Keeffe and Hyde, 1981). Thus, on the basis of this evidence and the calculations completed for the fluorite structure type, it is apparent that the oxide anion is appreciably more compressible along a bond than the Si cation. Promolecule calculations completed on a variety of coordination polyhedra indicate that the radius of oxide anion shows a much larger variation with bond length than the radius of a bonded cation, a result that suggests that the oxide anion should, in general, be more compressible along a bond than the cation (Feth et al., 1993). The f_i(SiO) value calculated for the SiO bond in the fluorite silica structure type is estimated to be ~0.75. However, the ionicity of the bond is indicated to decrease with increasing pressure as the bonded radius of the oxide ion decreases. In fact, Equation 4 suggests that the covalency of an XO bond should increase in a regular way with increasing pressure and that the ionicity of the bond should increase in a regular with increasing temperature. When other bonds like the CaO, BO and BeO bonds are considered, Equation 4 generates an f_i(CaO) value for the CaO bond in danburite of ~0.75, an f_i(BeO) value for the BeO bond in bromellite of ~0.63 and an f_i(BO) for the BO bond in danburite of ~0.55, compared with the respective values of 0.79, 0.63 and 0.43 estimated by Pauling (1960) from electronegativity considerations. With the exception of the estimate of the fractional ionic character of the BO bond, which departs by ~20% from the Pauling value, the agreement is reasonably good.

Numerous sets of ionic and crystal radii have been derived over the years for the main group cations, X^{+n}, assuming that the radius of the oxide ion is essentially constant (cf. Bragg, 1920; Goldschmidt et al., 1926; Pauling; 1927; Ahrens, 1952; Slater, 1964; Shannon and Prewitt, 1969; Whittaker and Muntus, 1970; Shannon, 1976). Given that the R(XO) bond lengths in oxides can be generated with the expression $R(XO) = 1.39p^{-2/9}$ for all main group cations to within 0.05Å, on average (Gibbs et al., 1987b), it is clear that any radius can be assumed for the oxide ion ranging between 0.60Å (the atomic radius of the O atom) and 1.40Å (the ionic radius of the oxide ion) and a set of cation radii can be derived. This is accomplished by simply subtracting the assumed radius of the oxide ion from the value of R(XO), calculated with the above expression, for a given cation with bond strength $p = s/r$ where s is the Pauling bond strength of the bond and r is the row number of the X–cation. Regardless of the assumed radius, the resulting set of cation radii, when added to the assumed radius of the oxide ion will reproduce XO bond lengths to within ~0.05Å, on average. If, for example, too large a radius is assumed, then one can expect negative radii to result for some of the cations (Shannon and Prewitt, 1969). Of course, the successful generation of bond lengths for a large variety of oxide crystals with a set of radii says little about the 'true' size of the oxide ion or the nature of the XO bond. Thus, the assertion that the radius assumed in one derivation would be a better measure of the true size of the oxide ion than that assumed in another is unfounded. Also the conclusion that the bonds in a material are ionic just because its bond lengths can be generated with a set of radii that were derived with an oxide ion

EBSCOhost - printed on 2/13/2023 4:48 AM via . All use subject to https://www.ebsco.com/terms-of-use

radius of 1.40Å is unfounded as well. These arguments also apply to sets of ionic and crystal radii derived for sulfides, nitrides and fluorides crystals (Bartelmehs, 1989; Buterakos, 1992; Nicoll et al., 1994).

A DISCUSSION

The SiO bond embodies a highly complex interaction between Si and O that has not only eluded our understanding, but it has also eluded a simple definition, if indeed such a definition even exists. In recent attempts to improve our understanding of its structural properties and its character, experimental and theoretical bond lengths and angles and electron density distributions have been recorded for a number of chemically related molecules and crystals containing SiO bonds. A careful scrutiny of these results has generated a variety of conclusions about the character of the bond ranging from a bond that is predominately ionic to one that is predominately covalent. For example, Tsirelson et al. (1990) have concluded that the SiO bond is predominately covalent with some double bond character on the basis of the heights, shapes and the positions of the peaks in assorted deformation electron density maps recorded for a variety of silicate crystals. In addition, a multipole electron density distribution obtained from a set of precise X–ray diffraction data recorded for quartz has yielded net residual charges of +1.0 on Si and −0.5 on O. Defining the ionic character of the bond to be $i = 100\times$ residual charge/formal charge, Stewart et al. (1980) concluded that the SiO bond is ~75% covalent in character. In addressing the question, 'Is silicon dioxide covalent or ionic?', Harrison (1978) interpreted evidence provided by an LCAO study of the electronic structure of SiO_2 as indicating that 'There would seem little question but what we should regard SiO_2 as a covalent solid.' He went on to say that this result conforms with the relatively open structure of quartz with two–coordinate oxide atoms and four–coordinated Si atoms in contrast with more dense, close–packed structures of ionic materials. On the other hand, the conclusion that the SiO bond is predominantly ionic in character was reached by Kudo and Nagase (1985) in a study of the deformation electron density distribution of the SiO bonds in $H_4Si_2O_2$, where they found that the peaks in the bonds are closer to the more electronegative oxide ion than to Si. In a more recent analysis of the total electron density distribution of the molecule, Gordon et al. (1991) concluded that its SiO bonds exhibit ionic closed shell interactions because electron density is concentrated more in the regions of the bonded atoms than between them along their bond paths. In MO calculations completed for disiloxane, Oberhammer and Boggs (1980) and more recently Nicholas et al. (1992a) have concluded, on the basis of charges obtained in a Mulliken population analysis for Si and O, that the ionic character of the bond is much greater than 50% and that the ionicity of the bond increases by as much as 25% as the SiOSi angle widens and the SiO bond shortens. It is evident from these results that there is an assortment of distinct viewpoints on the amount of ionic character that should be assigned to the SiO bond.

Several of the above conclusions have since been reevaluated with several important observations being made. In particular, Stewart and Spackman (1981) reconsidered the connection between the covalency of the SiO bond and the residual charges on Si and O and discovered that the strategy used to determine the charges is 'hopelessly dependent' on the form of the function over which the electron density was integrated. With this discovery, they concluded that the net residual charges obtained earlier have little or no experimental basis. As these charges were used to estimate covalency, the earlier conclusion that the bond is highly covalent can be considered to have little or no chemical significance. In a similar vein, as the absolute numerical values of the Mulliken charges generated in a population analysis are con-

EBSCOhost - printed on 2/13/2023 4:48 AM via . All use subject to https://www.ebsco.com/terms-of-use

sidered by Tossell and Vaughan (1992) and others to be essentially without meaning, conclusions about the highly ionic character of the bond and how the bond character changes with bond length and angle and coordination number should be softened and viewed with circumspection.

In addition, the assumption that the character of a bond is reflected in the sizes and positions of the peaks of a deformation electron density map has been critically examined by Spackman and Maslen (1985). As stated by Feynman (1939), the strongest and the most important attractive forces arise when there is an accumulation of electron density in the total electron density distribution in the region between a pair of bonded atoms like Si and O (see also Berlin, 1951). With this observation, not only has it been assumed that similar accumulations of electron density should occur in deformation electron density distributions, but it has also been assumed that the extent of such an accumulation should be directly related to the character of a bond such that the greater the accumulation, the more covalent the bond. In fact, in a study of such distributions, Spackman and Maslen (1985) observed that a peak of electron density in a bond is neither a necessary nor a sufficient condition for binding, although such features are often observed. More importantly, they were unable to establish a connection between the magnitude of the peak and the covalency of the bond (see also Catlow and Stoneham, 1983). This result agrees with the discovery of covalent and partly covalent NN, OO and CO bonds 'without bonding electron density'. Surely, in spite of an absence of appreciable electron density between the atoms of these bonds, few would interpret them as being ionic bonds. Thus, conclusions about the covalency or the double bond character of a bond based on features in deformation electron density maps should be made with the reservations outlined by Spackman and Maslen (1985) in mind (also see Hirshfeld, 1985 and Tossell and Vaughan, 1992).

Because of the difficulty in making meaningful inferences about the nature of a bond from its deformation electron density distribution, Bader (1990) and his students have studied such topological mappings as the gradient and the Laplacian of the electron density distribution. With the value of $\rho(\mathbf{r_c})$ evaluated at a bond critical point along with the eigenvalues provided by the Hessian of the electron density distribution evaluated at that point, they found that they could make meaningful inferences about atomic interactions and bond type. To gain insight into interactions that obtain between Si and O and the kind of bond that obtains, the topological properties of the total electron density distributions for several silicates and molecules were studied using the strategies devised by Bader (1990). As observed above, such studies indicate a closed shell interaction between Si and O and a bond that is intermediate in character between ionic and covalent. In addition, theoretical calculations completed for the disilicic acid molecule indicate that the concentration of the electron density in the valence shell of the oxide ion is locally depleted upon bond formation where the shell crosses the bond and that it is locally concentrated in the direction of the Si cation. This results in the electron density distribution of the oxide ion being highly polarized in its concentration in the direction of the Si cation. The calculations also indicate that the value of the electron density in the bond increases as the bond decreases in length. They also indicate that the polarity of the bond increases as the bond length shortens, a result that can be ascribed to either an increase in the ionic character of the bond or to an increase in the participation of the $d-$type AOs on Si. A calculation of the ellipticity of the bond indicates that the bond becomes more anisotropic in cross section as the SiOSi angle narrows and the SiO bond length increases. Given that the electron density in the bond increases as the angle widens, it can be concluded that the ionic character of the bond decreases as the bond shortens. With this result, it can be concluded that the progressive increase in the polarity of

EBSCOhost - printed on 2/13/2023 4:48 AM via . All use subject to https://www.ebsco.com/terms-of-use

the bond that accompanies a bond length decrease can be ascribed, at least in part, to a progressive increase in π-bonding as the SiO bond shortens and the SiOSi angle widens.

As we have seen, it is difficult if not impossible to assess the extent to which the $d-$type AOs on Si are involved in $\pi-$bond formation with the $p-$AOs on the oxide ion. As observed above, it is well established that bond lengths and angles, dipole moments and electron density distributions are reproduced better in theoretical calculations when the $d-$type AOs of Si are included in the basis set. But the same is true for analogous carbon compounds. It is not clear whether the $3d-$AOs serve as polarization functions in these calculations in compensating for a deficient $sp-$basis set, whether they mimic ionic effects or whether they are actually used in $\pi-$bonding. However, the Si K and $L_{2,3}$ and the O K X-ray emission spectra measured for quartz conform with a picture of charge transfer from the oxide ion that can involve the $d-$type AOs on Si. In order to explain the energy and the intensity distribution of the Si $L_{2,3}$ X-ray emission spectra, Tossell (1987) states that one 'must' include $d-$type AOs in the wave functions for a silicate coordination polyhedron. He continues by observing that even though their contributions to the wave function may not be large, the contracted components of the $d-$AOs can contribute strongly to the spectral intensity and the minimum energy geometry of a coordination polyhedron (see also Tossell and Vaughan, 1992). Also, as observed in a number of studies, it is clear that $d-$type polarization functions are required to generate the SiO bond lengths and angles observed for silicate crystals and organsilioxane molecules. As observed above, a calculation of the Laplacian of the electron density distribution for the bonds in coesite yield results that conform with a $\pi-$bonding model, but whether the bonds are $[2p(\mathrm{O})\text{–}3p(\mathrm{Si})]\pi$ or $[2p(\mathrm{O})\text{–}3d(\mathrm{Si})]\pi$ bonds or both is debatable. But, given the evidence that the $d-$AOs are required to explain the Si $L_{2,3}$ X-ray emission spectra, it is likely that both $\pi-$systems obtain as suggested by calculations completed by Tossell (1975) and Newton and Gibbs (1980).

To summarize, notwithstanding the many studies that have been completed, the SiO bond remains an elusive and poorly understood entity defying a simple description. For example, the binding forces that govern the geometry of a locally charge balanced silicate coordination polyhedron in a crystal behave as if short ranged in nature and largely independent of the force fields of the ions that comprise the periodic structure of a silicate crystal. Yet the theoretical and experimental evidence indicates that the SiO bonds in these crystals are of intermediate type with about equal amounts of covalent and ionic character. If such is the case, then the effective charges of ions in a silicate structure are either small, in conformity with the electroneutrality principle, or the Si cation has such a strong binding interaction with its coordinating oxide ions that the average bond length of the coordination polyhedron is largely unaffected by the force fields of the neighboring cations and anions. In addition to being a bond of intermediate type as originally proposed by Pauling (1939), the evidence indicates the covalent character of the bond increases as its length decreases. Also, as originally proposed by Pauling (1952), the $d-$AOs on Si seem to play an important role in the wavefunctions of the silicate coordination polyhedron in governing the geometry, electron density distribution and spectral properties of a silicate crystal, thereby reducing the electrostatic interactions that impact a silicate coordination polyhedron. In addition, the anisotropy of the bond in an Si_2O_7 dimer indicates that the $d-$AOs play a role in a $\pi-$system also as proposed by Pauling (1952). These AOs are also required to describe correctly the energy and the intensity of the X-ray emission spectra and the correct ordering of the energies of quartz and stishovite. But as we have seen, the extent to which the $d-$AOs play a role in the wavefunctions of a silicate anion is as elusive today as is the nature of the SiO bond

EBSCOhost - printed on 2/13/2023 4:48 AM via . All use subject to https://www.ebsco.com/terms-of-use

itself. Nonetheless, no model has provoked more discussion and research and provided more insight into the nature of the bond than the one set forth in 1939 by Linus Pauling in his classic book, *The Nature of The Chemical Bond.*

ACKNOWLEDGMENTS

The National Science Foundation is thanked for supporting this study with grant EAR-9303589. An early version of this review paper was written when one of us (GVG) was a JSPS Fellow at Kyoto University, Kyoto, Japan during the Fall of 1993. GVG wishes to thank Professor Osamu Tamada and the faculty of Kyoto University for making his visit a very pleasant and rewarding experience. We wish to thank Professor Linus Pauling who suggested, upon reading the paper by Gibbs, Boisen and Spackman (1992), that the connection between bonded radius and electronegativity be examined. Professor Leland C. Allen of the Chemistry Department at Princeton University, Dr. Michael Hochella and Frances Hill of Virginia Tech are also thanked for reviewing the manuscript and for making a number of helpful suggestions that improved the text. The manuscript has also benefited a great deal from the exciting discussions that we have had over the years with our very good friend and colleague Professor Mark Bukowinski at UC, Berkeley. Fran Hill is also thanked for kindly making available her PhD thesis results on the electron density distribution properties for $(HO)_3SiOSi(OH)_3$.

REFERENCES

Ahrens LH (1952) The use of ionization potentials. Geoch Cosmo Acta 16:155–169

Almennigen A, Bastiansen O, Ewing V, Hedberg K, Traetteberg M (1963) The molecular structure of disiloxane, $(SiH_3)_2O$. Acta Chem Scand 17:2455–2460

Allan, DC, Teter MP (1990) Local density approximation total energy calculations for silica and titania structure and defects. J Am Chem Soc 73:3247-3250

Apeloig Y (1989) Theoretical aspects of organosilicon compounds. In The Chemistry of organic silicon compounds, Edited by S. Paul and Z. Rappoport, Chapter 2. 57–224 John Wiley & Sons Ltd, New York

Bader RFW, Essén H (1984) The characterizations of atomic interactions. J Chem Phys 80:1943–1960

Bader RFW, MacDougall PJ, Lau CDH (1984) Bonded and nonbonded charge concentrations and their relation to molecular geometry and reactivity. J Am Chem Soc 106:1594–1605

Bader RFW (1990) Atoms in molecules. Oxford Science Publications Oxford, UK

Bartelmehs KL, Gibbs GV, Boisen MB (1989) Bond-length and bonded-radii variations in sulfide molecules and crystals containing main-group cations: A comparison with oxides. Am Min 74:620-626

Baur WH (1970) Bond length variation and distorted coordination polyhedra in inorganic crystals. Trans Am Crystal Assoc 6:129–154

Baur WH (1971) The prediction of bond length variations in silicon–oxygen bonds. Am Min 56:1573–1599

Baur WH (1977) Variation of mean SiO bond lengths in silicon–oxygen octahedra. J Sol State Chem 22:445–446

Belokoneva EL, Smirnitskaya YY, Tsirelson VG (1993) Electron density distribution in topaz $Al_2[SiO_4](F,OH)_2$ as determined from high–precision X–ray diffraction data. Russ J Inorg Chem 38:1251–1263

Belokoneva EL, Tsirelson VG (1993) Electron density distribution and chemical bonding peculiarities in tourmaline-elbaite from the precise X–ray diffraction data. Russ J Inorg Chem 38:1351–1358

Berlin T (1951) Binding regions in diatomic molecules. J Chem Phys 19:208–213

Binggeli N, Troullier N, Luís Martins J, Chelikowsky JR (1991) Electronic properties of α–quartz

EBSCOhost - printed on 2/13/2023 4:48 AM via . All use subject to https://www.ebsco.com/terms-of-use

under pressure. Am Phys Soc 44:4771–4777
Boisen MB, Gibbs GV, Downs RT, D'Arco P (1990) The dependence of the SiO bond length on structural parameters in coesite, the silica polymorphs and the clathrasils. Am Min 75:748–754
Boisen, M.B., Jr., Gibbs, G.V. and Bukowinski, M.S.T (1994) Framework silica structures generated using simulated annealing with a potential energy function based on a $H_6Si_2O_7$ molecule. Phys Chem Min xx:xx–xx
Born M, Landé A (1918) Über die absolute berechnung der kristalleigenschaften mit hilfe bohrsscher atommodelle. Sitzungsberichte der Preussischen Akademie der Wissenschaften Berlin 45:1048–1068
Bragg WL (1920) The arrangement of atoms in crystals. Phil Mag 40169-189
Bragg WH (1921) The intensity of X–ray reflection by diamond. Proc Phys Soc London 33:304–311
Brown GE, Gibbs GV, Ribbe PH (1969) The nature and variation in length of the SiO and AlO bonds in framework silicates. Am Min 54:1044–1061
Brown GE, Gibbs GV (1970) Stereochemistry and ordering in the tetrahedral portion of silicates. Am Min 55:1587–1607
Brown, I.D. and Shannon, R.D. (1973) Empirical bond–strength bond–length curves for oxides. Acta Cryst A29:266-282
Bukowinski MST, Wolfe GH (1986) Equation of state and stability of fluorite–structured SiO_2. J Geophys Res 91:4704–4710
Bukowinski MST (1994) Quantum geophysics. Annu Rev Earth Planet Sci 22:167–205
Burdett JK, McLarnan SL (1984) An orbital interpretation of Pauling's rules. Am Min 69:601–621
Burdett JK, Caneva, CC (1985) Energetic description of solids in terms of small fragments. Inorg Chem 24:3866–3873
Burdett JK, Hawthorne FC (1993) An orbital approach to the theory of bond valence. Am Min 78:884–892
Burkhard DJM, DeJong BHWS, Meyer AJHM Van Lenthe (1991) $H_6Si_2O_7$: Ab initio molecular orbital calculations show two geometric conformations. Geoch Cosmo Acta 55:3453–3458
Burnham, CW (1990) The ionic model: Perceptions and reality in mineralogy. Am Min 75:443–463
Buterakos, L.A., Gibbs, G.V., and Boisen Jr., M.B. (1992) Bond length variation in hydronitride molecules and nitride crystals. Phys Chem Min 19:127-132
Catlow CRA, Stoneham AM (1983) Ionicity in solids. J Phys C: Sol State Phys 16:4321–4338
Chakoumakos BC, Hill RJ, Gibbs GV (1981) A molecular orbital study of rings in silicates and siloxanes. Am Min 66:1237–1249
Cohen RE (1991) Bonding and elasticity of stishovite SiO_2 at high pressure: Linearized augmented plane wave calculations. Am Min 76:733–742
Collins GAD, Cruickshank DWJ, Breeze A (1972) *Ab initio* calculations on the silicate ion, orthosilicic acid and the $L_{2,3}$ X–ray spectra. J Chem Soc Fara Trans 686:1189–1195
Craven BM, Stewart RF (1993) Electrostatic properties of crystals from accurate diffraction data. Trans Am Crystal Assoc 26:41–54
Cremer D, Krakar E (1984) Chemical bonds without bonding electron density–Does the difference electron–density analysis suffice for a description of the chemical bond? Angew Chem Int Engl 23:627–628
Cremer D (1987) New ways of analyzing chemical bonding. In Modelling of structure and properties of molecules, Editor: ZB Macsić 128–144
Cruickshank DWJ (1961) The role of 3d–orbitals in π–bonds between (a) silicon, phosporus, sulphur, or chlorine and (b) oxygen or nitrogen. J Chem Soc 1961:5486–5504
Downs JW, Gibbs GV (1987) An exploratory examination of the electron density and electrostatic potential for phenakite. Am Min 72:769–777
Downs JW (1990) Electrostatic properties of minerals from X–ray diffraction data: A guide for accurate atomistic models. In J Ganguly, Ed, Diffusion, Atomic Ordering, and Mass Transport, Advances in Physical Geochemistry, Vol 8 Springer–Verlag Berlin
Downs JW, Swope RJ (1992) The Laplacian of the electron density and the electrostatic potential of danburite, $CaB_2Si_2O_8$. J Phys Chem 96:4834–4840
Downs JW (1994) The charge density of coesite. Trans Am Geophy Union Abstract 187
Downs RT (1992) Librational displacements of silicate tetrahedra in response to temperature and pressure. PhD dissertation, 75 pp. Virginia Polytechnic Institute and State University, Blacksburg, Va

EBSCOhost - printed on 2/13/2023 4:48 AM via . All use subject to https://www.ebsco.com/terms-of-use

Dunitz JD, Sieler P (1983) The absence of bonding electron density in certain covalent bonds as revealed by X–ray analysis. J Am Chem Soc 105:7056–7058

Dyatkina ME, Klimenko NM (1973) Hypothese of the participation of outer vacant atomic orbitals in the formation of molecules in the light of modern quantum–chemical calculations. Zhur Struk Khim 14:173-207

Ernst CA, Allred AL, Ratner MA, Newton MD, Gibbs GV, Moskowitz JW, Topiol S (1981) Bond angles in disiloxane: A pseudo–potential electronic structure study. Chem Phys Lett 81:424–429

Feth S, Gibbs GV, Boisen MB, Myers RH (1993) Promolecule radii for nitrides, oxides and sulfides. A comparison with effective ionic and crystal radii. J Phys Chem 97:11445–11450

Feynman, RP (1939) Forces in Molecules. Phys Rev 56:340–343

Finger LW, Hazen RM (1991) Crystal chemistry of six–coordinated silicon: a key to understanding the earth's deep interior. Acta Cryst B47:561–580

Fyfe WS (1954) The problem of bond type. Am Min 39:991–1004

Geisinger, K.L., Gibbs, G.V. and Navrotsky, A. (1985) A molecular orbital study of bond length and angle variations in framework structures. Phys Chem Min 11:266-283

Geisinger KL, Spackman MA, Gibbs GV (1987) Exploration of structure, electron density distribution and bonding in coesite with Fourier and Pseudoatom refinement methods using single crystal X–ray diffraction data. J Phys Chem 91:3237–3244

Gibbs GV, Meagher EP, Newton MD, Swanson DK (1981) A comparison of experimental and theoretical bond length and angle variations for minerals, inorganic solids, and molecules. In O'Keeffe M, Navrotsky A, Eds., Structure and Bonding in Crystals, Vol. 1 195–225 Academic Press, New York

Gibbs GV (1982) Molecules as models for bonding in silicates. Am Min 67:421–450

Gibbs GV, Boisen MB (1986) Molecular mimicry of structure and electron density distributions in minerals. Mat Res Soc Symp Proc 73:515–527

Gibbs GV, D'Arco P, Boisen MB (1987a) Molecular mimicry of the bond length and angle variations in germanate and thiogermanate crystals: a comparison with variations calculated for carbon–, silicon–, and Sn–containing oxide and sulfide molecules. J Phys Chem 91:5347–5354

Gibbs, G.V., Finger, L.W. and Boisen, M.B. (1987b) Molecular mimicry of the bond length–bond strength variations in oxide crystals. Phys Chem Min 14:327–331

Gibbs GV, Spackman MA, Boisen MB (1992) Bonded and promolecule radii for molecules and crystals. Am Min 77:741–750

Gillespie, RJ (1963) The valence–shell electron–pair repulsion (VSEPR) theory of directed valency. J Chem Edu 40:295–301

Goldschmidt VM, Barth T, Lunde G, Zachariasen, WH (1926) Geochemical distribution law of the elements. Skrif Norske-Videnskaps, Akademi, Oslo 2:1–117

Gordon MS, Packwood TJ, Carroll MT (1991) Structure, bonding, and relative stabilities of four–membered disiletane rings. J Phys Chem 95:4332–4337

Grigoras S, Lane TH (1987) Ab initio calculations on the effects of polarization functions on disiloxane. J Comp Chem 8:84–89

Griscom DL (1977) The electronic structure of SiO_2: A review of recent spectroscopic and theoretical advances. J Non–Cryst Sol 24:155–234

Harrison WA (1978) Is silicon dioxide covalent or ionic? In ST Pantelides, Ed., The physics of SiO_2 and its interfaces 105–110 Pergamon Press, New York

Hehre WJ, Radom L, Schleyer PR, Pople JA (1986) Ab initio molecular orbital theory. John Wiley and Sons New York

Hess AC, McMillan PF, O'Keeffe M (1986) Force fields for SiF_4 and H_4SiO_4: Ab initio molecular orbital calculations. J Phys Chem 90:5661–5665

Hess AC, McMillan PF, O'Keeffe M (1988) Torsional barriers and force fields in H_4TO_4 molecules and molecular ions (T = C, B, Al, Si). J Phys Chem 92:1785–1791

Hill FC, Gibbs GV, Boisen, MB (1995) Bond stretching force constants and compressibilities of nitride, oxide and sulfide coordination polyhedra in molecules and crystals. Struct Chem xx:xx

Hill FC (1995) In preparation. PhD dissertation, xx pp Virginia Polytechnic Institute and State University, Blacksburg, Va.

Hill RJ, Newton MD, Gibbs GV (1983) A crystal chemical study of stishovite. J Sol State Chem 47:185–200

Hill RJ, Gibbs GV (1979) Variations in d(T–O), d(T$\cdots$T) and ⟨TOT in silica and silicate minerals,

EBSCOhost - printed on 2/13/2023 4:48 AM via . All use subject to https://www.ebsco.com/terms-of-use

phosphates and aluminates. Acta Cryst B35:25-30
Hirshfeld, FL (1985) Accurate electron densities in molecules. J Mole Struct 130:125-141
Hubner K (1979) Chemical bond and related properties of SiO_2. Phys Stat Sol 52:541–547
Hylleras EA (1930) Wave–mechanical calculations of the lattice energy and lattice constant of lithium hydride. Zeits Physik 63:771–794
Jackson MD, Gibbs GV (1988) A modeling of the coesite and feldspar framework structure types of silica as a function of pressure using modified electron gas methods. J Phys Chem 92:540–545
Jaffe, HH (1954) Studies in molecular orbital theory of valence. III. Multiple bonds involving d–orbitals. J Am Chem Soc 58:185–190
Johnson O (1973) Ionic radii for spherical potential ions. I. Inorg Chem 12780-785
Karle IL, Karle JM, Nielson CJ (1986) On the SiOSi angle in 1,2–di–tert–butyl–1,1,2,2–tetraphenyl–disiloxane. Acta Cryst C42:64–67
Keskar NR, Chelikowsky JR (1991) Structural properties of nine silica polymorphs. Phys Rev D 46:1–13
Koput J (1990) Ab initio study of the molecular structure and potential energy surface of disiloxane. Chem Phys 148:299–308
Kubicki JD, Sykes D (1993) Molecular orbital calculations on $H_6Si_2O_7$ with variable SiOSi angle: Implications for the high pressure vibrational spectra of silicate glasses. Am Min 78:253–259
Kudo T, Nagase S (1985) Theoretical Study of dimerization of silanone and the properties of the polymeric Products $(H_2SiO)_n$ ($n = 2$, 3 and 4): Comparison with dimers $(H_2SiS)_2$ and $(H_2CO)_2$. J Am Chem Soc 107:2589–2595
Kutzelnigg W (1984) Chemical bonding in higher main group elements. Angew Chem Int Engl 23:272–295
Kwart H, King KG (1977) d–orbitals in the chemistry of silicon, phosphorous and sulfur. Springer–Verlag Berlin
Lasaga, AC and Gibbs, GV (1987) Applications of quantum mechanical potential surfaces to mineral physics calculations. Phys Chem Min 14:107–117
Lasaga, AC and Gibbs, GV (1990) *Ab initio* quantum mechanical calculations of water–rock interactions: Adsorption and hydrolysis reactions. Am J Sci 290:263–295
Lewis GN (1916) The atom and the molecule. J Am Chem Soc 38:762–785
Lewis GN (1923) Valence and the structure of atoms and molecules. The Chemical Catalog Company, Inc. New York
Liebau, F (1961) Untersuchungen über die groöβe des Si–O–Si – valenzwinkels. Acta Cryst 14:1104–1109
Liebau F (1985) Structural Chemistry of Silicates: Structure, Bonding, and Classification. Springer–Verlag Berlin
Liu F, Garofalini SH, King–Smith D, Vanderbilt D (1994) First–principles study of crystalline silica. Phys Rev B 49:12528–12534
Luke BT, Pople JA, Krogh–Jesperson M, Apeloig Y, Chandrasekhar J, Schleyer P (1986) A theoretical survey of singly bonded silicon compounds. Comparison of the structures and bond energies of silyl and methyl derivatives. J Am Chem Soc 108:260–269
Meier R, Hu T (1980) A theoretical study of the electronic structure of disiloxane $[(SiH_3)_2O]$ and its relation to silicates. Phys Chem Min 6:37–46
Michalske TA, Bunker, BC (1984) Slow fracture model based on strained silicate structures. J Appl Phys 56:2686–2693
Mitchell KAR (1969) The use of outer d orbitals in bonding. Chem Rev 69:157–178
Morse PM, Feshbach H (1953) Methods of Theoretical Physics. McGraw–Hill Book Company New York 157–178
Navrotsky, A., Geisinger, K.L., McMillian, P. and Gibbs, G.V. (1985) The tetrahedral framework in glasses and melts - Interferences from molecular orbital calculations and implications for structure, thermodynamics, and physical properties. Phys Chem Min 11:284-298
Newton MD, Gibbs GV (1980) *Ab initio* calculated geometries and charge distributions for H_4SiO_4 and $H_6Si_2O_7$ compared with experimental values for silicates and siloxanes. Phys Chem Min 6:221–246
Newton MD (1981) Theoretical probes of bonding in the disiloxy group. In O'Keeffe M, Navrotsky A, Eds., Structure and Bonding in Crystals, Vol. 1 176–193 Academic Press, New York
Nicholas JB, Winans RE, Harrison RJ, Iton LE, Curtiss LA (1992a) An *Ab initio* investigation of

EBSCOhost - printed on 2/13/2023 4:48 AM via . All use subject to https://www.ebsco.com/terms-of-use

disiloxane using extended basis sets and electron correlation. J Phys Chem 96:7958–7965
Nicholas JB, Winans RE, Harrison RJ, Iton LE, Curtiss LA (1992b) *Ab initio* molecular orbital study of the effects of basis set size on the calculated structure and acidity of hydroxyl groups in framework molecular sieves. J Phys Chem 96:10247–10257
Nicoll JS, Gibbs GV, Boisen MB, Downs RT, Bartelmehs KL (1994) Systematics of bond lengths and radii variations in fluoride and silicate molecules and crystals. Phys Chem Min 20:617–624
Noda R, Catlow CRA, Dovesi R, Pisani C (1990) An *Ab initio* Hartree–Fock study of α–quartz and stishovite. Phys Chem Min 17:353–362
Noll W (1968) Chemistry and technology of silicones. Academic Press, Inc London
Oberhammer H, Boggs JE (1980) Importance of (p–d)π bonding in the siloxane bond. J Am Chem Soc 102:7241–7244
O'Keeffe M (1981) Some aspects of the ionic model of crystals. In O'Keeffe M, Navrotsky A, Eds., Structure and Bonding in Crystals, Vol. 1 299–322 Academic Press, New York
O'Keeffe M, Hyde BG (1981) The role of nonbonded forces in crystals. In O'Keeffe M, Navrotsky A, Eds., Structure and Bonding in Crystals, Vol. 1 226–254 Academic Press, New York
O'Keeffe M, Domengès B, Gibbs GV (1985) *Ab initio* molecular orbital calculation on phosphates: Comparison with silicates. J Phys Chem 89:2304–2309
O'Keeffe M, McMillan PF (1986) The SiOSi force field: *ab initio* MO calculations. J Phys Chem 90:341–342
Pacansky J, Hermann K (1978) *Ab initio* SCF calculations on molecular silicon dioxide. J Chem Phys 69:963–967
Pauling L (1927) The sizes of ions and the structure of ionic crystals. J Am Chem Soc 49:765–790
Pauling L (1929) The principles determining the structure of complex ionic crystals. J Am Chem Soc 51:1010–1026
Pauling L (1939) The nature of the chemical bond. Cornell University Press Ithaca, NY
Pauling L (1952) Interatomic distances and bond character in the oxygen acids and related substances. J Phys Chem 56:361–365
Pauling L (1960) The nature of the chemical bond, 3rd Ed. Cornell University Press Ithaca, NY
Pauling L (1980) The nature of silicon–oxygen bonds. Am Min 65:321–323
Pietsch U, Hubner K (1986) Quantum–chemical approach to the dependence of oxygen charge on bond angle in SiO_2. Crys Res Tech 21:353–360
Sasaki S, Fujino K, Takeuchi Y, Sadanaga R (1980) On the estimation of atomic charge by X–ray method for some oxides and silicates. Acta Cryst A36:904–915
Sauer J, Zurawski B (1979) Molecular and electronic structure of disiloxane. An ab initio MO study. Chem Phys Lett 65:587–591
Sauer J (1983) Molecular structure of orthosilicic acid and importance of (p–d)π bonding. An ab initio molecular study. Chem Phys Lett 97:275–278
Sauer J (1989) Molecular models in *ab initio* studies of solids and surfaces: From ionic crystals and semiconductors to catalysts. Chem Rev 89:199–255
Savariault JM, Lehmann MS (1980) Experimental determination of the deformation electron density in hydrogen pyroxide by combination of X–ray and neutron diffraction measurements. J Am Chem Soc 102:1298–1302
Shannon RD, Prewitt CT (1969) Effective ionic radii in oxides and fluorides. Acta Cryst B25:925–946
Schomaker V, Stevenson DP (1941) Some revisions of the covalent radii and the additivity rule for the lengths of partially ionic single covalent bonds. J Am Chem Soc 63:37–40
Shannon, R.D. and Prewitt, C.T. (1976) Effective ionic radii in oxides and fluorides. Acta Cryst B25:925-946
Shannon RD (1976) Revised effective ionic radii and systematic studies of interatomic distances in halides and chalcogenides. Acta Cryst A32:751–767
Sheldrick WS (1989) Structural chemistry of organic silicon compounds. Chemical organic silicon compounds Editor, Patai, S 227–302 John Wiley and Sons New York
Shi Z, Boyd RJ (1988) The shell structure of atoms and the Laplacian of the charge density. J Chem Phys 88:4375–4377
Sherman J (1932) Crystal energies of ionic compounds and thermochemical applications. Chem Rev 11:93–170
Slater JC (1930) Atomic screening constants. Phys Rev 36:57–64

EBSCOhost - printed on 2/13/2023 4:48 AM via . All use subject to https://www.ebsco.com/terms-of-use

Slater JC (1964) Atomic radii in crystals. J Chem Phys 41:3199–3204
Slater JC (1965) Symmetry and energy bands in crystals. Dover Publications New York, NY
Smith JV, Bailey SW (1963) Second review of AlO and SiO tetrahedral distances. Acta Cryst 16:801–811
Smith, J.V. (1953) Reexamination of the crystal structure of melilite. Am Min 38:643-661
Spackman MA, Maslen EN (1985) Electron density and the chemical bond. Reappraisal of Berlin's theorem. Acta Cryst A41:347–353
Spackman MA, Maslen EN (1987) Chemical properties from the promolecule. J Chem Phys 90:2020–2027
Spackman MA, Stewart RF, LePage Y (1981) Maps of electrostatic properties from X–ray data from α–SiO_{2s} and Al_2O_{3s}. Acta Cryst Sup A Abstract A37:C–138
Spackman, MA, Hill RJ, Gibbs GV (1987) Exploration of structure and bonding in stishovite with Fourier and pseudoatom refinement methods using single crystal and powder x–ray diffraction data. Phys Chem Min 14:139–150
Stewart RF, Whitehead MA, Donnay G (1980) The ionicity of the SiO bond in quartz. Am Min 65:324–326
Stewart RF, Spackman MA (1981) Charge density distributions. In O'Keeffe M, Navrotsky A, Eds., Structure and Bonding in Crystals, Vol. 1 279–298 Academic Press, New York
Stone FGA, Seyferth D (1955) The chemistry of silicon involving probable use of d–type orbitals. J Inorg Nucl Chem 1:112–118
Swanson DK, Prewitt CT (1983) The crystal structure of $KSi^{IV}Si_3^{VI}O_9$. Am Min 68:581–585
Tossell JA (1975) The electronic structures of silicon, aluminum, and magnesium in tetrahedral coordination with oxygen from SCF–X_α calculations. J Am Chem Soc 97:4840–4844
Tossell JA (1984) A qualitative MO model for bridging bond angle variations in minerals. Phys Chem Min 11:81–84
Tossell JA (1987) Quantum mechanical studies of Si–O and Si–F bonds in molecules and minerals. Phys Chem Min 14:320–326
Tossell JA, Vaughan DJ (1992) Theoretical Geochemistry: Applications of quantum mechanics in the earth and mineral sciences. Oxford University Press New York
Trefry MG, Maslen EN, Spackman, MA (1987) Electrostatic, Madelung and cohesive energies for solids. J Phys C: Sol State Phys 20:19–28
Tsirelson VG, Evdokimova OA, Belokoneva EL, Urusov VS (1990) Electron density distribution and bonding in silicates: A review of recent data. Phys Chem Min 17:275–292
Uchino T, Sakka T, Ogata Y, Iwasaki M (1992) Changes in the structure of alkali–metal silicate glasses with the type of network modifier cation: An ab initio molecular orbital study. J Phys Chem 96:2463–2466
Verhoogen J (1958) Physical properties and bond type in Mg–Al oxides and silicates. Am Min 43:552–579
Voronkov MG, Mileshkevich VP, Yuzhelevski (1975) The siloxane bond and its influence on the structure and physical properties of organosilicon compounds. Russ Chem Rev 44:355–372
Whittaker EJW, Muntus R (1970) Ionic radii for use in geochemistry. Geoch Cosmo Acta 34:945–956
Xu Y, Ching, WY (1991) Electronic and optical properties of all polymorphis forms of silicon dioxide. Phys Rev B 44:11048–11058

EBSCOhost - printed on 2/13/2023 4:48 AM via . All use subject to https://www.ebsco.com/terms-of-use

FIRST-PRINCIPLES THEORY OF CRYSTALLINE SiO_2

Ronald E. Cohen

Geophysical Laboratory and Center for High Pressure Research,
Carnegie Institution of Washington
Washington, DC 20015 U.S.A.

ABSTRACT

This chapter reviews first-principles theory, ranging from potential models to self-consistent electronic structure methods, for bonding, structure, equations of state, dynamics, and phase transitions in crystalline SiO_2. Silica is of interest in many fields, including geology, geophysics, crystallography, high pressure research, materials science, solid state physics, and chemistry, and the breadth of work on silica reflects this breadth of interest. Silica is an excellent test material for new methods, and it is becoming a benchmark system for theoretical study.

INTRODUCTION

Silica forms the basis of most rock-forming minerals, and it is also essential to modern technology. This review considers the physical mechanisms that govern the behavior of crystalline SiO_2 at low and high pressures. (A treatment of lattice dynamical simulations of temperature-induced silica transformations may be found in the chapter by Dolino and Vallade.) Since so many different theoretical techniques have been applied to the silica system, this discussion offers an opportunity to describe some of the theoretical methods that have been formulated to study crystalline solids. Most of the methods and results considered in this chapter involve first-principles techniques; the only exceptions include cases in which researchers have adjusted the parameters of their models to obtain better agreement with experiment. A vast literature exists for both amorphous and crystalline SiO_2, and this chapter deals only with crystalline SiO_2. The area of high-pressure amorphization (Tsuneyuki et al., 1989; Chelikowsky et al., 1990; Tse and Klug, 1991; Binggeli and Chelikowski, 1991, 1992; Kingma et al., 1993) is not discussed, nor does this chapter describe defects (Purton et al., 1992) or surface structures. Rather, this discussion focuses on studies of bulk periodic systems. A review of molecular studies is given in the chapter by Gibbs et al. (this volume) and in Gibbs (1982).

Role of theory in mineralogy and solid state physics

The fields of *theoretical* solid state physics and chemistry are well established, and in those fields it is probably unnecessary to point out the current utility and future promise of theoretical techniques; this soon may be the case in mineralogy as well. However, some geoscientists may not be familiar with recent advances in solid state theory, and they may be confused by the differences between first-principles methods and theoretical modeling, that has long been a part of mineralogical studies. In empirical models, one fits experimental data to a model potential, such as a pair potential model that includes interactions between spherical atoms or ions, or a shell model, which includes dipolar distortions of ions. Such empirical models can be very successful in furthering our understanding of the physics of phase transitions and equations of state at the microscopic scale (Price et al., 1989; Catlow and Price, 1990). In a *first-principles* approach, one uses fundamental quantum physics to obtain the energetics and the static and dynamic properties

EBSCOhost - printed on 2/13/2023 4:48 AM via . All use subject to https://www.ebsco.com/terms-of-use

of a system, without fitting *any* experimental data. The advantages of first-principles approaches are many. First-principles approaches have a greater chance of being applicable outside the range of current experiments, since no experimental data are fit. By contrast, use of empirical models outside the range of experimental data necessarily involves extrapolation, which is always risky. For example, if one fits low-pressure data and applies the resulting potential to high pressures, one is extrapolating the interatomic potential to closer distances, which is highly uncertain because the functional form for interatomic interactions is generally unknown. Secondly, first-principles approaches have a better chance of describing correctly the microscopic physics that leads to macroscopic behavior. Fitting parameters to experiments usually leads to correlations or "trade-offs" in parameter values. For example, if one fits pair potentials or shell models to experiment, there is usually a high correlation between the charges on the ions and the values of the short-range repulsive parameters. Finally, since in first-principles methods one does not fit experimental measurements, bad or misinterpreted data cannot skew the model, and the results of first-principles methods can help support or invalidate experimental conclusions.

Electronic structure and bonding

Electronic structure methods. Before discussing the results of various studies of silica, it is necessary to review the methods applied and the underlying theory. This discussion is not intended as a full tutorial on first-principles techniques, but only as an outline of the methods and their capabilities. Nevertheless, it is important to understand the overall differences among the various methods: All theory is not created equal! Clearly one would not compare different experiments, such as non-hydrostatic versus hydrostatic, static versus dynamic, high-resolution versus low-resolution, and simply say, "Experiments show such and such..." Yet how often in the literature does one see the expression, "Compared with theoretical results,..." without regard to the accuracy, precision, or approximations of the method. It is still amazing to consider the accuracy of many of these first-principles methods, which can correctly predict physical properties that often depend on changes in the seventh to ninth significant figure in the total energy.

Two major classes of methods have been applied to silica: density functional theory and Hartree-Fock theory. Density functional theory is exact in principle for ground state properties, but in practice the Local Density Approximation (LDA) is used. Both classes of methods share many features, and they differ only in their treatments of the electron-electron interactions. In a non-magnetic system for a given configuration of nuclei, there is a single lowest energy configuration for the electron density $\rho(r)$. The electrons experience the potential due to the nuclei and to each other. Their interactions with each other can be separated into two parts. The first part is a self-consistent field, or so-called Hartree potential, which arises from the electrostatic field of the average electronic charge density. Up to this point, both LDA and Hartree-Fock (HF) are identical. The differences involve the treatments of the local *correlation*, which is due to the instantaneous interactions that cannot be ascribed to the average electrostatic field, and the quantum mechanical *exchange* interactions, which derive from the Pauli exclusion principle. The correlation is neglected in Hartree-Fock theory, but it is included in an average way in the LDA. The exchange interactions are treated exactly in Hartree-Fock theory (when completely converged), and in an average way in LDA. The Hartree-Fock method cannot be used with metallic systems, for which it gives crazy results due to the neglect of correlation effects. The LDA can be used for metals as well as insulators, and it also works well for ionic and covalent systems.

Both Hartree-Fock and the LDA can be applied self-consistently, which means that an iterative process is used to find the solution. One starts with a guess for the charge density

EBSCOhost - printed on 2/13/2023 4:48 AM via . All use subject to https://www.ebsco.com/terms-of-use

(LDA) or orbital occupations (Hartree-Fock), and one then evaluates the potential and the output charge density (LDA) or the HF matrices and output orbitals (Hartree-Fock). If the output differs from the input, the input and output are mixed together, and this process is iterated until the input and output are identical.

However, all self-consistent calculations are not the same. The quality of a calculation is greatly affected by the basis set that is used. The basis set describes the orbitals, and the final result can depend strongly on the accuracy of this description. There are many different types of basis sets that can be used. The Hartree-Fock program for periodic crystals, called CRYSTAL, uses a gaussian basis set, which typically consists of a small number of gaussians centered at each atomic nucleus. The periodic Hartree-Fock method is described well in a paper on cristobalite (Silvi et al., 1992) as well as in a text by Pisani et al. (1988). A gaussian basis set is very efficient, but it is incomplete. Basis set superposition error is typical in such total energy calculations, and it results from changes in the quality of the description of the states on one atom as the basis functions of a second atom are moved closer. This might cause significant problems in studies of pressure effects or phonons if not tested. Gaussians are often used as basis functions in LDA calculations as well, and a gaussian basis is usually called *linear combination of atomic orbitals*, or LCAO, in such applications. Another commonly used basis for LDA crystal calculations is a *plane wave* basis, which is ideal in several ways and problematic in others. Plane wave bases are advantageous in that they are fast, and matrix elements (such as those needed to calculate forces, the dynamical matrix, or optical properties) are easily evaluated. Convergence is also straightforward because there is one primary parameter to vary to test convergence, related to the number of plane waves; this parameter simply relates the shortest distance that can be described accurately by the basis. The disadvantage of plane waves is that they cannot account for the rapid variations around the core and nucleus of an atom. This drawback was solved by the development of pseudopotentials, which remove the core states from the problem and replace the real, rapidly varying potential with a smoother potential. The resulting pseudo-wave functions by construction agree with the correct wave functions outside some distance r_c from the nucleus, but they differ inside r_c. Until recently, pseudopotentials that allowed for reasonable plane wave basis set sizes did not exist for oxides and many transition metals, but recently ultra-soft pseudopotentials have been developed that do allow application of plane wave methods to oxides and silicates. Thus we have the distinction between all-electron calculations and pseudopotential methods.

At this point it is necessary to discuss another concept, that of full-potential versus non-full-potential methods. Full potential means that the potential (and charge density) is described in a flexible way that allows all variations in the molecule or crystal being studied. On the other hand, "muffin-tin" potentials force the potential to be spherical inside a sphere around each atom (called a muffin-tin) and constant outside the sphere. In other methods, such as LCAO, the potential and/or charge density is sometimes sphericalized as well. The loss of accuracy that is entailed by such shape approximations is most acute for total energy calculations, which are used to calculate phase transitions, phonon frequencies, and equations of state.

The last two basis sets to be discussed are: the Linearized Muffin Tin Orbital (LMTO) (Methfessel et al., 1989) and the Linearized Augmented Plane Wave (LAPW) (Wei and Krakauer, 1985; Singh, 1994) methods. The LMTO method is applied in different degrees of accuracy ranging from muffin-tin potential and the atomic sphere approximation (ASA) (which is very fast) to full-potential methods, which appear to be as accurate as any self-consistent method. The basis set in LMTO consists of roughly radial solutions to

EBSCOhost - printed on 2/13/2023 4:48 AM via . All use subject to https://www.ebsco.com/terms-of-use

Schrodinger's equation inside the muffin-tin spheres, and spherical waves outside the spheres. The LAPW method uses the same kinds of basis inside the spheres, but in the interstitial volume between spheres plane waves are used, and the plane waves are joined smoothly onto the basis functions in the spheres. The LAPW method is probably the most accurate of basis sets, since it is ideally suited to both the interstitial regions and the rapidly varying regions in the interior of an atom. It is discussed fully in a book by Singh (1994).

The fundamentals of density functional theory (DFT) were originally developed by Hohenberg and Kohn (1964) and Kohn and Sham (1965). The basic idea is that the exact ground state properties of a substance, including the ground state energy, are functions of the charge density alone. Kohn and Sham showed how to calculate the ground state charge density and total energy by solving a set of single-particle Schroedinger-like equations self-consistently, with an effective potential (using units such that $h^2/2m = 1$) given by :

$$V_{KS} = -\nabla^2 + V_{e\text{-}n} + V_{e\text{-}e} + V_{xc} \quad (1)$$

where $V_{e\text{-}n}$ is the nuclear electrostatic potential, $V_{e\text{-}e}$ is the electronic electrostatic (Hartree) potential, and V_{xc} is the quantum mechanical exchange-correlation potential. The total energy is given by:

$$E = T + U + E_{xc}, \quad (2)$$

where T is the kinetic energy of a system of non-interacting electrons with the same density as the interacting system, U is the electrostatic energy (including the electrostatic energy between the nuclei) and E_{xc} is the exchange-correlation energy. The beauty of the method is that the exact, many-body ground state energy can be found by solving a set of single particle equations. Unfortunately, the exact solution requires the exact exchange-correlation functional, which is unknown, and it is undoubtedly extremely complicated and non-local. Fortunately, a simple functional based on the homogeneous electron gas works very well. In this approximation, one simply uses a local exchange-correlation potential, which corresponds at each point in space to the exchange-correlation functional appropriate to a homogeneous electron gas with a density corresponding to the charge density at that point in space. This is known as the Local Density Approximation (LDA). Reviews of the LDA are given by Pickett (1985) and Schluter and Sham (1982).

The LDA is not a "one-electron" theory, because the exchange-correlation effects are included in a mean field way in the exchange-correlation potential V_{xc}. However, there is no explicit dependence in the LDA potential on orbital occupation, and some believe this to be a source of error in the LDA when applied to some magnetic systems. Electrons see the same spatial potential regardless of their energy, angular momentum, etc. Nevertheless, the DFT implies that only the charge density is required, and no orbitally-dependent potential should be necessary.

Self-consistent LDA Computations. The only inputs to a self-consistent calculation within the LDA are the nuclear charges and positions. No parameters are fit to experiment. Thus, the method can be considered a first-principles technique, although this does not imply that there are no approximations. In LDA calculations, the following set of equations is solved for the eigenvalues $\varepsilon_i(k)$ and eigenvectors $\psi_i(\mathbf{k},\mathbf{r})$:

$$H_{ij}\ \psi_j(\mathbf{k},\mathbf{r}) = \varepsilon_i(\mathbf{k})\ O_{ij}\ \psi_j(\mathbf{k},\mathbf{r}) \quad (3)$$

where

$$H_{ij}(\mathbf{k}) = \int \psi_i^* V_{KS}\ \psi_j\ d^3r \quad (4)$$

EBSCOhost - printed on 2/13/2023 4:48 AM via . All use subject to https://www.ebsco.com/terms-of-use

and

$$O_{ij}(\mathbf{k}) = \int \psi_i^* \psi_j \, d^3 \tag{5}$$

The charge density $\rho(\mathbf{r})$ is given by a sum over occupied states:

$$\rho(\mathbf{r}) = \int \sum \psi_i^*(\mathbf{r},\mathbf{k}) \, \psi_i(\mathbf{r},\mathbf{k}) \, \theta \, (E_f - \varepsilon_i(\mathbf{k}))d^3k \tag{6}$$

where θ is the step function and E_f is the Fermi level chosen to give the correct total charge in the system. From the charge density the effective potential V_{KS} is obtained, and the self-consistent solution where the input and output charge densities agree is found by iteration. Typically 10 to 15 iterations are required to reach self-consistency. The time-consuming steps involve setting up the Hamiltonian and overlap matrices (Eqns. 4 and 5) and solving the generalized eigenproblem (Eqn. 3).

The functions ψ_i above are represented as sums over basis functions φ_j:

$$\psi_i(\mathbf{k},\mathbf{r}) = \sum c_{ij}(k) \, \varphi_j(\mathbf{k},\mathbf{r}) \tag{7}$$

What follows is a thumbnail sketch of the solid state theory needed to understand the succeeding discussion: The space filled by the vectors **k** is known as *reciprocal space* or **k**-*space*; it is the same mathematical construct used in crystallography for periodic crystals. The vector **k** can be regarded as the coefficient in a plane wave given by $\exp[i\mathbf{k} \cdot \mathbf{r}]$ where **r** is a real space lattice vector. The eigenvalues $\varepsilon_i(\mathbf{k})$ form the *band-structure*, and the quasiparticle dispersion for occupied states often corresponds well with that given by the density functional bands, although there is no fundamental reason for a correspondence since density functional theory only gives measurable ground state properties in principle, and the bands are measurable only by exciting electrons.

First-principles models

Gordon-Kim models. Accurate self-consistent calculations are extremely computationally intensive, and in general it is impossible to study very large systems or to perform dynamical simulations for sufficient lengths of time to determine dynamical properties or to study the dynamics of phase transitions with such methods. There are several types of modeling techniques that allow for much faster computations while sacrificing a certain amount of accuracy. There are three main types of first-principles models. The first are Gordon-Kim type models (Gordon and Kim, 1972), in which the total charge density is modeled as overlapping ions, and the total energy is calculated using the LDA on that charge density. For oxides there is a problem because the O^{2-} ion is not stable in the free state. The solution is to include a positively charged "Watson-sphere" in the atomic calculation for the ionic charge density of the O^{2-} that stabilizes the ion (Muhlhausen and Gordon, 1981). Several improvements have been added that allow for spherical (Mehl et al., 1986) and non-spherical (Ivanov and Maksimov, 1992; Jackson and Gordon, 1988; Lacks and Gordon, 1993) charge relaxation of the ions. This technique is fast and quite accurate for ionic solids, such as alkali halides and some oxides. There are several different variants of Gordon-Kim type models. In the Potential Induced Breathing (PIB) model (Mehl et al., 1986; Cohen et al., 1987a,b; Cohen, 1987a,b), the Watson-sphere radius is chosen so that the electrostatic potential inside the sphere is equal to the Madelung potential at the nucleus in the crystal. This gives a dynamical coupling between the size of the oxygen ion and its electrostatic environment in the crystal. In the Variationally Induced Breathing (VIB) variant (Wolf and Bukowinski, 1988), the Watson-sphere radii are chosen variationally by minimizing the total model energy. There are

EBSCOhost - printed on 2/13/2023 4:48 AM via . All use subject to https://www.ebsco.com/terms-of-use

several approaches to account for non-sphericity of ions. Each ion can be modeled as consisting of two or more overlapping spherical densities (Jackson and Gordon, 1988), or the ions can be described by a non-spherical basis perturbed by an external field (Ivanov and Maksimov, 1992; Lacks and Gordon, 1993).

Potential models. Another approach is to use a parametrized interatomic potential function, which is fit to the results of first-principles calculations. This approach is very similar to empirical models in application except that first-principles "data" are fit rather than experimental data. One advantage of this approach over the empirical approach is that it offers access to the underlying potential energy surface, which cannot be directly obtained experimentally. Also, one can include unusual structural configurations or even transition state configurations in order to constrain properties outside the experimentally studied range or the processes associated with phase transitions. This approach has been used very successfully for SiO_2 (Purton et al., 1993; Tsuneyuki et al., 1988; van Beest et al., 1990). The main problem with the technique is that the best functional form for the potential is unknown, and it is often a matter of art to find a good potential for a material. Once a potential is derived, however, its evaluation is quite fast, and one can study molecular dynamics (Tsuneyuki et al., 1988) and lattice dynamics (Purton et al., 1993) with relative ease.

It is also possible to hybridize the above two model approaches. In the PIB++ model (Cohen et al., 1994) the PIB potential is augmented by parametrized pair potential terms

$$(a + b\mathbf{r} + c\mathbf{r}^2) \exp[-d\mathbf{r}^2] \tag{8}$$

where the parameters a, b, c, and d are fit for each atom pair type, and many-body self-energy terms

$$e\,\rho^{2/3} + f\,\rho^{4/3} \tag{9}$$

$$\rho = \Sigma\, \mathrm{Exp}[-g^2\,\mathbf{r}] \tag{10}$$

with fitted parameters e and f for each pair type and g for each atom type. The static ionic charges are obtained by fitting the self-consistent LAPW charge density to spherical overlapping ions, and charges of -1.4 and +2.8 are used for O and Si, respectively, for SiO_2.

Tight-binding models. A third major type of model is the tight-binding model, where the Hamiltonian (Eqn. 4) and overlap (Eqn. 5) elements are parametrized rather than obtained using the self-consistent potential (Harrison, 1980). There are many different levels of accuracy possible using this approach, ranging from rough heuristic arguments to models that have nearly the accuracy of self-consistent approaches (Cohen et al., 1994). It seems likely that eventually this approach will be commonly used for ionic crystals, but in its accurate forms so far it has mainly been applied to purely covalent or metallic systems.

MOLECULAR DYNAMICS AND MONTE CARLO SIMULATIONS

Once one has a technique for calculating the energy as a function of nuclear positions, in principle, any property that depends on energetics or dynamics can be obtained. In a molecular dynamics simulation (Hoover, 1986; Allen and Tildesley, 1989), one uses Newton's second law (F=ma) to calculate the classical dynamics of atoms in a system. Molecular dynamics can be used to study the dynamics of phase transitions and to calculate transport properties, as well as to search for ground state structures. In a Monte Carlo simulation, one uses the Metropolis Monte Carlo (Binder, 1986) technique; rather than solving Newton's law. one induces the system to make random moves and evaluates the

EBSCOhost - printed on 2/13/2023 4:48 AM via . All use subject to https://www.ebsco.com/terms-of-use

probability factor exp(-ΔE/RT). By following a well-defined procedure, one can thereby obtain statistical averages of thermodynamic properties, as well as search for local or global energy minima.

Lattice dynamics

Another very effective technique makes use of lattice dynamics (Born and Huang, 1954). The second-derivative matrix for atomic displacements is obtained either analytically or numerically, and the matrix is diagonalized. This gives the eigenfrequencies and eigenvectors that describe the atomic motions for each eigenmode. For a quasi-harmonic system this gives the phonon density of states, and it allows calculations of thermodynamic properties such as thermal expansivity and thermal equations of state. Quasiharmonic is the term for the assumption that the phonon spectrum varies with volume or crystal structure, and it neglects intrinsic anharmonicity, such as changes in the spectrum with temperature at constant volume or structure.

For additional information on the basic characteristics of first-principles models, the reader is referred to a recent review by Bukowinski (1994).

ELECTRONIC STRUCTURE AND BONDING OF CRYSTALLINE SILICA

Even if silica were not so important for the Earth sciences and technology, it would be a fascinating system to study. Linus Pauling classified the Si-O bond in silicates as 50% ionic and 50% covalent (Pauling, 1960). This description, however, is really only appropriate for low pressures, at which Si is tetrahedrally coordinated. Rather small compressions lead to stabilization of octahedrally coordinated Si, which is much more ionic. At pressures above 10 GPa, stishovite (rutile structure) is the stable phase of SiO_2 (see chapter by Hemley et al., this volume), and all of the other known polymorphs of silica occupy a very small region of pressure-temperature space. In fact, one could say that SiO_2 exists *primarily* as the stishovite structure. We think of silica as being highly covalent because we live at low pressures. The situation for silica is similar to that of elemental silicon, which shows even more extreme changes in bonding. At low pressures and temperatures, Si is very covalent with strong $sp\sigma$ bonding (Fig. 1a), and it is tetrahedrally coordinated in the diamond structure. At high temperatures, however, Si melts to a close-packed, twelve-coordinated metallic liquid, and at high pressure Si undergoes a series of transitions to close-packed metallic structures (Yin and Cohen, 1982). SiO_2 is held together by a combination of covalent $sp\sigma$ bonding and ionic bonding between the highly charged tetravalent Si^{4+} and O^{2-} ions at low pressures. The SiO_4 unit, however, is very incompressible, and with increasing pressure the short-range repulsive overlap forces become increasingly important relative to the rather small covalent energy, and they drive the structure into octahedral coordination. Covalent interactions are still important in the six-coordinated structures, (Burdett, 1985) but much less so than in the more open tetrahedral structures, and at high pressures ionic forces dominate. In stishovite the Si ion is octahedrally coordinated by O, and the O ions are surrounded by three Si ions in a planar configuration; the covalent bonding includes both relatively strong $sp\sigma$ bonds and weaker $pd\pi$ bonds (Fig. 1b) between O p orbitals perpendicular to the coordinating Si plane and d orbitals on Si. There are also strong interactions among the Si ions across the shared faces of the stishovite structure; the normal bonded Si-Si distance is 2.3Å, but the Si-Si distance in stishovite at zero pressure is 2.7Å. The O-O distance is also very short (2.3Å) so the O ions are strongly non-spherical . The change of behavior from strongly covalent tetrahedral structures to more ionic octahedral structures with increasing pressure is one of the most fascinating features of silicates.

EBSCOhost - printed on 2/13/2023 4:48 AM via . All use subject to https://www.ebsco.com/terms-of-use

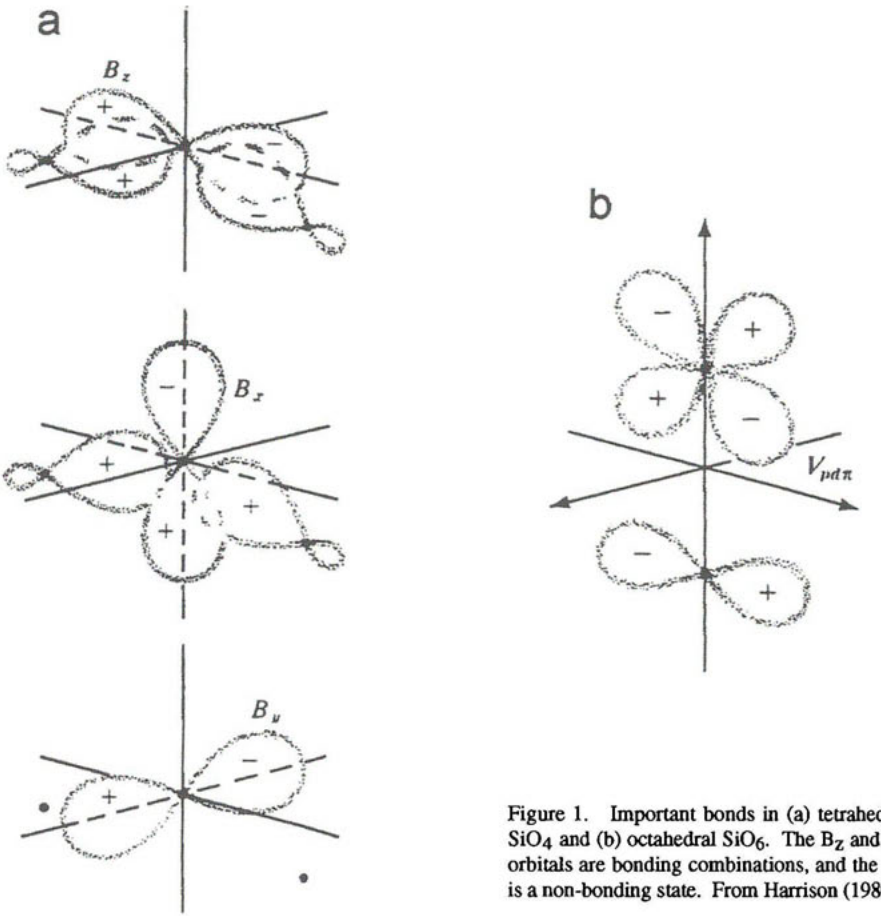


Figure 1. Important bonds in (a) tetrahedral SiO_4 and (b) octahedral SiO_6. The B_Z and B_X orbitals are bonding combinations, and the B_Y is a non-bonding state. From Harrison (1980).

The strength of the $pd\pi$ bonding is critical to the stability of the rutile structure since it stabilizes the planar anion coordination (Burdett, 1985). With increasing pressure, repulsive overlap begins to dominate the strength of the π bonding. The rutile structure becomes unstable with respect to the $CaCl_2$ structure (Cohen, 1992), and pyramidal rather than planar coordination of the oxygens results. This transition will be discussed more below.

Figure 2 shows calculated band structures of quartz and stishovite. Band structures can be quite inscrutable to the uninitiated. The combinations of Greek and Roman letters along the abscissa can certainly seem mysterious. Nevertheless, they also are quite esthetic in design, and they carry a lot of information. The band structure reveals the dispersion of eigenvalues (band energies) as a function of wavevector. The different letters indicate different wavevectors. For example, Γ is k = (0,0,0) and X is generally (π/a,0,0), although in some space groups it is (π/a, π/a,0)! One standard reference for these symbols is Koster (1957). The most important things to examine in a band structure are the band widths in energy, the gaps between bands, and the amount of dispersion of individual bands. (In a metal, the characteristics of bands as they cross the highest occupied energy, the Fermi energy, are also very important.) The band widths indicate the amount of overlap between atoms or different states, and the dispersion indicates the

EBSCOhost - printed on 2/13/2023 4:48 AM via . All use subject to https://www.ebsco.com/terms-of-use

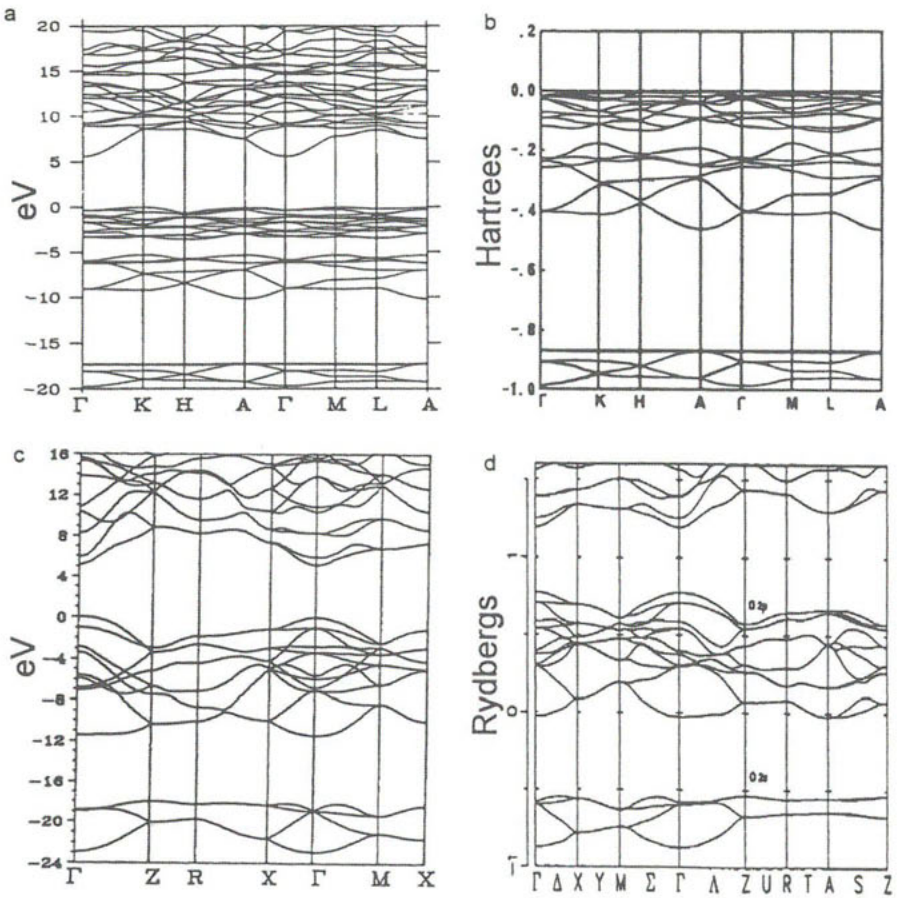


Figure 2. Band structures of quartz and stishovite. (a) Quartz OLCAO from (Xu and Ching, 1991), (b) Hartree-Fock from (Dovesi et al., 1987), (c) stishovite OLCAO from (Xu and Ching, 1991), (d) stishovite LAPW from (Cohen, 1991). In quartz the valence band is split into bonding and non-bonding manifolds. In stishovite the O 2*p* valence band is wide, but not split by a gap.

amount of hybridization between states. Also confounding for the novice is the variety of units used in first principles studies. The most common length units are Ångstroms (1Å = 10^{-10} m) and bohr or atomic units (1 au = 0.52917706 Å). A wide range of energy units is used, with "atomic unit" used for two different units(!), Rydbergs (1 Ryd = 13.605 eV; 1eV = 1.6022 10^{-19} J) and Hartrees (1 Hartree = 2 Ryd).

The band structures for silica are quite instructive. In quartz there are two sets of Si-O valence bands. The lower set contains the $sp\sigma$ bonding states (B_z and B_x in Fig. 1) and the upper set contains the non-bonding states (B_y in Fig. 1). Stishovite is quite different; there is only one valence manifold. The lower bands within this set are $sp\sigma$ bonding states,

EBSCOhost - printed on 2/13/2023 4:48 AM via . All use subject to https://www.ebsco.com/terms-of-use

and upper bands have $pd\pi$ bonding character (Harrison, 1980; Burdett, 1985). The density of states is the number of band states between E and E+dE, and it is an integral over the band structure. The density of states can be further decomposed into partial densities of states for each atomic state to show where different states contribute to bonding. These partial densities of states can sometimes be misleading, however, since they do depend on the basis, or on how the different contributions are calculated. Figure 3 shows the density of states for quartz and stishovite calculated using Hartree-Fock. It is found that there is significant Si *d* character in the valence band for quartz, indicating $pd\pi$ bonding as well as the normally considered $sp\sigma$ bonding in tetrahedral silica. It is also possible that this is an artifact from the relatively small basis set size, although LDA OCLAO calculations give similar results (Ching, pers. comm.).

The degree to which ionic bonding is important is evident in the success of purely ionic models to SiO_2. Even with spherical ions, a qualitatively correct picture is obtained. For example, the elasticity of stishovite has been studied using the PIB model (Cohen, 1987a). PIB with ionic interactions between Si^{4+} and O^{2-} gives interactions that are too stiff for stishovite, but they are not completely unreasonable. Even for quartz, which the band structure shows to be quite covalent, the PIB model gives some qualitatively correct results, as is seen by the PIB prediction of the α-β quartz transition with volume (Cohen et al., 1987a). However, in a quantitative sense, the PIB model with spherical ions fails to

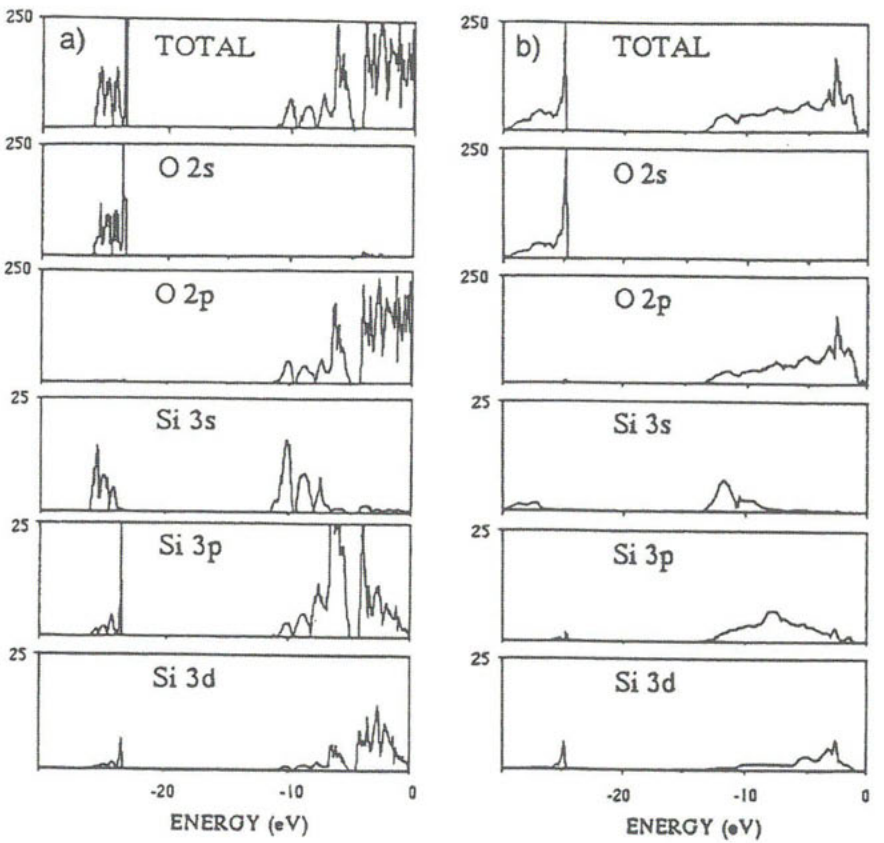


Figure 3. Hartree-Fock densities of states for (a) α-quartz and (b) stishovite, from Nada et al. (1990).

EBSCOhost - printed on 2/13/2023 4:48 AM via . All use subject to https://www.ebsco.com/terms-of-use

describe quartz. It predicts β-quartz to be the ground state zero pressure structure, rather than α-quartz. Using non-spherical ions impressively improves the picture (Jackson and Gordon, 1988; Lacks and Gordon, 1993). So energetically the ionic representation does not fare any worse than a purely covalent model, although ionicity fails quantitatively (Burdett, 1985).

The charge density complements the band structure (Fig. 2) and bond orbitals (Fig. 1). Images of the total charge density have almost no useful information content since they simply show overlapping densities that are almost spherical, and they are dominated by core and semi-core states. Usually the spherical atoms (or sometimes ions) are subtracted from the total density so that the non-spherical and charge transfer character is illustrated, or only the valence density is shown. Figure 4 shows the valence density for stishovite calculated using the LAPW method (Cohen, 1991). Most of the valence density resides on the oxygens, indicating the essentially ionic character of stishovite. However, note that the oxygens are highly nonspherical and are polarized towards the Si ions. A small amount of valence density resides as well on the Si ions.

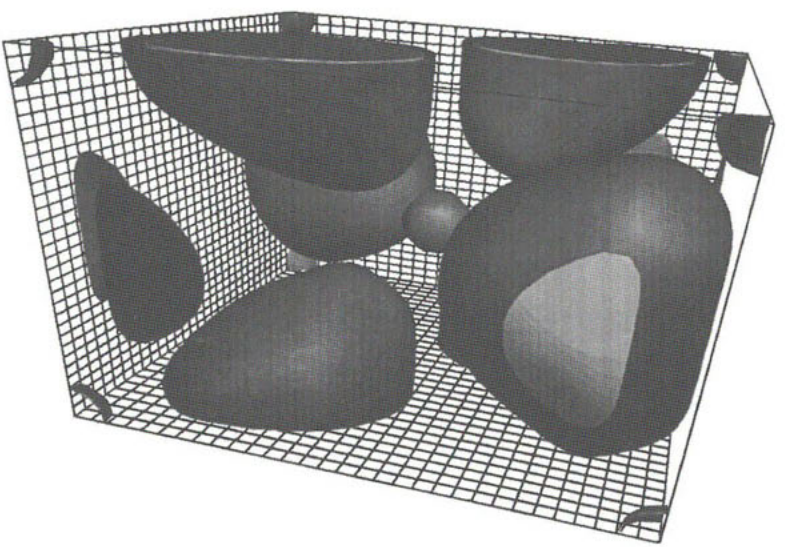


Figure 4. Valence charge density for stishovite calculated using the LAPW method. The isosurface levels are 0.06 and 0.08 $e^-/bohr^3$. From computations in Cohen (1991).

There are very few accurate experimental charge densities for minerals, but fortunately one is available for stishovite (Spackman et al., 1987), and it is considered to be among the most accurate. Figure 5 shows the deformation densities (total minus atomic densities). Note that the experimental study focused on the non-spherical deformations and not on the charge transfer, which was assumed to be zero (neutral Si and O). The theory and experiment are in excellent agreement, showing the same bonding and non-bonding features. The non-bonding features, such as the lobes directed perpendicular to the Si-O bond are often called "lone pairs," but this terminology is deceptive since there is no requirement that

EBSCOhost - printed on 2/13/2023 4:48 AM via . All use subject to https://www.ebsco.com/terms-of-use

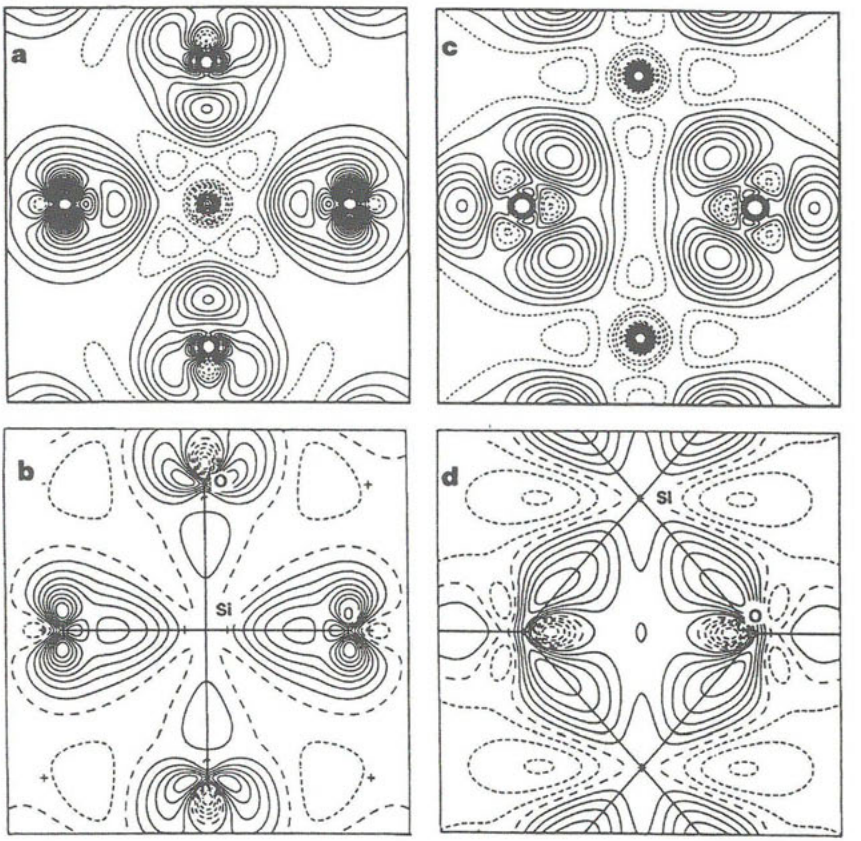


Figure 5. Deformation densities for stishovite obtained experimentally (Spackman et al., 1987) and from LAPW calculations (Cohen, 1991). (a) LAPW results for axial-equatorial bond plane (5 Å × 5 Å) (b) Experimental model of same section as a. (c) LAPW result for shared edge between two SiO_6 octahedra (4 Å × 4 Å). (d) Experimental model of same section as c. Contour interval is 0.05 $e^-/Å^3$.

two electrons reside in these features. Hartree-Fock and LDA deformation densities for quartz are shown in Figure 6. Both the bonding and non-bonding features are evident.

Deformation densities also cast light on the relative importance of covalency and ionicity in SiO_2. The deformation densities in Figure 6 show clearly that SiO_2 is very ionic; the silicon and oxygen are nearly fully charged Si^{4+} and O^{2-} ions rather than as neutral atoms with covalent bonds, as in diamond or silicon. Static ionic charges cannot be measured directly by experiment and are hard to quantify, but they are important in the development of simple models. One way to compute static charges is by comparing the self-consistent charge densities with overlapping ions; or, more precisely, one compares them with non-self-consistent charge density obtained from the potential that is generated by overlapping ions (Cohen, 1991; Cohen and Krakauer, 1990). For stishovite, static charges of -1.4 for O and +2.8 for Si were obtained this way (Cohen, 1991). Dynamic effective charges are well-defined, and they are related to experimentally observable longitudinal optic (LO) - transverse optic (TO) splitting (Schober and Strauch, 1993), although it is difficult to obtain accurate values since the LO-TO splitting is related to both the unknown dynamic charges and the unknown polarizabilities. The difference

EBSCOhost - printed on 2/13/2023 4:48 AM via . All use subject to https://www.ebsco.com/terms-of-use

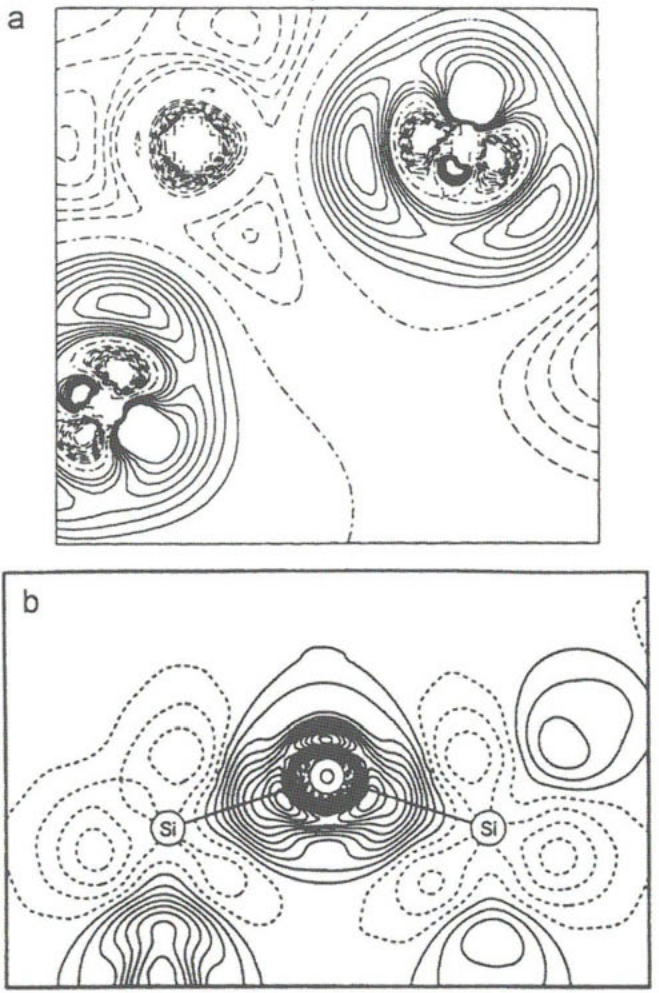


Figure 6. Deformation densities for quartz calculated using (a) Hartree-Fock (Nada et al., 1990) and (b) LDA pseudopotentials (Binggeli and Chelikowski, 1991).

between LO and TO mode frequencies with the same displacement pattern is due to the macroscopic electric field set up by LO modes. The presence of large LO-TO splittings in silica minerals is prima facie evidence that long-range forces and ionicity are important in SiO_2. The effective charge tensors have been calculated from first-principles for α-quartz (Gonze et al., 1992) and stishovite (Lee and Gonze, 1994). The effective charge depends on displacement direction, and the diagonal elements range from +3.0 to +3.6 for Si and -1.3 to -2.0 for O in quartz, and from +3.8 to +4.1 for Si and -1.9 to -2.0 in stishovite. The variations in these numbers with direction indicates the importance of covalency; in a rigid ionic crystal the effective charges are scalars. The magnitude of the numbers indicates the strongly ionic nature of silica. The results are also consistent with the lesser covalence in stishovite than in quartz. Experimental LO-TO splittings also indicate large effective charges (Schober and Strauch, 1993).

EBSCOhost - printed on 2/13/2023 4:48 AM via . All use subject to https://www.ebsco.com/terms-of-use

It has been suggested that the ionicity in silica polymorphs is very sensitive to structural parameters and thus to temperature (Kramer et al., 1991), to such a strong degree that the α- to β-quartz transition is ascribed to increasing ionicity with temperature. This interpretation appears very unlikely and seems never to have been observed in any first-principles calculations, nor has it been supported by experimental observations that are directly dependent on ionicity, such as LO-TO splitting. The authors of this study reached their conclusion on finding that the energetics of a silicon tetrahedron could be fit equally well with different sets of ionic charges in addition to parametrized short-range potentials. They furthermore found that despite similar fits the resulting crystalline energies varied. However, the insensitivity of the fits to assumed charges indicates that the energies for a tetrahedron contains insufficient information to constrain the ionicity, but it says nothing about the ionicity in crystalline silica. We move now to a discussion of the energetic properties of crystalline SiO_2.

STRUCTURE AND EQUATIONS OF STATE

Gordon-Kim models

The structural properties of several SiO_2 polymorphs have been studied using Gordon-Kim type models (Tossell, 1980; Post and Burnham, 1986; Cohen, 1987a; Cohen et al., 1987a; Jackson and Gordon, 1988; Lacks and Gordon, 1993). Using closed shell, spherical Si^{4+} and O^{2-} ions, 95% of the cohesive energy is accounted for in quartz (Jackson and Gordon, 1988). However, the ionic model for quartz gives a bulk modulus that is almost an order of magnitude too large (300 GPa instead of 35 GPa)! The zero-pressure static structure obtained by the fully charged spherical ionic model is β-quartz (Post and Burnham, 1986; Cohen et al., 1987a) rather than α-quartz, and the Si-O-Si bond angles are too large (163° rather than 145°). However, the structural variation with volume is fascinating. The PIB model (Fig. 7) shows that the α-quartz structure becomes stable at slightly expanded volumes, and in fact the atomic positional parameter u(Si), which is 0.5

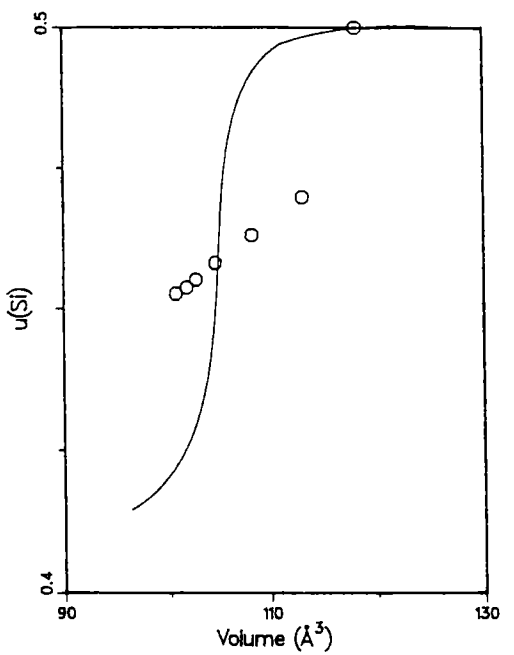


Figure 7. Internal parameter u(Si) vs volume for α-quartz calculated with PIB and compared with experiment (Levien et al., 1980). From Cohen et al. (1987a).

EBSCOhost - printed on 2/13/2023 4:48 AM via . All use subject to https://www.ebsco.com/terms-of-use

in β-quartz and 0.47 in α-quartz, varies continuously with volume, as is consistent with experiment. This volume dependence complicates discussions of the temperature-induced α- to β- phase transition, since thermal expansion decreases the potential barrier between so-called α_1 and α_2 configurations. The transition therefore cannot be considered as an excitation of atomic vibrations over a simple static double-well potential. This transition will be discussed in more detail below.

Similar to the problem with the quartz structure, Gordon-Kim models with spherical ions give ideal β-cristobalite with 180° Si-O-Si angles as the stable structure, rather than α-cristobalite with 149° angles (Jackson and Gordon, 1988). The problems with quartz and cristobalite can be solved by allowing the oxygen ions to distort non-spherically (Jackson and Gordon, 1988; Lacks and Gordon, 1993). Jackson and Gordon used a model with the O^{2-} ion represented as a core plus two spherical clouds, or shells, each containing four electrons, which can be displaced relative to the core to give a non-spherical oxygen density. Lacks and Gordon used a model with non-spherical O^{2-} ions calculated in an effective non-spherical potential simulated by point charges. Both approaches give good structures for SiO_2 polymorphs, but not much has been done beyond static energy minimizations. Ionic models work somewhat better with stishovite since it is more ionic than the tetrahedral polymorphs (Cohen, 1987a). The PIB volume is 7% too small and the bulk modulus is 40% too large, but this is an improvement over the PIB results for quartz.

Potential models

A number of potential models have been developed for SiO_2 based on fitting self-consistent results (Kramer et al., 1991; Lasaga and Gibbs, 1987; Lasaga and Gibbs, 1988; Stixrude and Bukowinski, 1988; Lasaga and Gibbs, 1991; McMillan and Hess, 1990; Purton et al., 1992; Purton et al., 1993; Tsuneyuki et al., 1988; van Beest et al., 1990). These models calculate the energy versus distortion for a molecule, and then fit that energy surface to a potential function. Most of these studies employ the Hartree-Fock method with small molecules such as H_4SiO_4 (van Beest et al., 1990; Kramer et al., 1991) and $H_6Si_2O_7$ (Stixrude and Bukowinski, 1988; Lasaga and Gibbs, 1991; McMillan and Hess, 1990). An SiO_4^{4-} molecule surrounded by 4 point charges was studied by Tsuneyuki et al. (1988). The difference between this calculation and those using H_4SiO_4 is that in the former case there are no basis functions on the point charges, so no bonds can form to the protons. Larger clusters up to 33 atoms ($Si_5O_{16}H_{12}$) have been studied using LDA (Purton et al., 1992; Purton et al., 1993); these studies fit the second derivatives of the energy surface instead of fitting the energy directly. McMillan and Hess (1990) did not find a potential but obtained the second derivatives and applied them directly to quartz; such an approach assumes completely harmonic behavior.

There are also important differences in the functional form chosen to represent the potential. Some potentials include no ionic terms (Lasaga and Gibbs, 1987; Stixrude and Bukowinski, 1988; Lasaga and Gibbs, 1988; Lasaga and Gibbs, 1991). Several researchers (van Beest et al., 1990; Kramer et al., 1991a,b) have argued that the self-consistent calculations include insufficient information in order to obtain ionicities, but it is possible to extract them from the actual orbital occupations (Tsuneyuki et al., 1988) or charge density (Cohen and Krakauer, 1990; Cohen, 1991). Some have assumed full ionic charges, 4+ for Si and 2- for O (Purton et al., 1992; Purton et al., 1993). What seems clear is that the energies of small clusters cannot be used to constrain the long-range electrostatic versus short-range interactions, and indeed the results for crystals with potentials fitted to the same molecular energy surface but with different charges give different structures and phase diagrams (van Beest et al., 1990; Kramer et al., 1991a,b).

EBSCOhost - printed on 2/13/2023 4:48 AM via . All use subject to https://www.ebsco.com/terms-of-use

This again indicates the importance of ionicity and long-range forces in silica. Finally, in some cases structural and/or compression data have been used to obtain more accurate potentials, giving a semi-empirical model (Stixrude and Bukowinski, 1988).

The structural properties of quartz are generally in good agreement with each other and with experiment. For example, the calculated Si-O-Si angles vary from 144° to 148° compared with the experimental value of 143.7°. The versatility of these potentials is quite astounding. For example, the Tsuneyuki potential (Tsuneyuki et al., 1988) works reasonably well even for stishovite with octahedrally coordinated Si, even though it was fitted to a single Si tetrahedron, in spite of its simple pair-wise rigid ion form! This potential has been tested in a number of papers (Swainson and Dove, 1993; Matsui and Tsuneyuki, 1992; Cowley and Gross, 1991; Yamada et al. 1992; Della Valle and Andersen, 1991; Keskar et al., 1991).

The success of the Tsuneyuki potential illustrates the importance of the functional form chosen for the potential. Tsuneyuki et al. only used results obtained for a single tetrahedron and obtained an excellent potential. However, when HF results for larger molecules are used, the derived potential can be less successful. For example, a simple covalent model fit to results for $H_6Si_2O_7$, which contains direct information on bond-bending forces, is less accurate, and gives a very small K' for quartz (Stixrude and Bukowinski, 1988), or even a negative value (Lasaga and Gibbs, 1987). When O repulsions are included, constrained by the known quartz equation of state, a much more reliable model emerges. For example, this model yields an accurate transition pressure from quartz to coesite (Stixrude and Bukowinski, 1988). The Tsuneyuki potential, on the other hand, includes no bond-bending terms; it infers that much of the energetics are due to O-O repulsions, which were determined from the data for a single tetrahedron, producing a model that is quite reliable.

Self-consistent calculations

Numerous self-consistent methods have been applied to SiO_2, and silica is fast becoming a benchmark for modern codes and methods, similar to the role played by Si for the previous generation. Table I summarizes structural and equation-of-state parameters obtained in the various self-consistent studies. Both HF and LDA have been used to study the zero-pressure structures and equations of state. All of the known polymorphs of SiO_2 have a number of structural parameters, and optimization of the structures is a non-trivial problem when individual energy calculations are expensive. The problem is not only the amount of computer time required to perform a self-consistent total energy calculation, but also the time necessary to set up the problem with displaced atoms, and the care necessary to ensure convergence with respect to basis set, etc. In fact, convergence is not always demonstrated due to the computational expense, and thus the source of discrepancies among different sets of calculations is not always easy to determine. In some cases discrepancies may be of fundamental interest, such as those due to different modeling methods, such as HF versus LDA, but in other cases they may simply arise from lack of convergence.

Early HF studies did not attempt full structural optimization (Dovesi et al., 1987; Silvi and D'Arco, 1990) but showed that the basic properties of quartz, such as the volume and tilt angle between tetrahedra, could be given by periodic Hartree-Fock models. However, agreement obtained with small basis sets was not perfect. For example, the tilt angle obtained was 23°, rather than the observed value of 15.9°. Of great importance in these studies was the mapping of the energy surface versus tilt (Silvi and D'Arco, 1990), which is of great importance in the α to β phase transitions in silica minerals. Geometry

EBSCOhost - printed on 2/13/2023 4:48 AM via . All use subject to https://www.ebsco.com/terms-of-use

optimization within LDA was first performed (Allan and Teter, 1987) using a plane wave basis and pseudopotentials using a Car-Parrinello (Car and Parrinello, 1985) technique, in which the electronic structure and crystal structure are simultaneously optimized The zero-pressure α-cristobalite structure, which has twelve atoms in the primitive cell, symmetry $P4_12_12$, and six structural parameters was fully optimized. The structural parameters were all within 0.6% of the experimental values, indicating that LDA is an excellent approximation for SiO_2. Pressure effects were not studied.

APW total energy calculations for fluorite showed that SiO_2 with the fluorite structure is not much more dense than an extrapolation of the experimental equation of state for stishovite, limiting the possibilities of a transition to fluorite (Bukowinski and Wolf, 1986). Furthermore, they found that an ionic model predicts that SiO_2-fluorite is dynamically unstable.

Early LAPW total energy calculations (Park et al., 1988) for stishovite gave an internal parameter [O(uu0)] of 0.303 in good agreement with the experimental value 0.306. Park et al. did not report the *c/a* value. Their calculated bulk modulus of 288 GPa is only 8% lower than the experimental value (Ross et al., 1990). Park et al. also studied the cubic pyrite-like $Pa\bar{3}$ structure for SiO_2 and found an internal parameter of 0.344 and K = 335 GPa. The predicted pressure-induced phase transition to $Pa\bar{3}$ will be discussed below. Later full-potential LAPW calculations (Cohen, 1991) gave somewhat different results; the earlier calculations were repeated with larger basis set sizes, and agreement with the later results was found (Terakura, pers. comm. and Kobayashi et al., 1993). For stishovite, Cohen (1991) found *c/a* = 0.640 in excellent agreement with the experimental value of 0.638, u=0.306 identical with experiment, V = 46.16Å^3 compared with 46.60 from experiment, and K = 314 GPa at the experimental volume, in near-perfect agreement with the experimental value of 313 GPa.

The agreement between the different methods presented in Table 1 is outstanding in light of the complexities of the structures, and indicates that both LDA and HF methods are excellent approximations for SiO_2 structural properties. Table 1 also documents the high reliability of modern pseudopotentials for SiO_2. Large differences are found between HF and LDA, however, when the energy differences between structures that are needed to calculate transition pressures and relative phase stability are studied.

LATTICE DYNAMICS AND ELASTICITY

Lattice dynamics is a much more stringent test of a model or method than structural properties or equations of state because it explores the potential surface for all possible small distortions of the structure. Lattice dynamics also provides information that offers insight into vibrational spectroscopy, phase transitions, and elastic properties. The elastic constants give us the speed of sound through a material, which is also of great importance in seismology. Elastic constants are given by the energy change with homogeneous strains only for simple crystals, such as rock salt, where there are no internal structural parameters, or more precisely structures for which there are no Raman active modes. In crystals with Raman modes, such as all of the silica minerals, the internal structural parameters are correlated with lattice strains, and elastic constants contain inhomogeneous contributions. A further complication, which will not be discussed here due to the absence of much first-principles theoretical work on silica, is that in piezoelectric crystals such as quartz the elastic constants couple with electric fields, so that the elastic constants at constant electric field are different from those obtained in open circuit conditions. These effects are very important in such technological applications as transducers.

EBSCOhost - printed on 2/13/2023 4:48 AM via . All use subject to https://www.ebsco.com/terms-of-use

EBSCOhost - printed on 2/13/2023 4:48 AM via . All use subject to https://www.ebsco.com/terms-of-use

Table 1. Zero pressure structural and equation of state parameters for silica minerals from optimized self-consistent studies compared with experiment.

quartz: Z=3	V(Å^3)	c/a	u(Si)	O(x)	O(y)	O(z)	K (GPa)
exp. (Levien et al., 1980)	113.1	1.100	0.470	0.414	0.267	0.119	35
(Nada et al., 1990) hf	114.2	1.086	***				
(Chelikowsky et al., 1990a; Binggeli and Chelikowsky, 1991) pp	107.4	1.124	0.469	0.418	0.274	0.118	38
(Keskar and Chelikowsky, 1992) pp	113.6*						
(Gonze et al., 1992) pp	106.9	1.105	0.461	0.410	0.282	0.108	
(Liu et al., 1994) pp	111.3	1.109	0.465	0.412	0.274	0.114	37
α-cristobalite: Z=4	V(Å^3)	c/a	Si(x=y)O(x)	O(y)	O(z)	K (GPa)	
exp. (Pluth et al., 1985)	169.31	1.390	0.305	0.238	0.111	0.183	
exp. (Parise et al., 1994; Palmer, 1994)							15.0
(Allan and Teter, 1990) pp	169.83	1.393	0.303	0.238	0.111	0.183	
(Keskar and Chelikowsky, 1992) pp	164.3	1.347	0.330	0.231	0.140	0.190	20.0
(Liu et al., 1994) pp	169.8	1.393	0.303	0.238	0.109	0.182	14.8
stishovite Z=2	V(Å^3)	c/a	O(x=y)	K (GPa)			
exp. (Spackman et al., 1987)	46.513	0.638	0.306				
exp. (Ross et al., 1990)				313			
(Cohen, 1987a) PIB	43.39	0.708	0.306	399			
(Park et al., 1988) LAPW	47.51	***	0.303	288			
(Allan and Teter, 1990) pp	47.145	0.612	0.308				
(Nada et al., 1990) hf	46.70	0.643	***				
(Cohen, 1991) LAPW	46.16	0.640	0.306	324****			
(Keskar et al., 1991; Keskar and Chelikowsky, 1992) pp	45.64	0.645	0.305	292			
(Sherman, 1993) hf	46.2	0.648**	0.306**	328			
(Kobayashi et al.1993) pp	46.93	0.638	0.306				
(Liu et al., 1994) pp	46.2	0.641	0.306	282			
(Lee and Gonze, 1994) pp	45.59	0.643	0.305				
(Jolly et al., 1994) hf	45.99	0.642	0.307	327			
(Cohen et al., 1994) PIB++	46.09	0.638	0.304	330			

EBSCOhost - printed on 2/13/2023 4:48 AM via - All use subject to https://www.ebsco.com/terms-of-use

Table 1, continued. Zero pressure structural and equation of state parameters for silica minerals from optimized self-consistent studies compared with experiment.

Pa3 Z=4	V(Å^3)	u	K
(Park et al., 1988) LAPW	89.49	0.344	335
(Keskar and Chelikowsky, 1992) pp	94.2		349
(Cohen, 1992) LAPW	86.62	0.344	351
(Sherman, 1993) hf	85.8	0.347	387
Fluorite: Z=4	V(Å^3)	K	
(Bukowinski and Wolf, 1986) APW	92.82	310	
(Park et al., 1988) LAPW	90.91	328	
(Keskar and Chelikowsky, 1992) pp	94.16	327	

*same as (Chelikowsky et al., 1990b; Binggeli and Chelikowsky, 1991) but different volume quoted
**not fully optimized
***experimental internal parameters used
****314 at experimental volume

Table 2. Elastic constants (GPa) at zero pressure.

α-quartz	method	c_{11}	c_{12}	c_{13}	c_{14}	c_{33}	c_{44}
(Mcskimin et al., 1965)	exp	87	7	19	-18	106	58
(Tse and Klug, 1991b)	van Beest	86	-2	4	-17	93	43
(Cowley and Gross, 1991)	Tsun.	70	9	12	-14	93	40
(Purton et al., 1993)	Pur.	90	6	14	-18	100	45

stishovite		c_{11}	c_{12}	c_{13}	c_{33}	c_{44}	c_{66}
(Weidner et al., 1982)	exp.	453	211	203	776	252	302
(Cohen, 1987a)	PIB	607	435	137	956	341	417
(Tse and Klug, 1991b)	van Beest	703	314	281	1072	287	260

Models

Few Gordon-Kim derived lattice dynamics results have been published for silica. A study of fluorite-structured SiO_2 using the MEG version of Gordon-Kim indicates that it is dynamically unstable, as mentioned above. In a study of stishovite as a function of pressure (Cohen, 1987a), single-crystal elastic constants were computed using the PIB model and the long wavelength limit of lattice dynamics (Table 2, above). This method is based on the fact that the slopes of the acoustic phonon branches with respect to q-vector give the elastic constants. The PIB model is a purely ionic model, and the results are significantly too stiff compared with experiment (Weidner et al., 1982). Qualitatively, however, many features are given correctly by the ionic model. For example, the stiffest elastic constant is c_{33}, for compressions along *c*, and the next stiffest is c_{11}. The correct sign for anisotropies with respect to shear are also given correctly, although the quantitative agreement is not exceptional. However, the net result is not terrible; the longitudinal acoustic velocity is 8% greater than experiment, and the shear velocity is 7% greater than experiment. The greater stiffness of the lattice may be due largely to the reduced volume obtained by PIB (7% smaller than experiment). The most significant result of that study is probably the smallness of the prediction for the shear modulus derivative with pressure, a value that is still unknown experimentally, and the prediction that the shear anisotropy increases with increasing pressure.

In two studies the lattice dynamics of several silica minerals were explored using the Tsuneyuki potential (Della Valle and Andersen, 1991; Cowley and Gross, 1991), and the results are shown in Tables 2 and 3. This simple potential works surprisingly well in light of the fact that it was fit only to the properties of a single silicon tetrahedron and is a simple central two-body ionic potential. A great accomplishment of this potential is its success in predicting dynamically stable structures for all of the observed low-temperature polymorphs of silica. The success of this model shows that explicit bond-bending forces are not required to model silica, as had been widely believed (Lasaga and Gibbs, 1991). Even more surprising, the Tsuneyuki potential also gives reasonable results for octahedral silica, such as stishovite. The success of this potential illustrates the importance of art and intuition in designing potentials, because previously it had been believed that two-body potentials could not model silica and that they certainly would not be transferable from tetrahedral to octahedral structures.

Thermodynamic properties can also be calculated using the phonon density of states and/or perturbation theory. For quartz, the Tsuneyuki potential gives excellent agreement with experiment for c_η (Fig. 8a), the quasiharmonic heat capacity at constant strain up to temperature approaching the α-β transition (Cowley and Gross, 1991). Cowley and Gross also obtained the linear expansivities, shown in Fig. 8b, and again agreement is quite good at low temperatures away from the phase transition. The deviations as the phase transition is approached is due to the perturbation expansion and not to the potential (Tsuneyuki et al., 1990). The potential also gives the current anomalous low-temperature expansion; the *c*-axis has a negative expansivity at low temperatures, and the coefficients to T^3 at low T are -14.9 K^{-1} and 17.4 K^{-1} parallel and perpendicular to *c* compared with the experimental values of -14.5 K^{-1} and 10.5 K^{-1} (Barron et al., 1982).

The Purton potential (Purton et al., 1993) was fit to large clusters rather than a single tetrahedron, and it also gives quite good results for the lattice dynamics model of quartz (Tables 2 and 3, Fig. 9). Again it is surprising that a simple two-body potential does a such a good job of modeling the dispersion of the phonon modes.

EBSCOhost - printed on 2/13/2023 4:48 AM via . All use subject to https://www.ebsco.com/terms-of-use

EBSCOhost - printed on 2/13/2023 4:48 AM via . All use subject to https://www.ebsco.com/terms-of-use

Table 3. Optical frequencies (cm-1) at zero pressure.

α-quartz	Exp.[1]	Tsun.[2]	Tsun.[3]	Purton[4]	LDA PP[5]	stishovite	Exp.[6]	LAPW[7]	Tsun.[2]	LDA PP[8]	HF[9]
A_1						B_{1g}	231, 234	224	270	214	225
	206, 219	243	239	201	239	E_g	589, 586		456	585	
	355, 358	403	400	347	339	A_{1g}	753, 751	751	596	755	
	464, 469	541	539	494	462	B_{2g}	967,964		1053	954	
	1085, 1082	980	979	1152	1061	A_{2g}	silent		909	599	
A_2						B_{1u}	silent		390	384	
TO	361	437	436	348	341	B_{1u}	silent		661	761	
LO	385	471	470	-	366	E_u TO	470		483	469	
TO	499	622	614	525	493	LO	565		511	569	
LO	553	678	674	-	540	TO	580		527	595	
TO	778	696	693	820	762	LO	700		790	705	
LO	791	778	773	-	784	TO	820		792	822	
TO	1072	1007	1003	973	1056	LO	1020		1007	1043	
LO	1230	1126	1120	-	1218	A_{2u} TO	650		530	649	
E						LO	950		1021	1049	
TO	128,133	163	161	142	133						
LO	128,133	163	161	142	133						
TO	265,269	301	299	266	261						
LO	265,269	301	299	268	263						
TO	394,393	426	427	399	378						
LO	401,402	440	442	406	389						
TO	450,452	580	573	442	444						
LO	511,512	637	632	457	499						
TO	697,698	663	661	729	691						
LO	697,701	675	674	730	695						
TO	796,799	706	702	834	792						
LO	808,812	779	777	848	804						
TO	1069,1066	990	987	980	1045						
LO	1162,1227	1094	1092	-	1209						
TO	1162,1158	1110	1110	1057	1128						
LO	1230,1155	1134	1129	1059	1124						

[1] (Gervais and Piriou, 1975; Hemley, 1987)
[2] (Della Valle and Andersen, 1991)
[3] (Cowley and Gross, 1991)
[4] (Purton et al., 1993)
[5] (Gonze et al., 1992)
[6] (Hemley et al., 1986; Vigasina et al., 1989; Hofmeister et al., 1990)
[7] (Cohen, 1991; Cohen, 1992)
[8] (Lee and Gonze, 1994)
[9] (Jolly et al., 1994)

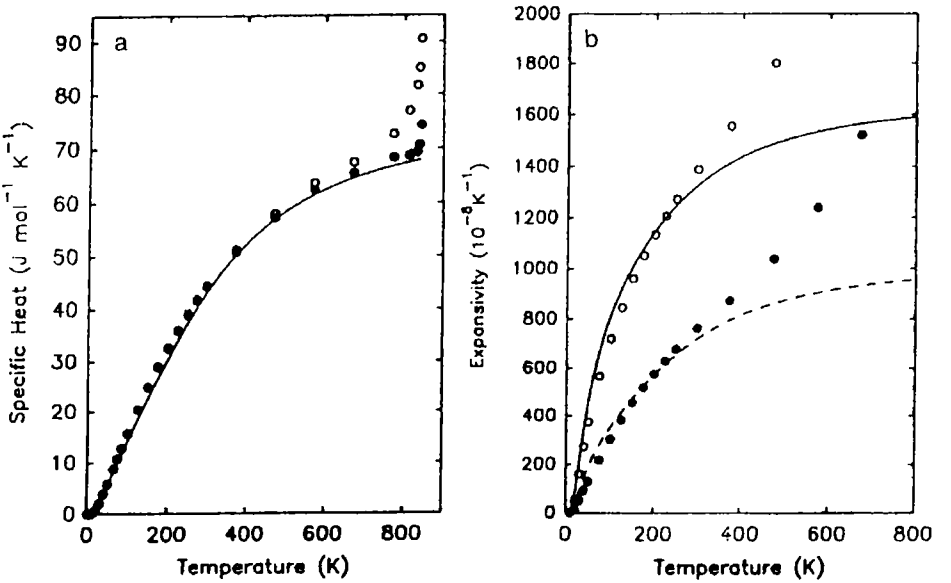


Figure 8. Quasiharmonic thermodynamic properties obtain using the Tsuneyuki potential. (a) Specific heat; (b) linear expansivity. From Cowley and Gross (1991).

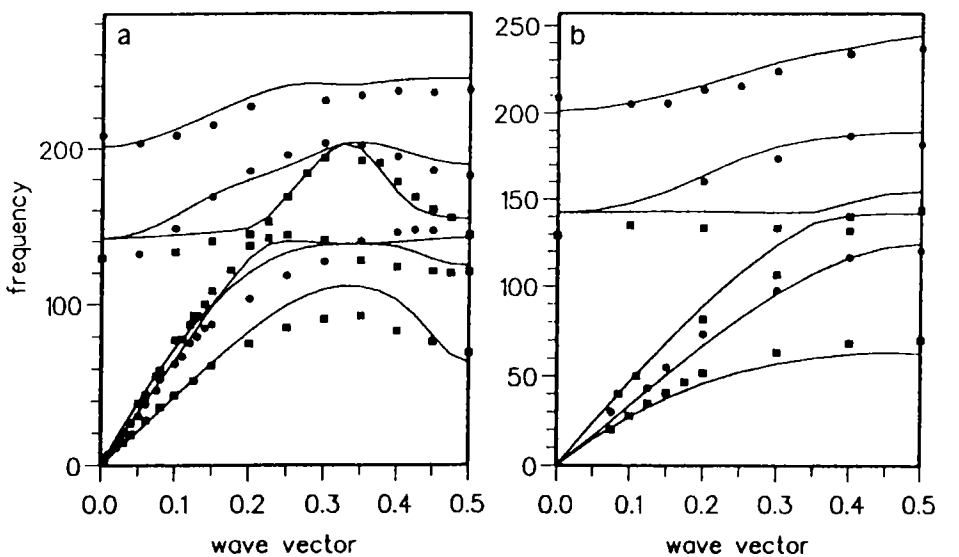


Figure 9. Phonon dispersion curves for α-quartz obtained from the Purton potential (Purton et al., 1993) compared with experiment (Dorner et al., 1980; Strauch and Dorner, 1993). From (Purton et al., 1993). (a) (qq0); (b) (q00).

EBSCOhost - printed on 2/13/2023 4:48 AM via . All use subject to https://www.ebsco.com/terms-of-use

Elastic constants can also be calculated using molecular dynamics, which has the advantage of taking full account of anharmonicity. MD calculations (Tse and Klug, 1991) using the van Beest (van Beest et al., 1990) potential gave quite reasonable results for quartz, but values for stishovite are too stiff, as with the PIB results (Table 1). It is not too surprising that the van Beest potential works better for quartz since it was designed to fit tetrahedral structures. Tse and Klug also studied the optical vibrations and obtained quite good agreement with experiment.

Results of the PIB++ look quite promising. Figure 10 shows both the LAPW and PIB++ Raman frequencies compared with experiment. The E_g and B_{2g} modes, which were not fit, are in good agreement with empirical values. The infrared modes, which also were not fit, also agree well with experiment (Hofmeister et al., 1990).

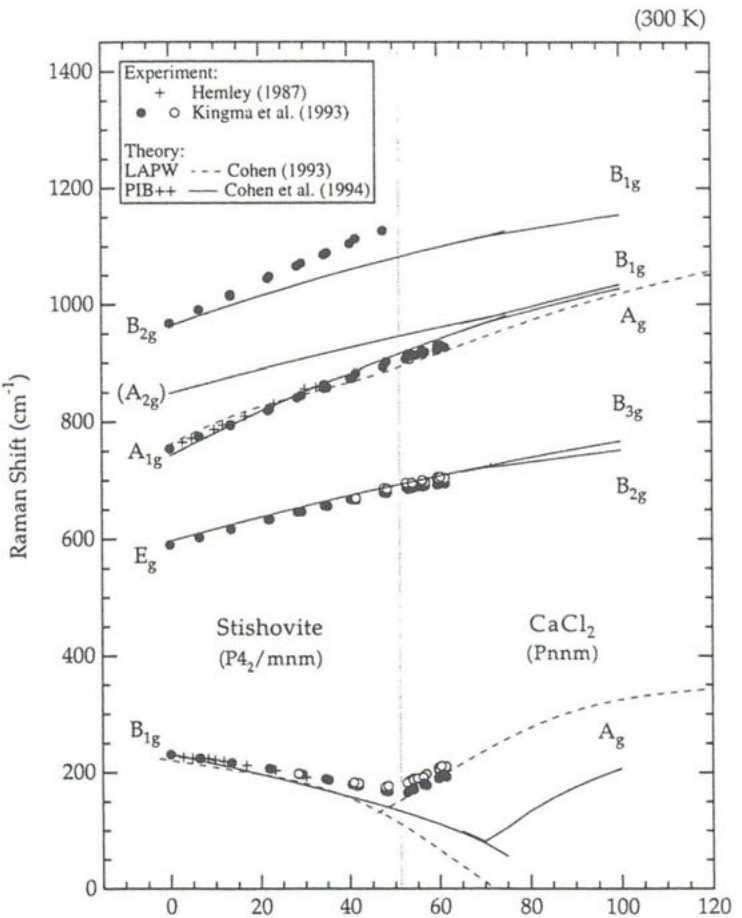


Figure 10. Raman frequencies for stishovite obtained using the LAPW (Cohen, 1991; Cohen, 1992) and PIB++ (Cohen et al., 1994) methods compared with experiment (Hemley et al., 1987; Kingma et al., 1993).

EBSCOhost - printed on 2/13/2023 4:48 AM via . All use subject to https://www.ebsco.com/terms-of-use

Self-consistent calculations

Only recently have self-consistent lattice dynamics calculations become feasible, compared with well-established lattice dynamics methods using interatomic potentials. Two main methods can be used. In the frozen phonon method, self-consistent calculations are performed for different structural configurations, and vibrational frequencies and elastic constants are obtained from the curvature of the potential surface. In the linear response method, the second derivatives of the potential surface are obtained directly by assuming the small distortion limit and expanding the wave functions in displacement. The advantage of the linear response method is that the full phonon dispersion curves can be obtained within the quasiharmonic approximation. The frozen phonon method is much more computationally intensive and requires the use of supercells to study $q \neq 0$ modes, so that dispersion curves cannot be mapped out throughout the zone. The advantage of the frozen phonon method is that anharmonic potential surfaces can be mapped out since there is no approximation of small distortions.

Frozen phonon calculations for stishovite using the LAPW method (Cohen, 1991; Cohen, 1992) give excellent agreement with experiment for the few modes studied (Table 3, Fig. 10). The LAPW calculations are within experimental error of the measurements at pressures below the phase transition discussed below. The B_{1g} mode was also studied using frozen phonons within the HF method, and agreement is also quite good (Jolly et al., 1994).

The ability to calculate dispersion curves self-consistently using linear response theory is a major advance that will revolutionize the ability to predict thermodynamic, elastic, and vibrational properties. As discussed above, they also give insight into bonding and ionicity and will also help in understanding phase transitions. Results are now available for α-quartz (Gonze et al., 1992) and stishovite (Lee and Gonze, 1994) and are shown in Table 3. The accuracy of these calculations for silica rivals experiment and is truly phenomenal and unexpected. That the properties of such complicated structures could be studied with such accuracy with fundamental methods is a surprise even to first-principles practitioners, and many would assume that such excellent agreement is fortuitous. However, it seems highly unlikely that such a broad range of agreement for all of the optical modes of quartz and stishovite could be obtained if the physics were not correctly described, and the possibility that agreement is fortuitous seems highly unlikely. It is also surprising that the pseudopotentials are so accurate for silica, but their accuracy is clearly demonstrated in these studies.

PHASE TRANSITIONS

Perhaps the most exciting aspects of silica minerals are their temperature- and pressure-induced phase transitions. Because of the large amount of energy required to break the Si-O bond, metastable structures and phase transitions are often observed. Whereas in *reconstructive* transitions the bonds must be broken to form a new structure, *displacive* transitions involve small motions that do not break the connectivity. There are an infinite number of ways to connect silica tetrahedra and/or octahedra, and only a small number of the possible structures have been observed, probably because most of these structures are dynamically unstable. Nevertheless, a rich set of transitions have been studied, and many more may be found in the future. Some of these transitions may be geophysically important, such as phase transitions in stishovite; other transitions are interesting in terms of crystal chemistry, such as high-pressure transitions in cristobalite

EBSCOhost - printed on 2/13/2023 4:48 AM via . All use subject to https://www.ebsco.com/terms-of-use

(Palmer, 1994). Metastable transitions are just as amenable to theory as stable transitions. A number of metastable transitions have been studied, for example, by pressurizing quartz, cristobalite, and coesite in MD simulations using the Tsuneyuki potential (Tsuneyuki et al., 1989). MD simulations with the Tsuneyuki potential were also recently used to help solve a structure observed in quartz pressurized beyond its stability field just before it amorphizes (Somayazulu et al., 1994).

The stishovite-II story

For years much interest has revolved around post-stishovite phase transitions in SiO_2. One much discussed candidate is fluorite, with tetrahedral coordination for the anion and eight-fold coordination for the cation. However, both Gordon-Kim (Bukowinski and Wolf, 1986) and empirical potentials (Matsui and Kawamura, 1987) show SiO_2-fluorite to be dynamically unstable. MD simulations typically relax to the α-PbO_2 structure when one starts with SiO_2-fluorite (Matsui and Kawamura, 1987). However, one run out of several hundred MD simulations resulted in a new structure, with space group $Pa\bar{3}$ (Matsui and Matsui, 1988). Indeed this new structure turned out to have lower energy. The $Pa\bar{3}$ structure is a distorted fluorite structure, and it has the same space group and occupancies as pyrite, except that the single positional parameter is smaller, so that O-O dimers are not evident. This may be the first time that an MD simulation has actually given a new stable structure for a mineral that had not been previously considered. The question remained whether this new structure was simply an artifact of the empirical potential or actually a post-stishovite phase? In 1988, Park et al. performed the first high-level calculation using the LAPW method to look for a transition from stishovite to the $Pa\bar{3}$ structure. Park et al. found a phase transition from stishovite to $Pa\bar{3}$ at 60 GPa, which was very exciting since it implied that free silica in the deep lower mantle might possibly not be stishovite.

Shortly after this prediction, Tsuchida and Yagi (1989) undertook high-pressure diamond anvil experiments to pressures over 100 GPa to search for this transition, but instead of observing the $Pa\bar{3}$ phase, these researchers inferred a transition to the $CaCl_2$ structure. They observed that some diffraction peaks exhibited a small shift, which led to anomalous behavior of the volume. The experiments were non-hydrostatic, so some questions remained with regard to the pressure of the phase transition. Because of the importance of such a phase transition to geophysicists, further LAPW calculations were undertaken, with special attention paid to convergence (Cohen, 1992). Convergence is especially a sensitive issue when energetics of totally different structures are compared. Those calculations clearly indicated a transition pressure from stishovite to $Pa\bar{3}$ at 150 GPa, rather than the 60 GPa predicted by Park et al (1988). In fact, the latter group repeated the calculations with higher convergence levels and also obtained 150 GPa (Terakura, pers. comm.). The $CaCl_2$ transition was also studied by LAPW, and the transition pressure obtained was 45 GPa.

The transition in stishovite is fascinating because it is a ferroelastic transition for which a shear elastic constant vanishes at the transition. It is surprising that such a small structural distortion, a small rotation of the octahedra around c, gives rise to such large changes in elastic properties. Since elastic constants govern the velocities of sound through a material, and since what we know of the deep earth is largely obtained from seismology, an elastic instability could be very important. The presence of an elastic instability in stishovite and the presence or absence of its seismological signal may give a boundary for the amount of free silica present in the deep earth.

EBSCOhost - printed on 2/13/2023 4:48 AM via . All use subject to https://www.ebsco.com/terms-of-use

Figure 11 shows the elastic constant c_{11}-c_{12} predicted by frozen phonon LAPW calculations. At the phase transition this modulus vanishes. The transition is driven by a soft Raman mode, the B_{1g} mode, but the transition occurs long before the Raman mode goes unstable. At the phase transition the soft mode becomes a hard mode of A_g symmetry. This indicates that Raman is perhaps the best way to study the transition, since it is a continuous transition and the deviation of *b/a* from 1 for the orthorhombic structure would be vanishingly small at the transition itself. Only when *b/a* became significantly different from 1 would a powder X-ray diffraction experiment detect the transition. Kingma et al. (1993) performed such Raman experiments on single crystals under quasihydrostatic pressure and found the transition at ~50 GPa. In Figure 10 the LAPW predictions are compared with experiment. Agreement is excellent, and this is perhaps one of the best cases for the verification of a quantitative theoretical prediction of a phase transition. Not only is the transition pressure very close to that predicted, but the behavior of the Raman modes agrees quite well with theory. Figure 10 also shows results of the PIB++ model, which gives a higher transition pressure of ~70 GPa, but it gives reasonable results for the other Raman modes, including the splitting of the E_g-modes at the transition. The transition has also been studied using Car-Parrinello methods and plane wave pseudopotentials, and a transition of 45 GPa was found (Kobayashi et al.1993), in perfect agreement with the LAPW frozen phonon study.

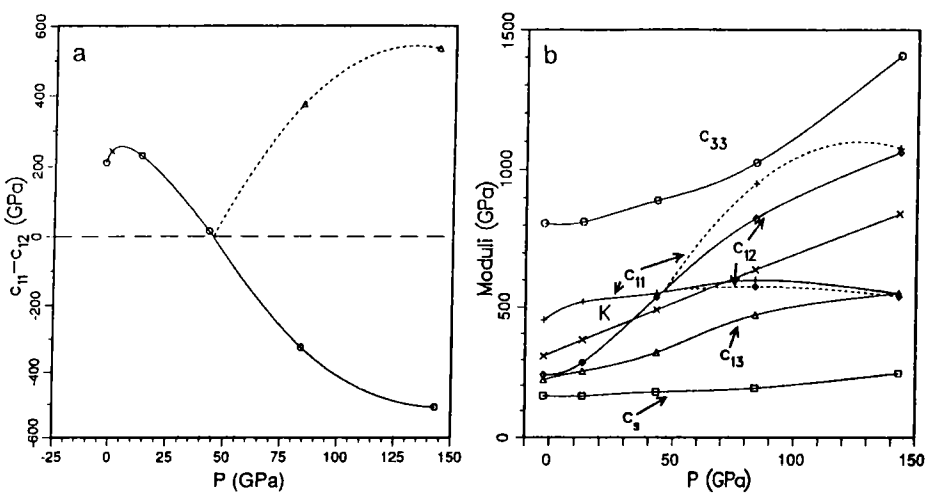


Figure 11. Elastic constants predicted for stishovite using the LAPW method. (a) Elastic constant c_{11}-c_{12}. The predicted transition is at ~45 GPa (Cohen, 1992). (b) The (incomplete) set of elastic constants so far obtained using LAPW.

All of the measurements so far performed on stishovite at high pressure were made at room temperature, and the published computations assume static low temperatures (Cohen, 1992) or room temperature (Matsui and Tsuneyuki, 1992). What happens at high temperatures? Will stishovite transform in the Earth? Experimental measurements of the transition at high temperatures will be exceedingly difficult (although almost nothing seems impossible!), and theoretical estimates again are required. The best way to study this problem would involve MD simulations that focus on the effect of temperature on the transition. Unfortunately, there is no potential that accurately reproduces the transition

EBSCOhost - printed on 2/13/2023 4:48 AM via . All use subject to https://www.ebsco.com/terms-of-use

pressure; the closest is the PIB++ model fit to LAPW calculations. As a first step before performing MD simulations, an estimate of thermal effects can be made using quasiharmonic lattice dynamics. Normally this sort of transition could not be studied well by lattice dynamics because there are unstable modes at the transition. However, in this case the instability occupies a very small part of phase space near q = 0 along the [110] direction, and even moderately large q-vector sets do not sample any unstable modes.

Thus, free energy minimizations have been performed as a function of temperature and pressure, and the phase transition has been mapped out using the PIB++ potential (Cohen et al., 1994). Figure 12 shows the resulting internal distortion parameter as a function of pressure and temperature. Even at 2000 K the transition is only shifted by 10 GPa, so that it would still occur in the Earth's mantle. Clearly single crystal studies are much more sensitive to such a transition than powder studies of lattice parameters, because the changes in the *b/a* ratio are quite small, whereas the internal distortions are larger. Also, it is clearly not reasonable to extrapolate measurements from lower temperatures in order to predict a thermally-induced transition from data. At all pressures the structure becomes more symmetric with increasing temperature, but this trend does not reliably indicate whether a transition occurs below melting or not.

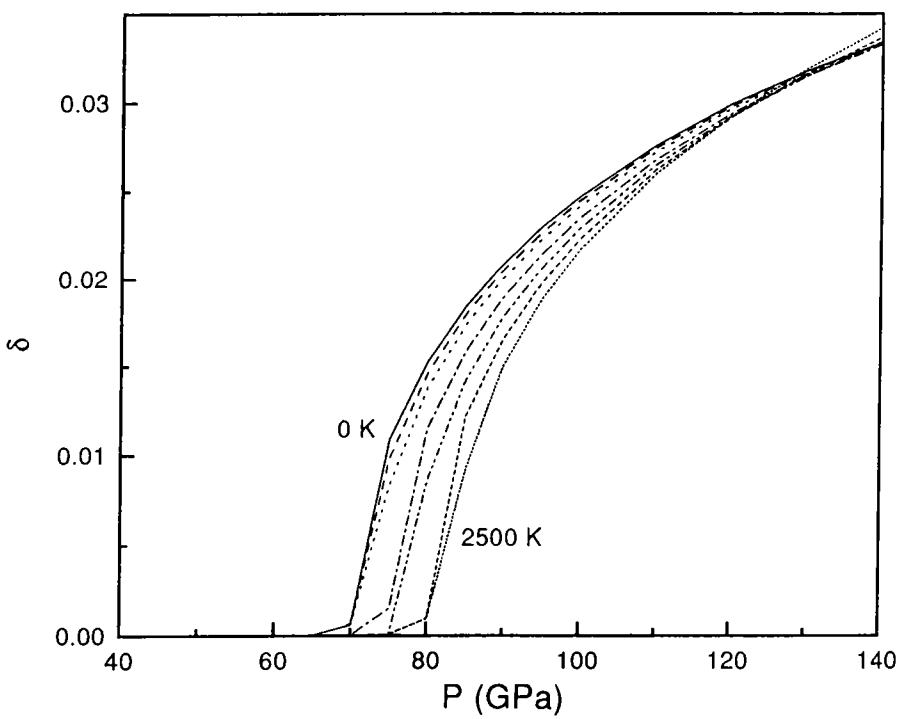


Figure 12. Quasiharmonic lattice dynamics predictions for stishovite with the Pressure PIB++ model. The internal distortion parameter δ = O(x)–O(y) is shown at 0, 300, 500, 1000, 1500, 2000, and 2500 K. The effect of temperature is not huge; 2000 K shifts the transition pressure by about 10 GPa. Note that PIB++ overestimates the transition pressure, and the actual thermal effects at 50 GPa may be somewhat larger. The predictions of a model such as PIB++ are much less reliable than those obtained using self-consistent methods.

EBSCOhost - printed on 2/13/2023 4:48 AM via . All use subject to https://www.ebsco.com/terms-of-use

The stishovite transition is probably one of the best cases of theory and experiment working together to solve a problem. Two kinds of questions remain. What are the dynamical and anharmonic properties of the transition? MD simulations using the Tsuneyuki potential show similar characteristics to the α- to β-quartz transition (Tsuneyuki et al., 1990), with complicated anharmonic dynamics at the transition (Matsui and Tsuneyuki, 1992). A thermodynamic Ginzberg-Landau study of the transition has been performed to better understand the nature of the transition (Yamada et al.1992). Further experimental measurements of properties at the transition, particularly elastic properties, will be particularly exciting and give better indications of whether a seismological signal for the transition should be observable.

Another basic question involves possible transformations at still higher pressures. New candidate structures are proposed periodically (Tse et al., 1992). The relative energies of different phases seems to be given quite differently by HF and LDA. For instance, HF computations reveal no ground state stability field for the $Pa\bar{3}$ structure, and it predicts that α-PbO_2 is lower in energy than $Pa\bar{3}$ (Sherman, 1993) . Since LDA has been demonstrated repeatedly to give accurate phase-transition pressures, the LDA results are considered more reliable. It is unclear how much of the difference is due to the diverse techniques of LDA and HF and how much may be ascribed to insufficient testing of convergence in the HF calculations, which have many different convergence parameters. In contrast, the LAPW method has only one parameter that controls convergence of the basis set, so that convergence is easily tested.

Displacive transitions in quartz, tridymite, and cristobalite

One of the most exciting and controversial areas in the physics of silica are the high-temperature transitions observed in quartz, tridymite, and cristobalite. The details of the transitions are different among these three materials, but the controversy over the phase transition mechanism encompasses them all. In each case, at high temperatures the average structure changes from a lower symmetry phase to a higher symmetry phase by a small tilt of tetrahedra. These are classic displacive transitions, and no bonds are broken at the transitions. Symmetry requires that the ground state contain multiple-well potentials with minima for the different twins. These potential surfaces have been partially mapped out for quartz, cristobalite, and idealized tridymite using periodic Hartree-Fock (Silvi et al., 1991). The barrier height between minima is a crucial quantity for better understanding these transitions. For example, the Hartree-Fock computations give a barrier height of 0.07 eV/molecule between two twins of α-cristobalite and ideal β-cristobalite. LDA calculations for the same potential barrier, however, give 0.3 eV, a significant difference (Liu et al., 1993). Whether this difference is due to lack of relaxation in the HF calculations as suggested by Liu et al., or whether there is a true difference between HF and LDA, or whether there was some other difference in the calculations, remains to be seen.

Cristobalite has been much discussed, since there are several candidate models for the high-temperature structure, and without theoretical input it is difficult to distinguish among the different models. As has been discussed many times, high temperature β-cristobalite on average appears to have 180° Si-O-Si angles and Si-O bond distances that are too short compared with other silicates. The conclusion of many studies is that the real structure is disordered, statically or dynamically, and that the ideal structure is only an average structure. The discussion then has centered on the nature of the disorder, which theory has helped to solve, but not with unanimity! On the basis of LDA pseudopotential calculations, Liu et al. supported the idea that β-cristobalite results from static disorder of regions of $F\bar{4}d2$ symmetry based on lower total energies for $F\bar{4}d2$ than for $P2_13$ or the ideal $Fd3m$

EBSCOhost - printed on 2/13/2023 4:48 AM via . All use subject to https://www.ebsco.com/terms-of-use

structures (Liu et al., 1993). However, they found that the $P4_12_12$ α-cristobalite structure, which differs from $F\bar{4}\,d2$ in the relative orientations of the tilts, has the same energy as $F\bar{4}\,d2$, so that they admit that they cannot rule out disordered domains of $P4_12_12$ α-cristobalite in β-cristobalite (Hatch and Ghose, 1991).

MD simulations using the Tsuneyuki potential show a quite different picture (Swainson and Dove, 1993), although they are not incompatible with any of the computation results of Liu et al. Swainson and Dove argue that β-cristobalite is most reasonably considered to be a dynamically disordered structure in which the oxygen atoms rotate freely around annular sites rather than hopping among distinct minima. Their results are compatible with experimental data and with computed potential surfaces.

Similar controversies swarm around β-quartz and the α-β quartz transition. The transition in quartz is complicated by the presence of an incommensurate phase stable for a small temperature region around the transition that consists of microdomains of α-quartz with mobile Dauphiné twin boundaries. MD simulations using the Tsuneyuki potential give excellent agreement with the observed properties of the α-β transition (Fig. 13) (Tsuneyuki et al., 1990), except for the incommensurate phase, which cannot be studied in small periodic systems. Tsuneyuki et al. carefully quantified the nature of the anharmonicity in the β-quartz structure, and they point out that whether β-quartz is a dynamical average structure or a disordered structure of α_1 and α_2 domains depends entirely on the time and length scales as a function of temperature. In the transition region (850 K) on a short time scale of 4 ps (which is still long compared with vibrational time scales), the structure is found to remain in either the α_1 or α_2 configurations, but when averaged over 12 ps it shows the average ideal β-quartz structure. At higher temperatures, the correlation time becomes shorter and shorter.

Tsuneyuki et al. also point out that the potential surface is volume dependent and that thermal expansivity is an essential part of the problem. This feature is very important and generally neglected or underemphasized. The PIB calculations for quartz (Fig. 7) show that with increasing volume the β-quartz structure becomes dynamically stable. This trend is evident in self-consistent calculations (Liu et al., 1993, Fig. 3; Silvi and D'Arco, 1990, Fig. 1), although the authors do not examine the expanded, static negative pressure regime where the potential surface will contain only a single minimum. This effect leads to the rapid change in the β-quartz structure from an anharmonic disordered structure to a more harmonic structure with increasing temperature. The fact that the transition pressure changes with temperature has been partly responsible for the many different conclusions drawn from experimental studies on quartz that ignore this possibility. An intriguing experiment would be the study of the anharmonicity in β-quartz as a function of pressure.

CONCLUSIONS

Clearly silica is an excellent case study for learning about phase transitions, electronic structure methods, and chemical bonding. This is an active field, and this review can only present a snap shot. If pure SiO_2, a closed shell system with "simple" chemistry is so complicated, can there be any end to discovery in mineralogy?

ACKNOWLEDGMENTS

Many thanks to R.J. Hemley, K.J. Kingma, and L. Stixrude for useful discussions. This research is supported by NSF grant EAR-9117932 and the National Center for Supercomputing Applications and the Pittsburgh Supercomputer Center sponsored by NSF.

EBSCOhost - printed on 2/13/2023 4:48 AM via . All use subject to https://www.ebsco.com/terms-of-use

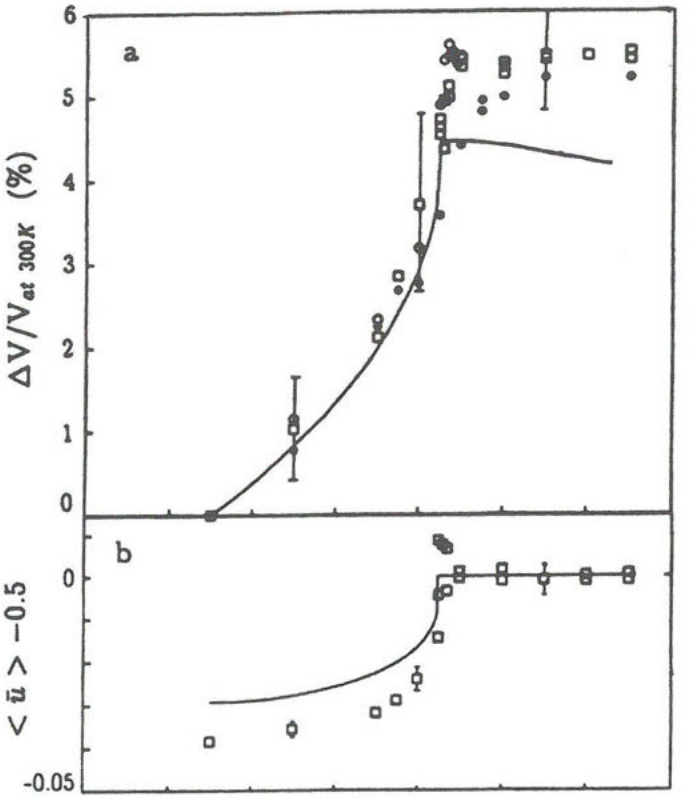


Figure 13. MD results for the α-β quartz transition (Tsuneyuki et al., 1990) compared with experiment. (a) Change in volume (simulations--points; experiment--solid line). (b) Average internal parameter (points--MD; curve--experiment).

EBSCOhost - printed on 2/13/2023 4:48 AM via . All use subject to https://www.ebsco.com/terms-of-use

REFERENCES

Allan DC, Teter MP (1987) Nonlocal pseudopotentials in molecular-dynamical density-functional theory: Application to SiO_2. Phys Rev Lett 59:1136-1139

Allan DC, Teter MP (1990) Local density approximation total energy calculations for silica and titania structure and defects. J Am Ceram Soc 73:3247-3250

Allen MP, Tildesley DJ. (1989) Computer Simulation of Liquids. Clarendon Press, Oxford, UK

Barron THK, Collins JF, Smith TW, White GK (1982) Thermal expansion, Gruneisen functions and static lattice properties of quartz. J Phys C 15:4311-4326

Binder K. (1986) Introduction: theory and technical aspects of Monte Carlo simulations. In: Binder K (ed) Monte Carlo Methods in Statistical Physics. Springer-Verlag, New York, p 1-45.

Binggeli N, Chelikowski JR (1991) Structural transformation of quartz at high pressures. Nature 353:344-346

Binggeli N, Chelikowsky JR (1992) Elastic instability in α-quartz under pressure. Phys Rev Lett 69:2220-2223

Born M, Huang K. (1954) Dynamical Theory of Crystal Lattices. Clarendon Press, Oxford, UK

Bukowinski MST. (1994) Quantum geophysics. In: Wetherill GW (ed) Ann Rev Earth Planetary Sci, Annual Review, Inc. Palo Alto, CA, p 167-205.

Bukowinski MST, Wolf GH (1986) Equation of state and stability of fluorite-structured SiO_2. J Geophys Res 91:4704-4710

Burdett JK (1985) Electronic control of the geometry of rutile and related structures. In Chem 24:2244-2253

Car R, Parrinello M (1985) Unified approach for molecular dynamics and density-functional theory. Phys Rev Lett 55:2471-2474

Catlow CRA, Price GD (1990) Computer modelling of solid-state inorganic materials. Nature 347:243-248

Chelikowsky JR, King HE, Jr., Glinnemann J (1990a) Interatomic potentials and the structural properties of silicon dioxide under pressure. Phys Rev B 41:10806-10869

Chelikowsky JR, King HE, Jr., Troullier N, Martins JL, Glinnnemann J (1990b) Structural properties of α-quartz near the amorphous transition. Phys Rev Lett 65:3309-3312

Cohen RE (1987a) Calculation of elasticity and high pressure instabilities in corundum and stishovite with the potential induced breathing model. Geophys Res Lett 14:37-40

Cohen RE (1987b) Elasticity and equation of state of $MgSiO_3$ perovskite. Geophys Res Lett 14:1053-1056

Cohen RE (1991) Bonding and elasticity of stishovite at high pressure: Linearized augmented plane wave calculations. Am Min 76:733-742

Cohen RE. (1992) First-principles predictions of elasticity and phase transitions in high pressure SiO_2 and geophysical implications. In: Syono Y, Manghnani MH (eds) High-Pressure Research: Application to Earth and Planetary Sciences. Terra Scientific/AGU, Washington, DC, p 425-431

Cohen RE, Boyer LL, Mehl MJ (1987a) Theoretical studies of charge relaxation effects on the statics and dynamics of oxides. Phys Chem Min 14:294-302

Cohen RE, Boyer LL, Mehl MJ (1987b) Lattice dynamics of the Potential Induced Breathing model: First principles phonon dispersion in the alkaline earth oxides. Phys Rev B 35:5749-5760

Cohen RE, Kingma KJ, Hemley RJ, Mao H (1994) Temperature-dependence of the $CaCl_2$ transition in stishovite and implications for the earth. EOS Trans Am Geophys Union 75:347

Cohen RE, Krakauer H (1990) Lattice dynamics and origin of ferroelectricity in $BaTiO_3$: Linearized augmented plane wave total energy calculations. Phys Rev B 42:6416-6423

Cohen RE, Mehl MJ, Papaconstantopoulos D (1994) A new tight-binding total energy method for transition and noble metals. Phys Rev B 50:14,694-14,697

Cowley ER, Gross J (1991) Lattice dynamics of a pair potential model of α-quartz. J Chem Phys 95:8357-8361

Della Valle RG, Andersen HC (1991) Test of a pairwise addittive ionic potential model for silica. J Chem Phys 94:5056-5060

Dorner B, Grimm H, Rzany H (1980) Phonon dispersion branches in α-quartz. J Phys Chem 13:6607-6612

Dovesi R, Pisani C, Roetti C, Silvi B (1987) The electronic structure of α-quartz: A periodic Hartree-Fock calculation. J Chem Phys 86:6967-6971

Gervais F, Piriou B (1975) Temperature dependence of transverse and longitudinal optic modes in the α and β phases of quartz. Phys Rev B 11:3944-3950

Gibbs GV (1982) Molecules as models for bonding in silicates. Am Min 67:421-450

Gonze X, Allan DC, Teter MP (1992) Dielectric tensor, effective charges, and phonons in α-quartz by variational density-functional perturbation theory. Phys Rev Lett 68:3603-3606

Gordon RG, Kim YS (1972) Theory for the forces between closed-shell atoms and molecules. J Chem Phys 56:3122-3133

EBSCOhost - printed on 2/13/2023 4:48 AM via . All use subject to https://www.ebsco.com/terms-of-use

Harrison WA. (1980) Electronic Structure and the Properties of Solids: The Physics of the Chemical Bond. W.h. Freeman and Company, San Francisco

Hatch DM, Ghose S (1991) The α-β phase transition in cristobalite, SiO_2. Phys Chem Min 17:554-562

Hemley RJ. (1987) Pressure dependence of Raman spectra of SiO_2 polymorphs: α-quartz, coesite, and stishovite. In: Manghnani MH, Syono Y (eds) High-Pressure Research in Mineral Physics. Terra Scientific, Tokyo, p 347-359.

Hemley RJ, Jackson MD, Gordon RG (1987) Theoretical study of the structure, lattice dynamics, and equations of state of perovskite-type $MgSiO_3$. Phys Chem Min 14:2-12

Hemley RJ, Mao H, Chao ECT (1986) Raman spectrum of natural and synthetic stishovite. Phys Chem Min 13:285-290

Hofmeister AM, Xu J, Akimoto S (1990) Infrared spectroscopy of synthetic and natural stishovite. Am Min 75:951-955

Hohenberg P, Kohn W (1964) Inhomogeneous electron gas. Phys Rev B 136:864-871

Hoover WG. (1986) Molecular Dynamics. Springer-Verlag, New York

Ivanov OV, Maksimov EG (1992) Microscopic calculations of phonons in polarizable-ion approach. Phys Rev Lett 69:108-111

Jackson MD, Gordon RG (1988) MEG investigation of low pressure silica--shell model for polarization. Phys Chem Min 16:212-220

Jolly LH, Silvi B, D'Arco P (1994) Periodic Hartree-Fock investigation of the stishovite $CaCl_2$-like phase transition of silica. J de Chime Phys Phys -Ch Biol 90:1887-1895

Keskar NR, Chelikowsky JR (1992) Structural properties of nine silica polymorphs. Phys Rev B 46:1-13

Keskar NR, Troullier N, Martins JL, Chelikowsky JR (1991) Structural properties of SiO_2 in the stishovite structure. Phys Rev B 44:4081-4088

Kingma KJ, Cohen RE, Hemley RJ, Mao H-K (1993) Compression of stishovite: Evidence for anomalous behavior from low frequency Raman spectra. EOS Trans Am Geophys Union 74:676

Kingma KJ, Meade C, Hemley RJ, Mao H, Veblen DR (1993) Microstructural observations of α-quartz amorphization. Science 259:666-669

Kobayashi K, Kokko K, Terakura K, Matsui Y. (1993) First-principles molecular dynamics study of pressure induced structural phase transition of silica. In: Doyama M, Kihara J, Tanaka M, Yamamoto R (eds) Computer Aided Innovation of New Materials II. Elsevier, p 121-124.

Kohn W, Sham LJ (1965) Self-consistent equations including exchange and correlation effects. Phys Rev A 140:1133-1140

Koster GF. (1957) Space groups and their representations. In: Seitz F, Turnball D (eds) Solid State Physics. Academic Press, New York, p 173-254.

Kramer GJ, Farragher NP, van Beest BWH, van Santen RA (1991a) Interatomic force fields for silicas, aluminophosphates, and zeolites: Derivation based on ab initio calculations. Phys Rev B 43:5068-5080

Kramer GJ, van Beest BWH, Santen RA (1991b) Relation between crystal symmetry and ionicity in silica polymorphs. Nature 351:636-638

Lacks DJ, Gordon RG (1993) Crystal structure calculations with distorted ions. Phys Rev B 48:2889-2908

Lasaga AC, Gibbs GV (1987) Applications of quantum mechanical potential surfaces to mineral physics calculations. Phys Chem Min 14:107-117

Lasaga AC, Gibbs GV (1988) Quantum mechanical potential surfaces and molecular clusters I. STO-3G and 6-31G* results. Phys Chem Min 16:29-41

Lasaga AC, Gibbs GV (1991) Quantum mechanical Hartree-Fock potential surfaces and calculations on minerals. Phys Chem Min 17:485-491

Lee C, Gonze X (1994) Lattice dynamics and dielectric properties of SiO_2 stishovite. Phys Rev Lett 72:1686-1689

Levien L, Prewitt CT, Weidner DJ (1980) Structure and elastic properties of quartz at pressure. Am Min 65:920-930

Liu F, Garofalini SH, King-Smith D, Vanderbilt D (1994) First-principles study of crystalline silica. Phys Rev B 49:12528-12534

Liu F, Garofalini SH, King-Smith RD, Vanderbilt D (1993) First-principles studies on stuctural properties of b-cristobalite. Phys Rev Lett 70:2750-2753

Matsui Y, Kawamura K. (1987) Computer experimental synthesis of silica with the α-PbO_2 structure. In: Manghnani MH, Syono Y (eds) High Pressure Research in Mineral Physics. Terra/AGU, Tokyo/Washington, DC, p 305-311.

Matsui Y, Matsui M. (1988) Molecular dynamics studies of polymorphism of SiO_2 at high pressures: A possible new cubic polymorph with high density. In: Ghose S, Salje E, Coey JMD (eds) Structural and Magnetic Phase Transitions in Minerals. Springer, New York, p 129-140

Matsui Y, Tsuneyuki S. (1992) Molecular dynamics study of rutile $CaCl_2$ type phase transition of SiO_2. In: Syono Y, Manghnani MH (eds) High-Pressure Research: Application to Earth and Planetary Sciences. Terra Scientific/AGU, Washington, DC p 433-439

EBSCOhost - printed on 2/13/2023 4:48 AM via . All use subject to https://www.ebsco.com/terms-of-use

McMillan PF, Hess AC (1990) Ab initio valence force field calculations for quartz. Phys Chem Min 17:97-107

Mcskimin J, Andreatch P, Thurston RN (1965) Elastic moduli of quartz versus hydrostatic pressure at 25° and -195.8°C. J Appl Phys 36:1624-1632

Mehl MJ, Hemley RJ, Boyer LL (1986) Potential induced breathing model for the elastic moduli and high-pressure behavior of the cubic alkaline-earth oxides. Phys Rev B 33:8685-8696

Methfessel M, Rodriguez CO, Andersen OK (1989) Fast full-potential calculations with a converged basis of atom-centered linear muffin-tin orbitals: Structural and dynamic properties of silicon. Phys Rev B 40:2009-2012

Muhlhausen C, Gordon RG (1981) Electron-gas theory of ionic crystals, including many-body effects. Phys Rev B 23:900-923

Nada R, Catlow CRA, Dovesi R, Pisani C (1990) An ab-initio Hartree-Fock study of α-quartz and stishovite. Phys Chem Min 17:353-362

Palmer D (1994) Pressure-induced phhase transition in cristobalite: An X-ray powder diffraction study to 4.4 GPa. Am Min 79:1-8

Parise JB, Weidner DJ, Yeganeh-Haeri A, Jorgensen JD, Saltzberg MA (1994) Pressure-induced phase transition and pressure dependence of crystal structure in low (α) and Ca/Al-doped cristobalite. J Appl Phys 75:1361-1367

Park KT, Terakura K, Matsui Y (1988) Theoretical evidence for a new ultra-high pressure phase of SiO_2. Nature 336:670-672

Pauling L. (1960) The Nature of the Chemical Bond. Cornell University Press, Ithaca, New York

Pickett WE (1985) Density functionals in solids I. Ground state. Comments Solid State Phys 12:1-15

Pisani C, Dovesi R, Roetti C. (1988) Hartree-Fock ab Initio Treatment of Crystalline Systems. Springer, New York

Pluth JJ, Smith JV, Faber J (1985) Crystal structure of low cristobalite at 10, 293, and 473 K: Variation of framework geometry with temperature. J Appl Phys 57:1045-1049

Post JE, Burnham CW (1986) Ionic modeling of mineral structures and energies in the electron gas approximation: TiO_2 polymorphs, quartz, forsterite, diopside. Am Min 71:142-150

Price GD, Wall A, Parker SC (1989) The properties and behavior of mantle minerals: a computer-simulation approach. Phil Trans R Soc London A 328:391-407

Purton J, Jones R, Catlow CRA, Lesie M (1993) Ab initio potentials for the calculation of the dynamical and elastic properties of α-quartz. Phys Chem Min 19:392-400

Purton J, Jones R, Heggie M, Oberg S, Catlow CRA (1992) LDF pseudopotential calculations of the α-quartz structure and hydrogarnet defect. Phys Chem Min 18:389-392

Ross NL, Shu JF, Hazen RF, Gasparik T (1990) High-pressure crystal chemistry of stishovite. Am Min 75:739-747

Schluter M, Sham LJ (1982) Density functional theory. Physics Today 35:36-43

Schober H, Strauch D (1993) Investigation of the LO-TO splitting in complex binary crystals. J Phys: Condens Matter 5:6165-6182

Sherman DM (1993) Equation of state and high-pressure phase tranistion of stishovite (SiO_2): ab initio (periodic Hartree-Fock) results. J Geophys Res 98:11865-11873

Silvi B, D'Arco P, Saunders VR, Dovesi R (1991) Periodic Hartree-Fock study of minerals: Tetra-coordinated silica polymorphs. Phys Chem Min 17:674-680

Silvi B, Allave M, Hannachi Y, Philippe D (1992) Pseudopotential periodic Hartree-Fock study of the cristobalite phases of silica and germanium dioxide. J Am Ceram Soc 75:1239-1246

Silvi B, D'Arco P (1990) Periodic pseudopotential Hartree-Fock study of α-quartz structure SiO_2 and GeO_2. J Chem Phys 93:7225-7229

Singh DJ. (1994) Planewaves, Pseudopotentials, and the LAPW Method. Kluwer Academic Publishers, Boston, MA

Somayazulu MS, Sharma SM, Sikka SK (1994) Structure of a new high pressure phase in α-quartz determined by molecular dynamics studies. Phys Rev Lett 73:98-101

Spackman MA, Hill RJ, Gibbs GV (1987) Exploration of structure and bonding in stishovite with Fourier and pseudoatom refinement methods using single crystal and powder X-ray diffraction data. Phys Chem Min 14:139-150

Stixrude L, Bukowinski MST (1988) Simple covalent potential models of tetrahedral SiO_2: Applications to α-quartz and coesite at pressure. Phys Chem Min 16:199-206

Strauch D, Dorner B (1993) Lattice dynamics of α-quartz: I. Experiment. J Phys: Condens Matter 5:6149-6154

Swainson IP, Dove MT (1993) Low-frequency floppy modes in β-cristobalite. Phys Rev Lett 71:193-196

Tossell JA (1980) Theoretical study of structures, stabilities, and phase transitions in some metal dihalide and dioxide polymorphs. J Geophys Res 85:6456-6460

EBSCOhost - printed on 2/13/2023 4:48 AM via . All use subject to https://www.ebsco.com/terms-of-use

Tse JS, Klug DD (1991a) Mechanical instability of α-quartz: A molecular dynamics study. Phys Rev Lett 67:3559-3562

Tse JS, Klug DD (1991b) The structure and dynamics of silica polymorphs using a two-body effective potential model. J Chem Phys 95:9176-9185

Tse JS, Klug DD, Le Page Y (1992) Novel High Pressure Phase of Silica. Phys Rev Lett 69:3647-3649

Tsuchida Y, Yagi T (1989) A new, post-stishovite high-pressure polymorph of silica. Nature 340:217-220

Tsuneyuki S, Matsui Y, Aoki H, Tsukada M (1989) New pressure-induced structural transformations in silica obtained by computer simulation. Nature 339:209-211

Tsuneyuki S, Tsukada M, Aoki H, Matsui Y (1988) First-principles interatomic potential of silica applied to molecular dynamics. Phys Rev Lett 61:869-872

Tsuneyuki S, Aoki H, Tsudaka M, Matsui Y (1990) Molecular-dynamics study of the α to β structural phase transition of quartz. Phys Rev Lett 64:776-779

van Beest BWH, Kramer GJ, van Santen RA (1990) Force fields for silicas and aluminophosphates based on ab initio calculations. Phys Rev Lett 64:1955-1958

Vigasina MF, Guseva EV, Orlov RY (1989) Vibrational spectrum of stishovite and analysis of its crystal lattice dynamics. Sov Phys Solid State 31:747-749

Wei SH, Krakauer H (1985) Local density functional calculation of the pressure induced phase transition and metallization of BaSe and BaTe. Phys Rev Lett 55:1200-1203

Weidner DJ, Bass JD, Ringwood AE, Sinclair W (1982) The single-crystal elastic moduli of stishovite. J Geophys Res 87:4740-4746

Wolf GH, Bukowinski MST (1988) Variational stabilization of the ionic charge densities in the electron-gas theory of crystals: Applications to MgO and CaO. Phys Chem Min 15:209-220

Xu Y, Ching WY (1991) Electronic and optical properties of all polymorphic forms of silicon dioxide. Phys Rev B 44:11048-11059

Yamada Y, Tsuneyuki S, Matsui Y. (1992) Pressure-induced phase transitions in rutile-type crystals. In: Syono Y, Manghnani MH (eds) High-Pressure Research: Application to Earth and Planetary Sciences. Terra Scientific/AGU, Washington, DC, p 441-446.

Yin MT, Cohen ML (1982) Theory of lattice-dynamical properties of solids: Application to Si and Ge. Phys Rev B 26:3259-3272

EBSCOhost - printed on 2/13/2023 4:48 AM via . All use subject to https://www.ebsco.com/terms-of-use

LATTICE DYNAMICAL BEHAVIOR OF ANHYDROUS SILICA

Gérard Dolino and Marcel Vallade

Laboratoire de Spectrométrie Physique
(URA CNRS 008) - Université Joseph Fourier - Grenoble I
B.P. 87 - 38402 Saint-Martin-d'Hères Cedex, France

ABSTRACT

The lattice dynamics properties of silica polymorphs are reviewed. The extensive investigations on quartz, performed at room and low temperature by infrared, Raman, Brillouin and neutron spectroscopy are presented. The soft mode of the $\alpha-\beta$ incommensurate β phase transitions has been measured by Raman scattering in the low temperature α phase, and by inelastic neutron scattering and hyper-Raman effect in the high temperature β phase. The temperature behavior of the other normal modes is described. For the other crystalline silica polymorphs, one can distinguish the low pressure polymorphs (cristobalite, tridymite), with symmetry related transitions from the high pressure phases (coesite, stishovite). Furthermore silica can easily be produced in an amorphous state. Cristobalite has only one transition, of the order-disorder type, while tridymite displays several transitions. All the silica polymorphs are built from SiO_4 tetrahedra, except stishovite (and silica glass at very high pressure), where SiO_6 octahedra are present.

The lattice dynamics of the silica polymorphs has been the subject of many theoretical studies, first with force models and later with empirical potentials (either with two-body or three-body interactions). Recently ab-initio models have been considered, starting either from molecular groups to determine the parameters of the interaction potentials, or taking into account the periodic crystal structure. In some cases, ab initio models give a rather complete description of crystal structure and vibrational properties.

INTRODUCTION

In a crystal at finite temperature, atoms vibrate around their equilibrium positions; lattice vibration modes depend not only on crystal structure and symmetry but also on the interaction potential. Measurements and calculations of lattice vibration are a strong test of our knowledge about crystal structures and atomic interactions. In previous volumes of Reviews in Mineralogy the theoretical and experimental bases of lattice dynamics have been presented: "Infrared and Raman spectroscopy" by McMillan and Hofmeister (1988) and "Inelastic neutron scattering" by Ghose (1988).

Silica polymorphs are very interesting materials for lattice dynamics as one can observe the interactions between Si and O atoms in different crystalline or amorphous structures (presented in other chapters of this book). Furthermore lattice dynamics is closely related to the different kinds of phase transitions:

- *reconstructive transitions*, between polymorphs with different structures; the temperature dependence of the free energy and the phase diagram, are related to lattice vibrations.

- *symmetry-breaking transitions,* existing in the low pressure polymorphs. These structural transitions can be described by Landau theory, and exhibit two typical mechanisms: *displacive transitions* with a soft mode or *order-disorder transitions*. The α-β transitions of quartz and cristobalite, are good examples of these two kinds of transition.

EBSCOhost - printed on 2/13/2023 4:48 AM via . All use subject to https://www.ebsco.com/terms-of-use

A crystal with n atoms in the unit cell has 3n phonon branches (with 3 acoustic branches and 3n-3 optical branches) which can be measured by inelastic neutron scattering, inside the whole Brillouin zone. In contrast, infrared (IR) and Raman spectroscopy can measure vibrational frequencies only for very small wavevectors q. These modes, close to the Brillouin zone center, can be classified according to their transformation properties with respect to the symmetry elements of the crystal point group. The atomic displacements generate a reducible representation which can be decomposed into its irreducible components. The polar optical modes which transform as a vector component P_i are infrared-active. The optical modes which transform as a symmetrical 2nd rank tensor component α_{ij} are Raman active. Symmetry classifications of the vibrational modes of silica polymorphs are given in Table 1.

In this review, we first present experimental results on lattice vibrations of quartz, at room and at low temperatures, and then at high temperature in connection with the α-β transition and the presence of an incommensurate phase. Then we review experimental studies of lattice vibrations in the other low and high pressure crystalline silica phases and in amorphous silica. (We do not review the properties of high pressure transitions and amorphization, presented in another chapter of this book). Finally, theoretical studies of the lattice dynamics of silica polymorphs are presented, separating empirical models from ab-initio calculations.

LATTICE DYNAMICS MEASUREMENTS IN QUARTZ

Introduction

Quartz is the crystalline phase stable in the lower temperature and pressure part of the SiO_2 phase diagram. Its structure is a helicoidal arrangement of corner-sharing SiO_4 tetrahedra, with space group $P3_121$ (or the enantiomorphic one $P3_221$) with three SiO_2 formula units in the cell, giving 27 vibration modes (24 optical and 3 acoustic modes). Upon heating to 847 K, there is a displacive first order phase transition, from the low temperature α phase to the high temperature β phase of space group $P6_222$ (or $P6_422$), always with three SiO_2 groups in the unit cell. Since its discovery in 1889, the α–β transition of quartz has been the subject of continuous interest, recently increased by the observation of an incommensurate phase. This is a good example of a transition with an order parameter, here the rotation of SiO_4 tetrahedra, well described by Landau theory (Dolino, 1988; Dolino and Bastie, 1994).

Owing to the large size and excellent quality of quartz samples, many optical properties of crystals have been discovered in quartz. Optical studies of quartz vibrational properties have also a long history, starting with the infrared (IR) studies of Nichols (1897). The first observation of Raman scattering in a crystal was performed in quartz, by Landsberg and Mandelstham (1928), a few months after the discovery of the Raman effect in liquids. The Brillouin effect was discovered in quartz by Gross (1930). Finally, the first observation of a soft mode was performed in quartz: Landsberg and Mandelstham (1929) described briefly the decreasing intensity and the increasing width of the 207 cm^{-1} line, upon heating in the α phase and its disappearance in the β phase; Raman and Nedungadi (1940) observed the decreasing frequency of this mode upon heating in the α phase and suggested a relation to the mechanism of the α–β transition. This was the first observation of a soft mode.

In this section, we describe the results of vibrational studies performed at room and low temperatures. Then, we present the high temperature studies of the α-β soft mode, by Raman measurements in the α phase and by neutron and hyper-Raman measurements in

EBSCOhost - printed on 2/13/2023 4:48 AM via . All use subject to https://www.ebsco.com/terms-of-use

EBSCOhost - printed on 2/13/2023 4:48 AM via . All use subject to https://www.ebsco.com/terms-of-use

Table 1. Symmetry classification of the optical modes of silica polymorphs.

Phase	Space group	+Number of modes	(R)	(R, IR)*	(IR)	(Silent)
α-quartz	$P3_121$	27	$4A_1$	+ 8E*	+ $4A_2$	
β-quartz	$P6_222$	27	$1A_1+4E_2$	+ $4E_1$*	+ $2A_2$	+ $3B_1$ + $2B_2$
α-cristobalite	$P4_12_12$	36	$4A_1+5B_1$ + $4B_2$	+ 8E*	+ $4A_2$	
β-cristobalite	$Fd\bar{3}m$	18	$1F_{2g}$		+ $2F_{1u}$	+ $1A_{2u}$ + $1E_u$ + $1F_{2u}$
Tridymite	$P6_3/mmc$	36	$1A_{1g}$ + $1E_{1g}$ + $2E_{2g}$		+ $3A_{2u}$ + $4E_{1u}$	+ $1A_{1u}$ + $2B_{1g}$ + $1B_{1u}$ + $3B_{2u}$ + $4E_{2u}$
Coesite	C2/c	72	16Ag + 17 Bg		+ 18 A_u + 18 B_u	
Stishovite	$P4_2/mnm$	18	$1A_{1g}$ + $1B_{1g}$ + $1B_{2g}$ + 1Eg		+ $1A_{2u}$ + 3 E_u	+ 1 A_{2g} + $2B_{1u}$

Notes A and B modes are nondegenerate; E modes and F modes are doubly and triply degenerate respectively; (R) Raman active; (IR) Infrared active.
+ The number of modes includes the 3 acoustic modes.

Table 2. Symmetry classification and frequencies (in cm^{-1}) of vibration modes in α– and β–quartz

α-phase			β-phase			α-phase			β-phase		
$4A_1$ (R)			$1A_1$ (R) + $3B_1$ (*)			8E (R, IR)			$4E_1$ (R, IR) + $4E_2$ (R)		
ω			ω			ω_t	ω_l	S	ω_t	$\omega_l(E_1)$	S(c)
207			*			128		0.0027(b)	96	96	?
356			*			265		0.05 (b')	E_2 245		
464			459			394	401	0.33	E_2 404		
1085			*			450	509	0.82	423	494	1.30
$4A_2$ (IR)			$2A_2$ (IR) + $2B_2$ (*)			697		0.018	E_2 685		
ω_t	ω_l (a)	S	ω_t	ω_l	S (c)	795	807	0.11	784	797	0.14
364	388	0.68	*			1072	1235	0.67	1065	1235	0.70
495	548	0.66	435	527	1.58	1162		0.01	E_2 1172		
778	790	0.10	*								
1080	1239	0.67	1061	1227	0.73						

Notes ω, mode frequencies ; ω_t , ω_l: transverse and longitudinal frequencies ; S: IR oscillator strength.
α phase :Raman measurements of Scott and Porto (1967), IR results from Spitzer and Kleinman (1961).
(a) calculated by Merten (1968). (b) at 1.5 K from Loewenstein et al. (1973), (b') from Russel and Bell (1967).
β phase : from Fries and Claus (1973) ; (c) from Gervais and Piriou (1975); * silent B modes.

the β phase. The high temperature behavior of the other vibrational modes is described and finally, some specific results obtained in the incommensurate phase are reported. But first, in Table 2, we give the measured optical mode frequencies in the α and in the β phases. Owing to the absence of a center of symmetry, α phase E modes and β phase E1 modes are both Raman and IR active. The observed LO-TO splittings are also given: four of the eight E modes show visible LO-TO splittings at room temperature. The correspondence with the four Raman and IR active E_1 modes of the β phase is not complete: the 128 cm^{-1} mode, which becomes an E_1 mode in the β phase, shows no apparent LO-TO splitting, while the split 394/401 cm^{-1} mode becomes an IR inactive E_2 mode in the β phase.

Infrared studies

References to the earlier IR studies can be found in Saksena (1940), Simon and McMahon (1953), Spitzer and Kleinman (1961), McCarty (1963) and Farmer (1974). For strong IR modes, the best results are obtained by measuring the reflectivity of single crystals using polarized light. High reflectivity is observed between the LO and TO frequencies of IR active modes. These features can be calculated from the complex dielectric constant ε (ω) given by a classical dispersion formula

$$\varepsilon(\omega) = \varepsilon_\infty + \sum_{j=1}^{N} \frac{S_j \omega_j^2}{\omega_j^2 - \omega^2 + i\omega\gamma_j} \tag{1}$$

where ε_∞ is the value for frequency $\omega \to \infty$; S_j, ω_j and γ_j are the oscillator strength, frequency and damping of the j^{th} mode [we recall that the TO frequencies correspond to $\varepsilon(\omega) \to \infty$, while LO frequencies correspond to $\varepsilon(\omega) = 0$]. In quartz, IR reflection measurements performed by Spitzer and Kleinman (1961), Gervais and Piriou (1975), whose results are plotted below in Figure 5, and by Camassel et al. (1988), are all in fair agreement with the results of Table 2. (The dip at 509 cm^{-1}, often observed for the A_2 mode reflection, is due to a contamination by the LO mode of E symmetry, as shown in the detailed studies of Onstott and Lucovsky (1970) and of Duarte et al. (1987)). The agreement with the classical dispersion formula is not very good, and in addition to the 509 cm^{-1} contamination, Spitzer and Kleinman (1961) introduced supplementary resonances to fit the high frequency side of the broad reflection bands. On the other hand, Gervais and Piriou (1975) used a factorized formula for the dielectric constant ε(ω), with four parameters per mode

$$\varepsilon(\omega) = \varepsilon_\infty \prod_{i=1}^{N} \frac{\left(\omega_{lj}^2 - \omega^2 + i\omega\gamma_{lj}\right)}{\left(\omega_{tj}^2 - \omega^2 + i\omega\gamma_{tj}\right)} \tag{2}$$

As shown in Figure 5, this formula gives a good fit to the experimental data. The weak low frequency E modes (128 and 265 cm^{-1}) were measured at room temperature by Russell and Bell (1967) and at low temperature by Plendl et al. (1967), Loewenstein et al. (1973) and by Gerbaux and Hadni (1982). Ocana et al. (1987) studied the modification of IR absorption spectra in small crystal powders.

High pressure IR studies of quartz were performed by Ferraro et al. (1972), Wong et al. (1986), who observed a frequency decrease of some E lines at high pressure, Velde and Couty (1987) and by Williams et al. (1993).

EBSCOhost - printed on 2/13/2023 4:48 AM via . All use subject to https://www.ebsco.com/terms-of-use

Raman studies

Room and low temperature studies. References to the earlier Raman studies can be found in Saksena (1940) and Krishnamurti (1958). Although the theoretical symmetry classification of quartz vibrational modes was established already by Saksena (1940), the full assignment of α-quartz vibrational modes with LO-TO splittings, given in Table 2, was only proposed by Scott and Porto (1967), after the introduction of laser light scattering techniques, which increased greatly the efficiency of Raman experiments. Typical room temperature Raman spectra, obtained by Shapiro et al. (1967), in good agreement with the frequencies of Table 2, are shown in Figure 1a for the A_1 modes and in Figure 1b for the E modes. In Figure 1a, in addition to the four A_1 lines (with the soft mode at 207 cm^{-1}), there

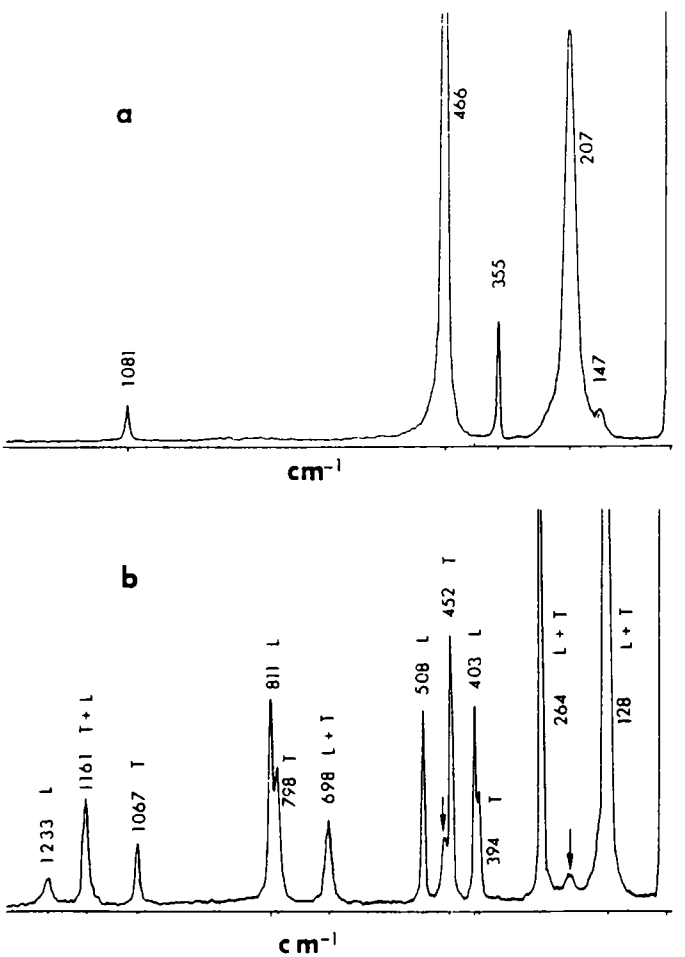


Figure 1. Room temperature Raman spectra of α-quartz: (a) for the A_1 modes; (b) for the E modes. The arrows indicate polarization leaking from the two intense A_1 modes. [Used by permission of the editor of Phys Rev Letters, from Shapiro et al. (1967), Fig 1, vol. 19, p. 362.]

EBSCOhost - printed on 2/13/2023 4:48 AM via . All use subject to https://www.ebsco.com/terms-of-use

is a supplementary line at 147 cm^{-1}, due to two-phonon scattering (Scott,1968). Among the eight E modes, four modes show visible LO-TO splittings: note the peculiar position of the 1162 cm^{-1} line, between the TO and LO components (at 1072 and 1235 cm^{-1}) of the highest frequency E mode. As discussed by Gervais and Piriou (1975), Raman spectra of quartz have been measured in several experiments, confirming the frequencies of Table 2. Zakharova et al. (1975) have performed detailed measurements of line widths. More recently, all the optical modes of quartz have been observed by Denisov et al. (1986) using the hyper-Raman effect.

Upon cooling to low temperature, Raman line widths are reduced and high resolution studies can be performed (Pine and Tannenwald, 1969). Pine and Dresselhaus (1969) observed a shift of the 128 cm^{-1} E line, proportional to the wavevector q, for phonons propagating along the OZ axis. This is a direct consequence of the helicoidal structure of quartz, which induces a linear dispersion of E modes, also observed on the neutron dispersion curves of Figure 2. Another way of obtaining further information on vibrational modes is by isotopic substitution: Sato and McMillan (1987) have measured the shifts of Raman and IR lines produced by substitution of ^{30}Si for ^{28}Si and of ^{18}O for ^{16}O.

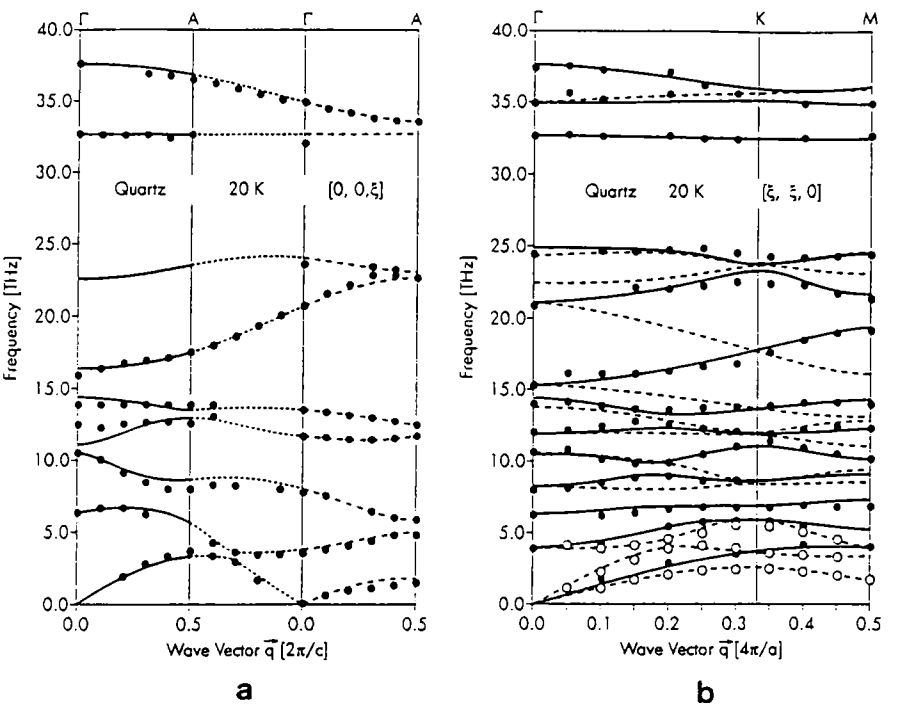


Figure 2. Dispersion curves of α-quartz at 20 K; (a) along Γ-A direction (Z axis); (b) along Γ-K-M direction (X axis). Circles: experimental frequencies; curves: theoretical results from a shell model; full curve: symmetric representation; dashed curve: antisymmetric representation. [Used by permission of the editor of J Phys: Condens Matter, from Strauch and Dorner (1993), Figs. 2 and 3, vol. 5, p. 6152.]

EBSCOhost - printed on 2/13/2023 4:48 AM via . All use subject to https://www.ebsco.com/terms-of-use

Uniaxial stress. Further information on vibrational modes, can be obtained by studying the Raman line on application of a symmetry breaking uniaxial stress, a technique used by Harker et al. (1970) at room temperature. Higher resolution results can be obtained at low temperature, as shown by several experiments performed in the same laboratory (Tekippe et al., 1973; Grimsditch et al., 1977; Briggs and Ramdas, 1977). They observed linear shifts of A_1 line frequencies and linear splittings of all E lines as a function of stress giving a determination of IR mode strenght.

High pressure. Vibration mode frequencies are modified by the application of hydrostatic pressure. High pressure Raman studies of quartz, up to 4 GPa, started with Asell and Nicoll (1968). They observed that the frequencies of several lines increase with pressure, with the largest effect (18 cm^{-1}/GPa) for the 207 cm^{-1} soft mode. They also noted the inverse relation between pressure and temperature frequency shifts. Similar Raman studies have been performed by Dean et al. (1982), Hemley (1987) and Jayaraman et al. (1987). In this last study, going to 20 GPa, non linear variations of frequency with pressure were observed, in particular for the soft mode. Raman studies have also been performed in relation with high pressure amorphization, a phenomenon presented in another chapter of this book. Quartz is also amorphized by neutron irradiation, an effect which has been studied by Raman effect (Zubov and Osipova, 1977).

LO-TO splittings and polaritons. In a crystal, there are short range interactions (which are often represented by force constants) and long range electric interactions. For degenerate E type modes, the degeneracy can be lifted by these electric interactions, and longitudinal and transverse optical modes are found with different frequencies. In fact this LO-TO splitting arises because IR and Raman measurements are performed at a small but finite wavevector q (and not at the zone center with $q = 0$). At very small q, polar phonons are coupled with electromagnetic modes, giving rise to "polariton" modes with anisotropic frequencies variations.

A review of these effects in quartz has been published by Merten and Borstel (1981). Several observations of small-q polariton have been reported: Scott et al. (1967) observed, at room temperature, the polaritons associated to the E modes at 1072, 795 and 450 cm^{-1}. Fries and Claus (1973) observed similar polariton behavior in the β phase of quartz. Polaritons have also been observed with non linear optical techniques in the α phase, by Biraud-Laval et al. (1976), Chapet-Rousseau et al. (1988) and Bogani et al. (1990).

The anisotropic variations of LO mode frequencies, were studied by Onstott and Lucovsky (1970) with IR and by Shapiro and Axe (1972) with Raman measurements. In contrast, the ordinary vibration E modes keep a TO character and have no anisotropic dispersion. These angular variations of LO-TO splitting are in good agreement with the theoretical results of Loudon (1968) and Merten (1968).

Non-linear optics. The high intensity of laser beams has opened the field of non-linear optics, with the possibility of mixing different light beams and exciting coherent vibrational modes. Stimulated Raman effects for the 128 cm^{-1} E mode and for the 466 cm^{-1} A_1 mode were observed at low temperature by Tanenwald and Weinberg (1967) and Aref'ev et al. (1968). This last work also reported non linear generation of IR, an effect also observed with stimulated polaritons (Biraud-Laval and Chartier, 1969).

The low temperature variation of the damping of the 466 cm^{-1} A_1 line has been measured (Gale and Lauberau, 1983), as well as the temperature variation of the stimulated

EBSCOhost - printed on 2/13/2023 4:48 AM via . All use subject to https://www.ebsco.com/terms-of-use

threshold for the 128 cm^{-1} E line, taking into account the effect of polariton dispersion (Amler et al., 1993).

Brillouin measurements of acoustic modes

The three acoustic modes can be measured in Brillouin scattering (with frequency shifts of the order of 1 cm^{-1}) and by inelastic neutron scattering for higher frequency. The complete Brillouin spectrum of quartz with one longitudinal acoustic (LA) and two transverse acoustic (TA) modes, was obtained in a laser experiment by Shapiro et al. (1966). Stimulated Brillouin effects in quartz were observed by Chiao et al. (1964).

Dispersion curves measurements by inelastic neutron scattering

A full study of dispersion curves inside the Brillouin zone is possible only by inelastic neutron scattering, an experiment first performed in quartz by Elcombe (1967), who measured the seven lower frequency modes along the Z axis. She used an ionic model to calculate dispersion curves. Dorner at al. (1980) measured the six lower frequency modes in the XY plane, while Joffrin et al. (1980) performed a detailed measurement of the three acoustic modes along the Z axis, in relation with the phenomena of acoustical rotation. Strauch and Dorner (1993) presented recently a rather complete investigation of all 27 vibrational modes of quartz, along Z and X axis, as shown in Figure 2. Along the Z axis, the results were plotted in an extended zone, which shows explicitly the linear dispersion of doubly degenerate E modes at small q. A remarkable feature is the strong dispersion of some high frequency modes, attributed to electrostatic effects. The soft mode is identified as the mode at 7 THz, with eigenvector similar to the atomic displacements of the α-β transition.

Soft mode in the α phase: Raman studies

After the work of Raman and Nedungadi (1940), the softening of the 207 cm^{-1} mode was observed again by Narayanaswamy (1948). However, it was only with the use of laser techniques that Shapiro et al. (1967) were able to observe the full behavior of the soft mode in the α phase: Figure 3 shows the interaction of the 207 cm^{-1} soft mode with the supplementary line at 147 cm^{-1}. The presently accepted interpretation of these features was proposed by Scott (1968): the 147 cm^{-1} line is a two-phonon mode coming from the lower transverse acoustic mode (TA_1), at the zone boundary, which is coupled to the 207 cm^{-1} soft mode. With increasing temperature, there is an anticrossing of the soft mode and of the two-phonon mode, which exchange their positions: at high temperature, the soft mode is the lower frequency line, decreasing to 30 cm^{-1} at the α-β transition while the two-phonon line is observed around 160 cm^{-1} and is always present in the β phase. (Similar effects are observed at the α-β quartz transition of $AlPO_4$ (Scott, 1970; 1974)).

The results of Shapiro et al. (1967, 1968) have been confirmed by several studies (Laulicht et al., 1972; Scott, 1974; Shigenari et al., 1980; Berge et al., 1984b; Gorelik et al., 1987). Anik'ev et al. (1984) have made further theoretical studies of the two-phonon mode. No value of the soft mode frequency smaller than 30 cm^{-1} has been observed. However the exact variation of the soft mode frequency ω_0 as a function of the temperature is not clear: several papers have used a "critical" formula $\omega_0 = a(T-T^*)^\gamma$ (in mean field theory, $\gamma = 0.5$ for a second order transition, where $\omega_0 = 0$ at $T = T^*$) . In their first paper, where the discontinuous character of the transition was not mentioned, Shapiro et al. (1967) gives $\gamma = 0.25$ with T^* close to the transition temperature T_c, for the coupled low frequency branch. Scott (1968) gives $\gamma = 0.33$ for the temperature dependence of the bare

EBSCOhost - printed on 2/13/2023 4:48 AM via . All use subject to https://www.ebsco.com/terms-of-use

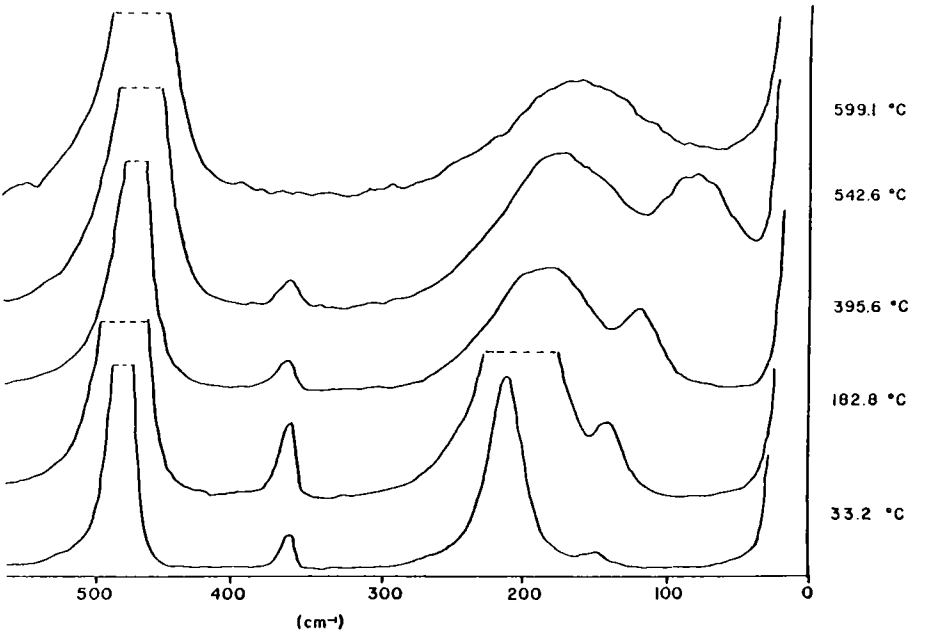


Figure 3. Variations of the low frequency A_1 modes in quartz. Upon heating from room temperature to the β phase, there is an anti-crossing interaction between the 207 cm^{-1} soft mode and the 147 cm^{-1} two-phonon mode. [Used by permission of the editor of Phys Rev Letters, from Shapiro et al.. (1967), Fig. 2, vol. 19, p. 362.]

soft mode. In another paper using a different coupling formula, Scott (1974) gives $\gamma = 0.31$ but with $T^* = T_c + 5$ K so that at the transition temperature T_c, the soft mode frequency ω_0 has a finite value around 30 cm^{-1}. Finally Shigenari et al. (1980) gives $\gamma = 0.2$ for the coupled low frequency branch, also with $T^* = T_c + 5$ K. However, as discussed for the order parameter variation of quartz (Bachheimer and Dolino, 1975), these power formulae have no fundamental meaning for a first order phase transition and are only numerical representations of a discontinuous mean field behavior.

Soft mode in the β phase

Neutron studies. Symmetry considerations show,that in the β phase, the soft mode has a B_1 character and is Raman and IR inactive. Then the soft mode can be observed only by inelastic neutron scattering or by hyper-Raman effect. The first technique was used by Axe and Shirane (1970). The soft mode, observed at the zone center, remains overdamped even at 1060 K, the highest temperature investigated. However the temperature variation of the integrated scattering intensity (proportional to ω_0^{-2}) has a mean field behavior, corresponding to $\omega_0^2 = a(T - T_0)$. Their value of $T_0 = T_c - 10$ *K*, is consistent with the first order nature of the α-β transition. They also measured the eigenvectors of the zone center soft mode, in the β phase and at room temperature, which were found similar to the atomic displacements of the α-β transition. They observed a low frequency branch along the OY axis (<q 0 0> direction of the reciprocal space) resulting from the interaction of the soft mode with a transverse acoustic (TA_2) mode. Boysen et al. (1980) observed the interaction

EBSCOhost - printed on 2/13/2023 4:48 AM via . All use subject to https://www.ebsco.com/terms-of-use

of this low frequency branch with the lowest acoustic mode (TA_1), around the transition temperature.

New neutron scattering studies were started after the discovery of the incommensurate phase (Berge et al., 1986). The gradient interaction, introduced by Aslanyan and Levanyuk (1979) to explain the origin of the incommensurate phase, induces an anisotropic coupling between the soft mode, the TA_2 and the LA modes. Bethke et al. (1987) observed in the XY plane the anisotropy of the soft mode, of the TA_2 and of the LA modes, produced by this coupling. A complete test of the theoretical model was obtained in high resolution inelastic neutron scattering experiments (Dolino, 1990; Dolino et al., 1992; Vallade et al., 1992a). At 1250 K, an underdamped soft mode was observed at 1 THz (i.e. 33 cm^{-1}) at the zone center, as shown in Figure 4. Along <q 0 0 > there is a strong coupling of the soft mode with the TA_2 mode, producing an anticrossing with a large gap of 0.7 THz. With decreasing temperature, the zone center soft mode frequency ω_0 decreases with a mean field behavior ($\omega_0^2 = a\,(T - T_0)$ with $T_0 = T_c - 4\ K$) so that at the transition temperature T_c, $\omega_0 \sim 0.1$ THz. Along <q 0 0>, the mixed low frequency branch softens and a dip appears at $q \simeq 0.05$, around T_c +20 K where this branch becomes overdamped. Upon decrasing further the temperature, the frequency of this mixed branch becomes zero for $q = 0.033$ at a temperature $T_i = T_c + 1.5$ K, where the incommensurate phase appears. Vallade et al. (1992a) have shown that this behavior of the soft mode is in good agreement with the gradient coupling model. They also give a more microscopic model of rigid tetrahedra rotations, showing that a whole vibration band along <q 0 0> has a low frequency.

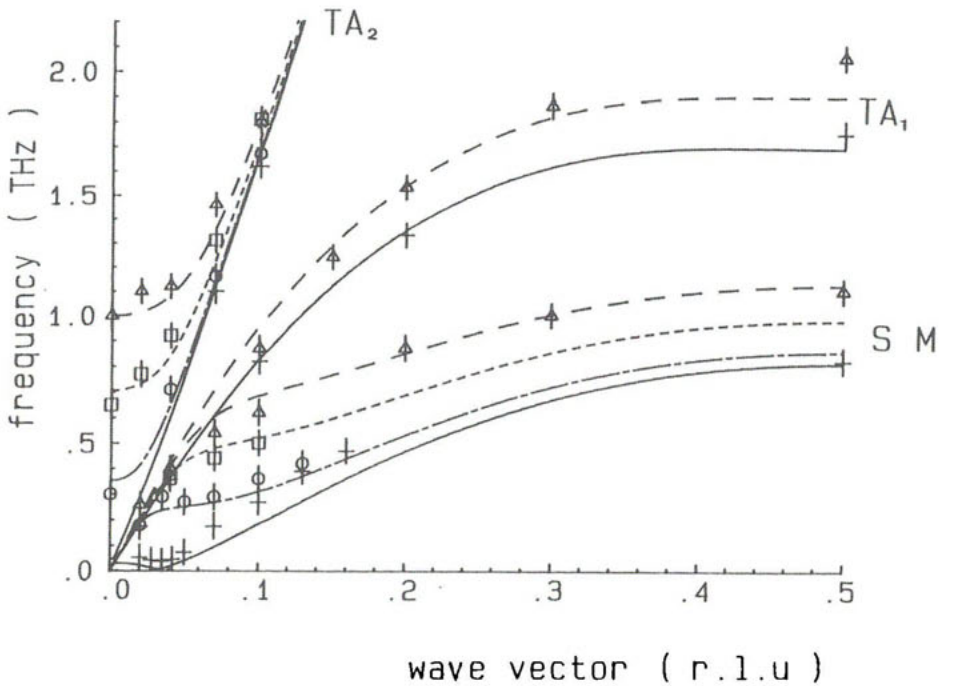


Figure 4. Temperature variations of the dispersion curves of the three lower frequency modes in the β phase of quartz at: Δ: 1250 K; □: 1050 K; O: 900 K; +: T_i = 847 K. The experimental points were obtained from inelastic neutron scattering measurements; the curves were calculated from a model of nearly rigid tetrahedra. [From the authors' work.]

EBSCOhost - printed on 2/13/2023 4:48 AM via . All use subject to https://www.ebsco.com/terms-of-use

Hyper-Raman study. The β phase soft mode can be observed (at the zone center) by hyper-Raman effect, an experiment performed by Tezuka et al. (1991). Above Tc + 100 K the soft mode is underdamped, while it is overdamped below. The soft mode frequency follows a mean field behavior ($\omega_o^2 = a(T - T_o)$ with $T_o = T_c - 5K$.) There is rather good agreement between hyper-Raman and neutron results. Both experiments show the displacive character of the β phase, at least at high temperature. Closer to the transition where the soft mode is heavily overdamped, the distinction between displacive and order-disorder transition is less clear and within a few K of the transition, the possibility of non classical effects remains an open question. One must also note the dissymetry of soft mode frequency variations in the α and in the β phases: in a temperature range of 400 K, the zone center soft mode increases from about 3 to 33 cm^{-1} in the β phase and from 30 to 200 cm^{-1} in the α phase. This dissymmetry is probably the consequence of the large value of the SiO_4 rotation in the α phase (16° at room temperature).

Temperature-dependence of other vibrational modes

Raman measurements. The temperature variations of the other Raman lines have been measured several times, either in the α phase or in the β phase (Narayanaswamy, 1948; Shapiro et al., 1968; Bates and Quist, 1972; Fries and Claus, 1973; Gillet et al., 1990). Their results are in agreement with symmetry considerations, with three of the four A_1 lines vanishing in the β phase. However the 355 cm^{-1} A_1 mode has been observed, with a small intensity, in the β phase 2K above the transition (Shapiro, 1968; Berge, reported in Salje et al., 1992). A detailed discussion of the Raman spectra in the β phase was given by Bates and Quist (1972). Their vibration frequencies are in fair agreement with those given in Table 2, from the work of Fries and Claus (1973) who observed the LO-TO splittings of three of the four E_1 modes (only the 96 cm^{-1} E_1 mode shows no visible LO-TO splitting). In general the frequencies of the Raman modes decreases slightly (less than 10 cm^{-1}) upon heating from room temperature to the β phase. However, in addition to the soft mode, some low frequency modes (at 128, 265 and 450 cm^{-1}) show large temperature decrease, a result which is consistent with their large increase under high pressure (Asell and Nicol, 1968; Jayaraman et al., 1987). However the frequencies of the E modes at 394 and 1162 cm^{-1} increase upon heating. These temperature and pressure variations of mode frequencies can be related to the volume variation by introducing positive and negative Gruneisen coefficients. However there is also a direct effect of anharmonicity, discussed by Gillet et al. (1990).

Infrared measurements. High temperature IR spectra of quartz have been measured by Simon and McMahon (1953) and by Gervais and Piriou (1975), whose results are shown in Figure 5: the full lines are fitted curves, given by the four parameter formula of equation (2) for $\varepsilon(\omega)$. In general, frequencies decrease upon heating, except for the 364 cm^{-1} A_2 mode and for the 394 cm^{-1} E mode, which increase. The dampings of several modes increase in the α phase close to the transition, while the intensities of the modes, which become IR inactive in the β phase, decrease upon heating in the α phase and disappear in the β phase (Gervais et al., 1975; Dolino et al., 1983). Recently Salje et al. (1992) have followed the disappearance of IR lines at the α-β transition, and concluded on the absence of a disordered structure in the β phase. The temperature variations of Raman and IR mode frequencies and intensities in the α phase are related to order parameter variations (Gervais and Piriou, 1975). In the β phase only purely anharmonic effects are present and smaller variations are expected (with the exception of the soft mode).

Brillouin measurements. Close to the α-β transition, Shapiro et al. (1968) have mesured the variations of Brillouin spectra. There is a continuous decrease of the

EBSCOhost - printed on 2/13/2023 4:48 AM via . All use subject to https://www.ebsco.com/terms-of-use

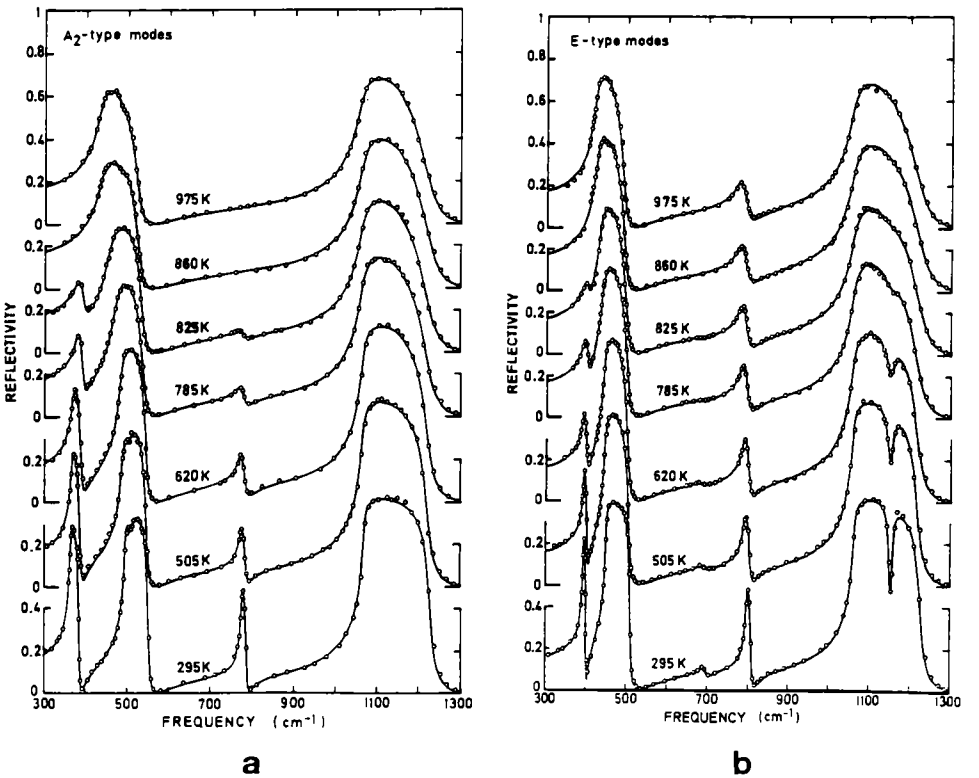


Figure 5. Temperature variations of the infrared reflectivity of quartz: (a) for the A_2 modes; (b) for the E modes. The curves are obtained from $\varepsilon(\omega)$ given by equation 2. [Used by permission of the editor of Phys Rev, from Gervais and Piriou (1975), Figs. 1 and 2, vol. 11, p. 3945.]

longitudinal Brillouin line frequency in the α phase, followed by a discontinuous increase above the transition. On cooling, the transition to the α phase occurs at a temperature lower by 1 K, with a smoother variations of this Brillouin line frequency, and an anomalous increase of the damping; (in fact the anomalous behavior upon cooling is due to the presence of the incommensurate phase). Pelous and Vacher (1976) measured the temperature variation of the frequency and damping of the longitudinal modes associated with the elastic constants C_{11} and C_{33}; Unoki et al. (1983) have measured several elastic constants up to 650°C. Anomalous damping of the TA_2 mode related to the incommensurate phase has been observed by Berge et al. (1984).

Elastic light scattering. A spectacular phenomenon, discovered by Yakolev et al. (1956), is the strong light scattering occuring just at the α-β transition, which was first interpreted as a critical opalescence at a continuous transition. However Shapiro et al. (1967) observed that this light scattering is static and that the transition is discontinuous, thereby excluding the critical opalescence explanation. More recent studies have shown that the light scattering is anisotropic (occuring only in the direction perpendicular to the Z axis) and that two different scattering phenomena occur at small angle and at large angle (Dolino,

EBSCOhost - printed on 2/13/2023 4:48 AM via . All use subject to https://www.ebsco.com/terms-of-use

1979). These phenomena are probably related to the presence of the incommensurate phase, although no detailed explanation has been proposed.

Low frequency spectra in the incommensurate phase. Between the classical α and β phases, there is an incommensurate phase in a small temperature interval of 1.5 K, which has recently been much studied (Dolino, 1988; Dolino and Bastie, 1994). Following the model of Aslanyan and Levanyuk (1979), the origin of the incommensurate phase is due to the coupling between the soft mode and the TA_2 acoustic mode, shown in Figure 4. Here we report the results of low frequency light scattering measurements around the α-incommensurate-β transitions (Berge et al., 1984b; Abe et al., 1989). Already in α and β phases, a broad hump is observed close to the transition, in a frequency range of ± 20 cm^{-1}. In the incommensurate phase, the low frequency intensity increases and a sharp feature appears at 7 cm^{-1}. In agreement with more recent measurements (Vallade et al., 1992b) this is interpreted as a contribution from acoustic branches at the position of the incommensurate wave modulation q_0. In the incommensurate phase, the intensity between the Brillouin line and the intensity of the central Rayleigh peak increase; this is due to the contributions of several effects: broad and narrow intrinsic central peaks, effect of incommensurate phase defects (Berge et al., 1984b; Shigenari and Abe, 1989).

Nature of the α-β transition. The displacive or order-disorder nature of the α-β transition has been the subject of many discussions. From X-ray measurements, Young (1962) and Kihara (1993) concluded on an ordered structure for the β phase, while from neutron measurements Wright and Lehman (1981) deduced a disordered structure. A recent NMR study was also interpreted as evidence for a dynamic disorder of the β phase (Spearing et al., 1992). The direct observations of a soft mode in the α and β phases confirm unambiguously the displacive nature of the α-β transition of quartz. However, owing to the large damping of the β phase soft mode close to the transition, it is difficult to distinguish displacive from order-disorder behavior. Indeed large variations are observed in this temperature range in many physical properties as, for example, the elastic constant measurements by Brillouin effect (Shapiro et al., 1968; Berge et al., 1984a), while the observation of the 355 cm^{-1} line above the transition (Shapiro, 1968; Salje et al., 1992) points to the presence of fluctuations with the α phase symmetry. Further theoretical and experimental work is needed to clarify the behavior of quartz just above the α-β transition.

LATTICE DYNAMICS OF OTHER SILICA POLYMORPHS

Introduction

After the extensive results on quartz, we review the more scattered data existing for the other silica polymorphs, presented in the following order:

- *Low pressure polymorphs, cristobalite and tridymite,* have been known for more than a century; they can also be produced by high temperature treatment of silica materials. Upon heating, cristobalite has two symmetry related phases, while several phases have been reported in tridymite.

- *High pressure polymorphs, coesite and stishovite,* first synthetized under high pressure, were later discovered at meteorite impact sites.

- *Amorphous silica,* is easily obtained by quenching silica melt. In addition to the usual low density glass,there is a compacted glass obtained under high pressure.

EBSCOhost - printed on 2/13/2023 4:48 AM via . All use subject to https://www.ebsco.com/terms-of-use

[Keatite, microcrystalline silica and zeolite type silica will not be considered in this chapter.] The symmetry classification of the vibrational modes of these crystalline polymorphs (restricted to the high temperature phase for tridymite) are given in Table 1; however, comparison with experimental results is often difficult, as experiments can be performed only on powders or on very small crystals.

Low pressure polymorphs

Upon heating at atmospheric pressure, the stable SiO_2 phases are tridymite, between 870 and 1470 °C and cristobalite between 1470 °C and the melting temperature of 1720 °C (Frondel, 1962); these phases exist in quenched metastable state at room temperature. The structure of the "ideal" high temperature phase of cristobalite can be obtained from the diamond lattice structure of silicon by placing an oxygen atom in the middle of each Si-Si bond, giving the cubic space group $Fd\bar{3}m$. However in this structure, the Si-O bond length is only 1.54 Å, instead of the normal value around 1.61 Å, and the Si-O-Si angle is 180°, instead of the usual value around 144°. To recover the usual characteristics of the SiO bond, it is necessary to displace O atoms perpendicularly to the Si-Si direction in a disordered way to get the average $Fd\bar{3}m$ symmetry. There is general agreement about the existence of disorder in the β phase of cristobalite, although various models have been proposed, as reviewed by Hatch and Ghose (1991) and by Schmahl et al. (1992). Rings of six SiO_4 tetrahedra are found in the (111) planes of cristobalite; similar rings exist also in tridymite, but with a different stacking, giving a hexagonal space group P63/mmc. The single α-β transition of cristobalite and the various transitions of tridymite are obtained by symmetry breaking SiO_4 rotations, as discussed respectively by Hatch and Ghose (1991) and by Hofmeister et al. (1992).

Cristobalite. The first vibrational studies were performed with powder IR measurements, often with simultaneous measurements on tridymite (Simon and McMahon, 1953; Sevchenko and Florinskaia, 1957; Lippincott et al., 1958; Plendl et al., 1967). A typical IR spectrum of cristobalite, measured at room temperature by Plyusnina et al. (1970) is shown in Figure 6. Three absorption bands (490, 790 and 1100 cm^{-1}) are in the same frequency range as in quartz, while a new characteristic line appears at 620 cm^{-1}. The Raman measurements of Bates (1972b) give high frequency spectra similar to those of quartz, but with a new characteristic line at 416 cm^{-1} which has been used to identify cristobalite in volcanic ash (Gage and Farwell, 1981). Table 3 gives the frequencies obtained by Cherukuri et al. (1985) in their IR and Raman measurements, and gives their symmetry assignments obtained from a valence force model. These results are in fair agreement with the results of Bates (1972b), Etchepare et al. (1978) and Ocana et al. (1987). The recent high pressure IR measurements of Yahagi et al. (1994) show the apparition of two new crystalline phases around 1.5 and 10 GPa. Elastic constants of cristobalite, at room temperature, have been measured by Brillouin spectroscopy (Yeganeh-Haeri et al., 1992) giving a negative Poisson ratio; powder neutron scattering measurements give frequencies of 40 and 85 cm^{-1} for the acoustic modes at the Brillouin zone boundary (Leadbetter, 1969).

In the β phase of cristobalite, with the mean $Fd\bar{3}m$ cubic symmetry, only two IR and one Raman active modes are expected. High temperature IR measurements in the β phase (Simon and McMahon, 1953; Swainson and Dove, 1993) are in agreement with these symmetry requirements, with only two broad bands around 450 and 1100 cm^{-1}; however Gaskell (1967) observed a third weak IR band around 800 cm^{-1}. The Raman measurements of Bates (1972b) show three lines: in addition to the expected F_{2g} mode at 777 cm^{-1}, there is a two-phonon line at 292 cm^{-1} and a supplementary line at 1077 cm^{-1},

EBSCOhost - printed on 2/13/2023 4:48 AM via . All use subject to https://www.ebsco.com/terms-of-use

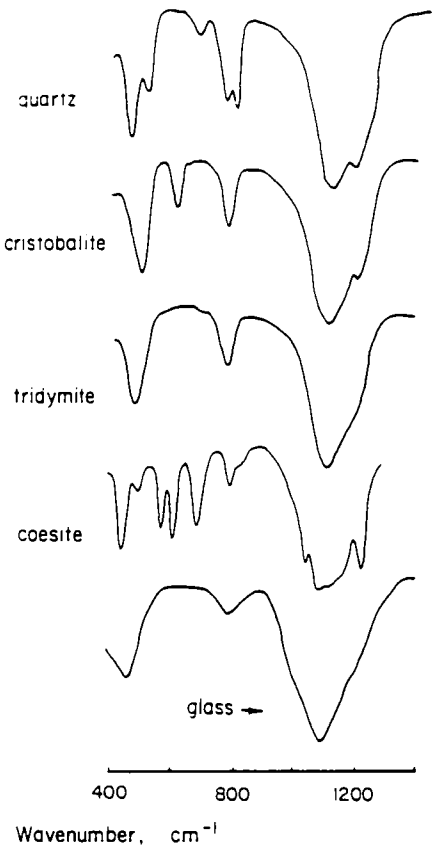


Figure 6. Infrared absorption spectra of silica polymorphs. [Used by permission of the editor of Phys Chem Minerals, from Dowty (1987), Fig. 7, vol. 14, p. 134.]

Table 3. Symmetry classification and frequencies (in cm^{-1}) of vibration modes in the α and β phases of cristobalite.

α- phase			β-phase
$4A_1$ (R)	$5B_1$ (R)	8E (R, IR)	$1\ F_{2g}$ (R)
	94 (a)	147	
233	110 (b)		
374	374	276	
421	783	387	777 (c)
1077	1013 (a)		
		480	
$4A_2$ (IR)	$4B_2$ (R)	618	$2\ F_{1u}$ (IR)
297	288	791	
481	447	1107	450 (d)
709 (a)	783	1195	
1033	1193		1100 (d)

Notes α phase : from Cherukeri et al. (1985); (a) lines not observed, calculated values are given ; (b) from Etchepare et al. (1978).
β phase : (c) from Bates (1973) ; (d) from Gaskell (1967).

EBSCOhost - printed on 2/13/2023 4:48 AM via . All use subject to https://www.ebsco.com/terms-of-use

identified with the IR active F_{1u} line. The supplementary IR and Raman lines have been attributed to disorder effects. Upon heating in the α phase, the IR experiments of Simon and McMahon (1953) and of Swainson and Dove (1993) and the Raman experiment of Bates (1972b) show that the intensity of the lines which become inactive in the β phase decreases, before disappearing at the α-β transition. Only small temperature shifts of Raman lines have been observed, even for the mode at 230 cm^{-1} which, according to Etchepare et al. (1978), corresponds to the atomic displacements of the α-β transition. In agreement with the order-disorder nature of the transition, no soft mode has been observed in cristobalite. Direct evidence of a disordered structure is given by the observation of a strong diffuse electron scattering in the β phase (Hua et al., 1988) and of a weaker one in the α phase (Withers et al., 1989). The dynamic nature of the diffuse scattering in the β phase has recently been demonstrated by the powder neutron measurements of Swainson and Dove (1993). The NMR measurements of Spearing et al. (1992) and of Phillips et al. (1993) are also in favor of a dynamic averaging of the disordered β phase structure.

Tridymite. The first vibrational studies of tridymite were often performed in relation with the cristobalite measurements given above. The IR tridymite spectra of Figure 6, shows the three absorption bands, corresponding to the major absorption bands of quartz and of amorphous silica. Görlich et al. (1983) have observed the modifications of IR spectra in four phases obtained upon cooling from the high temperature phase. Recently Hofmeister et al. (1992) started a new study of the temperature variation of IR spectra in various tridymite phases. They also observed frequency shifts produced by isotopic substitutions and studied the possible symmetry of the different tridymite phases. Raman spectra of tridymite, at room temperature, have been published by Etchepare et al. (1978) and by Gage and Farwell (1981) but with quite different results, showing the variability of tridymite samples. Indeed the main problem with tridymite is the difficulty of identifying the phase under study, as the existence of six phases (one of them incommensurate) have been reported by Xiao et al. (1993), with large variations among different samples. Vibration frequencies of high tridymite have been calculated by Etchepare et al. (1978) and by Della Valle et al. (1991).

High pressure polymorphs

Coesite. This is the stable phase of SiO_2 at intermediate pressure, with a structure built from rings of four interconnected SiO_4 tetrahedra, giving a higher density than for the low pressure polymorphs with rings of six tetrahedra. Owing to the large number (48) of atoms in the unit cell and its low-symmetry space group (C2/c), no classification of the observed vibration modes has been proposed, and only one calculation of vibration frequencies has been reported (Della Valle et al., 1991). IR spectra were obtained by Lippincott et al. (1958), Kieffer (1979) and Williams et al. (1993), who have studied high pressure variations. Raman spectra of coesite have been observed by Sharma et al. (1981), Boyer et al. (1985), Hemley (1987) as a function of pressure (with the observation of a phase transition to another crystalline phase, also observed by Williams et al., 1993), and by Gillet et al. (1990), as a function of temperature. Some observed IR and Raman frequencies are given in Table 4. Elastic constants of coesite have been measured in a Brillouin experiment by Weidner et al. (1977).

Stishovite. This is the silica phase stable at high pressure; it is the only classical SiO_2 phase built from SiO_6 octahedra with the rutile structure of TiO_2 (existing also for SnO_2 and GeO_2). Owing to this simple structure and to the possible existence of phases with SiO_6 octahedra in the earth's interior, the properties of stishovite have been much investigated. The IR spectra of stishovite, measured in several experiments (Sclar, 1962;

EBSCOhost - printed on 2/13/2023 4:48 AM via . All use subject to https://www.ebsco.com/terms-of-use

Table 4.
Vibration frequencies (cm^{-1}) of coesite

IR		R
(a)	(b)	(c)
	140	77
	265	116
	296	151
	337	176
	375	204
	394	269
	420	326
430	438	355
	448	427
490	490	466
557		521
600		
683		661
796		795
813		815
1040		1036
1098		1065
1170		1144
1225		1164

Notes (a) Williams et al. (1993).
(b) Kieffert (1979).
(c) Hemley (1987).

Table 5. Vibration frequencies (cm^{-1}) of stishovite

IR (a)		R (b)
ω_t	ω_l	ω
470	570 E_u	231 B_{1g}
580	700 E_u	589 E_g
650	910 A_{2u}	753 A_{1g}
820	1050 E_u	967 B_{2g}

Notes (a) Hofmeister et al. (1990).
(b) Hemley et al. (1986).

Lyon, 1962; Kieffer, 1979; Von Czarnowski et al., 1987; Hofmeister et al., 1990) are quite different from the spectra of the silica phases with SiO_4 tetrahedra: the high frequency stretching SiO band is now at a lower frequency (between 850 and 1000 cm^{-1}), adjacent to a group of medium frequency lines. Hofmeister et al. (1990) have proposed an analysis of these IR bands, according to the symmetry of the rutile structure, with three E_u and one A_u bands, given in Table 5. Williams et al. (1993) have observed the high pressure shifts of IR lines up to 30 GPa. Raman spectra of stishovite, with the four lines expected from the rutile structure, have been obtained by Hemley et al. (1986b) in synthetic stishovite (see Table 5). In natural samples, they observed an additional broad band (300-500 cm^{-1}) attributed to poor sample quality. Other Raman studies have been performed by Vigasina et al. (1989), Hemley (1987) under high pressure and Gillet et al. (1990) as a function of temperature. Several calculations of vibration frequencies have been published (Striefler and Barsch, 1976; Von Czarnowski et al., 1987; Vigasina et al., 1989; Lee et al., 1994). Elastic constants of stishovite have been measured by Weidner et al (1982) in a Brillouin scattering experiment.

Amorphous silica

Silica can easily be obtained in an amorphous state (a-SiO_2) by quenching from the liquid. This is also an important material for microelectronics, as the best passivation of silicon is obtained with a-SiO_2. An exhaustive discussion of vibrational properties a-SiO_2 has been given by Galeener et al. (1983), to explain the origin of the three major vibration modes observed around 450, 800 and 1000-1300 cm^{-1} in IR, Raman and neutron experiments. The presence of two peaks in the high frequency band was attributed to a LO-

EBSCOhost - printed on 2/13/2023 4:48 AM via . All use subject to https://www.ebsco.com/terms-of-use

TO splitting. Specific features have been observed in a-SiO_2 , in particular by Raman spectroscopy :

- Low frequency excitations, related to anomalous low temperature properties, are observed in many glasses, and in particular in a-SiO_2; the relation between these vibrational properties and the medium range order of glass has been much investigated recently (Elliot, 1992).

- Two sharp lines (D_1 and D_2 at 495 and 606 cm^{-1} respectively) are observed in the Raman spectra of a-SiO_2. Galeener (1982) attributed these narrow lines to the existence in a-SiO_2 of planar 4- and 3-rings (i.e. rings formed by 4 or 3 Si-O units). More recently Barrio et al. (1993) have given new arguments for these ring models: the assignment of the 606 cm^{-1} D_2 line to a planar 3-ring was confirmed, while the 495 cm^{-1} D_2 line was attributed to puckered 4-rings.

Finally in addition to the normal a-SiO_2 state, there is a compacted state of a-SiO_2 obtained under high pressure, which was observed in an in- situ Raman experiment by Hemley et al. (1986a); compacted a-SiO_2 is presently the subject of many studies in relation to the high pressure amorphization of crystalline silica polymorphs.

THEORY OF LATTICE DYNAMICS OF SILICA POLYMORPHS

Many models have been proposed (and are still proposed) to explain the lattice dynamical properties of silica polymorphs. Before entering into the details of these models, it seems worthwhile to make some general remarks about these systems:

-The nature of the bonding in SiO_2 is partly ionic and partly covalent. This is a major source of difficulty in calculations since either simple ionic point charge models or purely covalent models, that neglect long range electrostatic forces, are unable to give a full description of the vibrational spectrum.

-By far the strongest interaction in silicate is that of the Si-O bond stretching (see the review by McMillan (1984)). As shown by Sen and Thorpe (1977), to explain the presence of vibrational bands at 1000-1200 cm^{-1} and 400-700 cm^{-1}, it is enough to consider only the Si-O stretching force constant. For an SiO_4 molecule, two stretching modes are found (one symmetric non degenerate ν_1 mode and one asymmetric triply degenerate ν_3 mode). In tetrahedrally coordinated SiO_2 materials, these modes are coupled and give rise to out-of phase and in-phase Si motions, which correspond respectively to the high and low frequency bands observed in silica crystals and glass. The low frequency modes (450 cm^{-1}) involve mainly oxygen displacements in the plane bisecting Si-O-Si and the high frequency modes (1100 cm^{-1}) correspond to motions of both O and Si along the bonds.The presence of a vibrational band around 800 cm^{-1} may be accounted for by considering, in addition, O-Si-O bending forces (Bell et al., 1976; Laughlin et al., 1977). Therefore purely intra-tetrahedral forces are able to explain the salient features common to the high frequency part (> 400 cm^{-1}) of the phonon spectra of most of the SiO_2 polymorphs (including vitreous silica). It is clear however that the above picture is rather over simplified and cannot describe the details, in particular the LO-TO splittings which are the finger prints of electrostatic interactions.

Furthermore all inter-tetrahedral forces have been neglected. A question then arises: is this assumption compatible with crystal stability? It is clear that this cannot be the case if there are modes which leave the SiO_4 units undistorted. As a matter of fact, in the absence

EBSCOhost - printed on 2/13/2023 4:48 AM via . All use subject to https://www.ebsco.com/terms-of-use

of intertetrahedral forces, these modes would have zero frequency (free rotations of SiO_4 around a common oxygen). The crystal is therefore unstable and it is easy to show that its bulk modulus is zero. A systematic investigation of these "rigid unit modes" (RUM) can be made on the ground of purely geometrical considerations (Berge et al., 1986; Giddy et al., 1993). An interesting result is that such modes do exist in most SiO_2 polymorphs (β-quartz, ideal cristobalite and tridymite ...) but only for well defined wave-vectors at special points, lines or planes of reciprocal space. Since inter-tetrahedral forces are actually not all zero, owing in particular to Si-Si interactions or to Si-O-Si bending forces, all the RUM do not lead necessarily to crystal instability, although the corresponding frequencies are expected to be low. Some RUM however also leave the Si-Si distance approximately unchanged and involve mainly torsional motions of tetrahedra. These latter modes are expected to be very soft modes which can trigger displacive phase transitions. It was recognized a long time ago, that the α-β transition in quartz corresponds to alternate rotations of SiO_4 units around 2-fold symmetry axes with practically no change in Si-Si distances (Grimm and Dorner, 1975). It has been later shown that this property also holds for a whole phonon branch and that this can explain the onset of an incommensurate phase transition corresponding to the "freezing" of a phonon lying on this branch (Vallade et al., 1992a). The α-β transition in cristobalite has also been analysed along these lines (Swainson and Dove, 1993). The existence of low frequency RUM along well defined directions of the reciprocal space can also be related to the observation of intense diffuse lines in X-rays, neutron or electron scattering by Hua et al. (1988) for cristobalite and by Kihara (1993) for quartz.

In the following sections, we review the various microscopic models used to describe SiO_2 polymorphs. As they are very numerous, we shall restrict ourselves to those which have been explicitly used to calculate vibrational properties. (Other discussions can be found in other chapters of this book). We shall distinguish two broad classes of models: empirical and ab-initio.

Empirical models

The first lattice dynamical calculations used *force constant models*. In the harmonic approximation the potential energy of the system is written as a quadratic expansion of the atomic displacements, the coefficients of which have the meaning of force constants. These coefficients however are too numerous to be determined and the choice of a specific model consists in keeping only those that are thought to be the most relevant. Two main kinds of force constant have been used for SiO_2 : *valence force constants* and *central force constants*. The former use as independant variables, the changes in bond lengths (Si-O, O-O, Si-Si) and bond angles (O-Si-O , Si-O-Si), giving two and three body interactions respectively. The latter take only into account pair interactions between atoms with one longitudinal and one transverse force constant (with respect to the interatomic direction). In both cases, the eigenmodes and eigenfrequencies are calculated by diagonalization of a dynamical matrix.

Valence force models, first proposed by Saksena (1942), Barriol (1946) and Kleinman and Spitzer (1962), were fitted to several zone center phonon frequencies of α-quartz. Kleinman and Spitzer (1962) also proposed a model of charges and polarizabilities which accounts for the relative infrared and Raman intensities. Extension of these models were later proposed (Bates, 1972a; Yamaguchi et al., 1971; Mirgorodski and Lazarev, 1973; Etchepare et al., 1974). The number of adjustable force constants was increased to include non-diagonal terms in the potential energy and in some cases torsional forces between SiO_4

EBSCOhost - printed on 2/13/2023 4:48 AM via . All use subject to https://www.ebsco.com/terms-of-use

units (to stabilize the β phase of quartz). With nine force constants, Etchepare et al. (1974) were able to calculate fairly well the zone center phonon frequencies, not only for α and β quartz but also for other polymorphs (α and β cristobalite, β tridymite) using the same set of force constants. Relative intensities of infrared and Raman spectra of quartz were also approximately reproduced. Dowty (1987) applied similar models to various silicate glasses and crystals. The common drawback of all these valence force models is their inability to predict LO-TO splittings since all ionic contributions are neglected. Iishi et al. (1983) and Lazarev et al. (1986) attempted to improve these models by adding Coulombic contributions within the "deformable dipole model" and the "polarizable ion model" respectively.

Calculations using *central force* constants (Born-Von Karman models) were initiated in SiO_2 by Elcombe (1967). She took into account (Si-O) and (O-O) nearest neighbour interactions (4 parameters) to interpret the phonon dispersion curves of α and β quartz. She found that the introduction of Coulombic interactions (rigid ion approximation, with fractional charges) improves the fit significantly. Her model however was unable to explain the values of the elastic constants. Later Barron et al. (1976) and Strieffler and Barsch (1975, 1976) extented this rigid ion model by introducing non nearest neighbour oxygen interactions and Keating angle bending forces respectively. They emphasize that in Elcombe's model, the force constants are incompatible with the equilibrium condition for zero atomic displacement. By imposing equilibrium conditions, they reduce the number of adjustable parameters. A better agreement with elastic and dielectric properties of quartz is then achieved, but the LO-TO splittings are poorly reproduced, probably because the ionic polarisability is neglected. Cristobalite was also described using a Born-Von Karman model (Hua et al., 1988) and a Born-Keating model (Ahmad et al., 1988). More recently central force models were used to interpret new inelastic neutron scaterring data in β-quartz (Bethke et al., 1987) and α-quartz (Schober et al., 1993). The latter authors proposed several models which all include ionic polarizability through the shell model. Their models which provide the best fit to dispersion curves used a Born-Mayer potential (with an exponential repulsion between nearest neighboor atoms) and Keating angular force constants (eleven parameters). The equilibrium conditions are only approximately fulfilled

Over the last fifteen years numerical simulation techniques (molecular dynamics and Monte Carlo methods) have been used frequently to calculate static and dynamical properties of SiO_2. They offer the possibility of investigating disordered systems such as vitreous silica, defects, and surface effects, where normal mode analysis is not appropriate. The basic ingredient is then a model potential (rather than force constants). Various empirical potentials have been used: Ionic pair potentials (Erickson and Hostetler, 1987) supplemented by three-body potentials to better describe covalency (Vashishta et al., 1990). Most of these works, however, concentrated more on static structural properties than on lattice dynamics. The vibrational spectrum, calculated as the Fourier transform of the velocity autocorrelation function, was reported by Jin et al. (1993) for amorphous silica. Molecular dynamics simulation was also applied to study crystalline quartz by Vos Burchart et al. (1992). They reported an original study of the behavior of zone center phonons as a function of the density at zero temperature, which predicts the α-β displacive transition at a critical density. Anderson et al. (1993) calculated the vibrational spectra of cristobalite and amorphous silica. They found a reasonably good agreement with infrared spectra. Sanders et al. (1984) and Catlow et al. (1988) used static simulation techniques to calculate phonon dispersion curves and elastic and dielectric constants of quartz. They chose a fourteen-parameter shell model with Buckingham short range interactions and O-Si-O bond-bending force constant.

EBSCOhost - printed on 2/13/2023 4:48 AM via . All use subject to https://www.ebsco.com/terms-of-use

Ab initio calculations

Most of the recent lattice dynamical calculations have tried to achieve a more ambitious program than fitting empirical models to experimental data. They aim at deriving interatomic potentials using first principle quantum mechanical calculations (see the chapter by Gibbs in this book). Pioneering attempts to apply quantum chemistry to silicate are due to Gibbs and co-workers (Gibbs, 1982; Lasaga and Gibbs, 1991). The Schrödinger equation for a "silicate molecule" (H_4SiO_4, $H_6Si_2O_7$) is solved at the Hartree-Fock self consistent level using one-electron orbitals expanded as linear combinations of atomic orbitals. The potential surfaces for various geometries allow the calculation of equilibrium structures and of the "molecular" force constants. Usually the potential surfaces are fitted by analytical expressions similar to empirical potentials with the hope that they are transferable to the condensed state. Calculations along these lines have been made by Lasaga and Gibbs (1991) and by McMillan and Hess (1990). When applied to α-quartz, they found phonon frequencies that are systematically too high (by about 15 %) although the correct ordering of modes is nearly exactly obtained. These models however ignore all kinds of long-range fields and are unable to predict LO-TO splittings. Attemps to introduce electrostatic interactions into similar models have been made by Lazarev and Mirgorodski (1991). Tsuneyuki et al. (1988) fitted to the Hartre-Fock energy calculation of a SiO_4^{4-} cluster a pair potential of the form :

$$\phi_{ij} = \frac{q_i\, q_j}{r_{ij}} + f_0 \left(b_i + b_j\right) \exp \frac{\left[\left(a_i + a_j\right) - r_{ij}\right]}{b_i + b_j} - \frac{C_i\, C_j}{r_{ij}^6} \qquad (3)$$

This was then put in a molecular dynamics simulation program and proved to be able to reproduce reasonably well the structure of various SiO_2 polymorphs (α-quartz, α-cristobalite, coesite, stishovite). Della Valle et al. (1991) used these results for lattice dynamics calculations and they found that the vibrational frequencies of the five silica polymorphs are approximately in agreement (better than 30 %) with experimental results, which is remarkable for such a simple pairwise additive potential. Calculated elastic and thermodynamic properties of α-quartz are also in fairly good agreement with experiments (Cowley and Gross, 1991). Recently Binggeli et al. (1994) used Tsuneyuki et al. potential to study the mechanism of quartz amorphisation under high pressure, via phonon softening at the Brillouin zone boundary. A slightly different potential (restricted to Si-O and O-O interactions), was used by van Beest et al. (1990), after a fit to the ab-initio energy of a H_4SiO_4 molecule, with

$$\phi_{ij} = \frac{q_i\, q_j}{r_{ij}} + a_{ij} \exp\left(-\, b_{ij}\, r_{ij}\right) - \frac{c_{ij}}{r_{ij}^6} \qquad (4)$$

These authors noted that the effective charges cannot be determined unambiguously from such a small cluster and they used this flexibility to adjust these parameters to get the better fit to α-quartz structural and elastic properties. The resulting potential is thus "semi-empirical". Kramer et al. (1991) and Tse and Klug (1991) used this potential to calculate static and dynamic properties of SiO_2 polymorphs. The results are somewhat better than those derived from Tsuneyuki et al. model but they are still not accurate for vibrational frequencies (especially for the bending modes). Part of the discrepancies are thought to be related to the inaccuracy of the ab-initio calculation. Recently "local density functional" methods (LDA) have been used as an alternative procedure to Hartree-Fock type

EBSCOhost - printed on 2/13/2023 4:48 AM via . All use subject to https://www.ebsco.com/terms-of-use

approximations. Their main advantage is to take into account electronic exchange and correlation. Purton et al. (1993) applied this method to a silicate molecule ($H_{12}Si_5O_{16}$) with 33 atoms. They found that the total energy can be well fitted by a potential of the same form as that used by Sanders et al. (1984). The overall agreement with respect to phonon dispersion curves, dielectric and elastic data of α quartz is quite good (except for the LO-TO splittings of some high energy modes). The transferability of this model to other polymorphs however has not yet been tested. Surprinsingly enough this potential contains no direct Si-Si or Si-O-Si interactions (this is probably implicitly taken into acount through other interactions). Local density functional methods have also been used by Gonze et al. (1992) for α-quartz, Liu et al. (1993) for β-cristobalite and by Lee et al. (1994) for stishovite. Lattice dynamics and dielectric properties of quartz and stishovite have been calculated and are in good agreement with experiments particularly for stishovite: zone center phonon frequencies agree to within 4 % and the LO-TO splittings, which are large in this crystal, are well reproduced. Lee et al. (1994) evaluated the relative proportion of Coulombic and covalent contributions and they emphasize the importance of many-body potential. These results show that rather accurate determinations of the lattice dynamics of silica polymorphs can now be obtained from ab-initio calculations, at least for the simpler structures.

CONCLUSION

As shown in this review, lattice dynamics properties of the various silica polymorphs are known in quite different ways. Vibrational properties of α-quartz are known in a coherent and detailed way and a large amount of results have been obtained on amorphous silica, although their interpretation in a disordered material is more complex. The studies of the other crystalline polymorphs are limited by the lack of large single crystals. However as impressive progress have been made with ab-initio calculations, rather detailed informations on structure and lattice dynamics can now be obtained from theoretical studies starting with the electronic properties of Si and O atoms.

An important progress was the finding of simple "transferable" pair potentials that are able to explain the structure of various polymorphs (including stishovite) and (to a lesser extent) their vibrational frequencies and their electric and elastic properties. (To be true, these potentials are not strictly speaking fully ab-initio, since the electrostatic charges are adjusted to fit some crystalline properties). The fact that pair potentials are able to describe so strongly covalent materials as silica polymorphs seems surprising. This is probably due to the fact that Si-O bonding being so strong, Si-O length-changes are small and angular O-Si-O bending can be described by direct O-O interactions. Fully ab-initio calculations have also been reported for some polymorphs that explain rather accurately the lattice dynamics properties, even as subtle features as the LO-TO splittings.

A major interest of silica materials is their extensive polymorphism, which leads to many phase transitions. The symmetry related phase transitions of the low pressure polymorphs occurs upon heating. In a first approximation they are produced by the rotation of rigid interconnected tetrahedra but with different mechanism:

-The α–β phase quartz transition (and the existence of an incommensurate phase) is described by the variation of an order parameter, following Landau theory. This is a displacive transition with a soft mode corresponding to SiO_4 rotations; the high temperature phase structure is locally of high symmetry.

- The α–β cristobalite transition, is more discontinuous, and is of the order-disorder type. The high symmetry of the high temperature phase is due to a

EBSCOhost - printed on 2/13/2023 4:48 AM via . All use subject to https://www.ebsco.com/terms-of-use

dynamical averaging, produced by the jumps of oxygen atoms between several symmetry related positions. The behavior of tridymite is more complex, with the existence of at least six phases, with poorly reproducible properties.

Theoretical models with various degrees of sophistications have been used to describe these transitions, from simple mean field Landau theory to molecular dynamical simulation. Tsuneyuki et al. (1990), using their ab-initio potential, obtained a rather accurate description of the α-β transition of quartz (with a surprisingly accurate value of the transition temperature); they are in favor of a disordered structure for the β phase. In contrast, van Beest et al. (1990), using a closely related potential, showed that the transition properties are too sensitive to small variations of the potential parameters, to be determined only from small molecular clusters calculations. For cristobalite, ab-initio models lead systematically to a disordered structure, but with different models of disorder proposed (Liu et al., 1993; Swainson and Dove, 1993). Although encouraging results have been obtained, more work is needed to understand fully the high temperature transition behavior of the low-pressure polymorphs.

The reconstructive transition between different polymorphic phases depends on the temperature and pressure variations of the free energy. It is well known that thermodynamics properties are closely related to vibrational properties. This idea has been developped by Kieffer (1979, 1985), using simplified but realistic models of vibrational mode densities. More recently, Gillet et al. (1990) have considered the effects of anharmonicity. The study of the high pressure behavior of silica polymorphs, related to a change of silicon coordination from four to six is a very active research subject. Some models attribute the occurence of high pressure amorphization, to the existence of a lattice instability (Binggeli et al., 1993). Here also the possibility to treat realistic theoretical models can be of great value to understand these phenomena.

Although started more than a century ago, the study of silica vibrational properties is always very active and is closely related to the existence of polymorphic phase transitions. The recent progress in ab-initio calculations open the way to a detailed understanding of the lattice dynamics of silica polymorphs.

REFERENCES

Abe K, Kawasaki K, Koike T, Shigenari T (1989) Dynamical central peak near the incommensurate phase transition of quartz. J Phys:Condens Matter 1:8741-8746

Ahmad N, Nex CMM, Phillips WA (1988) Lattice dynamics of cristobalite. Phil Mag B 57:677-683

Amler H, Pichlmaier S, Ramm P, Maier M (1993) Polariton dispersion relation and stimulated Raman scattering from the 132 cm^{-1} E mode in α–quartz. Optics Commun 97:397-408

Anderson DC, Kieffer J, Klarsfeld S (1993) Molecular dynamic simulations of the infrared dielectric response of silica structures. J Chem Phys 98:8978-8986

Anik'ev AA, Gorelik VS, Umarov BS (1984) Effects of resonance interaction between a soft mode and two-phonon excitation in Raman spectra of quartz. Sov Phys Solid State 26:1679-1682

Aref'ev IM, Krivokhiza SV, Kyzylasov YI, Starunov VS, Fabelinskii IL (1968) Stimulated Raman scattering and generation of infrared radiation in quartz at low temperature. JETP Lett 8:84-86

Asell JF, Nicol M (1968) Raman spectrum of α-quartz at high pressures. J Chem Phys 49:5395-5399

Aslanyan TA, Levanyuk AP (1979) On the possibility of the incommensurate phase near α–β transition point in quartz. Solid State Commun 31:547-550

Axe JD, Shirane G (1970) Study of the α–β quartz phase transformation by inelastic neutron scattering. Phys Rev B 1:342-348

Bachheimer JP, Dolino G (1975) Measurement of the order parameter of α-quartz by second harmonic generation of light. Phys Rev B 11:3195-3205

EBSCOhost - printed on 2/13/2023 4:48 AM via . All use subject to https://www.ebsco.com/terms-of-use

Barrio RA, Galeener FL, Martinez E,Elliot RJ (1993) Regular ring dynamics in AX_2 tetrahedral glasses. Phys Rev B 48:15672-15689
Barriol J (1946) Etude des vibrations du quartz actives dans les spectres de diffusion et d'absorption infrarouge. J Phys France 8:209-216
Barron THK, Huang CC, Pasternak A (1976) Interatomic forces and lattice dynamics of α-quartz. J Phys C: Solid State Phys 9:3925-3940
Bates JB (1972a) Dynamics of β-quartz structures of vitreous SiO_2 and BeF_2. J Chem Phys 56:1910-1917
Bates JB (1972b) Raman spectra of α and β cristobalite. J Chem Phys 57:4042-4047
Bates JB, Quist AS (1972) Polarized Raman spectra of β-quartz. J Chem Phys 56:1528-1533
Bell RJ, Hibbins-Butler DC (1976) Infrared activity of normal modes in vitreous silica, germania and beryllium fluoride. J Phys C:Solid State Phys 9:1171-1175
Berge B, Dolino G, Vallade M, Boissier M, Vacher R (1984a) Incommensurate phase of quartz. II:Brillouin scattering studies. J Phys France 45:715-724
Berge B, Vallade M, Martinez G (1984b) Raman scattering investigation of the α–β transition and of the incommensurate phase in quartz. J Phys C: Solid State Phys 17:L167-171
Berge B, Bachheimer JP, Dolino G, Vallade M, Zeyen C (1986) Inelastic neutron scattering study of quartz near the incommensurate phase transition. Ferroelectrics 66:73-84
Bethke J, Dolino G, Eckold G, Berge B, Vallade M, Zeyen C, Hahn T, Arnold H, Moussa F (1987) Phonon dispersion and mode coupling in high-quartz near the incommensurate phase transition. Europhys Letters 3:207-212
Binggeli N, Keskar NR, Chelikovsky JR (1994) Pressure induced amorphization, elastic instability and soft modes in α-quartz. Phys Rev B 49:3075-3081
Biraud-Laval S, Chartier G (1969) Observation of infrared emission from stimulated polaritons in quartz. Phys Letters 30A:177-178
Biraud-Laval S, Reinisch R, Paraire N, Laval R (1976) Raman susceptibility damping constant and oscillator strengh determination from stimulated polaritons in quartz. Phys Rev B 13:1797-1801
Bogani F, Carraresi L (1990) Anomalies in the polarized Raman spectrum of crystal quartz. Nuovo Cimento 12 D:915-925
Boyer H, Smith DC, Chopin C, Lasnier B (1985) Raman microprobe determinations of natural and synthetic coesite. Phys Chem Min 12:45-48
Boysen H, Dorner B, Frey F, Grimm H (1980) Dynamic stucture determination for two interacting modes at the M-point in α–and β–quartz by inelastic neutron scattering. J Phys C: Solid State Phys 13:6127-6146
Briggs RJ, Ramdas AK (1977) Piezospectroscopy of the Raman spectrum of α-quartz. Phys Rev B 16:3815-3826
Camassel J, Goullet A, Pascual J (1988) Infrared activity of α-$AlPO_4$. Phys Rev B 38:8419-8430
Catlow CRA, Freeman CM, Islam MS, Jackson RA, Leslie M, Tomlinson SM (1988) Interatomic potentials for oxides. Phil Mag 58:123-141
Chapet-Rousseau M, Paraire N, Laval S (1988) A determination of transverse and longitudinal frequencies and oscillator strengh of the E modes in synthetic and natural α-quartz crystals from optical heterodyne measurements. J Phys C: Solid State Phys 21:3813-3825
Cherukuri SC, Pye LD, Chakraborty IN, Condrate RA, Ferraro SJR, Cornilsen BC, Martin K (1985) The vibrational spectra and normal coordinate analysis of ^{28}Si- and ^{29}Si-substituted α-cristobalite. Spectroscopy Letters 18:123-137
Chiao RY, Townes CH, Stoicheff BP (1964) Stimulated Brillouin scattering and coherent generation of intense hypersonic waves. Phys Rev Letters 12:592-595
Coes L Jr (1953) A new dense crystallite silica. Science 118:131
Cowley ER, Gross J (1991) Lattice dynamics of a pair potential model of α-quartz. J Chem Phys 95:8357-8361
Dean KJ, Sherman WF, Wilkinson GR (1982) Temperature and pressure dependence of the Raman active modes of vibration of α-quartz. Spectrochemica Acta 38A:1105-1108
Della Valle RG, Andersen HC (1991) Test of a pairwise additive ionic potential model for silica. J Chem Phys 94:5056-5060
Denisov VN, Mavrin BN, Podobedov VB, Sterin KE (1986) Two frequency excitation, anisotropy of the intensity and effects of asymmetry of the tensor of hyper-Raman light scattering in crystalline quartz. Sov Phys JETP 63:338-343
Dolino G (1979) Elastic light scattering and birefringence measurements in the coexistence state of α– and β-quartz. J Phys Chem Solids 40:121-128
Dolino G (1988) Incommensurate phase transitions in quartz and berlinite. In: Ghose S, Coey JMD, Salje E (eds) Structural and magnetic phase transitions in minerals. Springer-Verlag, New York, p 17-38
Dolino G (1990) The α–inc–β transition of quartz:a century of research on displacive phase transitions. Phase Transitions 21:59-72

EBSCOhost - printed on 2/13/2023 4:48 AM via . All use subject to https://www.ebsco.com/terms-of-use

Dolino G, Bachheimer JP, Gervais F, Wright AF (1983) La transition α–β du quartz:transition ordre-desordre ou displacive, comportement thermodynamique. Bull Min 106:267-285

Dolino G, Berge B, Vallade M, Moussa F (1992) Origin of the incommensurate phase of quartz:I. Inelastic neutron scattering study of the high temperature β phase of quartz. J Phys I France 2:1461-148

Dolino G, Bastie P (1994) Phase transition in quartz: α-incommensurate-β. (to be published, Trans Tech Publications)

Dorner B, Grimm H, Rzany H (1980) Phonon dispersion branches in α-quartz. J Phys C: Solid State Phys 13:6607-6612

Dowty E (1987) Vibrational interactions of tetrahedra in silicate glasses and crystals:II. Calculations on melilites, pyroxenes, silica polymorphs and feldspars. Phys Chem Min 14:122-138

Duarte JL, Sanjuro JA, Katiyar RS (1987) Off-normal reflectivity in uniaxial crystals:α-LiO_3 and α-quartz. Phys Rev B 36:3368-3372

Elcombe MM (1967) Some aspects of the lattice dynamics of quartz. Proc Phys Soc 91:947-958

Elliott SR (1992) A unified model for the low energy vibrational behaviour of amorphous solids. Europhys Letters 19:201-206

Erickson RL, Hostetler CJ (1987) Application of empirical ionic models to SiO_2 liquid:potential model approximations and integration of SiO_2 polymorph data. Geochim Cosmochim Acta 51:1209-1218

Etchepare J, Merian M, Smetankine L (1974) Vibrational normal modes of SiO_2. I. α and β quartz. J Chem Phys 60:1873-1876

Etchepare J, Merian M, Kaplan P (1978) Vibrational normal modes of SiO_2. II. Cristobalite and tridymite. J Chem Phys 68:1531-1537

Farmer VC (1974) The infrared spectra of minerals. Mineralogical Soc, London

Ferraro JR, Manghnani MH, Quattrochi A (1972) Infrared spectra of several glasses at high pressures. Phys Chem Glasses 13:116-121

Fries J, Claus R (1973) Phonon and polariton spectra of β-quartz. J Raman Spectroscopy 1:71-81

Frondel C (1962) The system of mineralogy, 7th ed, vol III. Wiley, New York

Gage DR, Farwell SO (1981) Laser Raman spectrometry for the determintion of crystalline silica polymorphs in volcanic ash. Analyt Chem 53:2123-2127

Gale GM, Lauberau A (1983) Direct measurement of picosecond and sub-picosecond phonon lifetime in α-quartz. Optics Commun 44:273-276

Galeener FL (1982) Planar rings in glasses. Solid State Commun 44:1037-1040

Galeener FL, Leadbetter AJ, Stringfellow MW (1983) Comparison of the neutron, Raman and infrared vibrational spectra of vitreous SiO_2, GeO_2 and BeF_2. Phys Rev B 27:1052-1078

Gaskell PH (1967) The vibrational spectra of silicates. Phys Chem Glasses 8:69-80

Gerbaux X, Hadni A (1982) Etudes en fonction de la temperature des vibrations polaires du quartz a 129 et 265 cm^{-1}. J Phys C: Solid State Phys 15:3821-3828

Gervais F, Piriou B (1975) Temperature dependence of transverse and longitudinal optic modes in the α and β phases of quartz. Phys Rev B 11:3944-3950

Gervais F, Piriou B ,Billard D (1975) Infrared damping divergence in quartz. Solid State Commun 17:861-865

Ghose S (1988) Inelastic neutron scattering. Rev Min 18:161-192

Gibbs GV (1982) Molecules as models for bonding in silicates. Am Min 67:421-450

Giddy AP, Dove MT, Pawley GS, Heine V (1993) The determination of rigid unit modes as potential soft modes for displacive phase transitions in framework crystal structures. Acta Cryst A 49:697-703

Gillet P, Le Cleac'h A, Madon M (1990) High temperature Raman spectroscopy of SiO_2 and GeO_2 polymorphs:anharmonicity and thermodynamic properties at high temperatures. J Geophys Res 95:21635-21655

Gonze X, Allan DC, Teter MP (1992) Dielectric tensor, effective charges and phonons in α-quartz by variational density-functional perturbation theory. Phys Rev Letters 68:3603-3606

Gorelik VS, Tochilin SD (1987) Inelastic opalescence near phase transition point in quartz crystals. Sov Phys Crystallogr 32:562-564

Görlich E, Blaszczak K, Handke M (1983) Infrared spectra of silica polymorphs. Mineralogica Polonica 14:3-17

Grimsditch MH, Ramdas AK, Rodriguez S, Tekippe VJ (1977) Piezospectroscopy of Raman lines exhibiting linear wavevector dependence: α-quartz. Phys Rev B 15:5869-5876

Grimm H, Dorner B (1975) On the mechanism of the α–β transformation of quartz. J Phys Chem Solids 36:407-413

Gross E (1930) Uber Anderung der Wellange bei Lichtzerstreuung in Kristallen. Zeit Phys 60:685-687

Harker YD, She CY, Edwards DF (1970) Raman spectra of α quartz under uniaxial stress. J Appl Phys 41:5274-5278

Hatch DM, Ghose S (1991) The α–β transition in cristobalite, SiO_2. Phys Chem Min 17:554-562

EBSCOhost - printed on 2/13/2023 4:48 AM via . All use subject to https://www.ebsco.com/terms-of-use

Hemley RJ, Mao HK, Bell PM, Mysen BO (1986a) Raman spectroscopy of SiO_2 glass at high pressure. Phys Rev Letters 57:747-750
Hemley RJ, Mao H-K, Chao ECT (1986b) Raman spectrum of natural and synthetic stishovite. Phys Chem Min 13:285-290
Hemley RJ (1987) Pressure dependence of Raman spectra of SiO_2 polymorphs:α-quartz, coesite and stishovite. In:Manghnani MH, Syono Y, ed. High-pressure research in mineral physics. Am Geophys Union, Washington, pp 347-359
Hofmeister AM, Xu J, Akimoto S (1990) Infrared spectroscopy of synthetic and natural stishovite. Am Min 75:951-955
Hofmeister AF, Rose TP, Hoering TC, Kushiro I (1992) Infrared spectroscopy of natural, synthetic and ^{18}O-substituted α-tridymite: structural implications. J Phys Chem 96:10213-10218
Hua GL, Welberry TR, Withers RL, ThompsonJG (1988) An electron diffraction and lattice dynamical study of the diffuse scattering in cristobalite SiO_2. J Appl Cryst 21:458-465
Iishi K, Miura M, Shiro Y, Murata H (1983) Lattice dynamics of α–quartz including the effect of the width of the atomic electron distribution. Phys Chem Min 9:61-66
Jayaraman A, Wood DL, Maines RGSr (1987) High pressure Raman study of the vibrational modes in $AlPO_4$ and SiO_2 (α-quartz). Phys Rev B 35:8316-8321
Jin W, Vashishta P, Kalia RK, Rino JP (1993) Dynamic structure factor and vibrational properties of SiO_2 glass. Phys Rev B 48:9359-9368
Joffrin C, Dorner B, Joffrin J (1980) Activite acoustique et loi de dispersion:le quartz et le chlorate de sodium. J Phys France Lettres 41:L391-395
Kihara K (1993) Lattice dynamical calculations of anisotropic temperature factors of atoms in quartz and the structure of β-quartz. Phys Chem Min 19:492-501
Kieffer SW (1979) Thermodynamics and lattice vibrations of minerals:2. Vibrational characteristics of silicates. Rev Geophys Space Phys 17:20-34
Kieffer SW (1985) Heat capacity and entropy:systematic relations to lattice vibrations. Rev Min 14:65-125
Kleinman DA, Spitzer WG (1962) Theory of the optical properties of quartz in the infrared. Phys Rev 125:16-30
Kramer GJ, Farragher NP, van Beest BWH, van Santen RA (1991) Interatomic force fields for silica, aluminophosphates and zeolites:derivation based on ab initio calculations. Phys Rev B 43:5068-5080
Krishnamurti D (1958) The Raman spectrum of quartz and its interpretation.Proc Ind Acad Sci A47:276-291
Landsberg G, Mandelstam L (1928) Eine neue Erscheinung bei der Lichtzerstreuung in Krystallen. Naturwiss 28:557-558
Landsberg G, Mandelstam L (1929) Lichtzerstreuung in Kristallen bei hoher Temperatur. Zeit Phys 58:250
Lasaga AC, Gibbs GV (1991) Quantum mechanical Hartree-Fock potential surfaces and calculations on minerals. Phys Chem Min 17:485-491
Laughlin RB, Joannopoulos JD (1977) Phonons in amorphous silica. Phys Rev B 16:2942-2952
Laulicht I, Bagno I, Schlesinger Y (1972) The temperature dependence of the soft mode linewidth of quartz. J Phys Chem Solids 33:319-326
Lazarev AN, Mirgorodsky AP, Smirnov MB (1986) Vibrational spectra and dynamic properties of ionic covalent crystals. Solid State Commun 58:371-377
Lazarev AN, Mirgorodsky AP (1991) Molecular force constants in dynamical model of α-quartz. Phys Chem Min 18:231-243
Leadbetter AJ (1969) Inelastic cold neutron scattering from different forms of silica. J Chem Phys 51:779-786
Lee C, Gonze X (1994) Lattice dynamics and dielectric properties of SiO_2 stishovite. Phys Rev Letters 72:1686-1689
Lippincott ER, Van Valkenburg A, Weir CE, Bunting EN (1958) Infrared studies on polymorphs of silicon dioxide and germanium dioxide. J Res Nat Bureau Standards 61:61-70
Liu F, Garofalini SH, King-Smith RD, Vanderbilt D (1993) First principles studies on structural properties of β-cristobalite. Phys Rev Letters 70:2750-2753
Loewenstein EV, Smith DR, Morgan RL (1973) Optical constants of far infrared materials. 2:Crystalline solids. Appl Optics 12:398-406
Loudon R (1968) Polaritons, Raman scattering, electro-optic effect and parametric amplification. In: Whright GB, ed. Light Scattering Spectra of Solids. Springer-Verlag, New-York, pp 25-42
Lyon RJP (1962) Infrared confirmation of 6-fold coordination of silicon in stishovite. Nature 196:266-267
McCarthy DE (1963) The reflection and transmission of infrared materials:II, bibliography. Appl Optics 2:596-600
McMillan PF (1984) Structural studies of silicate glasses and melts-applications and limitations of Raman spectroscopy. Am Min 69:622-644
McMillan PF, Hofmeister AM (1988) Infrared and Raman spectroscopy. Rev Min 18:99-159

EBSCOhost - printed on 2/13/2023 4:48 AM via . All use subject to https://www.ebsco.com/terms-of-use

McMillan PF, Hess AC (1990) Ab initio valence force field calculations for quartz. Phys Chem Min 17:97-107

Merten L (1968) Directional dispersion of extraordinary optical phonons of α-quartz. Phys Stat Sol 28:111-119

Merten L, Borstel G (1981) Bulk and surface phonon-polaritons in anisotropic crystals. J Raman Spec 10:205-211

Mirgorodskii AN, Lazarev AN (1973) Calculations of intensities in an α-quartz crystal as a method of checking on the shapes of the vibrations. Opt Spectrosc 34:514 517

Narayanaswamy PK (1948) The α–β transformation in quartz. Proc Ind Acad Sci A 28:417-422

Nichols EF (1897) A method for energy measurements in the infrared spectrum and the properties of the ordinary ray in quartz for waves of great wavelength. Phys Rev 4:297-305

Ocana M, Fornes V, Garcia-Ramos JV, Serna CJ (1987) Polarization effects in the infrared spectra of α-quartz and α-cristobalite. Phys Chem Min 14:527-532

Onstott J, Lucovsky G (1970) Directional dispersion of extraordinary optical phonons in α-quartz in the frequency domain from 380 to 640 cm^{-1}. J Phys Chem Solids 31:2171-2184

Pelous J, Vacher R (1976) Thermal Brillouin scattering in crystalline and fused quartz from 20 to 1000 °C. Solid State Commun 18:657-661

Phillips BL, Thompson JG, Xiao Y, Kirkpatrick RJ (1993) Constraints on the structure and dynamics of the β-cristobalite polymorphs of SiO_2 and $AlPO_4$ from ^{31}P, ^{27}Al and ^{29}Si NMR spectroscopy to 770K. Phys Chem Min 20:341-352

Pine AS, Tannenwald PE (1969) Temperature dependence of Raman linewidth and shift in α-quartz. Phys Rev 178:1424-1430

Pine AS, Dresselhaus G (1969) Linear wavevector shifts in the Raman spectrum of α-quartz and infrared optical activity. Phys Rev 188:1489-1496

Plendl JN, Mansur LC, Hadni A, Brehat F, Henry P, Morlot G, Naudin F, Strimer P (1967) Low temperature far infrared spectra of SiO_2 polymorphs. J Phys Chem Solids 28:1589-1597

Plyusnina II, Maleyev MN, Yefimova GA (1970) Infrared spectroscopic investigation of cryptocristalline varieties of silica. Int Geol Rev 13:1750-1754

Purton J, Jones R, Catlow CRA, Leslie M (1993) Ab initio potentials calculation of the dynamical and elastic properties of α-quartz. Phys Chem Min 19:392-400

Raman CV, Nedungadi TMK (1940) The α–β transformation of quartz. Nature 145:147

Russell EE, Bell EE (1967) Measurement of the optical constants of crystal quartz in the far infrared with the asymetric transform method. J Opt Soc Am 57:341-348

Saksena BD (1940) Analysis of the Raman and infrared spectra of α-quartz. Proc Ind Acad Sci A 12:93-139

Saksena BD (1942) Force constants and normal modes of the totally symmetric vibrations in α–quartz at room temperature. Proc Ind Acad Sci A 16:270-280

Salje EKH, Ridgwell A, Guttler B, Wruck B, Dove MT, Dolino G (1992) On the displacive character of the phase transition in quartz:a hard-mode spectroscopy study. J Phys: Condens Matter 4:571-577

Sanders MJ, Leslie M, Catlow CRA (1984) Interatomic potentials for SiO_2. J Chem Soc Chem Commun 1984:1271-1273

Sato RK, McMillan PF (1987) An infrared and Raman study of the isotopic species of α-quartz. J Phys Chem 91:3494-3498

Schmal WW, Swainson IP, Dove MT, Graeme-Barber A (1992) Landau free energy and order parameter behaviour of the α-β phase transition in cristobalite. Zeit Krist 201:125-145

Schober H, Strauch D, Nutzel K, Dorner B (1993) Lattice dynamics of α- quartz:II. Theory. J Phys:Cond Matter 5:6155-6164

Sclar CB, Carrison LC, Schwartz CM (1962) Relation of infrared spectra to coordination in quartz and two high pressure polymorphs of SiO_2. Science 138:525-526

Scott JF (1968) Evidence of coupling between one and two phonon excitations in quartz. Phys Rev Letters 21:907-910

Scott JF (1970) Hybrid phonons and anharmonic interactions in $AlPO_4$. Phys Rev Letters 24:1107-1110

Scott JF (1974) Soft mode spectroscopy:experimental studies of structural phase transitions. Rev Mod Phys 46:83-128

Scott JF, Porto SPS (1967) Longitudinal and transverse optical lattice vibrations in α-quartz. Phys Rev 161:903-910

Scott JF, Cheesman LE, Porto SPS (1967) Polariton spectrum of quartz. Phys Rev 162:834-840

Sen PN, Thorpe MF (1977) Phonons in AX_2 glasses:from molecular to band like modes. Phys Rev B 15:4030-4038

Sevchenko NA, Florinskaia VA (1956) Reflection and transmission of 7-24 μm waves by silica modifications. Sov Phys Doklady 1:508-511

EBSCOhost - printed on 2/13/2023 4:48 AM via . All use subject to https://www.ebsco.com/terms-of-use

Shapiro SM (1968) Light scattering studies of the α–β phase transition in quartz. Ph D Thesis, The John Hopkins University, Baltimore, MD (unpublished)
Shapiro SM, Gammon RW, Cummins HZ (1966) Brillouin scattering spectra of crystalline quartz, fused quartz and glass. Appl Phys Letters 9:157-159
Shapiro SM, O'Shea DC, Cummins HZ (1967) Raman scattering study of the α–β transition in quartz. Phys Rev Letters 19:361-364
Shapiro SM, Cummins HZ (1968) Critical opalescence in quartz. Phys Rev Letters 21:1578-1581
Shapiro SM, Axe JD (1972) Raman scattering from polar phonons. Phys Rev B 6:2420-2427
Sharma SK, Mammone JF, Nicol MF (1981) Raman investigation of ring configurations in vitreous silica. Nature 292:140-141
Shigenari T, Imura Y, Takagi Y (1980) Light scattering study of α–β transition of quartz. J Phys Soc Japan 49 Suppl B:29-31
Shigenari T, Abe K (1989) Optical study and light scattering studies on the incommensurate phase in quartz. Ferroelectrics 95:253-257
Simon I, McMahon HO (1953) Study of quartz, cristobalite and vitreous silica by reflection in infrared. J Chem Phys 21:23-30
Spearing DR, Farnan I, Stebbins JF (1992) Dynamics of the α–β transitions in quartz and cristobalite as observed by in situ high temperature ^{29}Si and ^{17}O NMR. Phys Chem Min 19:307-321
Spitzer WG, Kleinman DA (1961) Infrared lattice bands of quartz. Phys Rev 121:1324-1335
Strauch D, Dorner B (1993) Lattice dynamics of α-quartz: I Experiment. J Phys: Condens Matter 5:6149-6154
Striefler ME, Barsch GR (1975) Lattice dynamiccs of α-quartz. Phys Rev B 12:4553-4566
Striefler ME, Barsch GR (1976) Elastic and optical properties of stishovite. J Geophys Res 81:2453-2466
Swainson IP, Dove MT (1993) Low frequency floppy modes in β-cristobalite. Phys Rev Letters 71:193-196
Tannenwald PE, Weinberg DL (1967) Stimulated Raman scattering in an infrared active nontotally symmetric vibration of α-quartz. IEEE J Quantum Electr 3:334-335
Tekippe VJ, Ramdas AK, Rodriguez S (1973) Piezospectroscopic study of the Raman spectrum of α-quartz. Phys Rev B 8:706-717
Tezuka Y, Shin S, Ishigame M (1991) Observation of the silent soft phonon in β-quartz by means of hyper-Raman scattering. Phys Rev Letters 66:2356-2359
Tse JS, Klug DD (1991) The structure and dynamics of silica polymorphs using a two body effective potential model. J Chem Phys 95:9176-9185
Tsuneyuki S, Tsukuda M, Aoki H, Matsui Y (1988) First principle interatomic potential of silica applied to molecular dynamics. Phys Rev Letters 61:869-872
Tsuneyuki S, Aoki H, Tsukuda M, Matsui Y (1990) Molecular dynamics study of the α–β structural phase transition of quartz. Phys Rev Letters 64:776-779
Unoki H, Tokumoto H, Ishiguro T (1983) Brillouin Scattering from quartz. Jpn J Appl Phys Suppl 22-3:187-789
Vallade M, Berge B, Dolino G (1992a) Origin of the incommensurate phase of quartz:II. Interpretation of inelastic neutron scattering data. J Phys I France 2:1481-1495
Vallade M, Abe K, Berge B, Shigenari T (1992b) Evidence of folded acoustic phonon modes in the light scattering spectrum of incommensurate quartz. J Phys Condens Matter 4:9931-9938
van Beest BWH, Kramer GJ, van Santen RA (1990) Force fields for silicas and aluminophophates based on ab initio caculations. Phys Rev Letters 64:1955-1958
Vashishta P, Kalia RK, Rino JP, Ebbsjö I (1990) Interaction potential for SiO_2: a molecular dynamics study of structural correlations. Phys Rev B 41:12197-12209
Velde B, Couty R (1987) High pressure infrared spectra of silica glass. J Non-Cryst Solids 94:238-250
Vigasina MF, Guseva EV, Orlov RY (1989) Vibrational spectrum of stishovite and analysis of its crystal lattice dynamics. Sov Phys Solid State 31:747-749
Von Czarnowski, Hübner K (1987) Raman and infrared investigation of stishovite and their interpretation. Phys Stat Sol (b) 142:K91-96
Vos Burchart E, van Bekkum H, van de Graaf B (1992) Molecular study on the α-quartz/β-quartz transition. J Chem Soc Faraday Trans 88:1161-1164
Weidner DJ, Carleton HR (1977) Elasticity of coesite. J Geophys Res 82:1334-1346
Weidner DJ, Bass JD, Ringwood AE, Sinclair W (1982) The single crystal elastic moduli of stishovite. J Geophys Res 87:4740-4746
Williams Q, Hemley RJ, Kruger MB, Jeanloz R (1993) High pressure infrared spectra of α-quartz, coesite, stishovite and silica glass. J Geophys Res 98:22157-22170
Withers RL, Thomson JG, Welberry TR (1989) The structure and microstructure of α-cristobalite and its relationship to β-cristobalite. Phys Chem Min16:517-523

EBSCOhost - printed on 2/13/2023 4:48 AM via . All use subject to https://www.ebsco.com/terms-of-use

Wright AF, Lehmann (1981) The structure of quartz at 25 and 590°C determined by neutron diffraction. J Solid State Chem 36:371-380
Wong PTT, Baudais FL, Moffat DJ (1986) Hydrostatic pressure effects on TO-LO splitting and softening of infrared active phonons in α-quartz. J Chem Phys 84:671-674
Xiao Y, Kirkpatrick RJ, Kim YJ (1993) Structural phase transitions of tridymite: a ^{29}Si MAS NMR investigation. Am Min78:241-244
Yahagi Y, Yagi T, Yamawaki H, Aoki K (1994) Infrared absorption spectra of the high pressure phases of cristobalite and their coordination numbers of silicon atoms. Solid State Commun 89:945-948
Yakolev IA, Mikheeva LF, Velichkina TS (1956) The molecular scattering of light and the α-β transformation in quartz. Sov Phys Crystallogr 1:91-98
Yamaguchi H, Iishi K, Umegaki Y (1971) Study on the force field of quartz. J Sci Hiroshima Univ C 6:309-321
Yeganeh-Haeri A, Weidner DJ, Parise JB (1992) Elasticity of α-cristobalite:a silicon dioxide with a negative Poisson ratio. Science 257:650-652
Young RA (1962) Mechanism of the phase transition in quartz. Office Sci Res Rep No 2569
Zakharova EK, Zubov VG, Osipova LP (1975) Temperature dependence of the frequencies and widths of the Raman lines of single crystals of quartz. Sov Phys Crystallogr 19: 489-491
Zubov VG, Osipova LP (1977) Radiation and temperature induced changes in the width and intensity of the Raman spectral lines of α-quartz. Sov Phys Crystallogr 22:61-63

EBSCOhost - printed on 2/13/2023 4:48 AM via . All use subject to https://www.ebsco.com/terms-of-use

EBSCOhost - printed on 2/13/2023 4:48 AM via . All use subject to https://www.ebsco.com/terms-of-use

COLORED VARIETIES OF THE SILICA MINERALS

13 George R. Rossman 13

Division of Geological and Planetary Sciences
California Institute of Technology
Pasadena, California 91125 U.S.A.

INTRODUCTION

Quartz, when chemically pure SiO_2, is colorless and transparent from about 145 nm in the ultraviolet to about 2700 nm in the infrared when in mm to cm thickness. Natural quartz has three important colored varieties: amethyst (violet), citrine (yellow to brown) and smoky (dark smoky quartz is sometimes called morion). A fourth variety, prasiolite (green) also exists. Each of these varieties exhibits either a substitutional or interstitial component other than Si. In addition to chemical substitutions, development of color in some of these varieties requires exposure to ionizing radiation or heat. Each of these varieties can be produced through heat-treatment or irradiation of natural quartz of a different color and can also be produced by direct synthesis or through synthesis followed by irradiation. Other colored varieties of natural quartz (rose, blue, chrysoprase, jasper, etc.) are, in fact, mixtures of quartz and other phases (although there may be a type of rose quartz from substitutional causes alone).

Reviews and techniques

The colors of the silica minerals have been reviewed previously by Frondel (1962), Lehmann and Bambauer (1973), and Hutton (1974). While many of the major conclusions regarding color presented in these articles are generally unchanged, much research has been conducted since they were written which has resulted in a better understanding of the detailed origin of color and in the case of some varieties, a complete revision of the interpretation.

The primary tools for studying color centers in quartz are electron paramagnetic resonance (EPR) spectroscopy and optical absorption spectroscopy. EPR can detect on the order of 10^{11} to 10^{12} centers. It is 1000 times more sensitive than optical absorption for detecting centers which produce the strongest colors (charge-transfer bands) and 100,000 times more sensitive than optical absorption for detecting centers produced by isolated metal ions (ligand-field bands). Consequently, EPR may readily detect paramagnetic centers in quartz which are present at concentrations too low to have any effect upon the color of the mineral. Because absolute concentrations are rarely reported in EPR studies, it is often difficult to correlate the results of optical absorption and EPR studies. In spite of the quantitative limitations, EPR has proven the most informative method used to examine the detailed origin of color in quartz. The general field of EPR studies of color centers in quartz was reviewed by Wiel (1984) and updated in Wiel (1993).

IRON-SUBSTITUTION IN QUARTZ

Association of color with iron

Small amounts of iron can occur naturally in quartz and can also be introduced into synthetic quartz. The color of both amethyst and some types of citrine derives from an iron component. A green color seen in synthetic crystals grown in steel autoclaves and in some

EBSCOhost - printed on 2/13/2023 4:48 AM via . All use subject to https://www.ebsco.com/terms-of-use

heated amethyst, but rarely observed in natural samples, also comes from iron. In some specimens, amethyst, citrine and green coloration can be interchanged through the application of heat and irradiation.

Iron sites in quartz

Iron can occupy both substitutional (S sites) and interstitial (I sites) sites in quartz. The substitutional site is the tetrahedral, oxygen-coordinated silicon site. At least two interstitial positions exist (Fig. 1). The I1 position is on the *c*-axis midway between two silicon atoms; I1 cations are coordinated by two oxygens at 1.92 Å and two more at 2.52 Å. Two additional oxygen anions are within interaction distance, so the site can be considered to be a distorted octahedral site, [FeO_6]. The I2 position is on an *a*-axis with nearly regular tetrahedral coordination from two oxygens at 1.99 Å and two at 2.03 Å; it is also called the [FeO_4] interstitial site.

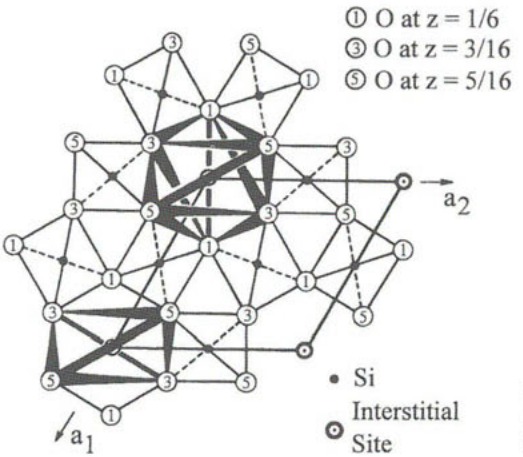


Figure 1. The interstitial sites in quartz in heavy outline. Modified from Figure 4 of Lehmann and Moore (1966).

Different configurations of the iron site are possible; they depend on the identity and geometry of the second-nearest neighbors. In the language of EPR spectroscopy, these configurations are called "centers." The substitutional centers are designated by two parallel terminologies -- "S_j" and "[FeO_4/M]^n", where j is an integer index, M is the compensating cation and n is the local charge.

The best understood and most studied centers in quartz are the Fe^{3+} substitutional centers. They involve replacement of a $[SiO_4]^0$ unit with either an electrically-uncompensated substitution, the $[FeO_4]^-$ center, or with a variety of monovalent cations functioning as electrical compensators, the $[FeO_4/M]^0$ centers. Fe^{3+} substitutional centers are present at low concentrations and have comparatively little direct influence on the color of quartz varieties, but can be important precursors to other color centers. The prominent iron centers are briefly summarized before the colored varieties of quartz associated with these centers are discussed.

The $[FeO_4/Li]^0$ center = The S1 center. This center, described by Hutton (1964) and Barry et al. (1965), is a substitutional Fe^{3+} at the Si site with Li^+ in an adjacent interstitial site on the twofold axis (Stegger and Lehmann, 1989a). At 20 K, two symmetry-distinct centers are represented by two forms, called $[FeO_4/Li]^0\alpha$ and

EBSCOhost - printed on 2/13/2023 4:48 AM via . All use subject to https://www.ebsco.com/terms-of-use

$[FeO_4/Li]^0\beta$ by Minge et al. (1989a) and Halliburton et al. (1989). These forms differ in the location of the compensating ion, which can occur positioned on either the long-bond side (α) or the short-bond side (β) of the FeO_4 tetrahedron. Additional complexity is observed in the EPR spectra, from which a family of closely related $[FeO_4/Li]^0$ centers has been identified (Choi and Wiel, 1990). These centers probably correspond to long-range electric field effects, possibly originating from twin or surface boundaries. As a substitutional Fe center, the S1 configuration has little direct effect upon the color of the host crystal.

The $[FeO_4/H]^0$ center = The S2 center. This center, described by Lehmann (1967), is a substitutional Fe^{3+} at the Si site with a H^+ bound to one of the oxide ions in the immediate coordination environment. Most commonly, H is bonded to distant oxygens at 2.52 Å, creating the $[FeO_4/H]^0\alpha$ = the S2(D) center. In the less abundant center, the $[FeO_4/H]^0\beta$ = the S2(C) center, hydrogen is bonded to one of the closer oxygens at 1.92 Å (Mombourquette et al., 1989; Stegger and Lehmann, 1989). As a substitutional Fe^{3+} center, it has little influence upon the color of the host.

The $[FeO_4/Na]^0$ center = The S3 center. This center has been observed in synthetic iron-doped quartz electrodiffused with sodium ions, which replace most of the Li interstitial ions (Minge et al., 1989b). Its EPR pattern is observed only at temperatures below 70 K as line broadening from motion of the sodium ions at higher temperatures. No claims have been presented that this center is important for the color of natural iron-bearing quartz.

The $[FeO_4]^0$ center = The S0 center = The I center. The interpretation of this Fe^{3+} center remains the subject of controversy. Recognized by its EPR pattern, it is found in amethyst, citrine and synthetic brown quartz. It is due to Fe^{3+} without observed local charge compensation. Most studies of this center have relied upon analysis of the EPR pattern, but there are differing interpretations as to whether the Fe^{3+} is in a substitutional site or in an interstitial site.

Discovered by Matarrese et al. (1964) in synthetic brown quartz, it was initially assigned to Fe in an interstitial site by Lehmann and Moore (1966b), who concluded that the Si site is too small for Fe^{3+} and argued in favor of Fe^{3+} occupation of one of the larger channel sites, creating an I center. Matarrese et al. (1969) established that the Fe^{3+} is located on a twofold axis, and they proposed that it substituted for Si^{4+}. However, they could not rule out the possibility that located on an interstitial channel site. On the basis of optical spectra, Lehmann (1971a,b) argued in favor of the tetrahedral interstitial site (I4). Scala and Hutton (1976) re-analyzed the data of Matarrese et al. and concluded that Fe^{3+} is located on the Si^{4+} site. Mombourquette et al. (1986) examined synthetic brown quartz and concluded that the I4 center is, in fact, a substitutional center at the Si^{4+} site, and they proposed the label $[FeO_4]^-$ for the center. Behner et al. (1986) concluded that the zero-field splitting pattern of the EPR spectrum supports the interstitial assignment. Stegger and Lehmann (1989a) point out that the hyperfine splitting in the EPR pattern is not consistent with a substitutional site, but rather indicates that Fe^{3+} is in an interstitial site, possibly in association with two additional anions (either O or OH) in the *c*-axis channel $[FeO_6]$. Publications from the labs directed by Lehmann and Wiel recognize that the issue of the $[FeO_4]^-$ site is not resolved.

The Fe^{4+} site: $[FeO_4]^0$. The Fe^{4+} ion is formed from Fe^{3+} by the action of ionizing radiation and is important for the coloration of amethyst. The EPR and optical spectra of this site (Cox, 1976, 1977) are the basis of the assignment of the unusual

EBSCOhost - printed on 2/13/2023 4:48 AM via . All use subject to https://www.ebsco.com/terms-of-use

oxidation state Fe^{4+}. The site assignment remains controversial. Cox assigned it to a substitutional site, although Cohen (1985) suggests that it is in an interstitial site.

The Fe^{2+} interstitial center: $[FeO_6]$ = The I6 site. Lehmann and Bambauer (1973) present the model for an Fe^{2+} I6 site, which is an interstitial Fe^{2+} in a channel site of distorted octahedral symmetry. This center is important in green quartz and is observed occasionally in amethyst and citrine.

The Fe^{2+} interstitial center: $[FeO_4]$ = The I4 site. This site consists of Fe^{2+} in the approximately tetrahedral interstitial site. It is believed to be an intermediary in the formation of the Fe^{2+} I6 site in amethyst (Lehmann and Bambauer, 1973).

CITRINE

Classification

Citrine is a variety of quartz which ranges from yellow to orange to orange-brown. Although citrine occurs naturally, most of the citrine available today is produced by heat-treating amethyst. In this heat-treated material, Fe^{3+} is the cause of the color. A discussion of citrine is complicated by the fact that a number of yellow, greenish-yellow, and orange-brown colors are produced in quartz by irradiation (natural or laboratory) with or without subsequent heat-treatment, and these specimens are also called citrine. Irradiation may be an important factor in naturally colored crystals, since quartz can receive enormous doses of radiation from the decay of nearby ^{40}K, uranium, thorium, and their daughter products. An excellent, illustrated review on the topic of citrine color and the methods used to distinguish among the various origins of color has been presented by Schmetzer (1989).

Following, in part, the classification of Schmetzer (1989), a discussion of citrine must consider the following:

(1) orange-brown iron-containing natural quartz;
(2) yellow to orange-brown colors produced by heating amethyst;
(3) yellow to orange-brown colors in synthetic quartz grown in the presence of iron;
(4) light-yellow irradiation-induced color found naturally in quartz or produced by heating dark smoky quartz; and
(5) greenish-yellow color produced by irradiation (with or without subsequent heat-treatment) of either natural colorless quartz or synthetic colorless quartz.

Unfortunately, much of the early literature did not distinguish clearly among these different types of citrines. Furthermore, it is not possible to determine whether the "natural" citrine samples used in early studies had a history of heat-treatment.

Natural orange-brown iron-containing citrine. Natural iron-containing citrine can occur as zones of citrine in amethyst at localities such as Hyderabad, India; Minas Gerais, Brazil; and as the spectacular bicolored material from the Anahí mine, Bolivia. On surface exposures, crystals containing citrine regions in otherwise colorless sun-bleached amethyst can occasionally be found. Comparatively little published information is available about this type of naturally occurring citrine (Vasconcelas et al., 1994).

EBSCOhost - printed on 2/13/2023 4:48 AM via . All use subject to https://www.ebsco.com/terms-of-use

Early researchers pinpointed substitutional Fe^{3+} as the cause of color. Although substitutional Fe^{3+} is undoubtedly present in citrine, as evidenced by the EPR pattern (Barry and Moore, 1964), analysis of the optical absorption spectrum indicates that it plays a minimal role in causing color (Lehmann and Moore, 1966b). Lehmann and Moore attribute the color of citrine to sub-microscopic particles of a presumed iron oxide dispersed in the quartz based upon the similarity of the EPR and optical absorption patterns with those of heated amethyst (see below). The optical spectrum of undisputedly natural iron-containing citrine (Fig. 2) shows strong absorption in the ultraviolet region. The tail of the absorption band extends to the short wavelength region of the visible spectrum. A weak band centered at 476 nm is superimposed on the tail.

Aines and Rossman (1986) observed that in Bolivian and Indian bicolor amethyst-citrine, the hydrogen species in the citrine zones is predominantly molecular water whereas the amethyst zones have mostly hydroxide ion.

Heated amethyst. When amethyst is heated over the range 300 to 560°C, it loses the amethyst color and may become yellow, yellowish-brown, brown, green or colorless. These changes have been reviewed and investigated by Neumann and Schmetzer (1984a,b) and are summarized in Table 1. When amethyst is initially heated, the violet color begins to bleach. As the heating proceeds, amethyst may become completely colorless, or yellow or green colors may develop. At higher temperatures, some samples develop yellow color from colorless or light-green regions, or brown color from yellow regions. These changes in color are accompanied by the loss of the amethyst band at 545 nm and increases of the green-quartz band at 741 nm and the yellow-quartz band in the ultraviolet region. The role of H_2O and OH^- in the color changes associated with amethyst and citrine is largely unexplored.

The optical absorption spectrum of heated amethyst consists of intense, isotropic absorption in the ultraviolet region that tails into the visible region (Fig. 3). The particular color of the sample is determined by the rate of the increase in the absorption over the short wavelength region of the spectrum. This, in turn, is determined by the amount of iron contributing to the absorption. Spectra of samples from a number of localities have been presented by Schmetzer (1989). The ultraviolet spectrum has been examined in detail by Stock and Lehmann (1977).

Table 1. Color changes which result from heating amethyst.

Color Change	Amethyst localities
violet → colorless	Madagascar; Mexico; Serra, Brazil; synthetic amethyst from Japanese and Russian producers
violet → colorless → yellow	Brazilian Localities: Paraguay Mine; Bolivia Mine; Bahia; Cerar ; Cabeluda; Palmeira
violet → yellow	Brazilian Localities: Rio Grande do Sul; Area; Jakobina; Vaequem Pode; Bahia
violet → yellow → brown	Serra, Brazil; Uruguay
violet → light green → yellow	Blattfeld, Namibia; Tanzania
violet → green	Zambia, Montezuma Mine, Brazil; Four Peaks, Arizona

EBSCOhost - printed on 2/13/2023 4:48 AM via . All use subject to https://www.ebsco.com/terms-of-use

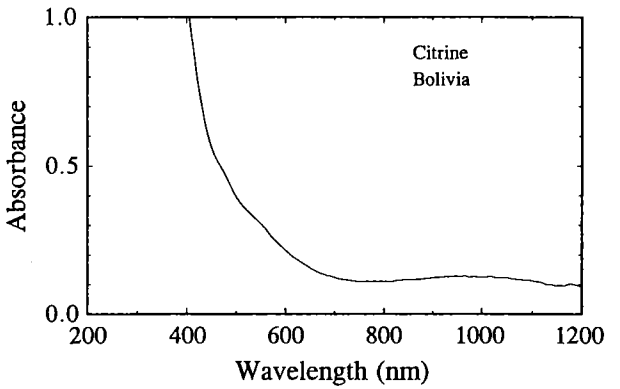


Figure 2. Optical absorption spectrum of natural citrine from the Anahí Mine, Bolivia. 1.0 cm thick. Data from Vasconcelos and Rossman, in preparation.

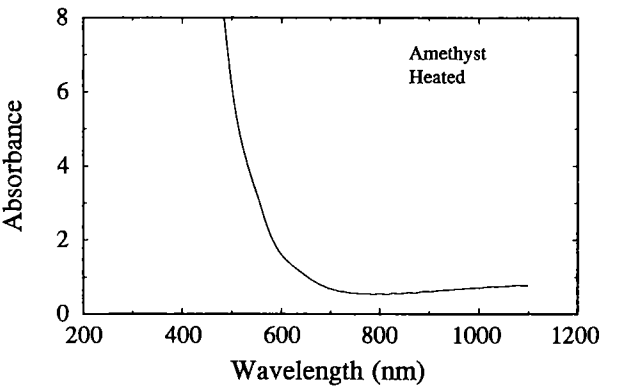


Figure 3. Spectrum of heated amethyst from Rio Grande do Sul, Brazil. The absorption is isotropic and arises from small clusters of an iron-rich phase. Data presented normalized to 1 cm thickness.

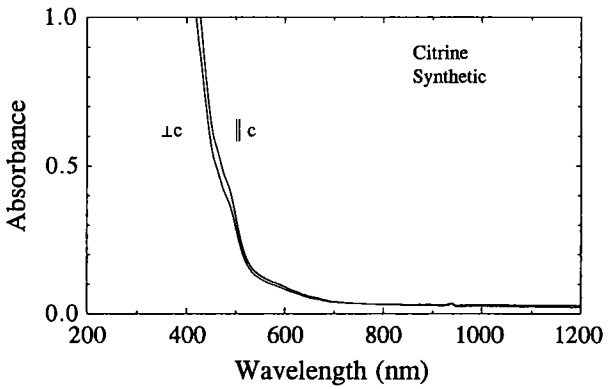


Figure 4. Spectrum of synthetic iron-containing yellow-brown quartz manufactured by Sawyer corporation. Data presented are normalized to 1 cm thickness.

EBSCOhost - printed on 2/13/2023 4:48 AM via . All use subject to https://www.ebsco.com/terms-of-use

The color is caused by sub-microscopic iron-containing particles, presumed to be Fe_2O_3, dispersed in the crystal through exsolution (Lehmann and Moore, 1966b; Lehmann, 1971a,b). These particles were identified by the width of their isotropic EPR line and its lack of temperature dependence (Hutton and Troup, 1966; Lehmann, 1967). The intensity of this EPR line is proportional to the intensity of the citrine color. Stock and Lehmann (1977) estimate that the size of the particles is on the order of 100 nm based on the width of the EPR line. The identification of the iron-containing particles as Fe_2O_3 suffers from the absence of the characteristic hematite absorption band near 850 nm, which can be clearly seen in the spectrum of jasper (Fig. 19) but not in that of heated amethyst.

Synthetic iron-containing quartz. Yellow and brown citrine can be synthesized in hydrothermal vessels from iron-containing solutions of silica in either alkaline K_2CO_3 or KCl/NaCl (Tsinober and Chentsova, 1959; Ballman, 1961; Khadzhi and Reshetova (1977); Hosaka and Taki, 1983; Hosaka, 1990). The color of the synthetic citrines results from the superposition of three different Fe-bearing centers: colloidal particles of a presumed iron oxide, Fe^{3+} in the $[FeO_4]^-$ site, and Fe^{2+} in the I6 site. The absorption spectrum of a synthetic citrine is presented in Figure 4.

Citrine color produced by irradiation. Citrine colors can occur in naturally irradiated quartz, or they can be produced by artificial irradiation of natural quartz from certain localities, by heat-treatment of natural smoky quartz, or by heating quartz turned smoky through laboratory irradiation. In addition, Krefft (1975) reports that after quartz is subjected to extended electrolysis in water vapor and then exposed to ionizing radiation, citrine color centers are produced. Yellow coloration can also be produced by heating natural dark-brown or black smoky quartz to about 300°C (Bank, 1976). Samoilovich et al. (1976) and Lehmann (1977;1978) emphasize that the origin of these colors is intrinsically different from that of heat-treated amethyst.

EPR spectra. The EPR spectrum of this type of citrine was studied by Maschmeyer et al. (1980), who found two paramagnetic centers. They distinguish this type of natural yellow citrine from heated amethyst which usually has a more intense brownish color than this citrine. Maschmeyer and Lehmann (1983a) describe seven centers in citrine that originate from irradiation.

Optical spectra. Optical absorption spectra have been presented by Lehmann (1977), Maschmeyer et al. (1980) and Schmetzer (1989). The spectrum of the radiation-induced citrine resembles that of heat-treated amethyst. It consists of an intense absorption centered in the ultraviolet region that extends into the visible region and preferentially absorbs in the violet and blue region (Fig. 5). Unlike the spectrum of heat-treated amethyst, this absorption is slightly pleochroic. Unlike the greenish-yellow irradiated quartz discussed below, the spectrum of this material does not have a distinct absorption band at 400 nm.

Greenish-yellow irradiation colors. Greenish-yellow hues result when quartz from certain localities is irradiated. This unusual coloration arises through the following processes: (1) irradiation of colorless quartz by gamma rays; (2) irradiation of colorless quartz to turn it smoky followed by heat-treatment at low (150-250°C) temperatures; or (3) heat treatment of naturally smoky quartz at the same low temperatures. The relationships among the colors are summarized in Figure 6.

EBSCOhost - printed on 2/13/2023 4:48 AM via . All use subject to https://www.ebsco.com/terms-of-use

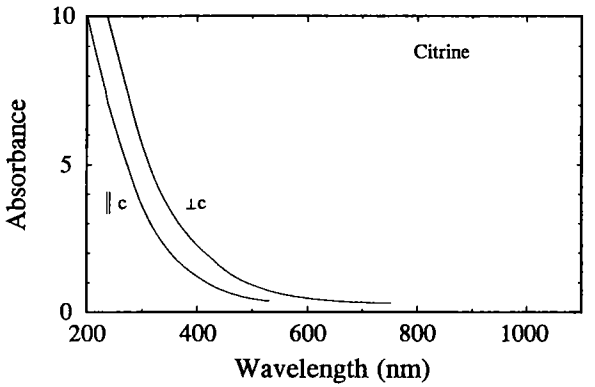


Figure 5. Optical spectrum of yellow-brown citrine of the irradiation type. These data are from Lehmann (1977) and are have been normalized to 1 cm thickness.

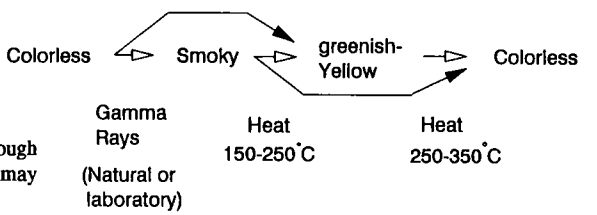


Figure 6. Interconversions of quartz through irradiation and heat-treatment which may lead to greenish-yellow colors.

Samoilovich et al. (1969) recognized two different types of citrine. One type they associated with iron impurity ions in the quartz and was not attributable to irradiation. The other type they called irradiated yellow quartz and prepared by exposing natural quartz to 2-10 MRads of ^{60}Co gamma rays followed by annealing at 200°C. Crystals that turned yellow had high Al, H and Li contents, an observation confirmed by Lehmann and Bambauer (1973). Bukanov and Markova (1969) observed that citrine color occurred naturally in quartz crystal deposits in the USSR with high Li contents ($>10^{-4}$ % Li). The depth of citrine color as developed by irradiation with 25 MRads of ^{60}Co gamma rays was directly proportional to the Li content, which could be measured by the Li-OH vibration at 3384 cm^{-1} in the infrared spectrum. The optical spectra reported by both of these groups identifies their specimens as greenish-yellow citrine.

Lehmann (1971a) recognized that pale yellow colors could be obtained by irradiation (1 Mrad gamma rays) of natural quartz with high Al and H contents. Unlike citrine produced from heat-treated amethyst, the products of this irradiation had a comparatively low thermal stability; they would bleach at 170°C.

Optical spectra of greenish-yellow citrine. The optical absorption spectrum of the citrine described by all of these reports is dominated by a band at 400 nm (the A2 band) on a tail of a more intense absorption band centered in the ultraviolet. An additional band at about 670 nm (the A1 band) is usually present at lower intensity (Fig 7). The color is due to the predominance of absorption in the violet and blue end of the spectrum.

EBSCOhost - printed on 2/13/2023 4:48 AM via . All use subject to https://www.ebsco.com/terms-of-use

EPR spectra. Samoilovich et al. (1969) presented a model for the color center in greenish-yellow citrine in which Si sites are substituted with Al^{3+} with charge-compensating H^+ and Li^+ nearby. Irradiation would generate a hole center (an electron deficient oxide ion analogous to the smoky center discussed in a later section) near which the H^+ and Li^+ would remain: $[AlO_4/H,Li]^0$. Other EPR spectra of this center are presented by Lehmann (1971a), Lehmann and Bambauer (1973), Samoilovich et al. (1976) and Maschmeyer et al. (1980) with some scatter in the relevant spectral parameters.

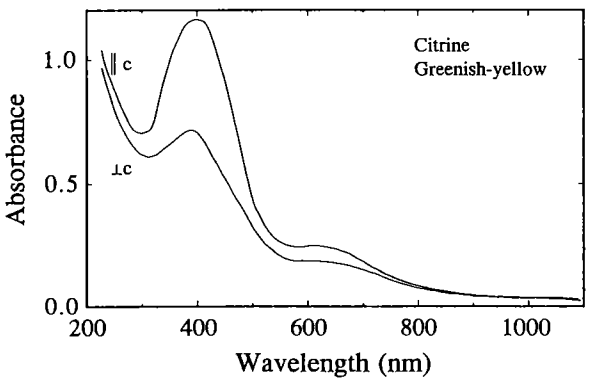


Figure 7. Optical absorption spectrum of a greenish-yellow citrine showing the band at 400 nm. Prepared from the data in Samoilovich (1969); normalized to 1 cm thickness.

New interpretations

In an extensive study of the irradiation behavior of natural quartz, Nassau and Prescott (1975, 1977a) further describe greenish-yellow colors produced by irradiation of both natural and synthetic quartz with gamma rays (and followed in some instances by heat-treatment). They view the spectra of most irradiated quartz (smoky, yellow, greenish yellow, etc.) as a superposition of five absorption bands that can only be resolved with curve-fitting methods (Table 2). The relative proportions of the centers corresponding to the components in the spectrum will determine the color of a particular specimen. In most cases, the color is dominated by the tail of a strong absorption band in the ultraviolet and is modified by the components in the visible region. Smoky color comes from absorption by the A3 band. Blue color originates from the A1 and A2 bands, and greenish-yellow from the C band. The A3 band correlates with the aluminum-hole EPR center. Meyer et al. (1984) determined that the A3 band is actually a doublet with the major component at 435 nm and a minor component at 633 nm. The relationship of the other bands to the EPR centers has not been determined.

Table 2. Positions of component bands in the smoky quartz spectrum. From Nassau and Prescott (1977)

band	nm	wavenumbers	electron volts	
A1	670	14,900	1.85	blue band
A2	486	20,600	2.55	blue band
A3	427	23,400	2.90	smoky band
B	314	31,900	3.95	
C	<270	>48,000	>6.00	UV tails

EBSCOhost - printed on 2/13/2023 4:48 AM via . All use subject to https://www.ebsco.com/terms-of-use

Mössbauer spectra

Ideally, Mössbauer spectroscopy would be of great value in studying the origin of color of Fe-containing varieties of quartz. However, because of the low Fe concen-trations in citrine (and other varieties of quartz), little Mössbauer spectroscopy work has been conducted on quartz. Vereshchak et al. (1973) examined the Mössbauer spectrum of synthetic quartz diffused under hydrogen at 1100°C with ^{57}Co (which decays to ^{57}Fe) and concluded that the iron was present predominantly in the 2^+ oxidation state. This result appears to be of little value for interpreting the state of Fe in natural quartz.

AMETHYST

Amethyst is the violet variety of α–quartz. Amethyst color develops only in iron-containing quartz (Holden, 1925). However, iron alone cannot account entirely for amethyst color, as evidenced by other iron-containing varieties of quartz such as citrine and green quartz. In 1906, Berthelot recognized that the development of amethyst color is associated with ionizing radiation . Amethyst color is destroyed by heat but may be restored by ionizing radiation, if the heating is not excessive.

Early ideas

Early ideas involving gold or titanium as a source of amethyst color are now discredited, as is the proposal by Berthelot (1906) that Mn is responsible for amethyst color. This idea came from the similarity of the color of amethyst to the color of potassium permanganate solutions ($KMnO_4$) and the observation that amethyst color is generated in Mn-containing glasses upon exposure to ionizing radiation.

Iron centers in amethyst

In amethyst, three prominent Fe^{3+} centers have been identified primarily through the interpretation of EPR spectra. They are the S1, S2 and I6 centers. According to the generally accepted model of Lehmann (1967), amethyst is formed through a process involving irradiation in which an Fe-containing precursor (Fe^{3+} on the Si site) interacts with the radiation and gives rise to a new color center, Fe^{4+}, which actually produces the amethyst color. The energy of a gamma ray photon is large compared to the binding energy of an electron on an Fe^{3+} ion. The gamma ray effectively strips the electron away from the Fe^{3+} (thereby oxidizing $Fe^{3+}$to Fe^{4+}) and sends the electron through the host crystal until it decelerates and becomes metastably attached to an electron trap. This trap is believed to be interstitial Fe^{3+}, which is then reduced to Fe^{2+}.

Barry et al. (1965) proposed that Fe^{3+} in a Si^{4+} site is the precursor for amethyst color, and Lehmann and Moore (1966a) and Lehmann (1967) proposed that Fe^{4+} in the Si site was the source of the amethyst color. Cox (1976) undertook a study of the EPR spectrum of amethyst in an attempt to provide direct evidence of Fe^{4+}. Fe^{3+} in quartz (in multiple sites) gives rise to hundreds of EPR lines (Hutton, 1964; Barry et al., 1965; Lehmann and Moore, 1966b; Matarrese et al., 1969; Zaitov et al., 1975) so Cox obtained amethyst spectra under conditions (4 K, high microwave power) which would saturate the Fe^{3+} contributions. The center Cox discovered corresponded to a $\Delta M = \pm 4$ transition of a center with spin $S = 2$. Such a transition could be caused by either Fe^{4+} or Fe^{2+}. Because this center has C_2 symmetry, it must be located on each of the three symmetry-related Si-sites on the C_2 axes. However, the EPR data indicate that the three C_2 sites are not equally

EBSCOhost - printed on 2/13/2023 4:48 AM via . All use subject to https://www.ebsco.com/terms-of-use

populated even though they should be equivalent in a mineral of trigonal symmetry. The concentration of the paramagnetic center in one of the C_2 sites is 10 to 100 times greater than in the other two in a given crystal sector. The same unequal distribution was observed for the Fe^{3+}, in accord with earlier observations (Barry et al., 1965; Lehmann and Moore, 1966b).

Cohen and Hassan (1974) suggested that substitutional Fe^{3+} (the S1 site) is charge compensated by Fe^{3+} in interstitial voids (the I site), and they proposed that this combination is the precursor to amethyst color. They wrote the amethyst-forming reaction in terms of a hole center and its associated trapped electron:

$$(Fe^{3+})_{sub} + (Fe^{3+})_{int} \Rightarrow \text{hole center } (Fe^{4+}) + \text{trapped electron } (Fe^{2+})$$

Cohen (1985) recognized that minor amounts of Al in amethyst could potentially form smoky centers; in nature, however, amethyst color dominates even in cases where Al content exceeds the Fe content. Thus, Cohen (1985) suggested a more complicated mechanism involving a role for both substitutional Al and interstitial alkali ions. This model requires interstitial Fe^{4+}. The postulated sequence of events when quartz is subjected to ionizing radiation is:

(1) $Al\text{-}O^- \Rightarrow Al\text{-}O^0 + e^-$ (formation of a trapped hole center on substitutional Al)

(2) $Na^+ + e^- \Rightarrow Na^0$ (formation of an atomic alkali atom which diffuses to form the trapped electron center)

(3) $Fe^{3+} \Rightarrow Fe^{4+} + e^-$ (oxidation of interstitial Fe)

(4) $Al\text{-}O^0 + e^- \Rightarrow Al\text{-}O^-$ (quenching of the hole by the electron).

Several difficulties arise from this model, including the lack of optical and EPR spectral features from atomic sodium. Furthermore, the validity of this proposal with regard to synthetic amethyst should be examined for those cases in which the amount of Fe greatly exceeds the amount of Al.

Adekeye and Cohen (1986) provide additional arguments in favor of interstitial Fe^{4+} based upon a consideration of the pervasive twinning of the amethyst color sectors in quartz crystals. Stegger and Lehmann (1989a) focus on the role of Fe and postulate that the S1 center loses an electron to form the substitutional Fe^{4+} center characterized by Cox (1976), and the I center evidently captures the electron to form Fe^{2+}:

$$[Fe^{3+}O_4 \cdots Li] + [Fe^{3+}O_6] \Rightarrow [Fe^{4+}O_4 \cdots Li] + [Fe^{2+}O_6] \ .$$

These models are complicated by the observations of Cressey et al. (1993) who obtained *L*-edge X-ray absorption spectra (transitions to the 2s orbital) on an amethyst. They found no indication of Fe^{4+} in the 2p absorption spectrum and concluded that two-thirds of the iron in amethyst is Fe^{2+}. Such results need to be examined in view of the optical absorption spectrum of the same amethyst samples to see whether the amount of Fe^{2+} indicated by the optical spectrum is consistent with the interpretation of the X-ray spectrum.

Although the roles of Fe and irradiation in the formation of amethyst are broadly established, these studies illustrate that the details regarding the Fe^{4+} site and its local environment are not unequivocally established, and additional work on the Fe^{4+} center is needed.

EBSCOhost - printed on 2/13/2023 4:48 AM via . All use subject to https://www.ebsco.com/terms-of-use

Color and optical spectrum

The amethyst optical absorption spectrum has been extensively examined. The salient features of the spectrum were presented by Cohen (1956a), who also reviewed earlier studies. The spectrum consists of absorption bands at 950, 545 and 357 nm, which define the transmission windows in the 460 nm region and in the red portion of the spectrum (Fig. 8). The spectra of natural and synthetic amethysts are similar, but the natural material tends to have higher levels of absorption in the ultraviolet region due to contributions from other iron centers and aluminum centers. Numerous other papers have addressed the spectrum of both natural and synthetic amethyst and have extended the study to include the intense ultraviolet bands at 200 nm, 225 nm, and 280 nm (Tsinober and Chentsova, 1959; Lehmann and Moore, 1966b; Schlesinger and Cohen, 1966; Lehmann, 1967; Lehmann and Bambauer, 1973; Hassan and Cohen, 1974; Cohen and Hassan, 1974; Stock and Lehmann, 1977; Balitsky, 1977; Balitsky and Balistkya, 1986). Cox's (1977) study, in particular,was important in demonstrating that the optical absorption is consistent with Fe^{4+} but not Fe^{2+}. The color tends to be localized to the (1011) faces, often in bands of color that parallel the (1011) face.

Dotto and Isotani (1991) put amethyst through heating and irradiation cycles and show that the bands at 545 nm and 357 nm have the same origin. The 950 nm band is most intense for light polarized perpendicular to the *c*-axis; the 545 nm band has about the same intensity in both polarizations; and the 357 nm band is more intense with light polarized parallel to the *c*-axis (Balitsky, 1977). The deep ultraviolet region absorbs more intensely when the electric vector is polarized parallel to the *c*-axis (Stock and Lehmann, 1977).

Amethyst displays biaxial optical absorption. The experimental measurement of the orientation of the bands is complicated both by the uniaxial optics imposed by the host crystal and by the optical rotation of plane polarized light. Cox (1977) determined that the 945 nm band is completely polarized parallel to a 2-fold axis (a_i-axis) and that the ~545 nm band has three components. A component centered at 527 nm is polarized in the $\mathbf{E} \parallel a_i$ direction. Two other components at 538 and 600 nm are polarized in the plane perpendicular to the a_i-axis but are not aligned with the *c*-axis.

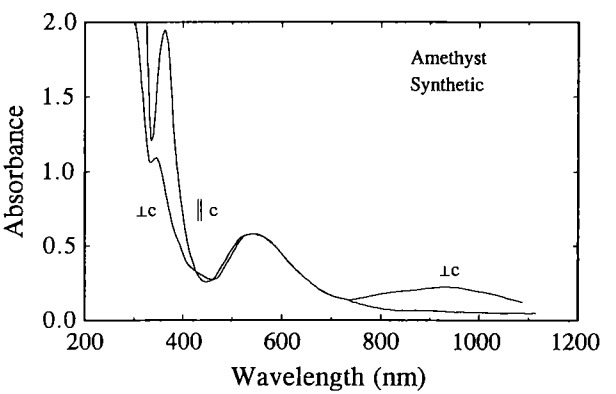


Figure 8. The optical absorption spectrum of a synthetic amethyst. Prepared from the data presented in Balitsky (1977).

EBSCOhost - printed on 2/13/2023 4:48 AM via . All use subject to https://www.ebsco.com/terms-of-use

Synthesis of amethyst

The ultimate proof of the contribution of irradiation to amethyst color came with the laboratory synthesis of amethyst crystals, first accomplished with relatively large crystals by Tsinober and Chentsova (1959). The process involves first making near-colorless or slightly yellow Fe^{3+}-doped synthetic quartz crystals. These are subsequently treated with ionizing radiation (X-ray or gamma-ray) to generate the amethyst color (Zaitov et al., 1975; Balitsky, 1977; Hosaka and Taki, 1983). Not all synthetic iron-containing quartz will turn to amethyst in response to irradiation; only those crystals in which the appropriate precursor sites are occupied will change. A history of synthetic amethyst and its growth methods is presented in Balitsky (1980). The gemological distinction between synthetic and natural amethyst is discussed by Schmetzer and Bank (1980), who present infrared spectral criteria, and Schmetzer (1985) and Crowningshield et al. (1986) who present criteria based on Brazil law twinning in natural amethyst, although subsequently, it has been demonstrated that the twinning criteria do not always allow distinction.

Irradiation dose

When synthetic amethyst is irradiated in a laboratory setting, the amethyst color reaches a saturation level after exposure to radiation in the 2 to 6 Mrad range (Balitsky, 1977; Hosaka and Taki, 1983). The author has developed amethyst color from surface exposures of colorless, sun-bleached Bolivian amethyst through 2 Mrad of gamma-ray irradiation. This dosage of gamma radiation is comparatively low for a natural setting. Gamma radiation from ^{40}K alone could provide this dose in 6×10^6 years in a granitic pegmatite environment (Reinitz and Rossman, 1988). In quartz-vein-hosted amethyst deposits, potassic clays are often present, and these could be a source of radiation. The intensity of color of natural amethyst is not necessarily saturated. Lehmann and Moore (1966a) report that irradiation of a Brazilian amethyst with X-rays increased the intensity of its color fivefold.

Distribution of amethyst color

The color of amethyst is usually unevenly distributed in natural crystals. It is usually concentrated under the major rhombohedral face $r=\{1011\}$ and often consists of a series of thin, dark bands which parallel the r and occasionally the $z=\{0111\}$ faces. Polysynthetic twinning on the Brazil law is commonly observed in the major rhombohedral sector, with alternating lamellae of left-handed and right-handed quartz. Schmetzer (1987) discusses the twinning microstructure in natural amethyst as observed with the optical microscope. Bands of extinction (called Brewster fringes) about one third as wide as the individual lamellae of left- or right-handed quartz separate the lamellae. Schlössin and Lang (1965) concluded that iron is present preferentially in the Brewster fringes. Similarly, McLaren and Phakey (1965) and McLaren and Pitkethly (1982) show that the iron impurities are concentrated in the Brazil twin boundaries; they suggest that any impurity atoms diffusing along the c-axis channels could become trapped in the twin boundaries because of the relative displacement across them. Such an argument necessarily supports a role for interstitial iron in the amethyst coloration.

Analytical aspects

The iron content of amethysts runs from a few tens of ppm to 350 ppm by wt (Barry et al., 1965; Dennen and Puckett, 1972; Lehmann and Bambauer, 1973; Marfunin, 1979;

EBSCOhost - printed on 2/13/2023 4:48 AM via . All use subject to https://www.ebsco.com/terms-of-use

Cohen, 1984). Cohen (1984) attempts to determine the intensity of the Fe^{4+} absorption at 545 nm and suggests that the oscillator strength (0.10) indicates that the absorption has some charge-transfer character.

Color stability

Amethyst color is unstable in light. While systematic investigation of the photostability of amethyst has not been conducted, informal fading experiments have shown that much of the color of amethyst geodes from southern Brazil is lost after three year's exposure to direct sunlight (Currier, 1985). Bolivian amethyst loses one-third of its color after two months in sunlight (Vasconcelos et al., 1994). This is not unexpected given the metastable nature of many electron traps. A careful observer can readily observe that many of the large amethyst geodes used for decorative purposes have unexpectedly pale color after residing in bright locations. This is certainly the result of photochemical decay of the amethyst center. In a few instances the color of faded amethyst can be restored by gamma-ray irradiation, but for material from most localities, the irradiation process co-generates smoky color (from Al centers) which either overwhelms the amethyst color or detracts from the quality of the hue.

In the laboratory, amethyst color bleaches out at temperatures greater than 400°C with the possible formation of citrine, or colorless or green quartz. This is discussed in a preceding section on citrine. Hassan (1972) and Dotto and Isotani (1991) present detailed studies of the thermal fading characteristics of the amethyst spectrum and its regeneration in response to irradiation. Studies of Thunder Bay, Ontario amethyst suggest that in the natural setting where prolonged exposure to magmatic heat occurs, amethyst color is thermally bleached at temperatures as low as 145°C (McArthur et al., 1993).

Amethyst-citrine (ametrine)

Rarely, quartz with both amethyst and citrine zones are encountered. The most striking example of amethyst-citrine that is now the source of commercial gemstones is the Anahí mine, Bolivia (Vasconcelos et al., 1994). Bicolor quartz from this locality is marketed under the name 'ametrine'. The origin of this material at one time was controversial (Nassau, 1981) because of the concern that it had been produced through heat-treatment or synthesis (Balitsky and Balitskaya, 1986). Less-striking occurrences of citrine in amethyst are Hydrabad, India (Aines and Rossman, 1986), Mato Grosso, Brazil (Bensusan and Bensusan, 1958), and unspecified localities in Minas Gerais, Brazil.

Optical biaxial behavior

Although colorless α–quartz (including colorless portions of amethyst crystals) is uniaxial in keeping with its trigonal symmetry, amethyst is often biaxial with 2V ranging from near 0 to 12° (Melankolin and Tsinober, 1963; Frondel, 1962). As noted earlier, EPR studies show that Fe^{3+} does not equally occupy the three equivalent Si positions (Barry et al., 1965). When amethyst crystals are heated to remove the amethyst color, the crystals become nearly uniaxial, but they will become biaxial upon irradiation with X-rays. This observation is strong evidence that the color centers (Fe^{4+}) are responsible for the biaxial character.

The optical anisotropy is more complex than would be predicted for a trigonal crystal. Striking color changes from red to purple to blue seen when some amethyst crystals are

EBSCOhost - printed on 2/13/2023 4:48 AM via . All use subject to https://www.ebsco.com/terms-of-use

rotated (Pancharatnam, 1954) are a result of the biaxial character of the absorbing species. Pancharatnam investigated the pleochroism of amethyst and found the following pleochroic scheme for an untwinned sector: 1) Along the *a*-axis, light orange; 2) Along two directions in the plane perpendicular to the *a*-axis and inclined approximately +45° and -45° to the *c*-axis, one deep red and the other blue. Which direction is red and which is blue depends upon the optical handedness of the sector and whether the sector is within a major or minor rhombohedron. Hassan and Cohen (1974) and Cox (1977) examined the optical absorption pattern of amethyst in detail, and they established the polarization directions of the visible bands. These do not necessarily correspond to the conventional ordinary and extraordinary rays because of the lower symmetry of the Fe^{4+} center originating from the unequal distribution of the Fe ions. In a (0001) section, the absorption bands (and color) are maximized when the incident light is polarized parallel to an *a*-axis, and the color is at a minimum when the polarization vector is 90° from the axis. In an *a-c* section, amethyst is pleochroic with the 357 nm band more intense with $\mathbf{E} \parallel c$, the 545 nm essentially unpolarized, and the 957 nm band more intense with $\mathbf{E} \perp c$. The position of the 545 nm band differs by about 75 nm among these polarizations.

GREEN QUARTZ

Green quartz, also called prasiolite or greened-amethyst, is produced when amethyst from certain localities (Four Peaks, Arizona; Montezuma Mine, Minas Gerais, Brazil; Zambia) is heated between 300° and 600°C (Sinkankas, 1957; Neumann and Schmetzer, 1984a,b). Neumann and Schmetzer discuss in detail the changes that occur when amethyst is heated to form green quartz. The color is caused by a transmission window defined by an absorption band centered at 741 nm (Rose and Lietz, 1954) that arises from interstitial Fe^{2+} (Lehmann, 1967) and a tail from a strong absorption band in the ultraviolet. An additional Fe^{2+} absorption band occurs in the near-infrared region at 950 nm (Fig. 9). These wavelengths are typical for six-coordinated Fe^{2+} in a slightly distorted octahedral site rather than for tetrahedral Fe^{2+}. The spectrum, including the ultraviolet region, is presented in Cohen and Hassan (1974).

Lehmann and Bambauer (1973) present a model for the formation of green quartz in which the green color arises from interstitial Fe^{2+} in a channel site of distorted octahedral symmetry [I6 = FeO_6]. This site is formed by reduction of Fe^{2+} in a tetrahedral interstitial site [I4 site] followed by its migration along the *c*-direction ~0.9 Å to the I6 site. The blue, synthetic iron-containing quartz discussed below in the section on blue quartz and the fact

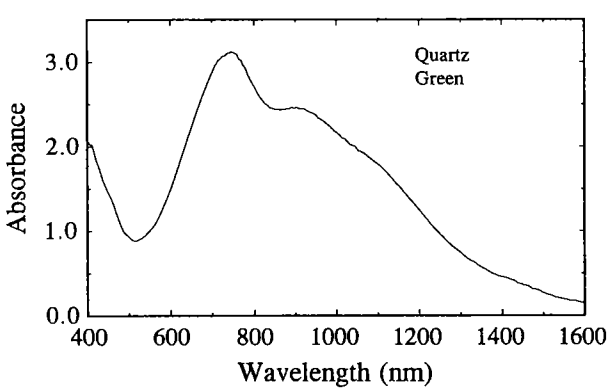


Figure 9. Optical absorption spectrum of a synthetic green quartz showing the absorption bands of Fe^{2+} in the intersitial site. Presented normalized to 1 cm thickness.

EBSCOhost - printed on 2/13/2023 4:48 AM via . All use subject to https://www.ebsco.com/terms-of-use

that some heat-treated amethyst turnsa blue-green rather than pure green indicates that the green color is a blend of blue color from Fe^{2+} in the I6 site and yellow from another iron component (Fe^{3+}).

Natural occurrences

Natural occurrences of green quartz are rare. Platonov et al. (1991) describe quartz crystals with green tips inside quartz-agate geodes from Poland collected in the late 19th century. Their optical absorption spectra demonstrate that iron occupies the same sites as in the synthetic green quartz. An occurrence north of Reno, Nevada is described by Paradise (1982); a vesicular, amethyst-bearing basalt was covered by another basalt flow, and the amethyst near the contact with the hot basalt was turned to green quartz. McArthur et al. (1993) discuss the Thunder Bay amethyst deposit, in which the amethyst was thermally-bleached to form pale green quartz in parts of the deposit. The optical absorption pattern of a Brazilian green quartz of uncertain history was described by Nassau and Prescott (1977b).

Green color through irradiation

A greenish-yellow color can be produced through the irradiation (sometimes followed by gentle heating) of many specimens of natural or synthetic quartz (Nassau and Prescott, 1977a). This color is discussed further in the section above on citrine irradiation colors.

Synthesis of green quartz

Synthetic green quartz (Tsinober and Chentsova, 1959) is grown in steel utoclaves with aqueous K_2CO_3. It becomes green with the uptake of Fe^{2+} released from the corrosion of the pressure vessel. Ballmann (1961) provides additional information about the synthesis of green quartz, indicating that coupling Fe^{2+} (in an interstitial position) with Be^{2+} (which would be substitutional at a Si site) produces a deep green product.

SMOKY QUARTZ

Smoky quartz is a yellowish-brown to black variety of quartz. It occurs in nature as a result of natural radiation acting upon Al-containing quartz. It can be made in the laboratory by irradiation of colorless quartz from many localities worldwide, and by irradiation of synthetic quartz. The topic of aluminum centers in quartz was reviewed by Wiel (1975) and is further discussed in a series of articles (Nuttall and Weil, 1980a,b; 1981a,b,c; Meyer et al., 1984).

Aluminum centers

Smoky quartz is associated with substitutional Al. Concentrations of aluminum in smoky quartz range up to a few thousand Al atoms per million silicon atoms. Although the detailed interpretation of the optical absorption spectrum (and thus the color) is not yet available, the dominant cause of color is now thought to be the oxygen ion, O^- (with a single unpaired electron), bound to a substitutional Al ion.

Griffiths et al. (1954a,b) first demonstrated that smoky quartz has an electron paramagnetic resonance spectrum and that the intensity of the signal is proportional to the depth of the smoky absorption. They also presented evidence that smoky color and the

EBSCOhost - printed on 2/13/2023 4:48 AM via . All use subject to https://www.ebsco.com/terms-of-use

resonance signal are associated with small quantities of aluminum in the crystal. The details of the hyperfine structure in the spectrum, which arises from nuclear magnetic moments of atoms in proximity to the unpaired electron, clearly show that the unpaired electron is adjacent to an atom with nuclear spin 5/2, namely aluminum.

The model for the smoky center was outlined by O'Brien and Pryce (1955) and developed in detail by O'Brien (1955) based on the EPR spectrum of X-ray irradiated smoky quartz. The main features of the spectrum were attributed to an unpaired electron in a localized orbital on an oxygen atom next to an aluminum atom. The unpaired electron is formed by the removal of one electron from an electron pair on the oxide ion (yielding a hole center). Mackey (1963) determined that a monovalent cation is associated with the original substitutional Al, an $[AlO_4/M]^0$ center where M = H, Li, or Na, by examining the EPR pattern of irradiated quartz at low temperature where the compensating cation still remains in the vicinity of the Al ion. The charge compensation cation diffuses away from the hole center at room temperature. The fate of the liberated electrons is not established. Substitutional Ge and Ti can trap electrons (Rinneberg and Wiel, 1972), but their concentration in most quartz crystals is not comparable to the number of Al centers.

Schnadt and Schneider (1970) confirm the interpretation of O'Brien (1955) that the SiO_4 tetrahedron contains two pairs of non-equivalent oxygens, that the hole center is confined to just one of those pairs, and that the hole is thermally delocalized between the two equivalent oxides at room temperature. They present a detailed model for the electronic structure of the hole center based on an O^- ion which accounts for the experimental EPR data. Nuttall and Weil (1981a) confirm that $[AlO_4]^0$ is the appropriate model and determine that the missing electron is on one of the oxygens on a long (1.796 Å) Al-O bond.

E centers

A variety of other paramagnetic centers are observed in the EPR spectrum of smoky quartz (and other quartz varities). Several are related to point defects in the quartz structure and may present traps for liberated electrons or may be color centers themselves. Best studied are the E centers related to oxide vacancies in the quartz structure (Weil, 1993):

E'_1 center: $[O_3Si \cdot SiO_3]^+$	Electron trapped on a silicon with a missing O^{2-}.
E'_2 center: $[O_3Si \cdot H^+O_3]$	Electron trapped at site of a missing Si and a O^- with H (Weeks and Lell, 1964).
E'_4 center: $[O_3Si{:}H \cdot SiO_3]^0$	Electron trapped near a silicon missing O^{2-} with H.

Optical spectra

The optical absorption spectra of smoky quartzes are variable, but they are commonly dominated by bands near 427 and 670 nm, which are on the tail of more intense absorption in the ultraviolet region (Ditchburn et al., 1954; Mitchell and Paige, 1955, 1956). The absorption is anisotropic (Fig. 10) and more intense with light polarized parallel to the *c*-axis (Mitchell and Paige, 1955; Cohen, 1956b).

Nassau and Prescott (1975, 1977a) irradiated nearly 400 colorless natural and synthetic specimens and studied the resulting colors. They found that smoky quartz absorption is a superposition of 5 Gaussian components (Fig. 11, Table 2). Meyer et al. (1984) further refined the decomposition of the smoky quartz spectrum into its Gaussian components. Earlier, only two bands in the visible region were recognized (A1 and A2). (Griffiths et al., 1954b; O'Brien, 1955; Mackey, 1963; Schnadt and Schneider, 1970); A1 and A2 were assumed to be correlated with aluminum content, but in a later study (Weeks,

EBSCOhost - printed on 2/13/2023 4:48 AM via . All use subject to https://www.ebsco.com/terms-of-use

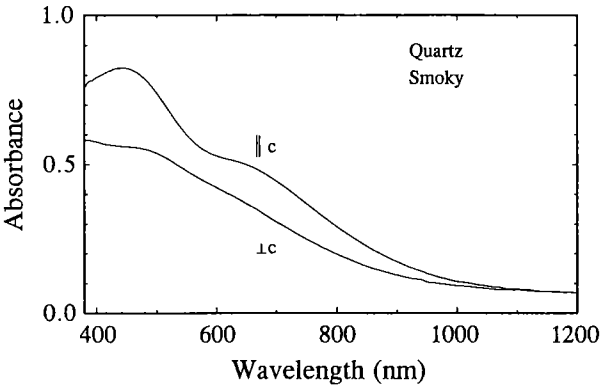


Figure 10. Optical absorption spectrum of smoky quartz from Drun Bugneig, Switzerland normalized to 1 cm thickness.

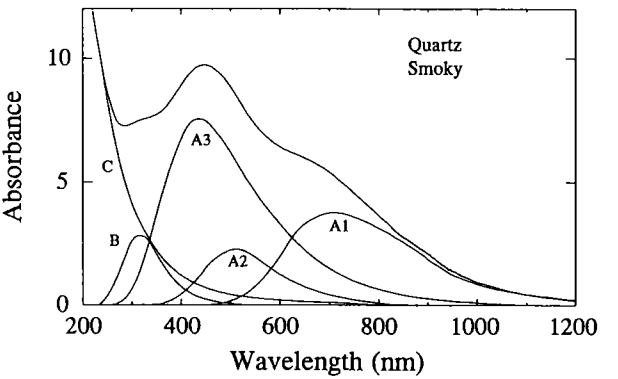


Figure 11. A model fit to the smoky quartz spectrum consisting of a superposition of five independent color centers. The component bands are asymmetric because the data are presented on a wavelength coordinate, rather than on an energy coordinate. Data from Nassau and Prescott (1977).

1970) the bands were shown not to be correlated with the $[AlO_4]^0$ center. Nassau and Prescott also showed that the A1 and A2 bands are not associated with the smoky color and the $[AlO_4]^0$ EPR spectrum, later refined by Meyer et al. (1984). Instead, they found that, by curve-fitting the spectrum, the intensity of the smoky color and the $[AlO_4]^0$ EPR pattern is correlated with the A3 band at 427 nm. Other studies confirmed that the A1 and A2 bands are not necessarily correlated with smoky color (van den Brom and Volger, 1974).

Schnadt and Schneider (1970) attempted to model the absorption spectrum of smoky quartz using an ionic model based on a singly negatively charged oxygen ion with the $2s^22p^2$ electronic configuration in an asymmetric Al-O-Si coordination environment. They predicted two optical transitions within the non-degenerate p-orbitals ($2p_x^2 2p_y^2 2p_z^1$) ⇒ ($2p_x^1 2p_y^2 2p_z^2$ and $2p_x^2 2p_y^1 2p_z^2$). They estimated the energies of these absorptions using parameters from the EPR spectrum, but predicted absorption in the near-infrared and ultraviolet regions, which did not agree with the experimental optical absorption spectrum.

Schirmer (1976) proposed that the light absorption process in smoky quartz involves the transfer of the hole between equivalent oxygen ions on the AlO_4 tetrahedron (small hole polaron model). This model is consistent with the gross features of the dominant A3 absorption band in smoky quartz, although several details remain incompletely understood.

EBSCOhost - printed on 2/13/2023 4:48 AM via . All use subject to https://www.ebsco.com/terms-of-use

Cohen and Makar (1982) point out the analogies between the centers in smoky quartz and soda-silica glass. Based on these analogies they propose the following assignments to the other centers in the smoky quartz spectrum (Fig. 12).

A1	is associated with a trapped hole center and consists of three non-bonded oxygens attached to an aluminum with an associated trapped hole.
A2	is associated with a trapped hole center and consists of two non-bonded oxygens attached to an aluminum with an associated trapped hole.
A3	is associated with a trapped hole center and consists of one non-bonded oxygen attached to an aluminum with an associated trapped hole.
B	is associated with a trapped-electron center associated with a tetrahedron containing two non-bonded oxygens.

Partlow and Cohen (1986) determined that the A2 and B centers are in a 1:1 relationship, suggesting that the electron lost from the A2 center is captured by the B center.

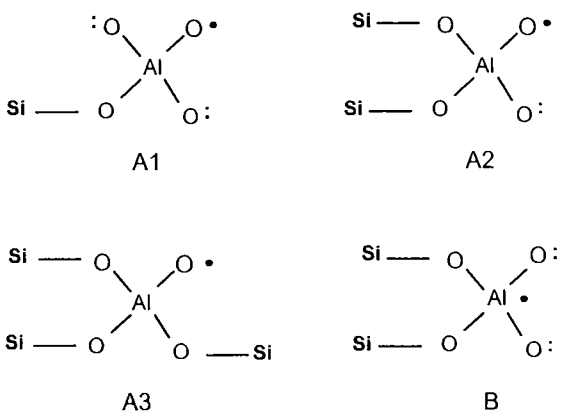


Figure 12. Representation of various centers found in smoky quartz after the assignment of Cohen and Makar (1982).

A quote from Wiel (1984) remains appropriate at this point in time: "The whole field of optical spectroscopy of the defects in quartz is still close to its infancy. Unfortunately, interpretation of optical bands attributed to specific defects in α–quartz has often led to unsatisfactory and controversial results."

E centers. These centers absorb well into the ultraviolet region (Weeks and Lell, 1964) and have little impact on the color of smoky quartz. For example, the E1' center has an absorption band centered at 210 nm.

Biaxiality

Biaxial character, also referred to as anomalous pleochroism (Tsinober, 1962; Tsinober et al., 1967), is seen in synthetic quartz grown on a minor rhombohedron seed and turned smoky by irradiation. The anisotropy originates in a non-random occupancy by Al in the three symmetry-equivalent Si sites (Nassau and Prescott, 1978). Heating above 490°C removes most of the anomalies through homogenization of the light-absorbing A3 centers. Nassau and Prescott proposed that the incorporation of Al is site selective and that possibly site selectivity of the charge-compensating cations was involved as well. Partlow and Cohen (1986) found that the orientation of the maximum intensity for the A2 and A3 optical absorption bands in the basal plane of quartz varies from crystal to crystal. The B

EBSCOhost - printed on 2/13/2023 4:48 AM via . All use subject to https://www.ebsco.com/terms-of-use

band was isotropic in the samples they examined, and A1 was too strongly overlapped to establish minor differences in its orientation.

Electrolytic smoky quartz

Smoky quartz can be generated electrolytically by passing current through a plate of quartz heated to 800°C (Laves et al., 1961). Its optical spectrum and EPR pattern are similar to that of natural smoky quartz (Weaver and Schindler, 1964; Krefft, 1975). If the electrolysis is conducted in vacuum the product is thermal stability up to 1000°C compared to the 300-350°C for natural smoky quartz. The implication is that charge-compensating cations (Na^+, H^+) are swept out of the crystal under vacuum and are not available for thermal recombination with the $[AlO_4]^0$ center.

Other irradiation colors related to smoky quartz

By a combination of irradiation and heat-treatment, some natural quartz crystals and some synthetic quartz crystals can be turned from colorless to smoky, blue, green or greenish-yellow. The relationship among the less-common irradiation colors and smoky quartz is discussed by Nassau and Prescott (1975;1977a). Each of these colors is a superposition of the A1, A2, A3, B and C bands discussed above. The particular color of a given specimen depends upon the relative proportions of these various components. The spectrum of a synthetic quartz turned blue by irradiation followed by heat treatment at 280°C is shown in Figure 13. The spectrum differs from that of smoky quartz by the relative absence of the A3 band near 427 nm.

Thermal and optical stability

Smoky quartz thermally bleaches at 350°C (O'Brien, 1955; Griffiths et al., 1954b; Nassau and Prescott, 1977a). Smoky quartz generated by X-irradiation of colorless synthetic quartz can be decolorized by exposure to ultraviolet irradiation (Griffiths et al., 1954b). No details were presented. This author's opinion is that smoky color in quartz is only moderately stable over geologic time. The doses of laboratory irradiation needed to intensify and saturate the color of a naturally pale smoky crystal are much lower than the dose such crystals should have experienced in nature. This suggests that there is a spontaneous (thermal) decay process that competes against the formation of smoky color in nature.

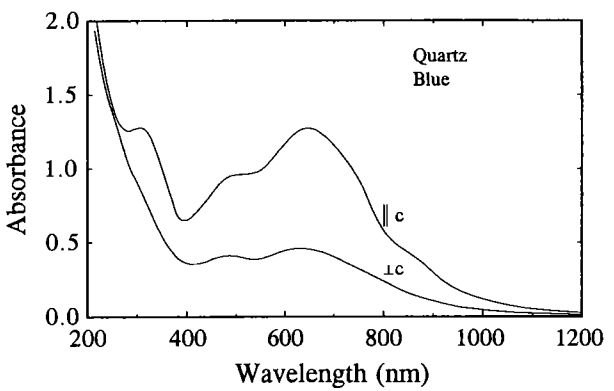


Figure 13. Optical absorption spectrum of a blue synthetic quartz in which the color was generated by irradiation. Data are from Nassau and Prescott (1975).

EBSCOhost - printed on 2/13/2023 4:48 AM via . All use subject to https://www.ebsco.com/terms-of-use

ROSE QUARTZ

Rose quartz usually occurs in massive vein deposits and rarely as isolated euhedral crystals. Massive and euhedral rose quartz appear to be fundamentally different, in terms of their optical absorption spectra, their photostabilities, and their origin of color. Since the properties of the two types of rose quartz are not identical, they will be discussed separately. Possibly the color of some rose quartz comes from a mixture of causes.

Massive rose quartz originates in pegmatites with giant potassium feldspar crystals, often without other gemstones, but occasionally with beryl. Rose quartz from massive vein deposits is inevitably slightly to highly cloudy. The haze arises from needles about 0.1 mm long and 0.05 to 0.4 μm in width that were formerly assumed to be rutile (Vultée, 1955a,b; Vultée and Lietz, 1956), but were more recently identified as dumortierite $[Al_3(BO_3)(SiO_4)_3O_3]$ by Applin and Hicks (1987). The color is thermally stable up to about 575°C. The Brazilian occurrences that produce much of the massive vein material and most of the crystallized rose quartz are described in Cassedanne and Roditi (1991).

Euhedral crystals of rose quartz occur near the end of the pegmatitic evolution in Na-rich environments, often with gem tourmaline and phosphate minerals. Its color, like most amethyst, is dominantly on the r {1011} growth sector, but bleaches upon exposure to light. The crystallized rose quartz is transparent and may have a substitutional origin.

Massive vein rose quartz

Cause of color. The color is due to an absorption band centered at 490 nm superimposed on background absorption that rises towards shorter wavelength (Fig. 14). Rose quartz is dichroic: $\mathbf{E} \perp c$ = pink; $\mathbf{E} \parallel c$ = nearly colorless (Holden, 1924b; Vultée and Lietz, 1956).

Over time, a variety of explanations have been presented for the origin of color in rose quartz. Early ideas centered on the possibility of colloidal gold causing color analogous to that in ruby glass. Holden (1924a,b) concluded that Mn^{3+} was the cause of the color based on his wet chemical analyses, which indicated that rose quartz from 21 localities contained 0.000x % MnO and noted that more intensely colored samples tended to have more Mn. Masgutov (1962) also expressed the opinion that Mn^{3+} was the coloring agent.

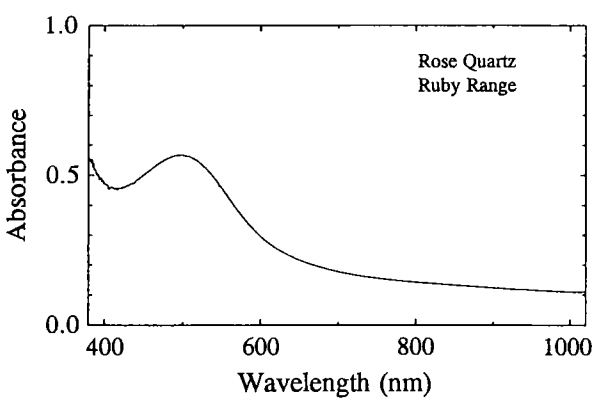


Figure 14. Optical absorption spectrum of massive rose quartz from the Ruby Range, Montana. This particular piece of rose quartz was shown by Applin and Hicks (1987) to contain dumortierite fibers. Additional studies showed that the fibers are pink.

EBSCOhost - printed on 2/13/2023 4:48 AM via . All use subject to https://www.ebsco.com/terms-of-use

Vultée and Lietz (1956) concluded that the 490 nm band in the rose quartz spectrum comes from absorption by the Ti^{3+} ion. Lehmann (1969a) concludes that the color is from Ti^{3+} in the interstitial *c*-axis channel sites of distorted octahedral symmetry, and he notes that the color of rose quartz fades in daylight, suggesting that radiation defects are a second cause of color.

Lehmann (1969a) and Lehmann and Bambauer (1973) suggested that Ti^{3+} in the interstitial channel sites is responsible for the rose color. They reasoned as follows: Because the haze in rose quartz had been attributed to rutile needles, it was assumed that rose quartz was Ti-saturated. The optical absorption spectrum of rose quartz is similar to Ti^{3+} in an octahedral site. Because Ti^{3+} substituting in the Si (tetrahedral) site would not give such an absorption pattern, the Ti was presumed to occupy an interstitial site that approximated an octahedral environment. Lehmann and Bambauer (1973) attributed the formation of reduced Ti to the reducing action of the growth solutions.

A small amount of Ti does, in fact, enter the Si site, and this can be reduced by the action of ionizing radiation (Wright et al., 1963). Smith et al. (1978) show that Ti^{3+} cannot be the cause of the color but suggest instead that the color originates from a charge transfer between interstitial Fe^{2+} and substitutional Ti^{4+}.

Scattering and inclusions. Like blue quartz, rose quartz displays properties that suggest that scattering of light by a second phase in the quartz is an important aspect of the color. Holden (1924a) identified small amounts of long, slender rutile needles in all samples he examined. Vultée (1955a,b; 1956) noted the earlier reports of Postelmann (1937) regarding submicrometer rutile needles in blue quartz, and he observed submicrometer needles in rose quartz. He assumed that the inclusions were rutile and presented structural models for their incorporation in the quartz structure. Von Vultée and Lietz (1956) concluded that the steep absorption towards the ultraviolet in the rose quartz spectrum comes from the scattering of light by the rutile needles and that the Ti^{3+} absorption is superimposed upon it. Dennen and Puckett (1971) concluded that the color results from Tyndall scattering by tiny oriented rutile needles. Although rutile is well entrenched in the literature as the cause of the haze in rose quartz, dumortierite [$Al_3(BO_3)(SiO_4)_3O_3$] fibers were identified under the SEM in hydrofluoric acid-etched rose quartz from Montana and North Dakota (Applin and Hicks, 1987). Dumortierite can be pink, so it is an obvious candidate for the origin of color of at least some rose quartz. The author has observed that when rose quartz from a variety of localities is dissolved in hydrofluoric acid, a mat of fine rose fibers remains after the quartz is dissolved. These fibers are dumortierite.

Inclusions of pink dumortierite, visible under the optical microscope, have been recognized in rose colored quartz for some time. Schaller (1916) noted that rose quartz from Humbolt Co., Nevada is colored by numerous fine inclusions of pink dumortierite. Ignatov et al. (1990) likewise identified microscopic dumortierite fibers in rose metamorphic vein quartz from the Caucasus Mountains and concluded that they were the cause of the rose color. They attributed the 490 nm absorption band to Fe^{2+}-Ti^{4+} intervalence charge transfer occurring in the dumortierite.

Absorption intensity. The intensity of absorption by rose quartz is comparatively low. Lehmann (1969a) reports 0.06 per cm and Vultée and Lietz (1956) report 0.32 per cm from a sample with 0.016 % TiO_2.

EBSCOhost - printed on 2/13/2023 4:48 AM via . All use subject to https://www.ebsco.com/terms-of-use

Chemical analysis. Using wet chemical methods, Holden (1924a) measured 0.000x % MnO in rose quartz from 21 localities and noted that more intensely colored samples tended to have more Mn. This observation formed part of the basis for the former assignment of the color to Mn. Small quantities of iron and titanium were also present in his analyzed samples. Vultée (1955) found 0.048% TiO_2 in a sample of rose quartz. Dennen and Puckett (1971) conducted emission spectrographic analyses of a comprehensive set of samples and found no Mn (<5 ppm) in any of their samples. Li and Al were the dominant trace components, and Fe and Ti were present in concentrations of about 10 and 20 ppm, respectively. Boron analyses have not been reported.

Substitutional Ti. EPR studies of laboratory-irradiated rose quartz identify a signal from substitutional Ti^{3+}, indicating that Ti^{4+} replaces some of the Si in this material (Wright et al., 1963; Bailey et al., 1992). Wright et al. found no indication that Ti^{3+} was important in natural, un-irradiated rose quartz and concluded that titanium, by itself, played no role in the color mechanism. Similar conclusions were reached by Smith et al. (1978).

Radiation effects. It has never been possible to reproduce the color of rose quartz by the action of radium either upon naturally colorless quartz or upon heat-decolorized rose quartz (Holden, 1924a). All of the author's attempts to augment the color of massive rose quartz result in the generation of a smoky color rather than an increase in the depth of rose color.

Thermal stability. The color of rose quartz is stable up to about 575°C (Holden, 1924b).

Photo stability. There are many indications that the color of rose quartz is unstable in sunlight, but some of the information is conflicting. Holden (1924a) repeats statements that long exposure to sunlight diminishes the color of rose quartz, but suggests that this has probably been exaggerated in view of his and others' observations that surface exposures of rose quartz exist that have probably been exposed to sunlight for extended periods of time. Frondel et al. (1962) report that rose quartz fades in daylight, a statement repeated by Lehmann (1969a). Cassedanne and Roditi (1991) state that rose quartz from some deposits fades after long exposure to light. The author has personally observed mine dumps at rose quartz deposits in Southern California where within two years after mining activity stops, no rose quartz remains visible on the sun-exposed surface and has seen rose quartz which has persisted in full exposure to the sun for at least 50 years. At some mines in Minas Gerais, Brazil, the owners take pains to protect their higher grade rose quartz from sunlight to prevent it from fading. These contradictory observations suggest that multiple origins of color occur in many specimens, including centers that fade (such as discussed in the next section) and ones that do not. It is also worth noting that the photostability of the pink color of dumortierite has not been carefully investigated, although there is no a priori reason to expect it to be unstable.

Single-crystal rose quartz

Single-crystal rose quartz is uncommon. Maschmeyer and Lehmann (1983b) studied the rare aggregates of small, transparent crystals with well-developed faces from the Sapucaia pegmatite, Minas Gerais, Brazil. They recognized that these specimens differ from common, massive rose quartz. Their chemical analysis found 118 phosphorus atoms per million silicon atoms and essentially no titanium. The color has low thermal stability and disappears at about 200°C. Furthermore, it is subject to bleaching in ultraviolet light. The optical absorption spectrum is dominated by bands at 338 and 524 nm (Fig. 15).

EBSCOhost - printed on 2/13/2023 4:48 AM via . All use subject to https://www.ebsco.com/terms-of-use

The crystals are moderately dichroic with the stronger absorption perpendicular to *c*.

EPR spectra identify an Al-O^--P center (a hole center formed when ionizing radiation removes an electron from a substitutional Al-O-P unit). This center is slowly bleached by UV light and is enhanced by ionizing radiation. The assignment of the optical absorption to this center was suggested, but was not considered certain. The synthesis of phosphorus-containing synthetic rose quartz discussed below adds support for this color mechanism. Crystals from the Sapucaia pegmatite, Minas Gerais, Brazil, were also examined by Cohen and Makar (1985). They found that the crystals become deeper rose upon irradiation. The color-causing mechanism they favored for a crystal containing 4 Ti atoms per 10^6 Si atoms was charge transfer between substitutional Ti^{4+} and interstitial Ti^{3+}. They observed that even in the (0001) plane, the absorption was anisotropic, inconsistent with the trigonal symmetry of quartz. Their favored explanation was that interstitial ions are involved.

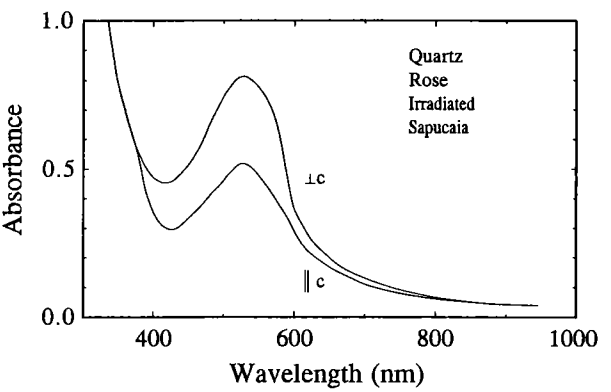


Figure 15. Optical absorption spectrum of single-crystal rose quartz from the Sapucaia pegmatite, Brazil. Data from Maschmeyer and Lehmann (1983) are presented for 1 cm thickness.

Synthetic rose quartz

A synthetic precursor to rose quartz has been grown from hydrothermal solutions with added Ti (Hosaka et al., 1986). This precursor material is essentially colorless. Rose color is developed through subsequent heat treatment at 1200°C in an iron-containing charge. During the heat treatment iron diffuses into the crystal, and rose color associated with weak absorption bands at 365, 470 and 500 nm develops. Like natural rose quartz, the synthetic crystal was translucent. Balitsky (1993) described a synthetic P-bearing hydrothermal rose quartz, grown at comparatively low temperature and pressure, and then irradiated to develop the color. Its optical spectrum is identical to that of single-crystal rose quartz. Further characterization is in progress (Balitsky, in preparation; E. Fritsch, pers. comm.)

OTHER VARIETIES OF SILICA MINERALS COLORED BY INCLUSIONS AND ADMIXED PHASES

Blue quartz

Natural blue quartz. The color of natural blue quartz is due to scattering of incident light by minute inclusions (Jayaraman, 1939). This can be convincingly demonstrated by holding a thin slab of blue quartz so that light can reflect off the surface. Under these conditions, the blue color is observed. When the same slab is held so that it can be observed in transmitted light, the blue color is replaced by an orangish-brown color. These phenomena mimic the behavior of the atmosphere. Scattered light from the day sky

EBSCOhost - printed on 2/13/2023 4:48 AM via . All use subject to https://www.ebsco.com/terms-of-use

is blue, but at sunset, we see only the remaining transmitted light, which is dominantly red. The optical transmission spectrum (Fig. 16) confirms that red light is preferentially transmitted. An early study by Vultée and Lietz (1956), which concluded that the color of blue quartz was the result of Rayleigh scattering from inclusions of rutile needles, has been widely quoted. This study, in turn, was influenced by the work of Postelmann (1937), who concluded that oriented rutile needles are the cause of color in blue quartz. The crystals, typically <0.5μm wide and present at a concentration of ~5000/mm^3, were identified on the basis of twin angles, morphology, etc. More recently, the source of the scattering has been identified in a TEM investigation of blue quartz phenocrysts from the Llano Uplift, Texas by Zolensky et al. (1988). They found that the inclusions in the quartz are rounded ilmenite grains averaging ~0.06 mm in diameter with a density of about 125 per cubic micrometer and that the depth of color correlated with the density of the inclusions. Likewise, a sub-micrometer iron-titanium oxide (presumed to be ilmenite) was found in blue quartz from the Roseland district, Virginia, and was presumed to be the cause of the color (Nord, cited in Herz and Force, 1984).

Zolensky et al. (1988) review earlier proposals for the origin of blue coloration which include scattering from fluid inclusions, strain deformation, apatite and zircon, and discuss the potential parameters of magma equilibrium that restrict blue quartz to rocks of middle to late Proterozoic age.

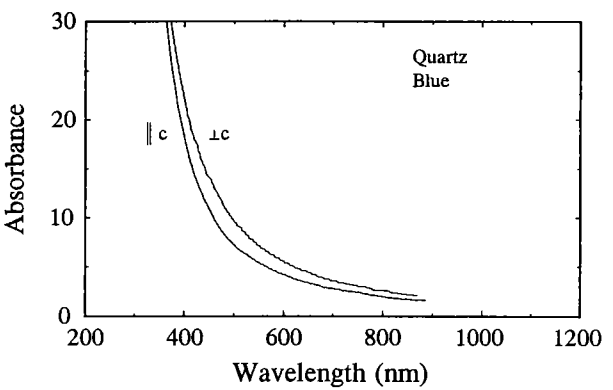


Figure 16. Optical absorption spectrum of blue quartz from Philadelphia, Pennsylvania. Replotted from the data of von Vultée and Lietz (1956). Presented normalized to 1 cm thickness.

Other blue colors. Large crystals of clear, synthetic blue quartz are available primarily for lapidary purposes. They are synthesized in the presence of Co^{2+}, which enters a tetrahedral site and is responsible for the color (Wood and Ballman, 1966). They can also be synthesized in a process where Co^{3+} is first incorporated in the interstitial I6 site to form yellow quartz. This material is then heated at 500°C to change the crystal to blue due to the formation of Co^{2+} in the I4 position (Lehmann, 1969b). The optical spectrum (Fig. 17) is distinctive and characteristic of Co^{2+}. There is no natural equivalent of this material.

Pale blue color has been observed in iron-containing synthetic quartz. Its color origin is similar to that of green quartz with Fe^{2+} in the interstitial position. Less yellow component is present than in the green quartz, so more transmission in the blue end of the spectrum occurs. A blue color unrelated to natural blue quartz has also been produced through irradiation of synthetic quartz (Nassau and Prescott, 1977a). This color was previously discussed in the section on other irradiation colors.

EBSCOhost - printed on 2/13/2023 4:48 AM via . All use subject to https://www.ebsco.com/terms-of-use

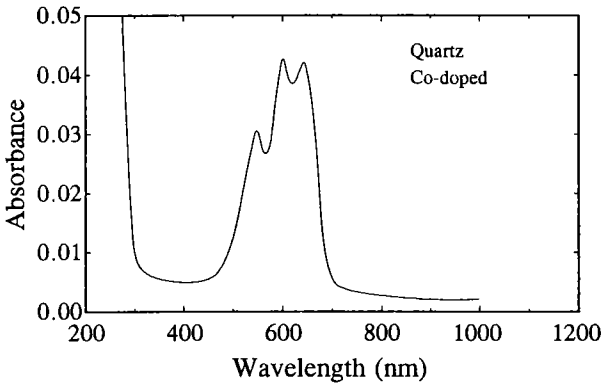


Figure 17. Optical absorption spectrum of synthetic blue quartz. Replotted from the data of Wood and Ballman (1966). Presented normalized to 1 cm thickness.

Chrysoprase

Chrysoprase color can vary from olive-green to a pale sea-green. While its physical properties are similar to those of chalcedony, both tridymite and cristobalite have been identified in some samples. It usually has a fibrous structure, but may also be microgranular. It is found in quartz veins in nickel-bearing rocks. Chrysoprase occurs as veins in laterites overlying Ni-containing serpentinites in Queensland (Brooks, 1965), and it is associated with jadeite in veins in serpentinized gabbroic and ultrabasic intrusions in Lower Silesia, Poland (Visser, 1947). Other localities include USA, India, Brazil, South Africa, and central Kazakhstan. Although early ideas about the color of chrysoprase included iron, cobalt, and copper, the color is now known to be directly related to its Ni content, which ranges from a few tenths of a percent to several percent by weight (Rehberg and Schlossmacher, 1944; Brooks, 1965). The color is from admixed fine-grained nickel compounds in the silica matrix rather than from substitutional Ni in the silica itself.

Heflik et al. (1989) review earlier studies on the mineralogiocal and color properties of chrysoprase, especially those in Russian- and Polish-language sources. They summarize two models for the origin of color. One associates the color with finely disseminated hydrous nickel silicates such as garnierite and saponites (Rehberg and Schlossmacher, 1944; Faust, 1966; Nikolskaya et al., 1975; Sachanbinski, 1980). These minerals are usually associated with chrysoprase deposits. The other model proposes that the color is from finely divided bunsenite (NiO) (Barsanov and Yakovleva, 1981; Heflik et al., 1989). The evidence for this phase is from cubic forms observed in TEM micrographs of replicas of fractured chrysoprase and a weak reflection at 2.39 Å in the X-ray pattern of chrysoprase from Kazakhstan (Barsanov and Yakovleva, 1981).

The optical absorption spectrum of chrysoprase from a variety of localities (Fig. 18) shows the features of octahedral Ni^{2+}. Absorption bands centered at about 652 and 1105 nm agree closely with published positions of garnierite bands at 658 and 1099 nm (Faye, 1974) but they do not coincide with those of NiO at 710 and 1142 nm (Rossman et al., 1981).

EBSCOhost - printed on 2/13/2023 4:48 AM via . All use subject to https://www.ebsco.com/terms-of-use

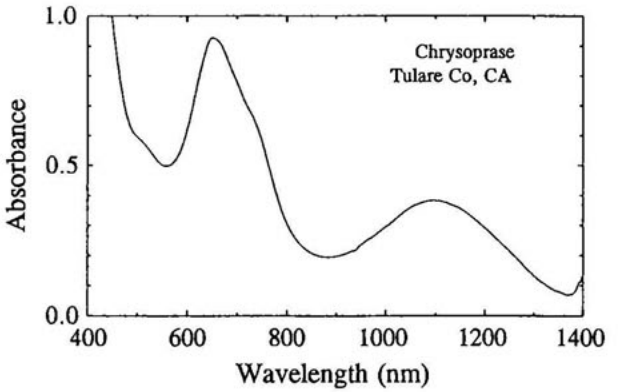


Figure 18. Diffuse transmission spectrum of chrysoprase from Tulare County, California, showing the absorption features of Ni^{2+}.

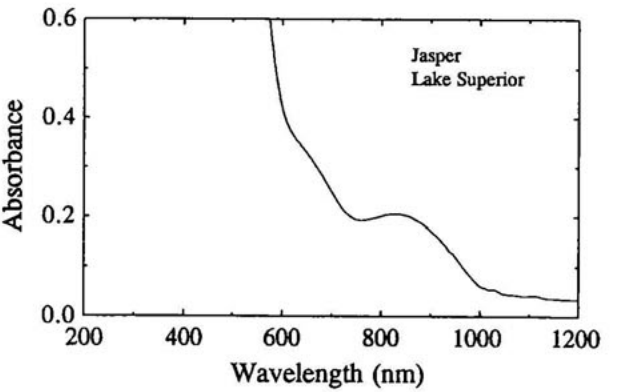


Figure 19. Diffuse reflection spectrum of the red jasper used by Heaney and Veblen (1991), showing the absorption features of hematite.

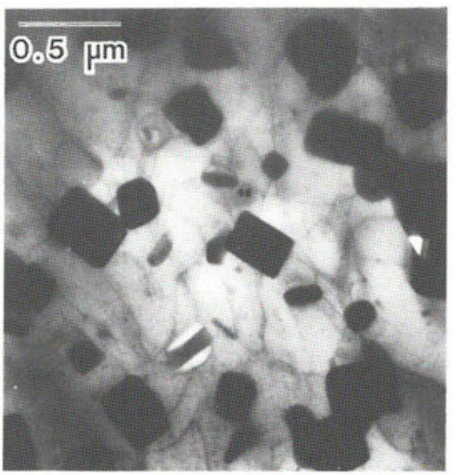


Figure 20. Bright-field transmission electron micrograph of jasper, showing Fe_2O_3 particles which are responsible for the red color. From Heaney and Veblen (1991).

EBSCOhost - printed on 2/13/2023 4:48 AM via . All use subject to https://www.ebsco.com/terms-of-use

Jasper

Jasper is a massive, fine-grained quartz with relatively large amounts of admixed material, chiefly iron oxide, up to 20% or more (Frondel, 1962, p. 224). It can also be brown, brownish-yellow or ocher-yellow, less commonly grayish-green. Various mineral pigments contribute to the color of jaspers. In the more common red jaspers, microcrystals of hematite produce the red color. The characteristic absorption bands of hematite can be seen in the optical spectrum of jasper (Fig. 19). Hematite crystals can be imaged in TEM photographs of jasper (Heaney and Veblen, 1991; Fig. 20). Goethite is believed to cause the color in yellow and brown types. Various clay minerals impart a white or gray color, and included chlorite may yield a variety of colors.

Chert

With decreasing amounts of foreign pigmenting substance, jasper grades into translucent fine-grained material, which may be variously termed chert, novaculite, etc. Colors range from gray-black, gray pale yellowish, brownish, reddish-brown to nearly white and arise from the same components found in jasper.

Plasma

Plasma is a microgranular or microfibrous variety of quartz colored various shades of green by disseminated particles of silicates: celadonite, chlorite, amphibole, etc. (Frondel, 1962, p 218). It is opaque with a conchoidal to smooth fracture.

Prase

Prase is more translucent than plasma and has a leek-green color. Its color is caused by aggregates of minute fibers of hornblende; chlorite has also been identified as a cause of color. (Frondel, 1962, p.219).

Heliotrope

Heliotrope, also called bloodstone, is a type of chalcedony or plasma, usually with a uniform green or grayish-green color, subtranslucent to opaque, containing red spots of iron oxide or red jasper resembling spots of blood. (Frondel, 1962, p219).

Agate

Some agates (such as the Lake Superior agates) naturally have reddish bands (from iron oxide), while others (such as those from some localities in southern Brazil) are often nearly devoid of color in their natural state. Bluish-grey colors can be seen in some as a result of light scattering off the fine chalcedony fibers. However, the colors of most agates are due to laboratory treatment rather than natural pigmentation (Nassau, 1994). Treatments can be based either on heating or dyeing. Heat treatment can dehydrate hydrous phases in the chalcedony (goethite to produce hematite). Dyeing can be conducted with a variety of inorganic (e.g., iron for red; chromium for green; ferric ferrocyanide or cobalt for blue) and organic chemicals (decomposed sugar for black).

OPAL

Both Baier (1932) and Raman and Jayaraman (1953) recognized that the high spectral purity of the color of precious opal indicated that a diffraction effect was responsible for the color. Bayliss (1965) recognized that the difference between colored

EBSCOhost - printed on 2/13/2023 4:48 AM via . All use subject to https://www.ebsco.com/terms-of-use

gem opal and common colorless opal from a given locality was not related to chemical compositional differences between the two materials. Jones et al. (1964) showed that precious opals are composed of spherical particles of amorphous silica 150 to 350 nm in diameter that are remarkably uniform in size and are packed together in a regular arrangement. Individual layers of particles occur as nearly perfect hexagonal arrays (Fig. 21). The unfilled void space between the silica particles provides the refractive index change that produces the diffraction effect.

The diffraction of light by gem opals was examined by in detail by Sanders (1968) who considered the color of opals in relation to the equations for diffraction gratings and showed that the physical phenomena observed in opal matched the predictions for a grating composed of spheres the size observed in TEM photographs of opal. The size of the spherical silica particles determines the lattice parameter of the grating, which in turn establishes the range of colors that are diffracted by the opal. The longest wavelength is diffracted by the "$10\bar{1}0$" planes of the hexagonal closest packed spheres, with a spacing of $r\sqrt{3}$, where r is the radius of the silica sphere. This corresponds to a maximum wavelength of

$$\lambda_{max} = 2\, n_\lambda\, r\sqrt{3} = 5.02\, r\ ,$$

where n_λ is the refractive index of the opal.

The spheres can be directly observed in SEM images (Fig. 22; Greer, 1969). Gem opals from sedimentary deposits show no microstructure in TEM images, and produce only

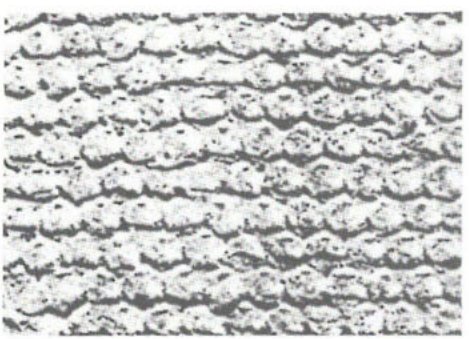


Figure 21. Transmission electron microscope image of a replica of a fracture surface of an Australian gem opal showing the regular hexagonal packing of the 0.15 μm diameter silica spheres. Illustration is modified from Figure 6 of Sanders (1968).

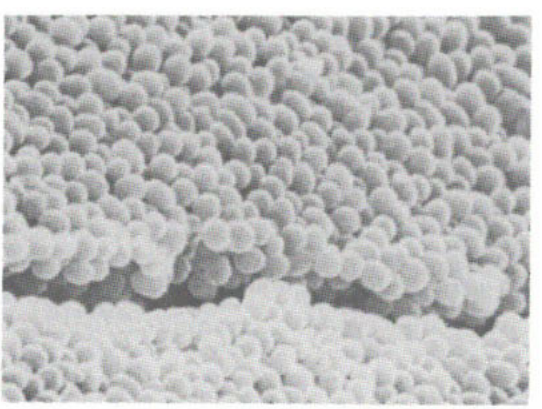


Figure 22. Scanning electron microscope photograph of silica spheres in low-quality gem opal from Tecopa Basin, California. Individual spheres are about 0.125 μm in diameter.

EBSCOhost - printed on 2/13/2023 4:48 AM via . All use subject to https://www.ebsco.com/terms-of-use

diffuse electron diffraction patterns indicating that they are truly amorphous. Opals from volcanic rocks are occasionally amorphous, but more often are partially crystalline and give diffractions patterns with prominent trydimite lines (Sanders, 1975). Interestingly, Dietz and Saunders (1967) observed that opals from Australia have characteristic voids between the silica spheres, whereas American opals appear not to have the voids. An excellent, illustrated summary of the microstructure of gem opal is presented by Sanders and Darragh (1971).

Color, particularly in red hues, often is found in opals both with and without diffraction colors. Such hues are commonly encountered in Mexican opals. As the similarity of the spectrum in Figure 23 to the hematite spectrum suggests, these red colors are associated with Fe^{3+} in the opals. Opals from some localities are colored blue from copper minerals.

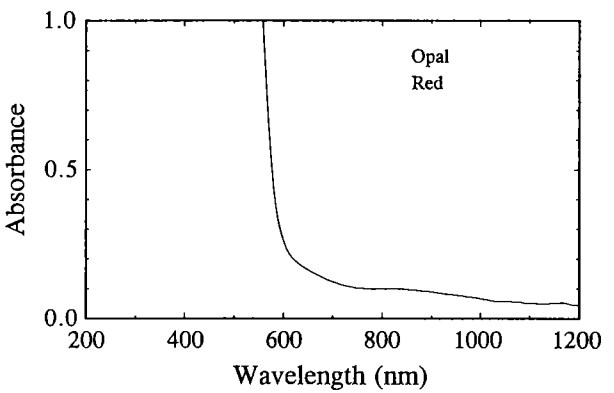


Figure 23. Optical absorption spectrum of a red variety of opal called cherry opal from Opal Mountain, San Bernardino Co., California. Presented for 1 mm thickness. Features of hematite (860 nm) are present in the spectrum of this clear material.

ACKNOWLEDGMENTS

Support for the original research which is part of this chapter was provided by the White Rose Foundation, whose interest in the scientific basis of the origin of color in minerals is highly appreciated. Assistance with the translation of Russian articles for this chapter was provided by Ruslan Mendybaev. Helpful discussions about quartz with Kurt Nassau, John Weil and Paulo Vasconcelos are particularly appreciated as are the numerous museums, miners and other donors who provided samples of quartz minerals over the years.

REFERENCES

Adekeye JID, Cohen AJ (1986) Correlation of Fe^{4+} optical anisotropy, Brazil twinning and channels in the basal plane of amethyst quartz. Appl Geochem 1:153-160

Aines RD, Rossman GR (1986) Relationships between radiation damage and trace water in zircon, quartz and topaz. Am Min 71:1186-1193

Applin KR, Hicks BD (1987) Fibers of dumortierite in quartz. Am Min 72:170-172

Baier E (1932) Structure of precious opal. Zeits Krist 18:183-218

Bailey P, Pawlik T, Söthe H, Spaeth J-M, Wiel JA (1992) $[TiO_4]^-$ in α–quartz studied by low-temperature electron paramagnetic resonance. J Phys: Condens Matter 4:4063-4073

Balitsky VS (1977) Growth of large amethyst crystals from hydrothermal fluoride solutions. J Crystal Growth 41:100-102

Balitsky VS (1980) Synthetic amethyst: Its history, methods of growing, morphology and peculiar features. Z Deutsch Gemmol Ges 29:5-16

EBSCOhost - printed on 2/13/2023 4:48 AM via . All use subject to https://www.ebsco.com/terms-of-use

Balitsky VS, Balitskaya OV (1986) The amethyst-citrine dichromatism in quartz and its origin. Phys Chem Min 13:415-421

Balitsky VS, Makhina IB, Prygov VI, Mar'in AA (1993) Man-made rose quartz. (abstr) 24th Int'l Gemmological Conf, Paris, Oct. 1993

Ballman AA (1961) The growth and properties of colored quartz. Am Min 46:439-446

Bank H (1976) Citrin. Z Deutsch Gemmol Ges 25:189-194

Barry TI, McNamara P, Moore WJ (1965) Paramagnetic resonance and optical properties of amethyst. J Chem Phys 42:2599-2606

Barry TI, Moore WJ (1964) Amethyst: Optical properties and paramagnetic resonance. Science 144:289-290

Barsanov GP, Yakovleva ME (1981) Mineralogical investigations of some precious and semi-precious varieties of cryptocrystalline silica. In: New Mineral Data. USSR Acad Sci 29 (in Russian; quoted in Heflik et al., 1989)

Bayliss P, Males PA (1965) The mineralogical similarity of precious and common opal from Australia. Min Mag 35:429-431

Behner T, Elbers G, Remme S, Prissok F, Stegger P Lehmann G (1986) Interstitial transition metal ipurities as a possible cause of enhanced reactivities. Ber Bunsenges Phys Chem 90:698-702

Bensusan K, Bensusan MB (1958) Cacoxenite. Gems & Minerals 1958:23; 86-87.

Berthelot M (1906) Synthesis of amethyst quartz. Researches on the color, natural or artificial, of some precious stones under radioactive influences. C R Acad Sci Paris 143:477-488

Brom WEvd, Volger J (1974) Electromodulated absorption in smoky quartz. Physica 75:245-267

Brooks JH (1965) Marlborough Creek chrysoprase deposits, Rockhampton district, central Queensland. Gems & Gemology 11:323-330, 351

Bukanov VV, Markova GA (1969) The smoky and citrine color of natural quartz. Dokl Akad Nauk SSSR 187:115-117 (translated from: Doklady Akademii Nauk SSSR 187:645-647)

Cassedanne JP, Roditi M (1991) Crystallized and massive rose quartz deposits in Brazil. J Gemmology 22:273-286

Choi D, Wiel JA (1990) EPR study of Fe^{3+} in α–quartz: Further lithium-compensated centers. Phys Rev B42:9759-9765

Cohen AJ (1956a) Color centers in the α–quartz called amethyst. Am Min 41:874-891

Cohen AJ (1956b) Anisotropic color centers in α–quartz. Part I. Smoky quartz. J Chem Phys 25:908-914

Cohen AJ (1975) On the color centers of iron in amethyst and synthetic quartz: A reply. Am Min 60:338-339

Cohen AJ (1984) The oscillator strength of Fe^{4+} in α–quartz. J Luminescence 31 & 32:302-304

Cohen AJ (1985) Amethyst color in quartz, the result of radiation protection involving iron. Am Min 70:1180-1185

Cohen AJ (1986) Optical studies of biaxial Al-related color-centers in smoky quartz. Am Min 71:589-598

Cohen AJ, Hassan F (1970) Iron in synthetic quartz: Heat and radiation induced changes. Science 167:176-177

Cohen AJ, Hassan F (1974) Ferrous and ferric ions in synthetic α–quartz and natural amethyst. Am Min 59:719-728

Cohen AJ, Makar LN (1982) Models for color-centers in smoky quartz. Phys stat solidi A73:593-596

Cohen AJ, Makar LN (1984) Differing effects of ionizing radiation in massive and single crystal rose quartz. N Jb Min Monat 1984:513-521.

Cohen AJ, Makar LN (1985) Dynamic biaxial absorption spectra of Ti^{3+} and Fe^{2+} in a natural rose quartz crystal. Min Mag 49:709-715

Cox RT (1976) ESR of an S = 2 centre in amethyst quartz and its possible identification as the d^4 ion Fe^{4+}. J Phys C: Solid State Phys 9:3355-3361

Cox RT (1977) Optical absorption of the d^4 ion Fe^{4+} in pleochroic amethyst quartz. J Phys C: Solid State Phys 10:4631-4643

Cressey G, Henderson CMB, van der Laan G (1993) Use of *L*-edge X-ray absorption spectroscopy to characterize multiple valence states of 3d transition metals; a new probe for mineralogical and geochemical research. Phys Chem Min 20:111-119

Crowningshield R, Hurlbut C, Fryer CW (1986) A simple procedure to separate natural from synthetic amethyst on the basis of twinning. Gems & Gemology 22:130-139

Currier, RH (1985) Natural fading of amethyst. Gems & Gemology 21:115-116

Darragh PJ, Gaskin AJ, Terrell BC, Sanders JV (1965) Origin of precious opal. Nature 209:13-16

Deitz R, Sanders JV (1967) Gems & Minerals, Sept. 1967 (quoted in Sanders, 1968)

Dennen WH, Puckett AM (1971) On the chemistry of color of rose quartz. Min Rec 2:226-227

Dennen WH, Puckett AM (1972) On the chemistry and color of amethyst. Canad Min 11:448-456

EBSCOhost - printed on 2/13/2023 4:48 AM via . All use subject to https://www.ebsco.com/terms-of-use

Ditchburn RW, Mitchell EWJ, Paige EGS, Clusters JF, Dyer HB, Clarke CD (1954) The optical effects of radiation damage in diamond and quartz. In: Defects in Crystalline Solids. Report of the conference on defects in crystalline solids, Bristol. The Physical Society, London, p. 92-107

Dotto CT, Isotani S (1991) Irradiation and heating effects in amethyst crystals fom Brazil. Radiation Effects and Defects in Solids 117:355-361

Faust GT (1966) The hydrous nickel-magnesium silicates. The garneirite group. Am Min 51:279-298

Faye GH (1974) Optical absorption spectrum of Ni^{2+} in garnierite: A discussion. Canad Min 12:389-393

Frondel C (1962) The System of Mineralogy, 7th ed, vol 3, Silica Minerals. J Wiley & Sons, New York

Greer RT (1969) Submicron structure of "amorphous" opal. Nature 224:1199-1200

Griffiths JHE, Owen J, Ward IM (1954a) Paramagnetic resonance in neutron-irradiated diamond and smoky quartz. Nature 173, 439-440

Griffiths JHE, Owen J, Ward IM (1954b) Magnetic resonance in irradiated diamond and quartz. In: Defects in Crystalline Solids. Report of the conference on defects in crystalline solids, Bristol. The Physical Society, London, p. 81-88.

Halliburton LE, Hantehzadeh MR, Minge J, Mombourquette MJ, Wiel JA (1989) EPR study of Fe^{3+} in quartz: A reexamination of the lithium-compensated center. Phys Rev B 40:2076-2081

Hassan F (1972) Amethyst. Min Rec 3:221-225

Hassan F, Cohen AJ (1974) Biaxial color centers in amethyst quartz. Am Min 59:709-718

Heaney PJ, Veblen DR (1991) An examination of spherulitic dubiomicrofissils in Precambrian banded iron formations using the transmission electron microscope. Precambrian Research 49:355-372

Heflik W, Kwiecinska B, Natkaniec NL (1989) Colour of chrysoprase in light of mineralogical studies. Australian Gemmologist 17:43-46; 58-59

Herz H, Force E (1984) Rock suites in Grenvillian terrane of the Roseland district, Virginia. Part I. Lithologic relations. Geol Soc Am Spec Paper 194:187-200

Holden EF (1924a) The cause of color in rose quartz. Am Min 9:75-88

Holden EF (1924b) The cause of color in rose quartz (concluded). Am Min 9:101-108

Holden EF (1925) The cause of color of smoky quartz and amethyst. Am Min 10:203-252

Hosaka M, Taki S (1983) Hydrothermal growth of amethyst and citrine in NaCl and KCl solutions. J Crystal Growth 64:572-576

Hosaka M, Miyata T, Shimizu Y, Okuyama O (1986) Synthesis of rose-quartz crystal. J Crystal Growth 78:561-562

Hosaka M (1990) Hydrothermal growth of gem stones and their characterization. Prog Crystal Growth and Charact 21:71-96

Hutton DR (1964) Paramagnetic resonance of Fe^{3+} in amethyst and citrine quartz. Phys Letters 12: 310-311

Hutton DR (1974) Defects in the coloured varieties of quartz. J Gemmology 14:156- 166

Hutton DR, Troup GJ (1966) Paramagnetic resonance centres in amehyst and citrine quartz. Nature 211:623

Ignatov SI, Platonov AN, Sedenko VS, Taran MN (1990) Rose color of quartz caused by dumortierite microinclusions (in Ukrainian). Dopovidi Akademii Nauk Ukrainskoi RSR Seriya B7:23-27

Jayaraman N (1939) The cause of colour of the blue quartzes of the charnockites of south India and of the champion gneiss and other related rocks of Mysore. Proc Indian Acad Sci A9: 265-285

Jones JB, Sanders JV, Segnit ER (1964) Structure of opal. Nature 204:990-991

Khadzhi VE, Reshetova GV (1977) Method of producing citrine crystals. US Patent 4,024,013

Koumvakalis N (1980) Defects in crystalline SiO_2: optical absorption of the aluminum-associated hole center. J Appl Phys 51:5528-5532

Krefft GB (1975) Effects of high-temperature electrolysis on the coloration characteristics and OH-absorption bands in α–quartz. Radiation Effects 26:249-260

Laves F, Schindler P, Weaver HE (1961) Eigenschaften von Elektrolyse-Farbzentren in Quartzkristallen. Naturwiss 48:714

Lehmann G (1967) Farbzentren des Eisens als Ursache der Farbe von Amethyst. Zeit Naturforsch 22a:2080-2086

Lehmann G (1969a) Zur Farbe von Rosenquarz. N Jb Min Monat 1969:222-225

Lehmann G (1969b) Interstitial incorporation of di and trivalent cobalt in quartz. J Phys Chem Solids 30:395-399

Lehmann G (1971a) Yellow color centers in natural and synthetic quartz. Phys kondens Materie 13:297-306

Lehmann G (1971b) The structure of yellow iron centers in quartz. Phys stat sol (b) 48:K65-K67

Lehmann G (1975) On the color centers of iron in amethyst and synthetic quartz: A discussion. Am Min 60:335-337

Lehmann G (1977) Über die Färbungsursachen natürlicher Citrine. Zeit Deutsch Gemmolog Ges 26:53-60

EBSCOhost - printed on 2/13/2023 4:48 AM via . All use subject to https://www.ebsco.com/terms-of-use

Lehmann G, Bambauer HU (1973) Quarzkristalle und ihre Farben. Angew Chem 85:281-289; Quartz crystals and their colors. Angew Chem Int'l Edn 12:283-291
Lehmann G, Moore WJ (1966a) Color center in amethyst quartz. Science 152:1061- 1062
Lehmann G, Moore WJ (1966b) Optical and paramagnetic properties of iron centers in quartz. J Chem Phys 44:1741-1745
Mackey JH (1963) An epr study of impurity related colour centres in aluminium-doped quartz. J Chem Phys 39:74-83
Marfunin AS (1979) Spectroscopy, Luminescence and Radiation Centers in Minerals. Springer-Verlag, Berlin
Maschmeyer D, Lehmann G (1983a) New hole centers in natural quartz. Phys Chem Min 10:84-88
Maschmeyer D, Lehmannn G (1983b) A trapped-hole center causing rose coloration of natural quartz. Zeit Kristallogr 163:181-196
Maschmeyer D, Niemann K, Hake H, Lehmann G, Räuber A (1980) Two modified smoky quartz centers in natural citrine. Phys Chem Min 6:145-156
Masgutov RV (1962) The coloring of rose quartz. Izv Akad Nauk Kaz SSR, Ser Geol 3:85-87 (not seen)
Matarrese LM, Wells JS, Peterson RL (1964) EPR spectrum of Fe^{3+} in synthetic quartz. Bull Am Phys Soc 9:502
Matarrese LM, Wells JS, Peterson RL (1969) EPR spectrum of Fe^{3+} in synthetic brown quartz. J Chem Phys 50:2350-2360
McArthur JR, Jennings EA, Kissin SA, Sherlock RL (1993) Stable-isotope, fluid- inclusion, and mineralogical studies relating to the genesis of amethyst, Thunder Bay Amethyst Mine, Ontario. Can J Earth Sci 30:1955-1969
McLaren AC, Phakey PP (1965) A transmission electron microscope study of amethyst and citrine. Austral J Phys 18:135-141
McLaren AC, Pitkethly DR (1982) The twinning microstructure and growth of amethyst quartz. Phys Chem Min 8:128-135
Melanckolin N, Tsinober L (1963) The biaxial nature of synthetic amethyst crystals. Sov Phys Crystallogr 8:83-84) (translated from: Kristallografiya 8:110-112)
Meyer BK, Lohse F, Spaeth JM, Weil JA (1984) Optically detected magnetic resonance of the $[ALO_4]^0$ centre in crystalline quartz. J Phys C: Solid State Phys 17:L31-L36
Minge J, Mombourquette MJ, Wiel JA (1989b) Dynamic interchange between $[FeO_4/Na]^0$ configurations in α–quartz. Phys Rev B 40:6523-6528
Minge J, Mombourquette MJ, Wiel JA (1990) EPR study of Fe^{3+} in α–quartz: The sodium-compensated center. Phys Rev B42:33-36
Minge J, Wiel JA (1989) ^{57}Fe Hyperfine structure of $[FeO_4/Li]^0$ center in α–quartz. J Phys Chem Solids 50:997-1001
Minge J, Wiel JA, McGavin DG (1989a) EPR study of Fe^{3+} in α–quartz: Characterization of a new type of cation-compensated center. Phys Rev B40:6490- 6498
Mitchell EWJ, Paige EGS (1955) The anisotropic absorption of the visible bands in irradiated α–quartz. Philos Mag 46:1353-1361
Mitchell EWJ, Paige EGS (1956) The optical effects of radiation induced atomic damage in quartz. Philos Mag 1:1085-1115
Mombourquette MJ, Tennant WC, Wiel JA (1986) EPR study of Fe^{3+} in α–quartz. A re-examination of the so-called I-center. J Chem Phys 85:68-79
Mombourquette MJ, Minge J, Hantehzadeh MR, Wiel JA, Halliburton LE (1989) Electron paramagnetic resonance study of Fe^{3+} in α–quartz: Hydrogen-compensated center. Phys Rev B39:4004-4008
Nassau K (1981) Artifically induced color in amethyst-citrine quartz. Gems & Gemology 17:37-39
Nassau K (1994) Gemstone Enhancement, 2nd ed. Butterworths, London
Nassau K, Prescott BE (1975) A reinterpretation of smoky quartz. Phys status solidi (a), 29:659-663
Nassau K, Prescott BE (1977a) Smoky, blue, greenish yellow, and other irradiation- related colors in quartz. Min Mag 41:301-312
Nassau K, Prescott BE (1977b) A unique green quartz. Am Min 62:589-590
Nassau K, Prescott BE (1978) Growth-induced radiation-developed pleochroic anisotropy in smoky quartz. Am Min 63:230-238
Nelson CM, Weeks RA (1960a) Trapped electrons in irradiated quartz and silica: I, Optical absorption. J Am Ceram Soc 43:396-399
Nelson CM, Weeks RA (1960b) Trapped electrons in irradiated quartz and silica: II, Electron spin resonance. J Am Ceram Soc 43:399-404
Neumann E, Schmetzer K (1984a) Mechanism of thermal-conversion of color and color-centers by heat-treatment of amethyst. N Jb Min Mh 6:272-282
Neumann E, Schmetzer K (1984b) Farbe, Farbursache und Mechanismen der Farbumwandlung von Amethyst. Zeit Deut Gemmol Ges 33:35-42

EBSCOhost - printed on 2/13/2023 4:48 AM via . All use subject to https://www.ebsco.com/terms-of-use

Nikolskaya LV, Samsonov YP, Guselnikov YB, Samoylovich MI (1975) About the nature of color and features of chrysoprase. Zap Vses Min Ob 4:104 (in Russian; quoted in Heflik et al., 1989)

Nuttall RHD, Wiel JA (1980a) Oxygen-17 hyperfine structure of trapped-hole center $[AlO_4]^0$ in α–quartz. Solid State Commun 35:789-791

Nuttall RHD, Wiel JA (1980b) Two hydrogenic trapped-hole species in α–quartz. Solid State Commun 33:99-102

Nuttall RHD, Wiel JA (1981a) The magnetic properties of the oxygen-hole aluminum centers in crystalline SiO_2. I. [AlO4]0. Canad J Phys 59:1696-1708

Nuttall RHD, Wiel JA (1981b) The magnetic properties of the oxygen-hole aluminum centers in crystalline SiO_2. II. $[AlO_4/H^+]^+$ and $[AlO_4/Li^+]^+$. Canad J Phys 59:1709-1718

Nuttall RHD, Wiel JA (1981c) The magnetic properties of the oxygen-hole aluminum centers in crystalline SiO_2. III. $[AlO_4]^+$. Canad J Phys 59:1886- 1892.

O'Brien MCM (1955) The structure of the colour centeres in smoky quartz. Proc Royal Soc A231:404-414

O'Brien MCM, Pryce MHL (1955) Paramagnetic resonance in irradiated diamond and quartz: Interpretation. In: Defects in Crystalline Solids. Report of the conference on defects in crystalline solids, Bristol. The Physical Society, London, p. 88-91

Pancharatnam S (1954) Pleochroism of amethyst quartz and its absorption spectra. Proc Indian Acad Sci 40A:196-210

Paradise TR (1982) The natural formation and occurrence of green quartz. Gems and Gemology 18:39-42.

Partlow DP, Cohen AJ (1986) Optical studies of biaxial Al-related color-centers in smoky quartz. Am Min 71:589-598

Platonov AN, Sakhanbinsky M, Vrublevsky P, Ignatov SI (1991) Rare varieties of green quartz from quartz-agate vugs of lower Silezia (Poland). Mineralogicheskiy Zhurnal 13:10-17 (in Russian)

Postelmann A (1937) Die Ursache der Blaufärbung gesteinsbildender Quarze. N Jb Min BB 72A:401-440

Raman CV, Jayaraman A (1953a) The structure of opal and origin of its irridescence. Proc Indian Acad Sci 38A:101-108

Raman CV, Jayaraman A (1953b) The structure and optical behaviour of irridescent opal. Proc Indian Acad Sci 38A:343-354

Rehberg CH, Schlossmacher K (1944) Die Farbe des Chrysoprases. N Jb Min Monat A 1944:81-85

Reinitz IM, Rossman GR (1988) The role of natural radiation in tourmaline coloration. Am Min 73:822-825

Rinneberg H, Wiel JA (1972) EPR studies of Ti^{3+} - H^+ centers in x-irradiated alpha-quartz. J Chem Phys 56:2019-2028

Rose H, Lietz J (1954) Ein grün verfärbbarer Amethyst. Naturwiss 41:448

Rossman GR, Shannon RD, Warring RK (1981) Origin of the yellow color of complex nickel oxides. J Solid State Chem 39:277-287

Sachanbinski M (1980) Mineralogy of chrysoprases of Lower Silesia deposits. Gem Minerals. Proc 11th Gen'l Meeting Int'l Mineralogical Assoc, Novosibirsk, USSR, 1978

Samoilovich MJ, Komarova LM, Khadzhi VY, Tsinober LI, Tsyganov LM, Shaposhnikov AA (1982) Optical spectrum characteristics of synthetic amethyst crystal. Int'l Geol Rev 24:41-43 (translation of Veses Mineralog Obshch Zapiski (1979) 584-587)

Samoilovich, M.I., Tsinober, L.I., Khadzhi, V.E. and Lelekova, M.V. (1968) Determining the activation energy of formation of smoky centeres in synthetic quartz containing aluminum. Soviet Phys Crystallog 13:734-736 (translation of Kristallografiya 13:850-853)

Samoilovich MI, Tsinober LI, Kreiskop VN (1969) The nature of radiation-produced citrine coloration in quartz. Sov Phys Cryst 13:626-628 (translation of Kristallografiya 13:727-730)

Samoilovich MI, Tsinober LI, Kreiskop VN (1970) Features of the smoky color of natural quartz crystals: morions. Sov Phys Crystallogr 15:438-440 (translation of Kristallografiya 15:519-522)

Samoilovich MI, Tsinober LI, Dunin-Barkavsky RL, Lisitsina EE, Khadzhy VE (1976) About the third type of citrine color of natural quartz. Zap Vses Min Obsh 105:223-227 (in Russian)

Sanders JV (1964) Colour of precious opal. Nature 204:1151-1153

Sanders JV (1968) Diffraction of light by opals. Acta Crystallogr 24:427-434

Sanders JV, Darragh PJ (1971) The microstructure of precious opal. Min Record 2:261-269

Sanders JV (1975) Microstructure and crystallinity of gem opals. Am Min 60:749- 757

Scala CM, Hutton DR (1976) Site assignment of Fe^{3+} in α–quartz. Phys stat sol (b) 73:K115-K117

Schaller WT (1916) Gems and precious stones. Mineral Resources of the United states 1916, II. Non-metals, p 893. Government Printing Office, Washington DC

Schirmer OF (1976) Smoky coloration of quartz caused by bound small hole polaron optical absorption. Solid State Commun 18:11349-11351

Schlesinger M, Cohen AJ (1966) Postulated structures causing the optical color center bands in amethyst quartz. J Chem Phys 44:3146-3148

EBSCOhost - printed on 2/13/2023 4:48 AM via . All use subject to https://www.ebsco.com/terms-of-use

Schlössin HH, Lang AR (1965) A study of repeated twinning, lattice imperfections and impurity distribution in amethyst. Philos Mag 12:283-296

Schmetzer K, Bank H (1980) Zur Unterscheidung natürlicher und synthetischer Amethyste. Zeit Deutsch Gemmol Ges 29:17-19

Schmetzer, K (1985) Ein verbesserter Probenhalter und seine Anwendung auf Probleme der Unterscheidung natüralicher und synthetischer Rubine sowie natüralicher und synthetischer Amethyste. Zeit Deutsch Gemmol Ges 34:30-47

Schmetzer K (1987) Microscopic observation of twinning microstructure in natural amethyst. N Jb Min Monat 1987:8-15

Schmetzer K (1988) Thermal stability of yellow colour and colour centres in natural citrine. N Jb Min Monat 1988:71-80

Schmetzer K (1989) Methods for the distinction of natural and synthetic citrine and prasiolite. J Gemmology 21:368-391

Schnadt R, Schneider J (1970) The electronic structure of the trapped-hole center in smoky quartz. Phys kondens Materie 11:19-42

Sinkankas J (1957) "Green" amethyst from Four Peaks, Arizona. Gems & Gemology 9:88-95

Smith G, Vance ER, Hasan Z, Edgar A, Runciman WA (1978) A charge transfer mechanism for the colour of rose quartz. Phys stat sol (a) 46:K135-K140

Stegger P, Lehmann G (1989a) The structures of three centers of trivalent iron in α–quartz. Phys Chem Min 16:401-407

Stegger P, Lehmann G (1989b) Dynamic effects in a new substitutional center of trivalent iron in quartz. Phys stat solidi (b)151:463-467

Stock HD, Lehmann G (1977) Phenomena associated with diffusion of trivalent iron in amethyst quartz. J Phys Chem Solids 38:243-246

Tsinober LI, Chentsova LG (1959) Synthetic amethyst quartz. Sov Phys Crystallogr 4:593-595 (translation of Kristallografiya 4:633-635)

Tsinober LI (1962) Feature of the pleochroism of colored synthetic quartz. Sov Phys Crystallogr 7:113-114 (translation of Kristallografiya 7:138-139) 261- 265.

Tsinober LI, Samoilovich MI, Gordienko LA, Chentsova LG (1967) Anomalous pleochroism in synthetic smoky quartz crystals. Sov Phys Crystallogr 12:53-56

Vasaconcelos PM, Wenk HR, Rossman GR (1994) The Anahí ametrine deposit, Bolivia. Gems and Gemology 30:4-23

Vereshchak MF, Zhetbaev AK, Kaipov DK, Satpaev KK (1973) Mössbauer effect in impurity atoms of Fe^{57} in quartz single crystals. Sov Phys Solid State 14:2638- 2639 (translation of Fizika Tverdogo Tela 14:3082-2083)

Visser JM (1947) Nephrite and chrysoprase of Silesia. Gemmologist 16:229-230

Vultée Jv (1955a) Über die orientierten Verwachsungen von Rutil in Quarz. N Jb Min Abh 87:389-415

Vultée Jv (1955b) Die Verwachsungsgesetze der orientierten Einlagerungen von Rutil in Quarz. Z Krist 107:1-17

Vultée Jv, Lietz J (1956) Über die Rolle des Titans als Färbungsursache von Blau- und Rosenquarzen. N Jb Min Monat 3:49-58

Weaver HE, Schindler P (1964) Paramagnetic Elektronenresonanz von fehlstellen in Quarzkristallen. Naturwiss 51:81-82

Weeks RA (1970) Paramagnetic resonance and optical absorption in gamma–ray irradiated α–quartz: the "Al" center. J. Am Ceram Soc 53:176-179

Weeks RA, Lell E (1964) Relation between E' centers and hydroxyl bonds in silica. J Appl Phys 35:1932-1938

Wiel JA (1975) The aluminum centers in α–quartz. Radiation Effects 26:261-265

Wiel JA (1984) A review of electron spin spectroscopy and its application to the study of paramagnetic defects in crystalline quartz. Phys Chem Min 10:149-165

Wiel JA (1993) A review of EPR spectroscopy of the point defects in α–quartz: the decade 1982-1992. In: Helms CR, Deal, BE (ed), The Physics and Chemistry of SiO_2 and the Si-SiO_2 Interface. 2. Plenum Press, New York, p 131-144

Wiel JA (1994) EPR of iron centres in silicon dioxide. Appl Magnetic Resonance. In press.

Wright PM, Wiel JA, Buch T, Anderson JH (1963) Titanium colour centres in rose quartz. Nature 197:246-248

Wood DL, Ballman AA (1966) Blue synthetic quartz. Am Min 51:216-220

Zaitov MM, Zaripov MM, Samoilovich MI, Khadzhi VE, Tsinober LI (1975) Fe^{3+} EPR spectrum in irradiated quartz. Sov Phys Crystallogr 19:674-675 (translated from Kristallografiya 19:1090-1092)

Zolensky ME, Sylvester PJ, Paces JB (1988) Origin and significance of blue coloration in quartz from Llano rhyolite (llanite), north central Llano County, Texas. Am Min 73:313-323

EBSCOhost - printed on 2/13/2023 4:48 AM via . All use subject to https://www.ebsco.com/terms-of-use

EBSCOhost - printed on 2/13/2023 4:48 AM via . All use subject to https://www.ebsco.com/terms-of-use

INDUSTRIAL APPLICATIONS OF SILICA

14 14

George H. Beall

Corning Incorporated
Sullivan Park FR-51
Corning, New York 14831 U.S.A.

INTRODUCTION

Silica in its various crystalline and amorphous forms has an extremely wide spectrum of industrial application. Its uses range from a simple raw material for glasses, ceramics, foundry molds and the production of silicon, to highly technical applications such as quartz oscillators and optical waveguides used in the long-distance telecommunications industry. Of the various polymorphs of crystalline silica, only α-quartz, and to a lesser extent cristobalite, have application in the pure siliceous form. α-quartz has many uses in the form of sand or as natural and synthetic single crystals. Cristobalite finds use as a synthetic phase in glass-ceramics, i.e., ceramics produced by the controlled crystallization of glass. The stuffed derivatives of the silica polymorphs are key crystalline components of many glass-ceramics. β-quartz and keatite solid solutions are commercially important because of their low thermal expansion characteristics and good chemical durability. Vitreous silica has a wide range of use where optical transmission and thermal or dimensional stability are important.

The crystalline polymorphs of silica are considered in the first portion of this paper, and stuffed derivatives of the crystalline polymorphs and their applications are treated next. The final section is concerned with vitreous silica and its many applications.

THE CRYSTALLINE SILICA POLYMORPHS

α-quartz

The stable low-temperature phase of silica, α-quartz, presents many features of industrial significance. First, it is abundant in relatively pure form in certain beach sands, sandstones, and quartzites. It also can be mined in highly pure form as quartz crystals in pegmatites, often accessible at the cores of these igneous veins. Second, many of the physical properties of α-quartz are unique. α-quartz is piezoelectric with extremely high Q (quality) values due to low internal friction, and the coefficient of thermal expansion of quartz is unusually high for a silicate material. Moreover, quartz exhibits excellent chemical durability, and it is readily synthesized as large single crystals of high purity by hydrothermal techniques.

Uses as a raw material. About 30 million short tons of industrial sand are produced in the U.S. annually, with a total value approaching $400 million (Minerals Yearbook, 1989). The five leading states in industrial sand production are (in descending order of volume): Illinois, Michigan, California, New Jersey, and Texas. Pure sandstones or orthoquartzites such as the Devonian Oriskany and the Ordovician St. Peter formations are typical sources. The Unimin and U.S. Silica corporations are the two leading producers. Major markets include glass and ceramic sands, foundry sands, stucco blast, and sands for golf courses and other specialty applications.

EBSCOhost - printed on 2/13/2023 4:48 AM via . All use subject to https://www.ebsco.com/terms-of-use

The purity of natural sands is important in glass and ceramic materials for which transition metal oxides, particularly iron oxides, cannot exceed 200 ppm. High purity quartz may be extracted from pegmatites, which may contain as little as 50 ppm iron oxides. Pegmatitic quartz is mined from such locations as the Black Hills of South Dakota, Zimbabwe, and Brazil.

Natural quartz as a ceramic component. In some cases, sand is not used merely as a batch material, e.g., for melting into glass, but it may eventually become an integral component of a finished product. For example, sand molds for metal casting may become sintered or partially converted to cristobalite by high temperature or may be cemented by the metal itself. These molds can be used many times in a foundry operation.

In addition, partially corroded quartz is often a major component in china and porcelain. Such ceramic bodies are typically cast at ambient temperature in the form of a slurry containing a mixture of feldspar, clay, and quartz (Kingery et al., 1976). During firing, the feldspathic ingredients completely melt, dissolving some of the quartz. The kaolinitic clay is converted to mullite, and the remaining silica enters the glassy phase. Porosity is significantly decreased by the partial vitrification procedure, but α-quartz and mullite are left as residual crystalline phases. The role of the α-quartz is particularly significant since its high coefficient of thermal expansion ($\sim 150 \times 10^{-7}$/°C) increases the thermal expansion coefficient of the ceramic body. This enables a vitreous glaze melted onto the surface of the ceramic to cool in mild compression because of its lower thermal expansion coefficient. The surface compression of the glaze on porcelain or china increases its strength and prevents crazing of the glossy skin.

Single crystal quartz. The explosion in high technology uses for minerals probably can be traced to early twentieth century experiments with crystalline quartz oscillators, the forerunners of the modern communications industry (Cady, 1946). The most important natural quartz deposits occur in Brazil and are widely distributed in the states of Minas Gerais, Santa Catarina, Sao Paulo, Paraiba, Parana, Bahia, and Rio de Janeiro. Other exporters of natural quartz crystals include Canada, Spain, Mexico, and the Netherlands.

The United States is the world leader in synthetic quartz production. Synthetic quartz has largely replaced natural quartz for most single crystal applications in the electronic and optical industries. Quartz crystals are mainly used in electronic applications including frequency controls for radio transmitters, RF telephone circuits, receiving circuit filters, transducers for interconversion of electronic and mechanical forces, oscillators for watches and clocks, frequency standards, and chemical and other sensors.

Single crystal quartz has been produced hydrothermally for many years by AT&T, General Electric, and other companies. The quartz crystals are synthesized in an autoclave or hydrothermal bomb (Laudise, 1970; Fig. 1), typically operating at 250 to 450°C under a pressure of 3.4×10^7 to 1.4×10^8 Pa. A difference in temperature of 150-200°C is maintained between the cool end where the crystals grow and the hot end where the raw material, usually quartz sand or crushed quartz, is inserted. Water charged with sodium carbonate or sodium hydroxide is the medium of transfer whereby quartz at the hot end is dissolved and transferred by convection to the cool end, where it crystallizes upon thin quartz seed plates. Typical growth rates of ~1 mm per day produce 4 cm × 4 cm × 15 cm crystals in a 20-day period. Material lost in processing synthetic quartz may exceed 50%, but it is less than that suffered in processing natural quartz for the same applications. The

EBSCOhost - printed on 2/13/2023 4:48 AM via . All use subject to https://www.ebsco.com/terms-of-use

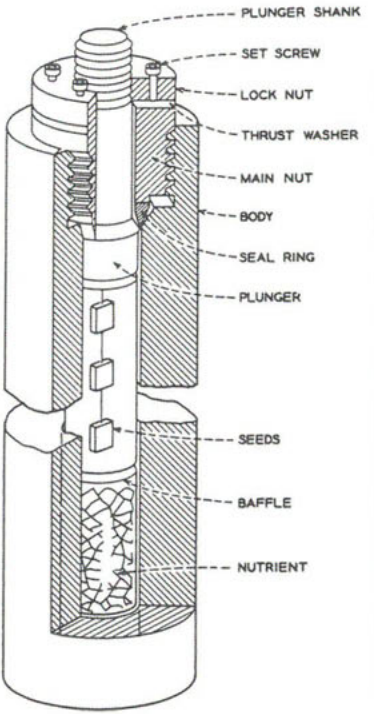




Figure 1. Modified Bridgman hydrothermal autoclave for growth of α-quartz single crystals (after Laudise, 1970).

formation of Dauphiné (electrical) twins is particularly troublesome, because this twinning neutralizes piezoelectric behavior.

Piezoelectric applications. The principal value of single crystal quartz derives from its piezoelectric property and high acoustic strength "Q" (inversely proportional to damping losses), which for natural quartz varies from about 10^5 to 3×10^6, and for synthetic quartz may be even higher. A piezoelectric material characteristically develops an electric polarization when mechanically stressed along an appropriate direction. In the converse effect, an applied electric field produces a mechanical distortion in the material.

Figure 2 illustrates a projection of silicon atoms along [001] in α-quartz (Vigoureux and Booth, 1950). Symmetry about 3 axes labeled XX can be observed. When the crystal is compressed along one of these lines, it becomes electrically polarized in that direction. In order to preserve twofold rotational symmetry with respect to the axis XX, as the projections of silicon centers like **b** and **c** move along horizontal lines **AB** and **CD, b´** and **c´** must move along corresponding lines. The rotations of the triangles **abc** and **ab´c´** are thus equal and opposite in sense. The distance between neighboring silicon atoms, such as **a** and **c**, is hardly altered in the process. When triangles like **abc** and **ab´c´** are distorted by pressure along **DA**, the centroids of the triangles move relative to **a** in the direction **DA**. Since the silicon atoms carry a positive charge, this distortion corresponds to a shift of positive charge from **D** towards **A**. There are also, as seen from Figure 2, two oxygen

EBSCOhost - printed on 2/13/2023 4:48 AM via . All use subject to https://www.ebsco.com/terms-of-use

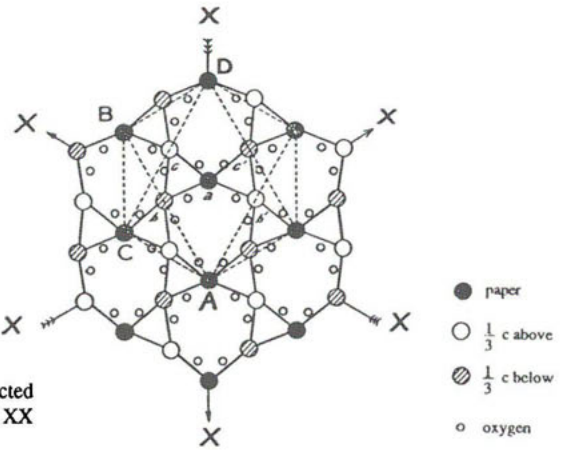


Figure 2. The structure of α-quartz projected along [001] showing piezoelectric axes XX (after Vigoreux and Booth, 1950).

triangles associated with **abc** and **ab´c´** whose centers of gravity are similarly shifted by pressure in the same direction as those of the silicon triangles. It was shown by Gibbs (1926) that the shift of the center of gravity of the oxygen triangle exceeds that of the silicon triangle by over an order of magnitude; the negative charges therefore move farther along direction **DA** than the positive charges. The crystal thereby becomes negatively electrified by compression in the direction indicated by the arrows along XX.

In the construction of quartz oscillators, thin plates of quartz are cut along particular lattice directions as dictated by the piezoelectric properties. The dimensions are carefully chosen to produce a desired resonant vibrational frequency, and the key faces are metallized. In addition, there are a number of orientations in which quartz shows zero or very low variation of frequency with temperature. These include the widely-used "AT" and "BT" cuts (Vigoreux and Booth, 1950) parallel to $(01\bar{1})$ and (023) respectively.

In the most general sense, a piezoelectric resonator is an elastic body capable of being excited to resonant vibration by an alternating electric field of the proper frequency (Cady, 1946). The field drives the resonator through the action of the converse piezoelectric effect. The vibrating crystal causes periodic piezoelectric charges on the electrodes that react on the driving circuit. Thus, an oscillating circuit can be controlled or stabilized within very narrow limits. The precision of frequency stabilization attainable depends on the narrowness of the response peak. There are several reasons why quartz is the material of preference in narrow band resonant uses despite low values of the piezoelectric coefficient. It has an exceptionally narrow resonance response curve due to low internal friction and resulting high Q values. It also allows reasonably good electro-mechanical coupling, and it is hard, chemically durable, and readily synthesized.

Quartz oscillators provide the basis for very stable crystal-controlled clocks that are constant to one part in 10^9. They are also widely used in microdevices (Danel and Delapierri, 1991) such as pressure sensors, gyroscopes, and galvanometers, and as fixed frequency standards in communications equipment of many types (e.g., telephone, radio, television, CB, ham, and military equipment, and in navigational systems such as LORAN).

EBSCOhost - printed on 2/13/2023 4:48 AM via . All use subject to https://www.ebsco.com/terms-of-use

Quartz transducers rely on the converse piezoelectric effect where an electric field induces a stress in the material. Their high sensitivity has recently been exploited in mass measurement techniques and in a variety of chemical and biological sensors (Ward and Buttry, 1990; Wang et al., 1993). These devices employ various films applied to quartz wafers. Interfacial chemical events result in mass changes that alter the frequency of acoustic waves that propagate through the quartz transducer and the adhered chemically active film. The most extensively studied transducer in this regard has been the shear-mode AT-cut quartz resonator, commonly referred to as the quartz crystal microbalance (QCM). This device uses an AT-cut crystal sandwiched between two metal excitation electrodes that generate a standing shear wave across the thickness of the quartz crystal. The thickness or mass per unit area of the film and the nature of the shear wave propagation in the film determine the frequency response. Minute mass changes of less than 10^{-9} g/cm^2 can be detected at surfaces of thin films and at electrode interfaces in liquid media as well. Such measurements are readily performed on a variety of interfacial processes, including reactions catalyzed by enzymes immobilized on surfaces, ion exchange and electron transfer in thin polymer films, and doping reactions in conducting polymers.

Optical applications. Because quartz is enantiomorphous, single crystals are distinctly right- or left-handed and will rotate plain polarized light. The extent of this rotation is expressed as the rotatory power which for the Na_D line is 27.71°/nm. Quartz is weakly birefringent with indices of refraction: $n_\omega = 1.5442$ and $n_\varepsilon = 1.5533$ at the Na_D line. It also transmits well in the near-ultraviolet. Optical uses for single-crystal quartz account for a minor fraction of its consumption. These include prisms and cells for spectrophotometers and quartz wedges and retardation plates for polarizing optical microscopes.

Cristobalite

Cristobalite is an important accessory mineral in ceramics because it readily crystallizes from glassy regions formed by siliceous liquid sintering. It has a high thermal expansion coefficient particularly in the low or α-cristobalite form, stable from 0 to 216°, where it averages over 500×10^{-7}/°C. It has good chemical durability over a wide range of pH, but it is very soluble in extremely alkaline solutions. It is found in a variety of glass-ceramics, the most important being magnesium aluminosilicate compositions where cordierite is the major phase, and in amphibole glass-ceramics widely used as tableware.

Cordierite-cristobalite glass-ceramics. Glass-ceramics are microcrystalline solids produced by the controlled devitrification of glass (Stookey, 1959; Aitken and Beall, 1994). Glasses are melted, fabricated to shape, and then converted by heat treatment to a predominantly crystalline state. The basis of controlled crystallization lies in efficient internal nucleation, which allows development of fine randomly-oriented grains without voids, microcracks, or other porosity. A unique manufacturing advantage of glass-ceramics over conventional ceramics is the ability to use high-speed plastic forming processes developed in the glass industry (e.g., pressing, blowing, rolling, etc.) to create complex shapes essentially free of internal inhomogeneities. Because glass-ceramic compositions are designed to crystallize, however, they cannot be held at temperatures below the liquidus during the forming process. Therefore, the viscosity at the liquidus temperature is critical, both in the choice of a forming process and in the choice of a glass composition. Cristobalite, as the most common form of free silica precipitating from glass, is therefore an expected phase in those siliceous compositions chosen to produce viscosity characteristics that are high enough for many forming processes.

EBSCOhost - printed on 2/13/2023 4:48 AM via . All use subject to https://www.ebsco.com/terms-of-use

Glass-ceramics based on the hexagonal form of cordierite, sometimes referred to as indialite, are strong and have excellent dielectric properties, including transparency over a wide range of microwave frequencies. They are stable to 1300°C and show excellent thermal shock resistance. Corning Code 9606, whose composition is given in Table 1, is the standard glass-ceramic used for over thirty years for radomes (missile nose cones). It is a multiphase material nucleated with titania, but it is largely based on cordierite of composition $Mg_2Al_4Si_5O_{18}$ with some solid solution toward Mg-beryl, i.e., $Mg^{2+} + Si^{4+} \leftrightarrow 2Al^{3+}$. This major phase is mixed with cristobalite, minor enstatite (~10%), rutile, magnesium dititanate, and glass, which is isolated at grain boundary nodes.

The choice of this composition was based primarily on glass-forming considerations. To optimize viscosity of the liquidus, the lowest ternary eutectic in the refractory system MgO-Al_2O_3-SiO_2 was approached from the direction of cordierite. The key properties of cordierite were maintained because it is the major crystalline phase in the subsolidus assemblage, even at the eutectic composition. Some cristobalite was necessarily incorporated, which had the immediate adverse effect of raising the coefficient of thermal expansion. This may have compromised thermal shock resistance, had not the mechanical strength of the cordierite-cristobalite mix proved unusually high for a ceramic material.

One of the difficulties in controlling the crystallization of glass-ceramics involves relieving stresses due to change in density accompanying phase transformation. This problem is well illustrated with Code 9606. Table 2 lists each phase assemblage and its corresponding density as the parent glass is heated to various temperatures for two-hour holds. There is a significant increase in density from glass to a dense metastable crystalline

Table 1. Commercial cordierite glass-ceramic (Corning 9606)

Composition		*wt %*	*mol %*	*Phases*
SiO_2		56.1	58.1	
Al_2O_3	xl	19.8	12.1	cordierite
MgO		14.7	22.6	cristobalite enstatite rutile
CaO		0.1	0.1	Mg-dititanate
TiO_2	n	8.9	6.9	
As_2O_3	f	0.3	0.1	
Fe_2O_3		0.1	0.1	

Use: Radomes

* xl, oxides concentrated in crystal; n, nucleating-agent oxides; f, fining-agent oxide

Table 2. Phase assemblages during crystallization of glass-ceramic 9606

Temp. (°C)	*Density (gcm^{-3})*	*Phases*
700	2.64	Glass
800	2.67	Glass, $MgTi_2O_5$
900	2.75	β-quartz ss, $MgTi_2O_5$, glass
1010	2.95	α-quartz, sapphirine, enstatite, $MgTi_2O_5$, rutile
1260	2.60	Cordierite ss, cristobalite, enstatite, rutile, $MgTi_2O_5$

EBSCOhost - printed on 2/13/2023 4:48 AM via . All use subject to https://www.ebsco.com/terms-of-use

assemblage at 1010°C, followed by a volume expansion to cordierite above that temperature. Clearly, in order to avoid extreme stresses and resulting cracking, the heat treatment schedule must be carefully adjusted to minimize extremes in metastable phase density and to allow sufficient viscous relaxation in the residual glassy phase at various stages to prevent cracking. This required rapid heating between 900 and 1100°C. The final phase assemblage developed at 1260°C consists of cordierite solid solution and cristobalite with minor enstatite, rutile, and magnesium dititanate (pseudo-brookite structure). These phases, including cristobalite, are stable even when held at lower temperatures for hundreds of hours.

It is interesting to note that enstatite is not a major phase in the glass-ceramic assemblage, despite the fact that the composition of Code 9606 lies between stoichiometric cordierite and the eutectic cordierite-enstatite-cristobalite. In fact, the normative composition of the glass-ceramic is roughly $Co_{63}En_{20}Qz_{17}$ (ignoring the nucleating component TiO_2), while the ternary eutectic is $Co_{50}En_{35}Qz_{15}$. In reality, however, the cordierite solid solution likely contains significant "Mg-beryl" component (Schreyer and Schairer, 1961b), and it has a composition between the maximum beryl solid solution: $MgO:Al_2O_3:SiO_2$ mole ratio of 2.3:1.5:5, and the stoichiometric 2:2:5. In addition, some of the titania, added for purposes of efficient internal nucleation, is combined with magnesium as the compound $MgTi_2O_5$. There is also a small amount of residual glass (<5%) of unknown composition. These factors may explain the low level of modal enstatite (~10%) even though the norm predicts 20%.

The microstructure of cordierite and cristobalite illustrated in Figure 3 shows a strong interlocking coast-and-island texture. This structure is largely responsible for the excellent mechanical properties of this glass-ceramic. A Weibull plot of flexural strength data from transverse ground bars hewn from a slab of this commercial composition is shown in Figure 4. Excellent consistency is demonstrated by a high Wiebull modulus of 9.3. Other important properties include a coefficient of thermal expansion (0-700°C) of 45×10^{-7}/°C, good fracture toughness (K_{1C} = 2.2 MPa $m^{1/2}$), thermal conductivity 0.009 cal/cm·sec/°C, Knoop hardness 700, dielectric constant and loss tangent at 8.6 GHz, 5.5 and 0.0003, respectively. It is this combination of good mechanical properties, microwave transparency, relatively high thermal conductivity for a silicate, and moderately low thermal expansion coefficient, that allow this material to be used in the difficult environment encountered by radar-guided high speed missiles.

Because of extreme surface abrasion from rain or hail in the troposphere, a special surface treatment was developed as a final finishing stage in radome production. This involved leaching with a hot caustic solution of sodium hydroxide. The cristobalite was selectively leached by the caustic, producing a porous silica-deficient skin on the radome. This skin tends to reduce both the initiation and the propagation of mechanical flaws caused by impact or abrasion.

Potassium fluorrichterite-cristobalite glass-ceramics. A new high strength tableware very similar in appearance to bone china and essentially nonreactive in the microwave oven was developed by Corning in the late 1980s. It is based primarily on the two-phase system potassium fluorrichterite ($KNaCaMg_5Si_8O_{22}F_2$) and cristobalite. The amphibole occurs in high-aspect-ratio rods which lend strength and toughness to the product (Beall, 1992).

Complex fluorosilicate glasses in the system SiO_2-MgO-CaO-Na_2O-K_2O-F with minor additions of Al_2O_3, P_2O_5, Li_2O, and BaO were optimized to produce this glass-ceramic

EBSCOhost - printed on 2/13/2023 4:48 AM via . All use subject to https://www.ebsco.com/terms-of-use

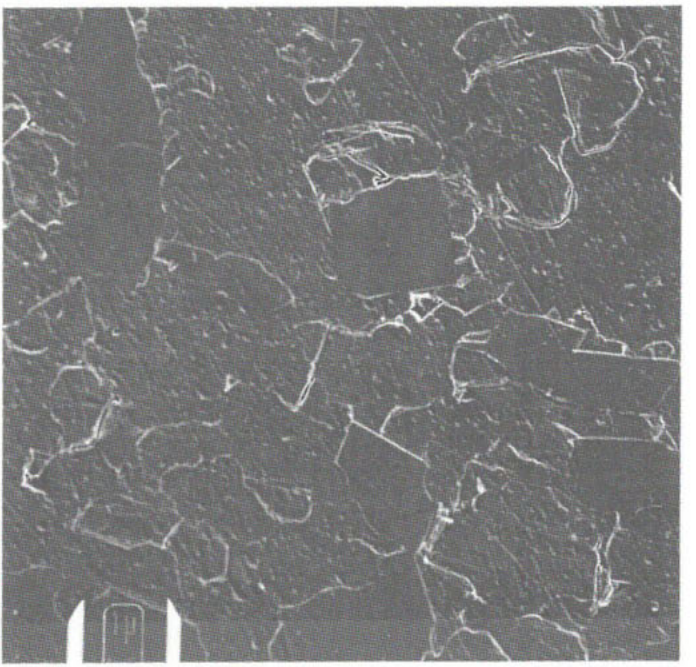


Figure 3. Interlocking "coast-and-island" structure of Code 9606 glass-ceramic showing cristobalite, enstatite and rutile in a cordierite matrix. Note the traces of easily etched glass at cordierite grain boundary nodes (replica electron microphotograph; 0.1% HF etch).

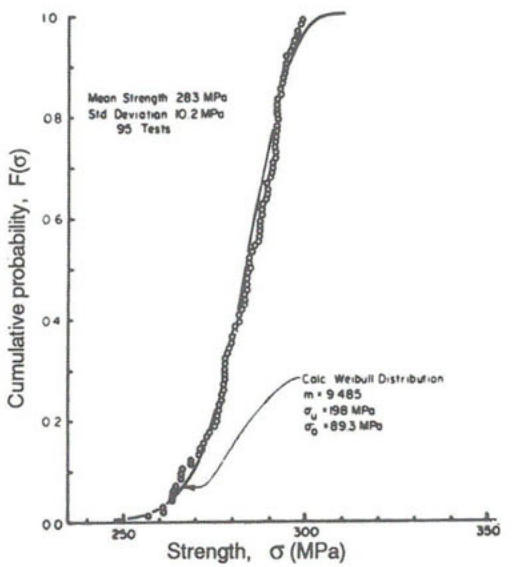


Figure 4. Flexural strength distribution of transverse ground bars of Corning Code 9606 glass-ceramic (after Lewis, 1982).

EBSCOhost - printed on 2/13/2023 4:48 AM via . All use subject to https://www.ebsco.com/terms-of-use

EBSCOhost - printed on 2/13/2023 4:48 AM via . All use subject to https://www.ebsco.com/terms-of-use

Table 3. K-F-richterite-cristobalite glass-ceramic: estimated phase assemblage and composition.

wt.%	Amphibole F-K-richterite	~50% F-K-R[a]	Mica taeniolite	~10% F-T[b]	Cristobalite	~20% Crb[c]	Total crystals	bulk	Residual glass ~20% (calc.)
	$KNaCaMg_5Si_8O_{22}F_2$		$KMg_2LiSi_4O_{10}F_2$		$95SiO_2 \cdot 5LiAlO_2$		80%	(anal.)	
SiO_2	57.3	28.7	59.3	5.9	95.0	19.0	53.6	67.1	68.6
Al_2O_3	--	--	--	--	4.0	0.8	0.8	1.8	5.1
MgO	24.1	12.1	19.9	2.0	--	--	14.1	14.3	1.5
CaO	6.7	3.4	--	--	--	--	3.4	4.7	6.6
Na_2O	3.7	1.9	--	--	--	--	1.9	3.0	5.6
K_2O	5.7	2.9	11.6	1.2	--	--	4.1	4.8	3.6
Li_2O	--	--	3.7	0.4	1.0	0.2	0.6	0.75	0.8
BaO	--	--	--	--	--	--	--	0.3	1.5
P_2O_5	--	--	--	--	--	--	--	1.0	5.1
Sb_2O_3	--	--	--	--	--	--	--	0.2	1.0
F	4.5	2.3	9.4	1.0	--	--	3.3	3.5	1.0
	102.0		103.9					101.5	100.4
	$0 \approx F\ 2.0$		$0 \approx F\ 3.9$					$0 \approx F\ 1.5$	$0 \approx F\ 0.4$
Totals	100.0		100.0					100.0	100.0

[a] F-K-R: fluorrichterite; [b] F-T: fluortaeniolite; [c] Crb: cristobalite

(after Beall, 1991)

product. Table 3 lists the commercial glass composition with its derivative glass-ceramic phases. It was found important to formulate a bulk composition substantially richer in silica than that of stoichiometric fluorrichterite. This yielded a stable glass with sufficient viscosity at the liquidus to meet high speed gobbing requirements. Plates and mugs are pressed from gobs of glass sheared at a platinum orifice from which the glass is delivered.

The excess silica required to meet the forming viscosity requirements of the glass was responsible for producing cristobalite in the final product. This phase increased the final thermal expansion coefficient of the glass-ceramic, thereby enabling a compressive glaze to be applied effectively.

The early stages of nucleation, as the parent glass is reheated, are controlled by an amorphous emulsion in which one of the two phases is evidently close to the tetrasilicic fluormica: potassium taeniolite solid solution ($KMg_{2+0.5x}Li_{1-x}Si_4O_{10}F_2$) in composition. Crystallization of this mica component is rapid near 600°C. Because fluormica incorporates the major fluxes in the system, the crystallization occurs at high viscosity (Fig. 5). Precipitation of diopside ($CaMgSi_2O_6$) follows above 700°C, and metastable mica and diopside then react above 850°C with the residual glass to produce the stable assemblage of potassium fluorrichterite and cristobalite, the latter growing above 900°C.

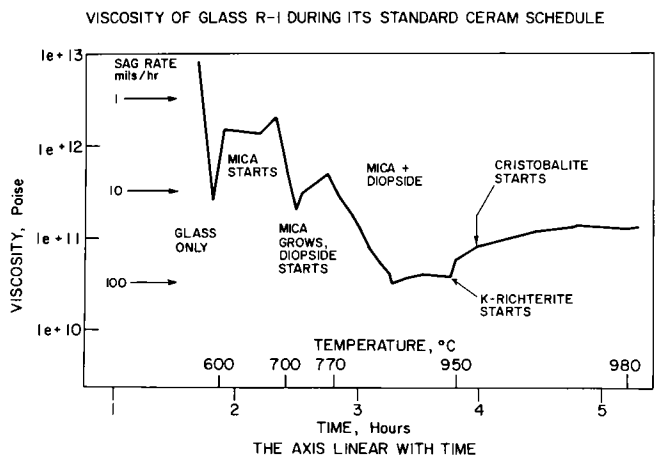


Figure 5. The viscosity of tableware glass (see Table 3) during its standard ceram schedule (after Beall, 1992).

Figure 5 shows the crystallization schedule and the viscosity corresponding to the various temperatures and corresponding crystal formation. It should be noted that at no time does the viscosity fall below 10^9 Pa sec (10^{10} P), very important for allowing glass articles to crystallize without distortion. The composition of the residual glass was calculated from the modal analysis to be siliceous and enriched in Al_2O_3 and P_2O_5, indicating strong chemical resistance. Combined with the chemical stability of the constituent crystals, K-F-richterite and cristobalite, this allows a glass-ceramic of exceptional chemical durability. Moreover, the high thermal expansion coefficient (115×10^{-7}/°C from 0-300°C) of this material enables the development of compressive stresses at the surface through the application of a conventional glaze. Thus, the flexural strength of the glass-ceramic body (150 ± 15 MPa) can be increased to 200 ± 15 MPa in the final article. This glazed material is high-gloss white and displays a translucency similar to that of bone china.

The composition of the cristobalite in this system is believed to be near pure silica because the inflection in the thermal expansion curve is close to 215°C, the transition

EBSCOhost - printed on 2/13/2023 4:48 AM via . All use subject to https://www.ebsco.com/terms-of-use

temperature from the tetragonal α to the cubic β form. Nevertheless, previous experience with cristobalite crystallizing in glasses containing both alumina and lithia suggests that a minor (~5%) incorporation of $LiAlO_2$ may be likely. If so, it has little effect on the phase transition.

Figure 6 illustrates the microstructure of the potassium fluorrichterite-cristobalite glass-ceramic. The most obvious features observed are the randomly-oriented amphibole rods reminiscent of natural nephrite jade or whisker-reinforced ceramics. The fracture toughness of this material has been measured at 3.2 ± 0.2 MPa $m^{1/2}$. The high strength and toughness produces exceptional durability in the final tableware product. This glass-ceramic is currently used widely as institutional tableware, i.e., in hotels, restaurants, etc., as well as for the cups and mugs of the CORELLE® retail line.



Figure 6. A fracture surface (replica electron micrograph) of K-F-richterite–cristobalite glass-ceramic showing the effects of rod reinforcement toughening from the amphibole (after Beall, 1991).

STUFFED DERIVATIVES OF SILICA POLYMORPHS

Buerger (1954) first recognized that certain aluminosilicate crystals composed of three-dimensional networks of SiO_4 and AlO_4 tetrahedra are similar in structure to one or another of the crystalline forms of pure silica. These aluminosilicates were termed stuffed derivatives because they may be considered silica structures with network replacement of Si^{4+} by Al^{3+}, accompanied by a filling of interstitial vacancies by larger cations to preserve electrical neutrality. As would be expected, considerable solid solution normally occurs between these derivatives and pure silica. The silica polymorphs cristobalite, tridymite, keatite, and quartz all have associated derivatives. Examples include the polymorphs carnegieite and nepheline ($NaAlSiO_4$), which are derivatives of cristobalite and tridymite, respectively; β-spodumene ($LiAlSi_2O_6$), a stuffed derivative of keatite; and β-eucryptite ($LiAlSiO_4$), a stuffed derivative of β-quartz.

Nomenclature of stuffed derivatives

There has been both confusion and misunderstanding concerning the nomenclature of stuffed derivatives of silica in both the lithium and magnesium aluminosilicate systems. Roy (1959) was the first to recognize a complete solid solution series between β-eucryptite ($LiAlSiO_4$) and silica with the structure of β-quartz. Members of this series with more silica than $Li_2O:Al_2O_3:3SiO_2$ were found metastable except very near the pure silica endmember. Roy coined the term "silica O" to describe this β-quartz solid solution. This term has been deemed inappropriate because these "silica O" phases are not of pure silica

EBSCOhost - printed on 2/13/2023 4:48 AM via . All use subject to https://www.ebsco.com/terms-of-use

composition; in fact, they may be as low as 50 mol % silica, as in the case of β-eucryptite. Moreover, the pure silica end member is β-quartz itself.

The term "virgilite" was more recently proposed (French et al., 1978) for naturally occurring representatives of lithium-stuffed β-quartz solid solutions falling between the spodumene stoichiometry $LiAlSi_2O_6$ and SiO_2. Virgilite was further defined as those compositions with more than 50 mol % $LiAlSi_2O_6$. Unfortunately, this definition specifies a part of the solid solution range in an arbitrary fashion. Moreover, the term virgilite was coined long after these materials had been widely referred to as β-quartz solid solution in the ceramic literature.

Similarly, the term "silica K" was coined by Roy (1959) to describe another series of solid solutions along the join SiO_2-$LiAlO_2$ that are stable over a wide range of temperatures. The compositions range from below 1:1:4 to about 1:1:10 proportions of Li_2O:Al_2O_3:SiO_2 (Fig. 7; Levin et al., 1964). Although it was initially recognized that tetragonal compounds in this series exhibit structures that are similar to keatite (Keat (1954), phase equilibria studies showed a large miscibility gap between pure silica keatite and the most siliceous end member of this series (Fig. 7). Since the term β-spodumene for the high temperature tetragonal polymorph of spodumene $LiAlSi_2O_6$ (1:1:4) was widely used, it seemed reasonable to refer to this more limited solid solution series as β-spodumene ss. The term "stuffed keatite" has also been used to describe this solid solution, but since there is no continuous composition series to the silica endmember, the mineral name β-spodumene, which identifies the general composition area, is preferred. This nomenclature is consistent with standard usage, as in the case of nepheline or carnegieite ($NaAlSiO_4$). These terms are preferred to "stuffed tridymite" or "stuffed cristobalite," because in these structures there is also no complete solid solution with SiO_2.

For all these reasons, the solid solutions along the SiO_2-$LiAlO_2$ join are herein referred to as β-quartz for the hexagonal solid solution series and β-spodumene for the tetragonal solid solution series. The term "high quartz solid solution" has been proposed (Ray and Muchow, 1968) instead of "β-quartz solid solution," but the Greek letter designations are generally preferred, not only for brevity but because more than two structural modifications are possible, as in the case of tridymite.

There has been similar confusion concerning the naming of metastable stuffed quartz derivatives in the system MgO-Al_2O_3-SiO_2. The terms "μ" $Mg_2Al_4Si_5O_{18}$ and

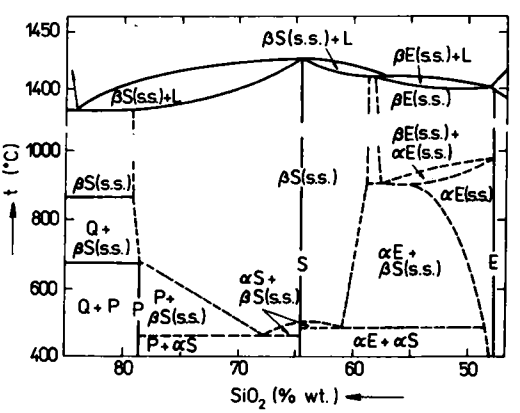


Figure 7. The phase diagram of the SiO_2–Li_2O•Al_2O_3•$2SiO_2$ system (after Levin et al., 1964, and Strnad, 1986). P – petalite, βS – β-spodumene, βE – β-eucryptite, Q – quartz, s.s. – solid solution, L – liquid.

EBSCOhost - printed on 2/13/2023 4:48 AM via . All use subject to https://www.ebsco.com/terms-of-use

"μ-cordierite" have priority (Karkhanavala and Hummel, 1953), but the crystal structure of cordierite basically different from the quartz-type phases described here, and there is evidence for a continuous metastable solid solution series from pure SiO_2 to the composition $MgO:Al_2O_3:2SiO_2$ and beyond (Schreyer and Schairer, 1961a). For these reasons the structural term β-quartz solid solution is again preferred.

β-quartz solid solutions

Composition and stability. A wide range of stuffed β-quartz compositions can be crystallized from simple aluminosilicate glasses with modifying cations capable of filling the cavities of the β-quartz structure. These cations exhibit a range of ionic sizes from 0.6 to 0.8 Å, and they include Li^+, Mg^{2+}, Zn^{2+}, and, to a lesser degree, Fe^{2+}, Mn^{2+}, and Co^{2+}. The solid solutions which have been most studied are described by the general formula

$$Li_{2-2(x+y)}Mg_xZn_yO{\cdot}Al_2O_3{\cdot}zSiO_2$$

(Strnad, 1986), where $x+y \leq 1$ and $z \geq 2$. The region of proven existence of quartz solid solutions in the pseudo-quaternary system SiO_2-$LiAlO_2$-$MgAl_2O_4$-$ZnAl_2O_4$ as crystallized from glass is illustrated in Figure 8 (Petzoldt, 1967).

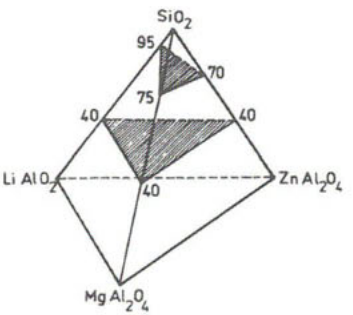


Figure 8. The region of proven existence of meta-stable solid solutions of β-quartz in the pseudo-quaternary system SiO_2–$LiAlO_2$–$MgAl_2O_4$–$ZnAl_2O_4$ (wt %) (after Petzoldt, 1967).

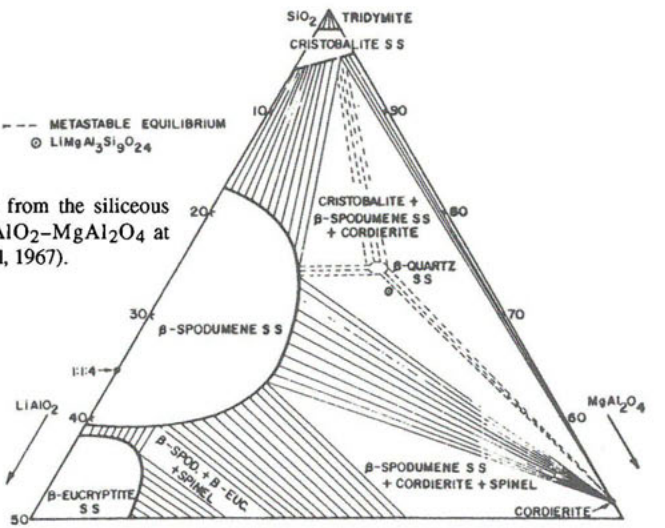


Figure 9. Isothermal section from the siliceous half of the system SiO_2–$LiAlO_2$–$MgAl_2O_4$ at 1230°C (wt %) (after Beall et al, 1967).

EBSCOhost - printed on 2/13/2023 4:48 AM via . All use subject to https://www.ebsco.com/terms-of-use

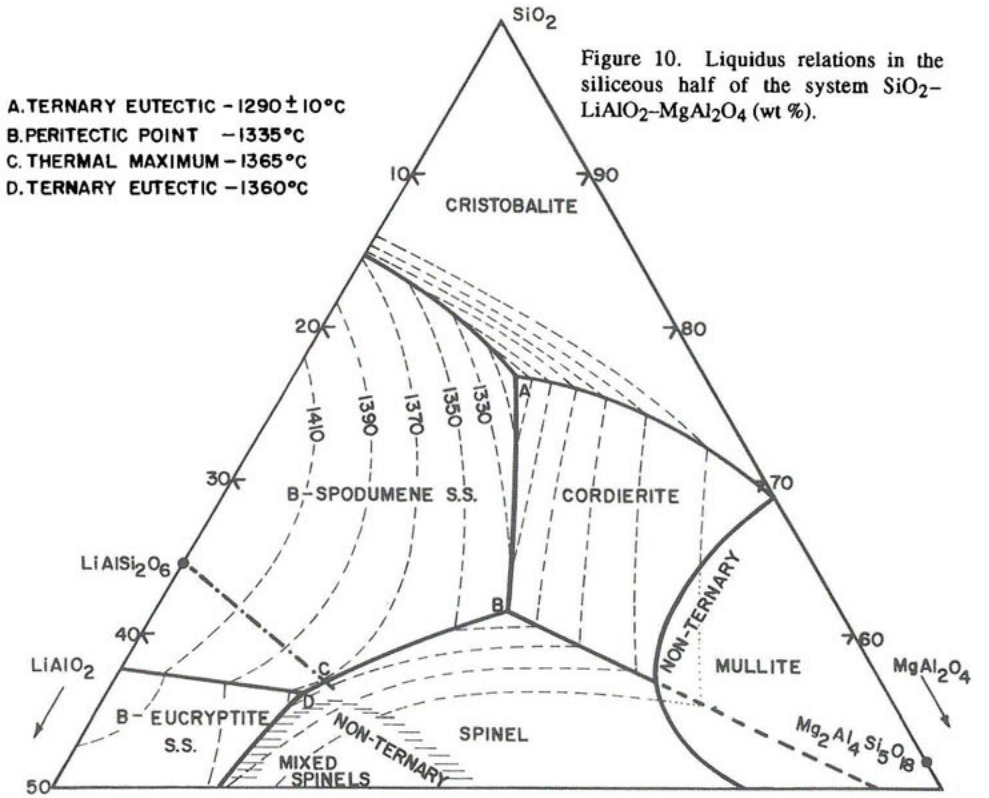


Figure 10. Liquidus relations in the siliceous half of the system SiO_2–$LiAlO_2$–$MgAl_2O_4$ (wt %).

Accessory solid solution components such as Li_2BeO_2 and $Al(AlO_2)_3$ have also been recognized (Beall et al., 1967). In other words, beryllium can substitute to a certain degree for silicon in the tetrahedral position, and some aluminum can enter an interstitial site in β-quartz if lithium is already present.

All of these β-quartz ss compositions are believed to be metastable, with the exception of β-eucryptite ss, whose stability region is shown in Figures 7 and 9, above. The latter depicts an isothermal slice of the pseudo-ternary system SiO_2-$LiAlO_2$-$MgAl_2O_4$ at 1230°C, about 60°C below the lowest melting eutectic in this system (see Fig. 10). Although all compositions in the siliceous half of this system can initially be crystallized from glass to a β-quartz ss, only those in the lower left corner near $LiAlSiO_4$ (eucryptite) have been shown to have any range of thermodynamic stability. On the other hand, there are some very persistent metastable β-quartz solid solutions in this pseudo-ternary system. These compounds can remain even when heated at 1200°C for 100 hours. The most persistent composition approaches the stoichiometry $LiMgAl_3Si_9O_{24}$. There may be some structural significance to this stoichiometry, but a single-crystal study would be necessary to determine whether ordered distributions of Li^+ and Mg^{2+} ions and SiO_4 and AlO_4 tetrahedra are present.

Structure and properties. The structure of a metastable quartz solid solution of composition $LiAlSi_2O_6$ or 1:1:4 has been determined by Li (1968) using a single crystal

EBSCOhost - printed on 2/13/2023 4:48 AM via . All use subject to https://www.ebsco.com/terms-of-use

grown from glass. The structure was confirmed as a stuffed derivative of β-quartz with random Si and Al distribution. Lithium ions were found to be four-coordinated and stuffed into interstitial positions with one lithium atom per unit cell. The lithium tetrahedra are irregular, and they share two edges with two (Si,Al) tetrahedra. The (Si,Al)-Li distance (2.609 Å) is exceptionally short, thereby producing strong cation repulsion. This repulsion is believed to play an important role in controlling the anomalously low thermal expansion behavior of this solid solution (Li, 1968). In this structure, the *a* and *b* axes are functions of the (Si,Al)-Li distance alone, and upon heating these axes tend to expand. On the other hand, the *c* axis, a function of the Li-O distance, would be expected to contract because increasing the (Si,Al)-Li distance decreases the shared edge and, hence, the Li-O bond length.

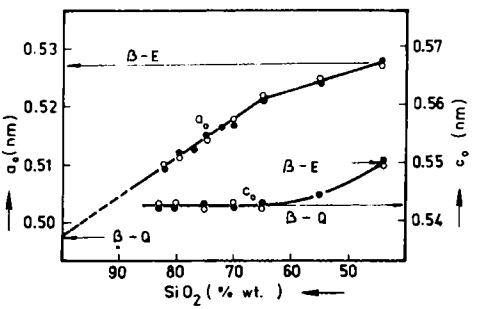


Figure 11. Unit cell dimensions *a* and *c* of β-quartz solid solutions between SiO_2 and β-eucryptite ($LiAlSiO_4$)—empty circles. Full circles correspond to peraluminous β-quartz solid solutions between $LiAl_{1.17}SiO_{4.25}$ and SiO_2 (after Nakagawa and Izumitani, 1972).

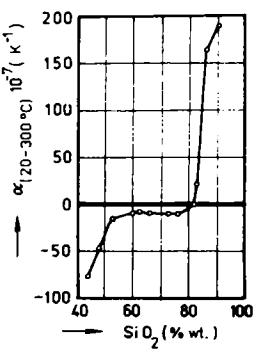


Figure 12 (left). Coefficient of thermal expansion of solid solutions of β-quartz crystallized from glasses in the SiO_2-$LiAlO_2$ system (after Petzoldt, 1967).

Figure 13 (right). Dilatometric curves of quartz solid solutions crystallized from glasses in the SiO_2-$LiAlO_2$ system: mol % Li_2O – (a) 5%, (b) 10%, (c) 15%, (Q) 0% = pure quartz (after Petzoldt, 1967).

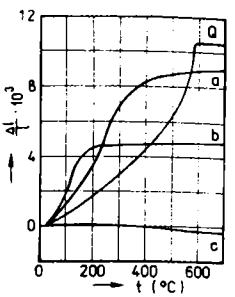


Figure 11 illustrates the lattice parameters a_0 and c_0 of the solid solutions of β-quartz between silica and eucryptite ($LiAlSiO_4$) (Nakagawa and Izumitani, 1972). Figure 12 shows the corresponding coefficients of thermal expansion of these solid solutions (Petzoldt, 1967). Note that this coefficient is heavily negative near β-eucryptite, plateaus at slightly negative values from 50 to 80 wt % SiO_2, approaches zero above 80%, and then becomes strongly positive. It is evident that the β-quartz solid solutions are incapable of persisting to room temperature when their composition is as siliceous as 82 wt %. This is illustrated in Figure 13, where compositions of 15, 10, and 5 mol % $LiAlO_2$ exhibit increasing inversion temperatures associated with the alpha-to-beta transformation (Petzoldt, 1967). Evidently, there is insufficient lithium to prop up the β-quartz structure much above 85 mol % SiO_2. The range of ultra-low expansivity important from practical melting considerations ranges from 52 to 75 wt % SiO_2.

EBSCOhost - printed on 2/13/2023 4:48 AM via . All use subject to https://www.ebsco.com/terms-of-use

The coefficients of thermal expansion of more complex solid solutions of β-quartz in the pseudoquaternary system SiO_2-$LiAlO_2$-$MgAl_2O_4$-$ZnAl_2O_4$ show a general decrease with increasing Li^+ and Zn^{2+}. On the other hand, Mg^{+2} increases the thermal expansion behavior (Strnad, 1986). For example, the thermal expansion of stuffed β-quartz at the cordierite stoichiometry ($Mg_2Al_4Si_5O_{18}$) from 25-870°C averages 47.2×10^{-7}/°C. The three cations Li^+, Mg^{2+}, and Zn^{2+} can therefore be used to tailor a thermal expansion coefficient very close to zero or, indeed, any value between -50 and $+50 \times 10^{-7}$/°C over a wide range of silica contents.

Similarly, the refractive index and birefringence of β-quartz solid solutions can be varied over a considerable range. Figure 14 shows the indices of refraction of quartz solid solutions along the SiO_2-$MgAl_2O_4$ join (Schreyer and Schairer, 1961a). It can be seen that optically positive quartz becomes isotropic at 72 wt % and negative at lower levels of silica. The existence of optically isotropic quartz suggests the possibility of transparency in polycrystalline β-quartz ceramics.

Glass-ceramics based on β-quartz solid solution. As we have seen, β-quartz solid solutions offer both a wide range of composition and a unique group of properties, especially low thermal expansivity. In order to manufacture these materials, they must also be formable as glasses by processes like casting, rolling, pressing, or blowing, and they must subsequently be crystallized through efficient internal nucleation. In commercial compositions, the silica levels tend to lie between 55 and 70 wt %, allowing appropriate viscosity for high speed forming. This brings the solid solutions into the metastable range where they will break down to other phases like β-spodumene, cristobalite, and cordierite if heated for prolonged periods above 900°C. Lithium is the preferred stuffing ion because of its dramatic ability to lower the thermal expansion of the crystal, but substitutions of Mg^{2+} and Zn^{2+} for $2Li^+$, as well as $AlPO_4$ for SiO_2, are useful in reducing both liquidus temperature and/or batch cost.

The combination of titania and zirconia has proven most effective in the nucleation of β-quartz ss and is used in most commercial glass-ceramic formulations (Beall, 1986). Both

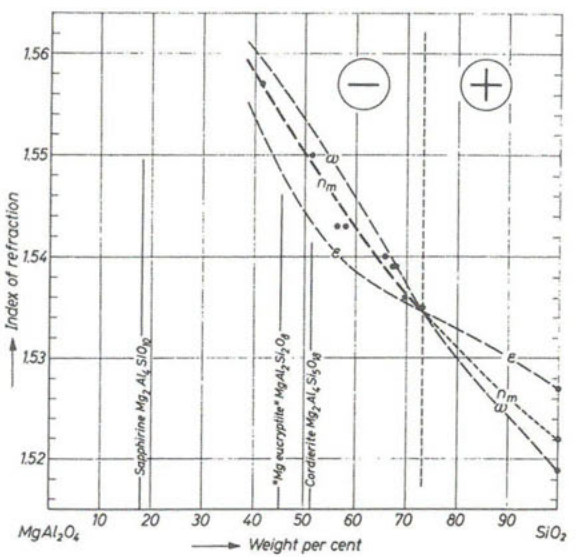


Figure 14. The refractive indices of metastable β-quartz solid solutions in the SiO_2—$MgAl_2O_4$ system (after Schreyer and Schairer, 1961a).

EBSCOhost - printed on 2/13/2023 4:48 AM via . All use subject to https://www.ebsco.com/terms-of-use

TiO_2 and ZrO_2 produce microphase separation in glasses near the join SiO_2-$LiAlO_2$-$MgAl_2O_4$ at levels above 3 mol %. Upon heat treatment of these glasses near the glass transition temperature, dispersed amorphous particles less than 10 nm in size and enriched in TiO_2 and ZrO_2 separate from the silicate matrix. Upon further heat treatment, about 50° to 100°C above the glass transition temperature or annealing point, oxide crystals such as zirconium oxide, zirconium titanate, aluminum titanate, or magnesium dititanate are precipitated from this dispersed amorphous phase. It is upon these oxide crystallites that the major silicate β-quartz ss phase crystallizes. A combination of TiO_2 and ZrO_2 at levels near 2 wt % each appears most effective in this nucleation process and is used in most commercial formulations, some of which are listed in Table 4.

Transmission electron microscopy can be used to study the development of the metastable quartz phase upon nuclei of zirconium titanate (Maier and Müller, 1987). In the Schott Zerodur® glass-ceramic (Table 4), for example, both nuclei and quartz are clearly visible in Figure 15. The efficiency of nucleation as a function of temperature for this composition has also been studied (Schiffner and Pannhorst, 1987). Homogeneous glass samples were heated for various times at temperatures within the nucleation range of zirconium titanate precipitation and were then heated to 1000°C for four minutes to ensure complete crystallization of β-quartz solid solution. The resulting crystal density as a function of nucleation temperature and time is shown in Figure 16. Nucleation rates show the classical form of temperature dependence (James, 1989) with a maximum in this case near 770°C.

Even higher crystal densities and finer microstructures are observed for the Corning VISIONS® glass-ceramic. Figure 17 shows a very fine-grained and highly crystalline microstructure after a heat treatment of 1.5 hours, including a nucleation hold near 780°C and a growth hold near 875°C. The particle density of the β-quartz ss phase is about $5 \times 10^{12}/mm^3$. The viscosity of the glass during the crystallization process for the VISIONS® product remains well above 10^9 Pa sec. The combination of efficient nucleation and sluggish grain growth allows crystals to impinge before they have grown much more than 50 nm. The extremely fine particle size and very low optical birefringence, particularly near 70 wt % SiO_2 (Fig. 14), allows the efficient transmission of light with minimum scattering (Beall and Duke, 1969). Obviously, both the compositions of the β-quartz ss and the crystallization thermal cycle have been adjusted to achieve very low thermal expansion coefficient in these products over their desired temperature range of application.

A convenient technique for displaying the relationship between metastable and stable phases for a glass-ceramic composition is the use of a "TTT" diagram, which plots phase transformation boundaries as a function of temperature and time. Figure 18 is a simple example for the experimental Corning β-quartz ss composition listed in Table 4. This type of diagram can predict the thermal stability of a metastable glass-ceramic at a specific temperature.

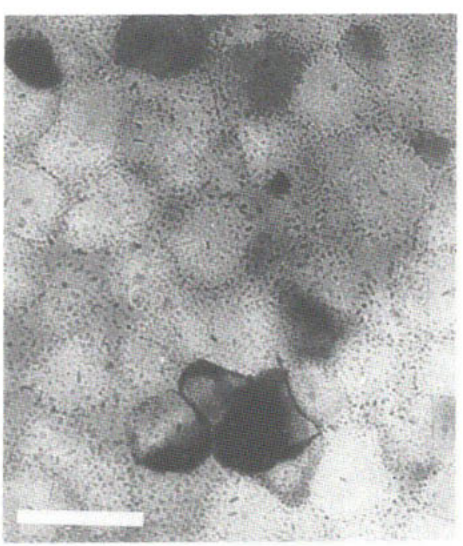
Some of the important applications for transparent β-quartz glass-ceramics are telescope mirror blanks, cookware, woodstove windows, infrared transmitting rangetops and laser gyroscopes. For telescope mirror blanks, the most important property is stable "zero" thermal expansion over the range of temperatures to be found at the telescope site. Perhaps equally important is the ability to produce a fine polish, the equivalent of glass. For this, the crystal size must not exceed 100 nm. Recent varieties of Schott Zerodur® show dimensional changes of less than 6 parts per million over the ambient temperature range of -30 to +40°C (Jacobs and Bass, 1989). The Zerodur® composition is modified by $AlPO_4$

EBSCOhost - printed on 2/13/2023 4:48 AM via . All use subject to https://www.ebsco.com/terms-of-use

Table 4. Composition of transparent glass-ceramics based on β-quartz solid solution (wt %)

		VISIONS® Corning	*ZERODUR®** Schott	*Narumi** Nippon Electric	*Experimental* Corning
SiO_2		68.8	55.5	65.1	65.0
Al_2O_3		19.2	25.3	22.6	23.0
Li_2O		2.7	3.7	4.2	3.8
MgO	xl	1.8	1.0	0.5	1.8
ZnO		1.0	1.4		1.5
P_2O_5			7.9	1.2	
F				0.1	
Na_2O		0.2	0.5	0.6	
K_2O	gl	0.1		0.3	
BaO		0.8			
TiO_2	n	2.7	2.3	2.0	2.0
ZrO_2		1.8	1.9	2.3	2.0
As_2O_3	f	0.8	0.5	1.1	0.9
Fe_2O_3		0.1	0.03	0.02	
CoO	c	50 ppm			
Cr_2O_3		50 ppm			
		Transparent cookware	Telescope mirrors	Rangetops Stove windows	

*As analyzed at Corning Incorporated, xl, oxides concentrated in crystal; gl, oxides concentrated in glass; n, nucleating-agent oxides; f, fining-agent oxide; c, colorant oxides



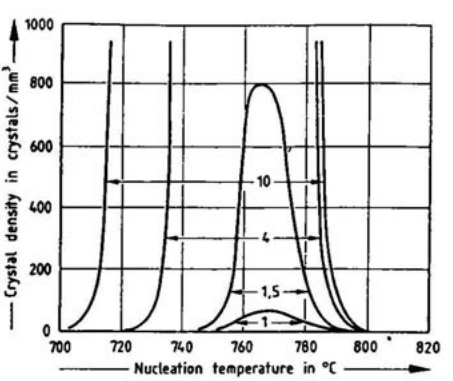


Figure 15 (left). Transmission electron micrograph of impinging β-quartz solid solution crystals showing tetragonal $ZrTiO_4$ nuclei at the center. Note continuous residual glass and precipitation of excess $ZrTiO_4$ along crystal boundaries (bar = 200 nm) (after Maier and Müller, 1987).

Figure 16 (right). Dependence of crystal density at constant nucleation times (min.) on nucleation temperature for Schott Zerodur® (after Schiffner and Pannhorst, 1987).

EBSCOhost - printed on 2/13/2023 4:48 AM via . All use subject to https://www.ebsco.com/terms-of-use

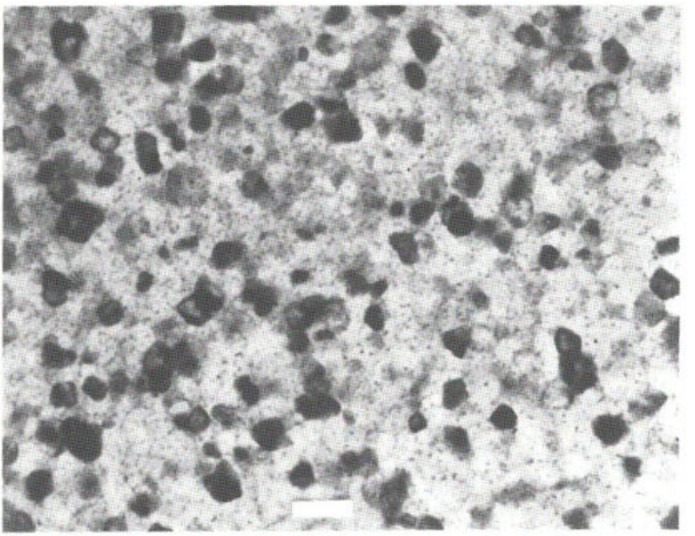


Figure 17 (above). The microstructure of Corning VISIONS® glass-ceramic as seen by transmission electron microscopy (white bar = 100 nm) (after Beall, 1986).

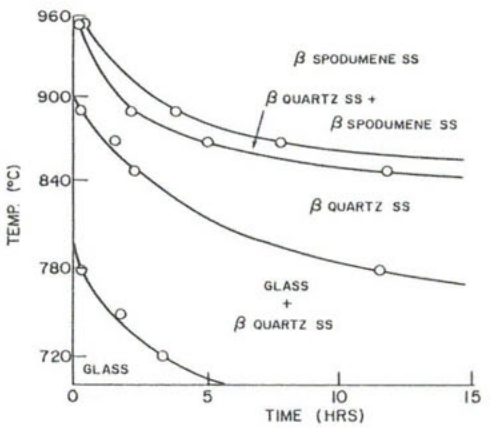


Figure 18 (left). The time–temperature–transformation (TTT) metastable phase diagram for experimental Corning glass-ceramic in Table 4 (after Beall and Duke, 1969).

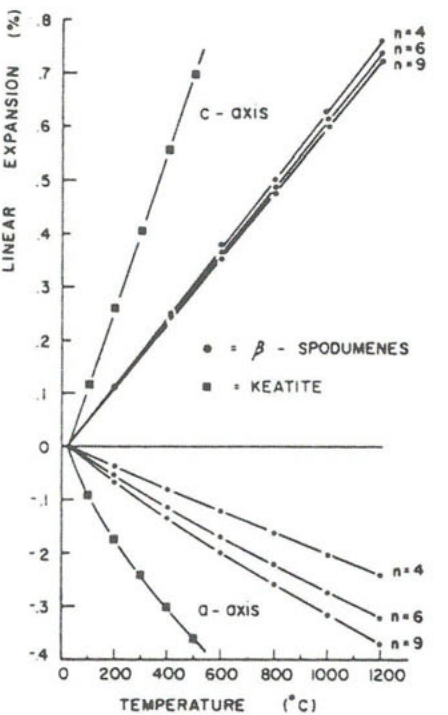


Figure 19 (right). Thermal expansion behavior of β-spodumene solid solution (stuffed keatite) crystals ($Li_2O{\cdot}Al_2O_3{\cdot}nSiO_2$) along tetragonal axes (after Ostertag et al., 1968).

EBSCOhost - printed on 2/13/2023 4:48 AM via . All use subject to https://www.ebsco.com/terms-of-use

partially substituted for silica (Table 4), and is therefore fluid enough to be spun cast over a diameter of 10 meters with a thickness less than 10 cm (Petzoldt and Pannhorst, 1991).

The transparent β-quartz glass-ceramic cookware sold by Corning as the product VISIONS® has sold well over 100 million pieces. For this application, transparency equivalent to glass is required. In addition, excellent chemical durability and strength well above that of glass are key benefits. Unlike glass products, this pressed glass-ceramic can be placed directly on the rangetop at temperatures as high as 700°C and then immediately quenched into cold water without breakage.

Another important commercial application is the flat stovetop or hob top. For this application, the β-quartz ss is doped with cobalt or vanadium to give a black appearance in reflected light, but it remains transparent in the near infrared. In this way, a resistance element or a tungsten halogen bulb placed below the glass-ceramic sheet can effectively radiate through the sheet to the overlying vessel. A similar application for transparent flat glass-ceramic sheet is woodstove windows or fire doors, where both thermal stability and thermal shock resistance are required.

A more recent technical application for these transparent β-quartz ss materials is as a ring laser gyroscope (Fig. 19), which is made from a slightly different composition than the cookware. The principle here is that two laser beams, one propagating clockwise and one counterclockwise, interfere according to tiny variations in path length created by motion of the platform to which the gyroscope is fixed. This application requires a thermal expansion coefficient in the host material below 10^{-8}/°C, which can be achieved by fine control of composition and thermal treatment for crystallization. Good transparency is required to allow the laser beam to travel without adverse scattering or absorption.

Stuffed derivatives of keatite (β-spodumene solid solution)

Composition and stability. Although keatite is a metastable form of SiO_2, its stuffed derivatives along the join SiO_2-$LiAlO_2$ are stable over a wide range of temperatures, at least at relatively low pressure. The composition range of β-spodumene solid solutions also coincides with practical glass-forming areas. Figure 7 shows the stable solid solution region from below 60 wt % to almost 80 wt % silica. The region of thermal stability is believed to be between 500°C and the solidus temperature, which, for the congruent melting $LiAlSi_2O_6$ composition, is maximum near 1425°C. A surprisingly large amount of MgO can be substituted for Li_2O in this solid solution, as is shown in Figure 9, but a decrease in thermal stability due to a lower solidus temperature (see Fig. 10) results. Unlike the metastable stuffed β-quartz solid solutions, however, little ZnO is permitted into the keatite (β-spodumene) structure, with over 1 wt % resulting in the presence of gahnite ($ZnAl_2O_4$).

Structure and properties. The β-spodumene framework has been confirmed to be isotypic with keatite (Li and Peacor, 1968). Lithium ions are coordinated to four oxygen atoms, and silicon and aluminum distributions in the tetrahedra are random. The structure consists of interlocking five-membered rings of (Si,Al) tetrahedra. These rings run parallel to *a* and *b*, thus creating channels that can be filled with lithium. As the temperature is increased, the *c*-axis expands while *a* and *b* are seen to contract. A structural explanation involving release of strain in the five-membered rings resulting in a change of tetrahedral orientation was offered by Li and Peacor (1968). The thermal expansion behavior of both tetragonal axes, as well as the average volume expansion of the unit cell, are given in Figures 19 (above) and 20. Note that the more siliceous compositions have the minimum

EBSCOhost - printed on 2/13/2023 4:48 AM via . All use subject to https://www.ebsco.com/terms-of-use

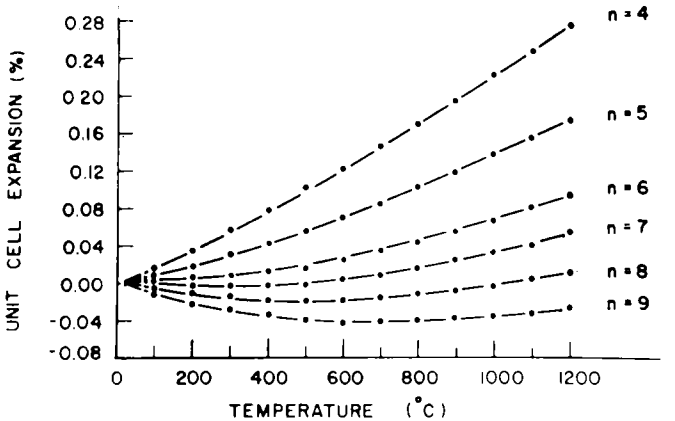


Figure 20. Volume thermal expansion in crystals of $Li_2O{\cdot}Al_2O_3{\cdot}nSiO_2$ β-spodumene solid solution (after Ostertag et al., 1968).

average expansion. These compositions are preferred in ceramic applications where very low thermal expansion behavior must be combined with thermal stability for both long-term high temperature use and thermal shock resistance.

β-spodumene solid solution glass-ceramics. Opaque glass-ceramics based on β-spodumene solid solution are readily crystallized from glasses in the system SiO_2-Al_2O_3-Li_2O-MgO, using either TiO_2 or combinations of TiO_2 and ZrO_2 as heterogeneous nucleating agents. As we have seen, metastable β-quartz solid solution is the first silicate phase to crystallize from such glasses (Figs. 15 and 17). The transformation from β-quartz to β-spodumene usually occurs between 900 and 1000°C. It is irreversible and is generally accompanied by an increase in grain size of almost an order of magnitude. When TiO_2 is used as a nucleating agent, significant rutile development accompanies the silicate phase transformation. Evidently, this component is less soluble in the keatite structure than in stuffed β-quartz.

Table 5. Composition of glass-ceramics based on β-spodumene solid solution (after Beall, 1986)

		CORNING WARE®		CERCOR® Corning	
		(wt %)	(mol %)	(wt %)	(mol %)
SiO_2		69.7	73.6	72.5	75.9
Al_2O_3		17.8	11.0	22.5	13.6
Li_2O	xl	2.8	5.9	5.0	10.5
MgO		2.6	4.1		
ZnO		1.0	0.8		
Na_2O	gl	0.4	0.4		
K_2O		0.2	0.1		
TiO_2	n	4.7	3.4		
ZrO_2		0.1	0.1		
Fe_2O_3	c	0.1	0.1		
As_2O_3	f	0.6	0.2		
		Cookware Hot plates		Heat exchangers Regenerators	

* xl, oxides concentrated in crystal; gl, oxides concentrated in glass; n, nucleating-agent oxides; f, fining-agent oxide; c, colorant oxides

EBSCOhost - printed on 2/13/2023 4:48 AM via . All use subject to https://www.ebsco.com/terms-of-use

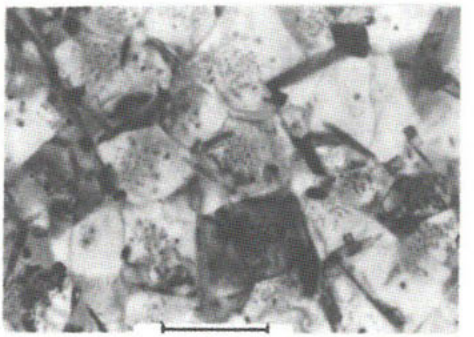


Figure 21. Microstructure of CORNING WARE® cookware, an opaque β-spodumene ss–rutile glass-ceramic, as shown by transmission electron microscopy (after Beall, 1986). Black scale bar = 1.0 μm.

The compositions of two commercial β-spodumene solid solution glass-ceramics, one used for CORNING WARE® cookware and the other for ceramic regenerators in turbine engines, are listed in Table 5. The former is melted as a multicomponent glass containing titania as the basic nucleating agent. Magnesia is partially substituted for lithia in order to lower the liquidus temperature, thereby allowing sufficient viscosity for the pressing and blowing procedures necessary to manufacture this form of cookware. The glass is crystallized by thermal treatment including a nucleation stage near 800°C and a maximum temperature hold at 1125°C, about 100° below the liquidus.

The sequence of crystallization involves the precipitation of $Al_2Ti_2O_7$ nuclei of the pyrochlore structure followed by basic crystallization of the major silicate component of the glass to β-quartz ss. The final assemblage reached near 1000°C includes β-spodumene ss and rutile. The β-spodumene crystals are lower in silica than the bulk composition. Therefore, total impingement of these crystals is prevented by the reluctance of the increasingly siliceous and viscous residual glass to crystallize. This glassy phase adheres to the impinging polyhedral grains (Fig. 21), forming a continuous membrane network throughout the body, even though it comprises less than 10 vol %.

Residual glass is beneficial in controlling secondary grain growth in glass-ceramics. As shown in Figure 22, β-spodumene ss crystals show isothermal grain growth dependence on the cube root of time (Chyung, 1969), and therefore it can be held for long

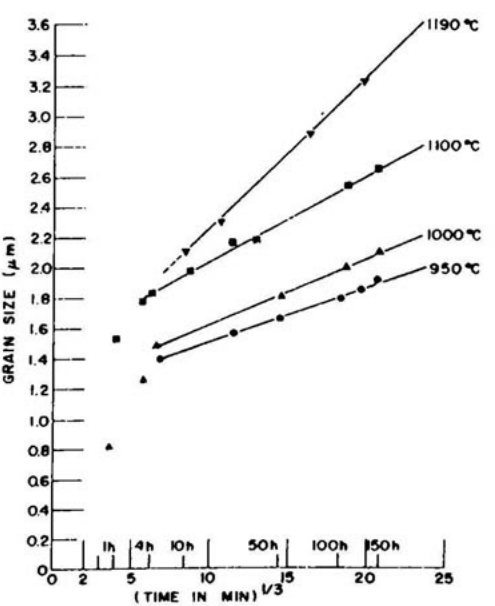


Figure 22. Grain size as a function of temperature and time for a typical β-spodumene ss glass-ceramic (after Chyung, 1969).

EBSCOhost - printed on 2/13/2023 4:48 AM via . All use subject to https://www.ebsco.com/terms-of-use

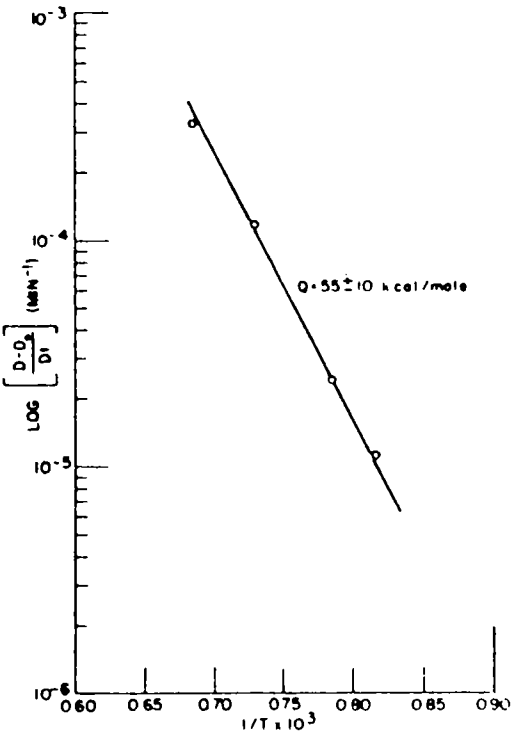


Figure 23. Arrhenius plot of secondary grain growth of a typical β-spodumene ss glass-ceramic (after Chyung, 1969).

periods at temperatures as high as 1200°C without serious coarsening. Because of the anisotropic thermal expansion of β-spodumene, crystals approaching 5 μm in size can produce microcracking, especially with repeated thermal cycling. This situation is avoided by the stabilizing effect of the siliceous, viscous and continuous glassy phase. An Arrhenius plot of the fractional increase in grain size as a function of time versus the reciprocal of temperature is shown in Figure 23. The activation energy for secondary grain growth is about 55 kcal/mole. This is similar to the activation energy of diffusion of Al^{+3} in SiO_2 glass, suggesting aluminum ionic migration across the glassy membrane between crystals is rate limiting.

β-spodumene ss glass-ceramics can also be reformed after their crystallization because of the continuous residual glass phase. Glass-ceramic sheet manufactured for laboratory benchtops and building cladding can therefore be vacuum-formed or otherwise molded into sinks and other complex shapes at temperatures well below the initiation of melting, even though the crystallinity is well over 90 percent. Plasticity at high temperatures in glass-ceramics has been correlated with unusually high rates of creep in these materials (Raj and Chyung, 1981). The high creep rates at subsolidus temperatures have been attributed to solution precipitation phenomena involving the glassy film wetting the spodumene grains. This model for creep envisions species transport through the glass phase. The applied stress is supported at grain boundary islands where the crystals meet. Grains tend to elongate in the direction of tensile stress. Creep studies are consistent with an interface-reaction-controlled creep model.

EBSCOhost - printed on 2/13/2023 4:48 AM via . All use subject to https://www.ebsco.com/terms-of-use

The regenerator glass-ceramic composition shown in Table 5 is a far more simple type of β-spodumene ss glass-ceramic. This material is produced as a honeycomb product for turbine engine heat exchangers. It is made from a peraluminous lithium aluminosilicate powdered glass frit which, as a slurry, impregnates paper that is wound as alternately corrugated sheets on a wheel. After firing and sintering, a porous ceramic regenerator wheel is produced that is mounted on the intake-exhaust portion of a turbine engine (Fig. 24). This regenerator slowly rotates, being heated to 1000°C from exhaust gases, and subsequently provides heat to inflowing cold gases, thereby improving the efficiency of the engine. Three properties are important here: very low coefficient of thermal expansion (5×10^{-7}/°C, 0-1000°C) to prevent the development of rupturing stresses in the wheel, high thermal stability (>1200°C), and very low secondary grain growth to insure against microcracking on grain boundaries. The latter is provided not only by a very small amount of siliceous residual glass, but by mullite precipitated along grain boundaries. Ceramic regenerators of this type are currently used in military power installations and have also been used in marine engines.

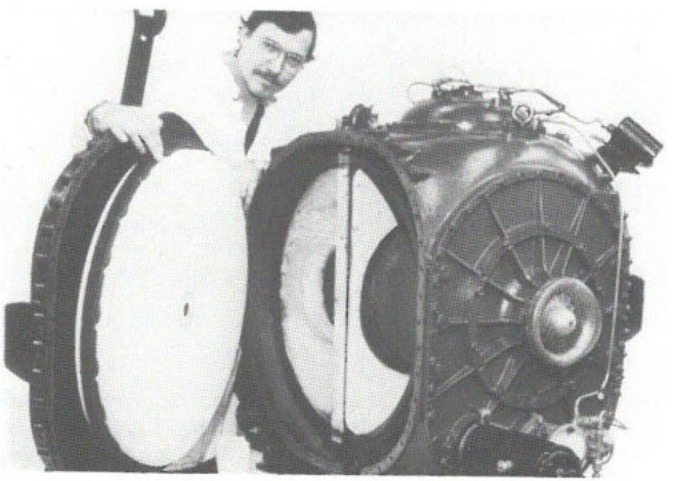


Figure 24. Turbine engine glass-ceramic regenerator wheel.

VITREOUS SILICA

Silica glass can be made in a very pure and stable form exhibiting unique and useful properties, such as high transparency from the ultraviolet to the near infrared, low thermal expansion with resulting high thermal shock resistance, good refractory and dielectric properties, and chemical inertness. Unfortunately, this simple glass is very stiff and difficult to shape, even at 2000°C. It is therefore not amenable to mass production plastic-forming methods. Nevertheless, novel methods have been developed to manufacture fused silica in either large shapes or in small dimensions such as fibers or soot.

Natural occurrences

A number of cases have been cited where vitreous silica has formed as the result of natural phenomena (Sosman, 1965). Quartz sand or sandstones can be locally fused by lightning to produce vitreous tubes called fulgurites. Larger deposits of this type of vitreous silica, commonly described as lechatelierite, occur in the Libyan desert. Natural fused quartz can also be produced by a combination of heat and pressure resulting from

EBSCOhost - printed on 2/13/2023 4:48 AM via . All use subject to https://www.ebsco.com/terms-of-use

meteoritic impact. In this case, instantaneous adiabatic heating of sandstone well above the melting point of quartz results in silica glass. It has been proposed (Skinner and Fahey, 1963) that the impact pressure first creates the high pressure form of SiO_2, stishovite, where silicon is in six-fold coordination. With the release of pressure, this mineral is vitrified, first to a dense octahedrally-coordinated glass and then to normal tetrahedrally-coordinated fused silica. This process can take place in less than two minutes at 800°C. Deposits of this type of natural fused quartz have been found near the Canyon Diablo crater in Arizona and in smaller meteorite craters in Australia and Saudi Arabia.

Structure

The first theory of the structure of vitreous silica was based on the coincidence of the maximum of broad X-ray diffraction humps for vitreous silica and sharp peaks of cristobalite. It was proposed that fused silica consisted of tiny units or crystallites of cristobalite about 1.5 to 2 nm in size or about 3 unit cells in length. These were believed randomly oriented and connected in such a way as to explain the X-ray diffraction pattern of broad diffuse rings. The Russian school of glass science led by Porai-Koshits (1958) has championed various forms of this crystallite theory.

A consensus of recent theories on the structure of vitreous silica all refer to the original random network theory of Zachariasen (1932), further developed by Warren (1937). In this theory, the structure is built up of silica tetrahedra where each oxygen apex is shared with another tetrahedron. In contrast to crystalline forms, the Si-O-Si bond angle varies throughout the network, ranging from 120-180° with an apparent maximum at 153°. The O-Si-O tetrahedral angle appears normal at 109.5°. X-ray, neutron, and electron diffraction studies have generally supported this simple model. The X-ray diffraction pattern is typical of an amorphous material having broad diffuse rings with no indication of crystallites of significant size. The radial distribution functions indicate that the separation between Si-O is in the 0.159-0.162 nm range. The nearest neighbor O···O distances similarly calculated are 0.260-0.265 nm, whereas Si to Si distances are 0.305-0.322 nm.

Computer modeling has generated theoretical structures based on these data. Evans and King (1966) constructed a tetrapod random structure of 651 units (see Fig. 25). This model produced a density of 2.08 g/cm^3, slightly less than the 2.20 g/cm^3 actually measured. Evans and Teter (1977) subsequently studied the influence of different model parameters on the resulting density.

Manufacture

Fused quartz. Quartz can be melted to silica glass by either of two methods (Danielson, 1982). In the first technique, known as the Osram process, fragmented quartz is fed into the top of a resistance-heated tubular furnace and melted in either a molybdenum or carbon crucible protected by an inert or reducing gas. Tubing is drawn from the bottom of the crucible. In a similar process, quartz is melted in an induction heated furnace in a hydrogen-helium atmosphere and drawn into tubing or rods.

In the second process, developed by Heraeus, quartz crystals are fed through an oxy-hydrogen flame onto a rotating fused quartz tube and withdrawn slowly from the burner as clear fused silica is built up. In order to maintain high purity, chlorine is introduced into the system above 1800°C. Impurities that form volatile chlorides, such as alkali, alkaline earths, aluminum, and transition metal ions are thereby removed.

EBSCOhost - printed on 2/13/2023 4:48 AM via . All use subject to https://www.ebsco.com/terms-of-use

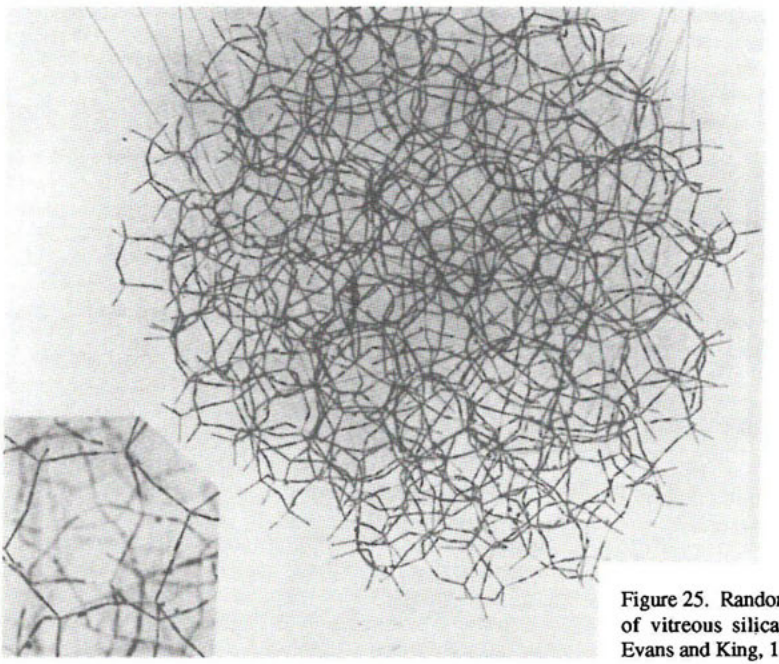


Figure 25. Random network model of vitreous silica structure (after Evans and King, 1966).

The primary sources of raw material for the fused quartz industry are in Brazil, although some quartz is imported from Namibia and the Malagasy Republic. The crystals are washed in hydrofluoric acid and distilled water to remove surface impurities. They are then dried, heated to about 800°C, and plunged into distilled water. Because of the large specific volume decrease during the transformation from β- to α-quartz and the subsequent further shrinkage of this phase to room temperature, massive microcracking is induced which minimizes the need for subsequent crushing.

Vapor phase hydrolysis. Synthetic silica may be prepared from silicon tetrachloride by oxidation or hydrolysis in a flame or plasma. The resulting soot is subsequently sintered to form silica glass. Typically, a vapor stream of $SiCl_4$ and O_2 is first passed through a methane-oxygen flame. Although a number of reactions occur in the flame, the fundamental one is: $SiCl_4 + O_2 \rightarrow SiO_2 + 2Cl_2$. Water, which is formed from the oxidation of methane, subsequently combines with the chloride formed by the reaction of silicon tetrachloride and oxygen producing hydrochloric acid and oxygen: $2H_2O + 2Cl_2 \rightarrow 4HCl + O_2$. Vitreous silica materials obtained by the vapor phase method can be formed in the shape of tubing rods, and boules, and may range in size up to hundreds of kilograms. Any of these may be subsequently reworked to make a variety of useful products, including telescope mirror blanks, high-temperature lamp tubing, crucibles, and optical fibers.

The largest commercial application for vitreous silica is optical fibers for telecommunications. The production of hair-thin strands of glass capable of low loss signal transmission over many kilometers was pioneered at Corning Glass Works (Kapron et al., 1970; Keck et al., 1973). This development required extremely pure raw materials and a process that allowed the control of dopant materials as a function of radial position within the fiber. The two principal methods of fiber manufacture are outside vapor

EBSCOhost - printed on 2/13/2023 4:48 AM via . All use subject to https://www.ebsco.com/terms-of-use

deposition (OVD) and modified chemical vapor deposition (MCVD) (Stroman, 1991). For each method, four processes are involved: lay-down or preformed deposition, consolidation, draw, and measurement.

In the OVD process, the reaction of oxygen with silicon tetrachloride (with germanium tetrachloride as a dopant) occurs in air while the materials being deposited are still in the vapor phase. This defines the first part of the lay-down process of soot deposition. Soot particles are typically less than 0.2 μm in diameter. The soot producing flame is directed towards a rod known as the target or bait rod which is rotated during lay-down. The preform is built up layer by layer, where the germanium doping of the vitreous silica can be controlled radially. The resulting translucent mass of porous soot must then be fully sintered. Sintering is conducted in a controlled atmosphere at temperatures from 1000-1600°C and results in a solid glass blank. The blank is placed in an electrically heated furnace where Cl_2 is introduced to the center hole of the preform created by removal of the target rod. This process removes residual water present in the form of OH^- ions and H_2O, as well as trapped transition metal ions. The resulting hydrochloric acid and other volatile chlorides are swept away in the exhaust gas flow.

The MCVD process chemistry is similar to that of the OVD, but in this case, a fused silica tube houses the reactants which are heated from the outside of the tube. Vitreous layers are formed by repeated passes of the torch. During each pass, soot is deposited and sintered as the torch passes over it. The last part of the process, fiber draw, is basically the same for both manufacturing techniques. A fiber blank is introduced into a furnace located at the top of a draw tower. A draw furnace produces temperatures in excess of 1800°C, causing the tip of the blank to flow. The plastic silica is pulled through a coating cup by a tractor-reel assembly. The diameter of the fiber is inversely proportional to the speed at which it is drawn by the tractor-pulleys. Very precise fiber diameter control, less than ±1 μm of variation, is achieved. The coating application system, necessary to preserve the pristine fiber surface and strength, uses two coats of polymer, typically acrylate urethane.

Sol-Gel processes. Vitreous silica can be produced by the sol-gel technique (Zarzycki, 1991). Gels may be formed by the destabilization of colloidal sols or by the hydrolysis of metal organic compounds. The latter is most common and involves hydrolyzed alkoxides, such as tetraethyl orthosilicate, which yields a silica-alcohol-water gel. The gel is dried and subsequently fused to silica glass. The expense of the raw materials and the difficulty in drying porous gels without massive shrinkage and cracking have so far limited manufacture of three-dimensional articles. Thin films have become the largest area of application. The films are applied by either dip or spin coating techniques using polymeric alkoxide sols. Hard antireflective coatings are based on a triple application of titania, silica-titania, and silica. They are used widely in architectural glass.

Physical properties

Optical properties. One of the unique features of bulk fused silica is its high ultraviolet transmission. The ultraviolet cutoff for ultrapure material of 1 cm thickness is slightly lower than 160 nm. In the infrared region, water incorporated in the structure as OH^- has a strong fundamental absorption band at 2.73 μm with overtones at 1.38 μm, 945 nm and 585 nm. The Si-O vibration has two strong fundamental absorption bands that affect the transmission of silica. The vibration at 8.83 μm has a strong overtone at 4.45 μm, which is therefore the practical infrared cutoff for vitreous silica of usable thickness.

EBSCOhost - printed on 2/13/2023 4:48 AM via . All use subject to https://www.ebsco.com/terms-of-use

Typical transmission curves of several types of vitreous silica are shown in Figure 26 (Danielson, 1982). Glasses corresponding to Curve A were prepared by vapor phase hydrolysis and those corresponding to Curve C were melted in a dry atmosphere or a vacuum. The refractive index of fused silica at 25°C is 1.53429 at 0.21386 μm, 1.46313 at 0.48613 μm, 1.45841 at 0.58926 μm, 1.45637 at 0.65627 μm, and 1.39936 at 3.7067 μm. Refractive index changes with temperature are about 1×10^{-5} from 0-100°C. The stress optical coefficient is 3.5×10^{-12}/Pa.

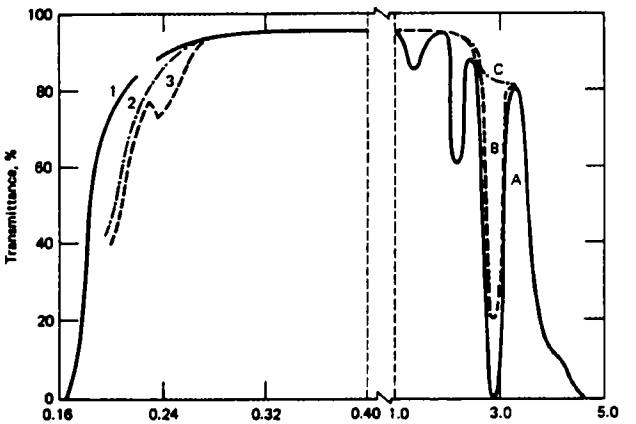
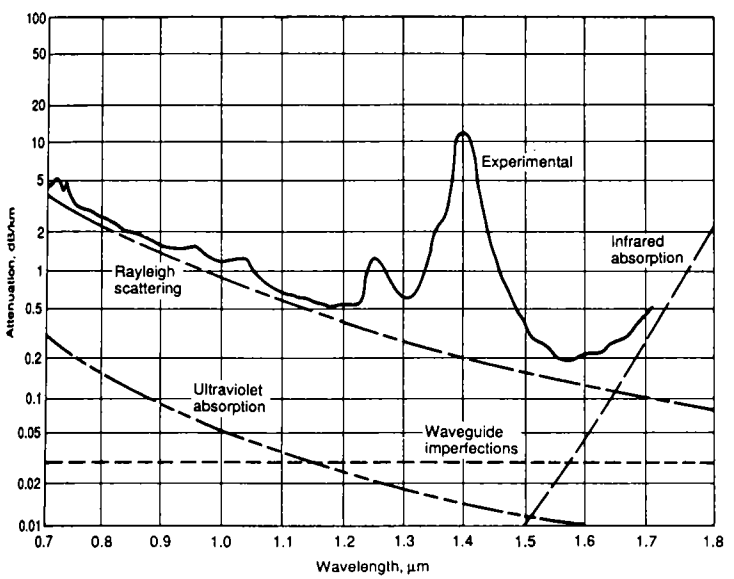


Figure 26 (above). Transmission curves for vitreous silica, 1 cm thick (after Danielson, 1982).

Manufacturer	*Type*	*UV curve*	*IR curve*
Amersil (Heraeus)	Ultrasil	2	B
Corning Incorporated	Code 7960	1	A
General Electric	Types 204, 214	3	C

Figure 27 (below). Optical loss behavior of telecommunciation fiber (after Stroman, 1991).



EBSCOhost - printed on 2/13/2023 4:48 AM via . All use subject to https://www.ebsco.com/terms-of-use

Ultra-pure silica with extremely high transparency is required for long distance telecommunications fiber optics. Dry glasses containing less than 0.1 ppm of transition metal ions yield attenuations as low as 0.2 dB/km at 1.55 μm (attenuation of 1 dB/km = 20.567% of the light absorbed). The transmission window for pure (optical-fiber-grade) fused silica depends on several attenuation mechanisms (Fig. 27, above; Stroman, 1991). It can be seen that the experimental attenuation curve is roughly bounded by Rayleigh scattering at the short wavelength and infrared absorption at the long wavelength of the region of interest. The position of remnant OH^- bands dictates regions of minimum absorption near 1.5 and 1.3 μm. These have become the accepted communication bands for optical waveguide fibers.

Radiation effects. Various types of radiation can affect the optical properties of vitreous silica. Significant structural changes can be caused by a neutron stream. A densification of vitreous silica that reaches a maximum value of 2.26 g/cm^3 (an increase of about 3%) may be caused by a dose of 1×10^{20} neutrons/cm^2. It is interesting to note that quartz, tridymite, and cristobalite attain the same density after similar irradiation. In each case, a glass-like material known as amorphous "silica M" (after metamict) is produced.

Ionizing radiation such as X-rays, γ-rays, electrons or protons produce absorption centers in vitreous silica, sometimes called color or defect centers. A characteristic band at 215 nm is produced by long-term X-ray radiation. This band is also observed in irradiated α-quartz, and is generally assigned to the presence of E′ centers. This type of defect is assumed to be a pyramidal SiO_3 unit with an unpaired electron in the dangling sp^3 orbital of Si. A schematic two-dimensional representation of SiO_2 glass showing several types of intrinsic (quench-disorder) and extrinsic (radiation-induced) defect centers is shown in Figure 28 (Friebele and Griscom, 1979).

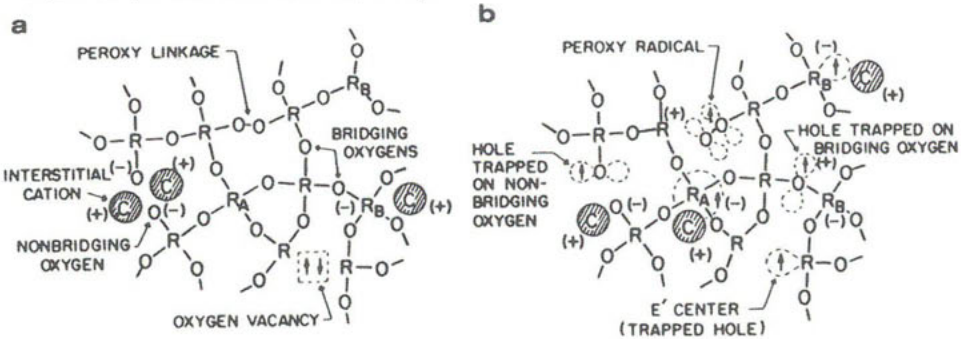


Figure 28. Schematic two-dimensional representation of several types of intrinsic and extrinsic defect centers (after Friebele and Griscom, 1979).

Thermal properties. The coefficient of thermal expansion of vitreous silica between 0-300°C ranges from 5.4 and 5.6×10^{-7}/°C. Titania substitution can reduce this to a near-zero or even negative value. With 7 wt % TiO_2, the CTE at 25°C is virtually zero; with 11% TiO_2, it falls to -3×10^{-7}/°C. Because of its low expansivity, vitreous silica can undergo thermal shock without cracking, and with titania doping, the CTE can be tailored to zero at any desired temperature.

The viscosity of vitreous silica in the glass transformation range depends primarily on thermal history and on level of impurities, particularly the hydroxyl content. Thus, the

EBSCOhost - printed on 2/13/2023 4:48 AM via . All use subject to https://www.ebsco.com/terms-of-use

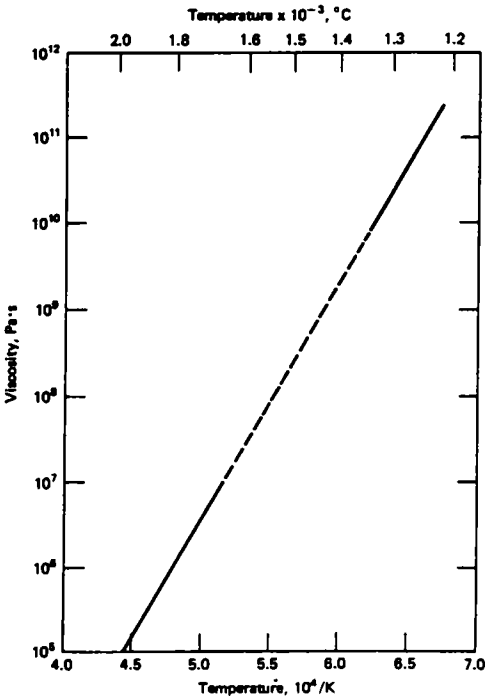


Figure 29. Viscosity-temperature curve for Amersil commercial grade vitreous silica (after Danielson, 1982).

annealing point for General Electric fused quartz, a very dry material, is 1213°C, whereas for Corning Code 7940 made by flame hydrolysis, it is 1075°C. A viscosity-temperature curve for Heraeus vitreous silica is shown in Figure 29. The thermal conductivity of vitreous silica ranges from 0.67 $Wm^{-1}K^{-1}$ at 100K to 1.74 at 600K.

Although vitreous silica is a stable glass from a practical point of view, it is nevertheless metastable below 1713°C, the melting point of cristobalite. The devitrification rate of vitreous silica for surface-nucleated cristobalite as a function of temperature shows a maximum at 1625°C of 28 μm/min (Danielson, 1982). This decreases to below 2 μm/min at temperatures below 1350°C for G.E. fused quartz treated in air. Devitrification is enhanced by either a high hydroxyl content in the glass, or the presence of water vapor and oxygen in the atmosphere. Neutral or reducing atmospheres inhibit devitrification.

Mechanical properties. The density of vitreous silica depends on its manufacturing and thermal history, but generally ranges from 2.20 to 2.21 g/cm^3. The Young's modulus of vitreous silica at 25°C is 73 GPa (1.06×10^7 psi), the shear modulus is 31 GPa, and Poisson's ratio is 0.17. Small differences of about 1 GPa may depend on the method of manufacture. A typical optical fiber can withstand tensile stresses of 3.4 to 4.8 GPa (Stroman, 1991). This extreme strength, over triple that of hardened steel, relies on a polymer coating being quickly applied to the cooling fiber before abrasion can occur. Mechanical abrasion in bulk fused silica products is unavoidable and dramatically reduces flexural strength. The modulus of rupture of a transparent rod abraded by sand blasting with a sand of 150-230 μm grit for 5 seconds is only 49 MPa. The Knoop indentation

EBSCOhost - printed on 2/13/2023 4:48 AM via . All use subject to https://www.ebsco.com/terms-of-use

hardness of vitreous silica is in the 473 to 593 kg/mm^2 range. The Vickers hardness (diamond pyramidal) lies between 600 and 750 kg/cm^2.

Electrical properties. The DC conductivity of vitreous silica is controlled by impurities, especially alkali ions. The difference in sodium content of a few parts per million significantly affects resistivity. At 225°C, the low sodium G.E. fused quartz shows a resistivity of $10^{11.5}$ ohm cm. Dielectric properties of vitreous silica are generally excellent, with low dielectric constants of 3.8-3.95 and loss tangents below 0.00005 over a wide range of frequencies and temperatures up to 300°C.

Other properties. High purity vitreous silica has an unusually low attenuation of high frequency ultrasonic waves. Its permeability to gaseous diffusion can be described as follows: for helium and hydrogen in the range 300-1000°C, the diffusion constant D_o is 7.4×10^{-4} for He and 5.65×10^{-4} for H, with E_d, the activation energy, 27.7 and 43.5 kJ/mole, respectively. The chemical durability of vitreous silica is excellent in most acids (except hydrofluoric) and moderate in strong bases. For example, at 95°C, the weight loss in 5% HCl is less than 0.01 mg/cm^2. By contrast, in 5% NaOH for 6 h, the weight loss is 0.7 mg/cm^2. Alkali metal vapors can attack silica at temperatures as low as 200°C. Carbon can reduce silica at temperatures at or above 1200°C. Although metals do not generally react with silica below 1000°C, magnesium, alkali metals, and aluminum are the exceptions, the latter readily causing reduction above 700°C.

Applications

Optical uses. As a result of its physical and chemical stability, excellent ultraviolet transmission, and resistance to ultraviolet radiation darkening, vitreous silica is an ideal refractive optic material. It is used for lenses, prisms, windows, solar cell covers, and other optical components where uv transmission is required. Every U.S. manned space vehicle has been equipped with vitreous silica windows (Corning Code 7940) for visual observation, photography, and television. The space shuttle uses triple layer windows with outer and central panes of vitreous silica and tempered aluminosilicate inner panes.

The ability of vitreous silica, particularly when doped with titania, to maintain dimensions with changing temperature has made this material a frequent choice for telescope mirror blanks. A recent example is the 35 ton mirror for Japan's Subaru telescope which is slated to begin operation in the year 2000 atop Mauna Kea, Hawaii. Forty-four hexagonal slabs were fused to make this 8.3 meter diameter mirror blank which is 30 cm thick. Figure 30 shows this mirror after fusion, but prior to sagging and final finishing.

Optical waveguides. Optical waveguides used for long distance telecommunications are based on composite fibers with a central or core refractive index of n_i and an outer or cladding refractive index of n_e such that $n_i > n_e$. A light ray propagating in the core n_i undergoes total internal reflection if its angle of incidence α is greater than the limiting reflection angle defined by $\sin \alpha_c = n_e/n_i$ (Fig. 31). A key factor in lining up the laser source or joining two fibers is β_c, the maximum entrance angle which will yield total internal reflection (Fig. 31). Following a ray from the entrance face of the fiber, application of Snell's law yields: $n_o \sin \beta_c \max = (n_i^2 - n_e^2)^{1/2}$. This is referred to as the numerical aperture (NA) of the fiber, which typically varies between 0.1 and 0.3.

Fibers can be single mode or multimode. In each case, various refractive index profiles are possible between the center of the core region and the core-cladding interface

EBSCOhost - printed on 2/13/2023 4:48 AM via . All use subject to https://www.ebsco.com/terms-of-use



Figure 30. Titania-doped ultra-low-expansion vitreous silica mirror for the Subaru telescope (courtesy of Corning Incorporated).

EBSCOhost - printed on 2/13/2023 4:48 AM via . All use subject to https://www.ebsco.com/terms-of-use

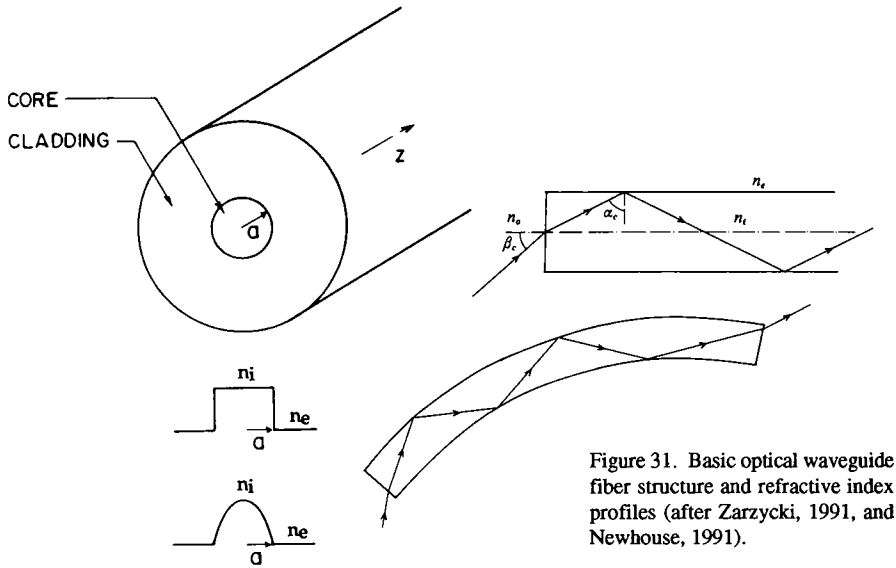


Figure 31. Basic optical waveguide fiber structure and refractive index profiles (after Zarzycki, 1991, and Newhouse, 1991).

(Newhouse, 1991). Most common are the stepped-index profile in which the refractive index is constant throughout the core region, and the graded index profile where the refractive index drops monotonically from the center to the core-cladding boundary. (In this way, dispersion caused by variations in distance that different rays travel is reduced.) The major dopant used to produce the required refractive index differences is GeO_2. The resulting refractive index of the core and the cladding deviate by generally less than 0.5%.

The diameter of telecommunications fibers is usually 125 μm. In single-mode fibers, the core diameter varies from 7 to 10 μm, whereas in multimode fibers, it ranges from 50-85 μm. For a particular optical waveguide, solutions to Maxwell's equations define the modes which are constrained by a set of boundary and continuity conditions. These modes are analogous to the modes of vibration in a circular stretched membrane. As the core radius is reduced, modes are cut off because the light of a finite wavelength cannot form the required mode pattern and still satisfy the continuity in boundary conditions. This cutoff condition is equivalent to the situation where the associated ray is no longer totally internally reflected.

In practice, multimode fibers for which the core diameter is much greater than the wavelength of propagating light (50-85 μm vs. 1.5 μm) have a usable bandwidth or analog transmission capacity of approximately 20 MHz km (Zarzycki, 1991). These fibers are restricted to short distance applications. Single mode fibers, on the other hand, with a diameter only somewhat greater than this wavelength (7-10 μm vs. 1.5 μm), can have bandwidths greater than 50 GHz-km. These single-mode fibers are used in the majority of long distance telecommunications systems because of their ability to transmit very high data rates.

In a multimode fiber, the signal is carried by a large number of modes or rays. The different optical path lengths of the various rays yield a spread of arrival times and therefore result in intermodal pulse spreading. To reduce this dispersion, multimode fibers typically

EBSCOhost - printed on 2/13/2023 4:48 AM via . All use subject to https://www.ebsco.com/terms-of-use

have graded index profiles. For single mode fibers, by contrast, a pulse traveling down an optical fiber will spread only in response to material and waveguide dispersion, which are much less than intermodal dispersion. The pulse spreading due to these effects is called intramodal or chromatic dispersion. While intermodal dispersion limits the bit rate in multimode fibers to less than 1 gigabit/second, single mode fibers are restricted only by intramodal dispersion, and can be operated at several gigabits/second.

The losses for current optical waveguide fibers approach the minimum theoretical limit at the telecommunications frequencies near 1.3 and 1.5 μm. The lowest reported loss is 0.15 dB/km at 1.6 μm where the minimum theoretical loss is believed to be 0.07 dB/km (Daglish, 1970). Standard commercial fibers have losses less than 0.25 dB/km at 1550 nm.

In addition to the development and widespread acceptance of optical fibers, excellent progress has been made in the area of passive components for optical fibers as subscriber loop systems. Functional requirements, such as interconnection, furcation, and filtration, currently are being met by discrete components that can be easily manufactured (Keck et al., 1989). Interconnection alignment is more easily achieved in multimode (large core) fibers, making these more suitable for local distribution. Depending on the system architecture, the cost and ease of placement of these components can play a pivotal role in allowing fiber deployment in the distribution loop. Ultimately, discrete components will be displaced by more highly integrated components and probably by optoelectronic systems in the more distant future.

Lighting. Clear fused quartz is used as an envelope material for mercury vapor lamps (Beggs, 1947). In this application, vitreous silica offers resistance to deformation at operating temperatures and pressures and allows sufficient ultraviolet transmission to permit color correction via phosphor coatings. Incandescent tungsten-halogen-cycle lamps operate at even higher temperatures where the glass envelope temperature may reach 600°C. Fused quartz can be used for long periods at these high temperatures, particularly when protected by reflective layers like zirconia or titanium silicate glass (Clausen, 1974; McVey and Uy, 1973). These lamps are used in the illumination of air fields, sports arenas, as automobile headlights, and in slide and film projectors.

Thermal applications. Vitreous silica tubing is sometimes used to protect precious-metal thermocouples in high-temperature pyrometry (Danielson, 1982). Radiant heaters use vitreous silica tubes to contain resistance wire. Immersion heaters for use in acid solutions are similarly constructed.

High-temperature thermal insulation has been made from vitreous silica fibers. In this way, low density tiles such as those used to protect the space shuttle are made. Vitreous silica rods are also used as standards for measurement of the thermal expansion of solids. This dilatometric application depends on the low and regular thermal expansion of amorphous silica.

Chemical applications. Because of its thermal stability, chemical durability, high purity, and thermal shock resistance, vitreous silica is commonly used in chemical analyses and preparations. Crucibles, tubing, rods, boats, and other containers, as well as special apparatus, can be made in both the normal transparent form and in opaque varieties sintered from glass powder.

EBSCOhost - printed on 2/13/2023 4:48 AM via . All use subject to https://www.ebsco.com/terms-of-use

Electronic applications. The major electronic applications for vitreous silica are associated with silicon wafer technology (Danielson, 1982). Silica glass crucibles and tubes are used as containers for silicon crystal growth, high temperature diffusion doping, and epitaxial growth processes on integrated circuit chips. Thin films of vitreous silica also serve as insulating layers between conductor strips and semiconductor surfaces, as well as surface passivation layers in planar diodes, transistors, and lasers. These films are generally formed by vapor deposition or RF-sputtering techniques. Vitreous silica is also used as a photomask substrate for very large scale integration (VLSI) of electronic circuits. Good ultraviolet transmission properties allow fast exposure of photoresists, and excellent dimensional stability prevents pattern distortions due to temperature gradients during processing.

Silica glass has been used as a connecting medium between transducers converting electrical signals to ultrasonic waves and vice-versa (Shand, 1958). Large signal delay depends upon an ultrasonic signal 100,000 times slower than that of an electronic signal in a conductor. Low ultrasonic transmission losses are important here. Silica delay lines are ground as flat polyhedral plates of high precision. They are used in electronic systems like radar where signal delay is sometimes necessary.

Other applications. Vitreous silica may be used in the form of powder or soot as an inert filler for polymers. This reduces the high thermal expansion coefficient of these materials.

Various complex silica molds can be made by extrusion or sintering of glass powders. These are used in investment casting of metal parts because of their dimensional stability at the temperatures where most alloys are cast. The cooled metal casting may subsequently be treated in hot caustic solutions to remove silica core material in articles where precisely shaped holes, cavities, and passages are involved.

SUMMARY

Silica has wide industrial application as single crystals, in polycrystalline glass-ceramics, and as ultrapure glass. The latter two materials allow a wide range of shapes from massive pieces through fibers, films, and soot. Crystalline silica and its stuffed derivatives are characterized by several unique and useful properties: low loss piezoelectric behavior, a wide spectrum of thermal expansion behavior from highly positive to negative, and good thermal stability and chemical durability. Vitreous silica has many applications which rely primarily on optical transmission and dimensional stability. These are basic to the concept of an information super highway, where silica fibers carry signals of great information density over many kilometers without boosting.

ACKNOWLEDGMENT

The writer thanks Mary Monger for invaluable help in preparing the manuscript and figures. He also thanks Drs. Jeffrey Kohli and J.B. MacChesney for critical reviews of the paper.

EBSCOhost - printed on 2/13/2023 4:48 AM via . All use subject to https://www.ebsco.com/terms-of-use

REFERENCES

Aitken BG, Beall GH (1994) Glass-ceramics. Materials Sci and Tech 11:267-294, eds: RW Cahn, P Haasen, EJ Kramer; Vol ed. M Swain. VCH Weinheim, New York

Beall GH, Karstetter BR, Rittler HL (1967) Crystallization and chemical strengthening of stuffed β-quartz glass-ceramics. J Am Ceram Soc 50, 4:181-190

Beall GH, Duke DA (1969) Transparent glass-ceramics. J Mater Sci 4:340-352

Beall GH (1986) Glass ceramics. Commercial Glasses, Boyd DC and MacDowell JF (eds) Adv Ceramics 18:157-173

Beall GH (1992) Design and properties of glass-ceramics. Ann Rev Mater Sci 22:91-119

Beggs EW (1947) New developments in mercury lamps and their applications. Illum Engr 42:435-465

Buerger MJ (1954) Stuffed derivatives of the silica structures. Am Min 39:600-614

Cady WG (1946) Piezoelectricity. McGraw Hill, New York

Chyung CK (1969) Secondary grain growth of Li_2O-Al_2O_3-SiO_2-TiO_2 glass-ceramics. J Am Ceram Soc 52:242-245

Clausen EM (1974) U.S. Pat. 3,988,628 (to General Electric Company)

Daglish NH (1970) Light scattering in selected optical glasses. Glass Technol 11:30-35

Danielson P (1982) Vitreous Silica. In Encyclopedia of Chem Tech 20:782-817, John Wiley & Sons, New York

Danel JS, Delapierri G (1991) Quartz: a material for microdevices. J Micromech Microeng 1:187-198

Evans DL, King SV (1966) Random network model of vitreous silica. Nature 212:1353-1354

Evans DL, Teter M (1977) p. 53 in The Structure of Non-Crystalline Materials, Gaskell PD (ed), Taylor and Francis, London

French BM, Jezek PA, Appleman DE (1978) Virgilite: a new lithium aluminum silicate mineral from the Macusani glass, Peru. Am Min 63:461-465

Friebele EJ, Griscom DL (1979) Radiation effects in glass. In Treatise on Materials Science and Technology, vol 17: Glass II, M Tomozowa, RH Doremus (eds) Academic Press, New York

Gibbs RE (1926) Structure of α-quartz. Proc Roy Soc A 110:443

Jacobs SF, Bass D (1989) Improved dimensional stability of Corning 9600 and Schott Zerodur glass-ceramics. Applied Optics 28, 19:4045-4047

James PF (1989) Volume nucleation in silicate glasses. In Glasses and Glass-Ceramics, ed. MH Lewis, Chapman and Hall, New York, pp 59-105

Kapron FP, Keck DB, Maurer RD (1970) Radiation loss in glass optical waveguide. Appl Phys Lett 17:423-425

Karkhanavala MD, Hummel FA (1953) Reactions in the System Li_2O-MgO-Al_2O_3-SiO_2: I. J Am Ceram Soc 36:393-397

Keat, PP (1954) A new crystalline silica. Science 120:328-330

Keck DB, Maurer RD, Schultz PC (1973) On the ultimate lower limit of attenuation in glass optical waveguides. Appl Phys Lett 22:307-309

Keck DB, Morrow AJ, Nolan DA, Thompson DA (1989) Passive components in the subscriber loop. J Lightwave Technol 7:1623-1633

Kingery WD, Bowen HK, Uhlmann DR (1976) Introduction to Ceramics. 2nd edn, John Wiley & Sons, New York

Laudise RA (1970) The growth of single crystals. Prentice-Hall, Englewood Cliffs, NJ

Levin EM, Robbins CR, McMurdie HF (1964) Phase diagrams for ceramists, Vol. 1. Fig. 456, System $Li_2O{\cdot}Al_2O_3{\cdot}2SiO_2$ (eucryptite)-SiO_2, p 168, Am Ceram Soc, Columbus, Ohio

Lewis D III (1982) Observations on the strength of a glass-ceramic. Am Ceram Soc Bull 61:1208-1214

Li C-T (1968) The crystal structure of $LiAlSi_2O_6$ III (high-quartz solid solution). Zeit Krist 127:327-348

Li C-T, Peacor DR (1968) The crystal structure of $LiAlSi_2O_6$-II ("β-spodumene"). Zeit Krist 126:46-65

Maier V, Müller G (1987) Mechanism of oxide nucleation in lithium aluminosilicate glass-ceramics. J Am Ceram Soc 70C:176-178

McVey CI, Uy OM (1973) US Pat. 3,879,625 (to General Electric Company)

Minerals Yearbook (1989) Vol 1, Metals and Minerals. US Dept of Interior, Bureau of Mines

Nakagawa K, Izumitani I (1972) Metastable phase separation and crystallization of Li_2O-Al_2O_3-SiO_2 glasses: determination of miscibility gap from the lattice parameters of precipitated β-quartz solid solution. J Non-Cryst Solids 7:168-180

Newhouse MA (1991) Optical fibers. In Optical Properties of Glass, DR Uhlmann, NJ Kreidl (eds), p 185-204, Am Ceram Soc, Columbus, Ohio

Ostertag W, Fisher GR, Williams JP (1968) Thermal expansion of synthetic β-spodumene and β-spodumene—Silica solid solutions. J Am Ceram Soc 51:651-654

EBSCOhost - printed on 2/13/2023 4:48 AM via . All use subject to https://www.ebsco.com/terms-of-use

Petzoldt J (1967) Metastabile Mischkristalle mit Quarzstruktur mit Oxidsystem Li_2O-MgO-ZnO-Al_2O_3-SiO_2. Glastechn Ber 40:385-396

Petzoldt J, Pannhorst W (1991) Chemistry and structure of glass-ceramic materials for high precision optical applications. J Non-Cryst Solids 129:191-198

Porai-Koshits EA (1958) The Structure of Glass. USSR Academy of Science Press, Moscow, Proc Conf on Structure of Glass, Leningrad, 1953; translation: Consultants Bureau, New York

Raj R, Chyung CK (1981) Solution-precipitation creep in glass-ceramics. Acta Met 29:159-166

Ray S, Muchow GM (1968) High-quartz solid solution phases from thermally crystallized glasses of compositions (Li_2O,MgO)•Al_2O_3•$n$$SiO_2$. J Am Ceram Soc 51:678-682

Roy R (1959) Silica O, a new common form of silica. Zeit Krist 111:185-189

Schiffner U, Pannhorst W (1987) Nucleation in a precursor glass for a Li_2O-Al_2O_3-SiO_2 glass ceramic. Part 1. Nucleation kinetics. Glastech Ber 60:99-109

Schreyer W, Schairer JF (1961a) Metastable solid solutions with quartz-type structures on the join SiO_2-$MgAl_2O_4$ (spinel). Zeit Krist 116:60-82

Schreyer W, Schairer JF (1961b) Compositions and structural states of anhydrous Mg-cordierites: A reinvestigation of the central part of the system MgO-Al_2O_3-SiO_2. J Petrol 2:324-406

Shand EB (1958) Glass Engineering Handbook, McGraw-Hill Book Company, New York, pp 354-355

Skinner BJ, Fahey JJ (1963) Observations on the inversion of stishovite to silica glass. J Geophys Res 68:5595-5604

Sosman RB (1965) The phases of silica. Rutgers Univ Press, New Brunswick, NJ

Stookey SD (1959) Catalyzed crystallization of glass in theory and practice. Indus Eng Chem 51:805-808

Strnad Z (1986) Glass-ceramic Materials. Elsevier, Amsterdam

Stroman JF (1991) Optical fibers. In Ceramics and Glass, Engineered Materials Handbook, ASM Int'l, Materials Information Soc 4:409-417

Vigoureux P, Booth CF (1950) Quartz vibrators and their applications. His Majesty's Stationery Office, London

Wang J, Ward MD, Ebersole RC, Foss RP (1993) Piezoelectric pH sensors: AT-cut quartz resonators with amphoteric polymer films. Analytical Chem 65:2553-2562

Ward MD, Buttry DA (1990) *In situ* interfacial mass detection with piezoelectric transducers. Science 249:1000-1007

Warren BE (1937) X-ray determination of the structure of liquids and glass. J Appl Phys 8:645-654

Zachariasen WH (1932) The atomic arrangement in glass. J Am Chem Soc 54:3841-3851

Zarzycki J (1991) Glasses and the vitreous state. In Cambridge Solid State Science Series, Cahn RW, Davies EA, Ward IM (eds), Cambridge University Press, Cambridge, UK

EBSCOhost - printed on 2/13/2023 4:48 AM via . All use subject to https://www.ebsco.com/terms-of-use

EBSCOhost - printed on 2/13/2023 4:48 AM via . All use subject to https://www.ebsco.com/terms-of-use

SILICA ZEOLITES AND CLATHRASILS

15 15

John. B. Higgins

Mobil Research and Development Corporation
Central Research Laboratory
P.O. Box 1025, Princeton, NJ 08540 U.S.A.
jbhiggins@crl.mobil.com

"Rarely in our technological society does the discovery of a new class of inorganic materials result in such a wide scientific interest and kaleidoscopic development of applications as has happened with the zeolite molecular sieves." (Breck, 1974)

INTRODUCTION

In 1756 the Swedish mineralogist Axel Fredrick Cronstedt (1722-1765) reported the discovery of a new class of silicate minerals that "exhibits so strange and peculiar behavior in a blowpipe flame that they are impossible to identify with any known family" (Cronstedt, 1756; Schlenker and Kühl, 1993). The two samples he examined from Iceland and the Svappavari copper mine in Finland emitted gas and puffed up like borax when heated in the blowpipe flame. He designated these minerals zeolites from the Greek words ζειν and λιθοσ (boiling stone). For almost 200 years zeolites remained an obscure group of minerals with rather unusual properties, and Cronstedt was remembered primarily for his discovery of the element nickel.

Cronstedt would probably have found it difficult to believe that synthetic analogs of the mineral group he described would play a major role in processing fuels and synthetic materials for our 20th century world. Today synthetic zeolites are the most important catalysts in petrochemical refineries. They catalyze the cracking of larger hydrocarbons into high octane gasoline, dewax diesel fuel, and separate xylene isomers for the production of synthetic polymers. Gasoline yield increases resulting from zeolite technology have exceeded 10% during the last two decades with an estimated added product value of $15 -20 billion per year. As commodity chemicals over 300,000 metric tons of synthetic zeolites are sold annually to consumers in powdered laundry detergents as environmentally friendly replacements for harmful polyphosphates. Synthetic and natural zeolites find numerous applications including water treatment, radioactive waste storage, gas separation and purification, desiccation, soil improvers, and animal feed supplements where their ion exchange and sorption properties are exploited (Dyer, 1984).

More recently there has been a growing interest in the applications of zeolitic materials for recognizing, discriminating, and organizing atoms, molecules and atomic clusters (Ozin et al., 1986; Ozin, 1992; Mac Dougall and Stucky, 1993; Terasaki, 1993; Borja and Dutta, 1993). Chiral molecules and polymers, small metal particles, and semiconductor clusters confined in zeolite pores and cages impart interesting electrical and optical properties that may be exploited in sensor, energy conversion, and other electronic technologies.

Their broad range of applications has spurred the development of new classes of zeolitic materials with novel chemistries, structures, and pore systems. One subclass is the silica zeolites (zeosils) and clathrasils that are the subject of this chapter. The literature on zeolites is voluminous and even the topic of silica zeolites could not be adequately reviewed

EBSCOhost - printed on 2/13/2023 4:48 AM via . All use subject to https://www.ebsco.com/terms-of-use

in one volume. This chapter will attempt to provide an introduction to silica zeolites with an emphasis on their preparation, structures, and structure-related properties. Informative reviews concerning zeolitic materials include Newsam (1986), Smith (1988), Gies (1991), Davis and Lobo (1992) and Suib (1993). No attempt will be made to review the extensive literature concerning the catalytic applications of high-silica (Si/Al > 5) zeolites. Recommended reviews in this area include Hölderich et al. (1988), Csicsery (1984), Jacobs and Martens (1991), Maxwell and Stork (1991) and Hölderich and van Bekkum (1991).

HISTORICAL DEVELOPMENT

High-silica zeolites were first synthesized in the early 1960s at the Paulsboro Research Laboratory of Mobil, Inc. A recent resurgence of interest in porous crystalline silicas is due primarily to their uses as chemically simple systems for elucidating synthesis mechanisms, computer modeling, and structural characterization. Because the development of high-silica zeolites and their silica analogues was closely related to other developments in zeolite technology (especially catalysis), their significance is best understood when placed in the historical context of zeolite development, as is summarized in Table 1 and briefly described below.

Table 1. Developments in zeolite science and technology

Early History		
1756	A.F. Cronstedt	described natural zeolites
1840	A. Damour	observed reversible dehydration
1858	H. Eichhorn	reported ion-exchange properties of zeolites
1862	H. de St. Claire-Deville	early hydrothermal synthesis (levyne)
1876	Lew	reported sedimentary zeolites in tuff deposit
1896	G. Friedel	observed organic liquid sorption; proposed open spongy framework structure
1909	F. Grandjean	reported gas sorption (NH_3, air, H_2)
1925	O. Weigel & F. Steinhoff	observed molecular sieve effect
1930	W.H. Taylor / L. Pauling	structure determinations of analcime and natrolite
1932-1940's	R.M. Barrer J. Sameshima	systematic studies of synthesis, ion-exchange sorption, and dehydration
Industrial Era		
1949-1954	Union Carbide	synthesis of zeolite A and zeolite X (synthetic faujasite)
1954	Union Carbide	commercialized zeolite-based gas purification and separation processes; early catalytic applications
1955-1962	Mobil	commercialized rare earth zeolite X cracking catalyst
1958-1964		discovery and commercialization of significant sedimentary zeolite deposits in western U.S. and Japan
1958	Mobil	zeolite synthesis with organic cations
1962-1980's	Mobil / Union Carbide	synthesis of high silica zeolites
1982	Union Carbide	synthesis of microporous $AlPO_4$ molecular sieves
Recent Developments		
1985 - 1994	Academic and industrial researchers	synthesis of "large pore" (e.g., VPI-5, cloverite), and mesopore (MCM-41) materials new silica zeolites and clathrates advanced materials applications

EBSCOhost - printed on 2/13/2023 4:48 AM via . All use subject to https://www.ebsco.com/terms-of-use

Early history

The discovery of zeolites is usually credited to A.F. Cronstedt because he recognized their intumescent properties. However, zeolites from Iceland are mentioned in the earlier writings of Horrebow (1752) and possibly those of other early naturalists (Betz, 1981). From Cronstedt's discovery in 1756 to the early 1930s, significant developments included descriptions of new zeolite species and occurrences and the discovery of their properties, including reversible dehydration, ion exchange, organic liquid and gas sorption, and the molecular sieve effect. In 1862 the hydrothermal synthesis of levyne was reported and in 1876 sedimentary zeolite deposits were described. Specific references to these early developments (listed in Table 1) may be found in several historical reviews (Milton, 1968; Flanigen, 1980; Mumpton, 1977; Milton, 1989; Flanigen, 1991).

Synthetic zeolite science

The 1930s began the era of modern zeolite science. Research programs initiated by R.M. Barrer in London and J. Sameshima in Japan dominated zeolite studies for almost two decades. Much of their work focused on the adsorption and ion exchange properties of natural and synthetic zeolites, especially mordenite and chabazite. Much of Barrer's work in sorption, diffusion, and synthesis is reviewed in two volumes (Barrer, 1978, 1982). In 1948 Barrer reported the synthesis of the first zeolite that did not have a natural counterpart. His long and prolific career earned him recognition as the father of modern zeolite science.

Early zeolite structures. The elucidation of silicate crystal structures by X-ray crystallography was developing rapidly in the late 1920s. Analcime, natrolite and cancrinite with their high symmetry and well-formed crystals were obvious candidates for early structure determinations. W.H. Taylor (1930) solved the crystal structure of analcime, and L. Pauling (1930) described the natrolite and cancrinite frameworks. These structure determinations showed that zeolites comprise corner-sharing tetrahedral aluminosilicate frameworks with precisely defined channels and pores that occluded charge balancing alkali or alkaline cations and water molecules. The previously observed sorption, exchange, and sieving properties of zeolites could not only be understood but even predicted from their framework structures. Pauling's brief article includes a description of the natrolite and cancrinite frameworks, but it does not include atomic coordinates or details of the way in which the structures were solved. By contrast, Taylor's manuscript includes not only structural details but also a lucid and detailed description of the structure solution process. His logic, insight, and novel assumptions in deducing correct atomic positions that eluded several previous workers provided a model for succeeding structural studies.

Taylor recognized that "zeolites are essentially silica-like structures, in which a portion of the silicon ... has been replaced by aluminum". This observation presaged the synthesis of the first silica zeolites by about 30 years. He also noted that feldspars have the same Si+Al:O ratio (2:1) and "considered it probable that this series also will be found to be built up on a basis of linked tetrahedra containing the silicon and aluminum ions". This prediction was confirmed on Christmas day, 1932 when he solved the sanidine structure (Taylor, 1933) and opened the field of feldspar crystallography that would have a significant impact on mineralogy and geological science.

In his effort "to test the suggested structure as completely as possible," Taylor conducted two experiments that involved changing the pore contents and comparing calculated with experimentally observed intensities. In one experiment analcime was dehydrated to remove water molecules from the pores and in another sodium cations were

EBSCOhost - printed on 2/13/2023 4:48 AM via . All use subject to https://www.ebsco.com/terms-of-use

ion-exchanged with silver cations. The cation exchange experiment was probably the first use of isomorphous substitution that plays an important role today in crystal structure solution, especially for macromolecules.

The industrial era

Synthesis and commercialization. In the late 1940s Robert Milton initiated a program of zeolite synthesis at the Union Carbide Corporation to develop new materials for the separation and purification of air. By crystallizing highly reactive alkali alumino-silicate gels, 16 new zeolite species were discovered, including zeolite A, which had not been found as a natural zeolite, and zeolite X, a synthetic faujasite (Milton, 1959; 1968). These zeolites had Si/Al ratios around one, which is the maximum Al content of a tetrahedral framework according to Lowenstein's rule (however, several sodalite materials have Si/Al ratios less than one, such as the mineral bicchulite with framework Si/Al = 0.5, and a synthetic strontium chromate aluminate with an all-aluminum tetrahedral framework). The high Al contents in these framework structures required large numbers of exchangeable cations for charge balance and their associated waters of hydration. These zeolites exhibited the highest known cation exchange and hydration/dehydration capacities of any materials. Their highly heterogeneous surfaces were very selective for the sorption of water and other polar molecules, and these properties served as the basis for their commercialization in gas drying and purification. Milton used powder diffraction techniques that were not commercially available at that time for characterization of synthesis products and obtained the first zeolite composition-of-matter patents with claims to X-ray diffraction data (Milton, 1959).

Catalytic applications. The potential application of zeolites as heterogeneous catalysts was recognized by industrial scientists in the mid-1950s. At that time several refinery processes (including catalytic cracking) employed amorphous aluminosilicate catalysts. Catalytic cracking reduces the molecular weight of the heavier crude oil components to lighter molecules that comprise gasoline and other fuel products. It was an obvious step to evaluate synthetic aluminosilicate zeolites for catalytic applications, and in 1959 Union Carbide commercialized zeolite Y (synthetic faujasite with a higher Si/Al ratio than Zeolite X) for the isomerization of pentane and hexane. However, the use of synthetic faujasites as cracking catalysts was hindered by their poor steam stability. This problem was solved by ion-exchanging rare earth cations into the faujasite pore system (Plank and Rosinski, 1964). The rare earth-exchanged zeolite X exhibited excellent stability in the steam environments of the catalytic cracking and regeneration units. The commercialization of the faujasite-based Durabead 5 in 1962 by Mobil provided the refining industry with a catalyst that significantly outperformed previous amorphous aluminosilicates. The cracking activity of this new catalyst was over 1000 times that of the conventional amorphous aluminosilicate catalysts. Within several years of their introduction more than 90% of the catalytic cracking units in the United States were using faujasite-based cracking catalysts with significantly greater product yields. Zeolites also exhibited broad utility for catalyzing other organic reactions that proceeded through carbonium ion intermediates, such as reforming, isomerization, and alkylation—all processes of commercial significance to the petroleum industry. The success of these catalytic applications assured a bright future for research on zeolitic materials.

Catalytic applications required materials not only with good thermal stability but also optimized levels of catalytic activity. The Al-rich synthetic zeolites exhibited such high catalytic activity levels that they often transformed feed stocks to coke, bypassing valuable intermediate products. Reducing the framework aluminum content improved thermal stability and moderated catalytic activity. Developing zeolites with higher Si/Al ratios

EBSCOhost - printed on 2/13/2023 4:48 AM via . All use subject to https://www.ebsco.com/terms-of-use

through the modification of framework chemistry and the synthesis of new materials became important industrial research targets that led to today's high-silica zeolites.

Synthesis with organic cations. In early 1958 G.T. Kerr at Mobil's Paulsboro Research Laboratory recognized the possibility of using organic cations instead of alkali cations in zeolite syntheses. Experiments with mixtures of tetramethylammonium (TMA) hydroxide and NaOH produced a zeolite designated ZK-4 with the zeolite A framework but with Si/Al ratios of 1.5-1.7 (compared with 1.0 for zeolite A). ZK-4 occluded both the large TMA and smaller Na cations in the pore system. The large size of the TMA cation relative to the Na cation resulted in fewer total cations in the pore system, thus limiting the positive charge available to balance framework Al substitution. In 1961 a letter was submitted for publication describing the properties of ZK-4, but for proprietary reasons the method of synthesis was not disclosed (Kerr and Kokotailo, 1961). Similar work with organic cations, including the preparation of high Si/Al ratio zeolite A, was also reported from Barrer's research group at about the same time (Barrer and Denny, 1961).

High-silica zeolites. The success with TMA cations led to further experiments with organic cations, and within a year two new zeolites without natural counterparts were synthesized. ZK-5 with Si/Al ratios of around 2 was prepared with 1,4-dimethyl-1,4-diazoniabicyclo[2.2.2]octane (DABCO) cations (Kerr, 1963), and zeolite β with Si/Al ratios from about 15-50 was crystallized with Na and tetraethylammonium (TEA) cations (Wadlinger et al., 1967). Zeolite β was the breakthrough—the first high-silica zeolite. Synthesis with organic cations produced most of the high-silica zeolites and silica zeolites that we have today. Before the synthesis of zeolite β, the most Si-rich zeolites were natural mordenites with Si/Al of around 5. Later syntheses produced "pure silica" β with aluminum contents determined by the purity of the silica starting materials (Fyfe et al. 1988). Syntheses continued with a variety of organic cations, resulting in many new high-silica zeolites including ZSM-5, ZSM-11, ZSM-12, ZSM-22, ZSM-23, ZSM-39, and ZSM-48. Several of these materials found applications in fuel and lubricant processing and chemicals production. One of the most unique applications was Mobil's methanol-to-gasoline (MTG) process (Chang and Silvestri, 1987). Methanol, derived cheaply from methane in natural gas, is converted directly to high octane gasoline and water when passed over a ZSM-5 catalyst at reaction conditions.

Pure silica zeolites (zeosils)? In 1978 Flanigen et al. announced the synthesis and characterization of silicalite, a purportedly pure silica zeolite with the ZSM-5 framework topology. Because only silica, water, and an organic template was used in the synthesis, the calcined organic free silicalite was initially claimed to be a pure silica polymorph. Subsequent Al NMR analyses of several silicalites revealed low levels of tetrahedral aluminum presumably from the silica reactants (see discussion below). The presence of tetrahedral aluminum showed that silicalite was a very high Si/Al ZSM-5 material. However, silicalite did generate considerable interest in the preparation and properties of very high-silica to pure silica zeolites. These materials exhibited properties quite distinct from low Si/Al zeolites (Table 2), including strongly hydrophobic/organophyllic internal surfaces. The preparations of high-silica/silica analogs of other synthetic zeolites (zeolite β, ZSM-11, ZSM-22, ZSM-48) were subsequently reported.

ZEOLITES AND ZEOLITIC MATERIALS

Before discussing the preparation and properties of silica-zeolites, it will be useful to review information concerning definitions, nomenclature and structures that may be unfamiliar to non-zeolite researchers and students.

EBSCOhost - printed on 2/13/2023 4:48 AM via . All use subject to https://www.ebsco.com/terms-of-use

Table 2. Transition in properties from low-silica zeolites to zeosils

	zeolites	zeosils
	Si/Al = 1.0 ——>	SiO_2
Acid resistance	low	high
Thermal stability	< 700°C	~ 1100°C
Surface selectivity	hydrophilic	hydrophobic
Acidity (catalytic activity)	high	none

modified after Flanigan (1991)

What is a zeolite?

"Zeolites and zeolite-like materials do not comprise an easily definable family of crystalline solids" (Meier and Olson, (1992). Meier (1986) and Smith (1988) pointed out that the definition of a zeolite has become a matter of debate in recent years and that the term zeolite is sometimes used in inconsistent ways. This becomes especially apparent when titles such as "When Is a Zeolite Not a Zeolite?" appear in journals like *Nature* (Rees, 1982). This situation results from the chemical and structural diversity of zeolitic minerals and synthetic materials. The mineralogical community provides the basic definition of a zeolite: A crystalline aluminosilicate with a 4-connected tetrahedral framework structure enclosing cavities occupied by large ions and water molecules, both of which have considerable freedom of movement, permitting ion exchange and reversible dehydration (Smith, 1988).

As with most definitions and classifications there are usually borderline examples, and zeolites are no exception. The Be-silicate mineral lovdarite (Merlino, 1990) and the new Zn-silicate mineral gaultite (Ercit and van Velthuizen, 1994) do not have framework aluminum. Roggianite (Giuseppetti et al., 1991) has silicon, aluminum, and beryllium ordered on an interrupted tetrahedral framework, and maricopaite (Rouse and Peacor, 1994) has an incompletely connected mordenite framework with one T site coordinated by three framework oxygens. All these minerals exhibit zeolitic properties but fail to meet one or more criteria of the mineralogical definition.

Synthetic zeolitic materials include numerous examples that do not meet the mineralogical criteria. Microporous aluminophosphates and silicas have neutral frameworks with no charge-balancing cations. They have low affinities for polar molecules such as water, but readily adsorb non-polar organic molecules. More than 100 metal-substituted aluminophosphates have been synthesized with over 13 elements in addition to Al and P. More recently zinc phosphate, berylloarsenate and gallogermanate materials with microporous tetrahedral frameworks and ion exchange capacity have been synthesized. These materials may reasonably be described as non-aluminosilicate zeolites.

The chemical and structural diversity of synthetic microporous materials has led many in the synthetic zeolite community to favor a broader usage of the term zeolite that is reflected in the literature and especially in publications such as the *Atlas of Zeolite Structure Types* (Meier and Olson, 1992), which is published on behalf of the International Zeolite Association. The Atlas contains entries not only for traditional aluminosilicate zeolites, but also for high-silica zeolites and clathrates, alumino-phosphates and other materials with microporous tetrahedral framework structures. Most of the materials discussed later in this chapter are included in the *Atlas of Zeolite Structure Types*.

EBSCOhost - printed on 2/13/2023 4:48 AM via . All use subject to https://www.ebsco.com/terms-of-use

Zeolite nomenclature

The nomenclature for natural zeolites and zeolitic minerals is straightforward, with mineral names approved by the International Mineralogical Commission on New Minerals and Mineral Names. The nomenclature for synthetic materials is at best complex and often discouraging. Academic and industrial synthesis programs have produced many new zeolitic materials, mixtures of materials, and duplication. Independent nomenclature schemes combined with the difficulty of structurally characterizing micron-sized white powders has resulted in a complex and often confusing nomenclature. This problem is compounded by the publication of much nomenclature information in the patent literature that is generally not as accessible as technical journals. As an example, Meier and Olson (1992) list 19 different designations for materials with the ZSM-5 framework structure, 17 of which are reported in the patent literature. Most synthetic materials are designated with a combination of letters and numbers like Mobil's ZSM-*n* series or Virginia Polytechnic Institute's VPI-*n* series. Unfortunately, a few synthetic materials have received names that sound like minerals (holdstite, silicalite, encilite, boralite, cloverite), a confusing practice that should be discouraged.

A comprehensive handbook of zeolite nomenclature, synthesis, and characterization data was compiled by Szostak (1992). A guide to the zeolite patent literature through 1987 with indices of materials was prepared by Michiels and de Herdt (1987). An invaluable reference to zeolite frameworks and materials is the previously mentioned *Atlas of Zeolite Structure Types* (Meier and Olson, 1992).

Classification of tetrahedral framework materials

In their continuing efforts to classify materials with structures based on condensed tetrahedra Liebau and colleagues (Liebau, 1983; Liebau et al., 1986) proposed a general classification for materials based on 4-connected tetrahedral frameworks. Table 3 includes the portion of their classification scheme related to silicates. It is based on framework chemistry (silicate or aluminosilicate) and the nature of the framework void spaces. Tetrahedral frameworks are classified according to their framework density (FD), which is the number of tetrahedra per 1000 Å^3 (Brunner and Meier, 1989). Dense frameworks with FD $\geq$ 21 have small voids that are either empty, as in quartz, cristobalite, and coesite, or contain non-exchangeable cations, as in the feldspars and nephelines. Materials with FD < 21 have larger channels and voids, and they are classified as porous. These porous frameworks may be subdivided into two classes, depending on the size of the T-atom-rings accessing the void spaces. Materials with frameworks in which access to void space is

Table 3. Classification of tectosilicates with representative examples

	Si		Si,Al	
Dense tectosilicates	**Pyknosils** quartz, cristobalite, coesite		**Pyknolites** feldspar, nepheline	
Porous tectosilicates	**Porosils**		**Porolites**	
	Clathrasils silica sodalite dodecasil 1H	**Zeosils** silica faujasite silica ZSM-12	**Clathralites** sodalite Linde N	**Zeolites** faujasite stilbite

modified after Liebau et al. (1986)

EBSCOhost - printed on 2/13/2023 4:48 AM via . All use subject to https://www.ebsco.com/terms-of-use

Table 4. Classification of porous silicate materials with known structures

Si/Al,(T) ≤ 2 low-silica		2 < Si/Al,(T) ≤ 5 intermediate-silica		5 < Si/Al,(T) < ∞ high-silica		Porosils	
mineral zeolites		**mineral zeolites**		**synthetic zeolites**		**synthetic zeosils**	
ANA	analcime	*BEA	tschernichite	AFI	SSZ-24 (B)	AFI	Si-SSZ-24
BIK	bikitaite	BOG	boggsite	*BEA	beta	*BEA	Si-beta
CAN	cancrinite	BRE	brewsterite	EUO	EU-1	FAU	Si-faujasite
EAB	bellbergite	CHA	chabazite	FAU	Linde Y	FER	Si-ferrierite
EDI	edingtonite	-CHI	chiavennite (Be)	FER	ZSM-35	MEL	Si-ZSM-11
FAU	faujasite	DAC	dachiardite	LEV	NU-3	MFI	Si-ZSM-5
GIS	amicite	EPI	epistilbite	MEL	ZSM-11	MTT	Si-ZSM-23
GIS	gismondine	FER	ferrierite	MFI	ZSM-5	MTW	Si-ZSM-12
GIS	gobbinsite	GOO	goosecreekite	MFS	ZSM-57	TON	Si-theta-1
GME	gmelinite	HEU	clinoptilolite	MOR	mordenite		Si-ZSM-48
LAU	laumontite	HEU	heulandite	MTT	ZSM-23		
LEV	levyne	LOV	lovdarite (Be)	MTW	ZSM-12		
LTL	perlialite	MAZ	mazzite	NES	NU-87		
NAT	natrolite	MER	merlinoite	TON	theta-1		
NAT	mesolite	MON	montesommaite		CIT-1 (B)	**synthetic clathrasils**	
NAT	scolecite	MOR	mordenite		MCM-22	AST	octadecasil
NAT	gonnardite	-MOR	maricopaite		NU-86	DDR	decadodecasil 3R
-PAR	partheite	OFF	offretite		SUZ-4	DOH	dodecasil 1H
PHI	phillipsite	PAU	paulingite		ZSM-48	MEP	Si-melanophlogite
-RON	roggianite (Be,Al)	STI	stilbite			MTN	dodecasil 3C
THO	thomsonite	YUG	yugawaralite			NON	nonasil
-WEN	wenkite	VSV	gaultite (Zn)	**synthetic clathralites**		SGT	sigma-2
				AST	Al-octadecasil	SOD	Si- sodalite
mineral clathralites		**synthetic zeolites**		MTN	ZSM-39		
AFG	afghanite	BPH	Linde type Q	RUT	RUB-10 (B)		
LIO	liottite	CAS	Cs-aluminosilicate	SOD	high Si-sodalite		
SOD	sodalite	EAB	TMA-E(AB)				
		EMT	EMC-2	**mineral clathralite**			
synthetic zeolites		FAU	Linde Y	MEP	melanophlogite		
ABW	Li-A(BW)	KFI	ZK-5				
EDI	Na K-F	LTA	ZK-4				
FAU	Linde X	LTL	Linde type L				
GIS	Na-P1	MEI	ZSM-18				
JBW	NaJ	RHO	rho				
LTA	Linde type A	VSV	VPI-7 (Zn)				
synthetic clathralites		**synthetic clathralite**					
LOS	losod	SOD	sodalite				
LTN	Linde type N						

limited by 6-rings or smaller and which tend to trap cations and organic molecules are classified as clathrasils (Si) or clathralites (Si,Al). Those with access by larger rings that usually permit ion exchange or diffusion of organic molecules are classified as zeosils (Si) or zeolites (Si,Al).

Table 4 classifies porous silicates with known structures based on the Liebau scheme. Minerals and synthetic materials are distinguished and aluminosilicates are subdivided into low-silica ($Si/Al \leq 2$), intermediate-silica ($2 < Si/Al \leq 5$), high-silica ($5 < Si/Al < \infty$) and SiO_2 (porosil) materials. The low, intermediate and high-silica divisions are rather arbitrary and are based on the historical development of synthetic materials; however, this usage is common in zeolite literature. Materials are identified by name and a three-letter structure type code described below. Table 4 contains examples of all published framework types (indicated by structure type codes) adopted by porous silicates, but the listing of specific materials is not exhaustive. Several porous silicates with published structures that have not yet been assigned structure codes are also included.

EBSCOhost - printed on 2/13/2023 4:48 AM via . All use subject to https://www.ebsco.com/terms-of-use

Tetrahedral frameworks & structure type codes. Tetrahedral frameworks comprise 3-dimensional arrays of 4-connected vertices and are defined by the connectivity (topology) of the tetrahedral vertex points. Framework properties such as symmetry and metrics may be applied to the framework topology. Tetrahedral frameworks possess a maximum topological symmetry when idealized into their most regular shape while preserving the framework topology (Smith, 1982). For real materials geometric distortions, ordering of different atoms on tetrahedral sites, and inclusion of ions or molecules in the pore system commonly results in symmetry lower than the maximum topological framework symmetry.

In the *Atlas of Zeolite Structure Types*, topologically distinct tetrahedral frameworks adopted by porous materials are designated by a structure type code that consists of three capital letters (e.g., FAU). Each code is mnemonically related to the name of a real material (e.g., faujasite) with a structure based on that framework. Structure type codes should not be confused or equated with actual materials. They do not depend on composition, cell dimensions or symmetry, but only on framework topology. The codes were established under the auspices of the IUPAC (International Union of Pure and Applied Chemistry, Barrer, 1979) and consist of three capital Roman letters. They are derived from the name of a type material that is usually the material from which the framework structure was determined. A hyphen (-PAR) or asterisk (*BEA) preceding the three-letter code indicates interrupted or faulted frameworks, respectively.

By referring to the structure type codes in Table 4, it is possible to determine the extent of Al substitution for any framework type. As an example, materials with the FAU framework span the entire Si/Al range with natural faujasite and synthetic Linde X as low-silica materials, synthetic Linde Y as intermediate- and high-silica materials, and a synthetic Si- faujasite as a pure silica material.

Aluminum content of porous silicates

As indicated in Table 4, porous silicates exhibit a wide range of aluminum contents. As tetrahedral framework aluminum decreases there is a gradual but distinct change in the properties of the materials, as summarized in Table 2. Catalytic activity and cation exchange capacities decrease, thermal stability increases and surface properties change from hydrophilic to hydrophobic.

Little is known about the distributions and locations of aluminum on tetrahedral sites in high-silica zeolites. In many of these materials the aluminum concentration can be varied continuously over many orders of magnitude. However, as the framework aluminum content decreases a point is reached where there is less than one aluminum per unit cell. For synthetic zeolite ZSM-5 with 96 T sites per unit cell, a Si/Al ratio of 95 would provide one aluminum per unit cell if the aluminum atoms were equally distributed throughout the crystal. For a Si/Al ratio of 1000, less than 10% of the unit cells could contain aluminum. At some point it becomes reasonable to ask when a high-silica zeolite is not a zeolite in the mineralogical sense and in what respects it differs from a silica polymorph. At higher Si/Al ratios, are these materials complex mixtures of zeolite (Al-containing) and non-zeolite (SiO_2) components or just impure forms of crystalline silica (Rees, 1982)?

Mineral silica polymorphs. Aluminum appears to be ubiquitous in silica polymorph minerals. Smith and Steele (1984) determined the aluminum content of eleven silica polymorphs (4 tridymites, 1 cristobalite, 1 melanophlogite, and 5 quartzes) with the electron and ion microprobe. They reported values ranging from 13 ppm-wt in quartz from

EBSCOhost - printed on 2/13/2023 4:48 AM via . All use subject to https://www.ebsco.com/terms-of-use

Herkimer, NY to over 7000 ppm-wt in tridymite from Pachuca, Mexico. Based on a good correlation between aluminum concentration in quartz and the measured α-β inversion temperatures (Ghiorso et al., 1979) and ^{27}Al NMR evidence (Smith and Blackwell, 1983) it was concluded that most of the aluminum is substituting for silicon in the tetrahedral framework. From the standpoint of tetrahedral aluminum content, most natural silica polymorphs appear quite similar to high-silica zeolites.

Synthetic porous silicas. Fyfe et al. (1982) obtained ^{27}Al NMR data from samples of silicalite (ZSM-5 framework) that purportedly contained no tetrahedral aluminum. They measured tetrahedral Si/Al ratios of $\geq$ 1000 and $\geq$ 200 in two silicalite materials and concluded that the aluminum was contributed by impurities in the silica sources used in the synthesis. The 100% isotopic abundance of ^{27}Al and its very short spin-lattice relaxation time results in an extremely sensitive aluminum probe with detection levels as low as 10 ppm-wt, corresponding to Si/Al ratios greater than 40,000.

Jansen (1991) reported the aluminum content of several silica sources commonly used for zeolite syntheses. Values ranged from < 10 ppm in fumed silicas such as Aerosil-200 (Degussa) and CAB-O-SIL M-5 (BDH) to < 500 ppm in colloidal silicas like Ludox-AS-400 (DuPont). High purity silicas such as Optipur (Merck) are reported to contain < 0.001 ppm aluminum. Organic silicon compounds such as tetraethyl-orthosilicate (TEOS) are also given an aluminum specification of < 0.2 ppm. These data suggest that aluminum-free SiO_2 polymorphs are difficult to prepare via hydrothermal synthesis with commonly available starting materials. Low ppm levels of aluminum in porous silicas will not be detectable with respect to many properties. However, Haag et al. (1984) demonstrated that the hexane cracking activity of ZSM-5 (α test) showed a high correlation with aluminum content down to around 20 ppm. As is the case with quartz, displacive phase transition inversion temperatures for high-silica zeolites and clathralites (see discussions of specific materials below) are probably sensitive to low level Al impurities.

The fourth column in Table 4 (Porosils) lists materials that have reportedly been synthesized without purposefully adding aluminum to the synthesis mixture. These materials are often described as silica molecular sieves, silica clathrates (clathrasils), or porous silica polymorphs to distinguish them from high-silica, aluminum-containing materials. Many of these "SiO_2" materials probably contain low levels of aluminum acquired from synthesis starting materials, and their distinction from high-Si zeolites is somewhat arbitrary from a practical standpoint. In the remainder of this chapter the designation porosil (or zeosil/clathrasil) will be used for materials synthesized without the deliberate addition of aluminum to the synthesis. However, much of the following discussion is also applicable to very high-silica zeolites.

PREPARATION OF POROSILS

Porous crystalline silicas have been prepared with 18 different tetrahedral frame-works by two different methods. Direct solvothermal synthesis with an aqueous (hydrothermal) or organic solvent is the most common technique. Chemical modification of a hetero-atom substituted SiO_2 framework (e.g., framework dealumination of an aluminosilicate zeolite) is the other. A brief overview of these preparation methods is presented below.

Solvothermal syntheses

Hydrothermal synthesis. The hydrothermal synthesis of high-silica zeolites and porosils has been described in numerous articles and several monographs. A compendium of recipes and extensive review of the hydrothermal synthesis literature is included in a

EBSCOhost - printed on 2/13/2023 4:48 AM via . All use subject to https://www.ebsco.com/terms-of-use

monograph by Jacobs and Martens (1987). A monograph which reviews the synthesis of a broad range of molecular sieve materials including zeolites and aluminophosphates was compiled by Szostak (1989). Because of simpler framework chemistry the synthesis of porosils may be considered as a less complex example of aluminosilicate zeolite synthesis.

A typical hydrothermal porosil synthesis uses several reactants including water, a silica source, an inorganic or organic base to assist in dissolving the silica and a soluble organic species which acts as a framework void space filler and/or structure directing agent. In the simplest cases the organic base may also act as the void filler and directing agent. The reactants are mixed in a prescribed order, aged for a prescribed time and then placed in an oven or autoclave at temperatures around 100-200°C for several days to several months. Many factors appear to influence which porosil framework(s) crystallize. These include the source of the reactants (colloidal, fumed or organic silica sources), order of mixing reagents, solution pH, aging history, thermal history (heating rate, reaction temperature and duration), reaction pressure, agitation, presence of seed crystals, and others. With this complexity it is not surprising that the synthesis of new porosils (and zeolites) has resulted mainly from trial and error efforts. These syntheses appear to involve multiple chemical reactions, equilibria and solubility variations in complex heterogeneous media. Finally the as-synthesized product is calcined usually between 500-800°C to remove the organic molecules and leave a porous crystalline tectosilicate.

The role of organic molecules. The role of organic molecules in porosil and zeolite synthesis has been reviewed by Lok et al. (1983), Gies and Marler (1992), Davis and Lobo (1992), and Lobo et al. (1994). Attempts to transform amorphous silicas into porosils without an organic usually result in dense crystalline phases or amorphous silica (Bettermann and Liebau, 1975). The organics used in porosil syntheses must be soluble and stable in the solvent system under reaction conditions. Commonly used organics include amines and quaternary ammonium hydroxides; less common are alkanes, alcohols, ethers, and thioethers. Gies and Marler (1992) synthesized small cage clathrasils (dodecasil 3C and Si-melanophlogite) in the absence of organics, but with Kr and Xe occupying small cages in the SiO_2 framework. They also detected the presence of gases including Ne, Ar, N, O, and CH_4 in porosils by mass spectroscopy and concluded that these "help gases" are entrapped in small framework voids and contribute to the stabilization of the framework.

Organic molecules probably play several roles in porosil synthesis:

(1) Basic organics (amines, quaternary ammonium hydroxides) modify the solution/gel chemistry by raising pH and increasing silica solubility.

(2) Organics may organize the dissolved silica by forming organosilicate species which may act as framework building units; however, this role is not well understood. Evidence for the existence of preorganized inorganic-organic moieties in tetrapropylammonium (TPA) ZSM-5 synthesis solutions is provided from two different sources. Using neutron H/D contrast variation experiments, Henderson and White (1988) detected scattering objects in room temperature synthesis solutions with neutron scattering length densities approximately that of TPA ZSM-5. More recently Burkett and Davis (1994) observed short range intermolecular interactions (~3Å) between TPA protons and Si atoms in a deuterated synthesis medium with ^{1}H–^{29}Si cross polarization MAS NMR prior to the crystallization of TPA Si-ZSM-5. Although these experiments indicate a direct interaction between the organic and silica components, the exact nature of the interaction and structures involved are unknown.

(3) Organics may protect the hydrophobic silica framework surfaces from the aqueous environment in hydrothermal syntheses.

EBSCOhost - printed on 2/13/2023 4:48 AM via . All use subject to https://www.ebsco.com/terms-of-use

(4) Finally, organics serve as space-fillers in framework channels and cages. The observation that at least 22 different organic molecules can synthesize ZSM-5 suggests a space-filling role rather than a structure specific templating role (Davis and Lobo, 1992).

Although organic molecules do not seem to template specific frameworks, their shapes and sizes do seem to affect the nature of the framework void spaces. Gies and Marler (1992) used 61 molecules including linear, branched and cyclic amines, and cyclic ethers and thioethers with different sizes, shapes and chemical characters to synthesize 13 different porosil frameworks. In all cases the molecules were occluded in the framework channel and cage voids. Excellent geometrical fits between the molecules and the void spaces were observed, with certain sizes and shapes of molecules exhibiting a clear preference for certain types of void spaces. The chemical character of the molecules seemed to be unimportant. Globular molecules stabilized clathrasils with cage-like voids. Long-chain amines were occluded in linear 1-dimensional channels with the molecule chain diameter determining the diameter of the framework channel. Branched molecules occurred in zeosils with intersecting channels. It was concluded that in these porosils the molecule-framework geometry is optimized for weak van der Waals interactions.

The role of alkali metals. Although not essential, alkali metal cations are often included in porosil syntheses as sources of hydroxide ions (NaOH) to help solubilize silica. The synthesis of porosils in alkali free systems often involve long crystallization times with some syntheses requiring six months (Gies and Marler, 1992). Goepper et al. (1992) studied the synthesis of Si-ZSM-12 (MTW) and observed that the addition of alkali metal ions at constant hydroxide concentration significantly increases the crystallization rate. They also observed that Si-ZSM-12 samples that were crystallized from solutions containing different potassium ion concentrations had similar morphologies. This morphology was different from Si-ZSM-12 crystallized without potassium ions, and it suggested that the alkali ions may affect both nucleation and crystal growth.

Non-alkaline solvents: replacement of OH^- by F^-. As described above, porosils may be synthesized from basic solutions (pH > 10) in which OH^- ions solubilize silica. In 1978 Flanigen and Patton disclosed a new synthesis route by substituting F^- for some OH^- ions. The addition of F^- ions (from NaF, HF, etc.), which were known to dissolve silica, reduced the pH of the synthesis solution below 10 and produced relatively large crystals with maximum dimensions of several hundred microns. Guth and coworkers (1986, 1989) extended this technique into acidic regimes with pH values as low as 1.5. Syntheses with F^- ions in neutral to acidic solutions produced porosils, aluminum- and boron-substituted zeolites, and microporous alumino-phosphates and gallophosphates (Kessler, 1989). An interesting material synthesized by this technique was the gallophosphate cloverite (-CLO) with the lowest known tetrahedral framework density (Eastermann et al., 1991). Caullet et al. (1991) reported a fluoride synthesis of octadecasil (AST), a clathrasil with a tetrahedral framework containing Si_8O_{12} cubes with a F^- ion located at the center of each cube. The F^- anions are charged-balanced by quinuclidinium cations located in large cages adjacent to the cubes. The silica framework partitions the ions into distinct void spaces. The analogous occurrence of partitioned F^- anions in $Ga_4P_4O_{12}$ cubes and organic cations in larger cages in the synthetic gallophosphate cloverite (-CLO) and a gallophosphate analog of Linde A (LTA) (Simmen et al., 1993) suggests that F^- ions may direct the formation of T_8O_{12} cubes in certain syntheses.

Non-aqueous solvents. In 1985 Bibby and Dale reported the synthesis of Si-sodalite (SOD) from a non-aqueous synthesis medium comprising fumed silica, ethylene

EBSCOhost - printed on 2/13/2023 4:48 AM via . All use subject to https://www.ebsco.com/terms-of-use

glycol, and NaOH or Na_2CO_3. Structural characterization revealed an ethylene glycol molecule occluded in the sodalite cage. More recently Kuperman et al. (1993) reported the synthesis of "giant" (up to ~0.5 mm) crystals of porosils and high-silica zeolites in systems containing an organic solvent, HF, an optional organic templating agent, and reagent amounts of water. Si-ZSM-5 (MFI), Si-ferrierite (FER), and dodecasil-3C (MTN) were prepared. Dissolving HF in pyridine and alkylamines produced remarkably stable polyhydrogen fluorides through hydrogen bonding. The small amounts of water in these systems hydrolyzed to produce OH^- ions that assisted in dissolving the silica. Supersaturation levels and nucleation rates are apparently lower in these organothermal systems relative to hydrothermal ones, resulting in larger crystals.

Framework modification

An alternative method to the direct synthesis of porosils is post-synthesis framework modification (dealumination) of an aluminosilicate zeolite. Chemical modification of zeolite frameworks is possible because most zeolites, unlike dense tectosilicates, have all tetrahedral sites accessible for chemical reactions at the internal or external surfaces of the crystal. Early aluminum extraction techniques included the use of strong mineral acids, aluminum chelating agents such as EDTA and AcAc, and treatment with steam. These treatments selectively remove aluminum from the zeolite framework, but leave framework defects, vacancies, or mesopores; under certain conditions, the reactions deposit some of the extracted aluminum as an aluminum oxide in the pore system. Beyer and Belenykaja (1980) described the modification of zeolites with $SiCl_4$ vapors, which remove aluminum and insert silicon in its place. The preparation of a Si-faujasite by this technique and its structural characterization have recently been reported (Hriljac et al., 1993). The most effective framework modification method for producing siliceous zeolites appears to be a relatively mild aqueous treatment with ammonium fluorosilicate ($(NH_4)_2SiF_6$) solution (Skeels and Breck, 1984). Ammonium fluorosilicate undergoes a stepwise hydrolysis in aqueous solution to form hydronium ions, fluoride ions, and monomeric silicon hydroxide species. Framework aluminum is removed by hydronium ions and complexed by ammonium and fluoride to form $(NH_4)_3AlF_6$ in an equilibrium reaction (Han et al., 1994). Silicon from the monomeric hydroxide is then inserted into framework defects or vacancies. With the appropriate metal fluoride this chemistry can also be used to insert other framework atoms, including aluminum, beryllium, boron, titanium, iron, tin, chromium, and gallium (Skeels, 1993). Reviews of framework modification techniques include Scherzer (1984) and Szostak (1991).

POROSIL MATERIALS

This section provides descriptions of porosil structures and structure-related properties. The large unit cells and complex pore systems often make description and visualization of these frameworks difficult. To simplify framework illustrations only the tetrahedral connectivities are shown. Si atoms occupy points or vertices of the nets, and straight lines represent Si-O-Si bridges. Polyhedral cage units are common constituents of these frameworks, especially clathrasils. These cages are defined by T-atom rings or polygons and are commonly designated $R_1^nR_2^n...$ where R is the ring size and n is the number of rings. Using this designation a cube is 4^6 and a hexagonal cylinder is 4^66^2. Stereographic drawings of most of the frameworks described below are included in the *Atlas of Zeolite Structure Types*. X-ray powder diffraction data for many of these materials has been compiled by von Ballmoos and Higgins (1990).

The majority of porosil structure refinements describe as-synthesized, organic-containing materials because of interest in the role of organics in the crystallization process.

EBSCOhost - printed on 2/13/2023 4:48 AM via . All use subject to https://www.ebsco.com/terms-of-use

Unfortunately these refinements have provided little insight into synthesis mechanisms except for the observation that the size and shape of the organic molecule is usually related to that of the channel or cage in which it is occluded. In most porosils the symmetry of the guest molecules is lower or different from that of the silica framework and the cages or channels they occupy. This symmetry problem along with the thermal motion of the molecules usually results in positionally disordered configurations from diffraction data. In many refinements the guest molecules are simulated by spherical scatterers with the appropriate number of electrons.

These materials, like other silica polymorphs, exhibit a rich variety of displacive phase transformations. These transitions are not only induced by the effects of temperature and pressure, but also by sorbing and desorbing molecules through the pore system. The ZSM-5 framework adopts at least three different space group symmetries at ambient conditions. Almost no high pressure studies of these materials have been reported. Such studies would almost certainly elucidate new phases and provide further insight into the nature of microporous silica frameworks and the interaction of sorbed or occluded molecules with the frameworks.

Very few physical property correlations have been reported for porosils. Marler (1988) observed an almost linear relationship between mean refractive index and density for 13 silica polymorphs with tetrahedral frameworks including eight porosils. Assuming the same atom polarizabilities for all silica polymorphs, he found that the general refractivity formula of Anderson and Schreiber (1965) best described the correlation.

Porosils are thermodynamically metastable with respect to dense silica phases. Their thermochemistry is discussed in the chapter by Navrotsky (this volume).

Zeosils

Si-theta-1 (TON). $24SiO_2$, $Cmc2_1$, a = 13.836(3) Å, b = 17.415(4) Å, c = 5.042(1) Å, (Papiz and Andrews, 1990 and Marler, 1987). A (001) projection of the framework is illustrated in Figure 1. Zig-zag -Si-O-Si- chains perpendicular to this projection form the 3-dimensional framework. The framework contains 1-dimensional linear channels parallel to c. The channels are defined by 10-member T-atom rings with elliptical pore openings of 4.7 Å × 5.5 Å. Twinning on (110) is common and Marler (1987) reported that no untwinned crystals had been detected. Periodic (110) twinning at $(a+b)/2$ intervals produces the ZSM-23 (MTT) framework described below (Fig. 1). Structure refinements of diethylamine containing and organic-free materials (Marler, 1987 and Papiz and Andrews, 1990) are very similar with respect to framework coordinates. No phase transformations have been reported for theta-1.

Si-ZSM-23 (MTT). $24SiO_2 \cdot 1.5NH_4F$, $P12_11$, a = 11.129(1) Å, b = 5.025(1) Å, c = 21.519(1) Å, β = 89.85(4)°, (Marler et al., 1993). Si-ZSM-23 was prepared by treating a calcined high-silica ZSM-23 with an aqueous ammonium fluoride solution and subsequent steaming at 1023 K. This treatment produced siliceous material with ammonium fluoride occluded in the pores and a small quantity of an unidentified impurity phase. The space group symmetry ($P12_11$) deduced from ^{29}SI NMR and high resolution synchrotron X-ray powder data was found to be lower than the maximum topological symmetry ($Pmmn$) of the ZSM-23 framework originally proposed by Rohrman et al. (1985). A (010) projection of the MTT framework showing the tear-drop shaped, 10-ring pore is illustrated in Figure 1. Zig-zag -Si-O-Si- chains perpendicular to the (010) projection complete the 3-dimensional framework. The structure refinement of Marler et al.

EBSCOhost - printed on 2/13/2023 4:48 AM via . All use subject to https://www.ebsco.com/terms-of-use

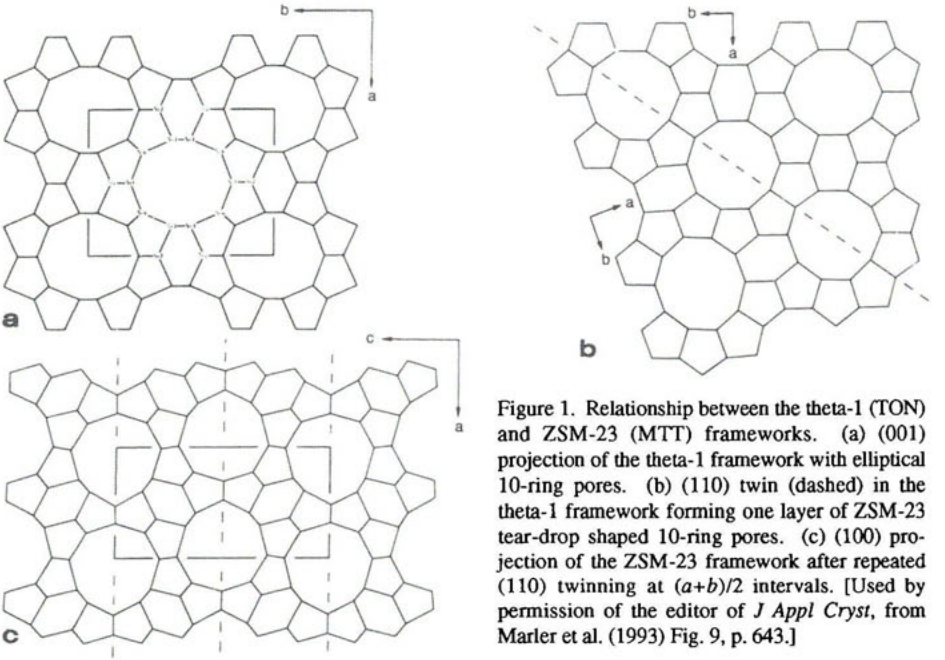


Figure 1. Relationship between the theta-1 (TON) and ZSM-23 (MTT) frameworks. (a) (001) projection of the theta-1 framework with elliptical 10-ring pores. (b) (110) twin (dashed) in the theta-1 framework forming one layer of ZSM-23 tear-drop shaped 10-ring pores. (c) (100) projection of the ZSM-23 framework after repeated (110) twinning at $(a+b)/2$ intervals. [Used by permission of the editor of *J Appl Cryst*, from Marler et al. (1993) Fig. 9, p. 643.]

located zig-zag chains of NH_4^+ and F^- ions in the linear 10-ring channels. Twinning on (110) is common in ZSM-23 materials. Repetitive (110) twinning at $(a+b)/2$ intervals converts the MTT framework into the TON framework.

Si-ferrierite (FER). $36SiO_2{\cdot}2NH_2C_2H_4NH_2{\cdot}2.5H_3BO_3{\cdot}4H_2O$, *Immm*, a = 18.557(6) Å, b = 13.889(3) Å, c = 7.249(9) Å, (Gies and Gunawardane, 1987). Ferrierite (Si/Al = 5) is the only natural zeolite that has been synthesized as a zeosil. Si-ferrierite was synthesized from an aqueous silica solution with ethylenediamine and boric acid as guest species. Boric acid was found to be essential for the crystallization. Syntheses with only ethylenediamine yielded no crystalline products even after nine months. This suggested that an ethylenediamine-boric acid complex (a Lewis acid-base pair) was occluded in the pore system. The SiO_2 framework was refined from a small 10 μm × 60 μm × 100 μm single crystal. The presence of (100) twins made selection of a larger defect-free crystal impossible. The FER framework can be constructed from small 5_4 polyhedra. These polyhedra share edges to form fairly dense corrugated layers perpendicular to [100] (Fig. 2). These layers are connected through oxygen atoms (one Si-O-Si bridge per polyhedron) to form the 3-dimensional framework. The framework contains linear 10-ring channels parallel to [001] that are interconnected by 8-ring pores. The Si-ferrierite framework is stable up to 900°C, but begins transforming to cristobalite at 1000°C.

Si-ZSM-48. $48SiO_2$, disordered framework, a = 14.24(3) Å, b = 20.14(4) Å, c = 8.40(2) Å, (Schlenker et al., 1985; Gunawardane et al., 1987, 1988). ZSM-48 was initially synthesized as a high-silica zeolite (Si/Al = 580) with several organic directing agents including 1,8-octanediamine (Schlenker et al.) and subsequently as a zeosil with eight different organic agents (Gunawardane et al.) Based on X-ray powder diffraction

EBSCOhost - printed on 2/13/2023 4:48 AM via . All use subject to https://www.ebsco.com/terms-of-use

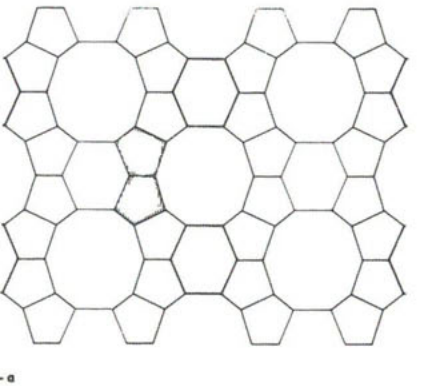


Figure 2. (a) (010) projection of the ferrierite (FER) framework with elliptical 10-ring pores. (b) (010) projection with 8-ring pores. Columns of high tetrahedral density are connected only by bridging oxygens. [Used by permission of the editor of *Zeolites*, from Gies and Gunawardane (1987) Figs. 3 and 4, pp. 444 and 445.]

data and model building, Schlenker et al. proposed a framework structure of ferrierite sheets (Fig. 2b) linked through bridging oxygen atoms. The X-ray powder data is consistent with *Pmma* symmetry, but all reflections inconsistent with both *C*- and *I*-centering are very weak and some are broadened. Models based on the stacking of ferrierite sheets have four unique T-sites for *C*- and *I*-centered cells and eight unique T-sites for primitive cells. In these models each T-atom is connected to three oxygens in the ferrierite sheet, leaving one T-O bond to point up (U) or down (D) to connect with adjacent ferrierite sheets to form a 3-dimensional framework. Considering the U and D permutations of unique T-sites there are seven frameworks each with *Cmcm*, *Cmmm*, *Immm*, and *Imma* symmetry for a total of 28 closely related hypothetical frameworks. For *Pmma* symmetry with 8 unique T-sites there are 128 hypothetical frameworks. These 156 frameworks differ only in the U/D connectivity of the ferrierite sheets. Simulated X-ray powder patterns of the UUDD *Cmcm*, UDUD *Imma*, and UUDDUDUD *Pmma* frameworks showed good agreement with the experimental pattern. Schlenker et al. concluded that random intergrowths of the UUDD *Cmcm* and UDUD *Imma* frameworks provided best agreement with the experimental data. The ZSM-48 framework contains linear channels defined by 10-membered T-atom rings with approximate pore diameters of 5.3 Å × 5.6 Å. The 10-ring channels in the UUDD *Cmcm* and UDUD *Imma* frameworks are defined entirely by 6-membered rings (Fig. 3) and are topologically identical. Because of the disordered nature of the ZSM-48 framework no structure refinement has been attempted and no structure type code has been assigned. Synthesis of an ordered framework member has not been reported.

Si-ZSM-5 (MFI). $96SiO_2$, $P2_1/n11$, a = 20.107(2) Å, b = 19.879(2) Å, c = 13.369(1) Å, α = 90.67(1)°, (van Koningsveld et al., 1990). ZSM-5 has been studied more than any other zeolitic material including over a dozen structure refinements. Interest

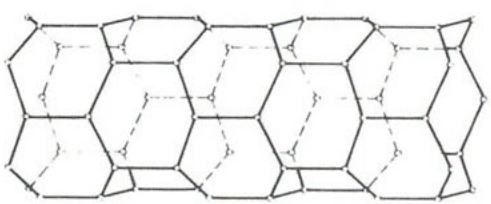
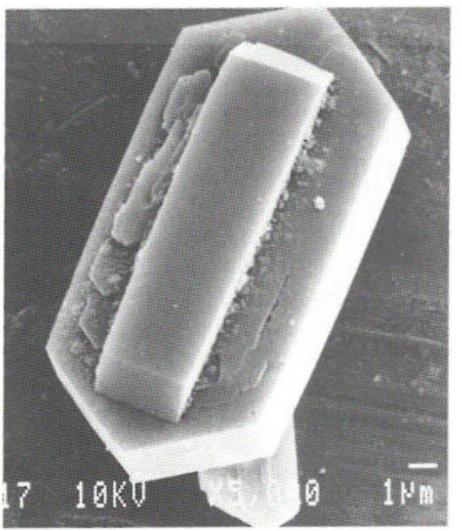


Figure 3. T-atom connectivity defining the 10-ring channel in the UDUD Imma and UUDD Cmcm models of ZSM-48. [Used by permission of the editor of *Zeolites*, from Schlenker et al. (1985) Fig. 2b, p. 356.]

EBSCOhost - printed on 2/13/2023 4:48 AM via . All use subject to https://www.ebsco.com/terms-of-use

in ZSM-5 has resulted from diverse catalytic applications including cracking, isomerization, dewaxing, methanol-to-gasoline conversion, and many others. ZSM-5 was originally synthesized with tetrapropylammonium (TPA) cations. Subsequently it has been synthesized with dozens of different organic molecules; non-organic syntheses have also been reported (Plank et al., 1979).

An optical study of TPA^+F^- Si-ZSM-5 crystals (Price et al., 1982) revealed interpenetrant twinning with twin components related by a 90° rotation about [001] (Fig. 4). Twinning results from the structural similarity between (100) and (010) slices. Measured refractive indices for Na D light are: $\alpha = 1.491$, $\beta = 1.493$, $\gamma = 1.496$. The optical symmetry is slightly monoclinic with an extinction angle of 0.3°



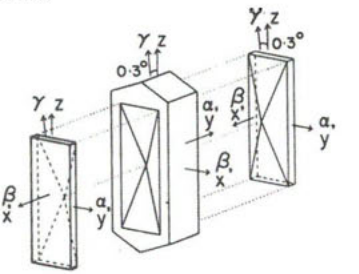


Figure 4. (a) Scanning electron micrograph of Si-ZSM-5 showing interpenetrant twinning. (b) Exploded illustration of interpenetrant twinning. The central twin component is related to the two outer components by a 90° rotation about [001]. [2b used by permission of the editor of *J Am Chem Soc*, from Price et al. (1982) Fig. 2, p. 5972.]

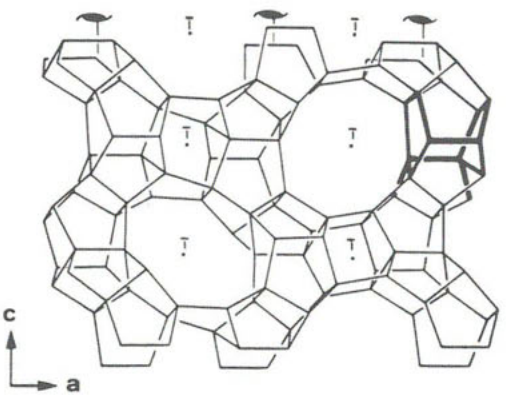


Figure 5. Framework topology and symmetry elements of the (010) pentasil layer in ZSM-5 (MFI). The 12 T-atom building unit is bolded. [By permission of the editor of *Zeolites*, from van Koningsveld et al. (1990) Fig. 1, p. 236.]

The structure of ZSM-5 is difficult to describe and depict because of the large unit cell and a 3-dimensional pore system. The simplest description is from van Koningsveld et al. (1990). The framework fragment (in bold) containing 12 T-sites in Figure 5 forms a chain along *c* by the application of a 2-fold screw axis parallel to *c*. Inversion centers produce additional chains and generate the (010) pentasil layer with 10-membered T-atom rings,

EBSCOhost - printed on 2/13/2023 4:48 AM via . All use subject to https://www.ebsco.com/terms-of-use

which define a linear channel parallel to [010]. Linking (010) pentasil layers with their mirror images completes the 3-dimensional framework and produces (100) pentasil layers (Fig. 6a), which also have 10-membered T-atom rings that define another sinusoidal channel system parallel to [100]. The MFI framework contains an intersecting, 3-dimensional, 10-ring pore system which is depicted schematically in Figure 7. The catalytic utility of aluminum-containing ZSM-5 results from the selectivity of this pore system for molecules of specific sizes and shapes and its 3-dimensional nature, which insures multiple diffusion paths through the crystal.

The high symmetry *Pnma* framework (Fig. 6a) may transform to $P2_1/n11$ symmetry through mutual shifts of successive (010) pentasil layers with equal probability along $+c$ or $-c$, producing aggregates of monoclinic twin domains (Fig. 6b). Twin domains of at least 50 unit cells (≈ 1000 Å) were reported by van Koningsveld et al. (1987) for one ZSM-5 sample. To obtain accurate structural data on the monoclinic phase, a ZSM-5 slab was subjected to a uniaxial compressive stress of about 2×10^6 Pa during slow cooling from 380 K to room temperature. X-ray photographs showed that the original twin fraction of 0.5 was reduced to about 0.06 after this treatment (van Koningsveld et al., 1989). ZSM-5 thus appears to be ferroelastic and it seems likely that ferroelastic behavior will be observed in other porosils. The twin-free monoclinic framework is illustrated in Figure 6c.

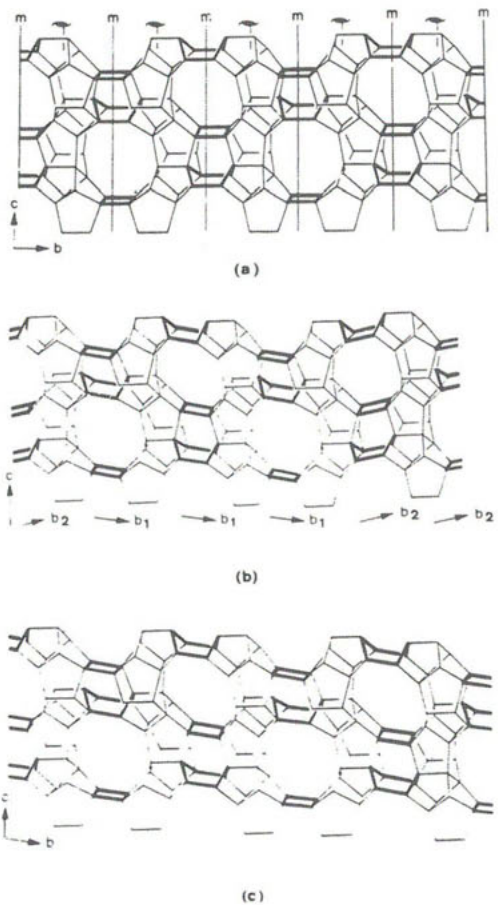


Figure 6. (a) (100) pentasil layer in Pnma (as-synthesized or high temperature) ZSM-5.

(b) (100) pentasil layer in P21/n11 ZSM-5 after inversion from the Pnma structure. The actual size of the twin domains are at least 50 unit cells in some crystals.

(c) (100) pentasil layer without twin domains in P21/n11 ZSM-5 formed by application of a uniaxial mechanical stress during the phase transition. [Used by permission of the editor of *Zeolites*, from van Koningsveld et al. (1990) Fig. 2, p. 236.]

EBSCOhost - printed on 2/13/2023 4:48 AM via . All use subject to https://www.ebsco.com/terms-of-use

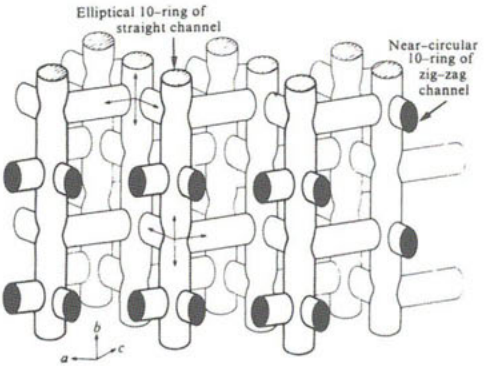


Figure 7. Schematic representation of the channel system in ZSM-5. [Used by permission of the editor of *Nature*, from Flanigen et al. (1978) Fig. 1, p. 512.]

Relative to the $P2_1/n11$ structure, the *Pnma* ZSM-5 structure is stable at higher temperatures, with higher framework aluminum contents, and with certain organics in the pore system (TPA fluoride, Price et al., 1981, 1982 and naphthalene, Mentzen et al., 1993). High-silica (Si/Al = 300) H^+ ZSM-5 undergoes the reversible $Pnma/P2_1/n11$ transition at about 340 K. Sorption of p-xylene or p-dichlorobenzene in the channels of high-silica ($P2_1/n1\bar{1}$) ZSM-5 induces displacive transformations to $P2_12_12_1$ symmetry with different framework geometries and sorbed molecule locations (van Koningsveld et al., 1989, 1992). Refinements of the *Pnma* TPA^+OH^- ZSM-5 (Si/Al = 300) and TPA^+F^- Si-ZSM-5 have been reported by van Koningsveld et al. (1987) and Price et al. (1982) respectively.

If adjacent chains in the (010) pentasil layer of *Pmna* ZSM-5 (Fig. 5) are related by (100) mirror planes instead of inversion centers, a new type of (010) layer is formed that builds the ZSM-11 (MEL) framework discussed below.

Si-ZSM-11 (MEL). $96SiO_2$, $I\text{-}4m2$ @ 373 K, a = 20.067(1) Å, c = 13.411(1) Å, (Fyfe et al., 1989). The framework structure of ZSM-11 is closely related to that of ZSM-5 described above. Rotation by 180° of alternate (100) layers in the MFI framework produces the MEL framework, in which adjacent (100) layers are related by mirror planes instead of inversion centers. The similarity of the frameworks often results in ZSM-5/ZSM-11 intergrowths on (100). While it is relatively easy to prepare structurally pure ZSM-5 materials, it is difficult to obtain ZSM-11 materials free of ZSM-5 intergrowths. The maximum topological symmetry of the MEL framework is $I\text{-}42m$. The framework contains two symmetrically equivalent, intersecting, linear, 10-ring channels that are topologically equivalent to the linear channel in the MFI framework. Fyfe et al. (1989) prepared intergrowth-free, high-silica ZSM-11, which was steamed at 77°C for seven days to dealuminate the framework and produce Si-ZSM-11. A variable temperature ^{29}Si NMR study showed a high temperature phase above 333 K and a low temperature phase below 278 K. However, between 283 K and 323 K changes occur in the number of Si resonances and in their positions and intensities. The phase transition is sluggish, occurring over about a 40° interval. The high temperature NMR data is consistent with the $I\text{-}4m2$ framework (7 T-sites with relative populations 1:2:2:2:1:2:2). The low temperature data indicates 12 T-sites and a lower symmetry framework. The 373 K $I\text{-}42m$ structure was refined from synchrotron X-ray powder data. Si-O distances were reasonable except those with O(13), which were 1.49 Å and 1.68 Å. A room temperature data set showed no deviation from I-centering; however, the structure would not refine in lower space group symmetries. The NMR data indicates that the phase transition is complete below room

EBSCOhost - printed on 2/13/2023 4:48 AM via . All use subject to https://www.ebsco.com/terms-of-use

temperature, so data at 253 K to 263 K may be required for successful refinement of the low temperature phase.

Si-ZSM-12 (MTW). $56SiO_2$, $C2/c$, a = 24.8633(3) Å, b = 5.01238(7) Å, c = 24.3275(7) Å, β = 107.7215(6)°, (Fyfe et al., 1990). Si-ZSM-12 was prepared by steaming a high-silica material to dealuminate the framework. The crystal structure was refined from synchrotron X-ray powder data with a framework model proposed by LaPierre et al. (1985). Single-crystal and powder X-ray data contained weak superstructure reflections that required doubling the c cell parameter of the LaPierre et al. model. ^{29}Si NMR data showed seven Si resonances of equal intensity, consistent with the structural model. A (010) projection of the ZSM-12 framework is illustrated in Figure 8. The short 5 Å repeat perpendicular to this projection consists of zig-zag -Si-O-Si- chains, which are evident in the channel topology illustration in Figure 9. These tubular, 12-ring channels are parallel to [010] and are defined by a cylindrical 6-ring net. Cylindrical 6-ring nets also form tubular channels in other silicate materials including SSZ-24 (AFI), ZSM-48, cancrinite (CAN), pentagonite and tridymite, and several aluminophosphates, including VPI-5 (VFI), $AlPO_4$-8 (AET), $ALPO_4$-5 (AFI), $AlPO_4$-11 (AEL), $AlPO_4$-31 (ATO), $AlPO_4$-41 (AFO), and $AlPO_4$-H2 (AHT). No phase transitions have been reported for Si-ZSM-12. (100) twins are present in most ZSM-12 materials. Samples prepared with 4,4'-trimethylenedipiperidine have very low twin densities while high densities are characteristic of other preparations. Periodic (100) twinning would produce a new *Pmcn* framework with a = 24.3 Å, b = 23.7 Å and c = 5.01 Å.

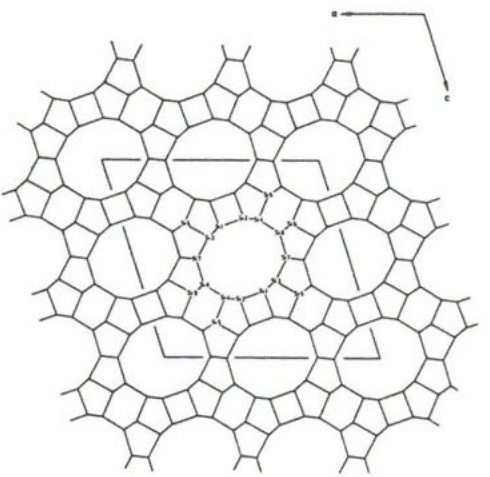


Figure 8. (010) projection of the ZSM-12 (MTW) framework. [Used by permission of the editor of *J Phys Chem* , from Fyfe et al. (1990) Fig. 2, p. 3720.]

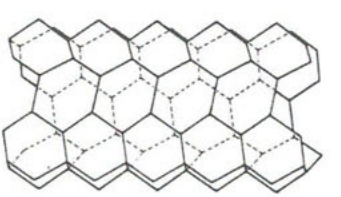


Figure 9. T-atom connectivity of the 12-ring channel in ZSM-12 viewed perpendicular to the channel axis. [Used by permission of the editor of *J Phys Chem*, from Fyfe et al. (1990) Fig. 4, p. 3720.]

EBSCOhost - printed on 2/13/2023 4:48 AM via . All use subject to https://www.ebsco.com/terms-of-use

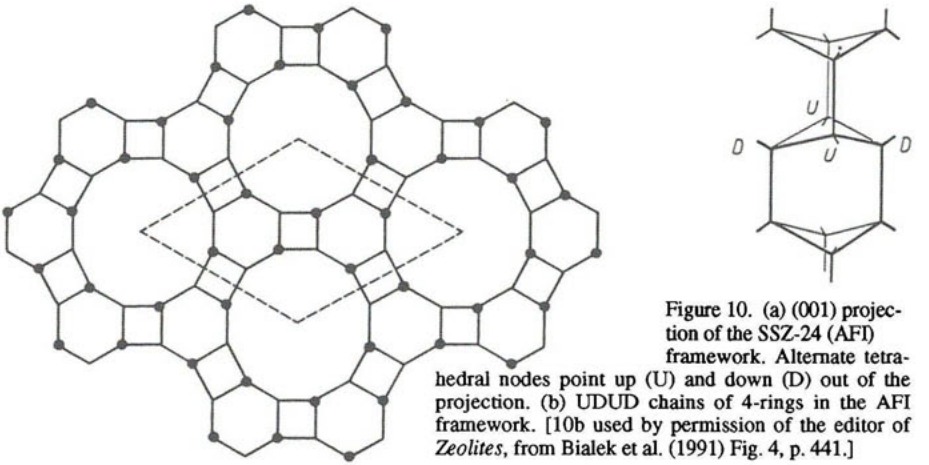


Figure 10. (a) (001) projection of the SSZ-24 (AFI) framework. Alternate tetrahedral nodes point up (U) and down (D) out of the projection. (b) UDUD chains of 4-rings in the AFI framework. [10b used by permission of the editor of *Zeolites*, from Bialek et al. (1991) Fig. 4, p. 441.]

SSZ-24 (AFI). 24 SiO_2, *P6/mmc* @ 370 K, a = 13.6495(1) Å, c = 8.3362(1) Å, @ 464 K a = 13.6553(1) Å, c = 8.3457(1) Å, (Richardson et al., 1990 and Bialek et al., 1991). SSZ-24 is synthesized with N,N,N-trimethyl-1-adamantammonium hydroxide (1-Ada^+OH^-). An (001) projection of the AFI framework is shown in Figure 10 where alternate tetrahedral nodes point up (U) or down (D) out of the projection. The 4-membered T-atom rings are projections of UDUD chains (narsarsukite chains) which build the 3-dimensional framework parallel to c. Room temperature X-ray (Bjalek et al.) and neutron (Richardson et al.) powder data sets contained weak reflections that could not be indexed on a hexagonal unit cell. These weak peaks disappeared upon heating above about 370 K and reappeared upon cooling in the neutron data. Neutron refinements at 370 K and 464 K showed strongly anisotropic thermal displacements for all four oxygens. Complete refinement of the room temperature structure was unsuccessful, but refinement of the pseudo-hexagonal structure revealed a trefoil-shaped O(2) peak in Fourier maps. In the high temperature maps this peak is nearly circular. Richardson et al. concluded that a key feature of the transition involves changes from large anisotropic displacements about a single oxygen centroid to smaller displacements about three oxygen centroids not related by symmetry. In the high temperature structures the average Si-O distance adjusted for riding motion is 1.622 Å at both temperatures. Bialek et al. refined the room temperature structure of calcined and as-synthesized material. Refinement of the calcined silica framework produced large, highly anisotropic oxygen thermal parameters and short Si-O(4) bond distances. Clearly the room temperature silica framework is not hexagonal. An ^{29}Si NMR study would probably provide more insight into the phase transition than the diffraction studies. Refinement of as-synthesized SSZ-24 confirmed one Ada^+OH^- ion pair per unit cell disordered in the 12-ring channel.

Si-beta (*BEA). 64SiO_2 for $P4_122$ structure, a = 12.47 Å, c = 23.33 Å, (Higgins et al., 1988 and Treacy and Newsam, 1988). Zeolite beta, the first high-silica zeolite, was synthesized from an aqueous aluminosilicate system with tetraethylammonium (TEA) cations. The preparation of Si-beta has been described by Marler et al. (1993) and van der Wall et al. (1994). Although ion-exchange, sorption, and catalytic properties confirmed that beta was indeed a zeolite, the X-ray powder diffraction pattern contained only six sharp and several broad reflections, indicating a highly disordered framework. The growth-faulted zeolite beta structure is most easily described in relation to an ordered $P4_122$ (or

EBSCOhost - printed on 2/13/2023 4:48 AM via . All use subject to https://www.ebsco.com/terms-of-use

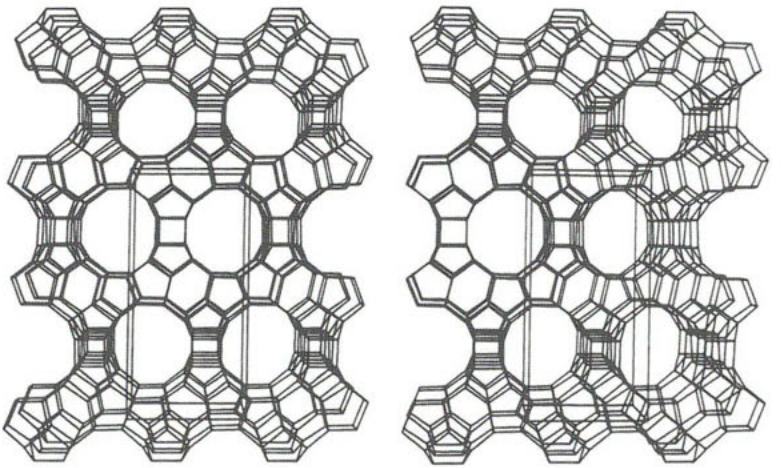


Figure 11. Stereo-view of the framework structure of polytype A ($P4_122$) viewed approximately along [010]. In this framework (00*l*) layers are stacked in an ABAB sequence. In zeolite beta *a*/3 and *b*/3 (00*l*) growth faults produce a disordered stacking sequence. [Used by permission of the editor of *Proc R Soc Lond*, from Newsam et al. (1988) Fig. 12, p. 389.]

$P4_322$) "end-member" structure designated polytype A. A stereographic drawing of polytype A viewed approximately along [010] is illustrated in Figure 11. In zeolite beta (001) growth faults with *a*/3 and/or *b*/3 displacements result in framework disorder along *c*. The faults occur in the 5-ring/6-ring layer between the layers of 12-ring channels. In polytype A, (00l) layers are stacked along *c* in an ABAB sequence. Other ordered polytypes with different stacking sequences have also been described (Treacy and Newsam, 1988, and Higgins et al., 1988). All zeolite beta materials examined thus far possess a disordered layer stacking sequence. The zeolite beta framework contains three intersecting 12-ring channel systems. The introduction of (00l) faults in this framework has no effect on the symmetrically related linear channels parallel to *a* and *b*. Faults do change the tortuosity of the channels along *c*. Large single crystals of Si-beta (110 μm × 110 μm × 210 μm) were synthesized from aqueous solutions containing silica, boric acid, and organic amines (4,4'-trimethylenedipiperidine) (Marler et al., 1993). These crystals exhibited the same structural disorder observed in all other beta preparations. Using only the sharp reflections, a superposition structure was refined which confirmed the framework models proposed earlier. To the surprise of most zeolite researchers, a mineral analogue of zeolite beta (tschernichite) was recently found in hydrothermally altered basalts from Oregon; in this natural sample, Si/Al = 3.7 and hydrated Ca ions occur in the pore system (Smith et al., 1991). X-ray diffraction patterns exhibited sharp and diffuse reflections similar to synthetic preparations, indicating similar framework disorder.

Si-faujasite (FAU). $192SiO_2$, $Fd3m$, a = 24.2576(3) Å (Hriljac et al., 1993). Si-rich faujasites (synthetic zeolites X and Y) have been studied extensively because of their catalytic applications in hydrocarbon cracking. Si-faujasite was prepared from an Na-Y material by framework dealumination with silicon tetrachloride vapor and subsequent heating at 550°C in air for 8 h to remove framework defects. ^{29}SI NMR spectra exhibited only one Si resonance characteristic of $Si(OSi)_4$ species. The sample was dehydrated for 12 h at 300°C under dynamic vacuum prior to collecting time-of-flight neutron powder diffraction data. The refined structure gave mean Si-O distances of 1.605 Å and mean Si-

EBSCOhost - printed on 2/13/2023 4:48 AM via . All use subject to https://www.ebsco.com/terms-of-use

O-Si angles of 143.7°. Neutron powder refinement of a benzene loaded Si-faujasite showed an increase in the cell edge (24.2823 Å) but only minor changes in the atomic coordinates. Surprisingly, the benzene molecules were not located in the refine-ment. It was concluded that relatively flat potential energy surfaces in the large α cage cause benzene molecules to be distributed over a range of low symmetry sites (disordered) which reduced the influence of the benzene molecules on the Bragg intensities. A portion of the FAU framework showing the large α cage accessed by four 12-ring pore openings is illustrated in Figure 12.

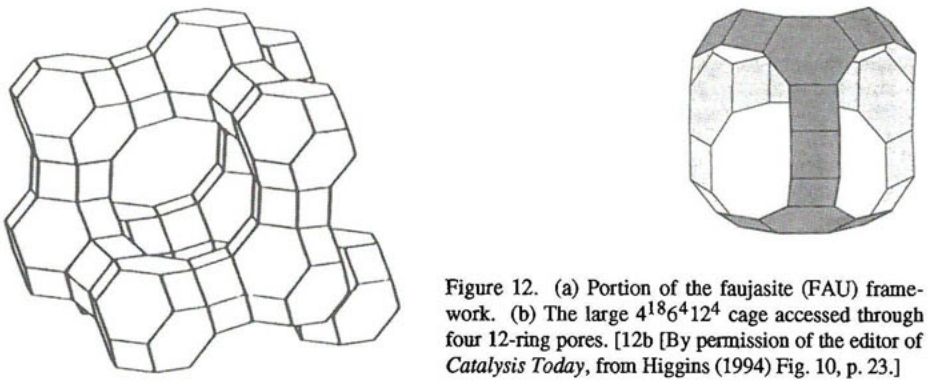


Figure 12. (a) Portion of the faujasite (FAU) framework. (b) The large $4^{18}6^{4}12^{4}$ cage accessed through four 12-ring pores. [12b [By permission of the editor of *Catalysis Today*, from Higgins (1994) Fig. 10, p. 23.]

Clathrasils

Table 5 summarizes nomenclature, structure type codes, crystallographic information and framework cages for clathrasils. In their as-synthesized form, clathrasil frameworks contain cage-like voids occupied by guest species. Large cages occlude organic molecules, and smaller cages occlude help gases (N_2, CO_2, CH_4, Ar). The smallest cages are usually empty. To convert these as-synthesized materials to porosils, the organic molecules and gases are removed by high temperature calcinations in air or oxygen. Because most of the polyhedral cages in clathrasils contain 6-membered or smaller T-atom rings, long calcination times are required to completely remove the organic molecules. Calcinations for short times (hours) often result in black or gray crystals due to retention of unoxidized carbonaceous material (coke) in the cages. The recently synthesized RUB-10 required calcination at 600°C for 100 days to completely remove all the organics. The retention of crystallinity after these treatments attests to the high thermal stability of the silica frameworks.

There is a recognized analogy between hydrogen bonds linking oxygens in water clathrates (OH_2) and oxygens linking Si atoms in silicas (SiO_2). Four clathrasil frameworks listed in Table 6 are isotopological to OH_2 clathrate hydrate frameworks.

melanophlogite (MEP). $46SiO_2{\cdot}6(CO_2,N_2){\cdot}2(CH_4,N_2)$, *Pm3n* @ 200°C, a = 13.436(3) Å, (Gies, 1983). The framework structure of melanophlogite was determined by Kamb (1965) who recognized that it was isostructural with the type I cubic gas hydrates (von Stackelberg and Müller, 1954). Mass spectroscopic analysis of six melanophlogites from 4 different localities indicated that CH_4, N_2 and CO_2 are the primary guest species (Gies at al., 1982). A tetragonal/cubic reversible displacive transformation was observed in natural samples (Gies and Liebau, 1981; Gies, 1983). The transformation temperature

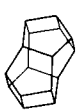
EBSCOhost - printed on 2/13/2023 4:48 AM via . All use subject to https://www.ebsco.com/terms-of-use

TABLE 5 Structural data for clathrasils

CODE	CLATHRASIL	COMPOSITION	SPACE GROUP
AST	octadecasil	20 SiO_2 • 2CH $C_6H_{12}NH^+F^-$ (1)	I4/m
DDR	deca-dodecasil 3R	120 SiO_2 • 9N_2 • 6 $C_{10}H_{15}NH_2$ (2)	$R\bar{3}m$
DOH	dodecasil 1H	34 SiO_2 • 5N_2 • $C_5H_{10}NH$ (3)	P6/mmm
MEP	melanophlogite	46 SiO_2 • 6 CO_2, N_2 • 2 CH_4, N_2	Pm3n (200°C)
MTN	ZSM-39 (dodecasil)	136 SiO_2 • 16N_2 • 8 $N(CH_3)_3$ (4)	Fd3
		136 SiO_2	Fd3m
		68 SiO_2 • 4 C_5H_5N (5)	$I\bar{4}2d$
NON	nonasil	88 SiO_2 • 4 $CH_3CH\ NH_2C_3H_7$ (6)	Fmmm
RUT	RUB-10	$Si_{32}B_4O_{72}$ • 4 $(CH_3)_4N^+$ (7)	$P2_1/a$
SGT	sigma-2		
SOD	Si-sodalite	12 SiO^2 • 2 $C_2H_4(OH)_2$ (8)	Im3m

(1) quinuclidinium flouride (2) 1-aminoadamantane (3) piperidine (4) trimethylamine

EBSCOhost - printed on 2/13/2023 4:48 AM via . All use subject to https://www.ebsco.com/terms-of-use

UNIT CELL PARAMETERS (A°)	REFERENCE	POLYHEDRAL CAGES		
a = 9.194 (2) c = 13.396 (4)	Caullet et al. (1991)	 [4^6]		 [$4^6 6^{12}$]
a = 13.860 (3) c = 40.891 (8)	Gies (1986)	 [5^{12}]	 [$4^3 5^{12} 6^1 8^3$]	
a = 13.783 (4) c = 11.190 (3)	Gerke and Gies (1984)	 [5^{12}]	 [$4^3 5^6 6^3$]	 [$5^{12} 6^8$]
a = 13.436 (3) (200°C)	Gies (1983)	 [5^{12}]	 [$5^{12} 6^2$]	
a = 19.402 (1)	Gies (1984)			
a = 19.369 (6)	Könnecke et al. (1992)	 [5^{12}]	 [$5^{12} 6^4$]	
a = 13.6620 (5) c = 19.5669 (7)	Chae et al. (1991)			
a = 22.232 (6) b = 15.058 (4) c = 13.627 (4)	Marler et al. (1986)	 [$4^1 5^8$]	 [$5^8 6^{12}$]	 [$5^5 6^4$]
a = 13.112 b = 12.903 c = 12.407	Gies and Rius (1994)	 [$4^4 5^4 6^2$]	 [$4^4 5^5 6^4 2^1$]	
b = 113.50		 [$4^3 5^4 6^1$]	 [$5^{12} 6^8$]	
a = 8.830 (1)	Richardson et al. (1988)			 [$4^6 6^8$]

(5) pyridine (6) 2-aminopentane (7) tetramethylammonium (8) ethylene glycol

EBSCOhost - printed on 2/13/2023 4:48 AM via . All use subject to https://www.ebsco.com/terms-of-use

Table 6. Structural analogy between SiO_2 and OH_2 frameworks

SiO_2 framework	**Isotopological OH_2 framework**
tridymite	hexagonal ice I
cristobalite	ice Ic
melanophlogite	12 Å cubic (type I) gas hydrate
dodecasil 3C	17 Å cubic (type II) gas hydrate
dodecadil 1H	synthetic clathrate hydrate
Si-sodalite	$HPF_6 \cdot 6H_2O$ and $(CH_3)_4N(OH) \cdot 5H_2O$

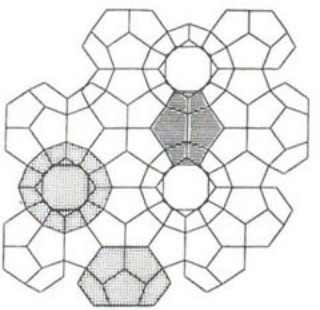


Figure 13. (100) projection of the melanophlogite framework. One 5^{12} cage and two $5^{12}6^2$ cages are emphasized. [Used by permission of the editor of *Z Kristallogr*, from Gies (1983) Fig. 2, p. 252.]

varied (40°C-65°C) among samples from different localities. Melanophlogite from Mt. Hamilton, CA transformed at 65°C with a transformation energy of 41 J/mole SiO_2 (Gies, 1983). At ambient conditions natural melanophlogite is tetragonal with transformation-twinned crystals; however, synthetic materials with CH_4, CO_2, N_2, Kr, or N_2 as occluded guest molecules are cubic (Gies and Liebau, 1981; Gies et al., 1982; Gies, 1983). Melanophlogite is unstable under shear stress (grinding) and transforms to quartz (Skinner and Appleman, 1963; Gies et al., 1982).

Gies (1983) refined the structure of a Mt. Hamilton crystal at 200°C. The unit cell contains two 5^{12} (pentagonal dodecahedron) cages with occluded CH_4 and N_2, and six $5^{12}6^2$ cages with occluded CO_2 and N_2 (Table 5). A projection of the melanophlogite framework down [100] is illustrated in Figure 13. A mean <Si-O> distance of 1.576 Å and <Si-O-Si> angle of 168.8° differ considerably from mean values of 1.61 Å and 144° reported for silica frameworks (Liebau, 1985). High oxygen temperature factors perpendicular to the direction of the Si-O bonds were interpreted as static or dynamic disorder of the oxygen atoms.

dodecasil 1H (DOH). $34SiO_2 \cdot 3N_2 \cdot C_5H_{10}NH$, *P6/mmm*, a = 13.783 (4) Å, c = 11.190 (3) Å (Gerke and Gies, 1984). Dodecasil 1H is the simplest member (1-layer) of the polytypic dodecasil series (Table 7). The dodecasil 1H framework is constructed from hexagonal layers of face-sharing 5^{12} pentagonal dodecahedra cages (Fig. 14). The layers are stacked in an AA sequence and form additional $4^3 5^6 6^3$ dodecahedra and $5^{12}6^8$ 20-hedra cages (Table 5) between the layers. The smaller dodecahedra cages occlude N_2 and the large 20-hedra cages occlude piperidine.

dodecasil 3C (MTN). $136SiO_2$, *Fd3m*, a = 19.369(6) Å (Könnecke et al., 1992; Chae et al., 1991; Gies, 1984; Schlenker et al., 1981). Dodecasil 3C is the most studied clathrasil material. The MTN framework topology was first determined from calcined

EBSCOhost - printed on 2/13/2023 4:48 AM via . All use subject to https://www.ebsco.com/terms-of-use

Table 7. Polytypic clathrasils with 5^{12} dodecasil layers

Designation	Code	Layer sequence	*a*	*c*
dodecasils				
dodecasil 1H	DOH	AA	13.8	11.3
dodecasil 2H		ABAB	13.8	22.4
dodecasil 3H		AABAAB	13.8	33.6
dodecasil 3C	MTN	ABCABC	19.4	——
.....				
dodecasil D		disordered	13.8	——
deca-dodecasils				
deca-dodecasil 1H		AA	13.8	13.6
deca-dodecasil 2H		ABAB	13.8	27.3
deca-dodecasil 3H		AABAAB	13.8	40.8
deca-dodecasil 3R	DDR	ABCABC	13.8	40.8
.....				
deca-dodecasil D		disordered	13.8	——

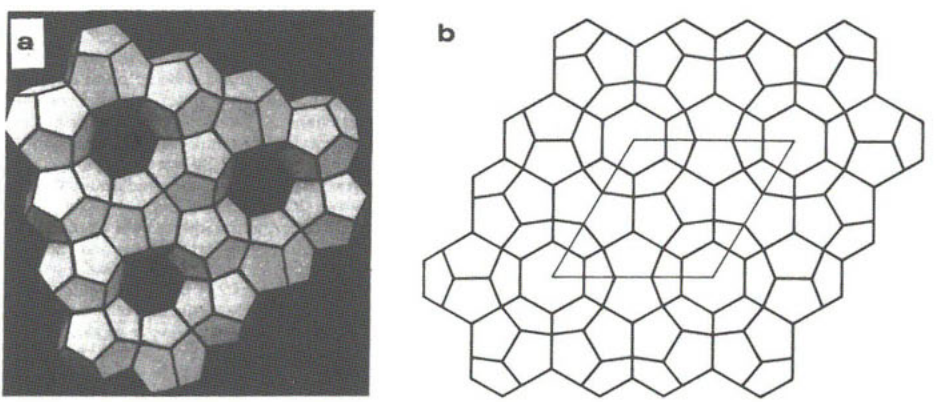


Figure 14. Arrangement of face-sharing 5^{12} cages in the (001) dodecasil layer which builds the DOH, MTN and DDR frameworks. (a) model, (b) projection. [Used by permission of the editors of (a) *Nature*, from Schlenker et al., (1981) Fig. 4a, p. 341. (b) *Z Kristallogr*, from Gies (1984) Fig. 1, p. 77.]

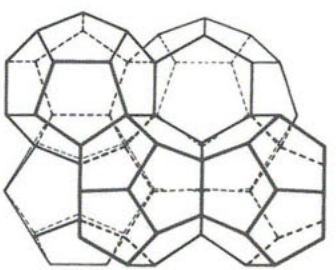


Figure 15. Portion of the dodecasil 1H (DOH) framework illustrating the 5^{12} cage and $5^{12}6^4$ cage between the dodecasil layers. [Used by permission of the editor of *Z Kristallogr* from Gies (1988) Fig. 2, p. 77.]

EBSCOhost - printed on 2/13/2023 4:48 AM via . All use subject to https://www.ebsco.com/terms-of-use

(0.5 h, 800°C) ZSM-39, a high-silica clathralite by Schlenker et al. (1981) who pointed out its structural relationship to the 17 Å type II gas hydrate framework. The framework contains 5^{12} dodecahedral cages that share faces to form the dodecasil layer illustrated in Figure 14. These layers are stacked in an ABCABC sequence forming additional 5^{12} cages and $5^{12}6^4$ cages between the layers (Fig. 15). An alternative description of the framework is $5^{12}6^4$ cages on a diamond lattice connected through 6-ring faces. Schlenker et al. reported the presence of weak X-ray reflections that could not be indexed on a face-centered lattice and concluded that the true symmetry is lower than *Fd*3*m*.

Gies (1984) prepared up to 200-μm, aluminum-free single crystals. He designated the silica end-member dodecasil 3C to indicate its relationship to other members of the polytypic framework series constructed from dodecasil layers. Table 8 summarizes materials prepared using different organic molecules and help gases. Materials with Kr, Xe, and trimethylamine occluded in the large cage were cubic; those prepared with tetrahydrofuran, tetrahydrothiophane, and piperdine were optically anisotropic. Under crossed nicols the anisotropic materials exhibited microtwinning with twin lamellae oriented parallel to [111] (dodecahedron faces). Differential scanning calorimetry on the tetrahydrofuran material indicated a displacive transformation to a cubic phase upon heating between 100 to 120°C with a transformation energy of ~100 J/mol SiO_2. On cooling, the transformation occurs between 95 and 105°C. These observations suggested that either preferred orientation of the guest molecules and/or framework relaxation are responsible for the transformation. A structure refinement of the trimethylamine material produced short mean Si-O distances (1.566 Å), high mean Si-O-Si angles (174.5°) and large oxygen temperature factors, which probably result from static or dynamic disorder of the silica framework.

Table 8. Cage content and symmetry of dodecasil 3C materials (Gies, 1984)

$5^{12}6^4$ cage content	5^{12} cage content	symmetry
Kr	?	cubic
Xe	?	cubic
$N(CH_3)_3$ trimethylamine, CO_2	N_2, CH_4, Ar	Fd3
C_4H_8O tetrahydrofuran	?	optically anisotropic
C_4H_8S tetrahydrothiophane	?	optically anisotropic
$C_5H_{10}NH$ piperidine		optically anisotropic

Chae et al. (1991) prepared 3-mm single crystals of pyridine-containing dodecasil 3C. Differential scanning calorimetry identified phase transitions around -46°C and 161°C. The high temperature cubic phase transforms to an *I*-42*d* phase around 161°C. The symmetry of the low temperature phase was not reported. Twin domains observed under crossed nicols disappeared when heated above 167°C, but they reappeared in their original configuration upon cooling below 159°C. When quickly heated above 700°C and cooled to below 159°C the domains acquired a new configuration, eliminating the memory effect. A memory effect was also observed in the low temperature phase transformation. Structure refinement at ambient temperature (a = 13.6620(5) Å, c = 19.5669(7) Å) on a fragment cut from a (110) face with only one set of twin domains produced unusually high oxygen temperature factors and resolved two statistically disordered sites for one oxygen atom. These results and SEM observations of oriented growth steps in the same orientation as domains

EBSCOhost - printed on 2/13/2023 4:48 AM via . All use subject to https://www.ebsco.com/terms-of-use

observed in the optical microscope suggest a twinned unit cell of lower (orthorhombic) symmetry with average tetragonal symmetry.

Könnecke et al. (1992) calcined 150-μm crystals of dodecasil 3C 48 h at 900°C to remove occluded pyrrolidine and help gases. The crystals turned black during calcination, retaining some carbonaceous material. Differential scanning calorimetry showed a small phase transition at 451 K. The structure of a calcined crystal was refined at 523±15 K, a = 19.369(6) Å, *Fd3m* symmetry. Anisotropic temperature factor refinement and Fourier analysis indicated split positions for three of the four oxygens. Short mean Si-O distances (1.581 Å) and high mean Si-O-Si angles (163.5°) suggested a disordered structure with *Fd3m* average symmetry. Because the differences in framework thermal parameters of this refinement and another at 623 K were small, the authors concluded that the disorder in dodecasil 3C is static. Comparison of the refined structure to lower symmetry DLS models showed that a model with *R*-3 symmetry explained part, but not all of the disorder.

deca-dodecasil 3R (DDR). $120SiO_2{\cdot}9N_2{\cdot}6C_{10}H_{15}NH_2$, *R*-3*m*, a = 13.806(3) Å, c = 40.891(8) Å. The deca-dodecasil framework comprises trigonal layers of face-sharing 5^{12} pentagonal dodecahedra cages analogous to those in dodecasil 1H (Fig. 14). These layers are stacked in an ABCABC sequence and interconnected through 6-membered rings of SiO_4 tetrahedra between the layers, forming two new cages (Fig. 16). A small $4^3 5^6 6^1$ decahedron contains no occluded molecules while the large $4^3 5^{12} 6^1 8^3$ 19-hedron occludes 1-aminoadamantane. The 19-hedra are interconnected through 8-membered rings producing a 2-dimensional interconnecting pore system between the dodecasil layers. Removing the 1-aminoadamantane molecules from the 19-hedron through calcination produces an accessible zeosil-like 8-ring pore system. Deca-dodecasil 3R is the only known member of another polytypic series (Table 7) and possesses framework voids characteristic of both zeosils and clathrasils.

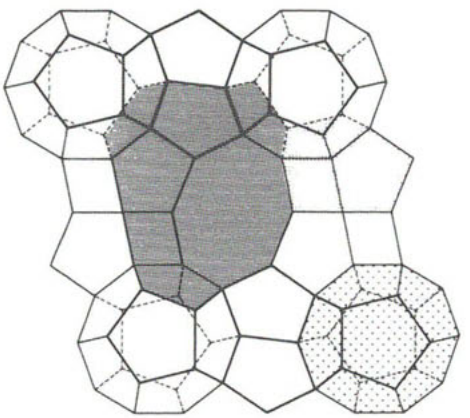


Figure 16. Projection of the deca-dodecasil 3R (DDR) framework parallel to the 5^{12} dodecasil layer. A small 5^{12} cage and a large $4^3 5^{12} 6^1 8^3$ cage is emphasized. [Used by permission of the editor of *Z Kristallogr*, from Gies (1986) Fig. 2, p. 98.]

nonasil (NON). $88SiO_2{\cdot}4C_5H_{11}NH_2$, *Fmmm*, a = 22.232(6) Å, b = 15.056(4) Å, c = 13.627(4) Å (Marler et al., 1986). Nonasils were synthesized with nine different organic molecules including 2-methylpyrrolidine, hexamethyleneimine, 2-methylpiperidine, 2-(aminomethyl)-tetrahydrofuran, 1,2-diaminocyclohexane, 2-methylpiperazine, 1-aminobutane, 2-aminobutane, and 2-aminopentane. The nonasil structure consists of small, empty $5^4 6^4$ octahedra and $4^1 5^8$ 9-hedra, and a larger $5^8 6^{12}$ 20-hedra which occludes the

EBSCOhost - printed on 2/13/2023 4:48 AM via . All use subject to https://www.ebsco.com/terms-of-use

organic molecule. Projections of the complex framework are illustrated in Figure 17. The nonasil structure was refined in space group *Fmmm* (maximum topological framework symmetry) with no observed violations of systematic extinctions for *Fmmm* in the data set. However, Weissenberg photographs exhibited weak intensities consistent with space group *Pbca*, a subgroup of *Fmmm*. Attempts to refine the structure in *Pbca*, *Pmmm* and *Pmm*2 were unsuccessful. It was suggested that the *Fmmm* structure might be some type of average structure.

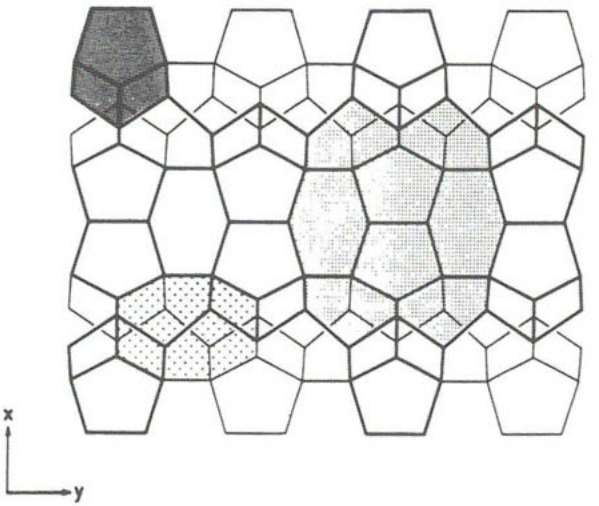


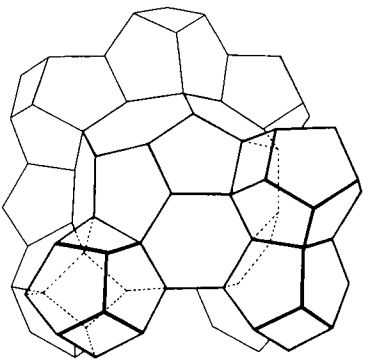
Figure 17. (010) projection of the nonasil framework with the $5^4 6^4$ and $4^1 5^8$ cages emphasized. [Used by permission of the editor of *J Inclusion Phenom*, from Marler et al. (1986) Fig. 2, p. 344.]

sigma-2 (SGT). $64SiO_2 \cdot 4C_{10}H_{15}NH_2$, $I4_1/amd$, a = 10.2387(1)Å, c = 34.3829(1) Å (McCusker, 1988). The sigma-2 structure was the first porosil structure determined with direct methods from powder diffraction data. The silica framework (Fig. 18) is composed of small $4^3 5^6$ cages and larger $5^{12} 6^8$ cages (Table 5) that contain a spatially disordered 1-aminoadamantane molecule.

Si-sodalite (SOD). $12SiO_2 \cdot 2C_2H_4(OH)_2$, $Im3m$, a = 8.830(1) Å, (Richardson et al., 1988). Si-sodalite was the first microporous silicate synthesized from an organic (ethylene glycol or 1-propanol) solvent system (Bibby and Dale, 1985). It was subsequently synthesized in an aqueous system with 1,3,5-trioxane ($C_3H_6O_3$) (Keijsper et al., 1989). The sodalite framework (Fig. 19) is one of the simplest tetrahedral frameworks with only $4^6 6^8$ cubooctahedra (sodalite) cages (Table 5).

Richardson et al. refined both single-crystal (from a 30-μm crystal) X-ray and powder neutron data from the as-synthesized material. The refinements showed the presence of one ethylene glycol molecule per sodalite cage. The ethylene glycol molecule does not conform to the cubic framework symmetry, and no specific conformation was determined from the diffraction data. Because the $Im3m$ symmetry of the fully expanded Si-sodalite framework may lower to $I\text{-}43m$ due to framework collapse, a careful check of the room temperature symmetry was undertaken. Refinement of the x coordinate of oxygen O(1), which would occupy position $0,y,z$ in $Im3m$ and x,y,y in $I\text{-}43m$ gave $x \sim 0.005(1)$. This small value suggested that the framework was fully expanded or nearly so. However, weak peaks in the neutron powder data that were indexed as (331) and (410)/(322) indicate that a small deviation from body centering may occur. The authors speculate that such a

EBSCOhost - printed on 2/13/2023 4:48 AM via . All use subject to https://www.ebsco.com/terms-of-use



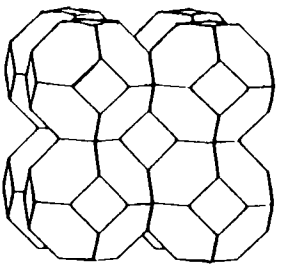


Figure 18 (left). Portion of the sigma-2 framework showing the small 4^35^6 cages and the large $5^{12}6^8$ cages. [Used by permission of the editor of *J Appl Cryst*, from McCusker (1988) Fig. 6, p. 309.]

Figure 19 (right). The sodalite (SOD) framework.

deviation might result from cooperative positioning of ethylene glycol molecules in adjacent cages and/or distortions of the silica framework.

Additional complexities were evident in the NMR data, which should have only one ^{29}Si resonance for *Im3m* symmetry. The splitting of the ^{29}Si NMR resonance into three components (-116.79, -117.13 and -117.37 ppm) is consistent with lower symmetry not detected by diffraction techniques. This information, combined with the presence of "unidentified" lines in X-ray powder data, suggests local distortions from cubic symmetry that are averaged out by the diffraction process but not by the NMR experiment.

Multiple splitting of peaks in neutron powder data obtained at 10 K may be due to ordering of the ethylene glycol molecules and "crinkling" of the silica framework. The phase transition appears to be sluggish, and it may exhibit hysteresis. The 10 K cell appears to be primitive monoclinic, but the precise symmetry was not determined.

The structural complexities of a "simple" organic-containing clathrasil are evident from the study of Richardson et al. It might be very informative to synthesize silica sodalite with a large occluded molecule possessing the same symmetry as the framework and to refine the structure of the organic-free SiO_2 framework.

octadecasil (AST). $20SiO_2{\cdot}2Q^+F^-$, *I4/m*, a = 9.194(2) Å, c = 13.396(4) Å, (Caullet et al., 1991). Unlike most other clathrasils, octadecasil was synthesized from fluorine-rich aqueous silica gels at near neutral pH with 1-azabicyclo[2.2.2]octane (quinuclidine = Q) as the organic directing agent. Octadecasil crystallizes as octahedra up to 200 μm in size. X-ray diffraction data from material calcined at 500°C for 4 h can be indexed to a cubic cell with a = 13.38 Å. As-synthesized material is twinned and birefringent with complex extinction behavior. These observations are consistent with a displacive framework transformation upon heating and/or removal of the organic template. The room temperature structure of as-synthesized octadecasil was refined from data collected on a 100-μm twinned crystal in space group *I4/m*. The silica framework (Fig. 20) is constructed from 4^66^{12} octadecahedra cages that share all their hexagon faces. Octadecahedra packed in this arrangement form another small cube (double 4-ring) 4^6 cage. The tetrahedral framework is topologically identical to that of $AlPO_4$-16 and is closely

EBSCOhost - printed on 2/13/2023 4:48 AM via . All use subject to https://www.ebsco.com/terms-of-use

related to the framework in the mineral zunyite. In zunyite sme of the tetrahedral nodes of the AST framework are vacant. A most interesting feature of the octadecasil structure is the nature and location of the non-framework atoms. ^{13}C NMR data suggest that quinuclidine is occluded in the 4^66^{12} cage as a quinuclidinium cation and not as the neutral molecule. The cation charge appears to be balanced by a fluoride ion occluded in the small 4^6 cube. If this interpretation is correct, octadecasil is unique among clathrasils in partitioning ion pairs into separate cages.

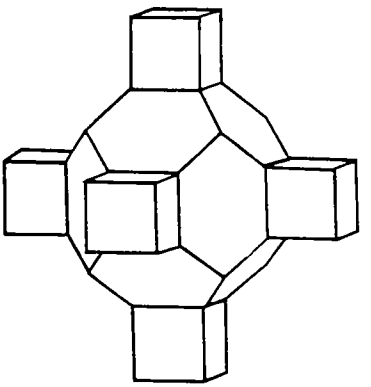


Figure 20. A portion of the octadecasil (AST) framework. [Used by permission of the editor of *Zeolites*, from Bennett and Kirchner (1991) Fig. 2, p. 505.]

Mean Si-O distances and Si-O-Si angles in octadecasil are 1.612 Å and 143.9° respectively. These are almost identical to the averages for dense silicas of 1.61 Å and 144° (Liebau, 1985). These reasonable distances and angles and normal oxygen thermal parameters indicate no oxygen disorder in the octadecasil framework. Static or dynamic oxygen disorder has been observed with most other clathrasils.

RUB-10 (RUT). $Si_{32}B_4O_{72}{\cdot}4(CH_3)_4N$, $P2_1/a$, a = 13.112Å, b = 12.903Å, c = 12.407 Å, β = 113.50° (Gies and Rius, 1994). Although strictly not a clathrasil because of boron in the framework, RUB-10 is of interest as a high-silica material (see Fig. 21).

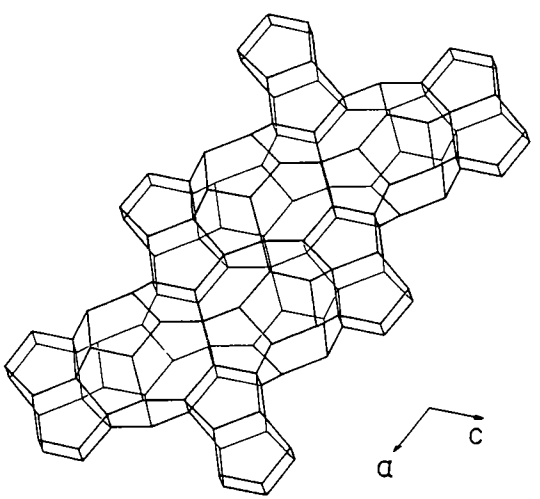


Figure 21. The framework topology of RUB-10 (RUT) illustrating connectivities of the small $4^45^46^2$ cages and the large $4^45^56^48^1$ cages. [Used by permission of the editor of *J Appl Cryst*, from Gies and Rius (1994) Fig. 5b.]

EBSCOhost - printed on 2/13/2023 4:48 AM via . All use subject to https://www.ebsco.com/terms-of-use

This new borosilicate clathrate was synthesized with tetramethylammonium cations that are occluded in 16-hedral $4^5 6^5 8^1$ cages (Table 5). Each 16-hedral cage is connected to 3 other 16-hedral cages, two through 6-rings and one through an 8-ring. Additional 10-hedral $4^5 4^6 2$ cages complete the complex framework (Fig. 21). These cages have not been encountered in other clathrasil frameworks. The results of a Rietveld structure refinement of as-synthesized material indicate that boron ordering reduces the maximum topological framework symmetry from *C2/m* to $P2_1/a$.

ACKNOWLEDGMENTS

Mobil Research and Development Corporation provided support for the preparation of this manuscript and permission to publish it. Scott Han, Mark Davis, Sandra Burkett, C-Y Chen, Raul Lobo and Herman Gies generously provided preprints of their research papers.

REFERENCES

Anderson OL, Schreiber E (1965) The Relation Between Refractive Index and Density of Minerals Related to the Earth's Mantle. J Geophys Res 70:1463-1471

von Ballmoos R, Higgins JB (1990) Collection of Simulated XRD Powder Patterns for Zeolites. Zeolites 10:313S-514S

Barrer RM (1948) Synthesis of a Zeolitic Mineral With Chabazite-like Sorptive Properties. J Chem Soc:127-132

Barrer RM (1978) Zeolites and Clay Minerals as Sorbents and Molecular Sieves. Academic Press, London

Barrer RM (1979) Chemical Nomenclature and Formulation of Compositions of Synthetic and Natural Zeolites. Pure and Appl Chem 51:1091-1100

Barrer RM (1982) Hydrothermal Chemistry of Zeolites. Academic Press, London

Barrer RM, Denny PJ (1961) Hydrothermal Chemistry of the Silicates: Part IX. Nitrogenous Aluminosilicates. J Chem Soc:971-982

Bennett JM, Kirchner RM (1991) The Structure of As-Synthesized $AlPO_4$-16 Determined by a New Framework Modelling Method and Rietveld Refinement of Synchrotron Powder Diffraction Data. Zeolites 11:502-506

Bettermann P, Liebau F (1975) Transformation of Amorphous Silica to Crystalline Silica Under Hydrothermal Conditions. Contrib Mineral Petrol 53:25-36

Betz V (1981) Zeolites From Iceland and the Faeroes. Mineralogical Record 12:5-26

Beyer HK, Belenykaja I (1980) A New Method for the Dealumination of Faujasite-Type Zeolites. In: Imelik B, Naccache C, Ben Taarit Y, Vedrine JC, Coudurier G, Praliaud H (eds) Catalysis By Zeolites, Studies in Surface Science and Catalysis 5:203-210

Bialek R, Meier WM, Davis M, Annen MJ (1991) The Synthesis and Structure of SSZ-24, the Silica Analog of AlPO4-5. Zeolites 11:438-442

Bibby DM, Dale MP (1985) Synthesis of Silica-Sodalite From Non-Aqueous Systems. Nature 317:157-158

Borja M, Dutta PK (1993) Storage of Light Energy by Photoelectron Transfer Across a Sensitized Zeolite-Solution Interface. Nature 362:43-45

Breck DW (1974) Zeolite Molecular Sieves, Structure, Chemistry, and Use, John Wiley & Sons, New York

Brunner GO, Meier WM (1989) Framework Density Distributions of Zeolite-Type Tetrahedral Nets. Nature 337:146-147

Burkett SL, Davis ME (1994) Mechanism of Structure Direction in the Synthesis of Si-ZSM-5: An Investigation by Intermolecular ^1H-^{29}Si CP MAS NMR. J Phys Chem: 98, 4647-4653

Burkett SL, Davis ME (1994) Synthetic Mechanisms and Strategies for Zeolite Synthesis. In: Lehn JM (ed) Comprehensive Supramolecular Chemistry, in press

Caullet P, Guth JL, Hazm J, Lamblin JM, Gies H (1991) Synthesis, Characteriaztion and Crystal Structure of the New Clathrasil Phase Octadecasil. Eur J Solid State Inorg Chem 28:345-361

Chae HK, Klemperer WG, Payne DA, Suchicital CTA, Wake DR, Wilson SR (1991) Clathrasils: New Materials for Nonlinear Optical Applications. In: Marder SR, Sohn JE, Stucky GD (eds) Materials for Nonlinear Optics: Chemical Perspectives. ACS Symposium Series 445, Am Chem Soc, Washington, DC, p 528-540

EBSCOhost - printed on 2/13/2023 4:48 AM via . All use subject to https://www.ebsco.com/terms-of-use

Cronstedt AF (1756) Rön och beskrifning om en obekant bärg art, som kallas Zeolites. Svenska Vetenskaps Akademiens Handlingar, Stockholm 17:120-123

Csicsery SM (1984) Shape-Selective Catalysis in Zeolites. Zeolites 4:202-213

Davis ME, Lobo RF (1992) Zeolite and Molecular Sieve Synthesis. Chem Mater 4:756-768

Dyer A (1984) Uses of Natural Zeolites. Chemistry and Industry: 241-245

Estermann M, McCusker LB, Baerlocher C, Merrouche A, Kessler H (1991) A Synthetic Gallophosphate Molecular Sieve With a 20-Tetrahedral-Atom Pore Opening. Nature 352:320-323

Ercit TS, van Velthuizen J (1994) Gaultite, a New Zeolite-Like Mineral Species From Mont Saint-Hilaire, Quebec, and Its Crystal Structure. Can Mineral, in press

Flanigen EM (1980) Molecular Sieve Zeolite Technology - The First Twenty-Five Years. In: Rees LVC (ed) Proc 5th Int'l Conf on Zeolites, Heyden and Sons Ltd., p 760-780

Flanigen EM (1991) Zeolites and Molecular Sieves an Historical Perspective. In: van Bekkum H, Flanigen EM, Jansen, JC (eds) Introduction to Zeolite Science and Practice. Elsevier, Amsterdam, p 13-34

Flanigen EM, Bennett JM, Grose RW, Cohen JP, Patton RL, Kirchner RM, Smith JV (1978) Silicalite, a New Hydrophobic Crystalline Silica Molecular Sieve. Nature 271:512-516

Flanigen EM, Patton RL (1978) Silica Polymorph and Process for Preparing Same. U.S. Patent 4,073,865

Fyfe CA, Gies H, Kokotailo GT, Marler B, Cox DE (1990) Crystal Structure of Silica-ZSM-12 by the Combined Use of High-Resolution Solid State MAS NMR Spectroscopy and Synchrotron X-ray Powder Diffraction. J Phys Chem 94:3718-3721

Fyfe CA, Gies H, Kokotailo GT, Pasztor C, Strobl H, Cox DE (1989) Detailed Investigation of the Lattice Structure of Zeolite ZSM-11 By a Combination of Solid-State NMR and Synchrotron X-ray Diffraction Techniques. J Am Chem Soc 111:2470-2474

Fyfe CA, Gobbi GC, Klinowski J, Thomas JM, Ramdas S (1982) Resolving Crystallographically Distinct Tetrahedral Sites in Silicalite and ZSM-5 by Solid-State NMR. Nature 296:530-533

Fyfe CA, Strobl H, Kokotailo GT, Pasztor CT, Barlow GE, Bragley S (1988) Correlations Between Lattice Structures of Zeolites and Their ^{29}Si MAS NMR Spectra:Zeolites KZ-2, ZSM-12, and Beta. Zeolites 8:132-136

Gerke H, Gies H (1984) Studies on Clathrasils. IV. Crystal Structure of Dodecasil 1H, A Synthetic Clathrate Compound of Silica. Z Kristallogr 166:11-22

Ghiorso MS, Carmichael IS, Moret LK (1979) Inverted High-temperature Quartz: Unit Cell Parameters and Properties of the α-β Inversion. Contrib Mineral Petrol 68:307-323

Gies H (1983) Studies on Clathrasils. III. Crystal Structure of Melanophlogite, a Natural Clathrate Compound of Silica. Z Kristallogr 164:247-257

Gies H (1984) Studies on Clathrasils. VI Crystal Structure of Dodecasil 3C, Another Synthetic Clathrate Compound of Silica. Z Kristallogr 167:73-82

Gies H (1986) Studies on Clathrasils. IX. Crystal Structure of Deca-dodecasil 3R, the Missing Link Between Zeolites and Clathrasils. Z Kristallogr 175:93-104

Gies H (1991) Clathrasils and Zeosils: Inclusion Compounds With Silica Host Frameworks. In: Atwood JL, Davies JED and MacNicol DD (eds) Inclusion Compounds 5:1-36. Inorganic and Physical Aspects of Inclusions. Oxford University Press, Oxford, UK

Gies H, Gerke H, Liebau F (1982) Chemical Composition and Synthesis of Melanophlogite, a Clathrate Compound of Silica. N Jb Mineral Mh, p 119-124

Gies H, Gunawardane RP (1987) One-step Synthesis, Properties and Crystal Structure of Aluminum-free Ferrierite. Zeolites 7:442-445

Gies H, Liebau F (1981) Melanophlogite: Composition, Thermal Behavior, and Structure Refinement. Acta Cryst A37:C-187 - C-188

Gies H, Marler B (1992) The Structure-Controling Role of Organic Templates for the Synthesis of Porosils in the System SiO2/Template/H2O. Zeolites 12:42-49

Gies H, Rius J (1994) Ab-Initio Structure Determination From Low Resolution (2 Å) X-ray Powder Diffraction Data: The Crystal Structure of the Zeolite RUB-10. J Appl Cryst, in press

Giuseppetti G, Mazzi F, Tadini C, Galli P, Galli E (1991) The Revised Crystal Structure of Roggianite: $Ca_2[Be(OH)_2Al_2Si_4O_{13}]<2.5H_2O$. N Jb Mineral Mh: 307-314

Goepper M, Li H-X, Davis ME (1992) A Possible Role of Al kali Metal Ions in the Synthesis of Pure-silica Molecular Sieves. J Chem Soc Chem Commun, 1665-1666

Gunawardane RP, Gies H, Liebau F (1987) Studies on Clathrasils X. The Effect of "Help Gases" on the Formation of Clathrasils. Z Anorg Allg Chem 546:189-198

Gunawardane RP, Gies H, Marler B (1988) Long-Chain Polyamines and Amine-Boric Acid Pairs as Templates for the Synthesis of Porous Tectosilicates. Zeolites 8:127-130

Guth JL, Kessler H, Higel JM, Lamblin JM, Patarin J, Sieve A, Chezeau JM, Wey R (1989) Zeolite Synthesis in the Presence of Fluoride Ions. In: Occelli ML, Robson HE (eds) Zeolite Synthesis, ACS Symposium Series 389, Am Chem Soc, Washington, DC, p 176-195

EBSCOhost - printed on 2/13/2023 4:48 AM via . All use subject to https://www.ebsco.com/terms-of-use

Guth JL, Kessler H, Wey R (1986) New Route to Pentasil-Type Zeolites Using a Non-Alkaline Medium in the Presence of Fluoride Ions. In: Murakami Y, Iijima A, Ward JW (eds) New Developments in Zeolite Science and Technology. Studies in Surface Science and Catalysis 28, Elsevier, Amsterdam, p 121-128

Han S, Schmitt KD, Schramm SE, Shihabi DS, Chang CD (1994) Evidence of Solution Equilibrium for Zeolite Isomorphous Substitution Using Aqueous Metal Fluoride Complexes. Inorg Chimica Acta, submitted

Haag WO, Lago RM, Weisz PB (1984) The Active Site of Acidic Aluminosilicate Catalysts. Nature 309:589-591

Hayhurst DT, Lee JC (1986) Parameters Affecting the Growth of Large Silicalite Crystals. In: Murakami Y, Iijima A, Ward JW (eds) New Developments in Zeolite Science and Technology. Studies in Surface Science and Catalysis 28, Elsevier, Amsterdam, p 113-120

Henderson SJ, White JW (1988) Microassembly by Intermolecular Forces. J Appl Cryst 21:744-750

Higgins JB (1994) Large Pore Zeolite Frameworks and Materials. Catalysis Today 19:7-26

Higgins JB, LaPierre RB, Schlenker JL, Rohrman AC, Wood JD, Kerr GT, Rohrbaugh WJ (1988) The Framework Topology of Zeolite Beta. Zeolites 8:446-452

Hriljac JA, Eddy MM, Cheetham AK, Donohue JA, Ray GJ (1993) Powder Neutron Diffraction and ^{29}Si NMR Studies of Siliceous Zeolite-Y. J Solid State Chem 106:66-72

Hölderich WF, Hesse M, Näumann F (1988) Zeolites: Catalysts for Organic Syntheses. Angew Chem Int Ed Engl 27:226-246

Hölderich WF, van Bekkum H (1991) Zeolites in Organic Synthesis. In: van Bekkum H, Flanigen EM, Jansen, JC (eds) Introduction to Zeolite Science and Practice. Elsevier, Amsterdam, p 631-726

Horrebow N (1752) Tilforladelige Efterredninger om Island. Copenhagen

Jacobs PA, Martens JA (1991) Introduction to Acid Catalysis With Zeolites in Hydrocarbon Reactions. In: van Bekkum H, Flanigen EM, Jansen, JC (eds) Introduction to Zeolite Science and Practice. Elsevier, Amsterdam, p 445-496

Jansen JC (1991) The Preparation of Molecular Sieves. In: van Bekkum H, Flanigen EM, Jansen, JC (eds) Introduction to Zeolite Science and Practice. Elsevier, Amsterdam, p 77-136

Kamb B (1965) A Clathrate Crystalline Form of Silica. Science 148:232-234

Keijsper J, Den Ouden CJJ, Post MFM (1989) Synthesis of High-Silica Sodalite From Aqueous Systems: A Combined Experimental and Model-Based Approach. In: Jacobs PA, van Santen RA (eds) Zeolites: Facts, Figures, Future. Elsevier Science Publishers B.V., Amsterdam, p 237-247

Kerr GT, Kokotailo GT (1961) Sodium Zeolite ZK-4, A New Synthetic Crystalline Aluminosilicate. J Am Chem Soc 83:4675

Kerr GT (1963) Zeolite ZK-5: A New Molecular Sieve. Science 140:1412

Kessler H (1989) Recent Advances in Zeolite Synthesis. In: Klinowski J, Barrie PJ (eds) Recent Advances in Zeolite Science, Studies in Surface Science and Catalysis 52:17-37, Elsevier, Amsterdam

van Koningsveld H, van Bekkum H, Jansen JC (1987) On the Location and Disorder of the Tetrapropylammonium (TPA) Ion in Zeolite ZSM-5 with Improved Framework Accuracy. Acta Cryst B43:127-132

van Koningsveld H, Jansen JC, van Bekkum H (1987) The Orthorhombic/Monoclinic Transition in Single Crystals of Zeolite ZSM-5. Zeolites 7:564-568

van Koningsveld H, Jansen JC, van Bekkum H (1990) The Monoclinic Framework Structure of H-ZSM-5. Comparison With the Orthorhombic Framework of as-synhesized ZSM-5. Zeolites 10:235-242

van Koningsveld H, Jansen JC, van Bekkum H (1992) The Influence of p-dichlorobenzene Adsorption on the H-ZSM-5 Framework Symmetry and Geometry. In: Higgins JB, von Ballmoos R, Treacy MMJ (eds) Extended Abstracts and Program, Ninth Int'l Zeolite Conf, Butterworth-Heinemann, Boston, abstract RP 201

van Koningsveld H, Tuinstra F, van Bekkum H, Jansen JC (1989) The Location of p-Xylene in a Single Crystal of H-ZSM-5 with a New, Sorbate-Induced, Orthorhombic Framework Symmetry. Acta Cryst B45:423-431

van Koningsveld H, Tuinstra F, Jansen JC, van Bekkum H (1989) On the Preparation of a Monoclinic (Nearly) Single Crystal of Zeolite HZSM-5. Zeolites 9:253-256

Konnecke M, Miehe G, Fuess H (1992) Static Disorder of Dodecasil 3C. A Single-Crystal Study With Synchrotron Radiation. Z Kristallogr 201:147-155

Kuperman A, Nadimi S, Oliver S, Ozin GA, Garces JM, Olken MM (1993) Non-aqueous Synthesis of Giant Crystals of Zeolites and Molecular Sieves. Nature 365:239-242

LaPierre RB, Rohrman AC, Schlenker JL, Wood JD, Rubin MK, Rohrbaugh WJ (1985) The Framework Topology of ZSM-12: A High-Silica Zeolite. Zeolites 5:346-348

Lawton SL, Bennett JM, Schlenker JL, Rubin MK (1993) Synthesis and Proposed Framework of Zeolite SUZ-4. J Chem Soc Chem Comm 894-896

EBSCOhost - printed on 2/13/2023 4:48 AM via . All use subject to https://www.ebsco.com/terms-of-use

Liebau F (1983) Zeolites and Clathrasils - Two Distinct Classes of Framework Silicates. Zeolites 3:191-193

Liebau F (1985) Structural Chemistry of Silicates, Structure Bonding and Classification. Springer-Verlag, Berlin, 374 p

Liebau F, Gies H, Gunawardane RP, Marler B (1986) Classification of Tectosilicates and Systematic Nomenclature of Clathrate Type Tectosilicates: A Proposal. Zeolites 6:373-377

Lobo RF, Zones SI, Davis ME (1994) Structure-Direction in Zeolite Synthesis. J Inclusion Phenomena, in press

Lok BM, Cannan TR, Messina CA (1983) The Role of Organic Molecules in Molecular Sieve Synthesis. Zeolites 3:282-291

Mac Dougall JE, Stucky GD (1993) Assembly of Supra-Nanoclusters Within Crystalline and Amorphous 3-D Structures. In: Reynolds PJ (ed) On Clusters and Clustering, From Atoms to Fractals, Elsevier Science Publishers, p 273-285

Marler B (1987) Silica-ZSM-22: Synthesis and Single Crystal Structure Refinement. Zeolites 7:393-397

Marler B (1988) On the Relationship Between Refractive Index and Density for SiO_2-Polymorphs. Phys Chem Minerals 16:286-290

Marler B, Bohme R, Gies H (1993) Single Crystal Structure Analysis of Zeolite Beta: The Superposition Structure. In: von Ballmoos R, Higgins JB, Treacy MMJ (eds) Proc Ninth Int'l Zeolite Conf. Butterworth-Heinemann, Boston, p 425-432

Marler B, Dehnbostel N, Eulert HH, Gies H, Liebau F (1986) Studies on Clathrasils VIII. Nonasils-$[4^15^8]$, $88SiO_2{\cdot}8M^8{\cdot}4M^{20}$: Synthesis, Thermal Properties, and Crystal Structure. J Inclusion Phenom 4:339-349

Marler B, Deroche C, Gies H, Fyfe CA, Grondey H, Kokotailo GT, Feng Y, Ernst S, Weitkamp J, Cox DE (1993) The Structure of Zeolite ZSM-23 (MTT) Refined from Synchrotron X-ray Powder Data. J Appl Cryst 26:636-644

Maxwell IE, Stork WHJ (1991) Hydrocarbon Processing with Zeolites. In: van Bekkum H, Flanigen EM, Jansen, JC (eds) Introduction to Zeolite Science and Practice. Elsevier, Amsterdam, p 571-630

McCusker L (1988) The *Ab Initio* Structure Determination of Sigma-2 (a New Clathrasil Phase) from Synchrotron Powder Diffraction Data. J Appl Cryst 21:305-310

Meier WM (1986) Zeolites, Zeolite-like Materials. Pure & Appl Chem 58:1323-1328

Meier WM, Olson DH (1992) Atlas of Zeolite Structure Types. 3rd Revised Edn, Butterworth-Heinemann, Boston, 200 p

Mentzen BF, Sacerdote-Peronnet M, Berar J-F, Lefebvre F (1993) Structural Study of an MFI/naphthalene System by X-ray Powder Diffraction, ^{29}Si MAS NMR, and Energy-Minimization Calculations. Zeolites 13:485-492

Merlino S (1990) Lovdarite, $K_4Na_{12}(Be_8Si_{28}O_{72}){\cdot}18H_2O$, A Zeolite-Like Mineral: Structural Features and OD Character. Eur J Mineral 2:809-817

Michaels P, de Herdt OCE (1987) Molecular Sieve Catalysts. European Patent Office Applied Technology Series, Vol 9, Pergamon Press, Oxford, UK

Milton RM (1959) Molecular Sieve Adsorbents. U.S. Patents 2,882,243 and 2,882,244

Milton RM (1968) Commercial Development of Molecular Sieve Technology. In: Molecular Sieves. The Society of Chemical Industry, London, p 199-203

Milton RM (1989) Molecular Sieve Science and Technology; A Historical Perspective. In: Ocelli ML, Robson HE (eds) Zeolite Synthesis. ACS Symposium Ser 398:1-10 Am Chem Soc, Washington DC, p 1-10

Muller U, Brenner A, Reich A, Unger KK (1989) Significant Parameters in the Synthesis of Large Alkaline-Free MFI-Type Zeolites and AFI-Type Aluminophosphates. In: Ocelli ML, Robson HE (eds) Zeolite Synthesis. ACS Symposium Series 398, Am Chem Soc, Washington DC, p 346-359

Mumpton, FA (1977) Natural Zeolites. In: Mumpton, FA (ed) Mineralogy and Geology of Natural Zeolites, Rev Min 4:1-17

Newsam JM (1986) The Zeolite Cage Structure. Science 231:1093-1099

Newsam JM, Treacy MMj, Koetsier WT, de Gruyter CB (1988) Structural Characterization of Zeolite Beta. Proc R Soc Lond A 420:375-405

Ozin GA (1992) Nanochemistry: Synthesis in Diminishing Dimensions. Adv Mater 4:612-649

Ozin GA, Kuperman A, Stein A (1989) Advanced Zeolite Materials Science. Angew Chem Int'l Ed Engl 28:359-376

Papiz Z, Andrews SJ (1990) Structure of the Zeolite Theta-1: Redetermination Using Single-Crystal Synchrotron-Rdiation Data. Acta Cryst C46:172-173

Pauling L (1930) The Structure of Some Sodium and Calcium Aluminosilicates. Proc Nat'l Academy of Sciences 16:453-459

Plank CJ, Rosinski EJ (1964) Process for Cracking Hydrocarbons With a Zeolite Catalyst. U.S. Patent 3,140,251

EBSCOhost - printed on 2/13/2023 4:48 AM via . All use subject to https://www.ebsco.com/terms-of-use

Plank CJ, Rosinski EJ, Rubin MK (1979) Method for Producing Zeolites. U.S. Patent 4,175,114
Price GD, Pluth JJ, Smith JV, Araki T, Bennett JM (1981) Crystal Structure of Tetrapropylammonium Fluoride Silicalite. Nature 292:818-819
Price GD, Pluth JJ, Smith JV, Bennett JM, Patton RL (1982) Crystal Structure of Tetrapropylammonium Fluoride Containing Precursor to Fluoride Silicalite. J Am Chem Soc 104:5971-5977
Ray GJ, Nerheim AG, Donohue JA (1988) Characterization of Defects in Dealuminated Faujasites. Zeolites 8:458-463
Rees LVC (1982) When Is a Zeolite Not a Zeolite? Nature 296:491-492
Richardson JW Jr, Pluth JJ, Smith JV, Dytrych WJ, Bibby DM (1988) Conformation of Ethylene Glycol and Phase Change in Silica Sodalite. J Phys Chem 92:243-247
Richardson JW Jr, Smith JV, Han S (1990) High-Low Displacive Transition in the All-Silica Form of the AlPO4-5 Topology. J Chem Soc Faraday Trans 86:2341-2342
Rohrman AC, LaPierre RB, Schlenker JL, Wood JD, Valyocsik EW, Rubin MK, Higgins JB, Rohrbaugh WJ (1985) The Framework Topology of ZSM-23: A High-Silica Zeolite. Zeolites 5:352-354
Rouse RC, Peacor DR (1994) Maricopaite, an Unusual Lead Calcium Zeolite With an Interrupted Mordenite-Like Framework and Intrachannel Pb4 Tetrahedral Clusters. Am Min 79:175-184
Scherzer J (1984) The Preparation and Characterization of Aluminum-Deficient Zeolites. In: White TE Jr, Dalla Betta RA, Derouane EG, Baker RTK (eds) ACS Symposium Series 248:157-200 Am Chem Soc, Washington, DC
Schlenker JL, Dwyer FG, Jenkins EE, Rohrbaugh WJ, Kokotailo GT, Meier WM (1981) Crystal Structure of a Synthetic High-silica Zeolite - ZSM-39. Nature 294:340-342
Schlenker JL, Kühl GH (1993) Observations and Descriptions: On an Unknown Mineral Species Called Zeolites by Axel Fredrick Cronstedt. In: von Ballmoos R, Higgins JB, Treacy MMJ (eds) Proc Ninth Int'l Zeolite Conf. Butterworth-Heinemann, Boston, p 3-9
Schlenker JL, Rohrbaugh WJ, Chu P, Valyocsik EW, Kokotailo GT (1985) The Framework Topology of ZSM-48: A High-silica Zeolite. Zeolites 5:355-358
Schlenker JL, Higgins JB, Valyocsik EW (1990) The Framework Topology of ZSM-57: A New Synthetic Zeolite. Zeolites 10:293-296
Simmen A, Patarin J, Baerlocher C (1993) Rietveld Refinement of F^--Containing GaPO4-LTA. In: von Ballmoos R, Higgins JB, Treacy MMJ (eds) Proc Ninth Int'l Zeolite Conf. Butterworth-Heinemann, Boston, p 433-440
Skeels GW (1993) Framework Substitution in Zeolites: Secondary Synthesis. Am Chem Soc Symposium Preprints, Division of Petroleum Chemistry, 38:484-485
Skeels GW, Breck DW (1984) Zeolite Chemistry V - Substitution of Silicon for Aluminum in Zeolites via Reaction With Aqueous Fluorosilicate. In: Olson DH, Bisio A (eds) Proc Sixth Int'l Zeolite Conf, Butterworths, Guilford, Surrey, UK, p 87-96
Skinner BJ, Appleman DE (1963) Malanophlogite, A Cubic Polymorph of Silica. Am Min 48:854-867
Smith JV (1982) Geometrical and Structural Crystallography. John Wiley & Sons, New York
Smith JV (1988) Topochemistry of Zeolites and Related Materials. 1. Topology and Geometry. Chem Rev 88:149-182
Smith JV, Blackwell CS (1983) Nuclear Magnetic Resonance of Silica Polymorphs. Nature 303:223-225
Smith JV, Steele IM (1984) Chemical Substitution in Silica Polymorphs. N Jb Mineral Mh: 137-144
Smith JV, Pluth JJ, Boggs RC, Howard DG (1991) Tschernichite, the Mineral Analogue of Zeolite Beta. J Chem Soc Chem Comm: 363-364
von Stackelberg M, Müller HR (1954) Feste Gashydrate II. Struktur und Raumchemie. Z Elektrochem 58:25-39
Suib SL (1993) Zeolitic and Layered Materials. Chem Rev 93:803-826
Szostak R (1989) Molecular Sieves: Principles of Synthesis and Identification, Van Nostrand Reinhold, New York, 524 p
Szostak R (1991) Modified Zeolites. In: van Bekkum H, Flanigen EM, Jansen, JC (eds) Introduction to Zeolite Science and Practice. Elsevier, Amsterdam, p 153-199
Szostak R (1992) Handbook of Molecular Sieves, Van Nostrand Reinhold, New York, 584 p
Taylor WH (1930) The Structure of Analcite ($NaAlSi_2O_6 \cdot H2O$). Z Kristallogr 74:1-19
Taylor WH (1933) The Structure of Sanidine and Other Feldspars. Z Kristallogr 85:425-442
Terasaki O (1993) HREM Study of the Fine Structures of Zeolites and Materials Confined in Their Spaces: Are Zeolites Good Enough as Containers for Confined Materials. J Solid State Chem 106:190-200
Treacy MMJ, Newsam JM (1988) Two New Three-Dimensional Twelve-Ring Zeolite Frameworks of Which Zeolite Beta Is a Disordered Intergrowth. Nature 332:249-251
Wadlinger RL, Kerr GT, Rosinski EJ (1967) Catalytic Composition of a Crystalline Zeolite. U.S. Patent 3,308,069
van der Wall JC, Rigutto MS, van Bekkum H (1994) Synthesis of All-silica Beta. J Chem Soc Chem Commun, 1241-1242

EBSCOhost - printed on 2/13/2023 4:48 AM via . All use subject to https://www.ebsco.com/terms-of-use

EBSCOhost - printed on 2/13/2023 4:48 AM via . All use subject to https://www.ebsco.com/terms-of-use

HEALTH EFFECTS OF SILICA DUST EXPOSURE

16 16

David F. Goldsmith

The Western Consortium for Public Health
2001 Addison Street, Suite 200
Berkeley, California 94704 U.S.A.

ABSTRACT

The health effects of exposure to crystalline silica dusts have been observed since Biblical times, and since the Renaissance the respiratory effects of silica dusts have paralleled many developments of occupational medicine and industrial toxicology. For the past century epidemiologists have recognized the debilitating effects on the lung of the inhalation of crystalline silica dust leading to silicosis or silicotuberculosis. Many of the "dusty trades"—mining, sand blasting, quarrying, metallurgy, and construction—reported either acute, accelerated, or chronic silicosis. Knowledge of the risks for silicosis resulted in the imposition of improved ventilation and wet methods, producing a decline in the incidence of silicosis and silica-related tuberculosis since the 1960s. There has been a history of concern about other health effects including lung and other cancers, kidney disease, and immunological ailments, but research linking silica exposure to these conditions has only emerged in the past decade. There is particular concern about the evidence linking silica exposure and cancer. An agenda for new research on the effects of silica exposure is necessary because of the fundamental issues related to the biology of inhaled particles.

INTRODUCTION AND HISTORY

The health effects of silica exposure have probably been known since Biblical times, when mining and smelting of precious ores, glass making, and stone cutting all produced dust diseases in the lungs. During the Renaissance dust diseases among miners and other trades became linked with the founding of occupational medicine and toxicology (Raffle et al. 1987). Gold and silver mining became an important source of wealth in Bohemia and Silesia between 1000 and 1400. The Bohemian towns of Schneeberg and Joachimsthal were the center of silver mining, metal smelting and coin minting. Georg Bauer, more commonly called Georgius Agricola (1499-1555) was appointed the physician in Joachimsthal in 1526. He wrote a 12-volume encyclopedia on all aspects of mining and smelting of precious metals, *De Re Metallica*, published in 1556 after his death. This work describes machinery and engineering, tools, ventilation, and drainage, and the last volume describes diseases among miners and means to prevent them (Agricola 1556).

Regarding poor air ventilation in underground mines, Agricola wrote:"....(W)hen a tunnel is of great length and no shaft reaches to it, then the air does not replenish itself. In such a case it weights heavily on the miners, causing them to breathe with difficulty, and sometimes they are suffocated and burning lamps are extinguished. There is therefore a necessity for machines which enable miners to breathe easily and carry on their work." He recommended the use of "loose veils" over the faces of miners to prevent excessive dust exposure. Although he did not identify the diseases, silicosis, silicotuberculosis, and lung cancer, Agricola (1556) observed that:

> "...(S)ome mines were so dry that they are entirely devoid of water and this dryness causes the workmen even greater harm, for the dust, which is stirred and beaten by

EBSCOhost - printed on 2/13/2023 4:48 AM via . All use subject to https://www.ebsco.com/terms-of-use

> digging, penetrates into the windpipe and lungs, and produces difficulty in breathing and the disease which the Greeks called asthma. If the dust has corrosive qualities, it eats away the lungs, and implants consumption in the body. In the mines of the Carpathian Mountains women are found who have married seven husbands, all of whom this terrible consumption has carried off to a premature death."

Eleven years after Agricola's treatise was published, Paracelsus (1493-1541) authored a book (published in 1567, 15 years after his death) on occupational medicine that described the lung diseases that afflict miners. Paracelsus, whose real name was Aureolus Theophrastus Bombastus von Hohenheim, was an experienced chemist and metallurgist, who studied medicine in Ferrara, Italy. He wandered throughout Europe, teaching in German (rather than in Latin), and wrote his monograph (Paracelsus, 1567) based on observations of mining and smelting. He observed that mining caused shortness of breath, cough, and wasting disease. He also recognized the importance of degree of exposure, and penned the watchword of toxicology: "The dose makes the poison."

The Renaissance physician, Bernardino Ramazzini (1633-1714), is often referred to as the "father of occupational medicine," because of his pioneering description of industrial environments and the common occupational diseases of his Italian patients. He systematically described respiratory ailments among miners of metals, tinsmiths, glass workers and mirror makers, blacksmiths, workers with gypsum and lime, and stone cutters, all of whom were exposed to silica dusts (Ramazzini 1700). He urged medical students and practicing doctors to amend their Hippocratic oath by always asking patients their occupations.

The industrial revolution brought to the workplace the need for power tools, leading to high dust exposures in occupations such as knife grinding, mining and tunneling, metallurgy, flint grinding, pottery making, and sandblasting. Workers in many of these jobs had severe respiratory diseases that shortened their lives greatly compared with employees in other trades (Raffle et al. 1987). The role silica played in conditions variously named "miners phthisis," "potters' rot or potters' asthma," and "industrial consumption" was not determined until the first decades of this century. The British physician Edgar Collis (1870-1957) demonstrated in a series of lectures in 1915 that the lung disease of many dusty trades workers was silicosis (or silicotuberculosis) caused by the inhalation of "free" or crystalline silica (Collis 1919). Much of our knowledge of industrial medicine in the twentieth century follows from the insights that Collis provided on silicosis.

BIOLOGY AND PHYSIOLOGY OF SILICA

Silica refers to silicon dioxide, SiO_2, the most common oxide in the earth's crust. Many publications in the health sciences do not clearly differentiate among the silica polymorphs known to mineralogists. The vast majority of these studies focus on quartz, the most abundant phase of silica. In most occupational articles that treat the subject, the term crystalline silica is used interchangeably with quartz. In this review, however, crystalline silica is employed in its more general (and mineralogically correct) meaning, and the phases quartz, cristobalite, and tridymite are specified where possible.

Routes of exposure

Inhalation is the usual route of crystalline silica entry into the body. Deposition within the respiratory tract is determined by particle size. Particles greater than 15 μm in mass median aerodynamic diameter (MMAD) are deposited in the outer portion of the nasal

EBSCOhost - printed on 2/13/2023 4:48 AM via . All use subject to https://www.ebsco.com/terms-of-use

passages; particles between 10 μm and 15 μm MMAD are deposited in the nasal turbinates and the pharynx. With decreasing size, regardless of chemical composition, particles penetrate further into the lungs. Particles between 5 and 10 μm MMAD are considered inhalable and can descend as far as the major airways, i.e., the trachea and main stem bronchi. Particles less than 5 μm MMAD are considered respirable and can penetrate as far as the terminal bronchioles and alveoli. The terminal bifurcation of the brochioles is considered to be the ultimate target of crystalline silica particle deposition (National Institute for Occupational Safety and Health (NIOSH), 1974; Warheit, 1992).

As highly insoluble inorganic material, crystalline silica experiences little or no metabolic breakdown (Federation of American Societies for Experimental Biology (FASEB), 1979). Thus, the human body relies on physical removal for elimination. After inhalation, respirable particles accumulate in the alveoli, the buds at the end of the airways where gas exchange occurs. Some particles will be removed from the larger airways by way of the mucociliary clearance mechanism that operates in the cells of the upper lungs; some will be engulfed by scavenger cells called macrophages; and some will be taken up by the pulmonary lymphatic system and be transported to the lymph nodes for ultimate excretion.

Particles engulfed by macrophages may be transported to the higher parts of the lung and eventually cleared by the mucociliary mechanisms, or may be retained and initiate a pathway of chronic inflammation. The exact mechanism of toxicity is unknown; many possible mechanisms have been postulated. Surface charge, irregularity of surfaces, and freshness of fracture are possible causes for silica's toxicity (Saffiotti, 1986; Bagchi, 1992; Shoemaker et al., in press). The cascade of toxic events within the scavenger cells after crystalline silica ingestion includes: (1) death of the macrophage and release of the contents, including lymphokines and other cytotoxic agents; (2) re-ingestion of silica particles by newly recruited macrophages and other cells; (3) stimulation of local factors in an attempt to wall off the inflammatory process; and (4) eventual formation of a fibrotic lesion and fibrosis (silicosis) in the lung tissue (Saffiotti, 1986). Entwined within the process of macrophage activation, recruitment, and death is a concomitant impairment of the cellular immunity at the local level. It is thought that reduced immune function also plays a role in the development of fibrosis in the lung.

Entry into the body by ingestion has been suggested by some researchers, especially in relation to pathologic changes in organ systems other than the respiratory tract. At present, ingestion is assumed to play a minor role in cases of renal disease and immunologic abnormalities associated with crystalline silica exposure. This assumption is based on the observation that most silica is passed through the gastrointestinal system with very little metabolism detected (FASEB, 1979).

Clearance of silica from the body

Normal clearance mechanisms of the lung play a role in silica's pulmonary toxicity. Davis (1986) found that after acute exposure of short duration, on long-term follow-up most respirable quartz particles are cleared from rat lungs. But even with long-term follow-up some material was retained. Clearance appeared to follow an exponential pattern, with the majority of particles cleared within the first 3 to 4 months. At 6 to 12 months up to 20% of the inhaled quartz remained within the lungs (Davis 1986). Other researchers have observed a more linear relationship between time and clearance of quartz particles (Pratt 1983), but in light of the persistent inflammatory process provoked by silica and its "recycling" in the lung tissue, it is likely that some quartz will persist after inhalation.

EBSCOhost - printed on 2/13/2023 4:48 AM via . All use subject to https://www.ebsco.com/terms-of-use

The alveolar macrophages have been shown to be instrumental in the clearance process for crystalline silica. Within three hours after inhalation, approximately two-thirds of the inhaled particles are engulfed (Brody et al., 1982). Some of these cells are moved out of the alveoli by the mucocilliary transport and clearance process. Eventually some of the free particles are translocated to the lung tissue, most likely by rupture of macrophages and release of previously phagocytized particles. Reuzel et al. (1991) observed accumulations of macrophages with granular quartz debris in pulmonary lymph nodes subsequent to inhalation exposure.

One research group has investigated alternate pathways of removal of crystalline silica from the body (King et al., 1933a,b), who observed minimal quantities of silicic acid in the urine after inhalation of quartz. More recent rodent ingestion studies (FASEB, 1979) found that 95% of silica is excreted unmetabolized; 4% is excreted in urine, and 1% remains in tissues. It seems clear that fluctuations in urinary levels of silicic acid are influenced more by dietary intake of crystalline silica than by inhalation, and that ingestion of silica seems to be nontoxic compared to inhalation (Proposition 65, 1988).

CLINICAL DESCRIPTION OF SILICA-RELATED DISEASES

Occupational exposure to respirable particles of crystalline silica produces several well-known conditions: silicosis, silicotuberculosis, enlargement of the heart (called cor pulmonale), interference with the body's immune system (called scleroderma or Caplan's syndrome), and damage to the kidneys. Extensive information on silicosis can be obtained from the work of several experts (Ziskind et al., 1976; Seaton, 1984; Peters, 1986; Craighead, 1988; Balaan and Banks, 1992). Silica-related health effects are likely to be detected among active or retired workers in the following industries: abrasives making; abrasive blasting; boiler and tank scaling; brick, tile, and clay production; cement production; ceramics; coal mining; diatomaceous earth calcining; enameling; farming; foundry work; glass making; metal ore mining and milling: paint blending; pharmaceuticals; quarrying and tunneling; sandblasting; scouring powder manufacturing and use; silica flour fillers; and synthetic mineral fibers production (Peters, 1986). There may be as many as 2,000,000 to 4,300,000 U.S. workers either currently or previously exposed to silica on the job (NIOSH, 1991).

Because of difficulties with historical measurements and recording techniques, research has not yet been able to quantitate the amount of crystalline silica that leads to specific degrees of silicosis. Most experts believe that the degree of silicosis increases with both increased intensity of exposure and increased duration of exposure (Heppleston, 1984; NIOSH, 1974; Rice, 1986; Davis, 1986). Other factors include particle size, individual susceptibility, age of crystalline surface (Shoemaker et al., in press), percentage of silica within total dust, and contributions of different polymorphs (Guthrie and Heaney, in press). Although seemingly controversial, the 1985 Surgeon General's Report concluded that smoking plays only a modest role, if any, in the risk of silicosis, and that cumulative dust exposure is the most important factor in pulmonary silicosis (U.S. Department of Health and Human Services, 1986)

Acute silicosis

Acute silicosis or silico-proteinosis is a rare and highly fatal disease, and it results from massive over-exposure to respirable-sized dusts with high quartz contents over a short time. Acute silicosis is the reaction of the lung to acute dust injury, resulting in the filling of air spaces with fluid containing lipid-rich protein debris from dismembered cells

EBSCOhost - printed on 2/13/2023 4:48 AM via . All use subject to https://www.ebsco.com/terms-of-use

in the respiratory tract (see Fig. 1a,b). Clinically, the condition is similar to pulmonary edema, and it includes shortness of breath, with fluid accumulations in the upper and middle areas of the lungs. TB infection has been a serious side effect, with death following a few months after diagnosis. The worst cluster of acute silicosis occurred during the building of the Gauley Bridge hydroelectric tunnel at Hawk's Nest, West Virginia during the Depression years of 1930-1931. In this disaster, there were 2000 black and white construction tunnel workers digging through high-silica rock with no respiratory protection; an estimated 400 died on site, and 1500 were disabled with silicosis (Cherniak, 1986). Despite its rarity, another cluster has been described with over 100 acute and accelerated cases of silicosis among Mexican sandblasters in Midland-Odessa, Texas (Fleming et al., 1990; Weisenfeld et al., 1993). As a result of this epidemic of acute silicosis, the National Institute for Occupational Safety and Health (NIOSH, 1992) issued an alert to make the health and industrial communities aware of this problem in order to prevent it.

Accelerated silicosis

Less devastating than acute silicosis, but often associated with it is accelerated silicosis. Accelerated silicosis results from exposure to high concentrations of silica over a period of 5 to 10 years. It is a disease seen in occupations without proper respiratory protection, including sandblasting, silica flour production, and diatomaceous earth calcining (Seaton, 1984). Silico-proteinosis and accelerated silicosis both are attributed to freshly fractured crystalline silica, which has greater toxicity than aged silicosis (Shoemaker et al., in press). Even if a worker is removed from sources of silica exposure, progression of the disease and premature death from respiratory failure is certain within as little as 10 years from first exposure.

Chronic silicosis

What are the symptoms of chronic silicosis? After 10 or more years employment at low dust concentrations, dusty trades workers may exhibit a dry cough, production of sputum (sometimes bloody), shortness of breath during exertion, reduced pulmonary function, and possibly right heart enlargement. These conditions result from the restriction of the airways by the presence of patches of fibrotic scarring (~1-3 mm in diameter) in the lung tissue at the ends of the alveolar sacs. These lesions are usually seen in the upper zones of the lung. Tuberculosis (TB) infection once was an immediate concern after diagnosis, but the availability of anti-TB drugs such as isoniazid has lessened those risks.

Along with lengthy occupational silica exposure and respiratory symptoms, diagnosis of chronic silicosis is confirmed with a positive X-ray. The radiology community has agreed upon a grading convention developed by the International Labour Organization(ILO) for assessing the severity of fibrotic lesions from silicosis (ILO, 1980). The opacities can range from mild (up to 1.5 mm); to moderate (1.5 to 3.0 mm); to severe (3 to 10 mm). These opacities are different from the diffuse lung changes that occur with age and cigarette smoking, but over time differentiation can be difficult. Silicosis in its simplest form can be detected in the absence of physical symptoms (see Figs. 2 and 3). There is autopsy evidence of simple silicosis in Vermont granite workers (including several who died of lung cancer) having neither symptoms nor X-ray findings of silicosis (Craighead and Vallyathan, 1980). Extensive research among South African gold miners shows that X-rays only predict about 30% of those with true silicosis when compared to autopsy results. This misclassification (or under-assessment) of disease is reduced when the cumulative exposure to silica dust is high (Hnizdo et al., 1993). Because diagnosing

EBSCOhost - printed on 2/13/2023 4:48 AM via . All use subject to https://www.ebsco.com/terms-of-use

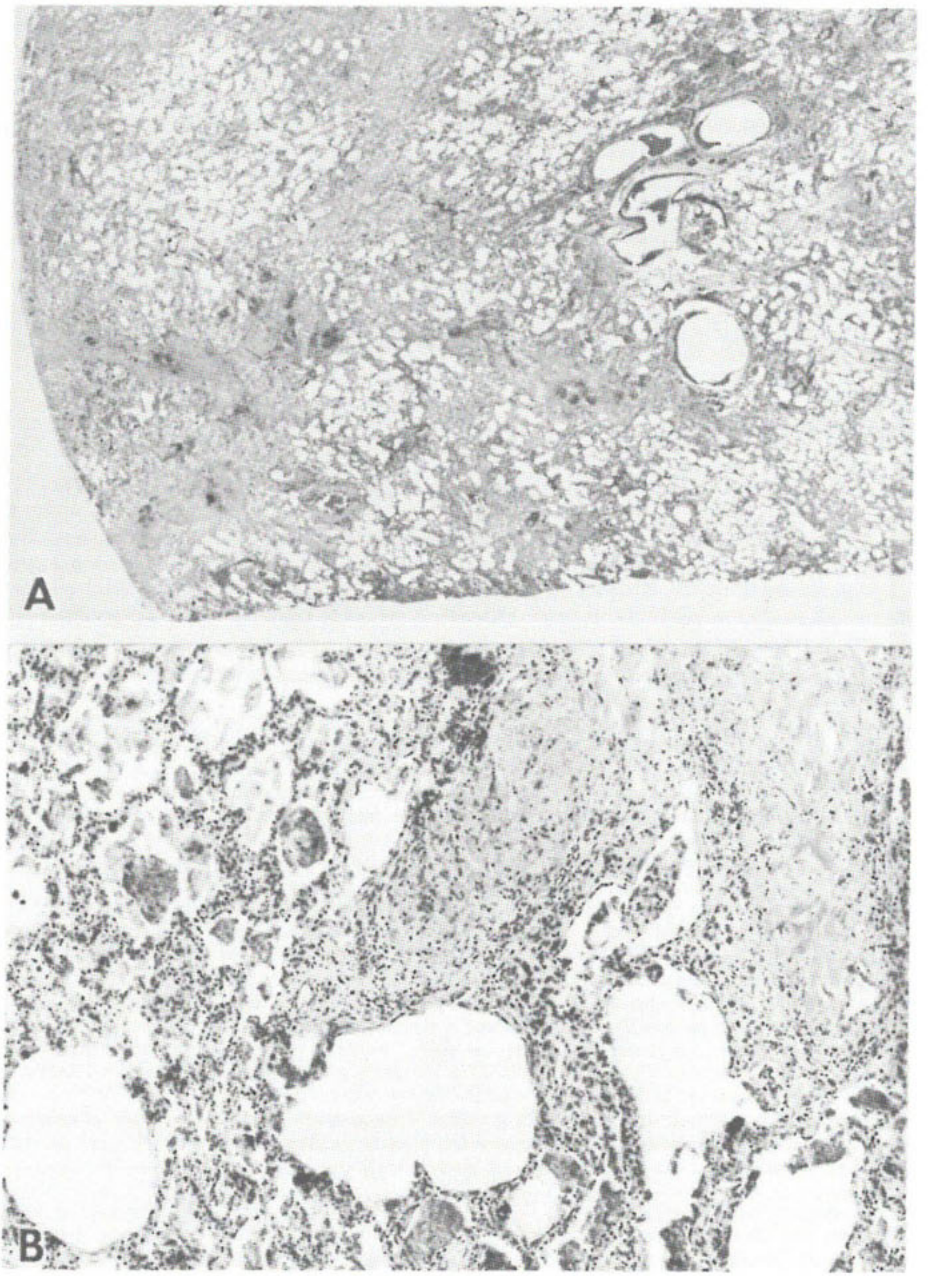


Figure 1. (A) Whole lung section of a worker employed in 1933 digging the Hawk's Nest Tunnel, Gauley Bridge, West Virginia. After 13 months employment, acute silicosis developed and he died 11 months later. From Vorwald Collection, Armed Forces Institute of Pathology (Craighead, 1988, used with permission of the American Medical Association). (B) At higher magnification, the early nodular fibrosis of acute silicosis and associated edema with alveolar proteinosis is visible. Small black dots are the silica dust particles imbedded in the lung. From Vorwald Collection, Armed Forces Institute of Pathology (Craighead, 1988, used with permission of the American Medical Association).

EBSCOhost - printed on 2/13/2023 4:48 AM via . All use subject to https://www.ebsco.com/terms-of-use

F 2,3

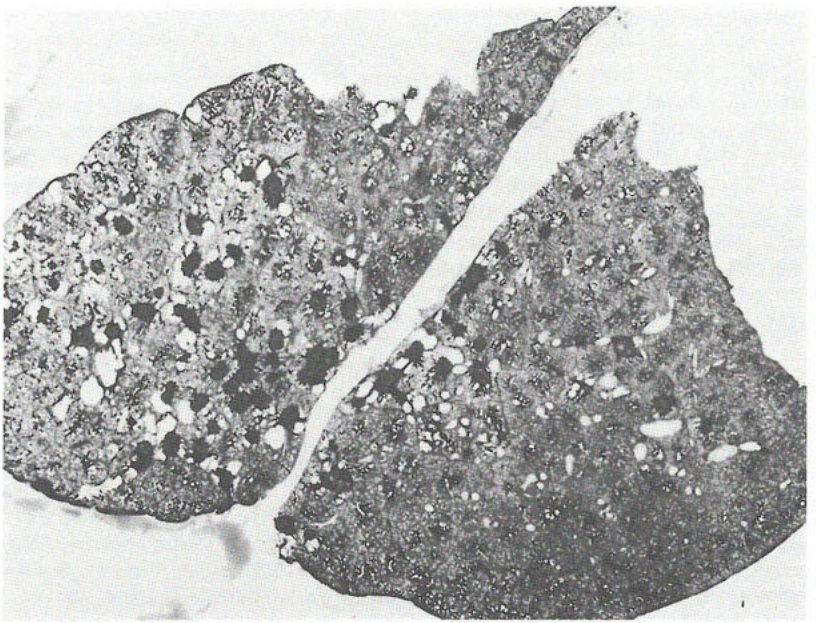


Figure 2. Simple (chronic) silicosis from whole lung section of a 61-year old tin miner from Cornwall, England. In simple silicosis, the fibrotic lesions are usually less than 1 mm in size, are difficult to detect on X-ray and appear in the upper areas of the lung field (Craighead, 1988, used with permission of the American Medical Association).

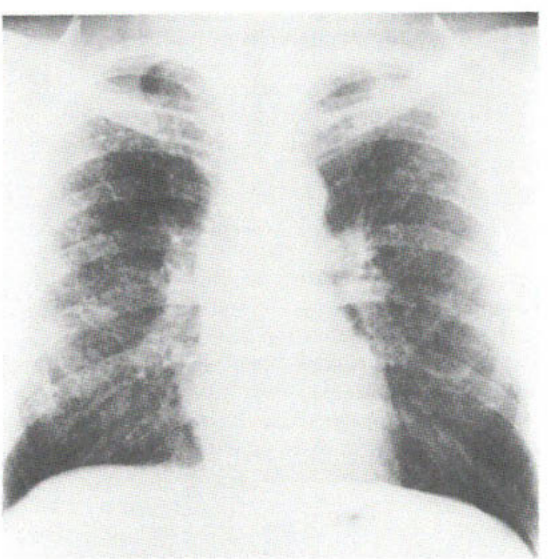


Figure 3. Chest X-ray showing simple silicosis, composed of multiple discrete rounded nodules (~1-3 mm in diameter) primarily seen in the upper mid-zones of the lungs (from Peters, 1986).

EBSCOhost - printed on 2/13/2023 4:48 AM via . All use subject to https://www.ebsco.com/terms-of-use

simple silicosis may be made difficult by confounding from smoking, Hnizdo et al. (1993) and the Surgeon's General Office on Smoking and Health agree that the amount of silica exposure, not smoking habits, are the best predictors of silicosis risk (U.S. Department of Health and Human Services, 1986)

Simple silicosis may progress to produce progressive massive fibrosis [PMF] (compare Figs. 4 and 5), even after workers are removed from exposure to silica dust. PMF is also referred to as complicated or conglomerate silicosis. Figure 6 is the gross evidence of PMF (seen in the upper lobes of the lung) in a granite worker who died with complicated silicosis. Figure 7 shows the X-ray evidence of PMF, with the involvement of the hilar lymph glands and emphysema. Figure 8 is a cross section of lung with PMF, revealing the tendency for the lesion to coalesce (at the top), and also showing that smaller fibrotic nodes can be present (at the bottom). With chronic silicosis small opacities coalesce into larger ones (>10 mm); the result is restricted lung volume, greatly elevated TB risk, decreased pulmonary compliance, and poor gas transfer (Balaan and Banks, 1992).

Complications following silicosis

The major source of co-morbidity with silicosis is infection by *mycobacterium—tuberculosis* (TB). Early descriptions of dust diseases of the lung did not distinguish between TB and silicosis, and as Seaton (1984) noted most fatal cases involved a combination of silicosis and TB. Currently, there is effective therapy for TB, but due to reactivation of old TB infections or the sharing of living quarters with someone who may be infected, TB infection remains a serious complication of silicosis. As an example, when examining mortality risks after filing Workers' Compensation claims in California from 1946 to 1975, male silicotics die of TB at a rate more than 50 times greater than that of the general maleU.S. population (Goldsmith et al., 1993). Because silicosis is prevalent in the dusty trades, it means that it is a disease of working people, many of whom are minorities or recent immigrants to the U.S. from countries where TB is endemic. Thus, preventing silicosis is also a vehicle for preventing TB. Seaton (1984) mentions other opportunistic infections as a consequence of silicosis: *Mycobacterium kansasii, Mycobacterium aviumintracellulare*, nocardiosis, sporotrichosis, cryptococcosis, and aspergillus may invade the injured lung of the silicotic.

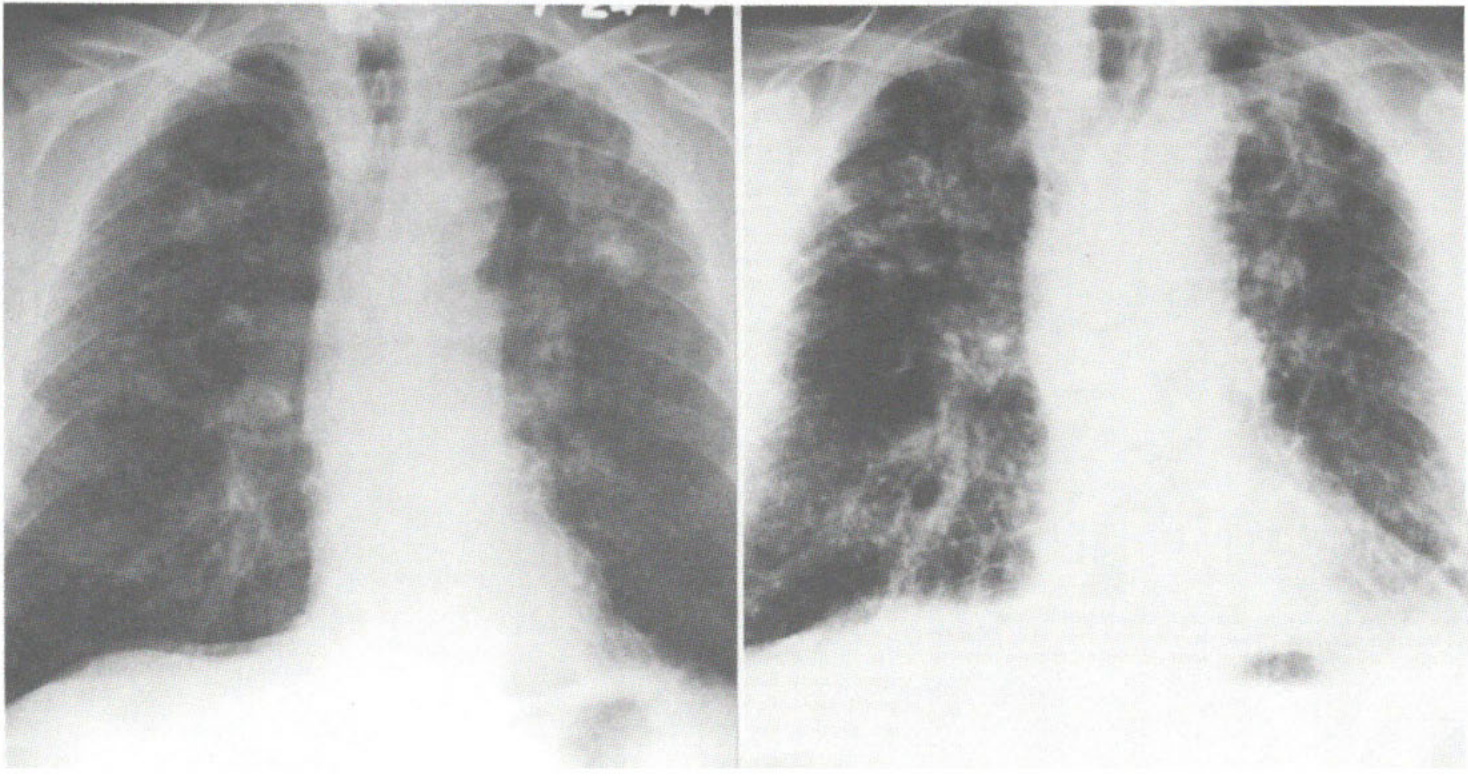
Entry of air through the lung's protective skin produces a collapsed lung, or pneumothorax, which also is a serious complication of PMF. It is rare in simple silicosis, but more common in PMF complicated by emphysema. In addition, the heart muscle is injured, and so another complication of silicosis is enlarge-ment and weakening of the right chambers of the heart. This condition is called *cor pulmonale* and was more common in older silicotics than is seen today.

Silicosis patients have altered immune systems. There have been case reports in the literature linking silica exposure and silicosis with auto-immune disorders and systemic sclerosis, a thickening of the skin with joint and muscle pain and weakness. In the last few years there is increasing evidence from research studies supporting the hypothesis that silicosis is linked to a wide variety of known or suspected auto-immune disorders, including rheumatoid arthritis, systemic sclerosis (scleroderma), systemic lupus, Sjogren's syndrome, and glomerular renal disease (Steenland and Goldsmith, 1994).

Silica's effects on the immune system may also lead to kidney disease and kidney damage. Thus, silicosis may involve complications of several types of kidney disease, including end-stage renal disease requiring dialysis (Goldsmith and Goldsmith, 1993).

EBSCOhost - printed on 2/13/2023 4:48 AM via . All use subject to https://www.ebsco.com/terms-of-use

EBSCOhost - printed on 2/13/2023 4:48 AM via . All use subject to https://www.ebsco.com/terms-of-use



Figures 4 (left) and 5 (right). The chest X-rays taken in 1974 and 1981 of a Vermont granite worker who died in 1982. The first, simple chronic silicosis was scored as a 2/1 by ILO scoring system (ILO, 1980), and the second, scored 2/2, showed the progression of the disease to PMF. Figure 5 shows eggshell calcification around many nodules in both lungs (Craighead, 1988, used with permission of the American Medical Association.)

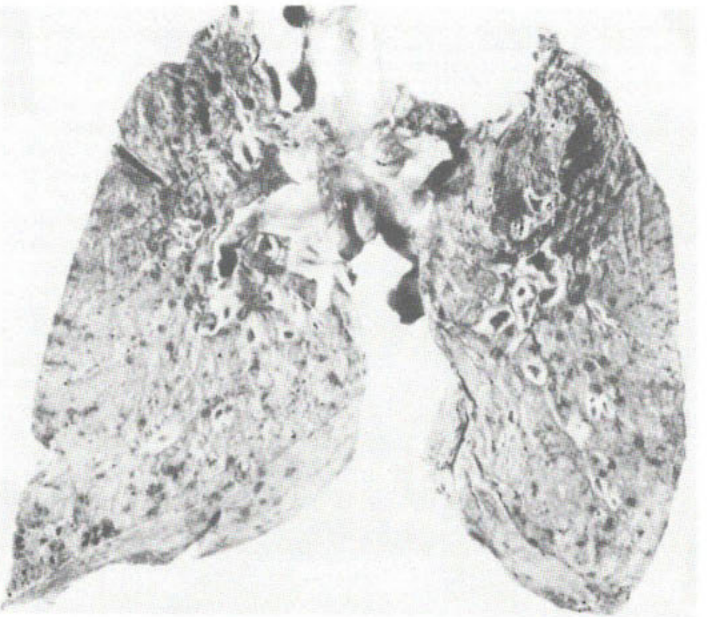
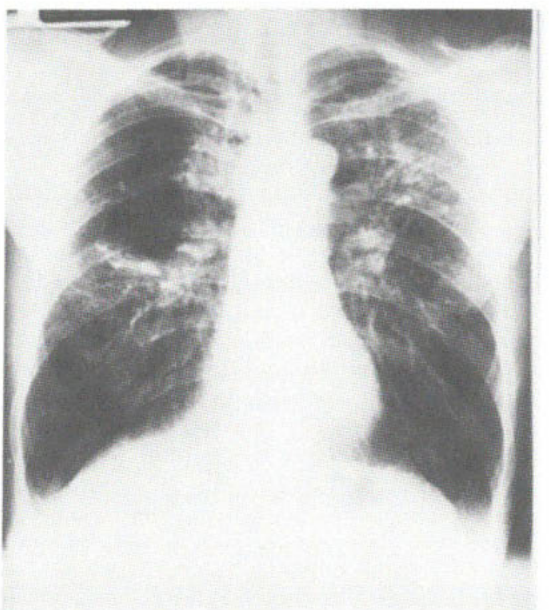


Figure 6 (above). A cross-section of the gross anatomy of the lungs of the granite worker whose X-rays are in Figures 4 and 5. The upper lobe shows the PMF seen in Figure 5 (Craighead, 1988, used with permission of the American Medical Assoc-iation).

Figure 7 (below). Chest X-ray of progressive massive fibrosis (PMF) showing the involvement of the hilar lymph glands, upper lobe conglomerate lesions, and emphysema (from Peters, 1986).



EBSCOhost - printed on 2/13/2023 4:48 AM via . All use subject to https://www.ebsco.com/terms-of-use



Figure 8. Whole lung cross-section of PMF diagnosed in a Welsh slate worker with 35 years of silica exposure. There are numerous well-marked nodules in the massive upper lobe lesion; the rest of the section shows simple and smaller conglomerate lesions of silicosis (Craighead, 1988, used with permission of the American Medical Association).

EBSCOhost - printed on 2/13/2023 4:48 AM via . All use subject to https://www.ebsco.com/terms-of-use

EPIDEMIOLOGY OF SILICA-RELATED DISEASES

What is epidemiology?

Epidemiology is the study of the causes of disease in groups of people. It is the basic science of public health, and its findings along with those in toxicology, medicine, industrial hygiene and statistics tell us the overall effects on health from exposure to environmental and occupational hazards, including silica dust. Epidemiology is a science that makes its judgments on the basis of comparisons, so if one wants to know the effects of silica exposure, one studies the diseases among those exposed to quartz and compares the probability of the same illness or death with a control group. A common control group is the U.S. population, and epidemiologists often ask how different the risk of disease or death is from that of the U.S. population. When this risk is determined, it is called a standardized (for age and sex and time) mortality ratio (SMR). Sometimes it is possible to compare silica-exposed workers to other blue-collar workers or to other unexposed sets of employees over 10 or 20 years in a large plant where silica exposure is only a single component. This type of risk is like a SMR, but is called a relative risk (RR). When there is interest in a single cause of death, such as cancer, epidemiologists compare the degree of exposure to a comparison or control group. This risk measure is called an odds ratio (OR) or a rate ratio (RR). For example, we could select a group of deaths in a mining company from tuberculosis, and we could choose a group of controls (otherwise similar in age, smoking, ioncome, etc.) with other diseases and then determine each group's exposure to silica dust or years underground. This study is called a nested case-control study, and it is a way to determine disease risk without spending time and resources obtaining exposure information on all employees. In so doing, one would be calculating an OR comparing cumulative exposure to dust among cases of TB and controls with other diseases.

When conducting epidemiology research, two critical questions being asked are: (1) Is the risk greater (or less) than the comparison group? and (2) How confident are we that the findings are not due to chance? When the disease or death rate is the *same* in the exposed group and the comparison group, then the risk measure equals 1 (or 100 if the risk is expressed as percentages). When the disease risk in the study group is greater than the comparison group, the risk is greater than 1, or when the exposed group is healthier, the risk is less than 1. A common example is that smokers have a relative risk (RR) of dying of lung cancer of at least 15.0 compared to those who do not smoke, and they have a RR of 1.9 for heart disease compared to those who do not smoke. That means that smokers run a 15 times greater risk of dying of lung cancer than nonsmokers, and that they run about twice the risk of dying from heart disease. One might ask, how sure are we of these figures? There are two common ways epidemiologists have of answering: with confidence intervals (CIs) and with p-values. Both provide an estimated degree of assurance that if a study were repeated, the results would come out the same. Usual minimum level of confidence is 95%, or a 5% probability that a result may be due to chance. Thus, the confidence limits are a measure of spread above and below the risk measure, and if the value 1.0 is not included in the CI, one can conclude that it is "statistically significant." If the 95% CIs around a smoking-lung cancer RR of 15 are 5 and 23 (95% CI = 5, 23), then the risk is significant, and if after the 1.9 RR for heart disease has a p-value of less than <0.01, then we say that there is less than 1/100 probability that the result of this study was due to chance.

Much of epidemiology research focuses on adjusting for differences between comparison groups. These difference factors are called confounding variables. As an example, to determine if silica exposure and lung cancer are related, one has to adjust for

EBSCOhost - printed on 2/13/2023 4:48 AM via . All use subject to https://www.ebsco.com/terms-of-use

differences between groups for factors that might provide alternative explanations for an elevated risk. Some of them, such as smoking, age, and gender are clear cut. Others factors for comparisons of pulmonary function are less obvious, such as race or height or weight. The greatest weakness for industrial epidemiology studies is the lack of contemporaneous exposure data. This weakness is especially true in studies of silica-exposed workers, and thus the development of surrogate measures of dust dose, such as employment duration, is required. Some of the epidemiology studies that follow will use the terminology described above. In case of confusion, the reader may consult either an epidemiology text (e.g., Mausner and Kramer, 1985) or an epidemiologist.

Non-malignant pulmonary effects

Epidemiologic studies of occupationally exposed cohorts provide most of the information about silicosis from inhalation of crystalline silica. There have been occasional case reports of pulmonary ailments suggestive of silicosis secondary to ambient exposure; most of these reports have been from underdeveloped arid portions of the world and are lacking in exposure assessment (Bar-Ziv and Goldberg, 1974; Norboo, 1991; Nouh, 1989; Saiyed, 1991). Furthermore, many of these reports also do not clearly differentiate between outdoor occupational exposures and ambient background environments.

Despite the early clinical knowledge of the threat to workers' pulmonary health discussed above, silicosis has continued to be a problem around the world during this century. Only since the 1940s have dust control measures such as wet-drilling methods gained acceptance. The many occupational reports of silicosis reflect the lack of application of adequate dust control measures. An early investigation by the U.S. Public Health Service of lead and zinc miners in Missouri in 1913 to 1915 found a 60% prevalence of silicosis (Lanza and Childs, 1917).

The U.S. Public Health service also studied Vermont granite workers during the early decades of the twentieth century (Russell et al., 1929). Employees of the granite shed were categorized as to the average dustiness of the work environment: mild (0.3 to 1.8 mg/m^3), moderate (1.8 to 2.4 mg/m^3), marked (2.4 to 3.3 mg/m^3), and massive (3.33 to 5.31 mg/m^3). The approximate crystalline silica content was 35%. Within the dustiness categories the percentage of workers with greater than 20 years of employment was 36, 31, 59, and 55%, respectively. The presence of silicosis was diagnosed by history and physical examination and supported by thoracic radiographs. Symptoms included cough, shortness of breath, chest pains, and pulmonary rales and ronchi. The dust exposure pattern may be presented with two gradients of increasing exposure: time, as measured by duration of employment; and dustiness, as measured by particulate levels. In the most heavily exposed group, some cases of silicosis appeared with as little as two years of exposure; all had some degree of silicosis after four years of exposure. Russell et al. (1929) felt that in the moderate and marked categories there was a qualitative increase in the proportion with silicosis depending on the intensity of dust exposure. In the lowest dust category, silicosis was less prevalent and took longer to develop. No consideration was given to smoking habits, but this is unlikely to have been an important factor as the prevalence of cigarette smoking was lower in the first quarter of the twentieth century than in later periods (U.S. Department of Health and Human Services, 1986).

Later studies of the Vermont granite shed workers (Theriault et al., 1974a,b; Theriault and Peters 1974) demonstrated a decreasing prevalence of silicosis in comparison to earlier research. This improvement occurred after the implementation of basic dust control measures in the 1940s reduced the total respirable dust level to an average of 0.52 mg/m^3

EBSCOhost - printed on 2/13/2023 4:48 AM via . All use subject to https://www.ebsco.com/terms-of-use

and a respirable silica level to an average of 0.05 mg/m^3. Of the 784 workers on which thoracic radiographs were taken, 70% were normal and 30% had some degree of fibrosis. Regular circular opacities were considered evidence of silicosis; their size and number tended to increase with greater dust exposures of longer duration. These chronic silicosis-related opacities were found in 19% of the abnormal radiographs. The remainder of the opacities were irregular and considered to be related to tobacco smoking, rather than dust exposure. This study also demonstrated the lack of diagnostic sensitivity of X-rays because pulmonary function changes could demonstrate ventilatory impairment 13.5 years before radiographic evidence appeared.

In a study of silica flour miners and millers evaluated by radiography, spirometry, and questionnaire, a team of NIOSH researchers found 26% had radiographic evidence of simple silicosis (Banks et al., 1981). Furthermore, 11% had evidence of PMF silicosis after 1 to 14 years of employment. The average length of exposure was not significantly different for the two silicotic groups; actual airborne silica concentrations were not reported. NIOSH industrial hygienists reported that total dust consisted of 99% crystalline silica, and 85% of the samples exceeded the NIOSH recommended exposure limit (REL) for crystalline silica of 0.05 mg/m^3 (Banks et al., 1981).

In 1985 Ng et al. (1985) described a number of cases of silicosis in Hong Kong jade workers exposed to silica flour during the polishing process. Early onset and rapid disease progression were noted. Respirable dust samples were found to contain 89% crystalline silica. Time weighted average (TWA) total dust concentrations varied depending on whether ventilation control efforts were functional (1.01 mg/m^3) or not (5.62 mg/m^3); respirable dust concentrations were 0.34 mg/m^3 and 0.72 mg/m^3 under the same conditions. These were case reports and did not reflect prevalence. In later reports Ng and co-workers used Hong Kong silicosis registry reports to describe development of silicosis in workers from other industries such as granite workers and underground construction employees (Ng and O'Kelly, 1987; Ng et al., 1987).

Landrigan et al. (1986) studied silicosis in iron foundry workers. The prevalence of silicosis increased from 17% in workers with less than 20 years of occupational exposure to greater than 50% in workers with more than 20 years of occupational exposure (Landrigan et al., 1986). Geometric mean respirable crystalline silica measurements were reported for various job categories at different sampling points: 1977, 1980, and 1983. A clear trend of decreasing exposure levels over time was evident, but there was no attempt beyond qualitative presentation to describe exposure levels resulting in silicosis. The highest exposure level was for coremakers in 1977, 1.05 mg/m^3, which decreased to 0.06 mg/m^3 by 1983. The lowest level was in sand preparation in 1977, 0.07 mg/m^3, settling in 1983 to <0.04 mg/m^3. Cigarette smoking habits were examined; the authors concluded that smoking may aggravate symptomatology but does not contribute to causation (Landrigan et al., 1986).

Since 1935 North Carolina has monitored the respiratory health of workers in that state's "dusty trades." Using this registry, Rice et al. (1986) performed a case-control study of 216 male silicotic workers versus 672 nonsilicotics. Four estimated exposure categories were constructed from exposure histories. The lowest category was considered a referent category which was close to zero; average quartz levels in the remaining categories 1, 2, and 3 were 0.09 mg/m^3, 0.225 mg/m^3, and 0.83 mg/m^3, respectively for a 40-year working history. Odds ratios (ORs) were used to compare the risk of silicosis for each exposure category to the referent category, and a dose-response effect was

EBSCOhost - printed on 2/13/2023 4:48 AM via . All use subject to https://www.ebsco.com/terms-of-use

observed. Compared with no exposure, the risk rose from 0.87 in Category 1 to 1.93 in Category 2 to 4.00 in Category 3 (χ^2 significant for trend). The increase was non-significant in category 1 and significant in categories 2 and 3. Smoking was assessed, but found not to influence the risks of silicosis (Rice et al., 1986).

Thomas and Stewart (1987) qualitatively ranked dust exposure levels for various job categories of pottery workers in the U.S. at a single company (none, low, high). The inclusion requirements were a minimum of one year of employment between 1939 and 1966. An increase in non-malignant respiratory disease mortality was observed in the highest exposure category (SMR = 226). The risk of respiratory disease also increased with years of employment. Again no information on smoking habits was available (Thomas and Stewart, 1987).

Checkoway et al. (1992, 1993) in studying diatomaceous earth workers at three sites (Lompoc, CA; Basalt, NV; Quincy, WA) developed an exposure matrix to describe qualitatively the exposure intensity in the calcining plant and patterns of change over time. The authors observed an increase in the mortality rate of non-malignant respiratory disease (NMRD), which they used in place of silicosis. This was done because they relied on information culled from death certificates where silicosis is uncommon. They found an increasing risk from NMRD with increasing exposure after a 15-year lag (Checkoway et al., 1992, 1993). The relative risks were 1.00, 1.13, 1.58, and 2.71 for the lowest to highest exposure levels. Exact exposure measurements were not provided and are the subject of ongoing investigation evaluating asbestos, quartz, and cristobalite.

Hnizdo and Sluis-Cremer (1993) examined the incidence of silicosis in a cohort of white South African goldmines. Miners included in the study had 24 years of occupational exposure between 1940 and the early 1970's. Evaluation was by radiography and follow-ups were continued until 1991. Radiographic pulmonary lesions were classified by standardized methodology (ILO, 1980). Fourteen percent of the miners developed silicosis; the average age of onset was 55.9 years, and 57% of the silicotics developed radiologic lesions after 7.4 years of exposure. The risk of silicosis increased exponentially as the cumulative dose increased above 7 mg/m^3-years. The highest exposure level, was 15 mg/m^3-years, which would be equivalent to 37 years of gold mining at a respirable dust concentration of 0.4 mg/m^3. At this level it was estimated that 77% of the miners would develop silicosis. Unlike other studies, Hnizdo and Sluis-Cremer (1993) found that latency was independent of dose and the risk of silicosis was more dose dependent than time dependent.

Steenland and Brown (1994) conducted a high-quality study of silica dust exposures and mortality among goldminers from South Dakota during the years 1940 to 1990. Overall, the SMR for nonmalignant respiratory diseases was 1.86 (95% CI = 1.58, 2.16); there were significant excesses for asthma with a SMR of 2.61 (95% CI = 1.09, 5.61), and for pneumoconioses, including silicosis with a SMR of 2.61 (95% CI = 2.11, 3.20). Comparing silica exposure <8000 dust days to >48,000 dust days, the risk of silicosis rose from 1.79 to 8.87—a significant increase of five times the risk from the lowest to the highest exposure.

The results of epidemiologic studies consistently show a graded response to either cumulative dust exposure or to length of employment in dusty jobs or industries. It is clear that high level exposure over time (usually decades) or cumulative silica dose can result in a sizable fraction of workers developing silicosis. As stated in the U.S. Surgeon General's Report on Smoking in the Workplace, simultaneous exposure to other agents (such as

EBSCOhost - printed on 2/13/2023 4:48 AM via . All use subject to https://www.ebsco.com/terms-of-use

smoking) appears to have less effect on the onset and/or progression of silicosis than the degree of respirable dust exposure (U.S. Department of Health and Human Services, 1986). Despite the fact that there is still evidence of silicosis in mines and factories where silica is used in the developed world, the apparent trend is towards an absolute reduction in the number and rate of industrial fibrosis in the U.S. (Frazier and Sundin, 1986).

In summary, three types of silicosis have been identified. The most common form of silicosis is the chronic or simple silicosis from prolonged quartz dust exposure at low doses. Acute (silicoproteinosis) and accelerated silicosis are both related to more intense exposures of shorter duration. All three varieties of silicosis have been observed with occupational exposure but not with ambient quartz exposure. The differentiation between acute and accelerated silicosis may not be clear and likely represents a continuous spectrum of human response rather than "clear-cut" arbitrary categories. Symptoms are variable, and with simple silicosis there is often no health impairment nor symptoms. As fibrosis progresses in any form of silicosis, symptoms develop, including chronic cough, dyspnea, and reduced pulmonary function. Silicosis can eventually result in respiratory failure and/or a type of heart disease called cor pulmonale.

Miscellaneous noncancer effects

As noted above, there have been repeated observations detecting an association between silicosis and tuberculosis (TB). Goldsmith and co-workers (1993) evaluated the mortality risk in a group of California employees filing Workers' Compensation claims for silicosis, and the SMR for TB was 56.35 (95% CI = 41.10, 75.40). Steenland and Brown (1994) examined the mortality from TB by cumulative silica dust exposure, and they found a highly significant SMR of 3.44 (95% CI = 2.44, 4.69). In addition, these two investigators demonstrated a dose-related gradient that rose from 0.52 for <8,000 dust days to 6.95 for >48,000 dust days. This association brings into question whether there is a localized immunosuppresive phenomenon or merely secondary infection of damaged pulmonary tissue. The idea that silica may be immunosuppresive is supported by the finding that quartz impairs macrophage function, and these cells are important to cell-mediated immunity. In turn, cell-mediated immunity is critical in the defense against infection by *Mycobacteria sp.*

Immunological effects of silica are supported by reports and studies showing associations between silica-exposed occupations and progressive systemic scleroderma, rheumatoid arthritis, and other immune markers. The U.S. gold miners cited above (Steenland and Brown 1994) had an SMR for musculoskeletal disease (including lupus and sclerosis) of 2.14 (95% CI = 1.03, 3.94), and an SMR for diseases of the skin (including scleroderma) of 2.45 (95% CI 1.17, 4.51). A study of U.S. granite workers (Steenland et al., 1992) found a significant excess of mortality from arthritis (proportionate mortality ratio of 2.01 (95% CI = 1.17, 3.21). Steenland and Goldsmith (1994) suggest that silica exposure may act directly on the immune system, and that more health surveillance may be needed to assess the strength of the association. From a research perspective, there is insufficient information to determine whether these reports are separate effects from silica exposure or sequalae of early stages of silicosis (Balaan and Banks, 1992), though it is interesting to note that scleroderma and other autoimmune illnesses among silica-exposed workers are being compensated in Ontario (Industrial Disease Standards Panel (ISDP), 1992).

As yet there are no indications that chronic crystalline silica exposure results in reproductive or developmental impairment in humans or in animals. Because the primary effects

EBSCOhost - printed on 2/13/2023 4:48 AM via . All use subject to https://www.ebsco.com/terms-of-use

of crystalline silica are contained at the site of entry—the respiratory system—it is unlikely that either reproductive or developmental impairment will be observed in the future.

CARCINOGENICITY OF CRYSTALLINE SILICA

In 1987 the International Agency for Research on Cancer (IARC) judged the evidence as *sufficient* for crystalline silica to be a carcinogen in laboratory animals and the evidence for carcinogenicity as *limited* in humans on the basis of epidemiologic reports available at that time. Thus, crystalline silica has been classified by IARC as a probable human carcinogen. Additional experimental and occupational epidemiologic research studies (Simonato et al., 1990; Goldsmith et al., 1993; Saffiotti et al., 1993; Goldsmith, 1994) published since IARC's review have reinforced the need for concern regarding the association between crystalline silica exposure and cancer, particularly lung cancer.

IARC's conclusion that crystalline silica is a probable human carcinogen was based on sufficient evidence of its carcinogenicity in one species of experimental animals—rats—and suggestive evidence in other animal species and in silica-exposed workers (IARC, 1987). In 1988 the Science Advisory Panel for California's Proposition 65 judged quartz to be carcinogenic in the the form of respirable airborne silica, and added quartz to the list of chemicals requiring warning labels (Proposition 65, 1988). California's Toxicology and Risk Assessment Section (TRAS) of the Department of Health Services has classified crystalline silica as a B1 carcinogen (California Air Pollution Control Officers Association (CAPCOA), 1991), i.e., a probable human carcinogen, using the U.S. EPA's classification scheme (U.S. Environmental Protection Agency, 1986). On the basis of IARC's evaluation, NIOSH and the National Toxicology Program also consider silica to be a carcinogen (U.S. Department of Labor, 1989).

This review is intended to be a comprehensive update of the literature, and is an expansion of that presented by Ross and colleagues (1993) and by Goldsmith (1994). Most of the focus will be on epidemiology studies of lung cancer risk among silica-exposed workers and among those with silicosis. Because of its importance to the assessment by IARC and other expert bodies and agencies, animal tumor findings will also be reviewed briefly.

Animal tumor research on silica

Five studies (of four experiments) provide evidence of a carcinogenic effect in laboratory rats from inhaled crystalline silica (Holland et al., 1983; Dagle et al., 1986; Holland et al., 1986; Muhle et al., 1989; Spietoff et al., 1992). The results of Holland et al. (1983, 1986) and Dagle (1986) were used by IARC (plus additional toxicolgy and tumorigenicity data) during the expert evaluation of silica's carcinogenic potential (IARC, 1987). However, the two most recent studies (Muhle et al., 1989 and Spietoff et al., 1992) were published subsequent to the evaluations of IARC and Proposition 65. Saffiotti and coworkers have reviewed these studies and recent research on silica's carcinogenic potential and mechanisms linking fibrogenicity and carcinogenicity (Saffiotti et al., 1993)

Inhalation studies using Fisher 344 rats exposed to crystalline silica demonstrated increased rates of lung tumors compared to unexposed control animals, as well as increased fibrotic lung changes. These studies also suggest that female rats are at greater risk than male rats. With the exception of Spietoff et al., the rodent studies fail to demonstrate a linear relationship between silica exposure doses and tumor rate. Studies of inhalation of crystalline silica in other animal species besides rats are scarce. Most experimental silica

EBSCOhost - printed on 2/13/2023 4:48 AM via . All use subject to https://www.ebsco.com/terms-of-use

studies in other species have used intratracheal injection (due to greater convenience of administration) and suggest variable species response to silica exposure because tumor rates are not uniform (Saffiotti, 1986). Hamsters appear more resistant to silica's carcinogenic and fibrogenic effects than rats (Saffiotti, 1986, 1992). The differential effect of crystalline silica on specific genetic strains of rats has not been examined; all but one study used the same variety of rat, Fisher 344. It is worth noting that Wagner and colleagues used several different polymorphs of silica and different strains of rats and consistently produced histiocytic lymphomas (cancers of the lymph system) via pulmonary injection proceedures (Wagner et al., 1980).

Although silica was judged by IARC to be a weak mutagen in short-term bioassays (IARC, 1987), new work by the U.S. National Cancer Institute indicates that quartz binds to DNA and is found in the nucleus of fetal rat lung epithelial cells (Saffiotti et al., 1993). Furthermore, the mechanism of carcinogenic action appears to follow immunohistochemical pathways via the induction of the cytokine transforming growth factor, TGF-β1 (Saffiotti et al., 1993)

Cancer epidemiology research on silica-exposed workers

The question of the carcinogenicity of crystalline silica has been debated in the scientific community since the 1930s. In the 1934, J. Henry Dible, a Liverpool pathologist published a review of 14 autopsied cases of silicosis in which four cancer cases were found, including one female with leukemia, two males with lung tumors (one also having a colon cancer), and a third male with liver cancer. On this basis he suggested a link between silica exposure and cancer (Dible, 1934). From that date until the 1980s there were periodic exchanges in the medical literature concerning the cancer risks among "dusty trades" workers, but most medical opinion held that silica produced lung fibrosis, but not cancer (Wagoner et al., 1963; Hueper, 1966; Ziskind et al., 1976; Selikoff, 1978; Heppelston, 1985; Craighead, 1988).

In the past 10 to 15 years, the link between silica exposure and cancer risk has undergone a transformation, and it started with a 1982 article in which evidence for lung cancer risks among silica-exposed workers and among laboratory animals were evaluated (Goldsmith et al., 1982). Since Goldsmith and colleagues raised the issue, researchers and agencies have given consideration to an alternative view: that silica may be a human carcinogen (IARC, 1987; Proposition 65, 1988; Simonato et al., 1990; Goldsmith et al., 1993). The foundation for this position is based on laboratory animal findings (Saffiotti, 1992; Saffiotti et al., 1993) and excess pulmonary cancer risks among silica-exposed workers, particularly among silicotics (summarized by Goldsmith et al., 1986; Amandus et al., 1991; Pairon, 1991; Goldsmith, 1994).

This review will canvas the cancer epidemiological research focusing on dusty trades workers and among silicotics. For the most part, the literature focuses on lung cancer, but other tumor sites, including lymphatic and gastrointestinal malignancies are relevant to this assessment. There are several salient points concerning the interpretation of these studies: the correlation of industrial hygiene data or any surrogate estimate of dust exposure or "dose" (such as length of employment); the means by which smoking is adjusted; and the presence of confounding from radon and other sources as possible explanations for any observed cancer risk.

Because occupational silica dust exposure is common in many dusty industries and occupations, the results of studies of workers are crucial for understanding the relationship

EBSCOhost - printed on 2/13/2023 4:48 AM via . All use subject to https://www.ebsco.com/terms-of-use

between quartz exposure and cancer risk (Goldsmith et al., 1986). This review is organized so that similar occupations can be examined together, i.e., general silica exposure; mining and quarrying; granite industry; ceramics and glass industry; and foundry work. Tables are included to assist the reader in evaluating the extent of association between silica and lung cancer.

Studies of generalized silica exposure

Dubrow and Wegman (1984) examined the mortality of all silica exposed workers in Massachusetts who died from 1971 to 1973 using a mortality odds ratio (MOR) adjusted for social class. They reported a MOR of 155 for respiratory cancer for ages 20 to 64. Based on a preventive medicine survey of nearly 250,000 workers conducted from 1950 to 1960, Neuberger et al. (1986) and Neuberger and Kundi (1990) conducted a follow-up study of 1,630 males employed in Vienna, Austria's dusty industries: foundries (employing about 50% of the sample), metal working, glass, ceramics, brick, stone, and other dusty trades. The authors compared the group with the mortality of Viennese male population and also compared it to a control group of unexposed men who were also enrolled in the same survey. The dust exposed workers had a lung cancer SMR of 148 ($p < 0.001$), while controls had a SMR of 110. They also reported SMRs for cancers of the following sites: stomach SMR = 161 ($p < 0.01$); and larynx SMR = 143. In the 1990 update the authors found significantly elevated lung and stomach cancer mortality for the cohort as a whole and for all industry groups (Neuberger and Kundi, 1990). The authors argued that confounding exposures were not an explanation of the lung cancer risk, and that silica and other respirable particulates were the likely explanation of the cancer excess (Neuberger et al., 1986; Neuberger and Kundi, 1990). However, there were no silica dust levels or smoking data available for analysis.

Siemiatycki et al. (1990) described a multi-use, multi-cancer case-control incidence series undertaken in Montreal, Canada that enabled the researchers to test the association between many different occupations having quartz exposure and cancer risk. Male cancer patients, aged 35 to 70 from Montreal were interviewed to obtain detailed work histories, and industrial silica exposures were translated by industrial hygienists for data analysis. The highest risks for silica exposure were among subjects with oat cell carcinomas of the lung (rate ratio [RR] = 1.4; 95% CI = 0.9-2.4), and squamous cell carcinomas of the lung (RR = 1.5; 95% CI = 1.0-2.1). Lifetime smoking levels appear to show a multiplicative effect of both exposures. The authors estimated that 7.4% of nonadenocarcinoma of the lung were attributable to silica dust exposures.

Hours and co-workers found a tobacco-adjusted Mantel-Haenszel OR of 1.89 (95% CI = 0.99, 3.52) for general silica exposure in a case-control study of lung cancer in the Lyon region of France (Hours et al., 1991).

Cancer risks and metal ore mining

Metal ore miners constitute one of the largest industrial groups occupationally exposed to silica dust. Underground miners are exposed to high levels of quartz during drilling, processing, and from many other jobs. Metal ores are often found in deposits having high quartz concentrations and, without proper exhaust, wet methods, and air recirculation, underground mining operations produce significant levels of respirable dust. As an example, Beadle and Bradley (1970) presented industrial hygiene data on the gold mines of South Africa. They estimated that 60 to 80% of the mined ore rock is quartz and about 30% of free silica is present in the respirable mine dust (Beadle and Bradley, 1970).

EBSCOhost - printed on 2/13/2023 4:48 AM via . All use subject to https://www.ebsco.com/terms-of-use

Respirable silica dust concentrations have ranged from 0.05 to 0.84 mg/m^3 in South African underground gold mines since the 1930s (Hnizdo and Sluis-Cremer, 1991). The high quartz levels are backed up by a recent survey showing persistently elevated silicosis risks among white South African gold miners (Hnizdo and Sluis-Cremer, 1993).

The initial concern about pulmonary cancer arose from the observations of Agricola in the 16th century that Schneeburg metal ore miners were dying of lung diseases (Agricola, 1556), which were later confirmed to be respiratory tumors (Darby and Samet, 1994). It was subsequently determined that radium ore decay products were the causes of high numbers of lung cancers. Contemporary miners are also exposed to diesel fumes, arsenic, and other occupational hazards that may confound any association with silica exposure. Of particular importance is gold ore mining, which often occurs in rock deposits containing high levels of quartz.

Metal ore miners (excluding coal, uranium, and asbestos miners) have been shown to have excessive lung cancer risks in four descriptive studies. Using Washington State death certificates from 1950 to 1971, Milham (1976) reported a significant excess proportionate mortality ratio (PMR) of 179 ($p < 0.05$) for cancers of the respiratory system among miners. Peterson and Milham (1980) reported that mine operatives and laborers dying in California from 1959 to 1961 had a PMR of 241 for ages 20 to 64. Williams et al. (1977) calculated odds ratios (OR) for the mining industry from the U. S. Third National Cancer Survey Study (1969 to 1971), adjusting for age, race, education, tobacco, alcohol and geographic location, and they reported an OR for pulmonary cancer of 1.77($p < 0.05$), and an OR of 5.2 for prostate cancer ($p < 0.05$). White male miners and drillers in California had a SMR of 217 ($p < 0.05$) for cancer of the trachea, bronchus, and lung, adjusted for smoking, alcohol, and socioeconomic status during 1979 to 1981 (Singleton and Beaumont, 1989).

Kjuss and colleagues conducted a case-referent study of lung cancer among 176 Norwegian males and an identical number of controls to assess which occupations showed elevated risks (Kjuss et al., 1986). They reported that the occupational group composed of mining and quarry work had a smoking-adjusted risk of 10.2 (95% CI = 2.0, 52.1). Lynge et al. (1990) used the Nordic census-based occupational registries to describe the lung cancer incidence and mortality risks for miners in Norway, Sweden, and Finland. Norwegian iron ore miners had a rate ratio (RR) of 1.36. Swedish iron ore miners had a significant RR of 3.19 (95% CI = 2.92-3.49), while other ore miners had a RR of 3.71 (95% CI = 3.1-4.44). In Finland there was a nonsignificant RR of 1.78 for iron ore miners, and a significant risk of 5.02 (95% CI = 3.11-7.68) for non-ferrous ore miners (Lynge et al., 1990).

Table 1 summarizes the general studies of miners and the ore-specific findings. Wagoner and colleagues studied a cohort of 1759 white male metal ore miners with generally low radon exposures. Follow-up was from 1937 through 1959, and the authors reported significant SMRs of 292 and 149 for respiratory and digestive cancers. They examined several factors, including smoking, immigration, urbanization, autopsy rates, and rejected them as possible causes. They also considered silica exposure, but consistent with medical views in the 1960s, rejected it. This determination was made despite the elevated mortality rates for TB, heart diseases, influenza and pneumonia, which are all consistent with strong effects of quartz dust exposure.

Costello (1983) conducted a retrospective cohort mortality study from 1958 to 1975 of U.S. metal ore miners employed in 50 different mines in 16 states. The study was a

EBSCOhost - printed on 2/13/2023 4:48 AM via . All use subject to https://www.ebsco.com/terms-of-use

Table 1. Summary of epidemiologic studies of lung cancer risk among metal ore miners

Authors (year) Country	Ore types	Risk Measures (95% CI/p value)	Comment
Wagoner et al. (1963) U.S.A.	Not specified	SMR=292 (p<0.01)	Digestive cancer SMR=149 (p<0.01); no smoking data; radon unlikely; no silica measures
Costello (1982) U.S.A.	All	SMR=127 (117-137)	Smokers and exsmokers show increased risk; no exposure measurements
	Lead-zinc	SMR=134 (102-174)	
	Mercury	SMR=355(177-635)	
	Chromium	SMR=347 (112-810) Matched OR=5.0 (0.6-24.9)	
	Gold & silver	Matched OR=9.0 (1.2-332.0)	
Amandus & Costello (1991) U.S.A.	All-silicotics	SMR=1.73 (0.94-2.90)	No silica exposure measurements; significant excess for current smokers; no confounding by radon
	All-nonsilicotics (NS)	SMR=1.18 (0.98-1.42)	
	All NS <20yrs	SMR=1.05 (0.82-1.31)	
	All NS ≥20 yrs	SMR=1.52 (1.10-2.03)	
	Mercury	SMR=2.66 (1.15-5.24)	Smoking explains risks of 1.3 only
	Copper	SMR=1.20 (0.87-1.61)	
	Lead-zinc	SMR=1.26 (0.86-1.29)	
Muller et al. (1983) Ontario, Canada	"mixed ores" some gold and other metals; excluded uranium	SMR=1.45 (p<0.001)	No exposure measurements; no adjustment for smoking; assumed to have low radon levels
Axelson & Sundell (1978) Sweden	Zinc-lead	SRR=16.6 (7.8-35.3)	With prior history of mining, the risk was greater among nonsmokers than smokers
Fox et al. (1981) Cornwall, U.K.	Tin Total Underground Surface	SMR=117 SMR=211 SMR=74	Stomach SMR=200; no silica exposure measures; assumed to be related to radon; "unlikely to be due to smoking."
Fu et al. (1994) Dachang, Guangxi Province, China	Tin Underground Silicosis Unconditional log. regression	OR=2.43 (1.40-4.21) OR=2.03 (1.25-3.29) Years of dust exposure and smoking (p<0.0001)	Radon negligible factor; no interaction between smoking and dust exposure
Carta et al. (1994) Sardinia, Italy	Lead-zinc Mine A (lo silica;↑radon) Mine B (↑silica; lo radon)	SMR=112 (71-166) SMR=128 (74-142) SMR=85 (34-175)	Trends for duration of employment in both mines; risk for airways obstruction, adjusted for age and smoking
Edling (1982) Sweden	Not specified	SRR=16.6 (7.7-35.3)	Compared underground miners with unexposed; no exposure information; radon and smoking possible causes

EBSCOhost - printed on 2/13/2023 4:48 AM via . All use subject to https://www.ebsco.com/terms-of-use

follow-up of a cross-sectional silicosis study conducted by the U.S. Public Health Service and the U.S. Bureau of Mines between 1958 and 1961 (U.S. Department of Health, Education and Welfare (DHEW), 1963). The original cohort consisted of 13,007 men involved in non-uranium metal ore mining. Costello (1983) examined white miners at risk for silicosis who mined eleven different metal ores or combinations of ores. Although there were no ore-specific silica dust concentrations presented, quartz constituted up to 40% of the airborne and settled particulate for all 50 mines surveyed (U.S. DHEW, 1963). These miners had elevated SMRs for all cancers of the respiratory tract and for cancer of the trachea, bronchus, and lung, but digestive tract cancers were significantly reduced (Costello, 1983).

Miners who smoked at the time of the 1958-61 USPHS survey exhibited a much higher risk of dying from respiratory cancer and lung cancer, compared to miners who did not smoke. By comparison, nonsmoking and exsmoking miners had significantly decreased SMRs of 35 and 57 for respiratory cancer. It is important to note that 85.1% of the entire cohort had a history of smoking. Thus, any elevated SMRs for lung cancer in the cohort could be due to confounding by smoking (Costello, 1983).

Costello used a matched, nested case-control analysis to further assess the lung cancer risk by type of ore, and demonstrated the following odds ratios (OR) organized by ore type: gold and gold silver (OR = 9.0; 95% CI = 1.2-332.3), chromium (OR = 5.0; 95% CI = 0.6-249.0), mercury (OR = 2.5; 95% CI = 0.7-10.9), and lead-zinc (OR = 1.63; 95% CI = 0.9-2.9); ORs were <1.0 for iron, and copper ores. Matched OR analysis for lung cancer showed increased risks for airways obstruction, diesel exhaust, and radon daughter exposure, but the risks were not statistically significant (Costello, 1983).

Amandus and Costello (1991) divided the same cohort of white miners into two groups of 369 silicotics and 9,543 miners without silicosis from the 1959-1961 US. Public Health Service study (U.S. DHEW, 1963). The authors excluded miners employed in mines where diesel equipment was used underground. They reported that silicotics had a SMR of 1.73 (95% CI = 0.94-2.90), while nonsilicotics had a SMR of 1.18 (95% CI = 0.98-1.42). Because the cancer risks among silicotics will be discussed below, attention will be focused on the nonsilicotic miners. Paralleling Costello's 1983 finding, smokers had significantly elevated lung cancer risks, and exsmokers and nonsmokers had significantly lowered risks. All ore types had elevated SMRs except iron ore miners; mercury ore miners had a SMR of 2.66 (95% CI = 1.15-5.24). Because diesel equipment was used during mining of chrome ore (reported by Costello (1983) to have an elevated SMR for lung cancer), chrome miners were excluded from this study. For those miners employed less than 20 years, the SMR was 1.05, while those employed 20 or more years had a SMR of 1.52 (95% CI = 1.10-2.03). Metal ore miners employed where radon levels were low had a higher SMR of 1.26 compared to those employed in higher radon mines (SMR = 1.04), although neither was significant (Amandus and Costello, 1991).

Muller et al. (1983) conducted a large mortality study of 50,201 Ontario, Canada, miners followed from 1955 to 1977. These authors evaluated the cancer risk for miners of nongold ores in Ontario. These ores include nickel copper, iron ore, "other ores," and "mixed ores." Of the 11,337 nickel-copper miners, there was only a nonsignificant SMR of 327 (based on three cases) for nasal cancer. There were too few deaths or person-years for any mortality excesses among the 1,735 iron ore miners. This limitation of small sample size was true for the 1,118 "other ore" miners. However, the cohort of 7,125 full-time underground "mixed ore" miners had a mortality profile very much like that for gold miners (see below): along with significant excesses of silicosis and other nonmalignant

EBSCOhost - printed on 2/13/2023 4:48 AM via . All use subject to https://www.ebsco.com/terms-of-use

respiratory diseases there was a highly significant SMR of 1.45 (see Table 1) for cancer of the trachea, bronchus, and lung ($p = 0.00078$) (Muller et al., 1983).

Lung cancer excesses have been reported in several metal ore mining groups; French iron ore miners (Roussel et al., 1964), British hematite miners (Boyd et al., 1970), Canadian flourspar miners (de Villiers and Windish, 1964), Swedish zinc/lead miners (Axelson and Rehn, 1971; Axelson and Sundell 1978), and Swedish iron ore miners (Jorgensen, 1973; St. Clair Renard, 1974; Edling, 1982).

Axelson and Rehn (1971) reported the results of a pilot study of lung cancer from 1956 to 1970 among miners from two adjacent Swedish zinc/lead mines. The authors reported highly significant excesses for both active and former miners compared to death rates for Swedish males, although they were unsure if the etiology stemmed from radon-daughter concentrations or metal ore dusts (including silica). Axelson and Sundell (1978) expanded the pilot study through 1976 and examined smoking using a matched Mantel-Haenszel case-referent approach. Using a local parish register of death, the authors found 29 lung cancer cases and 174 matched referents. Prior history of mining produced a standardized rate ratio (RR) of 16.6 (~95% CI = 7.8-35.3; $p < 0.0001$). Interestingly, the lung cancer risk was higher for nonsmokers than for smokers, and smoking miners worked an average about 50% less than nonsmokers (18 years versus 35 years), and smoking miners died 11 years earlier than nonsmokers. The authors assumed that radiation was the cause of the excess although no silica dust data were presented.

Edling (1982) conducted a similar matched case-referent study as that of Axelson and Sundell (1978), using data from the Swedish mining parish of Grangesberg from 1957 to 1980. Edling (1982) reported an age-standardized RR of 16.6 (95% CI = 7.7-35.3) for underground miners compared to unexposed persons in the parish. Smokers were shown to have a nonsignificant RR of 2.0 using matched pairs analysis. Thus, Edling concluded that the excess was due to radon exposure, although no quartz concentrations were presented.

Fox et al. (1981) assessed the mortality of Cornish tin ore miners followed from 1939 to 1976. Overall there was a SMR of 117 for lung cancer and a SMR of 141 for stomach cancer. When only underground miners were considered, the SMRs rose to 211 for lung cancer and 200 for stomach cancer. Although there were significant mortality excesses for silicotuberculosis and silicosis, the authors attributed the risk to radon exposures in the mines (Fox et al., 1981). Fu and colleagues examined the pulmonary cancer mortality risk for tin miners in Dachang mine in Guagxi Provence, China using case-control methods. Overall, they reported a signficiant OR of 2.43 for underground experience; silicosis had an OR of 2.03. Using unconditional logistic regression, they found the best predictors were years of underground dust exposure and smoking, but the risks were not synergistic. The authors examined the radon daughter levels in the mine, and felt that it did not contribute to the elevated lung cancer risk (Fu et al., 1994).

Two joint studies examined the mortality risks among South Central Chinese miners employed in ten tungsten mines, 6 copper/iron mines, and 4 tin mines (Chen et al., 1992; McLaughlin et al., 1992). Workers had to have completed one year of employment between 1972 and 1974, and their mortality was followed until 1989. For tungsten miners the SMR was 53 ($p < 0.05$), for copper/iron miners the SMR was 104, and for tin miners the SMR was 198 ($p < 0.05$) (Chen et al., 1992). Using a case-control analysis to adjust for age and smoking, McLaughlin et al. (1992) examined the risk by degree of cumulative exposure to respirable silica. There was a significantly negative trend for tungsten miners,

EBSCOhost - printed on 2/13/2023 4:48 AM via . All use subject to https://www.ebsco.com/terms-of-use

no trend among copper/iron miners, and a significant positive trend ($p = 0.004$) among tin miners. The OR rose from 1.5 for low cumulative exposure to silica (0.1-8.69 $\mu g/m^3$/year), to 1.9 for medium cumulative exposure to silica (8.7-26.2 $\mu g/m^3$/year), to 3.1 for high cumulative exposure to silica (>26.3 $\mu g/m^3$/year). The authors examined cumulative exposure to arsenic, polycyclic aromatic hydrocarbons, and radon decay products. Only arsenic produced a significant trend among tin miners, suggesting that arsenic and silica dusts may interact. The researchers also found silicosis to be a significant ($p < 0.05$) risk factor for lung cancer among copper/iron miners with OR = 3.1, and among tin miners OR = 2.0. The authors of both papers concluded that their findings offer only modest support for the silica-lung cancer association, but the results reported for tin miners were not due to smoking, radon, or PAH, but may be related to concomitant arsenic exposures (these studies are not included in Table 1).

The health risks of two cohorts of lead-zinc miners from Sardinia were studied by Carta et. al. (1994). One group of miners was exposed to mine air containing low radon and high silica dust levels (Mine A), with the other mine having elevated radon and low silica levels (Mine B). They found elevated lung cancer risks in Mine B, but not mine A, while the risk for lung cancer in both mines increased according to years underground. The authors concluded that the findings do not support a silica-effect related to lung cancer, though the number of study subjects may have been too small to detect an association (Carta et al., 1994).

Studies of iron ore miners

Jorgensen (1973) examined the lung cancer risk among iron ore miners using the death registry of the Swedish community of Kiruna from 1950 to 1970. Using the total cohort of miners for expected values, he obtained a SMR of 308 (13 observed and 4.2 expected) for underground workers, but dismissed diesel fumes and smoking as explanations. Jorgensen (1973) considered iron oxide, quartz, and radon daughter exposures but presented no dust sampling data.

Higgins et al. (1983) examined the mortality from 1952 to 1976 of 5,751 white male employees of Reserve Mining Company (exposed to iron oxide/taconite dust) compared to that of males from the state of Minnesota. Overall mortality showed a SMR of 87 ($p < 0.056$), strongly indicating a healthy worker cohort effect. Respiratory, digestive, urinary, and genital cancers had SMRs of 84, 114, 101, and 91, respectively (none significant). Total respirable and quartz dust concentrations were developed for all job codes (cumulative total dust exposure), and indicated no trends for respiratory or gastrointestinal cancers. Cumulative silica exposure suggested a modest gradient for lung cancer risk based on small numbers of cases; gastrointestinal cancer showed no response with cumulative silica exposure. Smoking appeared to explain the disease excess in this cohort for all causes, all cardiovascular diseases, and all neoplasms (Higgins et al., 1983).

Lawler and co-workers (1985) conducted a retrospective cohort study of 10,403 white male miners employed in hematite iron-ore extraction for at least 12 months prior to January 1, 1966 in St. Louis County, Minnesota. Cohort follow-up was from January 1, 1937 through December 31, 1978. Mortality results from the study population were compared to expected numbers based on the age-cause-time-specific mortality rates of the U.S. white male population. Iron ore dust and silica dust made-up approximately 20% and 24% of the dust exposure, respectively. No information was provided regarding average total dust concentrations in specific work areas. Except for elevated risks for accidental deaths and emphysema among surface miners, there were no elevated lung cancer SMRs.

EBSCOhost - printed on 2/13/2023 4:48 AM via . All use subject to https://www.ebsco.com/terms-of-use

Boyd et al. (1970) studied the mortality of Cumberland (UK) iron-ore miners by examining the death certificates of 5,811 miners who died between 1948 and 1967. The observed values were compared to an external standard population of local and national men not involved in mining. Radon concentrations were found to be well below permissible levels. Though silica constituted 10 to 12 % of the local iron-ore deposits, there was no specific information on dust concentrations in any of the mines surveyed. Along with excesses of silicosis and tuberculosis there were significant increases in deaths from lung cancer with a SMR = 152, (95% CI = 129-177), There was no mention of the effects of smoking or years employed underground (Boyd et al., 1970).

Radford and St. Clair Renard (1984) investigated cancer mortality from 1951 to 1976 among 1415 Swedish iron ore miners using the Malmberget area parish registry. Cumulative data were collected on radon daughter exposures, man-hours underground, and smoking histories. Smoking-specific Swedish national rates were used to determine expected values. Overall cancer mortality indicated a SMR of 156 ($p < 0.01$), with lung and stomach cancer SMRs of 342 and 189, respectively (both $p < 0.01$). There was no association with a prior diagnosis of tuberculosis or silicosis. Also ruled out as explanations were exposures to diesel exhaust or asbestos. Smoking and radon daughter exposure were additive, and the authors suggested that lifetime radiation exposures at 4 working level months (the current occupational standard for underground mining in the US and Sweden) may need to be reduced to prevent excess lung cancers. Silica dust levels were not assessed (St. Clair Renard, 1974).

Larsson and Damber (1982) conducted a case-control cancer study of nonuranium mining (iron and mixed sulfide ores) and smoking in Northern Sweden. No information of levels of silica exposure were presented. Comparing the 35 lung cancer cases among miners to the 554 cases among nonminers indicated that there was a higher proportion of nonsmokers (11.4% vs 7.6%) among miners and a lower-than-average tobacco consumption. When lifetime smoking levels were stratified into <150,000 cigarettes and >150,000 cigarettes, there was a clearer gradient of risk seen. In fact, miners who have smoked >150,000 cigarettes have an OR of 104.5 (95% CI = 35.3, 309.7) compared to nonsmokers, not employed as miners (Larsson and Damber, 1982). From these data, smoking and mining (including exposure to silica or radiation) may act synergistically (Goldsmith and Guidotti, 1986).

Chen and co-workers (1990) examined the mortality risks during the years 1970 to 1982 of 5,406 male underground hematite miners and 1,038 surface mine workers employed in Longyan and Taochong, China. Forty-two percent of the deaths were due to silicosis, and 20% were due to cancer. Compared with male Chinese rates, there was a SMR of 3.7 for lung cancer for underground workers (95% CI = 2.5, 5.3), with a SMR of 1.2 for unexposed miners. For stomach cancer the SMR was 0.8; for liver cancer the SMR was 0.8; and for esophageal cancer the SMR was 0.6. The greatest lung cancer risk (SMR = 4.8) occurred among miners first employed before the introduction of improved ventilation and wet drilling, with a SMR of 4.2 for heavy exposure to silica dust and radon. Those miners with a prior history of silicosis had a SMR of 5.3, and those with a history of silicotuberculosis had a risk of 6.6. For smokers, the risk rose with level of exposure to silica dust. The authors concluded that the lung cancer risk could not be attributable only to smoking, but given that silica dust and radon exposures overlapped extensively, they could not be evaluated separately.

In general, iron ore miners have some excess lung cancer risks (Jorgensen, 1973; Boyd et al., 1970; Radford and St. Clair Renard, 1984; Lawler et al., 1985; Chen et al.,

EBSCOhost - printed on 2/13/2023 4:48 AM via . All use subject to https://www.ebsco.com/terms-of-use

1990). However, it is unclear whether the risks are due to silica dust or to radon exposures or some combination of exposures. There was a modest dose-response observed in Higgins et al. (1983) for silica exposures, but the number of deaths was small. Based on the work of Larsson and Damber (1982), there is evidence that smoking and underground exposures (to either silica or to radon) among iron ore miners may act synergistically.

Studies of gold ore miners' cancer risk

Table 2 summarizes the lung cancer epidemiology studies of gold ore miners. Four studies (Gillam et al., 1976; McDonald et al., 1978; Brown et al., 1986; Steenland and Brown, 1994) examined the health risk to workers employed at the Homestake gold mine in Lead, South Dakota. The miners were exposed to silica dust and a fibrous amphibole, cummingtonite-grunerite (CG). Gillam et al. (1976) conducted a retrospective cohort study of 440 male miners from the Homestake gold mine in South Dakota identified during 1958-1961 by the U.S. Public Health Service study (U.S. DHEW, 1963) who were employed for at least 5 years underground and who had never worked in another underground mine. These men were followed from 1960 to 1973, and a significant SMR of 370 ($p < 0.01$) was calculated for pulmonary malignancies (Gillam et al., 1976). Crystalline silica concentrations were not apparently elevated and the following were present in trace concentrations: arsenic, chromium, and nickel; radon daughters were not detected. The authors postulated that the lung cancer excess was related to asbestos-like CG fibers in combination with cigarette smoking; a possible additive role for free silica also was proposed.

McDonald and colleagues (1978) conducted an enlarged follow-up study from 1937 to 1973 of the Homestake Veterans Association cohort that included 1,321 men with at least 21 years employment at the mine. SMRs were calculated using SD mortality rates as opposed to the use of US rates. SD, because of its mostly rural composition, has lower lung cancer rates than the US. For the years 1937 to 1955, the SMRs were 176 and 159 for respiratory and gastrointestinal cancer mortality, respectively, although there were no overall cancer excesses during the years 1937 to 1973. Using dust exposure data from company midget impinger samples, the authors examined the mortality risks in three categories of dustiness. They showed striking dose-response trends for tuberculosis and pneumoconiosis, but no correlations for respiratory or gastrointestinal cancers (McDonald et al., 1978).

Brown et al. (1986) and Steenland and Brown (1994) conducted the most thorough assessment of Homestake goldminers. The cohort included 3,328 white, male miners employed at least 1 year between 1940 and 1965 and followed up until June 1, 1977 and then to January 1, 1990. The authors calculated SMRs using person-years and contrasted mine mortality rates with U.S. white male rates. An index of dust exposure by job location was assembled for the purpose of assessing dose-response gradients. The SMR for malignant neoplasms of trachea, bronchus, and lung was 100 with no trends in latency for dust exposure or for length of employment (there was a SMR of 500 based on only three cases for cancer of the other parts of the respiratory system). There was a slight elevation (SMR = 169) for leukemia, and significant excesses were observed for respiratory tuberculosis and other respiratory diseases, especially for men employed before 1930 (Brown et al., 1986). Although none of the Homestake authors had any smoking data, it does not appear that its absence introduced any bias. In an update that extended mortality follow-up until 1990, Steenland and Brown (1993) showed that the SMR for lung cancer was 1.13, and that there remained significant excesses of lymphatic cancers, kidney disease, TB, and nonmalignant respiratory diseases/silicosis. All causes of death but

EBSCOhost - printed on 2/13/2023 4:48 AM via . All use subject to https://www.ebsco.com/terms-of-use

Table 2. Summary of epidemiologic studies of lung cancer risk among gold ore miners

Authors (date)	Country	Risk Measure (95% CI/p value)	Comment
Gillam et al. (1986)	South Dakota (U.S.A.)	SMR=370 (260-521)	No exposure measurements or smoking adjustment
McDonald et al. (1978)	South Dakota (U.S.A.)	SMR=103 (79-133)	Used SD rates as expected values; no risk gradient for dustiness
	Years 1937-55	SMR=176	
Brown et al. (1986)	Years 1940-77	SMR=100 (73-133)	No trends for latency or dust exposure; leukemia SMR = 169
		SMR=500 3 deaths other parts of the respiratory system	
Steenland & Brown (1994)	Years 1940-90	SMR=113	No trends for dust exposure;
Katsnelson & Mok-ronosova (1979)	Sverdlovsk Russia	RR=7.9 for males ($p<0.001$)	No smoking or exposure data
	Without silicotics	RR=3.1 ($p<0.02$)	
Armstrong et al. (1979)	Kalgoorlie, Westn Australia	SMR=145 (127-165)	Silicosis predicts lung cancer risk; risk remained after adjustment for smoking
de Klerk et al. (1995)	Expanded follow-up to 1991	OR=2.3 >40 yr worked (0.8, 6.5)	Strong smoking effect; no exposure information
Muller et al. (1983)	Ontario, Canada	SMR=145 (135-156)	No dust measurements, no smoking information
Shannon et al. (1987)	Ontario, Canada--expanded follow-up of Muller's cohort	SMR=141 (131-151)	Risk greatest for those employed <1936 with + gradient for time since first dust exposure
Miller et al. (1987)	Ontario, Canada--expanded follow-up of Muller's cohort	SMR=156 (145-167) Employee <1935-36 SMR=164; 1936-44 SMR=142; >1944 SMR=110	Smoking did not confound the results; + gradient by degree of silicosis
Kusiak et al. (1991)	Ontario, Canada more follow-up of	SMR=129 (115-145);	Stomach SMR = 152;
Kusiak et al. (1993)	Muller's cohort	Each yr employment <1945 ⇒ 6.5% incr risk ≥ 20yrs employment	Smoking unlikely explanation; radon and arsenic equally likely explanation as silica
Wyndham et al. (1986)	South Africa (whites miners)	SMR=161 (137-190)	Cumulative dust exposure had RR = 1.77 per 10 particle yrs underground, adjusted for smoking
Hnizdo & Sluis-Cremer(1991)	South Africa (whites miners)	Smoking adjusted RR for SiO_2 part-years/1000 (SPY) <15 SPY RR=1.00 15-30 SPY RR=1.54 31-40 SPY RR=2.07 ≥41 SPY RR=2.92	Dose-related gradient; apparent synergy between smoking and SiO_2 exposure; mostly on those with 35 pckyrs and >30 SPY; strong assn with hilar lymph nodes

EBSCOhost - printed on 2/13/2023 4:48 AM via . All use subject to https://www.ebsco.com/terms-of-use

pulmonary cancer showed dose-response gradients related to job exposure matrix (Steenland and Brown, 1994).

Katsnelson and Mokronosova (1979) examined the mortality at a Russian gold mine from 1948 to 1974 (data on silica fire brick mills were also collected and will be discussed below). Dust concentrations were not specifically stated for workers in the gold mine and a RR was calculated comparing the cancer risk among gold miners with that of a nearby town. Katsnelson and Mokronosova reported a RR of 7.9 ($p < 0.001$) for lung cancer among male underground gold miners; removing the silicotics left a RR of 3.1 ($p < 0.02$). No female lung cancer deaths occurred during these years. Underground male workers had a RR of 5.7 ($p < 0.001$) for stomach cancer; a RR of 4.4 ($p < 0.001$) resulted after silicotics were removed and a RR of 1.1 was reported for surface workers. For females there was a nonsignificant RR of 4.0 for stomach cancer among underground workers, with no change after silicotics were removed; and surface workers had a RR of 2.0. No smoking data were presented for gold mine workers. There appears to be an inverse gradient for the proportion of lung cancers by stage of silicosis and/or silicotuberculosis. The authors concluded that silica acts as a carcinogen with polycyclic aromatic hydrocarbons (PAH) in tobacco smoke.

Armstrong et al. (1979) studied 1,974 gold miners from Kalgoorlie, Western Australia who were first surveyed in 1961 and 1962 for silicosis and followed until 1975. Adjustment was made for cigarette smoking and silicosis prevalence in the analysis. The authors used a person-years analysis incorporating the age-specific death rates for Western Australia males as a source for expected values. Overall respiratory cancer had a SMR of 140. A diagnosis of silicosis in the early 1960s was demonstrated to be a modest predictive risk factor of mortality from respiratory cancer, as well as nonmalignant respiratory disease and all causes of death (Armstrong et al., 1979). The authors evaluated radon and arsenic levels in the gold ore and concluded that these did not confound the results because the concentrations were too low. de Klerk and co-workers (1995) have completed a partial follow-up to 1991 of the same cohort of gold workers, and reported that miners with greater than 40 years employment have an OR of 2.3. It appears that smoking is also a strong risk factor for lung cancer.

Muller and colleagues (1983) conducted a retrospective cohort study of 6,972 underground gold miners from the Province of Ontario, Canada who were employed at least 60 months in mining with a minimum 1/2 month spent in an Ontario mine. These gold ore miners were followed from 1955 to 1977 using tracing information from the Ontario Workers' Compensation Board (OWCB)/Mining Master File, death records from Statistics Canada, and Social Insurance files. Neither dust levels nor smoking habits of the miners were available, although later analysis demonstrated that smoking was not a confounder in the mortality rates (Industrial Disease Standards Panel (ISDP), 1987). SMRs were calculated using age- and calendar-specific mortality rates for the male population of Ontario. Cancers of the trachea, bronchus and lung had a significant SMR of 145 ($p < 0.0001$); for stomach cancer the SMR was 148 ($p = 0.0023$); silicotuberculosis and silicosis had SMRs of 6,140 and 1,688, respectively. With a deficit in bladder and kidney cancers (SMRs = 36 and 96, respectively), it is highly unlikely that the striking excesses were due to smoking (Muller et al., 1983).

In a report to the Ontario Workers' Compensation Board (OWCB) two additional analyses were undertaken of the lung cancer risk among the Province's gold miners (IDSP, 1987). Shannon et al. (1987) defined a larger cohort than Muller et al. that included 2,183 deaths of gold miners with a minimum 5 years in gold mining. Prior exposure to asbestos

EBSCOhost - printed on 2/13/2023 4:48 AM via . All use subject to https://www.ebsco.com/terms-of-use

or uranium eliminated the miner from entry to the expanded cohort. The comparison population was the mortality rate of the Ontario male population. Paralleling Muller et al. (1983), the lung cancer SMR was 141 (Shannon et al., 1987). The data suggested that the lung cancer risk was greatest for those first exposed before 1936, and a clear gradient emerged for time since first dust exposure, including a weighted duration of dust-years.

A second evaluation by Miller et al. (1987) accompanied the OWCB report. These authors also combined gold miner cohorts that Muller had described separately because they had worked <85% in gold ore mining. Miller and colleagues showed that year of first employment was a risk factor for lung cancer. For first employment prior to 1935-36, the SMR was 164, for first employment between 1935-36 to 1944 the SMR was 142, and for first employment after 1944, the SMR was 110. These findings were interpreted to be a function of the high silica dust exposure extant in the mines before 1945. Miller et al. considered that uncontrolled confounding by smoking may have been the reason the excess lung cancer was observed, but rejected that as an explanation because pulmonary cancer risk was not elevated among other Ontario miners with similar smoking histories. Elevated gastrointestinal cancer risks were also evaluated in the IDSP reports, and because they showed an inverse relationship with dust exposure and time employed, they were not considered related etiologically to gold mining or to silica exposure (IDSP, 1987)

The most recent review of lung cancer risk among Ontario gold miners included follow-up on 13,603 men from 1955 to 1986 (Kusiak et al., 1991). This analysis included some modest sampling for silica, radon, arsenic, and asbestiform fibers, and partial smoking histories. The investigators found that miners who began work before 1946 and never mined nickel had a SMR of 140 (95% CI = 122, 159); those who mined gold before 1946 and mined nickel before 1936 has a SMR of 181 (95% CI = 109, 283). Poisson regression models of mining before 1945 showed significant linear trends for arsenic exposure, lagged by 20 years, and for radon, lagged by 5 years. The best fitting model was for joint exposure to arsenic and radon; however, the model explaining the greatest variance included high silica exposure in combination with employment before 1945. Smoking and fibrous mineral exposure were found to be unlikely explanations for the lung cancer excess (Kusiak et al., 1991). Stomach cancer among gold miners was also assessed using similar methods and models; time underground and exposure to chromium dusts were considered a possible explanation for stomach cancer cases occurring before 60 years of age (Kusiak et al., 1993).

A cohort of 3,971 white South African miners born between 1916 and 1930 and who were alive in 1970, was followed for nine years. Wyndham et al. (1986) calculated SMRs using the mortality rates of white South African males as the comparison population. Using case-referent methods, the authors analyzed smoking, cumulative dust exposure, and years employed underground as risk factors for mortality from malignant and nonmalignant lung diseases, and from heart disease. There was an elevated risk for lung cancer (SMR = 161). The authors examined the employment underground risk factors such as cumulative dust exposure and length of service for lung cancer. Smoking was entered into the model before testing the mining factors, and the lung cancer model was statistically significant. Cumulative dust exposure had a smoking-adjusted rate ratio (RR) of 1.77 per 10 particle years of underground exposure [95% C.I. = 0.94-3.31 (p = 0.06)]. However, the smoking-adjusted RR was 1.14 per 10 years employed underground [95% C.I. = 0.63-2.05 (p = 0.65)] (Wyndham et al., 1986).

Hnizdo and Sluis-Cremer (1991) presented an important study of 2209 South African white male gold miners who began mining during the years 1936 to 1943 and were studied

EBSCOhost - printed on 2/13/2023 4:48 AM via . All use subject to https://www.ebsco.com/terms-of-use

for their risk of pulmonary disease, including smoking habits, during the years 1968 to 1971; mortality was followed from 1968 to 1986. The objectives of the study were to determine any dose-response relationship between silica dust and lung cancer risk; the combined effect of silica dust and smoking; and the association between lung cancer and silicosis at necropsy (the latter will be addressed below). The selection criteria for the 1968 to 1971 sample were attained age between 45 and 54, and a minimum of 10 years of underground gold mining experience. Vital status was ascertained using files of several South African sources, and causes of death were determined from the best available evidence, including the extensive postmortem records maintained for medicolegal purposes (84% of deceased subjects had an autopsy). Of the 945 deaths, there were 77 acceptable lung cancers (66 confirmed by necropsy, five by biopsy, and six from the death certificate).

The authors classified the gold mine jobs into 11 groups based on the average respirable silica dust concentrations developed by Beadle and Bradley (1970). Cumulative dust measures (in respirable particle-years/1000) [SPY] were calculated for each miner based on the number of shifts and occupations for each decade worked. Overall, the authors showed that in contrast with the rest of the cohort, the 77 cases of lung cancer had greater levels of silica particle-years exposure, and they smoked more, with greater pack-years; this group had a greater percentage of ever smokers (96% vs 88%), and they had poorer pulmonary function, with more symptoms of rhonchi and bronchitis.

Using a Cox proportional hazards model, smoking produced highly significant ($p < 0.001$) correlation with lung cancer risk in models that adjusted for age. In models that adjusted for age and cigarette equivalent pack-years (to account for pipe smoking), the following four cumulative dust variables were statistically significant: SPY to 1949/1000 ($p < 0.01$); SPY to 1959/1000 ($p < 0.05$); SPY to start of follow-up in 1968/1000 ($p < 0.01$); and SPY up to 1986/1000 ($p < 0.05$). The RR (adjusted for smoking) rose from 1.00 for ≤15 SPY/1000, to 1.54 for 16-30 SPY/1000, to 2.07 for 31-40 SPY/1000, to a RR of 2.92 for ≥41 SPY/1000 (95% CI = 1.02-8.4). The findings mean that miners with lung cancer had significantly higher silica exposures than miners free of lung cancer, and that risk rose in a dose-response fashion. According to the proportional hazards model, the relative risk for lung cancer per 1000 SPY (adjusted for smoking, year of birth, and age) was 1.023 (95% CI = 1.005-1.042. This means that the most veteran white gold miners (all employed ≥10 years) exposed to 50,000 SPY have 3.2 times greater likelihood of dying from lung cancer than those exposed to only 15,000 SPY. The data were also checked to determine if the combined effect of smoking and silica exposure were additive, and findings indicated the two exposures appeared to act synergistically. The synergy appears to be greatest for miners with more than 35 pack-years smoking and >30,000 SPY experience (Hnizdo and Sluis-Cremer, 1991).

With the exception of the studies by McDonald et al. (1978), Steenland and Brown (1993), and Brown et al. (1986), there is a consistent finding of an elevated respiratory tract cancer risk among gold ore miners throughout the world. This consistency is supported by the findings of many researchers (Gillam et al., 1976; Armstrong et al., 1979; Muller et al., 1983; Wyndham et al., 1986; Shannon et al., 1987; Miller et al., 1987; Kusiak et al., 1991; Hnizdo and Sluis-Cremer, 1991). The results among Ontario gold miners support the conclusion that highly exposed gold workers have increased risk for lung cancer, though from the latest assessment it is not clear whether the risk is a function of silica, radon, arsenic, or chromium (ISDP, 1994). This risk pattern appears not to be explained by smoking habits, but does show a positive correlation with degree of silicosis. There is also strong supporting evidence for the role of silica in the cancer excesses because

EBSCOhost - printed on 2/13/2023 4:48 AM via . All use subject to https://www.ebsco.com/terms-of-use

of the strong mortality risks from silicosis, other nonmalignant respiratory diseases, pneumoconiosis , and silicotuberculosis. Lastly, Wyndham et al. (1986) and Hnizdo and Sluis-Cremer (1991) have demonstrated that respirable silica exposures (measured in respirable particle-years) are significantly correlated with lung cancer risk, even after adjusting for smoking. Hnizdo and Sluis-Cremer (1991) also demonstrated a clear dose-response for cumulative silica exposures. These findings are summarized in Table 2.

Cancer risk for the granite industry, stone, and construction work

Workers employed in the granite, stone, and tunneling industries offer important insights into the question of the relationship between silica exposure and cancer. These cohorts are especially useful because they have lower confounding exposures to those substances found in metal ore mines, such as radon and diesel fumes .

Guralnick (1963) examined the 1950 U.S. occupational mortality among men 20 to 64 years old. She reported that stone masons had a lung cancer SMR of 148 while operatives in stone, clay, and glass products had a SMR of 117. Milham (1976) reported that Washington brick masons and stonemasons had a PMR of 141 ($p < 0.05$) for trachea, bronchus, and lung, and a PMR of 171 for stomach cancer ($p < 0.05$). Milham (1983) reported that sandblasters dying in Washington had a PMR of 348 ($p < 0.01$) for ages 20 to 64 during the years 1950 to 1979. Dubrow and Wegman (1984) calculated social class adjusted mortality odds ratios (MOR) for Massachusetts residents from 1971 to 1973. For brick masons and stonemasons the MOR was 143 for trachea, bronchus, and lung. Kjuus and colleagues (1986) reported a smoking-adjusted lung cancer OR of 1.9 for quartz/stone dust for industrial exposure in a case-control study. Lynge et al. (1990) used the Nordic Occupational mortality and cancer incidence registers to assess the lung cancer risk for granite, stone, and construction workers. In Norway the authors reported elevated RRs for other construction workers and for stone quarrying; in Sweden there was an increased risk for sand and clay pits; in Finland there was a significant risk for excavating and highway construction (RR = 1.97; 95% CI 1.32, 2.83), for limestone quarrying, and for stonecutting (RR = 1.75). In Denmark there was a RR of 2.10 for stonecutting, and a significant RR of 2.9 (95% CI 1.17, 5.98) for self-employed stonecutters.

Table 3 summarizes the epidemiologic studies of granite workers, tunnelers, and sandblasters. Vermont granite workers are exposed to quartz dust with a concentration of approximately 30% free silica. Thus data from the Vermont granite industry and the Vermont Division of Industrial Hygiene (DIH) can provide clues about the carcinogenicity of silica, unconfounded by extraneous exposures such as metal oxide fumes, radiation, or asbestisform fibers. Davis et al. (1983) conducted a PMR study of 969 deceased white granite workers whose X-rays were on file at DIH and who died between 1952 and 1978. The authors developed a dust index for the purpose of assessing exposure profiles for their study subjects. They analyzed the data excluding tuberculosis and silicosis after these 2 causes of death showed a powerful excess disease risk. Slight excesses for digestive tract, lung, larynx, and prostate cancers were reported, including a significant PMR of 1.3 for general respiratory cancer (95% CI = 1.0, 1.6). No apparent trends emerged relating dust exposure categories with respiratory cancer, but this may be due to insufficient person-time since dust controls were imposed in the 1940s. Smoking data were not available; interactions could not be assessed. In addition, the voluntary nature of the early participation in the DIH X-ray program suggests that there might be "volunteer bias," such that only healthy subjects entered the cohort before 1951 (Davis et al., 1983).

EBSCOhost - printed on 2/13/2023 4:48 AM via . All use subject to https://www.ebsco.com/terms-of-use

Table 3. Summary of epidemiologic studies of lung cancer risk among granite workers, tunnelers, and sandblasters

Authors (date) Country	Type of Exposure	Risk Measure (95%CI/pvalue)	Comment
Davis et al.(1983) Vermont, U.S	Granite	PMR=1.3 (1.0-1.6)	No apparent trends for dust index
Costello & Graham (1986) Vermont, U.S	Granite	SMR=104	Excess observed among workers hired before 1940 when dust levels were high
Steenland & Beaumont (1986) U.S.A.	Members of Granite Workers' Union	PMR=119	No time trends or gradients for duration; no dust exposures
		OR=3.16 (p<0.001)	Mention of silicosis on the death certificate; no smoking data
Koskela et al. (1990) Finland	Granite workers	SMR=156 (p<0.05)	No individual dust levels; no smoking data
	≥ 25 yrs	SMR=281(p<0.001)	
Selikoff (1978) New York City U.S.A.	Unionized tunnel workers Employed	SMR=160	No smoking data
	<20 yrs	SMR ~100	Dose-response for duration employment
	20-29yrs	SMR=210	
	≥30 yrs	SMR=430	
Puntoni et al. (1979) Genoa, Italy	Sandblasters	RR=3.76 (p<0.0.05)	No smoking or dust exposure data; possible confounding by solvents and asbestos
Guenel et al(1989) Denmark	Stone workers	SIR=200 (149-189)	No smoking data; no exposure data. National incidence rates adjusted for region
Copenhagen	All skilled stone workers	SIR=306 (181-482)	
	Sandstone	SIR=808 (323-1657	
	Granite	SIR=404 (202-723)	
Bornholm	Mixed skilled & unskilled	SIR=119 (51-235)	
Other Denmark	Skilled workers	SIR=192 (167-303)	
Mehnert et al. (1990) Germany	Slate quarry workers	SMR=109	Positive risk gradient for time since first exposure and duration of employment; no smoking data

Costello and Graham (1986) conducted a cohort study of 5,414 Vermont granite workers from 1950 to 1982. The authors used the personnel information on file in the Occupational Hygiene Division of Vermont State Health Department to ascertain date of hire and date of death. There were no increased risks for either respiratory system or lung cancer, although there was approximately a 25% excess mortality from pulmonary cancers among workers hired before 1940. Latency time or follow-up may be too short to determine the lung cancer risk among granite workers hired after 1940. Information was lacking on smoking, on dust exposure, and on the completeness of the Vermont records regarding employees at risk.

Steenland and Beaumont (1986) conducted a PMR study of 1905 white members of the Granite Cutters Union using U.S. death rates as a comparison population. Mortality

EBSCOhost - printed on 2/13/2023 4:48 AM via . All use subject to https://www.ebsco.com/terms-of-use

from nonmalignant respiratory disease (mostly silicosis) and tuberculosis and silico-tuberculosis was highly significant, with PMRs = 442 and 1358, respectively. The authors also reported a significant deficit for leukemia (PMR = 38), and significant excesses for bone cancer (PMR = 316) and arthritis (PMR = 333). The gastrointestinal cancer risk was not elevated; lung cancer was elevated (PMR = 119), but not significant. Furthermore, there were no trends for lung cancer risk over duration of exposure or calendar time. The authors used a case-control analysis to contrast the mention of silicosis or silicotuberculosis on the death certificate of 97 lung cancers and 135 other cancer deaths (excluding bone cancer and leukemia). They obtained an OR of 3.16 ($p < 0.001$), thus supporting a strong association between the two conditions.

Kurppa et al. (1982) and Koskela et al. (1984) provided some insight to the cancer risks among a cohort of Finnish granite workers. The geometric mean quartz dust levels ranged from 1.0 to 1.5 mg/m^3, with the highest concentrations found in drilling jobs. Kurppa et al. (1982) indicated that among 1,087 male workers employed for at least 3 months between 1940 and 1971 and followed until 1975, there was a 2-fold excess of gastrointestinal cancer (SMR = 202, $p < 0.02$); nonmalignant respiratory disease had a SMR of 265 ($p < 0.01$). Koskela et al. (1984) expanded the follow-up of granite workers and demonstrated that there was a slight peak for digestive cancers about 22 years after beginning observation. The authors noted that cancer excesses do not appear until at least 20 years after initiating observation. Koskela and colleagues demonstrated that there was a maximum SMR of 350 for lung cancer at 27 years after follow-up. Koskela et al. (1990) continued the follow-up to 1985, and they reported that the SMR for lung cancer was 156 ($p < 0.05$). Latency, as defined as years since entry into granite work, showed a steadily rising SMR from 156 for any exposure rising to 281 ($p < 0.001$) for employment ≥ 25 years; employment ≥ 30 years showed a SMR of 226 based on 7 deaths. Although the authors did not have smoking information on their subjects, they did not feel it biased their findings because granite workers' tobacco habits did not differ from those of all Finnish males.

Selikoff (1978) examined a 932-man cohort of unionized New York City tunnel workers from 1955 to 1972. These workers were exposed to siliceous dusts containing sizable amounts of quartzites, schists, and gneisses, though no dust concentrations were presented. There was an overall SMR of 160 for lung cancer and a gradient in the risk of respiratory cancer according to the number of years worked. The SMR was 100 for employment <20 years, increasing to 210 for 20-29 years and to 430 after 30 years or more. Similar to asbestos-exposed workers, there appears to be a minimum 20-year induction period needed to detect an elevated lung cancer risk. No smoking data were available and it is possible that this elevated risk may only be a reflection of long-term smoking habits or interactive effects of silica exposure and smoking.

Sandblasting produces a large quantity of silica dust, and workers often blast in confined spaces so that exposures can be very high. Because sandblasters are known to be heavy smokers (Jones et al., 1986), this seems to be a particularly good occupation to determine the link between silica exposure, smoking, and cancer. Puntoni et al. (1979) are the only investigators to have examined this occupation using epidemiologic follow-up methods. These researchers compared the lung cancer risk among 190 sandblasters employed in a cohort of 2,190 Genoa, Italy shipyard workers with the general male population of the same city. These men had RRs of 3.76 ($p < 0.05$) for lung cancer and 5.04 ($p < 0.05$) for laryngeal cancer (based on only 3 cases). However with possible confounding by solvents, likely asbestos exposure, and without dust measures or smoking

EBSCOhost - printed on 2/13/2023 4:48 AM via . All use subject to https://www.ebsco.com/terms-of-use

information, little can be determined about the joint cancer risk among smoking sandblasters.

Lynge et al.'s survey (1990) of Nordic dusty trades indicated that stone cutting conferred a doubling of the lung cancer mortality risk in Denmark. To elaborate on that association, a standardized incidence rate (SIR) study of Danish stone workers was conducted by Guenel et al. (1989). The authors followed 2071 skilled and unskilled stone workers from 1943 to 1984. Male lung cancer incidence rates were adjusted for age and region of Denmark. For the whole cohort, the SIR was 200 (95% CI = 149-269); for Copenhagen the SIR was 306 (95% CI = 181-482); for Bornholm (a center of road and building materials industry and stonecutting) the SIR was 119 (95% CI = 51-235); and for other parts of Denmark the SIR was 192 (95% CI = 167-303). Among skilled workers from Copenhagen, sandstone workers had a SIR of 808 (95% CI = 323-1657), granite workers had a SIR of 404 (95% CI = 202-723). Among unskilled workers the overall the SIR was 181 (95% CI 116-270), while the road building materials industry showed significant SIR of 246 (95% CI = 143-394). The authors concluded that stone construction workers, with no other workplace confounding exposures, had significantly elevated lung cancer risks, and these results support a relationship between respirable silica dust and cancer (Guenel et al., 1989).

Mehnert et al. (1990) evaluated the mortality risks of 2,483 German slate quarry workers. The cohort was defined as those employed at least one year between 1953 and 1985 and followed-up from 1970 to 1985. Lung cancer had a nonsignificant SMR of 109, but it rose to 183 when the risk of silicotic workers was examined separately. Lung cancer showed a positive risk-response gradient with time since first exposure and it showed increasing gradient for duration of employment among slate workers who survived 20 years after first exposure. This pattern of positive gradients remained among workers with silicosis and nonsilicotics.

In general there appears to be some consistent increase in lung cancer risk among granite workers and tunnelers, and that risk only appears after decades of work. The work of Guenel et al. (1979) gives some strong evidence that silica exposure in construction work presents significant lung cancer risks for Danish stone workers. Selikoff (1978) and Mehnert et al. (1990) suggest some experience-related risk gradients, although specific workplace exposure data are needed to provide more powerful evidence.

Cancer risks among ceramics, glass, and diatomaceous earth industries

Using the records of the UK National Health Service Central Register and the Office of Population Censuses and Surveys, McDowall (1984) examined the risk of death among 607 cement workers employed in 3 areas in North Kent from 1948 to 1981. For lung cancer there was a SMR of 85. Dubrow and Wegman (1984) reported that glass workers had an adjusted (for social class) MOR of 314 for trachea, bronchus, and lung. Lynge et al (1990) reported that in Norway glass, ceramic, and clay workers had a lung cancer RR of 1.79 (95% CI = 1.00-2.95), and a similar risk (RR = 1.75) was observed for ceramic modelers and formers. In Sweden glass-makers had a RR of 1.23. Finnish glass, ceramic, and clay workers had a RR of 1.27, and glass molders had a RR of 1.16. In Denmark glass makers had a RR of 1.62 and unskilled glass workers had a RR of 1.75 (95% CI = 1.09-2.68).

From some descriptive data, there is a suggestion of a lung cancer excess among glass workers. However, Sankila et al. (1990) were the first investigators to conduct an

EBSCOhost - printed on 2/13/2023 4:48 AM via . All use subject to https://www.ebsco.com/terms-of-use

epidemiologic study of glass workers. The authors studied two cohorts of Finnish glass workers to assess their cancer incidence from 1953 to 1986. Combining both cohorts produced a lung cancer SIR of 130 (95% CI = 100-167) for males, while females had a SIR of 111 (95% CI = 45-229). Glass blowers from the first cohort had a SIR of 85 (95 % CI = 28-198), while all other glass workers had a SIR of 133 (95% CI = 93-183), about the same rate as the second cohort with SIR = 134 (95% CI = 88-194). The borderline excesses could be explained by lack of adjustment for smoking, and there were no dust measurements of silica particulate. Furthermore, studying the whole cohort rather than the workers at the beginning of the manufacturing process where silica exposure was likely to have been high may have missed finding an effect. Recently IARC reviewed the cancer risks in the glass industry, and concluded that "the manufacture of art glass, glass containers, and pressed ware entails exposures that are probably carcinogenic to humans (IARC Group 2A); and occupational exposure in flat-glass and special glass manufacture are not classifiable as to their carcinogenicity to humans (Group 3)" (IARC, 1993).

Employment in the pottery industry was characterized by an apparent lung cancer excess as early as the 1920s and 1930s (Kennaway and Kennaway 1947), but no additional follow-up was carried out until the 1980s. Thomas (1982) examined the mortality of members of the (U.S.) Pottery and Allied Workers Union from 1955 to 1977. For males there was significant ($p < 0.01$) PMR lung cancer localized among workers in sanitary-ware production (Thomas, 1982). Thomas and Stewart (1987) conducted a follow-up study of 2055 white male sanitary-ware workers employed between 1939 and 1966 and followed until 1980. Despite the lack of specific industrial hygiene data, the authors categorized exposure to silica and nonfibrous talc. Overall there was a SMR of 1.43, with the lung cancer excesses occurring in the high silica exposure jobs (SMR = 181; $p < 0.05$) and in jobs characterized by high silica and high exposure to nonfibrous talc (SMR = 2.54; $p < 0.05$). Further analysis suggested that years exposed to talc provided greater risk gradients than exposure to silica, although possible interaction was not ruled out (Thomas, 1990). No smoking data were available for any of these studies.

Forastiere et al. (1986), using the death registry of Civitacastellana, Italy, for the years 1968 to 1984, examined the lung cancer risk among pottery workers using matched case-referent methods. The study examined 72 lung cancer cases and 319 matched controls; subjects' next-of-kin were interviewed by public health nurses blinded to study objectives including smoking and occupational histories. Disability from silicosis was also obtained for all subjects from the Italian National Institute for Compensation of Occupational Diseases. The time-, age- and smoking-adjusted results showed a Mantel-Haenszel RR of 1.0 for quarry work and an RR of 2.0 (95% CI = 1.1-3.5) for ceramics manufacturing. When the ceramic workers were compared for silicosis status, those compensated with silicosis had a smoking-adjusted OR of 3.9 (95% CI = 1.8-8.3) while those without silicosis had an OR of 1.4 (Forastiere et al., 1986). Further analysis by Lagorio et al. (1990) suggested that silicosis and smoking enhances the lung cancer risk when comparing the risk among those who were either unexposed to ceramics or those without silicosis. Firing and repairing and cleaning jobs confer a significant RR of 2.2 and 3.1, respectively (Lagorio et al., 1990). Duration of employment showed no gradients either for silicotics or for nonsilicotics. Both studies concluded that there is an excess lung cancer risk among ceramic workers, and the authors suggested that silicosis plays an etiologic role in the development of pulmonary tumors.

Winter and co-workers (1990) examined a cohort of 6187 British pottery workers who were surveyed in 1970-71 and whose mortality was ascertained from 1970 to 1985. The authors focused on males who were <60 years old at the time of the survey, and they

EBSCOhost - printed on 2/13/2023 4:48 AM via . All use subject to https://www.ebsco.com/terms-of-use

reported that there was a significant SMR of 1.40 (95% CI =1.07-1.80) for lung cancer using national rates and a significant SMR of 1.32 (95% CI = 1.00-1.69) using locally adjusted rates. There was a modest gradient of risk for the categories of years since entering employment. Although employment in several ceramic products or job groups showed increased SMRs, only employment in glazing and decorating jobs produced a significant smoking-adjusted SMR of 2.82 (95% CI = 1.03-6.13). Lung cancer risk was assessed by exposure categories based on industrial hygiene sampling at the time of the survey, but little relationship emerged for cross-sectional respirable quartz levels. For cumulative exposure up to 1970-71 of >50 mg/m^3, a 50 to 60% increase in risk was demonstrated. These data suggest that British pottery workers have elevated risks for lung cancer, unexplained by smoking, with some relationship with cumulative silica exposures.

When Chen et al. (1992) and McLaughlin (1992) examined the lung cancer risk among metal ore miners (see above) in Southern China, they also examined the pulmonary cancer risk in 8 pottery factories. The lung cancer SMR for pottery workers from 1972 to 1989 was 58 ($p < 0.05$). In the case-control analysis, the OR (adjusted for age and smoking) was not significant for cumulative exposure to respirable silica, nor was there any association with cumulative exposure to all dusts, arsenic, PAH, or radon. Furthermore, the OR was 0.5 for a prior history of silicosis among pottery workers.

Katsnelson and Mokronosova (1979), whose study was described above under gold mines, also examined lung cancer at 2 aluminosilicate fire clay plants and at a silica firebrick plant. Although the firebricks and fire clay dusts contain high levels of quartz, there were no dust samples collected in the plants. Male workers at the fireclay plants had RRs for lung cancer of 4.0 ($p < 0.01$) and 4.5, while a nonsignificant respiratory cancer SMR of 5.1 was reported for female workers at the first plant. At the firebrick plants the RR was 2.0 ($p < 0.05$) for male workers; for females it was 0.8. The authors suggested a link between smoking and silica exposure in the risk of lung cancer, but their findings lack any empirical measurements of silica dust or smoking rates.

Puntoni et al. (1988) conducted a follow-up study of 211 workers employed in a refractory silica brick plant near Genoa, Italy. Their mortality from 1960 to 1979 was compared to the age-specific male population of Genoa from 1960 to 1980. There was an overall SMR of 122 for all deaths with an equal risk for all tumors (SMR = 121). Based on <5 deaths in all sites, excesses were reported for the following tumors: colon (SMR = 250), rectum (SMR = 256), and larynx (SMR = 405). Cancers of the respiratory tract showed a SMR of 208 (95% CI = 113, 349). There was a striking excess of nonmalignant respiratory disease (SMR = 304; $p < 0.01$). When the cohort was divided into silicotics and nonsilicotics, the excess for laryngeal cancer was confined to the silicotic group, while there was a respiratory tract cancer risk of approximately 2-fold for both groups—SMR = 223 (95% CI = 102-420) for silicotics and SMR = 185 for nonsilicotics (Puntoni et al., 1988). Although cross-sectional industrial hygiene data for respirable and silica dust were presented for work areas in the brick plant, they were not applied to the risk measures. A limited amount of smoking data indicated that 4 of the 14 deaths from lung and laryngeal tumors were among nonsmokers. The authors concluded that their findings support a hypothesis that silica may be carcinogenic, with or without silicosis as a premalignant condition; smoking may also play a role.

Producing refractory brick uses extensive amounts of fine, high purity silica. Merlo et al. (1991) examined the lung cancer risk among 1200 Italian refractory brick workers and followed them up to 1986. Overall the lung cancer SMR was 132 with a nonsignificant SMR of 201 for laryngeal cancer (Merlo et al., 1991). These investigators

EBSCOhost - printed on 2/13/2023 4:48 AM via . All use subject to https://www.ebsco.com/terms-of-use

found an increasing lung cancer risk for >20 years latency (SMR = 188; $p < 0.05$), and increased risk for those hired before 1960 (SMR = 167; $p < 0.05$). Although there was no information about smoking or about levels of quartz exposure, the authors concluded that the findings provided additional evidence of the link between silica exposure and lung cancer.

Silica exposure occurs during the mining of diatomaceous earth (DE) and in preparation of the finished product. During the extraction of DE most of the exposure is to amorphous silica, though miners can be exposed to low levels of quartz. However, when DE is calcined (heated in a kiln to temperatures of 800 to 1000°C with a sodium chloride or sodium carbonate flux), high levels of exposure to crystalline silica and cristobalite occur. Checkoway et al. (1992) have conducted a landmark study of the health of 2570 white male DE workers employed at least one year in the western states' DE industry and followed from 1942 to 1987. Overall the all-causes SMR was 1.12 (95% CI = 1.03, 1.21), with a SMR of 1.43 for lung cancer (95% CI = 1.09, 1.84) and NMRD with a SMR of 2.59 (95% CI = 1.79, 2.83). There were slight elevations for cancers of the colon (SMR = 1.19), pancreas (SMR = 1.11), larynx (SMR = 1.15), and brain and central nervous system (SMR = 1.53), but none was statistically significant. The authors found dose-related gradients for duration of employment and a semiquantitative silica exposure index for both lung cancer and NMRD with lagged exposure for 15 years. The risks were adjusted for age, calendar year, duration of follow-up, and ethnicity (Hispanic versus other white). The lung cancer risk rose from 1.00 for <50 exposure intensity-years, to 1.19 for 50 to 99 exposure intensity-years, to 1.37 for 100 to 199 exposure intensity-years, to 2.74 for ≥200 intensity-years. Having limited smoking histories on the DE workers, Checkoway et al. reported that smoking could not account for all the strong links between silica exposure and lung cancer, and they concluded that high dust exposure prior to the 1950s was the most etiologically significant contributor to the lung cancer and NMRD risks detected in the cohort (Checkoway et al., 1992, 1993). Future research will examine comparisons between silica, cristobalite, and possible confounding from asbestos.

Cancer risk among foundry workers and in metallurgical industries

The manufacture of cast parts in metallurgical foundries is an old and relatively simple process requiring the use of large quantities of sand and binders to make the molds into which the molten metal is poured. After the piece cools, the mold must be broken during the "knockout" process. The next step is the cleaning of the sand from the piece's surface using abrasive grinders. It is important to recognize that metallurgy production entails exposures to many known and potential carcinogens such as benzo[a]pyrene, metal oxide fumes, acid mists, and high electrical fields, though silica is ubiquitous in foundries.

Kennaway and Kennaway (1947) reported that metal grinders and foundry sandblasters had elevated lung cancer SMRs, while only metal grinders had elevated cancer of the larynx. Guralnick (1963) reported that for deaths from ages 20 to 64 among steel workers classified as blacksmiths, forgemen, etc., there were SMRs of 190 ($p < 0.05$) and 139 for lung and stomach cancer, respectively. For metal molders, the SMR was 227 ($p < 0.05$); for operatives and kindred workers in primary metal industries the lung cancer SMR was 147 ($p < 0.05$). Milham (1976) reported that Washington metal molders had a PMR of 312 for ages 20 to 64 for cancer of the bronchus and lung (similar to the PMR of 348 [$p < 0.01$] for sandblasters, some of whom may have worked in the metal industry). In California, metal molders had a PMR of 192 ($p < 0.05$) for cancer of the respiratory tract (Peterson and Milham, 1980). Williams et al. (1977) reported smoking-adjusted ORs of 2.97 and 2.23 for laryngeal and stomach cancers from the metal industries; pulmonary

EBSCOhost - printed on 2/13/2023 4:48 AM via . All use subject to https://www.ebsco.com/terms-of-use

cancer risks were less the null value for metal and fabricated metal industries. Dubrow and Wegman (1984) reported the following occupational excesses, adjusted for social class: foundry workers for cancers of the trachea, bronchus, and lung (TBL) MOR = 412 and MOR = 183 for large intestine and rectum (LIR); forgemen and hammermen MOR = 967 for TBL and MOR = 676 for gastric cancers; for abrasive workers MOR = 235 for respiratory system, MOR = 202 for LIR, and MOR = 322 for urinary tract; for steelworkers MOR = 198 for TBL; for heated metal workers MOR = 422 for cancer of the tongue, MOR = 289 for rectum, MOR = 259 for larynx, and MOR = 196 for bladder. In addition, for other metal workers there were excesses of cancer of the esophagus, pancreas, myeloid leukemia, and large intestine. Lynge and co-workers (1990) reported in their study of lung cancer that foundry workers in Norway had a RR of 1.73 (95% CI = 1.12-2.25); in Sweden foundry workers have a RR of 1.38 (95% CI = 1.16-1.64); Finnish workers in metallurgical smelting had a RR of 1.56 (95% CI = 1.31-1.86); and skilled molders from Denmark have a RR of 1.6.

Gallagher and Threlfall (1983) examined the cancer risk among metal workers in British Columbia from 1950 to 1978. The PMR was 110 for all cancers combined (95% CI = 105, 116). Most of the excesses were accounted for by lung cancer with a PMR of 134 (95% CI = 123, 145). There were nonsignificant elevations for stomach and rectal cancers and for Hodgkin's disease and multiple myeloma. The authors examined occupational groups of metal workers and showed that metal mill workers had significant PMRs of 248, 168, and 356 for rectum, lung, and leukemia, respectively. Boilermakers and structural iron workers had a significant PMR of 157 for lung cancer; sheet metal workers shared the pulmonary cancer risk with a PMR of 138.

Table 4 summarizes the epidemiologic studies of foundry workers. Siltanen et al. (1976) as part of a thorough examination of the Finnish foundry industry, measured the work areas with the highest levels of silica and total dust concentrations. These work areas include sand preparation, furnace repair, shake-out, and cleaning (fettling); moderate levels were found in coremaking and molding; and the lowest levels were measured during melting and pouring. Koskela et al. (1976) studied the lung cancer risk in a sample of 3,876 iron, steel, and nonferrous Finnish foundry workers, reporting an overall SMR of 151 ($p < 0.05$). The excess was confined to iron foundries, especially to molders with more than 5 years of experience. However, the sample size appears not to have been large enough to examine other work areas in depth, and the authors noted that company personnel records underestimated subjects exposure. Of the 21 lung cancer cases, only one never smoked, but the smoking habits of the rest of the cohort were not obtained. However, the authors indicated that based on survey studies of workers employed at that time, foundrymen smoked to the same degree as the general male population, so that the excess could not have been due solely to smoking. Koskela et al. (1976) also proposed that smoking may be a co-carcinogen with the organic toxic emissions characteristic of the foundry environment.

Tola et al. (1979) conducted an expanded study of 3,425 iron foundry workers with at least one year's employment, and they reported an overall PMR of 144. The authors then conducted a nested case-control study of lung cancer and reported that molders and casters combined had significant ($p < 0.01$) odds ratios (ORs) of 4.2 and 4.6, respectively. In-depth exposure histories were obtained by contacting all previous employers. The authors examined gradients of PAH exposure (but not silica or total dust exposure), which suggested a reason for the excess. However, comparing heavy versus low PAH exposure produced a nonsignificant risk ratio of 1.7. From survey data of current workers, the authors reported that smoking did not vary much between jobs and there-

EBSCOhost - printed on 2/13/2023 4:48 AM via . All use subject to https://www.ebsco.com/terms-of-use

Table 4. Summary of epidemiologic studies of lung cancer among foundry workers

Authors (date)	Occupation or Source of SiO_2	Risk Measure (95% CI/p value)	Comment
Koskela et al. (1976) Finland	Iron, steel and nonferrous foundry workers	SMR=151(p<0.05)	Excess centered on iron foundries w 5 yrs employment; neither smoking nor exposure data available
	Iron foundries only	SMR=270 (p<0.05)	
Tola et al. (1979) Finland	Iron foundry workers	PMR=144	No smoking or dust exposure information
	Molders	OR=4.2 (p<0.01)	
	Molders & casters	OR=4.6 (p<0.01)	
Gibson et al. (1977) Ontario, Canada	Foundry workers	RR=5.0 (p<0.0005)	Compared with non-foundry workers; no smoking information
	Steel casting	SMR=250 (p<0.05)	
	Crane Operators	SMR=714 (p<0.01)	Compared with Toronto male mortality rates
	Finishers	SMR=314	Highest mean total suspended particulates
	Molders	SMR=255	
Redmond (1975); Redmond et al. (1981) U.S.A., members of United Steelworkers of America — 7 plants	Foundry Dept. (whites only)	SMR=162	Elevated for 1953-66 only; indirect adjustment for smoking; no exposure data
	Mason Dept. (whites only)	SMR=21	
	Blacksmith Dept. (whites only)	SMR = 242	Consistent excess for 1953-75
Decoufle & Wood (1979) U.S.A.	Foundry workers w/5 yrs service	SMR=200	No smoking or exposure information
U.S.A. Members Internal Molders &Allied Workers	Union member ≥11 yrs	PMR=147 (p<0.05)	No smoking or exposure information
Egan-Baum et al. (1981) Expanded follow-up	For whites	PMR=144 (p<0.05)	No smoking or exposure information
	For blacks	PMR=176 (p<0.05)	
	Iron foundries Among those aged 42-64 yrs	OR=2.36 (1.01-5.53)	Compared to steel & nonferrous foundries
Blot et al. (1983) U.S.A. Pennsylvania	Steel industry—usual occup 15 years foundry workers and/or moldmakers	OR=1.8	Adjusted for smoking, age, education, other hazardous employment; no exposure data
		OR=7.1 (1.2-42.3)	
Andjelkovich et al. (1990); Andjelkovich et al. (1992) U.S.A.	Gray iron foundry	SMR=1.23 whites (0.96-1.54) SMR=1.32 non-whites(1.02-1.67)	SMR=1.67 stomach SMR=1.57 rectum; SMR=1.43 pancreas; SMR=1.47 prostate
	Entire plant	SMR=1.27 (p<0.01) [race-adjusted]	Excesses for molding, finishing, general service, pattern making; smoking most likely w/SiO_2 possible
Fletcher (1986); Fletcher & Ades (1984) U.K.	Steel foundries	SMR=149 (p<0.001)	No adjustment for smoking; significant trend for >20 yrs employment
	Silica group	SMR=180 (p<0.001)	

EBSCOhost - printed on 2/13/2023 4:48 AM via . All use subject to https://www.ebsco.com/terms-of-use

fore did not introduce confounding into the case-control study. Because the authors could not measure dustiness, this study makes only modest contribution to the question of silica and cancer.

Gibson and co-workers (1977) conducted a retrospective cohort study of Dofasco steel mill workers in Hamilton, Ontario, Canada from 1967 to 1976. The authors compared foundry workers to nonfoundry workers and reported the overall lung cancer relative risk to be 5.0 ($p < 0.0005$). Gibson et al. (1977) used metropolitan Toronto male mortality rates to calculate expected values and reported elevated lung cancer SMRs for the following job titles based on where employees spent the majority of their work time: crane operators (SMR = 714, $p < 0.01$), finishers (SMR = 314), molders (SMR = 255), coremakers (SMR = 108), and furnace operators (SMR = 114). The authors noted that the finishing area had the highest mean level of total suspended particulates (much of it silica), respirable particulates, and benzene soluble fraction of total suspended particulates. After the finishing area, the molding and furnace work areas had similar industrial hygiene characteristics. No smoking histories were available for the cohort as a whole, although two surveys taken in 1973 and 1976 showed that foundry workers smoke no more than the general male population (~55%). Of the 24 lung cancers, 22 were among men who were cigarette smokers. The authors proposed that smoking and particulate exposure (containing adsorbed organic material) might be an explanation for the lung cancer excess. In a later study, Gibson et al. (1986) demonstrated that foundry particulate was mutagenic and that a gradient of mutagenicity correlated well with particulate samples from the foundry where the elevated lung cancer SMRs had been observed. The excess findings for crane operators were not supported by data from the U.S. steel industry (Lerer et al., 1974), and are likely to be an artifact of in-plant job mobility in which workers transfer from dustier, entry level jobs to positions requiring greater skill and/or paying higher wages.

Redmond (1975) and Redmond et al. (1981) have conducted two major cancer mortality studies among nearly 59,000 members of the United Steelworkers of America, initially studied in 1953 and followed until 1975. Using deaths from 1953 to 1966, the first study found elevated SMRs for pulmonary cancer among whites employed in the foundry, mason, and blacksmithing departments; complete follow-up to 1975 indicated that only blacksmithing showed a consistent lung cancer excess (Redmond et al., 1981). Workers in the mason department remove, clean, and repair silica brick linings in the blast furnaces, and they had significant SMRs ranging from 169 to 307 for nonmalignant respiratory disease mortality. Nonwhite workers had excesses of digestive and lymphatic cancers; whites have significantly lower risks of digestive malignancies in the mason department. No smoking data were available in these studies, but by using the rest of the steelworker cohort not employed in the department under study as the comparison group provides an internal control for smoking and social class.

Although the findings by Redmond et al. (1981) do not show an overall excess mortality from employment in the foundry department, several smaller studies support the view that foundry workers have excess lung cancer risks (Decoufle and Wood, 1979; Egan et al., 1979; Egan-Baum et al., 1981; Silverstein et al., 1986). Decoufle and Wood (1979) examined the lung cancer risk among employees of a gray-iron foundry, and those with at least 5 years experience had a SMR of 200. Egan et al. (1979) studied the male members of the International Molders and Allied Workers Union, and they found a PMR of 147 for pulmonary cancer. Egan-Baum et al. (1981) updated the previous study and confirmed the previous result with significant PMRs for whites of 144 and for blacks of 176 (both having $p < 0.05$). Silverstein et al. (1986) reported that white and nonwhite males employed in a ferrous foundry had standardized PMRs of 146 ($p < 0.05$) and 106, respectively, for

EBSCOhost - printed on 2/13/2023 4:48 AM via . All use subject to https://www.ebsco.com/terms-of-use

respiratory system cancers. White workers having their longest employment duration in finishing had a SPMR of 179 ($p < 0.05$). These authors had good dust sampling data, but they were not linked directly to the mortality findings. Despite showing similar risks, these studies lack smoking data, usually lack dust estimates, and in some cases sufficient sample sizes. Future work is needed to determine if silica dust interacts with other hazards in the foundry environment.

Blot et al. (1983) conducted a case-control study of lung cancer among white males in eastern Pennsylvania to assess the association with employment in the steel industry. Interviews with next-of-kin provided information about residential, occupational, and smoking histories. The authors demonstrated a smoking-adjusted OR of 2.2 for usual employment in the steel industry (95% CI = 1.5, 3.3). For the job category "foundry worker, mold maker," there was an odds ratio of 7.1 (95% CI = 1.2, 42.3) based only on six cases. Although the authors obtained smoking histories, the next of kin could only provide a surrogate measure of silica exposure by naming the subjects' departments, and thus no assessment of joint risk could be undertaken.

Sherson and Iversen (1986) evaluated the lung cancer risk among a cohort of 5,579 Danish male foundry workers. When these workers were examined in national surveys from 1967 to 1969 and 1970 to 1974, work histories were obtained and stored in the Danish Foundry Worker Register. However, smoking habits were not included. Job exposures were ranked by industrial hygienists so that work histories could be scored for exposures to dust, PAH, and carbon monoxide. However, some jobs could not be classified, limiting the conclusions that could be drawn. The authors observed excess deaths from lung cancer (SMR = 115); urogenital cancer (SMR = 130), nonmalignant respiratory diseases [NMRO] (SMR = 157, $p < 0.01$); and NRD without silicosis (SMR = 118). The authors observed a slight excess from lung cancer (SMR = 115), which was stronger when examining the risk with 25+ years employment. A dose-response gradient emerged for years of employment. The authors, despite their lack of smoking data, argued that their results were unlikely to be significantly confounded. Sherson and Iversen also reported that there were 8 deaths from lung cancer among 163 foundrymen with extant silicosis, suggesting a possible synergistic or additive effect between quartz and PAH from either the foundry environment or from smoking (study was not included in Table 4).

Andjelkovich et al. (1990; 1992) evalated the cancer risk for foundry workers from 1950 to 1984. Overall, there were elevated lung cancer risks for white and nonwhite male employees, with SMRs of 1.23 and 1.32, respectively. For whites, there was also a 1.67 SMR for stomach cancer, and for blacks there were elevated risks for rectum, pancreas, and prostate. When work-area specific risks were assessed, the authors found a race-adjusted significant excess of 1.27 ($p < 0.01$), and elevated lung cancer risk for molding, finishing, general service, and pattern making. The authors considered whether silica exposure could be part of the lung cancer excess, but concluded that smoking was a better explanation (Andjelkovich et al., 1990; 1992).

Fletcher and Ades (1984) and Fletcher (1986) conducted three studies of U.K. foundry workers. The first was a cohort study of 11,048 workers from 9 steel foundries who began work between 1946 and 1965 and were followed until 1978. Overall there was a significant SMR of 149 ($p < 0.001$) for lung cancer, a risk shared by many dusty occupations in the plant. The authors divided the work areas into the foundry, fettling shop, and other jobs, with highly significant lung cancer SMRs for the foundry and fettling shop. In the second study, Fletcher (1986) organized occupations into a "silica group" including sand preparation, molding coremakers, furnace repair, mold knockout men,

EBSCOhost - printed on 2/13/2023 4:48 AM via . All use subject to https://www.ebsco.com/terms-of-use

shotblasters, and dressers. The overall risks for NMRD (SMR = 135; $p < 0.05$), lung cancer (SMR = 171; $p < 0.001$), and stomach cancer (SMR = 171; $p < 0.001$) were significantly elevated. Furthermore, significant χ^2 for trend for length of employment was demonstrated for NMRD. Lacking any direct data on past dust exposures, Fletcher examined the length of employment which was used to estimate dust "dose." He contrasted the lung cancer risk among "silica group" workers with the unexposed jobs, excluding the first 10 years of follow-up. The overall SMR was 89 for the unexposed group; for the "silica group" the SMR was 180 ($p < 0.001$) with a significant χ^2 for trend for 20+ years of employment. Despite the lack of smoking data, the author argues that nearly 100% of foundry workers would need to be smokers to account for the lung cancer excesses. A smoking prevalence survey conducted in 1964 suggests that 73.9% and 70.4% of foundrymen and male engineering workers were smokers, respectively. This is about the same as the U.K. national average in 1964—70%. Fletcher and Ades (1984) adjusted for region of the country, but this made a negligible difference. The third study presented PMRs for death benefits paid to British foundry union members from 1979 to 1982 (Fletcher, 1986). Four job categories of skilled molders, semi-skilled molders, dressers, and laborers were formed and the findings indicated that lung cancer appears to be increasing or is constant among foundry molders.

Employment in foundries is dirty and dusty, and there appears to be excess lung cancer among foundry workers. Some work areas in foundries such as mason and fettling work where there is high silica dust exposure show excess lung cancer risks, and the work of Fletcher (1986) comparing the silica exposed jobs with other jobs in British foundries suggests that silica plays a role in lung cancer among these workers. However, lack of adjustment for smoking and other respiratory hazards in the metallurgy environment (including polycyclic aromatic hydrocarbons, heavy metal fumes, and other chemicals) make silica's etiologic role difficult to interpret.

Cancer risks among silicotics

There is an extensive literature examining the association of silicosis and lung cancer from autopsy studies showing little association between the two conditions, but these studies use methods that are not acceptable by current scientific standards, including selection errors and a lack of adjustment for age and gender (reviewed by Goldsmith, 1994). Data from silicotics are extremely important because these workers have high exposure to silica dust, sufficiently high either to cause these subjects to become ill with silicosis or to have applied for compensation for their disease. Tables 5 and 6 summarize contemporary epidemiologic studies of lung cancer among silicotics in Sweden, Ontario, Canada, Switzerland, Austria, Finland, Italy, Japan, China, and the U.S. Table 5 presents studies that used standardized mortality ratio (SMR) or standardized incidence ratio (SIR) study design, while Table 6 lumps all other study approaches: proportional cancer mortality ratio (PMR), mortality odds ratio (MOR), and Mantel-Haenszel odds ratio (M-HOR).

Westerholm et al. (1986) conducted a follow-up study from 1961 to 1980 of 712 silicotics and 810 noncases from the same industries. The controls were matched for age, industry, and occupation. For silicotics from the mining, quarrying, and tunneling industries, the SMR was 538 ($p < 0.05$) and for the steel and iron industry, the SMR was 385 ($p < 0.05$) (Westerholm et al., 1986).

Tornling et al. (1990) examined the lung cancer incidence and mortality among 280 silicotic men employed in the Swedish ceramics industry. Follow-up was from 1958 to 1983, and it demonstrated that there was a SMR of 188, with 95% CI = 85-356. For

EBSCOhost - printed on 2/13/2023 4:48 AM via . All use subject to https://www.ebsco.com/terms-of-use

Table 5. Summary of lung cancer epidemiology studies of silicotics using standardized mortality/incidence ratio methods

Authors (date)	Country (industry)	SMR or SIR (95% CI/p value)	Comment
Westerholm et al. (1986)	Sweden (Mining, quarry, tunneling) (Foundries)	441 (p<0.05) 538 (p<0.05) 529 (p<0.05) SIR 385 (p<0.05) 182 SIR	Matched for occupation, age, year of first exposure to silica; indirect adjustment for smoking
Finkelstein et al. (1982)	Ontario, Canada (Underground miners) (Above ground	198 (p<0.01)	No adjust. for smoking; although authors estimate that 20% of excess
Finkelstein et al. (1987)	occupations)	302 (173-489)	explained by smoking
Neuberger et al. (1986)	Austria (All occupations)	140 (p<0.05)	No adjustment for smoking
Kurppa et al. (1986)	Finland (Mining) (Rock & stone) (Steel casting) (Foundries) (Other)	312 (230-414) 436 (246-670) 271 (112-549) 184 (54-451) 225 (88-464) 343 (168-628)	No adjustment for smoking; all CIs are 99%. All categories of radio -graphic findings show significant SMRs
Gudbergsson et al. (1984)	Finland	3.0 (1.5-5.3) SIR	CIs are 99%
Zambon et al. (1986)	Veneto Area, Italy (Mining) (Tunneling) (Quarrying) (Mixed mine) (Others)	228 (169-302) 156 (68-871) 239 (145-376) 569 (200-1187) 190 (90-347) 279 (78-732)	Smoking explains part of the excess; apparent dose-response for years since first exposure with 20 years minimum
Chiyotani (1984)	Japan	653 (p<0.05)	Elevated risks for all smoking categories
Chiyotani et al. (1990)	(Mining)	6.03 (5.29-6.77) 1.83 (Nested case/control[NCC])	including 2.22 for never smokers; inverse association for category of
	(Mining/tunnling) (Ceramics) (Quarrymen) (Quary/coalminrs) (Kilnmen/casters)	1.75 NCC ∞ (p <0.05) NCC 1.33 NCC 0.57 NCC ∞ (p<0.05) NCC	pneumoconiosis
Miller et al. (1987)	Ontario, Canada (Goldminers) (Nonsilicotic) ((Mild silicosis) Severe silicosis)	156 (145-167) 134 (122-147) 201 (175-232) 242 (191-303)	Employment before 1945; Smoking examined, but not thought to confou results
Infante-Rivard et al., 1989	Quebec, Canada (Mining) (Mining, quarry) (Foundries) (Ceramics) (Other)	3.5 (p<0.05) 3.8 (p<0.05) 2.0 (p<0.05) 3.0 (p<0.05) 5.0 (p<0.05) 6.9 (p<0.05)	Smoking data unavailable
Amandus and Costello (1991)	U.S.A. (Metal ore miners) (Copper ore) (Lead-zinc ore) (Iron ore) (Mercury ore) (Other ores)	1.73 (0.94-2.90) 1.96 (1.19-3.23)# 0.96 (0.2-2.81) 2.42 (0.66-6.21) 1.77 (0.21-6.38) 14.03 (2.89-40.99) 1.01 (0.12-3.68)	Risk 2-3 times greater for smokers; radon levels does not explain the risk #Compared to non-silicotics, and adjusted for age and smoking
Amandus et al., (1991); (1992)	North Carolina U.S.A.	2.6 (1.8-3.6) 3.9 (2.4-6.4) when compared to non-silicotic metal ore miners	Risks not explained by smoking Risk not altered by re-reading chest films

EBSCOhost - printed on 2/13/2023 4:48 AM via . All use subject to https://www.ebsco.com/terms-of-use

Table 5. Summary of lung cancer epidemiology studies of silicotics using standardized mortality/incidence ratio methods

Authors (date)	Country (industry)	SMR or SIR (95% CI/p value)	Comment
Chia et al. (1991)	Singapore (Chinese ancestry)	2.01 (0.92-3.81) SIR	No adjustment for smoking; risk increases with length of employment
	(Granite & gravel work)		
	(Mild silicosis)	1.40 SIR	
	(Moderate silicosis)	2.79 SIR	
	(Severe silicosis)	5.11 SIR	
Merlo et al., (1990)	Genoa, Italy	6.85 (4.47-10.0)	Indirect adjustment for smokin explains 12-30% of risk
Ng et al. (1990)	Hong Kong, China	203 (1.35-2.93)	All deaths were among smokers, but only 50% of the risk was due to unadjusted confounding
Goldsmith et al. (1993)	Selected regions of California, U.S.A.	1.90 (1.35-2.60)	Only 1.3 risk explained by smoking; SMR = 2.08 for large intestine
	Construction	4.04 ($p<0.05$)	
	Mining &quarry	1.65	
	Metallurgy	0.57	
	Utilities/Misc	0.76	

those subjects whose lung cancer occurred >10 years following diagnosis of silicosis, the SMR was 236 (95% CI = 107-448). No smoking or industrial exposure measurements were available for this study.

Finkelstein et al. (1982) conducted a follow-up study of 1190 Ontario, Canada silicotics who had been employed underground from 1940 to 1975 comparing the lung cancer risk to that of Ontario males. The authors reported an overall SMR of 198 ($p < 0.01$) with SMRs of 303 ($p < 0.01$) and 195 ($p < 0.05$) for silicotics diagnosed between 1940 to 1949 and between 1950 and 1959, respectively. Finkelstein et al. (1987) examined the lung cancer risk among 276 silicotics from 1940 to 1985 employed in above-ground industries (excluding foundries). Overall the SMR for lung cancer was 302 (95% CI = 173-489).

Miller et al. (1987) obtained X-rays of Ontario gold miners and demonstrated that the risk of lung cancer increased with degree of silicosis, as shown by severity of chest film reading, but this pattern was confined only to those employed before 1945. Those gold miners without silicosis had a SMR of 134 (95% CI = 122, 147); those with mild silicosis had a SMR of 201 (95% CI =175, 232); and those with severe silicosis had a SMR of 242 (95% CI =191, 303).

Infante-Rivard et al. (1989) assessed the lung cancer risk among 1,165 silicotics in Quebec who were diagnosed from 1938 to 1985 and followed until 1986. Overall the lung cancer risk was 3.5 ($p < 0.05$). This risk remained elevated in all the industries: mining, quarrying and tunneling, metallurgy, and ceramics with SMRs that ranged from 2.0 to 6.9. Neuberger et al. (1986) examined the relative risk for lung cancer among Austrian silicotics using death certificates from 1955 to 1979. The overall SMR was 140 ($p < 0.05$).

Gudbergsson et al. (1984) examined the cancer incidence among 331 silicotics identified from the Finnish Registry of Occupational Diseases who were compensated between 1964 and 1974, and followed through 1975. Compared to the age-adjusted lung cancer incidence in the Finnish male population, the SIR was 3.0 (99% CI = 1.5-5.3). Kurppa and colleagues (1986) presented the lung cancer mortality rate among 961 cases of

EBSCOhost - printed on 2/13/2023 4:48 AM via . All use subject to https://www.ebsco.com/terms-of-use

silicosis diagnosed from 1935 to 1977. Using the Finnish male population as a comparison, they observed 80 lung cancer deaths versus 25.5 expected, a SMR of 312 (99% CI = 230-414). Silicotics from the mining industry had a SMR of 436 (99% CI = 246-670); the rock and stone industry had a SMR of 271 (99% CI = 112-549); the SMR for steel casting was 184 (99% CI = 54-451); and the SMR for iron foundries was 225 (99% CI = 88-465).

Zambon et al. (1987) examined a cohort of 1,234 silicotics from the Veneto Region of Italy diagnosed from 1959 to 1963 and followed through 1980. Overall, there was a significant SMR for lung cancer of 228 (95% CI =169-302). For the mining industry , the SMR was 156 (95% CI = 68-871); for tunneling the SMR was 239 (95% CI = 145, 376); and for quarrying the SMR was 569 (95% CI = 200-1187). An earlier examination of this cohort suggested that smoking acted synergistically with silicosis in the risk of lung cancer (Mastrangelo et al., 1983)

Merlo and co-workers (1990) conducted a follow-up study of 520 male silicotic patients seen at San Marco Hospital in Genoa, Italy from 1961 to 1981. The SMR for respiratory tract cancers was 6.85 (26 observed, 3.8 expected based on Italian national mortality for males) with 95% CI = 4.47-10.0. Using Alexson's (1978) method for indirect adjustment for smoking, the authors estimated that between 12% and 30% of the excess cancer risk could be attrubuted to unadjusted confounding from smoking.

Chiyotani (1984) showed that the SMR among silicotics rose from 178 to 573 when comparing the lung cancer risk for the periods 1971-1975 to 1976-1981 in Japanese males aged more than 50 years. The author then calculated the risk for lung cancer for the years 1979 to 1981 using patients from 11 pneumoconiosis clinics throughout Japan, and found a SMR of 575 (48 obs v 8.35 exp); for silicotics the SMR was 653, and for anthrocosilicosis the SMR was 491. Chiyotani et al. (1990) extended follow-up another two years and reported a SMR of 6.03 (95% CI = 5.29-6.77). In a case-control analysis (matching on hospital, age, and smoking), there were elevated odds ratios for mining, for quarry work, and for ceramics manufacturing.

Amandus and Costello (1991) examined the lung cancer risk among silicotics diagnosed in the 1959-1961 U.S. Public Health Service study of metal ore miners. Overall these men had a SMR of 1.73 (95% CI = 0.94-2.90). Lung cancer risk was two to three times greater for current and ex-smokers at the time of the survey. Although the numbers of deaths were small, there were elevated risks for the following ores: lead-zinc, iron, and mercury mining. Compared with nonsilicotics and adjusting for age and smoking, silicotics had a rate ratio of 1.96 (95% CI = 1.19-3.23). This risk was not explained by levels of radon in the mines, and there did not appear to be interaction between silicosis and smoking .

Amandus et al. (1991) published an important paper on the the lung cancer risk among 760 silicotics from the North Carolina Dusty Trades surveillance program who were diagnosed from 1940 and whose vital status was followed until 1983. The authors compared mortality rates of silicotics with U.S., North Carolina, and the nonsilicotics in the U.S. Public Health survey of metal ore miners described above. Among white silicotics the SMR was 2.6 (95 % CI = 1.8-3.6) based on U.S. rates and the SMR was 3.0 (95% CI = 2.0-4.2) based on North Carolina rates. Cigarette smokers had a SMR of 3.4 (95% CI = 2.0-5.3) and nonsmokers had a SMR of 1.7 (95% CI = 0.5-3.9). Compared to metal ore miners, North Carolina silicotics had a lung cancer RR of 3.9 (95% CI = 2.4-6.4) that was adjusted for smoking. Interestingly, never smokers had a RR of 8.6

EBSCOhost - printed on 2/13/2023 4:48 AM via . All use subject to https://www.ebsco.com/terms-of-use

while smokers had a RR of 3.2, comparing silicotics with metal ore miners. The authors re-read the chest films, and found similar lung cancer excesses as those observed previously (Amandus et al., 1992)

Chia and colleagues (1991) examined the lung cancer incidence in 159 cases of silicosis among Chinese males registered between 1970 and 1984 in Singapore. All subjects were employed in granite excavation and gravel crushing. The standardized incidence ratio (SIR) was 2.01 (95% CI = 0.92-3.81), with the risk rising from 1.76 with 20 to 40 years employment to 2.54 for employment >40years. There was a gradient for three categories of severity based on positive X-rays: Category 1 (mild silicosis) had a SIR of 1.4; Category 2 (moderate profusion) had a SIR of 2.79; and Category 3 (severe silicosis) had a SIR of 5.11 (Chia et al., 1991).

Ng and colleagues (1990) conducted a follow-up study of 1,419 men registered as silicotics in Hong Kong, China. They reported a SMR of 2.03 (95% CI = 1.35-2.93), 28 observed lung cancers, and 13.8 expected. All pulmonary cancer deaths occurred among smokers; tuberculosis was also demonstrated to be a risk factor (SMR = 2.52; 95% CI = 1.52-3.94). There was an increasing trend showing a lung cancer association with severity of opacities from pulmonary X-rays. Using Alexson's (1978) approach for estimating degree of confounding from smoking, the authors suggested that perhaps 50% of the risk may be due to confounding by tobacco, and they also suggest that smoking and silicosis may act synergistically.

Goldsmith and co-workers conducted a follow-up study of 590 Workers' Compensation claims for silicosis in California from 1946 to 1991 (Goldsmith et al., 1993). The authors compared mortality with U.S. males, adjusting for age, race and time period. In addition to high risks for tuberculosis (TB) (SMR = 56.34; 95% CI = 41.0, 75.40) and for NMRD (SMR = 6.80; 95% CI = 3.11, 8.63), the study demonstrated a SMR of 1.90 (95% CI = 1.35, 2.60) for cancer of the lung, and SMR of 2.08 (95% CI = 1.14, 3.50) for cancer of the large intestine. Cancers of the the lung and large intestine showed SMRs of 4.04 and 3.28 among silicotics from the construction industry; mining and quarrying had SMRs of 1.65 and 2.01; metallurgy had SMRs of 0.57 and 0.86; and utilities, transportation and miscellaneous industries had SMRs of 0.76 and 2.83, though the latter two industry groups were based on small numbers of deaths. Evaluating the lung cancer risk indicated that only a SMR of 1.30 could be explained by unadjusted confounding by smoking. When the risks were assessed by amount of compensation awarded, positive gradients emerged for TB, NMRD, and lung cancer, though not for cancer of the large intestine (Goldsmith et al., 1993)

Table 6 presents the results of other epidemiological study methods (odds ratios [ORs], proportionate mortality ratios [PMRs], or mortality odds ratios [MORs]) in which the association between silicosis and lung cancer has been examined. Westerholm (1980) used a PMR approach to examine the lung cancer risk among silicotics enrolled in the Swedish Pneumoconiosis Register. For those whose silicosis arose from employment in mining, quarrying, and tunneling between 1931 and 1948, the PMR was 5.9 ($p < 0.01$); for those whose pneumoconiosis was diagnosed between 1949 and 1969 the PMR was 3.8 ($p < 0.01$). For silicotics employed in the steel and iron industry and whose conditions were presented between 1949 and 1969, the PMR was 2.2 ($p < 0.05$) .

Hessel and Sluis-Cremer (1986) tested the association of underground exposure and silicosis in a matched case-control study of lung cancer among white South African gold miners. Matching was on year of birth, minimal employment of 4 years, and tobacco

EBSCOhost - printed on 2/13/2023 4:48 AM via . All use subject to https://www.ebsco.com/terms-of-use

Table 6.
Summary of lung cancer epidemiology studies of silicotics using other study methods

Authors (date)	Country (Industry)	Measure of Effect* (95% CI/p value)	Comment
Westerholm (1980)	Sweden (All)	PMR =2.7 (p<0.05)	No smoking information
	(Mining, quarry & tunneling 1931-48)	PMR = 5.9 (p<0.01)	
	(Mining, quarry & tunneling 1949-69)	PMR =3.8 (p<0.01)	
	(Steel & iron foundries 1949-69)	PMR=2.2 (p<0.05)	
	(Ceramics)	PMR=1.3	
	(Other)	PMR=3.3	
Hessel & Sluis-Cremer(1986)	South Africa (White goldminers)	OR =1.1 (p=0.87)	Matched for year of birth, tobacco consumption, and min. # of dusty shifts
Hessel et al. (1990)	(Parenchmal silicosis)	OR =1.10 (0.79-1.60)	Matched only on age and min. # of dusty shifts;
	(Pleural silicosis [PS])	OR = 0.80 (0.54-1.20)	Adjusted for smoking, age, and dust exposure
	(Silicosis hilar glands [SHG])	OR = 1.29 (0.83-2.00)	
Hnizdo & Sluis-Cremer (1991)	(White goldminers surveyed 1968-71 aged 45 to 54 with 10 yrs min underground)	OR=0.9 (0.5-1.6) for silicosis of lung OR=1.2 (0.7-2.0) for PS OR=3.9 (1.2-12.7) for SHG	Adjusted for age, smoking, & cumulative dust exposure; gradient for degree of SHG and lung cancer
Schuler & Ruttner (1986)	Switzerland (Mining)	MOR=2.0 (p<0.001)	No smoking data
	(Stone & quarry)	MOR=2.3 (p<0.001)	
	(Ceramics)	MOR=1.2 (p>0.6)	
	(Foundry)	MOR=2.0 (p=0.25)	
	(Others + ceramics)	MOR=3.3 (p<0.001) MOR=2.4 (p<0.05)	
Steenland & Beaumont (1986)	U.S.A. (Members of the Granite Workers Union)	OR =3.2 (p<0.001) Nested case-control study	No smoking data
Rubino et al. (1985)	Piedmont area, Italy	PMR=1.54 (p<0.05)	No smoking data
Forastiere et al. (1986)	Civitacastellana, Italy (Ceramics)	OR=3.9 (1.8-8.3)	Adjusted for smoking
Forastiere et al. (1989)	Latium area, Italy	MOR =1.5 (1.1-1.9)	
Rosenman et al. (1995)	U.S.A. (States of Michigan and New Jersey)	PCMR=1.82 (1.04, 2.95) for white males PCMR=1.73 (0.83, 3.18) for black males	Risk is not related to those who filed Workers' Compensation or to smoking
Goldsmith et al. (1990)	California, U.S.A.	PMR=2.2 (1.4-3.4) for whites	No adjustment for smoking

* PMR = proportionate mortality ratio; OR = odds ratio; MOR = mortality odds ratio; PCMR = proportionate cancer mortality ratio

consumption 10 years prior to death. The authors found 127 death certificates and an equal number of controls from the the files of the gold miners' pension fund from January, 1979 through October, 1983. The pulmonary cancers were verified by autopsy or biopsy record. Matched pairs analysis revealed that there was no association between silicosis (or cumulative dust exposure) and lung cancer; the matched OR was 1.1. Hessel et al. (1990) conducted an expanded case-control study of necropsied miners that included 231 primary lung tumors and 318 controls who died from 1975 to 1986 (excluding those in the prior

EBSCOhost - printed on 2/13/2023 4:48 AM via . All use subject to https://www.ebsco.com/terms-of-use

study). Their findings showed no differences in cumulative dust exposure, dust intensity, shifts employed underground and shifts in high dust jobs. The OR (adjusted for age, smoking, and cumulative dust exposure by conditional logistic regression) for silicosis of the parenchyma was 1.10 (95% CI = 0.79-1.60); for silicosis of the pleura the OR was 0.80 (95% CI = 0.54-1.20); and for silicosis of the hilar lymph glands the OR was 1.29 (95% CI = 0.83-2.00). Hnizdo and Sluis-Cremer (1991) also examined the association between silicosis and lung cancer in a nested case-control study of their cohort of miners (see above for details). They reported that the adjusted (for age, cumulative dust particle-years, and cigarette smoking) OR for silicosis of the lung was 0.9 (95% CI = 0.5-1.6); for silicosis of the pleura the OR was 1.2 (95% CI = 0.7-2.0); and for silicosis of the hilar lymph glands the OR was 3.9 (95% CI = 1.2-12.7). There was also a significant association for trend ($p = 0.035$) for the degree of silicosis of the hilar glands (comparing slight, moderate, and marked with no silicosis).

Schüler and Rüttner (1986) examined the mortality from 1960 to 1978 of 2,399 cases of silicosis in Switzerland using the MOR. The overall lung cancer risk was 2.2 ($p < 0.05$). For mining the MOR was 2.3 ($p < 0.001$); the MOR for stone and quarry work was 1.2; for the foundry industry the MOR was 3.3 ($p < 0.001$); and for the ceramic industry the MOR was 2.0. Steenland and Beaumont (1986) in a study of the mortality of granite workers conducted a nested case-control study that showed a 3.2-fold OR ($p < 0.001$) when comparing lung cancer cases with other causes of death for mention of silicosis on the death certificate.

Rubino et al. (1985) conducted a PMR study of 746 silicotics from the Piedmont area of Italy during the years 1970 to 1983. They reported a significant PMR of 1.4 for lung cancer ($p < 0.05$). Carta et al. (1991) reported on the lung cancer risks for a cohort of 724 silicotics from Sardinia. They reported a SMR of 1.29 (95% CI = 0.8-2.0) for lung cancer, with an increasing trend for latency of 10 and 15 years from diagnosis. The authors reported a SMR of 4.11 among heavy smokers, and a SMR among those with airflow obstruction of 2.83. There was no association with severity of silicosis or with cumulative silica exposure. The authors concluded that smoking and airflow obstruction were greater risk factors for lung cancer than either silicosis or silica exposure.

Forastiere et al. (1986) demonstrated that among Italian ceramic workers with silicosis there was a smoking- and age-adjusted Mantel-Haenszel OR of 3.9 (95% CI = 1.8-8.3). A more recent report of the lung cancer risk among 595 Latium region silicotics showed a MOR of 1.5 (95% CI = 1.1-1.9), with significant risks demonstrated for mining and for pottery work (Forastiere et al., 1989). Goldsmith et al. (1990) reported a PMR of 2.2 for lung cancer (95% CI = 1.4-3.4) among silicotics identified from 1945 to 1963 in the California Silicosis Registry and followed until 1984. McLoughlin et al. (1992) reported lung cancer ORs of 0.5 for tungsten ore miners, 2.0 ($p < 0.05$) for tin miners, and 3.1 for copper/iron ore miners. These findings were adjusted for age and smoking.

Rosenman and colleagues (1995) found that silicotics in New Jersey and in Michigan had elevated cancer proportional mortality ratios for both whites and blacks (Rosenman et al. 1995).

Interaction between silica exposure or silicosis and other factors

The question of whether simultaneous exposure to tobacco smoke and inhaled crystalline silica elevate the risk for both non-malignant respiratory disease and lung cancer is controversial. There are a number of epidemiologic studies that suggest that simultaneous exposure to tobacco smoke and crystalline silica increases the cancer risk

EBSCOhost - printed on 2/13/2023 4:48 AM via . All use subject to https://www.ebsco.com/terms-of-use

(Goldsmith & Guidotti, 1986; Hnizdo & Sluis-Cremer, 1991; Ng et al., 1985; Zambon et al., 1986) while others suggest smoking plays little role in the risk of silicosis (Landrigan et al., 1986; Rice et al., 1986; Sluis-Cremer, 1986). This position is supported by the 1986 Surgeon General's Report on smoking in the workplace, which conludes that smoking and silica exposure may interact for other nonmalignant respiratory illnesses (such as bronchitis and small airways disease), but smoking plays little role in the risk of silicosis (U.S. DHHS, 1986). There is also the possibility that silica, smoking and radon progency may interact (Abelson 1991). These relationships have not been examined in an experimental animal setting and so the immunologic and molecular chemical mechanisms of interaction are poorly defined and not well understood.

Does silica exposure or silicosis cause lung cancer?

Determining whether silica causes lung cancer is a question of comparing the evidence with some standard criteria for determining causation. This assessment has been undertaken by IARC (1987) and by the State of California (Proposition 65, 1988). This assessment will use the criteria spelled out by (Hill 1965) with some modifications, and the review will examine silica exposure and silicosis separately. In both cases, one must ask if the data comply with the following criteria: strong relative risk; dose-response; consistency; control for confounding; temporal cogency; biological specificity; positive animal model; reliable exposure data; and overall coherence. Table 7 compares these criteria for both silica exposure and for silicosis.

Table 7.
Criteria for causation for silica exposure and for silicosis

Point of evidence	Silica-exposed workers	Workers with silicosis
• Strong relative risk	✓	✓✓✓
• Consistent findings	✓✓	✓✓✓
• Dose-response gradients	✓✓	✓
• Controlled confounding	✓	✓
• Reliable exposure data	✓	more research needed
• Biological specificity	✓✓	more research needed
• Temporal cogency	✓	✓
• OVERALL COHERENCE	YES	YES

Strong relative risk

Strong relative risk is usually defined as a risk measure of 2.0 or greater. For silica-exposed workers, the risk levels seem to be consistently elevated, but the risk levels tend to be in the 1.3 to 1.7 ranges. Especially noteworthy is the relatively low risks for granite workers, tunnelers, and sandblasters seen in Table 3. Gold miners from throughout the world seem to have elevated lung cancer risks, with the exception of Homestake miners in South Dakota as seen in Table 2. Foundry workers have some elevated lung cancer risks, but with the exception of the study by Fletcher (1986), linkage with silica exposure remains elusive.

For silicotics, there is a strong set of relative risks. With the exception of the autopsy studies that show risks less than the null value (relative risk of 1.0), 27 out of 29 studies of

EBSCOhost - printed on 2/13/2023 4:48 AM via . All use subject to https://www.ebsco.com/terms-of-use

silicotics throughout the world show striking risks that range from 1.4 in Austria (Neuberger, et al., 1986) to 6.5 in Japan (Chiyotani et al., 1990). Only Hessel and co-workers have shown no association between silicosis and lung cancer, and that has now been challenged by his colleagues, Hnizdo and Sluis-Cremer (1991) with their finding of 3.9 relative risk among those with silicosis of hilar lymph glands. Also noteworthy are the recent elevated risks for silicotics in North Carolina and among a national sample of metal ore miners by Amandus et al. (1991) and by Amadus and Costello (1991).

Consistent findings

The relative risks for silica-exposed workers and for silicotics have been consistent between investigators and accross national boundries. An exception appears to be iron ore miners, who do not seem to have the elevated risks that other silica-exposed groups have. The consistency for the findings among epidemiologic studies of silicotics is impresssive, and these associations hold true in Europe, Asia, and North America.

Dose-response gradients

For a material to be biologically active, it must demonstrate that increasing the dose or exposure level produces increasing risk. Among silica-exposed workers, there are several examples of dose-related gradients, but they tended to be be indirect measures of exposures such as length of time employed (such as Selikoff, 1978) or increased risk for dustier jobs (such as Fletcher, 1986). However, the work of Hnizdo and Sluis-Cremer (1991) and Checkoway et al. (1993) demonstrating a dose-response for cumulative industrial hygiene respirable particle exposure confirms the previous indirect associations and strengthens the link between silica dust and lung cancer. Among silicotics, there is only indirect data linking workplace silica concentrations to lung cancer risk. However, there are four positive studies showing a gradient for the degree of silicosis disability being a risk factor for lung cancer (Chia et al., 1991; Ng et al., 1990; Miller et al., 1987); and Hnizdo and Sluis-Cremer, 1991). To the extent that severity of silicosis reflects silica exposure, then silicotics share the dose-related gradients demonstrated in studies of silica exposure.

Controlled for confounding

Lack of adjustment for smoking was the biggest confounder in both types of early studies. However, adjusting for smoking where it is missing and when data are present does not alter the risk. In studies of foundry workers, there are other environmental exposures that may continue to confound a suggestive link with silica dust. IARC (1987) observed that selection bias may play a role in the elevated risk for silicotics because they were more likely to have physicians' attention and thus lung tumors were more likely to be found because of their having chronic pulmonary disease. However, given the strong likelihood of histological confirmation for lung cancers, and the findings of Amandus et al. (1992) and Merlo et al. (1990), this arguement does not blunt the strong and consistent finding of significantly elevated lung cancer rates among silicotics.

Reliable exposure data

All of the occupational/industrial groups reviewed above have high dust exposure to crystalline silica though not recorded accurately. The best exposure data exist for quartz-exposed workers rather than for silicotics, because obtaining individual dust concentrations is not practical. The exception to that situation is sampling from the North Carolina Dusty Trades monitoring, but Amandus et al. (1991) did not present them in this paper. The most powerful exposure data are those presented for respirable quartz in the South African gold

EBSCOhost - printed on 2/13/2023 4:48 AM via . All use subject to https://www.ebsco.com/terms-of-use

mines by Checkoway et al. (1993), Wyndham et al. (1986), and Hnizdo and Sluis-Cremer (1991), and all studies found measurable lung cancer risks correlated with cumulative silica exposures.

Biological specificity

Respirable silica interacting with pulmonary tissue producing lung cancer is the pathway outlined by Goldsmith et al. when this issue arose in 1982. Silica exposure is multi-pathological causing silicosis, cor pulmonale, silicotuberculosis, and possibly nephritis. Understanding the precise mechanism for quartz's ability to produce cancer does not mean that it cannot induce cancer through different pathways. Goldsmith et al. (1982) suggested that quartz could act directly or via some fibrotic mechanism (similar to foreign body tumorigenesis), and there is no agreement as to which is more likely. Saffiotti (1986) suggested that release of cell mediators during the fibrotic process could stimulate cell proliferation in adjacent tissue and ultimately neoplasia. His recent work demonstrates silica binds with DNA, and/or enhances access to reactive oxygen species (Saffiotti et al., 1993).

Positive animal findings

There is ample animal evidence in support of silica's carcinogenity, an attribute recognized by IARC (1987) which judged the findings to be sufficient. Since 1987, Muhle et al. (1989) demonstrated that lifetime exposure to DQ12 quartz is carcinogenic via inhalation at $1 mg/m^3$. It is also clear that quartz produces fibrosis in the lung and that either preceedes or appears simultaneously with respiratory tumors. These positive animal results appear to show some species specificity, because rats (along with humans) demonstrate that silica produces fibrotic and neoplastic diseases, while other rodents (such as hamsters and guinea pigs) do not. This issue has perplexed Saffiotti (1986; 1992) who has developed several lines of research to try to explain this paradox, and the mechanisms for carcinogenesis (Saffiotti, et al., 1993).

Temporal cogency

In both silica-exposed workers and among silicotics, the data support appropriate time-related events. That is, cancer risk is not elevated until at least 20 years employment, which is consistent with what has been learned about other workplace carcinogens such as asbestos and arsenic. The lung cancer excesses among silicotics have arisen after the diagnosis of silicosis (not coincidentally), and again after usually decades of employment/exposure to silica.

Overall coherence

For silica-exposed workers, there is a moderate relative risk, it is consistent across industries and countries and investigators, and there are excellent dose-response data from South Africa. Confounding for age and smoking have been adjusted and the lung cancer risk remains; there are good exposure data, with biological specificity and a powerful animal model; and no chronological violations of temporal cogency. On these bases, it is logical to conclude that occupational silica exposure is carcinogenic for humans.

For silicotics, there are very strong relative risks for lung cancer, and they are consistent between countries, investigators and among industries giving rise to the fibrotic lung disease. Although there is little silica exposure data, there are several studies supporting an increased risk according to severity of fibrosis, and selection, smoking, and radon do not account for the risk. The animal model is less clear cut, but the findings are

EBSCOhost - printed on 2/13/2023 4:48 AM via . All use subject to https://www.ebsco.com/terms-of-use

consistent with biological specificity and are temporally correct. Thus, it is rational to argue that silicosis predisposed to an increased lung cancer risk, and that risk is either due to high silica exposure or to the fibrotic processes or both.

SUMMARY OF HUMAN HEALTH RELATED TO SILICA EXPOSURE

Many studies have examined the cancer risk in silicotics (Amandus and Costello; 1991; Chia et al.; 1991; Ng et al., 1990; Zambon et al, 1987) and non-silicotics separately. The presence of silicosis itself may be a separate risk factor for pulmonary neoplasia, an indicator variable for duration and/or intensity of exposure, or a marker of genetic suseptibility to pulmonary damage by inhalable crystalline silica. The general trend is that silicotics show increased risk of pulmonary neoplasia as compared to both those exposed to silica without silicosis and the general population.

Hnizdo and Sluis-Cremer (1991) and Checkoway et al. (1993) studies both demonstrated excess risk associated with occupational exposure to crystalline silica and a dose-response relationship. Both studies also demonstrated greater than additive inter-action between crystalline silica and tobacco smoke. Other epidemiologic studies have demonstrated a dose-response gradient for the association between silicosis and lung cancer (Chia et al.; 1991; Ng et al., 1990), but questions of confounding exposures from polycyclic aromatic hydrocarbons, metal oxide fumes, and radon, exist (Goldsmith et al. 1986; Goldsmith, 1994; McLaughlin, 1992).

Besides increases in pulmonary cancer in silicotics and non-silicotic workers exposed to crystalline silica, epidemiologic studies have occasionally demonstrated evidence of increases in other varieties of cancer. Increses in the rate of lymphatic malignancies were demonstrated by Brown et al. (1986) and Steenland and Brown (1993), Kurppa et al. (1986), Silverstein et al. (1986), and Redmond et al. (1981). Similarly, Wagner et al. (1980) demonstrated increases in lymphatic cancers in crystalline silica expsoed animals. Finkelstein et al. (1982, 1987) showed a consitent excess of gastric cancer among Ontario, Canada silicotics, but recent analyses differ regarding the associations among Ontario gold miners (IDSP, 1987; Kusiak et al., 1993). Goldsmith et al. (1993) observed a two-fold excess for cancer of the large intestine among silicotics in California.

Taken together with the positive animal findings and the ability of silica to bind with DNA, IARC's assessment (IARC, 1987) that there is sufficient evidence for the carcinogencity of quartz does not appear to be in doubt. Furthermore the human evidence for silica's carcinogencity appears to sufficient based on the epidemiology findings for both silica-exposed workers and for silicotics as well (Goldsmith, 1994).

Many scientists express the view that silica exposure and silicosis are unrelated to cancer risk (Heppleston 1985; Craighead 1988; McDonald 1989; Pairon et al. 1991) . In some cases their objections are to aspects of research which they feel need attention. As an example, McDonald (1989) has expressed the view that silicotics from compensation registries contain too many individuals with smoking-related (rather than true silicosis) claims, and thus a finding of elevated lung cancer was purely a function of smoking and not of silica exposure or silicosis. The high lung cancer findings of Merlo et al. (1990) who used hospitalized silicosis patients, Amandus and colleagues (1992) who re-evaluated their 1991 results using only the positive x-rays for silicosis in the North Carolina data and found nearly identical lung cancer risks, and Goldsmith et al. (1993) who showed a lung cancer gradient for level of compensation compared to workers who received none stand in response to McDonald's observations. Heppleston (1985) argued against silicosis and

EBSCOhost - printed on 2/13/2023 4:48 AM via . All use subject to https://www.ebsco.com/terms-of-use

lung cancer being related because autopsy findings comparing silicotics and general necropsies suggested no association. That position appears to have less support because of the powerful epidemiology findings of elevated lung cancer risk among silicotics since 1980, a risk both too high to be explained by smoking and independent from smoking as well.

The work of Frazier and Sundin (1986) showed a decline in the number and rate of silicosis cases and deaths in the U.S; these data matched a common industry perspective indicating that silicosis declined after the introduction of wet methods in the Vermont granite sheds (Costello and Graham, 1986; Davis et al., 1983) in the 1940s. However, new epidemiology research suggests that extensive residual risks remain for common noncancer health risks. Specifically, the report of over 100 cases of acute and accelerated silicosis among Mexican and Mexican-American sandblasters detected over the past 5 years in Texas (Weisenfeld et al., 1993) is very distressing from a public health perspective. The most recent follow-up mortality studies by Hnizdo and Sluis-Cremer (1993), Steenland and Brown (1994 in press), and Checkoway et al.(1993) strongly suggest that silicosis and associated lung diseases,including TB, remain elevated. Additional health problems including kidney diseases (Goldsmith and Goldsmith, 1993) and autoimmune disorders (Steenland and Goldsmith, 1994 submitted), are emerging as areas of concern for those occupationally exposed to silica.

CONCLUSION

Occupational silica exposure is causally related to silicosis, silicotuberculosis, and right heart enlargement, and appears to be related to kidney disease and to autoimmune disorders. Consistent with IARC's (1987) assessment of silica being a probable human carcinogen, the evidence for silica's carcinogenicity is strongly related to a prior diagnosis of silicosis, and there is also substantial evidence of silica's direct carcinogenic risk.

From the perspective of science, medicine, and public health, future research should be expanded to address the following issues: the biological and physical interaction between silica exposure, radon, and smoking; differential cancer and noncancer risks according to the polymorphs of silica; develop improved and simplified means of measuring different polymorphs in dusty work areas and in exposed workers; mechanistic research on the link between silica, fibrosis, and cancer; the biology and epidemiology of silica exposure and kidney diseases and autoimmune disorders; and improvements in silica exposure dose reconstruction. The final recommendations are the simplest and most difficult because they involve industry taking risks of detecting and preventing illnesses: improve and expand the health surveillance of silica-exposed workers,and via workplace engineering, lower dust levels so that all silica-related diseases can be prevented.

ACKNOWLEDGMENTS

Randall Ruble, DVM, MPVM, contributed to parts of this review, and the author was supported by Contract #324A-8702-S0370 from the U.S. Department of Energy to the California Public Health Foundation.

EBSCOhost - printed on 2/13/2023 4:48 AM via . All use subject to https://www.ebsco.com/terms-of-use

REFERENCES

Abelson, P. (1991) Mineral dusts and radon in uranium mines. Science 254:777.

Agricola, G. (1556) De Re Metallica. Basel, Switzerland, Dover Publications, New York.

Amandus, H., Costello, J. (1991) Silicosis and lung cancer in U.S. metal miners. Arch Environ Health 46:82-89.

Amandus, H.E., Castellan, R.M., Shy, C.M., Heineman, E.F., Blair, A. (1992) Reevaluation of silicosis and lung cancer in North Carolina dusty trades workers. Am J Indust Med 22:147-153.

Amandus, H.E., Shy, C.M., Wing, S., Blair, A., Heineman, E.F. (1991) Silicosis and lung cancer in North Carolina dusty trades workers. Am J Indust Med 20:57-70.

Andjelkovich, D.A., Mathew, R.M., Richardson, R.B., Levine, R.L. (1990) Mortality of iron foundry workers: I. Overall findings. J Occup Med 32:529-540.

Andjelkovich, D.A., Mathew, R.M., Yu, R.C., Richardson, R.B., Levine, R.L. (1992) Mortality of iron foundry workers II. Analysis by work area. J Occup Med 34:391-401.

Armstrong, B.K., McNulty, J.C., Levitt, L.J., Williams, K.A., Hobbs, M.S.T. (1979) Mortality in gold and coal miners in Western Australia with special reference to lung cancer. Brit J Indus Med 36:199-205.

Axelson, O., Rehn, M. (1971) Lung cancer in miners. Lancet ii:706-707.

Axelson, O., Sundell, L. (1978) Mining, lung cancer and smoking. Scand J Work Environ Health 4:46-52.

Bagchi, N. (1992) What makes silica toxic? Brit J Indus Med 49:163-166.

Balaan, M.R., Banks, D.E. (1992) Silicosis. Environmental and Occupational Medicine, 2nd edn, Rom WN (ed) Boston, Little, Brown & Co, p 345-358.

Banks, D.E., Morring, K.L., Boehlecke, B., Althouse, R.B., Merchant, J.A. (1981) Silicosis in silica flour workers. Am Rev Respir Dis 124:445-450.

Bar-Ziv, J., Goldberg, N. (1974) Simple siliceous pneumonoconiosis in Negev Bedouins. Arch Environ Health 29:121-126.

Beadle, D., Bradley, A. (1970) The composition of airborne dust in South African gold mines. Proc Int'l Pneumoconiosis Conf, Johannesburg, Shapiro H.A. (ed) Cape Town, Oxford University Press, p 462-466.

Blot, W.J., Brown, L.M., Pottern, L.M., Stone, B.J., Fraumeni, J.F. Jr (1983) Lung cancer among long-term steel workers. Am. J. Epidemiol 117:706-716.

Boyd, J.P., Doll, R., Faulds, J.S., Keiper, J. (1970) Cancer of the lung in iron ore (haematite) miners. Brit J Indus Med 27:97-105.

Brody, A., Roe, M.W., Evans, J.N., Davis, G.S. (1982) Deposition and translocation of inhaled silica in rats. Quantification of particile distribution, macrophage participation, and function. Laboratory Investigations 47:533-542.

Brown, D.P., Kaplan, S.D., Zumwalde, R.D., Kaplowitz, M., Archer, V.E. (1986) Retrospective cohort mortality study of underground gold mine workers. In: Silica, Silicosis, and Cancer: Controversy in Occupational Medicine. Goldsmith DF, Winn DM, Shy CM (eds) New York, Praeger. p 335-350.

CAPCOA (California Air Pollution Control Officers Association) (1991) Air Toxics "Hot Spots" Program, Risk Assessment Guidelines for AB 2588. California Air Pollution Control Officers Assoc, Risk Assessment Comm of CAPCOA, Sacramento, CA.

Carta, P., Cocco, P., Picchiri, G. (1994) Lung cancer mortality and airways obstruction among metal miners exposed to silica and low levels of radon daughters. Am J Indust Med 25:489-506.

Carta, P., Cocco, P. L., Casula, D. (1991) Mortality from lung cancer among Sardinian patients with silicosis. Brit J Indus Med 48:122-129.

Checkoway, H., Heyer, N.J., Demers, P.A., Breslow, N.E. (1992) A Cohort Mortality Study of Workers in the Diatomaceous Earth Industry—Report to Int'l Diatomite Producers Assoc, Univ Washington, School of Public Health and Community Medicine, Seattle, WA.

Checkoway, H., Heyer, N.J., Demers, P.A., Breslow, N.E. (1993) Mortality among workers in the diatomaceous earth industry. Brit J Indus Med 50:586-597.

Chen, J., McLaughlin, J.K., Zhang, J.-Y., Stone, B.J., Luo, J., Chen, R.-A., Dosemeci, M., Rexing, S.H., Wu, Z., Hearl, F.J., McCawley, M.A., Blot, W.J. (1992) Mortality among dust-exposed Chinese mine and pottery workers. J Occup Med 34:311-316.

Chen, S.Y., Hayes, R.B., Liang, S.R., Li, Q.G., Stewart, P.A., Blair, A. (1990) Mortality experience of haematite mine workers in China. Brit J Indus Med 47:175-181.

Cherniak, M. (1986) The Hawk's Nest Incident: America's Worst Industrial Disaster. New Haven, CT, Yale University Press.

Chia, S.-E., Chia, K.-S., Phoon, W.-H., Lee, H.-P. (1991) Silicosis and lung cancer among Chinese granite workers. Scand J Work Environ Health 17:170-174.

EBSCOhost - printed on 2/13/2023 4:48 AM via . All use subject to https://www.ebsco.com/terms-of-use

Chiyotani, K. (1984) Excess risk of lung cancer deaths in hospitalized pneumoconiotic patients. Proc 6th Int'l Conf on Pneumoconiosis, 1983. Bochum, Germany, Int'l Labor Organization. p 228-236.

Chiyotani, K., Saito, K., Okubo, T., Takahashi, K. (1990) Lung cancer risk among pneumoconiosis patients in Japan, with special reference to silicotics. In: Occupational Exposure to Silica and Cancer Risk. Simonato L, Fletcher AC, Saracci R, Thomas TL (eds) Int'l Agency for Research on Cancer (IARC), Lyon, France, p 95-104.

Collis, E.L. (1919) Industrial Pneumoconioses with Special Reference to Dust Phthisis. Milroy Lectures. His Majesty's Medical Inspectorate, London.

Costello, J. (1983) Mortality of metal miners-a retrospective cohort and case-control study. Health Issues Related to Metal and Nonmetal Mining. Wagner WL et al. (eds) Boston, Butterworth. p 226-240.

Costello, J., Graham, W.G.B. (1986) Vermont granite workers' mortality study. Silica, Silicosis, and Cancer: Controversy in Occupational Medicine. Goldsmith DF, Winn DM, Shy CM (eds) New York, Praeger, p 437-440.

Craighead, J.E. (chair) (1988) Silicosis and Silicate Disease Committee of NIOSH: Diseases associated with exposure to silica and nonfibrous silicate materials. Arch Path Lab Med 112:673-720.

Craighead, J.E., Vallyathan, N.V. (1980) Cryptic pulmonary lesions in workers occupationally exposed to dust containing silica. J Am Med Assoc 244:1939-1941.

Dagle, G.E., Wehner, A.P., Clark, M.L., Buschbom, R.L. (1986) Chronic inhalation exposure of rats to quartz. In: Silica, Silicosis, and Cancer: Controversy in Occupational Medicine. Goldsmith DF, Winn DM, Shy CM (eds) New York, Praeger. p 255-266.

Darby, S.H., Samet, J.M. (1994) Radon. Epidemiology of Lung Cancer. Samet JM (ed) New York, Marcel Dekker, p 219-243.

Davis, G.L. (1986) Pathogenesis of silicosis: current concepts and hypotheses. Lung 164:139-154.

Davis, L.K., Wegman, D.H., Monson, R.R., Froines, J. (1983) Mortality experience of Vermont granite workers. Am J Indust Med 4:705-723.

de Klerk, N.H., Musk, A.W., Tetlow, S., Hansen, J., Eccles, J.L. (1995) Lung cancer mortality in Western Australian goldminers exposed to silica. Scand J Work Environ Health, Proc 2nd Int'l Symp' of Silica, Silicosis, and Cancer (in press)

de Villiers, A.J., Windish, J.P. (1964) Lung cancer in a flourspar mining community. I. Radiation, dust and mortality experience. Brit J Indus Med 21: 94-109.

Decoufle, P., Wood, D.J. (1979) Mortality patterns among workers in a gray iron foundry. Am J Epidem 109:667-675.

Dible, J.H. (1934) Silicosis and malignant disease. Lancet ii: 982-983.

Dubrow, R., Wegman, D.H. (1984) Occupational Characteristics of Cancer Victims in Massachusetts: 1971-1973. U S Dept Health and Human Services, Public Health Service, Centers for Disease Control, Nat'l Inst Occupational Safety and Health, Div of Surveillance, Hazard Evaluations, and Field Studies.

Edling, C. (1982) Lung cancer and smoking in a group of iron ore miners. Am J Indust Med 3:191 -199.

Egan, E., Waxweiler, R.J., Blade, L., Wolfe, J., Wagoner, J.K. (1979) A preliminary report of mortality patterns among foundry workers. J Environ Path Toxic 2.

Egan-Baum, E., Miller, B.A., Waxweiler, R.J. (1981) Lung cancer and other mortality patterns among foundrymen. Scan J Work Environ Health 7 (Supp 4):147-155.

FASEB (Federation of American Societies for Experimental Biology) (1979) Evaluation of the Health Aspects of Certain Silicates as Food Ingredients. Federation of American Societies for Experimental Biology, Food and Drug Administration, Washington, DC

Finkelstein, M., Kusiak, R., Suranyi, G. (1982) Mortality among miners receiving workmen's compensation for silicosis in Ontario: 1940-1975. J Occup Med 24:663-667.

Finkelstein, M.M., Liss, G.M., Kramer, F., Kusiak, R.A. (1987) Mortality among surface-industry workers receiving Workers' Compensation awards for silicosis in Ontario: 1940-1984. Brit J Indus Med 44:588-594.

Fleming, D., Maynard, D., McKinney, B., Perotta, D.M., Schulze, L., Pichette, J. (1990) Silicosis: cluster in sandblasters—Texas and occupational surveillance for silicosis. Mortality and Morbidity Weekly Report 39:433-437.

Fletcher, A.C. (1986) The mortality of foundry workers in the United Kingdom. In: Silica, Silicosis, and Cancer: Controversy in Occupational Medicine. Goldsmith DF, Winn DM, Shy CM (eds) New York, Praeger. p 385-401.

Fletcher, A.C., Ades, A. (1984) Lung cancer mortality in a cohort of English foundry workers. Scandinavian Journal of Work Environment and Health 10:7-16.

Forastiere, F., Lagorio, S., Michelozzi, P., Cavariani, F., Arca, M., Borgia, P., Perucci, C., Axelson, O. (1986) Silica, silicosis and lung cancer among ceramic workers: a case-referent study. Am J Indust Med 10:363-370.

EBSCOhost - printed on 2/13/2023 4:48 AM via . All use subject to https://www.ebsco.com/terms-of-use

Forastiere, F., Lagorio, S., Michelozzi, P., Perucci, C.A., Axelson, O. (1989) Mortality patterns of silicotic subjects in the Latium region, Italy. Brit J Indus Med 46:877-880.

Fox, A.J., Goldblatt, P., Kinlen, L.J. (1981) A study of the mortality of Cornish tin miners. Brit J Indus Med 38:378-380.

Frazier, T.M., Sundin, D.S. (1986) Industrial demographics and populations at risk for silica exposures. In: Silica, Silicosis, and Cancer: Controversy in Occupational Medicine. Goldsmith DF, Winn DM, Shy CM (eds) New York, Praeger. p 3-9.

Fu, H., Gu, X., Jin, X., Yu, S., Wu, K., Guidotti, T.L. (1994) Lung cancer among tin miners in Southeast China: Silica exposure, silicosis, and cigarette smoking. Am J Indust Med (in press)

Gallagher, R.P., Threlfall, W.J. (1983) Cancer mortality in metal workers. Can Med Assoc J 129:1191-1194.

Gibson, E.S., Martin, R.H., Lockington, J.N. (1977) Lung cancer mortality in steel foundries. J Occup Med 19:807-812.

Gibson, E.S., McCalla, D.R., Kaiser-Farrell, C., Kerr, A.A., Lockington, J.N. (1986) Industrial mutagenicity testing: Assessing silica's role in lung cancer among foundry workers. In: Silica, Silicosis, and Cancer: Controversy in Occupational Medicine. Goldsmith DF, Winn DM, Shy CM (eds) New York, Praeger. p 167-176.

Gillam, J.D., Dement, J.M., Lemen, R.A., Wagoner, J.R., Archer, V.E., Blejer, H.P. (1976) Mortality patterns among hard rock gold mines exposed to an asbestiform mineral. New York Acad Sci 271:335-344.

Goldsmith, D.F. (1994) Silica exposure and pulmonary cancer.In: Epidemiology of Lung Cancer. Samet JM (ed) New York, Marcel Dekker, p 245-298.

Goldsmith, D.F., Beaumont, J.J., Lutzenhiser, S., Schenker, M.B. (1990) Silicosis and Lung Cancer: Preliminary Results from the California Silicosis Registry. Proceedings for the 7th Int'l Conf Pneumoconioses, 1988., Pittsburgh, U S Dept of Health and Human Services, DHHS (NIOSH) Publ. No. 90-108.

Goldsmith, D.F., Beaumont, J.J., Morrin, L.A., Schenker, M.B. (1993) Respiratory cancer and other chronic disease mortality among silicotics in California (submitted to Am J Indust Med) 2nd Int'l Symp on Silica, Silicosis, and Cancer, San Francisco, CA, Western Consortium for Public Health, Berkeley, CA

Goldsmith, D.F., Guidotti, T.L. (1986) Combined silica exposure and cigarette smoking: a possible synergistic effect. In: Silica, Silicosis, and Cancer: Controversy in Occupational Medicine. Goldsmith DF, Winn DM, Shy CM (eds) New York, Praeger. p 451-459.

Goldsmith, D.F., Guidotti, T.L., Johnston, D.R. (1982) Does occupational exposure to silica cause lung cancer? Am J Indust Med 3:423-440.

Goldsmith, D.F., Hesterberg, T.W., Rabovsky, J., Saffiotti, U., Spear, R.C., Wagner, G.R., Weeks, J. (eds) (1993) 2nd Int'l Symp Silica, Silicosis, and Cancer. Berkeley, CA, Western Consortium for Public Health.

Goldsmith, D.F., Winn, D.M., Shy, C.M. (eds) (1986) Silica, Silicosis, and Cancer: Controversy in Occupational Medicine. New York, Praeger.

Goldsmith, J.R., Goldsmith, D.F. (1993) Fiberglass or silica exposure and increased nephritis or end-stage renal disease (ESRD). Am J Indust Med 23:873-881.

Gudbergsson, H., Kurppa, K., Koskenin, H., Vasama, M. (1984) An association between silicosis and lung cancer. A register approach. Proc 6th Int'l Conf Pneumoconiosis, 1983. Bochum, Germany, Int'l Labor Organization, Geneva, p 212-216.

Guenel, P., Hojberg, G., Lynge, E. (1989) Cancer incidence among Danish stone workers. Scand J Work Environ Health 15:265-270.

Guralnick, L. (1963) Mortality by Occupation and Cause of Death Among Men 20 to 64 Years of Age: United States, 1950. U S Dept of Vital Statistics, Washington DC.

Guthrie, G.D.J., Heaney, P.J. (1995 in press) Mineralogical characteristics of the silica polymorphs in relation to their biological activities. Proc 2nd Int'l Symp Silica, Silicosis, and Cancer. Goldsmith, DF, Wagner GR, Saffiotti U, Rabovsky J, Leigh J (eds) Scand J Work Environ Health.

Heppleston, A.G. (1985) Silica, pneumoconiosis, and carcinoma of the lung. Am J Indust Med 7:285-294.

Heppleston, A.G. (1984) The disposal of inhaled particulate matter; a unifying hypothesis. American Journal of Pathology 42:119-135.

Hessel, P.A., Sluis-Cremer, G.K. (1986) Case-control study of lung cancer and silicosis. In: Silica, Silicosis, and Cancer: Controversy in Occupational Medicine. Goldsmith DF, Winn DM, Shy CM (eds) New York, Praeger. p 351-355.

Hessel, P.A., Sluis-Cremer, G.K., Hnizdo, E. (1990) Silica exposure, silicosis, and lung cancer: a necropsy study. Br. J Ind Med 47:4-9. Brit J Indus Med 47:4-9.

Higgins, I.T., Glassman, J.H., Oh, M.S., Cornell, R. (1983) Mortality of reserve mining company employees in relation to taconite dust exposure. Am J Epidem 118:710-719.

EBSCOhost - printed on 2/13/2023 4:48 AM via . All use subject to https://www.ebsco.com/terms-of-use

Hill, A.B. (1965) The environment and disease: Association or causation? Proc Royal Society of Medicine 58:295-300.

Hnizdo, E., Murray, J., Sluis-Cremer, G.K., Thomas, R.G. (1993) Correlation between radiological and pathological diagnosis of silicosis—an autopsy population based study. Am J Indust Med 24:478f.

Hnizdo, E., Sluis-Cremer, G.K. (1991) Silica exposures, silicosis, and lung cancer: a mortality study of South African gold miners. Brit J Indus Med 48:53-60.

Hnizdo, E., Sluis-Cremer, G.K. (1993) Risk of silicosis in a cohort of white South African gold miners. Am J Indust Med 24:447-457.

Holland, L.M., Gonzales, M., Wilson, J.S., Tillery, M.I. (1983) Pulmonary effects of shale dusts in experimental animals. In: Health Issues Related to Metal and Nonmetal Mining. Wagner WL, Rom WN, Merchant J.A (eds) Boston, Butterworth Publishers. 485-496.

Holland, L.M., Wilson, J.S., Tillery, M.I., Smith, D.M. (1986) Lung cancer in rats exposed to fibrogenic dusts. In: Silica, Silicosis, and Cancer: Controversy in Occupational Medicine. Goldsmith DF, Winn DM, Shy, CM (eds) New York, Praeger. p 267-279.

Hours, M., Fevotte, J., Danache, B., Ayzack, L., Pallen, C., Bergeret, A., Etard, J.F., Cardis, E., Fabry, J. (1991) Lung cancer and occupational risk: results of case-control study conducted in Lyon (France) 1984-1990 (abstract). 8th Int'l Symp on Epidemiology and Occupational Health, Paris, France, Int'l Comm Occupational and Environmental Health.

Hueper, W.C. (1966) Occupational and environmental cancers of the respiratory system. Recent Results in Cancer Research 3:1-159.

IARC (1987) Evaluation of the Carcinogenic Risk to Silica and Some Silicates, Monogr 43. Int'l Agency for Research on Cancer, Lyon, France.

IARC (1993) Monograph on the Evaluation of the Carcinogenic Risks to Humans. Beryllium, Cadmium, Mercury, and Exposures to Glass Manufacturing. Int'l Agency for Research on Cancer (IARC), Lyon France.

Industrial Disease Standards Panel (1994) Report to the Workers' Compensation Board on Lung Cancer in the Hardrock Mining Industry. Industrial Disease Standards Panel, Toronto, Ontario.

Industrial Disease Standards Panel (ISDP) (1992) Interim Report to the Workers Compensation Board (of Ontario) on Scleroderma. Industrial Disease Standards Panel, Toronto, Ontario.

Industrial Disease Standards Panel (ISDP) (1987) Report to the Workers' Compensation Board on the Ontario Gold Mining Industry. Ontario Ministry of Labour, Toronto, Ontario.

Infante-Rivard, C., Armstrong, B., Petitclerc, M., Cloutier, L.G., Theriault, G. (1989) Lung cancer mortality and silicosis in Quebec, 1930-85. Lancet ii:23-30.

International Labor Organization (ILO) (1980) Guidelines for the Use of the ILO Int'l Classification of Pneumoconiosis. Geneva, Int'l Labor Office.

Jones, R.N., Hughes, J.M., Hammad, Y.Y., Weill, H. (1986) Sandblasting and Silicosis. In: Silica, Silicosis, and Cancer: Controversy in Occupational Medicine. Goldsmith DF, Winn DM, Shy CM (eds) New York, Praeger. p 71-75.

Jorgensen, H.S. (1973) A study of mortality from lung cancer among miners in Kiruna 1950-1970. Scand J Work Environ Health 10:126-133.

Katsnelson, B.A., Mokronosova, K.A. (1979) Non-fibrous mineral dusts and malignant tumors. J Occup Med 21:15-20.

Kennaway, E.L., Kennaway, N.M. (1947) A further study of the incidence of cancer. British Journal of Cancer 1:260-298.

King, E.J., Stantial, H., Dolan, M. (1933) The biochemistry of silicic acid II: the presence of silica in tissues. Biochemistry Journal 27:1002-1006.

King, E.J., Stantial, H., Dolan, M. (1933) The biochemistry of silicic acid III: the excretion of administered silica. Biochemistry Journal 27:1008-1014.

Kjuss, H., Skjaerven, R., Langard, S., Lien, J.T., Aamodt, T. (1986) A case-referent study of lung cancer, occupational exposures, and smoking. Scand J Work Environ Health 12:193-202.

Koskela, R.-S., Hernberg, S., Karava, R., Jarvinen, E., Nurminen, M. (1976) A mortality study of foundry workers. Scand J Work Environ Health 2 (Supp 1):73-89.

Koskela, R.-S., Jarvinen, E., Kolari, P.J. (1984) Effect of cohort definition and follow-up length on occupational mortality rates. Scand J Work Environ Health 10:311-316.

Koskela, R.-S., Klockers, M., Jarvinen, E., Rossi, A., Kolari, P.J. (1990) Cancer mortality of granite workers 1940-1985. In: Occupational Exposure to Silica and Cancer Risk. Simonato L, Fletcher AC, Saracci R, Thomas TL (eds) Int'l Agency for Research on Cancer (IARC), Lyon, France, p 43-53.

Kurppa, K., Gudbergsson, H., Hannunkari, I., Koskinen, H., Hernberg, S., Koskela, R.-S., Ahlman, K. (1986) Lung cancer among silicotics in Finland. In: Silica, Silicosis, and Cancer: Controversy in Occupational Medicine. Goldsmith DF, Winn DM, Shy CM (eds) New York, Praeger. p 311-319.

Kurppa, K., Koskela, R.-S., Gudbergsson, H. (1982) Gastrointestinal cancer in workers exposed to quartz (letter). Lancet ii:150.

EBSCOhost - printed on 2/13/2023 4:48 AM via . All use subject to https://www.ebsco.com/terms-of-use

Kusiak, R.A., Ritchie, A.C., Springer, J., Muller, J. (1993) Mortality from stomach cancer in Ontario miners. Brit J Indus Med 50:117-126.

Kusiak, R.A., Springer, J.C., Ritchie, A.C., Muller, J. (1991) Carcinoma of the lung in Ontario gold miners: possible aetiological factors. Brit J Indus Med 48:808-817.

Lagorio, S., Forastiere, F., Michelozzi, P., Cavariani, F., Perucci, C.A., Axelson, O. (1990) A case-referent study on lung cancer mortality among ceramic workers. In: Occupational Exposure to Silica and Cancer Risk. Simonato L, Fletcher AC, Saracci R, Thomas TL (eds) Int'l Agency for Research on Cancer (IARC), Lyon, France, p 21-28.

Landrigan, P.J., Lewis, F.A., Cherniack, M.G., Catlett, L.R. (1986) Silicosis in a grey iron foundry. The persistence of an ancient disease. Scand J Work Environ Health 12:329-339.

Lanza, A.J., Childs, S.B. (1917) Miners consumption: a study of 433 cases of the disease among zinc miners in southwestern Missouri. U S Public Health Service, Washington DC, U S Gov't Printing Office.

Larsson, L.-G., Damber, L. (1982) Interaction between underground mining and smoking in the causation of lung cancer: A study of nonuranium miners in northern Sweden. Cancer Detection and Prevention 5:385-389.

Lawler, A.B., Mandel, J.S., Schuman, L.M., Lubin, J.H. (1985) A retrospective cohort mortality study of iron ore (hematite) miners in Minnesota. J Occup Med 27:507-517.

Lerer, T.J., Redmond, C.K., Breslin, P.P., Salvin, L., Rush, H.W. (1974) Long-term mortality study of steelworkers: VII. Mortality patterns among crane operators. J Occup Med 16:608-614.

Lynge, E., Kurppa, K., Kristofersen, L., Malker, H., Sauli, H. (1990) Occupational groups potentially exposed to silica dust: a comparative analysis of cancer mortality and incidence based on the Nordic occupational mortality and cancer incidence registers. In: Occupational Exposure to Silica and Cancer Risk. Simonato L, Fletcher AC, Saracci R, Thomas TL (eds) Int'l Agency for Research on Cancer (IARC), Lyon, France, p 7-20.

Mastrangelo, G., Zambon, P., Saia, B., Brega, M., Crepet, M. (1983) Exposure to silica and lung cancer: A case-referent study (abstract). Scand J Work Environ Health 9:70-71.

Mausner, J.S., Kramer, S. (1985) Epidemiology: An Introductory Text. Philadelphia, PA, W B Saunders Company.

McDonald, J.C. (1989) Silica, silicosis and lung cancer (editorial) 46. Brit J Indus Med 46:289-291.

McDonald, J.C., Gibbs, G.W., Liddell, F.D.K., McDonald, A.D. (1978) Mortality after long exposure to cummingtonite-grunerite. Am Rev Respiratory Dis 118:271-277.

McDowall, M. E. (1984) A mortality study of cement workers. Brit J Indus Med 41:179-182.

McLaughlin, J.K., Chen, J.-Q., Dosemecci, M., Chen, R.-A., Rexing, S.H., Zhien, W., Hearl, F.J., McCawley, M.A., Blot, W.J. (1992) A nested case-control study of lung cancer among silica exposed workers in China. Brit J Indus Med 49:167-171.

Mehnert, W.H., Staneczek, W., Mohner, M., Konwtzke, G., Muller, W., Ahlendorf, W., Beck, B., Winkelmann, R., Simonato, L. (1990) A mortality study of a cohort of slate quarry workers in the German Democratic Republic. In: Occupational Exposure to Silica and Cancer Risk. Simonato L, Fletcher AC, Saracci R, Thomas TL (eds) Int'l Agency for Research on Cancer (IARC), Lyon, France.

Meijers, J.M.M., Swaen, G.M.H., Volovics, A., Slagen, J.J.M., Van Vliet, K. (1990) Silica exposure and lung cancer in ceramic workers: A case-control study. Int'l J Epidem 19:19-25.

Merlo, F., Costantini, M., Reggiardo, G., Ceppi, M., Puntoni, R. (1991) Lung cancer risk among refractory brick workers exposed to crystalline silica: a retrospective cohort study. Epidemiology 2:299-305.

Merlo, F., Doria, M., Fontana, L., Ceppi, M., Chesi, E., Santi, L. (1990) Mortality from specific causes among silicotic subjects: a historical prospective study. In: Occupational Exposure to Silica and Cancer Risk. Simonato L, Fletcher AC, Saracci R, Thomas TL (eds) Int'l Agency for Research on Cancer (IARC), Lyon, France, p 105-111.

Milham, S.J. (1976) Occupational Mortality in Washington State, 1950-1971. U S Dept of Health, Education and Welfare, Public Health Service, Center for Disease Control, Nat'l Inst Occupational Safety and Health, Cincinnati, Ohio.

Milham, S.J. (1983) Occupational Mortality in Washington State 1950-1979. U S Dept of Health and Human Services, Public Health Service, Center for Disease Control, Nat'l Inst Occupational Safety and Health, Cincinnati, Ohio.

Miller, A.B., Scarpelli, D., Weiss, N.S. (1987) Report to the Workers' Compensation Board on the Ontario Gold Mining Industry of the Scientific Panel on Mortality from Cancer Among Ontario Gold Miners 1955-1977. Industrial Disease Standards Panel Ontario Ministry of Labour, Toronto.

Muhle, H., Takenaka, S., Mohr, U., Dasenbrock, C., Marmelstein, R. (1989) Lung tumor induction upon long-term low-level inhalation of crystalline silica. Am J Indust Med 15:343-346.

EBSCOhost - printed on 2/13/2023 4:48 AM via . All use subject to https://www.ebsco.com/terms-of-use

Muller, J., Wheeler, W.C., Gentleman, J.F., Suranyi, G., Kusiak, R.A. (1983) Study of mortality of Ontario miners 1955-1977 Part I. Ontario Ministry of Labour, Ontario Workers Compensation Board, Atomic Energy Control Board of Canada.

Neuberger, M., Kundi, M. (1990) Occupational dust exposure and cancer mortality—results of a prospective cohort study. In: Occupational Exposure to Silica and Cancer Risk. Simonato L, Fletcher AC, Saracci R, Thomas TL (eds) Int'l Agency for Research on Cancer (IARC), Lyon, France, p 65-73.

Neuberger, M., Kundi, M., Westphal, G., Grundorfer, W. (1986) The Viennese dusty worker study. In: Silica, Silicosis, and Cancer: Controversy in Occupational Medicine. Goldsmith DF, Winn DM, Shy CM (eds) New York, Praeger. p 415-422.

Ng, P.N., Chan, S.L., Lee, J. (1990) Mortality of a cohort of men in a silicosis register: further evidence of an association with lung cancer. Am J Indust Med 17:163-171.

Ng, T.P., Allan, W.G.L., Tsin, T.W., O'Kelly, F.J. (1985) Silicosis in jade workers. Brit J Indus Med 42:761-764.

Ng, T.P., O'Kelly, F.J. (1987) Silicosis prevalence in granite quary and construction workers in Hong Kong. J Hong Kong Medical Assoc 39:160-162.

Ng, T.P., Yeung, K.H., O'Kelly, F.J. (1987) Silica hazard of caisson construction on Hong Kong. J Soc Occupational Med 37:62-65.

NIOSH (1974) Criteria for a Recommended Standard—Occupational Exposure to Crystalline Silica. Department of Health Education and Welfare, National Institute for Occupational Safety and Health, Cincinnati, Ohio.

NIOSH (1991) Work-related diseases surveillance report. National Institute for Occupational Safety and Health, Centers for Disease Control, U.S. Department of Health and Human Services, Public Health Service, Cincinnati, Ohio.

NIOSH (1992) Alert: Request for Assistance in Preventing Silicosis and Deaths from Sandblasting. Nat'l Inst Occupational Safety and Health, Centers for Disease Control, U S Dept of Health and Human Services, Public Health Service, Cincinnati, Ohio.

Pairon, J.C., Brochard, P., Jaurand, M.C., Bignon, J. (1991) Silica and lung cancer: A controversial issue. Eur Respiratory J 4:730-744.

Paracelsus, T. (1567) Von der Bergsucht. Dilingen, Germany.

Peters, J.M. (1986) Silicosis. In: Occupational Respiratory Diseases. Merchant JA, Boehlecke BA, Taylor G, Pickett-Harner M. (eds) Washington, DC, U S Dept of Health and Human Services, Public Health Service, Center for Disease Control, National Inst Occupational Safety and Health, U S Gov' Printing Office. p 219-238.

Peterson, G.R., Milham, S.J. (1980) Occupational Mortality in the State of California 1959-61. Nat'l Inst Health, Nat'l Cancer Institute, U S Dept of Health and Human Services, Public Health Service, Center for Disease Control, Nat'l Inst Occupational Safety and Health, Cincinnati, Ohio.

Pratt, P.C. (1983) Lung dust content and response in guinea pigs inhaling three forms of silica. Arch Environ Health 38:197-204.

Proposition 65 (1988) Chemicals known to the State (of California) to cause cancer or reproductive toxicity. Scientific Advisory Board, Proposition 65, State of California Safe Drinking Water and Toxic Enforcement Act of 1986.

Puntoni, R., Goldsmith, D.F., Valerio, F., Vercelli, M., Bonassi, S., DiGiorgio, F., Ceppi, M., Stagnaro, E., Filiberti, R., Santi, L., Merlo, F. (1988) A cohort study of workers employed in refractory brick plant. Tumori 74:27-33.

Puntoni, R., Vercelli, M., Merlo, F., Valerio, F., Santi, L. (1979) Mortality among shipyard workers in Genoa, Italy. Ann New York Acad Sci 330:353-377.

Radford, E.P., St. Clair Renard, K.G. (1984) Lung cancer in Swedish iron miners exposed to low doses of radon daughters. 310, . New Engl J Med 310:1485-1494.

Raffle, P.A.B., Lee, W.R., McCallum, R.I., Murray, R. (1987) Hunter's Diseases of Occupations. Boston, Little, Brown & Company.

Ramazzini, B. (1700) De Morbis Artificum Diatriba. Padua, Italy, University of Chicago Press, Chicago, 1940.

Redmond, C.K. (1975) Comparative Cause-Specific Mortality Patterns by Work Area Within the Steel Industry. U S Dept Health, Education and Welfare, Public Health Service, Center for Disease Control, Nat'l Inst Occupational Safety and Health, Rockville, Maryland.

Redmond, C.K., Weiand, H.S., Rockette, H.E., Sass, R., Weinberg, G. (1981) Long-term Mortality Experience of Steelworkers. U S Department of Health and Human Services, Public Health Service, Center for Disease Control, Nat'l Inst Occupational Health, Cincinnati, Ohio.

Reuzel, P.G. J., Bruijntjes, J.P., Feron, V.J., Woutersen, R.A. (1991) Subchronic inhalation toxicity of amorphous silicas and quartz dust in rats. Food Chem Toxicol 29:341-354.

Rice, C.H., Harris, R.L., Checkoway, H., Symons, M.J. (1986) Dose-response relationships for silicosis from a case-controls study of North Carolina dusty trades workers. In: Silica, Silicosis, and Cancer:

EBSCOhost - printed on 2/13/2023 4:48 AM via . All use subject to https://www.ebsco.com/terms-of-use

Controversy in Occupational Medicine. Goldsmith DF, Winn DM, Shy CM (eds) New York, Praeger. p 77-86.

Rosenman, K.D., Stanbury, M.J., Reilly, M.J. (in press) Mortality among persons with silicosis reported to two state based disease surveillance systems. In: Proc 2nd Int"l Symp on Silica, Silicosis, and Cancer, Goldsmith DF et al. (eds) Scand J Work Environ Health.

Ross, M., Nolan, R.P., Langer, A.M., Cooper, W.C. (1993) Health effects of mineral dusts other than asbestos. In: Health Effects of Mineral Dusts. Guthrie, GD, Mossman BT (eds) Rev Mineralogy 28:362-407.

Roussel, J., Pernot, C., Shoumacher, P., Pernot, M., Kessler, Y. (1964) Consideration statistique sur le cancer brouchique des mineurs de fer du bassin de Lorraine. J Radiol Electr 45: 541-546.

Rubino, G.F., Scansetti, G., Coggiola, M., Pira, E., Piolatto, G., Coscia, G.C. (1985) Epidemiologic study of the mortality of a cohort of silicotics in Piedmont. Silice, Silicosi e Cancro Eds. Deutsch, E. I., Marcato, A. Padua, Univ Padua. 121-132.

Russell, A.E., Britten, R.H., Thompson, L.R., Bloomfield, J. (1929) The health of workers in dusty trades, II: exposure to siliceous dust (granite industry). U S Public Health Service, U S Treasury Dept, U S Gov't Printing Office, Washington, DC.

Saffiotti, U. (1986) The pathology induced by silica in relation to fibrogenesis and carcinogenesis. In: Silica, Silicosis, and Cancer: Controversy in Occupational Medicine Goldsmith DF, Winn DM, Shy CM (eds) New York, Praeger. 287-307.

Saffiotti, U. (1992) Lung cancer induction by crystalline silica. In:. Relevance of Animal Studies to the Evaluation of Human Cancer Risk. D'Amato R, Slaga TJ, Farland WH, Henry C (eds) New York, Wiley-Liss. p 51-69.

Saffiotti, U., Daniel, L.H., Mao, Y., Williams, A.o., Kaighn, M.E., Ahmed, N., Knapton, A.D. (1993) Biological studies on the carcinogenic mechanisms of quartz. In: Health Effects of Mineral Dusts. Guthrie, GD, Mossman BT (eds) Rev Mineralogy 28:523-544.

St Clair Renard, K.G. (1974) Respiratory cancer mortality in an iron ore in Northern Sweden. Ambio 2:67-69.

Sankila, R., Karjalainen, S., Pukkala, E., Oksanen, H., Hakulinen, T., Teppo, L., Hakama, M. (1990) Cancer risk among glass factory workers: an excess of lung cancer? Brit J Indus Med 47:815-818.

Schuler, G., Ruttner, J.R. (1986) Lung cancer and silicosis in Switzerland. In: Silica, Silicosis, and Cancer: Controversy in Occupational Medicine. Goldsmith DF, Winn DM, Shy CM (eds) New York, Praeger. p 357-366.

Seaton, A. (1984) Silicosis. Occupational Lung Diseases Eds. Morgan, W. K. C., Seaton, A. Philadelphia, PA, W. B. Saunders. second, ed. 250-294.

Selikoff, I.J. (1978) Carcinogenic potential of silica compounds. Biochemistry of Silicon and Related Problems Eds. Benz, G., Lindquist, I. New York, Plenum. 311-336.

Shannon, H., Heller, J.G., Pron, G., Gallina, P., MacRae, J. (1987) Report of the Special Panel on the Ontario Gold Mining Industry, Appendix A of Industrial Disease Standards Panel Report to the Workers Compensation Board on the Ontario Gold Mining Industry, Toronto. Ontario Ministry of Labour.

Sherson, D., Iversen, E. (1986) Mortality among foundry workers in Denmark due to cancer and respiratory and cardiovascular diseases. In: Silica, Silicosis, and Cancer: Controversy in Occupational Medicine. Goldsmith DF, Winn DM, Shy CM (eds) New York, Praeger. p 403-414.

Shoemaker, D.A., Pretty, J.R., Ramsey, D.M., McLaurin, J.L., Khan, A., Teass, A.W., Castranova, V., Pailes, W.H., Dala, N.S., Miles, P.R., Bowman, L., Leonard, S., Shumaker, J. Vallyathan, V., Pack, D. (in press) Genration of aerosols of freshly milled and aged α-quartz: Analysis of differences in particle activity and in vivo pulmonary response. In: Proc 2nd Int"l Symp on Silica, Silicosis, and Cancer, Goldsmith DF et al. (eds) Scand J Work Environ Health.

Siemiatycki, J., Gerin, M., Dewar, R., Lakhani, R., Begin, D., Richardson, L. (1990) Silica and cancer associations from a multicancer and occupational exposure case-referent study. In: Occupational Exposure to Silica and Cancer Risk. Simonato L, Fletcher AC, Saracci R, Thomas TL (eds) Int'l Agency for Research on Cancer (IARC), Lyon, France.

Siltanen, E., Koponen, M., Kokko, A., Engstrom, B., Reponen, J. (1976) Dust exposure in Finnish foundries. Scand J Work Environ Health 2 (Suppl 1):19-31.

Silverstein, M., Maizlish, N., Park, R., Silverstein, B., Broadsky, L., Mirer, F. (1986) Mortality among ferrous foundry workers. Am J Indust Med 10:27-43.

Simonato, L., Fletcher, A. C., Saracci, R., Thomas, T.L. (eds) (1990) Occupational Exposure to Silica and Cancer Risk. Int'l Agency for Research on Cancer (IARC), Lyon, France, p

Singleton, J.A., Beaumont, J.J. (1989) COMS I California Occupational Mortality, 1979-1981 Adjusted for Smoking, Alcohol, and Socioeconomic Status. December 21. Health Demographics Section, Health Data and Statistics Branch, California Dept of Health Services, Sacramento.

EBSCOhost - printed on 2/13/2023 4:48 AM via . All use subject to https://www.ebsco.com/terms-of-use

Spietoff, A., Wesch, H., Wegener, K., Klimisch, H. (1992) The effects of thoratrast and quartz on the induction of lung tumors in rats. Health Physics 63:101-110.

Steenland, K., Beaumont, J. (1986) A proportionate mortality study of granite cutters. Am J Indust Med 9:189-201.

Steenland, K., Brown, D.P. (in press) Mortality study of goldminers exposed to silica and nonasbestiform amphibole minerals: an update. Am J Indust Med 25.

Steenland, K., Goldsmith, D.F. (1994) Silica exposure and auto-immune diseases. Submitted to Lancet.

Steenland, K., Nowlin, S., Ryan, B. (1992) Use of multiple cause mortality data in epidemiologic analyses. Am J Epidem 136:855-862.

Theriault, G., Burgess, W.A., DiBerardinis, L.J., Peters, J.M. (1974) Dust exposure of the Vermont granite sheds. Arch Environ Health 28:12-17.

Theriault, G.P., Peters, J.M. (1974) Pulmonary function and roetgenographic changes in granite dust exposure. Arch Environ Health 28: 23-27.

Theriault, G.P., Peters, J.M., Fine, L.J. (1974) Pulmonary function in granite shed workers in Vermont. Arch Environ Health 28:18-22.

Thomas, T.L. (1982) A preliminary investigation of mortality among workers in the pottery industry. Int'l J Epidem 11:175-180.

Thomas, T.L. (1990) Lung cancer mortality among pottery workers in the United States. In: Occupational Exposure to Silica and Cancer Risk. Simonato L, Fletcher AC, Saracci R, Thomas TL (eds) Int'l Agency for Research on Cancer (IARC), Lyon, France, p 75-81.

Thomas, T.L., Stewart, P.A. (1987) Mortality from lung cancer and respiratory disease among pottery workers exposed to silica and talc. Am J Epidem 125:35-43.

Tola, S., Koskela, R.-S., Hernberg, S., Jarvinen, E. (1979) Lung cancer mortality among iron foundry workers. J Occup Med 21:753-760.

Tornling, G., Hogstedt, C., Westerholm, P. (1990) Lung cancer indicence among Swedish ceramic workers with silicosis. In: Occupational Exposure to Silica and Cancer Risk. Simonato L, Fletcher AC, Saracci R, Thomas TL (eds) Int'l Agency for Research on Cancer (IARC), Lyon, France, p 113-119.

U.S. Department of Health and Human Services (1986) The Health Consequences of Smoking: Cancer and Chronic Lung Disease in the Workplace—A report of the Surgeon General. Office on Smoking and Health, Public Health Service, Rockville, Maryland.

U.S. Department of Health Education and Welfare (1963) Silicosis in the metal mining industry: a re-evaluation, 1958-1961. U.S. Public Health Service, Washington DC.

U.S. Department of Labor Occupational Safety and Health Administration (1989) Air Contaminants, Final Rule. Federal Register.

U.S. Environmental Protection Agency (1986) Guidelines for carcinogen risk assessment. Federal Register 51:33992-34003.

Wagner, M.M.F., Wagner, J.C., Davies, R., Griffiths, D.M. (1980) Silica-induced malignant histiocytic lymphoma: incidence linked with strain of rat and type of silica. Brit J Cancer 41:908-917.

Wagoner, J.K., Miller, R.W., Lundin, F.E., Fraumeni, J.F. Jr., Haij, M.E. (1963) Unusual cancer mortality among a group of underground metal miners. New England J Med 269:284-289.

Warheit, D.B. (1992) The importance of deposition and clearance to risk assessment research. The Emerging Risk Assessments for Crystalline Silica, Monterey, CA, Western Consortium for Public Health, Berkeley, CA.

Weisenfeld, S.L., Perotta, D.M., Abraham, J.L. (1993) Epidemic of accelerated silicosis in West Texas sandblasters. 2nd Int'l Symp on Silica, Silicosis, and Cancer, San Francisco, CA, Western Consortium for Public Health, Berkeley, CA

Westerholm, P. (1980) Silicosis—observation on a case register. Scand J Work Environ Health 6 (suppl 2):1-86.

Westerholm, P., Ahlmark, A., Maasing, R., Segelberg, I. (1986) Silicosis and lung cancer—a cohort study. In: Silica, Silicosis, and Cancer: Controversy in Occupational Medicine. Goldsmith DF, Winn DM, Shy CM (eds) New York, Praeger. p 327-333.

Williams, R.R., Stegens, N.L., Goldsmith, J.R. (1977) Associations of cancer site and type with occupation and industry from the Third National Cancer Survey interview. J Nat'l Cancer Inst 59:1147-1185.

Winter, P.D., Gardner, M.J., Fletcher, A.C., Jones, R.D. (1990) A mortality follow-up study of pottery workers: Prelimary findings on lung cancer. In: Occupational Exposure to Silica and Cancer Risk. Simonato L, Fletcher AC, Saracci R, Thomas TL (eds) Int'l Agency for Research on Cancer (IARC), Lyon, France, p 83-94.

Wyndham, C.H., Bezuidenhout, B.N., Greenacre, M.J., Sluis-Cremer, G.K. (1986) Mortality of middle aged white South African gold miners. Brit J Indus Med 43:677-684.

EBSCOhost - printed on 2/13/2023 4:48 AM via . All use subject to https://www.ebsco.com/terms-of-use

Zambon, P., Simonato, L., Mastrangelo, G., Winkelmann, R., Saia, B., Crepet, M. (1987) A mortality study of workers compensated for silicosis during 1959 to 1963 in the Veneto region of Italy. Scand J Work Environ Health 13:118-123.

Ziskind, M., Jones, R.N., Weill, H. (1976) Silicosis—State of the art review. Am Rev Respiratory Dis 113: 643-665.

EBSCOhost - printed on 2/13/2023 4:48 AM via . All use subject to https://www.ebsco.com/terms-of-use